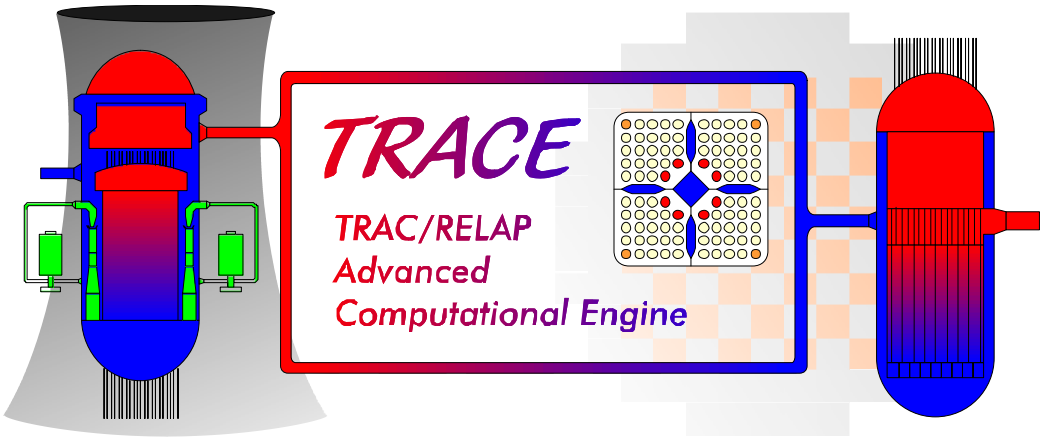

TRACE V5.0
ASSESSMENT MANUAL

Appendix B: Separate Effects Tests

Division of Risk Assessment and Special Projects
Office of Nuclear Regulatory Research
U. S. Nuclear Regulatory Commission
Washington, DC 20555-0001

This page intentionally left blank

Break Flow Tests

B.1. Marviken Full Scale Critical Flow Experiments

Author(s): Justin K. Watson, William J. Krotiuk

Affiliation: PennState ARL, NRC

Code Version: TRACE V5.0

Platform and Operating System: Intel x86, Windows XP

B.1.1. Introduction

The calculation of critical flow is an important consideration in the area of nuclear reactor safety. The fluid velocity at nozzles, breaks, or other restrictions can exceed the local sound speed which causes the fluid flow rate to become insensitive to downstream pressure changes. Of particular importance are choking conditions at pipe break locations where fluid at high pressure-temperature conditions is subjected to large decreases in pressure. In order to account for fluid choking effects, the TRACE computer code employs a one-dimensional critical flow model. The TRACE critical flow model comprises of three separate models; a subcooled liquid choked-flow model, a two-phase, two-component choked-flow model, and a single-phase vapor choked-flow model.

The subcooled liquid choked-flow model is based on the Burnell model. The subcooled liquid choked-flow model is used where subcooled liquid persists through the choking plane. The two-phase, two-component choked-flow model is based on first principles and calculates flow limitations for a two-phase fluid which can consist of two different fluids such as water and an inert-gas such as air. Finally, the single-phase vapor choked-flow model is based on the theory describing an isentropic expansion of an ideal-gas. The choking models employed by TRACE are more fully described in the TRACE Theory Manual (Ref. 1).

The Marviken full-scale critical-flow experiments were designed to simulate pressure-vessel blowdown. These experiments provide experimental data for subcooled and two-phase water critical-flows exiting a simulated break from a tank pressurized to about 5-MPa. Flow exited from a pipe test section attached to the bottom of the tank. The TRACE computer code was used to predict critical flow conditions for six tests at the Marviken facility. Five of the analyzed tests had approximately a 0.5-m exiting pipe diameter; the remaining test had a 0.2-m exit pipe diameter. The lengths of the test sections varied from 0.391-m to 1.99-m for the exit pipe with the 0.5-m diameter. The length of the exit pipe with a 0.2-m diameter was 0.69-m. These conditions and geometries are typical of a full scale nuclear reactor. The critical-flow tests were performed at the Marviken Power Station, located in Sweden, which was originally built for use as a boiling

heavy-water, direct cycle nuclear reactor. However, nuclear fuel was never loaded in the reactor, and the facility was used to perform full-scale safety experiments.

B.1.2. Test Facility Description

The Marviken test facility has four main components; a pressure vessel, a discharge pipe, a test nozzle, and a rupture disk. A number of different test nozzle-rupture disk assemblies were used during testing. The diameter and length of the nozzle-rupture disk assembly were varied for different tests in order to simulate different design and operating conditions. The pressure vessel and discharge pipe are shown in Figure B.1-1. and Figure B.1-2.. The pressure vessel, which was originally intended to be a reactor pressure vessel, includes part of the core superstructure and three gratings to limit vortex formation.

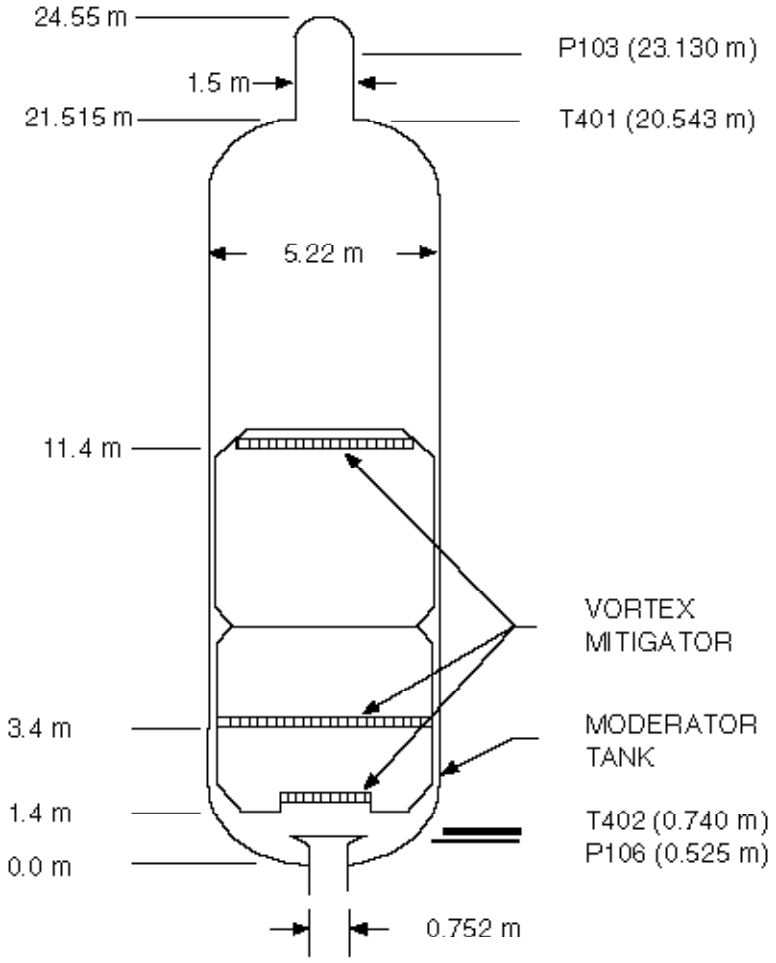

Figure B.1-1. Marviken Pressure Vessel

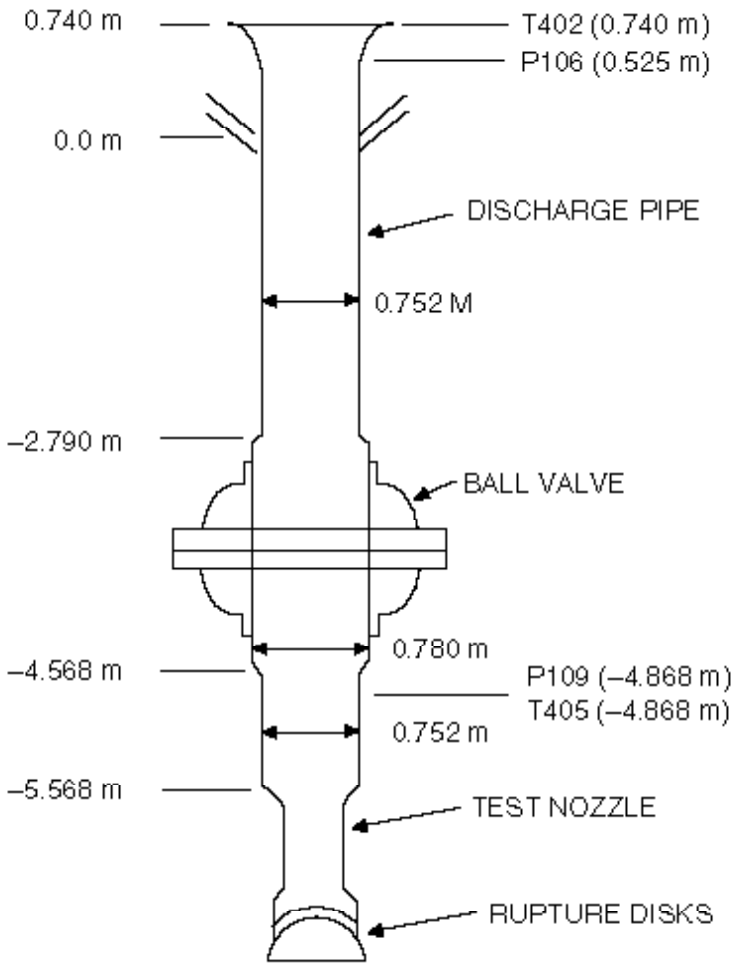

Figure B.1-2. Marviken Discharge Pipe and Test Nozzle

For each experiment the vessel is partially filled with deionized water. The water is taken from the bottom of the vessel, heated and then returned to the to the top of the pressure vessel. Consequently, complex temperature distributions can be produced. The pressure in the upper vessel vapor space is maintained about 5-MPa. After the desired initial conditions are achieved, the test is initiated by rupturing the disk at the end of the test nozzle allowing flow to enter the containment environment which is at atmospheric conditions. Because of the large pressure drop from the test nozzle to the containment pressure, the flow exiting the test nozzle is expected to choke. The test is completed when either the valve in the discharge line is closed at a specific time, or vapor flow is detected in the discharge pipe. If vapor flow is detected, valve closure is started immediately after detection.

Pressure and temperature measurements were taken at a number of locations in the test assembly. Figure B.1-1. and Figure B.1-2. indicate the pressure and temperature measurement locations which will be compared against computer code predictions. The break flow was measured by

pitot-static pressure measurements near the discharge pipe entrance. These readings were augmented with density measurements provided by a gamma densitometer and/or temperature measurements. The probable measurement errors are ±9 kPa for the absolute pressure measurements, ±0.6 C for the temperature measurements, and ±3- to 10-percent and ±8- to 15-percent for subcooled and saturated two-phase flows determined by the pitot-static method. However, the maximum pressure measurement error is ±90 kPa for the absolute pressure measurements, and ±2 C for the temperature measurements.

B.1.3. TRACE Model Description

The TRACE model for all six Marviken tests include 4 components. A zero velocity FILL component is used a the top of the pressure vessel as a boundary condition. A TEE component is used to represent the pressure vessel. The main leg of the TEE is used to model the pressure vessel, discharge pipe, test nozzle and rupture disk assembly. The side leg of the TEE is used to model the volume at the bottom of the vessel which lies below the entrance to the discharge pipe. A zero velocity FILL is used as the side-leg boundary condition. A BREAK is used as the pressure boundary condition at the rupture disk. The TRACE nodalization diagram for Marviken Test 4 is on Figure B.1-3. All test cases run in this analysis utilize the same nodalization diagram except for cell 47 of the TEE component. This cell represents the test nozzle and rupture disk assembly, which changes for each of the tests. Table B.1.1 summarizes the computer code inputs used to model the six Marviken critical flow tests. The default values for any multipliers to the choked-flow model calculations were used during the execution of the computer code. The initial temperature profile and water level indicated on Table B.1.2 was used as the starting input condition for each computer code model before the transient calculations. Table B.1.2 lists the initial pretest mass determined from test data and calculated using the water property tables included in each computer code.

B.1.4. Tests Simulated with TRACE

A series of 27 critical flow tests were performed at the Marviken facility. These tests were performed with different test nozzles and with different initial pressure vessel temperature distributions. All testing was performed at a pressure of about 5-MPa. Table B.1.2 shows the characteristics of the six tests that have been chosen for comparison with computer code predictions. As indicated in Table B.1.2, the initial temperature distribution in the vessel is described by three categories. The Category I profile has the upper part of the vessel liquid higher in temperature than the lower part. The Category II profile attempts to maintain a constant temperature in the vessel liquid region. The Category III low subcooling profile attempts to maintain a constant temperature in the vessel liquid region. Figure B.1-4. specifically plots the initial temperature distribution for the analyzed tests.

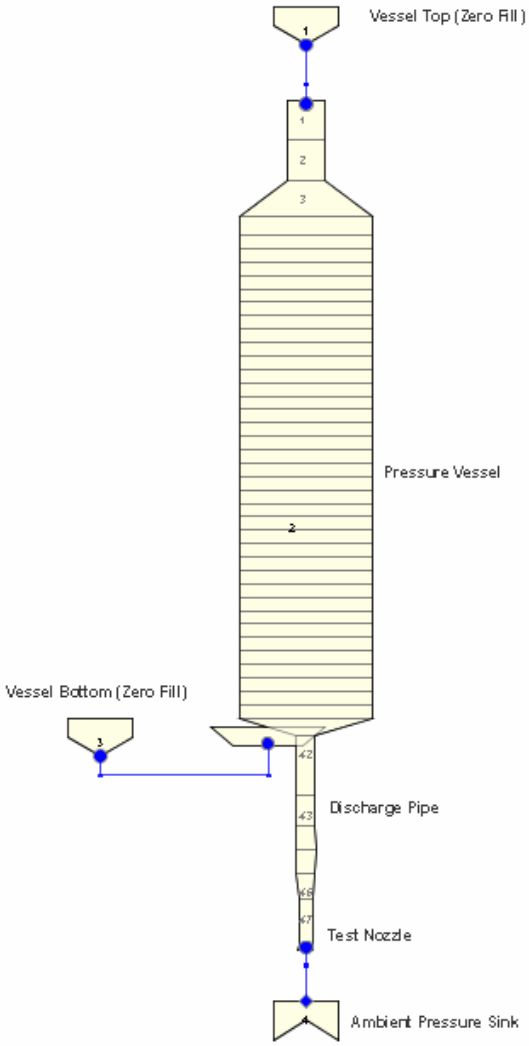

Figure B.1-3. Marviken TRACE Computer Code Model

Table B.1.1. Marviken Vessel and Discharge Line Geometry Model Input

Volume Number	Volume Length (m)	Volume Flow Area (m2)	Volume (m3)	Juncton Flow Area (m2)	Junction Irreversible Loss Coef.	Hydraulic Diameter (m)
Pressure Vessel						
				1.76175		1.5
2001	1.5	1.76175	2.6507			1.5
				1.76175		1.5

Table B.1.1. Marviken Vessel and Discharge Line Geometry Model Input

Volume Number	Volume Length (m)	Volume Flow Area (m2)	Volume (m3)	Juncton Flow Area (m2)	Junction Irreversible Loss Coef.	Hydraulic Diameter (m)
2002	1.535	1.76175	2.7126			1.5
				1.76175	0.8417	1.5
2003	1.4	Varies	9.5604			Varies
				21.4008		5.22
2004	0.715	21.4008	15.3016			5.22
				21.4008		5.22
2005	0.5	21.4008	10.7004			5.22
				21.4008		
2006 to 2039 repeat 2005 and its following junction.						
2040	0.5	21.4008	10.7004			5.22
				21.4008		5.22
2041	0.66	Varies	5.3538			Varies
				15.6930		4.47
2049	0.74	Varies	4.2066			Varies
Discharge Pipe						
				0.44415	0.0294	0.752
2042	2.3533	0.44415	1.0452			0.752
				0.44415		0.752
2043	1.1767	0.44415	0.5226			0.752
				0.44415	0.00497	0.752
2044	0.889	0.47784	0.4248			0.78
				0.47784		0.78
2045	0.889	0.47784	0.4248			0.78
				0.44415	0.03525	0.752
2046	1.0	0.44415	0.44415			0.752
Test Nozzle for Test 4						
				0.2035	0.01626	0.509
2047	1.745	0.2035	0.3994			0.509
				0.2035	0.0909	0.509
2048	0.175	0.2913	0.04856			0.609
				0.2913	1.0	0.609
Test Nozzle for Test 13						
				0.031416	0.02788	0.200
2047	0.690	0.031416	0.02639			0.200

Table B.1.1. Marviken Vessel and Discharge Line Geometry Model Input

Volume Number	Volume Length (m)	Volume Flow Area (m2)	Volume (m3)	Juncton Flow Area (m2)	Junction Irreversible Loss Coef.	Hydraulic Diameter (m)
				0.031416	0.5625	0.200
2048	0.120	0.12566	0.01508			0.400
				0.12566	1.0	0.400
Test Nozzle for Test 15						
				0.2035	0.01626	0.509
2047	1.990	0.2035	0.47776			0.509
				0.19635	1.0	0.500
Test Nozzle for Tests 20 and 22						
				0.2035	0.01626	0.509
2047	0.955	0.2035	0.2614			0.509
				0.19635	1.0	0.500
Test Nozzle for Test 24						
				0.19635	0.01674	0.500
2047	0.391	0.19635	0.14304			0.500
				0.19635	1.0	0.500

Table B.1.2. Marviken Tests Used for Critical Flow Assessments

Marviken Test	4	13	15	20	22	24
Initial Pressure in Vessel Steam Dome	4.94 MPa	5.09 MPa	5.04 MPa	4.99 MPa	4.93 MPa	4.96 MPa
Lover Vessel Initial Nominal Subcooling (relative to steam dome saturation temperature)	37 ^{o}C	31 ^{o}C	31 ^{o}C	7 ^{o}C	52 ^{o}C	33 ^{o}C
Initial Minimum Vessel Temperature	224 ^{o}C	236 ^{o}C	233 ^{o}C	257 ^{o}C	211 ^{o}C	230 ^{o}C
Initial Vessel Water Level Elevation	17.59 m	17.52 m	19.93 m	16.65 m	19.69 m	19.93 m
Category for Vessel Initial Temperature Profile[a]	I	I	II	III	II	II
Initial System Mass[b] Calculated by TRACE	2.86×10^{5} kg 2.94×10^{5} kg	2.82×10^{5} kg 2.85×10^{5} kg	3.27×10^{5} kg 3.33×10^{5} kg	2.67×10^{5} kg 2.69×10^{5} kg	3.34×10^{5} kg 3.39×10^{5} kg	3.30×10^{5} kg 3.36×10^{5} kg
System Volume	428.3 m^3	427.9 m^3	428.3 m^3	428.1 m^3	428.1 m^3	428.0 m^3

Table B.1.2. Marviken Tests Used for Critical Flow Assessments

Marviken Test	**4**	**13**	**15**	**20**	**22**	**24**
Test Nozzle Diameter	0.509 m	0.200 m	0.509 - 0.500 m	0.509 - 0.500 m	0.509 - 0.500 m	0.500 m
Test Nozzle Length (includes test nozzle entrance length)	1.745 m	0.690 m	1.99 m	0.955 m	0.955 m	0.391 m
Test Nozzle L/D (includes test nozzle entrance length	3.43	3.45	3.91	1.88	1.88	0.78
Test Duration (when steam enters discharge pipe or ball valve begins to close)	49 sec. (steam flow & start of valve closure)	148 sec. (start of valve closure)	55 sec. (Steam flow & start of valve closure)	58 sec. (Steam flow & start of valve closure)	48 sec. (Steam flow & start of valve closure)	54/55 sec. (Steam flow / start of valve closure)
Expected Choked-Flow Condition at Rupture Disk	1. Initial - Subcooled 2. Primary - Two-Phase	1. Initial - Subcooled 2. Final - Two-Phase	1. Initial - Subcooled 2. Final - Two-Phase	1. Initial - Subcooled 2. Primary - Two-Phase	1. Primary - Subcooled 2. Final - Two-Phase	1. Initial - Subcooled 2. Final - Two-Phase

a. The Category I profile has the upper part of the vessel liquid higher in temperature that the lower part. The Category II profile attempts to maintain a constant temperature in the vessel liquid region. The Category III low subcooling profile attempts to maintain a constant temperature in the vessel liquid region.

b. Value obtained from Reference 2.

B.1.4.1. Simulation of Marviken Test 4.

Marviken Test 4 is a category I test. The lower part of the vessel is subcooled liquid, and the upper liquid part of the vessel is elevated in temperature and close to saturation temperature. The initial water level before the start of the test is at elevation 17.50 m. The fluid above this elevation is a saturated vapor. After rupture of the disk in the test nozzle, the flow initially is subcooled flashing liquid. However, the exiting flow transitions, relatively rapidly, to two-phase water flow as the vessel pressure drops and the warmer liquid reaches the exiting flow location at the rupture disk. Consequently, the exiting flow is initially determined using the subcooled liquid choking model, and the two-phase choked-flow model determines exiting flowrate in the later stage of the test.

Figure B.1-5. shows flowrate comparisons between test data and predictions from TRACE. During the early part of the test when subcooled liquid flashing choked-flow is present at the exit flow location TRACE's flowrate predictions agree well with test data, and are within the measurement uncertainty. During the later part of the test when the exiting flow is two-phase, TRACE predicts flowrates close to data and within the measurement uncertainty. The TRACE, computer code successfully predicts the time when vapor flow enters the test nozzle.

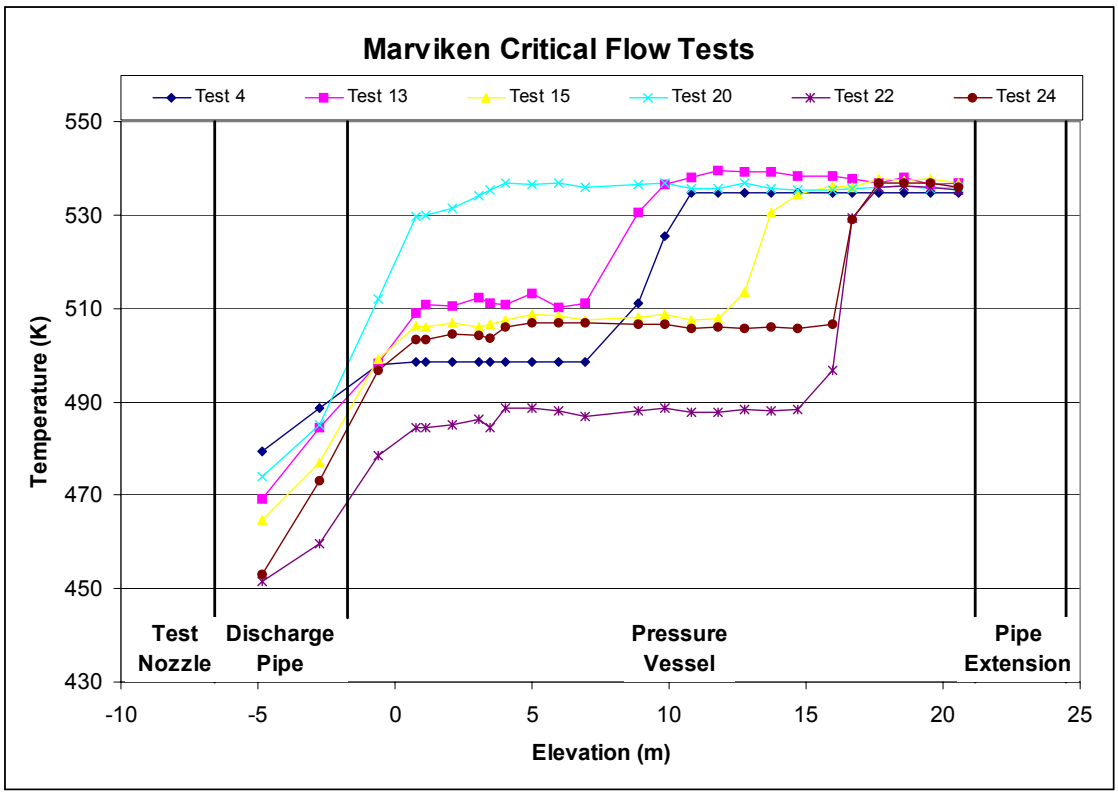

Figure B.1-4. Initial Temperature Distribution for the Analyzed Marviken Critical Flow Tests

It should also be noted that TRACE predicts unrealistic, small peaks in flowrate, between 50- and 54-seconds, after steam flow is predicted to exist in the test nozzle. The reasons for this anomaly should be determined and appropriate corrections must be implemented in TRACE.

Figure B.1-6., Figure B.1-7. and Figure B.1-8. compare pressure measurements with computer code predictions in the upper vessel space, the lower vessel at the discharge pipe entrance and the discharge pipe. The TRACE pressure predictions in the upper and lower vessel agree well with measurements. In the discharge pipe TRACE computer code predictions are close to measurements during the early period with subcooled flashing exit flow. TRACE predicted pressures approach measurements during the later period with two-phase exit flow. The three pressure measurements exhibit an initial drop in pressure immediately following the disk rupture in the test nozzle. This initial drop in pressure is due to delayed nucleation and subsequent flashing at the start of testing (Ref. 3). The models in the TRACE computer code assume that nucleation occurs immediately when the thermodynamic conditions are reached and consequently fail to calculate the initial pressure drop.

Figure B.1-9., Figure B.1-10. and Figure B.1-11. provide comparisons of temperature predictions and measurements. Figure B.1-9. provides temperature comparisons in the upper vapor space. TRACE predictions are almost identical to test measurements for the major portion of the transient. The test data exhibits a drop in temperature during the first seconds of the transient. As

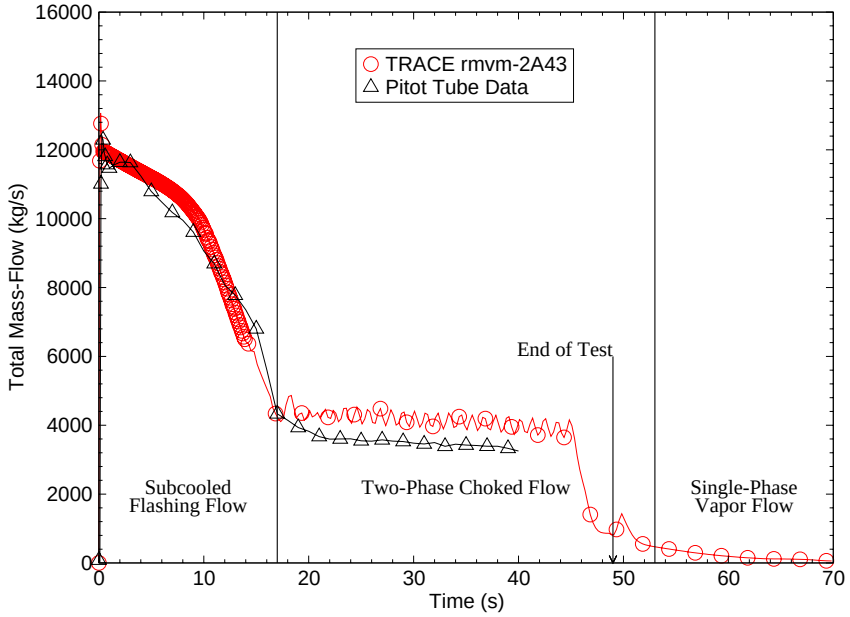

Figure B.1-5. Measured and Calculated Break Flows for Marviken Test 4

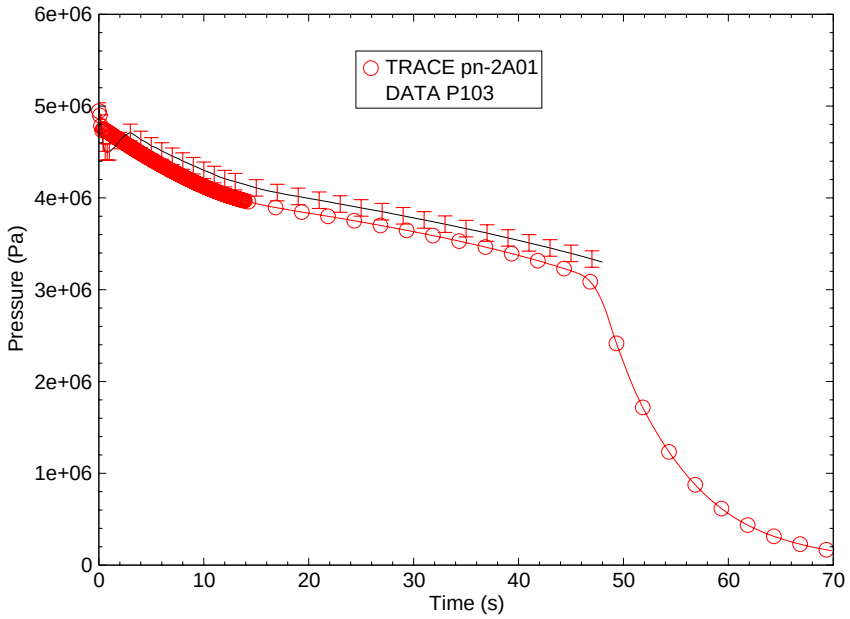

Figure B.1-6. Measured and Calculated Upper Vessel Pressures for Marviken Test 4

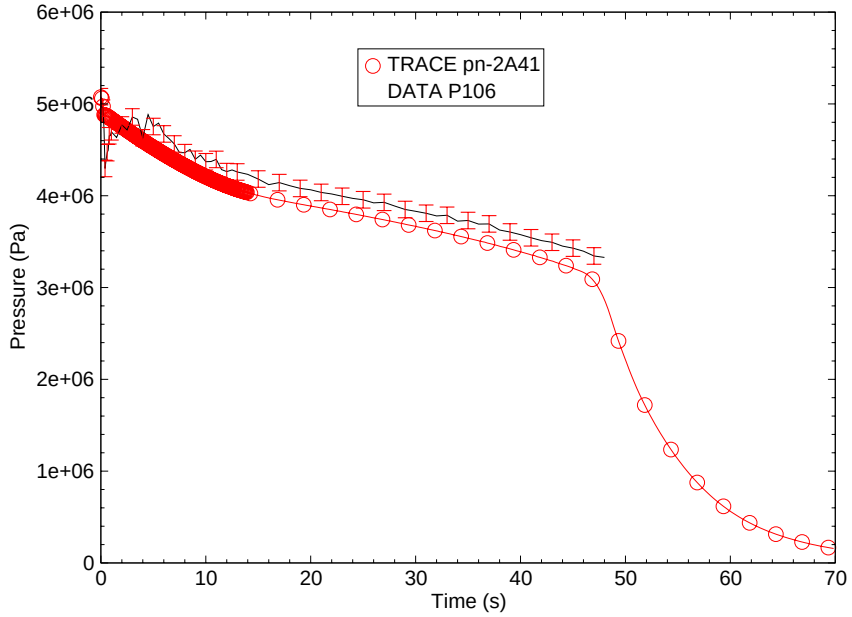

Figure B.1-7. Measured and Calculated Lower Vessel Pressures for Marviken Test 4

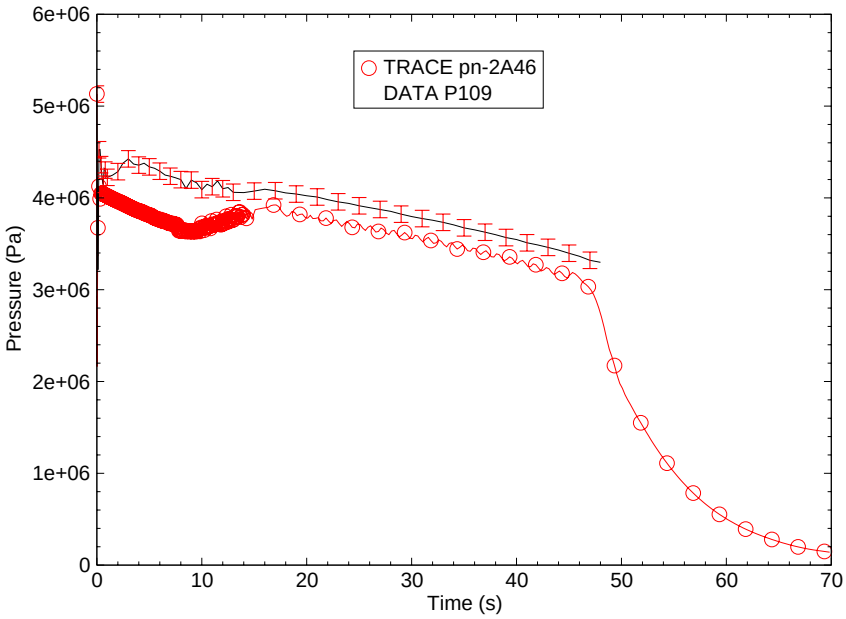

Figure B.1-8. Measured and Calculated Discharge Pipe Pressures for Marviken Test 4

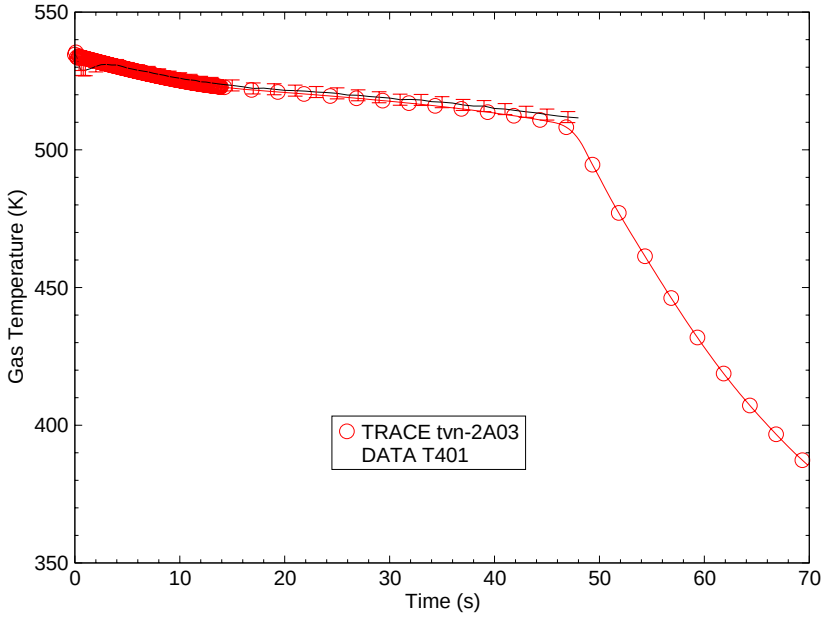

Figure B.1-9. Measured and Calculated Upper Vessel Temperatures for Marviken Test 4

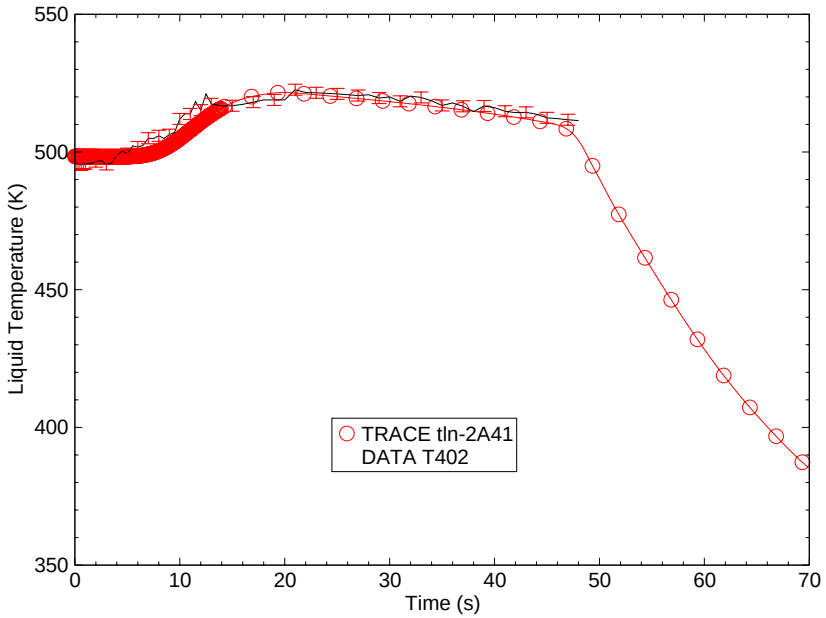

Figure B.1-10. Measured and Calculated Lower Vessel Temperatures for Marviken Test 4

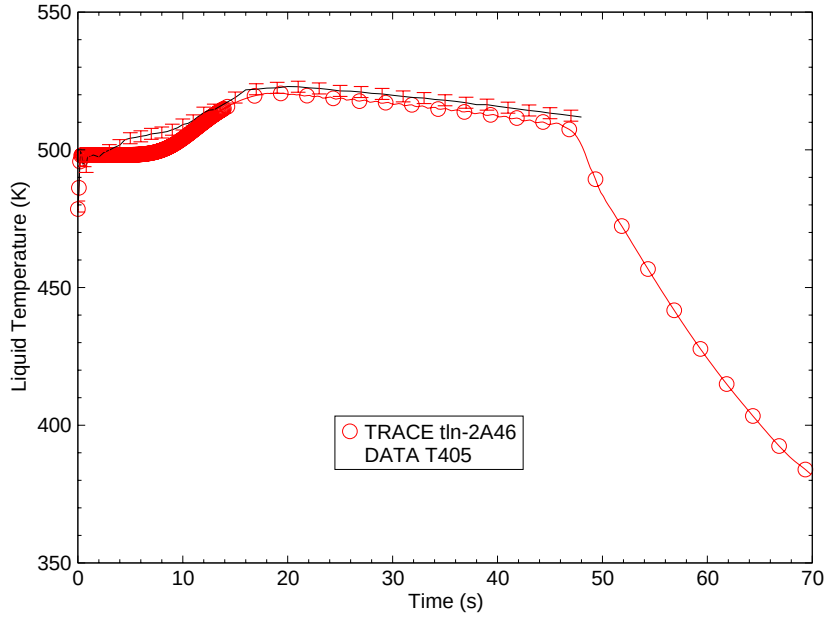

Figure B.1-11. Measured and Calculated Discharge Pipe Temperatures for Marviken Test 4

indicated in previous discussions regarding pressure, the temperature drop is caused by delayed nucleation at the start of the experiment.

The liquid temperature comparisons at the vessel bottom and in the discharge line are shown in Figure B.1-10. and Figure B.1-11.. The TRACE liquid temperature predictions at these locations are very close to measurements throughout the transient.

B.1.4.2. Simulation of Marviken Test 13.

As indicated in Table B.1.2 and Figure B.1-4., Test 13 is a category I test where the initial lower vessel temperature is lower than the upper vessel temperature. Consequently, the liquid on the lower part of the vessel is initially subcooled, whereas the initial upper vessel liquid temperature is at or close to saturation conditions. Therefore, immediately after the rupture of the disk in the test nozzle, the flow exiting the test nozzle is a subcooled flashing liquid. As the transient progresses, the vessel pressure drops and the initially higher temperature fluid at the top of the vessel reaches the exiting flow location at the rupture disk. At this time the flow in the test nozzle is two-phase, one-component water. Therefore, the choked-flow at the beginning of the transient is calculated using the subcooled liquid choking model, and the two-phase choked-flow model is used for the later stage of the transient.

As indicated on Table B.1.2, Test 13 has a test nozzle diameter of 0.2-m whereas all the other tests have test nozzle diameters about 0.5-m. Therefore, this test has the smallest exiting flowrate of the considered tests and, consequently, the longest test duration.

Figure B.1-12. provides a comparison of the calculated and measured break flows for the Marviken Test 13. During the early part of the transient when the exiting flow is determined using the subcooled flashing model, TRACE predicts flowrates within the uncertainty of the test data. During the later part of the transient when the exiting flow is two-phase, TRACE underpredicts the choked flowrate. The presence of nonequilibrium conditions in the short test nozzle during the two-phase saturated flow period explains the inability of TRACE to more accurately predict the two-phase choked-flow condition. The TRACE two-phase critical flow model assumes the presence of thermal equilibrium between phases (Ref. 3).

Figure B.1-13., Figure B.1-14. and Figure B.1-15. present comparisons of pressure measurements and predictions in the upper vessel vapor space, in the lower vessel at the entrance to the discharge pipe, and in the discharge pipe. The TRACE pressure predictions are close to data measurements and are within uncertainty bounds for most of the first part of the transient. The three pressure measurements exhibit an initial drop in pressure immediately following the disk rupture in the test nozzle. This initial drop in pressure is due to delayed nucleation and subsequent flashing at the start of testing (Ref. 3). The models in the TRACE computer code assume that nucleation occurs immediately when the thermodynamic conditions are reached and consequently fail to calculate the initial pressure drop.

Temperature measurements and predictions are plotted on Figure B.1-16., Figure B.1-17. and Figure B.1-18.. Figure B.1-16. displays the upper vessel vapor temperature measurements and predictions. The TRACE calculated vapor and liquid temperatures, which are almost identical, are slightly higher than measurements, but within the uncertainty bounds for the major portion of the transient.

B.1.4.3. Simulation of Marviken Test 15.

Marviken critical flow Test 15 was run with an category II initial temperature profile. Initially almost all the liquid in the vessel is subcooled. Only the upper part of the liquid close to the vapor-liquid interface in the vessel is close to saturation temperature. Consequently, the bulk of the flow exiting the test nozzle following disk rupture is calculated using the subcooled liquid choked-flow model. Only the flowrate for the last portion of the test is determined using the two-phase choking model.

The mass flow plots on Figure B.1-19. indicate that the TRACE predictions are always close to measurements and within the uncertainty bounds. TRACE slightly overpredicts the time for the start of vapor flow.

The pressure plots on Figure B.1-20., Figure B.1-21. and Figure B.1-22. show that the TRACE pressure predictions are within the uncertainty bounds. As with the previous test results TRACE is unable to capture the pressure drop at the start of the experiment caused by delayed nucleation.

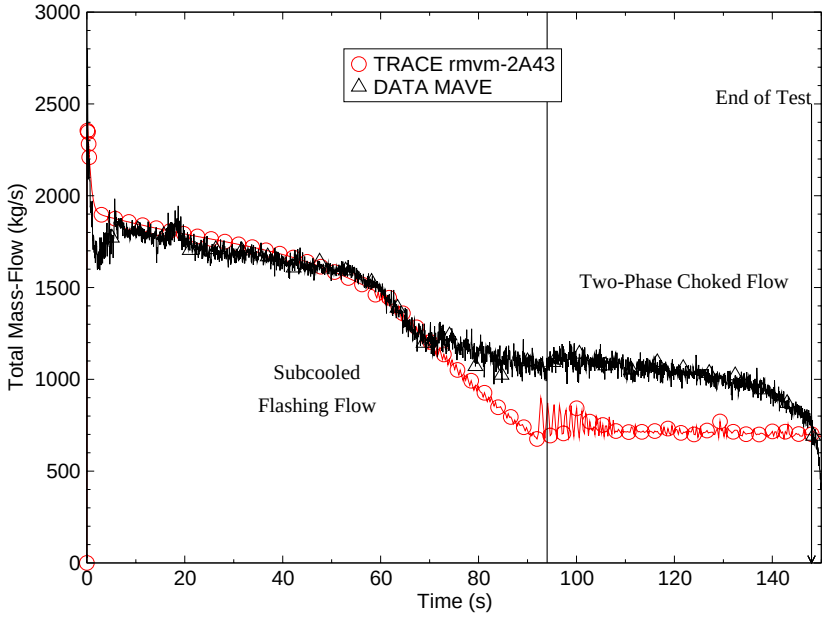

Figure B.1-12. Measured and Calculated Break Flows for Marviken Test 13

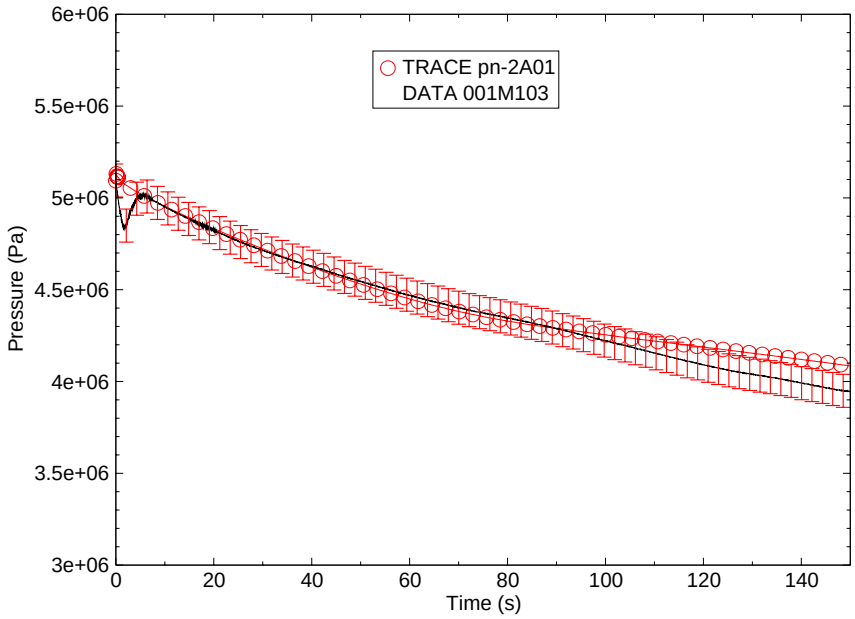

Figure B.1-13. Measured and Calculated Upper Vessel Pressures for Marviken Test 13

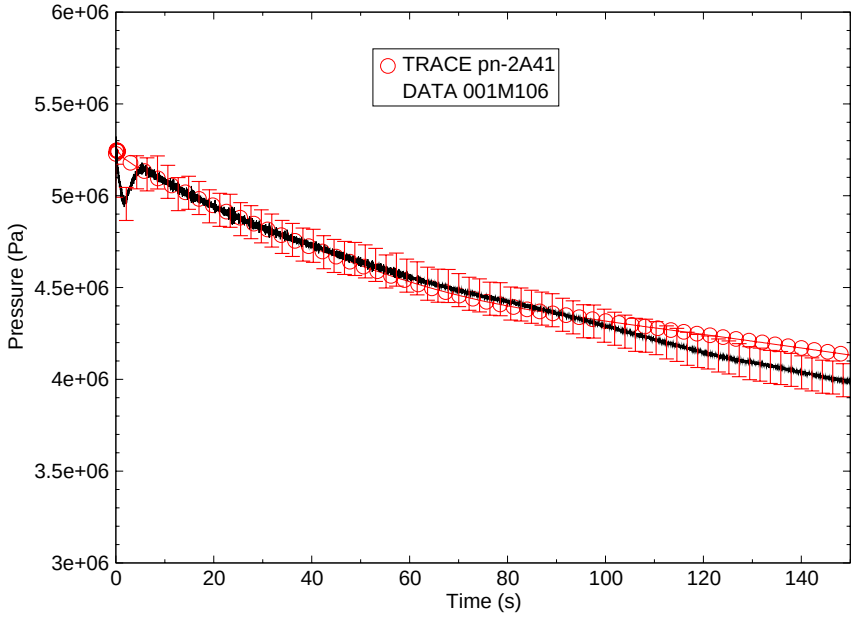

Figure B.1-14. Measured and Calculated Lower Vessel Pressures for Marviken Test 13

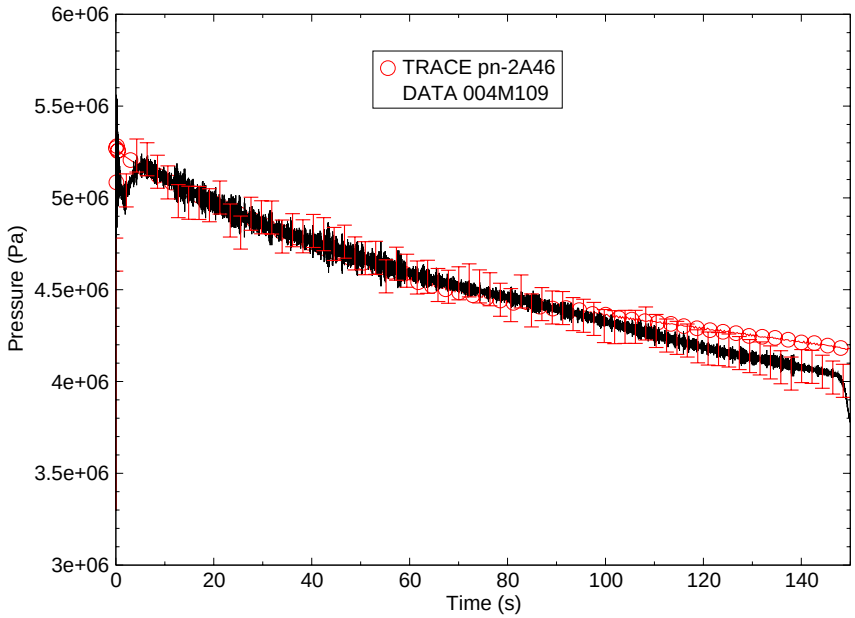

Figure B.1-15. Measured and Calculated Discharge Pipe Pressures for Marviken Test 13

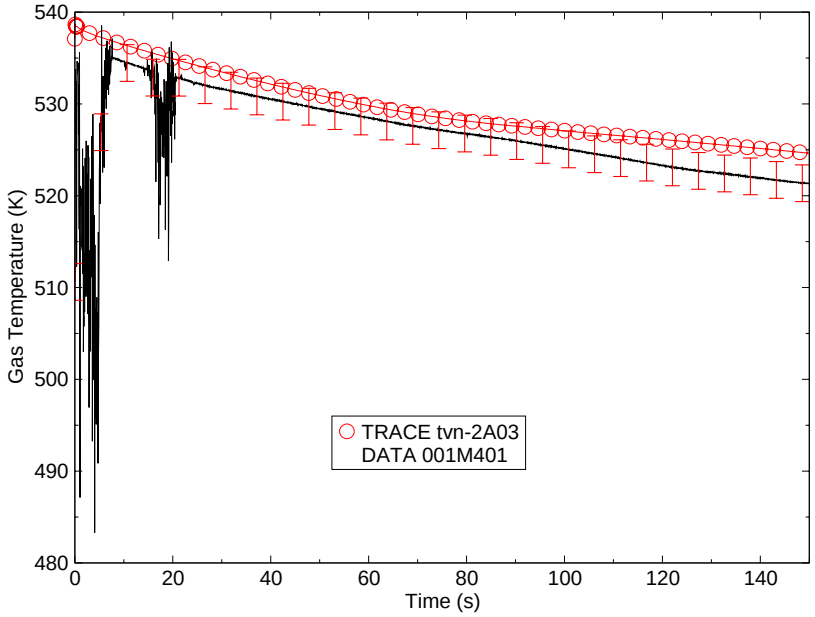

Figure B.1-16. Measured and Calculated Upper Vessel Temperatures for Marviken Test 13

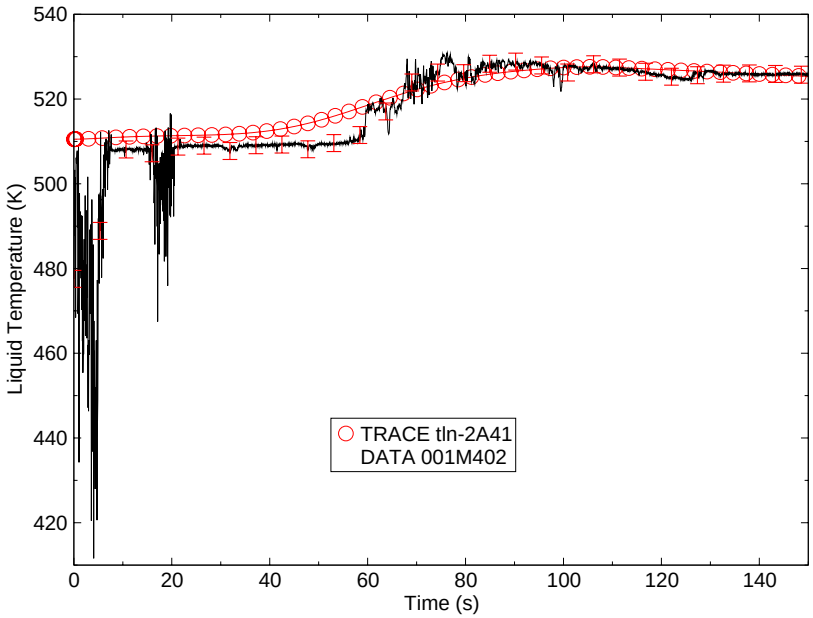

Figure B.1-17. Measured and Calculated Lower Vessel Temperatures for Marviken Test 13

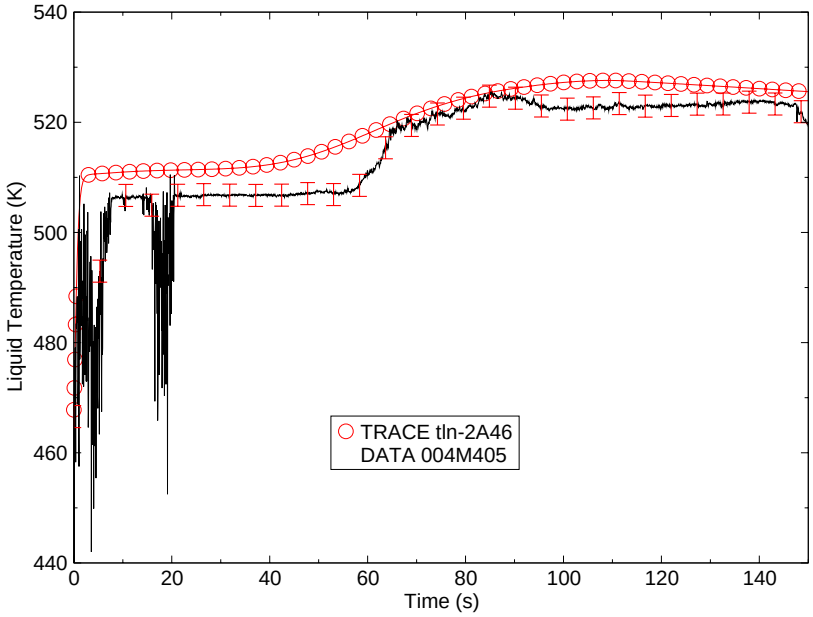

Figure B.1-18. Measured and Calculated Discharge Pipe Temperatures for Marviken Test 13

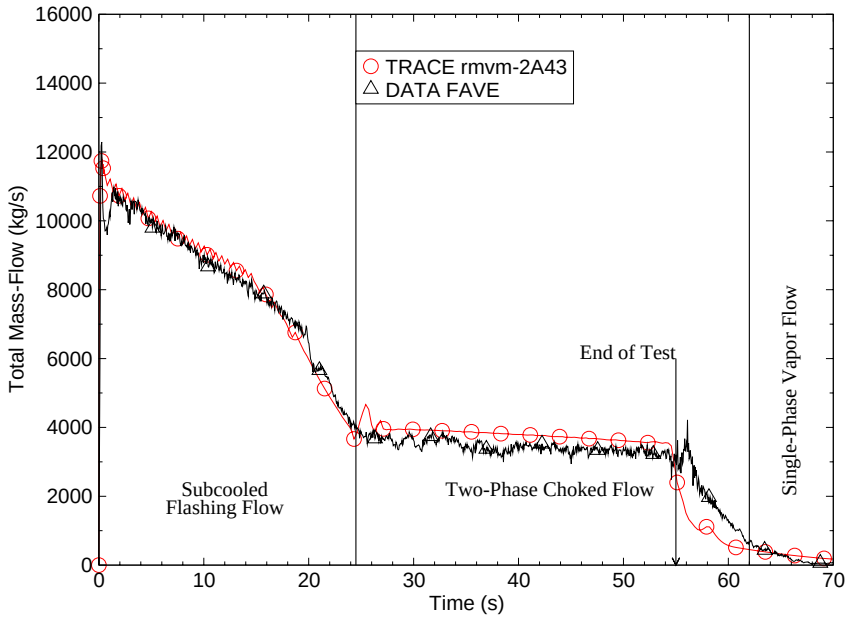

Figure B.1-19. Measured and Calculated Break Flows for Marviken Test 15

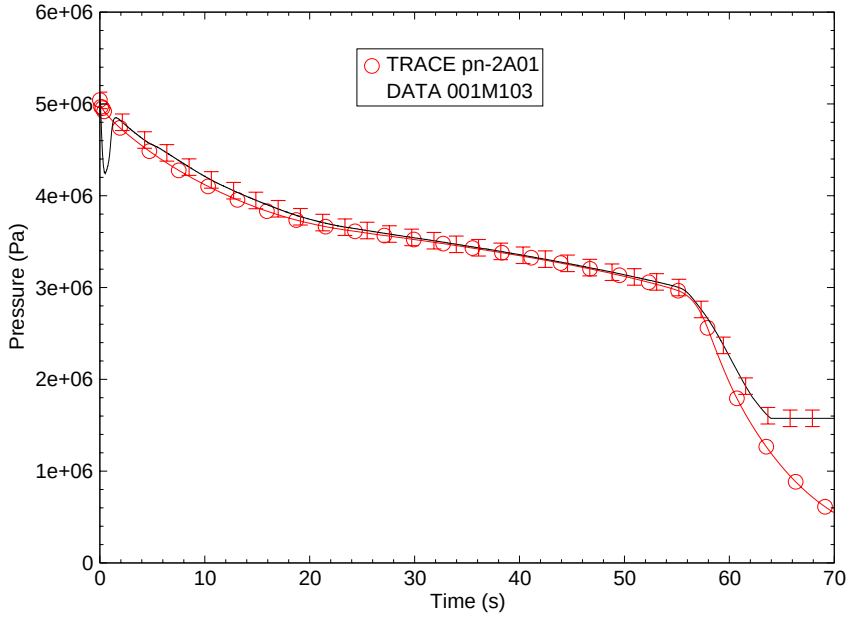

Figure B.1-20. Measured and Calculated Upper Vessel Pressures for Marviken Test 15

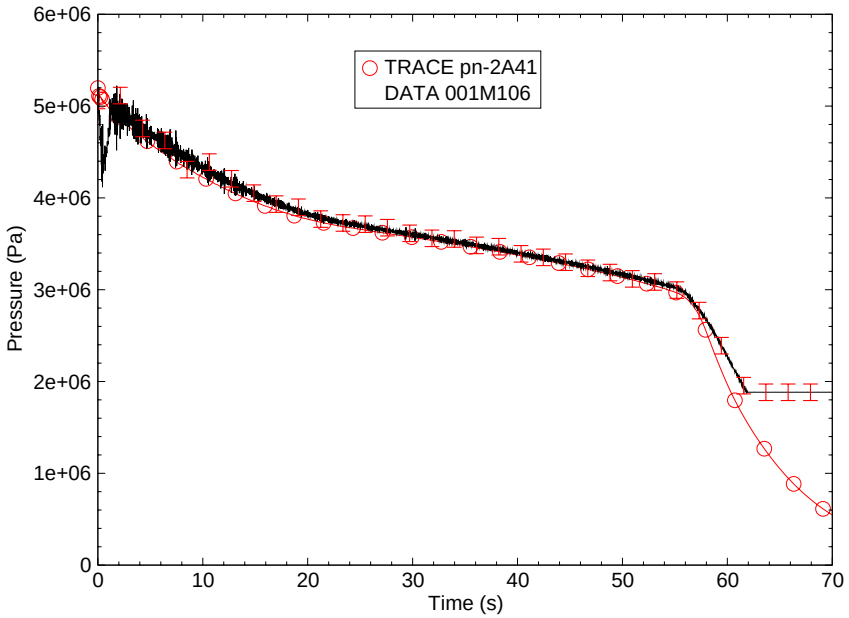

Figure B.1-21. Measured and Calculated Lower Vessel Pressures for Marviken Test 15

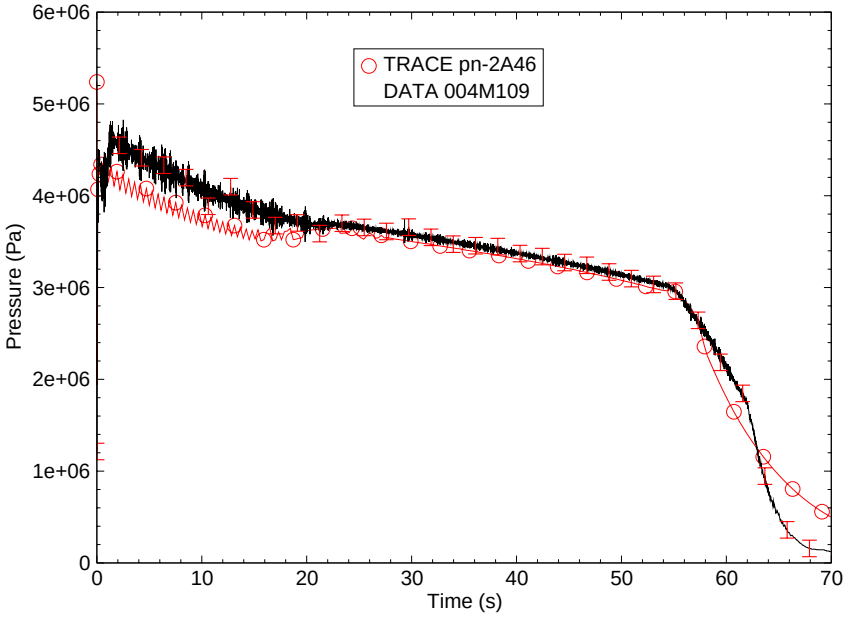

Figure B.1-22. Measured and Calculated Discharge Pipe Pressures for Marviken Test 15

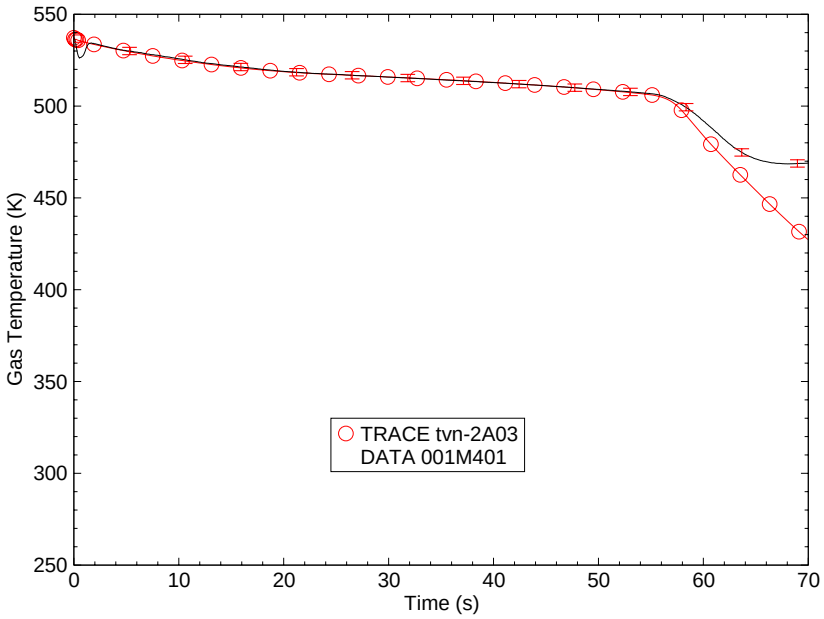

Figure B.1-23. Measured and Calculated Upper Vessel Temperatures for Marviken Test 15

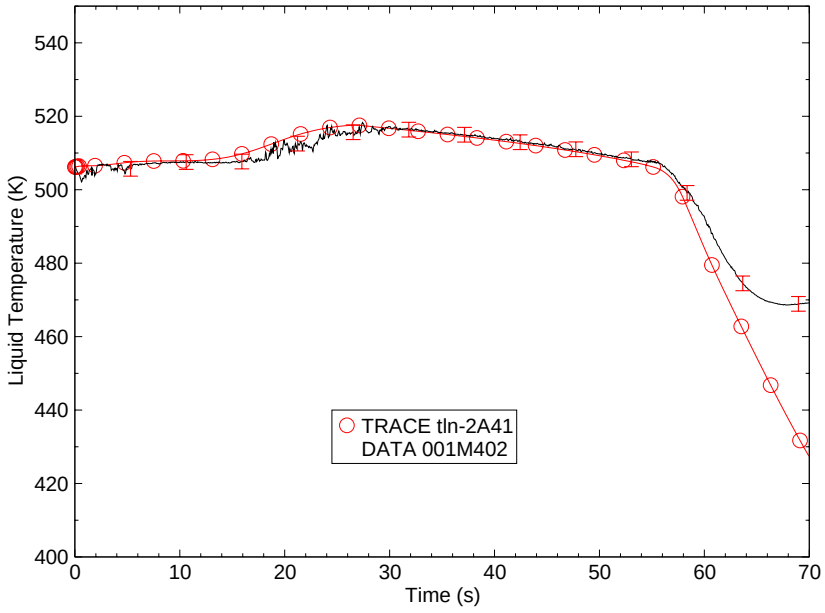

Figure B.1-24. Measured and Calculated Lower Vessel Temperatures for Marviken Test 15

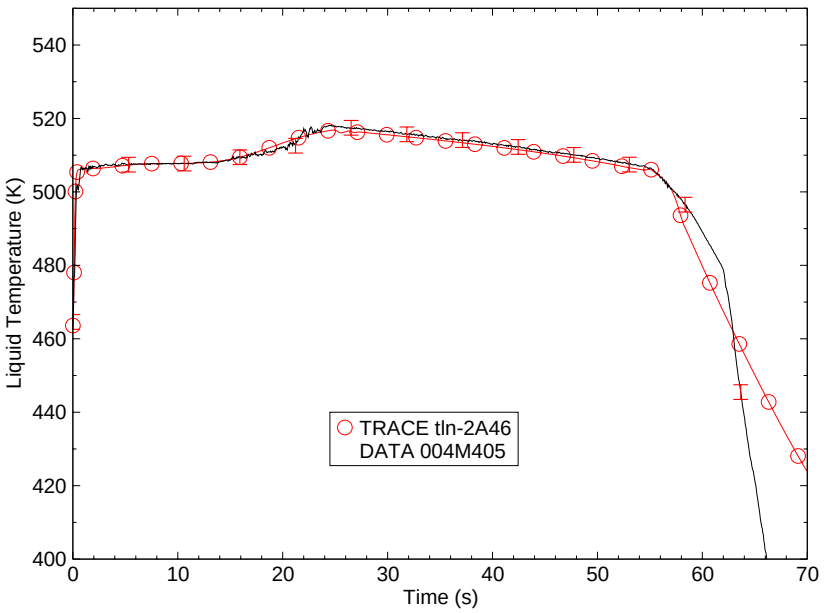

Figure B.1-25. Measured and Calculated Discharge Pipe Temperatures for Marviken Test 15

The upper vessel vapor temperature plot is supplied on Figure B.1-23.; liquid temperature plots are provided on Figure B.1-24. and Figure B.1-25.. TRACE provide an acceptable match with test data throughout the transient.

B.1.4.4. Simulation of Marviken Test 20.

The initial temperature profile for Test 20 is defined as category III. This test is a low subcooling test where the entire vessel liquid is close to the saturation temperature of the vapor in the upper part of the containment. This means that the appropriate choking relation for flow initially exiting the test nozzle would be the subcooled choking correlation; however, the flow transitions to the two-phase water choking flow model quickly after the start of flow.

Figure B.1-26. shows the measured and calculated flowrates following disk rupture. The flows calculated by TRACE closely match the measured flowrate within the uncertainty margin.

A comparison between pressure measurements and code predictions is provided on Figure B.1-27., Figure B.1-28. and Figure B.1-29.. TRACE predictions closely match measurements. As with the previous test results TRACE is unable to capture the pressure drop at the start of the experiment caused by delayed nucleation.

The comparisons of vapor and liquid temperature measurements and predictions shown on Figure B.1-30., Figure B.1-31. and Figure B.1-32., result in conclusions similar to those observed in the pressure comparison. TRACE predictions closely match measurements during the experiment time period.

B.1.4.5. Simulation of Marviken Test 22.

Test 22 starts from a category II temperature profile and has the largest amount of liquid subcooling of all the considered tests, a large initial portion of the flow through the rupture disk is limited by subcooled choking. As the system pressure drops toward the end of the test transient, the flow transitions to two-phase flow at the test nozzle. Consequently, two-phase choked-flow is present during that later time period.

Figure B.1-33. indicate good agreement between the measured flowrate and the values calculated by TRACE. TRACE overpredicts the time for transition to steam flow in the discharge line. Similar to the comparison for previous Marviken Tests, TRACE predicts an unrealistic, peak in flowrate, between 58- and 62-seconds, after steam flow is predicted to exist in the test nozzle. The reasons for this anomaly should be determined and appropriate corrections must be implemented in TRACE . . . . . .

As shown in Figure B.1-34., Figure B.1-35. and Figure B.1-36., TRACE underpredicts pressure during the initial period of the test. As previously indicated, the TRACE, computer code is not capable of predicting the drop in pressure due to delayed nucleation which appears to exist at the start of this test.

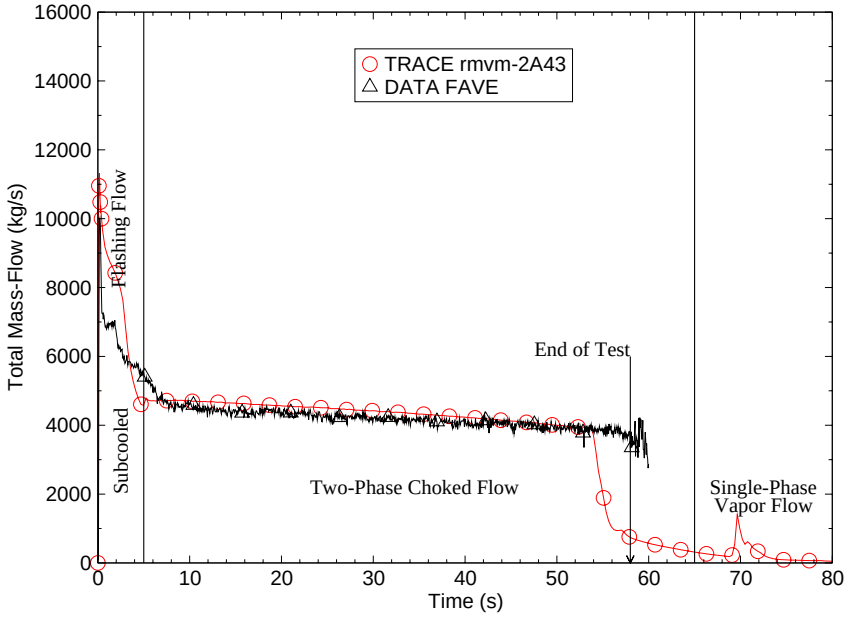

Figure B.1-26. Measured and Calculated Break Flows for Marviken Test 20

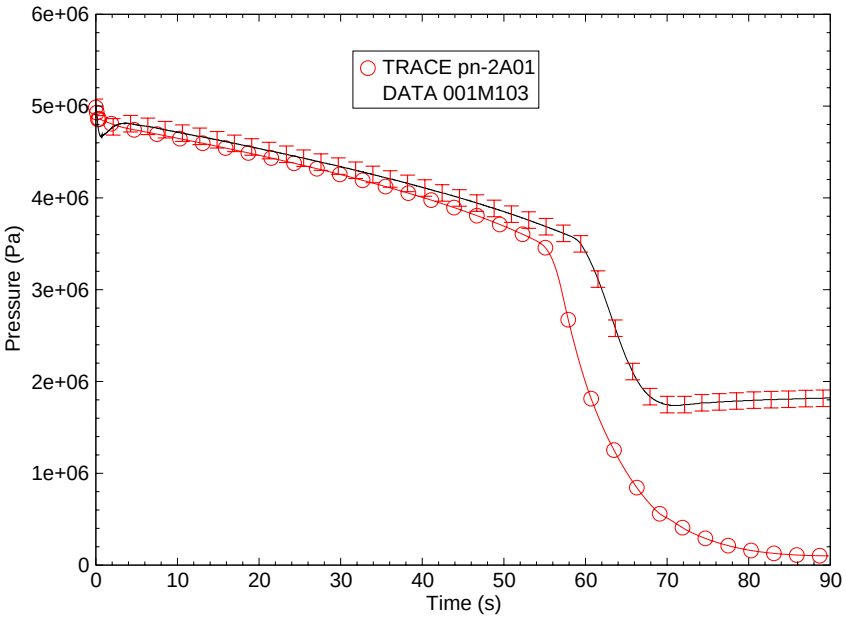

Figure B.1-27. Measured and Calculated Upper Vessel Pressures for Marviken Test 20

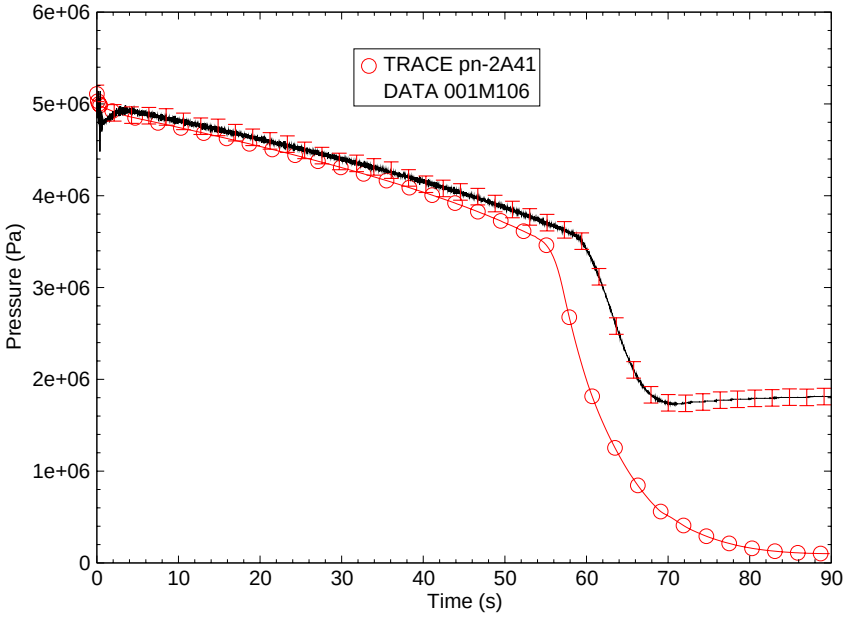

Figure B.1-28. Measured and Calculated Lower Vessel Pressures for Marviken Test 20

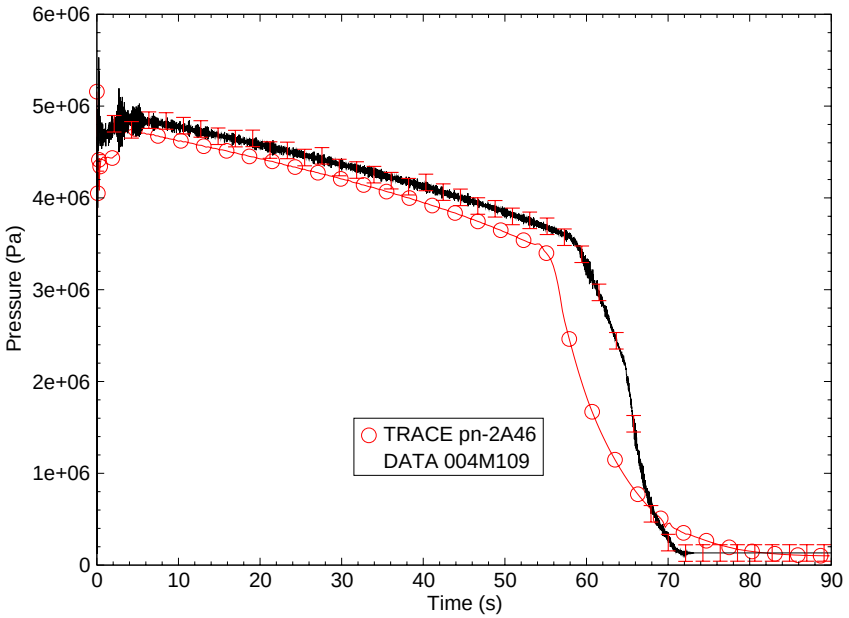

Figure B.1-29. Measured and Calculated Discharge Pipe Pressures for Marviken Test 20

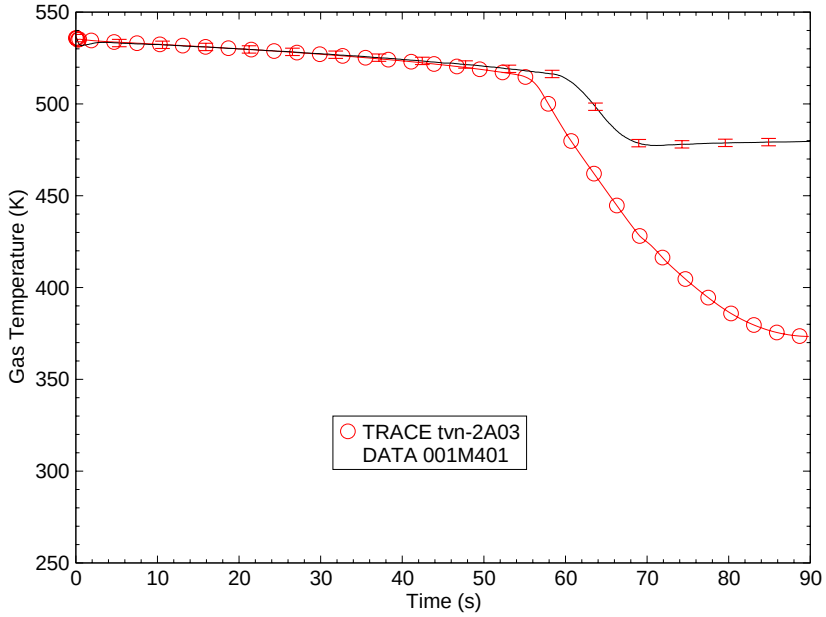

Figure B.1-30. Measured and Calculated Upper Vessel Temperatures for Marviken Test 20

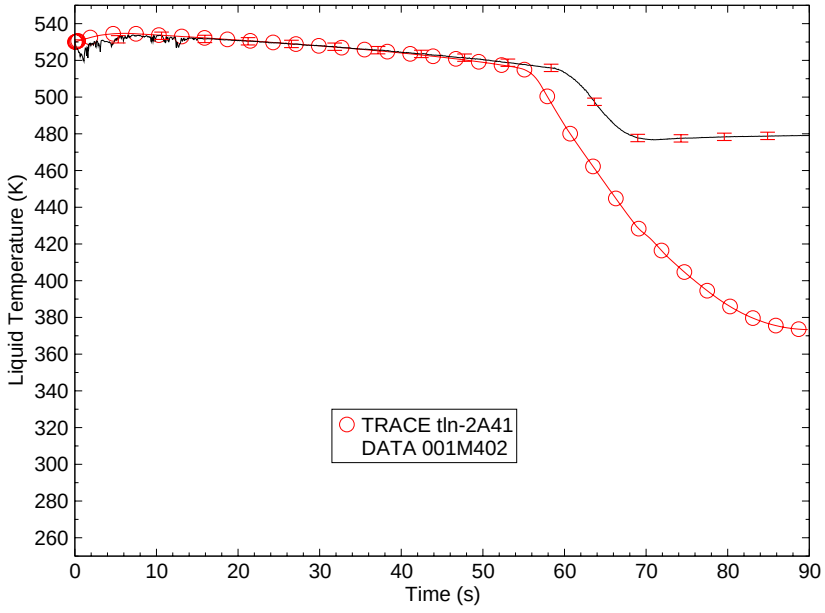

Figure B.1-31. Measured and Calculated Lower Vessel Temperatures for Marviken Test 20

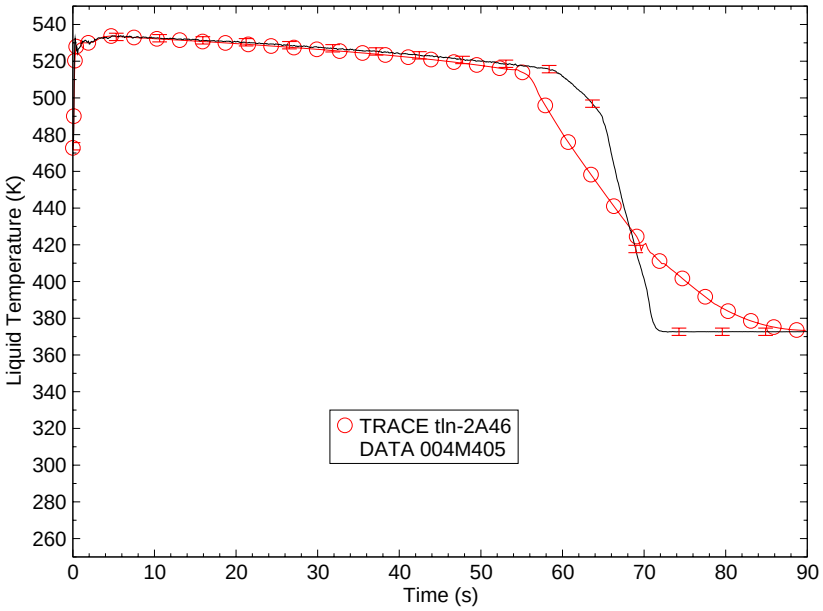

Figure B.1-32. Measured and Calculated Discharge Pipe Temperatures for Marviken Test 20

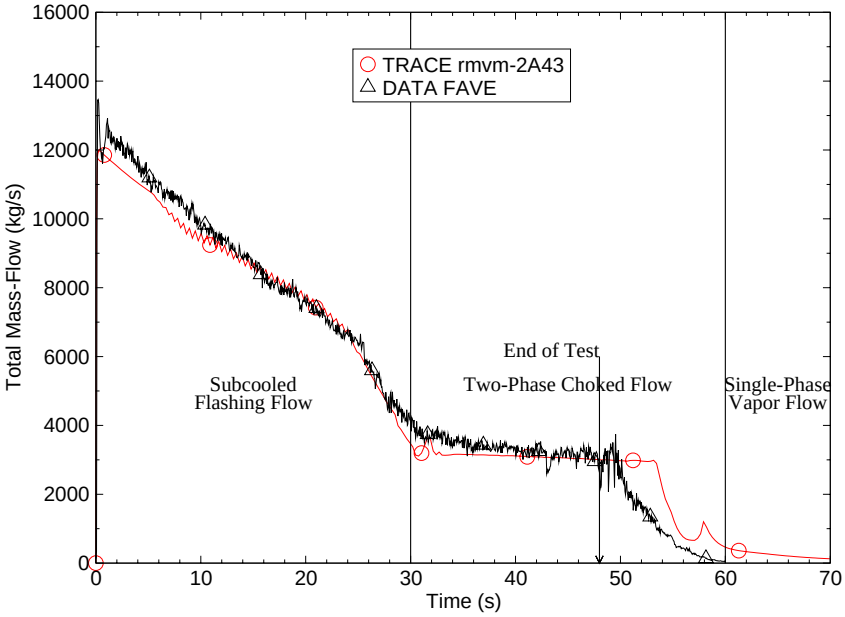

Figure B.1-33. Measured and Calculated Break Flows for Marviken Test 22

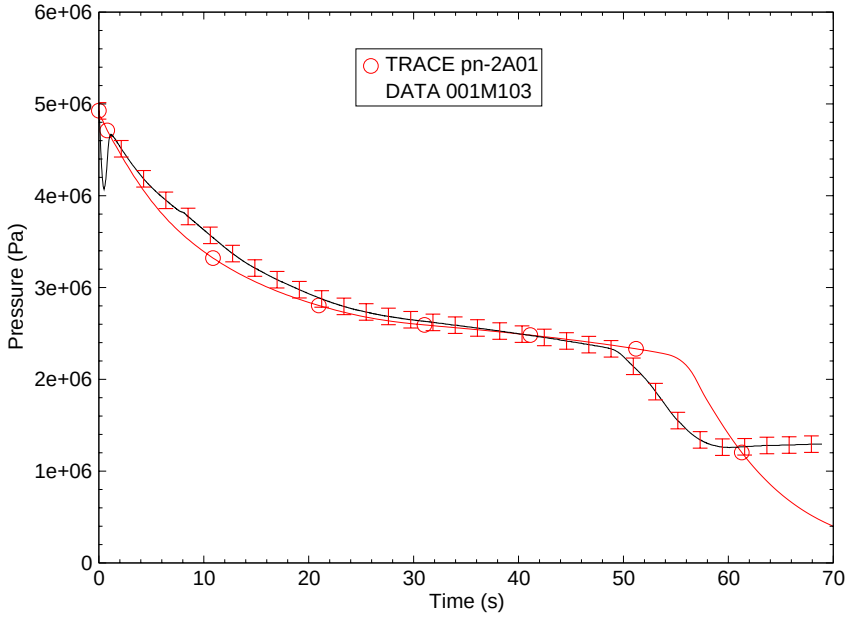

Figure B.1-34. Measured and Calculated Upper Vessel Pressures for Marviken Test 22

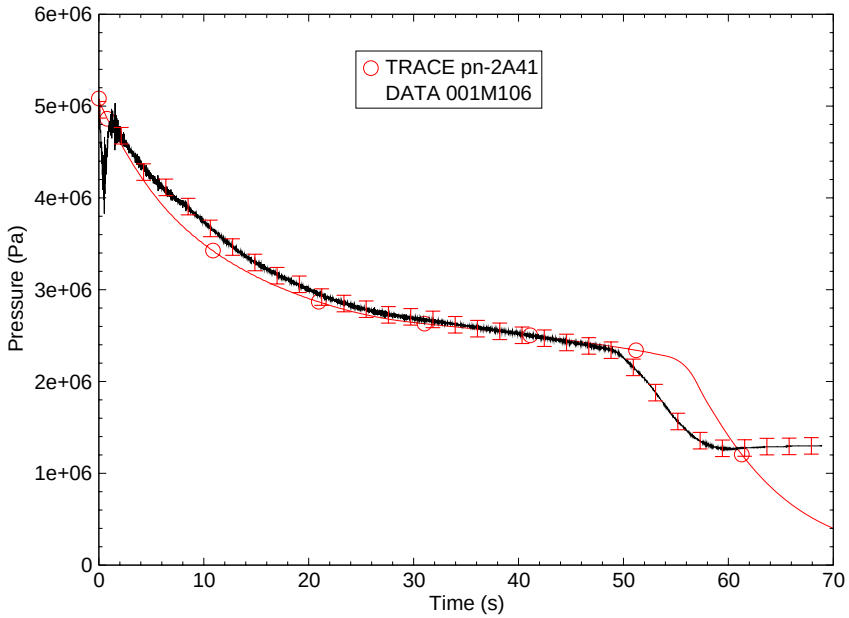

Figure B.1-35. Measured and Calculated Lower Vessel Pressures for Marviken Test 22

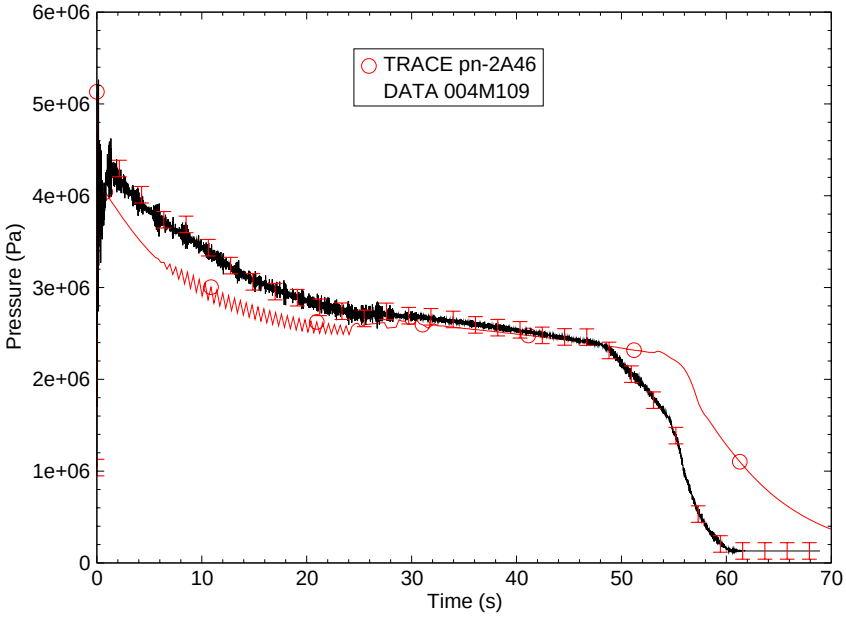

Figure B.1-36. Measured and Calculated Discharge Pipe Pressures for Marviken Test 22

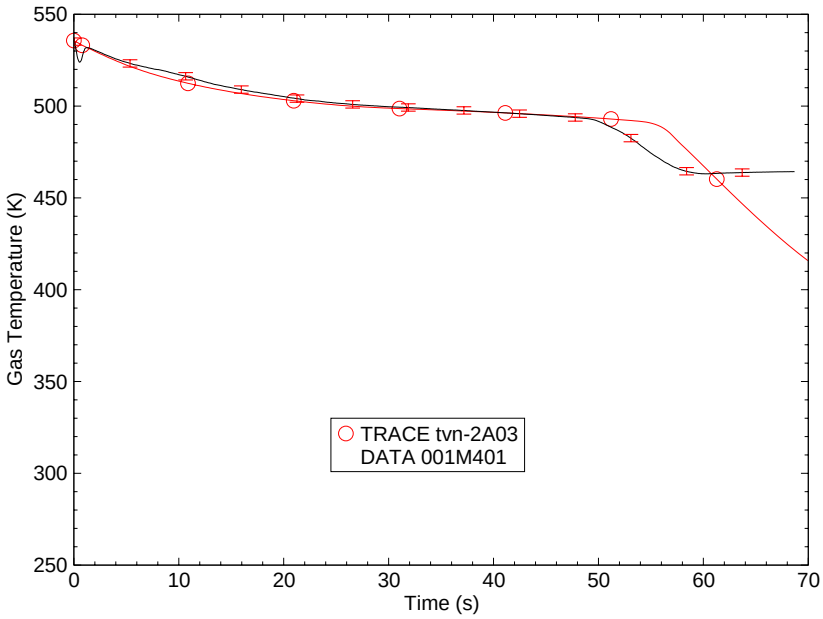

Figure B.1-37. Measured and Calculated Upper Vessel Temperatures for Marviken Test 22

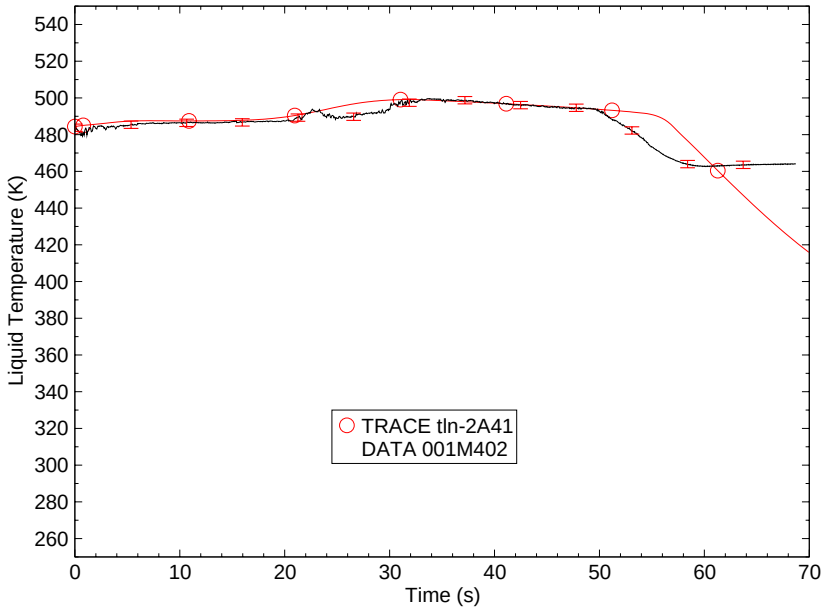

Figure B.1-38. Measured and Calculated Lower Vessel Temperatures for Marviken Test 22

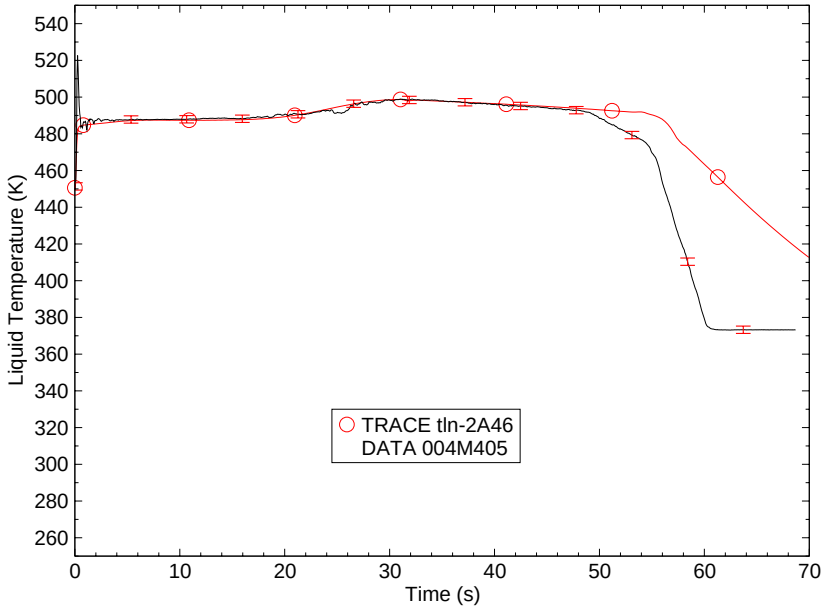

Figure B.1-39. Measured and Calculated Discharge Pipe Temperatures for Marviken Test 22

Figure B.1-37., Figure B.1-38. and Figure B.1-39. provide comparison of vapor and liquid temperature measurements and predictions for Test 22. TRACE predictions are agree well for the major portion of the test.

B.1.4.6. Simulation of Marviken Test 24.

The initial condition for Test 24 is a category II temperature profile. The initial flow period through the test nozzle is dominated by subcooled choking; the later part of the test is two-phase choked-flow.

The characteristics of the flowrates calculated by the computer codes are similar to those observed for Test 22. Figure B.1-40. shows that TRACE flowrate predictions are within the uncertainty bounds during the initial subcooled choked-flow conditions. During the later two-phase choked-flow period, TRACE provides good agreement with measurements. TRACE overpredicts the time for the steam flow transition.

As indicated in the pressure plots provided on Figure B.1-41., Figure B.1-42. and Figure B.1-43., TRACE provides acceptable agreement with measured pressures. TRACE is not capable of predicting the initial measured pressure drop in the first 2-seconds which has been postulated to be the results of delayed nucleation followed by flashing.

TRACE provides acceptable agreement with the vapor and liquid temperature measurements shown on Figure B.1-44., Figure B.1-45. and Figure B.1-46.. TRACE overpredicts the time for the temperature drop due to loss of mass inventory which occurs at the time steam flow enters the discharge pipe.

B.1.5. Assessment Results Summary

Table B.1.3 provides a summary of the comparisons between experimental measurements and code predictions for the six Marviken critical flow tests studied in this report. The TRACE pressure and temperature predictions are acceptable. The TRACE computer code appears able to acceptably predict choked-flow rates for subcooled and saturated flashing conditions. The TRACE predictions for two-phase choking are also acceptable, but TRACE did underpredict flowrates for Test 13.

Test data indicates a pressure drop at all measured locations immediately following the disk rupture. Previous analyses of the Marviken Test attribute the pressure drop to delayed nucleation at the liquid surface in contact with vapor. TRACE cannot predict pressure drop due to delayed nucleation. TRACE does not include detailed modeling of nucleation effects, pool flashing and their history. Detailed nucleation site modeling is impractical because nucleation predictions are greatly dependent on past history. Consequently, delayed nucleation calculations are impractical for most analyses. Initial nucleation delay is a short-term effect which does not drastically affect later results.

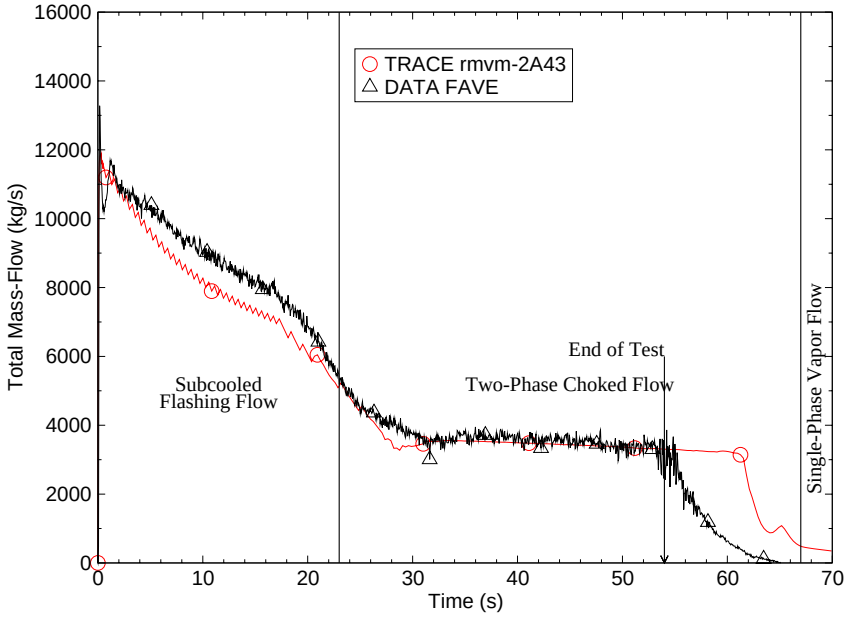

Figure B.1-40. Measured and Calculated Break Flows for Marviken Test 24

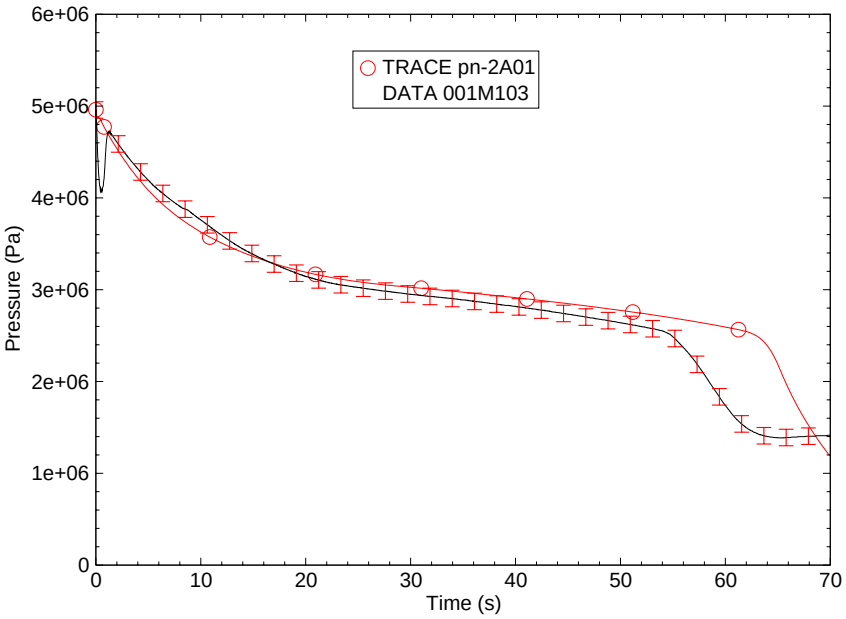

Figure B.1-41. Measured and Calculated Upper Vessel Pressures for Marviken Test 24

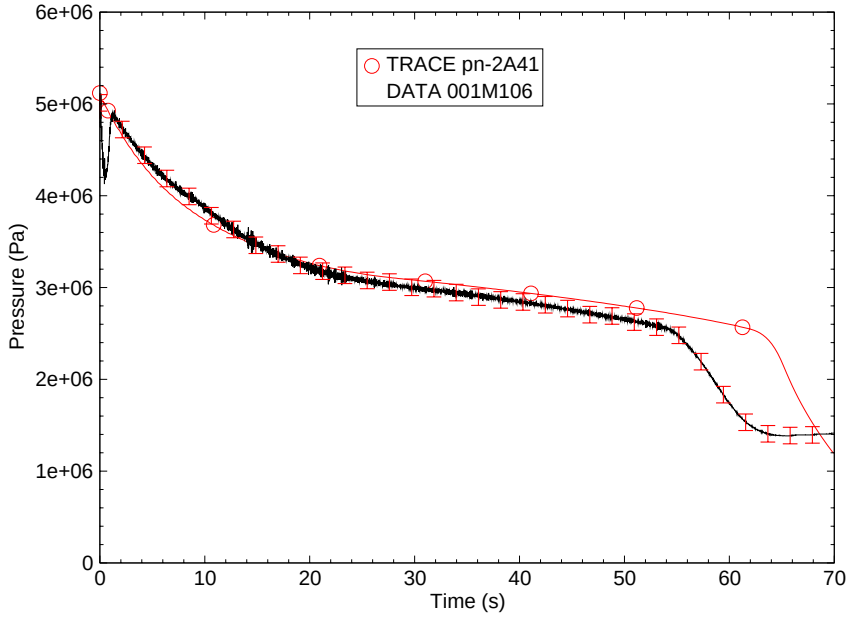

Figure B.1-42. Measured and Calculated Lower Vessel Pressures for Marviken Test 24

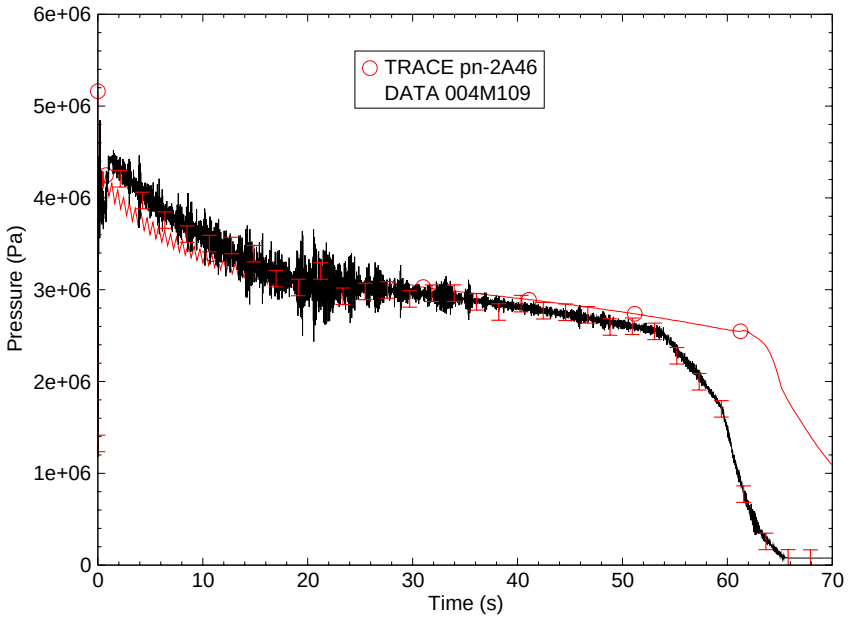

Figure B.1-43. Measured and Calculated Discharge Pipe Pressures for Marviken Test 24

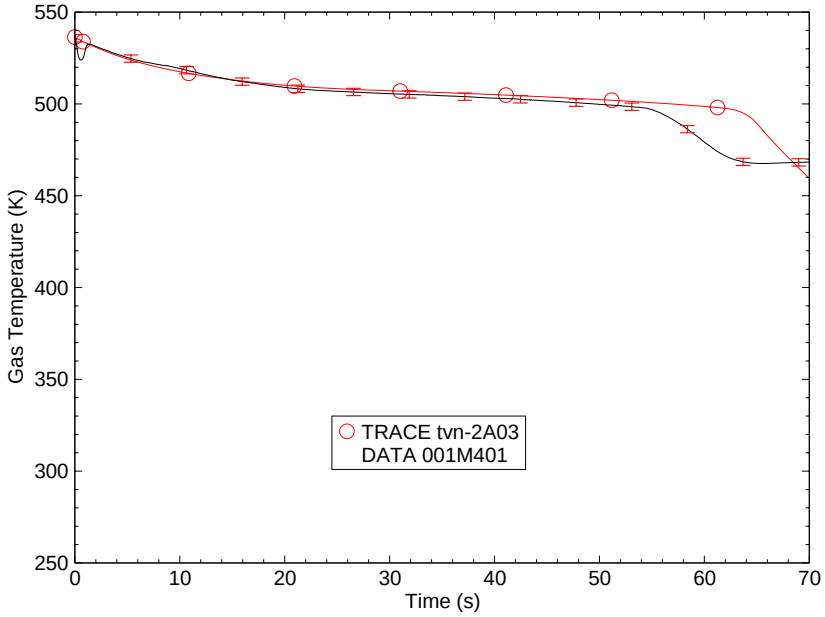

Figure B.1-44. Measured and Calculated Upper Vessel Temperatures for Marviken Test 24

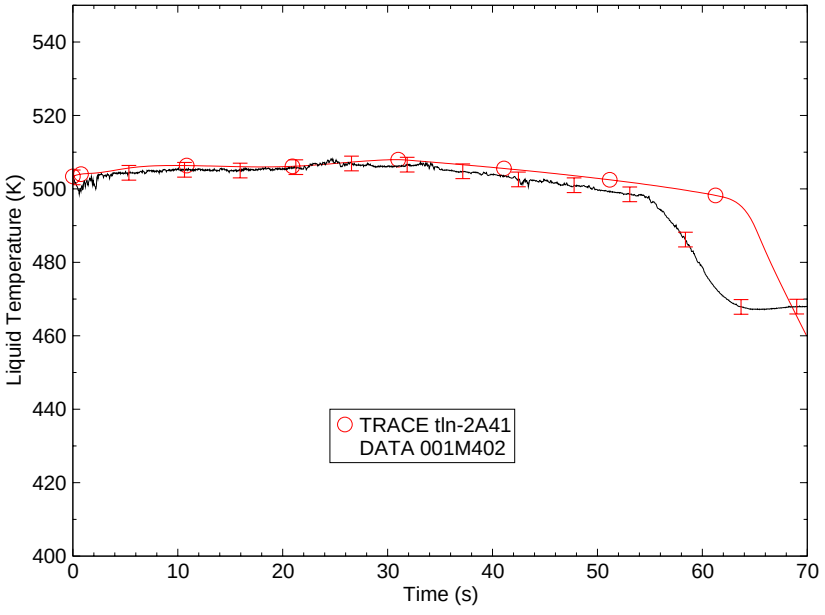

Figure B.1-45. Measured and Calculated Lower Vessel Temperatures for Marviken Test 24

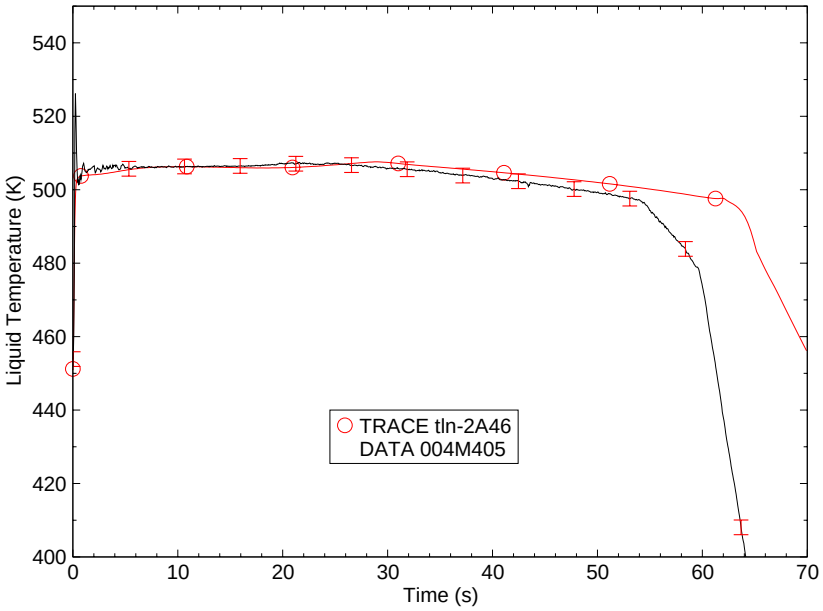

Figure B.1-46. Measured and Calculated Discharge Pipe Temperatures for Marviken Test 24

Table B.1.3. Summary of Comparisons Between Measurements and TRACE Predictions for Six Marviken Critical Flow Tests

Marviken Test	**Test 4**	**Test 13**	**Test 15**	**Test 20**	**Test 22**	**Test 24**
Test Nozzle ID	**0.509 m**	**0.200 m**	**0.509-0.500 m**	**0.509-0.500 m**	**0.509-0.500 m**	**0.500 m**
Nozzle L/D	**3.43**	**3.45**	**3.91**	**1.88**	**1.88**	**0.78**
Flashing Critical Flow Period						
Flowrate Comparisons						
	Good	Good	Good	Good	Good	Acceptable
Pressure Comparisons						
	Acceptable	Good	Acceptable	Good	Acceptable	Acceptable
Temperature Comparisons						
	Good	Marginal	Good	Good	Good	Good
Flowrate Comparisons						
	Good	Poor	Good	Good	Acceptable	Good
Pressure Comparisons						

Table B.1.3. Summary of Comparisons Between Measurements and TRACE Predictions for Six Marviken Critical Flow Tests

Marviken Test	**Test 4**	**Test 13**	**Test 15**	**Test 20**	**Test 22**	**Test 24**
Test Nozzle ID	**0.509 m**	**0.200 m**	**0.509-0.500 m**	**0.509-0.500 m**	**0.509-0.500 m**	**0.500 m**
Nozzle L/D	**3.43**	**3.45**	**3.91**	**1.88**	**1.88**	**0.78**
	Acceptable	Marginal	Good	Good	Good	Good
Temperature Comparisons						
a	Good	Marginal	Good	Good	Good	Good

a. Ratings are defined as follows;
Good
Acceptable
Poor

B.1.6. References

1 "TRAC-M/FORTRAN 90 Theory Manual," U. S. Nuclear Regulatory Commission, NUREG/CR-6724, July 2001.

2 "The Marviken Full Scale Critical Flow Tests, Summary Report," U. S. Nuclear Regulatory Commission, NUREG./CR-2671, MXC-301, May 1982.

3 "Assessment of Modernization and Integration of BWR Components and Spatial Kinetics in the TRACE, Version 3690, Code," U. S. Nuclear Regulatory Commission, NUREG-1752, December 200

B.2. Moby Dick Critical Flow Experiments

Author(s): Justin K. Watson, William J. Krotiuk

Affiliation: PennState ARL, NRC

Code Version: TRACE V5.0

Platform and Operating System: Intel x86, Windows XP

B.2.1. Introduction

The calculation of critical flow is an important consideration in the area of nuclear reactor safety. The fluid velocity at nozzles, breaks, or other restrictions can exceed the local sound speed which causes the fluid flow rate to become insensitive to downstream pressure changes. Of particular importance are choking conditions at pipe break locations where fluid at high pressure-temperature conditions is subjected to large decreases in pressure. In order to account for fluid choking effects, the TRACE computer code employs a one-dimensional critical flow model. The TRACE critical flow model comprises of three separate models; a subcooled liquid choked-flow model, a two-phase, two-component choked-flow model, and a single-phase vapor choked-flow model.

The subcooled liquid choked-flow model is based on the Burnell model. The subcooled liquid choked-flow model is used where subcooled liquid persists through the choking plane. The two-phase, two-component choked-flow model is based on first principals and calculates flow limitations for a two-phase fluid which can consist of two different fluids such as water and an inert-gas such as air. Finally, the single-phase vapor choked-flow model is based on the theory describing an isentropic expansion of an ideal-gas. The choking models employed by TRACE are more fully described in the TRACE Theory Manual (Ref. 1).

The Moby Dick Flow Experiments were performed at the Centre d'Etudes Nucleaires de Grenoble in France. The objective of this series of experiments was to study steady-state, two-phase, two-component critical flow in a vertical, divergent nozzle at low pressure. During testing, a low quality water and nitrogen mixture flowed at high velocity through a vertical test section which included a 7-degree divergent nozzle. Flashing was observed downstream of the divergent nozzle. Pressures and void fractions were measured at various points along the test section.

B.2.2. Test Facility Description

The Moby Dick test facility's primary loop has five main components; a pump, a preheater, a nitrogen injection system, a test section, and a condenser (Figure B.2-1). The test channel is located in the upper left-hand portion of the figure. Flow is directed vertically upward in the test section. The outlet of the vertical test section is located inside the condenser. Test flow conditions were obtained by maintaining constant inlet conditions to the test section and lowering the downstream pressure in the condenser to atmospheric pressure. Reference 5 describes the Moby Dick facility and provides the test data for the experiments.

Figure B.2-2 shows the major, fully instrumented portion of the test section. Nitrogen is injected into the pipe at a location 0.985 meters upstream of the expansion. The gas is injected through four porous screens surrounding the flow pipe (Figure B.2-3). Void fraction measurements were made for some tests at the entrance to the fully instrumented test section, position Xe indicated on Figure B.2-2, and at various location located before and within the nozzle. Pressure measurements are taken at the various positions labeled with P on Figure B.2-2. Water temperature was measured at the inlet to the test section; the temperature of the injected nitrogen was also measured. The accuracy of the temperature measurement is indicated to be ±0.2 C. The water mass flowrate was also measured. Table B.2.1 provides the dimensions of the test section.

Table B.2.1. Geometry for the Moby Dick Experiments

Straight Inlet Section	
Length	2.668 m
Internal Diameter	0.014 m
Nitrogen Injection	0.985 m Upstream of Nozzle
Conical Convergent Nozzle	
Length	0.2534 m
Divergent Angle	7^{o}
Straight Outlet Section	
Length	0.420 m
Internal Diameter	0.045 m

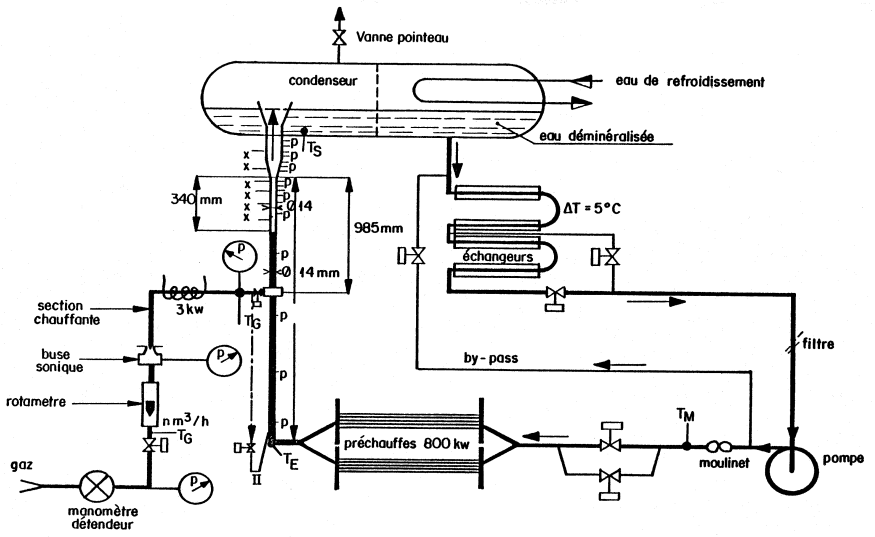

Figure B.2-1. Moby Dick Test Loop

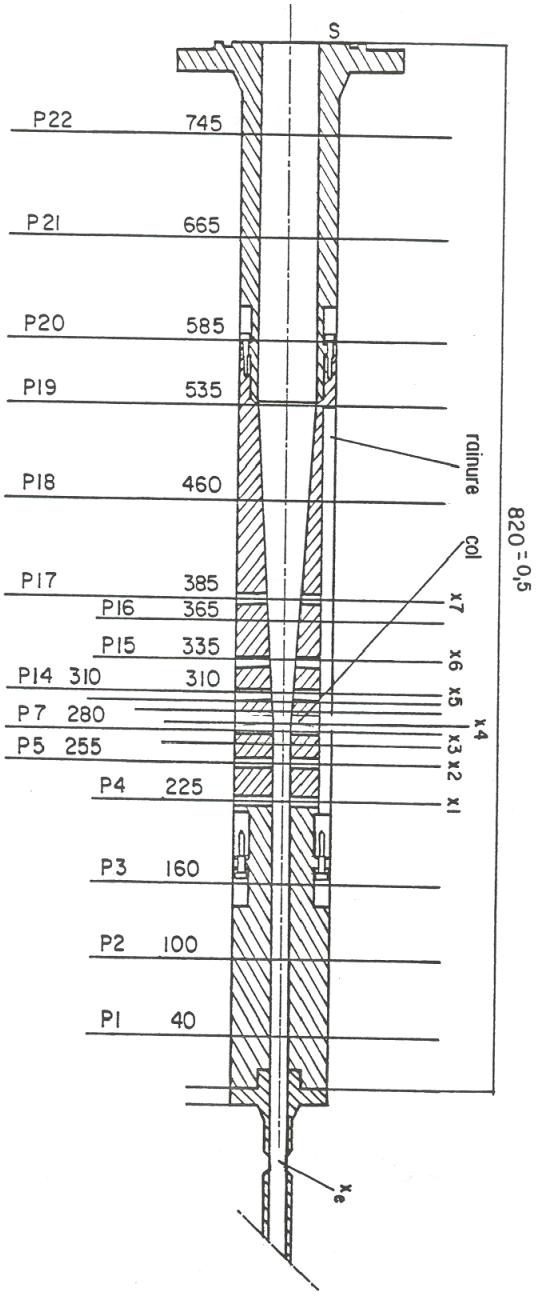

Figure B.2-2. Moby Dick Test Section

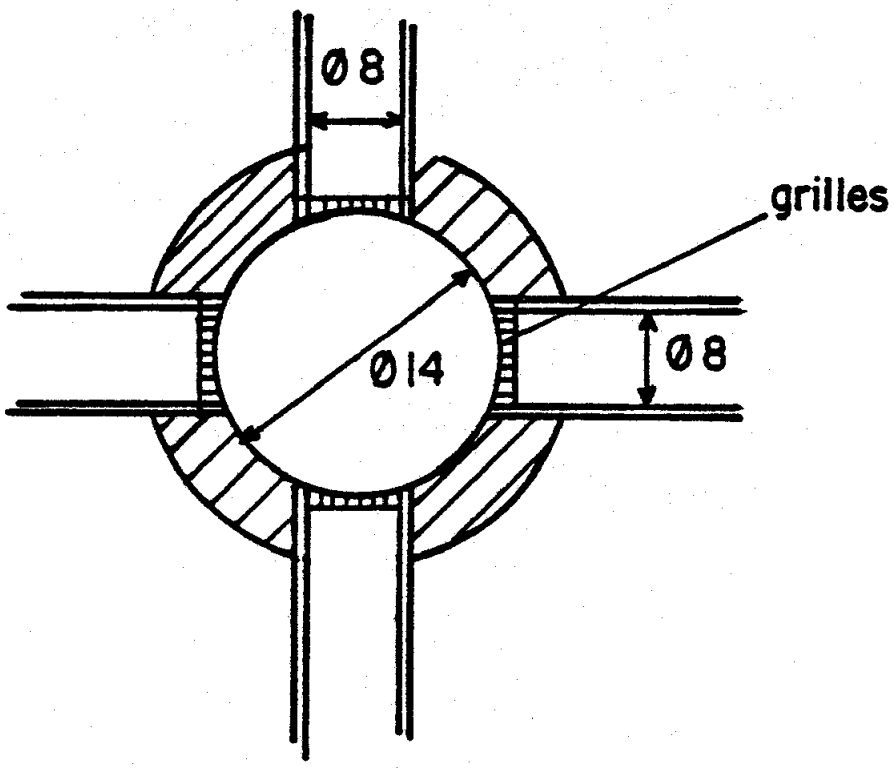

Figure B.2-3. Nitrogen Injection Section for Moby Dick Experiments

B.2.3. TRACE Model Description

The TRACE model for all tests except for 3170 include 4 components. A BREAK component is used to specify the test section inlet conditions. A TEE component is used to represent the test section. The side leg of the tee models the nitrogen injection. A BREAK component is also used to represent the condenser. A FILL component is used to inject the nitrogen. Figure B.2-4 shows the schematic of the TRACE model. The model used for test 3170 is the same a the others except the TEE component used to represent the test section is replaced by a PIPE component. This test has no nitrogen injection so the TEE component is unnecessary. The lengths of the control volumes in the straight sections are set approximately equal to the line diameter. The control volume length for the diverging section is defined to accommodate the gradual volume changes. Irreversible pressure drop loss coefficients for the divergent nozzle were obtained from the correlations provided by Reference 4.

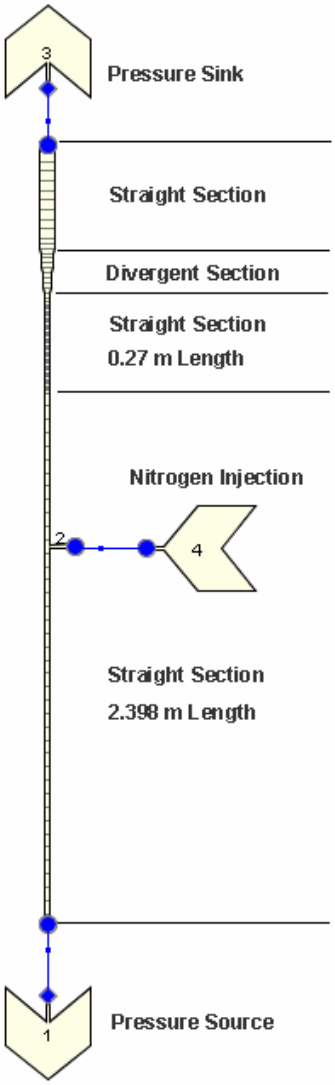

Figure B.2-4. TRACE Analytical Model for Moby Dick Experiment

B.2.4. Tests Simulated with TRACE

Ten tests were chosen to provide comparisons for computer code assessment. All but two of the chosen tests provide void fraction measurements. The two tests with no void fraction measurements were chosen because they were previously used for previous code assessments (Ref. 6). Additionally, despite the fact that the Moby Dick Critical Flow Tests were intended to

study critical flow conditions, the analytical assessments indicate that not all tests have critical flow conditions at the minimum area upstream of the divergent nozzle. Table B.2.2 lists the measured test conditions for the tests chosen for assessment. The general characteristics of the assessed tests include:

a. Baseline Non-Critical Flow Test Without Nitrogen Injection

Test 3170 - This test does not include nitrogen injection. This test was chosen to provide a baseline for comparison with those tests which included nitrogen injection. The single phase water was observed to flash downstream of the nozzle neck.

b. Non-Critical Flow Tests With Nitrogen Injection

Test 3174 - This test has nitrogen injection. Flashing is observed downstream of the nozzle neck.

Test 3177 - This test is similar to Test 3174. The test has nitrogen injection, and flashing is observed downstream of the nozzle neck.

Test 3167 - This test has nitrogen injection and a larger water flowrate resulting from a larger applied pressure drop across the test system. Reference 5 reports that a shock wave was present in the test section during this test.

Test 3087 - This test has a larger nitrogen injection, a large water flowrate and pressure drop, and operates at the highest water temperature of the chosen non-critical flow tests.

c. Critical Flow Tests With Nitrogen Injection

Test 3010 - This test with high temperature nitrogen injection operates has the largest upstream source pressure and inlet water temperature of the assessed tests.

Test 3030 - This test with high temperature nitrogen injection has a large upstream source pressure, but a lower inlet water temperature.

Test 3052 This low temperature nitrogen injection test has a lower upstream source pressure.

Test 3141 - This test has a low temperature, high flow nitrogen injection with a lower inlet water temperature.

Test 3151 - This test has the largest flow temperature nitrogen injection of the considered tests at a lower inlet water temperature.

Table B.2.2. Measured Test Conditions for Moby Dick Experiments Chosen for Computer Code Assessment

Test	3170	3174	3177	3167	3087

Table B.2.2. Measured Test Conditions for Moby Dick Experiments Chosen for Computer Code Assessment

Choking at Divergent Nozzle[a]	No	No	No	No	No
Upstream Liquid Temperature (^oC)	32.5	30.5	34.0	37.7	40.4
Upstream Pressure (Pe) (Pa)	627700	492400	487000	704900	570900
Condenser Pressure (Pcond) (Pa)	100943	149342	100113	154657	171793
Pe - Pcond (Pa)	526757	343058	386887	550243	399107
Liquid Entrance flux ($kg/m^2/sec$)	17260	13280	13400	17110	12440
Liquid Flowrate (kg/sec)	2.657	2.044	2.063	2.634	1.915
Liquid Entrance Velocity (m/sec)	17.3	13.3	13.5	17.2	12.5
Nitrogen Entrance Temperature (^oC)	NA	17	17	21	21
Void Fraction at Test Section Entrance (Xe)	0.0	0.054	0.062	0.044	0.191
Calculated N_2 Flowrate (kg/sec)	NA	$1.759x10^{-4}$	$1.867x10^{-4}$	$1.906x10^{-4}$	$1.086x10^{-3}$
Test	3010	3030	3052	3141	3151
Choking at Divergent Nozzle[a]	Yes	Yes	Yes	Yes	Yes
Upstream Liquid Temperature (^oC)	79.5	30.1	35.8	35.5	38.5
Upstream Pressure (Pe) (Pa)	765000[b]	757200[b]	625800	561900	566000
Condenser Pressure (Pcond) (Pa)	102566	99382	134360	103178	102186
Pe - Pcond (Pa)	662434	657818	491440	458722	463814
Liquid Entrance Flux ($kg/m^2/sec$)	13550	14260	12530	7940	7110
Liquid Flowrate (kg/sec)	2.086	2.195	1.929	1.222	1.094
Liquid Entrance Velocity (m/sec)	13.9	14.3	12.6	7.98	7.16
Nitrogen Entrance Temperature (^oC)	67	63	25	18	19
Void Fraction at Test Section Entrance (Xe)	0.217	0.198	0.229	0.554	0.612
Calculated N_2 Flowrate (kg/sec)	$1.549x10^{-3}$	$1.803x10^{-3}$	$1.632x10^{-3}$	$6.101x10^{-3}$	$6.252x10^{-3}$

a. Choking condition determined from analytical assessments.

b. Pressure estimated because recorded value is unrealistic.

B.2.4.1. Assessment of Tests With Non-Critical Flow

This section discusses the analytical predictions and test observations for the five assessed tests which were determined not to have critical flow.

Nitrogen is not injected into the test piping for Test 3170. Test 3170 does not run with this version of TRACE. This problem is not expected to have any choking at the divergent nozzle. TRACE is

predicting that the downstream pressure is greater than the upstream pressure while trying to calculate choked conditions at the nozzle. This is non-physical since you can not have a choked condition when the downstream pressure is greater than the upstream pressure.

Figure B.2-5, Figure B.2-7, Figure B.2-9, and Figure B.2-11 show pressure distributions for tests 3174, 3177, 3167, and 3087 respectively. TRACE does predict the pressure distribution in the straight pipes before and after the divergent nozzle. Figure B.2-7, Figure B.2-9,and Figure B.2-11 show that TRACE does not predict the pressure drop at the entrance of the divergent nozzle. In Figure B.2-6, Figure B.2-8, and Figure B.2-10 the experimental data shows flashing occurring in the diverging nozzle and condensing before the end of the expansion. In all cases TRACE over predicts the void distribution in the divergent nozzle. The pressure under prediction and the void over prediction in the nozzle is cased by a problem in the interfacial drag model. TRACE is predicting that the liquid velocity is greater than the vapor velocity which is causing a non-physical slip ratio. Table B.2.3 summarizes the system flowrates predicted by TRACE. This table also shows that TRACE did predict critical flow in the divergent nozzle for cases 3167 and 3177 when no critical flow was observed during the experiment. This can also be attributed to the pressure and interfacial drag problems discussed above. TRACE did do a good job of predicting the flowrates at the nozzle.

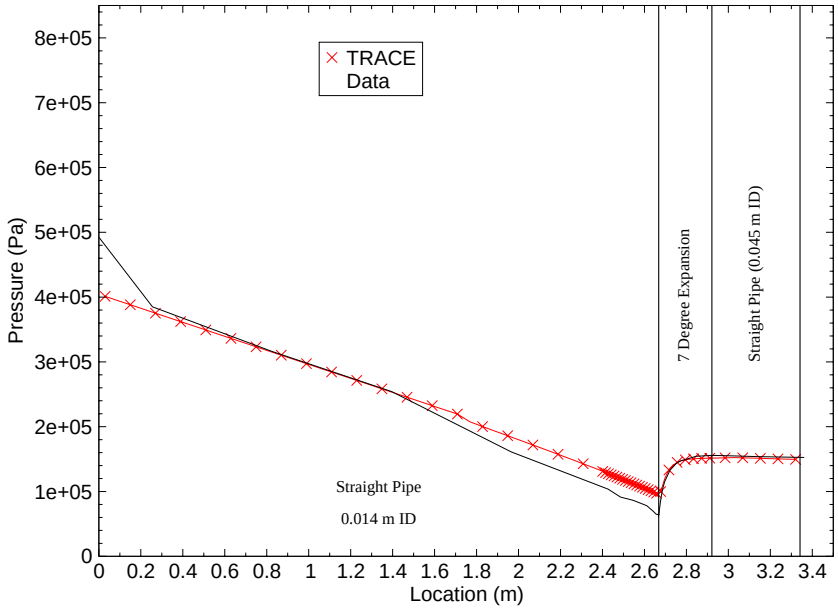

Figure B.2-5. Comparison Between Pressure Measurements and Code Predictions for Moby Dick Test 3174

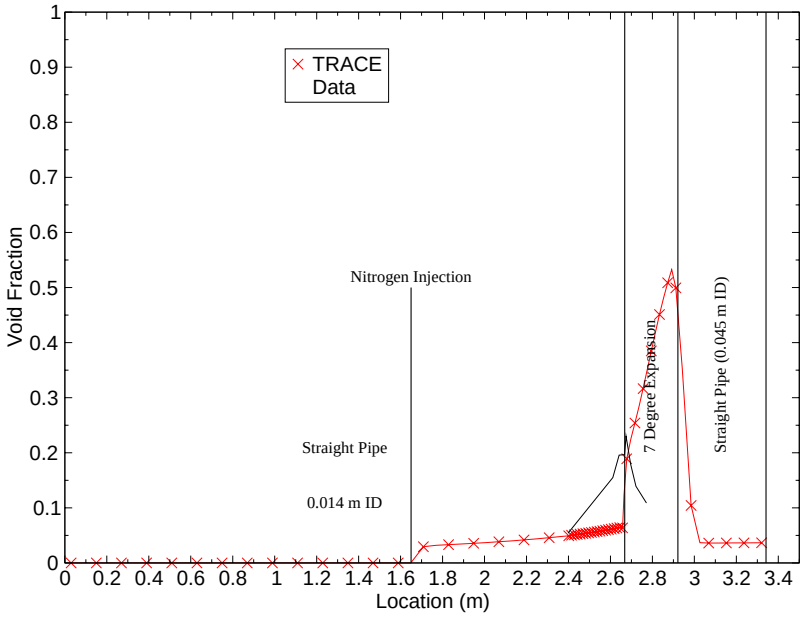

Figure B.2-6. Comparison Between Void Fraction Measurements and Code Predictions for Moby Dick Test 3174

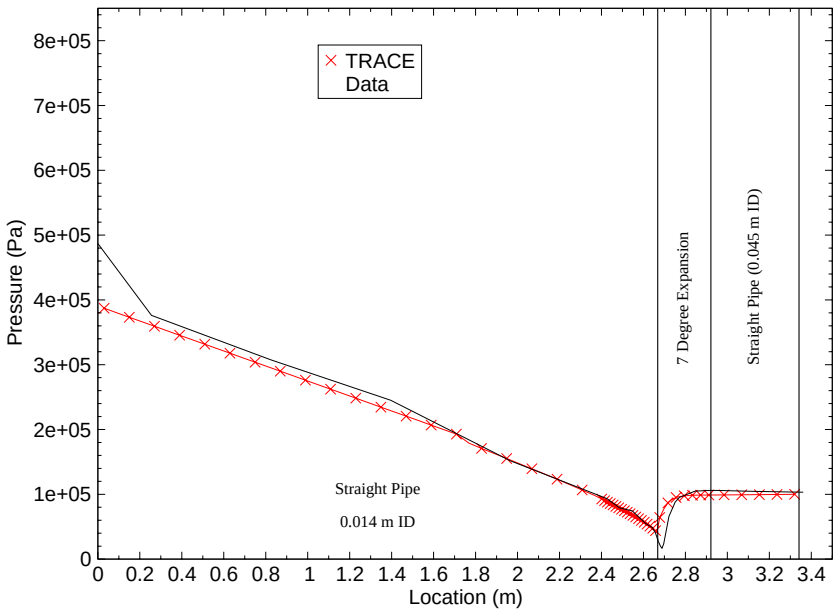

Figure B.2-7. Comparison Between Pressure Measurements and Code Predictions for Moby Dick Test 3177

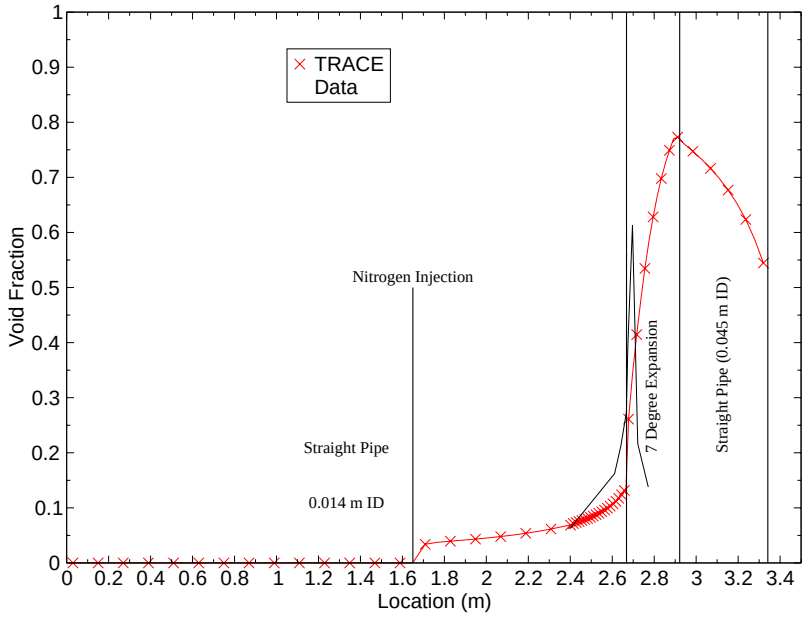

Figure B.2-8. Comparison Between Void Fraction Measurements and Code Predictions for Moby Dick Test 3177

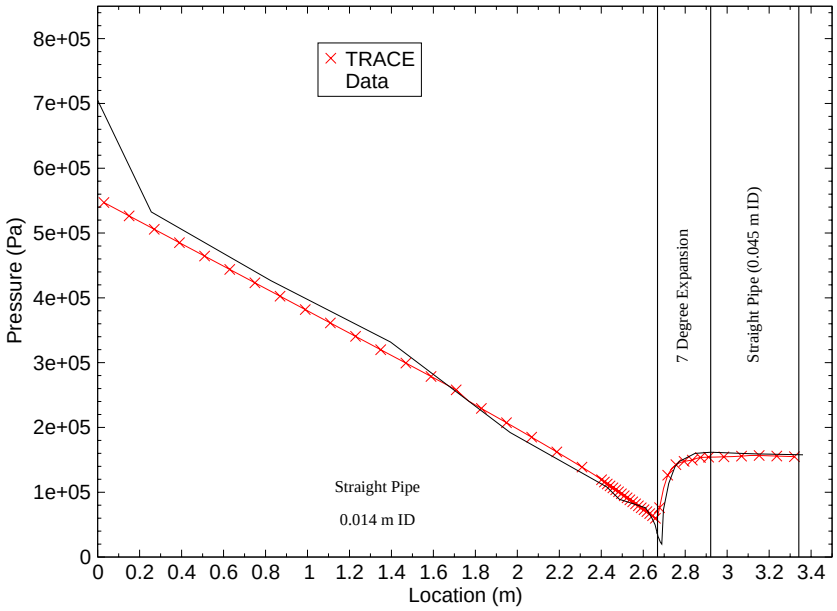

Figure B.2-9. Comparison Between Pressure Measurements and Code Predictions for Moby Dick Test 3167

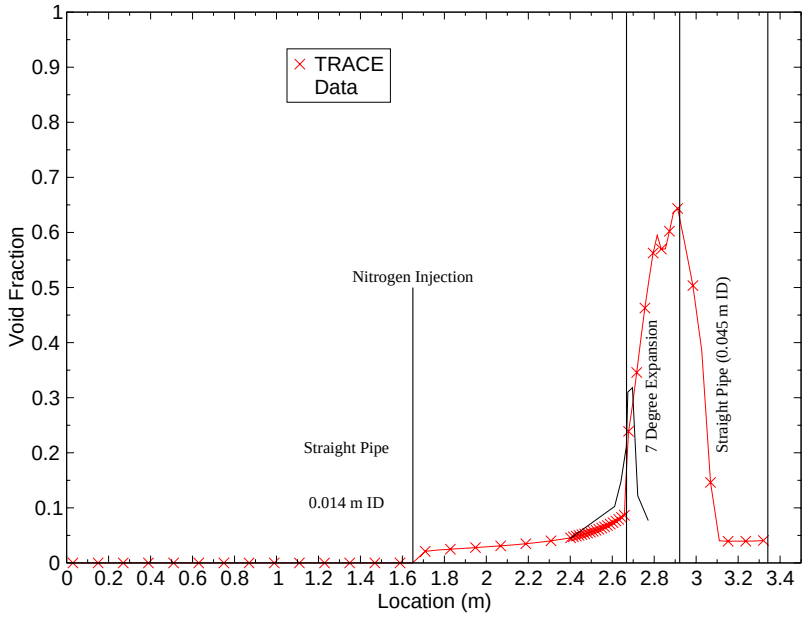

Figure B.2-10. Comparison Between Void Fraction Measurements and Code Predictions for Moby Dick Test 3167

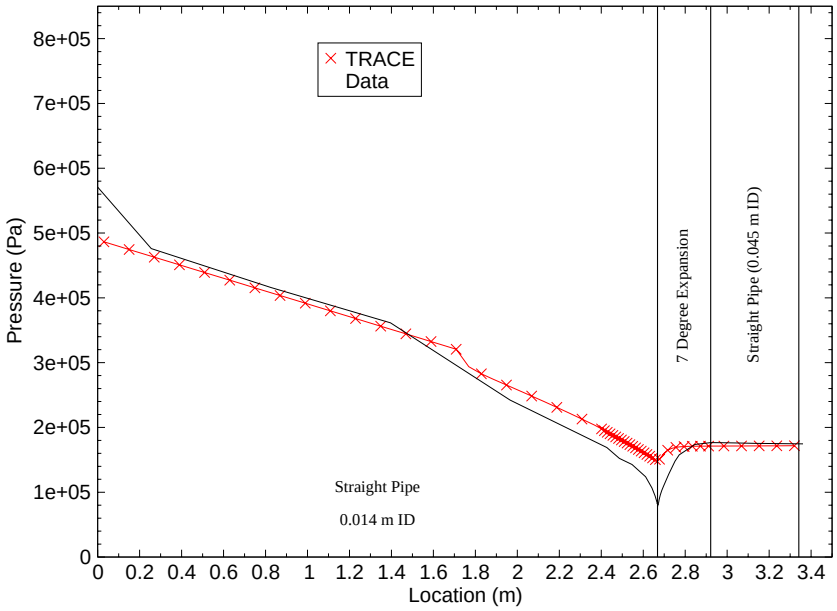

Figure B.2-11. Comparison Between Pressure Measurements and Code Predictions for Moby Dick Test 3087

B.2.4.2. Assessment of Tests With Critical Flow

This section discusses the analytical predictions and test observations for the five assessed tests which were determined to possess critical flow at the minimum flow area of the divergent nozzle in the Moby Dick test section.

Figure B.2-12, Figure B.2-14, and Figure B.2-16 show the comparison of pressure to measured data for tests 3030, 3052, and 3141. Test 3010 and 3151 do not run with this version of TRACE. The first three test results show that TRACE predicts the pressure gradient in the straight pipes before and after the divergent nozzle. Figure B.2-12 and Figure B.2-14 show that TRACE was unable to predict the pressure drop at the entrance to the divergent nozzle. Figure B.2-13 and Figure B.2-15 indicate that the TRACE void fraction predictions closely match measured test data at the nozzle entrance. TRACE over predicts the void fraction trends downstream of the start of the divergent section. Figure B.2-17 show the void fraction distribution predicted by TRACE for test 3141. No data is available for this test; however, the plot is shown for completeness. The pressure under prediction and the void over prediction in the nozzle is cased by a problem in the interfacial drag model. TRACE is predicting that the liquid velocity is greater than the vapor velocity which is causing a non-physical slip ratio.

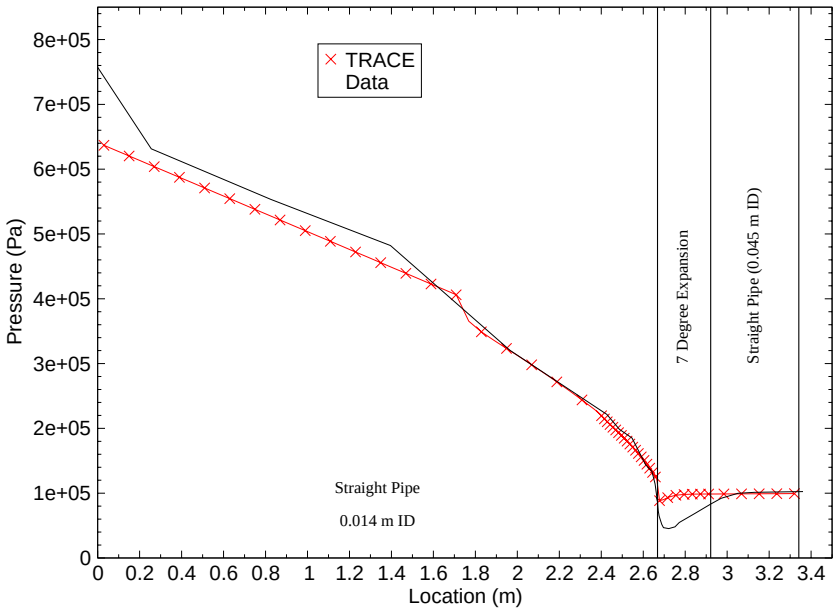

Figure B.2-12. Comparison Between Pressure Measurements and Code Predictions for Moby Dick Test 3030

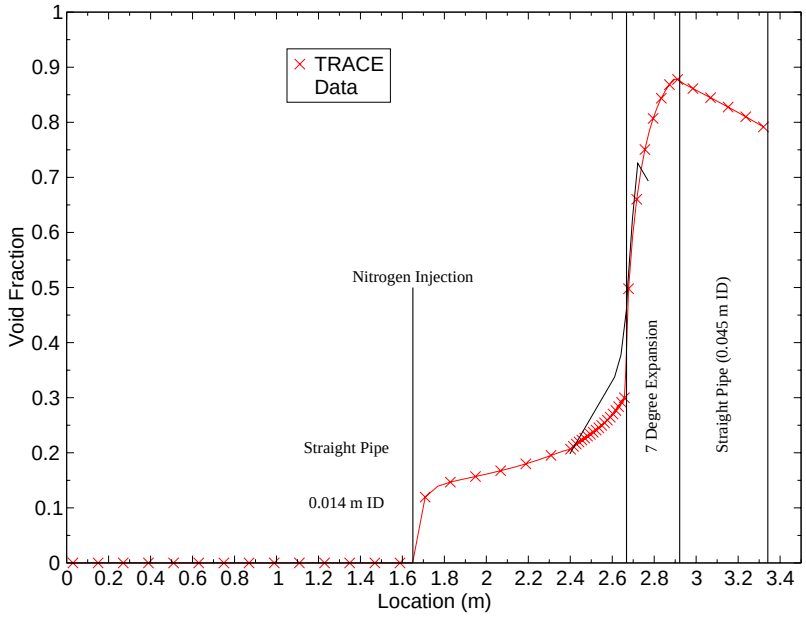

Figure B.2-13. Comparison Between Void Fraction Measurements and Code Predictions for Moby Dick Test 3030

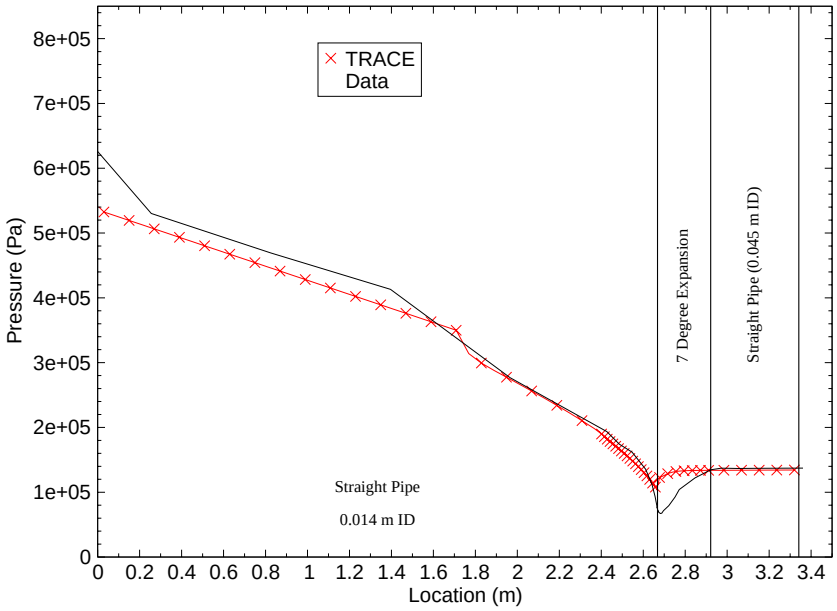

Figure B.2-14. Comparison Between Pressure Measurements and Code Predictions for Moby Dick Test 3052

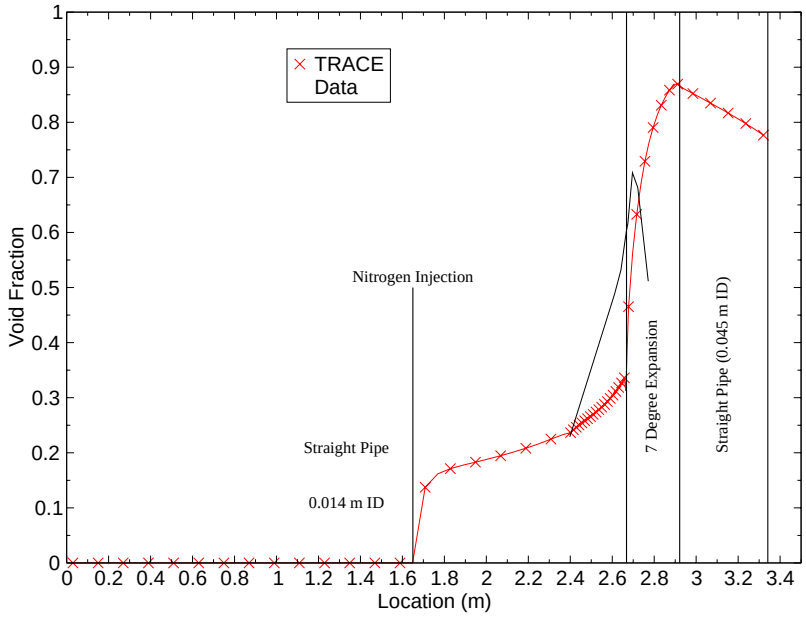

Figure B.2-15. Comparison Between Void Fraction Measurements and Code Predictions for Moby Dick Test 3052

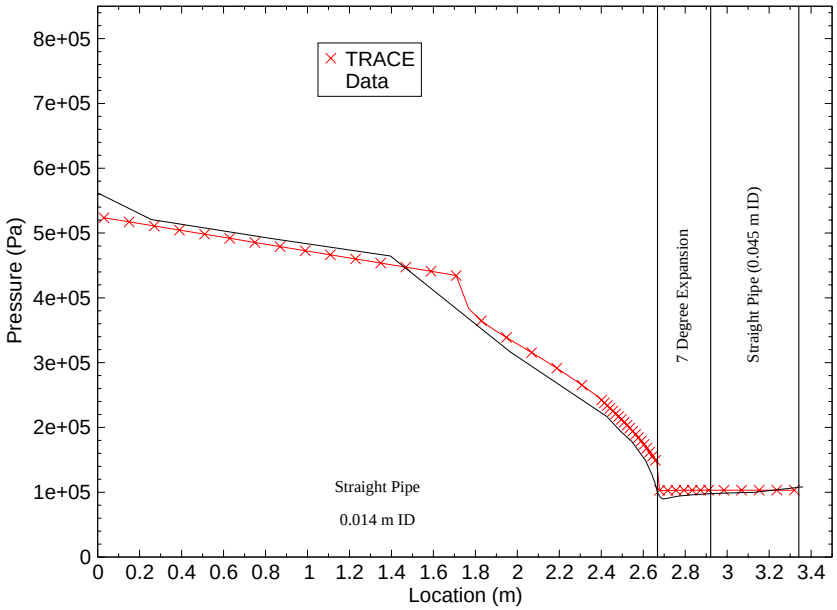

Figure B.2-16. Comparison Between Pressure Measurements and Code Predictions for Moby Dick Test 3141

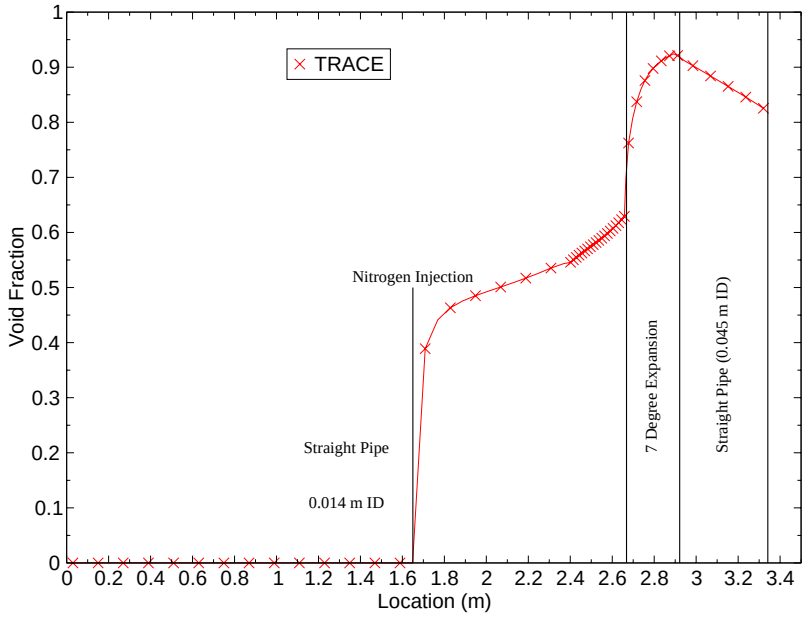

Figure B.2-17. Code Predicted Void Fraction for Moby Dick Test 3141

Table B.2.3 summarizes the system flowrates predicted by TRACE. This table also shows that TRACE did predict critical flow conditions at the minimum flow area at the start of the divergent nozzle for all of the tests that ran.

B.2.5. Assessment Results Summary

Table B.2.3 provides a summary of the comparisons between experimental measurements and TRACE predictions for the ten Moby Dick experiments studied in this assessment report. For the five test cases where critical flow was not expected, TRACE was unable to predict the pressure gradients at the divergent nozzle entrance. TRACE was also unable to accurately predict the flashing in the divergent nozzle.

TRACE was able to predict the pressure drop in the straight pipe before and after the divergent nozzle for the five tests where critical flow was expected. TRACE was unable to predict the pressure gradients at the divergent nozzle for these five tests. TRACE was unable to accurately predict the void fraction in the divergent nozzle, but was able to predict the mass flux at the minimum flow area at the start of the divergent nozzle for all of these test cases. TRACE did predict choked flow at the minimum flow area for all of the tests.

Table B.2.3. Table 4.3: Comparison Between Mass Flux Measurements and Predictions

Tests Without Critical Flow

	No N_2 Injection	With Nitrogen Injection			
Test	3170	3174	3177	3167	3087
Liquid Mass Flux ($kg/m^2/sec$)					
Data	17260	13280	13400	17110	12440
TRACE Predictions					
Choking	NA	NO	YES	YES	NO
Mass Flux	NA	13050	13648	17195	12537
$\frac{(\text{Mass Flux}_{calc} - \text{Mass Flux}_{data})}{\text{Mass Flux}_{data}}$	NA	-0.017	0.018	0.005	-0.008

Tests With Critical Flow

Test	3010	3030	3052	3141	3151
Liquid Mass Flux ($kg/m^2/sec$)					
Data	13550	14260	12530	7940	7110
TRACE Predictions					
Choking	NA	YES	YES	YES	NA
Mass Flux	NA	14999	13186	8418	NA
$\frac{(\text{Mass Flux}_{calc} - \text{Mass Flux}_{data})}{\text{Mass Flux}_{data}}$	NA	0.052	0.052	0.060	NA

B.2.6. References

1 "TRACE/FORTRAN 90 Theory Manual," U. S. Nuclear Regulatory Commission, NUREG/CR-6724, July 2001.

2 "Super Moby Dick Test Report 120B305C," USNRC Reactor Safety Data Bank, Office of Nuclear Regulatory Research.

3 "Flashing Flow," Rousseau, J. C., Multiphase Science and Technology, Volume 3, Hemisphere Publishing Corporation, 1987.

4 Handbook of Hydraulic Resistance, Idel'chik, I. E., U. S. Department of Commerce,

5 "Etude Experimentale d'Ecoulements Eau-Air a Grande Vitesse," Jeandey, C. and G. Barriere, CEA - Centre d'Edudes Nuclearires de Grenoble, Note T. T. Number 599, January 1997.

6 "Independent assessment of TRAC-PF1 (Version 7.0), RELAP5/Mod1 (Cycle 14), and TRAC-BD1 (Version 12.0) Codes Using Separate Effects Experiments", Saha P., J. H. Jo, L. Neymotin, U. S. Rohatgi, G. C. Slovik, and C Yuelys-Miksis, U. S. Nuclear Regulatory Commission, NUREG/CR-4359, August 1985.

B.3. Super Moby Dick Critical Flow Experiments

Author(s): Justin K. Watson, William J. Krotiuk

Affiliation: PennState ARL, NRC

Code Version: TRACE V5.0

Platform and Operating System: Intel x86, Windows XP

B.3.1. Introduction

The calculation of critical flow is an important consideration in the area of nuclear reactor safety. The fluid velocity at nozzles, breaks, or other restrictions can exceed the local sound speed which causes the fluid flow rate to become insensitive to downstream pressure changes. Of particular importance are choking conditions at pipe break locations where fluid at high pressure-temperature conditions is subjected to large decreases in pressure. In order to account for fluid choking effects, the TRACE computer code employs a one-dimensional critical flow model. The TRACE critical flow model comprises of three separate models; a subcooled liquid choked-flow model, a two-phase, two-component choked-flow model, and a single-phase vapor choked-flow model.

The subcooled liquid choked-flow model is based on the Burnell model. The subcooled liquid choked-flow model is used where subcooled liquid persists through the choking plane. The two-phase, two-component choked-flow model is based on first principals and calculates flow limitations for a two-phase fluid which can consist of two different fluids such as water and an inert-gas such as air. Finally, the single-phase vapor choked-flow model is based on the theory describing an isentropic expansion of an ideal-gas. The choking models employed by TRACE are more fully described in the TRACE Theory Manual (Ref. 1).

The objective of the Super Moby Dick Experiments, which were performed at the Centre d'Etudes Nucleaires de Grenoble in France, was to study steady-state critical flow in nozzles at medium to high pressure for various thermal-hydraulic conditions. TRACE was used to predict steady-state flow conditions for eight tests. Four of the tests simulate flow through a long divergent nozzle. The other four tests simulate flow through an abrupt expansion. The inlet pressure to the test section was about 12×10^6 Pa for six tests and about 4×10^6 Pa for the other two. Critical flow conditions were obtained by maintaining constant inlet conditions to the test section and lowering the downstream pressure until the drop in discharge pressure no longer influenced flow. Choked flow is defined to exist at that point. Pressures were measured at various points along the test section. Test data indicated a steady-state critical mass flux at the nozzle neck. Void fraction

measurements were available for one of the tests and density measurements were available for another.

B.3.2. Test Facility Description

The Super Moby Dick test facility's primary loop has four main components; a pump, a preheater, a test section, and a condenser (Figure B.3-1). Two different test sections are investigated in this assessment. The first nozzle consists of a smooth convergent section followed by a straight pipe with a constant cross section followed by a 6^{o} 57' diverging nozzle (Figure B.3-2). This test section is referred to as the "long nozzle" test in this assessment. The second nozzle is the same as the first except the diverging nozzle is replaced with a straight expansion (Figure B.3-3). This test section is referred to as the "abrupt expansion" test section in this assessment. Reference 2 supplies data for Test 120B305C which uses a long nozzle test section. Reference 3 provides data for several other tests which use a long nozzle test section or an abrupt expansion test section.

For each of the tests subcooled water is pumped vertically upward through the test section and is vented to the condenser. Critical flow conditions were obtained by maintaining constant inlet conditions to the test section and lowering the downstream pressure in the condenser until the drop in discharge pressure no longer influenced flow. Choked flow is defined to exist at that point.

B.3.2.1. The Long Nozzle Test Section

The long nozzle is a vertical stainless steel test section which consists of a smooth convergent section followed by a straight pipe with a constant cross section followed by a 6^{o} 57' diverging nozzle (Figure B.3-2). Table B.3.1 provides dimensions for the long nozzle test section. Pressures are measured at various points along the test section. Figure B.3-2 along with Table B.3.2 provide the data measurement identifications, locations and measured parameters for the long nozzle tests. This table also lists the equivalent measurement locations used for the data plots provided in this section. The pressure measurement accuracy is estimated to be ±20-kPa and the flow measurement accuracy is evaluated to be ±2-percent of the measured mass flux. The overall accuracy of the averaged density measurement is estimated to be ±2-percent.

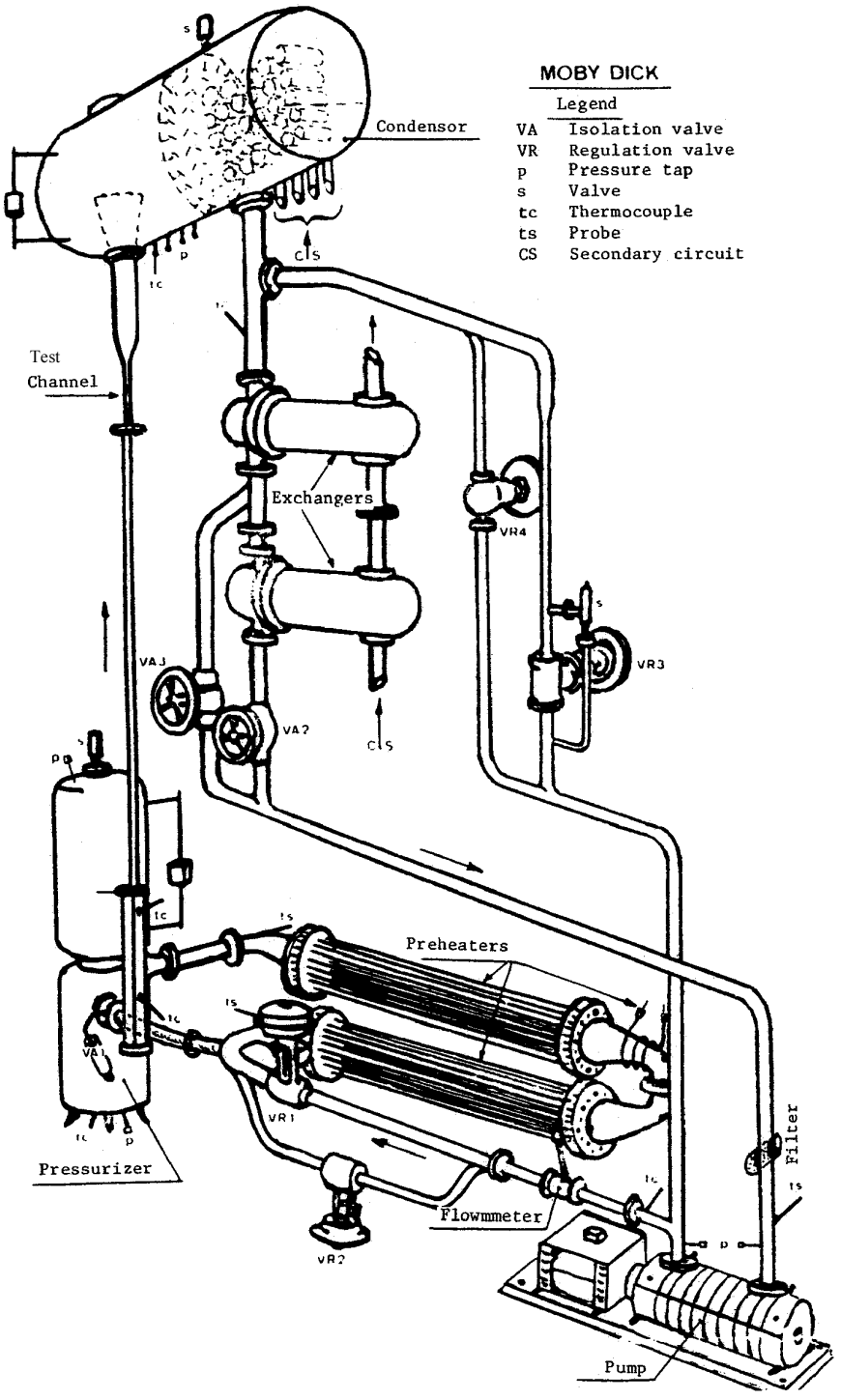

Figure B.3-1. Super Moby Dick Experimental Facility

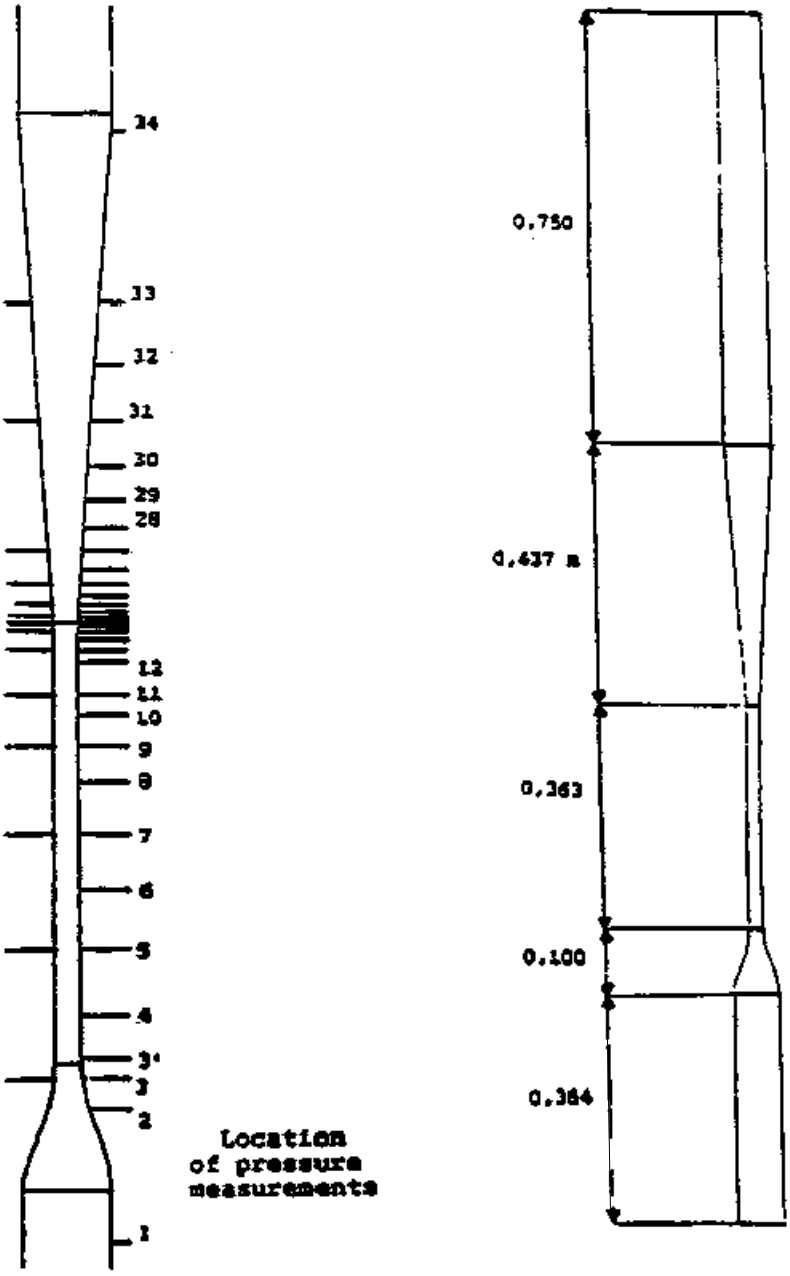

Figure B.3-2. Super Moby Dick Long Nozzle Test Section

Table B.3.1. Geometry for Super Moby Dick Long Nozzle Experiments

Geometry for Long Nozzle Test Section		
Straight Inlet Section	Length	0.364 m
	Internal Diameter	0.0667 m
Conical Convergent Nozzle	Length	0.1 m
Straight Neck Section	Length	0.363 m
	Internal Diameter	0.02013 m
Conical Divergent Section	Length	0.437 m
	Conical Divergent Angle	7^o
Straight Outlet Section	Length	0.75 m
	Internal Diameter	0.07359 (Calculated)

Table B.3.2. Data Measurement Identification and Locations for the Long Nozzle Tsets

Measurement Identification	**Measurement Location[a] (m)**	**Measured Parameter**	**Location on Plotting Axis (m)**
1	-0.5	Pressure	0.327
2	-0.397	Pressure	0.430
3	-0.372	Pressure, Density	0.455
3’	-0.358	Pressure	0.469
4	-0.322	Pressure	0.555
5	-0.272	Pressure, Density	0.653
7	-0.174	Pressure, Density	0.653
9	-0.104	Pressure, Density	0.723
11	-0.059	Pressure, Density	0.768
13	-0.032	Pressure, Density	0.795
15	-0.014	Pressure, Density	0.813
16	-0.008	Pressure	0.819
17	-0.004	Density	0.823
18	-0.002	Pressure	0.825
19	0.0[a].Top of straight nozzle section defined as the 0.0 meter location.	Pressure, Density	0.827
20	0.002	Pressure	0.829

Table B.3.2. Data Measurement Identification and Locations for the Long Nozzle Tsets

Measurement Identification	Measurement Location[a] (m)	Measured Parameter	Location on Plotting Axis (m)
21	0.004	Density	0.831
22	0.008	Pressure	0.835
23	0.014	Pressure, Density	0.841
25	0.032	Pressure, Density	0.859
27	0.059	Density	0.886
31	0.171	Pressure, Density	0.998
34	0.421	Pressure	1.248
Condenser	1.187	Pressure	1.248

a. Top of straight nozzle section defined as the 0.0 meter location.

B.3.2.2. The Abrupt Expansion Test Section

The abrupt Expansion is a vertical stainless steel test section which consists of a smooth convergent section followed by a straight pipe with a constant cross section followed by a straight expansion (Figure B.3-3). Table B.3.3 provides dimensions for the abrupt expansion test section. Figure B.3-3 along with Table B.3.4 show the pressure and density measurement identification numbers, their locations along the test section, and the corresponding location used for the analysis models and plots provided in this section. The estimated pressure measurement accuracy is ±20-kPa, the flow uncertainty is evaluated to be ±2-percent of the measured mass flux from 104 to 6.1x104 kg/m2/sec., and the overall accuracy of the averaged density measurement is estimated to be ±2-percent .

Table B.3.3. Geometry and Test Conditions for Super Moby Dick Abrupt Expansion Experiments

Geometry for Abrupt Test Section		
Straight Inlet Section	Length	0.3 m
	Internal Diameter	0.0875 m
Conical Convergent Nozzle	Length	0.1 m
Straight Neck Section	Length	0.4 m
	Internal Diameter	0.02005 m
Straight Outlet Section	Length	1.6 m
	Internal Diameter	0.135 m

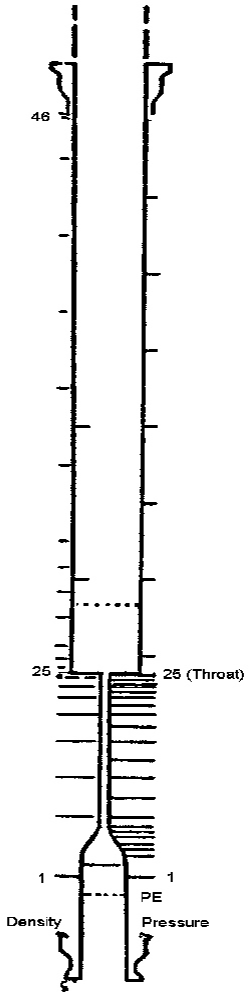

Figure B.3-3. Super Moby Dick Abrupt Expansion Test Section

Table B.3.4. Data Measurement Identification and Locations for the Abrupt Expansion Tests

Measurement Identification	Measurement Location[a] (m)	Measured Parameter	Location on Plotting Axis (m)
PE (Inlet)	-0.599	None	0.0
1	-0.529	Pressure, Density	0.070
2	-0.474	Pressure	0.125
3	-0.459	Pressure	0.104

Table B.3.4. Data Measurement Identification and Locations for the Abrupt Expansion Tests

Measurement Identification	Measurement Location[a] (m)	Measured Parameter	Location on Plotting Axis (m)
4	-0.444	Pressure	0.155
5	-0.429	Pressure	0.170
6	-0.414	Pressure	0.185
7	-0.399	Pressure	0.200
8	0.390	Pressure	0.209
9	-0.374	Pressure, Density	0.225
10	-0.324	Pressure	0.275
11	-0.274	Pressure, Density	0.325
12	-0.224	Pressure	0.375
13	-0.174	Pressure, Density	0.425
14	-0.134	Pressure	0.465
15	-0.104	Pressure, Density	0.495
16	-0.079	Pressure	0.520
17	-0.059	Pressure, Density	0.540
18	-0.044	Pressure	0.555
19	-0.032	Pressure, Density	0.567
20	-0.022	Pressure	0.577
21	-0.014	Pressure	0.585
22	-0.008	Pressure	0.591
23	-0.004	Pressure, Density	0.595
24	-0.002	Pressure	0.597
25 (Expansion)	0.0[a]	None	0.599
26	0.005	Density	0.604
27	0.020	Density	0.619
28	0.040	Density	0.639
30	0.080	Density	0.679
31	0.150	Density	0.749
32	0.213	Density	0.812
33	0.251	Pressure	0.850
34	0.278	Density	0.877
35	0.348	Density	0.947
37	0.548	Density	1.147
39	0.748	Density	1.347
41	0.948	Density	1.547

Table B.3.4. Data Measurement Identification and Locations for the Abrupt Expansion Tests

Measurement Identification	Measurement Location[a] (m)	Measured Parameter	Location on Plotting Axis (m)
43	1.149	Density	1.748
45	1.349	Density	1.948

a. Expansion Location is defined at the 0.0 meter location.

B.3.3. TRACE Model Description

The TRACE model for both the long nozzle and the abrupt expansion tests include 3 components. A BREAK component is used to specify the test section inlet conditions. A single PIPE component is used to represent the entire test section. A BREAK component is also used to represent the condenser. Figure B.3-4 and Figure B.3-5 show the TRACE schematics of the models used for the long nozzle and abrupt expansion test section. The length for the control volumes in the straight sections are set approximately equal to the diameter. The control volume length for the converging and diverging sections are defined to accommodate gradual volume changes. Irreversible pressure drop loss coefficient for the convergent nozzle and the conical divergent section were obtained from Reference 4.

B.3.4. Tests Simulated with TRACE

A series of 30 tests were performed at the Super Moby Dick test facility. Three different test sections were used with different initial pressure and temperature conditions. Eight of these tests have been analyzed using TRACE. Four of them from the tests with the long nozzle and four from the tests with the abrupt expansion. Table B.3.5 shows the upstream temperature and pressure, the down stream pressure, and the mass flux at the nozzle for each of the tests selected for this analysis.

B.3.4.1. Simulation of Super Moby Dick Long Nozzle Experiment.

Figure B.3-6, Figure B.3-8, Figure B.3-9 and Figure B.3-10 show comparisons between the steady-state pressures calculated using the TRACE and the pressure measurements for the four tests listed in Table B.3.5. Figure B.3-7 provides a comparison between the TRACE predictions and the measurements for void fraction for Test 40B240C provided in Reference 3.

Figure B.3-7 shows that TRACE over predicts the void fraction in the straight pipe region upstream of the expansion. This corresponds to the prediction of pressures lower than measured in the two-phase region shown in Figure B.3-6. Figure B.3-8, Figure B.3-9 and Figure B.3-10

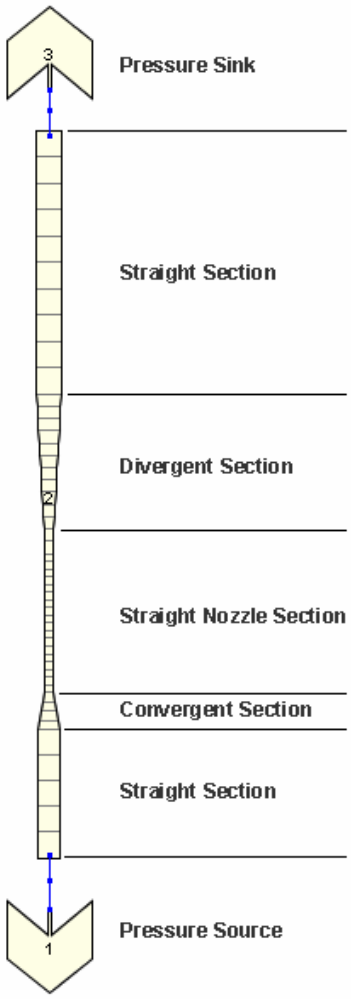

Figure B.3-4. TRACE Analysis Model of Long Test Nozzle for the Super Moby Dick Experiments

show similar results. TRACE does not accurately predict the pressure drop in the straight pipe where flashing is occurring.

Table B.3.6 provides a comparison between the measured and calculated mass flux through the test nozzle. For example, the measured mass flux at the convergent nozzle neck for Test 120B305C was 62200 kg/m^2/sec. The TRACE code calculated a steady-state flow of 19.32 kg/sec. which corresponds to a mass flux of 60697 kg/m^2/sec. at the 0.02013 m diameter nozzle neck. TRACE did not calculate critical flow at the convergent nozzle neck for cases 40B240C and 120B305C at the original choked flow location. The choking face was moved one face downstream into the neck where choking was observed. The TRACE calculated mass flux shows

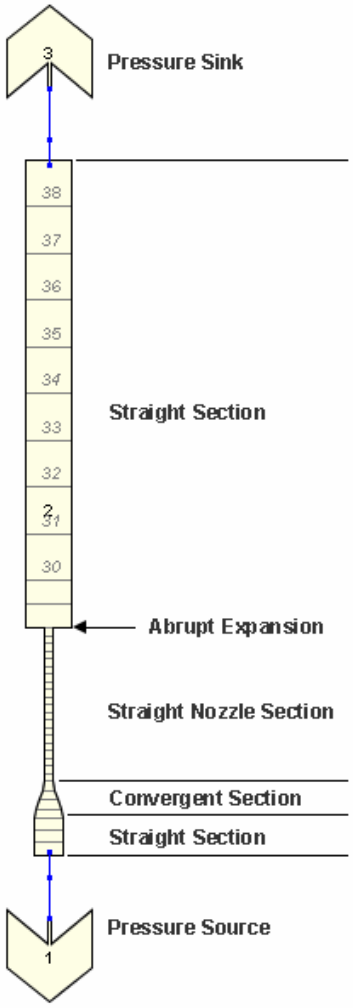

Figure B.3-5. TRACE Analysis Model for Super Moby Dick Abrupt Expansion Experiments

good agreement with the experimental data for all tests except 119B319. No test is below the reported measurement accuracy of ± 2%.

Table B.3.5. Operating Conditions for the Long Nozzle Tests and the Abrupt Expansion Tests

Long Nozzle Tests				
Test	40B240C	120B305C	119B319	119B324C
Upstream Temperature (^oC)	240.5	305.7	319.2	324.6
Upstream Pressure (Pa)	$40x10^6$	$12.006x10^6$	$11.995x10^6$	$11.992x10^6$
Downstream Pressure (Pa)	$2.311x10^6$	$7.678x10^6$	$8.038x10^6$	$8.327x10^6$
Mass Flux at Neck ($kg/m^2/sec$)	32800	62200	48200	40900
Abrupt Expansion Tests				
Test	40J227	120EB305	120EB319	120EB324
Upstream Temperature (^oC)	226.6	304.8	312.2	323.6
Upstream Pressure (Pa)	$4.005x10^6$	$11.885x10^6$	$12.013x10^6$	$11.998x10^6$
Downstream Pressure (Pa)	$1.709x10^6$	$6.866x10^6$	$6.979x10^6$	$8.810x10^6$
Mass Flux at Neck ($kg/m^2/sec$)	46300	61800	47100	41600

Table B.3.6. Measured and Calculated Mass Flux Comparisons for Long Nozzle Tests

Test	**40B240C**	**120B305C**	**119B319**	**119B324C**
Critical Mass Flux ($kg/m^2/sec.$)				
Data (Accuracy $\pm$2%	32800	62200	48200	40900
TRACE Calculated	30009	62582	57587	43952
Critical Flow Predicted	YES	YES	YES	YES
$\frac{(\text{Mass Flux}_{calc} - \text{Mass Flux}_{data})}{\text{Mass Flux}_{data}}$				
TRACE	-0.085	-0.006	0.195	0.074

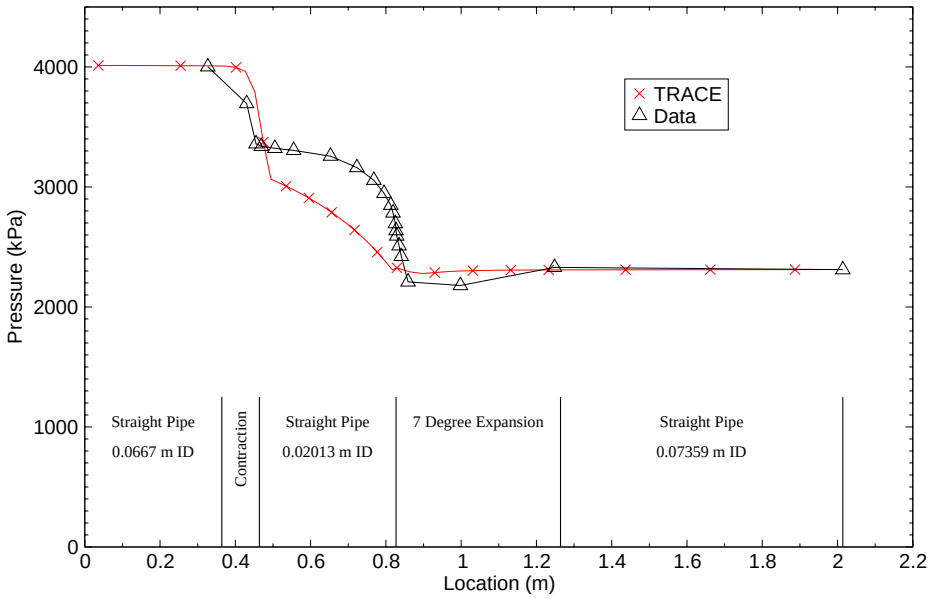

Figure B.3-6. Comparison Between Pressure Measurements and Code Predictions for Test 40B240C

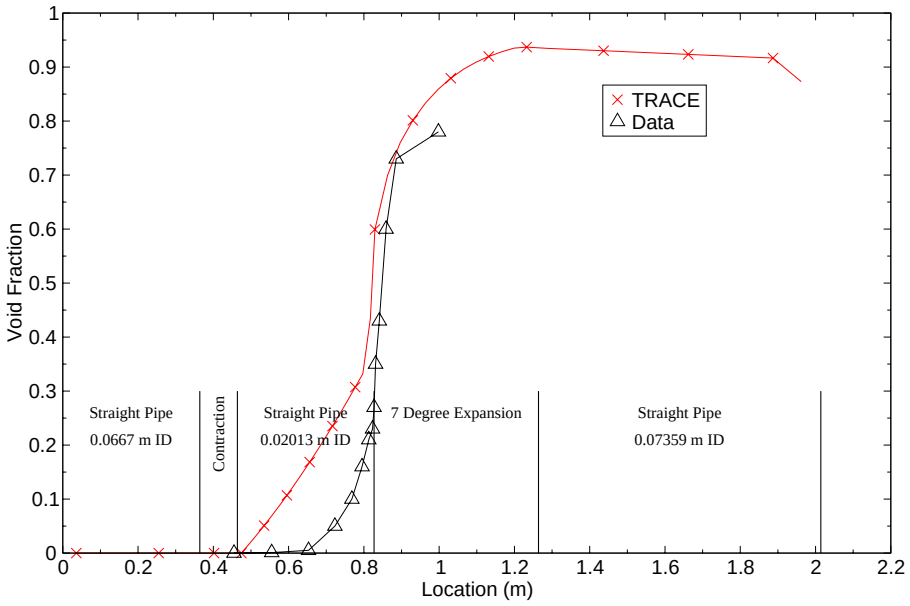

Figure B.3-7. Comparison Between Void Fraction Measurements and Code Predictions for Test 40B240C

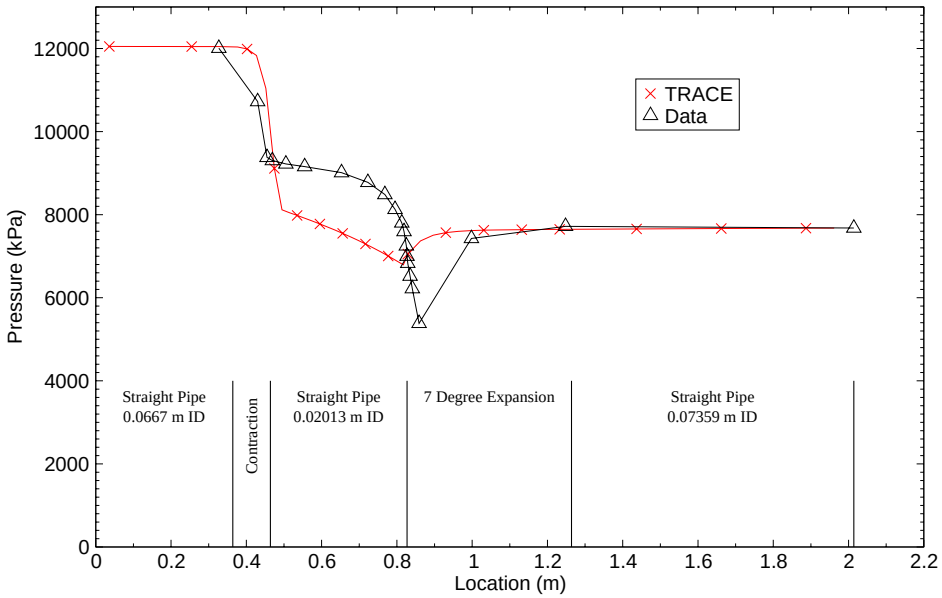

Figure B.3-8. Comparison Between Pressure Measurements and Code Predictions for Test 120B305C

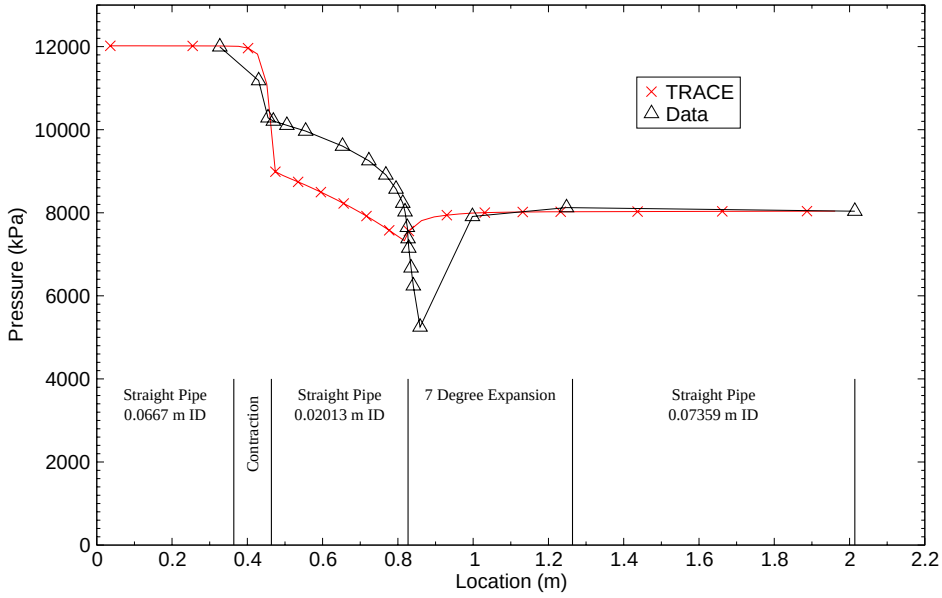

Figure B.3-9. Comparison Between Pressure Measurements and Code Predictions for Test 119B319

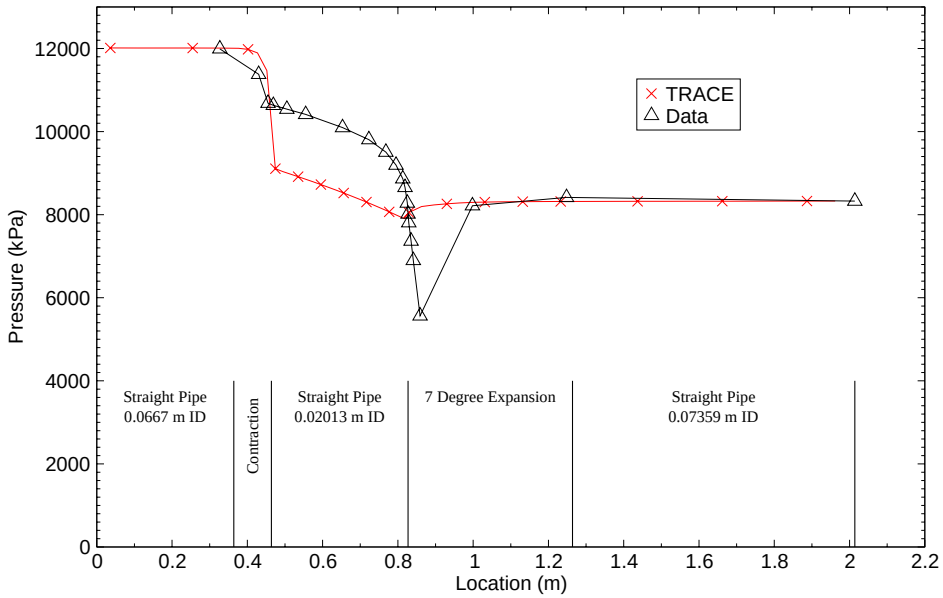

Figure B.3-10. Comparison Between Pressure Measurements and Code Predictions for Test 119B324C

B.3.4.2. Simulation of Super Moby Dick Abrupt Expansion Experiment.

Figure B.3-11, Figure B.3-13, Figure B.3-14 and Figure B.3-15 provide a comparison between measured pressure and pressure predictions calculated by the TRACE for the tests listed in Table B.3.7. Figure B.3-12 compares density measurements and code predictions for Test 40J227.

In all four test cases TRACE predicts lower pressures in the straight section of the pipe upstream of the abrupt expansion. Test 40J227 is the only test where TRACE accurately predicts the pressure at the convergent nozzle neck. TRACE was also unable to predict critical flow conditions in tests 40J227, 120EB305, and 120EB319. The choking face was moved one face downstream into the neck where choking was observed for test 120EB305 and 120EB319. Table B.3.7 provides a comparison between the measured and calculated mass flux through the test nozzle. The TRACE calculated mass flux shows good agreement with the experimental data for all tests. Test 120EB305 is below the reported measurement accuracy of ± 2%.

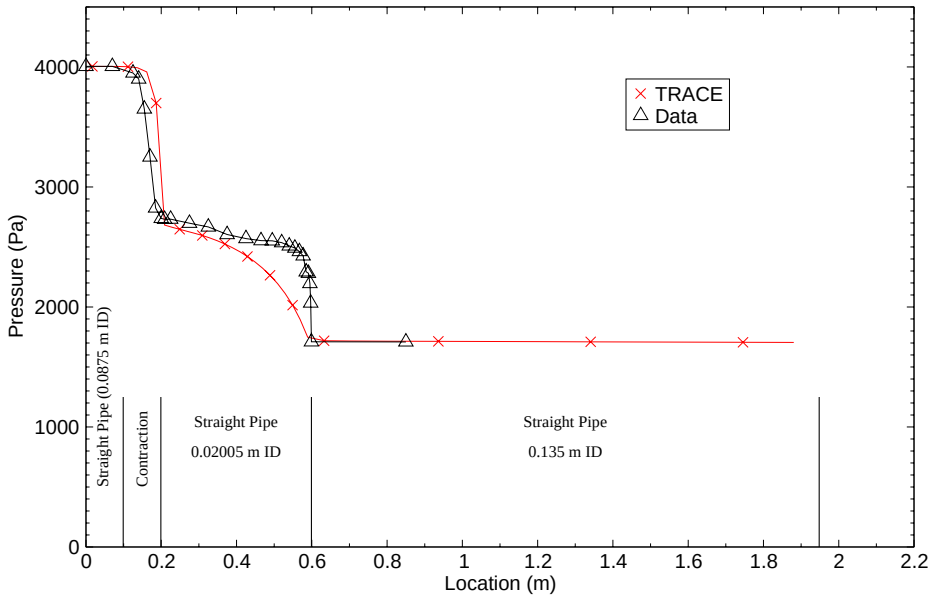

Figure B.3-11. Comparison Between Pressure Measurements and Code Predictions for Test 40J227

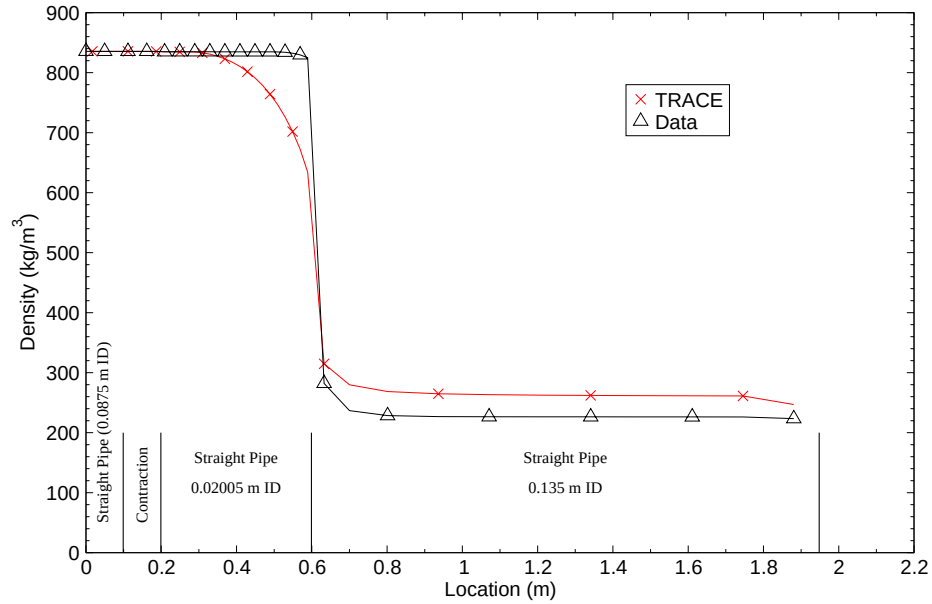

Figure B.3-12. Comparison Between Density Measurements and Code Predictions for Test 40J227

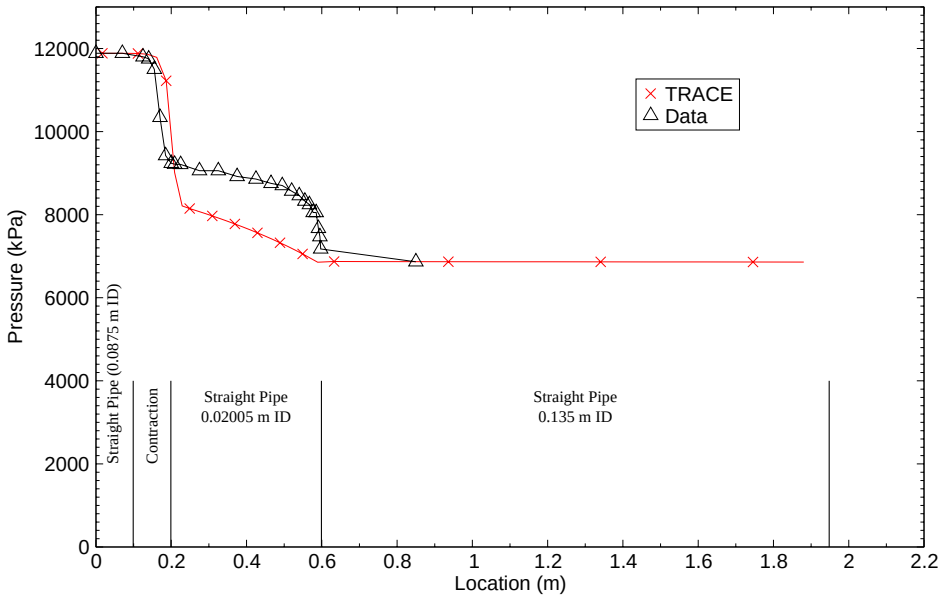

Figure B.3-13. Comparison Between Pressure Measurements and Code Predictions for Test 120EB305

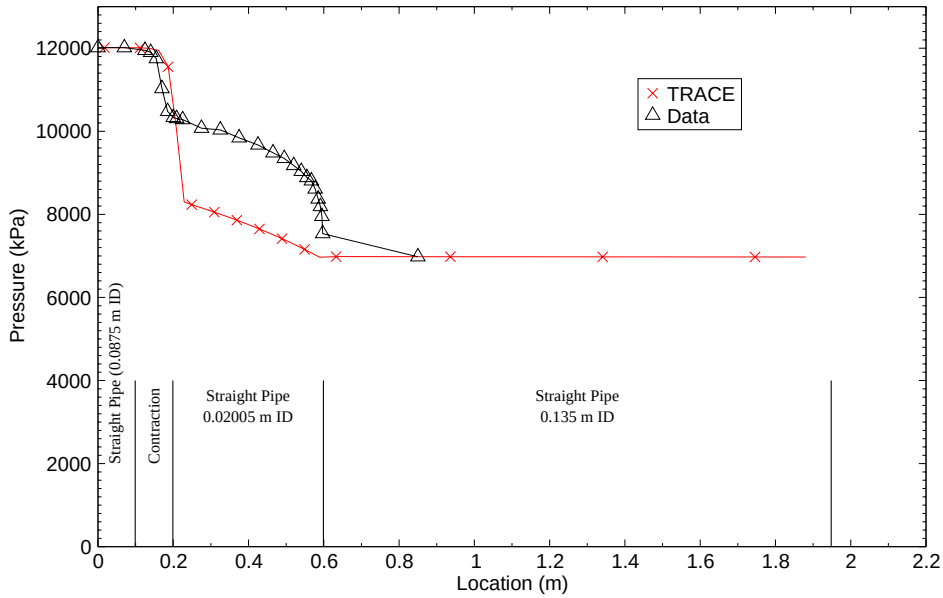

Figure B.3-14. Comparison Between Pressure Measurements and Code Predictions for Test 120EB319

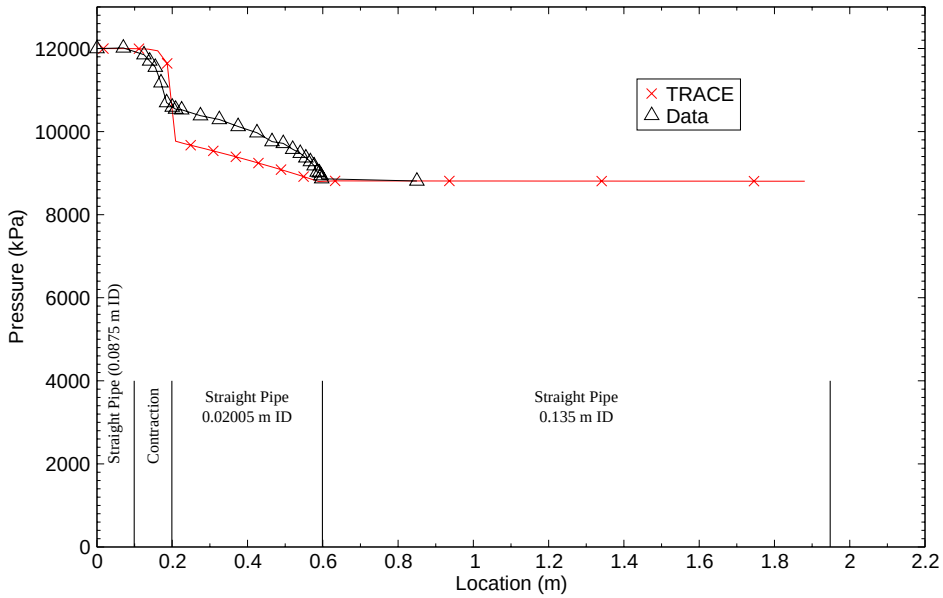

Figure B.3-15. Comparison Between Pressure Measurements and Code Predictions for Test 120EB324

Table B.3.7. Measured and Calculated Mass Flux Comparisons for Abrupt Expansion Tests

Test	**40J227**	**120EB305**	**120EB319**	**120EB324‘**
Critical Mass Flux ($kg/m^2/sec.$)				
Data (Accuracy ± 2%	46300	61800	47100	41600
TRACE Calculated	44979	61197	50871	43205
Critical Flow Predicted	NO	YES	YES	YES
$\frac{(\text{Mass Flux}_{calc} - \text{Mass Flux}_{data})}{\text{Mass Flux}_{data}}$				
TRACE	-0.028	-0.009	0.080	0.039

B.3.5. Assessment Results Summary

Table B.3.8 provides a summary of the comparisons between experimental measurements and TRACE predictions for the eight Super Moby Dick experiments studied in this assessment report. In general, TRACE does not accurately predict critical flow conditions for these test cases. TRACE was unable to predict critical flow at the convergent nozzle neck for one of the eight cases. TRACE consistently predicted lower pressures in the straight test section just upstream of the divergent nozzle or abrupt expansion. For one test case TRACE did predict the critical mass flux within the measurement uncertainty.

Table B.3.8. Comparisons Between Critical Flowrate Measurements and Code Predictions for the Super Moby dick Experiments

Tests With Long Divergent Nozzle				
Test	40B240C	120B305C	119B319	119B324C
Test Section ID (m)	0.02013	0.02013	0.02013	0.02013
Type of Critical Flow	Two-Phase Flashing	Two-Phase Flashing	Two-Phase Flashing	Two-Phase Flashing
Nozzle Pressure (Pa)				
Data Point 16 (Accuracy ±20 kPa)	2.784×10^6	7.593×10^6	8.024×10^6	8.655×10^6
TRACE Calc. Vol. 27	2.308×10^6	6.793×10^6	7.325×10^6	7.904×10^6
Nozzle Void Fraction				
Data Points 15/17	0.21/0.23	NA	NA	NA
TRACE Calc. Vol. 27	0.45	0.23	0.29	0.34
Mass Flux ($kg/m^2/sec.$)				
Data (Accuracy ±2%)	32800	62200	48200	40900
TRACE Calculated	30009	62582	57587	43952
$\frac{(\text{Mass Flux}_{calc} - \text{Mass Flux}_{data})}{\text{Mass Flux}_{data}}$				
TRACE	-0.085	-0.006	0.195	0.074
Tests With Abrupt Expansion				
Test	40J227	120EB305	120EB319	120EB324
Test Section ID (m)	0.02005	0.02005	0.02005	0.02005
Type of Critical Flow	Two-Phase Flashing	Two-Phase Flashing	Two-Phase Flashing	Two-Phase Flashing
Nozzle Pressure (Pa)				
Data Point 22 (Accuracy ±20 kPa)	2.281×10^6	7.669×10^6	8.190×10^6	9.008×10^6
TRACE Calc. Vol. 27	1.748×10^6	6.860×10^6	6.986×10^6	8.798×10^6

Table B.3.8. Comparisons Between Critical Flowrate Measurements and Code Predictions for the Super Moby dick Experiments

Nozzle Density (kg/m^3) Data Point 23 (Accuracy ±2%) TRACE Calc. Vol. 27	770 835	NA 707	NA 695	NA 668
Nozzle Void Fraction TRACE Calc. Vol. 27	0.24	0.138	0.214	0.206
Mass Flux ($kg/m^2/sec.$) Data (Accuracy ±2%) TRACE Calculated	46300 44979	61800 61197	47100 50871	41600 43205
$\frac{(\text{Mass Flux}_{calc} - \text{Mass Flux}_{data})}{\text{Mass Flux}_{data}}$ TRACE	-0.028	-0.009	0.080	0.039

B.3.6. References

1 "TRACE/FORTRAN 90 Theory Manual," U. S. Nuclear Regulatory Commission, NUREG/CR-6724, July 2001.

2 "Super Moby Dick Test Report 120B305C," USNRC Reactor Safety Data Bank, Office of Nuclear Regulatory Research.

3 "Flashing Flow," Rousseau, J. C., Multiphase Science and Technology, Volume 3, Hemisphere Publishing Corporation, 1987.

4 Handbook of Hydraulic Resistance, Idel'chik, I. E., U. S. Department of Commerce,

ECC Bypass Tests

B.4. UPTF ECC Bypass Tests

Authors: Jae Hoon Jeong [1], Chang Wook Huh [2], Ahn Dong Shin [3]

Affilation: Korea Nuclear Fuel Co., Ltd[1], Korea Institute of Nuclear Safety[2, 3]

Code Version: TRACE V5.0

Platform and Operation System: Intel x86, Windows XP

B.4.1. Introduction

In a hypothetical cold leg large break loss of coolant accident (LOCA) in a PWR, most of the initial reactor coolant inventory is rapidly expelled through the break and the pressure of the primary system decreases causing most of the liquid inventory to flash into steam. When the pressure has decreased below the accumulator setpoint, emergency core cooling (ECC) begins to be injected into the Reactor Coolant System (RCS). The purpose of the ECC injection is to rapidly refill the reactor vessel lower plenum and to reflood the reactor core. During the early part of blowdown, steam flows up the downcomer and out through the broken cold leg nozzle. This steam upflow prevents the ECC from penetrating the downcomer and refilling the lower plenum. The upflow of steam in the downcomer can entrain some or all of the ECC-water out the broken cold leg. This counter-current flow of steam and water in the downcomer is referred to as ECC bypass and is important because it determines how quickly the lower plenum refills. Rapid refilling of the lower plenum leads to a lower peak cladding temperature. As blowdown proceeds and the steam flow decreases, the bypass flow also decreases and ultimately the ECC is fully delivered to the lower plenum.

The Upper Plenum Test Facility (UPTF) (Ref. 1), was part of the international 2D/3D project, and was used to provide experimental data on thermal hydraulic steam/water behavior in the upper plenum, loops, and downcomer during end-of-blowdown, refill and reflood phases after LOCA. As part of the UPTF test matrix, Test 5, 6, 7 and 21 series were run as downcomer separate effects tests (SET), simulating cold leg breaks with either cold leg ECC injection (Test 5, 6, and 7) or downcomer ECC injection (Test 21).

UPTF Tests 5, 6, 7, and 21 were steady state, separate effects simulations of the counter-current flow which would occur during the end-of-blowdown and the refill phase of a LOCA. In these tests, counter-current flow in the downcomer was established by injecting single-phase steam through the core simulator while ECC flow was injected into the cold leg. These tests were

conducted to determine downcomer flooding characteristics. The four major parameters of interest were steam flow rate, ECC injection flow rate, ECC subcooling, and ECC injection location (i.e., the intact cold leg near the break or far away from the break). For UPTF Tests 5, 6, and 7, steam flow rates ranged from 30 to 440 kg/s, while the ECC injection rate per loop was either 490 or 735 kg/s. Four combinations of ECC injection locations were used, and the ECC subcooling ranged from 5 to 121 ^{o}C. Test configuration and conditions of UPTF Test 21 (Run 272) were similar to those of Test 5 except for the ECC injection location. Test 21 simulated direct downcomer injection through the two direct vessel injection (DVI) nozzles, while Test 5 used ECC injection into the cold legs.

In order to assess the TRACE code's ability to predict rates of ECC penetration into the lower plenum, simulations of UPTF Test 5, 6, 7 and 21 have been carried out with TRACE V5.0.

B.4.2. UPTF Test Facility Description

The UPTF facility was a full-scale representation of a 3900 MWt four-loop PWR. One of the four primary loops could simulate a hot leg (HL) or cold leg (CL) break (i.e., 3 intact loops and 1 broken loop). The facility contained all major components with the exception of the nuclear core, active pumps, steam generators (SG), and containment. The core, coolant pumps, steam generators, and containment were replaced by simulators to account for the thermal hydraulic behavior in these components during a large break LOCA. To evaluate different LOCA scenarios, the facility could simulate thermal hydraulic phenomena which could occur during the end-of-blowdown, refill, and reflood time period for breaks in the hot leg or cold leg with break sizes ranging from 0.25 to 2 times the pipe cross sectional area. The UPTF test facility had four reactor coolant loops, each containing a steam/water separator and variable flow resistance, to simulate the steam generators and reactor coolant pumps, respectively. The UPTF downcomer was a 0.25 m wide annulus formed by the 4.87 m diameter vessel wall and core barrel. This provided a flow area of 3.63 m^2. Four 0.75 m diameter cold leg nozzles were located 9.12 m above the bottom of the vessel and 6.64 m above the bottom of the downcomer skirt in a 45^{o} x 135^{o} circumferential spacing. An overview of the test facility and its major dimensions are shown in Figure B.4-1 and Figure B.4-2 A flow diagram of the facility is shown in Figure B.4-3. The vessel and its internals are shown in Figure B.4-4. The main components of UPTF are described below;

Test Vessel and Internals

The dimensions of the UPTF test vessel were nearly identical to the reactor vessel of the reference PWR except that the wall thickness was reduced to correspond to the necessary operating pressure loading. Penetrations were provided for instrumentation. The vessel internals consisted of the lower plenum internals, core simulator, dummy fuel assemblies, and upper plenum internals.

The core region contained the core simulator and 193 quarter-length dummy fuel assemblies with end boxes. The steam produced in an actual core was simulated by the core simulator. The core

simulator consisted of 17 injection pipes (17 zones) for both steam and water injection. These injection pipes subdivided into 193 steam/water injection nozzles, one below each dummy fuel assembly. Each of the injection zones had a separate injection control valve to simulate a lateral distribution of steam flow rates resulting from various local core power. Total flow capacities were 360 kg/s of steam.

The upper plenum had actual reactor dimensions and contained 61 control rod guide tubes and 16 support columns. Eight vent valves were mounted in the core barrel above the hot leg nozzle elevation for simulation of ABB and B&W PWRs. The vent valves could be locked or unlocked depending on the type of test.

Steam Generator Simulators

Each of the three intact loops contained a steam generator simulator to simulate a PWR steam generator. They were designed to measure water carried into the simulators and simulate the steam generator response to carryover while preserving the flow resistance of the reference steam generators. Water carryover was measured by separating the water from the steam flow using a set of 31 two-stage cyclone separators. A steam mass flow equivalent to the measured water entrainment could be injected into the simulator to simulate the thermal response of a PWR steam generator.

Steam/Water Separators

Steam/water separators were located in the hot and cold legs of the broken loop. They were configured similar to the steam generator simulators, except that the dimensions were adjusted to account for the larger mass flows expected in the broken loop.

Emergency Core Cooling System (ECCS)

The ECC injection systems were simulated using accumulators. There were a total of 4 accumulators; two with a capacity of 150 m^3 and two with a capacity of 125 m^3 each. Two of these could be used alternatively as nitrogen accumulators for simulation of accumulator nitrogen release.

Pump Simulators

UPTF simulated the flow resistance and key internal heights of a reactor pump with manually adjustable valves installed in each loop between the pump seal and the cold leg injection port.

Containment Simulator

The containment simulator was designed to simulate the containment pressure history following a LOCA in the PWR. It was divided into an upper dry well of about 500 m^3 and a wet well of about 1000 m^3. Vent pipes routed steam from the dry well into the water pool of the wet well, where it condensed.

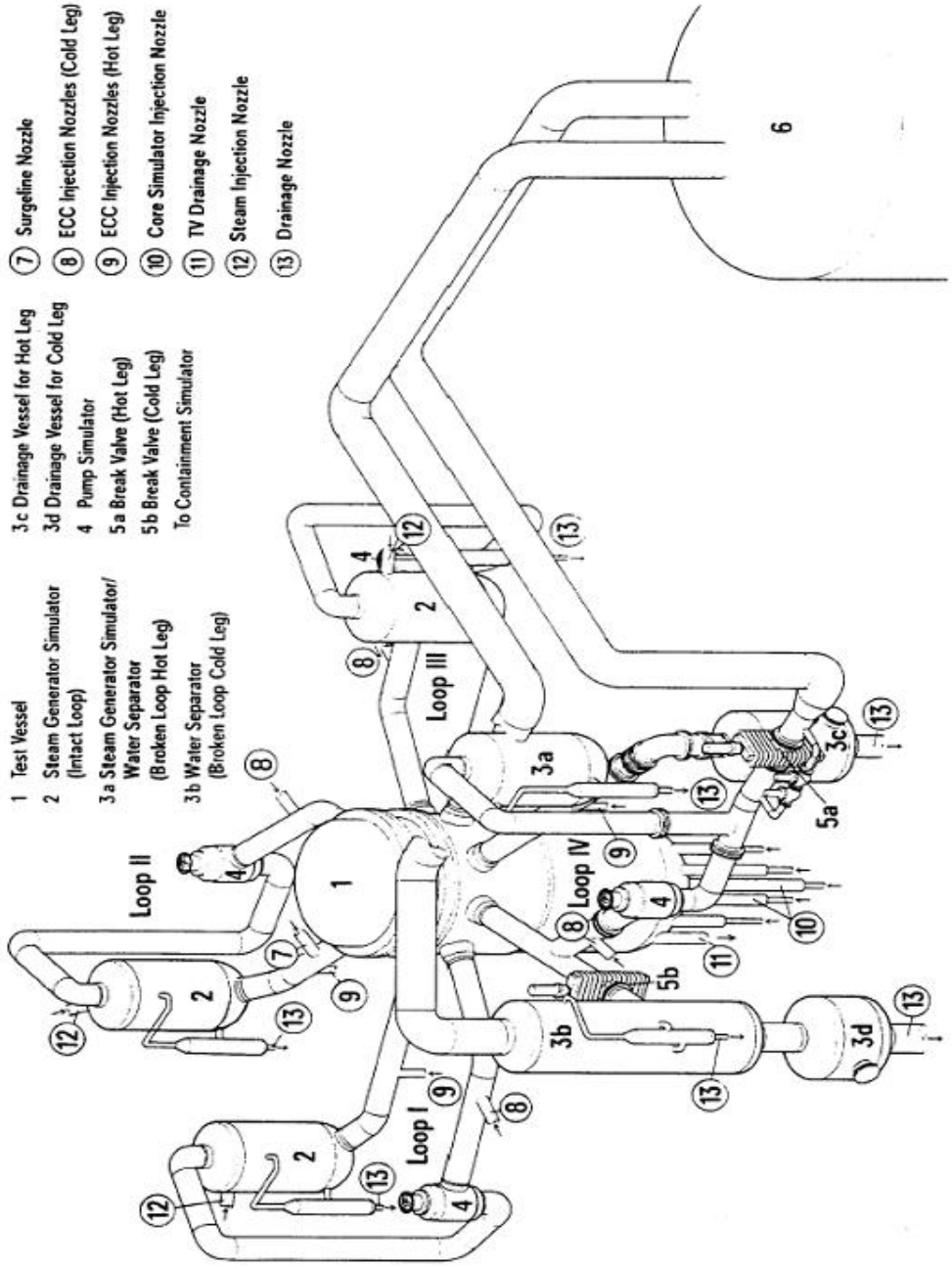

Figure B.4-1. Overview of UPTF Test Facility

B.4.3. TRACE Model Description

Noding diagrams for the TRACE model of the UPTF vessel are shown in Figure B.4-5 through Figure B.4-7. For UPTF Test 5, 6, and 7, the vessel is modeled with a VESSEL component with 13 axial levels, 8 azimuthal sectors, and 3 radial rings for a total of 312 computational cells. In

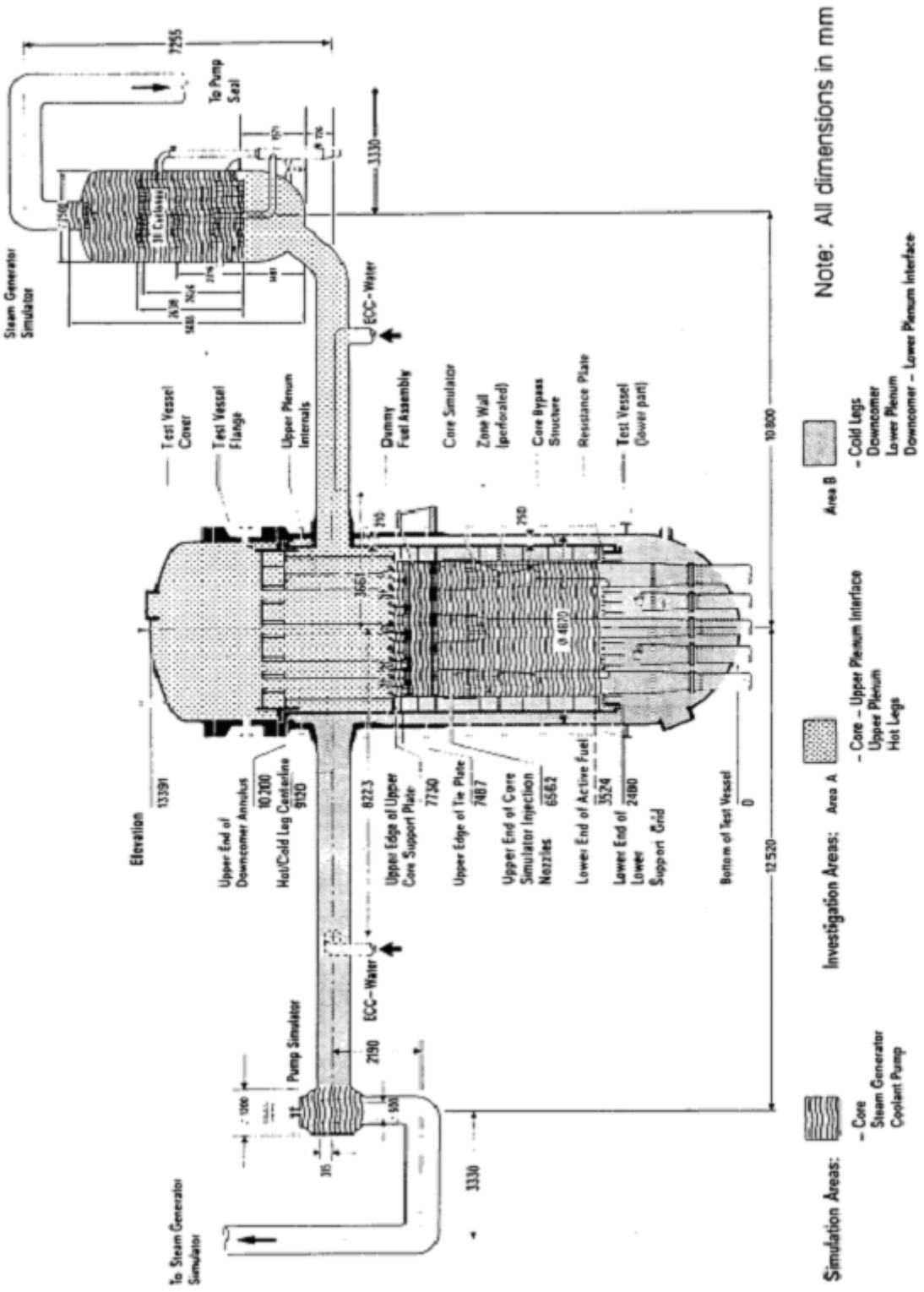

Figure B.4-2. Major Dimension of UPTF Facility

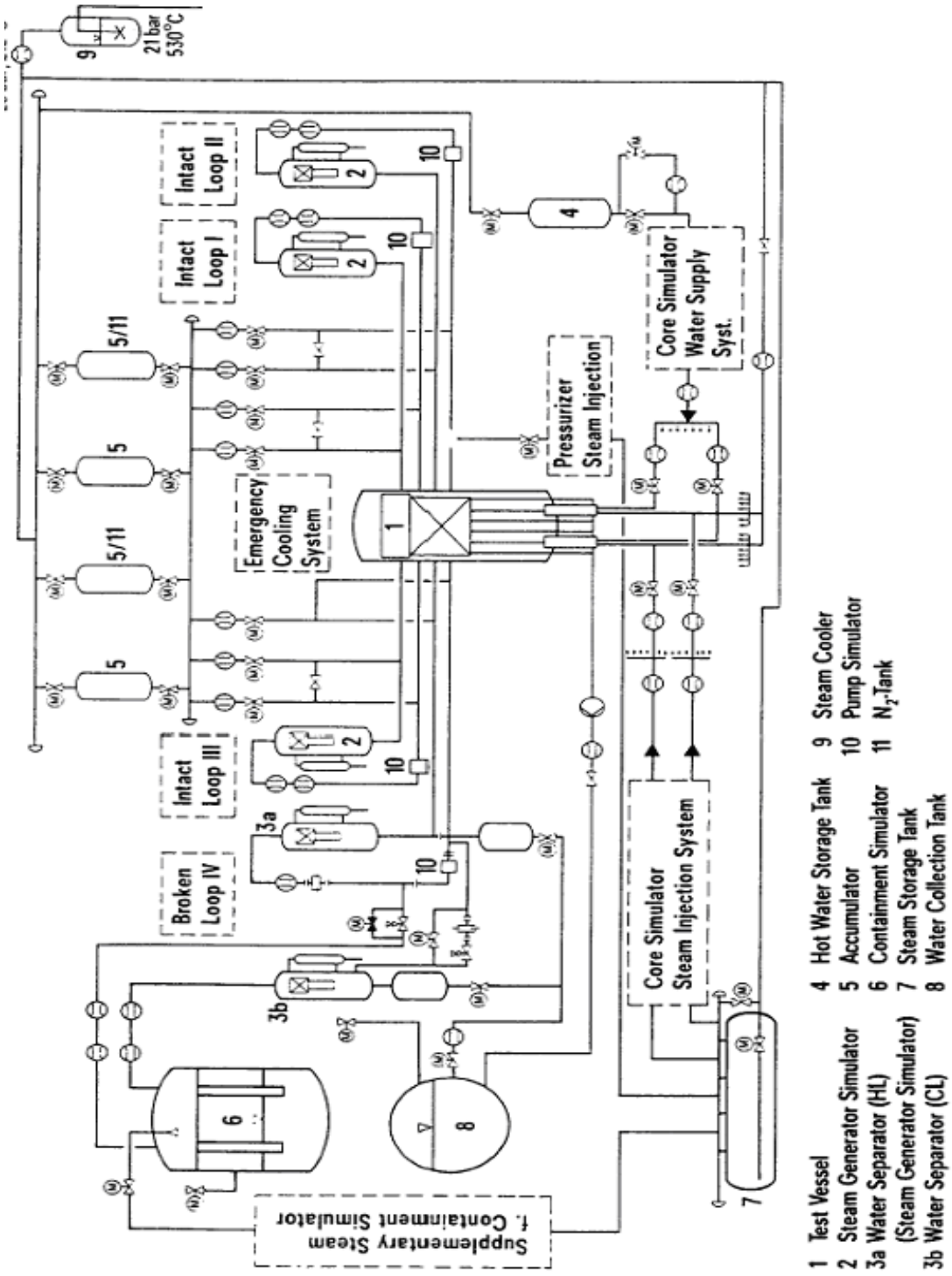

Figure B.4-3. UPTF Flow Diagram

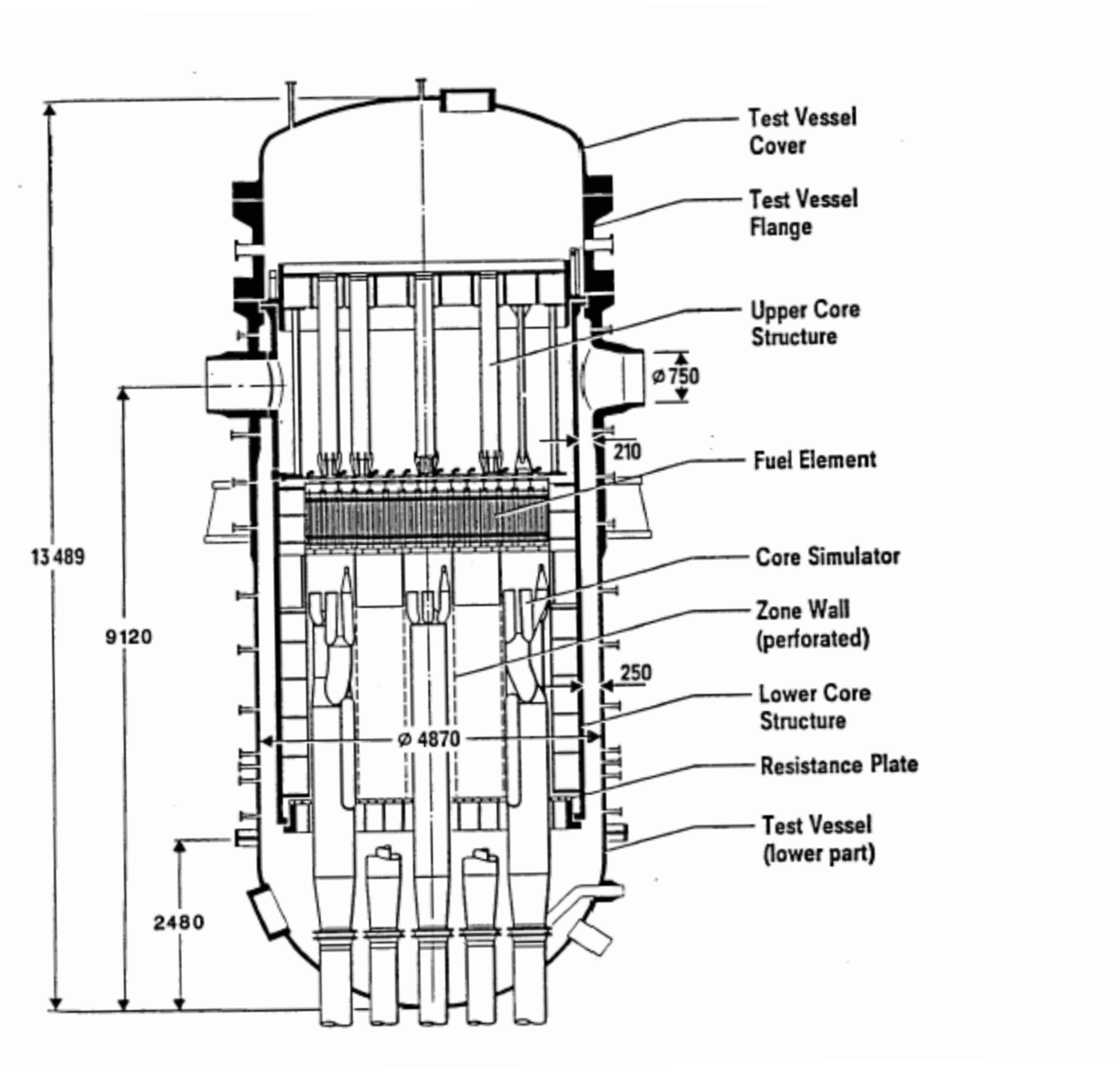

Figure B.4-4. UPTF Test Vessel and Vessel Internals

Figure B.4-5 the plan view of the UPTF test vessel and the azimuthal and radial noding distribution for the vessel are shown. For UPTF Test 21, since the ECC injection nozzle region in the upper downcomer needs to be modeled as its own computational volume, the VESSEL component is modeled with 13 axial levels, 10 azimuthal sectors, and 3 radial rings, with the outermost ring being used for downcomer injection as shown in Figure B.4-6. The core is represented by the inner two rings, and the downcomer is represented by the outer ring. The downcomer region is modeled in the outer ring and between axial levels 3 and 12 and lower plenum region is modeled within axial levels 1 and 2 with all three rings. The core simulator is modeled with core steam simulator FILL and TEE components, and the core steam is injected at

axial level 6 from each core region cell. The Intact cold legs and hot legs are connected at level 11. The vessel axial noding diagram is shown in Figure B.4-7.

Figure B.4-8 to Figure B.4-10 show the noding for intact loops 1, 2, and 3. In each loop the hot leg is modeled with a TEE component; the steam generator simulator is modeled with a combination of four TEE components and one VALVE component; and the crossover pipe, pump simulator, and cold leg are modeled with another TEE component. Steam injection into the top of the steam generator simulator is modeled with TEE and FILL components. This FILL component can be controlled by the mass flow of liquid into the hot leg. The drain line from the bottom of the secondary side to the steam generator simulator inlet plenum is modeled with another TEE and VALVE component. The pump simulator is modeled with a flow-area restriction and the correct volumes associated with the pump simulator component. ECC injections in both the hot and cold legs are modeled with the TEE and FILL components. The FILL components can invoke a time-dependent programmed ECC flow if desired. The loop 1 and loop 3 nodings are identical. In loop 2, modeling of the pressurizer in the hot leg requires the addition of an extra TEE component. A FILL component of this loop also may use a preprogrammed-type steam flow. Figure B.4-11 and Figure B.4-12 show the loop 4 (broken-loop) hot and cold leg nodings. The broken-loop cold leg consists of a VALVE component to model the main break valve, a TEE component to model the bottom of the steam/water separator and drain line, and another TEE component to model the upper part of the steam/water separator and piping to the containment. The bottom of the drain line is modeled with a VALVE component. This drain line drains off accumulated liquid during the course of the transient. The broken-loop also includes a TEE component for the hot leg, another TEE component for the steam generator simulator and drainage, and a VALVE component for the piping that runs to the containment tank. The containment tank is modeled with two BREAK components. These components provide a transient pressure boundary condition. Drain lines from the bottom of the vessel to the drain tank are completely modeled and are shown in Figure B.4-13.

The core steam/water injection sources are modeled with 16 individual TEE components each having the same noding as shown in Figure B.4-14. Each component is connected to one of the 16 core cells at the vessel axial level 6. The TEE components are able to combine the steam input from a feedback injection with the preprogrammed steam/water input. For UPTF test 5, 6,and 7, there is no feedback injection flow. The walls between the UPTF injection zones are solid; therefore, TRACE incorporates a zero flow area in the radial and azimuthal direction at level 6.

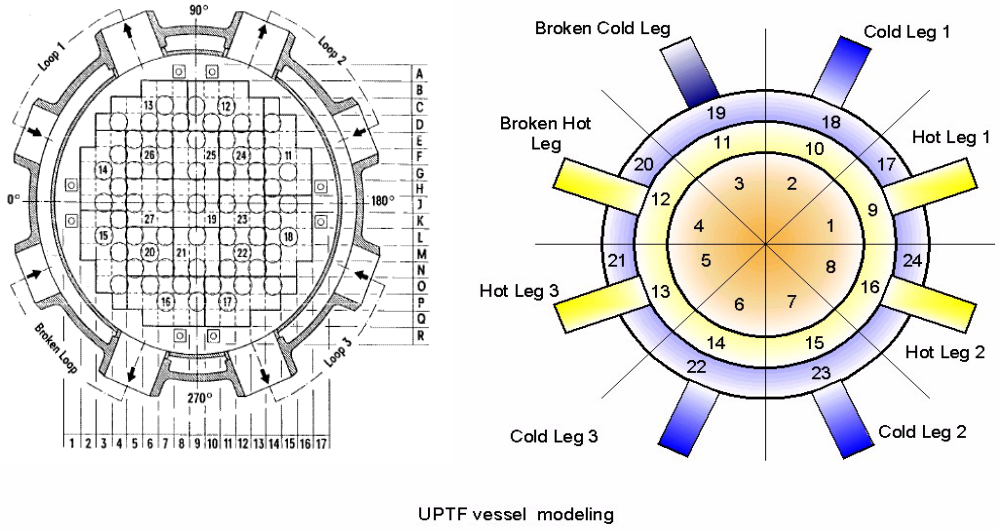

Figure B.4-5. UPTF Test Vessel plan view (left) and Noding Diagram (right) for Test 5, 6, and 7

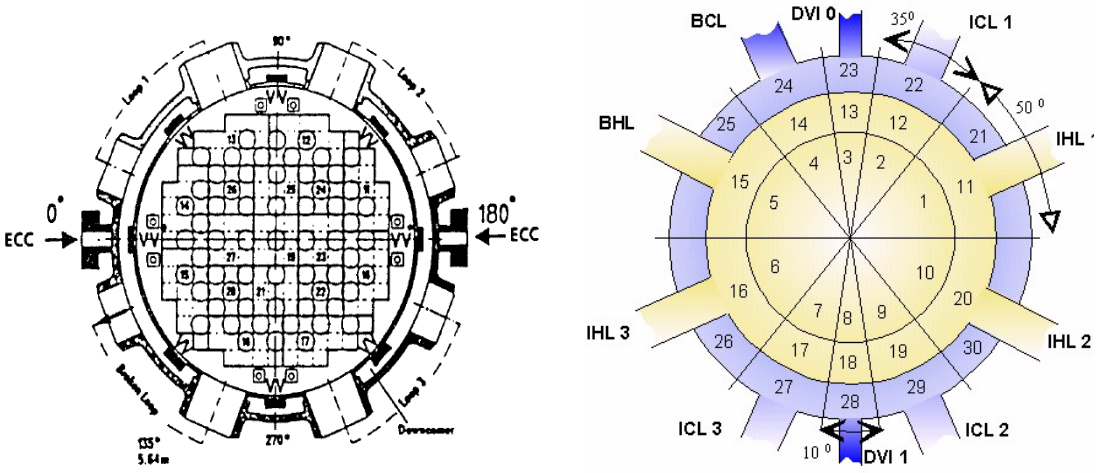

Figure B.4-6. UPTF Test Vessel Plan View (left) and Noding Diagram (right) for Test 21

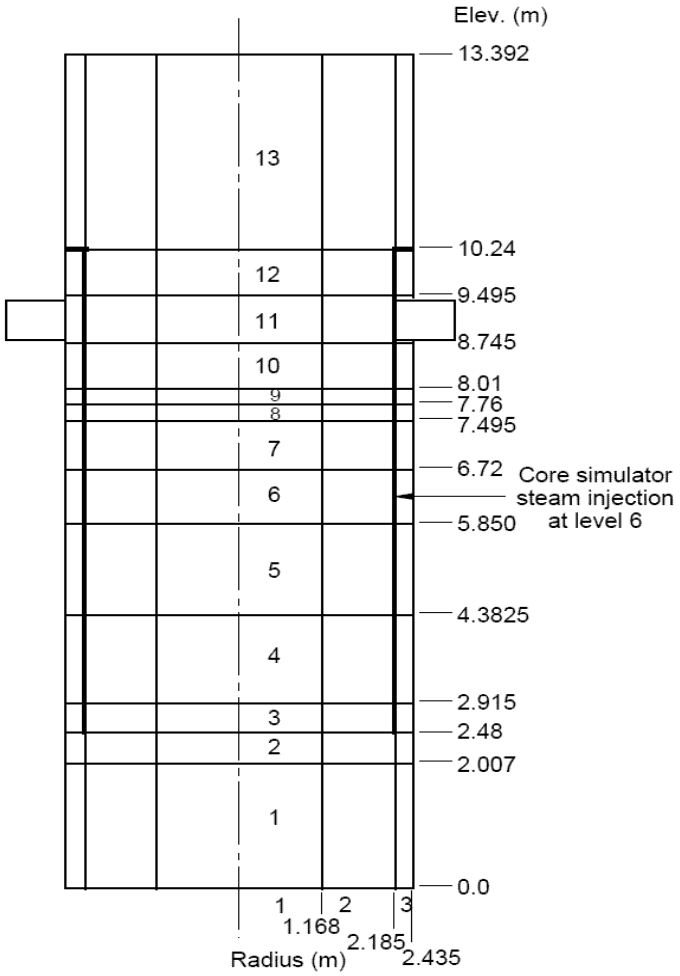

Figure B.4-7. UPTF Test Vessel Model Elevation View

B.4.4. UPTF Tests Simulated with TRACE

B.4.4.1. UPTF Test 6

B.4.4.1.1. System Configuration and Test Conditions

The test facility configuration for UPTF test 6 is shown in Figure B.4-15 Test 6 was a steady state separate effects test with blocked pump simulators, closed broken loop hot leg break valve, and fully opened broken loop cold leg break valve. The primary system and containment pressure was maintained at approximately 2.5 bar throughout the test. The initial lower plenum inventory was negligible. The test was conducted in five separate runs, each with different steam flows to determine the penetration of ECC water into the downcomer and lower plenum as a function of

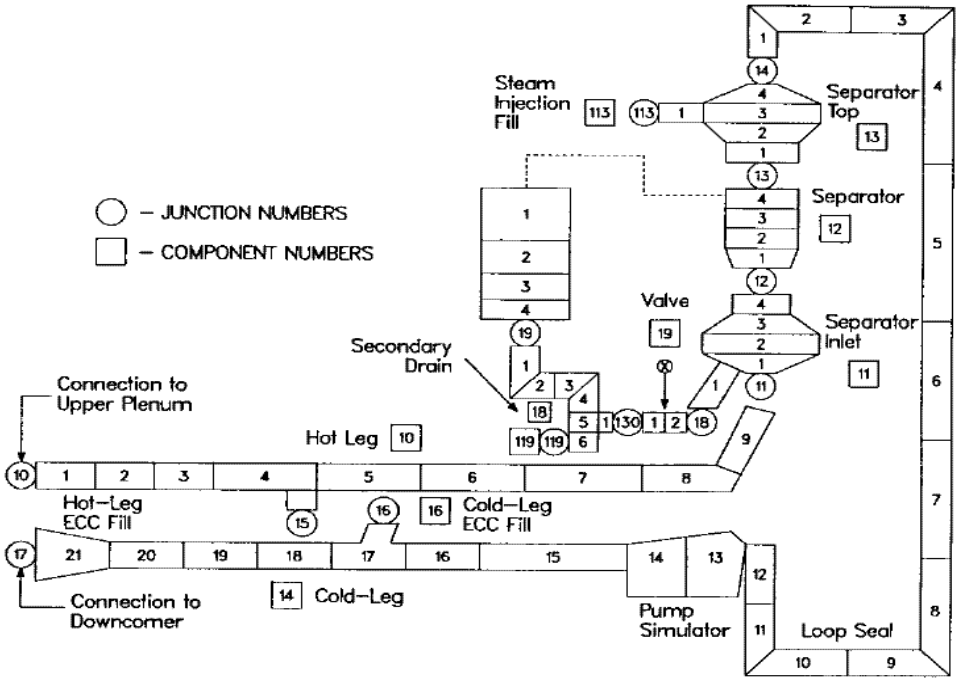

Figure B.4-8. UPTF Loop 1 Noding Diagram

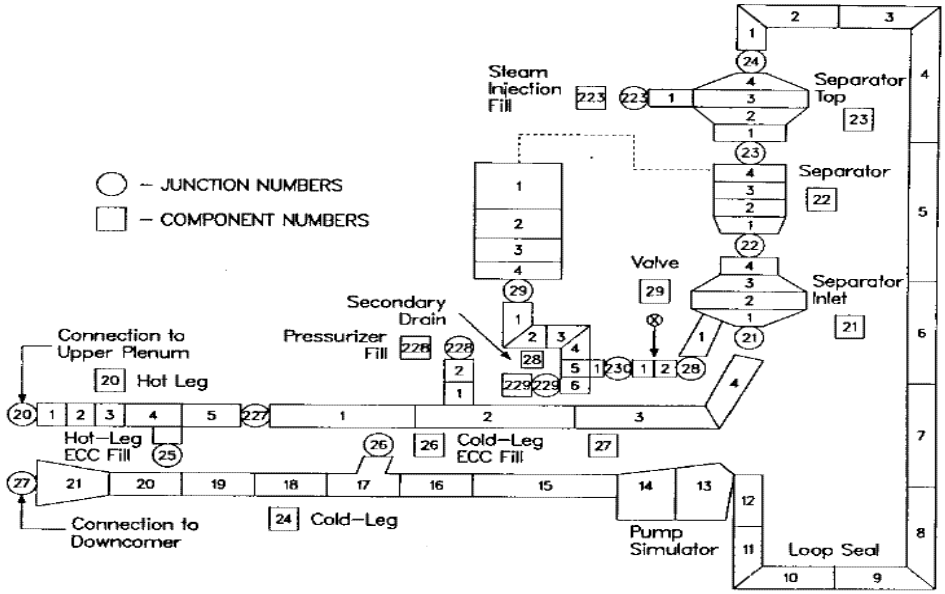

Figure B.4-9. UPTF Loop 2 Noding Diagram

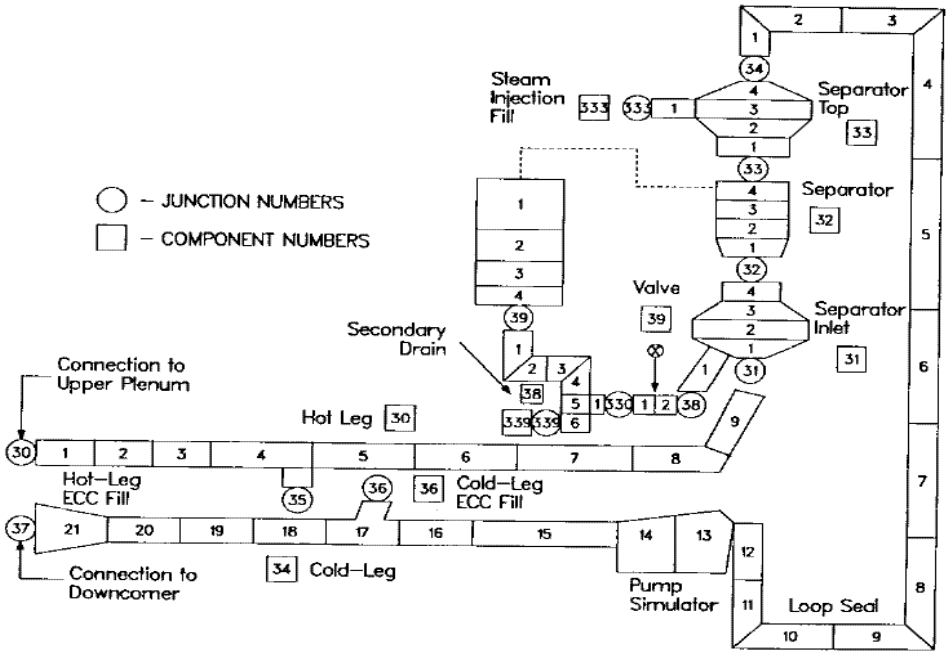

Figure B.4-10. UPTF Loop 3 Noding Diagram

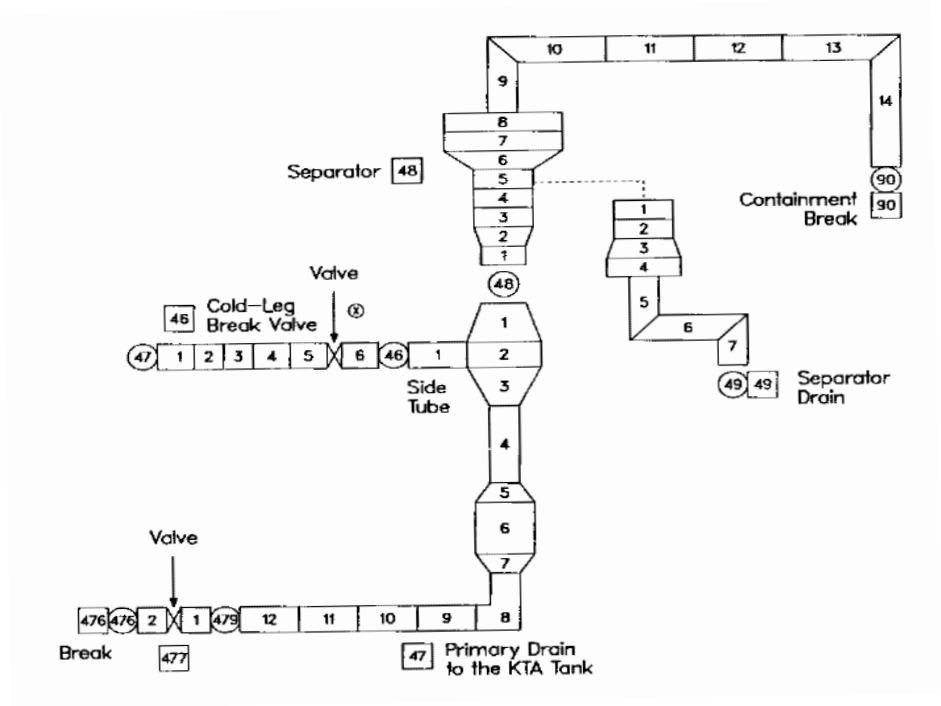

Figure B.4-11. UPTF Broken Loop 4, Cold-Leg Noding Diagram

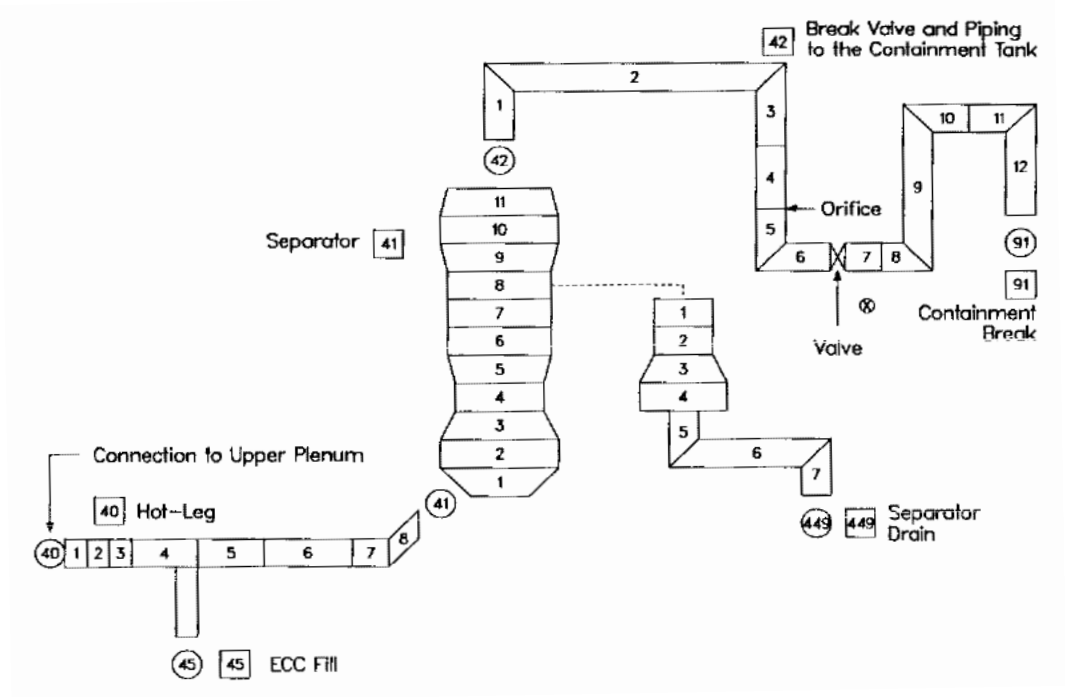

Figure B.4-12. UPTF Broken Loop 4, Hot-Leg Noding Diagram

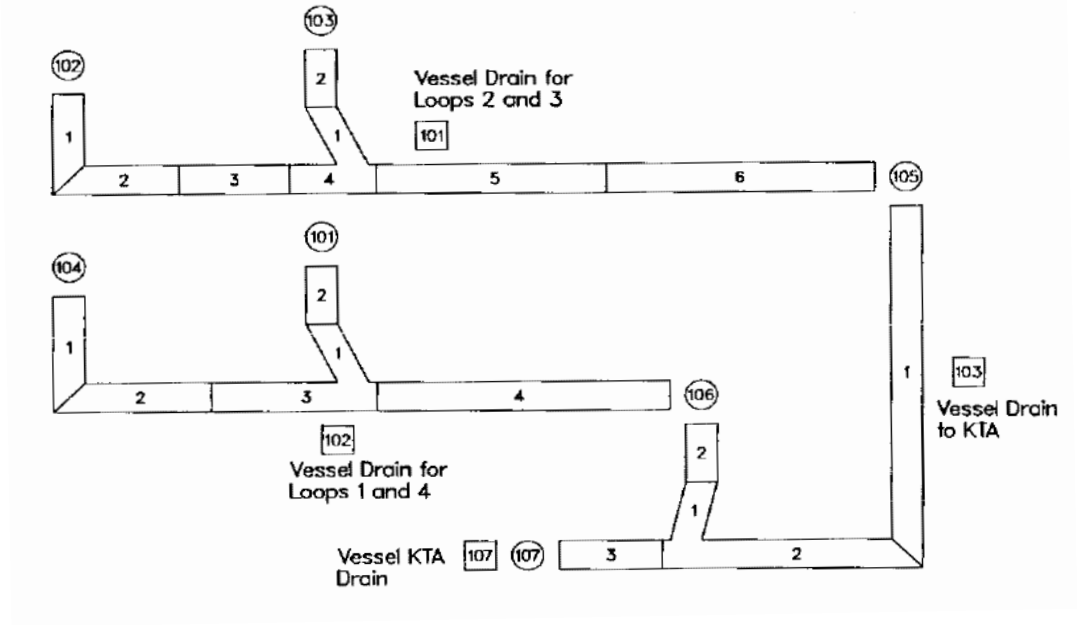

Figure B.4-13. UPTF Water Drainage System Noding Diagram

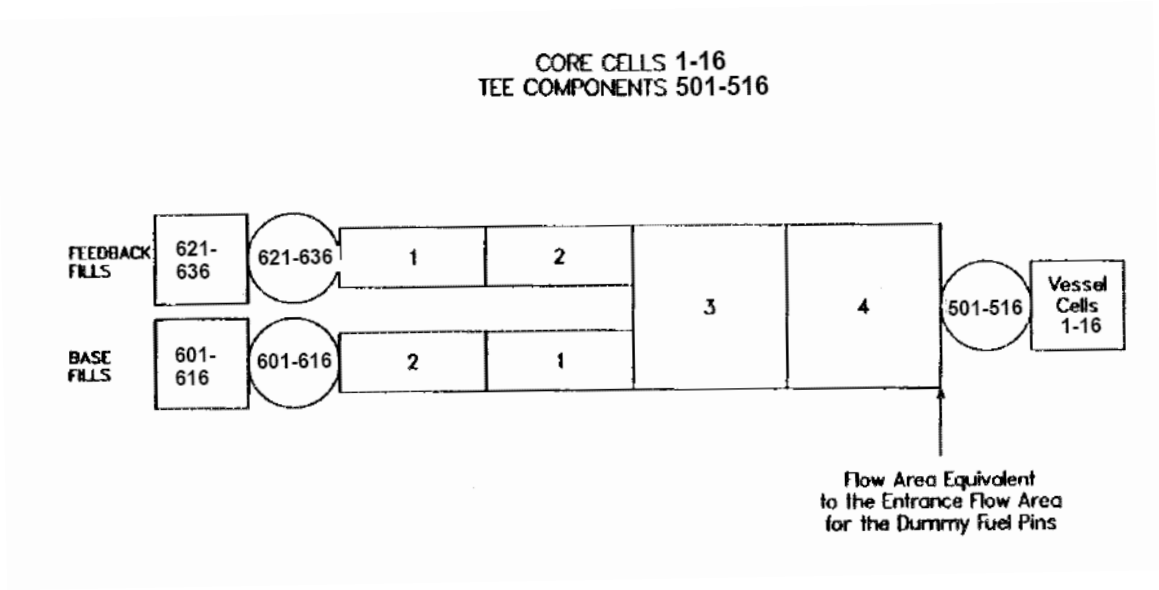

Figure B.4-14. UPTF Core Simulator Injection Noding Diagram

steam flow up the downcomer. The first four runs used steam flows of about 100, 200, 300, and 400 kg/s. The final run was performed at 440 kg/s, and the containment pressure was maintained at approximately 3.5 bar. The core simulator steam flow was equally distributed in all zones. Since the steam injection capacity of the core simulator was 340 kg/s, steam injection into both the core simulator and intact loop SG simulators was required for the high steam flow tests. The ECC temperature was maintained near saturation at 120 ^{o}C (248 ^{o}F) to minimize condensation and promote bypass. The ECC injection rate per loop was about 500 kg/s for each run. The ECC water temperature was somewhat higher for Run 135, about 130 ^{o}C (266 ^{o}F). In all runs, The ECC water was injected into the 3 intact cold legs. A small amount of nitrogen (0.33 kg/s per loop) was injected along with the ECC water to simulate the nitrogen dissolved in the ECC water. To begin each run, steam flow was first established and followed shortly thereafter by accumulator ECC injection to the three intact cold legs. The test conditions for each run are compared in Table B.4.1. After reaching the initial conditions as indicated in Table B.4.1, the data acquisition system was started.

B.4.4.1.2. Comparison of Simulation Results with Test Data

The core steam injection rate, steam generator simulator steam injection rate, ECC injection rate, nitrogen injection rate, and steam/water separator pressure of the test data are modeled as boundary conditions in TRACE simulations. The starting time of each TRACE simulation corresponds to the starting time of the data acquisition system.

The simulation results for five runs of UPTF Test 6 are compared with test data in Figure B.4-26 through Figure B.4-36. The presented results consist of 6 graphs for each test run (except for Run 131) as follows; Graph 1 for total steam injection flow rate and ECC injection flow rate of each

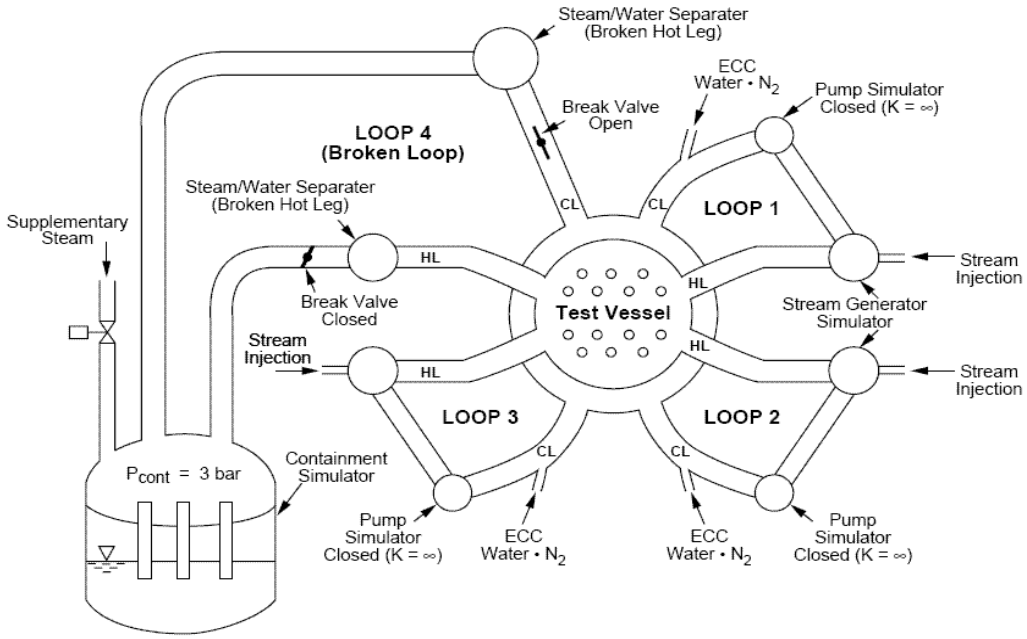

Figure B.4-15. System Configuration for UPTF Test 6

Table B.4.1. Test Conditions for UPTF Test 6

TEST Number **RUN number**	**6** **136**	**6** **133**	**6** **132**	**6** **131**	**6** **135**
Initial Conditions					
Pressure, bar	2.45	2.57	2.50	2.44	3.43
Lower Plenum Water Level, m	0.0	0.0	0.0	0.0	0.0
Inventory, kg	0.0	0.0	0.0	0.0	0.0
Wall Temperature, ^{o}C	167	187	172	173	196
Water Temperature, ^{o}C	N/A	N/A	N/A	N/A	N/A
Test Conditions					
Containment Pressure, bar	2.40	2.56	2.48	2.52	3.43
Core Simulator Steam Flow, kg/s	102	110	205	309	349
SG Steam Injection Flow/loop, kg/s	0.0	31.0	30.0	29.0	30.0
Total Steam Injection Flow, kg/s	102	202	295	396	436
ECC Injection Flow/loop, kg/s	490	491	490	482	476
ECC Temperature, ^{o}C	114	117	112	118	129
Total N_2 Injection, kg/s	1.0	1.0	1.0	1.0	1.0

intact cold leg to show the test conditions, Graph 2 for absolute pressure of downcomer and upper plenum, Graph 3 for steam mass flow out the break, Graph 4 for integrated total break flow,

Graph 5 for total mass inventory in the three intact cold legs and downcomer inventory, and Graph 6 for lower plenum inventory. For Run 131, three more graphs showing the mass inventory of each intact cold leg separately are included, as well. Graph numbers used in each figure are marked at the upper (or lower) right corner.

Total Steam Injection Flow Rate and ECC Injection Flow Rate of Each Intact Cold Leg

The total steam injection flow rate and the ECC injection flow rate to each intact cold leg are shown in Graph 1 of each figure to show the test conditions used for each test run. At about 30 seconds, the core simulator steam and the SG simulator steam were injected into the test vessel at a designated injection rate. The steam injection flow rate ranged from 102 kg/sec of Run 136 to 436 kg/sec of Run 135. Then nitrogen injection started at about 38 seconds. At about 40 ~ 45 seconds, ECC injection began at approximately 500 kg/s to each of the three intact cold legs. For all test runs, the ECC injection flow rate remained almost the same throughout all tests.

Downcomer and Upper Plenum Absolute Pressure

All test data show that the absolute pressure in the downcomer and in the upper plenum increases sharply owing to steam injection into the primary system as indicated in Graph 2 of each simulation result figure. Immediately after start of ECC injection, the condensation of superheated steam decreases the system pressure. Until about 5 seconds after steam injection, TRACE predicts the system pressure response nearly identical to the experimental data for all runs. After steam injection but before ECC injection, TRACE slightly over-predicts the system pressure for relatively high steam injection cases of Run 131, 132 and 135, while TRACE predicts the system pressure almost identical to the experimental data for the low steam injection case of Run 136. This over-prediction of the system pressure for relatively high steam injection tests is mainly because the calculated steam break flow is less than the data before ECC injection. From start of ECC injection to the end of simulated time periods, TRACE under-predicts the system pressure by about 20% for all the simulated runs except for Run 136. One reason for this under-prediction of the system pressure is a higher condensation rate of the injected steam as confirmed by the break steam flow rate being less than the test data as shown in Graph 3 of each figure. For Run 136, the predicted system pressure generally matches test data well except for the time period of ECC penetration to the lower plenum.

Break Steam Mass Flow

The TRACE-predicted break steam mass flow is compared with data in Graph 3 of each simulation result figure. During the early core steam injection phase, until about 5 seconds after steam injection, the TRACE-predicted break steam flow is nearly identical to the experimental data for all runs. Afterwards, TRACE slightly under-predicts the break steam mass flow for Run 131, 132 and 135. After the lower plenum inventory reaches to an equilibrium level, TRACE under-predicts the break steam mass flow by about 50%. The main reason for TRACE to predict less break steam flow is probably due to the higher condensation rate. TRACE predicts significant condensation (10 ~ 30 kg/m^3-s) to occur in the upper downcomer regions (axial node 11 and 10, where loop pipings are connected to and just below the loop piping connection) and at the broken cold leg. However, during the downcomer analysis period, i.e., after start of ECC injection and

before lower plenum inventory reaches to an equilibrium level, the TRACE-predicted break steam flow generally agree with data well. For the low steam injection case of Run 136, TRACE predicts the break steam flow fairly well throughout the entire simulation period.

Integrated Total Break Flow

The integrated total break mass flow calculated by TRACE is compared with data in Graph 4 of each simulation result figure. Since the data of the total break flow of steam and liquid are not available, the integrated total break flow from the evaluation performed by MPR Associates (Ref. 3) are digitized, and the TRACE-predicted total break mass flow of each test is integrated from ECC injection start time to compare with data. The digitized data shown in Graph 4 of each simulation result figure may contain uncertainty due to digitizing accuracy. TRACE predicts integrated total break mass flow somewhat higher than data in every simulation result. However, the extent of the over-prediction can not be quantified accurately because of potential uncertainty of the digitized data. The test data shows that the integrated total break flow decreases as the steam injection flow decreases, and TRACE's prediction follows this trend well.

Total Inventory in Three Intact Cold Legs and Downcomer Inventory

The total inventory in three intact cold legs calculated by TRACE is compared with data in Graph 5 of each simulation result figure. The test data of total inventory in three intact cold legs of each test is digitized from MPR report (Ref. 3). The predicted mass in the intact cold legs is determined by summing the fluid-cell masses in each of the intact cold legs, cells 14 through 21 of components 14, 24, and 34 of the loop models. During the time period approximately 5 ~ 10 sec after start of ECC injection, test data shows that most of the ECC injected accumulates in the intact cold legs. The duration of this short cold leg filling period increases with the higher steam flow due to the more rapid pressurization of the test vessel and the higher ECC bypass. The TRACE-predicted inventory in three intact cold legs matches data well during this short cold leg filling period. At the end of this period, the test data shows that the intact cold legs are filled about halfway and water begins penetrating into the downcomer and the lower plenum. Afterwards, the total intact cold leg inventory data reaches about 55 ~ 80% of the full inventory and is maintained whereas the TRACE-predicted total intact cold leg inventory reaches about 16 ~ 45% of the full inventory. The data shows that the total intact cold leg inventories are almost the same for all test runs except for Run 136 in which the total steam injection flow rate is low and the total intact cold leg inventory is lower than the other cases. TRACE predicts the same trend except for Run 135, a case of high steam injection flow, in which the total intact cold legs inventory is considerably higher than the other simulated runs. The total intact cold leg inventory of Run 136 is lower than the other runs in both test data and TRACE simulation.

Graphs 7, 8 and 9 in Figure B.4-28 show the inventory behavior of intact cold legs, i.e., cold leg 1, cold leg 2 and cold leg 3, respectively, for Run 131. The test data shows that the inventory of intact cold legs starts to increase and reaches about 80% full at around 60 seconds. As shown in Graph 7, the data shows that the inventory of cold leg 1 is higher than the other intact cold legs. The larger accumulation of ECC water in cold leg 1 which is adjacent to the broken cold leg is due to the higher steam flux on the water front facing the downcomer. TRACE does not predict such a geometric effect, and the calculated inventory of each intact cold leg is almost the same.

Since test data of downcomer inventory is unavailable, the TRACE-predicted downcomer inventory is not compared with the test data. TRACE predicts that the downcomer inventory starts to increase sharply in 2 ~ 4 sec. after the initiation of ECC accumulation in the intact cold legs. TRACE predicts that the start time and the rate of increase in downcomer inventory is faster for the lower steam injection flow rate cases. During the ECC water penetration period, the downcomer inventory is maintained at almost the same value, and the lower plenum inventory starts to increase. When the lower plenum inventory reaches an equilibrium level, the downcomer inventory starts to increase shortly and then remains fairly constant while the break flow increases continuously. TRACE predicts additional downcomer inventory accumulation as the steam injection flow rate decreases. The predicted downcomer inventory of Run 131 is almost the same as the inventory of intact cold legs whereas the predicted downcomer inventory of Run 136 is about 3 times the intact cold leg inventory at the equilibrium level.

Lower Plenum Inventory

The TRACE-predicted lower plenum inventory is compared with data in Graph 6 of each simulation result figure. The lower plenum inventory data is calculated using the lower plenum water level as indicated by a differential pressure measurement. All data show a small rise in inventory before ECC injection due to the dynamic pressure effect of the injected steam. The start time of ECC penetration into the lower plenum varies with the total steam injection rate as shown in Graph 6 of each simulation result figure. The beginning time of ECC penetration into the lower plenum is predicted to be almost the same as the data (for Run 131, Run 136) or faster by several seconds than the data (for Run 132, Run 135). The lower plenum refill period lasts about 15 to 25 seconds in the data whereas the lower plenum refill period lasts about 16 ~ 37 seconds in the simulations. TRACE predicts that the lower plenum refill period lasts longer than the data for all cases except for Run 136. The TRACE-predicted lower plenum refill period of Run 136 is shorter by about 6 seconds than the data. Test data shows an intermittent and discontinuous slug penetration for the higher steam flow rate runs (> ~ 300 kg/s) or a smooth and continuous penetration for the lower steam flow rate runs (< ~ 200 kg/s), whereas TRACE predicts a smooth and continuous penetration in all simulated runs. However, the TRACE-predicted penetration rates match data well. The penetration rates of TRACE simulations and the data are compared in section B.4.4.5

At the end of ECC penetration period, the data shows that the liquid inventory of the lower plenum reaches an equilibrium value which varies from 13000 kg to 17500 kg and the equilibrium level is inversely proportional to the steam injection flow rate. However the TRACE-predicted equilibrium inventories are nearly same at around 16000 kg and higher by about 10 ~ 23% than the data except for Run 136. This over-prediction of the lower plenum equilibrium inventory is due to the longer refill period, as indicated before. The TRACE-predicted equilibrium inventory of Run 136 matches data well at about 17500 kg. The TRACE-calculated lower plenum inventories are very similar to the data in spite of over-prediction of the total break flow in all simulated cases probably because more intact cold leg inventory is predicted to exit break instead of accumulating in the cold legs and, as indicated before, the digitized total break flow data could contain a large uncertainty.

B.4.4.2. UPTF Test 7

B.4.4.2.1. System Configuration and Test Conditions

The test facility for UPTF Test 7 was configured such that the pump simulators were blocked, and the flow path through the vessel was down the core, up the downcomer, and out the broken cold leg nozzle like as Test 6, but there was no steam injection through the steam generator simulator as shown in Figure B.4-16. The containment pressure was maintained at about 2.5 bar to match Test 6 conditions.

Four runs were conducted in Test 7, each with steam injection to the core simulator and ECC injection to the intact cold legs in various combinations. Lower plenum drainage was initiated in each run to maintain the lower plenum water level at approximately 2 m. Each run had several sequential parts, each with a different steam injection rate, ECC injection rate, and ECC injection location (i.e., Loop 1, Loop 2, Loop 3, or some combinations) to examine 3-dimensional effects. Subphase II of Run 201 and subphase I and III of Run 202 were considered unsuccessful because the lower plenum level exceeded 2 m or the required ECC injection rate was not established quickly enough. Test conditions for each successful part of the four runs are compared in Table B.4.2.

To provide a comparison to Test 6 and a base case for comparison of other Test 7 data, Run 201 Part III (Run 201-III) used 100 kg/s steam flow and 500 kg/s ECC flow in each loop. Also to supplement Test 6 data, Run 203-IV used 50 kg/s steam flow and the same ECC injection. To examine the effect of ECC injection location, Run 200-I had ECC injection only to loop 1 (closest to the broken loop) while Run 201-I had injection to loops 2 and 3 (farthest from the broken loop) with the same steam flow (100kg/s) and the same ECC injection rate (500 kg/s) in each loop. In Run 200-I and Run 200-III, the steam flow rate was maintained at 100 kg/s, and ECC was injected to loop 1 at 500 kg/s and 735 kg/s respectively in order to determine the effect of ECC flow rate. To determine the effect of steam flow rate by maintaining constant ECC injection and varying steam flow, the following steam flows were used with an ECC flow of 735 kg/s injected only to loop 1: 100 kg/s (Run 200-III), 70 kg/s (Run 203-I), 50 kg/s (Run 200-II), and 30 kg/s (Run 203-II). In addition, with an ECC flow of 500 kg/s injected to loops 2 and 3, steam flows of 130 kg/s (Run 202-II) were compared to 100 kg/s (Run 201-I).

B.4.4.2.2. Comparison of Simulation Results and Test Data

The simulation results of four runs of UPTF Test 7 are shown in Figure B.4-37 through Figure B.4-44. The simulation result figures consist of seven graphs for each test run as follows; Graph 1 for total steam injection flow rate and ECC injection flow rate of each intact cold leg to show the test conditions, Graph 2 for absolute pressure of downcomer and upper plenum, Graph 3 for break steam mass flow, Graph 4 for integrated total break flow, Graph 5 for total inventory in three intact cold legs and downcomer inventory, Graph 6 for lower plenum inventory, and Graph 7 for the lower plenum drain rate. Graph numbers used in each figure are marked at the upper right corner.

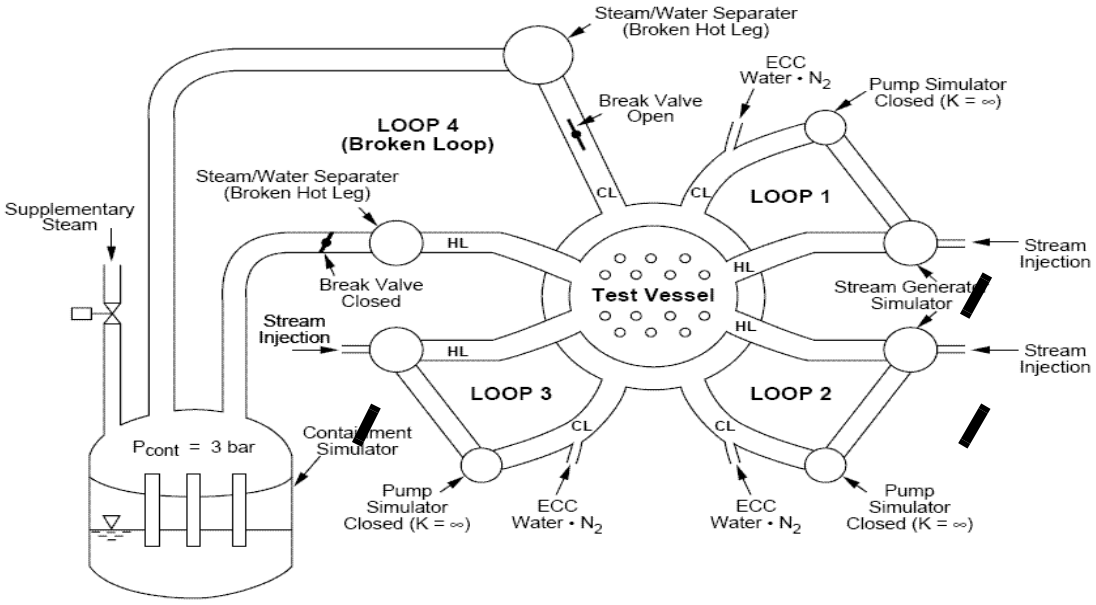

Figure B.4-16. System Configuration for UPTF Test 7

Table B.4.2. Test Conditions for UPTF Test 7

TEST/Phase **RUN**	**7/I** **200**	**7/II** **200**	**7/III** **200**	**7/I** **201**	**7/III** **201**	**7/II** **202**	**7/I** **203**	**7/II** **203**	**7/III** **203**	**7/IV** **203**
Initial Conditions										
Time at Start of Subphase, sec	40	100	159	40	167	106	40	100	173	256
Pressure, bar	3.0	4.6	3.4	2.5	3.3	3.8	2.6	4.2	2.9	4.0
Lower Plenum Water level, m	1.5	1.5	1.8	1.5	2.0	2.2	0.9	1.6	1.9	2.0
Inventory, kg	10000	10400	14000	10400	17700	19400	4000	10600	14100	17070
Wall Temp. C	128	144	136	130	138	138	150	144	134	142
Water Temp, C	126	132	138	132	145	140	148	140	133	144
Test Conditions										
Containment Pr, bar	2.5	2.5	2.5	2.5	2.5	2.5	2.5	2.5	2.5	2.5
Core Simulator Steam Flow, kg/s	104	54	102	102	102	128	69	30	71	51
SG Steam Injection Flow/loop, kg/s	0.0	0.0	0.0	0.0	0.0	0.0	0.0	0.0	0.0	0.0
ECC injection rat										
loop1, kg/s	494	736	735	0	493	0	735	737	737	493
loop 2, kg/s	0	0	0	487	487	486	0	0	0	485
loop 3, kg/s	0	0	0	490	489	491	0	0	733	487
ECC temp	126	128	129	127	131	132	131	133	133	133
Total N2 injection, kg/s	0.0	0.0	0.0	0.0	0.0	0.0	0.0	0.0	0.0	0.0

Each run is divided into 3 or 4 subphases according to the steam and ECC injection rate as well as the number of injecting cold legs as listed in Table B.4.2. It is noticed that since each subphase's phenomena are strongly dependent on the results of the previous subphase, even small deviation of TRACE simulation from the data in a subphase could cause a noticeable deviation in the subsequent subphase's result.

Total Steam Injection Flow Rate and ECC Injection Flow Rate of Each Intact Cold Leg

The total steam injection flow rate and the ECC injection flow rate to each intact cold leg are shown in Graph 1 of each result figure to show the test conditions used for each test run. At about 30 seconds, core simulator steam and SG simulator steam are injected into the test vessel at a designated injection rate. Total steam injection flow rate ranges about 30 ~ 130 kg/sec. The total ECC injection flow rate ranges about 500 ~ 1470 kg/sec. The steam injection flow rate, the ECC injection flow rate and the number of injection cold legs of each subphase are listed in Table B.4.2.

Downcomer and Upper Plenum Absolute Pressure

The TRACE-predicted absolute pressures of the downcomer and the upper plenum are compared with data in Graph 2 of each simulation result figure. During the steam injection period, TRACE predictions of downcomer and upper plenum pressure are almost identical to the data showing a sharp increase of pressure due to steam injection before ECC injection. After ECC injection, TRACE over-predicts the system pressure until a few seconds after the full development of ECC flow. TRACE over-predicts the system pressure more in the higher ECC flow rate cases, i.e., Run 201 and 202. Then, for all the cases, TRACE under-predicts the system pressure by about 10 ~ 30%. Similar to the simulation of Test 6, one of the reasons for this under-prediction of the system pressure is a higher condensation rate of the injected steam as confirmed by the break steam flow rate being calculated to be less than the test data. For all the cases, the data shows that the downcomer pressure is almost the same as the upper plenum pressure throughout the whole test period. In the cases of Run 200 and Run 203, TRACE predictions show that the pressure trend is the same as the data showing no pressure differences between the downcomer and the upper plenum, whereas TRACE predicts the downcomer pressure lower than the upper plenum pressure by about 3 ~ 5% for Run 201 and Run 202.

In spite of some deviations from the data, the TRACE-predicted system pressure trend follows the data trend reasonably well.

Break Steam Mass Flow

The break steam mass flow calculated by TRACE is compared with data in Graph 3 of each simulation result figure. TRACE slightly under-predicts the break steam flow for Run 201, 202 and 203, whereas TRACE under-predicts the break steam flow by about 50% for Subphase III of Run 200. The reasons for a significant discrepancy of break steam mass flow during the Subphase III of Run 200 are probably due to the over-prediction of condensation rate in TRACE and a large uncertainty of the data. The data shows that the measured break steam flow of Subphase III of Run 200 is about 175 kg/s which is significantly higher than the injected steam mass flow of

about 102 kg/s, whereas the other test data of Test 6 and 7 show that the measured break steam flow is nearly close to the injected steam mass flow. In the case of Run 203, TRACE calculates negative break steam mass flow during 163 ~ 169 sec due to the lower plenum drain, thus this time period is not considered in the analysis of ECC delivery behavior in **Section B.4.4.5.2.**. In general, the TRACE-predicted break steam flow rate agrees well with data.

Integrated Total Break Flow

The integrated total break mass flow calculated by TRACE is compared with data in Graph 4 of each simulation result figure. Since the data for total break flow of steam and liquid are not available, the integrated total break flow plots in the MPR report (Ref. 3) are digitized and the TRACE-predicted total break mass flow of each test is integrated from the ECC injection start time to compare with data. The digitized data shown in Graph 4 of each simulation result figure may contain a large uncertainty due to the digitizing accuracy. Nonetheless, the TRACE-predicted integrated total break mass flow follows the digitized data well for all simulated cases.

Total Inventory in Three Intact Cold Legs and Downcomer Inventory

The predicted total inventory in three intact cold legs is compared with data in Graph 5 of each simulation result figure. The test data of total inventory in three intact cold legs of each test is digitized from the plots in the MPR report (Ref. 3) and the predicted mass in the intact cold legs is determined by summing the fluid-cell masses in each of the intact cold legs, cells 14 through 21 of components 14, 24, and 34 of the loop models. Total intact cold leg inventory depends on the test conditions, i.e., the injected steam flow rate, ECC flow rate, etc., so that total intact cold leg inventory varies with each subphase of each test run. Both TRACE and test data show that the total intact cold leg inventory increases as the injected steam flow increases and/or ECC injection flow increases. As indicated by the simulations of Test 6, TRACE under-predicts the total intact cold leg inventory for all cases. In the case of Subphase IV of Run 203, TRACE under-predicts the total cold leg inventory up to 80%. However, the extent of the under-prediction can not be quantified well because the digitized data are expected to have a large uncertainty.

Since test data of downcomer inventory is unavailable, the TRACE-predicted downcomer inventory is not compared with the test data. As can be expected, for the cases of lower injected steam flow rate or higher ECC injection flow rate, TRACE predicts more downcomer inventory resulting from relatively easier ECC water penetration into the downcomer.

Lower Plenum Inventory and Lower Plenum Drain Rate

Lower plenum inventory calculated by TRACE and the lower plenum drain rate used in the simulation are compared with data in Graph 6 and Graph 7 of each simulation result figure respectively. The lower plenum inventory data is calculated using the lower plenum water level as indicated by a differential pressure measurement. As described before, since the forced steam flow would artificially prevent ECC penetration into the lower plenum when the liquid level reaches above about 2 m, the lower plenum drainage was initiated in each run to maintain the lower plenum water level at approximately 2 m for Test 7. Thus the total mass drained from the lower plenum should be added to the lower plenum inventory calculation. For TRACE

simulation, the lower plenum drain rate is modeled by a tabular input (i.e., time vs. drain rate) or the control system data (i.e., CONTROL BLOCK component of TRACE) which simulates the drain rate control logic.

During the first subphase of each test, TRACE reasonably predicts the increase of the lower plenum inventory before drainage is initiated for Run 201 and Run 202. For Run 203, the data shows that the lower plenum inventory increases continuously from about 49 sec, i.e., 9 sec after ECC injection, to about 115 sec, whereas the TRACE-predicted lower plenum inventory starts to increase briefly at the same time as data, but turns around to decrease soon and does not show such an increase as data until the end of Subphase I. In the case of Run 200, TRACE predicts a slight increase of the lower plenum inventory at around the end of first subphase while the data shows no increase during the first subphase.

During the subsequent phases of each test, the TRACE-predicted lower plenum inventories of Run 201 and Run 202 show a good agreement with data. However, the TRACE-predicted lower plenum inventories of Run 200 and Run 203 show a big difference probably due to the propagation effect of the first subphase's deviation and the drain rate.

Since the drain rate is very high in all runs of Test 7, a small difference of drain rate between the data and TRACE model can strongly affect the TRACE-predicted lower plenum inventory. Thus a comparison of ECC penetration rates with an appropriate consideration of drain rates is more meaningful than a direct comparison of the lower plenum inventories in assessing the capability of TRACE for predicting the ECC bypass processes. The penetration rates of TRACE simulations and the data are compared in section B.4.4.5.

B.4.4.3. Highly Subcooled Water Flow Test (UPTF Test 5)

B.4.4.3.1. System Configuration and Test Conditions

UPTF Test 5 Phase B (Run 062, pseudo-steady phase) was a separate effects test performed at almost constant pressure with downward ramping steam flow to the core simulator and highly subcooled (~120 ^{o}C) ECC water injection into the cold legs. There was no steam flow through the steam generator simulators. The system configuration for this test is shown in Figure B.4-17. The pump simulators of each intact loop were closed, and only the cold leg break valve was opened, forcing all steam injected in the core simulator to flow downward through the lower plenum, up the downcomer, and out the vessel through the broken cold leg.

Test was initiated by injecting steam through the core simulator at 22 seconds. Steam flow was decreased from the initial value of 320 kg/sec to the final value of 160 kg/sec after 160 seconds duration of steam injection. Shortly after the steam flow was established, accumulator ECC injection to the three intact cold legs was initiated at around 31 seconds. The ECC injection flow of 500 kg/sec per loop at 30 ^{o}C was selected based on the values of a typical PWR. Since the break valve was initially fully open and kept open throughout the experiment, the initial system pressure was the same as the containment pressure, 2.6 bar. The system was expected to

pressurize significantly to about 4.5 bar once steam injection was initiated. Thus the initial system temperature was chosen as 150 ^{o}C, the saturation temperature at 4.5 bar. The initial lower plenum water level was about 0.9 m (about 3700 kg). Test conditions are summarized in Table B.4.3.

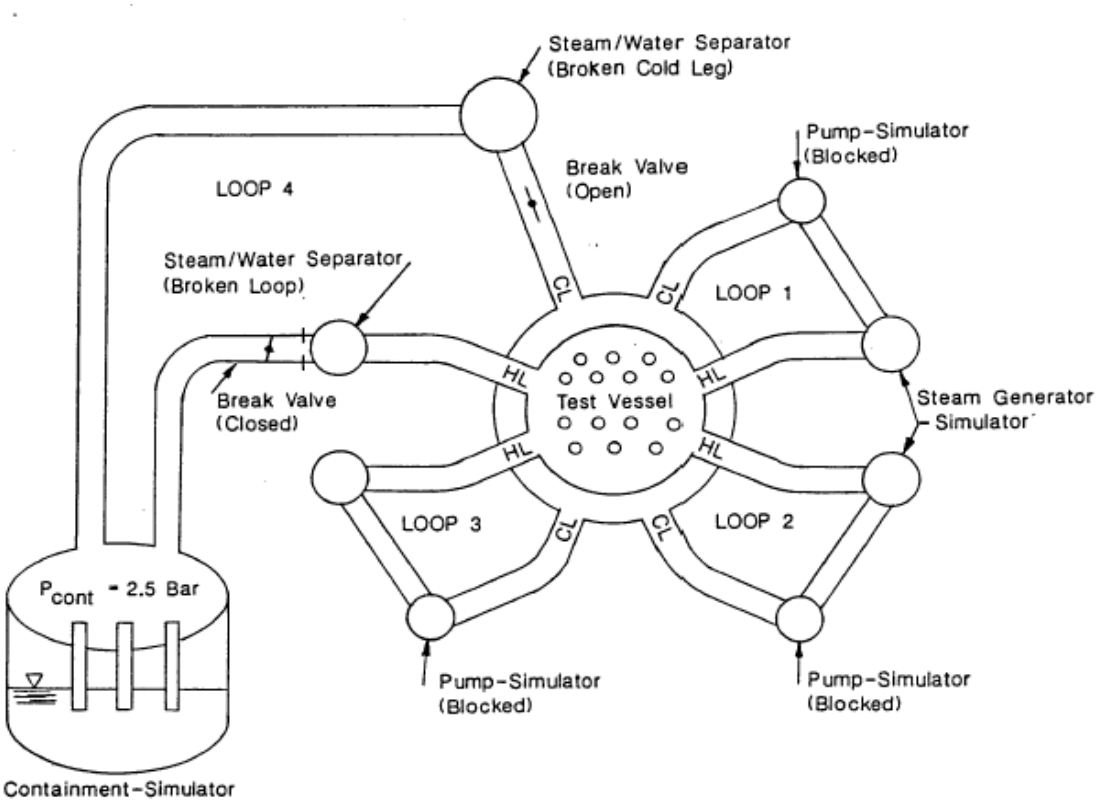

Figure B.4-17. System Configuration for UPTF Test 5

Table B.4.3. Test Conditions for UPTF Test 5

TEST Number **RUN number**	**5-B** **062**
Initial Conditions	
Pressure, bar	2.6
Lower Plenum Water Level, m	0.9
Inventory, kg	3700
Wall Temperature, ^{o}C	150
Steam Temperature, ^{o}C	129
Test Conditions	
Containment Pr, bar	2.6
Core Simulator Steam Flow, kg/s	320-160

Table B.4.3. Test Conditions for UPTF Test 5

TEST Number **RUN number**	**5-B** **062**
SG Steam Injection Flow/loop, kg/s	0.0
ECC Injection Flow/loop, kg/s	500
ECC Temperature, ^{o}C	30
Total N2 Injection, kg/s	0.93

B.4.4.3.2. Comparison of Simulation Results and Test Data

As shown in the Graph 1 of Figure B.4-45 and Table B.4.3, the core simulator steam injection started at 22 seconds and the nitrogen (21 ^{o}C) injection started at about 24 seconds. The ECC injection control valves were opened at 30 seconds and the highly subcooled ECC water was injected into intact cold legs.

Absolute pressures of the upper plenum and the downcomer calculated by TRACE are compared with data in Graph 2 of Figure B.4-45 Upper plenum and downcomer pressure before ECC injection are predicted to be higher than the test data. This over-predicted system pressure results from the less break steam flow that exit the system through the break as shown in the Graph 3 of Figure B.4-45. During the early phase of ECC injection, the test data shows that the system pressure decreases rapidly at 31 seconds as soon as the ECC injection starts and after about 2 seconds the pressure increases slowly to about 500 kPa whereas TRACE simulation results show a rapid pressure decrease at about 35 seconds.

As shown in Figure B.4-18, there are 4 thermocouple stalks in the cold leg of test facility and each stalk has 6 thermocouples which are located axially (Ref. 2). The fluid temperatures of stalk no. 5 of intact cold leg 2 are shown in Figure B.4-19

The fluid temperature at the bottom region (stalk05-6) is less than 50 ^{o}C while other higher thermocouples show at least 125 ^{o}C. This temperature profile data may show that there was cold water initially at the bottom of the cold leg. During the time period of from 31 seconds to 34 seconds, there may be condensation in cold leg between the steam in upper region of cold leg and water in the bottom of cold leg, and that seemed to cause an earlier pressure drop in the cold leg and downcomer before ECC water reached the cold legs. Since there is no data available for the initial water inventory in cold leg, the cold leg is modeled as containing no initial inventory in TRACE simulation. Thus the TRACE simulation results show that there is no condensation before ECC water reaches the intact cold legs, and the pressure decreases in the cold legs and downcomer are predicted to occur later than the test data. TRACE predicts the rapid pressure drop at 35 seconds when ECC flow is fully developed. From about 38 sec to the end of problem, TRACE slightly under-predicts the system pressure by about 5 ~ 25% due to more condensation than the experiment. During the lower plenum penetration period, the downcomer pressure data of this test (Run 062) is about 75 ~ 80% of Test 6-Run 132 of which test conditions are nearly similar to Run 062 except for ECC water temperature and initial lower plenum inventory. The

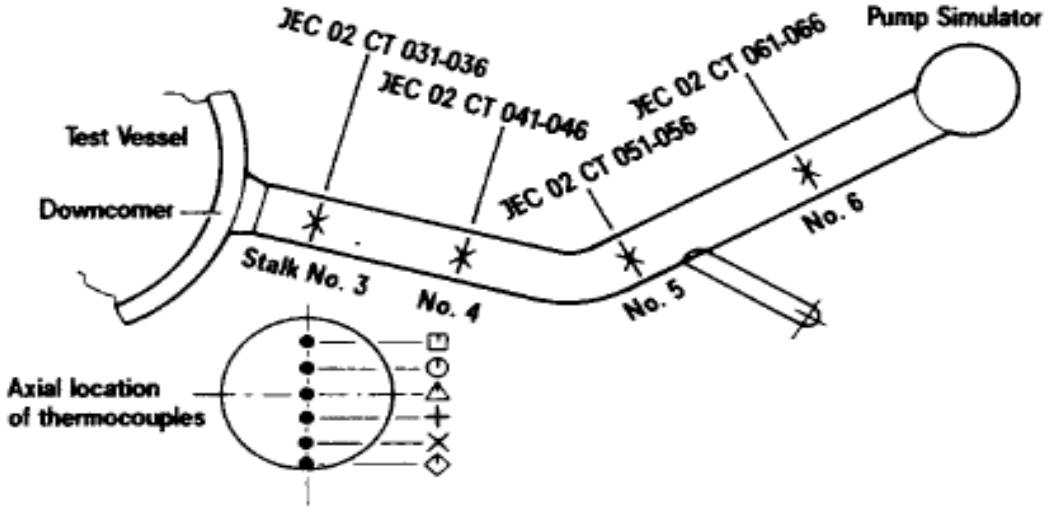

Figure B.4-18. Arrangement of Thermocouples and TC-Stalks in Cold Leg of Loop 02

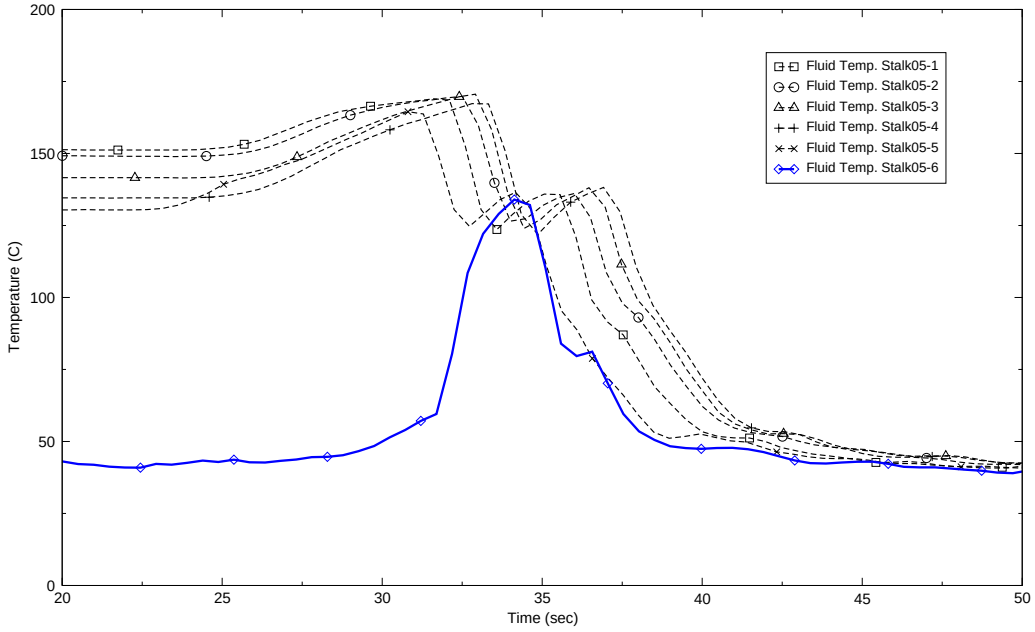

Figure B.4-19. Fluid Temperature Profile at Stalk No. 5 in Cold leg Loop 2

TRACE-predicted downcomer pressure of Run 062 is also about 75 ~ 80% of the predicted system pressure of Run 132, showing the effect of high subcooled ECC water.

The break steam mass flow calculated by TRACE is compared with data in Graph 3 of Figure B.4-45. When ECC flow is fully developed, the measured break steam flow decreases to about 30% of the injected steam flow due to the condensation by high subcooled ECC water whereas the data of Test 6 and Test 7 show that the break steam flow is nearly close to the injected steam flow, as indicated in the simulations of Test 6 and Test 7. Even though TRACE slightly under-predicts the break steam flow through the whole simulated period, TRACE predicts well the condensation effect of high subcooled ECC water on the break steam flow.

The integrated total break mass flow calculated by TRACE is compared with data in Graph 4 of Figure B.4-46. As described in the previous sections, the integrated total break flow data is obtained by digitizing plots in the MPR report (Ref. 3) and the TRACE-predicted total break mass flow is integrated from ECC injection start time to compare with data. The TRACE-predicted integrated total break flow increases noticeably from about 35 sec whereas the data shows a slight increase until about 50 sec. At 50 sec, the integrated total break flow calculated by TRACE is about 300% of the data. After 50 sec, both the TRACE-predicted integrated total break flow and data increase rapidly but the difference in their rate of increase is still significant. Since the digitized data may have a large uncertainty, the accuracy of the prediction can not be quantified well. From this graph, it is expected that the TRACE-predicted lower plenum inventory is much less than the data.

The total inventory in three intact cold legs calculated by TRACE is compared with data in Graph 5 of Figure B.4-46. The test data of total inventory in three intact cold legs is digitized from the plots in the MPR report (Ref. 3) and the predicted mass in the intact cold legs is determined by summing the fluid-cell masses in each of the intact cold legs, cells 14 through 21 of components 14, 24, and 34 of the loop models. During approximately 12 seconds after ECC injection, test data shows that most of the injected ECC water is accumulated in the intact cold legs, and at the end of this period, the intact cold legs are filled more than halfway and water begins to penetrate into the downcomer and the lower plenum as shown in Graph 6 of Figure B.4-46 The TRACE-predicted inventory in three intact cold legs reasonably follows the data during this short cold leg filling period. After a short cold leg filling time, the total intact cold legs inventory of test data reaches about 80% of the full inventory and this inventory is maintained thereafter whereas the TRACE-predicted total intact cold leg inventory decreases continuously after 52 sec as the calculated lower plenum inventory increases relatively faster than before as shown in Graph 6 of Figure B.4-46.

As might be expected from the over-prediction of the integrated total break flow, TRACE significantly under-predicts the lower plenum inventory as shown in Graph 6 of Figure B.4-46. As described before, the lower plenum inventory data is calculated using the lower plenum water level as indicated by a differential pressure measurement. Between 32 sec and 37 sec, test data shows a sharp increase in inventory before ECC injection, but this is due to an erroneous pressure measurement. The data shows that the lower plenum inventory level starts to increase sharply at around 43 sec and reaches an equilibrium level at around 53 sec. TRACE predicts the starting time of penetration into the lower plenum well. However, the calculated rate of increase in the lower plenum inventory is much lower than the data, and the lower plenum inventory reaches an equilibrium level at around 88 sec. Because of the steam mass condensed by the high subcooled ECC water, the data of this test shows a faster inventory increase than Run 132 of Test 6. Steam

injection flow and ECC injection flow of Test 6-Run 132 are nearly same as those of this test but ECC water temperature is close to the saturation temperature. As the data shows, TRACE calculates higher condensation rates in this simulation of high subcooled test than what is predicted in the simulation of Run 132 of Test 6. However, TRACE predicts the opposite lower plenum inventory behavior. A predicted rate of the lower plenum inventory increase in highly subcooled test is lower than what is predicted in Run 132 of Test 6. This discrepant lower plenum inventory behavior in the simulation of highly subcooled test is probably because TRACE calculates too high interfacial drag for highly subcooled water, resulting in excessive ECC bypass. The quantified penetration rates of TRACE simulation and the data are compared in section B.4.4.5

B.4.4.4. Direct Vessel Injection Test (UPTF 21)

B.4.4.4.1. System Configuration and Test Conditions

UPTF Test 21, a quasi-steady state experiment, investigated steam/water flow phenomena in the downcomer and lower plenum of a Babcock and Wilcox (B&W) PWR during the end-of-blowdown, refill and reflood phases of a cold leg break LOCA. Babcock and Wilcox PWRs differ from other US PWRs in that the ECC injection of accumulators and lower pressure injection pumps is through nozzles in the downcomer rather than through nozzles in the cold legs. B&W PWRs employ vent valves in the reactor upper plenum to vent steam from the upper plenum directly to the downcomer during a LOCA. The objective of UPTF Test 21 was to obtain data concerning steam/water interaction in the downcomer for downcomer ECC injection and to compare test results with the cold leg ECC injection results. UPTF Test 21 was run with locked closed vent valves. UPTF Test 21 was divided into four phases of A, B, C and D. Phase A and B were run with end of blowdown/refill conditions i.e., steam only core simulator injection and high ECC injection, and Phases C and D were run with reflood conditions.

To assess the capability of TRACE in predicting the ECC bypass processes, Phase A (Run 272) is selected. The other steady state test, i.e., Phase B (Run 274), is not selected since mass balance error is very large (about 54.6%) in Subphase I of this test. Test Run 272 is a counterpart of the experiments with cold leg ECC injection of Test 5. The flow conditions for this test are sufficiently similar to Test 5 of cold leg ECC injection test to allow comparison of downcomer phenomena for the different injection locations.

As shown in Figure B.4-20, the configuration of system for UPTF Test 21 was similar to the cold leg injection test (Test 6), except that ECC was injected from two downcomer injection nozzles which were located 350 mm (13.8 in) above the cold leg centerline in a 180^{o} circumferential spacing, with each nozzle azimuthally midway between adjacent cold leg nozzles. One downcomer injection nozzle was located between broken cold leg and cold leg 1 (0^{o}) and the other was located between cold leg 2 and 3 (180^{o}). All pump simulators were closed and the broken cold leg valve was fully open. No nitrogen was injected into the ECC-water, and ECC-water was injected directly into the downcomer. The primary system and the containment

simulator were initialized at 3 bar. Initial lower plenum waster level was 0.6 m to ensure that the vessel drain pipes were filled up.

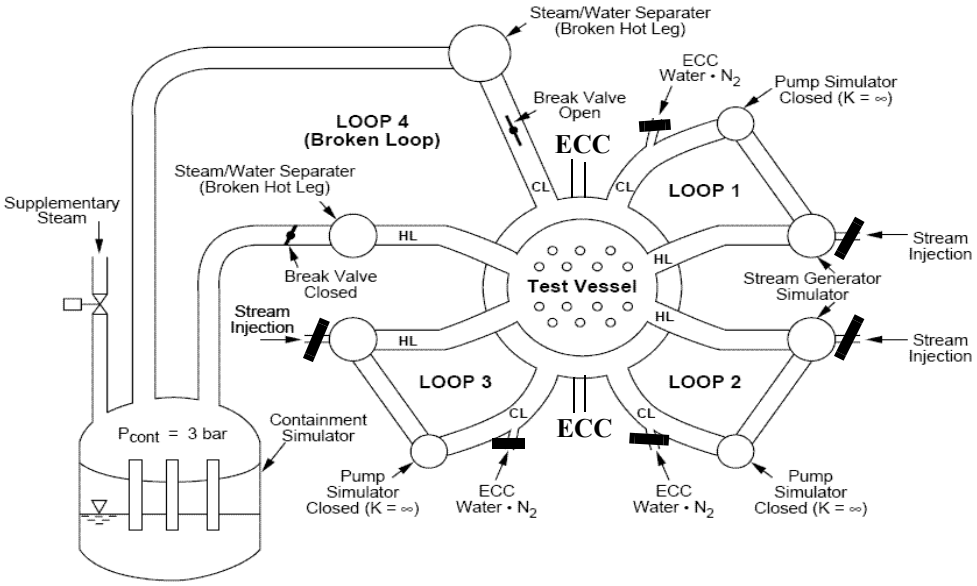

Figure B.4-20. System Configuration for UPTF Test 21

During Phase A, a total steam mass flow of 314 kg/s was introduced through the core and steam generator simulators and strongly subcooled ECC water of 912 and 910 kg/s was injected into the downcomer injection nozzles at 0^o and 180^o respectively. The extent of ECC water subcooling was about 117 K to investigate the effect of the subcooling of ECC on the penetration rate into the lower plenum. The test conditions are listed in Table B.4.4.

Table B.4.4. Test conditions for UPTF Test 21 Run 272

Test/Run/Subphase	**Test 21 Run 272**
Initial Conditions (in Test Vessel)	
Time at Beginning of Phase, sec	30
Pressure, bar	2.86
Lower Plenum Water Level, m	0.62
Wall Temperature, ^oC	172
Water Temperature, ^oC	130
Test Conditions	
Containment Pressure, bar	2.92
Core Simulator Steam Injection Rate, kg/s	225
SG Simulator Steam Injection Rate, kg/s	89
Total ECC Injection Rate, kg/s	1822
ECC Injection Rate at Nozzle 0^o, kg/s	912

Table B.4.4. Test conditions for UPTF Test 21 Run 272

Test/Run/Subphase	Test 21 Run 272
ECC Injection Rate at Nozzle 180^{o}, kg/s	910
ECC temperature, ^{o}C	34
ECC subcooling, ^{o}C	117

B.4.4.4.2. Comparison of Simulation Results and Test Data

The simulation results for Run 272 (Phase A) are shown in Figure B.4-47 and Figure B.4-48 The simulation result figures consist of 6 graphs as follows; Graph 1 for total steam injection flow rate and ECC injection flow rate of each intact cold leg to show the test conditions, Graph 2 for absolute pressure of downcomer and upper plenum, Graph 3 for break steam mass flow, Graph 4 for integrated total break flow, Graph 5 for downcomer inventory calculated by TRACE, and Graph 6 for lower plenum inventory. These graphs are distributed in two figures. Graph numbers used in each figure are marked at the upper right corner.

As shown in the Graph 1 of Figure B.4-47 and Table B.4.4, the core simulators and steam generator simulators started to inject steam at about 31 seconds and the ECC injection started at about 46 seconds. As described before, the highly subcooled ECC water of 912 and 910 kg/s was injected into the downcomer injection nozzles at 0^{o} and 180^{o} respectively and the extent of ECC water subcooling was about 117 K.

Absolute pressures of the upper plenum and the downcomer calculated by TRACE are compared with data in Graph 2 of Figure B.4-47. After start of steam injection, the data shows the sharp increase of the system pressure in the downcomer and upper plenum before ECC injection. TRACE slightly over-predicts the system pressures by about 7% during this period because the calculated break steam flow is slightly less than data as shown in Graph 3 of Figure B.4-47. At about 47 sec (1 sec after ECC injection), condensation of steam on high subcooled ECC leads to rapid pressure drop in both TRACE and the data. At the same time, a rapid reduction of steam flow caused by intensive steam condensation is observed in the test, and TRACE predicts well this condensation effect on break steam flow as shown in Graph 3 of Figure B.4-47. After then, TRACE reasonably predicts the system pressure and the break steam mass flow during this period.

The integrated total break mass flow calculated by TRACE is compared with data in Graph 4 of Figure B.4-48. As described in the previous sections, the integrated total break flow data is obtained by digitizing plots in the MPR report (Ref. 5) and the TRACE-predicted total break mass flow is integrated from the start time of test. The TRACE-predicted integrated total break flow increases noticeably from about 49 sec as shown by the data. After 49 sec, TRACE slightly over-predicts the integrated total break flow but the rate of increase calculated by TRACE matches data well. Since the digitized data may have a large uncertainty, the accuracy of the prediction may not be quantified.

The total inventory in three intact cold legs calculated by TRACE is compared with data in Graph 5 of Figure B.4-48. The total inventory in three intact cold legs is obtained from the data and TRACE simulation using the same way as described in the previous section. After start of ECC injection, the measured total intact cold legs inventory starts to increase sharply and reaches about 8880 kg at 70 sec whereas the TRACE-predicted inventory increases slowly and reaches 4550 kg (51% of the data) at 70 sec. TRACE under-predicts the intact cold legs inventory in all simulations of cold leg ECC injection tests (Test 5, 6 and 7) as well as in this simulation of downcomer ECC injection. The downcomer inventory calculated by TRACE increases sharply until about 52 sec, after which a nearly constant value is maintained during ECC penetration periods.

As shown in Graph 6 of Figure B.4-48, TRACE predicts no ECC water penetration into the lower plenum until 52 sec resulting in sharp increase in downcomer inventory, while the data shows no ECC water penetration until about 57 sec. Between 31 sec and 47.5 sec, test data shows a small rise of inventory due to the dynamic pressure effect of the injected steam, as described in the previous sections. During ECC penetration period, the TRACE-calculated lower plenum inventory shows a smooth increase whereas the data shows an intermittent increase by slugs or plugs of strongly subcooled water. However, TRACE reasonably predicts the rate of increase. The lower plenum inventory calculated by TRACE reaches the equilibrium value at about 82 sec. The predicted equilibrium inventory level is slightly higher than the data. The quantified penetration rate calculated by TRACE is compared with data in the following section.

B.4.4.5. Assessment Results

B.4.4.5.1. Evaluation of ECC Penetration Starting Time into the Lower Plenum

The starting time of TRACE-predicted ECC delivery into the lower plenum is compared with data as shown in Table B.4.5 and Figure B.4-21. The starting time of ECC penetration into the lower plenum is determined by selecting time point when the lower plenum inventory starts to increase. Since Test 7 series consists of 2 ~ 4 subphases, the predicted ECC penetration starting time of the first subphase of each test is compared with data. Test 6-Run 133 is not compared with data because the data is not available.

As the results of comparison, TRACE predicts well the starting time of ECC penetration into the lower plenum, and the difference between TRACE prediction and the data is within +15 ~ –15% of data except for Run 200 and 203 of Test 7. TRACE predicts the ECC penetration to start at 84 sec whereas the data shows no ECC penetration during the first subphase of Test 7-Run 200. In the case of the first subphase of Test 7-Run 203, TRACE predicts no ECC penetration into the lower plenum whereas ECC penetration starts at 48.6 sec in the data.

B.4.4.5.2. Evaluation of ECC Water Penetration Rate into the Lower Plenum

To assess the capability of TRACE in predicting the ECC bypass, the TRACE-predicted ECC penetration rate of each test is calculated and compared with data. In both test data and TRACE

Table B.4.5. Comparison of ECC Penetration Starting Time into LP Between Test Data and TRACE-predicted

Test-Run /subphase	Total Steam Injection Flow, kg/s	Total ECC Injection Flow, kg/s	ECC Injection Start Time, sec	ECC Penetration Beginning Time into LP, sec		Difference, % of Data
				DATA	TRACE	
6-131	396	1446	45.0	55.5	54	-3
6-132	295	1470	42.7	53.3	46.6	-13
6-133	202	1473	N/A	N/A	51.0	N/A
6-135	436	1428	42.3	56.8	48.5	-15
6-136	102	1470	42.5	46.1	48.5	+5
7-200/I	104	494	38.2	No penetration	84	N/A
7-201/I	102	977	40.1	49.3	43.1	-13
7-203/I	69	735	40.2	48.6	No penetration	N/A
5-062	310	1500	30.4	40.5	40.2	-1
21-272	314	1822	46.0	48	50.1	+4

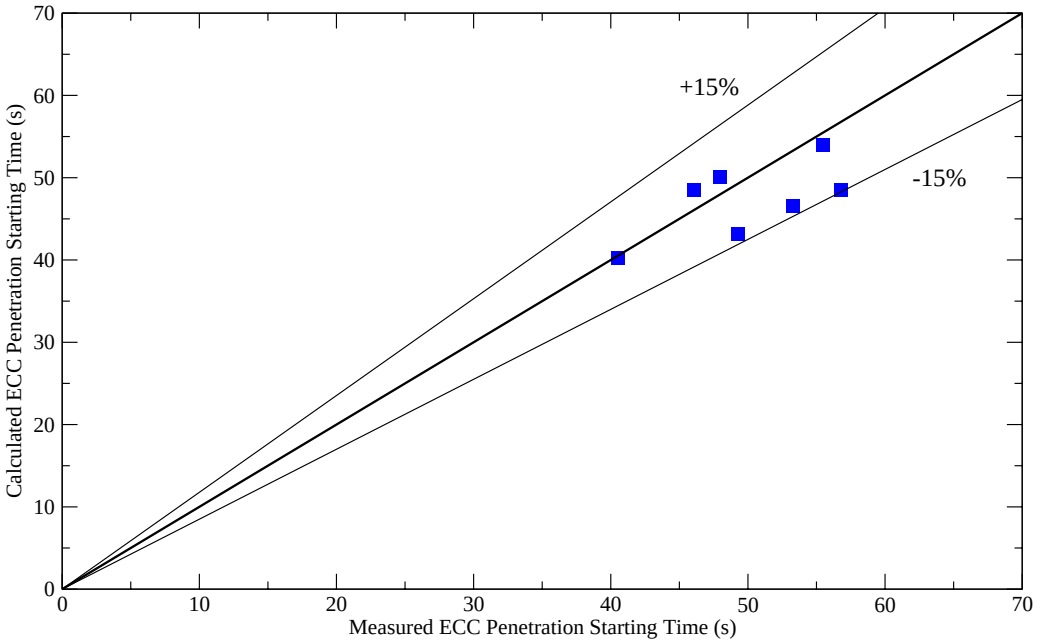

Figure B.4-21. Comparison of Calculated and Measured ECC Penetration Starting Time into the Lower Plenum

simulations, rates of ECC penetration into lower plenum are obtained using a simple method which is a direct way of calculating the rate of ECC water downflow into the lower plenum by considering the water inventory change in the lower plenum over the chosen time period to evaluate, i.e.,

$$\text{ECC Penetration Rate} = \frac{\text{LP Inventory (t2)} - \text{LP Inventory (t1)}}{\text{t2} - \text{t1}} \quad (4\text{-}1)$$

The criteria used to select the evaluation time period are; (1) steady state steam and ECC injection flow rate, (2) nearly constant pressure in the downcomer, and (3) similar water inventories in the intact loop cold legs and the downcomer at the two time points where the lower plenum inventory is calculated. But the evaluation time period of Test 6-Run 133 is obtained from the Quick Look Report for Test 6 (Ref. 4) since no data is available. The selected evaluation time period of each test is shown in Table B.4.6.

Table B.4.6. Selected Time Periods To Evaluate ECC Penetration

Test-Run /subphase	Evaluation Period, sec	
	DATA	TRACE
5-062	43.2 - 52	42 - 88
6-131	58.5 - 80	55 - 80
6-132	54 - 68	47 - 67
6-133	55 - 66	54 - 70
6-135	56.8 - 65	56 - 82
6-136	49.5 - 64.8	49 - 64.5
7-200/I	40 - 100	40 - 98
7-200/II	100 - 159	100 - 150
7-200/III	159 - 212	159 -212
7-201/I	50 - 106	43.5 - 106
7-201/III	167 - 225	167 - 225
7-202/II	106 - 168	106 - 168
7-203/I	40 - 100	40 - 100
7-203/II	100 - 173	100 - 160
7-203/III	190 - 256	190 - 250
7-203/IV	270 - 330	270 - 330
21-272	57 - 81	51.5 - 80.5

The predicted ECC water penetration rates from TRACE simulations are compared with data as shown in Table B.4.7 and Figure B.4-22. The TRACE-predicted ECC penetration rates reasonably match data, and the ECC penetration rate differences between data and TRACE are within 20% in most cases. Considering the experimental mass balance error of up to about 15% (Ref. 3), the TRACE-predicted ECC penetration rates are in good agreement with data, showing the reasonable capability of TRACE in predicting ECC bypass phenomena of cold leg ECC injection and downcomer ECC injection. However, TRACE simulation result shows a large deviation for the case of highly subcooled ECC cold leg injection (Test 5-Run 062) and the cases of ECC injection to only cold leg 1 (Subphase I and III of Test 7-Run 200 and Subphase I of Test 7-Run 203). TRACE under-predicts the ECC penetration rate by 75% for the Test 5-Run 062. For Subphase I of Test 7-Run 203, the TRACE-predicted ECC penetration rate is close to 0 kg/s whereas test data shows 108 kg/s of ECC water delivered into the lower plenum. For Test 7-Run 200, the TRACE-predicted penetration rates are 47 kg/s for the Subphase I, and 116 kg/s for subphase III, whereas test data shows that the penetration rate is close to 0 kg/s in both subphases. However, the simulation results of Test 7-Run 200 are somewhat dubious since the results

(especially behavior of inventory in the downcomer and the lower plenum) are very sensitive to input-data model.

For the cases of ECC injection into three intact cold legs, a flooding curve (i.e., "Steam Injection Flow Rate vs. ECC Penetration Rate") obtained from TRACE simulations, is compared with a flooding curve of the data in Figure B.4-23 Eight different steam flow rates are used ranging 51 ~ 436 kg/s, while the ECC injection rate per loop is about 490 kg/s for all eight cases. The rate of ECC penetration into the lower plenum decreases as steam injection flow rate increases in both TRACE simulations and test data except for Test 5-Run 062. TRACE significantly under-predicts ECC penetration rate for Test 5-Run 062, as described before. In the case of steam flow of 396 kg/s ~ 436 kg/s, the data shows that the whole ECC flow from cold leg 1 and about 40% of ECC flow from cold leg 2 and cold leg 3 are bypassed, and TRACE simulation results show almost the same ECC bypass behavior, i.e., the whole ECC flow from cold leg 1 and about 37% of ECC flow from cold leg 2 and cold leg 3 are predicted to bypass. In the case of steam flow rate of 202 kg/s ~ 295 kg/s, the whole ECC from cold leg 1 and about 17 ~ 18% of ECC from cold leg 2 and 3 are bypassed in the test, whereas the whole ECC from cold leg 1 and 23 ~ 26% of ECC from cold leg 2 and 3 are predicted to bypass in TRACE simulations, showing a small difference between TRACE predictions and data. In the cases of steam flow of 102 kg/s and higher, the ECC from cold leg 1 is fully bypassed in the test, whereas TRACE predicts that a small amount of ECC from cold leg 1 is delivered into the lower plenum for Test 6-Run 136. With steam flow rate of 51 kg/s, a small amount of ECC water from cold leg 1 and the whole ECC flow from cold leg 2 and 3 are delivered into the lower plenum in both TRACE simulation and the data. In all steam injection flow rates, the TRACE-predicted flooding curve is in good agreement with data-based flooding curve for the cases of ECC injection into the three intact cold legs except for Test 5-Run 062.

Table B.4.7. Comparison of Measured and Predicted ECC Penetration Rates into the Lower Plenum

Test-Run-Subphase	Steam Flow (kg/s)	ECC Injection Flow (kg/s)				ECC Penetration Rate (kg/s)		ECC Penetration Ratio (% of Total ECC Flow)	
		CL1	CL2	CL3	Total	Data	TRACE	Data	TRACE
ECC Injection to Cold Legs 1,2,3:									
6-135	436	480	480	481	1441	571	483	40	34
6-131	396	478	485	488	1451	582	617	40	43
5-062	310	500	500	500	1500	1020	257	68	17
6-132	295	494	489	489	1472	814	719	58	49
6-133	202	499	486	493	1478	802	756	66	52
6-136	102	494	488	489	1471	921	1074	63	73
7-201-III	102	493	487	489	1469	967	993	66	68
7-203-IV	51	493	485	487	1465	1023	1099	70	75
ECC Injection to Cold Legs 2 and 3:									
7-202-II	128	-	486	491	977	655	692	67	71
7-201-I	102	-	487	490	977	868	798	89	82
ECC Injection to Cold Leg 1 and 3:									

Table B.4.7. Comparison of Measured and Predicted ECC Penetration Rates into the Lower Plenum

Test-Run-Subphase	Steam Flow (kg/s)	ECC Injection Flow (kg/s)				ECC Penetration Rate (kg/s)		ECC Penetration Ratio (% of Total ECC Flow)	
		CL1	CL2	CL3	Total	Data	TRACE	Data	TRACE
7-203-III	71	737	-	733	1470	836	812	57	55
ECC Injection to Cold Leg 1 Only:									
7-200-I	104	494	-	-	494	~ 0	47	0	10
7-200-III	102	735	-	-	735	~ 0	116	0	16
7-203-I	69	735	-	-	735	108	~ 0	15	0
7-200-II	54	736	-	-	736	303	232	41	31
7-203-II	30	737	-	-	737	521	455	71	62
ECC Injection to Downcomer		DVI 0	DVI 180		Total				
21-272	314	912	910		1822	419	471	23	26

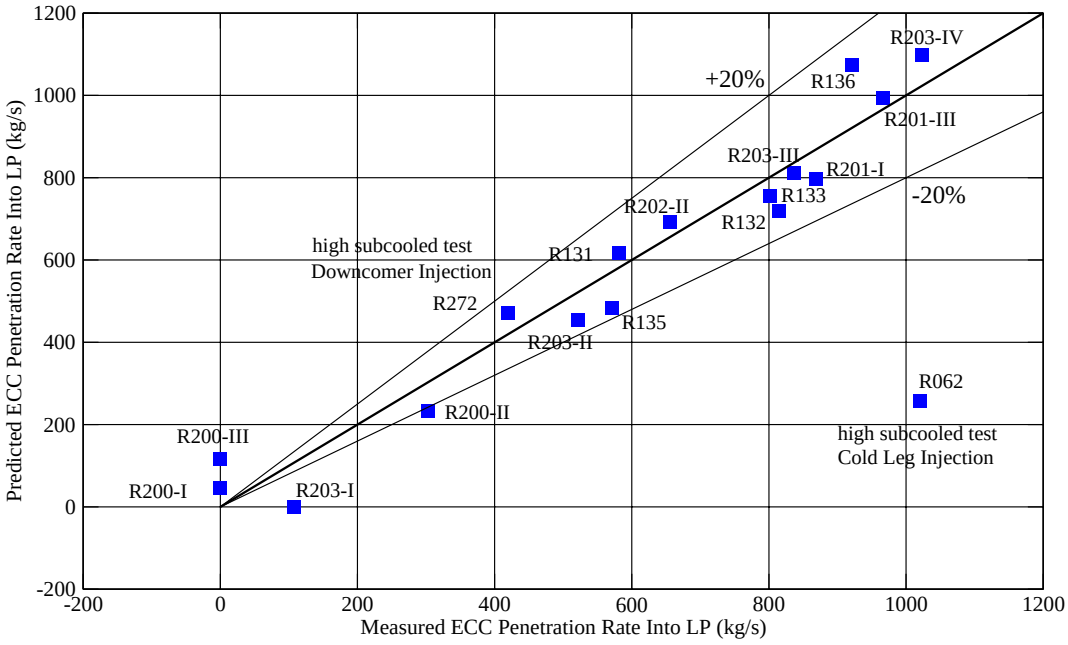

Figure B.4-22. Comparison of Calculated and Measured ECC Penetration Rate into the Lower Plenum

The TRACE-predicted flooding curves of the tests with the other ECC injection locations (i.e., ECC injection to only CL1, ECC injection to CL2/CL3, and ECC injection to CL1/CL3) are

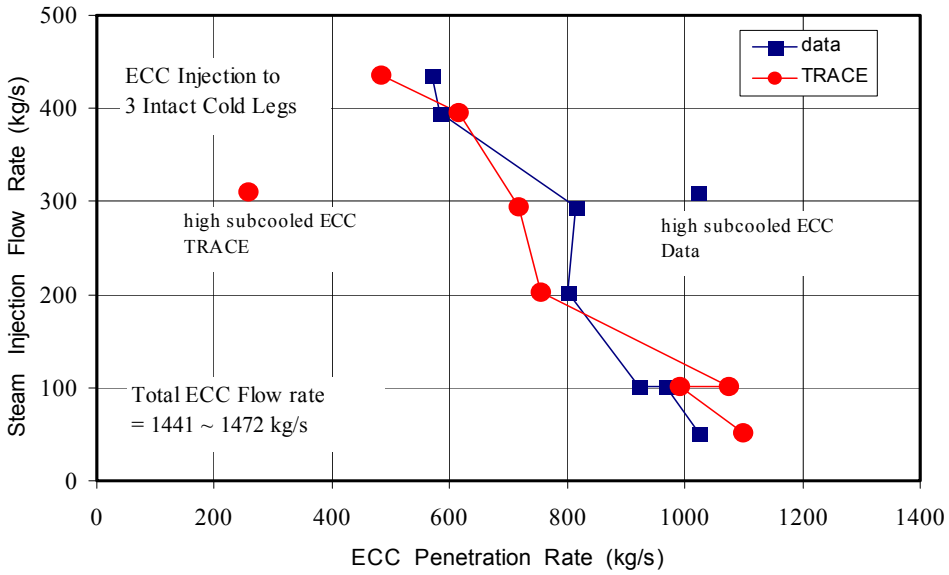

Figure B.4-23. Steam Injection Flow Rate vs. ECC Penetration Rate for ECC Injection to 3 Cold Legs Cases

compared with data in Figure B.4-23. For the flooding curve of ECC injection from only cold leg 1, the data-based flooding curve shows that the injected ECC water is completely bypassed at steam injection rates of 102 kg/s and above. However, the TRACE-predicted flooding curve shows an inconsistent bypass behavior with steam injection flow rates. This inconsistency in the TRACE-predicted flooding curve is caused by the unexpected results of Test 7-Run 200 simulation in which results are very sensitive to input-data model as described before. Excluding the simulation results of Test 7-Run 200, TRACE predicts that the injected ECC is completely bypassed at steam injection rate of 69 kg/s. The predicted flooding curve follows the data-based flooding curve well if steam injection flow is less than 69 kg/s. In the case of ECC injection from cold 2 and 3 far away from the broken cold leg, TRACE predicts penetration rates well, and the penetration rate difference between data and TRACE is about 13%. The predicted flooding curve follows the trend of data-based flooding curve well. The ECC penetration rate decreases as steam injection flow increases in both TRACE simulation and data. In the case of ECC injection from cold 1 and 3, the predicted penetration rate also matches data well, and the difference between data and TRACE is less than 3%.

TRACE reasonably predicts the ECC penetration rate well for the downcomer injection test with highly subcooled ECC (i.e., Test 21-Run 272), showing a 12% difference between data and TRACE. Data-based ECC penetration rate of Test 5-Run 062, in which test conditions are quite similar to those of Test 21-Run 272 except for cold leg ECC injection, is higher than Test 21-Run 272 by more than 2 times as previously shown in Table B.4.7 However, on the contrary, the TRACE-predicted ECC penetration of Test 21-Run 272 is much higher than what is predicted in Test 5-Run 062 since TRACE significantly under-predicts the ECC penetration rate of Test 5-Run 062.

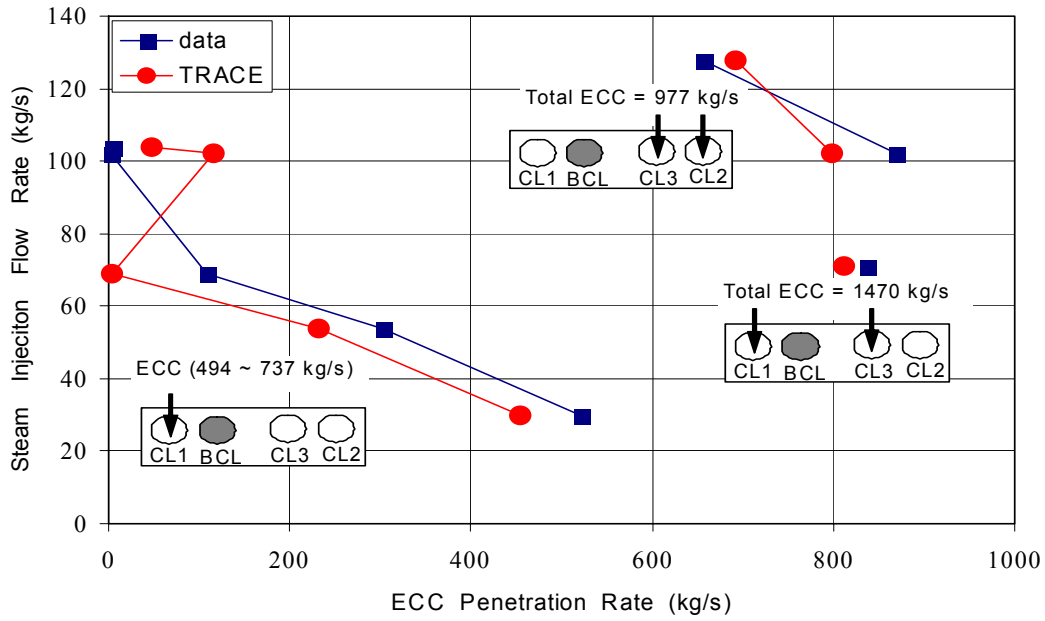

Figure B.4-24. Steam Injection Flow Rate vs. ECC Penetration Rate for Various Configurations of Cold Leg Injection

In general, data-based flooding curves can be characterized in 3 regions as follows:

1. For the steam flow rate of above 202 kg/s, the ECC delivery rate from cold legs 2 and 3 decreases with increasing steam mass flow rates, and no ECC water from cold leg 1 penetrates into the lower plenum.
2. For the steam flow rate of below 202 kg/s, the ECC from cold leg 2 and cold leg 3 is completely delivered into the lower plenum.
3. The ECC water from cold leg 1 is fully bypassed at the steam flow rate of 102 kg/s.

The TRACE-predicted flooding curves show a good agreement with region 1) and 2). However, TRACE predicts that the ECC water from cold leg 1 is fully bypassed at the steam flow rate of 69 kg/s. Although the point of steam flow rate, where the ECC water injected from cold leg 1 is completely bypassed, is estimated lower than the data, the TRACE-predicted ECC penetration rates agree with data well.

B.4.4.5.3. Condensation Efficiency

Steam condensation is one of the major parameters which significantly affect ECC bypass phenomenon. In the UPTF test data analysis (Ref. 3), the efficiency for condensation occurring in

the intact cold legs and downcomer was calculated by comparing average subcooling of ECC exiting the downcomer to the average subcooling of ECC entering the system. The average ECC subcooling exiting the downcomer was calculated by averaging the liquid temperature at the bottom of the downcomer and in the broken cold leg. The downcomer temperature was weighted by the fraction of ECC delivered to the lower plenum, while the broken cold leg temperature was weighted by the fraction of ECC bypassed to account for the distribution of ECC water. The condensation efficiency, f, was then calculated by comparing the outlet ECC subcooling to the inlet ECC subcooling:

$$f = \frac{\Delta T_{in} - \Delta T_{out}}{\Delta T_{in}} \tag{4-2}$$

where

ΔT_{in} = average ECC subcooling at the downcomer entrance (calculated in intact cold legs),

ΔT_{out} = average ECC subcooling at the downcomer exit (calculated at the bottom of the downcomer and in the broken cold leg)

The condensation efficiency of TRACE simulation is obtained according to the same method used in the data analysis report, in order to get a consistent evaluation results. The calculated condensation efficiency is compared with data in Table B.4.8, and Figure B.4-25. Both condensation efficiency of TRACE and data are evaluated only during the downcomer analysis period. The data-based condensation efficiency is obtained from the data analysis report (Ref. 3). The downcomer analysis period used in the data analysis report is different from those of TRACE simulation, but the difference is not significant.

The condensation efficiency of TRACE simulation is in the range of 54 ~ 90% whereas the data-based condensation efficiency is in the range of 40 ~ 80%. In the cases of Subphase I and IV of Test 7-Run 203, the calculated condensation efficiency is 100% probably because TRACE calculates lower pressure at downcomer region, which makes subcooling of ECC decrease during the analysis period. Average ECC subcooling at intact cold leg is close to 0.0 or even less than 0.0 for Subphase I and IV of Test 7-Run 203. For the cases of ECC injection to Loop 1 only, the calculated condensation efficiency, ranging 54 ~ 90%, is higher than the data which is ranging 40 ~ 68%. For the cases of ECC injection into three intact cold legs, the calculated condensation efficiency is in the range of 58 ~ 90% whereas the data-based condensation efficiency is in the range of 40 ~ 82%. For steam flow of > 202 kg/s, the calculated condensation is higher than the data, whereas for steam flow of < 202 kg/s, the calculated condensation is lower than the data. The data-based condensation efficiency of the cases with ECC injection into three intact cold legs is higher than that of the cases with ECC injection into the cold leg 1 only, but such a trend of condensation efficiency is not indicated in TRACE simulation. For downcomer ECC injection, the calculated condensation efficiency is slightly lower than the data, but the difference is not significant. As described in the data analysis report, the data-based condensation efficiency could not be accurately determined since the subcooling of water in downcomer could not be precisely measured with a limited number of thermocouples. Nonetheless, the difference of condensation

efficiency between TRACE simulation and data is within 25% in most simulated cases, showing a good agreement with data.

Table B.4.8. Comparison of Calculated and Data-Based Condensation Efficiency

Test-Run-Subphase	Condensation Efficiency, f	
	Data	TRACE
ECC Injection to Cold Legs 1, 2 and 3:		
6-135	0.8167	0.8963
6-131	0.7846	0.8804
5-062	0.7769	0.7666
6-132	0.7857	0.8080
6-133	0.6341	0.6788
6-136	0.6786	0.5800
7-201-III	0.7857	0.6169
7-203-IV	0.4	1.0
ECC Injection to Cold Legs 2 and 3:		
7-202-II	0.7333	0.6753
7-201-I	0.9412	0.5925
ECC Injection to Cold Leg 1 and 3:		
7-203-III	0.5	0.7993
ECC Injection to Cold Leg 1 Only:		
7-200-	0.6842	0.7134
7-200-III	0.6097	0.7783
7-203-I	0.4167	1.0
7-200-II	0.6	0.5447
7-203-II	0.4	0.8958
ECC Injection to Downcomer		
21-272	0.828	0.770

B.4.4.6. Conclusion

The simulations of UPTF tests using TRACE Version 5.0RC3 are performed and compared with data to assess the capability of TRACE for predicting ECC bypass phenomena. The simulated test series are chosen to cover various configurations of critical parameters on ECC bypass (steam injection flow rate, ECC injection location, ECC temperature, and ECC flow rate). The simulation results show that TRACE generally predicts the ECC penetration rate well, although there are some deficiencies. In most simulated cases, TRACE under-predicts the system pressure after start of ECC injection due to excessive condensation resulting in under-prediction of break steam flow. The other deficiency is the under-prediction of ECC penetration rate in highly subcooled ECC test with ECC injection into cold legs. The difference in ECC penetration rates between TRACE prediction and data is less than 20% in most simulated cases. Considering the experimental mass

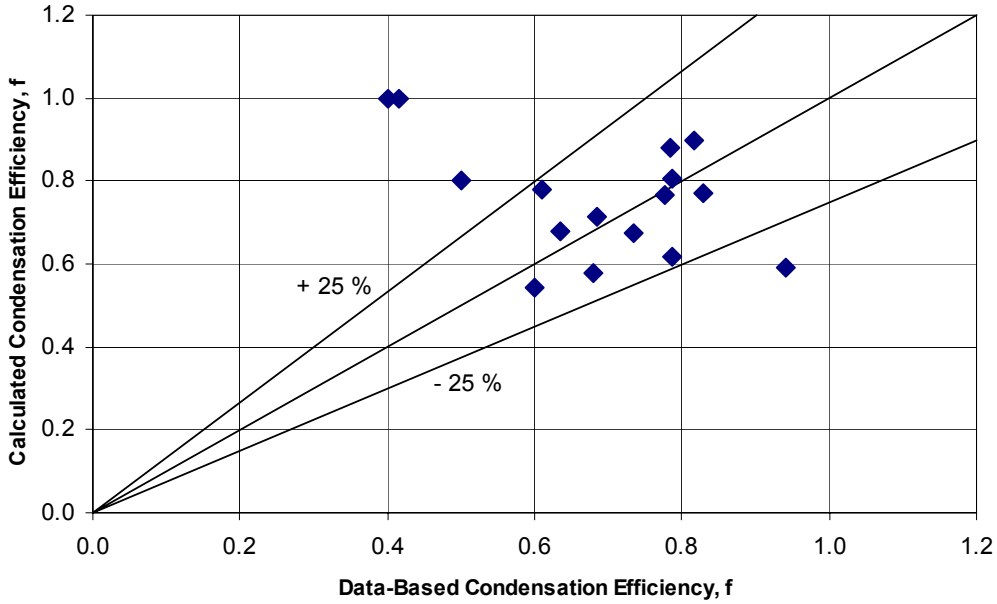

Figure B.4-25. Comparison of Calculated and Data-Based Condensation Efficiency

balance error of up to about 15%, the TRACE-predicted ECC penetration rates are in good agreement with data, showing the reasonable capability of TRACE in predicting the ECC bypass phenomenon during the cold leg ECC injection and the downcomer ECC injection.

B.4.5. References

1 "UPTF: Program and System Description", U9 414/88/023, UB KWU, Nov., 1988

2 "UPTF Test Instrumentation - Measure System Identification, Engineering Units and Computed Parameters", R 515/85/23, UB KWU, Sep., 1985

3 "Summary of Results from the UPTF Downcomer Separate Effects Tests, Comparison to Previous Scaled Tests, and Application to U.S. Pressurized Water Reactor", MPR Associates, INC., July, 1990

4 "UPTF Test No. 6 Downcomer Separate Effect Test, Quick Look Report", SIMENS AG, Mar. 1989.

5 "Summary of Results from the UPTF Downcomer Injection/Vent Valve Separate Effects Tests, Comparison to Previous Scaled Tests, and Application to Babcock & Wilcok Pressurized Water Reactors", MPR 1329, MPR Associates, INC., September 1992.

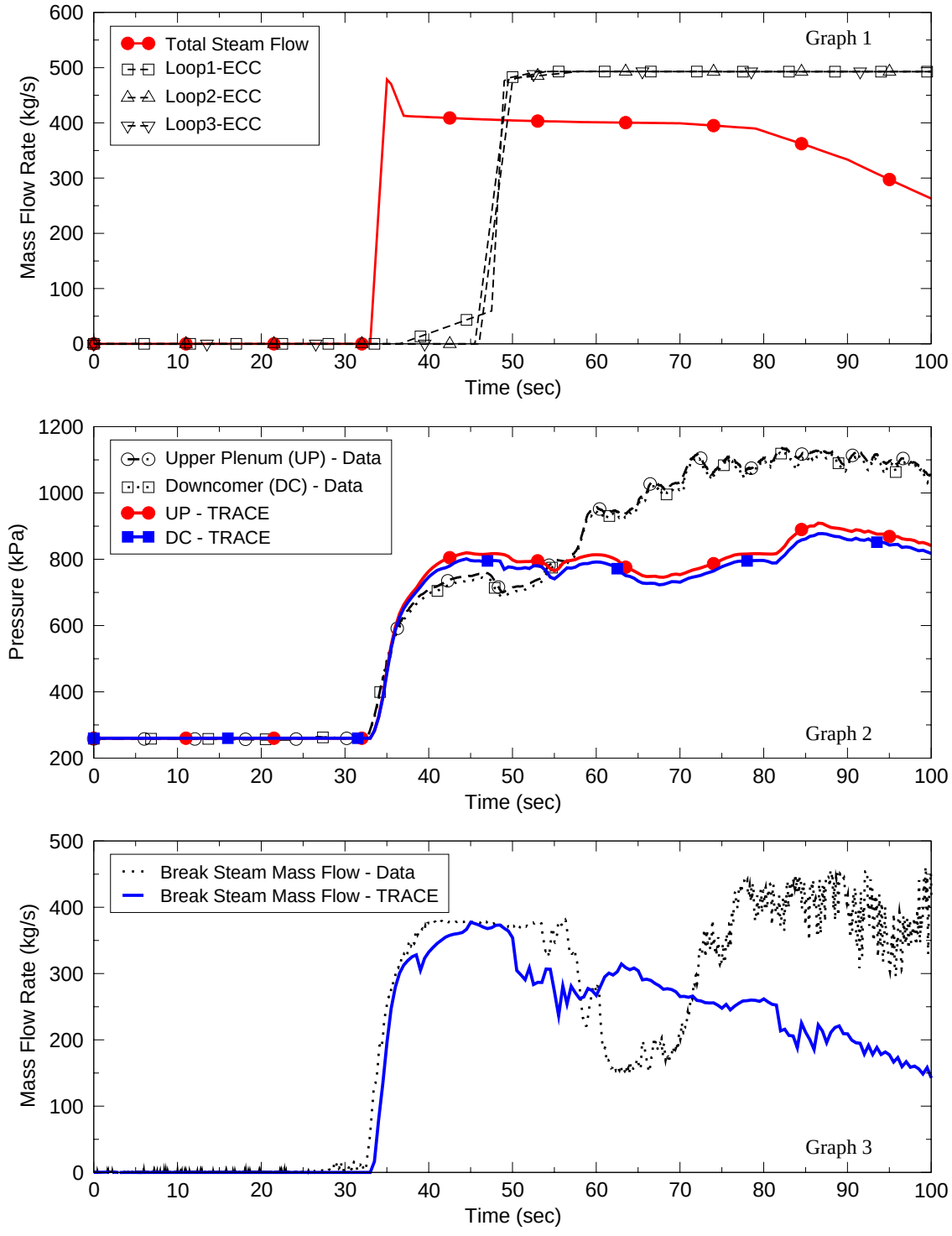

Figure B.4-26. Simulation Results for UPTF Test 6 Run 131 : (1/3)

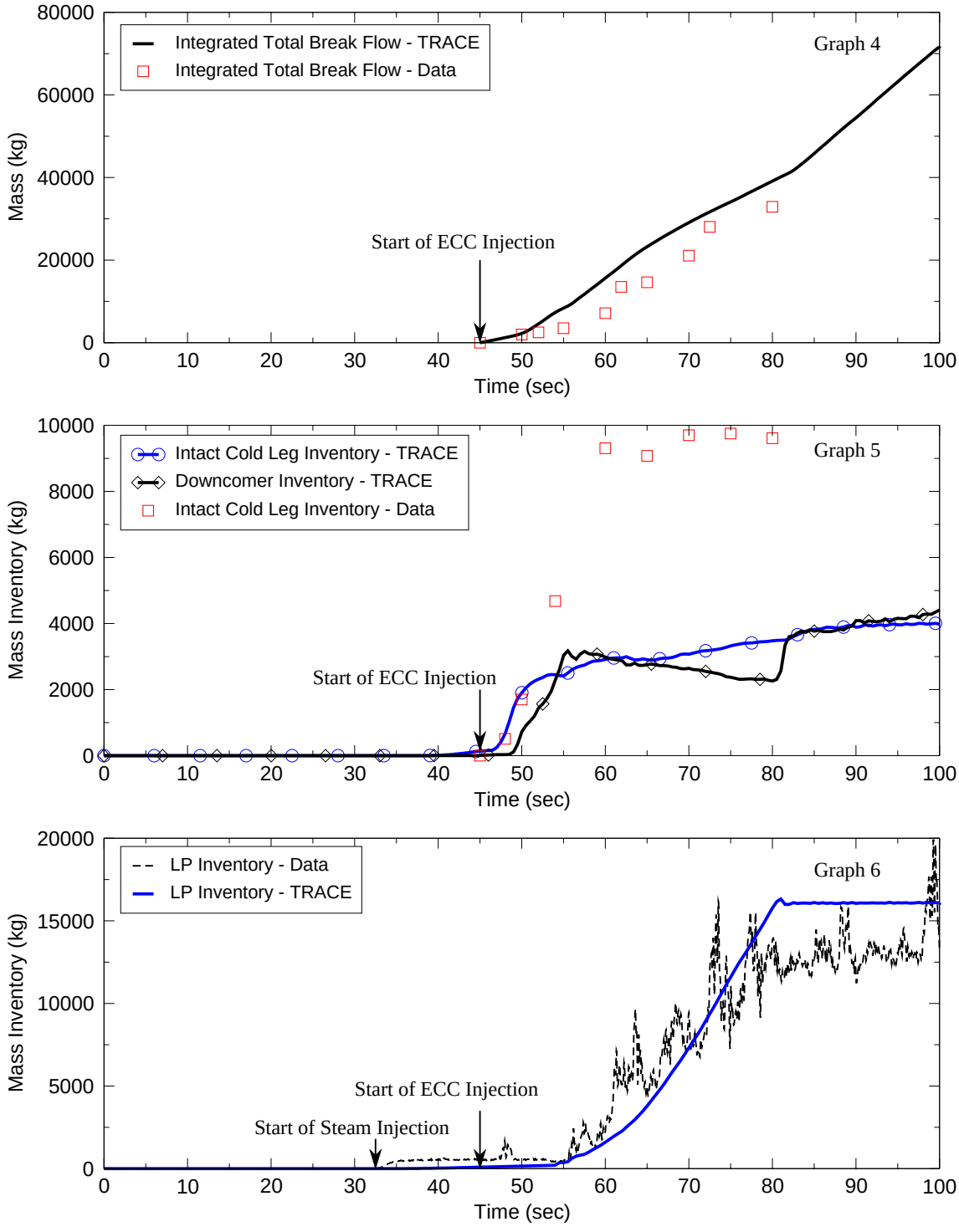

Figure B.4-27. Simulation Results for UPTF Test 6 Run 131 : (2/3)

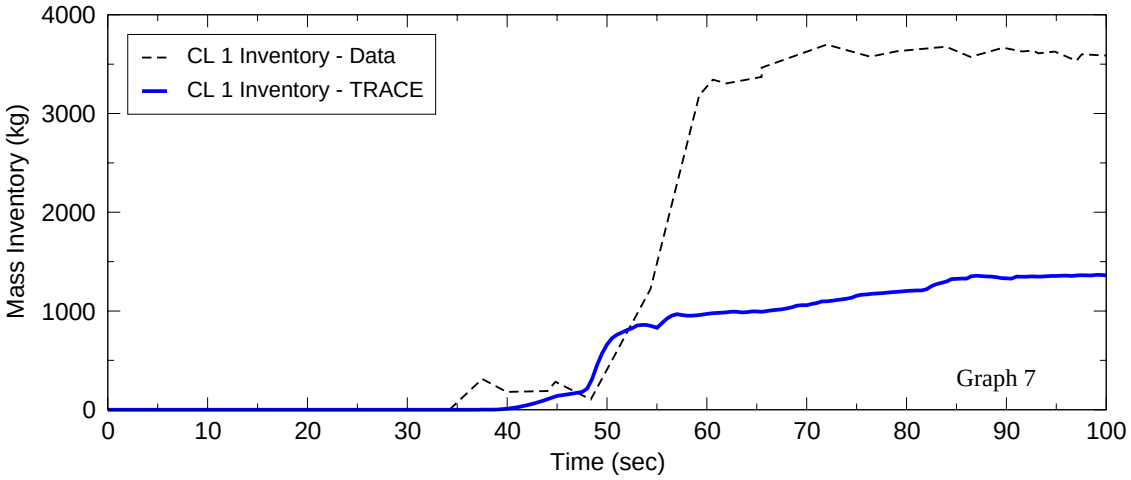

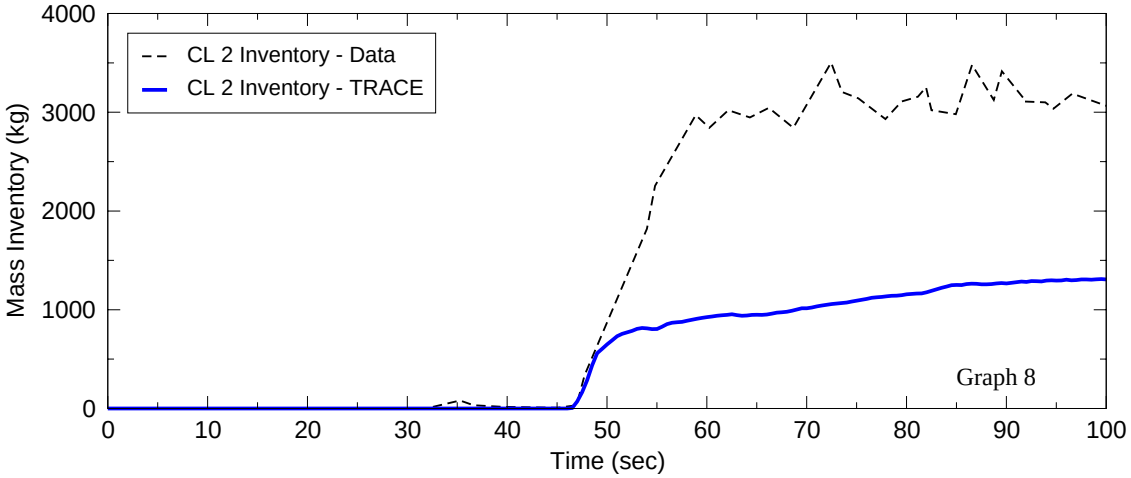

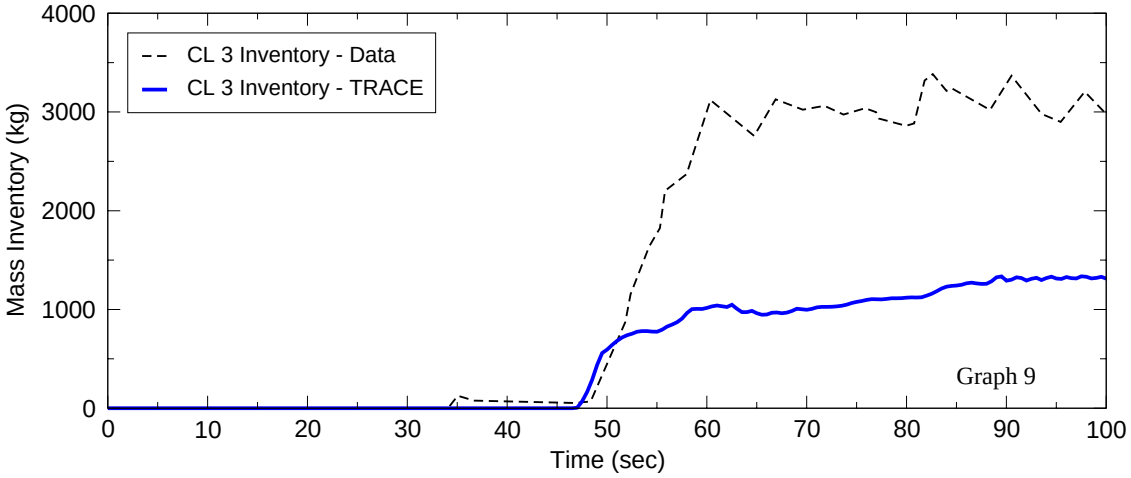

Figure B.4-28. Simulation Results for UPTF Test 6 Run 131 : (3/3)

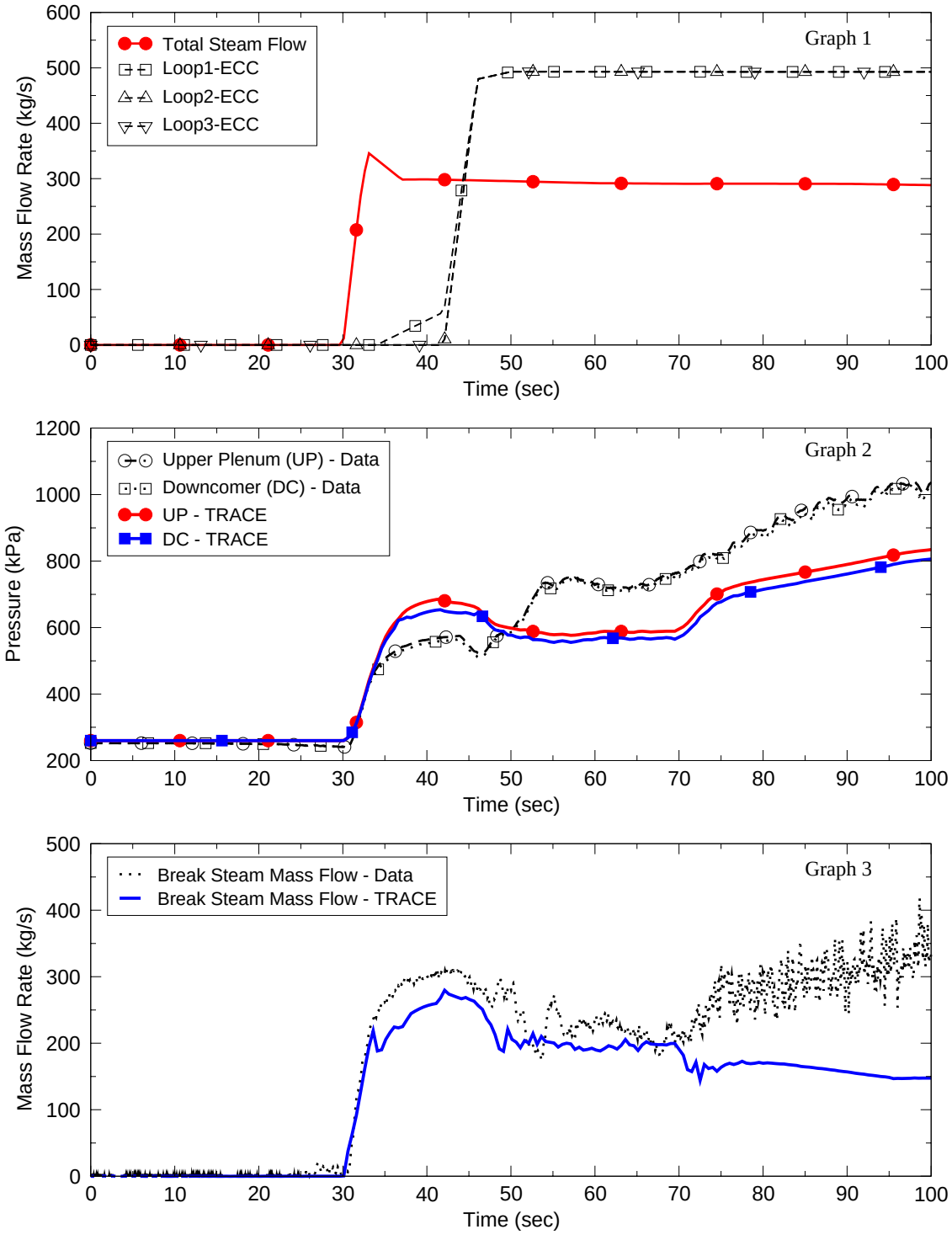

Figure B.4-29. Simulation Results for UPTF Test 6 Run 132 : (1/2)

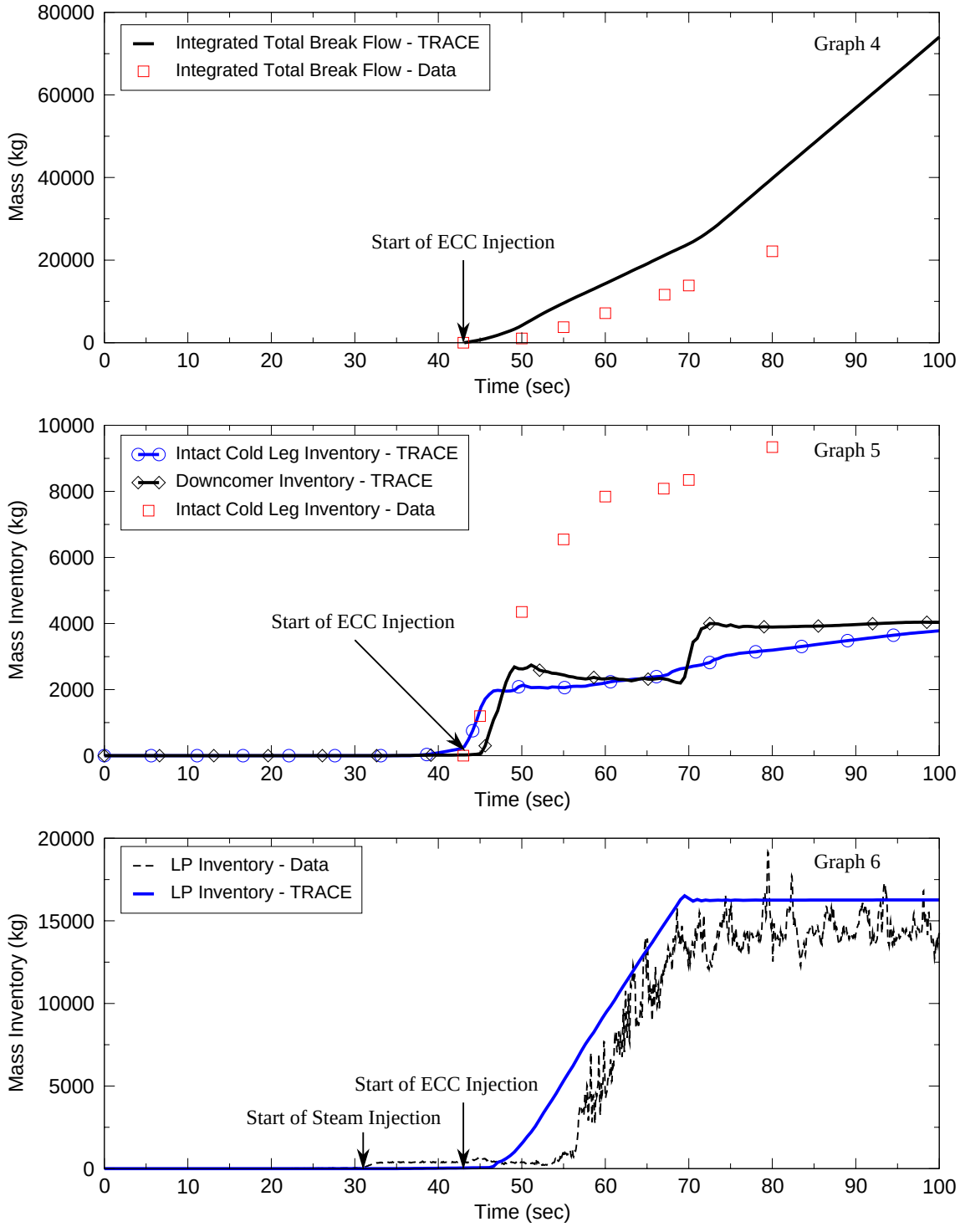

Figure B.4-30. Simulation Results for UPTF Test 6 Run 132 : (2/2)

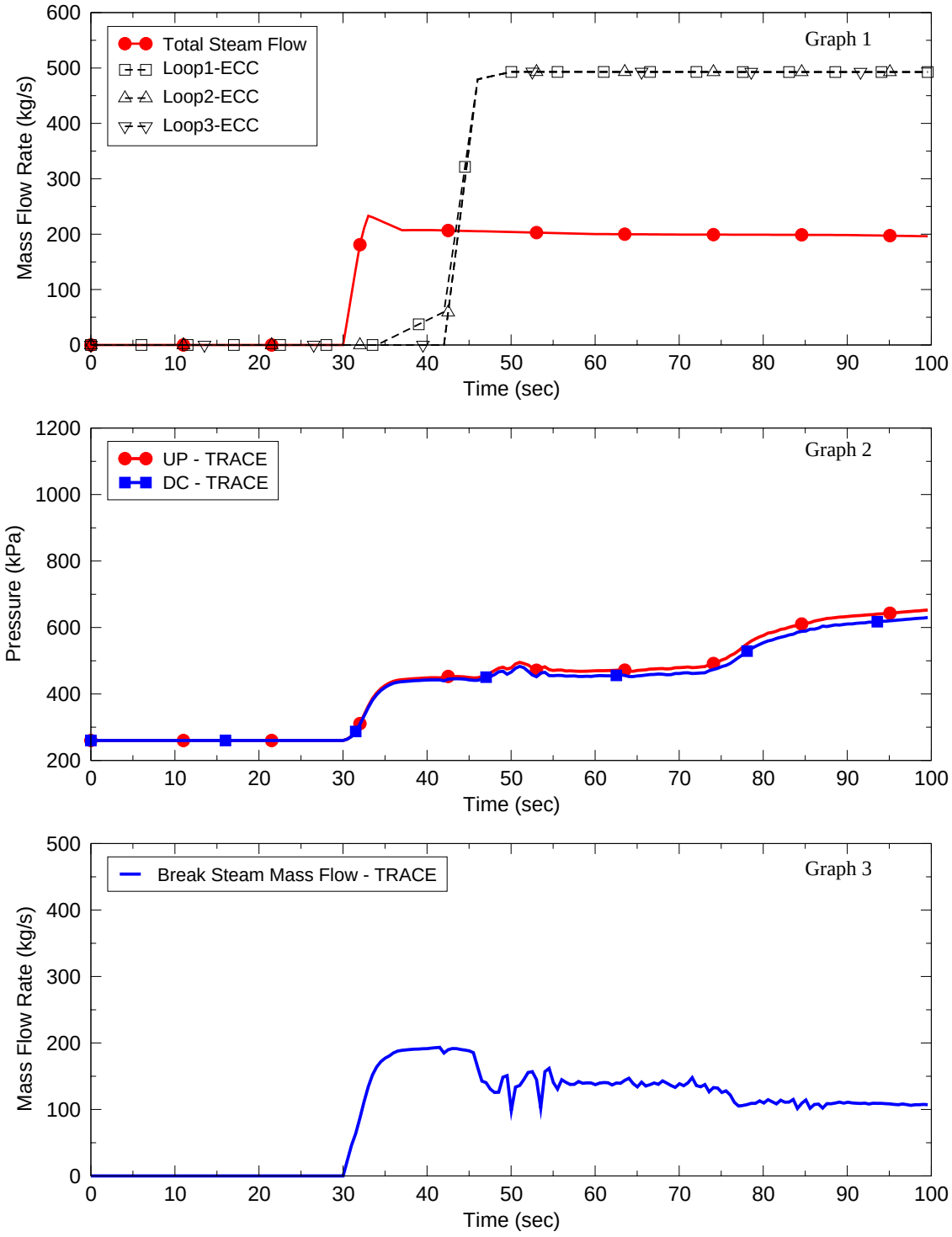

Figure B.4-31. Simulation Results for UPTF Test 6 Run 133 : (1/2)

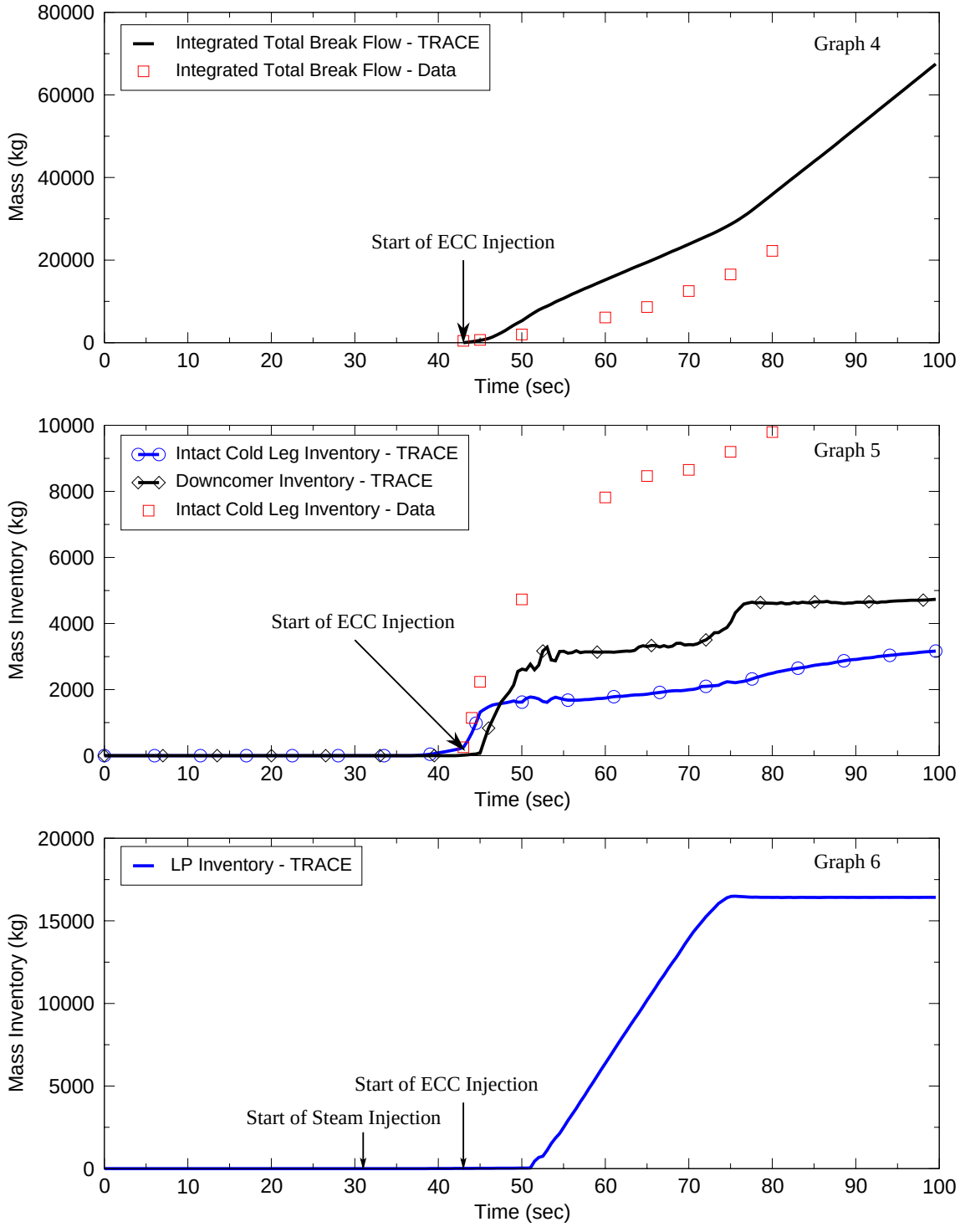

Figure B.4-32. Simulation Results for UPTF Test 6 Run 133 : (2/2)

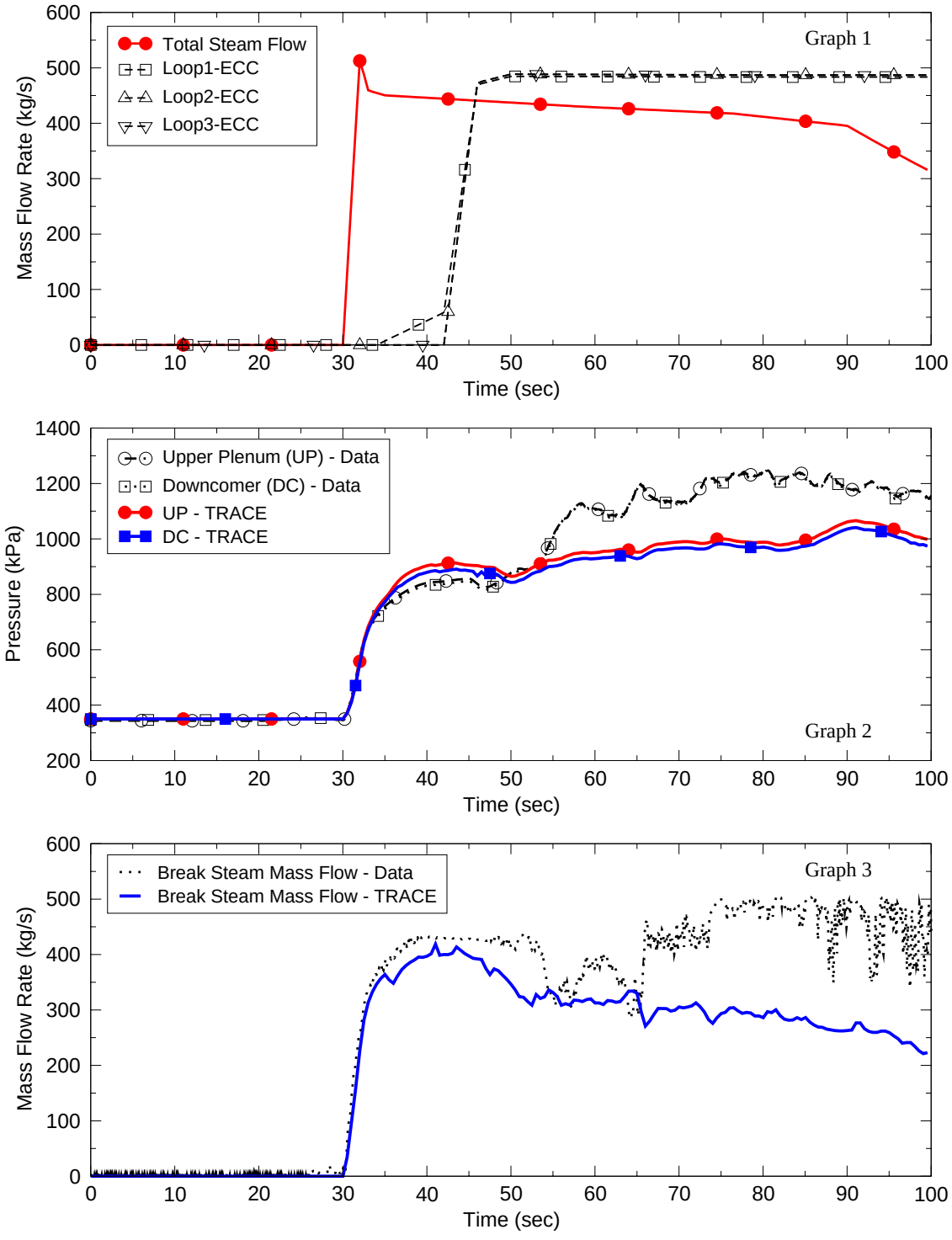

Figure B.4-33. Simulation Results for UPTF Test 6 Run 135 : (1/2)

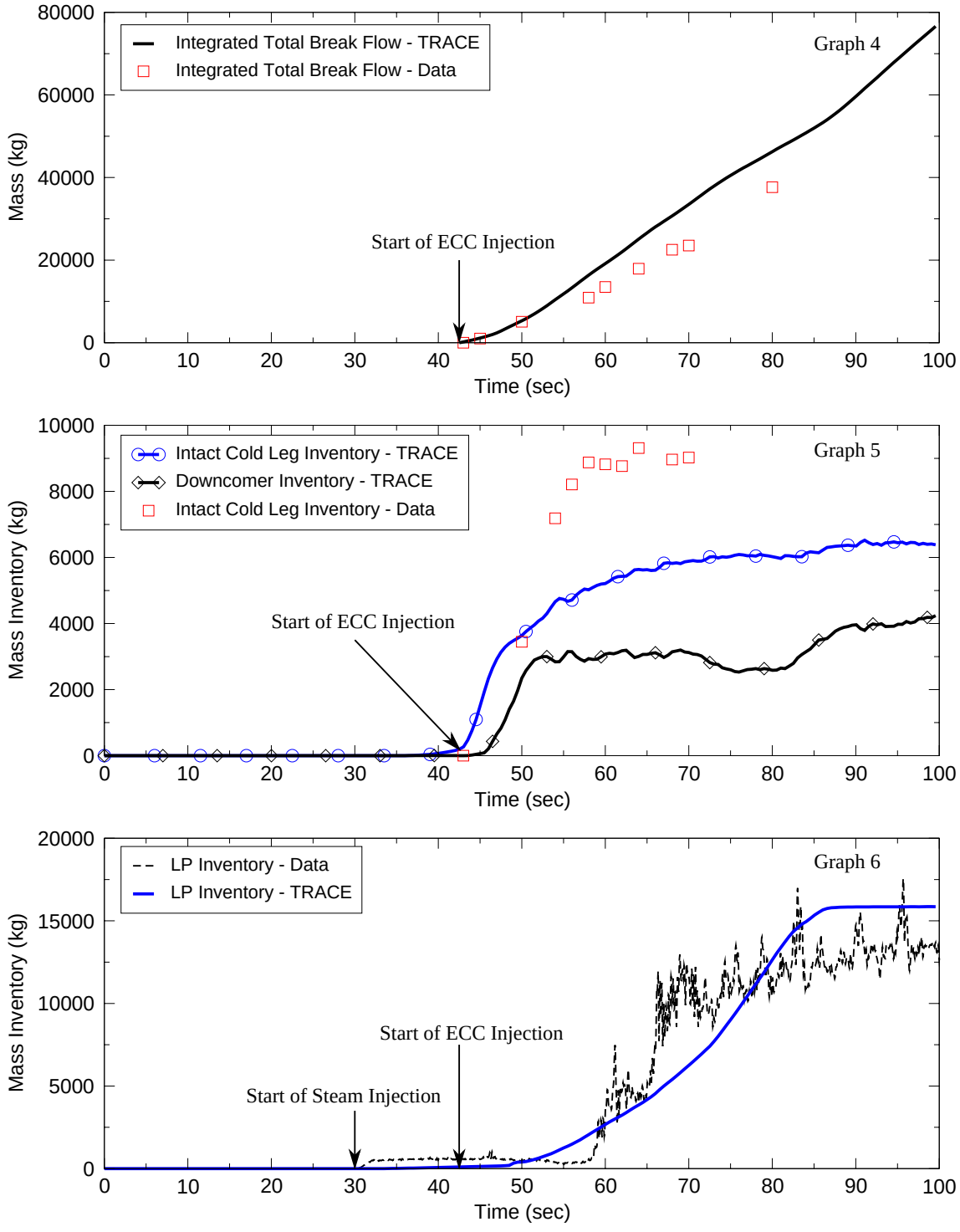

Figure B.4-34. Simulation Results for UPTF Test 6 Run 135 : (2/2)

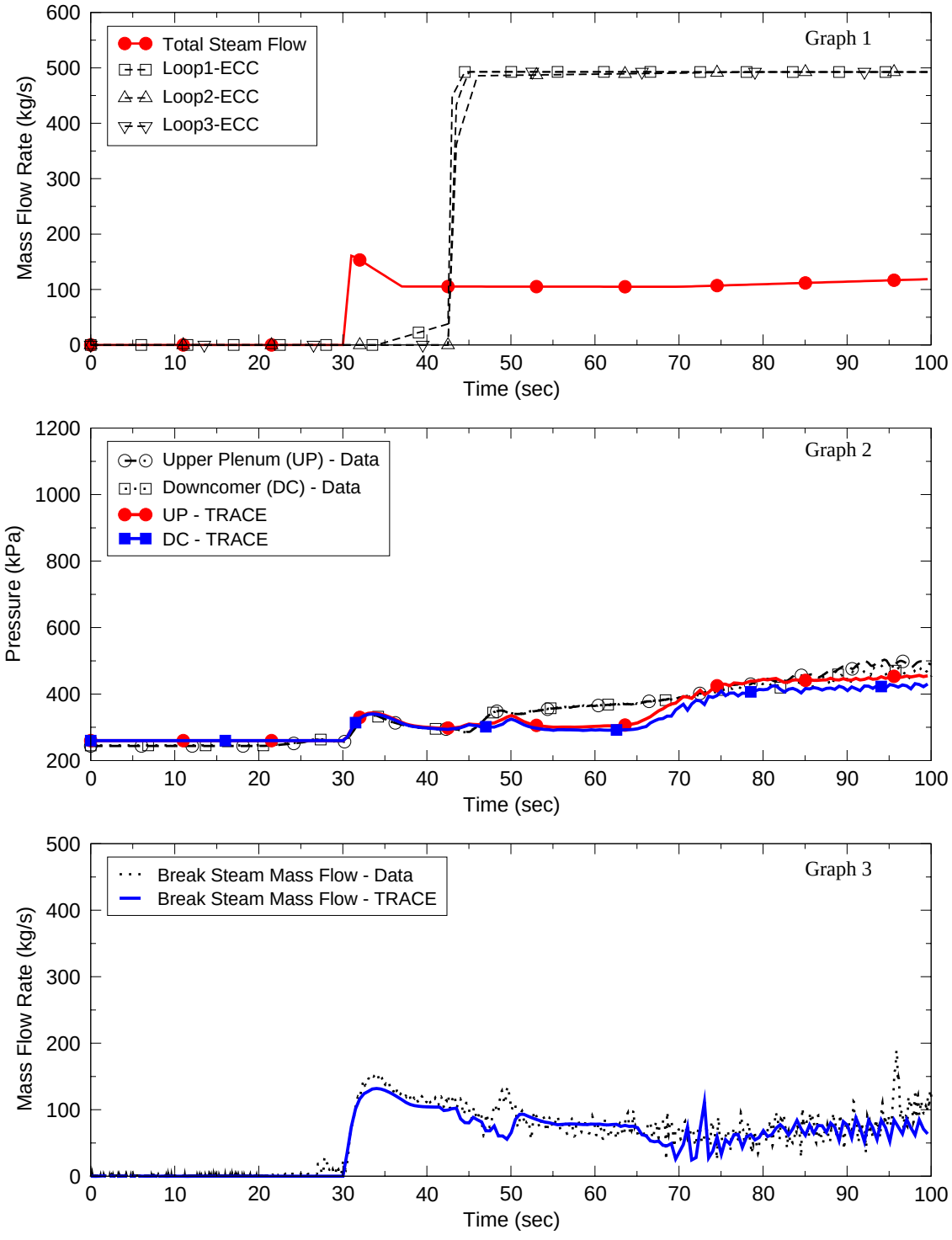

Figure B.4-35. Simulation Results for UPTF Test 6 Run 136 : (1/2)

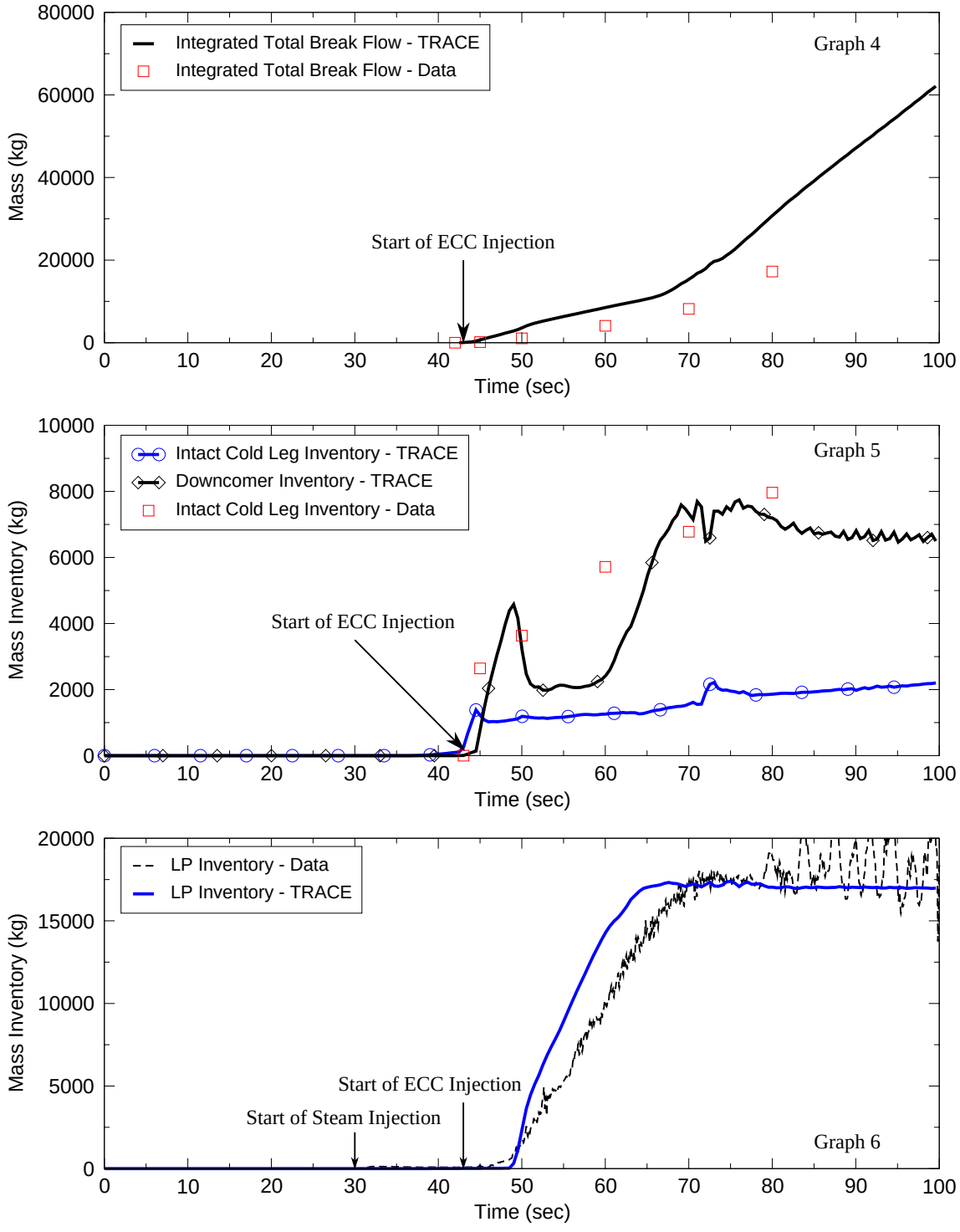

Figure B.4-36. Simulation Results for UPTF Test 6 Run 136 : (2/2)

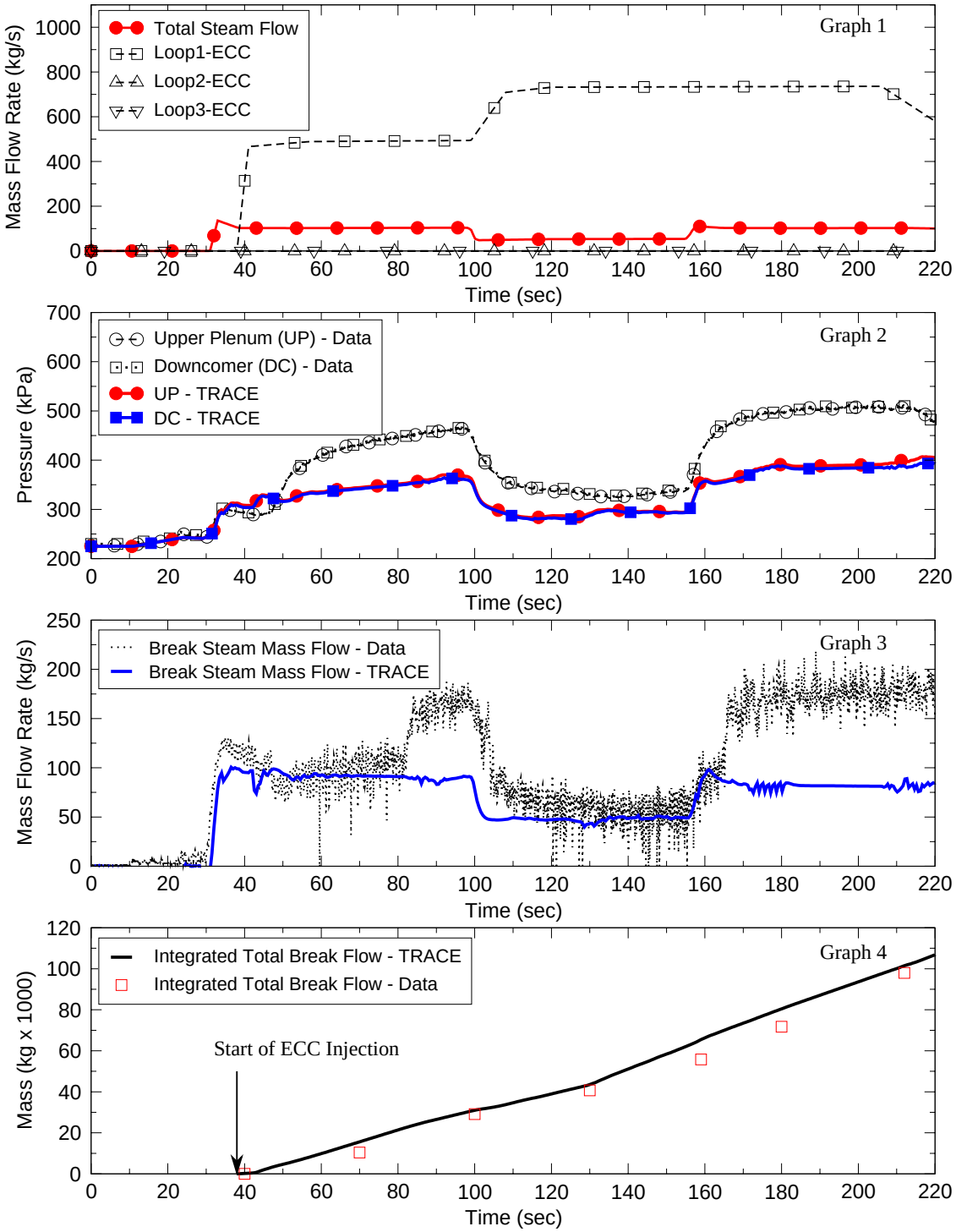

Figure B.4-37. Simulation Results for UPTF Test 7 Run 200 : (1/2)

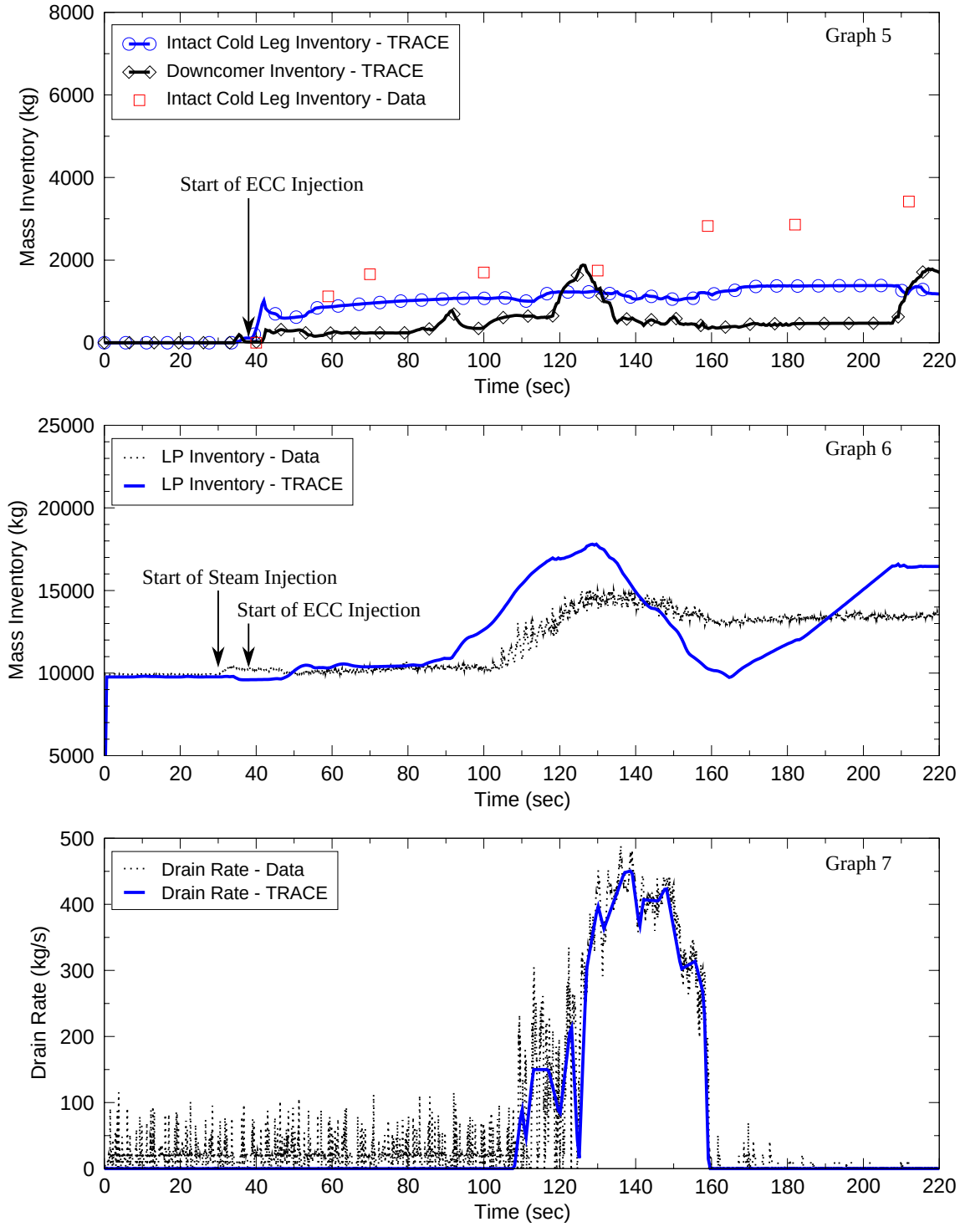

Figure B.4-38. Simulation Results for UPTF Test 7 Run 200 : (2/2)

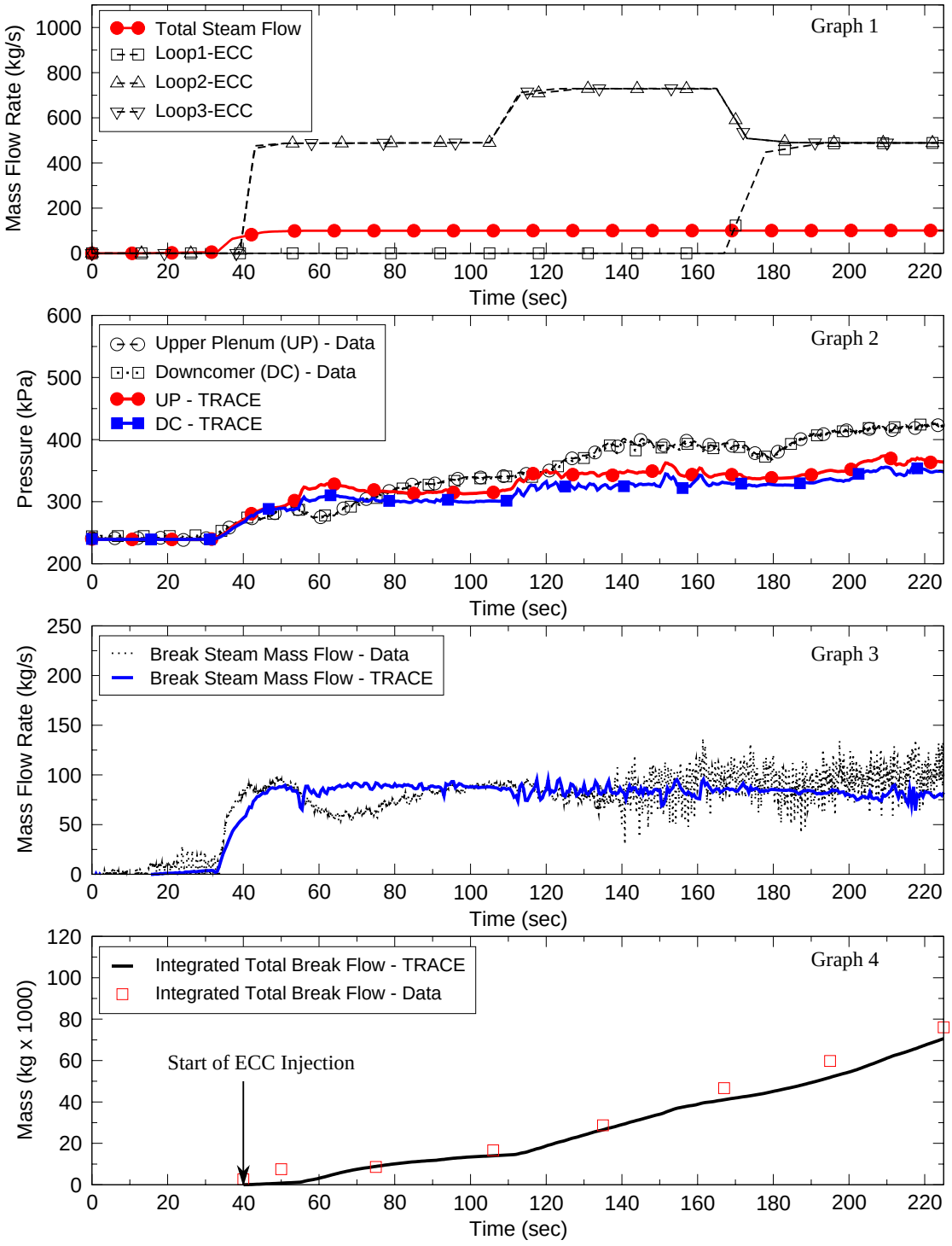

Figure B.4-39. Simulation Results for UPTF Test 7 Run 201 : (1/2)

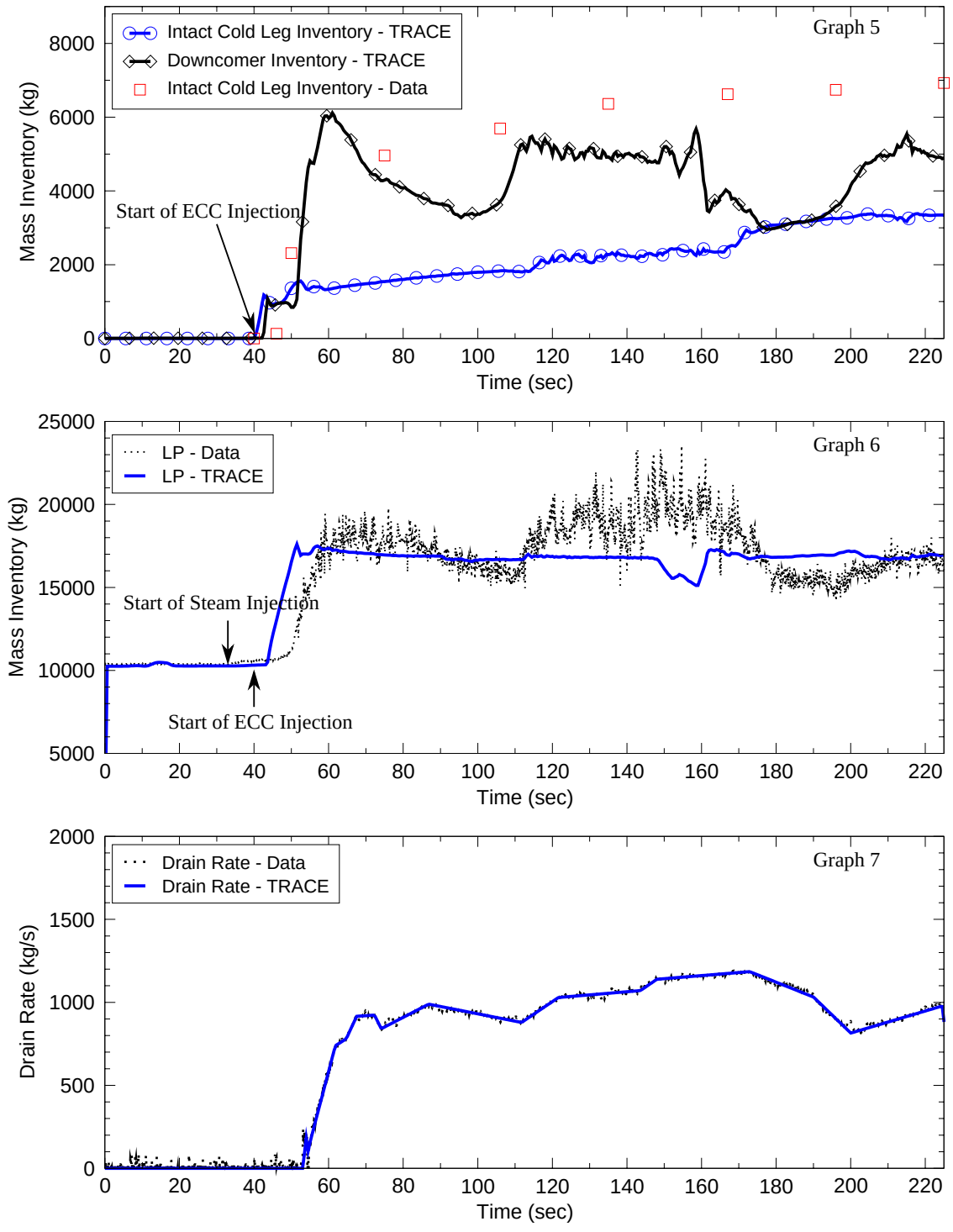

Figure B.4-40. Simulation Results for UPTF Test 7 Run 201 : (2/2)

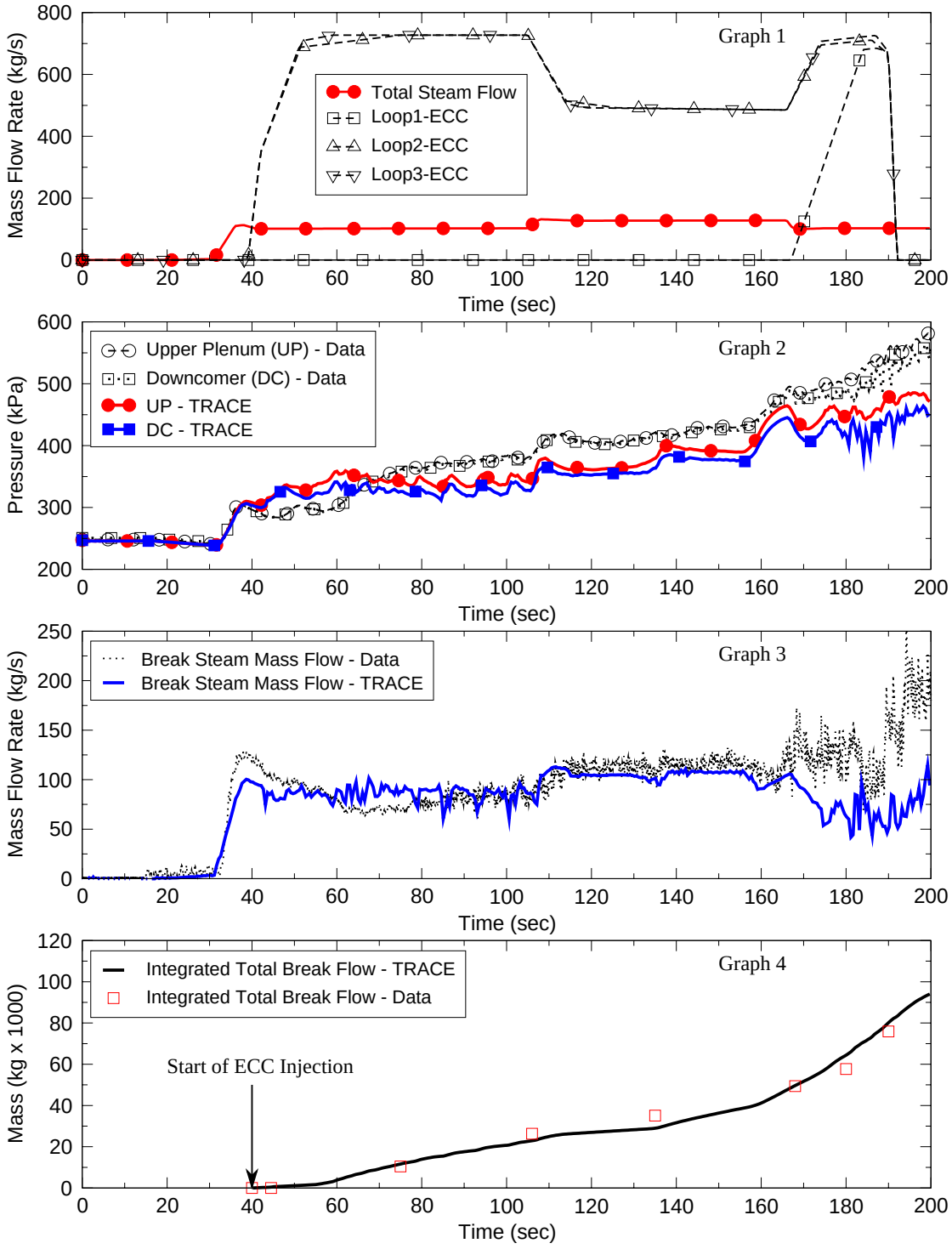

Figure B.4-41. Simulation Results for UPTF Test 7 Run 202 : (1/2)

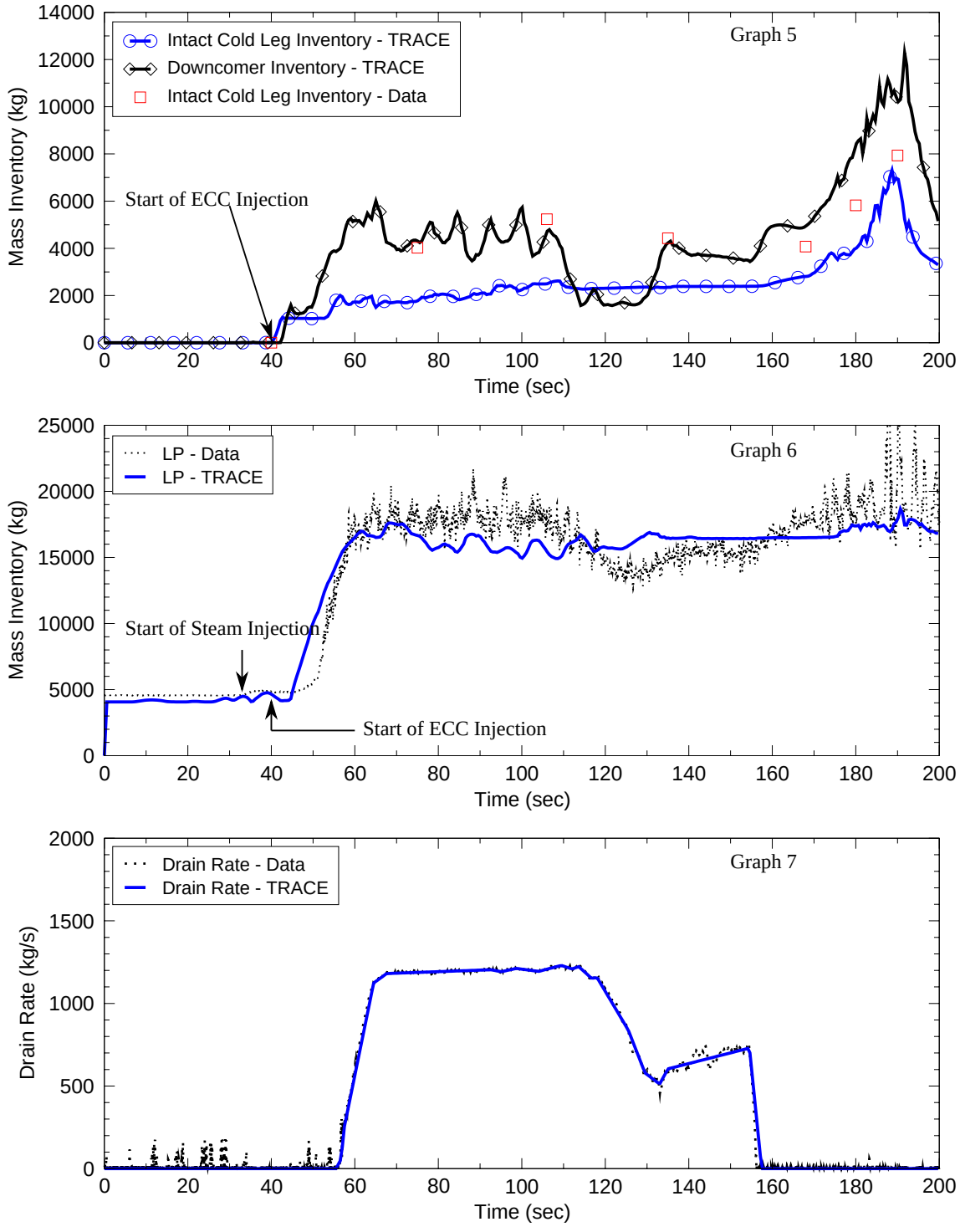

Figure B.4-42. Simulation Results for UPTF Test 7 Run 202 : (2/2)

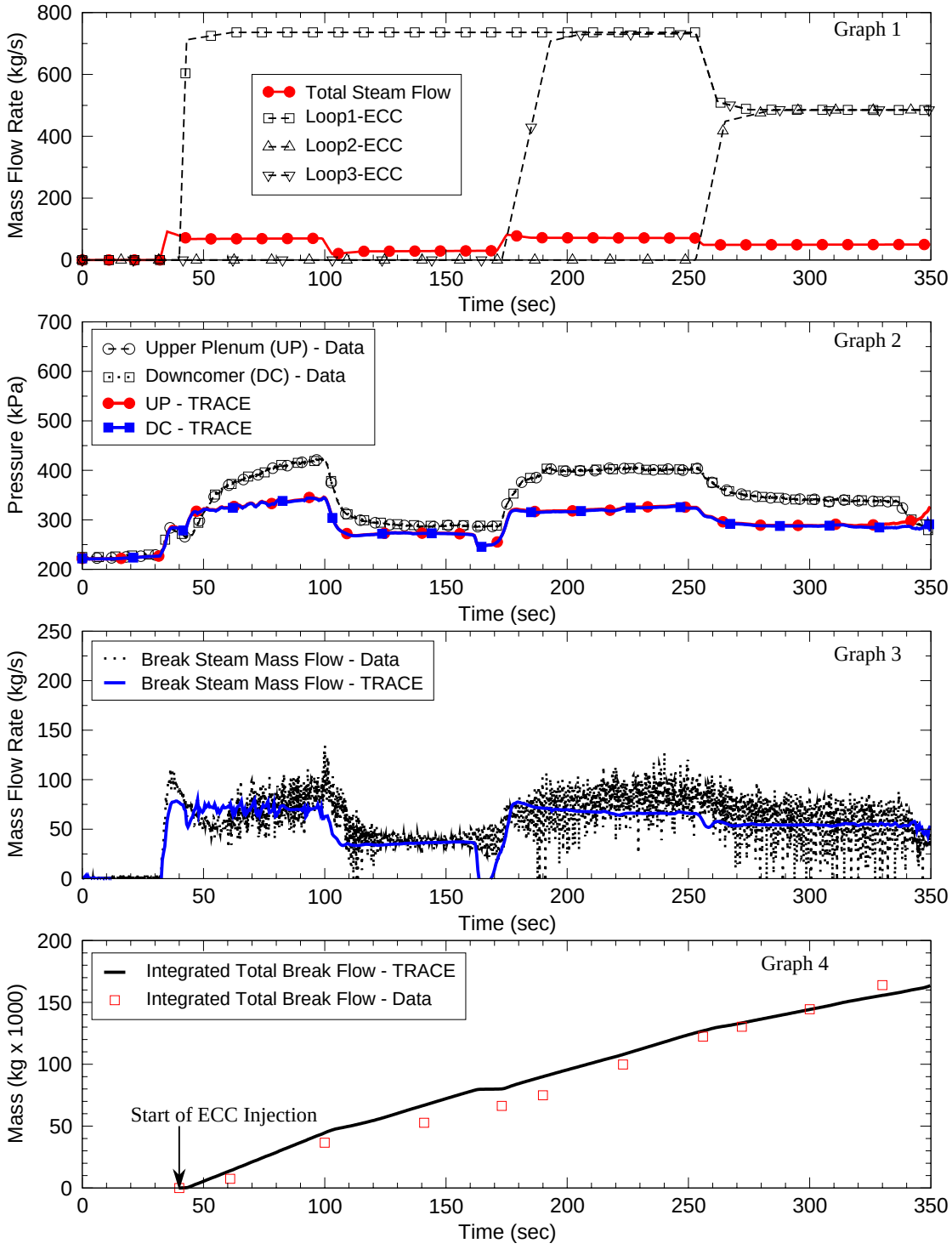

Figure B.4-43. Simulation Results for UPTF Test 7 Run 203 : (1/2)

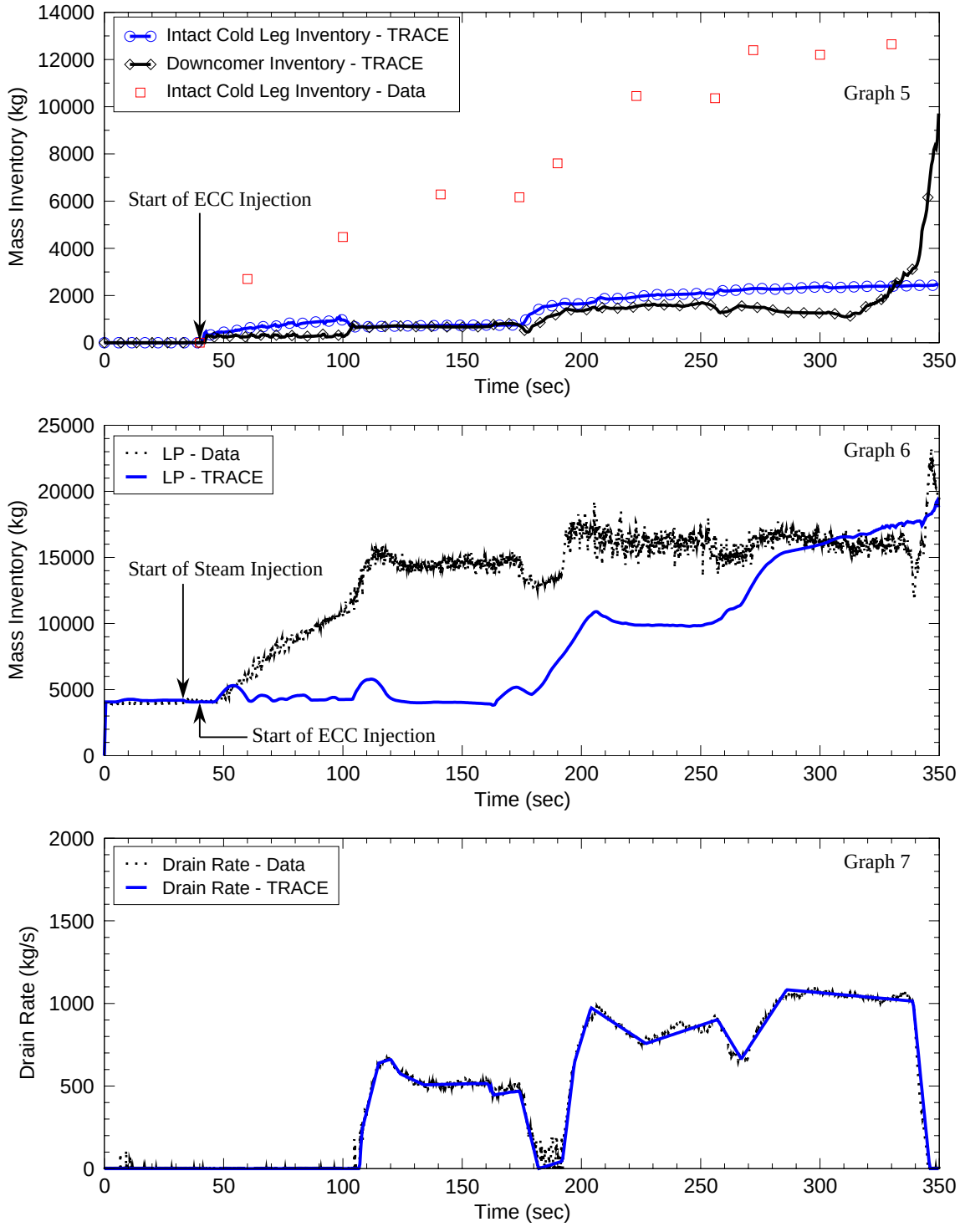

Figure B.4-44. Simulation Results for UPTF Test 7 Run 203 : (2/2)

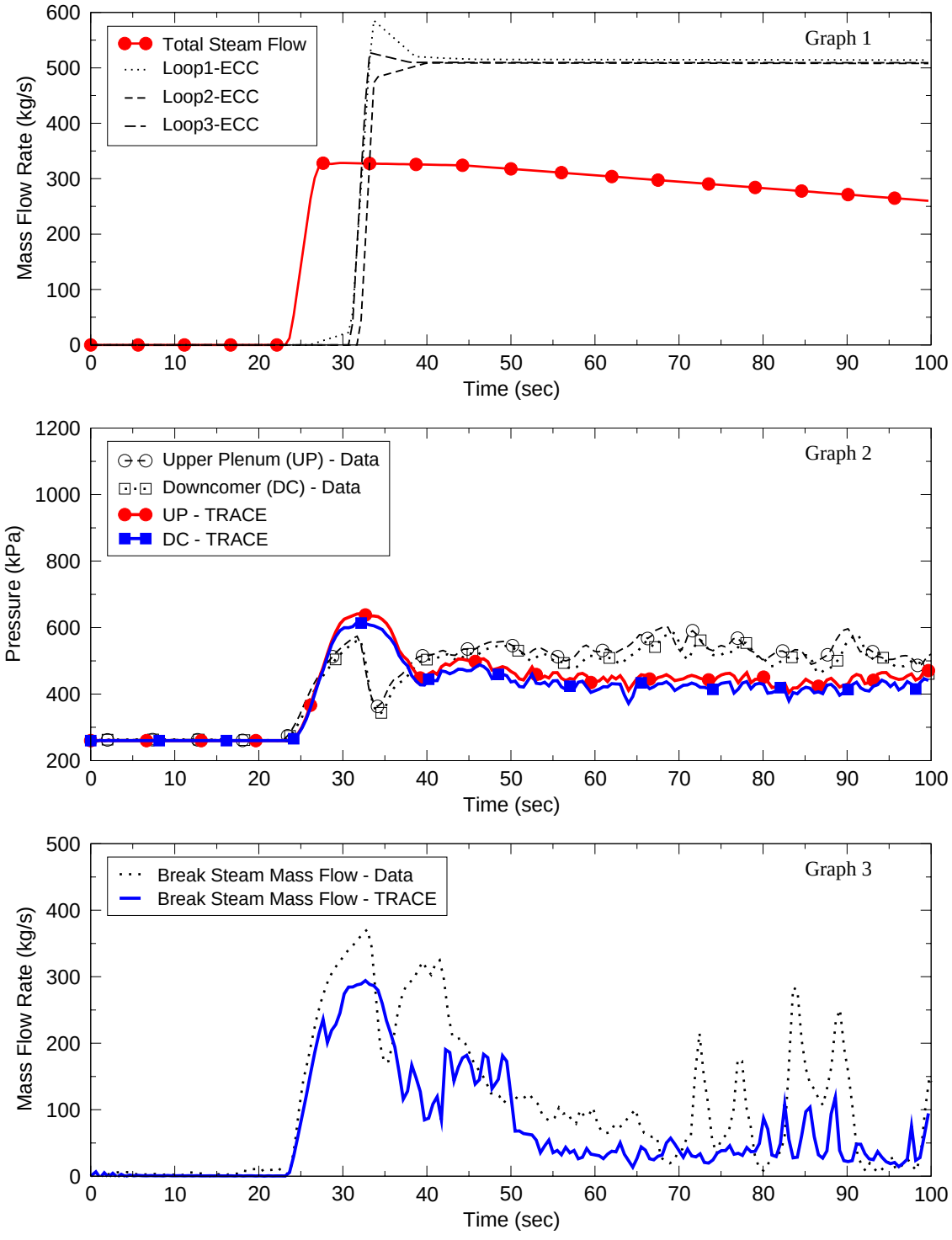

Figure B.4-45. Simulation Results for UPTF Test 5 Run 062 : (1/2)

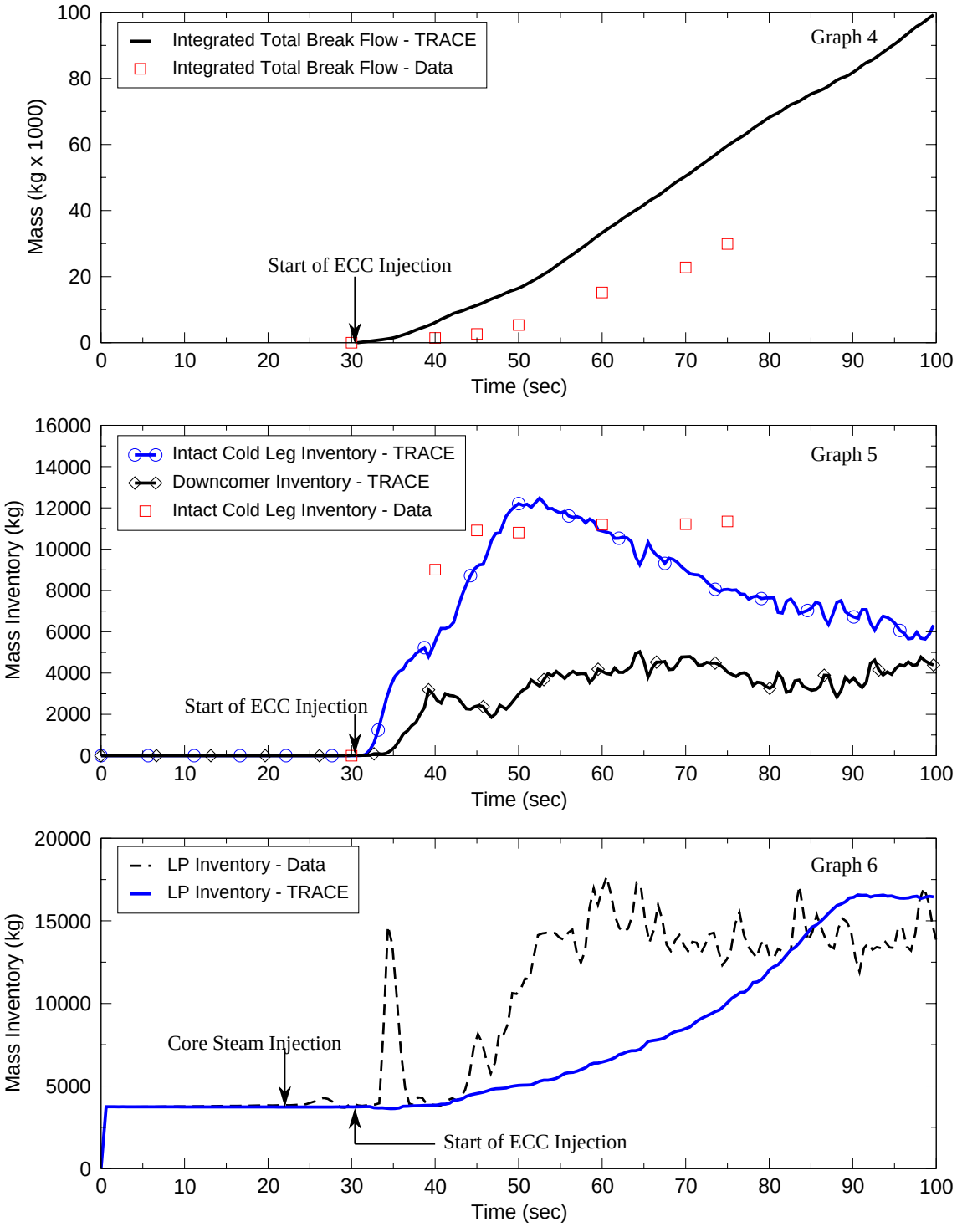

Figure B.4-46. Simulation Results for UPTF Test 5 Run 062 : (2/2)

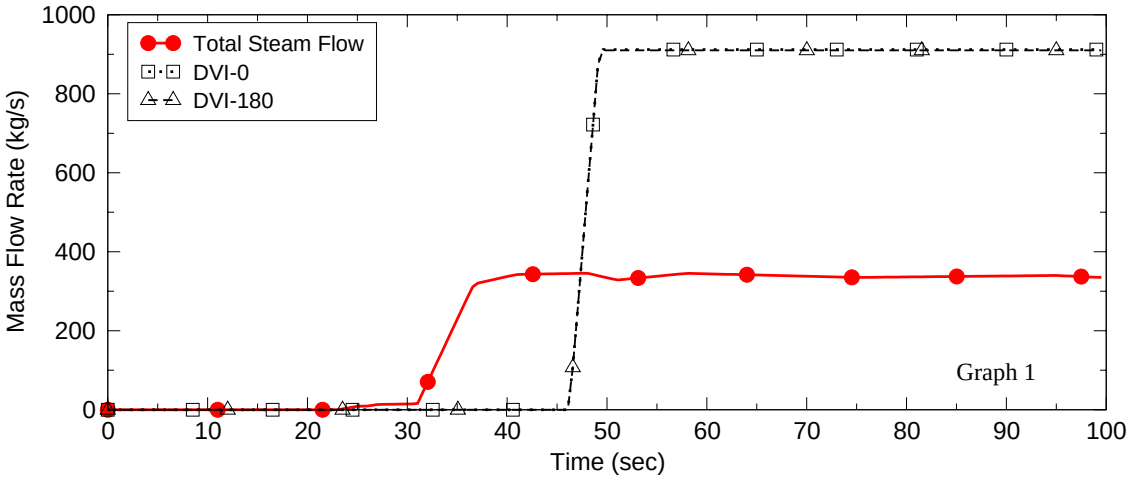

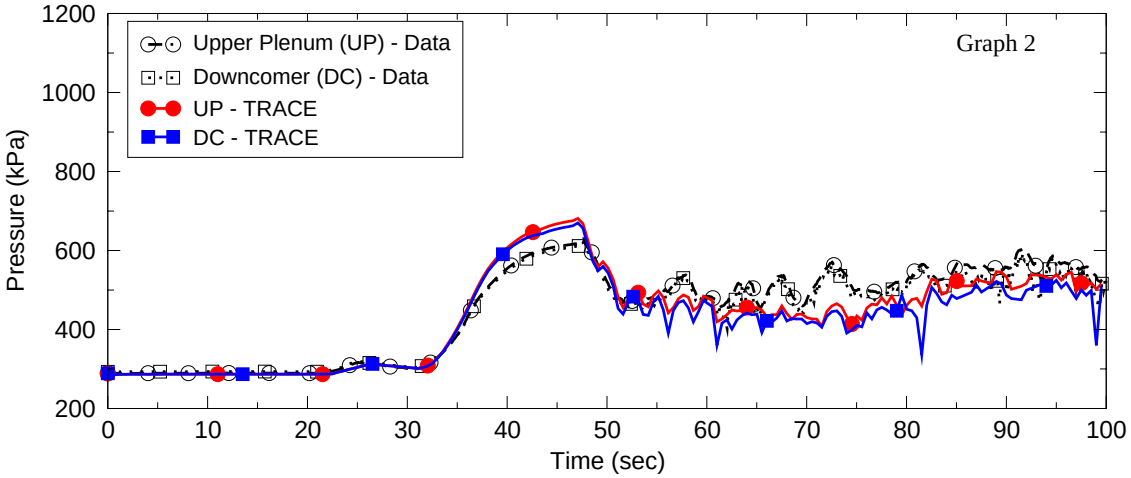

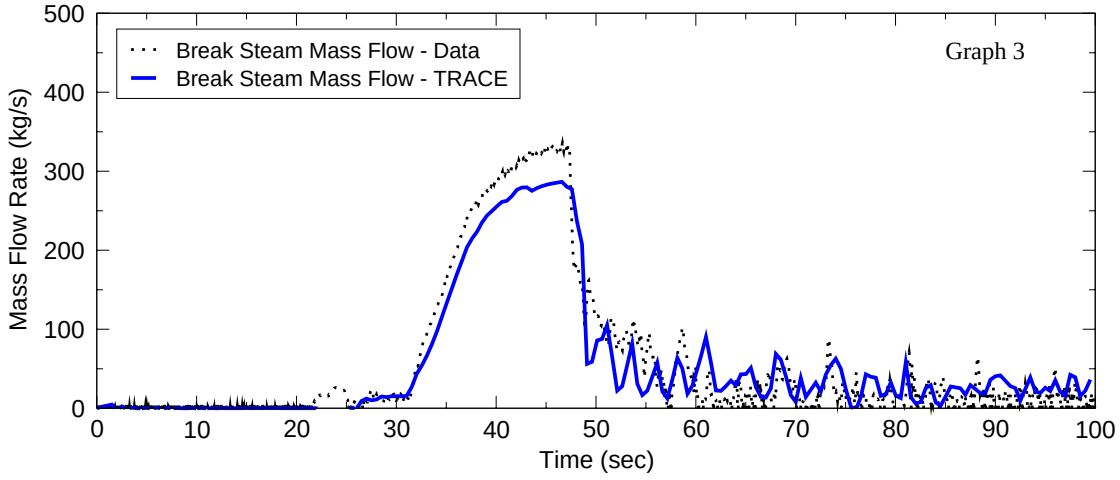

Figure B.4-47. Simulation Results for UPTF Test 21 Run 272 : (1/2)

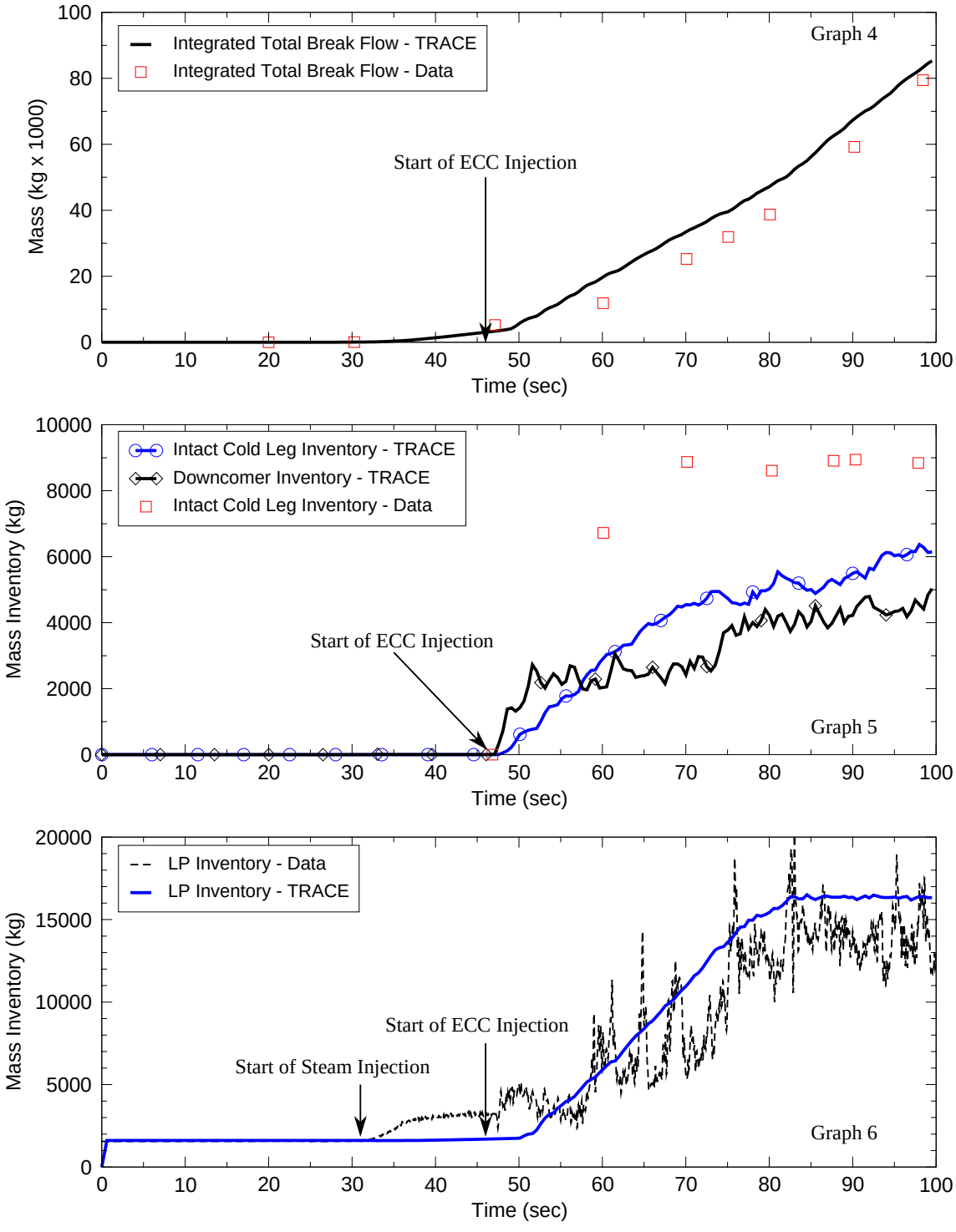

Figure B.4-48. Simulation Results for UPTF Test 21 Run 272 : (2/2)

Blowdown Heat Transfer Tests

B.5. THTF Steady State Tests Assessment

Author(s): Weidong Wang, Andrew Ireland

Affiliation: USNRC

Code Version: TRACE V5.0

Platform and Operating System: Intel x86, Windows XP

B.5.1. Introduction

The Oak Ridge National Laboratory (ORNL) Pressurized Water Reactor (PWR) Blowdown Heat Transfer (BDHT) program studied dispersed flow film boiling. The film boiling regime can occur during a large break loss-of-coolant accident (LBLOCA) when the liquid becomes depleted at the heated (or hot) surface. The purpose of this section is to document TRACE code simulations of four heat transfer experiments performed under the BDHT program. The assessment will show the capability of TRACE to predict the heat transfer dispersed flow film boiling. The experiments, performed in the Thermal-Hydraulic Test Facility (THTF), were steady state film boiling tests. The tests simulated and reported herein are the steady state film boiling tests 3.07.9B, 3.07.9H, 3.07.9N, and 3.07.9W. The test conditions for the TRACE assessment fit into three categories: high or medium pressure, high or low mass flux, and high or low heat flux.

This assessment report is based largely on the assessment report of Weidong Wang for the same steady state tests simulated with an older version of TRACE (Ref. 1).

B.5.2. Test Facility Description

THTF is a nonnuclear pressurized water loop containing 64 full-length rods arranged in an 8 x 8 bundle. Figure B.5-1 shows an isometric view of the facility. Sixty of the rods were electrically heated and four were unheated. Rod diameter (0.0095 m) and pitch (0.0127 m) are typical of a PWR with 17 x 17 fuel assemblies. Figure B.5-2 is a schematic of the THTF rod bundle cross section and shows the location of the four unheated rods. The axial and radial power profiles of the THTF bundle are flat. The heated length of the bundle is 3.66 m and there are six spacer grids in the heated length.

Figure B.5-3 is a simple diagram of the THTF to help describe the facility. In steady state mode, fluid flows from the pump through the horizontal inlet and vertical inlet spool pieces. From the vertical inlet spool piece, fluid enters the external downcomer spool piece and then flows into the

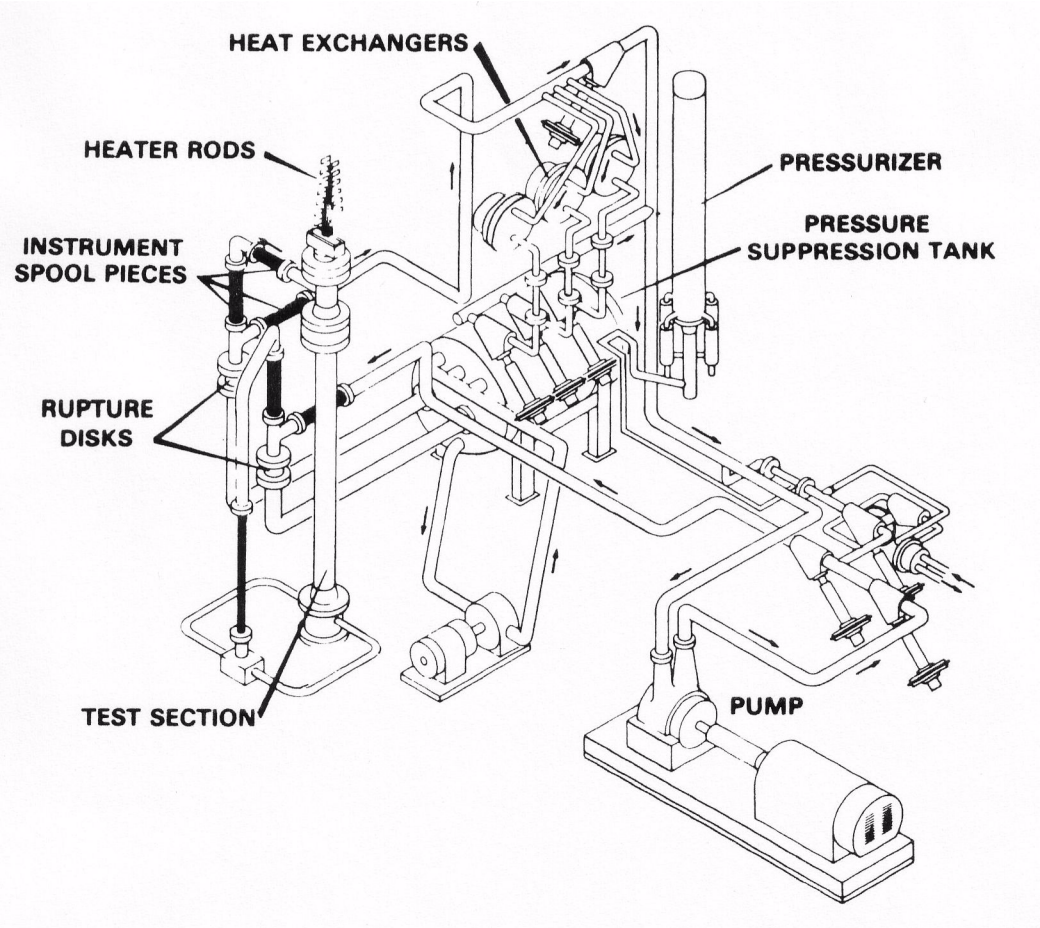

Figure B.5-1. Thermal-Hydraulic Test Facility

test section lower plenum. Fluid flows from the lower plenum up through the heated length of the bundle, into the test section upper plenum, through the outlet spool pieces, into the main heat exchangers, and back to the inlet of the pump. The steady state upflow film boiling experiments were conducted with the THTF slightly altered from its standard configuration. The alteration involved a relocation of the pressurizer from the horizontal outlet spool piece to the pump bypass piping.

The test facility was highly instrumented with pressure and differential pressure transducers, gamma densitometers for measuring in-bundle fluid density, fuel rod simulator (FRS) thermocouples, and thermocouples mounted to grid spacers for in-bundle fluid temperature. Figure B.5-4 shows the axial location of the grid spacers and the FRS thermocouples. For a detailed discussion of the test facility, refer to Reference 2.

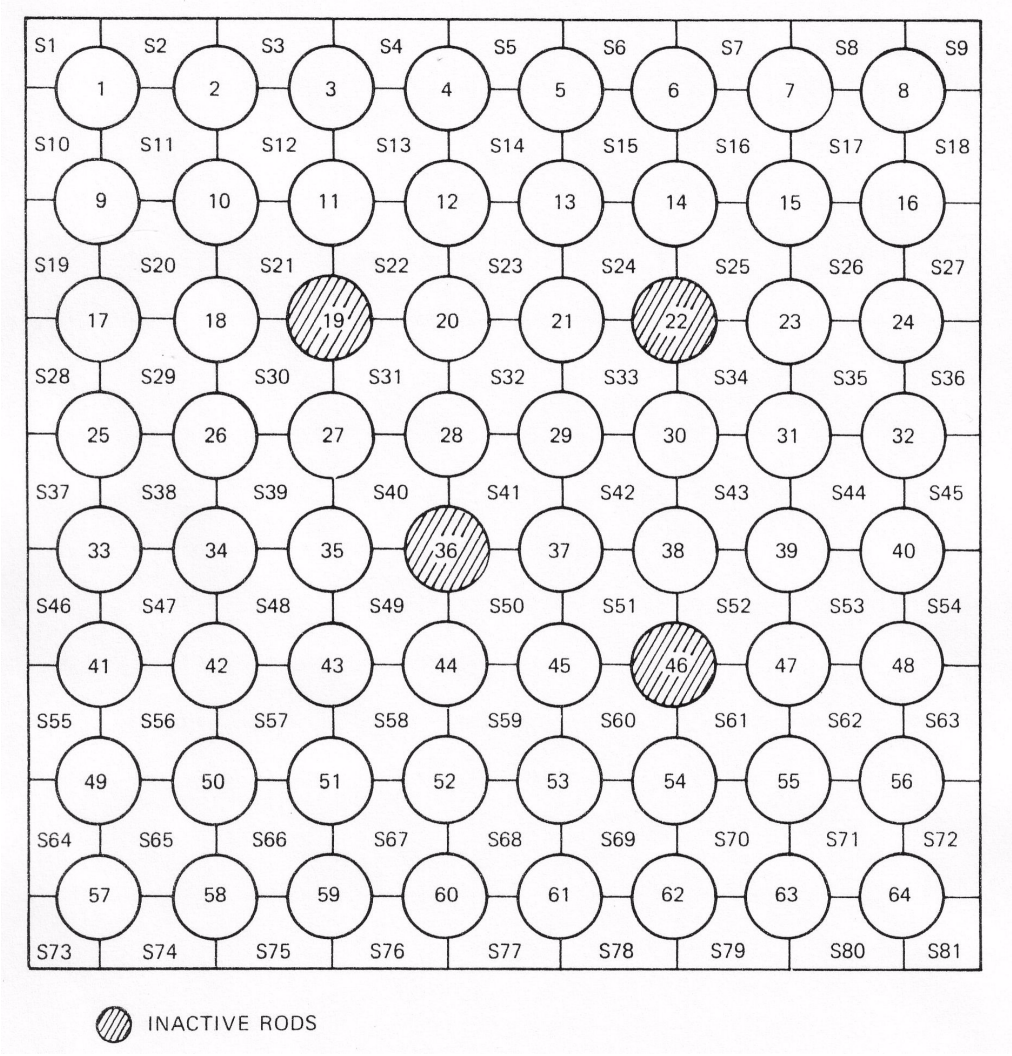

Figure B.5-2. Cross section of the THTF heated bundle showing location of the unheated rod

B.5.3. TRACE Model Description

Nodalization of the TRACE model of THTF is shown in Figure B.5-5. In order for the results of this assessment can be applied to both Pressurized Water Reactor (PWR) and Boiling Water Reactor (BWR) facilities, two TRACE input files were made: one input file contained a CHAN component (CHAN input deck) and the other input file contained a Vessel component (Vessel input deck). Both input files were similar, i.e. they both contained the same number of components and had identical cell and heat structure noding (heat structures for the heated and un-heated rods and the bundle wall are contained with in the CHAN component where as HTSTR components representing the heated and un-heated rods and the bundle wall were input for the Vessel input deck). Details of each component is given below.

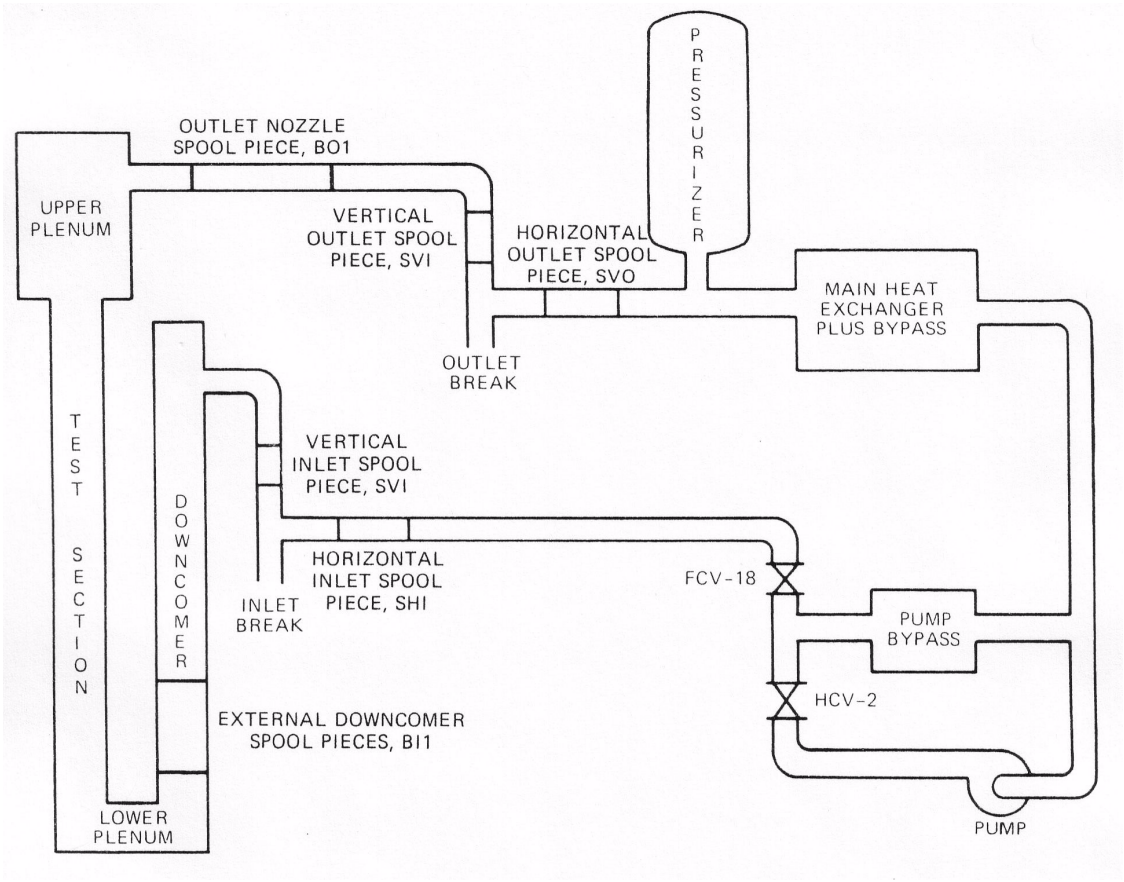

Figure B.5-3. Diagram of THTF

B.5.3.1. CHAN/Vessel Component

The 8 X 8 rod bundle extends the entire length of the test section. A bundle shroud box with a 0.1037 meter square inside dimension surrounds the rod bundle. The shroud box extends about 0.26035 meters below and about 0.2889 meters above the heated section of the rod bundle. The lower and upper plenums of the test section, below and above the shroud box, are bounded by a 10 inch, schedule 140 (8.75 inch ID), 316 stainless steel pipe. The CHAN/VESSEL component models the full length of the bundle shroud box. The component number for the CHAN/VESSEL is 222.

The CHAN and Vessel components are divided into 14 axial cells/levels. The hydraulic geometry in the Vessel component was modeled using cartesian coordinates in order to approximate the CHAN component. The core (heated rod section) is 3.6576 m long. There are 6 grid spacers in the heated rod section. Two hydro cells/levels were placed between each grid spacer (see Figure B.5-4 for the grid spacer locations) with a total of 12 cells/levels in the core (0.3048 m cell lengths). The heated section of the rod bundle begins at the bottom of cell/level 2 and ends at the top of cell/level 13. Cell/level 1 and 14 is the end and beginning of the lower and upper plenum

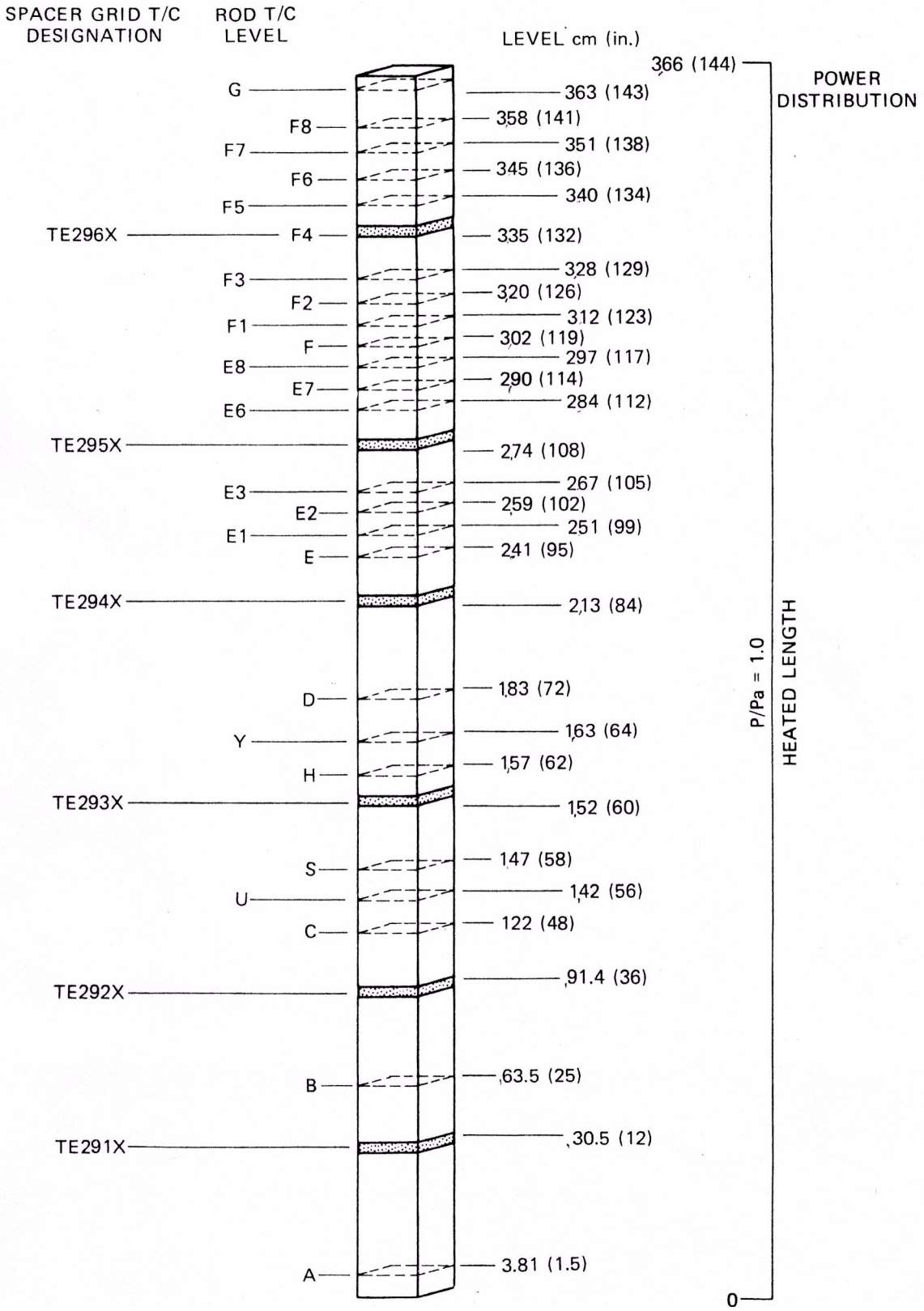

Figure B.5-4. Grid Spacer and fuel rod simulation thermocouple axial locations.

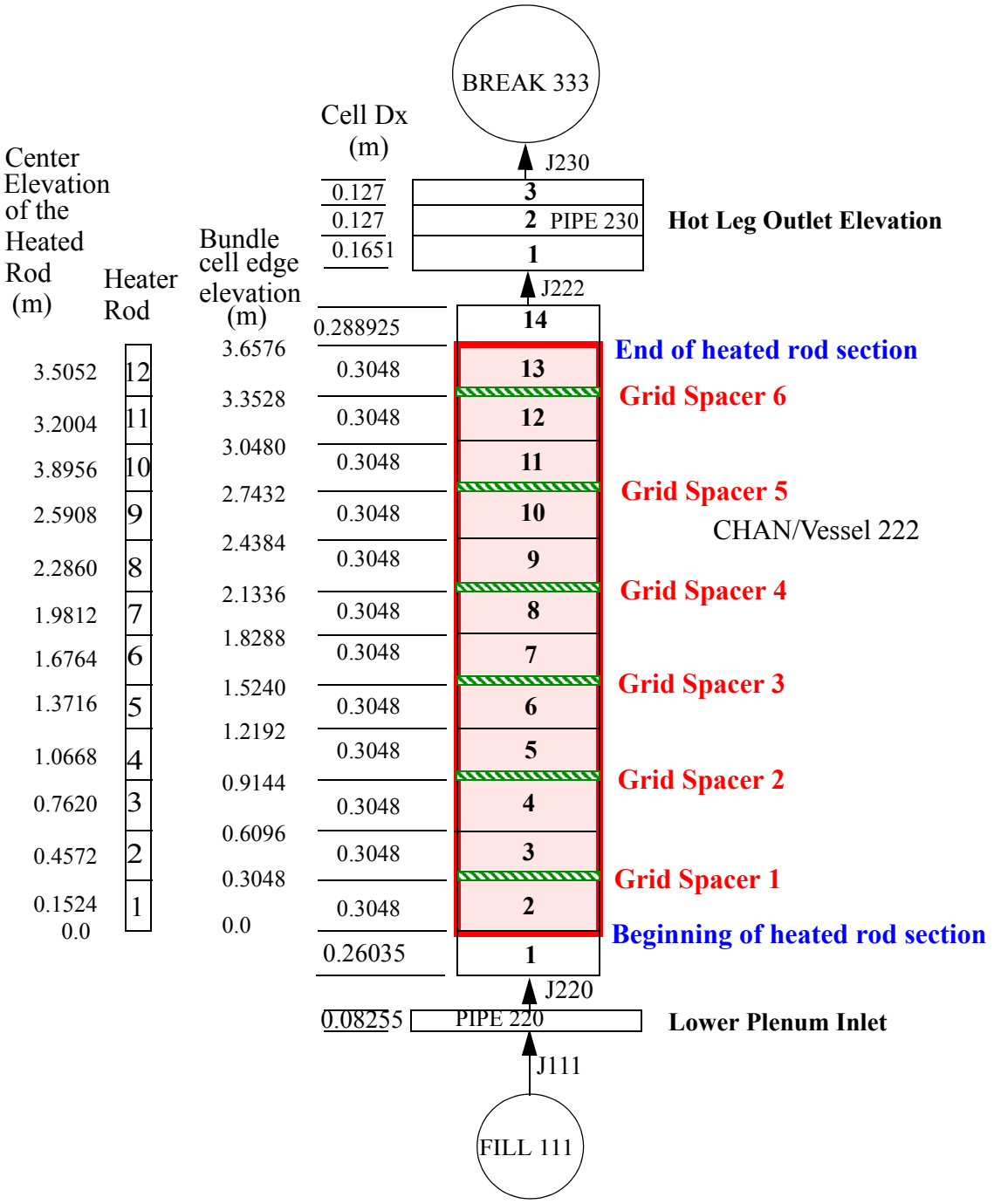

Figure B.5-5. TRACE nodalization of the Thermal-Hydraulic Test Facility.

respectively. The flow area is constant in the heated rod region at 0.0061752 m^2. The volume of the CHAN and VESSEL components is 0.02598 m^3.

The geometry describing the heated and un-heated rods and the bundle shroud box is included in the CHAN component input. TRACE uses this information and spawns heat structure components. The rods are divided into 2 rod groups in the CHAN component. Rod group 1 represents the 60 heated rods and rod group 2 represents the 4 unheated rods. The rods are divided into 10 radial nodes, representing the boron nitride insulating material, the constantan/nichrome heater wire and the stainless steel cladding. The bundle shroud wall was divided into 5 nodes. The heat structure cell height is the same as the hydro cell height. The heated rod diameter is 0.0095 m. The unheated rod diameter is 0.0102 m, slightly larger than the heated rod diameter. For simplicity, the four unheated rods were modeled the same as the heated rods except without power. This compromise is believed to have negligible consequences for the TRACE simulations.

Thomas (Ref. 8) reported a grid spacer loss coefficient of 1.216 for all mass flow rates in THTF. This was based on an earlier 49 rod bundle configuration. Assuming the grid spacer losses are similar in the 64 rod bundle configuration an equivalent resistance was calculated using the area ratio squared between the two bundle sizes. The equivalent loss coefficient was calculated to be 1.332.

Three HTSTR components were used in the Vessel input deck to model the heated and unheated rods and the bundle shroud box. The HTSTR components were modeled one-to-one with the CHAN internal heat structures. The CHAN internal heat structure component numbers and the corresponding Vessel input deck heat structure component numbers are given in Table B.5.1.

Table B.5.1. CHAN and Vessel heat structure component numbers.

Modeled component	CHAN component heat structure numbers	Vessel heat structure component numbers
heated rods	222002	888
unheated rods	222003	889
bundle shroud box	222004	890

Radiation heat transfer was modeled using the MROD array in the CHAN input. This was accomplished by setting the IBEAM input parameter in the CHAN input to 0 and entering the layout of primary and supplemental rod positions in the MROD array. The bundle shroud box is the last position in the MROD array. Figure B.5-6 illustrates the MROD array input. Once the MROD array is configured, TRACE calculates the view factors, and beam lengths. The view factors and beam lengths are printed in the output.

The RADENC component (component 895) was used in the Vessel input deck to model radiation heat transfer. The view factors and beam lengths calculated by TRACE for the CHAN component were used in setting up the RADENC component. NAMELIST variable nEnclosure was set to 1 (number of radiation heat transfer enclosures). Setting nEnclosure greater than 0 necessitated the addition of an extra card in the HTSTR components (888, 889, and 890). Input parameters IFRADI and IFRADO are flags to tell the code whether or not radiation heat transfer for the inner or outer surface of a particular HTSTR is desired. A zero specifies no radiation heat transfer and a one specifies radiation heat transfer. For the Vessel input deck IFRADO was set to 1 for HTSTR

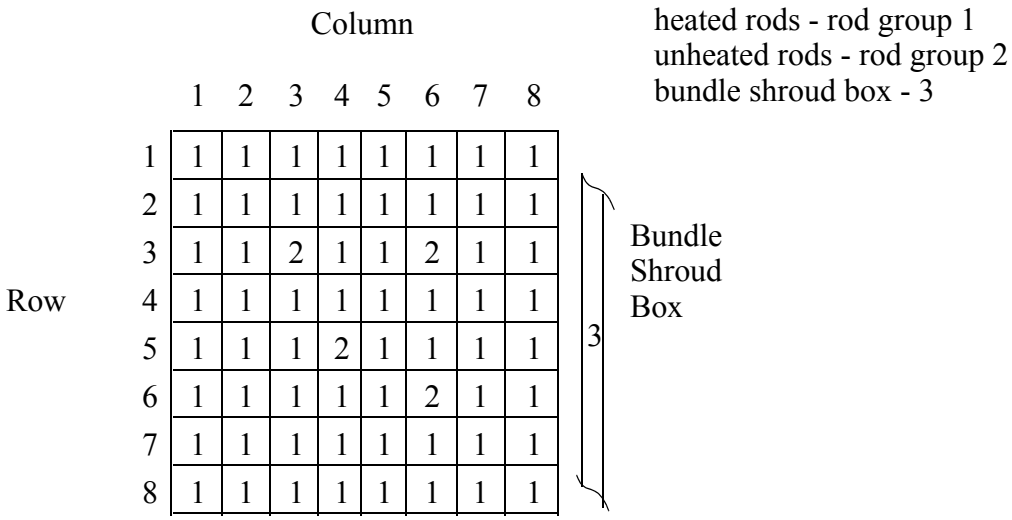

Figure B.5-6. MROD array configuration for the CHAN radiation heat transfer model.

components 888 and 889 (heated and unheated rods) and IFRADI was set to 1 for HTSTR component 890 (bundle shroud box).

B.5.3.2. Lower Plenum Inlet

Fluid enters the heated region of the test section through the lower plenum. As stated earlier, the lower plenum is constructed with a 10 inch schedule 140 stainless steel pipe. The unheated portion of the bundle rods extend down through the lower plenum. The external downcomer is connected to the lower plenum from two sides (see Figure B.5-1). PIPE component 220 (Figure B.5-5) represents the geometry of the lower plenum from the external downcomer connection elevation up to the bottom of the bundle shroud box. Junction 220 connects PIPE 220 to the CHAN or Vessel component.

B.5.3.3. Upper Plenum

Fluid exits the heated test section via the upper plenum and then out to the heat exchangers through the test section outlet piping (see Figure B.5-3). Like the lower plenum, the upper plenum is also constructed with a 10 inch schedule 140 stainless steel pipe that surrounds the unheated portion of the bundle rods above the heated rod zone. PIPE component 230 represents the upper plenum from the top of the bundle shroud box to the outlet pipe connection elevation. The PIPE component is divided into three cells. The CHAN or Vessel component is connected to PIPE 230 via junction 222.

B.5.3.4. Inlet Initial and Boundary Conditions

FILL component 111 was used to setup the test section inlet initial and boundary conditions for steady-state film boiling tests simulated with TRACE. FILL type 5 was used for the steady-state film boiling simulations. A type 5 FILL is mass flow rate versus the independent-variable form (time in this case). The inlet mass flow rates in the steady-state film boiling tests were constant. Table B.5.2 lists the reported initial and boundary conditions for the steady-state tests (see Reference 7) and the input to the FILL component. The mass flow rate for the FILL input was calculated multiplying the mass flux by the test section flow area. Inlet fluid temperatures were obtained with a standard steam table using the reported pressure and inlet quality.

Table B.5.2. Initial and boundary conditions used for the FILL component in the steady-state film boiling test simulations.

Test	3.07.9B	**3.07.9H**	**3.07.9N**	**3.07.9W**
Pressure (MPa)	12.76	8.89	8.52	12.55
Mass Flux (kg/m^2-s)	713	256	806	256
Heat Flux (kW/m^2)	910	417	940	380
Quality (X_o)	-0.107	-0.146	-0.056	-0.177
Inlet Mass Flow Rate (kg/s)	4.4029	1.5809	4.9772	1.5809
Inlet Fluid Temperature (K)	583.4	537.6	558.3	567.2
Inlet Subcooling (K)	19.1	38.0	14.2	34.0
Rod Power (kW)	5860.6	2731.1	6156.5	2488.8

B.5.3.5. Outlet Initial and Boundary Conditions

BREAK component 333 was used to setup the test section outlet pressure boundary conditions. Constant pressure was input for the steady-state film boiling simulations.

B.5.3.6. POWER Component

The TRACE POWER component (998) was used to model the power input to the THTF simulations. The axial and radial power profile of the THTF rod bundle was flat. The power input for the steady-state simulations was obtained by multiplying the reported heat flux by the total rod surface area (see Table B.5.2)

B.5.4. Tests Simulated with TRACE

Test conditions for the four steady-state film boiling upflow tests are shown in Table B.5.3 As shown, the test conditions fit into three categories: high or medium pressure, high or low mass flux, and high or low heat flux.

Table B.5.3. Test conditions for the steady-state film boiling upflow tests.

	Test 3.07.9B	**Test 3.07.9W**	**Test 3.07.9N**	**Test 3.07.9H**
Pressure (MPa)	12.76	12.55	8.52	8.89
Mass Flux (kg/m^2-s)	713	256	806	256
Inlet Mass Flow (kg/s)[a]	4.4029	1.5809	4.9772	1.5809
Avg Heat Flux (kW/m^2)	910	380	940	417
Bundle Power (MW)[b]	5.8606	2.4888	6.1565	2.7311
Inlet Fluid Temperature (K)[c]	583.4 (583.5)	567.2 (566.8)	558.3 (558.7)	537.6 (537.4)
Inlet Subcooling (K)	19.1	34.0	14.2	38.0
	High Pressure High Mass Flux High Heat Flux	High Pressure Low Mass Flux Low Heat Flux	Medium Pressure High Mass Flux High Heat Flux	Medium Pressure Low Mass Flux Low Heat Flux

a. mass flow rate = mass flux * area, where area is the test section flow area = 0.006175201 m^2.
b. bundle power = average heat flux * # of heated rods * surface area of one rod
c. based on pressure and inlet quality X_o documented in Table 1 of Reference 7. Values in parentheses are from TC probe TE-256.

During steady-state operation of the THTF, fluid flows from the pump to the external downcomer. The fluid then passes through the external downcomer and into the test section inlet plenum. The fluid passes up through the test section past the heated rods where it is heated. The fluid leaves the test section from the upper plenum proceeds through the heat exchangers and returns to the pump.

Inlet flow for each steady-state test was established and the loop was adjusted to provide the intended inlet fluid temperature and pressure. The bundle power was increased until the DNB point was at the desired position in the bundle. The steady-state operating point was assumed to have been reached when operating pressure and rod surface temperatures stabilized.

The results of the simulations are presented in the form of parameter versus elevation. Axial vapor temperature profiles are shown for the steady-state simulations. Only rod surface temperatures and bundle exit steam temperatures were measured during the experiment. The thermocouple probes were not aspirated. Therefore, the measured steam temperature may or may not reflect the actual temperature at the bundle exit. Most of the probes are at saturation. However, some of the simulated results show the vapor temperature to also be at saturation. Quenching front locations in

the assessment are hard wired to the test data by using namelist input *chfmult*. This hard wiring is help the heat transfer assessment in the dryout region.

B.5.4.1. Simulation of Test 3.07.9B

Test 3.07.9B is considered to be a high pressure, high mass flux and high heat flux test when compared to all of the tests performed in the 3.07.9 test series.

The predicted axial rod clad temperature profile is compared to data in Figure B.5-7. The elevation at which DNB occurs in the experiment is at about 1.5 m from the bottom of the heated core bundle. The CHAN and VESSEL calculations predict DNB occurring between 1.47m to 1.57m (due to the finite noding, it cannot predict the exact location), which is close to the data. The value of namelist input *chfmult* for adjust quenching front location used 0.8. At elevations above the DNB elevation, the CHAN and VESSEL model calculations predict the rod clad temperatures within the error bands, with the CHAN model predicting slightly lower temperatures. Both CHAN and VESSEL predicted temperature decrease trends downstream the DNB location. CHAN and VESSEL model failed to predict identical temperatures. This may be due to many factors. One known factor is VESSEL and CHAN used different wall friction models. As will be shown in the other plots, CHAN and VESSEL predictions are slightly different for the same reason and they will not be discussed repeatedly.

Predicted and measured heat transfer coefficients (HTC) are compared in Figure B.5-8 for elevations above the dryout location. Both the CHAN and VESSEL models were found to be in good agreement with the data, with the predicted heat transfer coefficients generally with the uncertainty of the data.

The predicted axial vapor temperature is shown on Figure B.5-9. The average measured core bundle exit steam temperature is also shown. The predicted exit vapor temperatures are higher than data. Since the vapor temperature data is near to the saturation temperature value, it is probable that the instrument is wetted and only recorded saturation temperature.

The predicted void fraction is shown in Figure B.5-10. The difference in the axial profile of void fraction between the CHAN and VESSEL models is small.

Scatter plots for TRACE calculated heat transfer coefficient verses data are provided in Figure B.5-11 and Figure B.5-12. These two figures are provided for additional comparison for the HTC prediction.

B.5.4.2. Simulation of Test 3.07.9W

Test 3.07.9W is considered a high pressure, low mass flux and low heat flux test (see Table B.5.3). It is a counter-part to Test 3.07.9B in that the mass and heat fluxes are low instead of high. The inlet subcooling for this test, however, is about two times larger.

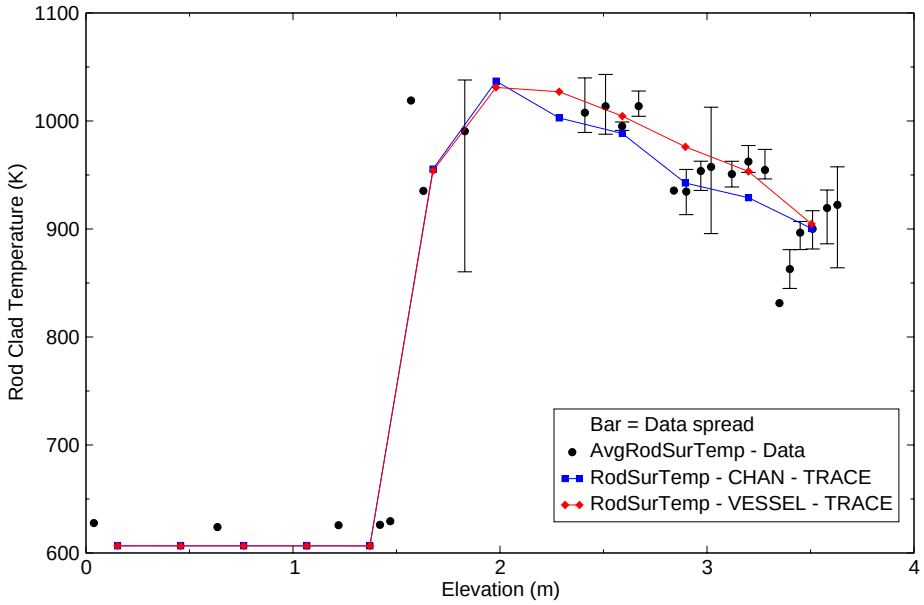

Figure B.5-7. Axial clad temperature comparison -THTF Test 3.07.9B

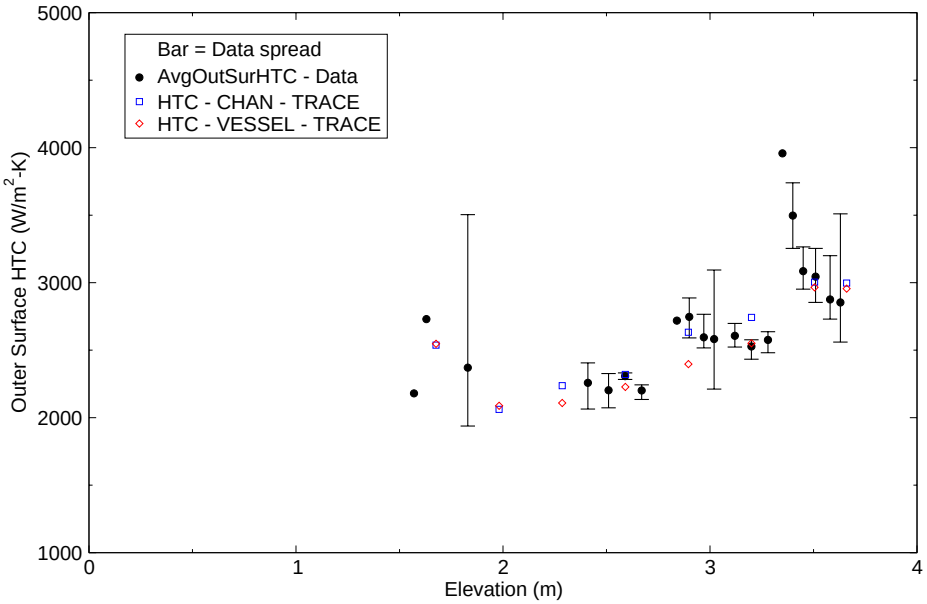

Figure B.5-8. Comparison of film boiling HTCsat - Test 3.07.9B

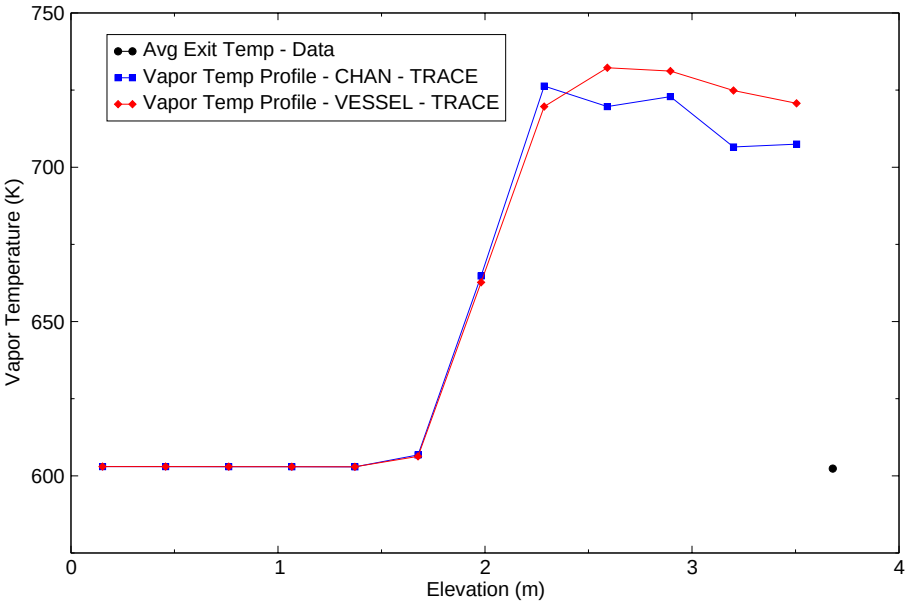

Figure B.5-9. Vapor temperature comparison - Test 3.07.9B

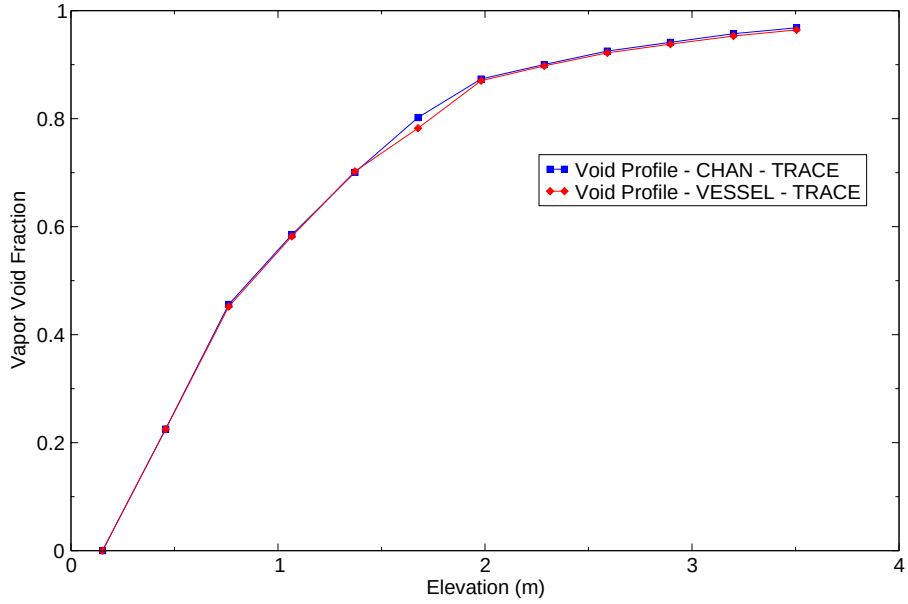

Figure B.5-10. Void fraction comparison - Test 3.07.9B

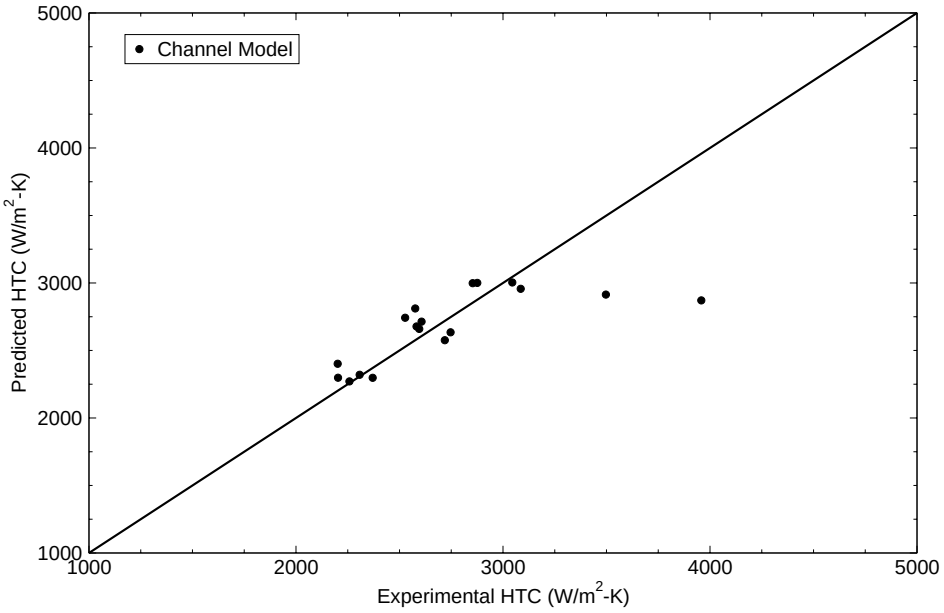

Figure B.5-11. Heat Transfer Coefficient Scatter plot for 3079B CHAN model.

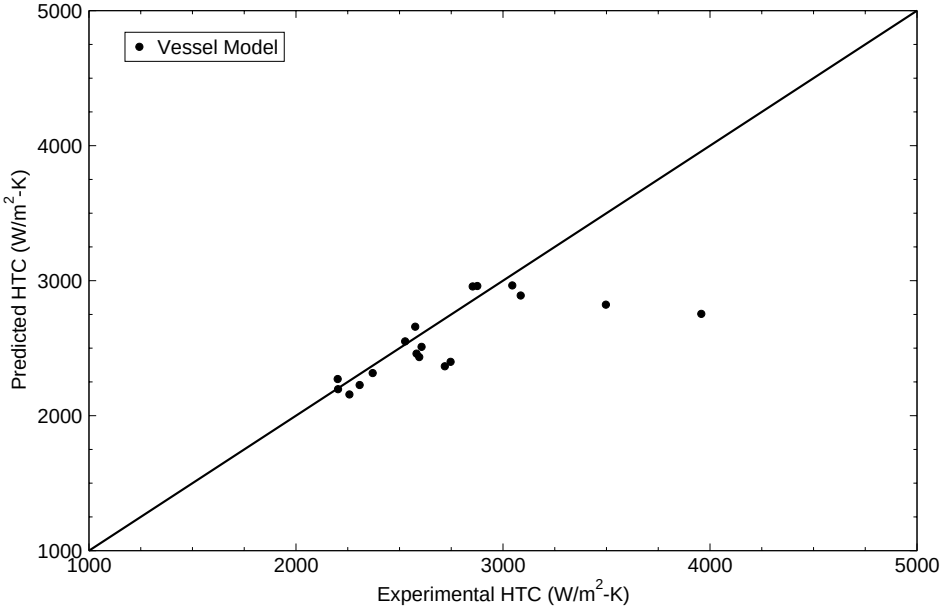

Figure B.5-12. Heat Transfer Coefficient Scatter plot for 3079B VESSEL model.

Figure B.5-13 compares the predicted axial rod clad temperature profile with data. Because the mass and heat flux is lower for this test, the axial location for DNB is higher as shown in Figure B.5-13. The value of namelist input *chfmult* for adjusting quenching front location used 0.7 and the code predicted DNB elevation reasonably. At elevations near the top of the bundle, the CHAN and VESSEL calculations calculate clad temperatures close to the data. But at elevation around 2.9m, the code underpredicted the data.

Predicted and measured heat transfer coefficients (HTC) are compared in Figure B.5-14 for elevations above the dryout location. The CHAN and VESSEL models were found to be in good agreement with the data near the top of the bundle, with the predicted heat transfer coefficients generally with the uncertainty of the data. But around 2.9m, both CHAN and VESSEL overpredicted data, which caused underprediction of rod temperatures at the same locations as shown in Figure B.5-13.

An examination of the vapor temperature comparison given in Figure B.5-15 shows a disagreement of the vapor temperatures at the exit for the CHAN and VESSEL calculation. This can be due to the accuracy of the measurement as discussed for Test 3079B.

The predicted void fraction is shown in Figure B.5-16. The difference in the axial profile of void fraction between the CHAN and VESSEL models is small.

Scatter plots for TRACE calculated heat transfer coefficient verses data are provided in Figure B.5-17 and Figure B.5-18. These two figures are provided for additional comparison for the HTC prediction.

B.5.4.3. Simulation of Test 3.07.9N

Boundary conditions for Test 3.07.9N are similar to Test 3.07.9B except the system pressure is lower (see Table B.5.3).

The predicted axial rod clad temperature profile is compared in Figure B.5-19. The data shows DNB occurring around the 2.6 meter elevation. The value of namelist input *chfmult* for adjusting quenching front location used 0.9 and the code predicted DNB elevation reasonably. However, beyond DNB location, the CHAN and VESSEL both underpredicted rod temperatures.

The predicted rod outer surface HTC in the film boiling region is compared in Figure B.5-20. Both CHAN and VESSEL calculation predict HTCs higher than the data average. In return, the code underpredicted rod temperatures as shown in Figure B.5-19.

The calculated vapor temperature profile is shown in Figure B.5-21. It shows a disagreement of the vapor temperatures at the exit for the CHAN and VESSEL calculation compared to the test data. This can be due to the accuracy of the measurement as discussed for Test 3079B.

The predicted void fraction is shown in Figure B.5-22. The difference in the axial profile of void fraction between the CHAN and VESSEL models is small.

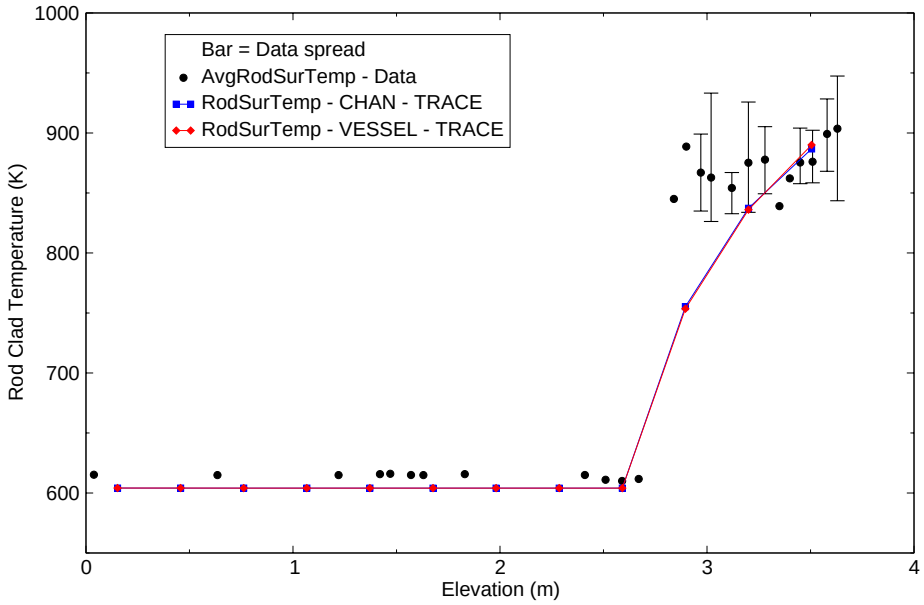

Figure B.5-13. Axial clad temperature comparison -THTF Test 3.07.9W.

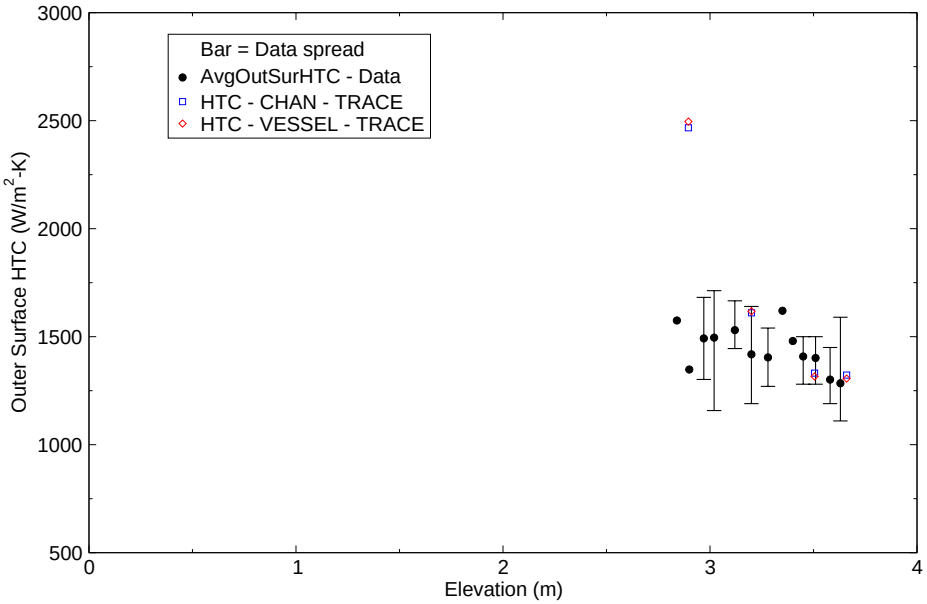

Figure B.5-14. Comparison of film boiling HTCsat - Test 3.07.9W.

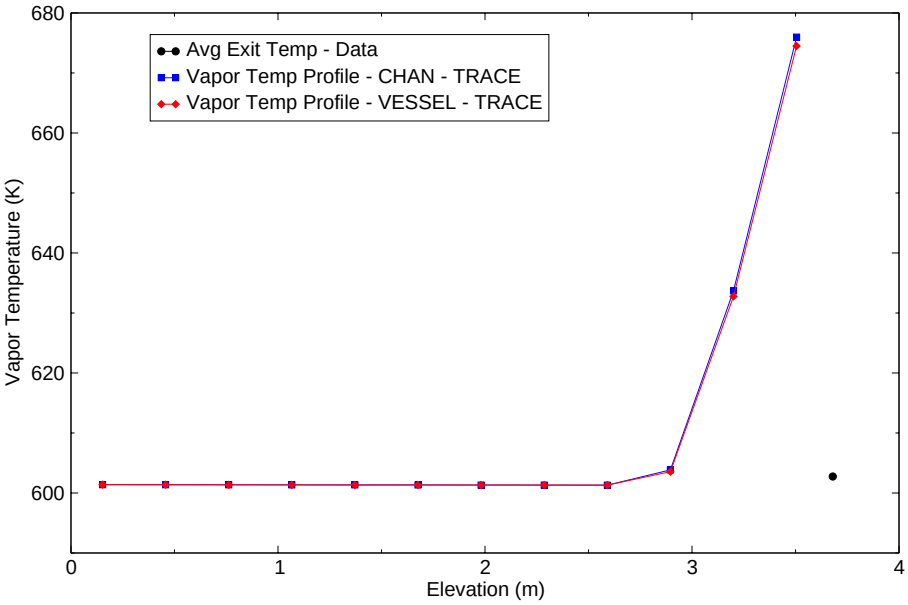

Figure B.5-15. Vapor temperature comparison - Test 3.07.9W.

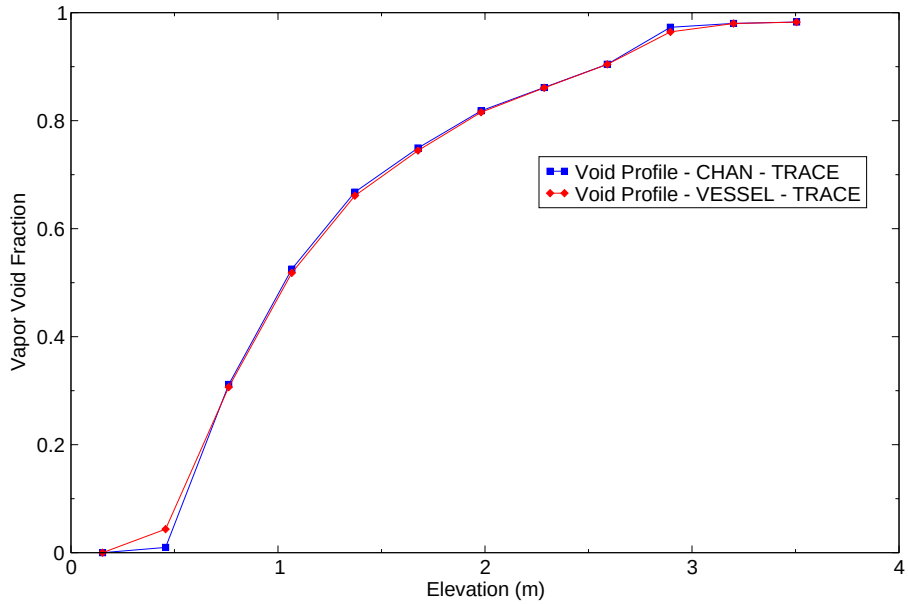

Figure B.5-16. Void fraction comparison - Test 3.07.9W

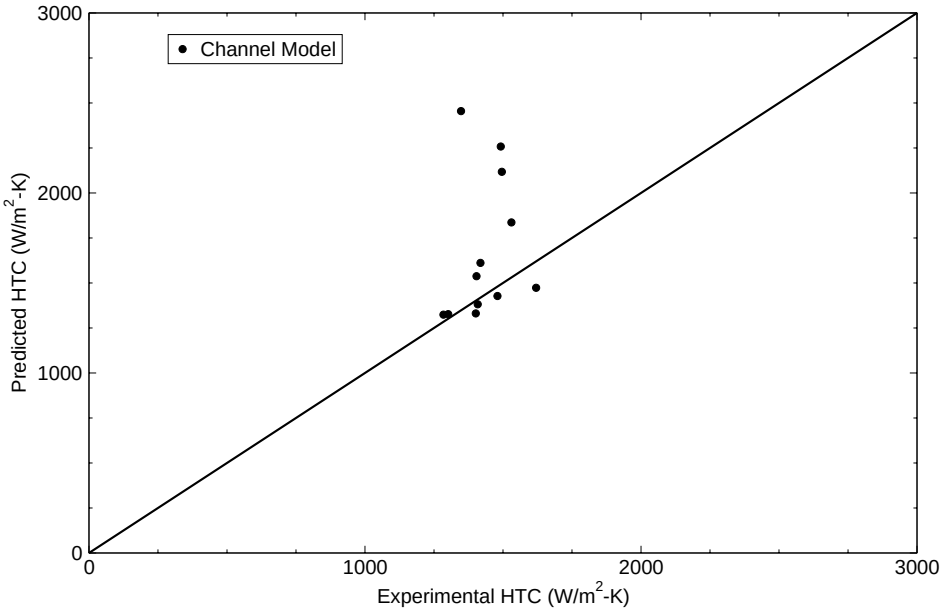

Figure B.5-17. Heat Transfer Coefficient Scatter plot for 3079W CHAN model.

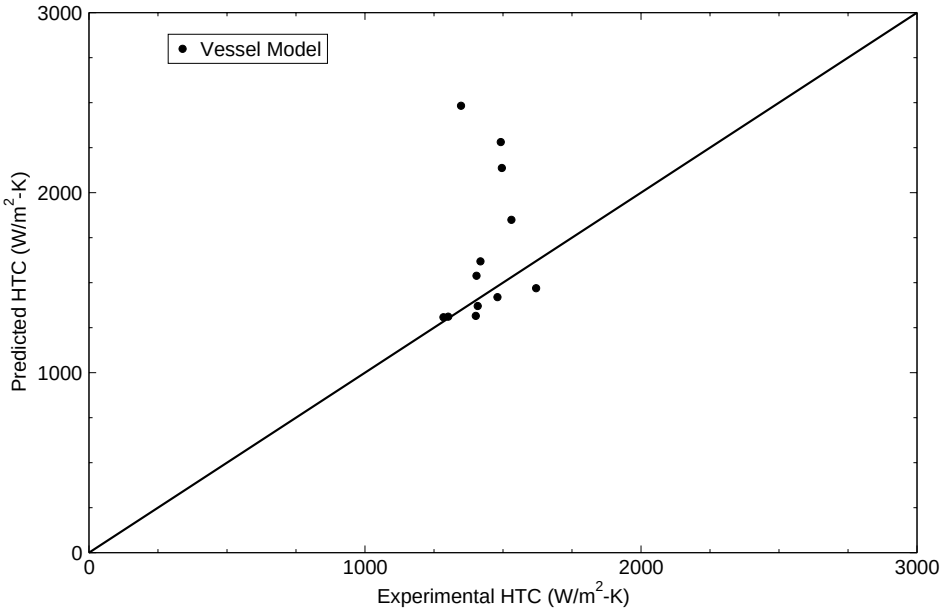

Figure B.5-18. Heat Transfer Coefficient Scatter plot for 3079W VESSEL model.

Scatter plots for TRACE calculated heat transfer coefficient verses data are provided in Figure B.5-23 and Figure B.5-24. These two figures are provided for additional comparison for the HTC prediction.

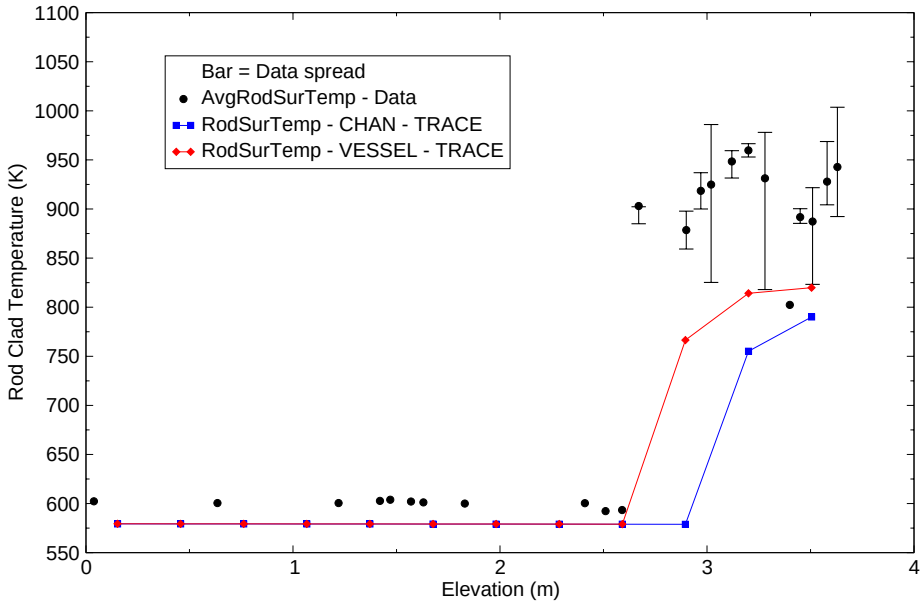

Figure B.5-19. Axial clad temperature comparison -THTF Test 3.07.9N

B.5.4.4. Simulation of Test 3.07.9H

Test 3.07.9H is considered to be a medium pressure, low mass flux and low heat flux test (see Table B.5.3). The boundary conditions for this test are similar to Test 3.07.9W except the system pressure is lower.

The predicted and measured axial rod clad temperature profile are compared in Figure B.5-25. The measured data indicates DNB occurring at about 2.7 meters in the bundle, similar to the location of DNB for Test 3.07.9W. With chfmult = 0.42, DNB location predicted are reasonable. Both the CHAN and VESSEL models underpredict the clad temperatures. Reasonable agreement is obtained only at the bundle exit.

The predicted and measured heat transfer coefficients are compared in Figure B.5-26.Figure only showed the HTC after the DNB locations. CHAN and VESSEL models predicted HTC correctly near the top of the bundle. But at around 2.9m, both CHAN and VESSEL overpredicted data, which caused underprediction of the rod temperatures at the same locations as shown in Figure B.5-25

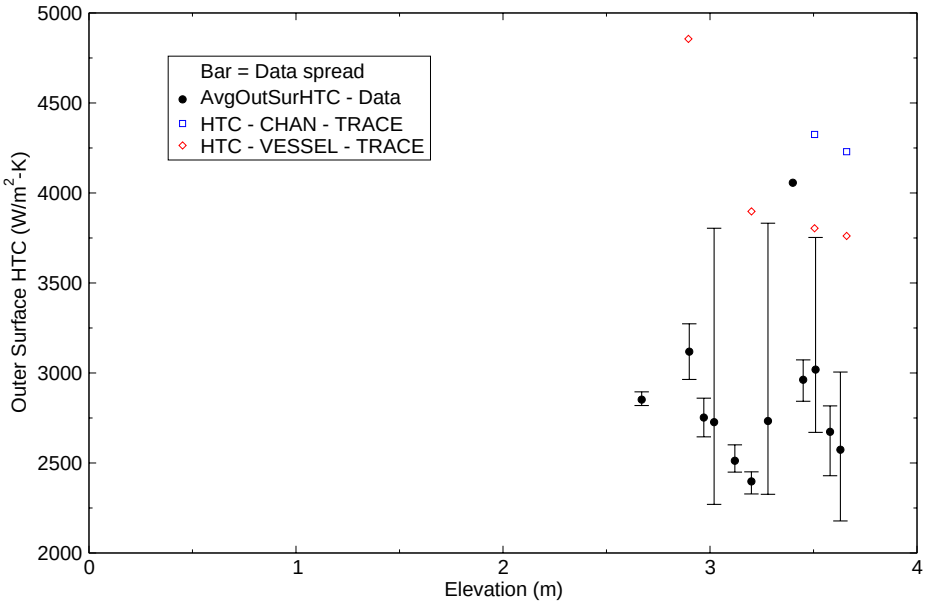

Figure B.5-20. Comparison of film boiling HTCsat - Test 3.07.9N

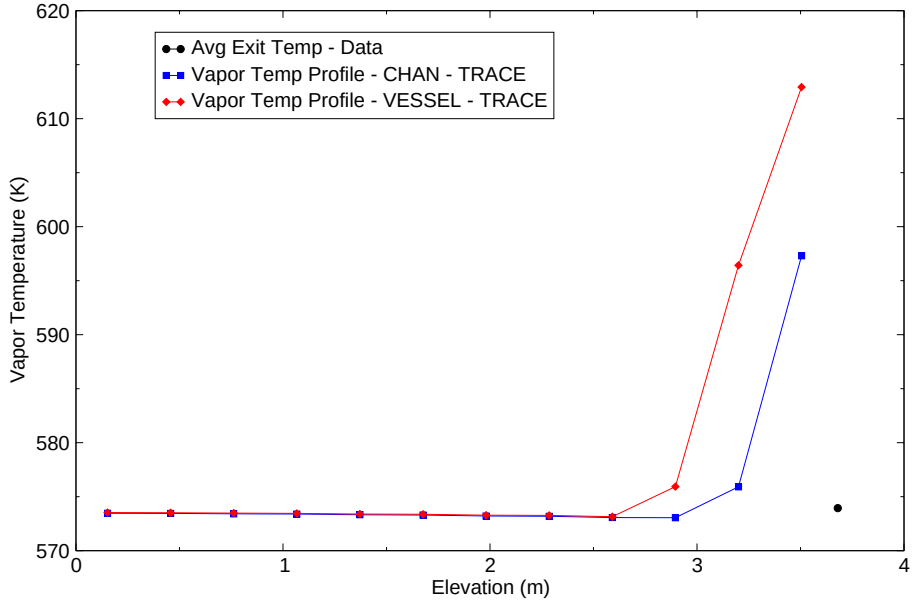

Figure B.5-21. Vapor temperature comparison - Test 3.07.9N

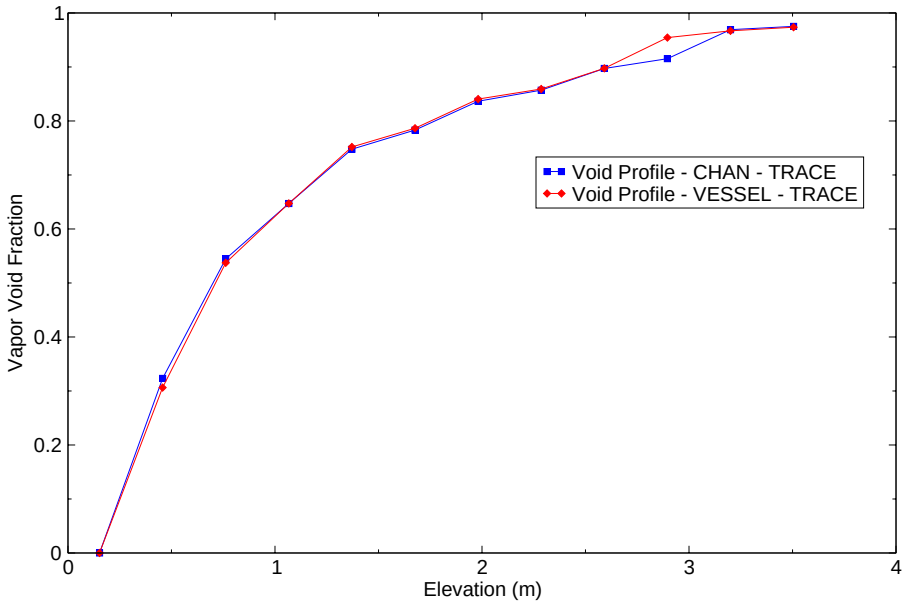

Figure B.5-22. Void fraction comparison - Test 3.07.9N.

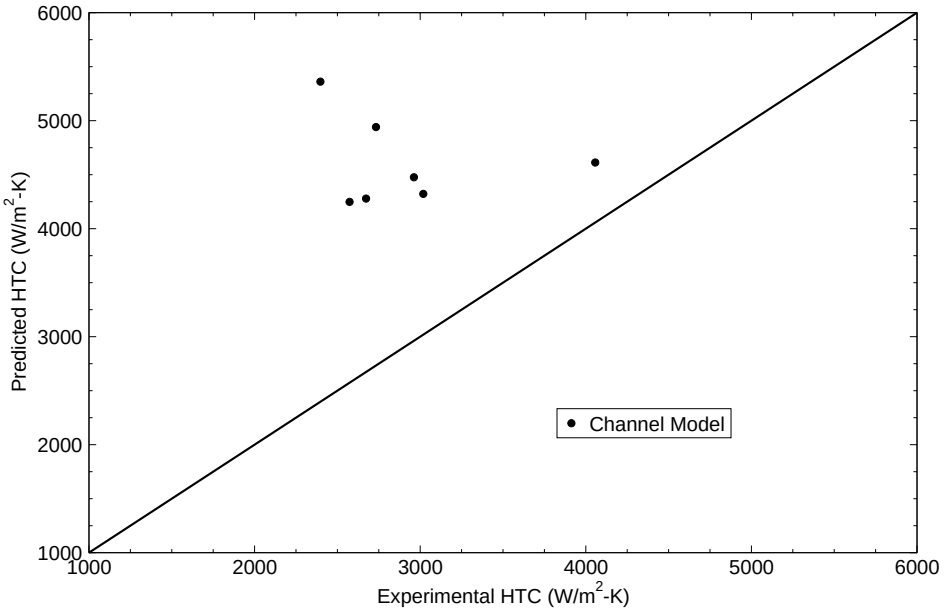

Figure B.5-23. Heat Transfer Coefficient Scatter plot for 3079N CHAN model.

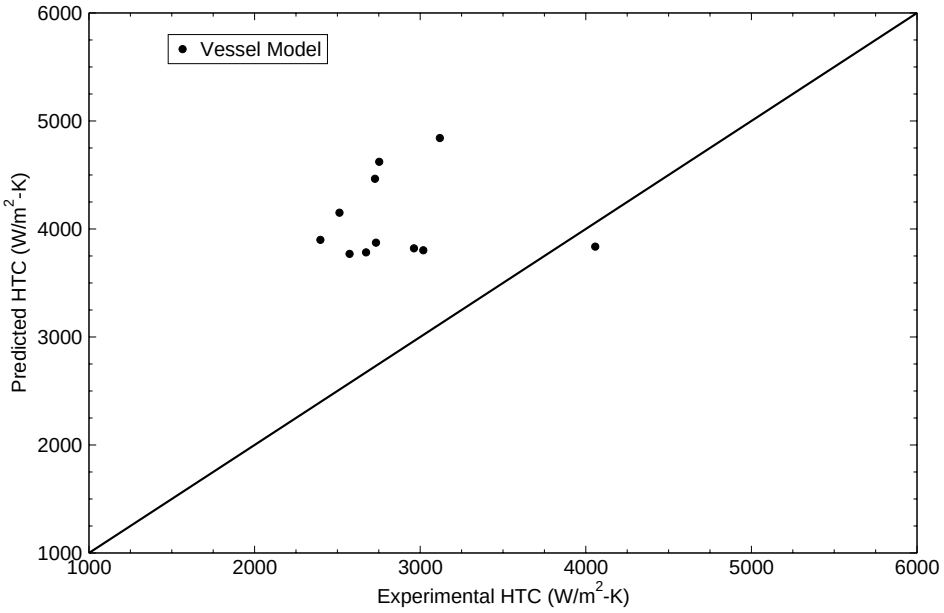

Figure B.5-24. Heat Transfer Coefficient Scatter plot for 3079N VESSEL model.

The prediction of the vapor temperature in the bundle affects the rod clad temperature prediction. The predicted axial vapor temperature profile is shown in Figure B.5-27. Also shown is the average measured bundle exit steam temperature. Calculations over-predict the steam temperature.

The predicted void fraction is shown in Figure B.5-28. The difference in the axial profile of void fraction between the CHAN and VESSEL models is small.

Scatter plots for TRACE calculated heat transfer coefficient verses data are provided in Figure B.5-29 and Figure B.5-30. These two figures are provided for additional comparison for the HTC prediction.

B.5.5. Assessment Results Summary

The DNB position in this set of assessment tests were adjusted to match the test data. With the hard wired DNB location setting, post-chf heat transfer were assessed using four THTF steady state tests. For Test 3079B, which is a high pressure, high mass flux and high heat flux test, showed good prediction for the rod temperature and HTCs using CHAN and VESSEL component. For Tests 3079W and H, which are at high pressure, low mass flux and low heat flux test and a medium pressure, low mass flux and low heat flux test, code predicted reasonable rod temperatures and HTCs near the bundle exit but underpredicted rod temperature right after the

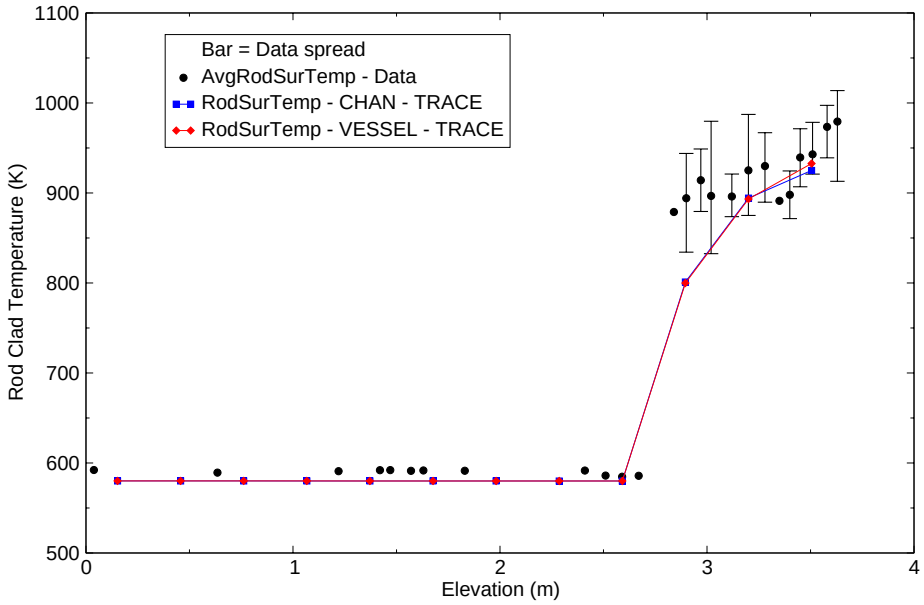

Figure B.5-25. Axial clad temperature comparison -THTF Test 3.07.9H

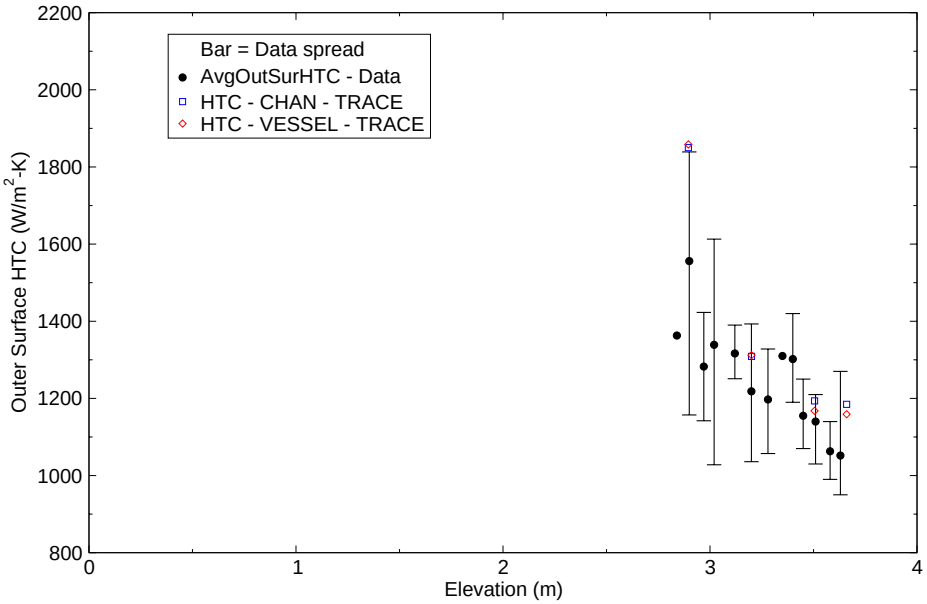

Figure B.5-26. Comparison of film boiling HTCsat - Test 3.07.9H

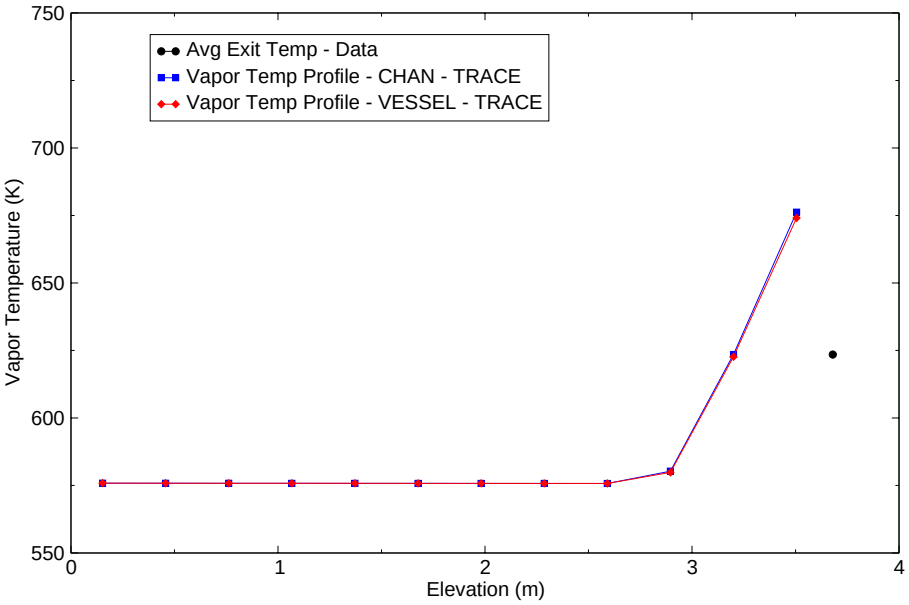

Figure B.5-27. Vapor temperature comparison - Test 3.07.9H

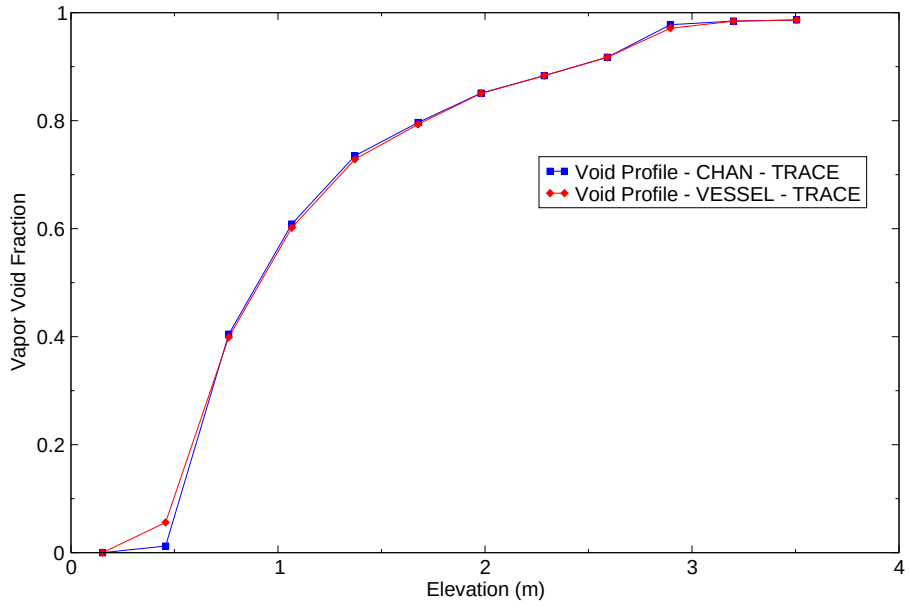

Figure B.5-28. Void fraction comparison - Test 3.07.9H.

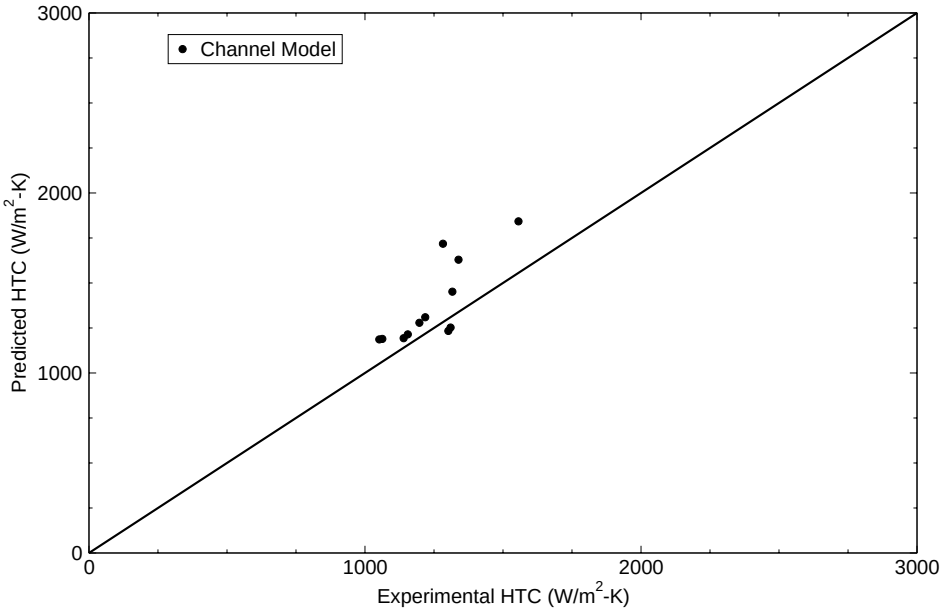

Figure B.5-29. Heat Transfer Coefficient Scatter plot for 3079H CHAN model.

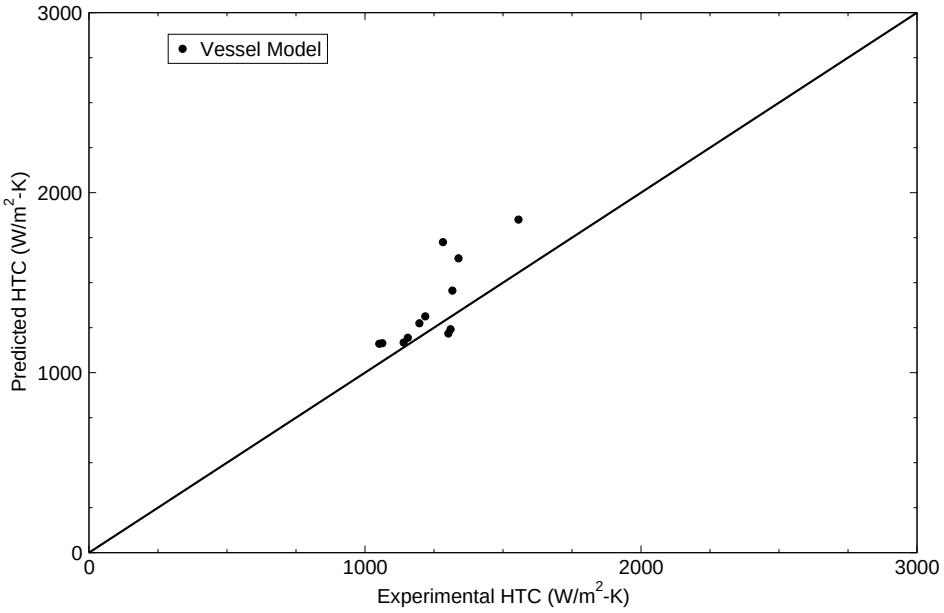

Figure B.5-30. Heat Transfer Coefficient Scatter plot for 3079H VESSEL model.

quench front. For Test 3079N, which is a medium pressure, high mass flux and high heat flux test, the code underpredicted rod temperature in dry-out region.

The steady-state film boiling simulations also have shown small difference between CHAN and VESSEL models. The differences can be caused by many reasons, one know reason is the difference of wall friction models for CHAN and VESSEL.

The measured steam temperatures for the tests simulated were not reliable. The temperature probes were not aspirated, therefore they were subject to early quench. Further assessment will be useful with data that has good steam temperature data.

B.5.6. References

1 Weidong Wang, THTF Steady State Tests Assessment Report for TRACE v. 4.269, ML061790094.

2 D. K. Felde, et. al., "Facility Description - THTF MOD 3 ORNL PWR BDHT Separate-Effects Program", ORNL/TM-7842, October 1982.

3 C. B. Mullins, et. al., "ORNL Rod Bundle Heat Transfer Test Data - Volume 2. Thermal-Hydraulic Test Facility Experimental Data Report for Test 3.03.6AR - Transient Film Boiling in Upflow", NUREG/CR-2525, Vol. 2, ORNL/NUREG/TM-407/V2, April 1982.

4 C. B. Mullins, et. al., "ORNL Rod Bundle Heat Transfer Test Data - Volume 3. Thermal-Hydraulic Test Facility Experimental Data Report for Test 3.06.6B - Transient Film Boiling in Upflow", NUREG/CR-2525, Vol. 3, ORNL/NUREG/TM-407/V3, May 1982.

5 C. B. Mullins, et. al., "ORNL Rod Bundle Heat Transfer Test Data - Volume 5. Thermal-Hydraulic Test Facility Experimental Data Report for Test 3.08.6C - Transient Film Boiling in Upflow", NUREG/CR-2525, Vol. 5, ORNL/NUREG/TM-407/V5, May 1982.

6 C. B. Mullins, et. al., "ORNL Rod Bundle Heat Transfer Test Data - Volume 7. Thermal-Hydraulic Test Facility Experimental Data Report for Test Series 3.07.9 - Steady-state Film Boiling in Upflow", NUREG/CR-2525, Vol. 7, ORNL/NUREG/TM-407/V7, May 1982.

7 G. L. Yoder, et. al., “Dispersed Flow Film Boiling in Rod Bundle Geometry - Steady-State Heat Transfer Data and Correlation Comparisons”, NUREG/CR-2435, ORNL-5822, March 1982.

8 D. G. Thomas, “PWR-Blowdown Heat Transfer Separate Effects Program”, Fourth Water Reactor Safety Research Information Meeting September 27-30, 1976.

B.6. THTF Transient Blowdown Assessment

Author(s): Weidong Wang, Andrew Ireland

Affiliation: USNRC

Code Version: TRACE V5.0

Platform and Operating System: Intel x86, Windows XP

B.6.1. Introduction

The Oak Ridge National Laboratory (ORNL) Pressurized Water Reactor (PWR) Blowdown Heat Transfer (BDHT) program (Ref. 1) studied heat transfer phenomena in PWRs during loss of coolant accidents (LOCAs). The film boiling heat transfer can occur during a large break LOCA when the liquid becomes depleted at the heated (or hot) surface. The purpose of this section is to document TRACE code simulations of three heat transfer experiments performed under the BDHT program. The assessment will show the capability of TRACE to predict the heat transfer during a blowdown. The tests simulated and reported herein are: 3.03.6AR, 3.06.6B, and 3.08.6C. A brief description of the test facility is given below, followed by a description of the tests. The TRACE input model of the facility is described followed by calculation results compared to data. Conclusions of the assessment are then given.

This assessment report is based largely on the assessment report of Weidong Wang for the same blowdown tests simulated with an older version of TRACE (Ref. 2).

B.6.2. Test Facility Description

THTF is a nonnuclear pressurized water loop containing 64 full-length rods arranged in an 8 x 8 bundle. Figure B.6-1shows an isometric view of the facility. Sixty of the rods were electrically heated and four were unheated. Rod diameter (0.0095 m) and pitch (0.0127 m) are typical of a PWR with 17 x 17 fuel assemblies. Figure B.6-2 is a schematic of the THTF rod bundle cross section and shows the location of the four unheated rods. The axial and radial power profiles of the THTF bundle are flat. The heated length of the bundle is 3.66 m and there are six spacer grids in the heated length.

Figure B.6-3 is a simple diagram of the THTF to help describe the facility. Fluid flows from the pump through the horizontal inlet and vertical inlet spool pieces. From the vertical inlet spool piece, fluid enters the external downcomer spool piece and then flows into the test section lower

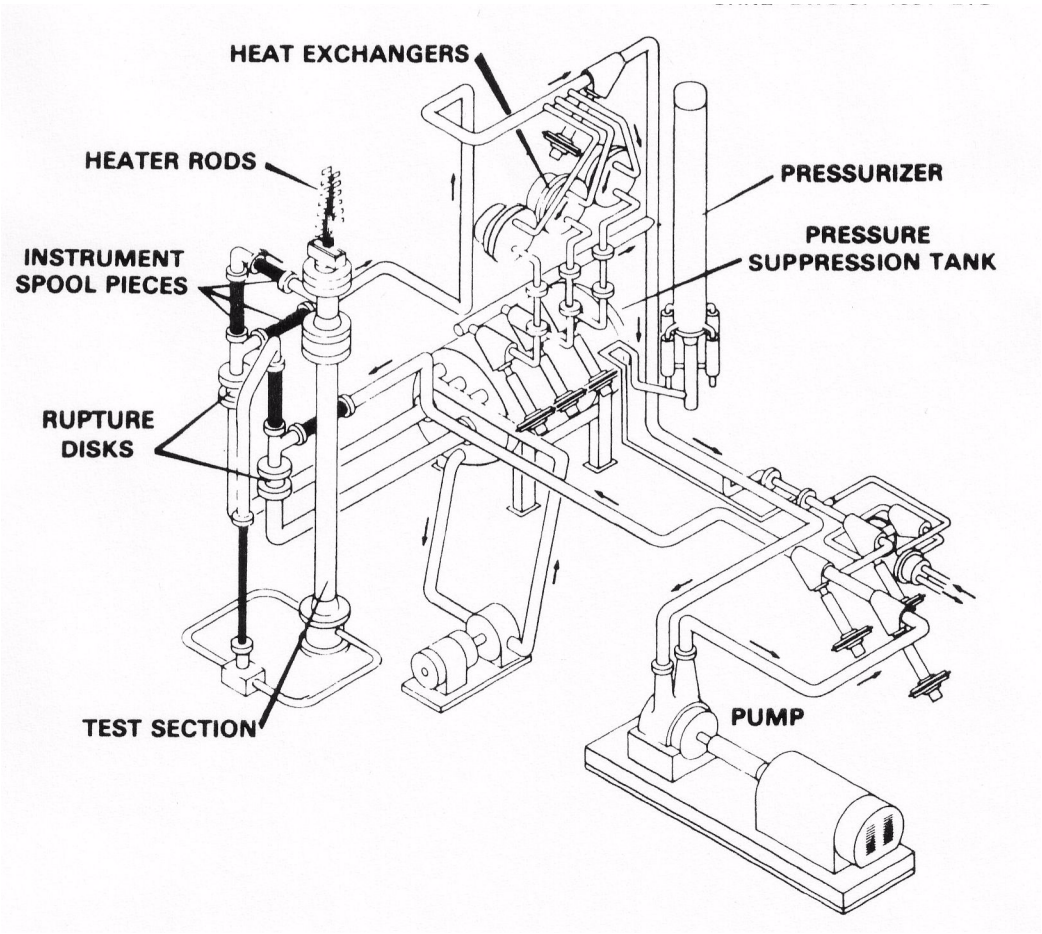

Figure B.6-1. Thermal-Hydraulic Test Facility

plenum. Fluid flows from the lower plenum up through the heated length of the bundle, into the test section upper plenum, through the outlet spool pieces, into the main heat exchangers, and back to the inlet of the pump.

The test facility was highly instrumented with pressure and differential pressure transducers, gamma densitometers for measuring in-bundle fluid density, fuel rod simulator (FRS) thermocouples, and thermocouples mounted to grid spacers for in-bundle fluid temperature. Figure B.6-4 shows the axial location of the grid spacers and the FRS thermocouples. For a detailed discussion of the test facility, refer to Reference 1.

B.6.3. TRACE Model Description

Nodalization of the TRACE model of THTF is shown in Figure B.6-5 In order for the results of this assessment to be applied to both Pressurized Water Reactor (PWR) and Boiling Water Reactor (BWR) facilities, two TRACE input files were made: one input file contained a CHAN component (CHAN input deck) and the other input file contained a Vessel component (Vessel

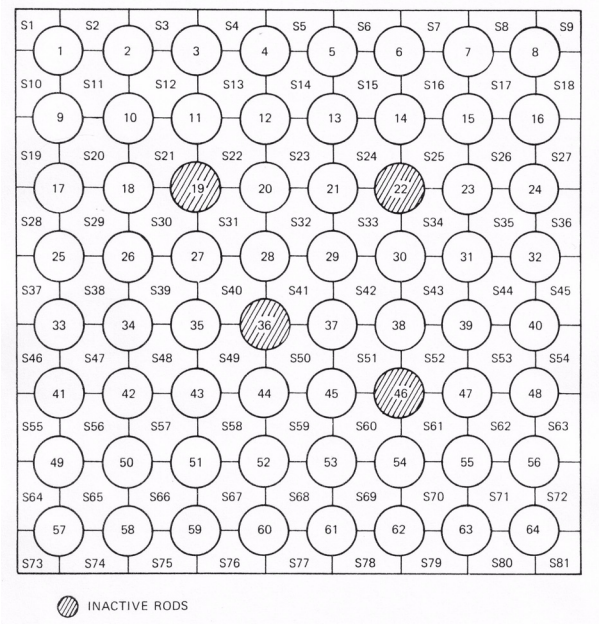

Figure B.6-2. Cross section of the THTF heated bundle showing location of the unheated rod

input deck). Both input files were similar, i.e. they both contained the same number of components and had identical cell and heat structure noding (heat structures for the heated and un-heated rods and the bundle wall are contained with in the CHAN component where as HTSTR components representing the heated and un-heated rods and the bundle wall were input for the Vessel input deck). Details of each component is given below.

B.6.3.1. CHAN/VESSEL Component

The 8 X 8 rod bundle extends the entire length of the test section. A bundle shroud box with a 0.1037 meter square inside dimension surrounds the rod bundle. The shroud box extends about 0.26035 meters below and about 0.2889 meters above the heated section of the rod bundle. The lower and upper plenums of the test section, below and above the shroud box, are bounded by a 10 inch, schedule 140 (8.75 inch ID), 316 stainless steel pipe. The CHAN/Vessel component models the full length of the bundle shroud box. The component number for the CHAN/Vessel is 222.

The CHAN and Vessel components are divided into 14 axial cells/levels. The hydraulic geometry in the Vessel component was modeled using Cartesian coordinates in order to approximate the CHAN component. The heated section is 3.6576 m long. There are 6 grid spacers in the heated rod section. Two hydro cells/levels were placed between each grid spacer (see Figure B.6-4 for the grid spacer locations) with a total of 12 cells/levels in the core (0.3048 m cell lengths). The heated section of the rod bundle begins at the bottom of cell/level 2 and ends at the top of cell/ level 13. Cell/level 1 and 14 is the end and beginning of the lower and upper plenum

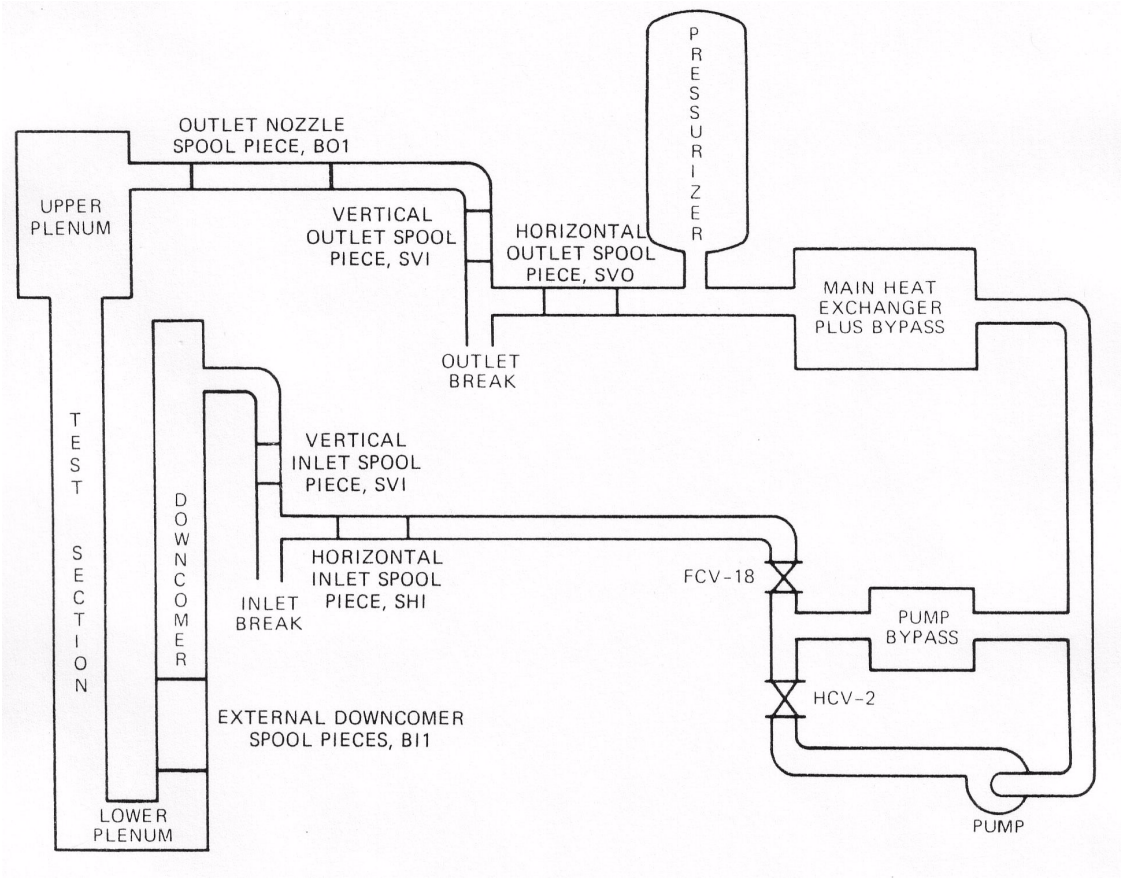

Figure B.6-3. Diagram of THTF

respectively. The flow area is constant in the heated rod region at 0.0061752 m^2. The volume of the CHAN and Vessel components is 0.02598 m^3.

The geometry describing the heated and un-heated rods and the bundle shroud box is included in the CHAN component input. TRACE uses this information and spawns heat structure components. The rods are divided into 2 rod groups in the CHAN component. Rod group 1 represents the 60 heated rods and rod group 2 represents the 4 unheated rods. The rods are divided into 10 radial nodes, representing the boron nitride insulating material, the constantan/nichrome heater wire and the stainless steel cladding. The bundle shroud wall was divided into 5 nodes. The heat structure cell height is the same as the hydro cell height. The heated rod diameter is 0.0095 m. The unheated rod diameter is 0.0102 m, slightly larger than the heated rod diameter. For simplicity, the four unheated rods were modeled the same as the heated rods except without power.

Thomas (Ref. 8) reported a grid spacer loss coefficient for all mass flow rates in THTF of 1.216. This was based on an earlier 49 rod bundle configuration. Assuming the grid spacer losses are similar in the 64 rod bundle configuration an equivalent resistance was calculated using the area

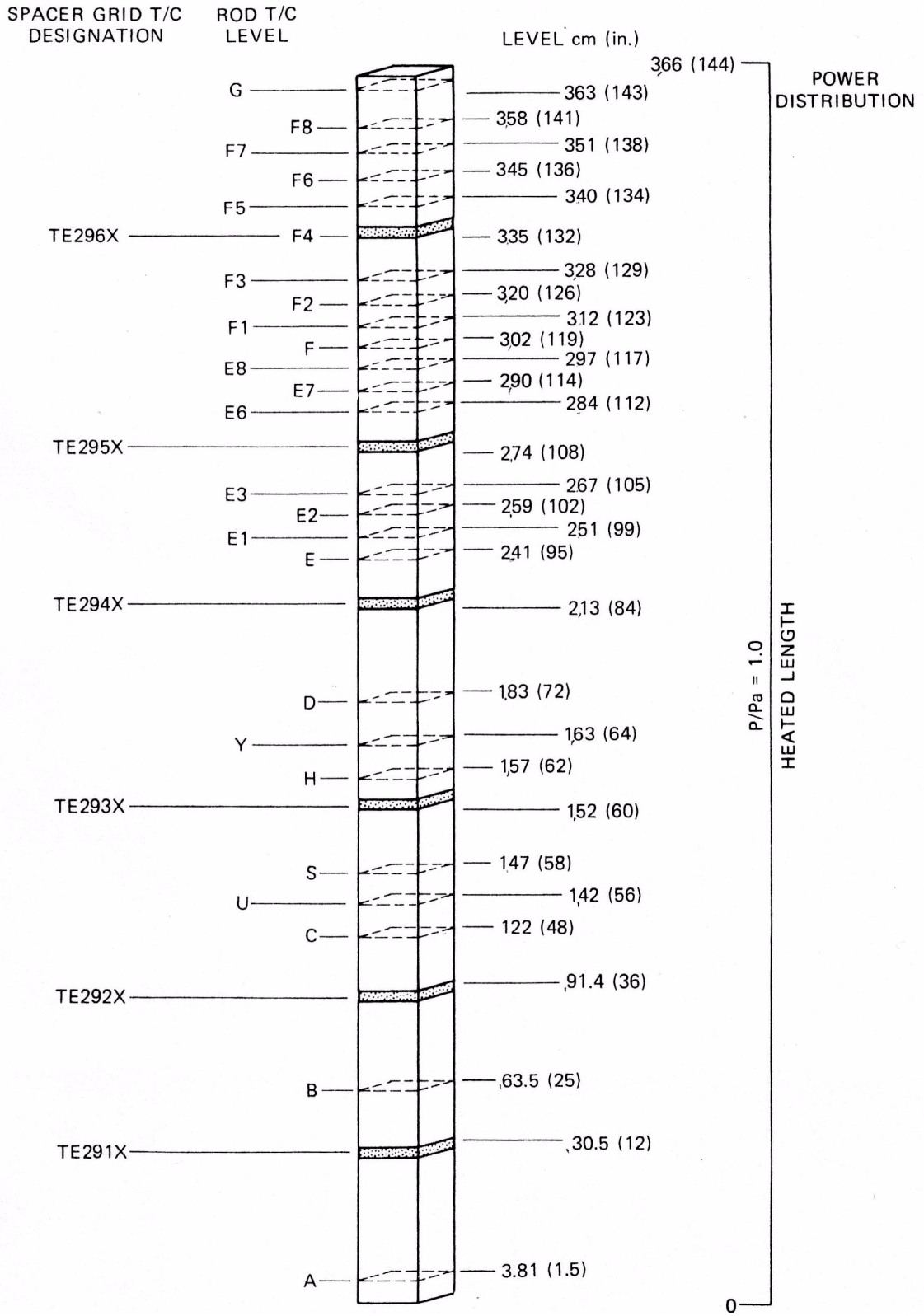

Figure B.6-4. Grid Spacer and fuel rod simulation thermocouple axial locations.

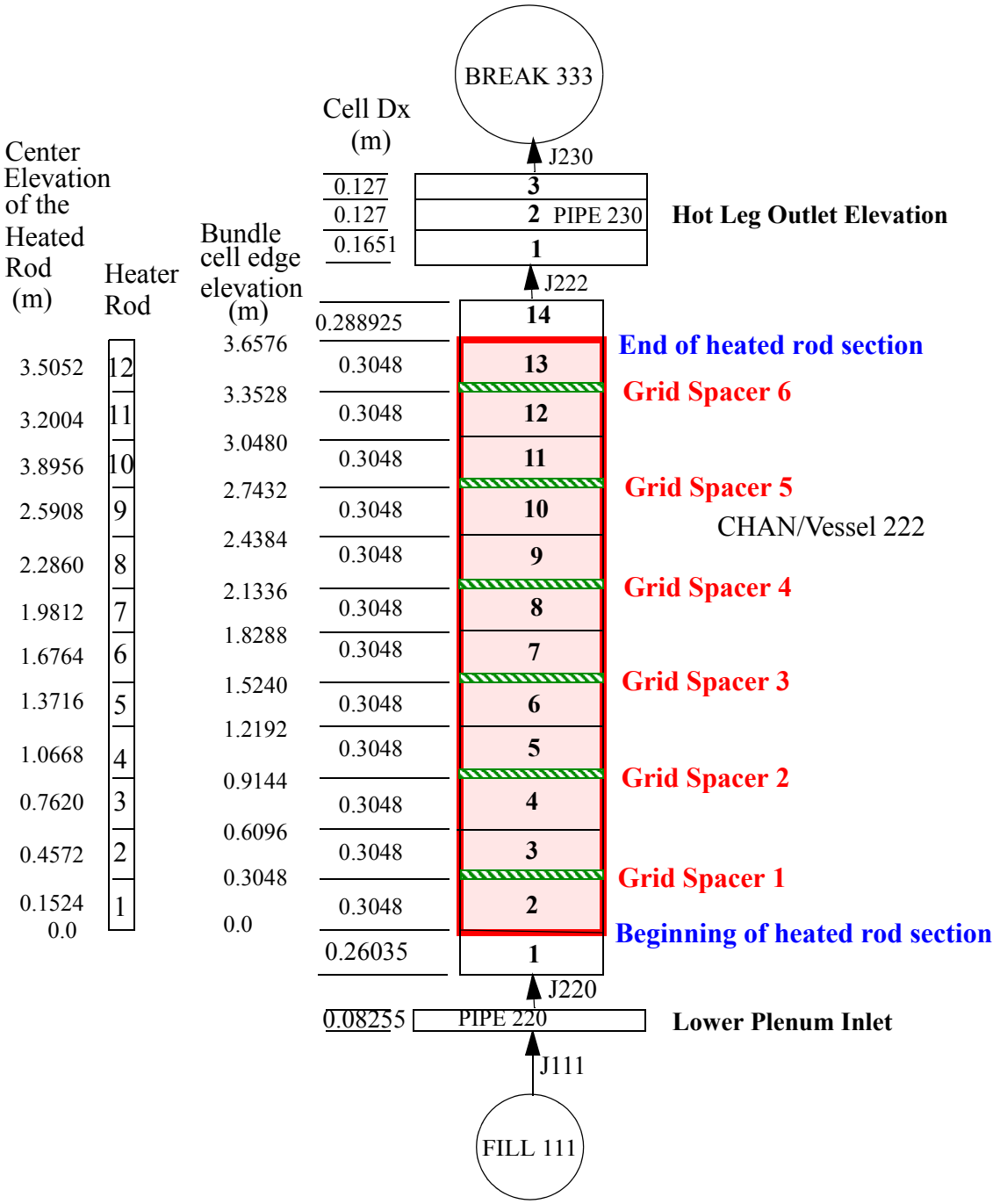

Figure B.6-5. TRACE nodalization of the Thermal-Hydraulic Test Facility.

ratio squared between the two bundle sizes. The equivalent loss coefficient was calculated to be 1.332.

Three HTSTR components were used in the Vessel input deck to model the heated and unheated rods and the bundle shroud box. The HTSTR components were modeled one-to-one with the

CHAN internal heat structures. The CHAN internal heat structure component numbers and the corresponding Vessel input deck heat structure component numbers are given in Table B.6.1.

Table B.6.1. CHAN and Vessel heat structure component numbers.

Modeled component	CHAN component heat structure numbers	Vessel heat structure component numbers
heated rods	222002	888
unheated rods	222003	889
bundle shroud box	222004	890

Radiation heat transfer was modeled using the MROD array in the CHAN input. This was accomplished by setting the IBEAM input parameter in the CHAN input to 0 and entering the layout of primary and supplemental rod positions in the MROD array. The bundle shroud box is the last position in the MROD array. Figure B.6-6 illustrates the MROD array input. Once the MROD array is configured, TRACE calculates the view factors, and beam lengths. The view factors and beam lengths are printed in the output.

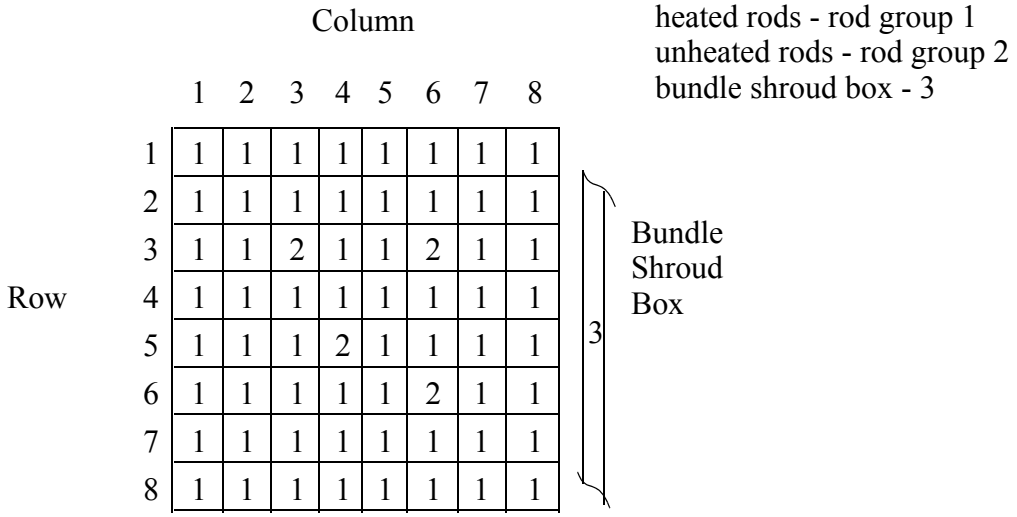

Figure B.6-6. MROD array configureation for the CHAN radiation heat transfer model.

The RADENC component (component 895) was used in the Vessel input deck to model radiation heat transfer. The view factors and beam lengths calculated by TRACE for the CHAN component were used in setting up the RADENC component.

B.6.3.2. Lower Plenum Inlet

Fluid enters the heated region of the test section through the lower plenum. As stated earlier, the lower plenum is constructed with a 10 inch schedule 140 stainless steel pipe. The unheated portion of the bundle rods extend down through the lower plenum. The external downcomer is connected to the lower plenum from two sides (see Figure B.6-1). PIPE component 220 (Figure B.6-5) represents the geometry of the lower plenum from the external downcomer connection elevation up to the bottom of the bundle shroud box. Junction 220 connects PIPE 220 to the CHAN or Vessel component.

B.6.3.3. Upper Plenum

Fluid exits the heated test section via the upper plenum and then out to the heat exchangers through the test section outlet piping (see Figure B.6-3). Like the lower plenum, the upper plenum is also constructed with a 10 inch schedule 140 stainless steel pipe that surrounds the unheated portion of the bundle rods above the heated rod zone. PIPE component 230 represents the upper plenum from the top of the bundle shroud box to the outlet pipe connection elevation. The PIPE component is divided into three cells. The CHAN or Vessel component is connected to PIPE 230 via junction 222.

B.6.3.4. Inlet Initial and Boundary Conditions

FILL component 111 was used to setup the test section inlet initial and boundary conditions. FILL type 6 was used for the transient film boiling simulations. A type 6 FILL is a generalized state versus independent-variable form table. The independent-variable is time, and the generalized state parameters are: liquid and vapor velocities, liquid and vapor temperatures, void fraction, pressure, and non-condensable gas partial pressure. The liquid and vapor velocities were derived from volumetric flow measurements taken upstream of the test section inlet (instrument tag FE-260) and assuming no slip between the two phases. The fluid temperature and the pressure were taken from instrument tags TE-256 and PE-258 respectively which are also located upstream of the test section inlet. Void fraction versus time was calculated using the following relationship:

$$\dot{m} = \rho_m Q_m = \rho_v A_T v_v \alpha + \rho_l A_T v_l (1 - \alpha \quad (6\text{-}1)$$

where: $\dot{m}$ = mass flow rate

ρ_m = measured density

Q_m = measured volumetric flow

ρ_v = vapor density

ρ_l = liquid density

A_T = total flow area

v_v = vapor velocity

v_l = liquid velocity

α = void fraction

If no slip is assumed between the liquid and vapor velocities, $v_v = v_l = v$ and $Qm = A_T v$ then (6-1) reduces to:

$$\rho_m = \rho_v \alpha + \rho_l (1 - \alpha) \quad . \tag{6-2}$$

Solving for the void fraction yields:

$$\alpha = \frac{\rho_m - \rho_l}{\rho_v - \rho_l} \tag{6-3}$$

The measured density is obtained from instrument tag DE-20 and the liquid and vapor densities are obtained with a simple TRACE PIPE input deck utilizing the test section inlet pressure measurement (PE-258).

The measured density has an error band of ± 5 kg/m3.

B.6.3.5. Outlet Initial and Boundary Conditions

BREAK component 333 was used to setup the test section outlet pressure boundary conditions. Pressure tap PE-201 was used to set the pressure-time history in the BREAK component for the transient film boiling tests.

B.6.3.6. POWER Component

The TRACE POWER component (998) was used to model the power input to the THTF simulations. The axial and radial power profile of the THTF rod bundle was uniform. The power input for the transient simulations was determined from the measured voltage and current applied to the rods.

B.6.4. Tests Simulated with TRACE

The results of the TRACE simulations of the THTF transient film boiling tests are presented in this section. The transient THTF tests simulated were 3.03.6AR, 3.06.6B, and 3.08.6C. Transient tests were initiated by breaking the outlet rupture disk assembly. Breaking only the outlet rupture disk assembly assured unidirectional flow up through the test section. At the same time the rupture disk was broken, the pump was tripped and bundle power was ramped up from the steady-state value to a predetermined value (~6.5 MW for Test 3.03.6AR, and ~7.8 MW for Tests 3.06.6B and 3.08.6C) for each of the tests over a period less than 3 seconds. The bundle power remained at this high value until 50% of the thermocouples at the 3.63 m elevation in the bundle reached 811 K. The bundle power was then ramped down until the bundle power was tripped by the high-rod-temperature trip. This procedure resulted in prolonged film boiling while safely operating the bundle. The Power curve used in the TRACE simulation is provided in Figure B.6-7.

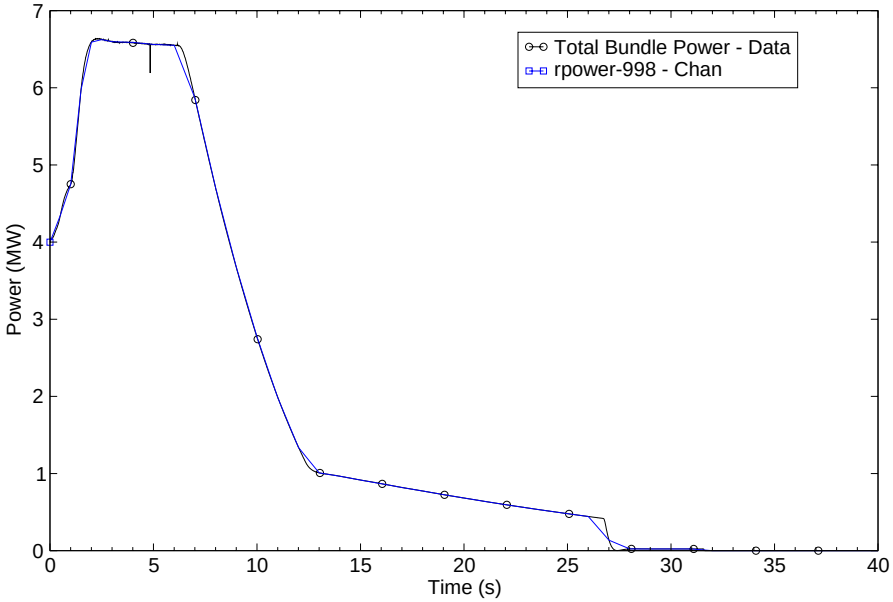

Figure B.6-7. Total bundle power comparison for Test 3036AR

Prior to simulating the transients, steady state calculations were made to initialize the thermal-hydraulic conditions. This was accomplished by setting the input parameters in the FILL, BREAK and POWER components to constant values and executing a null transient for about 1000 seconds to assure pressures, and temperatures had stabilized. After the problem had reached steady conditions, the output was processed to extract the end time results and create a new input

deck for the transient calculations. Table B.6.2 contains initial condition data and the calculated steady-state parameters for the input deck.

Table B.6.2. Initial conditions for the transient film boiling simulations

	Test 3.03.6AR		**Test 3.06.6B**		**Test 3.08.6C**	
	measured	**calculated**	**measured**	**calculated**	**measured**	**calculated**
Bundle Power (MW)	~4.0	3.998	~2.27	2.27	~2.4	2.2
Mass Flow Rate (kg/s)	14.01	14.08	5.99	5.97	~6.5	6.3
Average Pressure (MPa)	14.1	14.1	14.9	14.9	12.8	12.8
Inlet Temperature (K)	541.2	541.2	550	550	538.8	538.8
Outlet Temperature (K)	592.5	593.6	611.4	612	599	600
Test Section Differential Pressure[a] (kPa)	105[b]	122	~66	52	~66	55

a. Steady-state error band ±35 kPa

b. This DP is an overall test section DP (PDE-200). There are intermediate DP taps in the test section. A comparison of these DP taps with the overall DP tap suggests that there may have been some problems with the instrumentation during this experiment and the value listed in the table may be in error.

B.6.4.1. Simulation of Test 3.03.6AR.

The initial bundle power and inlet mass flow rate for Test 3.03.6AR was 4.0 MW and 14.01 kg/s respectively, about twice that of the other two tests.

At the initiation of the break, the system went through a rapid subcooled depressurization. When the pressure dropped below the saturation pressure of the liquid at the test section outlet, flashing occurred and the pressure recovered momentarily. At about 3.5 seconds the pressure then turned over and began a slow depressurization rate. The system pressure is shown in Figure B.6-8. This pressure is the input for the BREAK component.

A comparison of the predicted break mass flow rate with data is shown in Figure B.6-9. Mass flow rate is not directly measured, but is a product of the volumetric flow rate (FE-216) and the measured density (DE-218). During the subcooled portion of the blowdown, the predicted mass flow rate agrees well with the data. However, after flashing commences the break mass flow rate is over-predicted. The over-prediction results in about 30% more liquid mass leaving the system than the data as shown in Figure B.6-10. This is probably a result of too much entrainment. After 20 seconds the predicted break flow rate is close to the data.

A discussion on the methods used to calculate mass flux at the THTF test section boundaries and the estimated uncertainties in those calculations is presented in Reference 3 through Reference 5. Mass flow error for steady-state two phase flow using turbine-meter and gamma densitometer measurements was reported to be 60% of the reading. The uncertainty of transient effects on two-phase flow was reported to be an extra 30-50% of reading for mass flow greater than 3.79 kg/s.

Rod clad temperature comparisons are shown in Figure B.6-11 through Figure B.6-20. The axial elevations at the center of the heat structure cells of the predicted rod clad temperatures do not match exactly with the axial elevations of the thermocouples in the experiment. Plotting software function was used to plot a specified rod temperature at specified elevation by interpolation. The elevation for Rod clad temperature comparisons are Level B (0.635 m), Level U (1.42 m), Level Y (1.63 m), Level D (1.83 m), Level E (2.41m), Level F (3.02 m), and Level G (3.63 m) (see Figure B.6-4 and Figure B.6-5 for Level and cell locations). The rod clad thermocouples are located on the inside of the stainless-steel cladding. Shown are measured data compared to predicted results from the CHAN calculation and the Vessel calculation. Several thermocouples are located at each of the elevations. Therefore, a thermocouple representative of the data at that elevation is defined by the black curve in the figures. Error bands around the data are given. Additional data from other thermocouples are shown at Levels B, U, E, F, and G. Measured rod clad temperature data from the other thermocouples are defined by the small black dots.

The predicted rod clad temperature in the lower part of the rod bundle for the two TRACE calculations seems reasonable compared with the data (see Figure B.6-11). It slightly underpredicted the data in the first 15 seconds. After 15 seconds, the prediction of the rod temperature moves near to the lower band of the test data. The lower section of the heated bundle region remains in nucleate boiling. The initial condition are obtained from a steady state calculation with the initial rod temperatures below the test data (however, the initial inlet/outlet fluid temperature predictions are reasonable compared to the test data as shown in Table B.6.2). This results clad temperature prediction near the lower limit of the data band. Figure B.6-12 shows the predicted liquid heat transfer coefficients (HTC) for the two calculations at cell 3 (0.635 m). The rod temperature prediction implies these HTCs prediction are reasonable. Similar to Level B, rod temperature prediction at Level U (1.42 m) and Level Y (1.63 m) are shown in Figure B.6-13 and Figure B.6-14. At the 1.63 m elevation, a temperature excursion is predicted to occur briefly but this is not present in the test data. Overall, however, at these elevations the test data are underpredicted during the first 15 seconds and prediction stayed near the lower band of the test data afterward. The heat transfer regime for Level Y is shown in Figure B.6-15 and it shows that the heat transfer is in nucleate boiling mode for the entire test at this elevation for the channel model. However, the vessel model shows a brief period of transition boiling. Figure B.6-16 shows the void fraction transition for Level Y. These plots show only minor differences from results using CHAN and VESSEL models.

The measured rod clad temperature at Level D (HTSTR cell 7) is shown in Figure B.6-17. The data shows at this level some of the rods depart from nucleate boiling (shown by the black dotted curve) while the others remain in nucleate boiling (shown by the black solid curve). The code predicts that the rod clad temperature at this level transitions to film boiling.

At elevations greater than 2 meters (Levels E, F, and G), the data indicates that all the heater rods depart from nucleate boiling and transition into film boiling as shown in Figure B.6-18 through Figure B.6-20. Likewise, the code also predicts the heater rods going to film boiling. The rod clad temperature prediction does a good job at predicting the time of DNB compared with data. The calculation predicts the rod temperature a Level E within the scatter of the data (Figure B.6-18) up to 25 seconds. The code predicts the peak clad temperature correctly but it predicts a delayed quenching time. At Levels F and G, the code does a good job in predicting peak temperature, but over-predicts temperature after reaching the peak temperature. The code also predicts delayed quenching time. TRACE does not have model grid spacers, which would enhancing cooling.

Additional parameters are examined at Level E (at elevation 2.41 m with Cell 8) for understanding the modeling process. A comparison of the predicted vapor and liquid HTC for the powered rod is shown in Figure B.6-21 and Figure B.6-22, respectively. The predicted outer surface heat transfer regime at this elevation is shown in Figure B.6-23. For the first 5 seconds of the transient, the code predicts nucleate boiling liquid heat transfer mode. The wall heat is transferred to the liquid since the vapor HTC is zero. As the rod continues to heat up, the temperature excess (T_{wall} - T_{sat}) becomes larger and rod transitions from nucleate to film boiling as shown in Figure B.6-24. The calculation model divides the film boiling regime (post-CHF) into two parts: inverted annular (heat transfer regime = 4) and dispersed flow (heat transfer regime = 5). The code predicts the rods are in the dispersed film boiling regime (regime 5) for CHAN and dispersed, inverted annular, and transition boiling for VESSEL calculations during dry out. While in film boiling, the TRACE partitions the heat removed from the rod wall to the vapor phase and the wall heat transfer to the liquid is turned off as inferred by the vapor and liquid HTCs shown in Figure B.6-21 and Figure B.6-22 respectively. Around 32 seconds, the rod quenches at Level E and heat again transfers to liquid as shown in Figure B.6-21 and Figure B.6-22. The interfacial heat transfer coefficients are shown in Figure B.6-25 and it can greatly affect the rod clad temperature prediction.

Figure B.6-26 compares the measured heated bundle region exit temperature with available data. The steam probes were not aspirated and is quenched early by liquid droplets impinging on the thermocouple. Thus out past 11 seconds it is unknown what the steam temperatures were.

B.6.4.2. Simulation of Test 3.06.6B

The main differences between Test 3.03.6AR and Test 3.06.6B were the initial inlet mass flow rate and the initial rod bundle power. The initial bundle power and inlet mass flow rate for Test 3.06.6B was 2.27 MW and 5.99 kg/s respectively. The bundle power history was similar to Test 3.03.6AR, i.e. the power was ramped up to about 7 MW and remained at that power until 50% of the rods reached 811 K then ramped down until the rod protection system tripped the power. The time when the power was tripped was about 11 seconds. In general, the predicted results from the TRACE simulations of Test 3.06.6B are similar to those of Test 3.03.6AR.

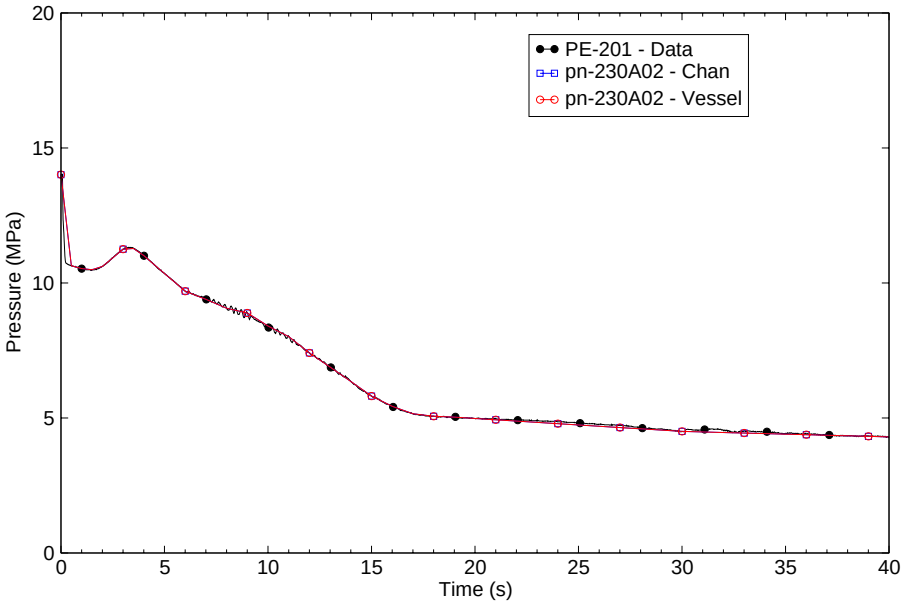

Figure B.6-8. System pressure response for Test 3036AR

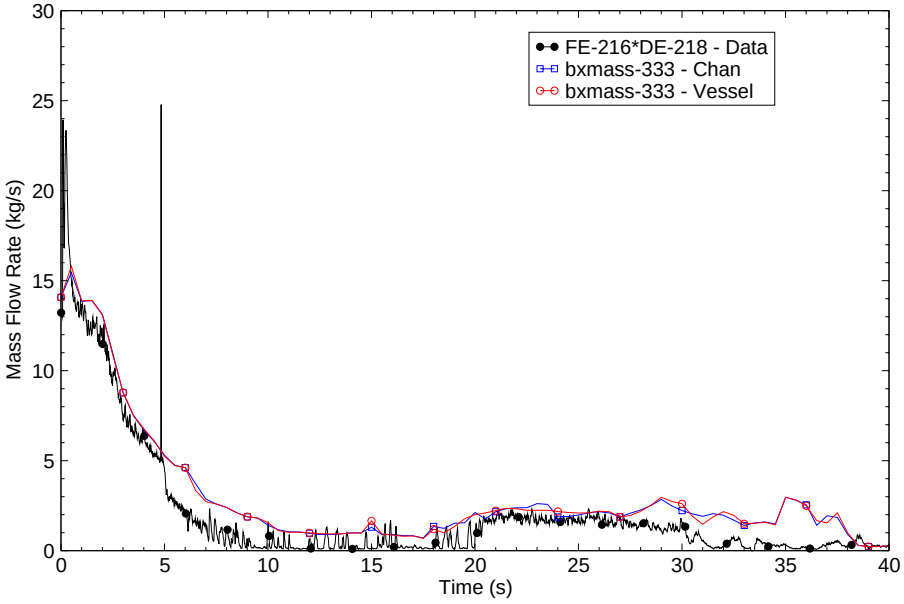

Figure B.6-9. Test section outlet mass flow rate for Test 3036AR

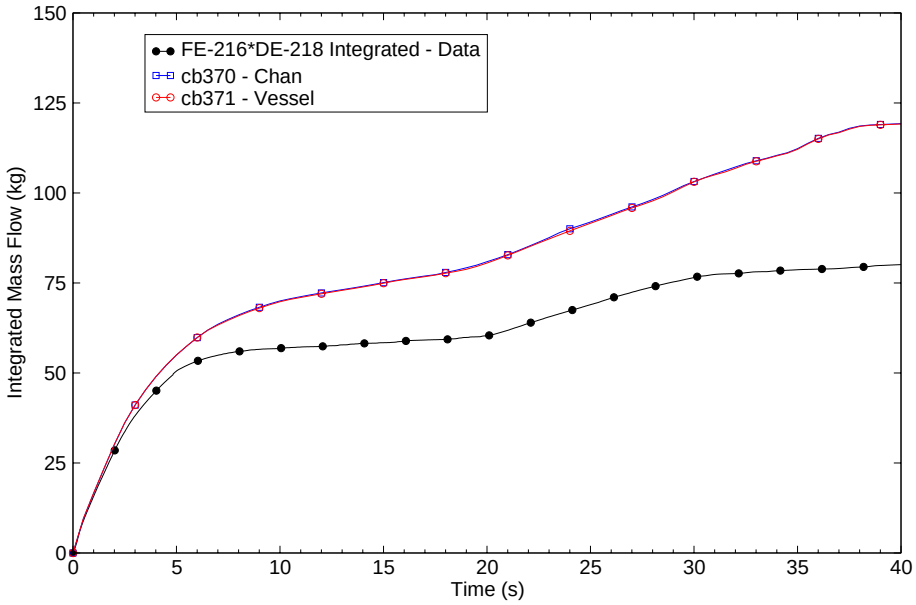

Figure B.6-10. Integrated outlet mass flow rate for Test 3036AR

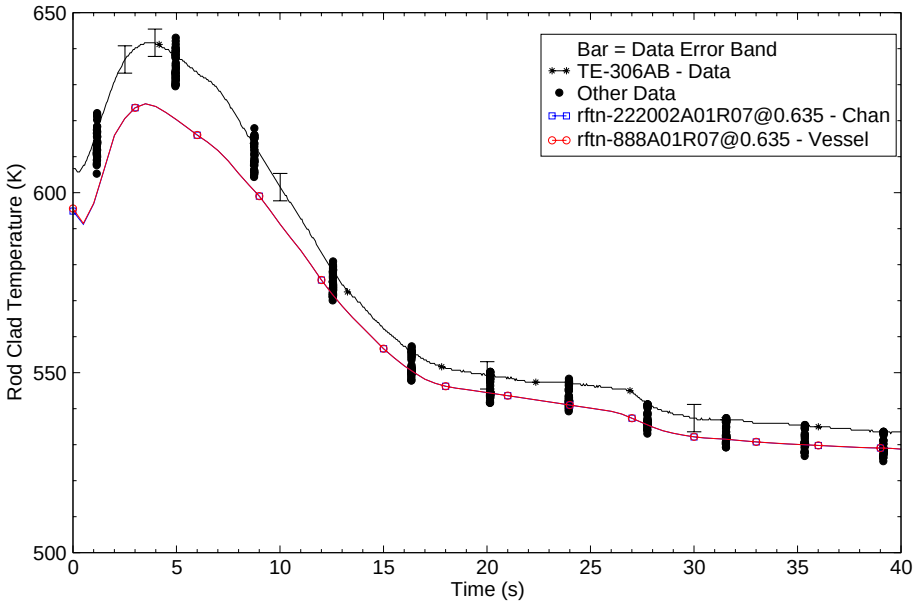

Figure B.6-11. Rod clad temperature at Level B (0.635m) for Test 3036AR

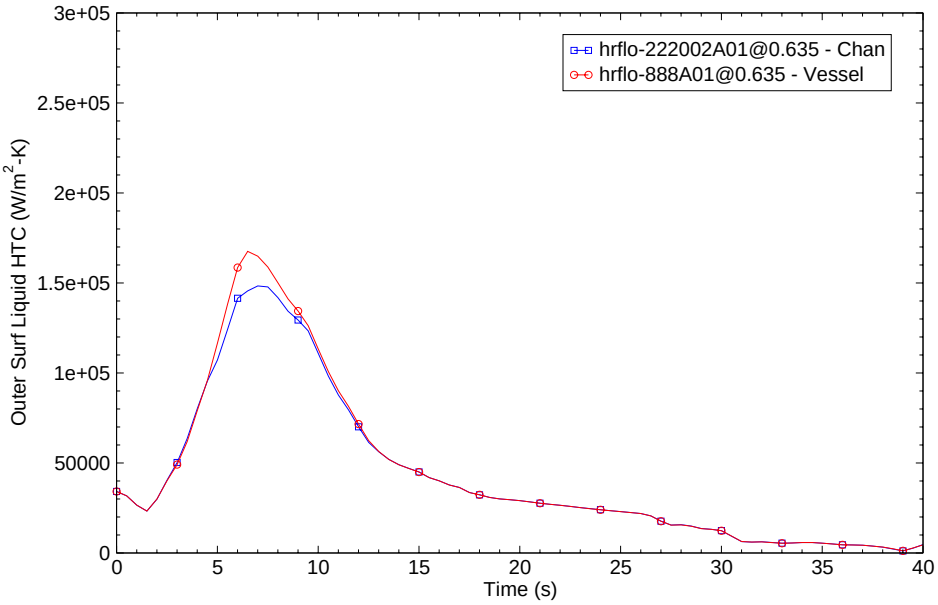

Figure B.6-12. Predicted liquid heat transfer coefficient @ 0.635 m for Test 3036AR

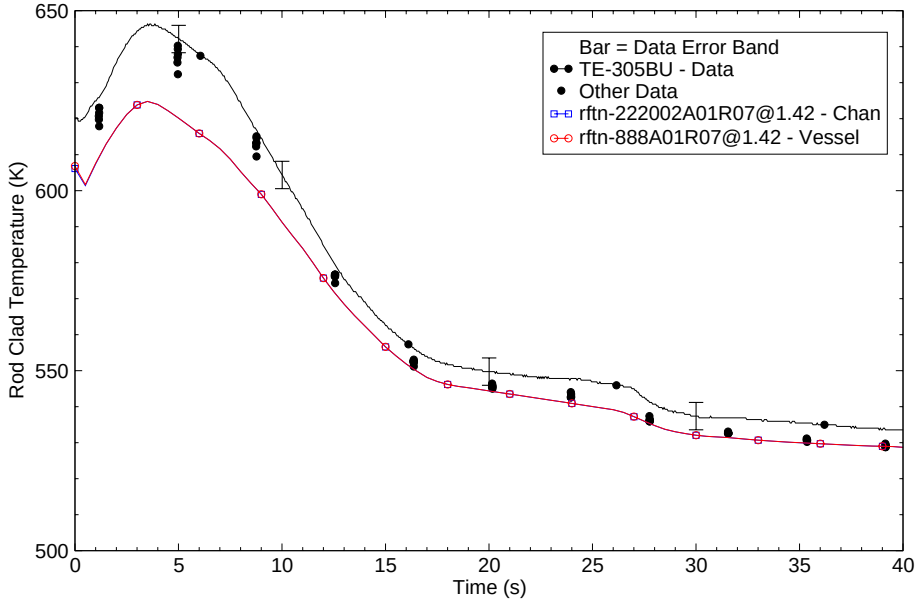

Figure B.6-13. Rod clad temperature at Level U (1.42 m) for Test 3036AR

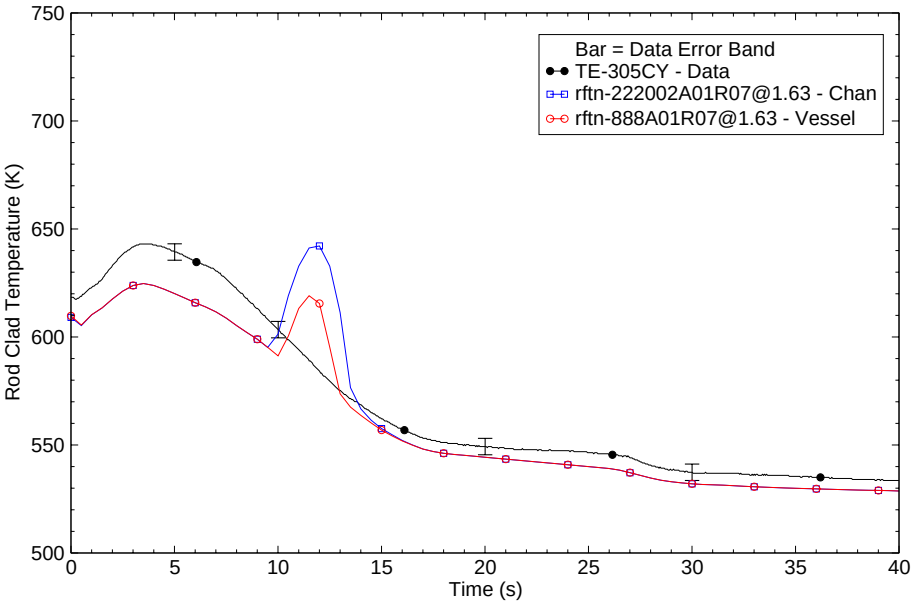

Figure B.6-14. Rod clad temperature at Level Y (1.63 m) for Test 3036AR

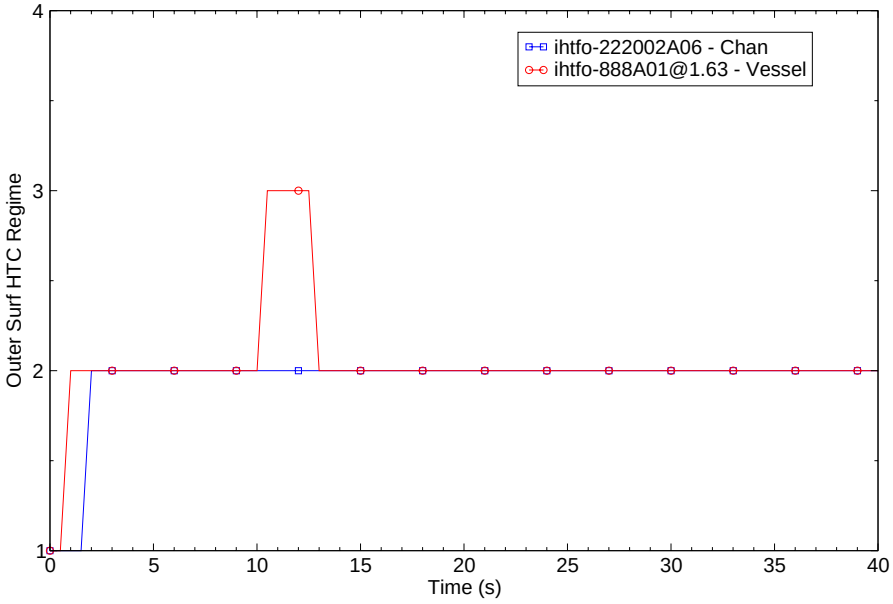

Figure B.6-15. Predicted heat transfer regime at level Y for Test 3036AR

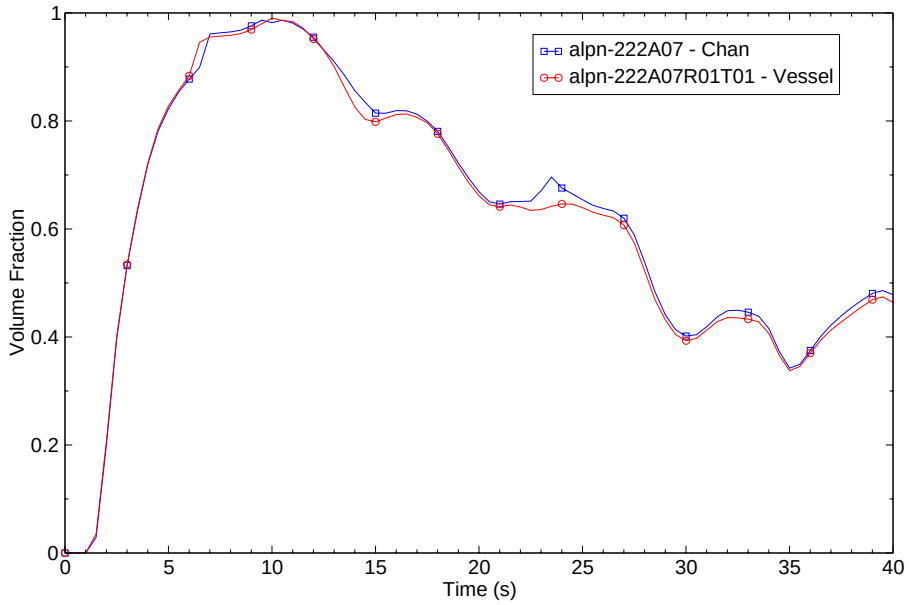

Figure B.6-16. Predicted void fraction at Level Y (1.63m) for Test 3036AR

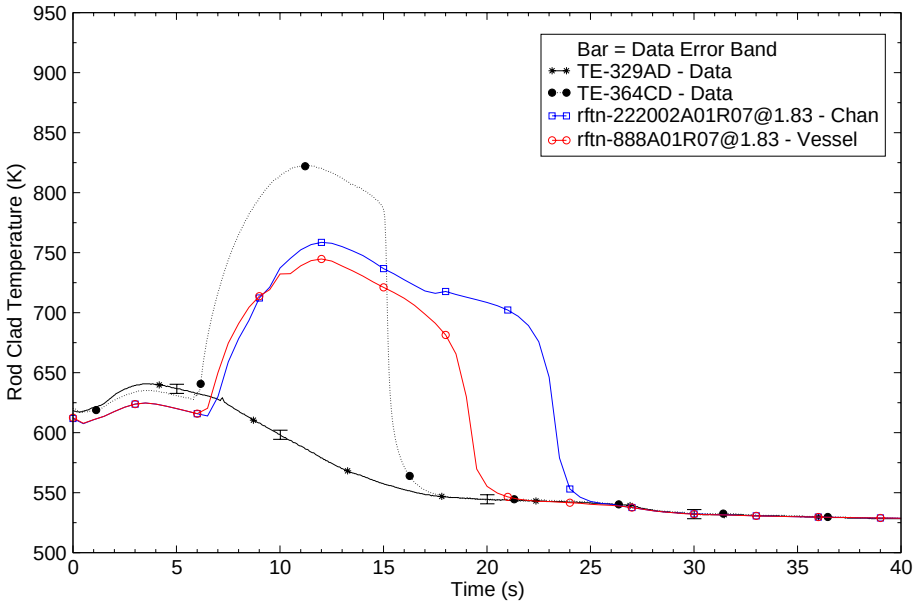

Figure B.6-17. Rod clad temperature at Level D (1.83 m) for Test 3036AR

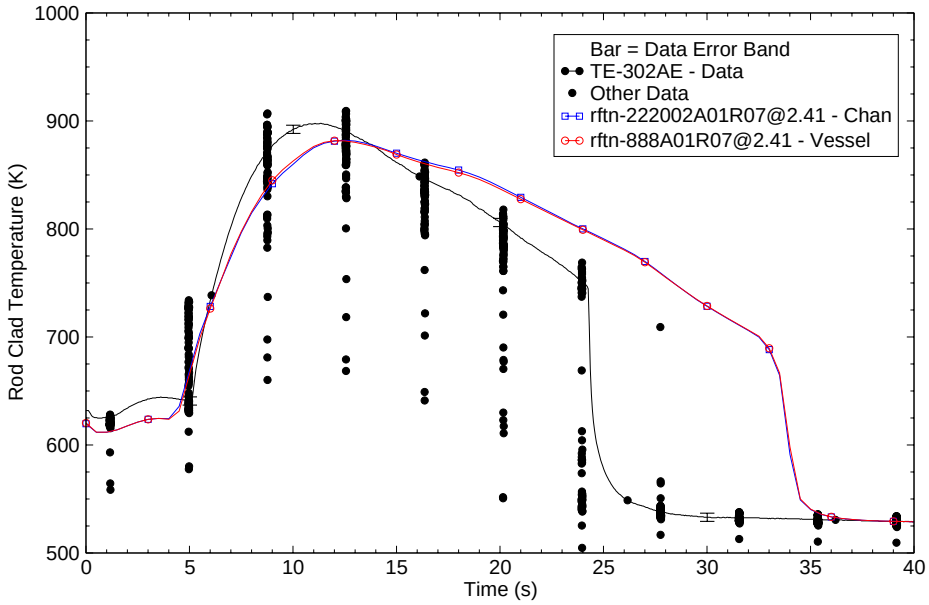

Figure B.6-18. Rod clad temperature at Level E (2.41 m) for Test 3036AR

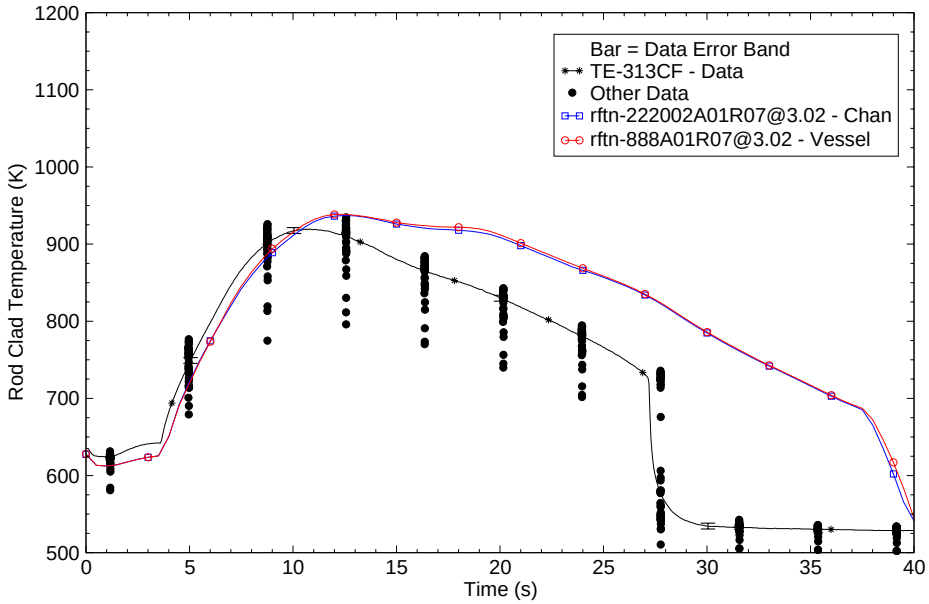

Figure B.6-19. Rod clad temperature at Level F (3.02 m) for Test 3036AR

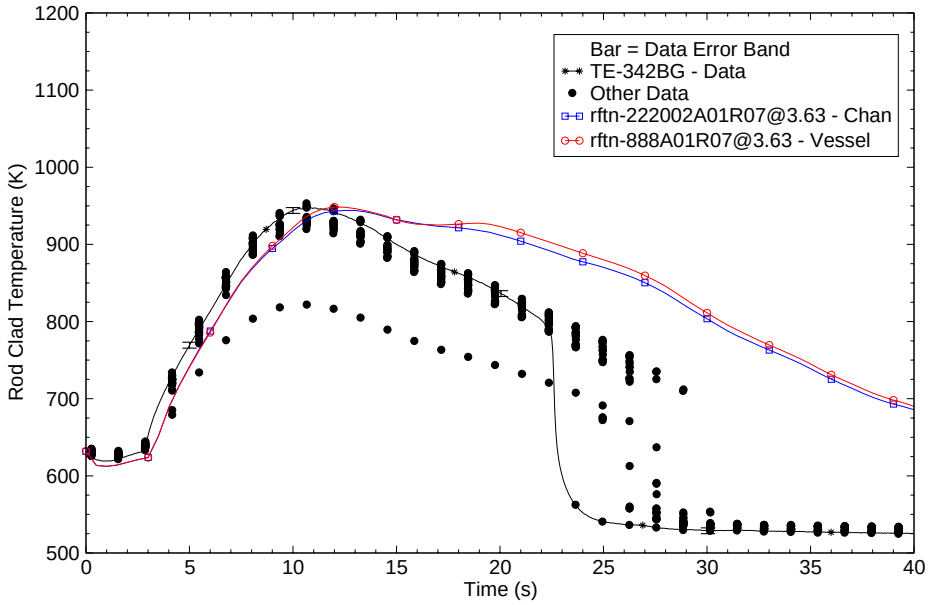

Figure B.6-20. Rod clad temperature at Level G (3.63 m) for Test 3036AR

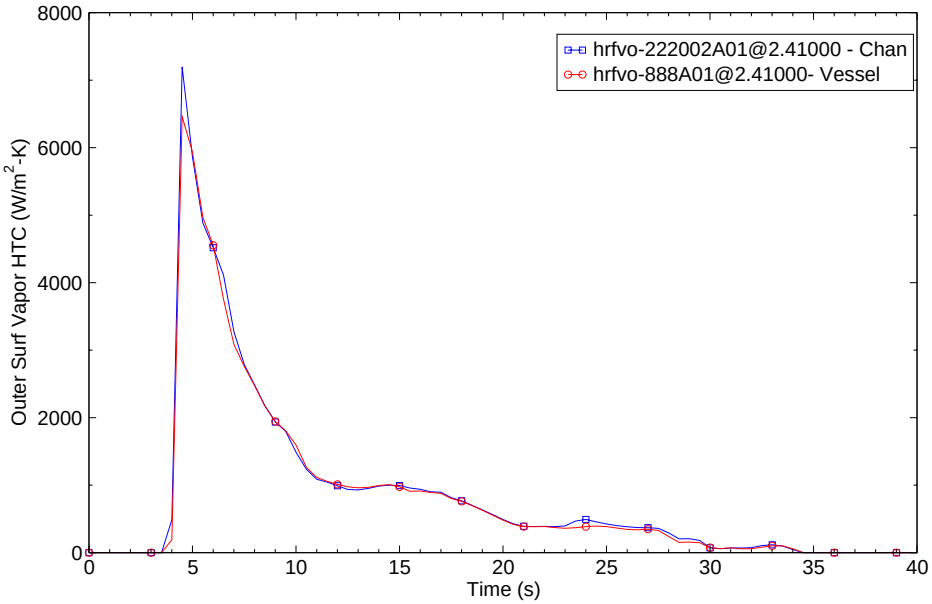

Figure B.6-21. .Predicted vapor HTC for Cell 8 (2.41 m) for Test 3036AR.

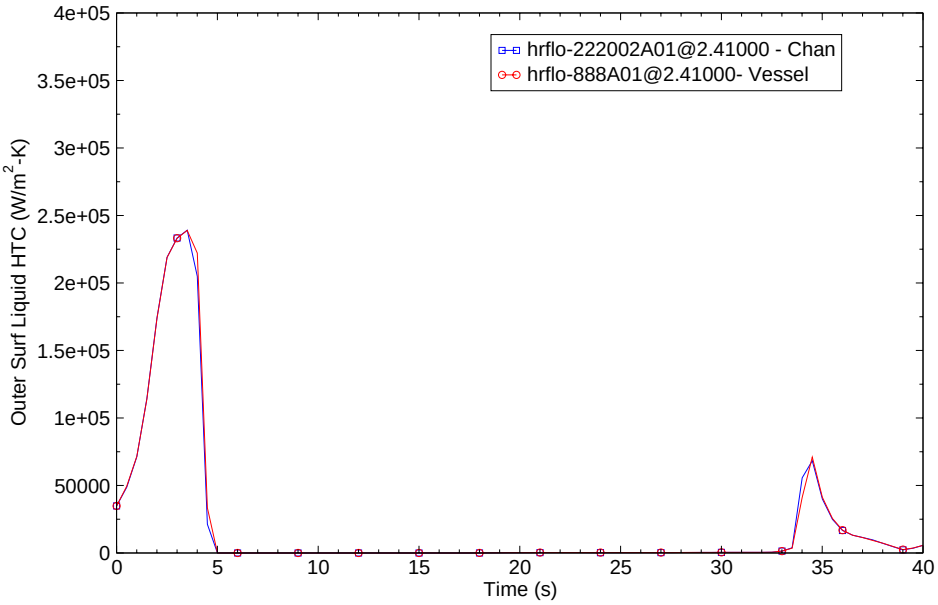

Figure B.6-22. Predicted Liquid HTC for Cell 8 (2.41 m) for Test 3036AR.

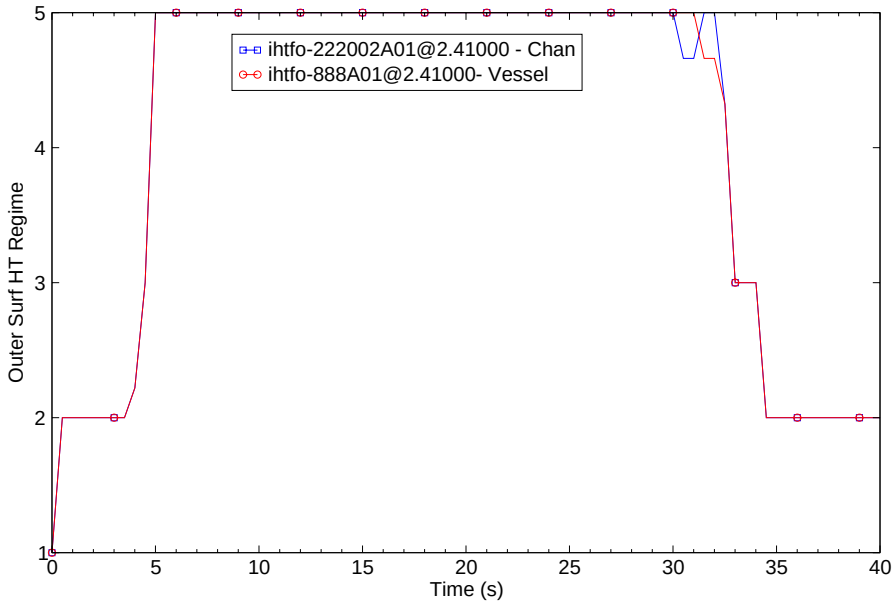

Figure B.6-23. Predicted heat transfer regime for Cell 8 (2.41 m) for Test 3036AR

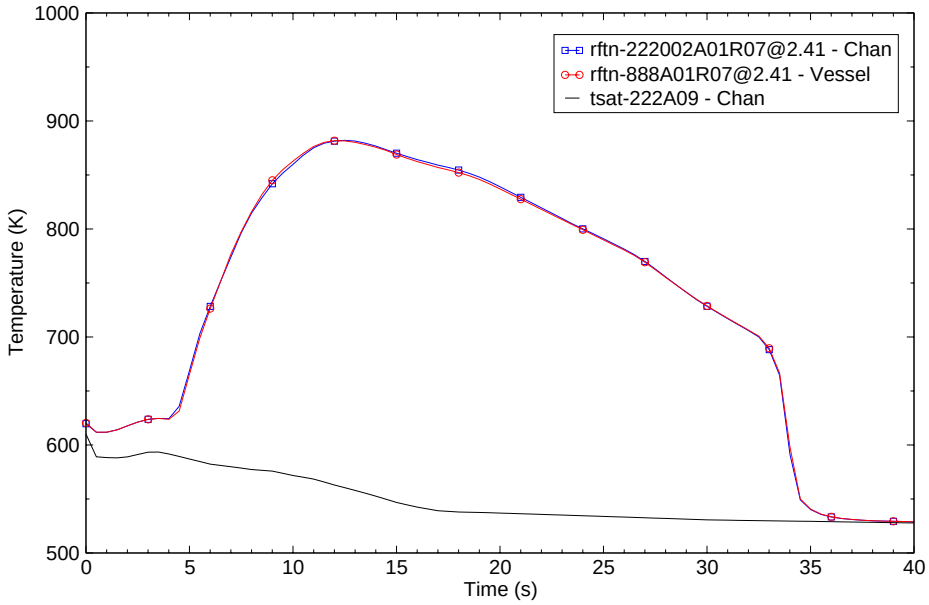

Figure B.6-24. Predicted rod outer surface temperature and saturation temperature at Cell 8 (2.41 m) for Test 3036AR.

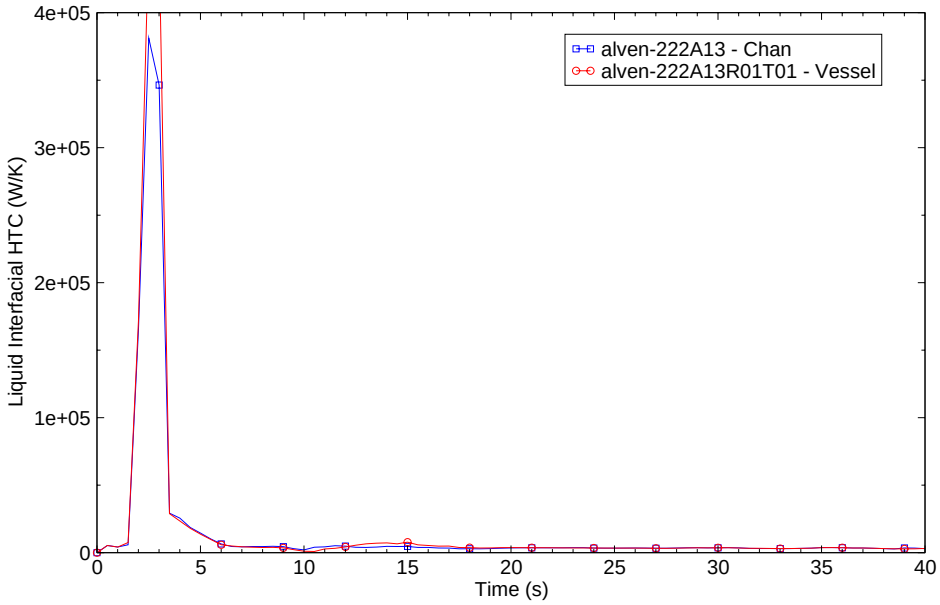

Figure B.6-25. Predicted liquid interfacial HTC at top of the heated bundle for Test 3036AR.

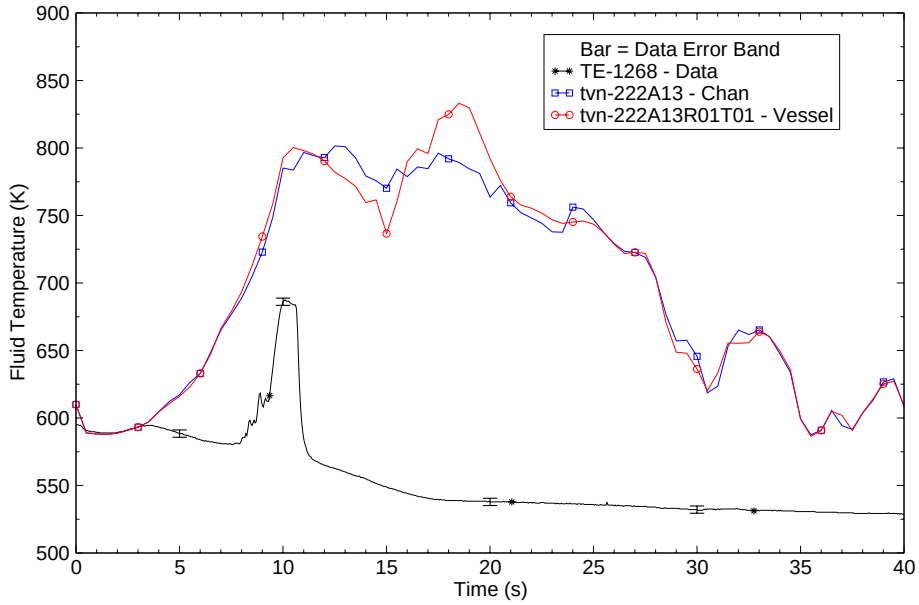

Figure B.6-26. Test Section exit steam temperatures for Test 3036AR.

A comparison of the predicted break mass flow rate with measured data is shown in Figure B.6-27. Generally, the predicted break mass flow rate compares reasonably with the data. At the beginning of the transient the break flow rate is under-predicted. However, after 5 seconds the predicted break flow rate becomes reasonable compared to the data. The integrated break flow rate comparison is shown in Figure B.6-28. Initially, the data shows more liquid leaving the system than the calculations. However, after 5 seconds the slope of the integrated mass flow rate curves are nearly parallel.

A discussion on the methods used to calculate mass flux at the THTF test section boundaries and the estimated uncertainties in those calculations is presented in Reference 3 through Reference 5. Mass flow error for steady-state two phase flow using turbine-meter and gamma densitometer measurements was reported to be 60% of the reading. The uncertainty of transient effects on two-phase flow was reported to be an extra 30-50% of reading for mass flow greater than 3.79 kg/s.

Rod clad temperature comparisons for Test 3.06.6B are shown in Figure B.6-29 through Figure B.6-35. The elevation/cell location at which the comparisons are made are the same as reported in section for Test 3.03.6AR.

DNB occurs at a much lower elevation in this test than in Test 3.03.6AR because of the lower power and inlet mass flow rate. Figure B.6-29 shows that some of the thermocouples at Level B are beginning to transition from nucleate to film boiling while code predicted nuclear boiling, which agrees to the most of the thermocouple reading. At Level U (Figure B.6-30) and above the rods have transitioned to film boiling. The time of DNB at each of the levels is well predicted by

two calculations. After transitioning to film boiling the predicted rod clad temperature from calculations matches the measured data reasonably well during the rod heatup portion of the transient at all levels.

At elevations greater than 1.42 m (Level U) the predicted rod clad temperatures are more typical of the predicted rod clad temperatures at Levels E, F, and G for Test 3.03.6AR (see Figure B.6-18 to Figure B.6-20). The peak clad temperature prediction are a little higher than the measured data. Quenching times at each levels are delayed and the cause is most likely due to the lack of grid spacer model in the current code version.

A comparison of the bundle region exit temperature is shown in Figure B.6-36. The steam probes for this test quench at 15 seconds. TRACE overpredicts the steam temperature measurement before 15 seconds and predicts superheat until 45 seconds.

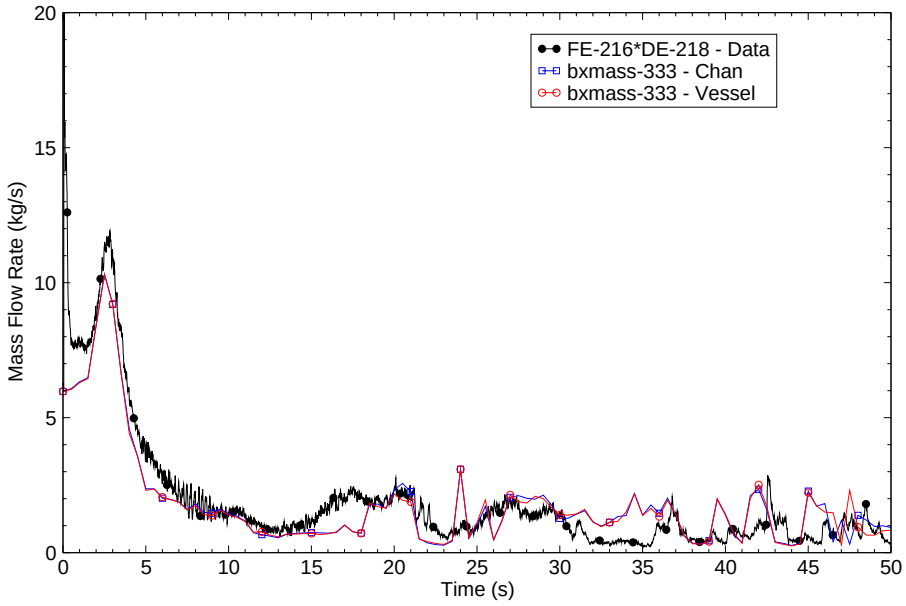

Figure B.6-27. Break mass flow rate for THTF Test 3.06.6B

B.6.4.3. Test 3.08.6C Simulation Results

The initial conditions for Test 3.08.6C are similar to Test 3.06.6B with the exception of the initial system pressure. Instead of 14.9 MPa, the initial pressure was 12.8 MPa. The test initial conditions for Test 3.08.6C are presented in Table B.6.2. Following the break of the rupture disk, bundle power was ramped from about 2.7 to about 7.8 MW over a period of 2 seconds. The bundle power was maintained at 7.5 to 7.6 MW for the next 18 seconds. At around 20 seconds the

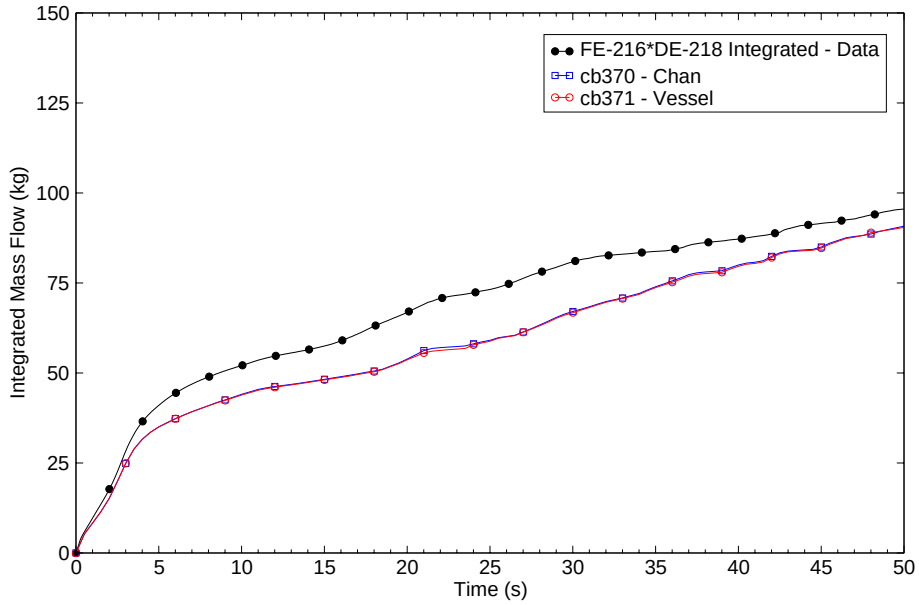

Figure B.6-28. Integrated outlet mass flow rate for THTF Test 3.06.6B

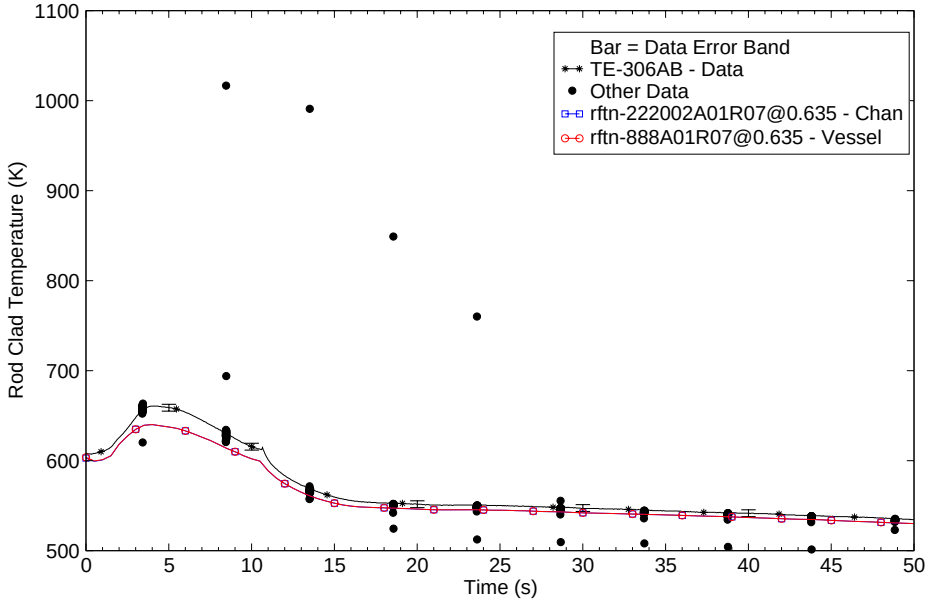

Figure B.6-29. Rod clad temperature at Level B (0.635 m) for THTF Test 3.06.6B

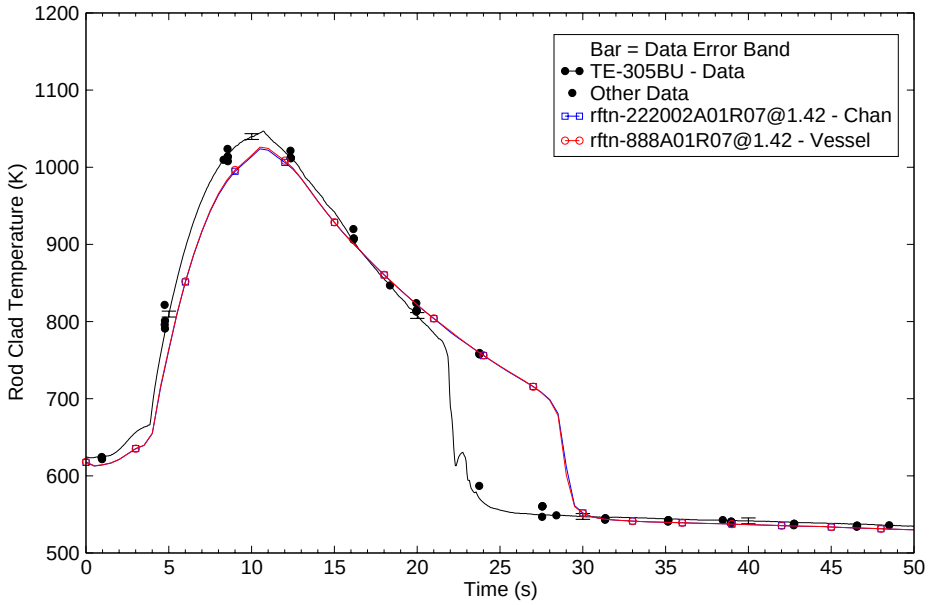

Figure B.6-30. Rod clad temperature at Level U (1.42 m) for THTF Test 3.06.6B

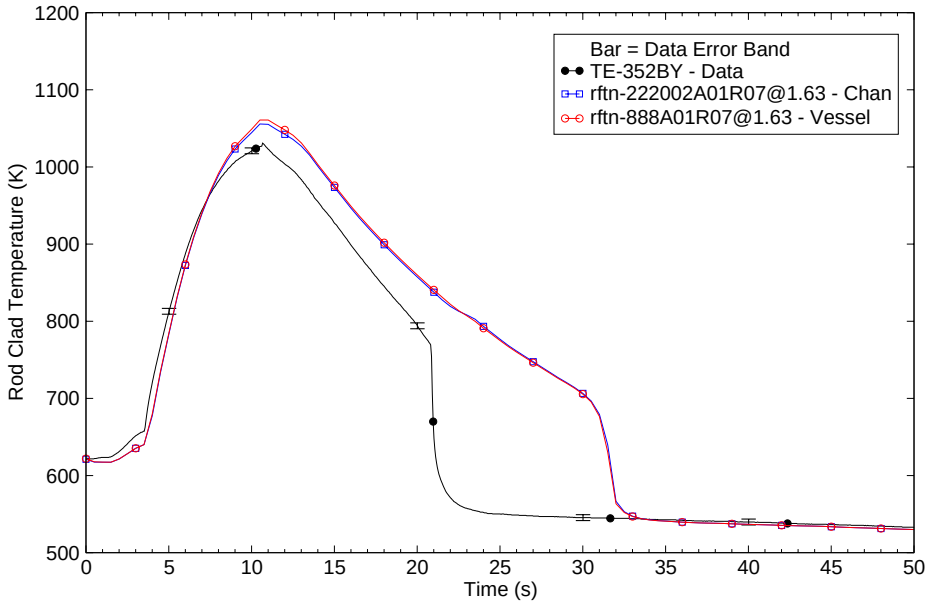

Figure B.6-31. Rod clad temperature at Level Y (1.63 m) for THTF Test 3.06.6B

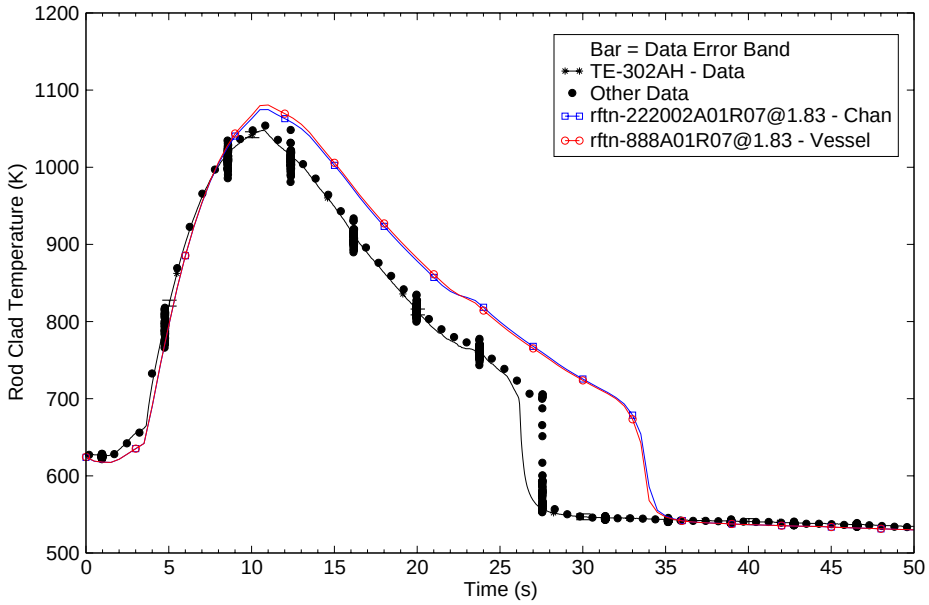

Figure B.6-32. Rod clad temperature at Level D (1.83 m) for THTF Test 3.06.6B

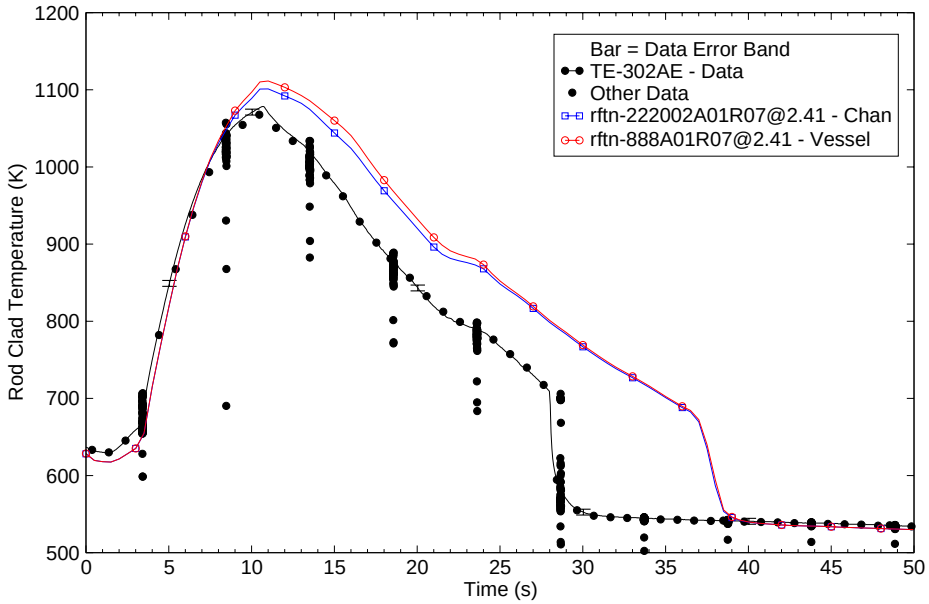

Figure B.6-33. Rod clad temperature at Level E (2.41 m) for THTF Test 3.06.6B

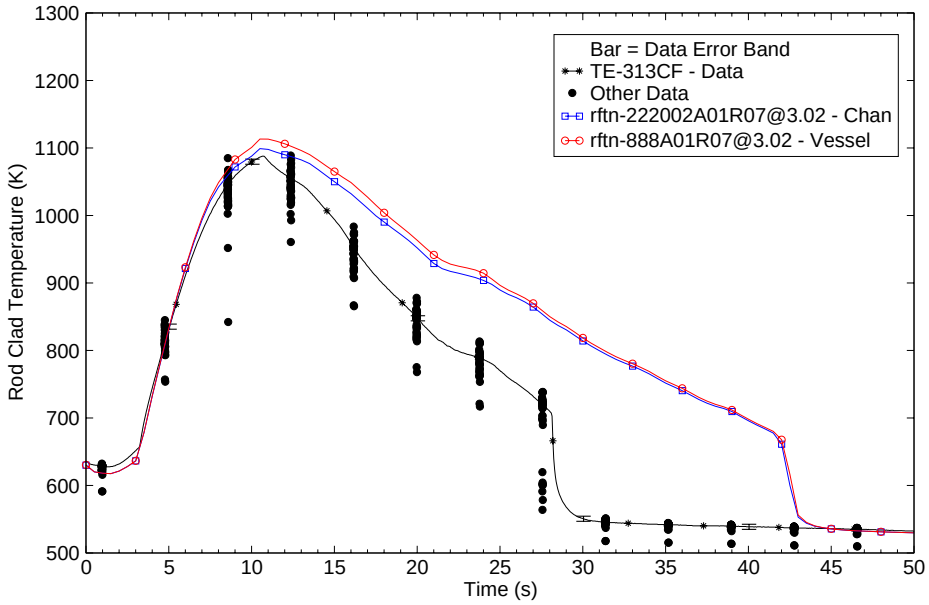

Figure B.6-34. Rod clad temperature at Level F (3.02 m) for THTF Test 3.06.6B

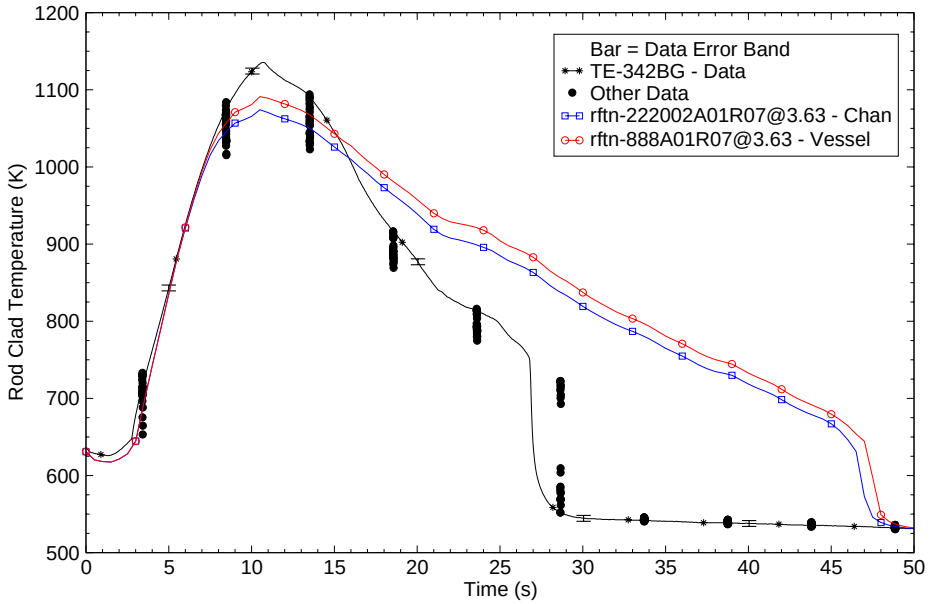

Figure B.6-35. Rod clad temperature at Level G (3.63 m) for THTF Test 3.06.6B

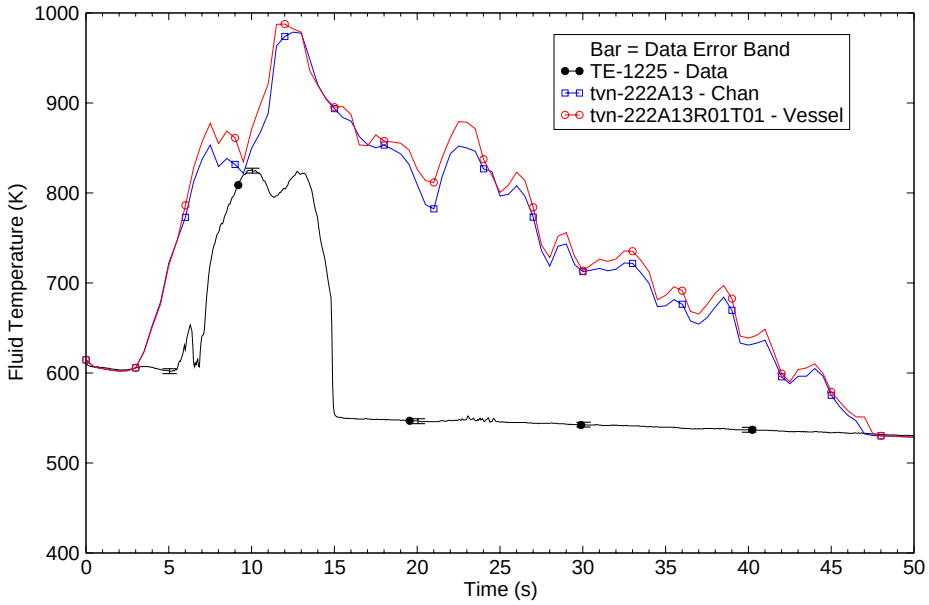

Figure B.6-36. Heat bundle exit steam temperature for THTF Test 3.06.6B

power was reduced to approximately 3.3 MW over a 4 second time period. The power remained at about 3.3 MW up to 36 second before a power trip. The power history for this test is shown in Figure B.6-37.

A comparison of the measured and predicted break mass flow rate is shown in Figure B.6-38. The predicted break mass flow rate compares well with the measured data. Figure B.6-39 shows excellent comparisons with the integrated break mass flow rates.A discussion on the methods used to calculate mass flux at the THTF test section boundaries and the estimated uncertainties in those calculations is presented in Reference 3 through Reference 5. Mass flow error for steady-state two phase flow using turbine-meter and gamma densitometer measurements was reported to be 60% of the reading. The uncertainty of transient effects on two-phase flow was reported to be an extra 30-50% of reading for mass flow greater than 3.79 kg/s.

The predicted rod clad temperatures are compared to data in Figure B.6-40 through Figure B.6-46. The measured rod clad temperatures indicate only the upper part of the bundle underwent departure from nucleate boiling. The thermocouples at Level D indicate only a few of the rods in the bundle underwent DNB. At levels below Y the rods remained in nucleate boiling.

At Levels B and U (Figure B.6-40 and Figure B.6-41), CHAN and VESSEL simulations under-predicted the rod clad temperature during the first 40 seconds of the transient. The initial rod temperature condition at these locations are comparable to the test data. The code may be predicting a higher liquid heat transfer coefficient. After the power was tripped at about 36 seconds simulations predict the clad temperature well.

At Level Y (1.63 m) (Figure B.6-42), the data showed a brief DNB period between 30 seconds to 38 seconds and the code predicted the on set of DNB and peak temperature very well. However, the code over predicts the rod temperature after the rod reached the peak temperature.

At Level D (1.83 m) (Figure B.6-43), some data showed early dry out starting around 4 seconds and some data showed nuclear boiling until heat up around 30 seconds. The code predicts nuclear boiling with lower temperature compared to the data for the first 30 seconds. At 30 seconds, the calculations predict rod temperature rising well. Similar to the other locations, the code predicted slow cooling beyond the peak temperature. From 45 seconds to the end of the transition, the power is tripped off and the code predict rod temperature reasonably.

At Levels E and F (Figure B.6-44 and Figure B.6-45), where the measured rod clad temperatures indicate film boiling, the predicted rod clad temperatures are typical of those predicted in Tests 3.03.6AR and 3.06.6B. The predictions fall within the scatted data except a slow cooling around the time for quenching.

At Level G (3.63 m) (Figure B.6-46), the code underpredicts the rod temperature.

The vapor temperature data showed oscillations and that may due to the condensation on the thermocouples. The code predict the a few ups and downs as well and predict the peak temperature of the steam reasonably as shown in Figure B.6-47.

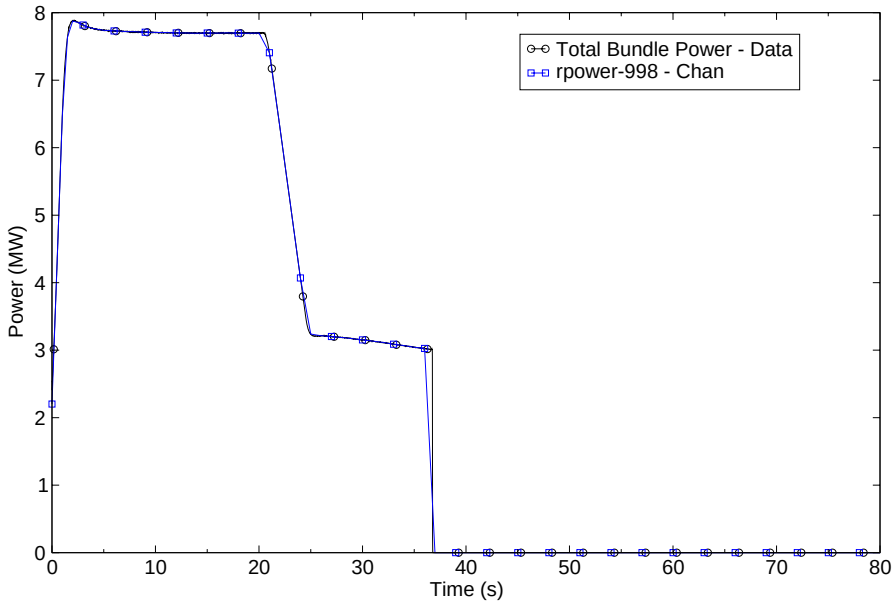

Figure B.6-37. Rod bundle power history for THTF Test 3.08.6C.

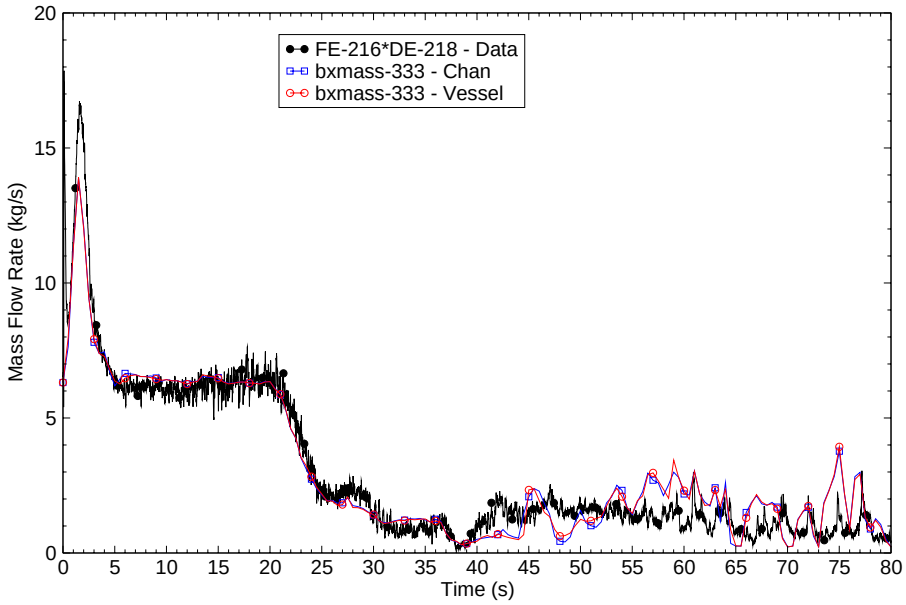

Figure B.6-38. Break mass flow rate comparison for THTF Test 3.08.6C.

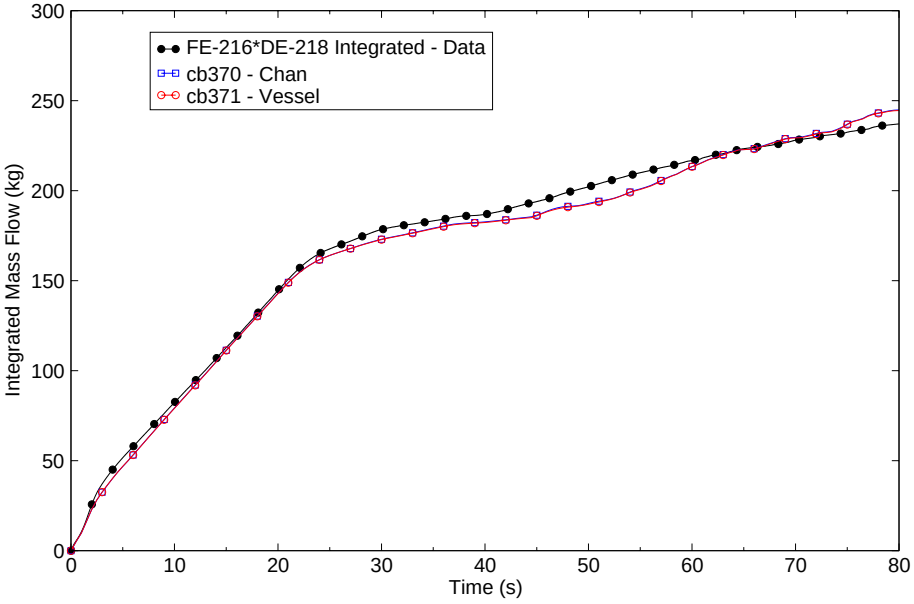

Figure B.6-39. Integrated outlet mass flow rate comparison for THTF Test 3.08.6C.

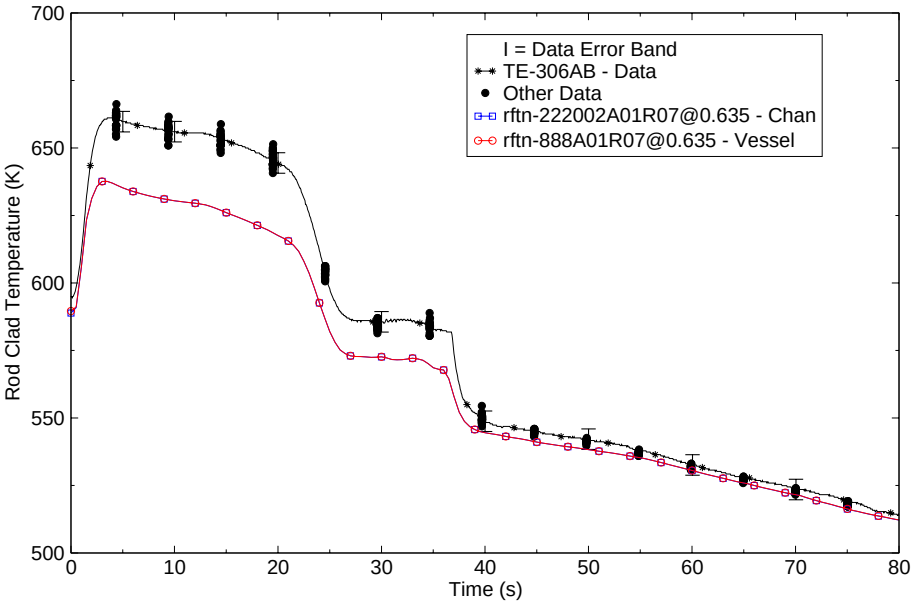

Figure B.6-40. Rod clad temperature comparison at Level B (0.635 m) for THTF Test 3.08.6C.

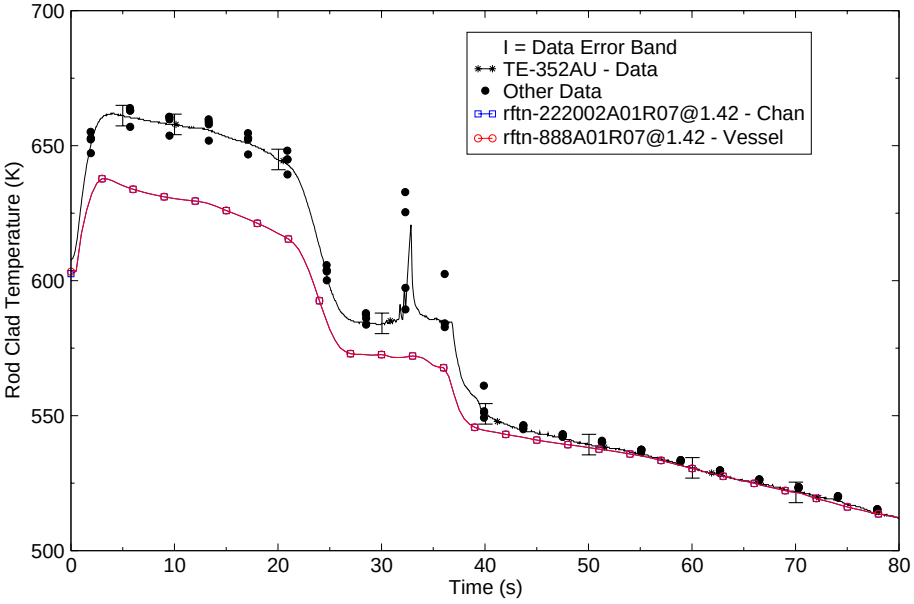

Figure B.6-41. Rod clad temperature comparison at Level U (1.42 m) for THTF Test 3.08.6C.

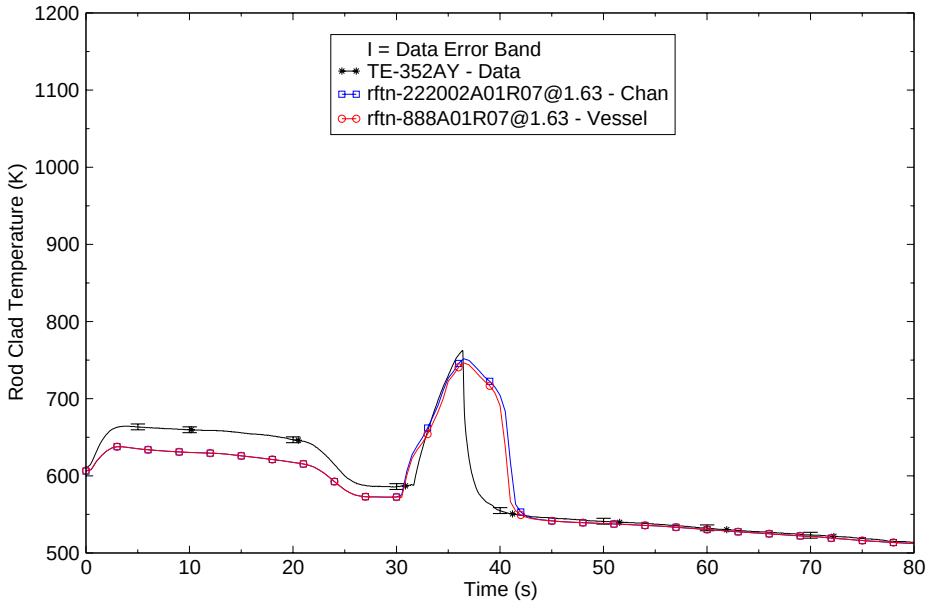

Figure B.6-42. Rod clad temperature comparison at Level Y (1.63 m) for THTF Test 3.08.6C.

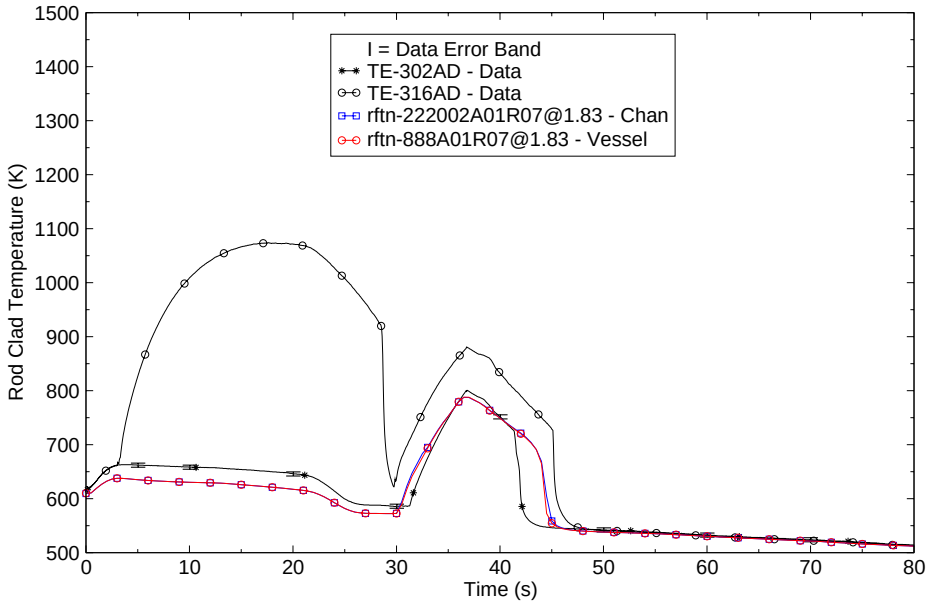

Figure B.6-43. Rod clad temperature comparison at Level D (1.83 m) for THTF Test 3.08.6C.

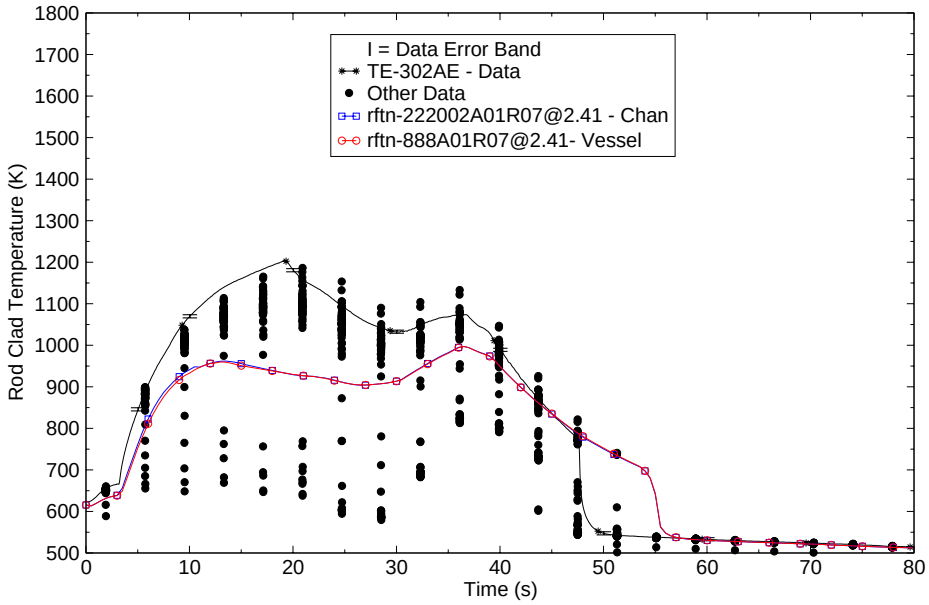

Figure B.6-44. Rod clad temperature comparison at Level E (2.41 m) for THTF Test 3.08.6C.

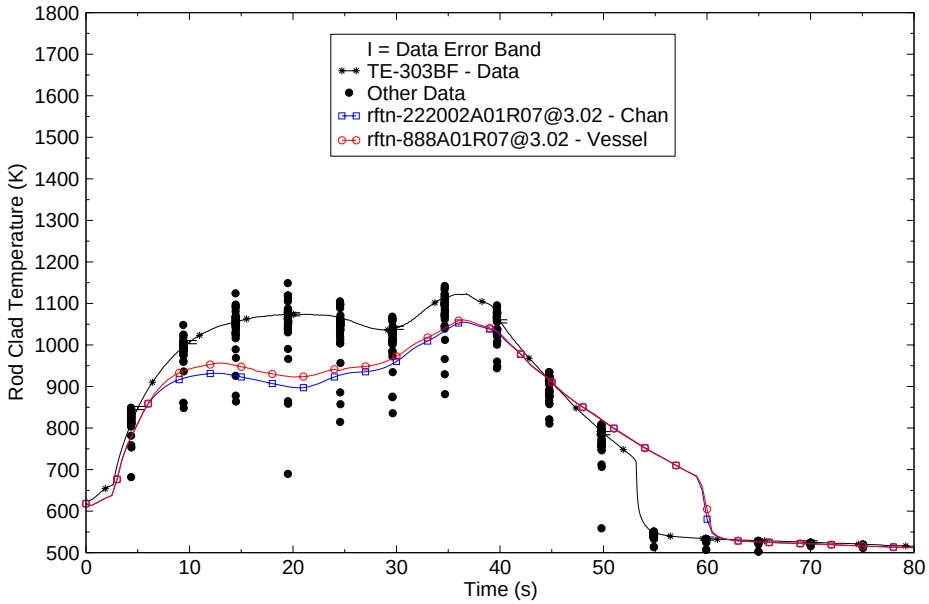

Figure B.6-45. Rod clad temperature comparison at Level F (3.02 m) for THTF Test 3.08.6C.

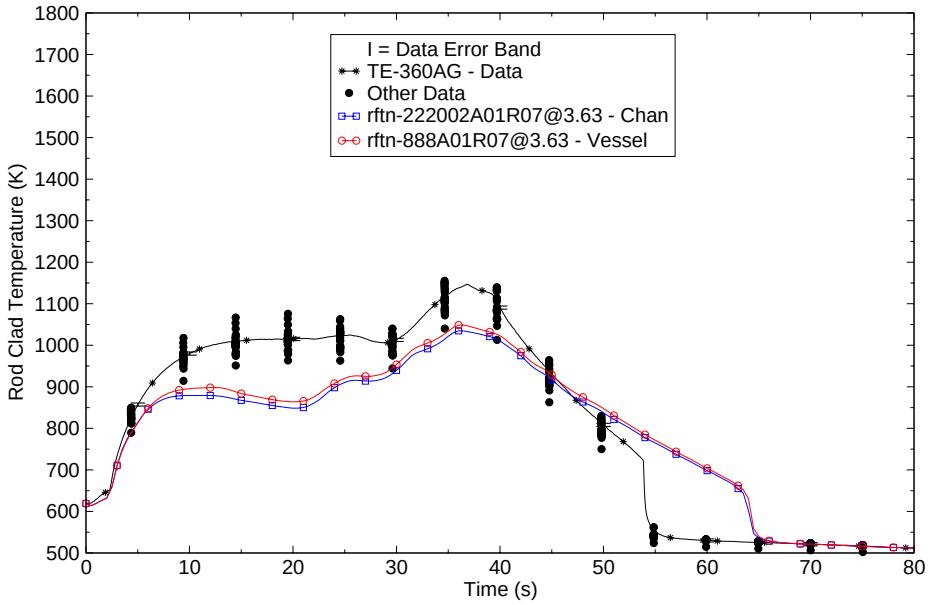

Figure B.6-46. Rod clad temperature comparison at Level G (3.63 m) for THTF Test 3.08.6C.

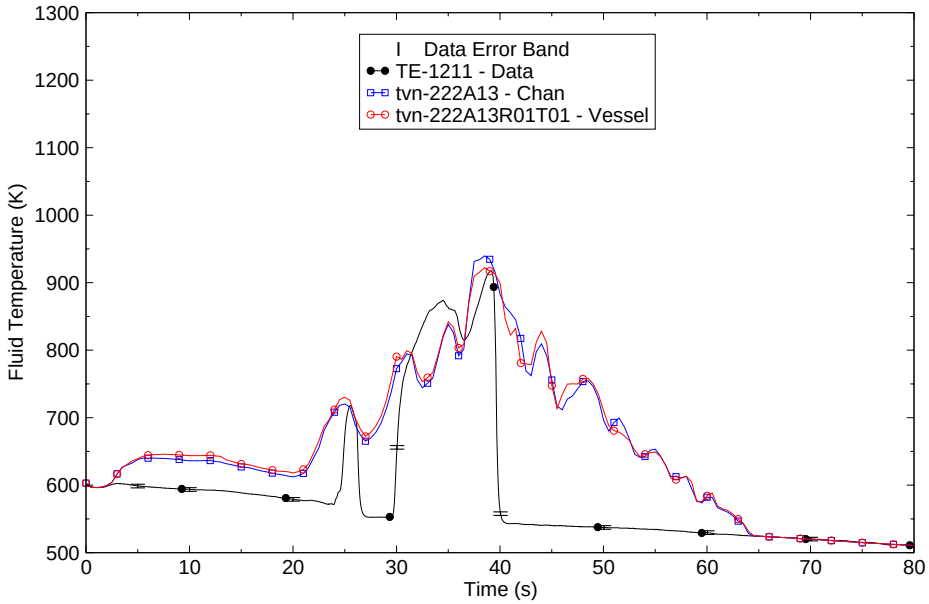

Figure B.6-47. Exit steam temperature for THTF Test 3.08.6C

B.6.5. Conclusions

TRACE predicts time of the film boiling onset and rod clad temperatures reasonably well in THTF transition calculations. The code also predicts rod cladding temperature well before the rod reaching the peak temperature. Table B.6.3 summarizes the peak clad temperature for each of the transients simulated. Peak clad temperatures summarized here are at rod bundle Levels E, F, and G and they are the maximum reading of the ensemble of thermal-couples at an elevation. The code overpredicted rod temperature after the rod temperature peaking and before quenching. This also resulted a delayed quenching time. Lack of a grid spacer model in the TRACE code contributes to inadequate cooling. CHAN and VESSEL models produced comparable results with minor differences. One reason for the differences is that a different wall friction model was used for CHAN and VESSEL components in dry out region.

Table B.6.3. Peak clad temperatures for the THTF transient simulations.

Test	Level (m)	Peak Clad Temperature (K)		
		Measured	CHAN Model	VESSEL Model
3.03.6AR	E (2.41)	897	882	881
	F (3.02)	919	938	939
	G (3.63)	946	941	943
3.06.6B	E (2.41)	1076	1102	1111
	F (3.02)	1086	1101	1113
	G (3.63)	1134	1075	1089
3.08.6C	E (2.41)	1202	996	995
	F (3.02)	1121	1054	1059
	G (3.63)	1144	1027	1036

B.6.6. References

1 D. K. Felde, et. al., “Facility Description - THTF MOD 3 ORNL PWR BDHT Separate-Effects Program”, ORNL/TM-7842, October 1982.

2 Weidong Wang, THTF Transient Blowdown Assessment Report for TRACE v. 4.269, ML061790151.

3 C. B. Mullins, et. al., "ORNL Rod Bundle Heat Transfer Test Data - Volume 2. Thermal-Hydraulic Test Facility Experimental Data Report for Test 3.03.6AR - Transient Film Boiling in Upflow", NUREG/CR-2525, Vol. 2, ORNL/NUREG/TM-407/V2, April 1982.

4 C. B. Mullins, et. al., "ORNL Rod Bundle Heat Transfer Test Data - Volume 3. Thermal-Hydraulic Test Facility Experimental Data Report for Test 3.06.6B - Transient Film Boiling in Upflow", NUREG/CR-2525, Vol. 3, ORNL/NUREG/TM-407/V3, May 1982.

5 C. B. Mullins, et. al., "ORNL Rod Bundle Heat Transfer Test Data - Volume 5. Thermal-Hydraulic Test Facility Experimental Data Report for Test 3.08.6C - Transient Film Boiling in Upflow", NUREG/CR-2525, Vol. 5, ORNL/NUREG/TM-407/V5, May 1982.

6 C. B. Mullins, et. al., "ORNL Rod Bundle Heat Transfer Test Data - Volume 7. Thermal-Hydraulic Test Facility Experimental Data Report for Test Series 3.07.9 - Steady-state Film Boiling in Upflow", NUREG/CR-2525, Vol. 7, ORNL/NUREG/TM-407/V7, May 1982.

7 G. L. Yoder, et. al., "Dispersed Flow Film Boiling in Rod Bundle Geometry - Steady-State Heat Transfer Data and Correlation Comparisons", NUREG/CR-2435, ORNL-5822, March 1982.

8 D. G. Thomas, "PWR-Blowdown Heat Transfer Separate Effects Program", Fourth Water Reactor Safety Research Information Meeting September 27-30, 1976.

Reflood Heat Transfer Tests

B.7. FLECHT-SEASET

Author(s): Gene Rhee[*] and Jae-Hoon Jeong[**]

Affiliation: U. S. NRC[*] and Korea Nuclear Fuel Co. Ltd.[**]

Code Version: TRACE V5.0

Platform and Operating System: Intel x86, Windows XP

B.7.1. Introduction

The FLECHT-SEASET (Full-Length Emergency Core Heat Transfer - Separate Effects And System Effects Test) data represent important data sources for reflood tests, even though the data were obtained over 30 years ago as a joint project among the NRC, the Electric Power Research Institute (EPRI), and Westinghouse Corp. (W), because the test facility was large and well instrumented and the tests were run at high temperatures exceeding the licensing limit of 1204 °C (2200 °F) in some cases. The ability of predicting the consequences of large-break (LB) loss-of-coolant-accidents (LOCAs), particularly the consequential reflood phase, is important to TRACE, as in any other thermal hydraulic codes, since the LB LOCA usually determines the reactor power design parameters and the maximum operation power level. Eight forced-feed reflood tests are selected to assess the capability of TRACE in predicting the reflood progression.

B.7.2. Test Facility Description

The FLECHT-SEASET Facility (Ref. 1) was constructed mainly for reflood experiments. The heater rod bundle contained 177 rods which consisted of 161 heater rods and 16 thimble rods. The 177 rods were placed in a cylinder of 0.194 m (7.625 in) diameter with a square lattice array similar to the 17x17 Westinghouse fuel bundle design. The heated part was 3.66 m (12 ft) long. Of the 161 heater rods, 68 rods were instrumented while the remaining 93 rods were not instrumented. The total power that could be provided to the rods was about 850 KW. The thimble rods were hollow and not heated, and four of them were instrumented. The bundle also contained 8 spacer grids, 12 steam probes, and 8 solid triangular fillers which were used to reduce the excess flow area near the housing wall. The facility layout is shown in Figure B.7-1, and the cross-sectional view of the bundle in Figure B.7-2 The test facility consisted of the following major components:

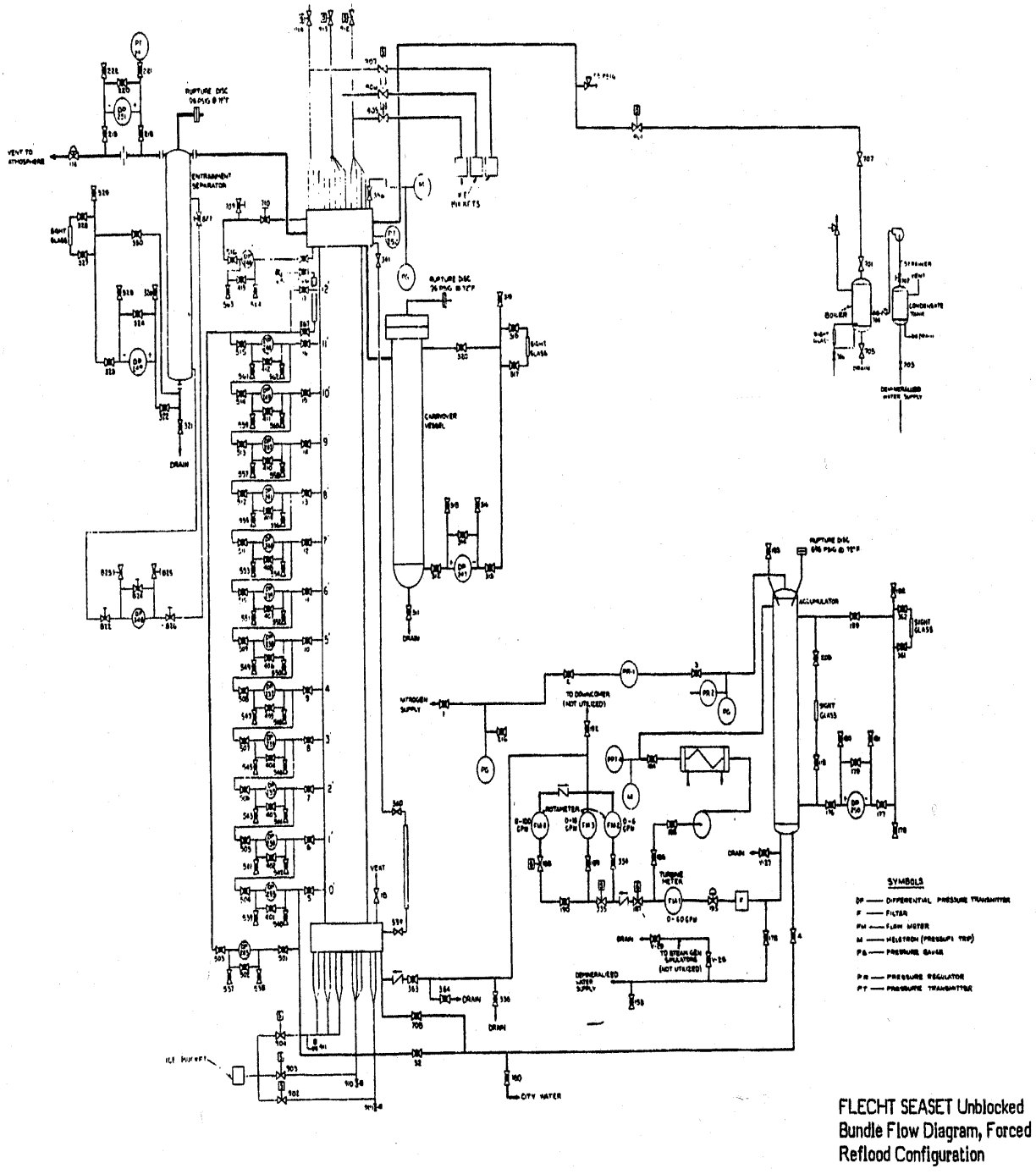

Figure B.7-1 FLECHT-SEASET Facility Flow Diagram for Forced Reflood Tests

- Cylindrical test section consisting of a lower plenum, low-mass housing containing the heater rod bundle, and an upper plenum,

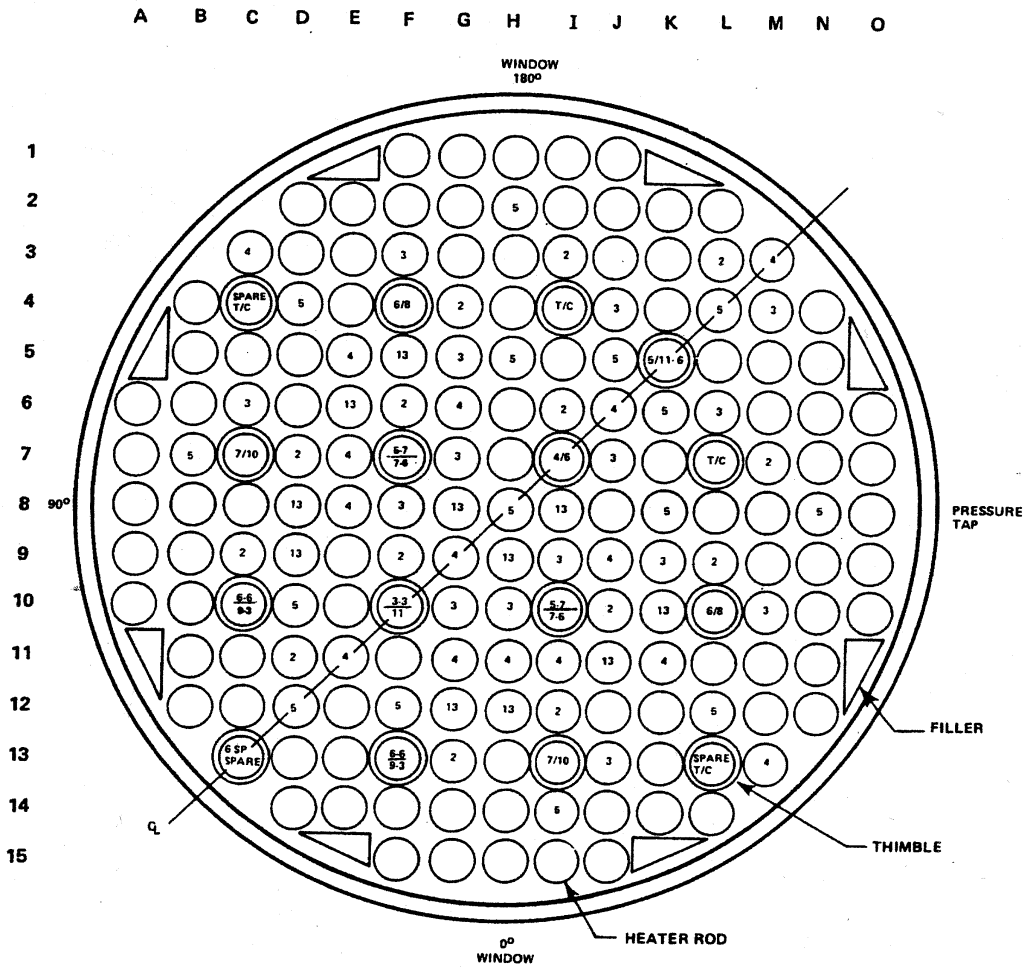

Figure B.7-2 Cross-sectional View of FLECHT-SEASET Bundle Heated Section

- Cooling water injection system,
-Entrained liquid separation tank,

-Carry-over liquid collection tank,

-External pipe downcomer, and

-Steam boiler for back-pressure control to get the desired bundle pressure.

The low-mass housing was designed to minimize the wall effects so that the rods one row or more away from the housing wall would be representative of a PWR (pressurized water reactor) core. An external pipe downcomer was connected to the bundle housing lower plenum for the gravity reflood tests. However, the downcomer was not used for the forced reflood tests which are used for the TRACE assessment described in this section.

The fuel rods were simulated with electrically heated rods. To preserve proper thermal scaling of the facility with respect to a PWR, the power-to-flow-area ratio, which was equivalent to power-to-volume ratio since the full height of the core was used, was nearly the same as that of a PWR fuel assembly. The heater rods were heated with a Kanthal heater coil which was imbedded in boron nitride encased with stainless steel cladding. Heater rod clad temperatures were measured by placing Type K (chromel-alumel) thermocouples at the inner surface of the stainless steel cladding. The heater rod had the outside diameter of 9.5 mm (0.374 inch), the wall thickness of 0.64 mm (0.025 inch), and the heated length of 3.66 m (12 ft), as shown in Figure B.7-3 A rod-to-rod pitch was 12.6 mm (0.496 inch). Each rod had a cosine axial power profile as shown in Figure B.7-4 The radial power distribution was uniform.

The test bundle was pre-heated to the desired pressure and temperature with dry steam, and then cooling water was delivered to the lower plenum of the bundle by a gas-charged accumulator for the forced reflood tests to quench the rods, simulating the reflood process.

The upper plenum was expanded to a diameter bigger than the heated section, and the heated section housing wall was extended into the upper plenum by about 0.15 m to prevent the de-entrained liquid from falling back into the heated section and to collect the liquid and drain it to a collection tank. The two-phase flow mixture exiting the bundle heated section was directed to move upward, outward, downward, and then upward again in the upper plenum to separate most of the liquid from the mixture, and subsequently the remainder was led to an exhaust pipe which was connected to a steam/water separator. The separator was designed to remove any remaining water droplets exiting the bundle so that a single-phase steam flow could be measured using an orifice positioned downstream of the separator.

The instrumentation of the FLECHT-SEASET Facility was extensive, including 205 heater rod thermocouples, 12 differential pressure cells positioned 0.3048 m (1 ft.) apart along the axial direction of the heated section, 12 steam probes, and inlet and outlet flow meters.

A FLECHT-SEASET data report (Ref. 1) indicates that the measurement uncertainties are as follows:

Temperature 1.39 °C (2.51 °F) for 277 °C (530 °F) > T

$\sqrt{(1.539 + (0.00217T)^2)}$ for 277 °C < T < 1316 °C (2400 °F)

(For T = 1000 °C (1832 °F), the uncertainty is 2.5 °C (4.5 °F))

Pressure 2.66 kPa (0.386 psi)

Power 2.14 kW

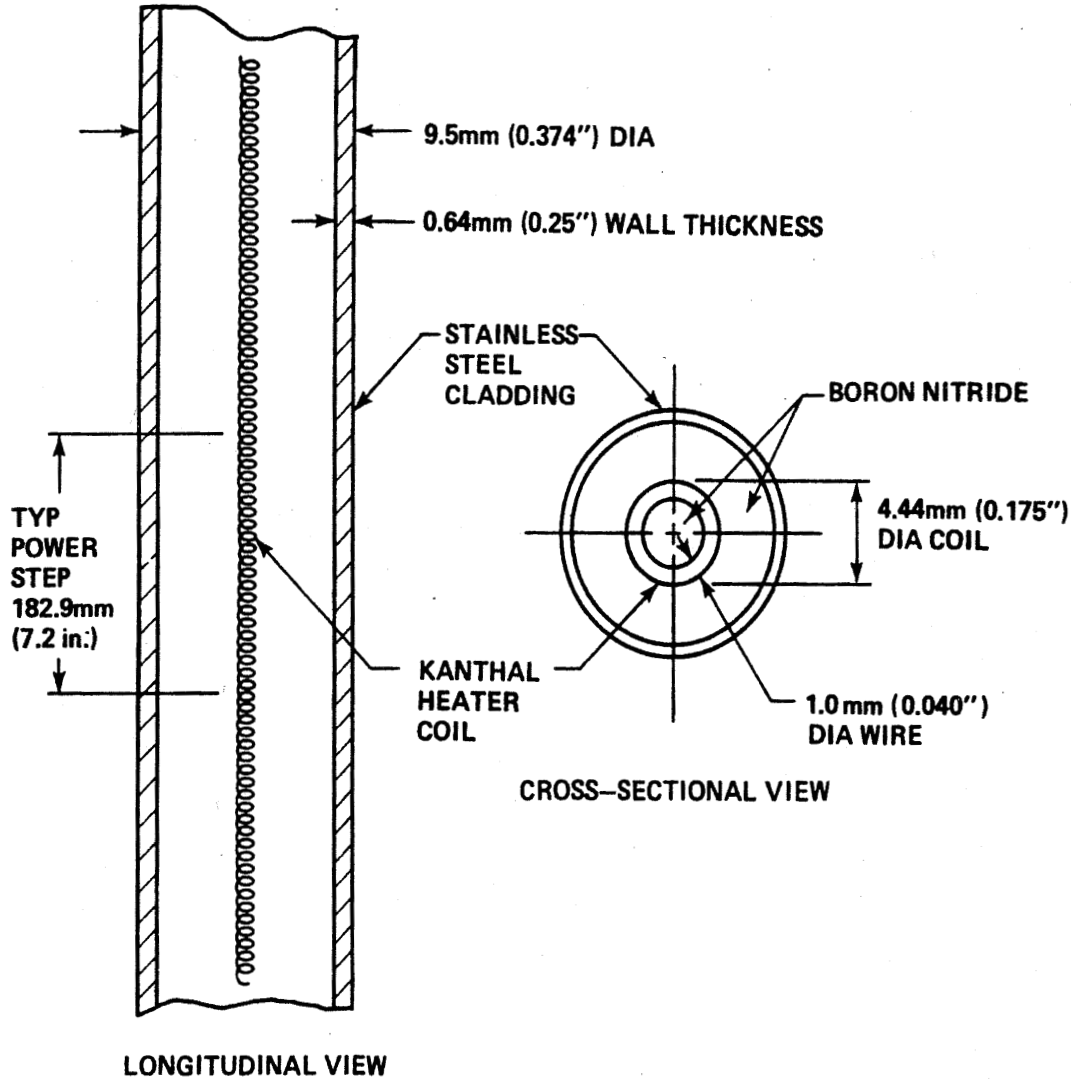

Figure B.7-3 Heater Rod Schematic Diagram

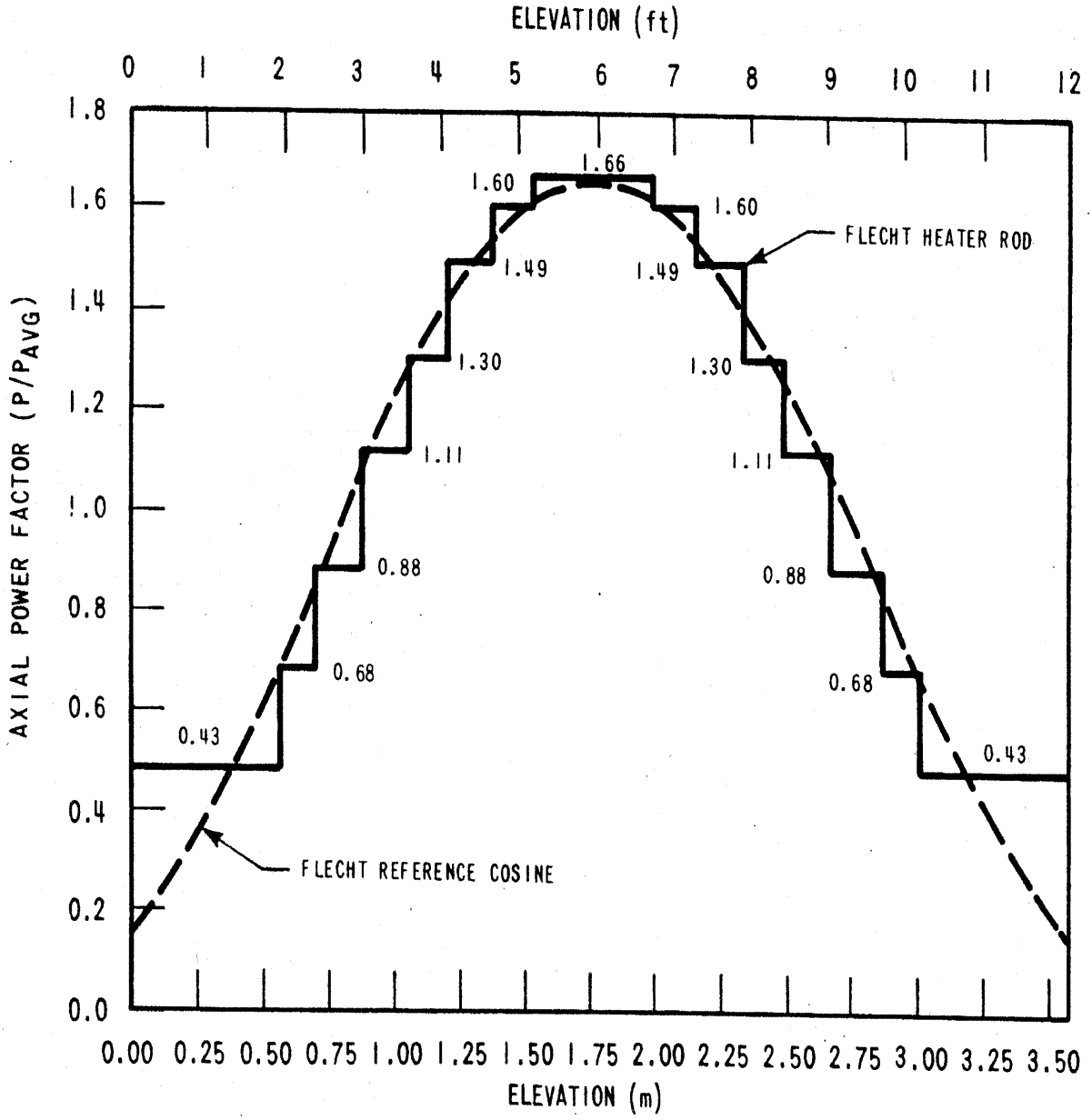

Figure B.7-4 Axial Power Profile of Heater Rods

B.7.3. TRACE Model Description

The FLECHT-SEASET Facility is modeled for TRACE calculations to the extent necessary for simulating the reflood process in the bundle test section. Thus the coolant injection system and the bundle flow exhaust system are greatly simplified. The Facility is represented with 5 fluid components, as shown in Figure B.7-5; FILL (Component 1), inlet PIPE (Component 2),

VESSEL (Component 5), outlet PIPE (Component 3), and BREAK (Component 4). The measured inlet flow rates and temperatures are set in the FILL component as a function of time, and the measured upper plenum pressure is set in the BREAK component as a function of time.

The VESSEL component is modeled in one dimension along the axial direction because the radial and azimuthal directions can be considered as uniform. The entire 161 heated rods are represented by a single heat structure (HTSTR, Component 6) while the bundle housing wall is represented by another heat structure (HTSTR, Component 7). The VESSEL component is divided into 16 nodes; one node for the lower plenum, one node for the upper plenum, and 14 nodes for the heated section.

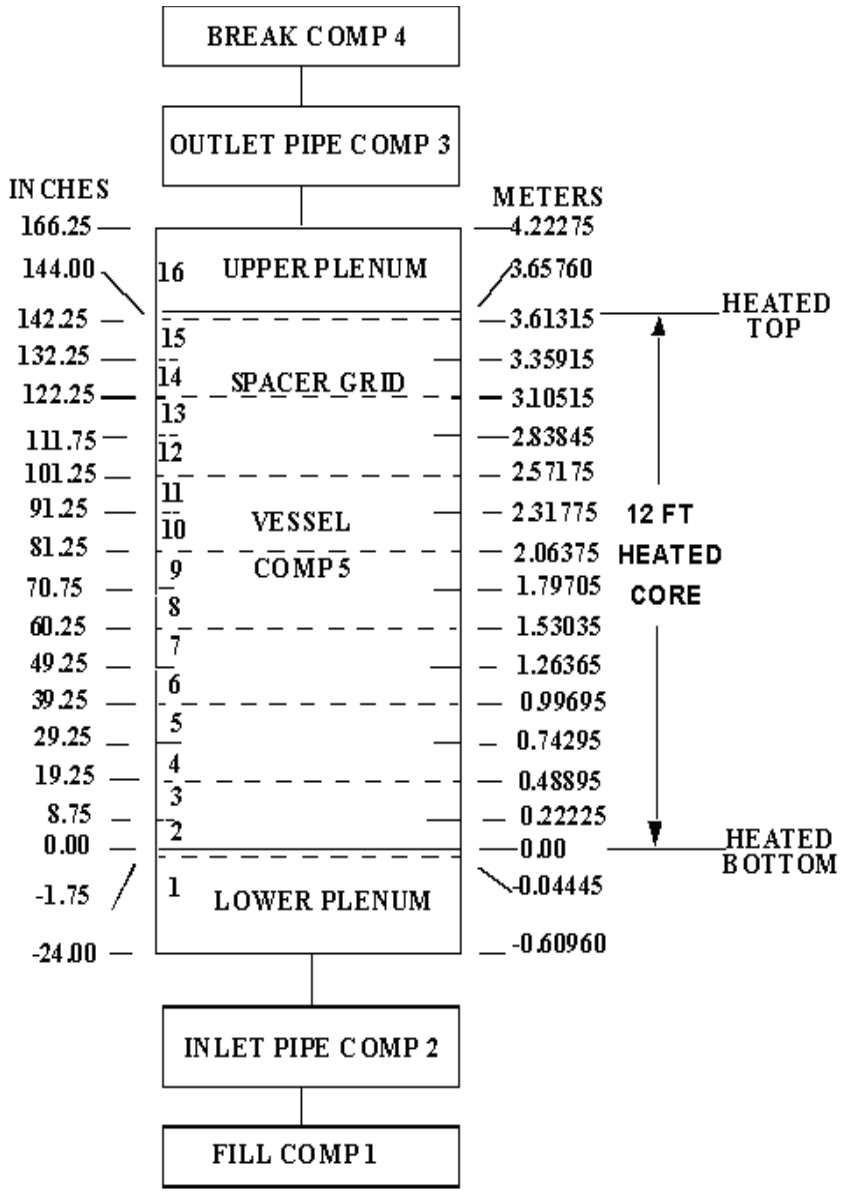

Figure B.7-5 FLECHT-SEASET TRACE Noding Diagram

It should be noted that the upper plenum modeled as a part of the VESSEL represents the unheated area of about 0.6 m (2 ft) long above the 3.6 m (12 ft) heated core but below the actual facility upper plenum. Since the upper plenum was designed to prevent any liquid from draining back into the core, unlike the upper plenum in the plant, the upper plenum in the FLECHT-SEASET Facility is included as a part of the outlet pipe in TRACE modeling.

A node boundary is established such that the bottom of a spacer grid coincides with the bottom of a computational node and each grid span has two equal distance nodes. Thus the bottom of every other node in the heated section has a grid. The spacer grids are modeled by specifying the pressure loss coefficient K to be 1.20.

The electrical power input to the rods is set in a POWER component (Component 8) as a function of time. The axial distribution of power is based on a cosine power shape with the peak power location at the mid-point of the heated section, as shown in Figure B.7-4. The radial and azimuthal power distributions are uniform. The heater rods are divided into 7 radial nodes which model a Kanthal heater coil insulated with boron nitride powder that is encased with stainless steel cladding. Additional details of nodalization are shown in the calculation note.(Ref. 2)

B.7.4. Tests Simulated with TRACE

Eight tests are selected for TRACE assessment as indicated in Table B.7.1 The flooding rate varies from 2.10 cm/sec (0.81 in/sec) to 15.50 cm/sec (6.10 in/sec), the upper plenum pressure from 0.13 MPa (19 psia) to 0.41 MPa (60 psia), and the coolant temperature from 33 °C (91 °F) to 125 °C (257 °F), but the initial rod power at the peak location is 2.3 KW/m (0.70 KW/ft) for all tests. The rod power is designed to represent the decay heat prescribed by 10CFR Part 50 Appendix K from 30 sec following a double-ended guillotine break.

The test conditions shown in Table B.7.1 are nominal values, and the actual values vary considerably with time. Therefore, the actual inlet flow rates and temperatures and the upper plenum pressures are all approximated as a function of time and then used as input to TRACE calculations. Since the rod power decreases with time according to the Appendix K formula, it is also approximated as a function of time. Initial conditions are set based on measured values.

Table B.7.1. FLECHT-SEASET Tests Used for TRACE Assessment

	Run No.	Flooding Rate cm/sec (in/sec)	Upper Plenum Pressure MPa (psia)	Coolant Inlet Temp. °C (°F)	Coolant Inlet Subcooling Temp. °C (°F)	Initial Rod Peak Power KW/m (KW/ft)
1	31108	7.90 (3.11)	0.13 (19)	33 (91)	74 (134)	2.3 (0.70)
2	31203	3.84 (1.51)	0.28 (40)	52 (126)	78 (141)	2.3 (0.70)
3	31302	7.65 (3.01)	0.28 (40)	52 (126)	78 (141)	2.3 (0.70)
4	31504	2.40 (0.97)	0.28 (40)	51 (124)	79 (143)	2.3 (0.70)

Table B.7.1. FLECHT-SEASET Tests Used for TRACE Assessment

	Run No.	Flooding Rate cm/sec (in/sec)	Upper Plenum Pressure MPa (psia)	Coolant Inlet Temp. °C (°F)	Coolant Inlet Subcooling Temp. °C (°F)	Initial Rod Peak Power KW/m (KW/ft)
5	31701	15.5 (6.10)	0.28 (40)	53 (127)	77 (140)	2.3 (0.70)
6	31805	2.10 (0.81)	0.28 (40)	51 (124)	79 (143)	2.3 (0.70)
7	32013	2.64 (1.04)	0.41 (60)	66 (150)	79 (143)	2.3 (0.70)
8	32114	2.5 - 3.1 (1.0 - 1.22)	0.28 (40)	135 (257)	5 (10)	2.3 (0.70)

Detailed comparisons between data and TRACE calculations are given in the following sections for each test. In each case, input boundary conditions (the inlet flow rate and temperature, the upper plenum pressure, and the total power supplied to the rods) are presented first to show how closely the measured values are represented. Heater rod and housing initial temperatures follow. Then TRACE-calculated values are presented and compared with data in the following order:

1. Heater rod clad temperatures at 8 different elevations; 0.6096 m (2 ft), 1.2192 m (4 ft), 1.8288 m (6 ft), 1.9812 m (6.5 ft), 2.4384 m (8 ft), 3.048 m (10 ft), 3.3528 m (11 ft), and 3.5052 m (11.5 ft) elevations as measured from the bottom of the heated region which is located 0.6096 m (2 ft) above the bottom of the bundle,

2. Vapor temperatures at the 1.8288 m (6 ft) and 3.048 m (10 ft) elevations,

3. Quench profile showing the quench front elevation as a function of time,

4. Integrated liquid mass flow rates into and out of the bundle,

5. Differential pressure for the entire 3.66 m (12 ft) core,

6. Differential pressure between the 1.83 m (6 ft) and 2.13 m (7 ft) elevations,

7. Differential pressure between the 3.05 m (10 ft) and 3.35 m (11 ft) elevations,

8. Heater rod clad temperature versus elevation at certain specific time chosen during the time period when the middle section of the core is being quenched, (For this plot the data is not included because the available automatic plotting script (avscript) can not generate such an axial plot).

9. Void fraction versus elevation at certain specific time chosen during the time period when the middle section of the core is being quenched, (For this plot the data is not included because the available automatic plotting script (avscript) can not generate such an axial plot. It should be noted that for this figure the elevation is measured from the bottom of the vessel while in all other

figures the elevation is measured from the bottom of the heated core. The bottom of the vessel is located 0.6 m (2 ft) below the bottom of the heated core.)

10. Heat transfer coefficients (HTCs) at 5 different elevations; 1.2192 m (4 ft), 1.8288 m (6 ft), 1.9812 m (6.5 ft), 2.4384 m (8 ft), and 3.048 m (10 ft) from the bottom of the heated core. HTCs are calculated from data using a program called IHCP1D (Inverse Heat Conduction Program 1 Dimension) Version 8 (Ref. 3). Three HTCs (minimum, maximum, and average) are calculated from data of each of the above 5 elevations at each second. The average is computed as the arithmetic average of HTCs from all instrumented rods which have valid clad temperature measurements at a given elevation. These three data-derived HTCs are compared with the TRACE-derived HTCs in all HTC figures.

In both test data and TRACE calculations, the HTC is defined as follows:

HTC = Heat Flux / (Clad Temp. - Saturation Temp.).

HTCs are also calculated using the DATARH program which was developed by Westinghouse Corp. as a part of the FLECHT-SEASET project which was a joint research project among the NRC, EPRI (Electrical Power Research Institute), and Westinghouse Corp. The main difference between DATARH-calculated HTCs and IHCP1D-calculated HTCs is that the DATARH-calculated HTCs are very oscillatory while the IHCP1D-calculated HTCs are fairly smooth. Both are close to each other in terms of the average value over about 10 seconds. The DATARH program does not use any averaging process while the IHCP1D program has an option of choosing the averaging period. Data-derived HTCs used in all HTC figures of this Flecht Seaset section are computed with the IHCP1D program using the 9 time step average option. Since DATARH-calculated HTCs are fairly close to the IHCP1D-calculated HTCs in terms of the 9-step average values (i.e., 9-sec average values since each time step is 1 sec), only IHCP1D-calculated HTCs are used in TRACE-data comparison figures, and DATARH-calculated HTCs are not used in the figures.

In the above TRACE-data comparisons, all valid data points are included in the figures. For instance, since there are 21 rod temperature measurements at the 1.8 m (6 ft) elevation, all 21 measured rod temperatures are plotted in the figures to compare with a single TRACE value at any given instant.

Since 5 tests are selected for variation of flooding rates ranging from 21.0 mm/sec (0.81 in/sec) to 155.0 mm/sec (6.10 in/sec), the assessment of TRACE is discussed first for these five tests, then two tests for variation of pressures, and finally one test for variation of inlet flow temperatures.

B.7.4.1. Flooding Rate Variation

The five tests of different flooding rates are presented from the lowest flooding rate (2.1 cm/s) test to the highest flooding rate (15.5 cm/s) test.

B.7.4.1.1. Simulation of Test 31805

a. Initial and Boundary Conditions

Nominal input boundary conditions are a flooding rate of 2.1 cm/s (0.81 in/s), inlet liquid temperature of 51 °C (124 °F), and upper plenum pressure of 0.28 MPa (40 psia), as indicated in Table B.7.1 However, the actual input conditions vary considerably with time and can not be treated as constants and thus are treated as time-dependent variables and approximated as shown in Figure B.7-6 through Figure B.7-8. The total power supplied to the bundle which decreases with time according to the Appendix K formula is approximated as shown in Figure B.7-9. The initial rod clad and housing temperatures are approximated as shown in Figure B.7-10.

b. Heater Rod Clad Temperatures

Heater rod clad temperatures calculated by TRACE are compared with the data at 8 different elevations, as indicated before, in Figure B.7-11 through Figure B.7-18. The maximum calculated peak clad temperature (PCT) is 1460 K at 1.9812 m (6.5 ft) from the heated core bottom as compared to the measured temperatures of 1353-1509 K at the same elevation which has 12 valid temperature measurements. Thus the calculated temperature is within the data spread range. TRACE predicts the peak clad temperatures very well below the 3 m (10 ft) elevation from the heated bottom. Between 3.0 m and 3.4 m, TRACE over-predicts the PCTs up to 106 °C (191 °F) based on a comparison between the calculated value and the average measured value at a given elevation. The primary reason for TRACE to predict higher temperatures at these elevations is probably due to lack of a spacer grid model in the current TRACE code. A spacer grid model is to be developed for a later version of the TRACE code. It is well known that spacer grids promote heat exchanges between rods and the surrounding fluid, particularly in the droplet dispersed flow regime, and thus clad temperatures at high elevations will be lowered if a spacer grid model is implemented in TRACE. At 3.5 m (11.5 ft), however, TRACE under-predicts the PCT by 83 °C (149 °F) based on a comparison between the calculated value and the average value of the data at that elevation. It is not clear why TRACE changes from over-prediction to under-prediction as the elevation changes from 3 m to 3.5 m.

The under-prediction of clad temperatures by TRACE near the top of the core occurs in all 4 tests (including this one) which have a flooding rate less than 31 mm/s (1.22 in/s) and which do not show an early top quench front in the data. The test data show that for these low flooding rate tests the liquid de-entrainment at the upper part of the core is not significant and thus does not cause the rods to be quenched early whereas for the other 4 high flooding rate tests the liquid de-entrainment at the top elevations is significant enough to cause an early top quench. Therefore, TRACE over-predicts PCTs even at the 3.5 m (11.5 ft) elevation for the four high flooding rate tests since TRACE does not have a top quench model.

The calculated temperatures turn around and decrease much faster than the data, typically turning around by about 100 sec faster than data above 3 m. Below 3 m the turn-around time difference between calculation and data becomes smaller as the elevation decreases.

c. Vapor Temperatures

Vapor temperatures calculated by TRACE are compared with the data at two different elevations (1.8 m (6 ft) and 3.0 m (10 ft)), as indicated before, in Figure B.7-19 and Figure B.7-20. TRACE reasonably predicts vapor temperatures at both elevations, considering that vapor temperature measurements may have a fairly large uncertainty.

d. Quench Profile

TRACE predicts the quench front very well for the entire core as shown in Figure B.7-21. The quench front progression upward in the core follows a reverse "s" shape. The quench front moves up quickly for the first 25% of the core, settles to a medium speed for the middle 50% of the core, and then moves up at a faster speed again for the last 25% of the core. The initial fast speed is probably due to explosive burst of liquid resulting in liquid drops and chunks thrown upward when the liquid comes into contact with hot rods for the first time, and a faster speed for the last 25% of the core is probably due to de-entrainment of liquid in the upper part of the core above the heated section. Another reason for the fast speed of quench front progression in the lowest and the highest regions of the core is that the power density is lower in these regions. The power density is highest in the central region according to the cosine power shape.

e. Liquid Carryout

The liquid carryout calculated by TRACE is compared with the data in Figure B.7-22 in terms of integrated values because instantaneous values oscillate too much. TRACE over-predicts the amount of the carried-out liquid by about 25% at the end of the test. However, the extent of the over-prediction can not be quantified very well because the data is expected to have a large uncertainty. Considering more reliable differential pressure comparisons which show that TRACE over-predicts the amount of liquid accumulated in the core, TRACE is expected to under-predict the liquid carryout since the liquid in the upper plenum is insignificant.

f. Differential Pressures (DPs)

Differential pressures (DPs) calculated by TRACE are compared with the data in Figure B.7-23 through Figure B.7-25 for the entire core region, a mid-level (1.83 m to 2.13 m (6 ft to 7 ft)), and a top region (3.05 m to 3.35 m (10 ft to 11 ft)), respectively. TRACE predictions of differential pressures are reasonable even though the predicted values for the entire core are about 1.5 kPa (0.22 psi) or 8% higher than the data. The difference between the calculated and the measured DPs for the entire core is well within the measurement uncertainty of 2.66 kPa (0.39 psi). The DP comparisons suggest that TRACE retains the correct amount of liquid (if the DP uncertainty is considered) or slightly more liquid in the core than the data since the DP represents the hydrostatic head essentially as the accelerational and frictional contributions are negligible.

g. Clad Temperature and Void Fraction versus Elevation at Some Time during the Middle Section Being Quenched

The calculated clad temperatures and void fractions at 200 sec after reflood initiation are plotted as a function of elevation in Figure B.7-26 and Figure B.7-27, respectively. The elevation in Figure B.7-26 is measured, as usual, from the bottom of the heated core whereas the elevation in Figure B.7-27 is measured from the bottom of the vessel which is located 0.6096 m (2 ft) below the bottom of the heated core. The data is not included in these figures because these figures along with all other figures are generated using a script which does not have the capability of generating such axial plots for the data. The clad temperature and void fraction plots show that the temperature and void fraction profiles are consistent in the sense that the temperature increases as the void fraction increases and reaches the maximum after the void fraction becomes nearly 1.0. The clad temperature decreases beyond 2.5 m because the power density decreases according to a cosine function. The clad temperature is strongly affected by the combined effect of void fraction and power density.

h. Heat Transfer Coefficients (HTCs)

The calculated heat transfer coefficients (HTCs) are compared with the data at 5 different elevations, as indicated before, in Figure B.7-28 through Figure B.7-32. As indicated previously, three HTCs are calculated from the data; the minimum, the maximum, and the average value of all rods which have valid temperature measurements at that elevation. As expected from the previous temperature comparisons, TRACE-predicted HTCs match data fairly well up to about 200 sec (except for the 10 ft elevation) beyond which the predicted values are bigger than the data as much as 180%. The largest discrepancy occurs at the 1.98 m (6.5 ft) elevation at about 320 sec just before the core is quenched at 360 sec; 280 (calculation) vs. 100 (data) W/(m^2-C). TRACE tends to predict HTCs better in the lower elevations (at or less than 6.5 ft) of the core in the early reflood period while it tends to predict HTCs better in the upper elevations (higher than 6.5 ft) of the core in the late reflood period. The comparison of HTCs at any instant is not very meaningful because TRACE-predicted values oscillate significantly since they are not averaged over a 9-sec. period. A more meaningful comparison is done later in the section of figure-of-merit where comparisons are made in terms of average values over some stable reflood period. Extraneous lines shown after 800 sec in the figures should be ignored because the test is terminated at about 800 sec. These lines result from applying the HTC calculation software beyond the valid data points.

B.7.4.1.2. Simulation of Test 31504

a. Initial and Boundary Conditions

Nominal input boundary conditions are a flooding rate of 2.4 cm/s (0.97 inch/s), inlet liquid temperature of 51 °C (124 °F), and upper plenum pressure of 0.28 MPa (40 psia), as indicated in Table B.7.1 However, the actual input conditions vary considerably with time and can not be treated as constants and thus are treated as time-dependent variables and approximated as shown in Figure B.7-33 through Figure B.7-35. The total power supplied to the bundle which decreases with time according to the Appendix K formula is approximated as shown in Figure B.7-36. The initial rod clad and housing temperatures are approximated as shown in Figure B.7-37.

b. Heater Rod Clad Temperatures

Heater rod clad temperatures calculated by TRACE are compared with the data at 8 different elevations, as indicated before, in Figure B.7-38 through Figure B.7-45. The highest PCT occurs at 1.9812 m (6.5 ft) from the core bottom for both TRACE and data; 1394 K for TRACE and 1322 to 1423 K for data which has 10 valid temperature measurements at this level. The predicted value is within the data spread range. TRACE predicts the PCTs very well below about 3 m (10 ft) from the heated bottom of the core. Between 3.0 m and 3.4 m, TRACE over-predicts the PCTs up to about 102 °C (184 °F), based on a comparison between the calculated value and the average measured value at a given elevation, with the deviation tending to be larger as the elevation increases. The primary reason for TRACE to predict higher PCTs at these elevations is probably due to lack of a spacer grid model in the current TRACE code. A spacer grid model is to be developed for a later version of the TRACE code. At 3.5 m (11.5 ft), however, TRACE under-predicts the PCT by 41 °C (74 °F), based on a comparison between the calculated value and the average measured value at this elevation. The under-prediction of PCTs by TRACE near the top of the core occurs in all 4 tests which have a flooding rate less than 31 mm/s (1.22 in/s) and in which the data do not show an early top quench front.

The calculated temperatures tend to turn around and decrease faster than the data. This tendency is stronger above 3 m; e.g., the calculated temperature turning around by about 100 sec faster than data at the 3.5 m (11.5 ft) elevation. Below 3 m the turn-around time difference between calculation and data becomes smaller as the elevation decreases.

c. Vapor Temperatures

Vapor temperatures calculated by TRACE are compared with the data at two different elevations, as indicated before, in Figure B.7-46 and Figure B.7-47. TRACE over-predicts peak vapor temperatures by about 70 °C (126 °F) at the 3 m (10 ft) elevation, if momentary fluctuations are ignored, whereas at the 1.8 m (6 ft) elevation the prediction is within the data spread. As in clad temperatures, the predicted vapor temperatures turn around faster than data by about 50 sec in both elevations, if momentary fluctuations of TRACE values are ignored.

d. Quench Profile

As in the case of clad temperature predictions, TRACE predicts the quench front very well for the lower 70% of the core as shown in Figure B.7-48. However, the calculated value starts deviating from the data at the 2.5 m elevation above which the data shows an accelerated progression of quench front probably because of the combined effect of low power density and liquid de-entrained on the rod surface above the heated region. TRACE calculation shows a similar trend but with a 30 sec delay.

e. Liquid Carryout

The liquid carryout calculated by TRACE is compared with the data in Figure B.7-49 in terms of integrated values because instantaneous values oscillate too much. TRACE over-predicts the

liquid carryout up to about 25% at the end of the test. However, the extent of the over-prediction can not be quantified because the data is expected to have a large uncertainty.

f. Differential Pressures (DPs)

Differential pressures calculated by TRACE are compared with the data in Figure B.7-50 through Figure B.7-52 for the entire core region, a mid-level (1.83 m to 2.13 m (6 ft to 7 ft)), and a top region (3.05 m to 3.35 m (10 ft to 11 ft)), respectively. TRACE over-predicts the overall differential pressures within 20% and the top level within a few percent for most of the times. In the case of the mid-level DP, TRACE under-predicts DP for the first 170 sec, over-predicts it between 210 and 340 sec, and then correctly predicts it for the rest of the test. The plots after 600 sec should be ignored because the test is terminated at about 600 sec. It appears that TRACE retains more liquid in the core than the data even though the liquid carryout comparison shows otherwise. Since the liquid carryout data would probably have a high uncertainty, we should rely on DP data more.

g. Clad Temperature and Void Fraction versus Elevation at Some Time during the Middle Section Being Quenched

The calculated clad temperatures and void fractions at 150 sec after reflood initiation are plotted as a function of elevation in Figure B.7-53 and Figure B.7-54, respectively. The elevation in Figure B.7-53 is measured, as usual, from the bottom of the heated core whereas the elevation in Figure B.7-54 is measured from the bottom of the vessel which is located 0.6096 m (2 ft) below the bottom of the heated core. The data is not included in these figures because these figures along with all other figures are generated using a script which does not have the capability of generating such axial plots for the data. The clad temperature and void fraction plots show that the temperature and void fraction profiles are consistent in the sense that the temperature increases as the void fraction increases and reaches the maximum after the void fraction becomes nearly 1.0. The clad temperature decreases beyond 2.3 m because the power density decreases according to a cosine function. The clad temperature is strongly affected by the combined effect of void fraction and power density.

h. Heat Transfer Coefficients (HTCs)

The calculated heat transfer coefficients (HTCs) are compared with the data at 5 different elevations, as indicated before, in Figure B.7-55 through Figure B.7-59. As indicated previously, three HTCs are calculated from the data; the minimum, the maximum, and the average value of all rods which have valid temperature measurements at that elevation. As expected from the previous temperature comparisons, TRACE-predicted HTCs match data fairly well up to about 200 sec for the lower elevations of the core, and beyond 200 sec the upper elevations show a better match. The largest discrepancy of 170 W/(m^2-C) or about 140% deviation occurs at 1.98 m (6.5 ft) from the heated bottom shortly before that elevation is quenched at 320 sec. The comparison of HTCs at any instant is not very meaningful because TRACE-predicted values oscillate significantly since they are not averaged over a 9 sec period. A more meaningful comparison is done later in the section of figure-of-merit where comparisons are made in terms of average values over some stable reflood period.

Extraneous lines shown after 600 sec in the figures should be ignored because the test is terminated at about 600 sec. These lines result from applying the HTC calculation software beyond the valid data points.

B.7.4.1.3. Simulation of Test 31203

a. Initial and Boundary Conditions

Nominal input boundary conditions are a flooding rate of 3.84 cm/s (1.51 in/s), inlet liquid temperature of 52 °C (126 °F), and upper plenum pressure of 0.28 MPa (40 psia), as indicated in Table B.7.1 However, the actual input conditions vary considerably with time and can not be treated as constants and thus are treated as time-dependent variables and approximated as shown in Figure B.7-60 through Figure B.7-62 It should be noted that the upper plenum pressure data fluctuates widely for the first 100 sec, and TRACE input is made to follow these fluctuations closely, too. The total power supplied to the bundle which decreases with time according to the Appendix K formula is approximated as shown in Figure B.7-63. The initial rod clad and housing temperatures are approximated as shown in Figure B.7-64.

b. Heater Rod Clad Temperatures

Heater rod clad temperatures calculated by TRACE are compared with the data at 8 different elevations, as indicated before, in Figure B.7-65 through Figure B.7-72. The highest PCT occurs at 1.9812 m (6.5 ft) from the bottom of the core for both TRACE and data; 1285 K for TRACE and 1240 to 1299 K for data which has 11 valid temperature measurements at this level. Thus, the calculated value falls within the data range. TRACE predicts the PCTs very well below the 3 m (10 ft) elevation from the bottom of the heated core. Between 3.0 m and 3.4 m, TRACE over-predicts the PCTs up to 131 °C (236 °F), based on a comparison between the calculated value and the average measured value at a given elevation, with the deviation tending to be larger as the elevation increases. The primary reason for TRACE to predict higher temperatures at these elevations is probably due to lack of a spacer grid model in the current TRACE code. A spacer grid model is to be developed for a later version of the TRACE code. At 3.5 m (11.5 ft), however, TRACE over-predicts the PCT only slightly (21 °C (38 °F)), based on the average value of the data at this level. The turn-around times are predicted very well in all elevations.

c. Vapor Temperatures

Vapor temperatures calculated by TRACE are compared with the data at two different elevations, as indicated before, in Figure B.7-73 and Figure B.7-74. TRACE over-predicts vapor temperatures significantly particularly at high elevations; e.g., by about 100 °C (180 °F) in terms of non-oscillatory peak values at 3 m (10 ft) from the heated bottom. However, since the data are not considered to be very accurate, the extent of deviation shown in the figures may not represent the reality.

d. Quench Profile

As in the case of clad temperature predictions, TRACE predicts the quench front very well for the lower 80% of the core as shown in Figure Figure B.7-75. However, the calculated value starts deviating from the data at 3 m (10 ft) from the bottom of the core, and the deviation increases as the elevation increases. The maximum deviation in quench elevation is about 50 cm at 400 sec and that in quench time is by about 30 sec at the 3.5 m elevation. In the top 15% of the core, the data shows a top quench behavior probably due to liquid de-entrained on the rod surface above the active core whereas TRACE does not show any such top quench behavior.

e. Liquid Carryout

The liquid carryout calculated by TRACE is compared with the data in Figure B.7-76 in terms of integrated values because instantaneous values oscillate too much. The liquid carryout data suggests that TRACE over-predicts the liquid carryout. However, the differential pressure (DP) data suggests otherwise. Since the entrainment data is expected to have a large uncertainty, we should rely on the DP data more and would conclude that TRACE would show the less entrainment than the data, if the data were to show the correct amount of liquid carryout. As an example of unreliable entrainment data, the data shows that the liquid carried out of the bundle does not increase much beyond about 350 sec probably because the liquid collection tank got filled up at 350 sec.

f. Differential Pressures

Differential pressures calculated by TRACE are compared with the data in Figure B.7-77 through Figure B.7-79 for the entire core region, a mid-level (1.83 m to 2.13 m (6 ft to 7 ft)), and a top region (3.05 m to 3.35 m (10 ft to 11 ft)), respectively. TRACE over-predicts differential pressures for the entire core generally within 20%, for the middle section within 50%, and the top level within 20%, when momentary fluctuations are ignored. As in previous tests, TRACE retains more liquid in the core than what data shows.

g. Clad Temperature and Void Fraction versus Elevation at Some Time during the Middle Section Being Quenched

The calculated clad temperatures and void fractions at 100 sec after reflood initiation are plotted as a function of elevation in Figure B.7-80 and Figure B.7-81, respectively. The elevation in Figure B.7-80 is measured, as usual, from the bottom of the heated core whereas the elevation in Figure B.7-81 is measured from the bottom of the vessel which is located 0.6096 m (2 ft) below the bottom of the heated core. The data is not included in these figures because these figures along with all other figures are generated using a script which does not have the capability of generating such axial plots for the data. The clad temperature and void fraction plots show that the temperature and void fraction profiles are consistent in the sense that the temperature increases as the void fraction increases and reaches the maximum shortly after the void fraction becomes nearly 1.0. The clad temperature decreases beyond 2.2 m because the power density decreases according to a cosine function. The clad temperature is strongly affected by the combined effect of void fraction and power density.

h. Heat Transfer Coefficients (HTCs)

The calculated heat transfer coefficients (HTCs) are compared with the data at 5 different elevations, as indicated before, in Figure B.7-82 through Figure B.7-86. As indicated previously, three HTCs are calculated from the data; the minimum, the maximum, and the average value of all rods which have valid temperature measurements at that elevation. As expected from the previous temperature comparisons, TRACE-predicted HTCs match data fairly well up to about 130 sec for the lower elevations of the core except for the 1.22 m (4 ft) elevation, and beyond 130 sec the upper elevations show a better match. The largest discrepancy of about 200 W/(m^2-C) or about 100% deviation occurs at 1.22 m (4.0 ft) from the heated bottom shortly before that elevation is quenched at 100 sec. The comparison of HTCs at any instant is not very meaningful because TRACE-predicted values oscillate significantly since they are not averaged over a 9-sec. period. A more meaningful comparison is done later in the section of figure-of-merit where comparisons are made in terms of average values over some stable reflood period.

Extraneous lines shown after quench time, which are signified by nearly vertical lines as HTCs become very large as a result of wall temperatures approaching the saturation temperatures, should be ignored because HTCs after rod quench would be very erratic as a result of a very small fluctuating number divided by a very small fluctuating number.

B.7.4.1.4. Simulation of Test 31302

a. Initial and Boundary Conditions

Nominal input boundary conditions are a flooding rate of 7.65 cm/s (3.01 in/s), inlet liquid temperature of 52 °C (126 °F), and upper plenum pressure of 0.28 MPa (40 psia), as indicated in Table B.7.1 However, the actual input conditions vary considerably with time and can not be treated as constants and thus are treated as time-dependent variables and approximated as shown in Figure B.7-87 through Figure B.7-89. The total power supplied to the bundle which decreases with time according to the Appendix K formula is approximated as shown in Figure B.7-90. The initial rod clad and housing temperatures are approximated as shown in Figure B.7-91.

b. Heater Rod Clad Temperatures

Heater rod clad temperatures calculated by TRACE are compared with the data at 8 different elevations, as indicated before, in Figure B.7-92 through Figure B.7-99. The highest PCT occurs at 1.83 m (6 ft) from the core bottom for both TRACE and data; 1196 K for TRACE and 1120 to 1190 K for data which has 19 valid temperature measurements at this elevation. Thus the TRACE-predicted value is 6 °C (11 °F) higher than the highest measured value or 34 °C (61 °F) higher than the average value (1162 K) of measured temperatures at this elevation. It is interesting to note that a high flooding rate of 7.65 cm/s (3.01 in/s) not only lowers the PCT but also lowers the elevation, where this PCT occurs, from 1.98 m (6.5 ft) to 1.83 m (6 ft). TRACE predicts the PCTs very well for the lower 55% of the core, below 1.98 m (6.5 ft). However, above 2.4 m (8 ft), TRACE over-predicts the PCTs up to 104 °C (187 °F), based on the average value of the temperature data at a given elevation, with the deviation tending to be larger as the elevation increases until the 3.4 m elevation is reached. At the 3.5 m elevation, the over-prediction by TRACE is much less; only 54 C at 3.5 m vs. 104 C at 3.0 m.

The calculated temperatures turn around and decrease much later than the data, turning around in about 130 sec after reflood initiation in the case of the top of the core for TRACE versus about 10-50 sec of turn-around time in the data at all elevations.

c. Vapor Temperatures

Vapor temperatures calculated by TRACE are compared with the data at two different elevations, as indicated before, in Figure B.7-100 and Figure B.7-101. TRACE over-predicts vapor temperatures significantly (up to 200 °C (360 °F) in peak values) particularly at high elevations. However, since the data are not considered to be very accurate, the extent of deviation shown in the figures may not represent the reality.

d. Quench Profile

As in the case of clad temperature predictions, TRACE predicts the quench front very well for the lower 60% of the core as shown in Figure B.7-102. However, the calculated value starts deviating from the data at about 2 m from the core bottom, and the deviation increases as the elevation increases. In the top 15% of the core, the data shows a top quench probably due to liquid de-entrained on the rod surface above the heated part of the core whereas TRACE does not show any top quench behavior. The maximum deviation is about 50 cm in elevation and 80 sec in quench time in the top quench region.

e. Liquid Carryout

The liquid carryout calculated by TRACE is compared with the data in Figure B.7-103 in terms of integrated values because instantaneous values oscillate too much. TRACE over-predicts the liquid carryout by about 40% at the end of the test. The over-prediction of the liquid carryout by TRACE is indicated by the liquid collection data of this test as well as by the data of all the other seven tests. However, more reliable differential pressure data indicates otherwise. Therefore, based on differential pressure comparisons as shown in Figure B.7-104, we should conclude that, if the liquid carryout data were correct, the data would show the same amount of liquid carryout as predicted by TRACE since the liquid remaining in the upper plenum is insignificant.

f. Differential Pressures (DPs)

Differential pressures calculated by TRACE are compared with the data in Figure B.7-104 through Figure B.7-106 for the entire core region, a mid-level (1.83 m to 2.13 m (6 ft to 7 ft)), and a top region (3.05 m to 3.35 m (10 ft to 11 ft)), respectively. TRACE predictions of differential pressures are reasonable in all three regions.

g. Clad Temperature and Void Fraction versus Elevation at Some Time during the Middle Section Being Quenched

The calculated clad temperatures and void fractions at 60 sec after reflood initiation are plotted as a function of elevation in Figure B.7-107 and Figure B.7-108, respectively. The elevation in Figure B.7-107 is measured, as usual, from the bottom of the heated core whereas the elevation in

Figure B.7-108 is measured from the bottom of the vessel which is located 0.6096 m (2 ft) below the bottom of the heated core. The data is not included in these figures because these figures along with all other figures are generated using a script which does not have the capability of generating such axial plots for the data. The clad temperature and void fraction plots show that the temperature and void fraction profiles are consistent in the sense that the temperature increases as the void fraction increases and reaches the maximum when the void fraction becomes 0.96. The clad temperature decreases beyond 2.2 m because the power density decreases according to a cosine function. The clad temperature is strongly affected by the combined effect of void fraction and power density.

h. Heat Transfer Coefficients (HTCs)

The calculated heat transfer coefficients (HTCs) are compared with the data at 5 different elevations, as indicated before, in Figure B.7-109 through Figure B.7-113. As indicated previously, three HTCs are calculated from the data; the minimum, the maximum, and the average value of all rods which have valid temperature measurements at that elevation. As expected from the previous temperature comparisons, TRACE-predicted HTCs match data fairly well up to about 80 sec for the lower elevations of the core except for the 1.22 m (4 ft) elevation, and beyond 80 sec the upper elevations show a slightly better match. The largest discrepancy of about 170 W/(m^2-C) or about 72% deviation occurs at 1.22 m (4.0 ft) from the heated bottom at about 50 sec shortly before 60 sec of quench time at that elevation. In the above comparisons, discrepancies very near to the quench time are not included because a very large discrepancy at or very near the quench time is not really relevant to judging the code capability of predicting HTCs applicable to the majority of the reflood period. In addition, extraneous lines shown after quench time, which are signified by nearly vertical lines as HTCs become very large as a result of wall temperatures approaching the saturation temperatures, should be ignored because HTCs after rod quench would be very erratic as a result of a very small fluctuating number divided by a very small fluctuating number. The comparison of HTCs at any instant is not very meaningful because TRACE-predicted values oscillate significantly since they are not averaged over a 9-sec. period. A more meaningful comparison is done later in the section of figure-of-merit where comparisons are made in terms of average values over some stable reflood period.

B.7.4.1.5. Simulation of Test 31701

a. Initial and Boundary Conditions

Nominal input boundary conditions are a flooding rate of 15.5 cm/s (6.10 in/s), inlet liquid temperature of 53 °C (127 °F), and upper plenum pressure of 0.28 MPa (40 psia), as indicated in Table B.7.1 However, the actual input conditions vary considerably with time and can not be treated as constants and thus are treated as time-dependent variables and approximated as shown in Figure B.7-114 through Figure B.7-116. The total power supplied to the bundle which decreases with time according to the Appendix K formula is approximated as shown in Figure B.7-117. The initial rod clad and housing temperatures are approximated as shown in Figure B.7-118.

b. Heater Rod Clad Temperatures

Heater rod clad temperatures calculated by TRACE are compared with the data at 8 different elevations, as indicated before, in Figure B.7-119 through Figure B.7-126. The rod temperatures are reasonably predicted. The maximum PCT occurs at the 1.83 m (6.0 ft) elevation for both TRACE and data; 1145 K from TRACE and 1114 to 1175 K from data which has 16 valid temperature measurements at this elevation. Thus, the predicted value falls within the data spread range. TRACE predicts the PCTs very well for the lower 70% of the core, at or below 2.4 m (8 ft). However, above 2.4 m, TRACE over-predicts the PCTs slightly; 49 °C (88 °F) at 3.0 m (10 ft), 39 °C (70 °F) at 3.4 m (11 ft), and 22 °C (40 °F) at 3.5 m (11.5 ft), all based on the average data value at a given elevation. The calculated temperatures turn around and decrease later than the data, turning around in about 60 sec after reflood initiation near the top of the core in the case of TRACE calculation versus about 10 sec of turn-around time in all elevations in the case of data.

c. Vapor Temperatures

Vapor temperatures calculated by TRACE are compared with the data at two different elevations, as indicated before, in Figure B.7-127 and Figure B.7-128. TRACE over-predicts vapor temperatures significantly at the 3 m (10 ft) elevation; up to 160 °C (288 °F) in terms of peak values. However, since the data are not considered to be very accurate, the extent of deviation shown in the figures may not represent the reality.

d. Quench Profile

As in the case of clad temperature predictions, TRACE predicts the quench front very well for the first 30% of the core as shown in Figure B.7-129. For the middle 30% between 1.5 and 3.05 m, data shows a faster quench by about 20-30 sec probably because a lot of liquid chunks are thrown up from below by high steam velocity associated with a high flooding rate of 15.5 cm/s (6.1 in/s), resulting in an improved heat transfer from rods to the surrounding fluid. The improvement in heat transfer in this region is more than what TRACE shows. In addition, the data shows that the liquid de-entrained on the rod surface above the heated region causes a top quench to occur for the top 40% of the core. Test 31302 and this test show that a top quench occurs for a flooding rate of 3.84 cm/s (1.51 inch/sec) or higher and that the top quench region expands as the flooding rate increases further from 3.84 cm/s. On the other hand, TRACE does not show such a top quench even though at upper elevations TRACE shows that the quench front progresses a little faster probably because of low power density and some de-entrainment of liquid.

e. Liquid Carryout

The liquid carryout calculated by TRACE is compared with the data in Figure B.7-130 in terms of integrated values because instantaneous values oscillate too much. TRACE over-predicts the liquid carryout by about 50% at the end of the test. However, it is suspected that the data has a large uncertainty because differential pressure comparisons show that TRACE retains about right amount of liquid in the core. Therefore, we would conclude that TRACE correctly predicts the amount of liquid carried out of the bundle since the amount of liquid in the upper plenum is insignificant.

f. Differential Pressures

Differential pressures calculated by TRACE are compared with the data in Figure B.7-131 through Figure B.7-133 for the entire core region, a mid-level (1.83 m to 2.13 m (6 ft to 7 ft)), and a top region (3.05 m to 3.35 m (10 ft to 11 ft)), respectively. TRACE predictions of differential pressures are reasonable except for the initial period of the middle region and the entire period of the top region where the calculation under-predicts the differential pressures by about 25%.

g. Clad Temperature and Void Fraction versus Elevation at Some Time during the Middle Section Being Quenched

The calculated clad temperatures and void fractions at 30 sec after reflood initiation are plotted as a function of elevation in Figure B.7-134 and Figure B.7-135, respectively. The elevation in Figure B.7-134 is measured, as usual, from the bottom of the heated core whereas the elevation in Figure B.7-135 is measured from the bottom of the vessel which is located 0.6096 m (2 ft) below the bottom of the heated core. The data is not included in these figures because these figures along with all other figures are generated using a script which does not have the capability of generating such axial plots for the data. The clad temperature and void fraction plots show that the temperature and void fraction profiles are consistent in the sense that the temperature increases as the void fraction increases and reaches the maximum when the void fraction becomes about 0.9. The clad temperature decreases beyond 2.2 m because the power density decreases according to a cosine function. The clad temperature is strongly affected by the combined effect of void fraction and power density.

h. Heat Transfer Coefficients (HTCs)

The calculated heat transfer coefficients (HTCs) are compared with the data at 5 different elevations, as indicated before, in Figure B.7-136 through Figure B.7-140. As indicated previously, three HTCs are calculated from the data; the minimum, the maximum, and the average value of all rods which have valid temperature measurements at that elevation. As expected from the previous temperature comparisons, TRACE-predicted HTCs match data fairly well for most of the core, in terms of the average values, except for 3.05 m (10 ft) from the heated bottom where data seem to spread to a wide range probably because of the non-uniform flow distribution along the radial and the azimuthal directions as a result of a high flooding rate of 15.5 cm/sec (6.1 inch/sec). In the above comparisons, discrepancies very near the quench time are not included because a very large discrepancy at or very near the quench time is not really relevant to judging the code capability of predicting HTCs applicable to the majority of the reflood period. In addition, extraneous lines shown after quench time, which are signified by nearly vertical lines as HTCs become very large as a result of wall temperatures approaching the saturation temperatures, should be ignored because HTCs after rod quench would be very erratic as a result of a very small fluctuating number divided by a very small fluctuating number. The comparison of HTCs at any instant is not very meaningful because TRACE-predicted values oscillate significantly since they are not averaged over a 9-sec. period. A more meaningful comparison is done later in the section of figure-of-merit where comparisons are made in terms of average values over some stable reflood period.

B.7.4.2. Pressure Variation

The two tests of different pressures are presented below from the lower pressure (0.13 MPa (19 psia)) test to the higher pressure (0.41 MPa (60 psia)) test. The five tests discussed in the previous section would serve as intermediate pressure (0.28 MPa (40 psia)) tests even though their flooding rates are not same.

B.7.4.2.1. Simulation of Test 31108

a. Initial and Boundary Conditions

Nominal input boundary conditions are a flooding rate of 7.9 cm/s (3.11 in/s), inlet liquid temperature of 33 °C (91 °F), and upper plenum pressure of 0.13 MPa (19 psia), as indicated in Table B.7.1 However, the actual input conditions vary considerably with time and can not be treated as constants and thus are treated as time-dependent variables and approximated as shown in Figure B.7-141 through Figure B.7-143. The total power supplied to the bundle which decreases with time according to the Appendix K formula is approximated as shown in Figure B.7-144. The initial rod clad and housing temperatures are approximated as shown in Figure Figure B.7-145.

b. Heater Rod Clad Temperatures

Heater rod clad temperatures calculated by TRACE are compared with the data at 8 different elevations, as indicated before, in Figure B.7-146 through Figure B.7-153. The maximum PCT of 1225 K occurs at the 1.98 m (6.5 ft) elevation in the calculation whereas maximum PCT of 1200 K occurs at the 1.83 m (6.0 ft) elevation in the data. The data range at 1.83 m is from 1126 to 1200 K, giving the average value of 1168 K with 12 valid temperature measurements. TRACE predicts the peak clad temperatures very well below the midpoint of the core, 1.83 m (6 ft). However, above the midpoint, TRACE over-predicts the PCTs up to 157 °C (283 °F), based on the average value of the data at each elevation, with the deviation largest at the 3.0 m (10 ft) elevation. The calculated temperatures turn around and decrease much later than the data at all levels above 1.2 m from the heated bottom, turning around in about 200 sec after reflood initiation near the top of the core in the case of TRACE calculations versus about 10-20 sec of turn-around times at all elevations in the case of data.

c. Vapor Temperatures

Vapor temperatures calculated by TRACE are compared with the data at two different elevations, as indicated before, in Figure B.7-154 and Figure B.7-155. TRACE over-predicts vapor temperatures significantly particularly at high elevations; e.g., 200 °C (360 °F) in terms of peak values at the 3 m (10 ft) elevation. However, since the data are not considered to be very accurate, the extent of deviation shown in the figures may not represent the reality.

d. Quench Profile

As in the case of clad temperature predictions, TRACE predicts the quench front very well for the lower half of the core as shown in Figure B.7-156. However, the calculated value starts deviating from data starting at about 2 m from the bottom of the core, and the deviation increases as the elevation increases. In the elevations between 2 m and 3 m from the bottom of the core, TRACE shows an earlier quench than the data even though rod temperatures are higher. In this region the TRACE calculates higher heat transfer rates than the data. In the top 20% of the core, the data shows a top quench probably due to liquid de-entrained on the rod surface above the heated region whereas TRACE does not show any top quench behavior.

e. Liquid Carryout

The liquid carryout calculated by TRACE is compared with the data in Figure B.7-157 in terms of integrated values because instantaneous values oscillate too much. As in all other tests, TRACE over-predicts the liquid carryout, as compared to the data. However, because of a large uncertainty in the data, it would not be correct to conclude that TRACE carries too much liquid out of the bundle. For instance, the data shows that the liquid carried out of the bundle does not increase much beyond about 150 sec probably because the liquid collection tank got filled up early since this is a high flooding rate test. More reliable differential pressure data-TRACE comparisons suggest that the liquid carryout predicted by TRACE would be about right or slightly less than the data, depending upon how accurate the DP data is. The liquid carryout collected and the liquid accumulated in the core are directly related since the amount of liquid retained in the upper plenum is insignificant.

f. Differential Pressures

Differential pressures calculated by TRACE are compared with the data in Figure B.7-158 through Figure B.7-160 for the entire core region, a mid-level (1.83 m to 2.13 m (6 ft to 7 ft)), and a top region (3.05 m to 3.35 m (10 ft to 11 ft)), respectively. TRACE over-predicts the overall pressure drop by about 13%. As in many other previous tests, TRACE appears to retain more liquid in the core than the data. For a mid-level, TRACE under-predicts the pressure drop by about 10-40% for the first 100 sec, reasonably predicts it between 100 and 180 sec, if momentary values are ignored, and slightly (by about 8%) under-predicts it between 180 and 250 sec before the region is completely filled with two-phase mixture. For the top region, TRACE shows a lot of big oscillations except for the middle of the testing period between 100 and 300 sec where TRACE under-predicts the pressure drop by about 10-25%.

g. Clad Temperature and Void Fraction versus Elevation at Some Time during the Middle Section Being Quenched

The calculated clad temperatures and void fractions at 100 sec after reflood initiation are plotted as a function of elevation in Figure B.7-161 and Figure B.7-162, respectively. The elevation in Figure B.7-161 is measured, as usual, from the bottom of the heated core whereas the elevation in Figure B.7-162 is measured from the bottom of the vessel which is located 0.6096 m (2 ft) below the bottom of the heated core. The data is not included in these figures because these figures along with all other figures are generated using a script which does not have the capability of generating such axial plots for the data. The clad temperature and void fraction plots show that the

temperature and void fraction profiles are consistent in the sense that the temperature increases as the void fraction increases and reaches the maximum shortly when the void fraction becomes about 0.96. The clad temperature decreases beyond 2.2 m because the power density decreases according to a cosine function. The clad temperature is strongly affected by the combined effect of void fraction and power density.

h. Heat Transfer Coefficients (HTCs)

The calculated heat transfer coefficients (HTCs) are compared with the data at 5 different elevations, as indicated before, in Figure B.7-163 through Figure B.7-167. As indicated previously, three HTCs are calculated from the data; the minimum, the maximum, and the average value of all rods which have valid temperature measurements at that elevation. As expected from the previous temperature comparisons, TRACE-predicted HTCs in the lower half of the core tend to match data better in the earlier period of the reflood while TRACE-predicted HTCs in the upper half of the core tend to match data better in the later period of the reflood. The maximum discrepancy of 180 W/(m^2-C) or 90% deviation occurs at 1.2 m (4 ft) at 55 sec shortly before the rod quenches at 65 sec. Extraneous lines shown after quench time, which are signified by nearly vertical lines as HTCs become very large as a result of wall temperatures approaching the saturation temperatures, should be ignored because HTCs after rod quench would be very erratic as a result of a very small fluctuating number divided by a very small fluctuating number. The comparison of HTCs at any instant is not very meaningful because TRACE-predicted values oscillate significantly since they are not averaged over a 9 sec. period. A more meaningful comparison is done later in the section of figure-of-merit where comparisons are made in terms of average values over some stable reflood period.

B.7.4.2.2. Simulation of Test 32013

a. Initial and Boundary Conditions

Nominal input boundary conditions are a flooding rate of 2.64 cm/s (1.04 in/s), inlet liquid temperature of 66 °C (150 °F), and upper plenum pressure of 0.41 MPa (60 psia), as indicated in Table B.7.1 However, the actual input conditions vary considerably with time and can not be treated as constants and thus are treated as time-dependent variables and approximated as shown in Figure B.7-168 through Figure B.7-170. The total power supplied to the bundle which decreases with time according to the Appendix K formula is approximated as shown in Figure B.7-171. The initial rod clad and housing temperatures are approximated as shown in Figure B.7-172.

b. Heater Rod Clad Temperatures

Heater rod clad temperatures calculated by TRACE are compared with the data at 8 different elevations, as indicated before, in Figure B.7-173 through Figure B.7-180. The maximum PCT occurs at the 1.98 m (6.5 ft) elevation for both TRACE calculation and data; 1369 K from calculation and 1306 to 1431 K from data which has 12 valid temperature measurements at this elevation. Thus, the calculated maximum PCT falls within the data spread range. TRACE predicts

the PCTs very well for the lower 80% of the core, below 3 m (10 ft). However, TRACE over-predicts the PCT by 38 °C (68 °F) at 3 m and by 50 °C (90 °F) at 3.4 m, but under-predicts it at 3.5 m by 48 °C (86 °F). The turn-around temperatures are predicted very well at all elevations.

TRACE tends to predict clad temperatures better as the pressure increases; i.e., best at 0.41 MPa (60 psia) followed by 0.28 MPa (40 psia) and worst at 0.13 MPa (19 psia).

c. Vapor Temperatures

Vapor temperatures calculated by TRACE are compared with the data at two different elevations, as indicated before, in Figure B.7-181 and Figure B.7-182. TRACE predicts vapor temperatures reasonably well for both elevations. However, since the data are not considered to be very accurate, the accuracy of prediction can not be determined.

d. Quench Profile

As in the case of clad temperature predictions, TRACE predicts the quench front reasonably well for the entire region of the core as shown in Figure B.7-183 In this test, the data does not show a top quench behavior since the flooding rate is not high, only 2.64 cm/s (1.04 in/s). However, the rate of quench advancement becomes faster for both TRACE calculation and the data at the top 15% of the core probably because of the low power density.

e. Liquid Carryout

The liquid carryout calculated by TRACE is compared with the data in Figure B.7-184 in terms of integrated values because instantaneous values oscillate too much. TRACE over-predicts the liquid carryout by about 30% at the end of the test. However, as discussed previously, the liquid carryout data has a large uncertainty, and thus the differential pressure data should be used to determine how much liquid is carried out of the bundle.

f. Differential Pressures

Differential pressures calculated by TRACE are compared with the data in Figure B.7-185 through Figure B.7-187 for the entire core region, a midlevel (1.83 m to 2.13 m (6 ft to 7 ft)), and a top region (3.05 m to 3.35 m (10 ft to 11 ft)), respectively. TRACE predictions of differential pressures are reasonable in all three regions for most of the time. Since TRACE correctly predicts the amount of liquid retained in the bundle, it would also correctly predict the liquid carried out of the bundle because the liquid remaining in the upper plenum is insignificant.

g. Clad Temperature and Void Fraction versus Elevation at Some Time during the Middle Section Being Quenched

The calculated clad temperatures and void fractions at 150 sec after reflood initiation are plotted as a function of elevation in Figure B.7-188 and Figure B.7-189, respectively. The elevation in Figure B.7-188 is measured, as usual, from the bottom of the heated core whereas the elevation in Figure B.7-189 is measured from the bottom of the vessel which is located 0.6096 m (2 ft) below

the bottom of the heated core. The data is not included in these figures because these figures along with all other figures are generated using a script which does not have the capability of generating such axial plots for the data. The clad temperature and void fraction plots show that the temperature and void fraction profiles are consistent in the sense that the temperature increases as the void fraction increases and reaches the maximum shortly after the void fraction becomes nearly 1.0. The clad temperature decreases beyond 2.45 m because the power density decreases according to a cosine function. The clad temperature is strongly affected by the combined effect of void fraction and power density.

h. Heat Transfer Coefficients (HTCs)

The calculated heat transfer coefficients (HTCs) are compared with the data at 5 different elevations, as indicated before, in Figure B.7-190 through Figure B.7-194. As indicated previously, three HTCs are calculated from the data; the minimum, the maximum, and the average value of all rods which have valid temperature measurements at that elevation. As expected from the previous temperature comparisons, TRACE-predicted HTCs in the lower half of the core tend to match data better in the earlier period of the reflood while TRACE-predicted HTCs in the upper half of the core tend to match data better in the later period of the reflood. The largest discrepancy of 180 W/(m^2-C) or about 80% deviation occurs at the 1.2 m (4 ft) elevation at 90 sec shortly before the rod quenches at 115 sec.

B.7.4.3. Inlet Subcooling Temperature Variation

There is only one test (Test 32114) which used significantly different subcooling of 5 °C (9 °F). All the other 7 tests selected for the TRACE assessment used a much higher and similar subcooling of 74 to 79 °C (134 to 143 °F).

B.7.4.3.1. Simulation of Test 32114

a. Initial and Boundary Conditions

Nominal input boundary conditions are a varying flooding rate ranging from 2.5 to 3.1 cm/s (1.0 to 1.22 in/s), inlet liquid temperature of 125 °C (257 °F), and upper plenum pressure of 0.28 MPa (40 psia), as indicated in Table B.7.1 However, the actual input conditions vary significantly with time and thus are treated as time-dependent variables and approximated as shown in Figure B.7-195 through Figure B.7-197. It should be noted that TRACE-input values are made to follow closely the data of the oscillatory inlet flow rate and temperature and upper plenum pressure to represent the test conditions accurately. The test input conditions for the first 200 sec oscillate significantly as shown in Figure B.7-195 through Figure B.7-197 The total power supplied to the bundle which decreases with time according to the Appendix K formula is approximated as shown in Figure B.7-198. The initial rod clad and housing temperatures are approximated as shown in Figure B.7-199.

b. Heater Rod Clad Temperatures

Heater rod clad temperatures calculated by TRACE are compared with the data at 8 different elevations, as indicated before, in Figure B.7-200 through Figure B.7-207. The maximum PCT occurs at the 1.98 m (6.5 ft) elevation for both TRACE calculation and data; 1408 K from calculation and 1292 to 1443 K from data which has 12 valid measurements at this level. Thus the calculated value falls within the data spread range. TRACE predicts the peak clad temperatures very well for the lower 60% of the core, below 2.4 m (8 ft). However, between 2.4 m and 3.4 m (11 ft), TRACE over-predicts the peak clad temperatures up to 135 °C (243 °F), based on the average of data value at each elevation, with the largest deviation at the elevation of 3.0 m (10 ft) from the bottom of the core. At 3.5 m (11.5 ft), TRACE under-predicts the PCT by 45 °C (81 °F), based on the average of data value at this elevation. The temperature turn-around times are predicted very well below 3.0 m (10 ft), but above it they are predicted to occur later than data by about 30 to 100 sec.

c. Vapor Temperatures

Vapor temperatures calculated by TRACE are compared with the data at two different elevations, as indicated before, in Figure B.7-208 and Figure B.7-209. TRACE-predicted vapor temperatures are highly oscillatory with a period of about 20 sec and an amplitude of 50 to 300 °C even though data are not so oscillatory. The calculated vapor temperature oscillation is driven by highly oscillatory upper plenum pressures for the first 240 sec of the test. In order to simulate the test accurately, the oscillatory upper plenum pressure data are accurately represented as input to TRACE calculations. The small oscillation of vapor temperatures after 240 sec is probably due to residual effect of oscillating upper plenum pressures which persist until 240 sec. The oscillation decreases gradually after 240 sec. Even though the calculated vapor temperatures are highly oscillatory for the first 240 sec, the average values are reasonably close to the data except for trailing ends. In any case, since the data are not considered to be very accurate, the extent of predictive accuracy can not be determined.

d. Quench Profile

As in the case of clad temperature predictions, TRACE predicts the quench front very well for the lower 60% of the core as shown in Figure B.7-210. However, the calculated value starts deviating from the data at about 2 m from the bottom of the core, and the deviation increases as the elevation increases. In the top 20% of the core, the data shows that the quench front moves up rapidly probably because of the combined effect of low power density and liquid de-entrained on the relatively cold rod surface above the heated region. TRACE shows a similar trend but the increased rate is delayed by about 50 sec.

e. Liquid Carryout

The liquid carryout calculated by TRACE is compared with the data in Figure B.7-211 in terms of integrated values because instantaneous values oscillate too much. TRACE over-predicts the liquid carryout by about 50% at the end of the test (600 sec). However, because of a large uncertainty in the data, it is not certain that TRACE really over-predicts the liquid carryout. In fact, a comparison of the more reliable core differential pressure between TRACE and data shows that TRACE retains more liquid in the core than the data, implying that the predicted carryout

would be less than the data, if the liquid carryout data were accurate. The amount of liquid in the core and the amount of liquid carried out of the bundle are directly related because the amount of liquid in the upper plenum is not significant.

f. Differential Pressures

Differential pressures calculated by TRACE are compared with the data in Figure B.7-212 through Figure B.7-214 for the entire core region, a mid-level (1.83 m to 2.13 m (6 ft to 7 ft)), and a top region (3.05 m to 3.35 m (10 ft to 11 ft)), respectively. TRACE-predicted differential pressures are very oscillatory, as in vapor temperatures, because of oscillating upper plenum pressures. However, the calculated average pressures are reasonably close to the data except for the pressure drop for the entire core for which the calculated values are higher than data by about 10 to 20%. If the differential pressure measurement uncertainty of 2.7 KPa is considered, the calculated values are close to the data even for the entire core.

g. Clad Temperature and Void Fraction versus Elevation at Some Time during the Middle Section Being Quenched

The calculated clad temperatures and void fractions at 200 sec after reflood initiation are plotted as a function of elevation in Figure B.7-215 and Figure B.7-216, respectively. The elevation in Figure B.7-215 is measured, as usual, from the bottom of the heated core whereas the elevation in Figure B.7-216 is measured from the bottom of the vessel which is located 0.6096 m (2 ft) below the bottom of the heated core. The data is not included in these figures because these figures along with all other figures are generated using a script which does not have the capability of generating such axial plots for the data. The clad temperature and void fraction plots show that the temperature and void fraction profiles are consistent in the sense that the temperature increases as the void fraction increases and reaches the maximum when the void fraction becomes nearly 1.0. The clad temperature decreases beyond 2.2 m because the power density decreases according to a cosine function. The clad temperature is strongly affected by the combined effect of void fraction and power density.

h. Heat Transfer Coefficients (HTCs)

The calculated heat transfer coefficients (HTCs) are compared with the data at 5 different elevations, as indicated before, in Figure B.7-217 through Figure B.7-221. As indicated previously, three HTCs are calculated from the data; the minimum, the maximum, and the average value of all rods which have valid temperature measurements at that elevation. TRACE predicts data-derived HTCs relatively well at all elevations, but predicted values tend to oscillate more than the data since TRACE-predicted HTCs are instantaneous values while data-derived HTCs are averaged over 9 sec. If extreme values are taken, the largest discrepancy of 140 W/(m^2-C) or about 100% deviation occurs at the 1.2 m (4 ft) elevation at 110 sec shortly before the rod quenches at 175 sec.

B.7.4.4. Figure of Merits (FOMs)

To present a concise picture of the predictive capabilities of TRACE with respect to the LOCA reflood process, three FOMs are selected; peak clad temperatures (PCTs), quench times, and heat transfer coefficients (HTCs). Each FOM is discussed for each test first and then combined for all 8 tests to provide a general and concise picture.

B.7.4.4.1. Individual Tests

a. Peak Clad Temperatures (PCTs)

TRACE-predicted and measured PCTs are compared for each test in Figure B.7-222 through Figure B.7-229 for all 8 different elevations. In general, PCTs are predicted within a 10% deviation. A slightly larger deviation occurs in the upper part of the core, usually 2.4 to 3.4 m (8 ft to 11 ft) from the bottom of the heated region. In terms of temperatures, a slightly larger deviation occurs in the temperature range of 600 to 1000 K for the tests which have either high flooding rates (Tests 31203 and 31302) or low pressure (Test 31108) and in the temperature range of 900 to 1300 K for the tests which have regular or low flooding rates (Tests 31504 and 31805) or low subcooling (Test 32114). The other two tests (Test 31701 which has a very high flooding rate of 15.5 cm/s (6.1 in/s) and Test 32013 which has high pressure of 0.41 MPa (60 psia)) do not have any point outside of a 10% deviation line.

b. Quench Time

TRACE-predicted and data-based quench times are compared for each test in Figure B.7-230 through Figure B.7-237 for all 8 different elevations. Quench times derived from rod temperature data are averaged at each elevation for each test, and thus each figure has eight points to be plotted. Quench times are predicted within a 10% deviation for four of the eight tests. These are Tests 31203, 31504, 31805, and 32013 which have flooding rates 3.8 cm/s (1.5 inch/s) or less and pressure 0.28 MPa (40 psia) or higher. The remaining 4 tests are 3 high flooding rate tests (Test 31108 (3.1 in/sec), Test 31302 (3.0 in/sec), and Test 31701 (6.1 in/sec)), and one low subcooling test (Test 32114 (10 °F subcooling as opposed to the usual 134 to 143 °F subcooling)). However, the low subcooling test shows that the maximum deviation between data and TRACE is only slightly higher than 10%. For the high flooding rate tests a deviation bigger than 10% is mostly due to the fact that data shows a top quench behavior whereas TRACE does not show such a behavior.

c. Heat Transfer Coefficients (HTCs)

TRACE-predicted and data-derived HTCs are compared for each test in Figure B.7-238 through Figure B.7-245 for all 5 different elevations. The HTCs used in these figures are the average values over some stable period of the reflood process as indicated in a table below.

In all 8 tests the deviations between TRACE-predicted and experimentally-derived HTCs are generally within 35%. In high flooding rate tests TRACE-predicted values are lower than the data

particularly in upper elevations where clad temperatures are over-predicted. This is mainly because the effect of the spacer grid has not been adequately accounted for in TRACE.

Table B.7.2. Time Intervals Used for Computing the Average Heat Transfer Coefficients

Elevation	Time Intervals in Seconds							
	Test 31108	**Test 31203**	**Test 31302**	**Test 31504**	**Test 31701**	**Test 31805**	**Test 32013**	**Test 32114**
1.2192 m (4 ft)	10 - 50	20 - 60	15 - 55	30 - 110	0 - 25	10 - 110	10 - 90	20 - 150
1.8288 m (6 ft)	30 - 130	30 - 170	30 - 110	30 - 220	5 - 40	40 - 270	40 - 180	30 - 300
1.9812 m (6.5 ft)	30 - 150	30 - 200	40 - 120	40 - 260	5 - 50	40 - 320	40 - 220	40 - 350
2.4384 m (8 ft)	30 - 220	40 - 280	40 - 170	40 - 370	5 - 70	40 - 440	40 - 300	40 - 440
3.048 m (10 ft)	30 - 270	40 - 340	40 - 190	40 - 480	10 - 50	60 - 540	40 - 370	40 - 520

B.7.4.4.2. All Eight Tests

a. Peak Clad Temperatures (PCTs)

TRACE-predicted and measured PCTs are compared for all tests in Figure B.7-246 TRACE predicts all PCTs within a 10% deviation except for high elevations (3.0-3.4 m (10-11 ft)) of the core where TRACE over-predicts PCTs mainly because the effect of the spacer grid is not adequately accounted for in the TRACE model. The upper and lower elevations correspond to the low temperature regions because of the low power density. TRACE tends to over-predict PCTs only in the low to moderate temperature regions (600 to 1200 K) while in the upper temperature region (1200 to 1500 K) TRACE tends to predict PCTs correctly. At the highest elevation of 3.5 m (11.5 ft), however, TRACE tends to under-predict PCTs although the deviation is still within 10%. It is not certain what causes TRACE to under-predict PCTs at the highest elevation.

b. Quench Time

TRACE-predicted and data-based quench times are compared for all tests in Figure B.7-247. TRACE predicts all quench times within a 10% deviation except for high elevations (3.0 m (10 ft) or higher) of the core where TRACE over-predicts quench times mainly because the effect of the spacer grid is not adequately accounted for in the TRACE model. As expected, higher clad temperatures predicted lead to slower quench times.

c. Heat Transfer Coefficient (HTC)

TRACE-predicted and data-derived HTCs are compared for all tests in Figure B.7-248. TRACE predicts all HTCs generally within a 35% deviation except for several points mostly at either low elevations (below 2 m (6.5 ft)) of the core where TRACE over-predicts HTCs or higher elevations (3.0 m (10 ft)) of the core where TRACE under-predicts HTCs and where data exhibits a top

quench behavior particularly for high flooding rate tests while TRACE does not show such a top quench behavior.

B.7.5. Assessment Results Summary

The TRACE capability of calculating the reflood process is assessed against data from 8 FLECHT-SEASET tests covering the flooding rate from 2.10 cm/sec (0.81 in/sec) to 15.50 cm/sec (6.10 in/sec), the upper plenum pressure from 0.13 MPa (19 psia) to 0.41 MPa (60 psia), the inlet coolant temperature from 33 °C (91 °F) to 125 °C (257 °F), and the initial rod peak power at 2.3 kW/m (0.70 kW/ft). The capability is summarized in terms of several important output variables as indicated below.

B.7.5.1. Peak Clad Temperatures (PCTs) and Quench Times of Heater Rods

Heater rod PCTs are plotted and compared between TRACE-calculated values and data at 8 different axial levels in the core ranging from 0.61 m (2 ft) to 3.51 m (11.5 ft) from the bottom of the heated core. In all 8 tests TRACE predicts heater rod PCTs reasonably well for the lower 50% of the core (at or below 6.0 ft elevation of the 12 ft core) where the largest discrepancy is 32 °C (58 °F) of over-prediction in a low pressure (19 psia) test. Above 1.8 m (6.0 ft) but at or below 3.4 m (11.0 ft) from the bottom of the heated core, TRACE over-predicts PCTs up to 157 °C (283 °F) which occurs at the 3.0 m (10 ft) elevation in a low pressure (19 psia) test. At 3.5 m (11.5 ft), TRACE under-predicts PCTs up to 83 °C (149 °F) for low flooding rate tests (flooding rates equal to or less than 2.4 cm/s), but over-predicts PCTs up to 51 °C (92 °F) for high flooding rate tests (flooding rates at or higher than 3.84 cm/s (1.5 inch/s)).

Both TRACE-calculated PCTs and measured PCTs decrease as the flooding rates increase, as expected, although the PCT difference between two high flooding rates of 7.65 cm/s (3.01 inch/s) and 15.5 cm/s (6.10 inch/s) is not significant. The TRACE predictive capability does not vary with the flooding rates even though there is a tendency that a high flooding rate (6.10 inch/s) test provides better predictions. The elevation where the PCT occurs tends to shift downward from 1.98 m (6.5 ft) to 1.83 m (6 ft) as the flooding rate increases beyond 7.7 cm/s (3 in/s).

Heater rods cool down faster than data after the clad temperatures reach the maximum in nearly all cases. The cool-down rate accelerates and becomes considerably faster than data particularly at elevations between 1.2 m (4 ft) and 2.4 m (8 ft) from the bottom of the heated core.

The TRACE predictive capability is better as the system pressure increases. For instance, at the 3.0 m (10 ft) elevation where TRACE over-prediction is greatest, the over-prediction of PCTs changes from 157 °C, to 21-135 °C, and to 50 °C, respectively, as the pressure increases from 0.13 MPa (19 psia), to 0.28 MPa (40 psia), and to 0.41 MPa (60 psia).

The TRACE predictive capability of PCTs for the low subcooling (5 C of subcooling) test (Test 32114) is somewhat worse than the other five high subcooling (51 to 53 °C of subcooling) tests with the same pressure of 0.28 MPa (40 psia).

The TRACE prediction of quench times varies from an earlier quench (up to 32 sec) to a later quench (up to 179 sec). Quench times are predicted reasonably well below 1.98 m (6.5 ft) for all 8 tests, with the maximum deviation being 31 sec of later-than-data quench. Above 1.98 m and for flooding rates less than 7.65 cm/s (3.01 inch/s), quench time differences between data and TRACE cover a range from an earlier quench of 13 sec to a later quench of 94 sec. For flooding rates at or above 7.65 cm/s, data shows a top quench and thus an earlier-than- TRACE (up to 179 sec) quench at high elevations at or above 2.4 m (8 ft). As in the case of PCTs, quench times are predicted better for the high pressure test (60 psia) where the deviation between TRACE and data is within 25 sec for all elevations.

Overall, both PCTs and quench times are predicted by TRACE within a 10% deviation for nearly all cases with a small fraction being excepted.

B.7.5.2. Vapor Temperatures

Vapor temperatures are plotted and compared between TRACE-calculated values and data at two different axial levels in the core; 1.83 m (6 ft) and 3.05 m (10 ft) from the bottom of the heated core. TRACE predicts peak vapor temperatures within 80 °C of deviation at the 1.8 m (6 ft) elevation and within 160 °C of deviation at the 3.0 m (10 ft) elevation for flooding rates equal to or less than 3.84 cm/s (1.51 inch/s) whereas for flooding rates higher than 3.84 cm/s TRACE predicts peak vapor temperatures within 110 °C at 1.8 m and within 195 °C at the 3.0 m elevation. For the high pressure (60 psia) test case, TRACE predicts vapor temperatures within 80 °C. In all cases, the measured vapor temperatures decrease much more quickly than TRACE-calculated values after going through the maximum values. This is consistent with TRACE-calculated rod temperatures cooling off more quickly than the data. However, since vapor temperature measurements are not considered very accurate, the TRACE capability of predicting vapor temperatures can not be assessed accurately.

B.7.5.3. Quench Profile

TRACE predicts the quench front propagation very well within a few percent for the lower 70% of the core. However, in the upper part of the core the discrepancy between the data and TRACE becomes large because of the lack of the top quench modeling in TRACE, particularly for high reflooding rate cases. The worst discrepancy occurs at the top elevation in the highest flooding rate case (15.5 cm/s (6.10 inch/s)) where the data shows both top and bottom quench (e.g., 1.1 m and 3.4 m elevations quenched at the same time at 28 sec) while TRACE shows only a bottom quench (e.g., 1.1 m elevation quenched at 28 sec). All three tests which have a flooding rate of 7.65 cm/s (3.01 inch/s) or higher show a very pronounced top quench behavior while TRACE does not.

B.7.5.4. Liquid Mass Carried out of the Bundle

TRACE predicts more liquid carried out of the bundle than what data shows. However, the liquid collection data appears to have a large uncertainty and seems to show too low values. TRACE-predicted liquid mass which is carried out of the bundle and which is integrated from time zero is higher than the data by 27 to 50% at the end of the tests. The high flooding rate (higher than 3.01 inch/s) tests and the low subcooling test all have a 40-50% discrepancy at the end of the tests. Two tests (31108 and 31203) have an obvious error in measurements because the amount of liquid collected does not increase much after some period of time. Since the liquid carryout collection data appears to have a large uncertainty, we can not judge how accurately TRACE predicts the liquid carryout. However, comparisons between the TRACE-predicted and measured DPs of the core suggest that TRACE would show either the correct amount or slightly less amount of liquid carryout than the data, if the liquid collection data were obtained accurately, since the liquid remaining in the upper plenum is insignificant.

B.7.5.5. Differential Pressures (DPs)

Differential pressures are plotted and compared between TRACE-calculated values and data at three different axial levels in the core; the entire core height of 3.66 m (12 ft), 1.83 to 2.13 m (6 to 7 ft), and 3.05 to 3.35 m (10 to 11 ft) from the bottom of the heated core. In terms of the overall DP for the entire core, TRACE over-predicts it for six of the eight tests, slightly under-predicts it for one test, and closely matches it for the remaining one test. A discrepancy between the prediction and the data varies from an over-prediction of up to 3.5 kPa for the lowest pressure (19 psia) test to an under-prediction of up to 0.2 kPa for the highest pressure (60 psia) test. In all but one test (the lowest pressure test) the discrepancy between the prediction and the data is less than the measurement uncertainty of 2.7 kPa. DP predictions in other elevations also reasonably match the data.

Since accelerational and frictional pressure losses are insignificant, DPs can be directly converted to the mass of liquid in the core. This means that in nearly all cases TRACE predicts either a correct amount or slightly more liquid than data being accumulated in the core which implies that the predicted amount of liquid carried out of the bundle would be the same as or slightly less than the data if the data were accurately obtained. The amount of liquid remaining in the upper plenum at the end of the tests is negligible since essentially all liquid drains out to the collection tank.

B.7.5.6. Heat Transfer Coefficients (HTCs)

HTCs are plotted and compared between TRACE-calculated values and data at five different axial levels in the core; 1.22 m (4 ft), 1.83 m (6 ft), 1.98 m (6.5 ft), 2.44 m (8 ft), and 3.05 m (10 ft) from the bottom of the heated core. TRACE tends to predict HTCs fairly well in the lower half of the core during the first half of the reflood period while it tends to predict HTCs well in the upper half of the core during the latter half of the reflood period.

Overall, TRACE predicts HTCs generally within a 35% deviation. The predicted and data-derived HTCs vary usually between 50 and 250 W/(m^2-C). During the cool-down period after clad temperatures turn-around, TRACE-predicted HTCs are usually higher than the data and thus predicted clad temperatures decrease faster than the data although the rate of the temperature decrease becomes slower as quench times are approached.

B.7.5.7. Comparison between Window and Linux Results

Comparisons of TRACE calculation results obtained from a Window computer and those from a Linux computer indicate that both results are essentially the same. For example, in PCT calculations there is a 3 K difference out of 1200 K which is a 0.25% difference. In addition, there are some differences in oscillatory values of differential pressures and heat transfer coefficients, but their average values are essentially the same.

B.7.6. Conclusion

The assessment of TRACE Version 5.0 against 8 FLECHT-SEASET tests shows that TRACE is capable of calculating the reflood process correctly, in general, although there are some deficiencies. The most important deficiency is the over-prediction of clad temperatures as much as 160 °C (288 °F) in the upper part of the core, usually at elevations of 3.0-3.4 m (10-11 ft) from the bottom of the 3.66 m (12 ft) core. This deficiency may be caused by lack of a spacer grid model in TRACE. It is well known that spacer grids promote heat exchanges between rods and the surrounding fluid, particularly in the droplet dispersed flow regime, and thus clad temperatures at high elevations will be lowered if a spacer grid model is implemented in TRACE. The second deficiency is the fact that TRACE does not have the capability of simulating top quench behavior. In high reflooding rate tests the data clearly shows top quench behavior by exhibiting quench front proceeding from both top and bottom regions toward the middle region. Another minor deficiency is the fact that TRACE retains slightly more liquid in the core than what differential pressure data indicates. However, this discrepancy between TRACE and data is not significant, less than 13%. Furthermore, if a differential pressure measurement uncertainty is applied, the maximum deviation reduces from 13% to 3%.

B.7.7. References

1 Loftus, M.J. et al., “PWR FLECHT SEASET Unblocked Bundle, Forced and Gravity Reflood Task Data Report”, Vol. 1 and 2, NUREG/CR-1532, June 1980

2 Rhee, G. S. and J. H. Jeong, “TRACE Calculation Notebook for FLECHT-SEASET Test Simulations”, Rev. 5, ADAMS ML071430006, March 2007.

3 Robb, K. and S. Bajorek, "Calculation Notebook for Heat Transfer Coefficients Generated with IHCP1D for FLECHT SEASET Reflood Tests", August 17, 2006.

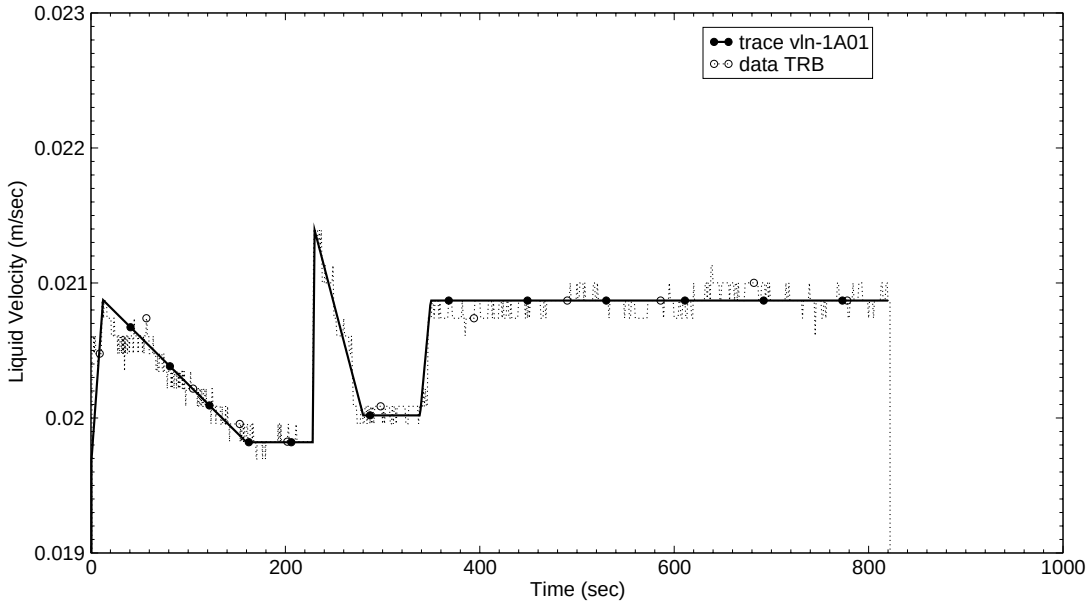

Figure B.7-6. Liquid Inlet Flow Rate for Test 31805

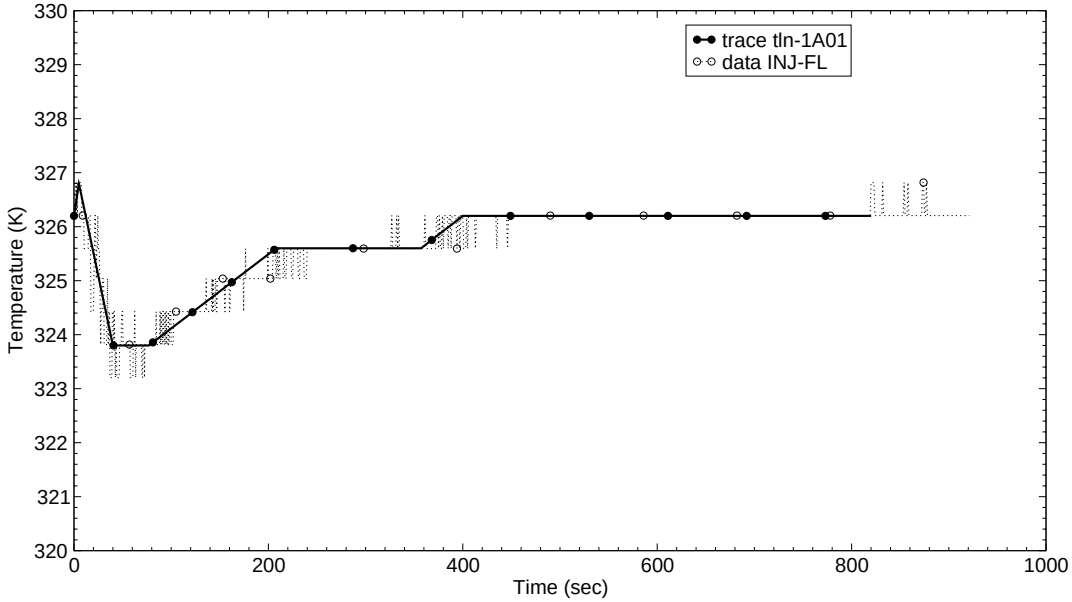

Figure B.7-7. Liquid Inlet Temperature for Test 31805

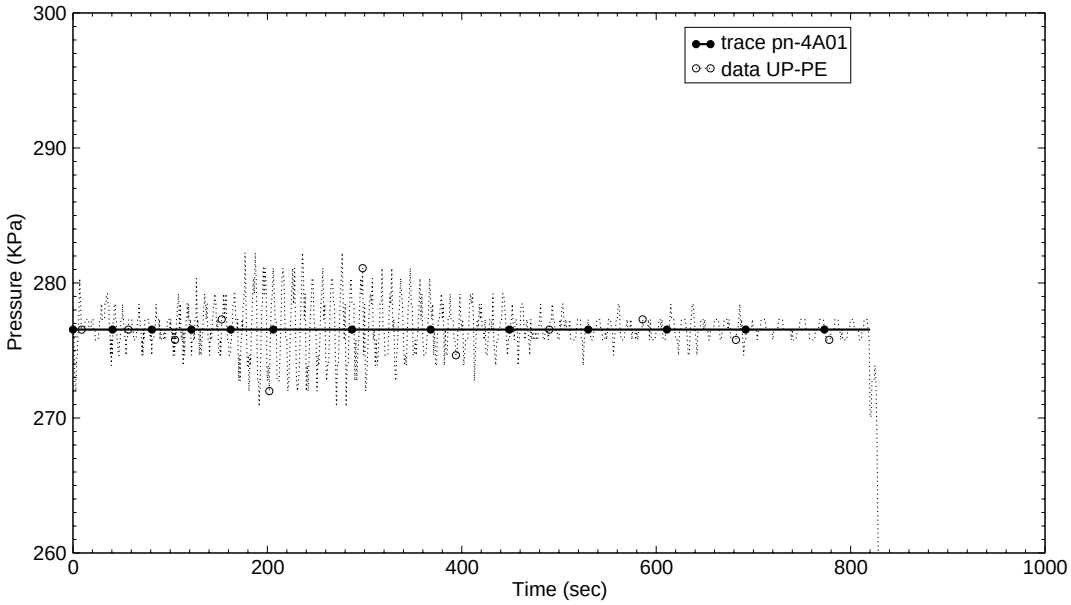

Figure B.7-8. Upper Plenum Exit Pressure for Test 31805

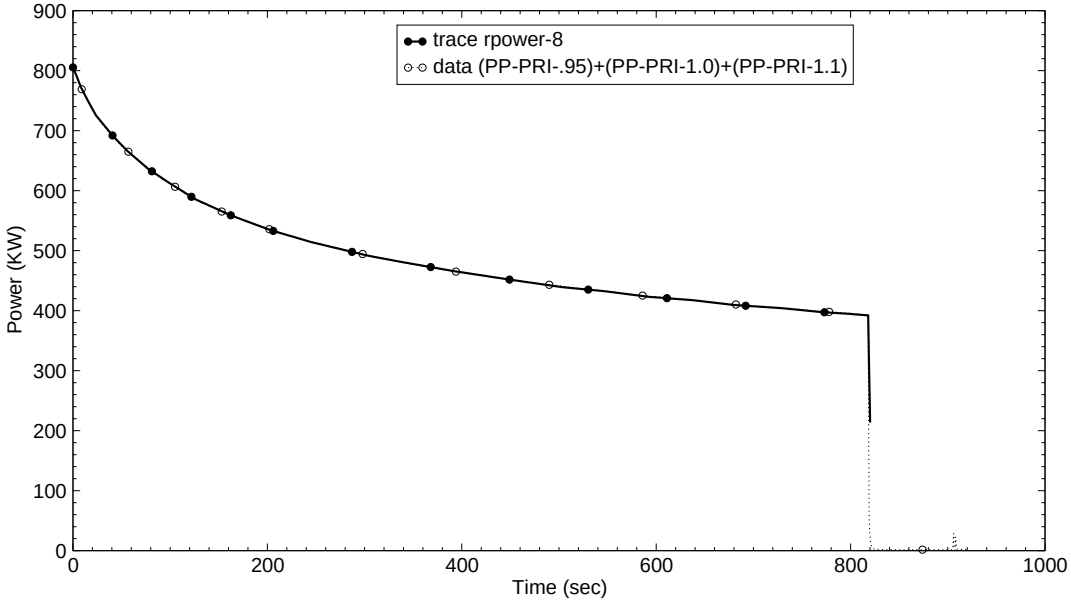

Figure B.7-9. Total Power to the Rod Bundle for Test 31805

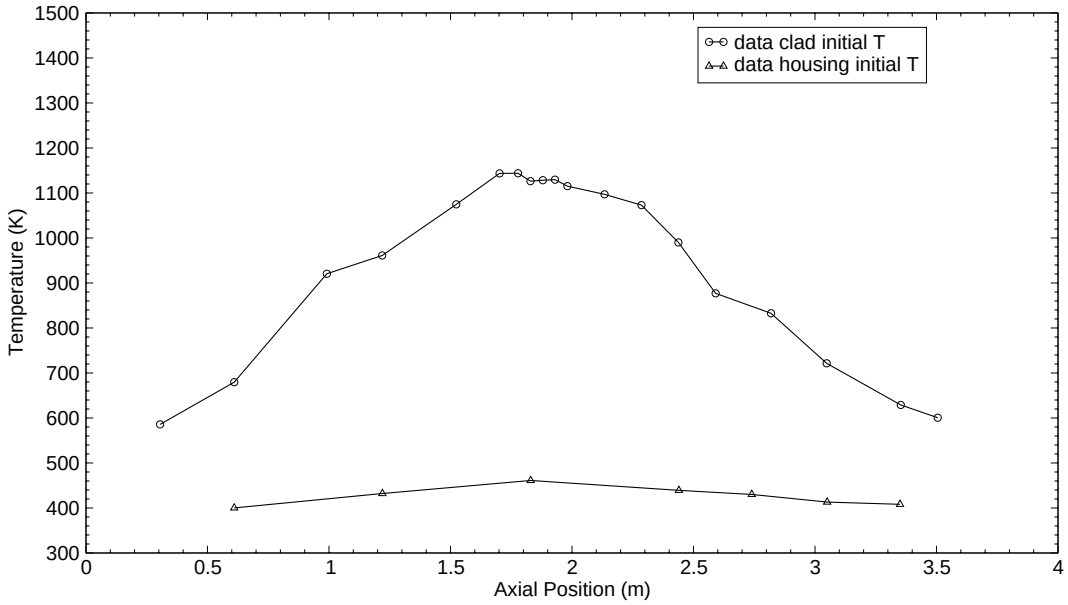

Figure B.7-10. Heater Rod Clad and Housing Initial Temperatures for Test 31805

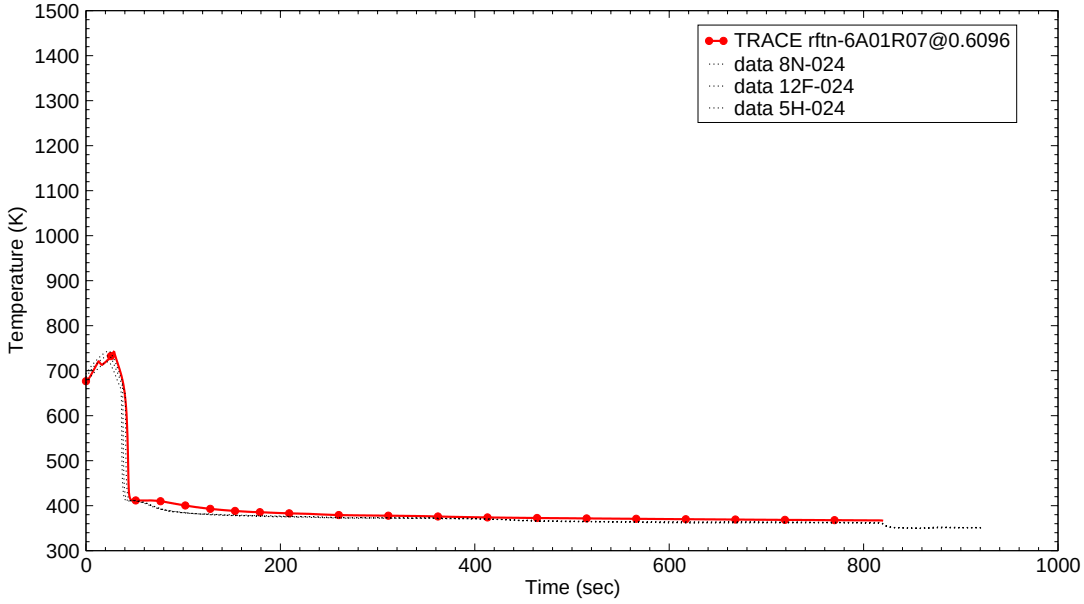

Figure B.7-11. Rod Clad Temperatures at 2 ft from Heated Bottom for Test 31805

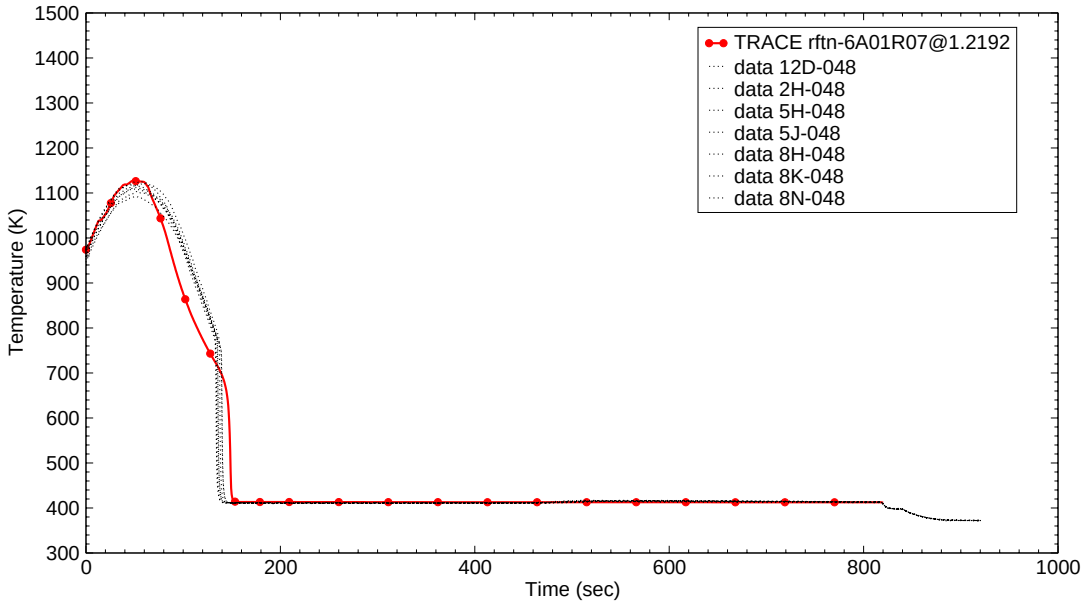

Figure B.7-12. Rod Clad Temperatures at 4 ft from Heated Bottom for Test 31805

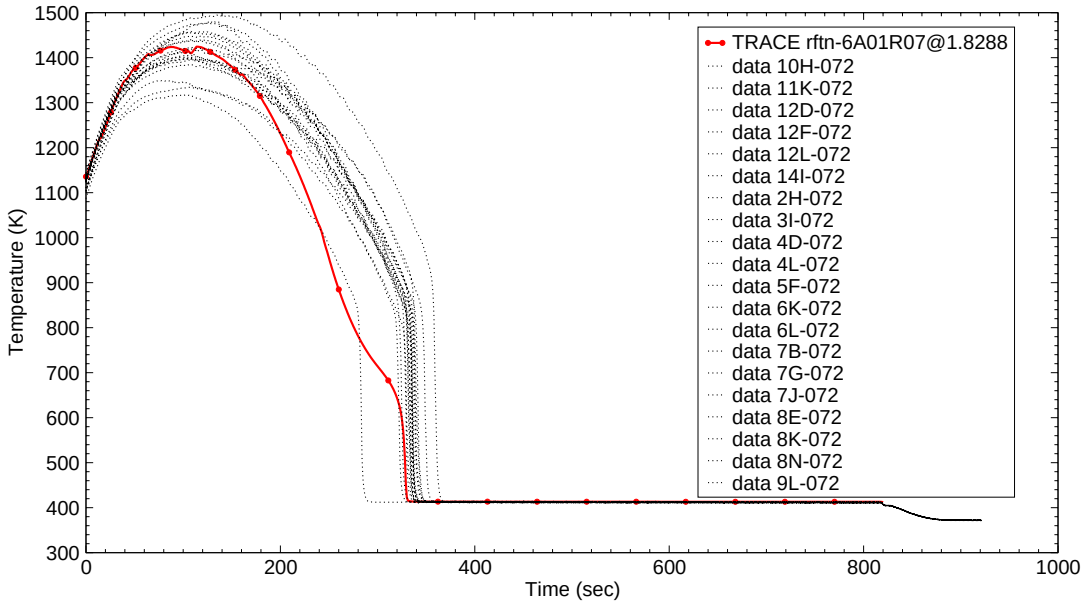

Figure B.7-13. Rod Clad Temperatures at 6 ft from Heated Bottom for Test 31805

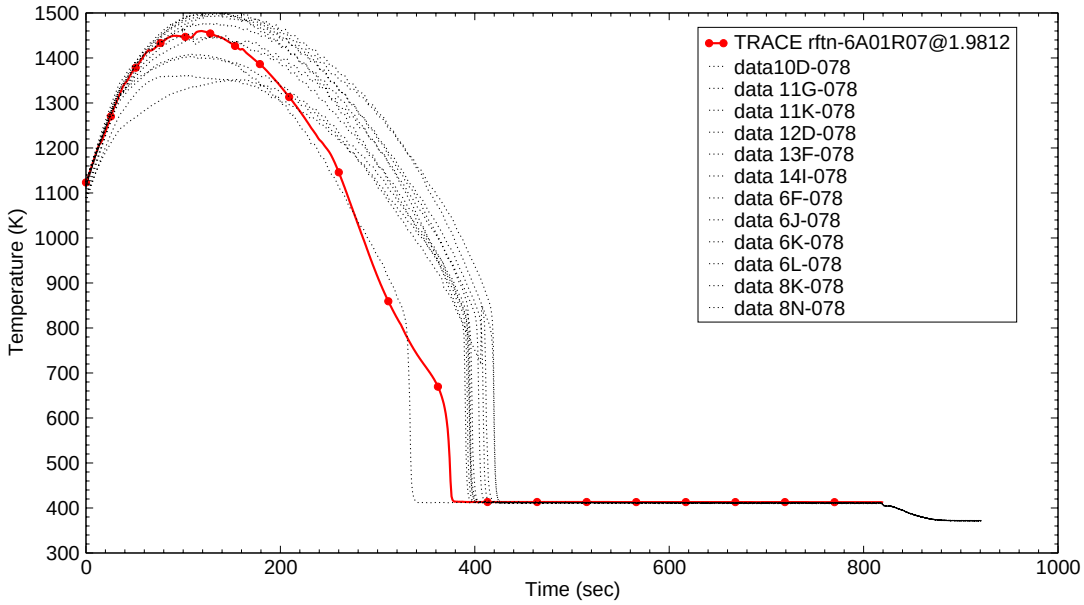

Figure B.7-14. Rod Clad Temperatures at 6.5 ft from Heated Bottom for Test 31805

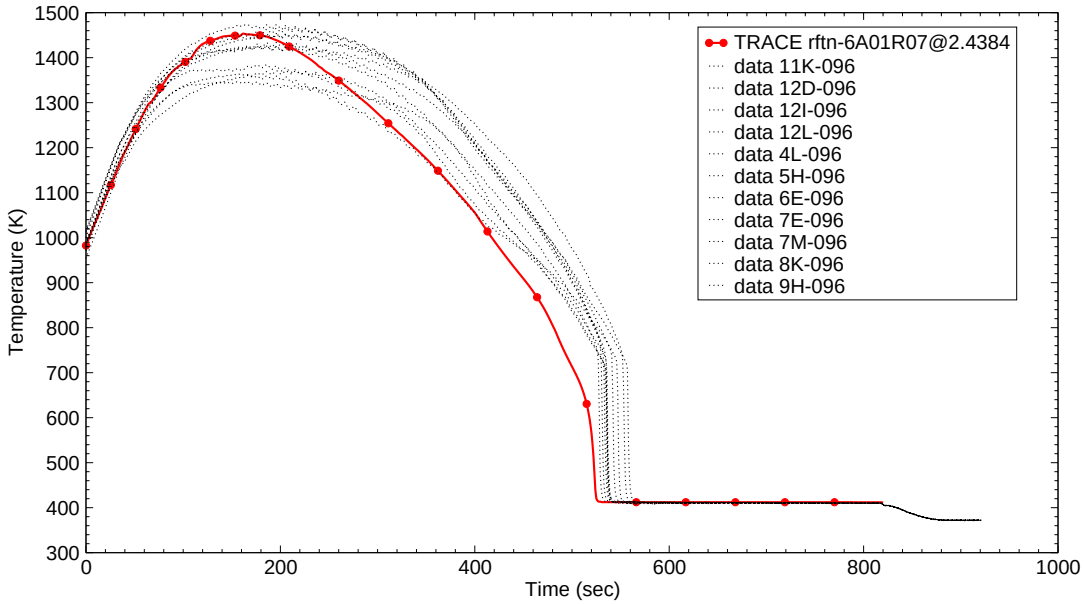

Figure B.7-15. Rod Clad Temperatures at 8 ft from Heated Bottom for Test 31805

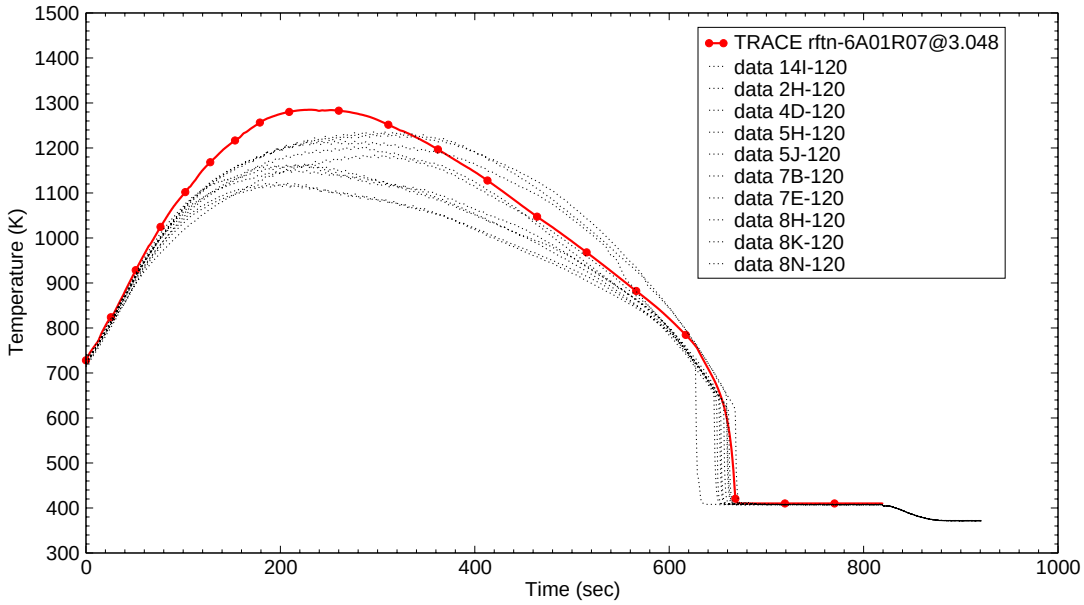

Figure B.7-16. Rod Clad Temperatures at 10 ft from Heated Bottom for Test 31805

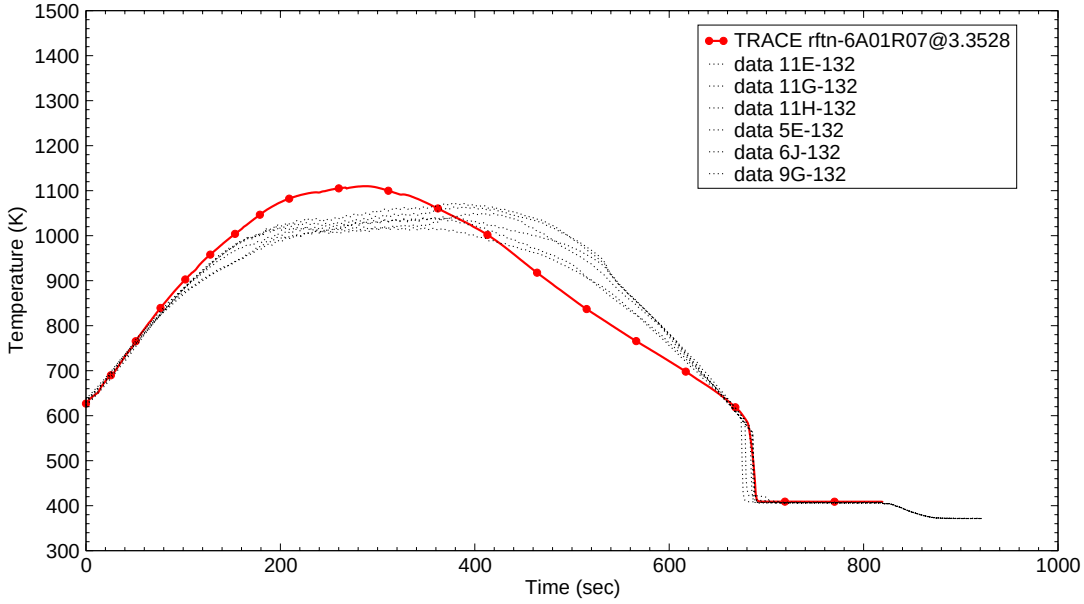

Figure B.7-17. Rod Clad Temperatures at 11 ft from Heated Bottom for Test 31805

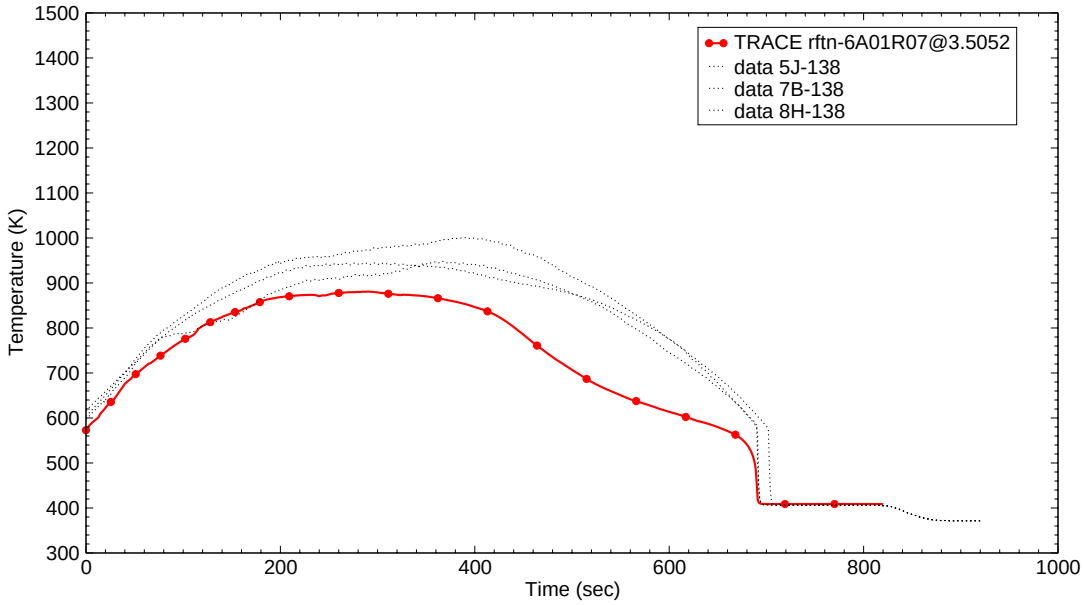

Figure B.7-18. Rod Clad Temperatures at 11.5 ft from Heated Bottom for Test 31805

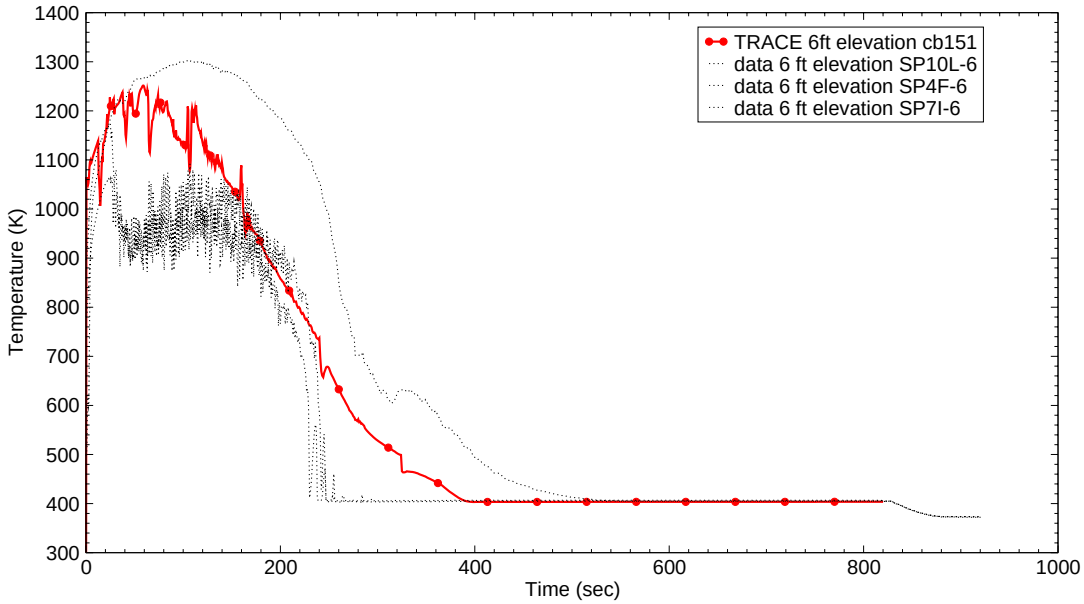

Figure B.7-19. Vapor Temperatures at 6 ft from Heated Bottom for Test 31805

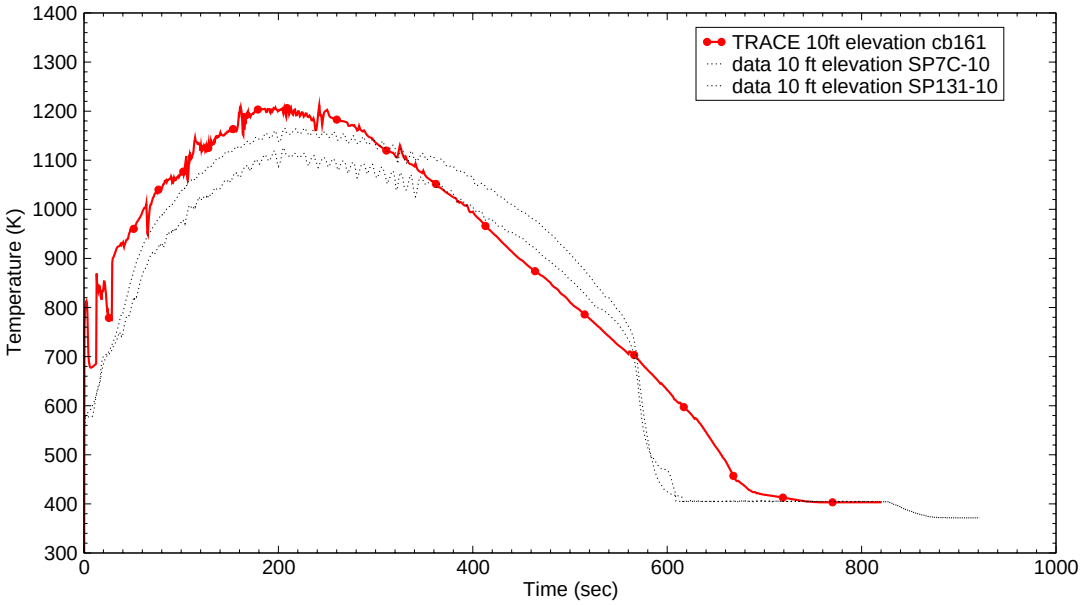

Figure B.7-20. Vapor Temperatures at 10 ft from Heated Bottom for Test 31805

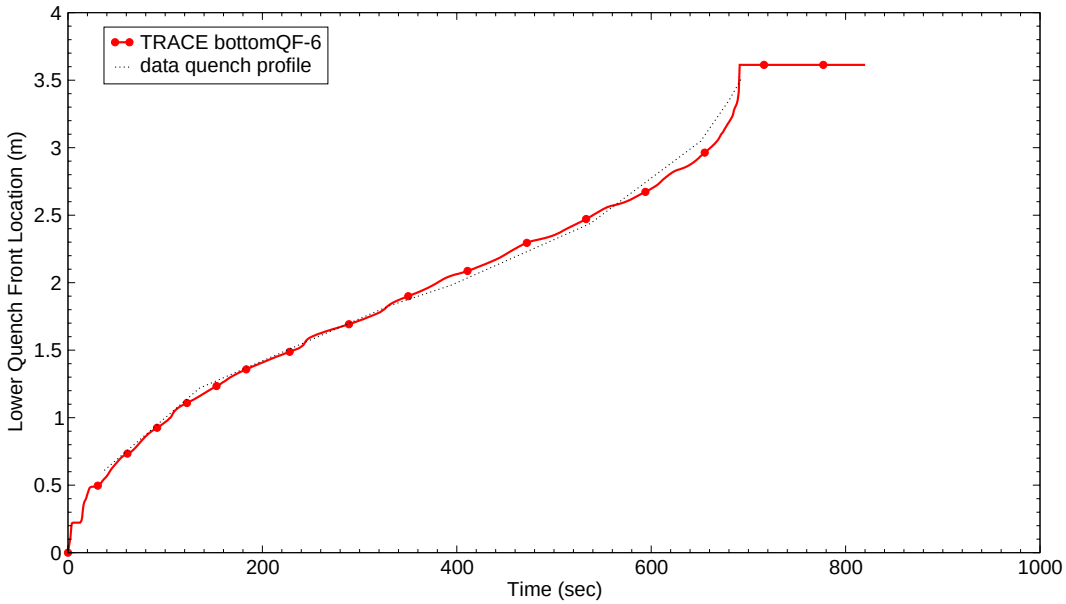

Figure B.7-21. Quench Profile as a Function of Time for Test 31805

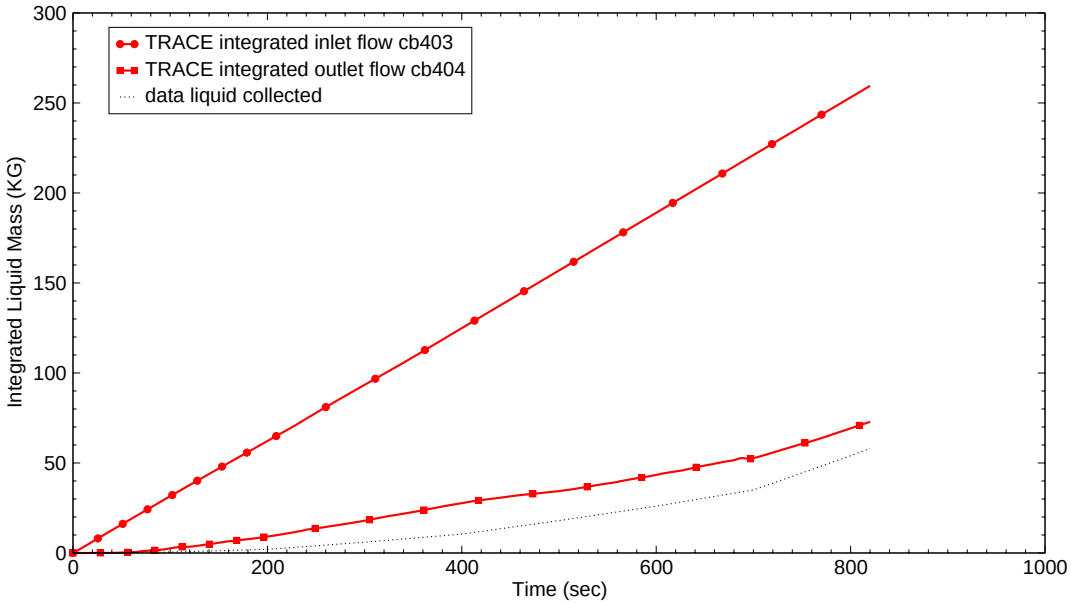

Figure B.7-22. Integrated Liquid Mass Flow into and out of Bundle for Test 31805

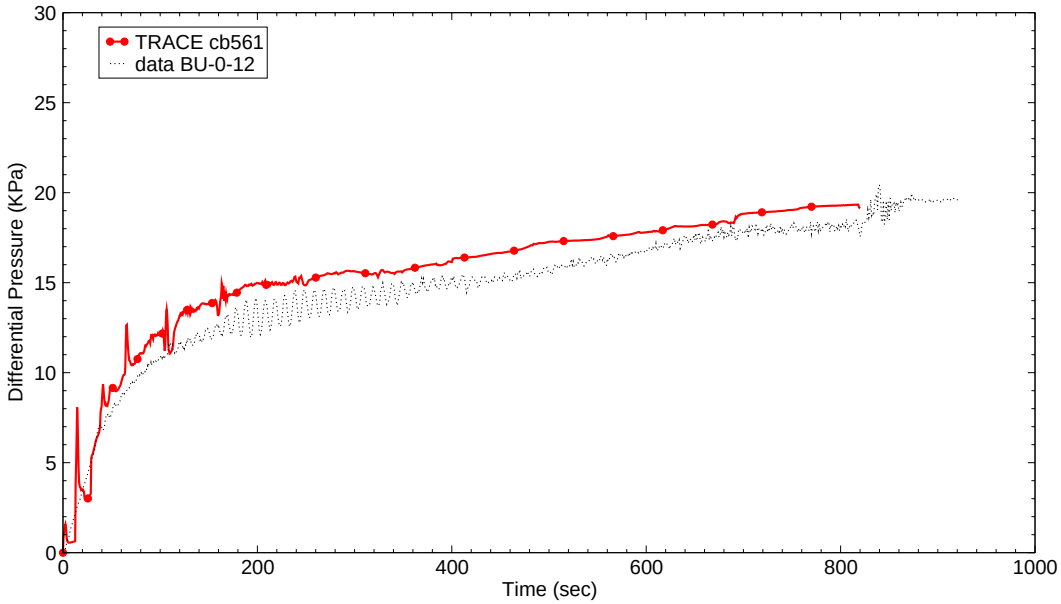

Figure B.7-23. Differential Pressure for the Entire 12 ft Core for Test 31805

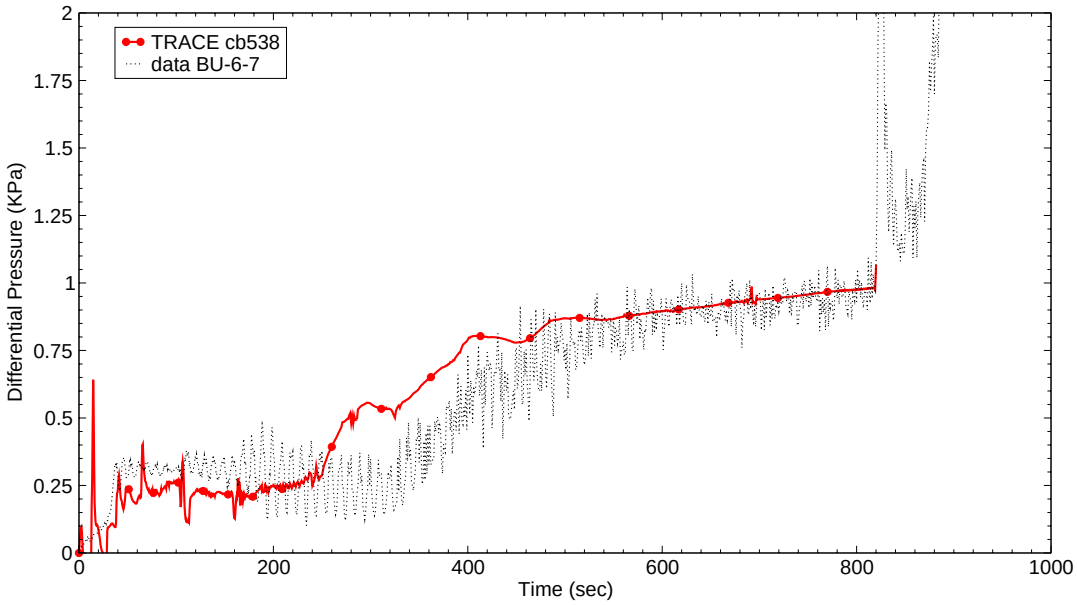

Figure B.7-24. Differential Pressure at 6-7 ft Elevation for Test 31805

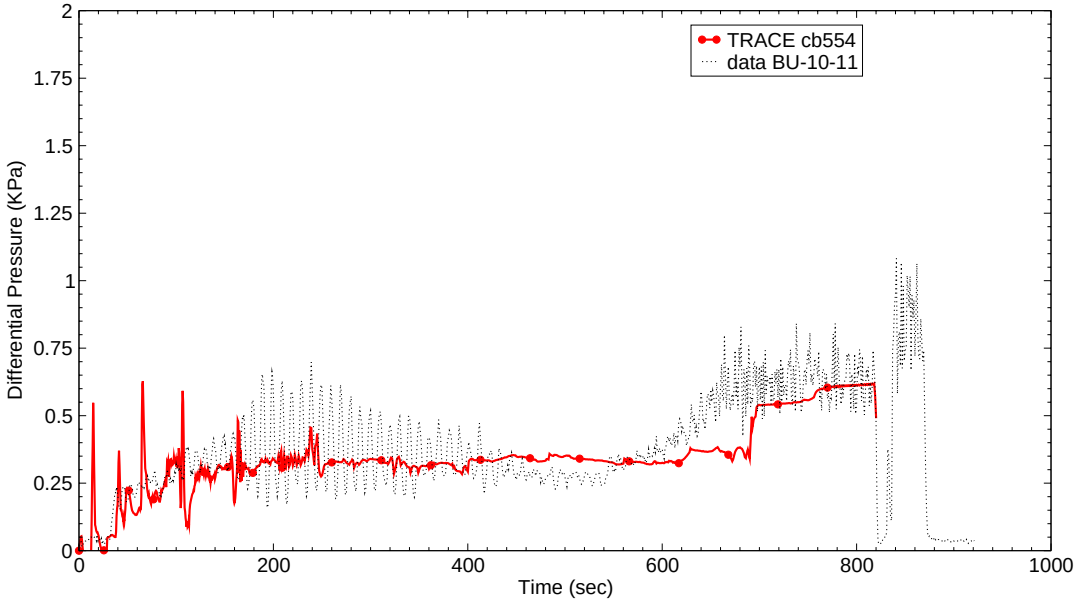

Figure B.7-25. Differential Pressure at 10-11 ft Elevation for Test 31805

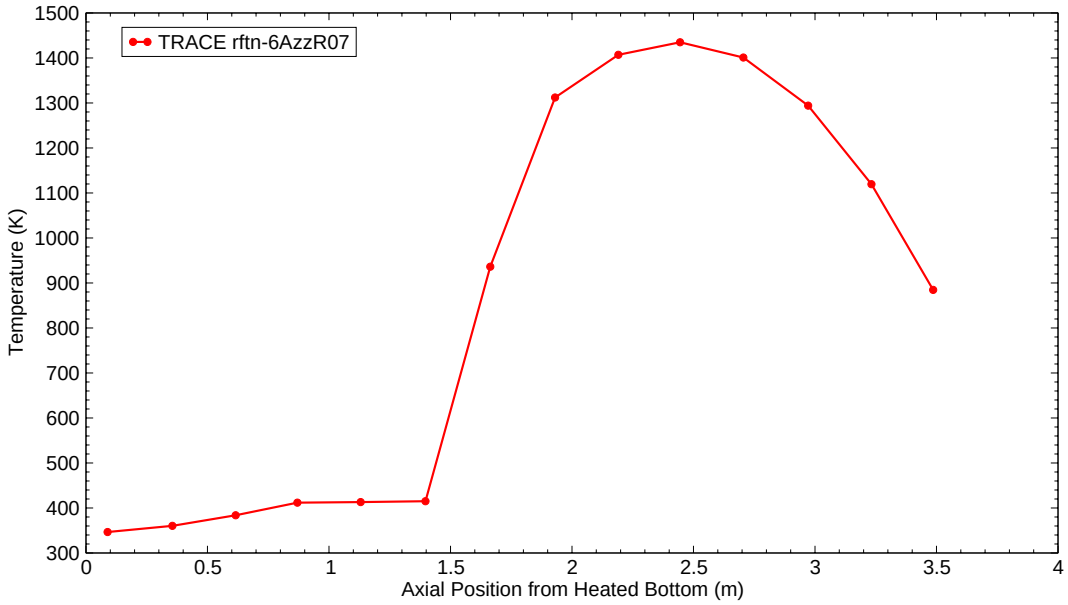

Figure B.7-26. Clad Temperature Profile at 200 sec after Reflood Start for Test 31805

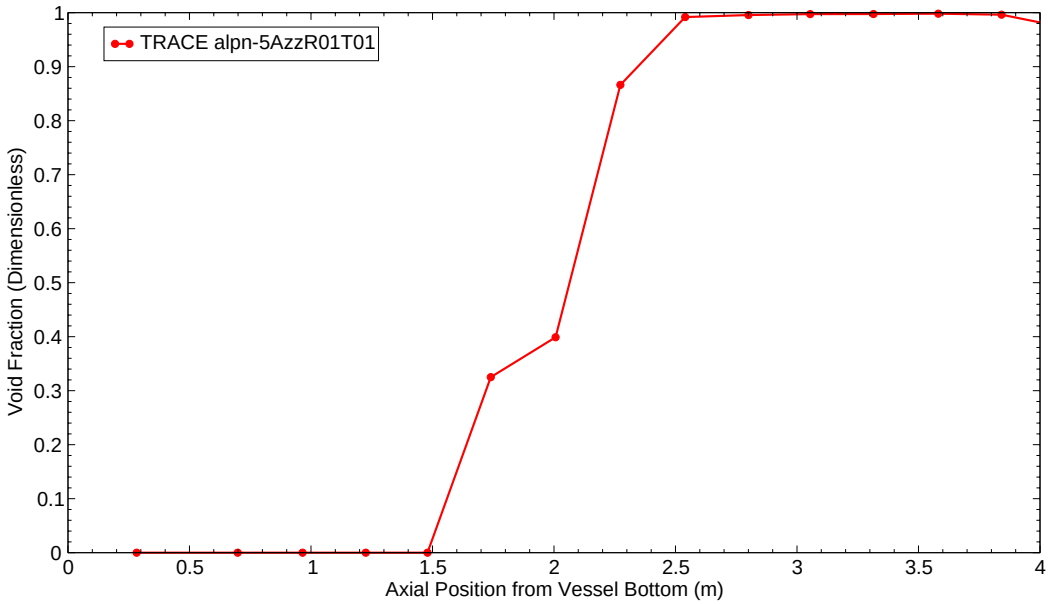

Figure B.7-27. Void Fraction Profile at 200 sec after Reflood Start for Test 31805

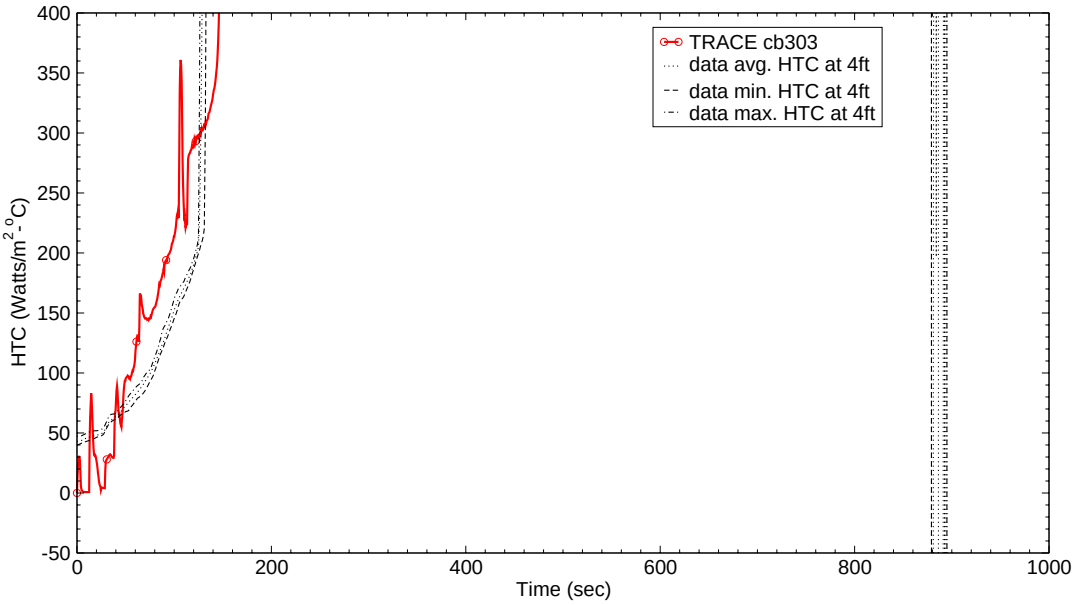

Figure B.7-28. Heat Transfer Coefficient at 4 ft from Heated Bottom for Test 31805

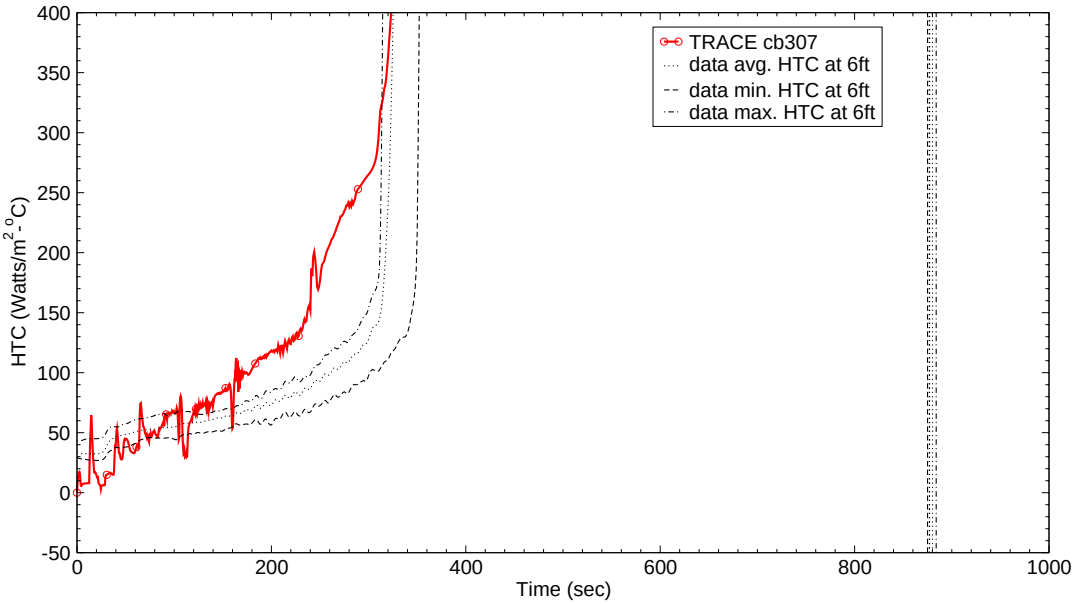

Figure B.7-29. Heat Transfer Coefficient at 6 ft from Heated Bottom for Test 31805

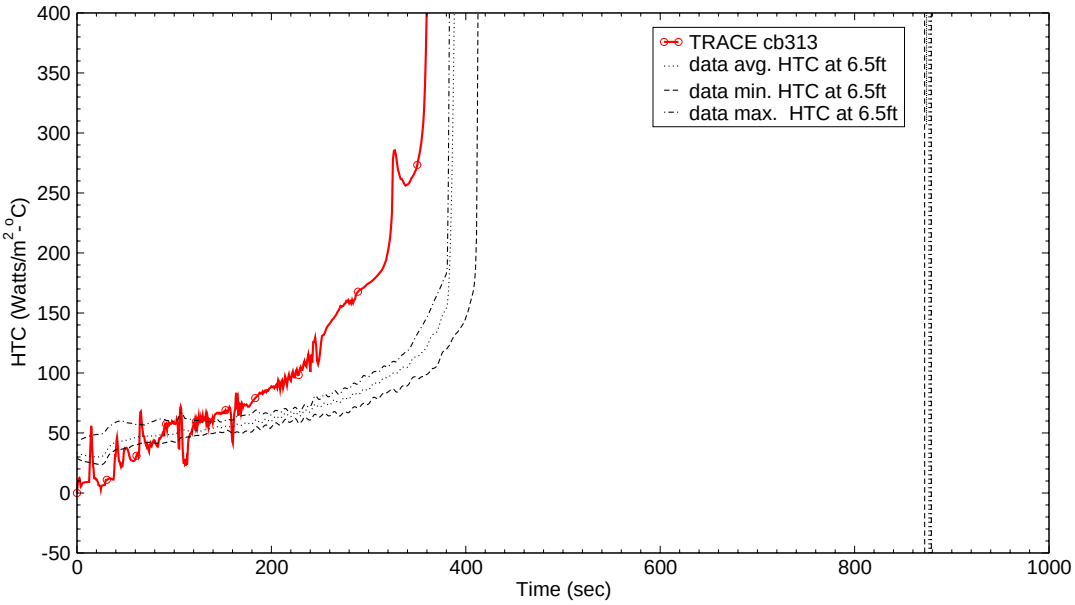

Figure B.7-30. Heat Transfer Coefficient at 6.5 ft from Heated Bottom for Test 31805

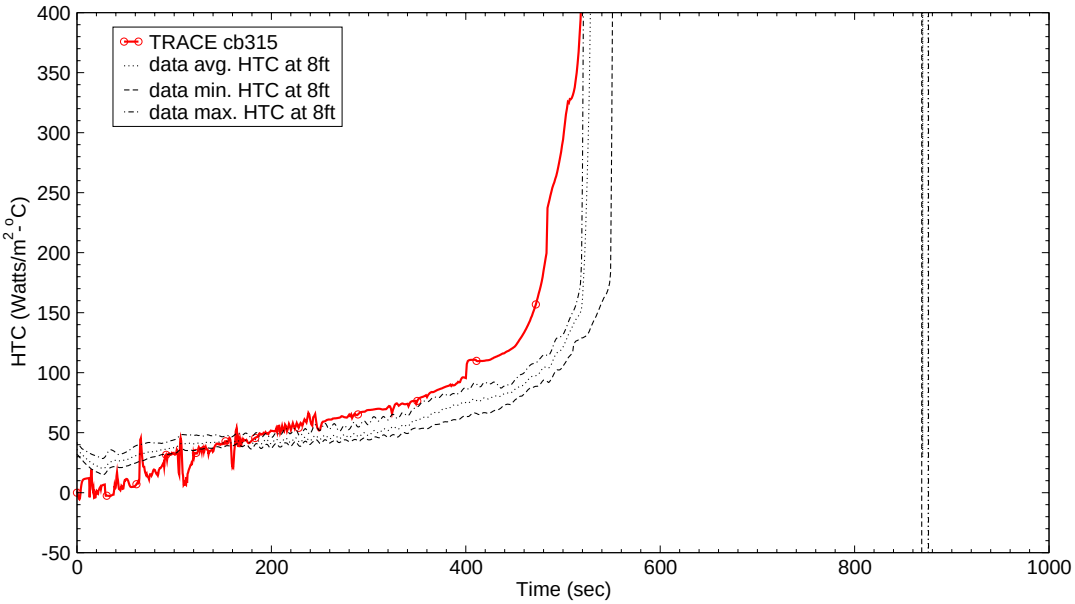

Figure B.7-31. Heat Transfer Coefficient at 8 ft from Heated Bottom for Test 31805

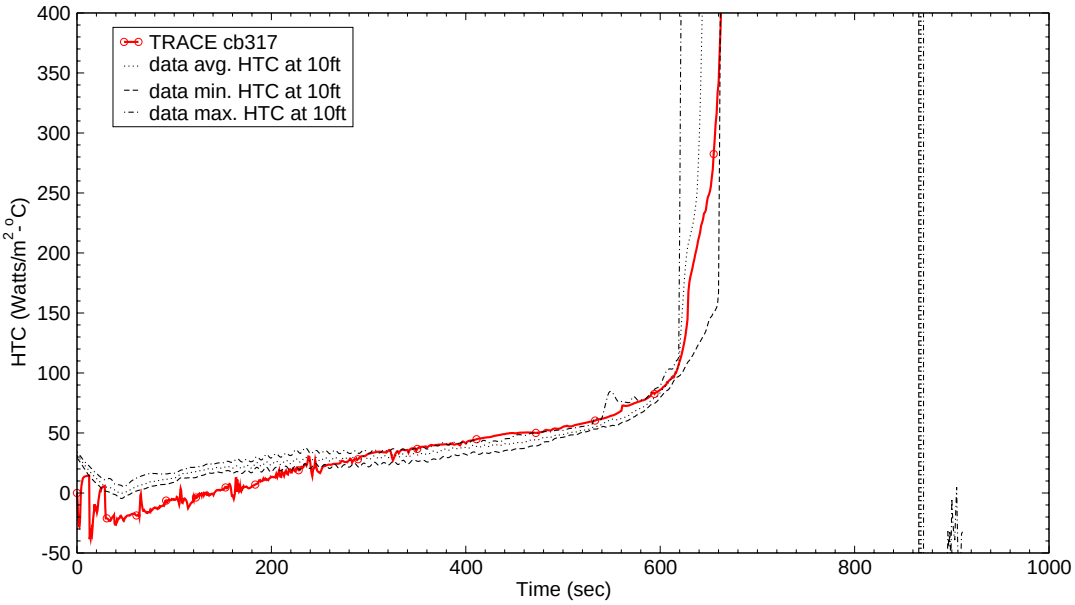

Figure B.7-32. Heat Transfer Coefficient at 10 ft from Heated Bottom for Test 31805

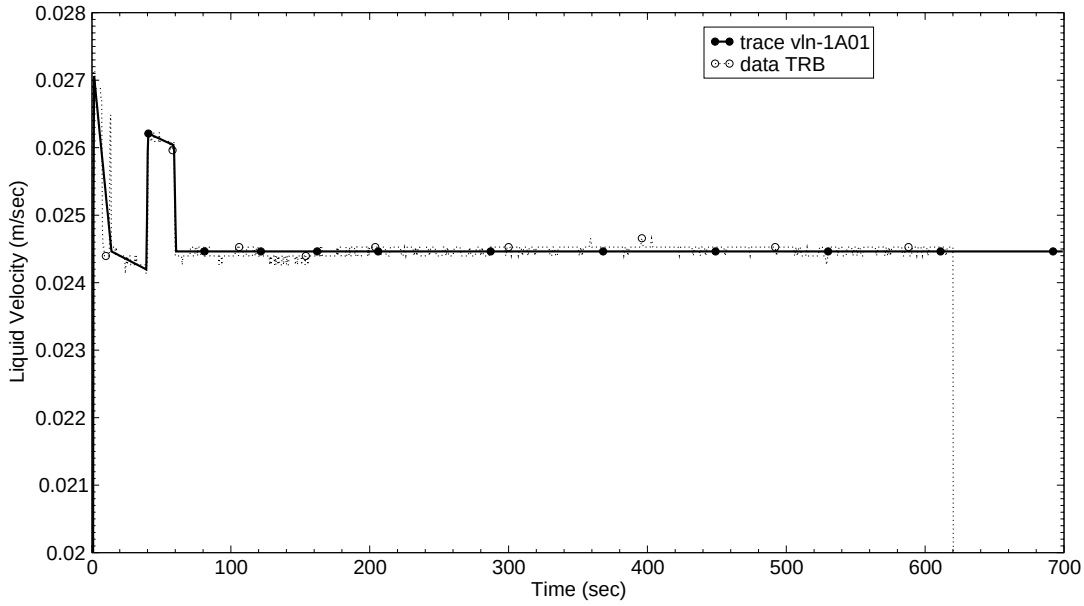

Figure B.7-33. Liquid Inlet Flow Rate for Test 31504

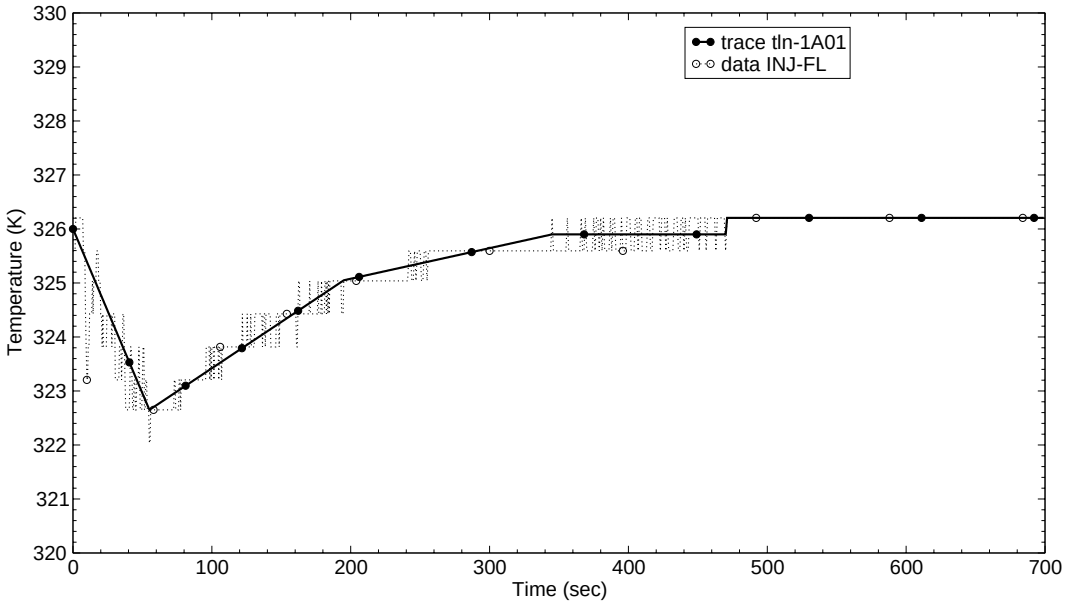

Figure B.7-34. Liquid Inlet Temperature for Test 31504

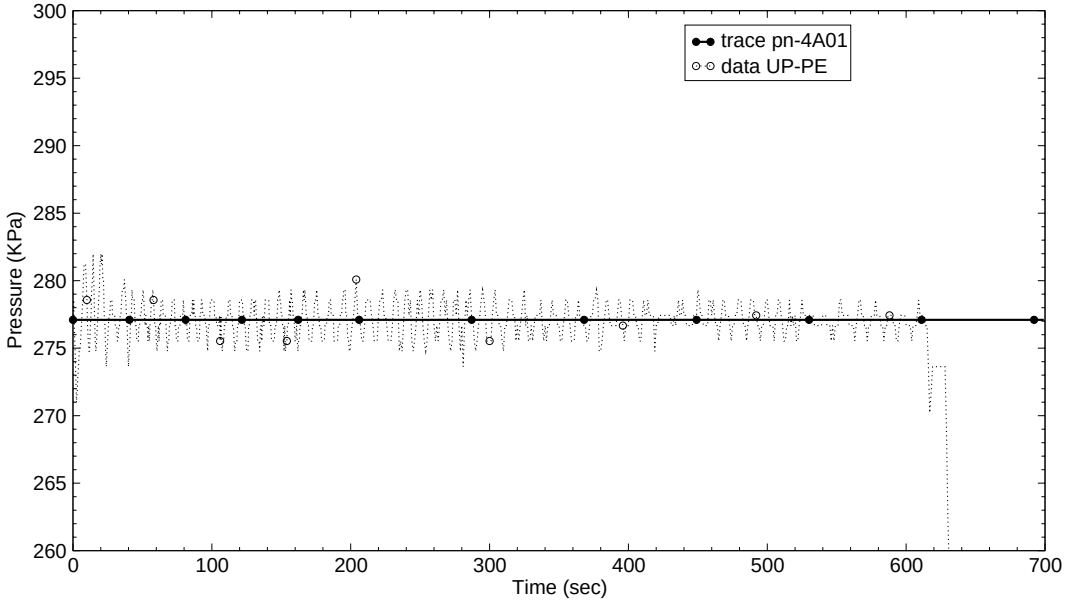

Figure B.7-35. Upper Plenum Exit Pressure for Test 31504

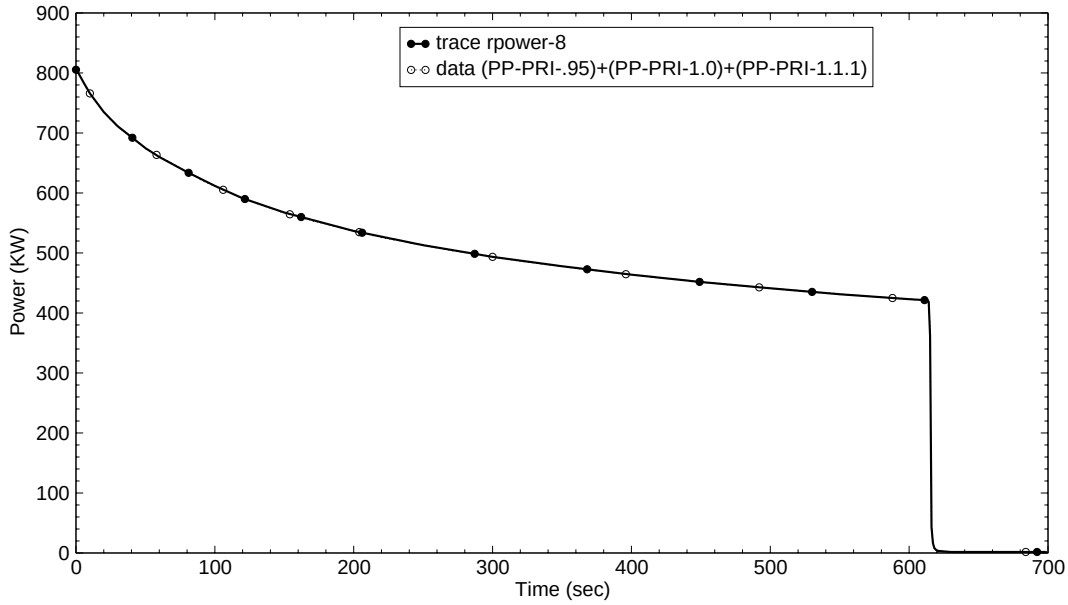

Figure B.7-36. Total Power to the Bundle for Test 31504

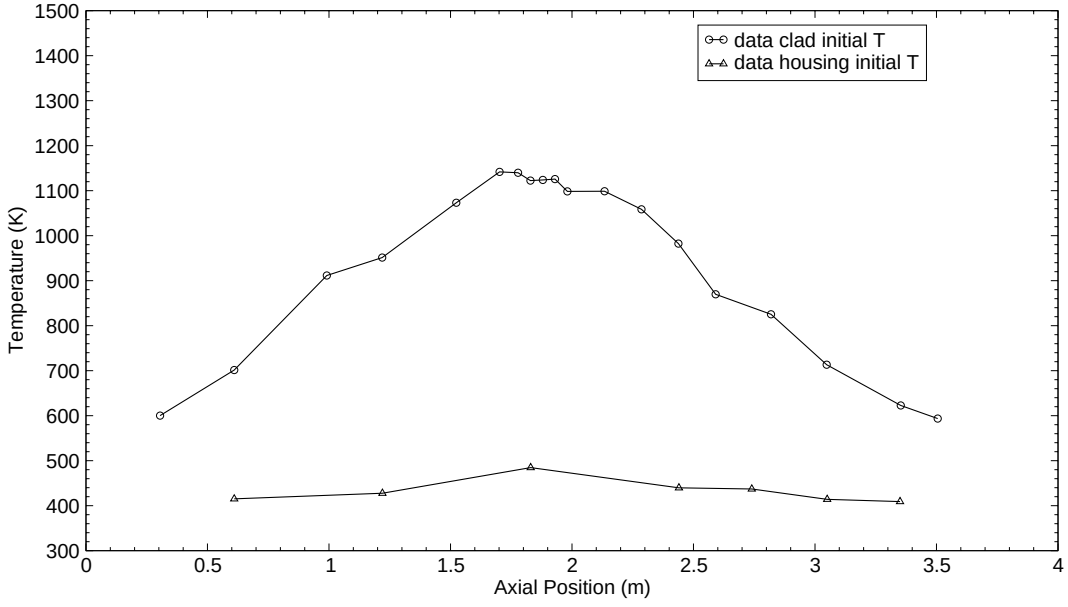

Figure B.7-37. Heater Rod Clad and Housing Initial Temperatures for Test 31504

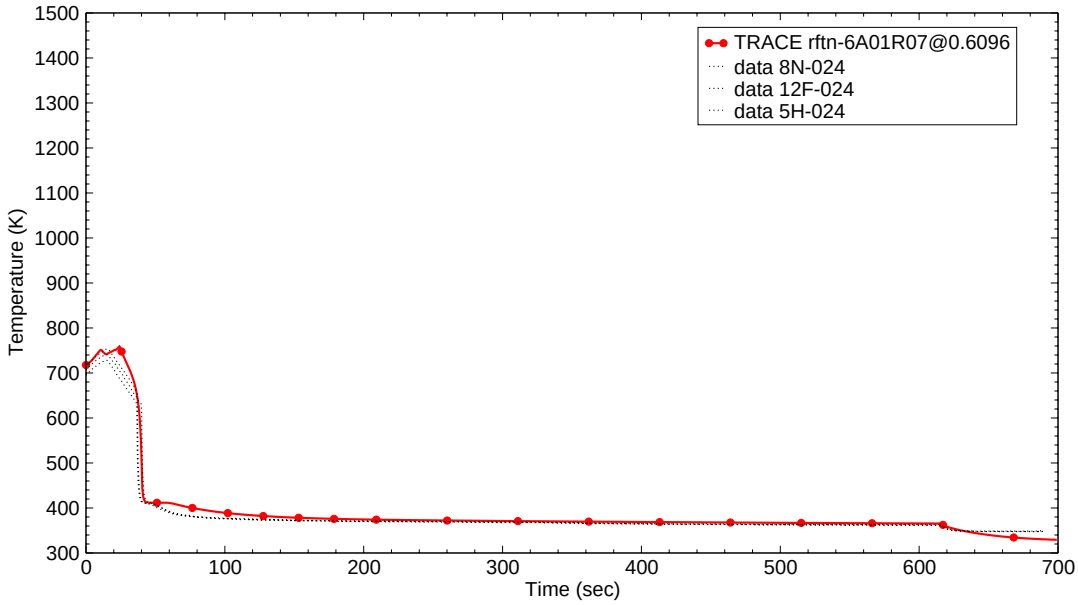

Figure B.7-38. Rod Clad Temperatures at 2 ft from Heated Bottom for Test 31504

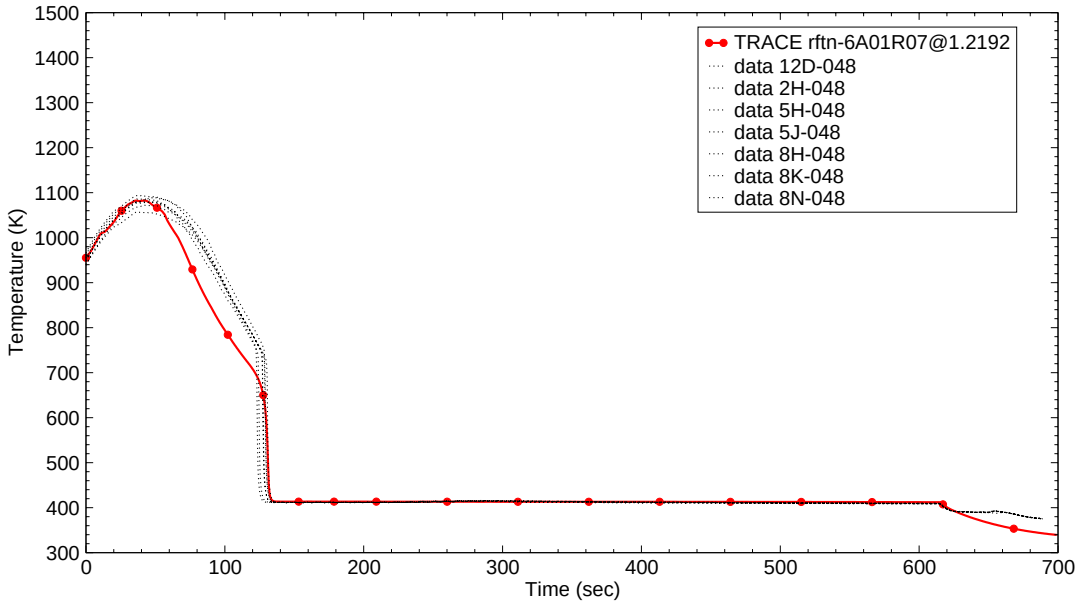

Figure B.7-39. Rod Clad Temperatures at 4 ft from Heated Bottom for Test 31504

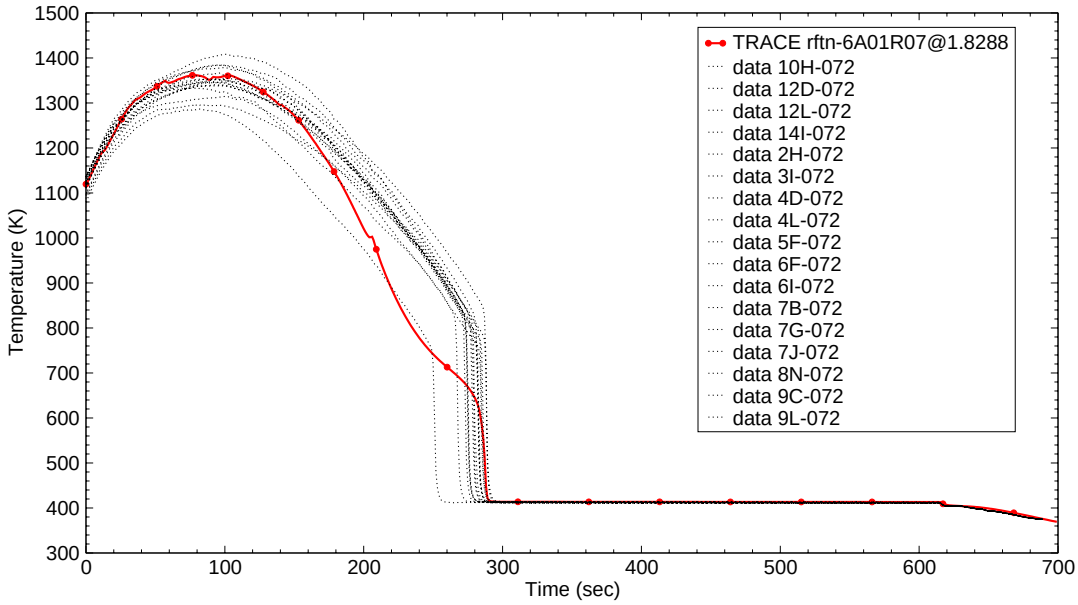

Figure B.7-40. Rod Clad Temperatures at 6 ft from Heated Bottom for Test 31504

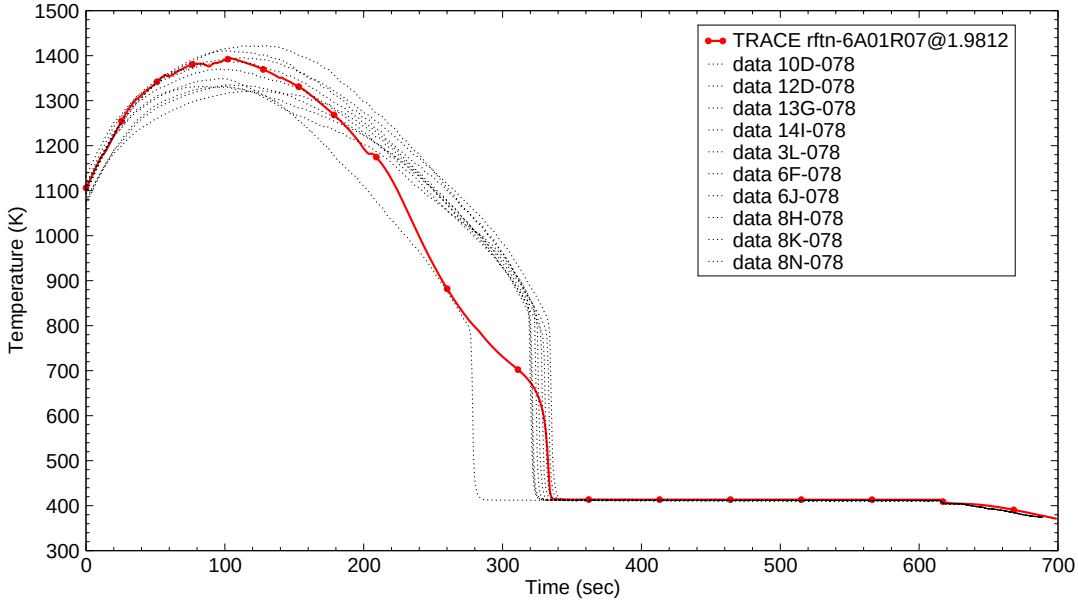

Figure B.7-41. Rod Clad Temperatures at 6.5 ft from Heated Bottom for Test 31504

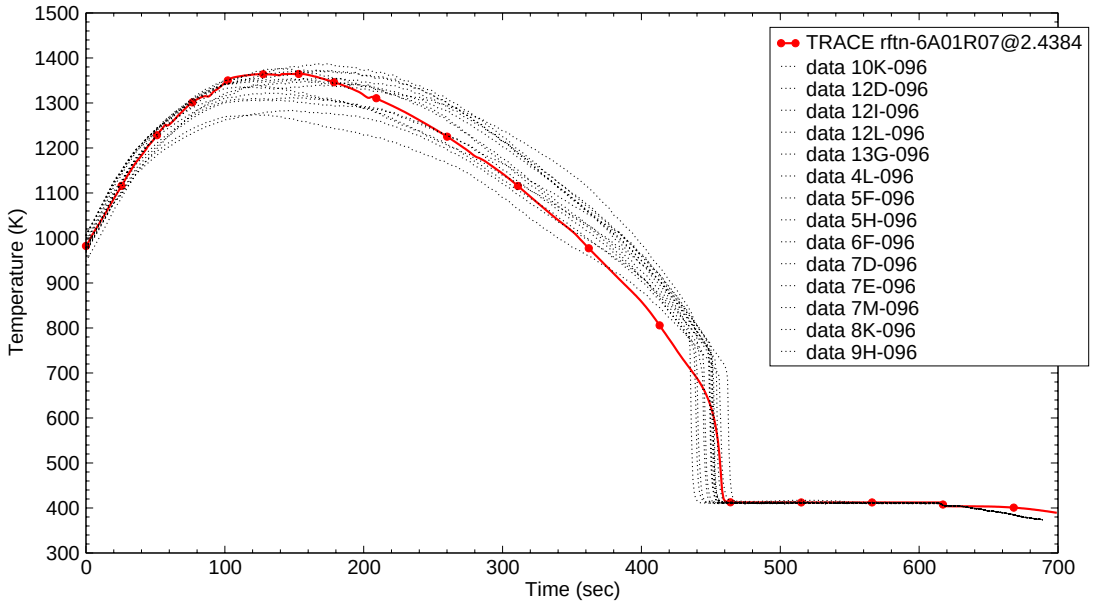

Figure B.7-42. Rod Clad Temperatures at 8 ft from Heated Bottom for Test 31504

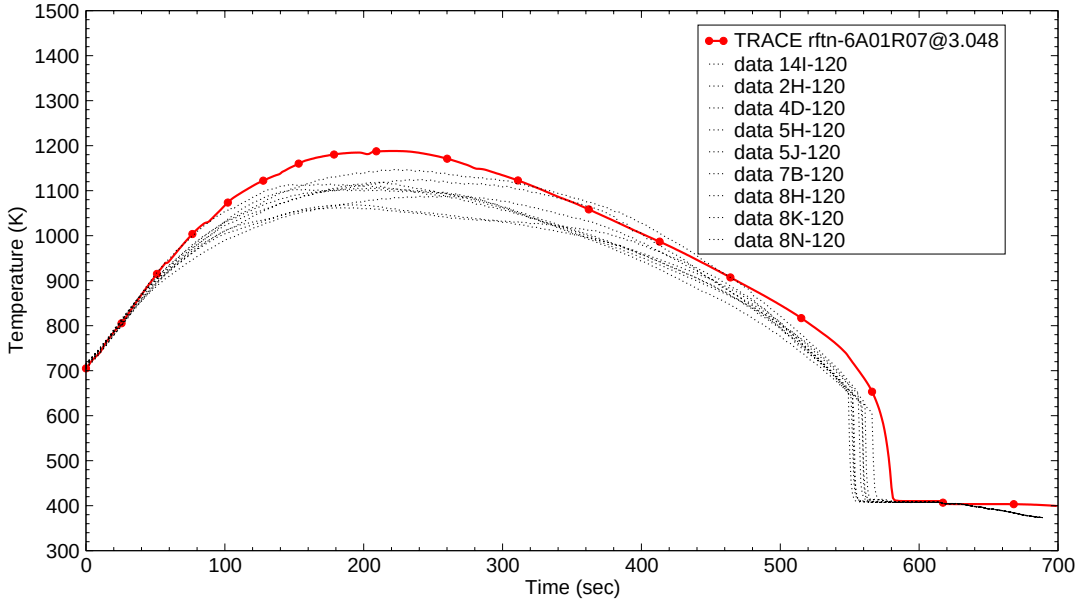

Figure B.7-43. Rod Clad Temperatures at 10 ft from Heated Bottom for Test 31504

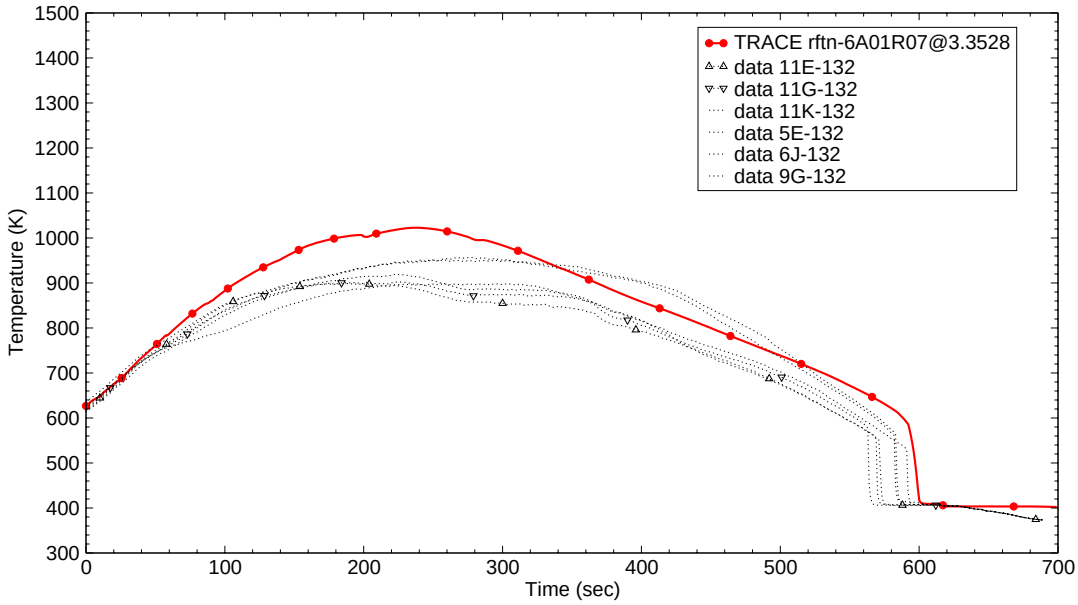

Figure B.7-44. Rod Clad Temperatures at 11 ft from Heated Bottom for Test 31504

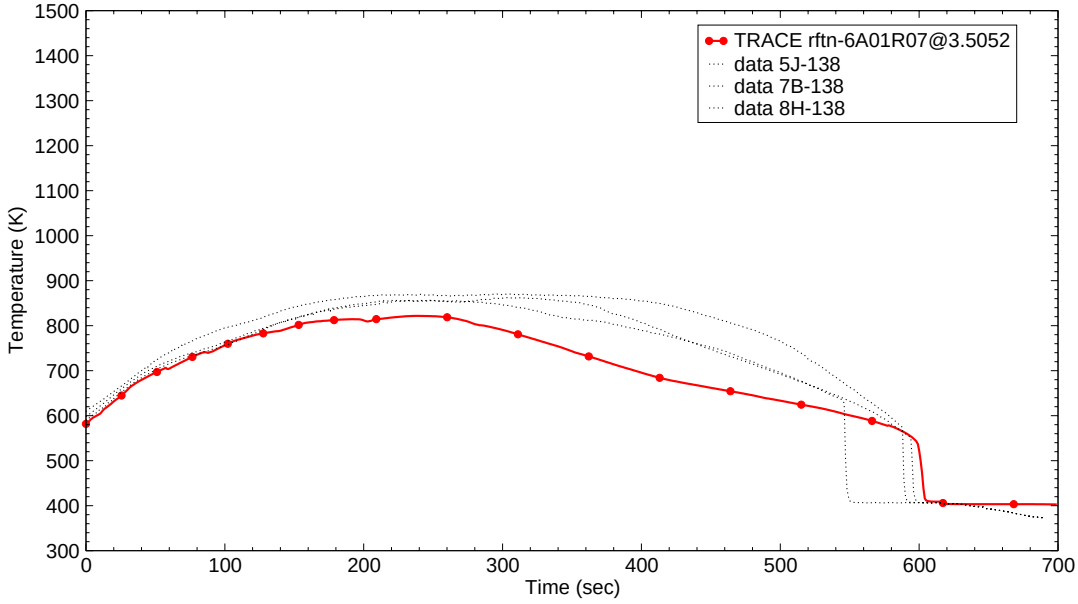

Figure B.7-45. Rod Clad Temperatures at 11.5 ft from Heated Bottom for Test 31504

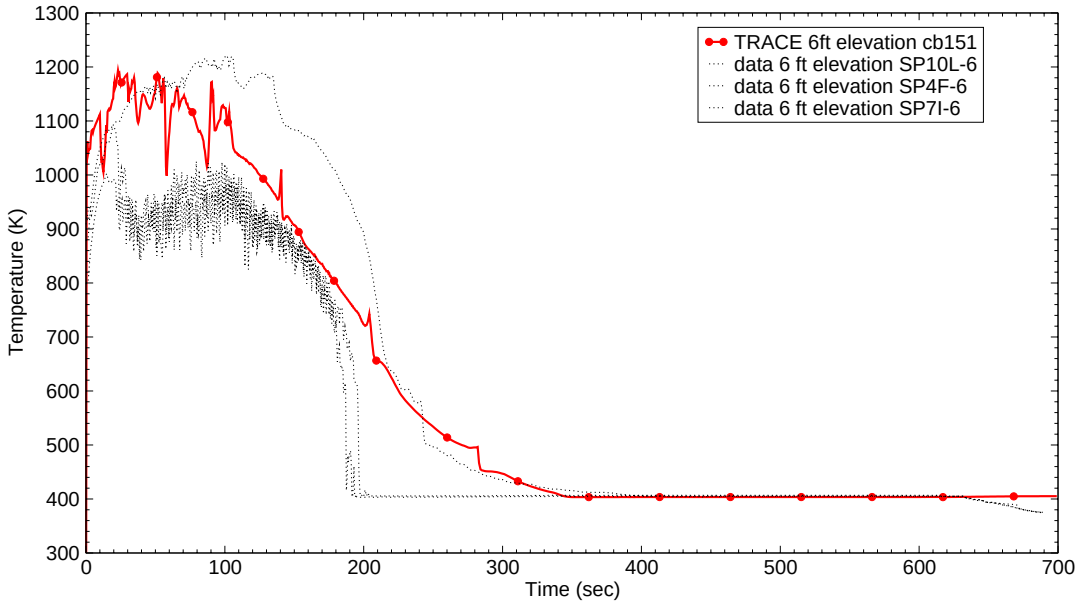

Figure B.7-46. Vapor Temperatures at 6 ft from Heated Bottom for Test 31504

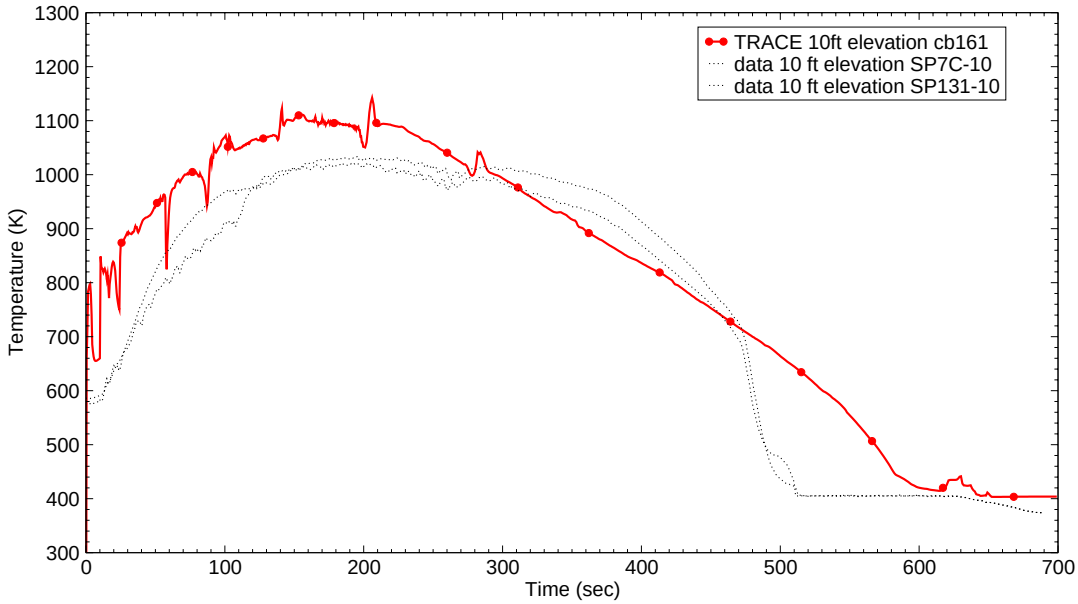

Figure B.7-47. Vapor Temperatures at 10 ft from Heated Bottom for Test 31504

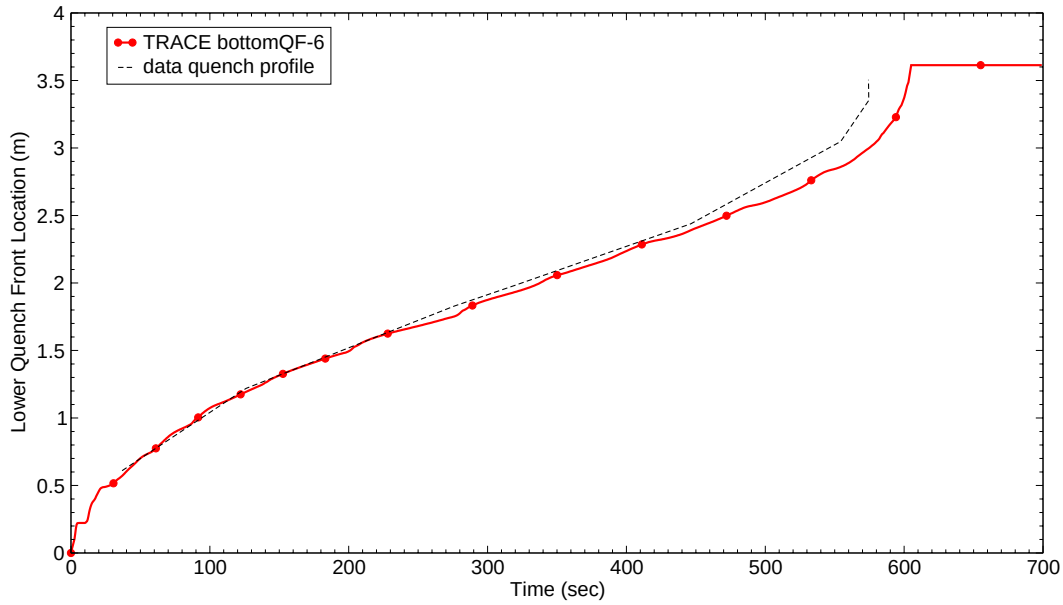

Figure B.7-48. Quench Profile as a Function of Time for Test 31504

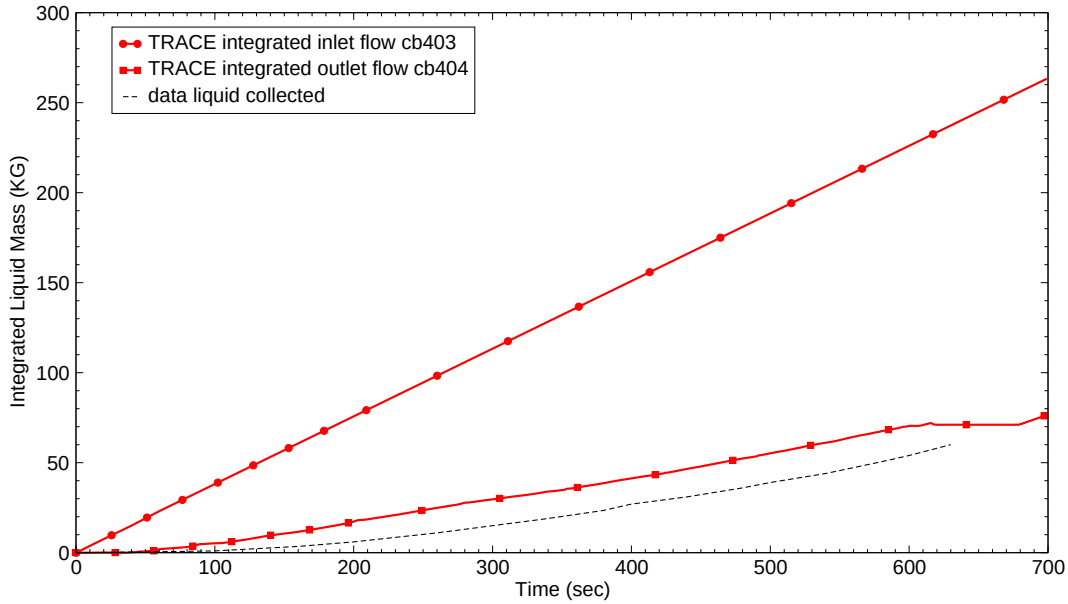

Figure B.7-49. Integrated Liquid Mass Flow into and out of Bundle for Test 31504

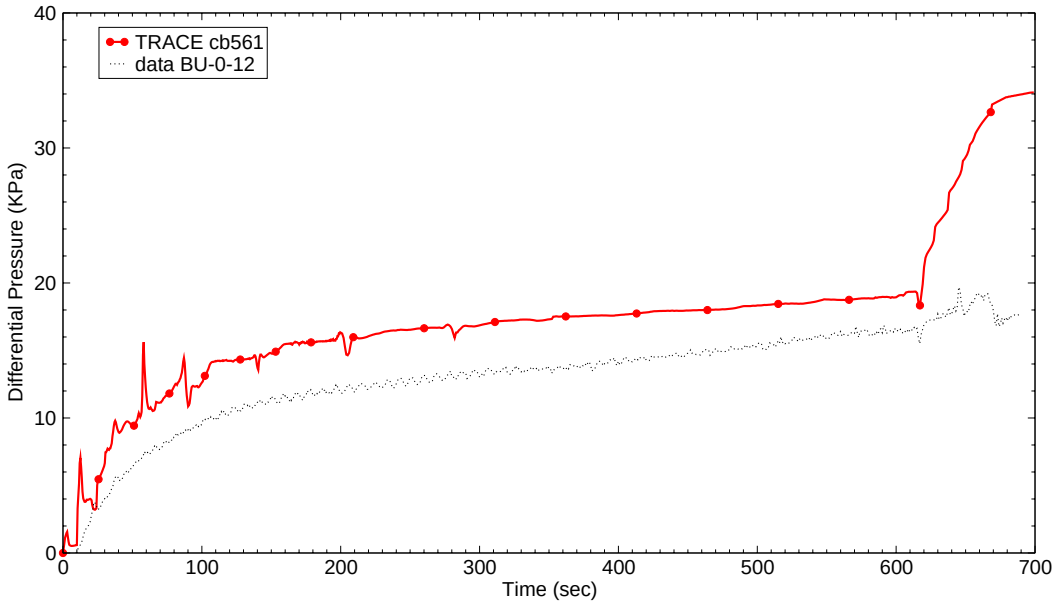

Figure B.7-50. Differential Pressure for the Entire 12 ft Core for Test 31504

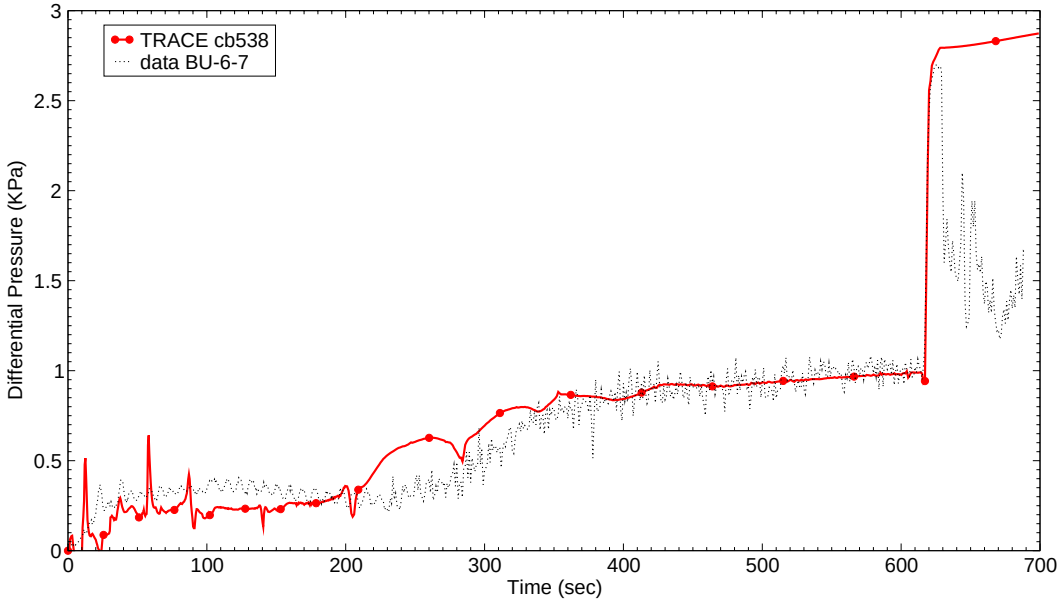

Figure B.7-51. Differential Pressure at 6-7 ft Elevation for Test 31504

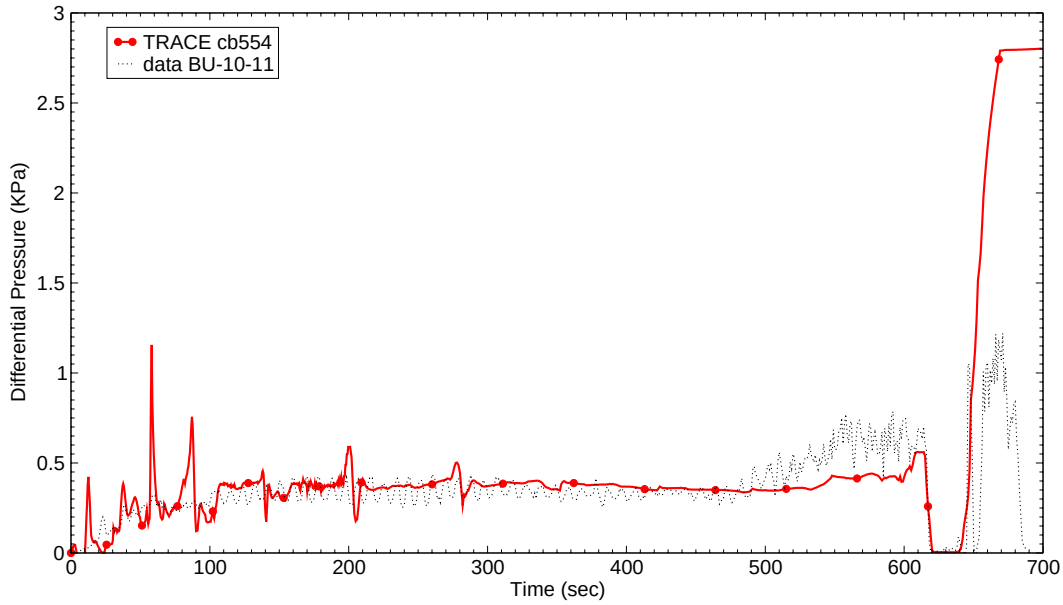

Figure B.7-52. Differential Pressure at 10-11 ft Elevation for Test 31504

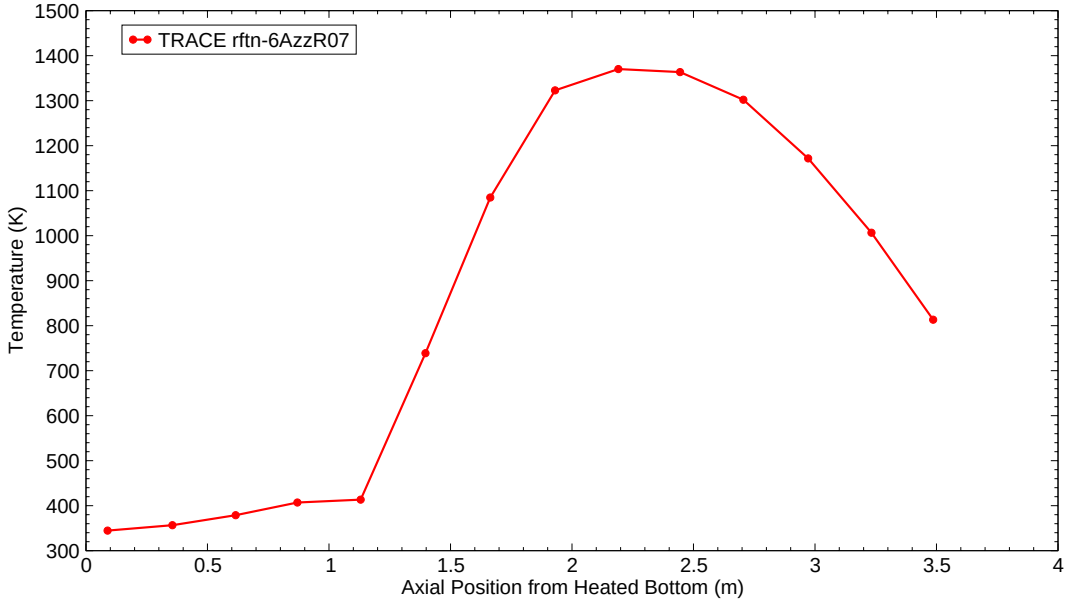

Figure B.7-53. Clad Temperature Profile at 150 sec after Reflood Start for Test 31504

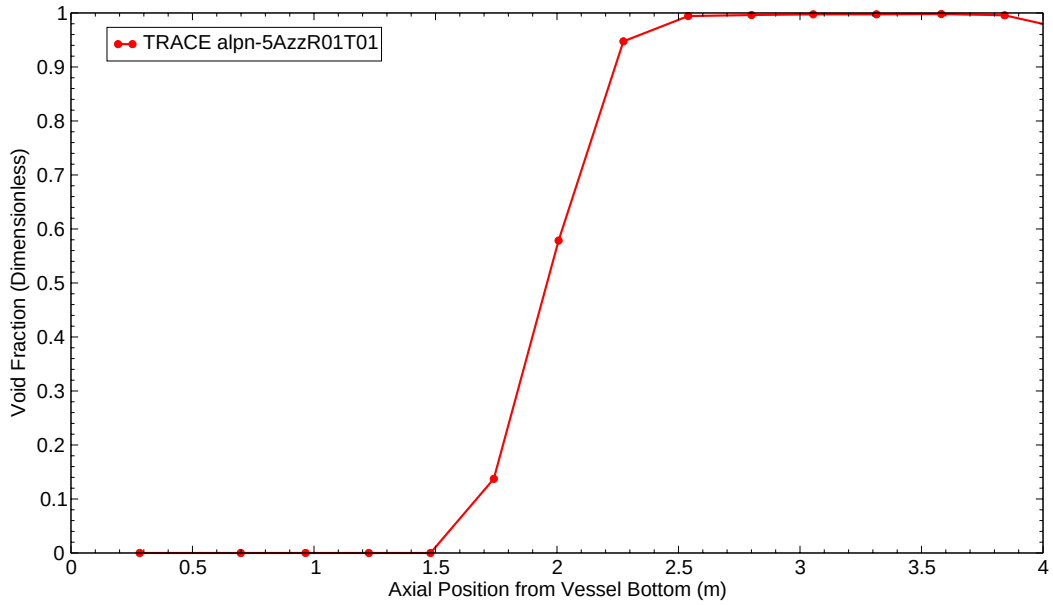

Figure B.7-54. Void Fraction Profile at 150 sec after Reflood Start for Test 31504

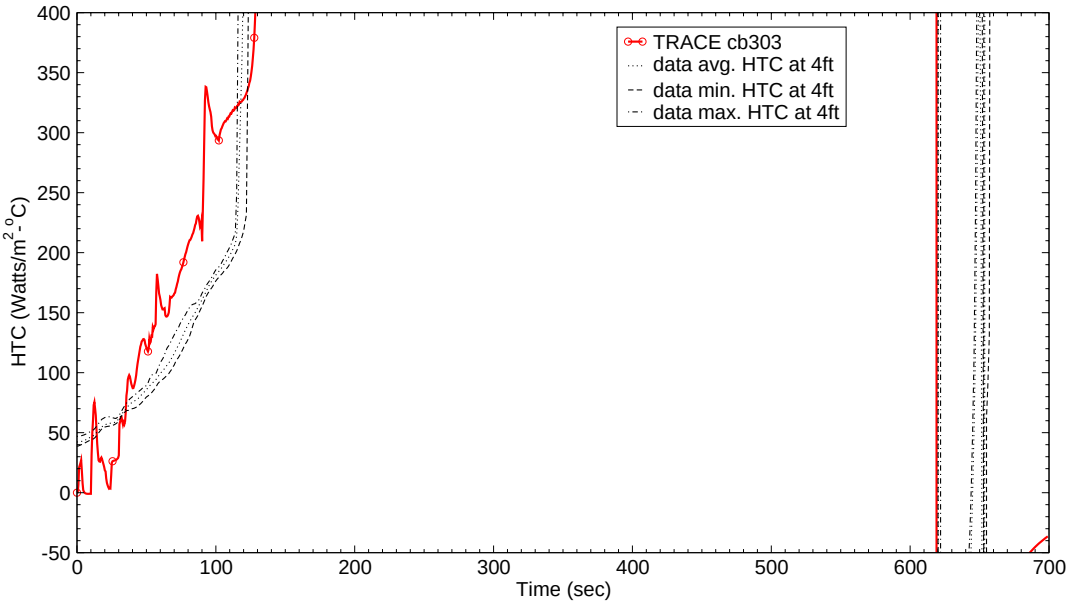

Figure B.7-55. Heat Transfer Coefficient at 4 ft from Heated Bottom for Test 31504

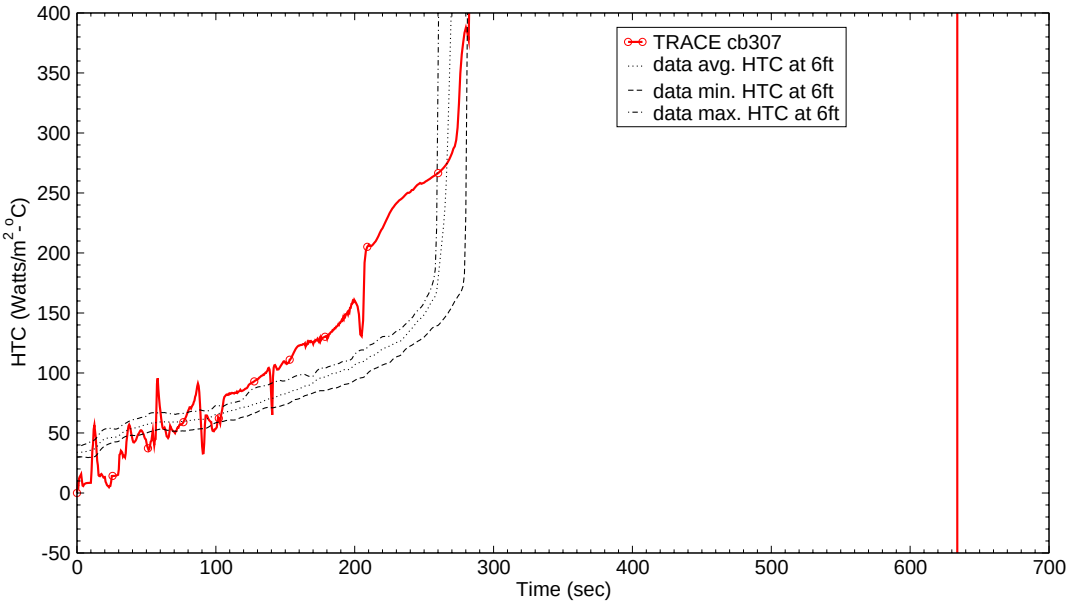

Figure B.7-56. Heat Transfer Coefficient at 6 ft from Heated Bottom for Test 31504

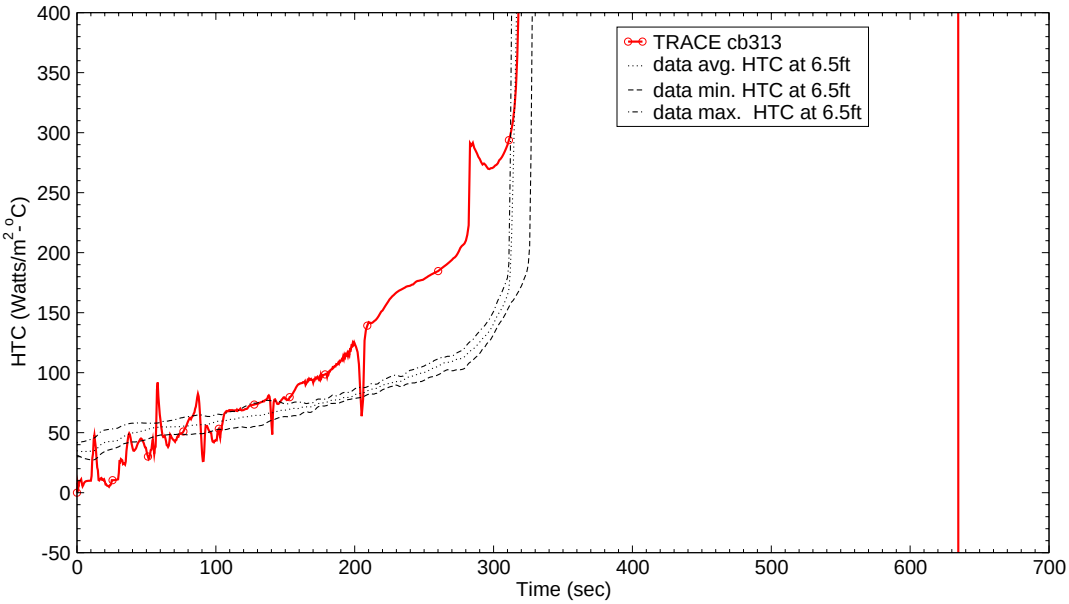

Figure B.7-57. Heat Transfer Coefficient at 6.5 ft from Heated Bottom for Test 31504

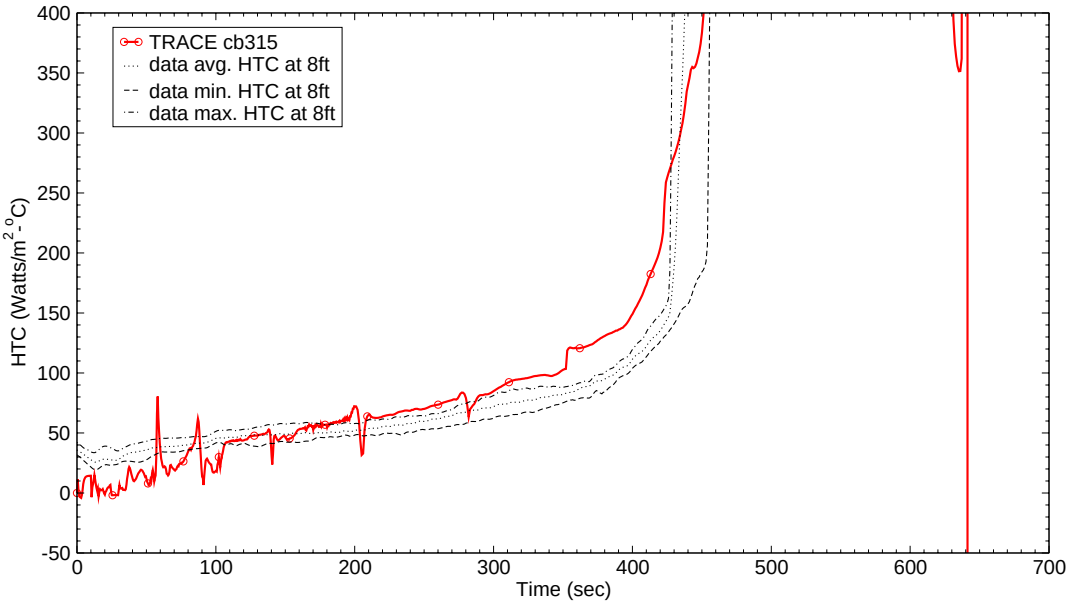

Figure B.7-58. Heat Transfer Coefficient at 8 ft from Heated Bottom for Test 31504

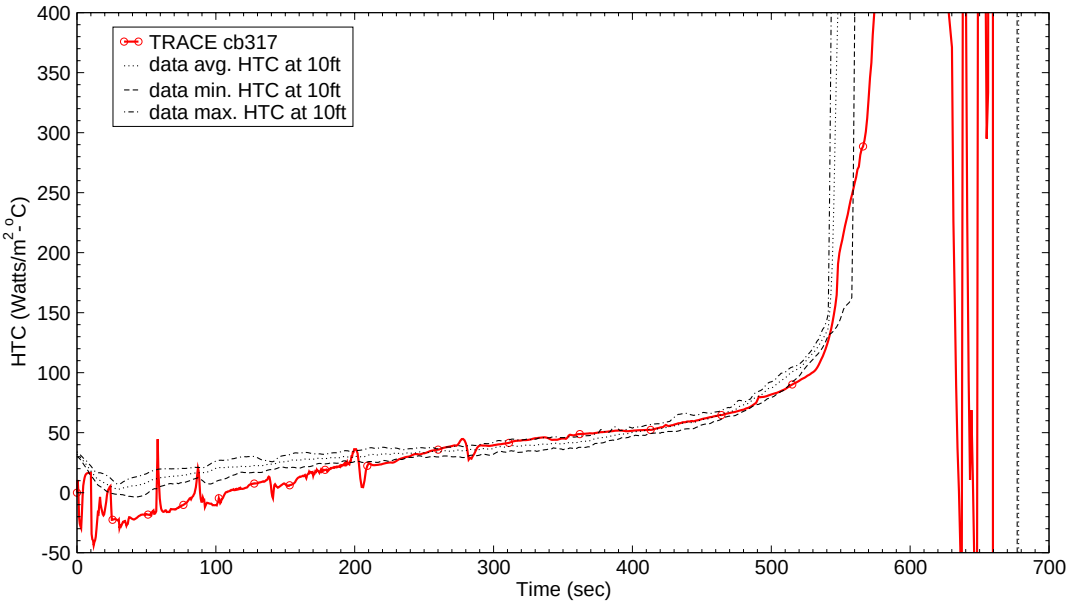

Figure B.7-59. Heat Transfer Coefficient at 10 ft from Heated Bottom for Test 31504

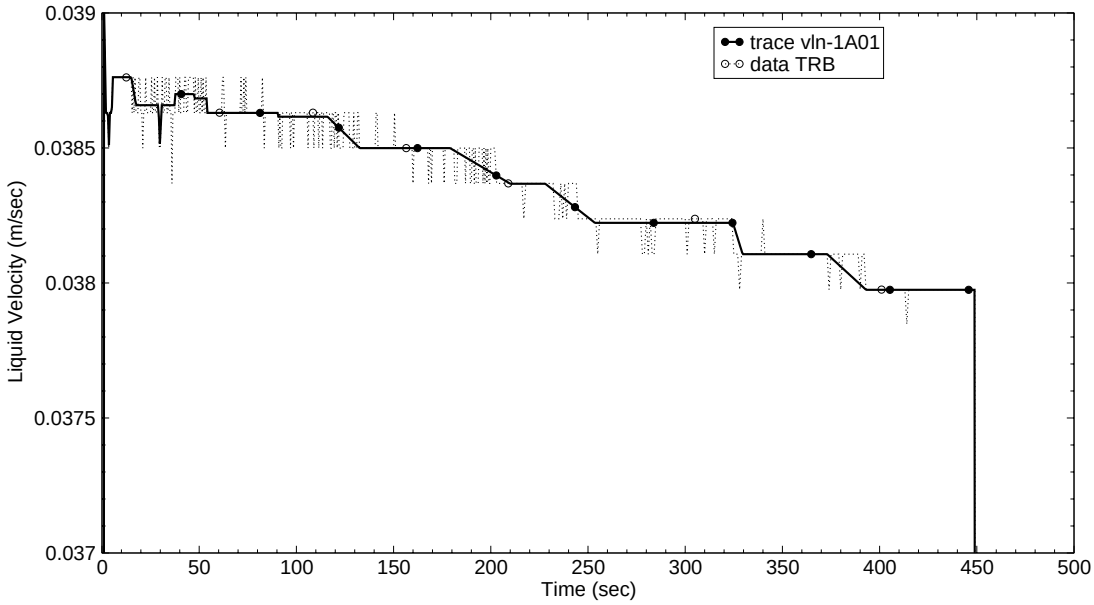

Figure B.7-60. Liquid Inlet Flow Rate for Test 31203

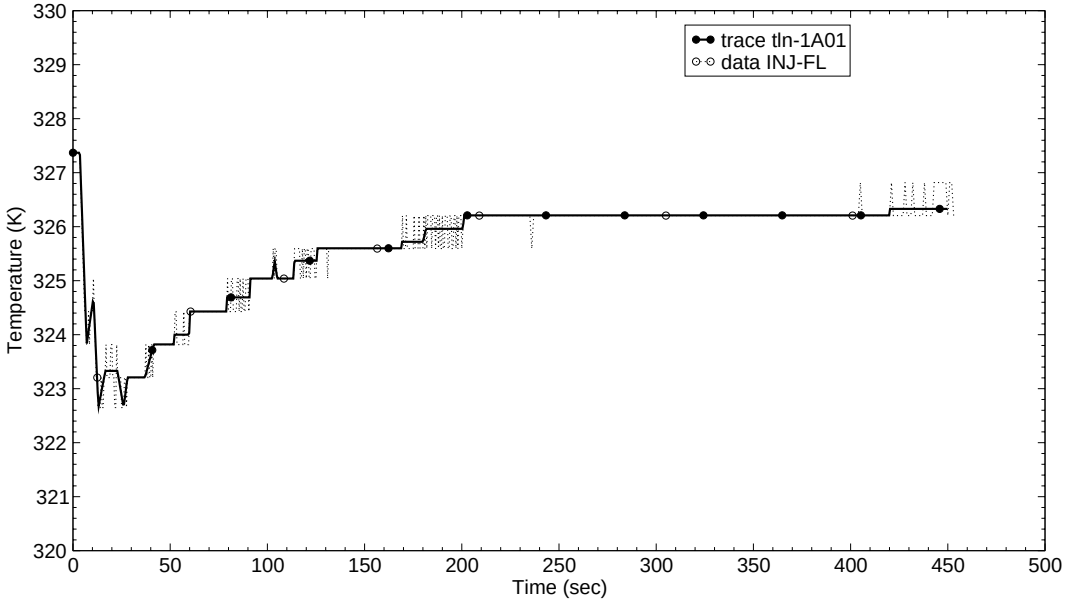

Figure B.7-61. Liquid Inlet Temperature for Test 31203

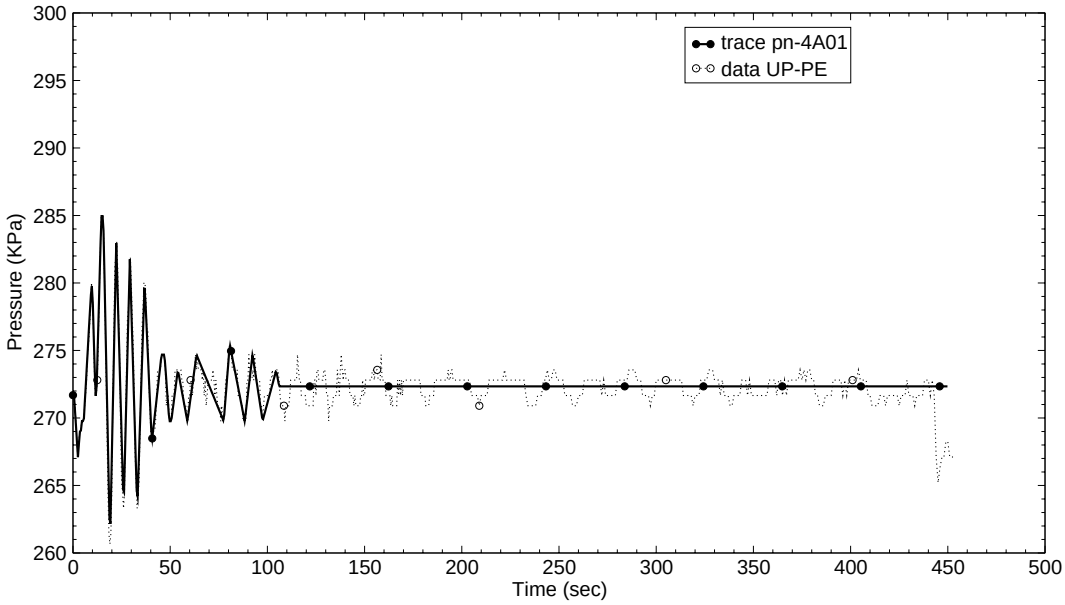

Figure B.7-62. Upper Plenum Exit Pressure for Test 31203

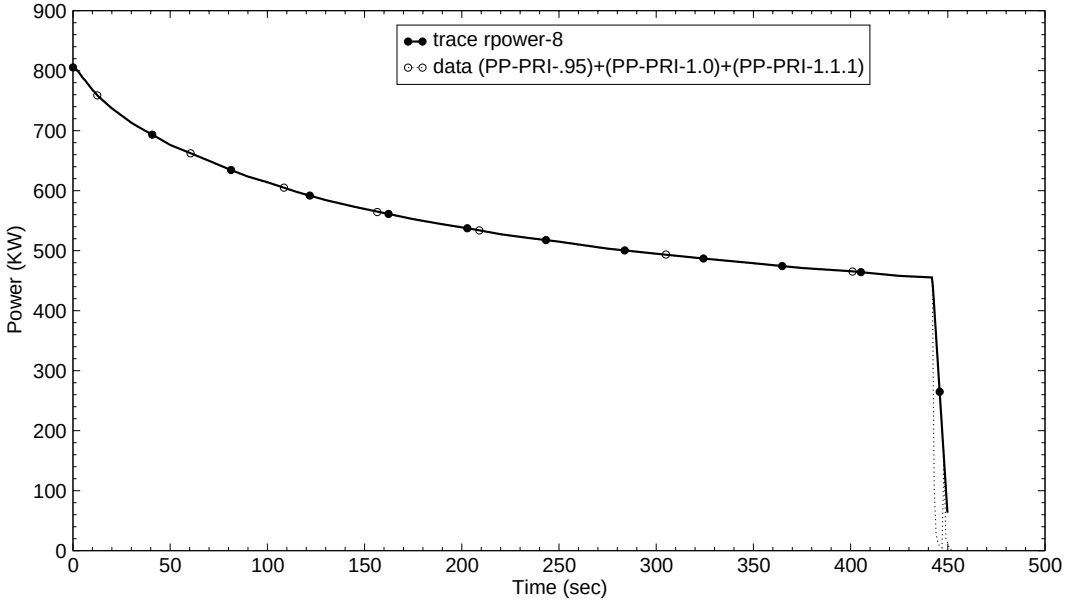

Figure B.7-63. Total Power to the Bundle for Test 31203

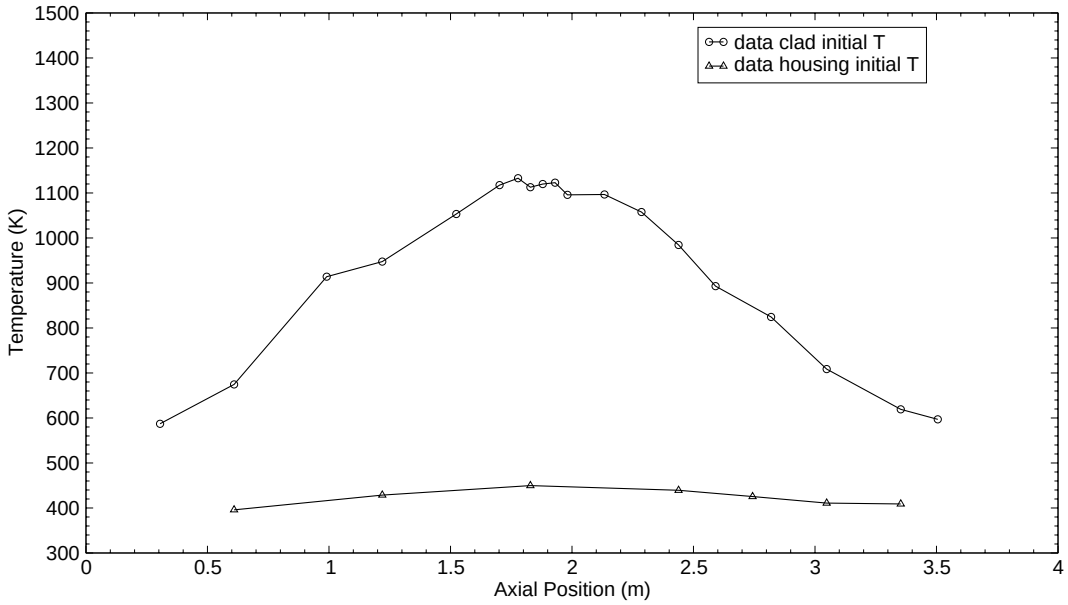

Figure B.7-64. Heater Rod Clad and Housing Initial Temperatures for Test 31203

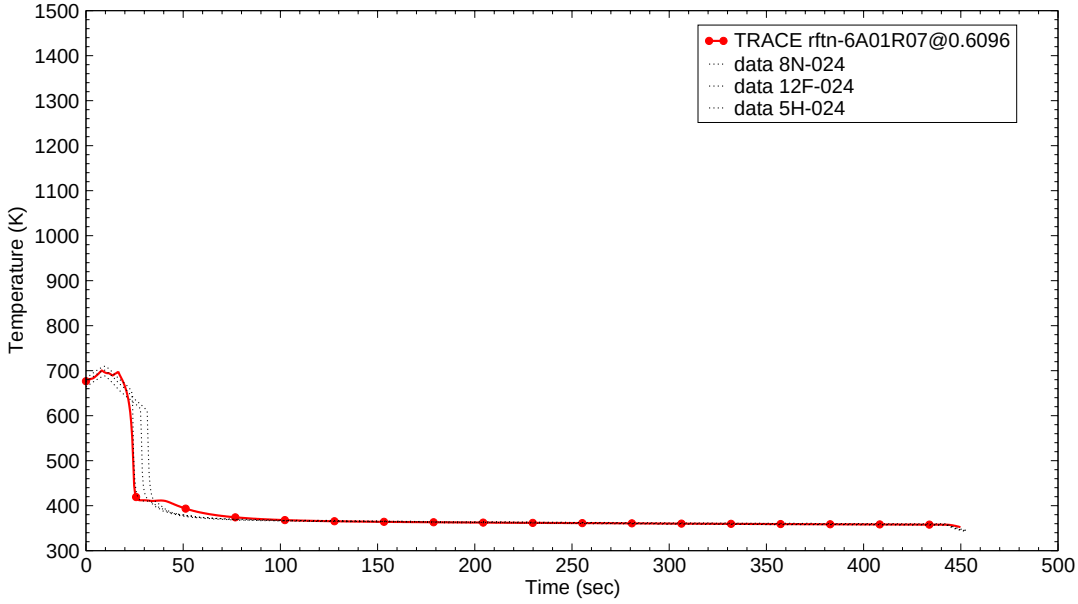

Figure B.7-65. Rod Clad Temperatures at 2 ft from Heated Bottom for Test 31203

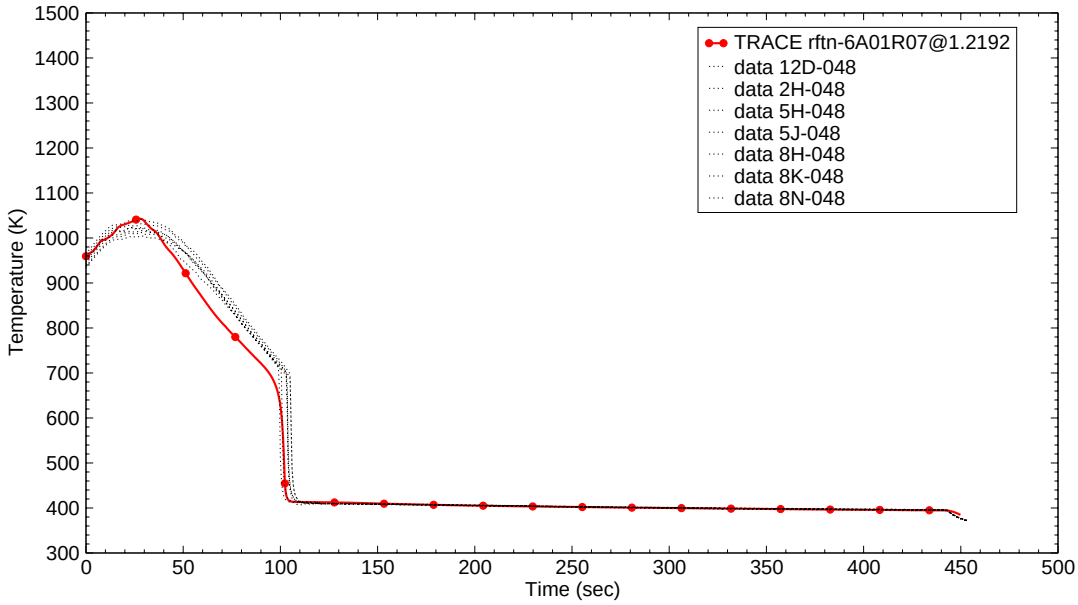

Figure B.7-66. Rod Clad Temperatures at 4 ft from Heated Bottom for Test 31203

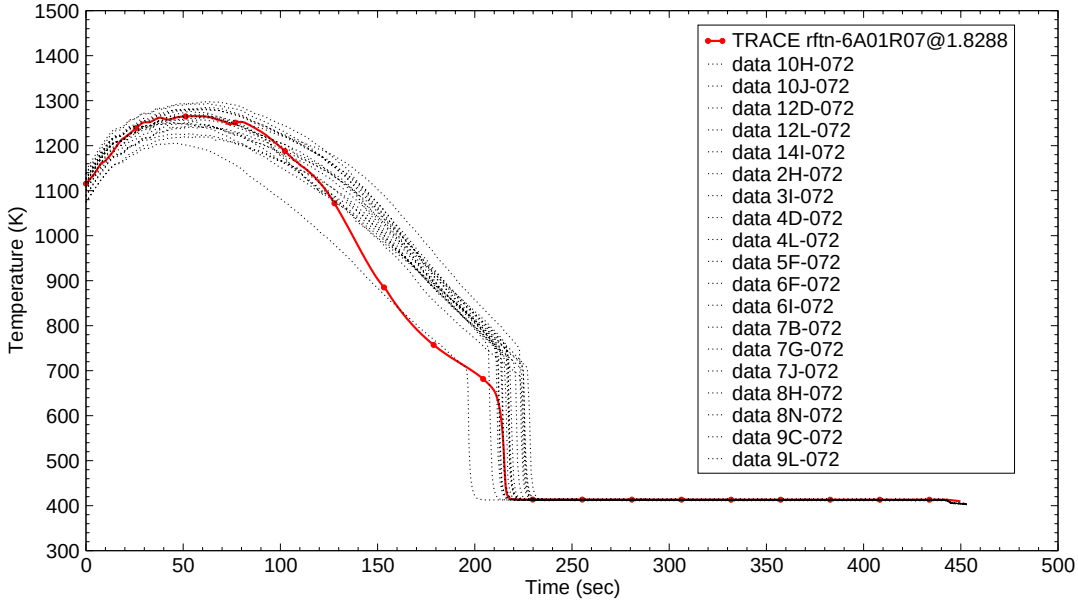

Figure B.7-67. Rod Clad Temperatures at 6 ft from Heated Bottom for Test 31203

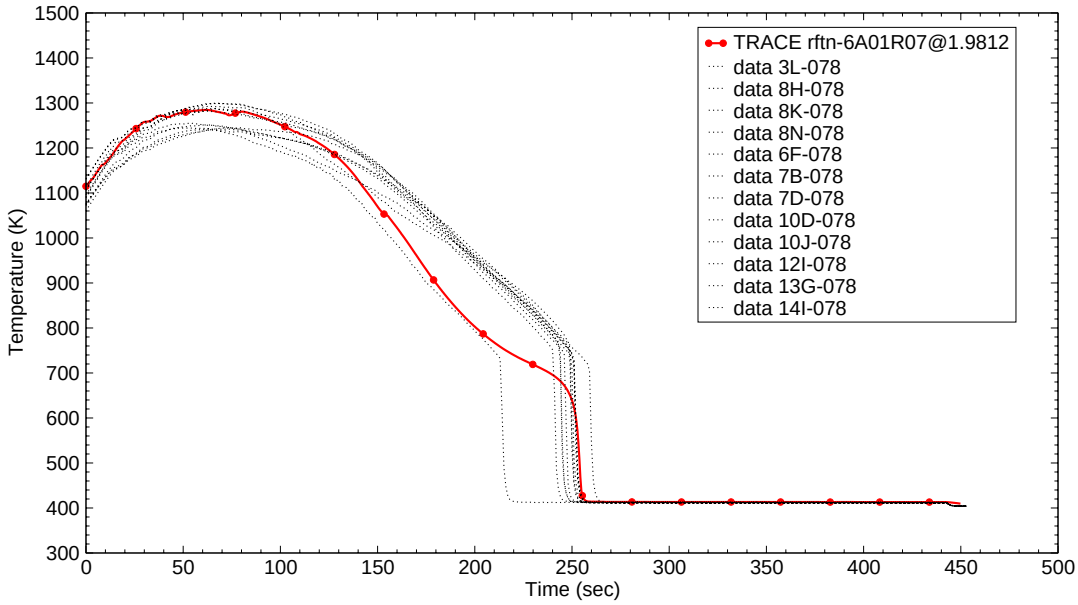

Figure B.7-68. Rod Clad Temperatures at 6.5 ft from Heated Bottom for Test 31203

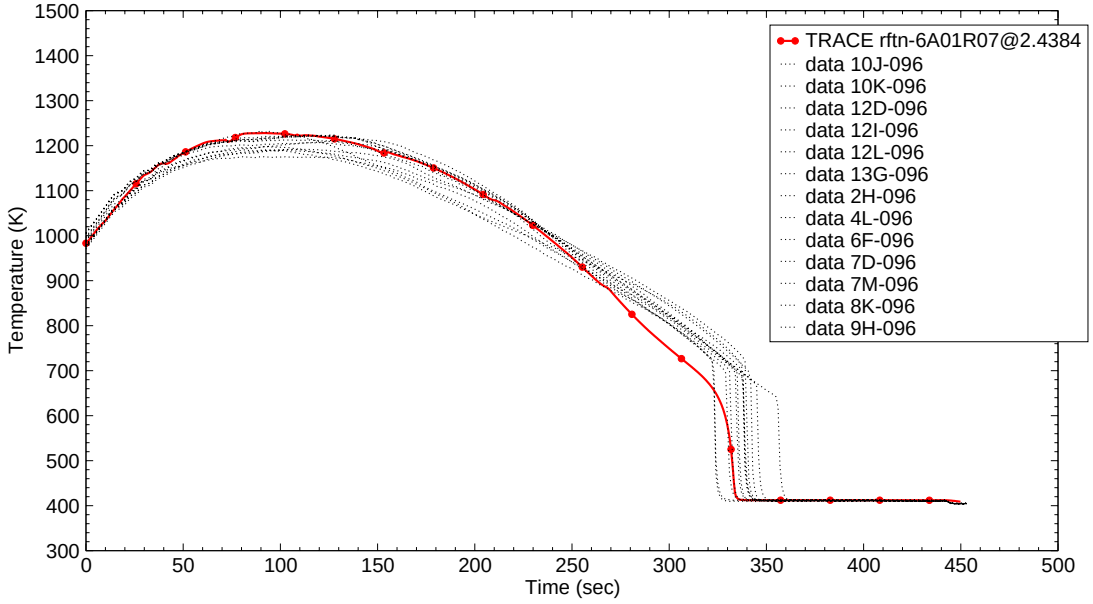

Figure B.7-69. Rod Clad Temperatures at 8 ft from Heated Bottom for Test 31203

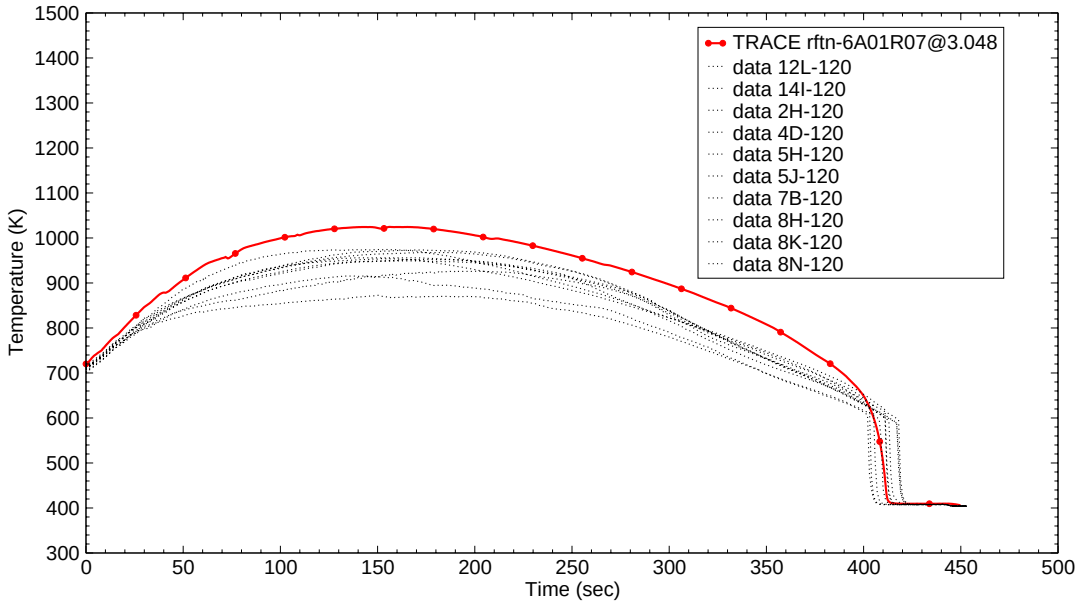

Figure B.7-70. Rod Clad Temperatures at 10 ft from Heated Bottom for Test 31203

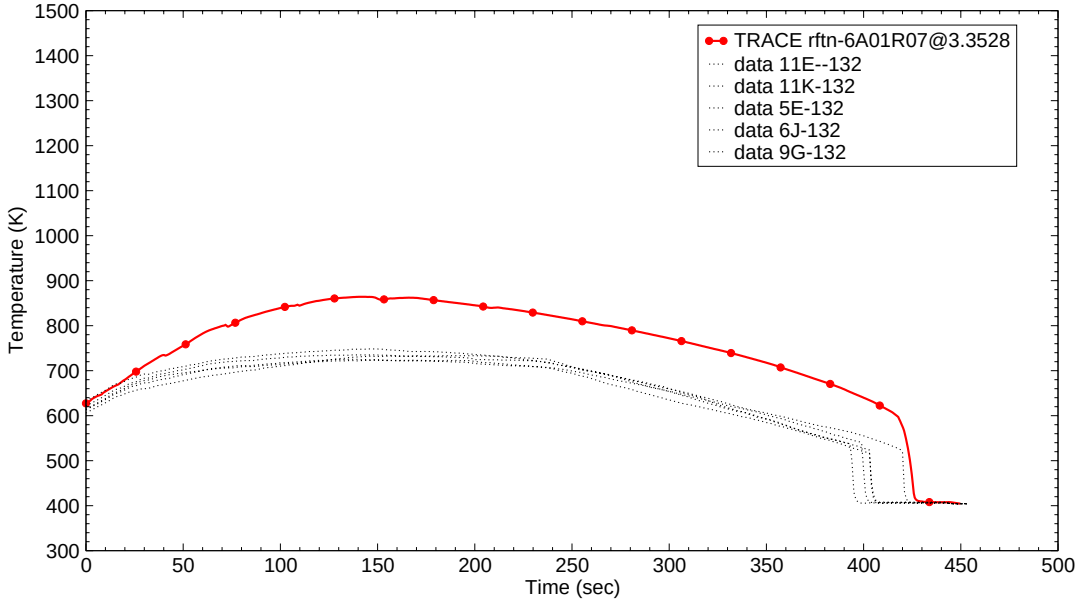

Figure B.7-71. Rod Clad Temperatures at 11 ft from Heated Bottom for Test 31203

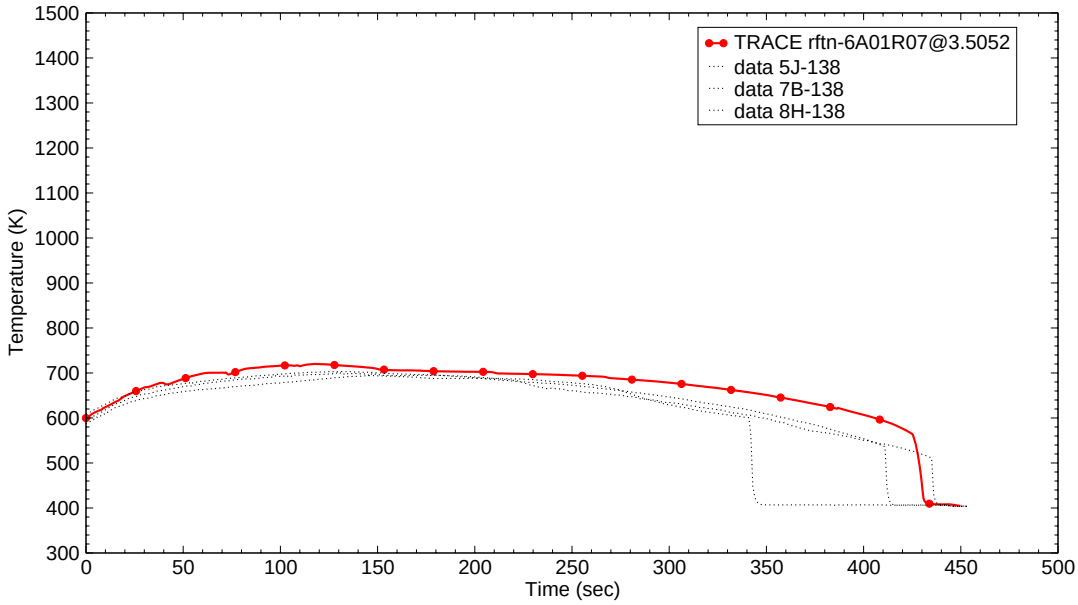

Figure B.7-72. Rod Clad Temperatures at 11.5 ft from Heated Bottom for Test 31203

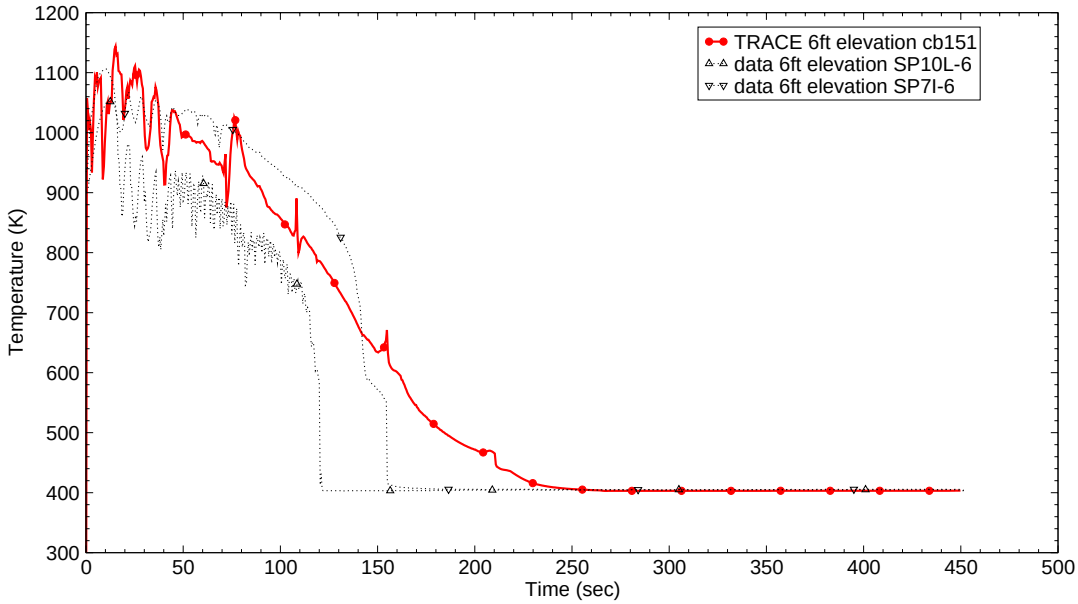

Figure B.7-73. Vapor Temperatures at 6 ft from Heated Bottom for Test 31203

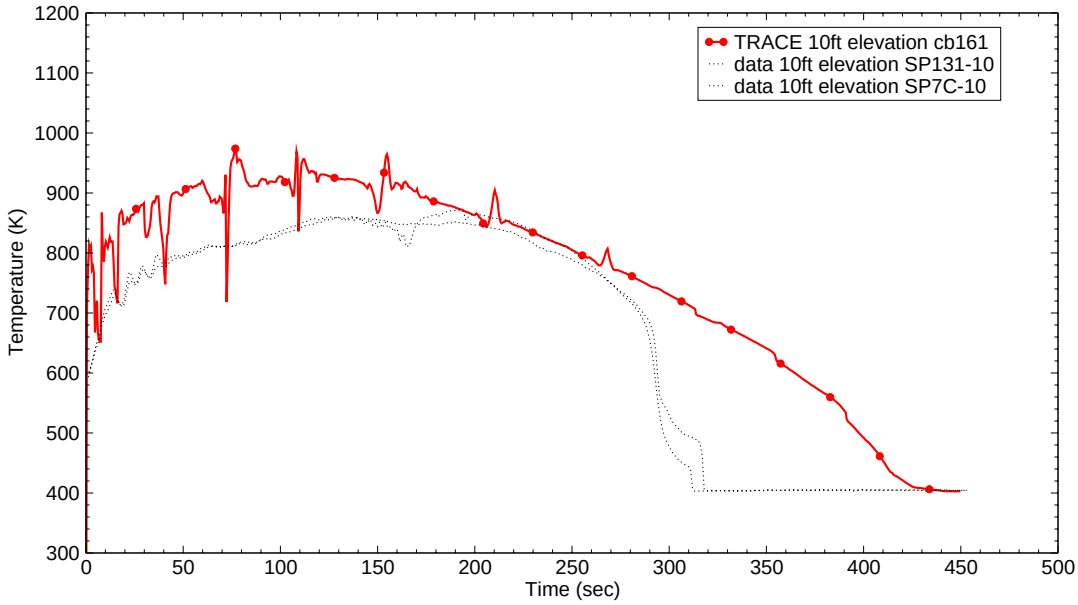

Figure B.7-74. Vapor Temperatures at 10 ft from Heated Bottom for Test 31203

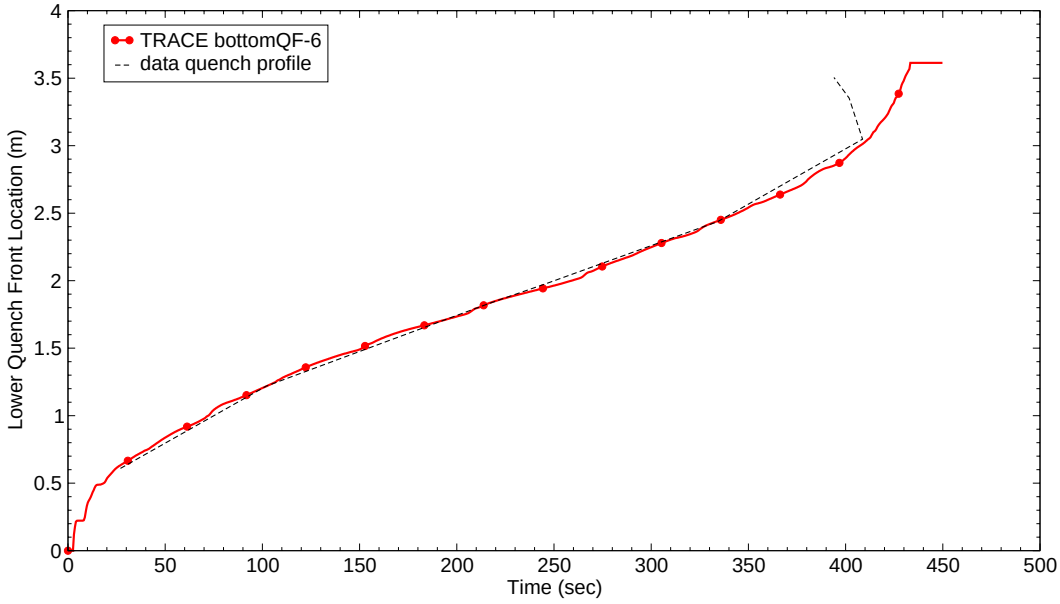

Figure B.7-75. Quench Profile as a Function of Time for Test 31203

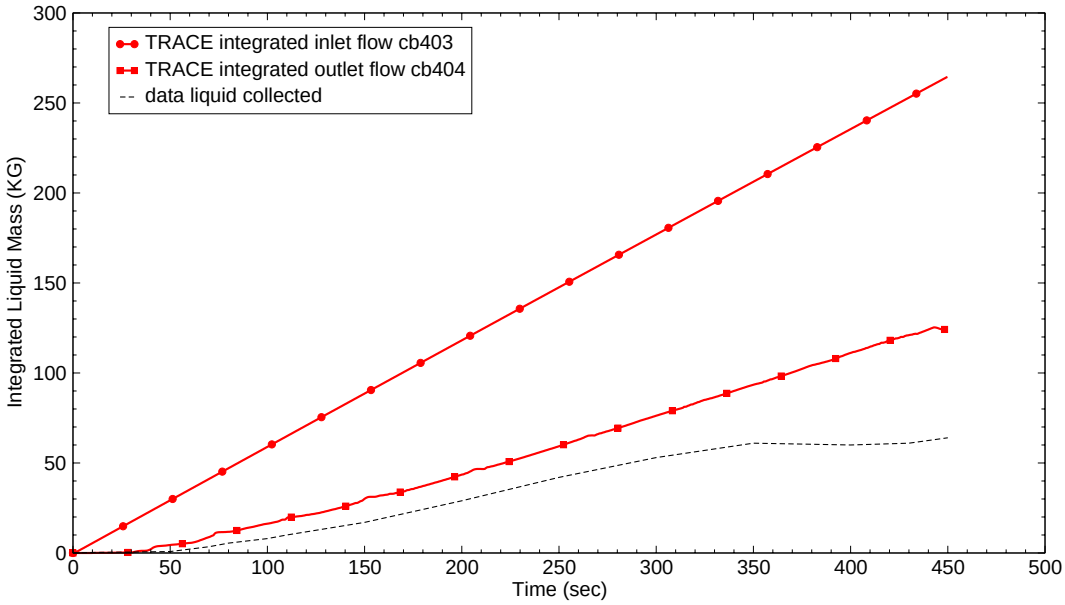

Figure B.7-76. Integrated Liquid Mass Flow into and out of Bundle for Test 31203

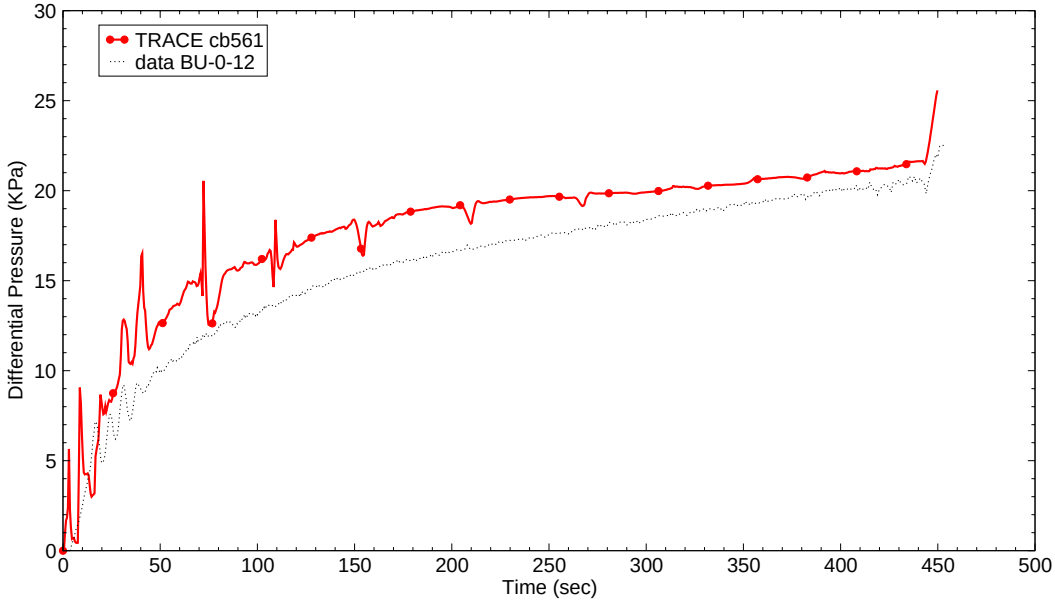

Figure B.7-77. Differential Pressure for the Entire 12 ft Core for Test 31203

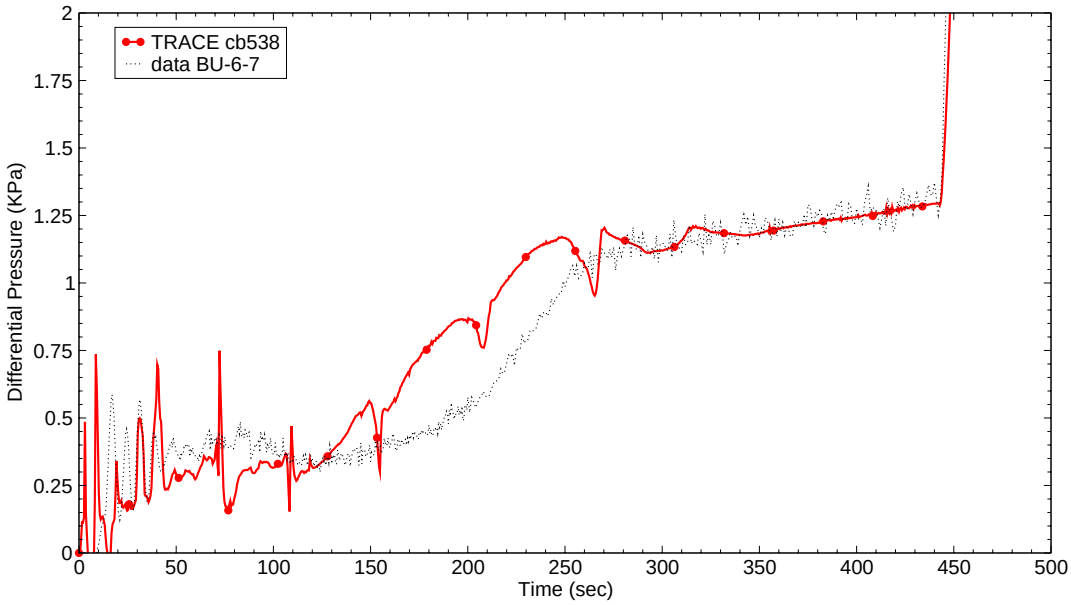

Figure B.7-78. Differential Pressure at 6-7 ft Elevation for Test 31203

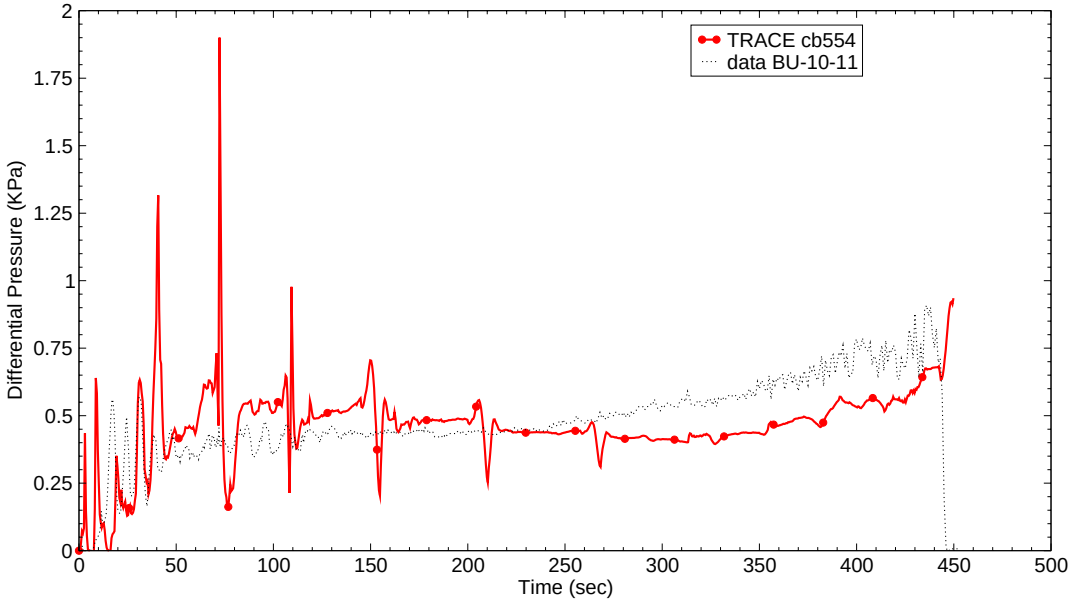

Figure B.7-79. Differential Pressure at 10-11 ft Elevation for Test 31203

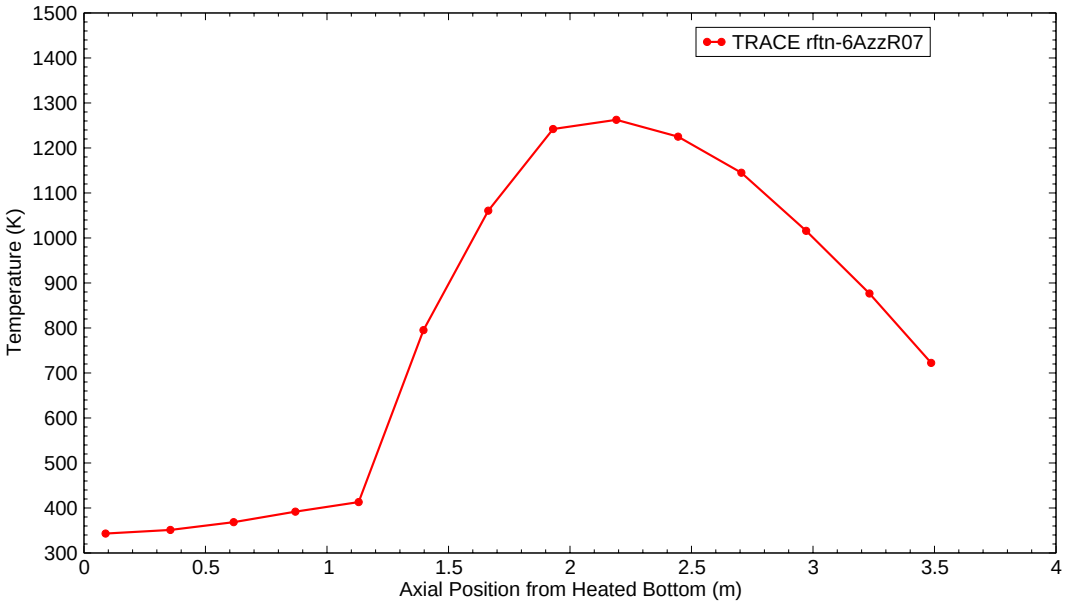

Figure B.7-80. Clad Temperature Profile at 100 sec after Reflood Start for Test 31203

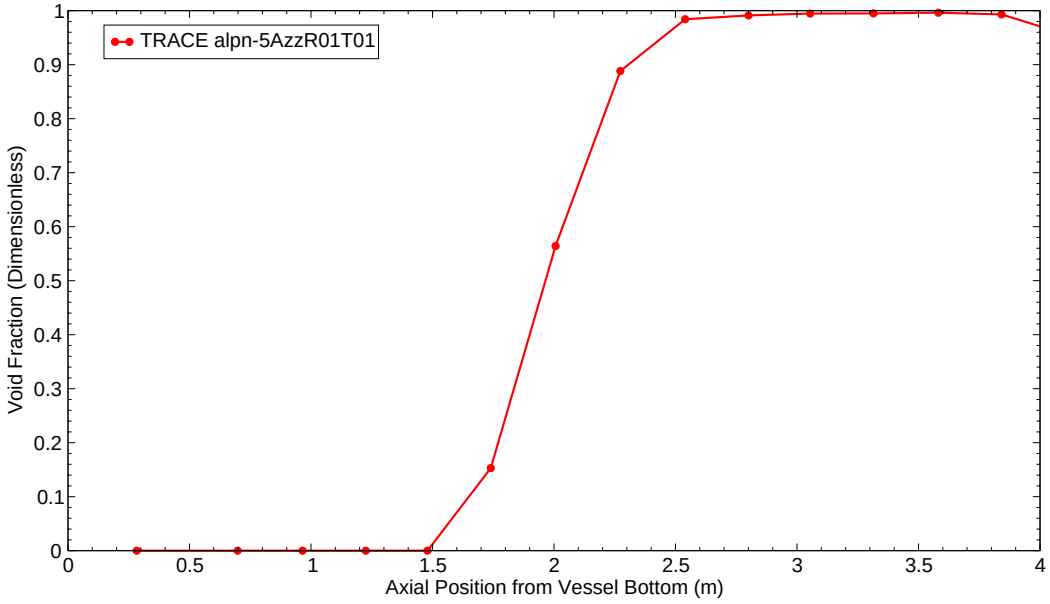

Figure B.7-81. Void Fraction Profile at 100 sec after Reflood Start for Test 31203

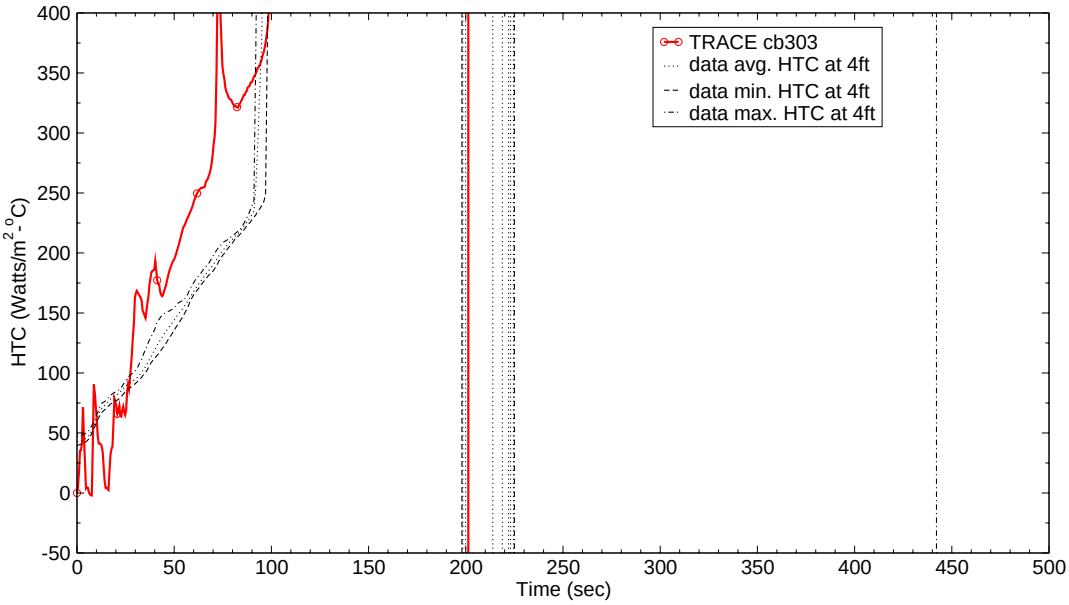

Figure B.7-82. Heat Transfer Coefficient at 4 ft from Heated Bottom for Test 31203

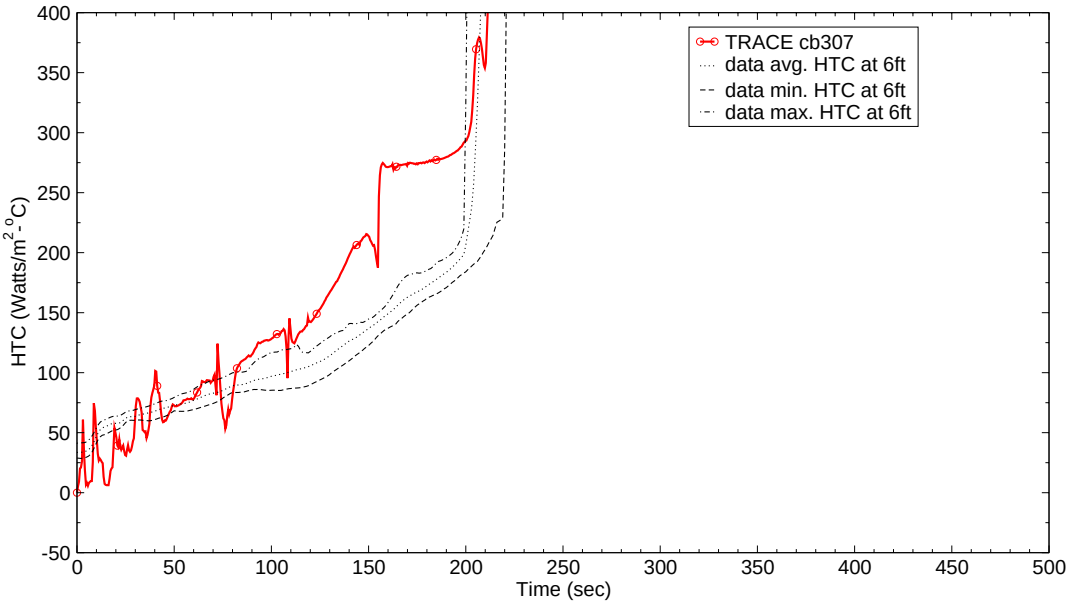

Figure B.7-83. Heat Transfer Coefficient at 6 ft from Heated Bottom for Test 31203

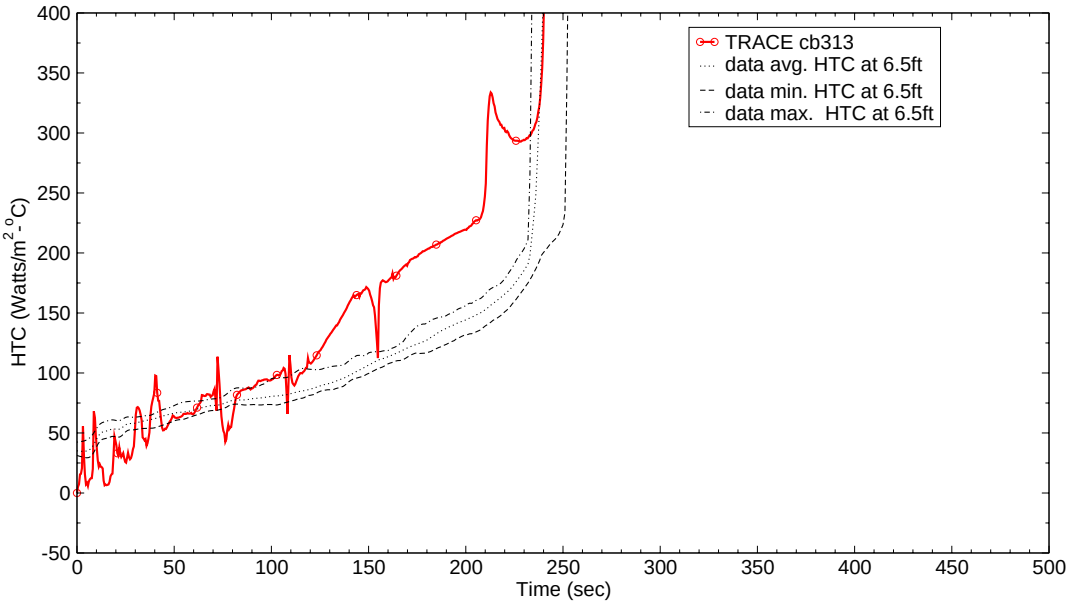

Figure B.7-84. Heat Transfer Coefficient at 6.5 ft from Heated Bottom for Test 31203

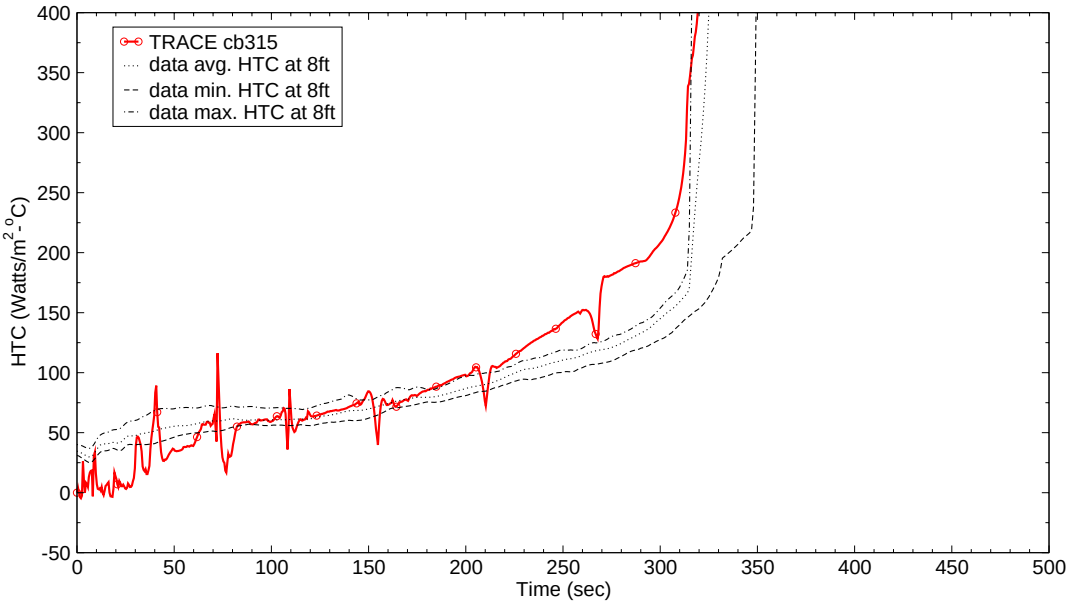

Figure B.7-85. Heat Transfer Coefficient at 8 ft from Heated Bottom for Test 31203

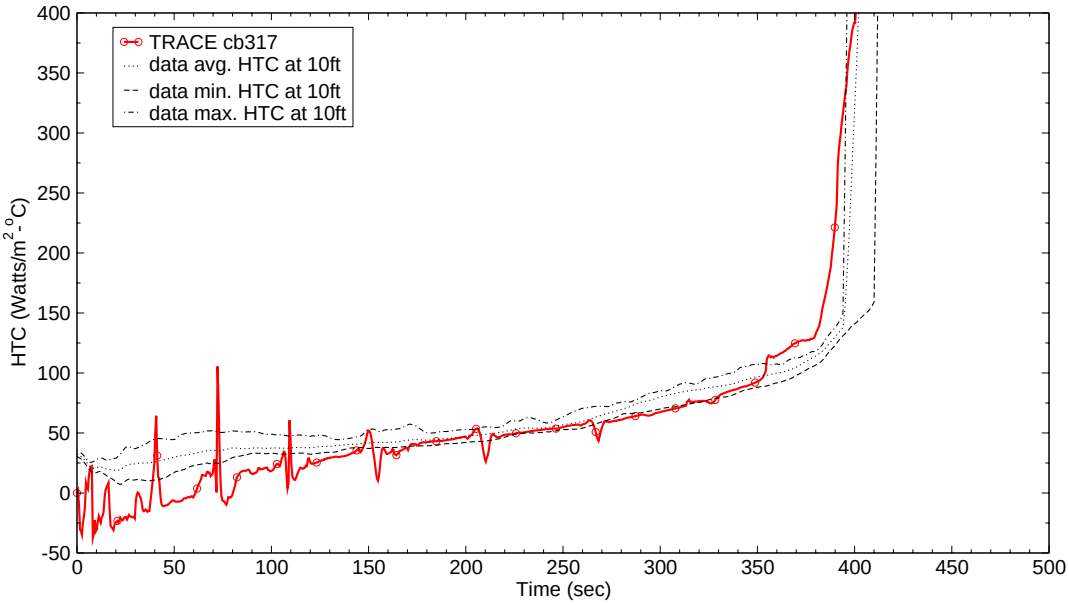

Figure B.7-86. Heat Transfer Coefficient at 10 ft from Heated Bottom for Test 31203

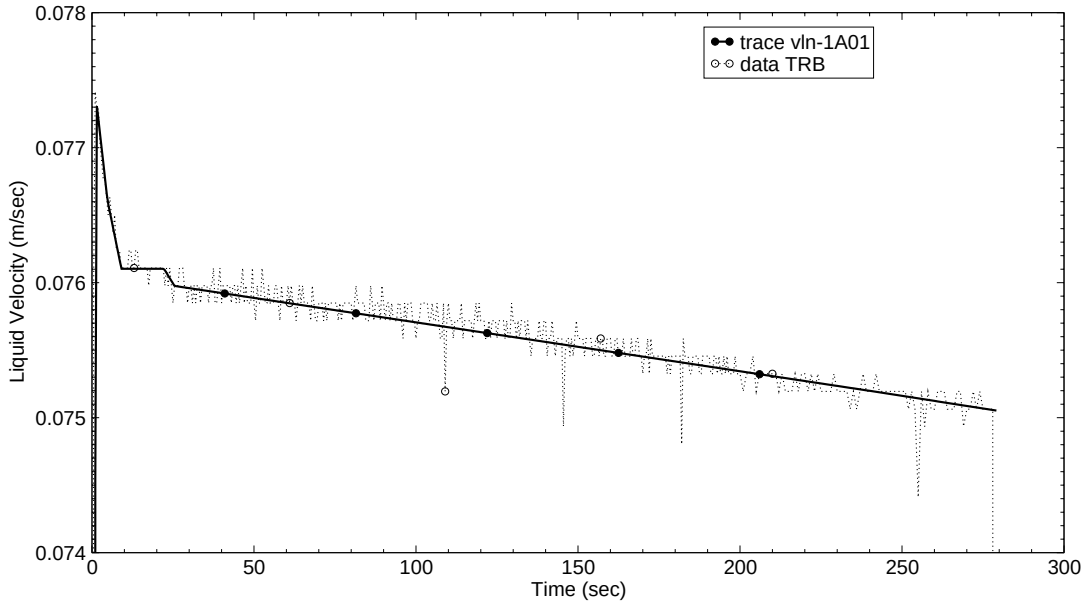

Figure B.7-87. Liquid Inlet Flow Rate for Test 31302

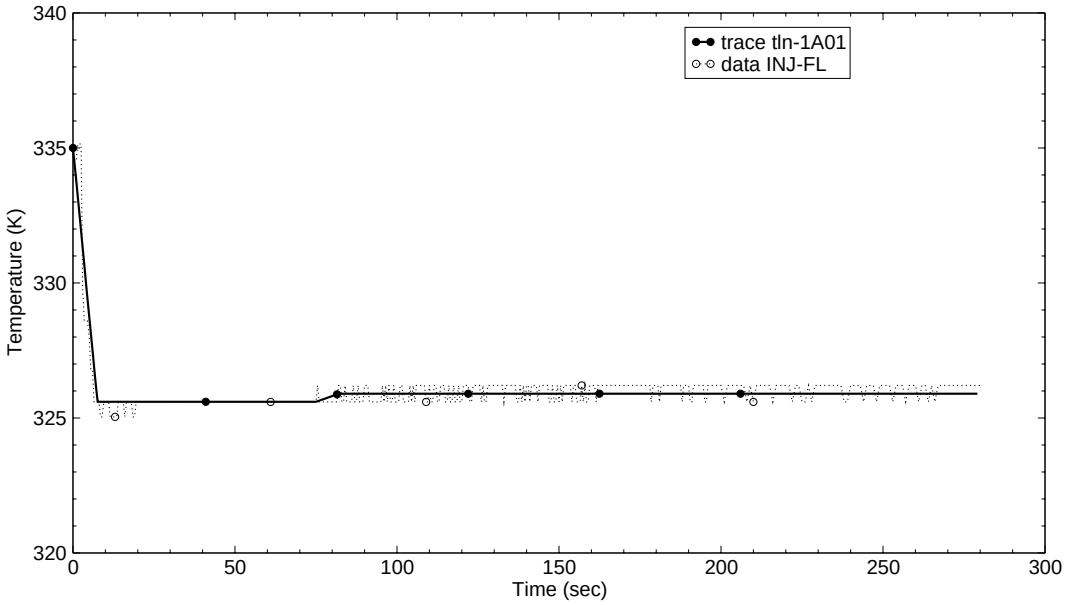

Figure B.7-88. Liquid Inlet Temperature for Test 31302

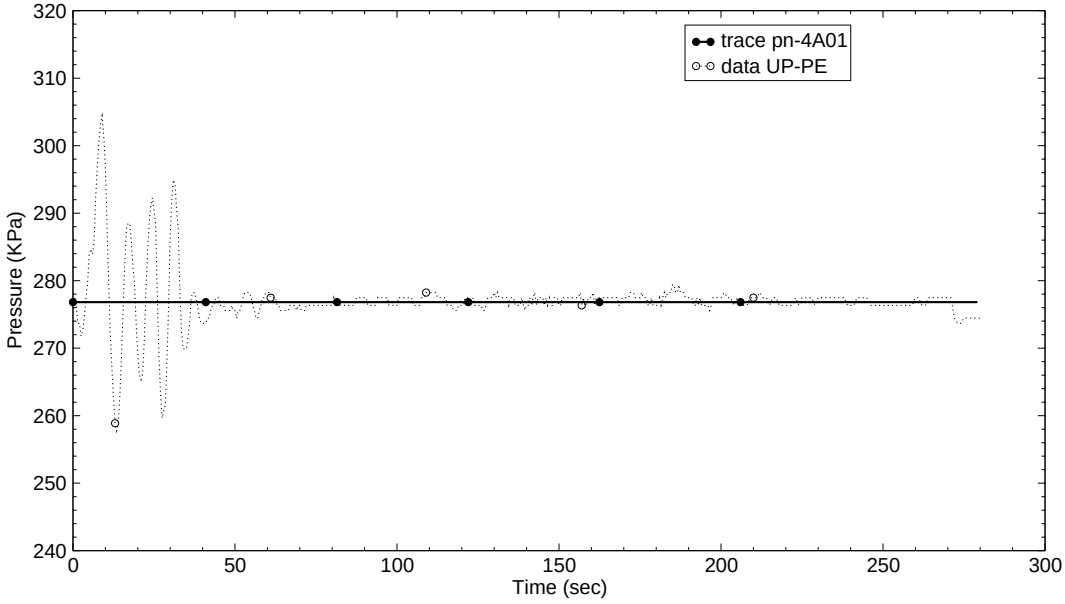

Figure B.7-89. Upper Plenum Exit Pressure for Test 31302

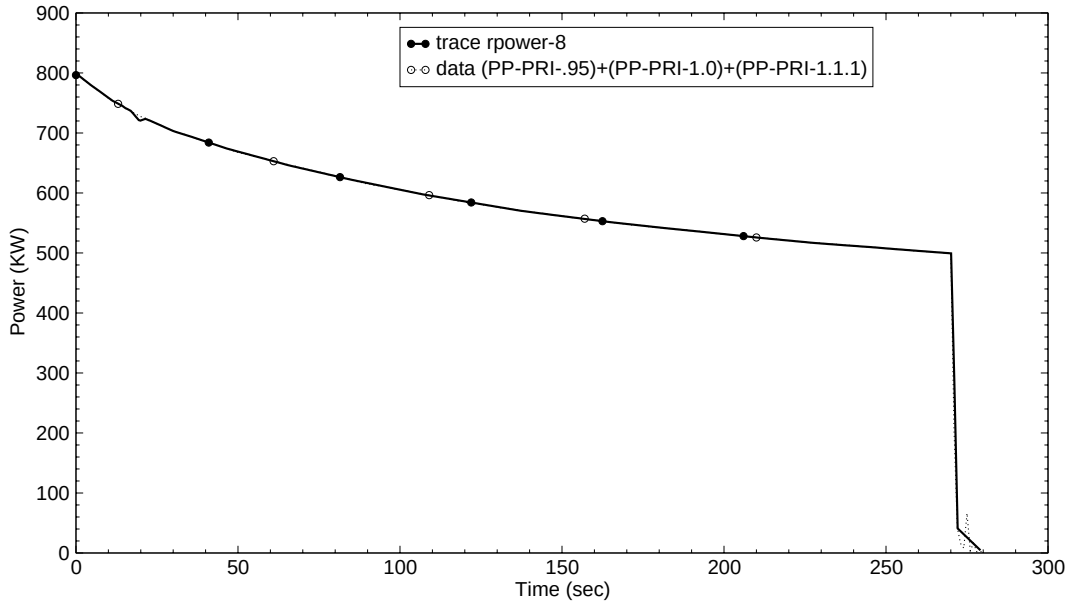

Figure B.7-90. Total power to the Bundle for Test 31302

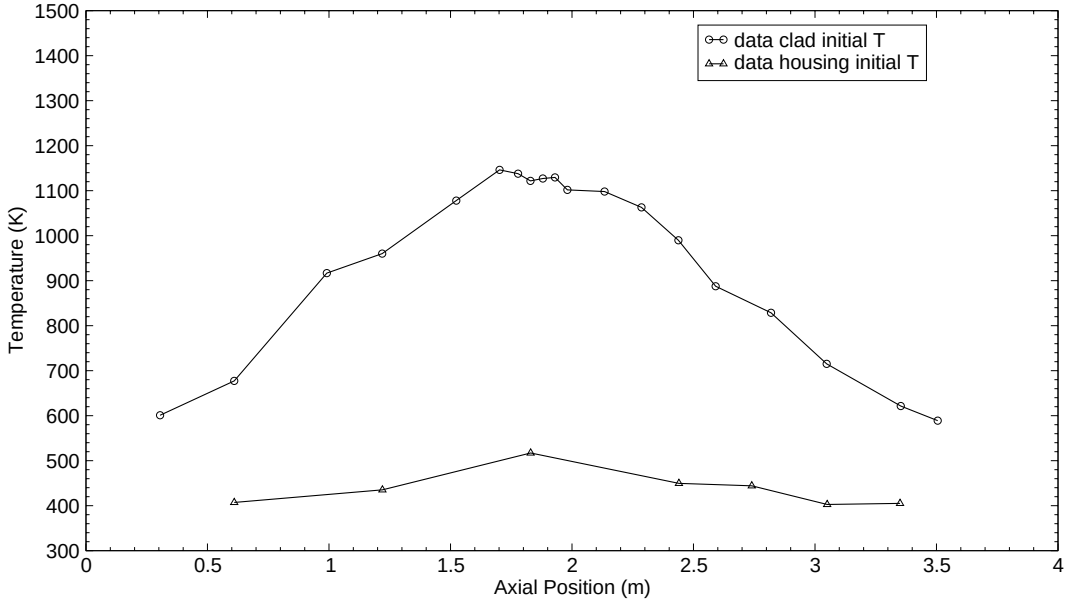

Figure B.7-91. Heater Rod Clad and Housing Initial Temperatures for Test 31302

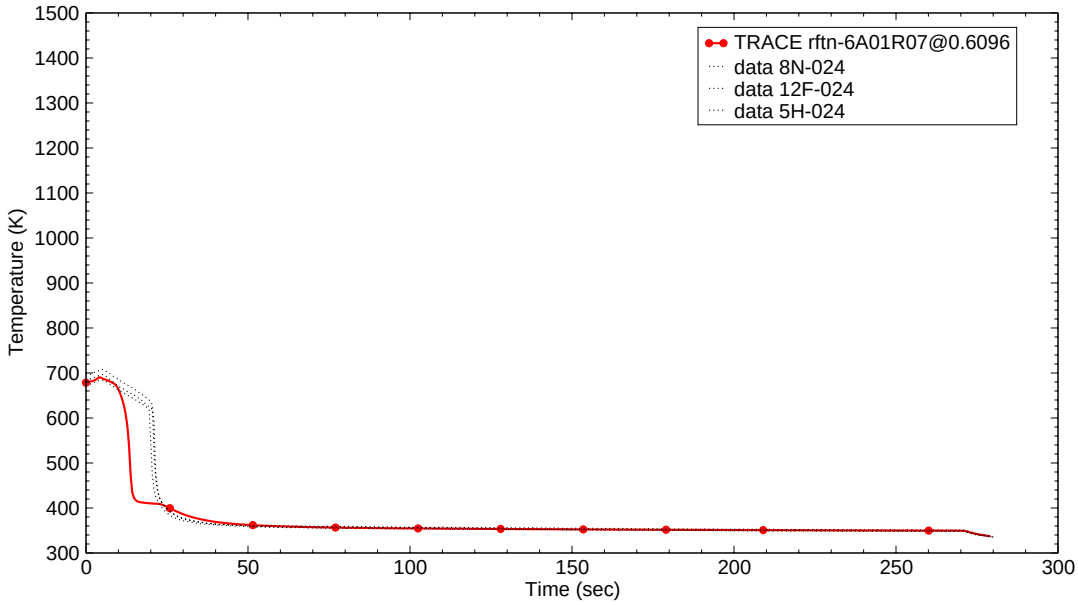

Figure B.7-92. Rod Clad Temperatures at 2 ft from Heated Bottom for Test 31302

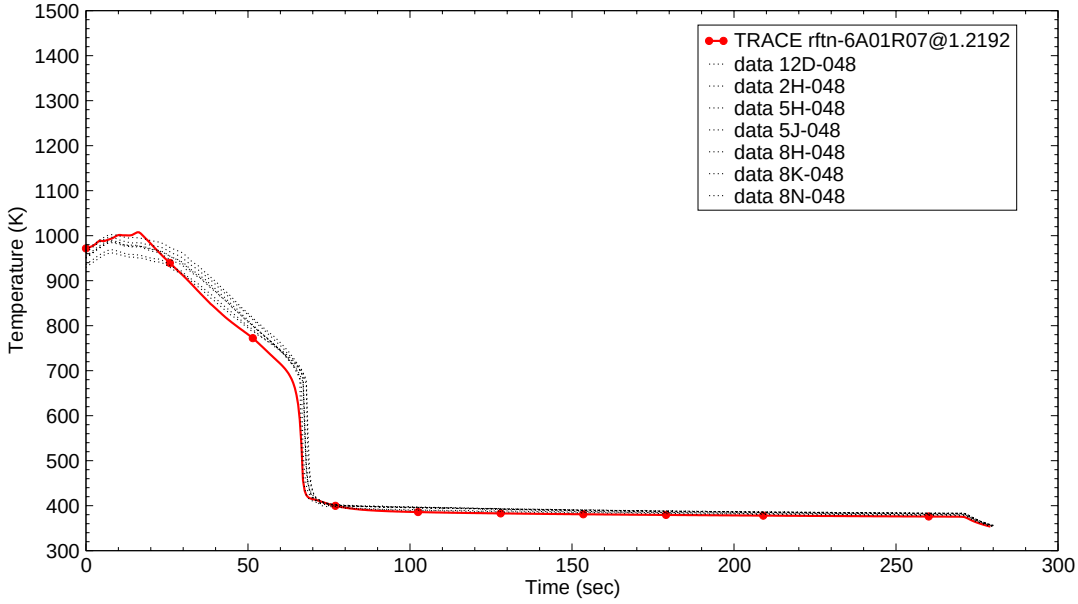

Figure B.7-93. Rod Clad Temperatures at 4 ft from Heated Bottom for Test 31302

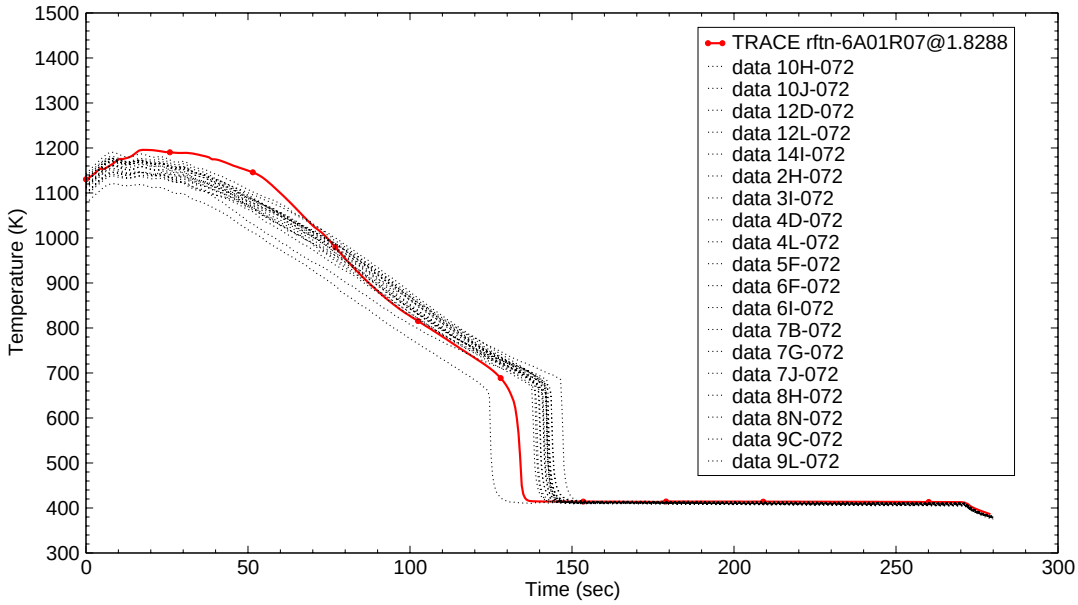

Figure B.7-94. Rod Clad Temperatures at 6 ft from Heated Bottom for Test 31302

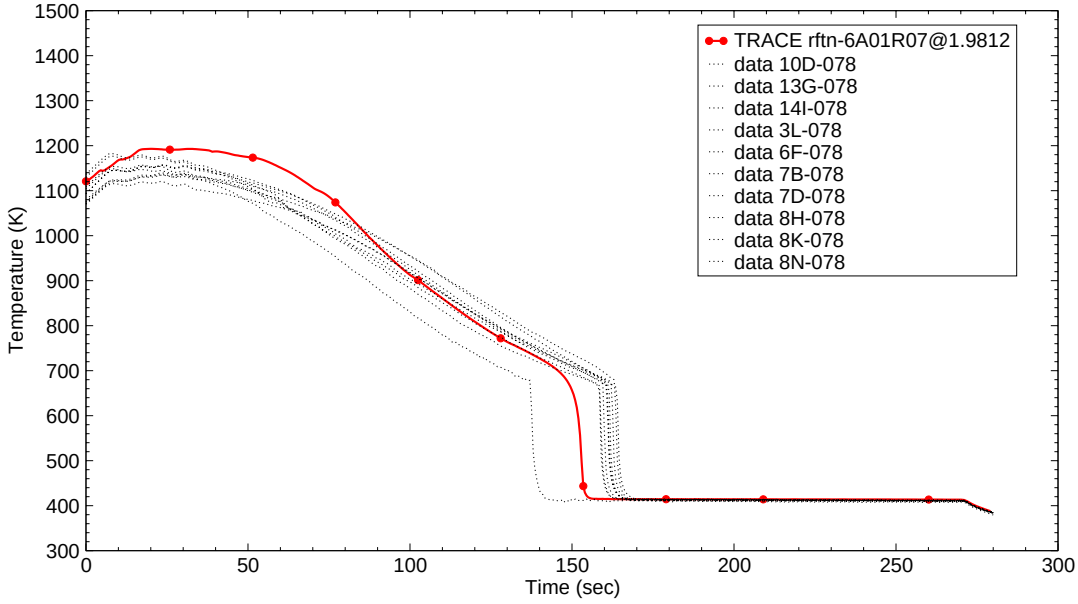

Figure B.7-95. Rod Clad Temperatures at 6.5 ft from Heated Bottom for Test 31302

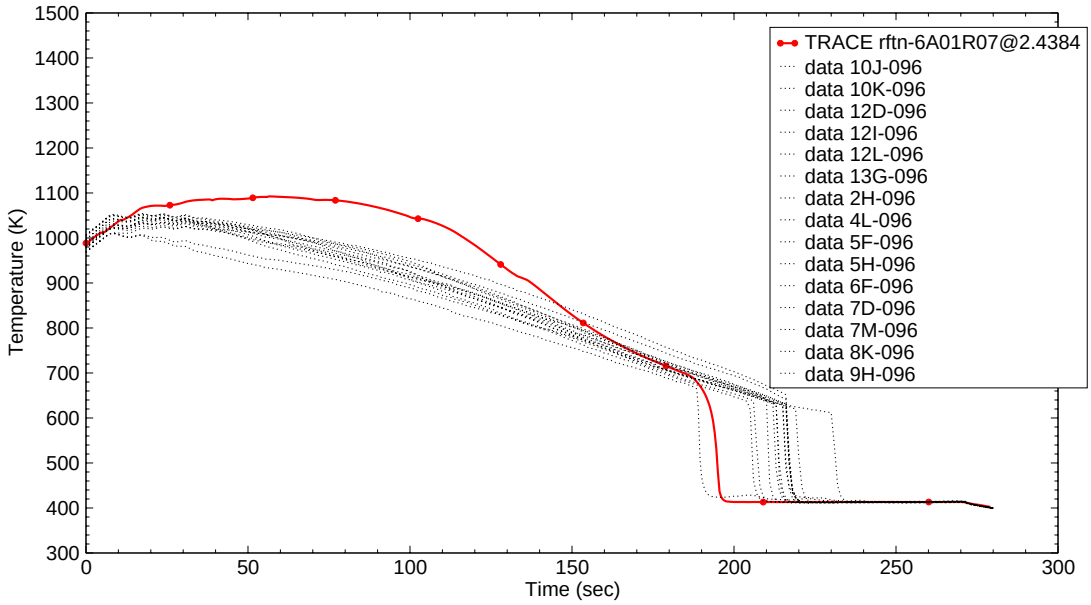

Figure B.7-96. Rod Clad Temperatures at 8 ft from Heated Bottom for Test 31302

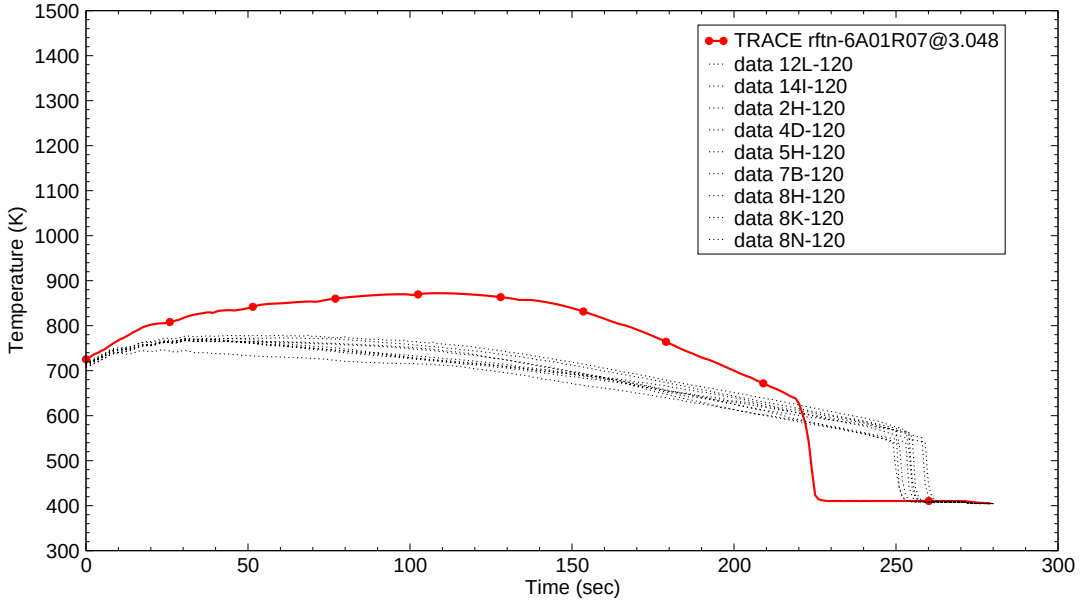

Figure B.7-97. Rod Clad Temperatures at 10 ft from Heated Bottom for Test 31302

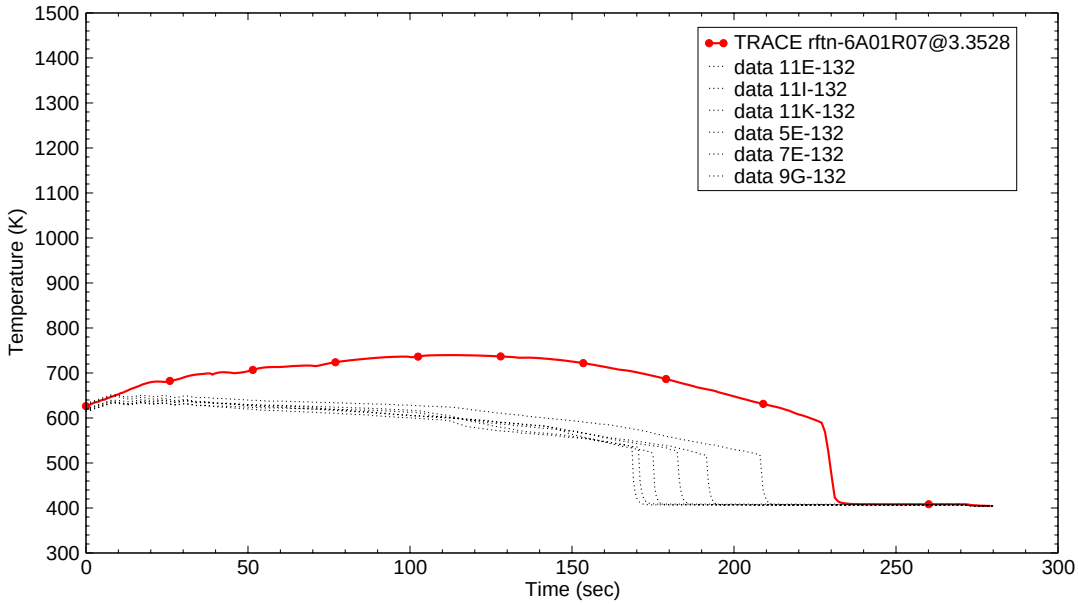

Figure B.7-98. Rod Clad Temperatures at 11 ft from Heated Bottom for Test 31302

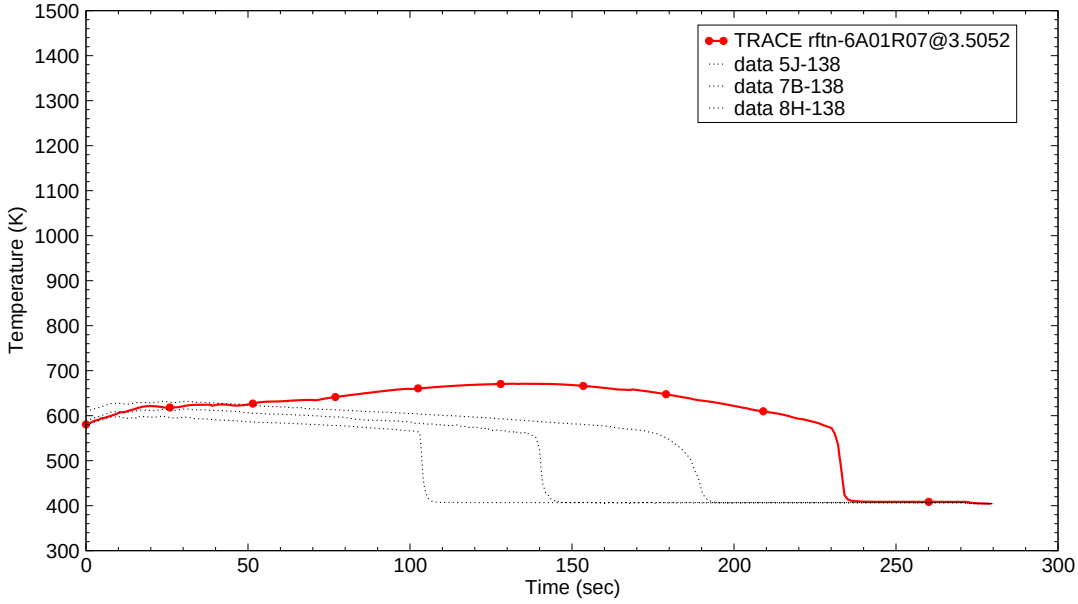

Figure B.7-99. Rod Clad Temperatures at 11.5 ft from Heated Bottom for Test 31302

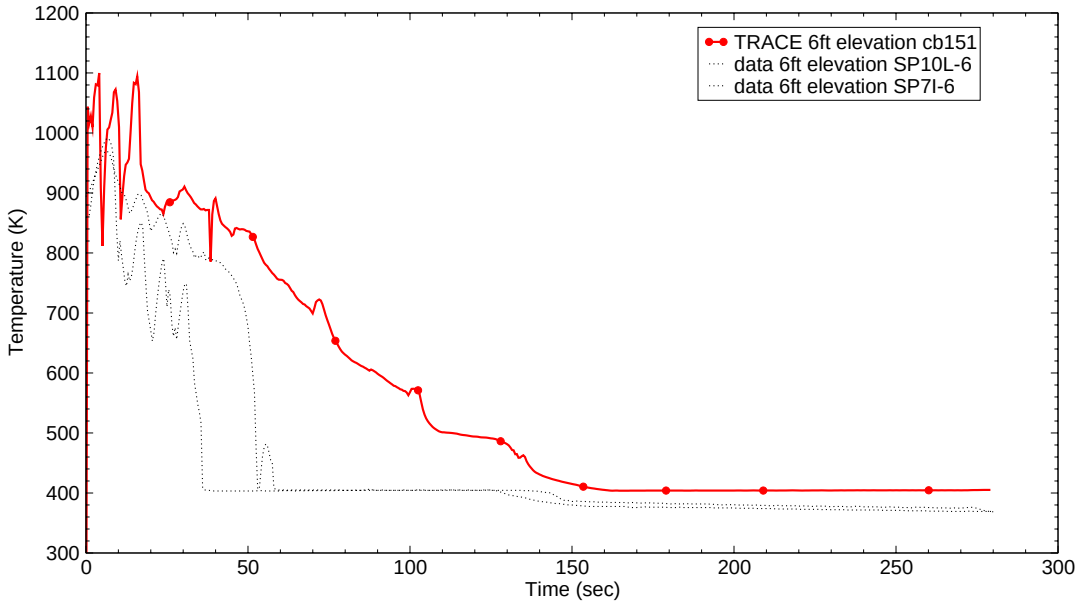

Figure B.7-100. Vapor Temperatures at 6 ft from Heated Bottom for Test 31302

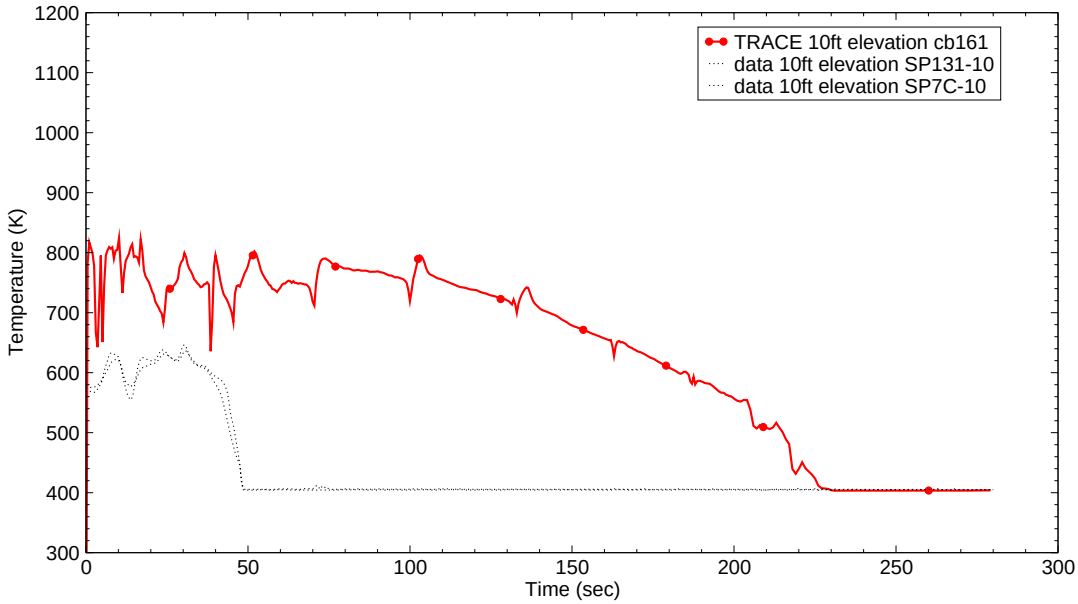

Figure B.7-101. Vapor Temperatures at 10 ft from Heated Bottom for Test 31302

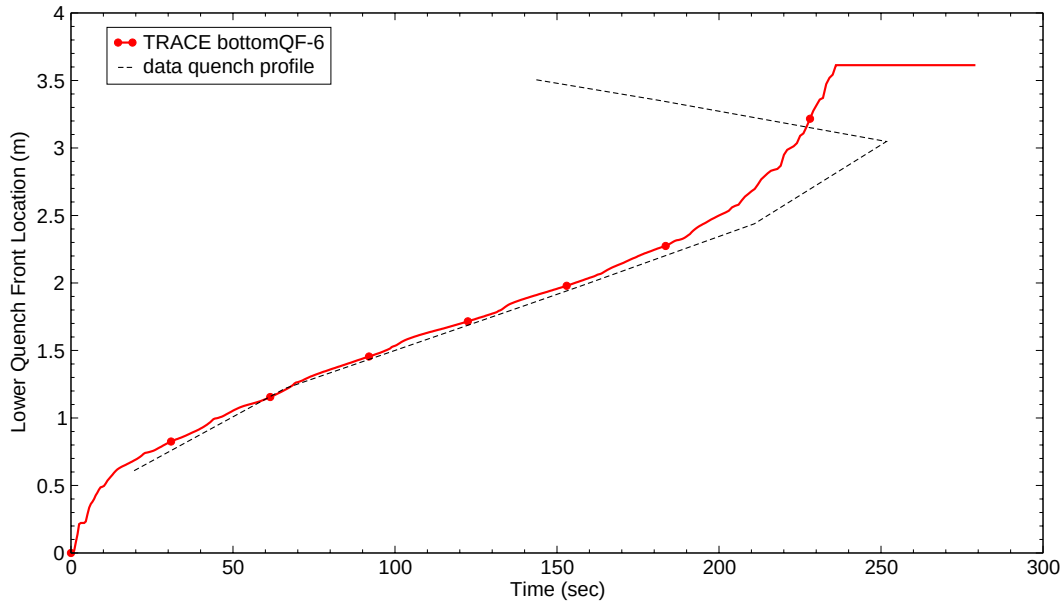

Figure B.7-102. Quench Profile as a Function of Time for Test 31302

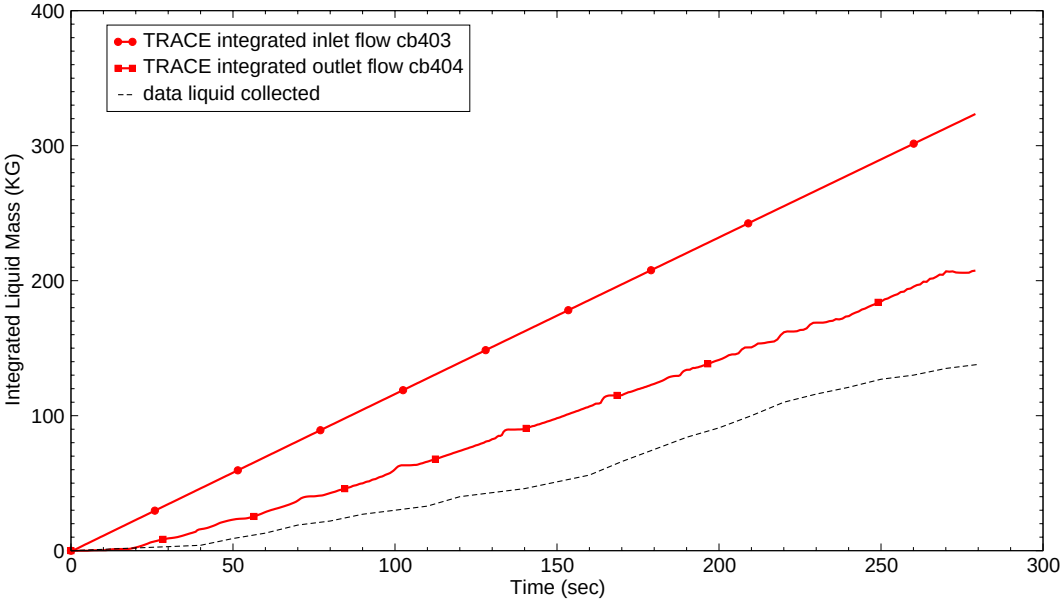

Figure B.7-103. Integrated Liquid Mass Flow into and out of Bundle for Test 31302

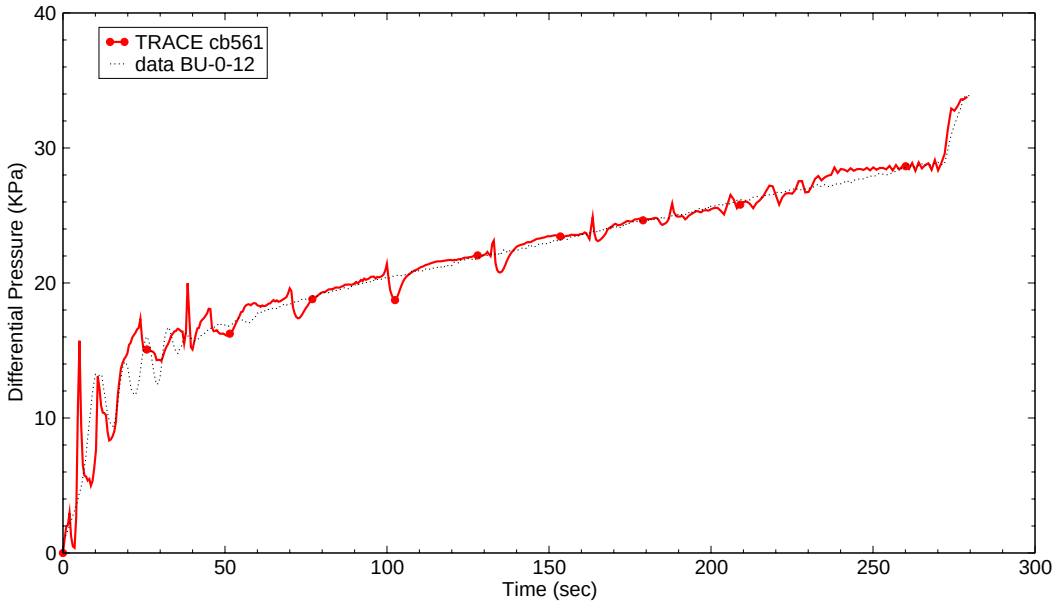

Figure B.7-104. Differential Pressure for the Entire 12 ft Core for Test 31302

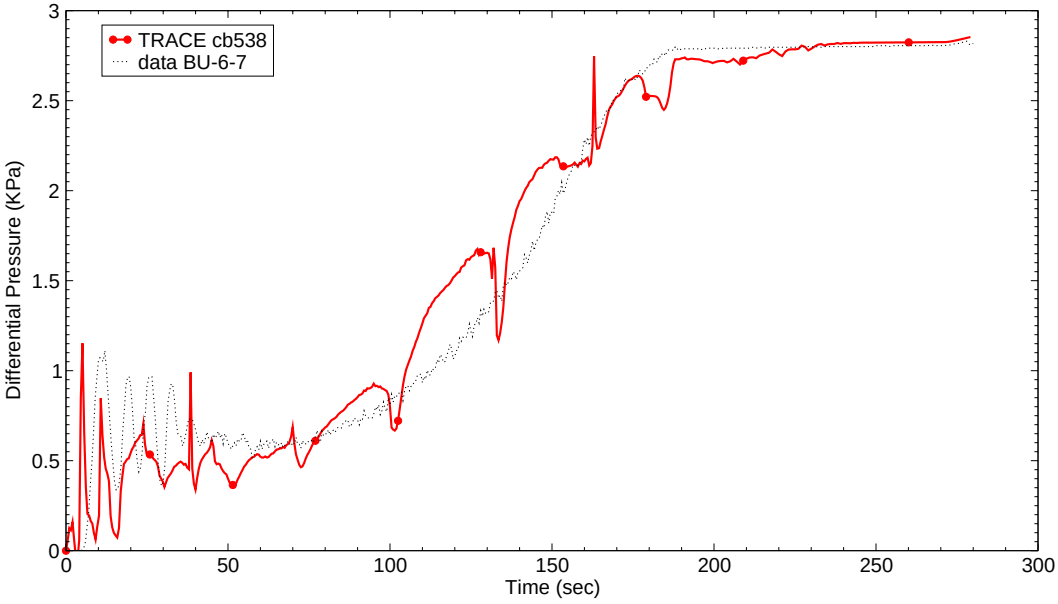

Figure B.7-105. Differential Pressure at 6-7 ft Elevation for Test 31302

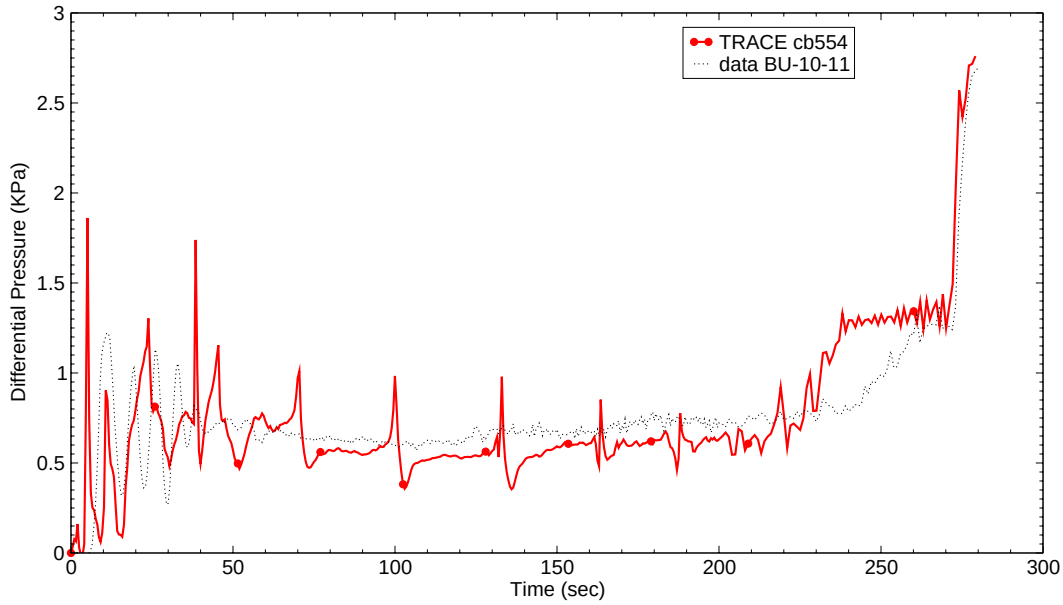

Figure B.7-106. Differential Pressure at 10-11 ft Elevation for Test 31302

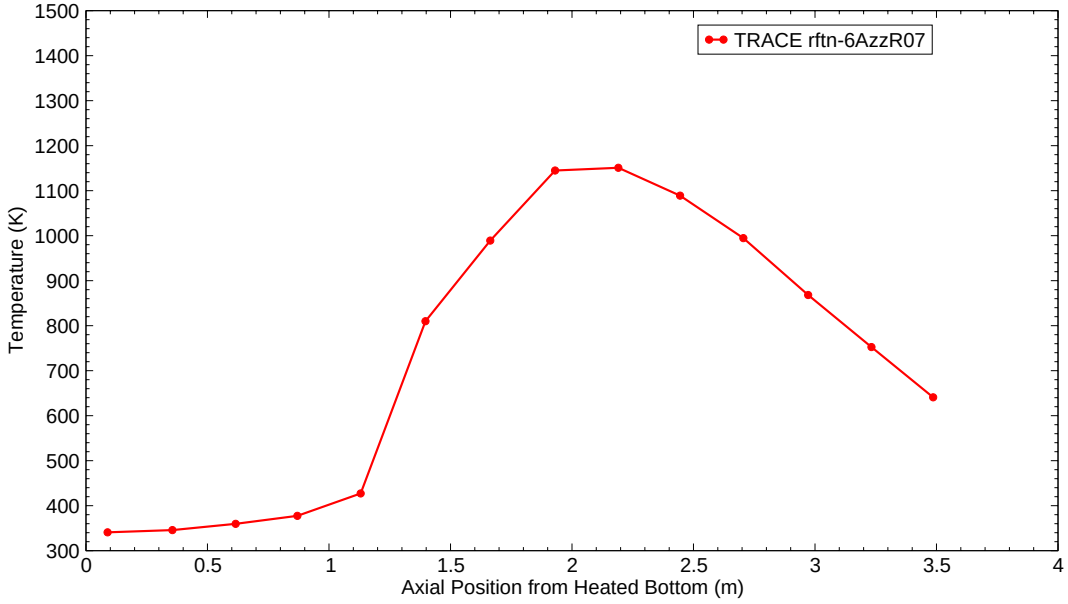

Figure B.7-107. Clad Temperature Profile at 60 sec after Reflood Start for Test 31302

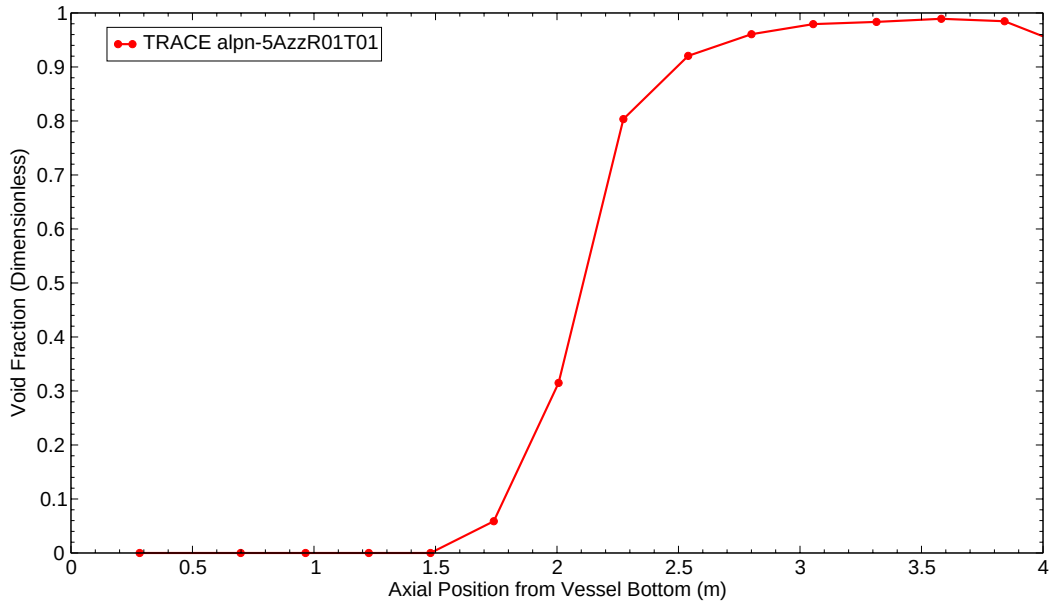

Figure B.7-108. Void Fraction Profile at 60 sec after Reflood Start for Test 31302

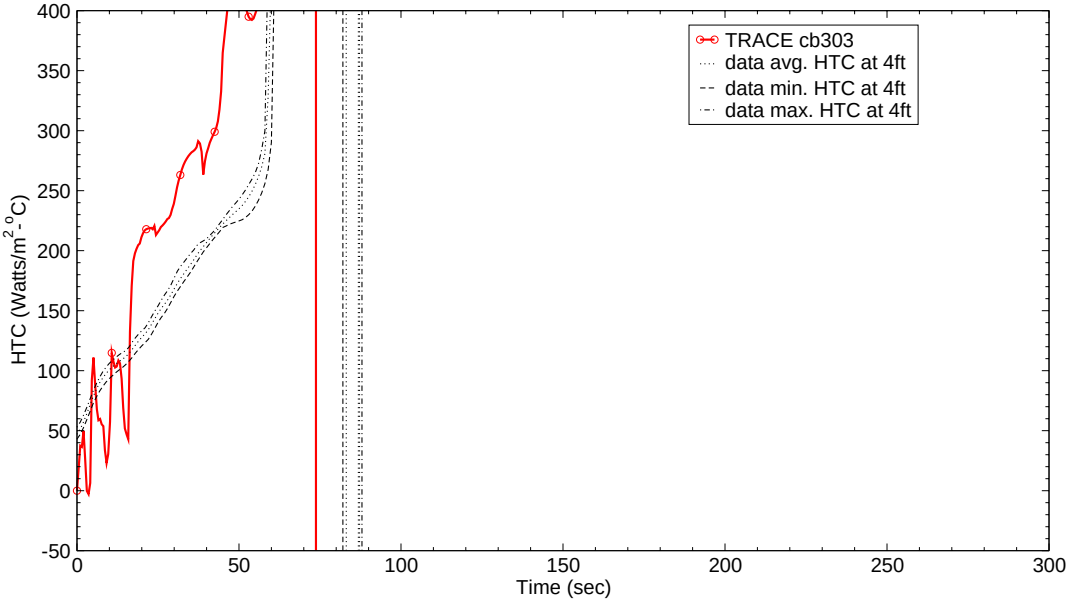

Figure B.7-109. Heat Transfer Coefficient at 4 ft from Heated Bottom for Test 31302

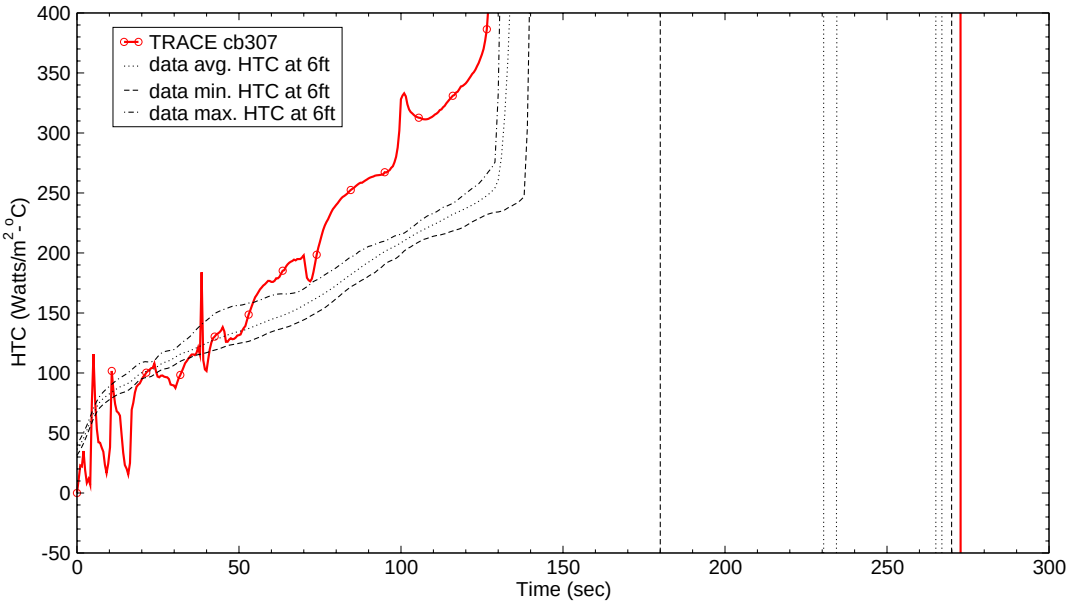

Figure B.7-110. Heat Transfer Coefficient at 6 ft from Heated Bottom for Test 31302

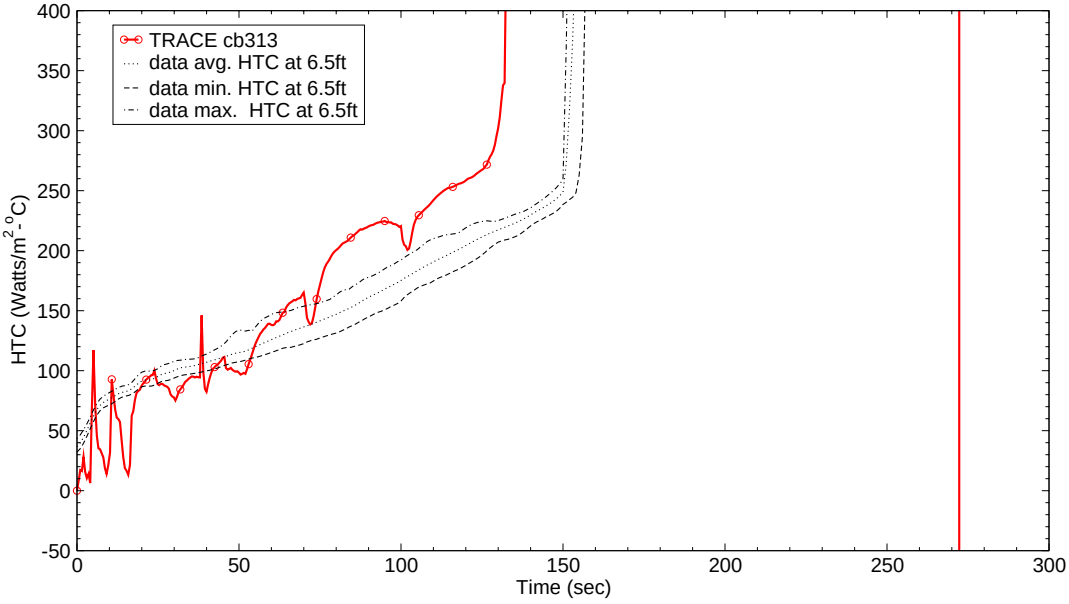

Figure B.7-111. Heat Transfer Coefficient at 6.5 ft from Heated Bottom for Test 31302

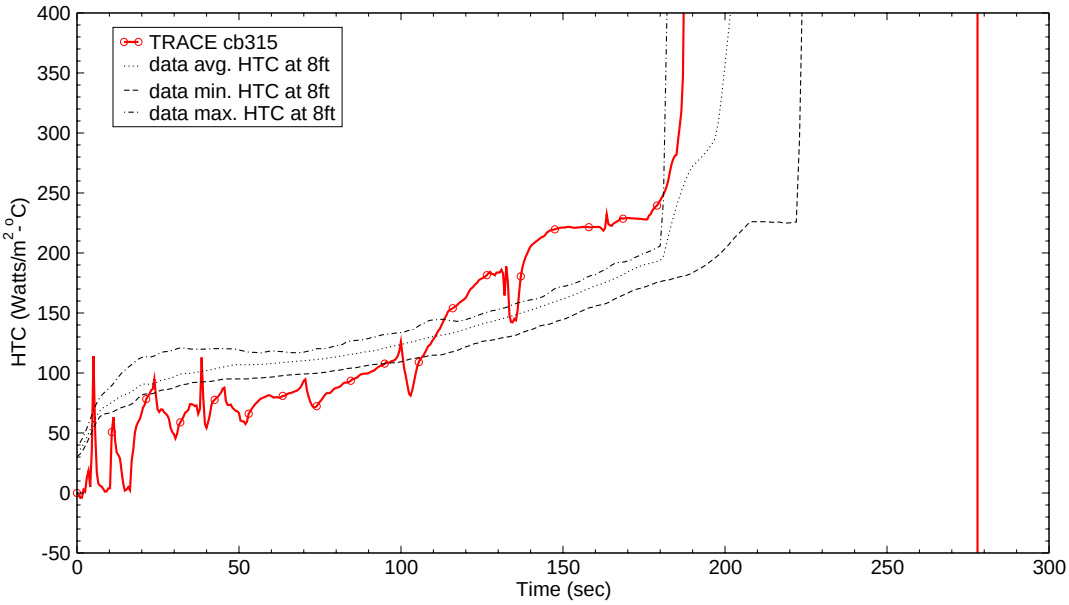

Figure B.7-112. Heat Transfer Coefficient at 8 ft from Heated Bottom for Test 31302

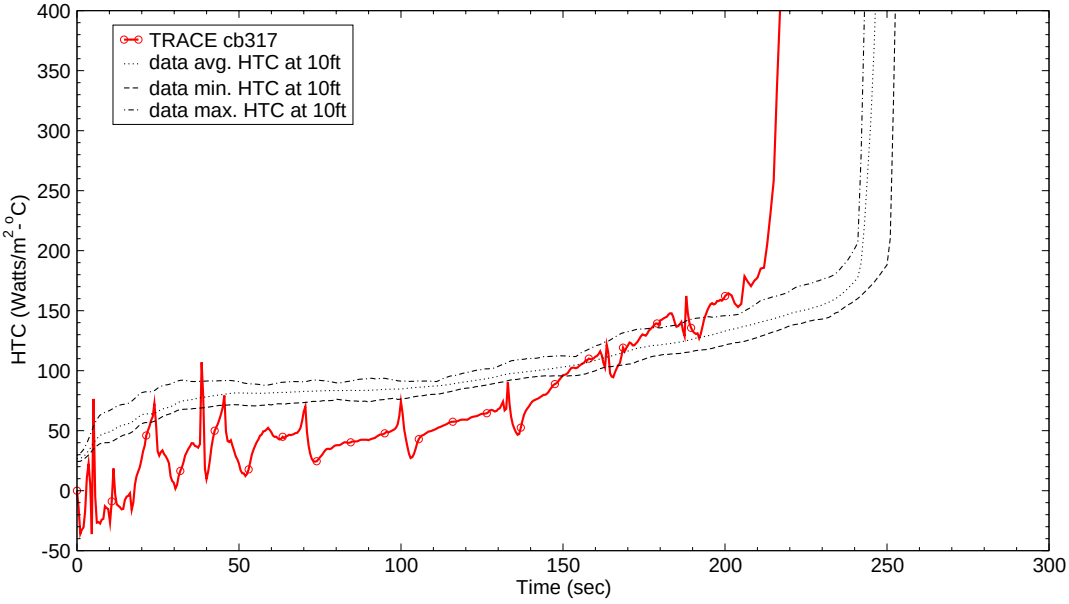

Figure B.7-113. Heat Transfer Coefficient at 10 ft from Heated Bottom for Test 31302

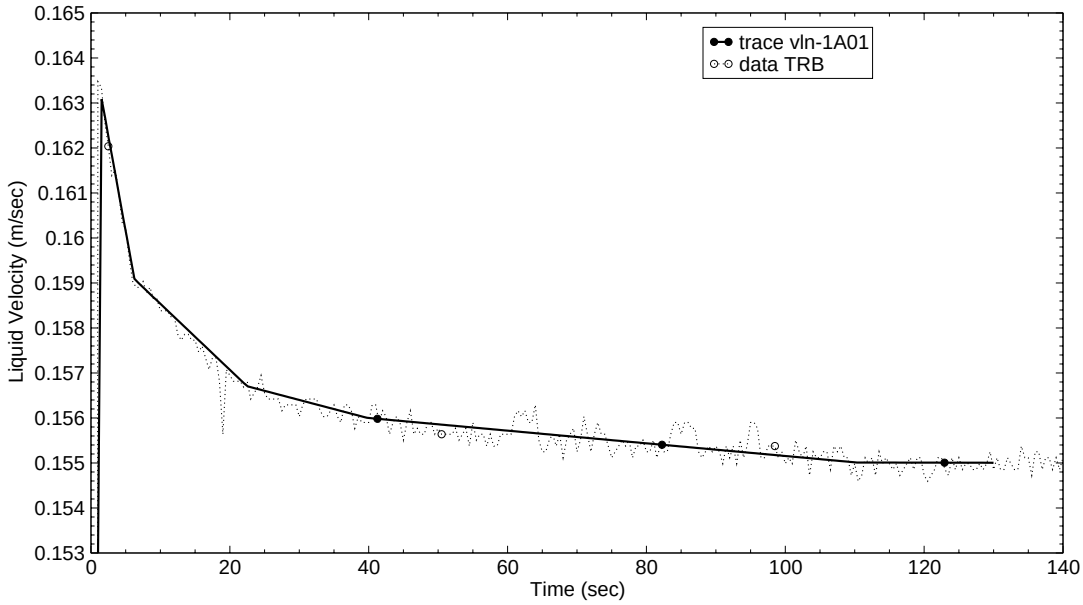

Figure B.7-114. Liquid Inlet Flow Rate for Test 31701

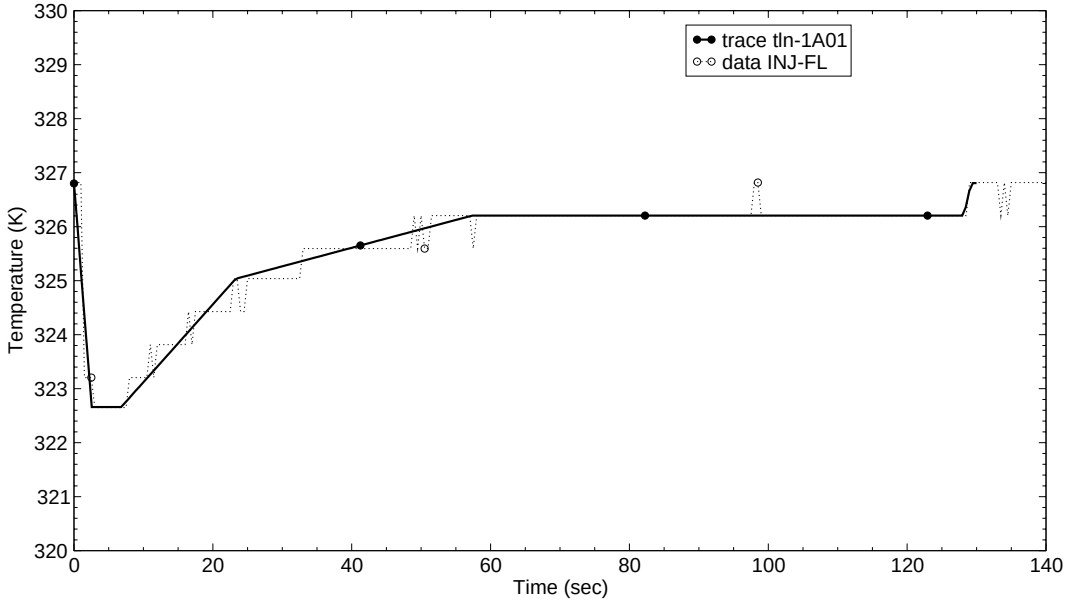

Figure B.7-115. Liquid Inlet Temperature for Test 31701

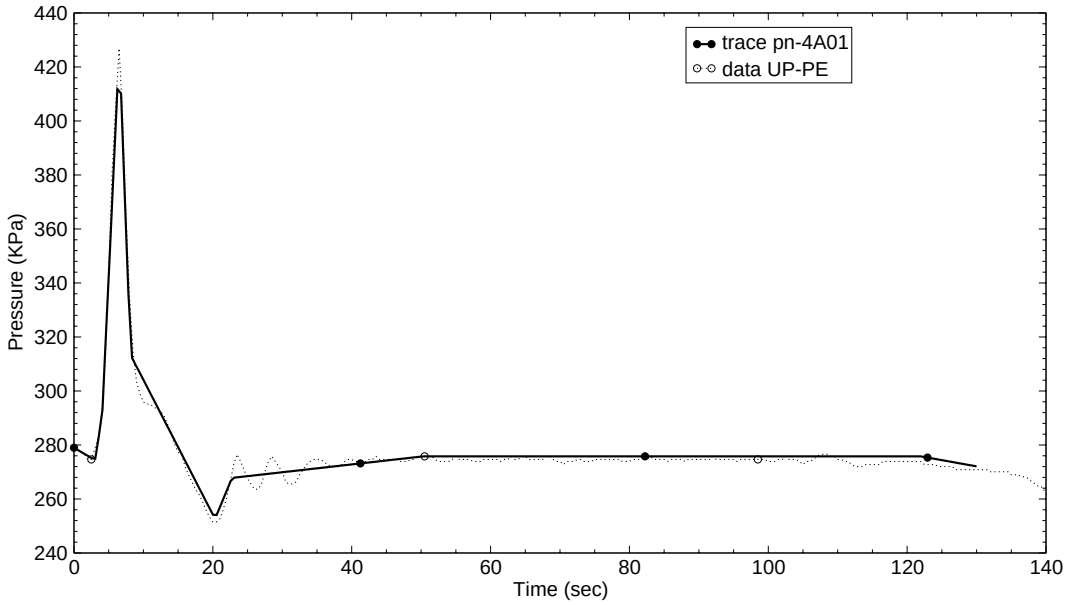

Figure B.7-116. Upper Plenum Exit Pressure for Test 31701

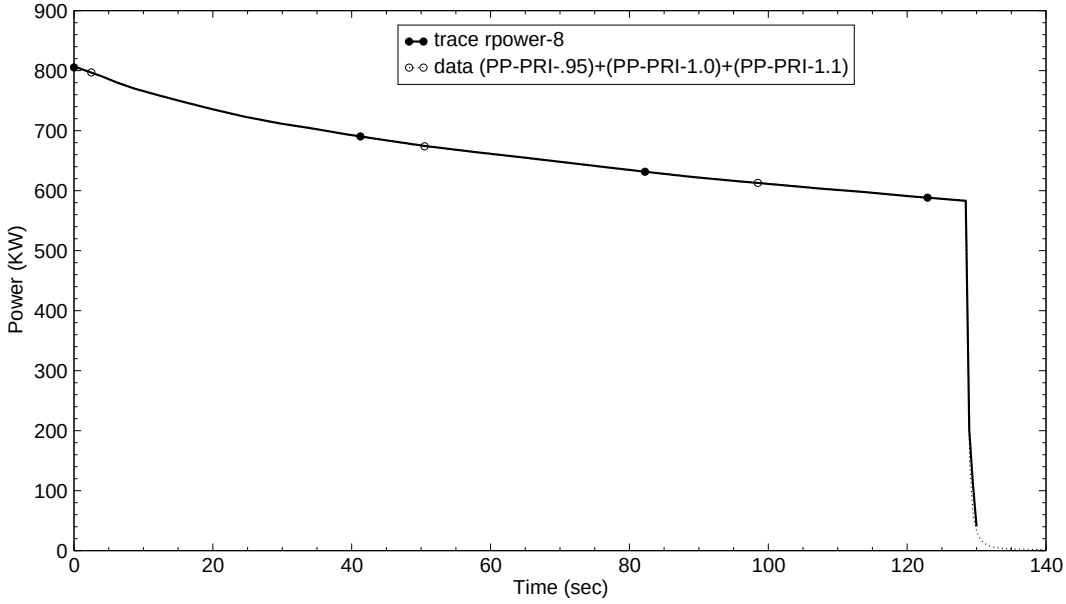

Figure B.7-117. Total Power to the Bundle for Test 31701

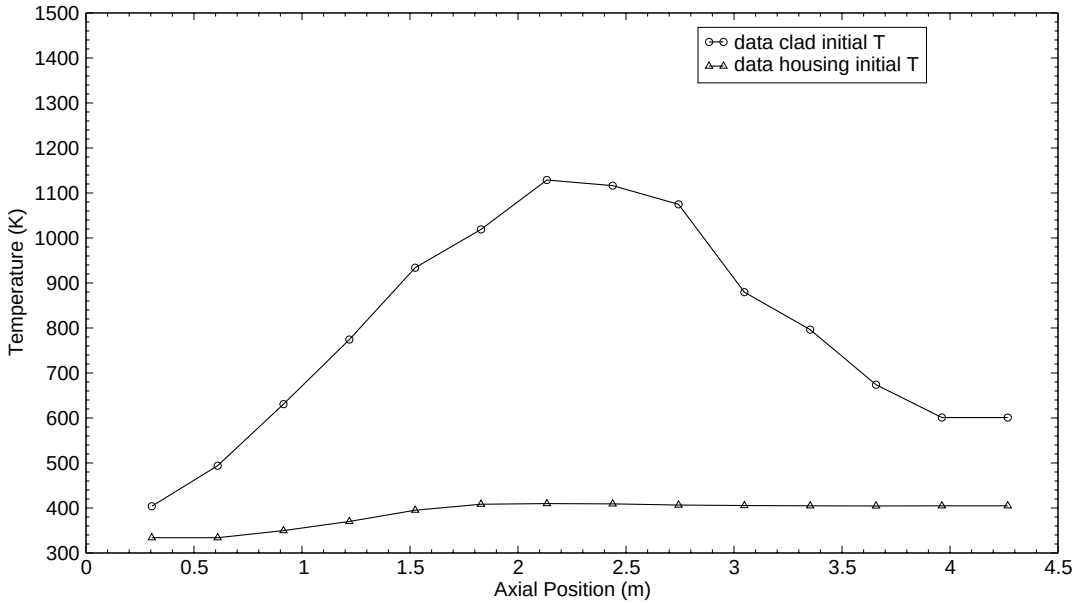

Figure B.7-118. Heater Rod Clad and Housing Initial Temperatures for Test 31701

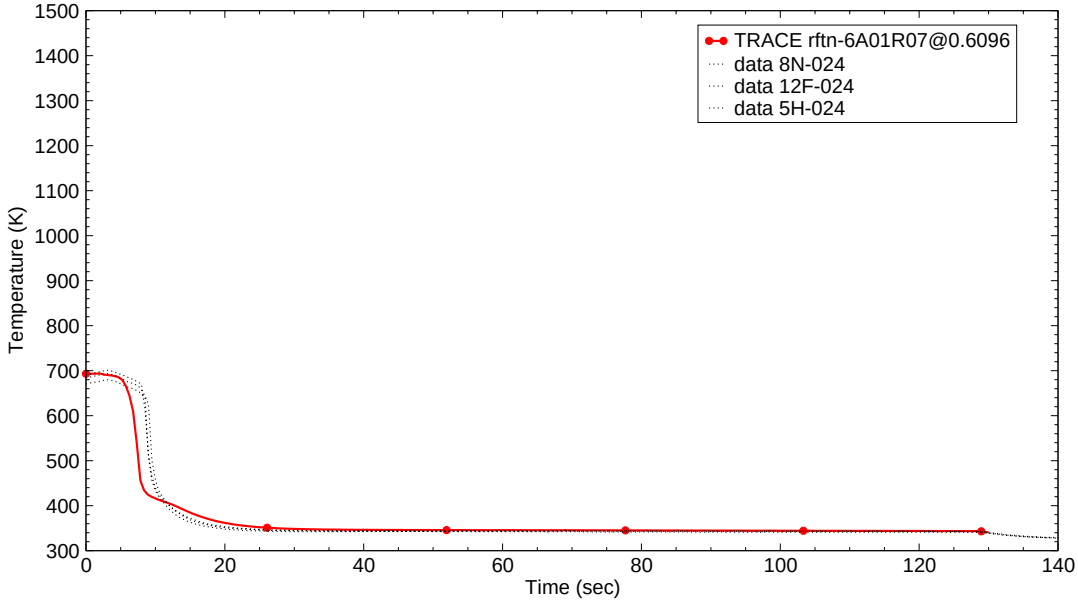

Figure B.7-119. Rod Clad Temperatures at 2 ft from Heated Bottom for Test 31701

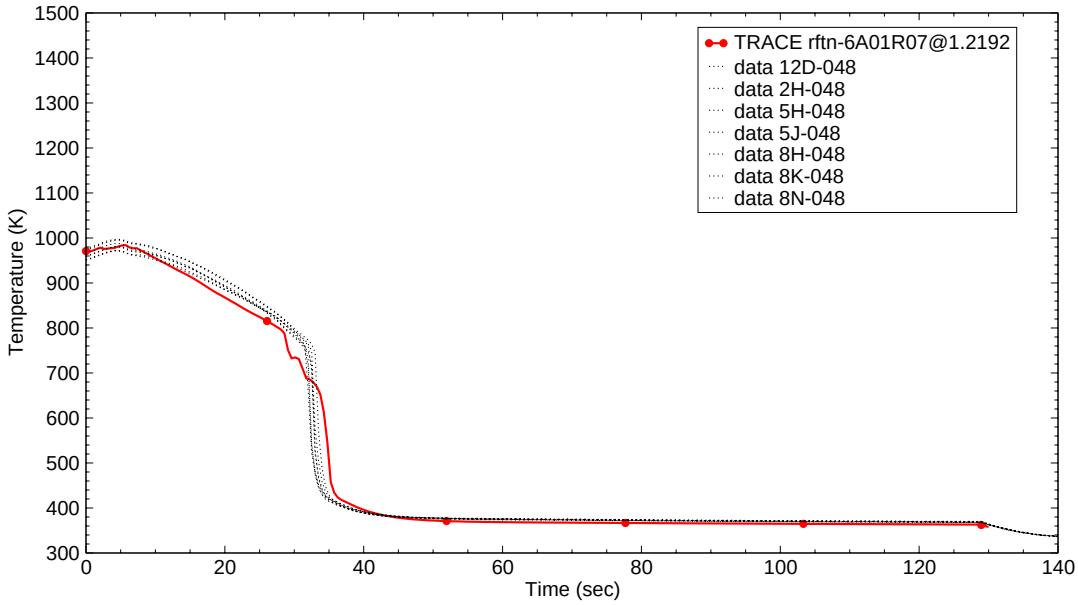

Figure B.7-120. Rod Clad Temperatures at 4 ft from Heated Bottom for Test 31701

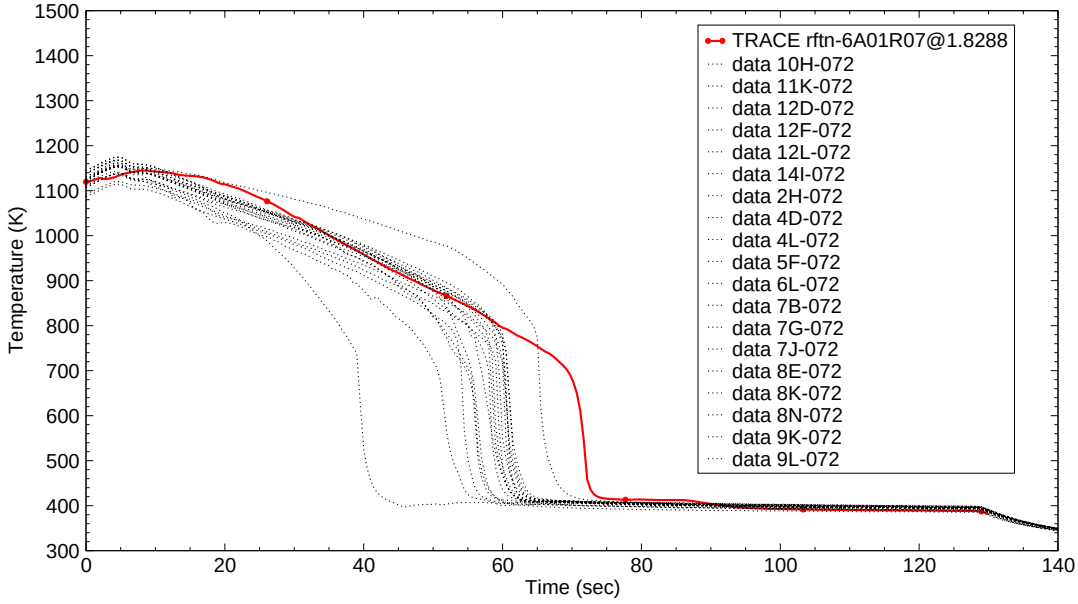

Figure B.7-121. Rod Clad Temperatures at 6 ft from Heated Bottom for Test 31701

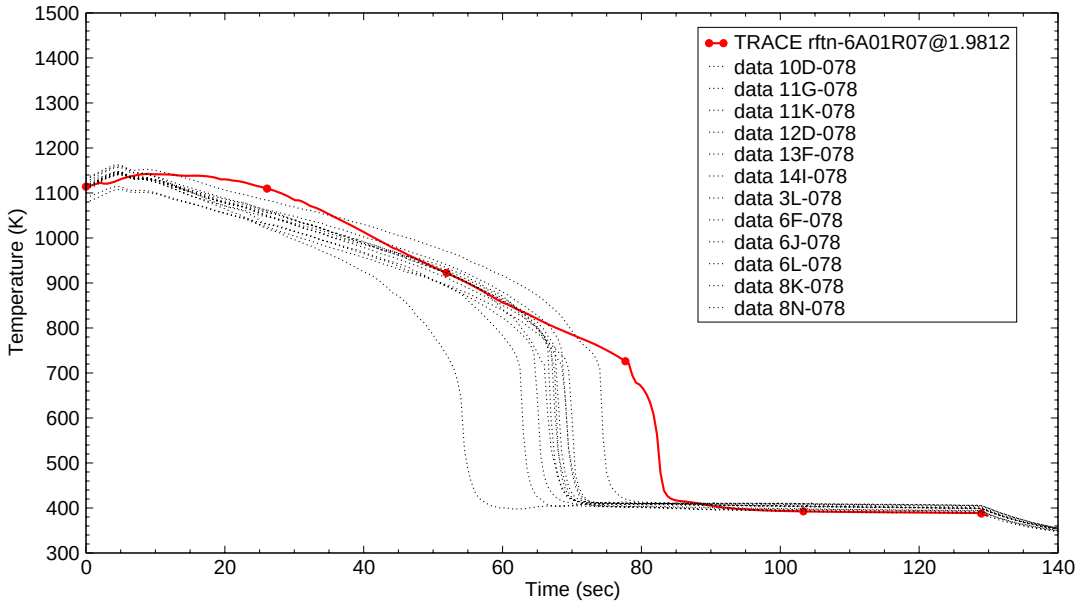

Figure B.7-122. Rod Clad Temperatures at 6.5 ft from Heated Bottom for Test 31701

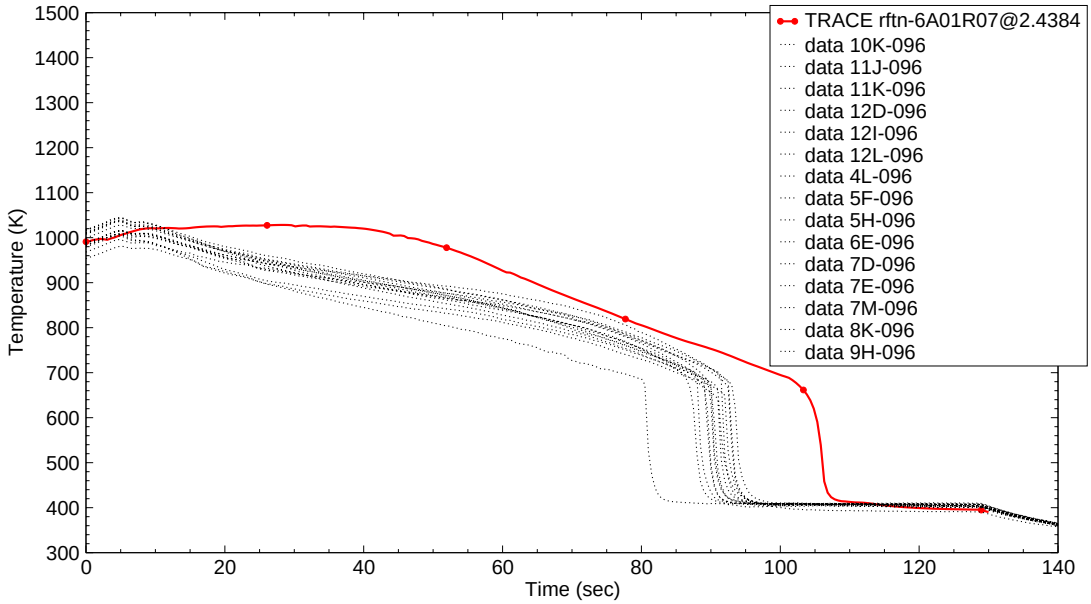

Figure B.7-123. Rod Clad Temperatures at 8 ft from Heated Bottom for Test 31701

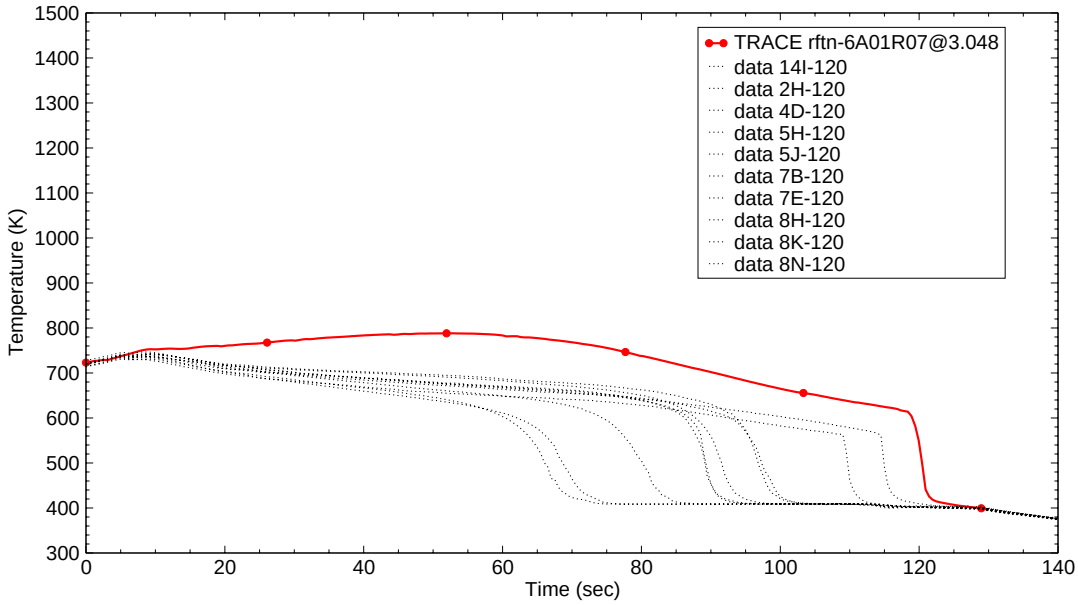

Figure B.7-124. Rod Clad Temperatures at 10 ft from Heated Bottom for Test 31701

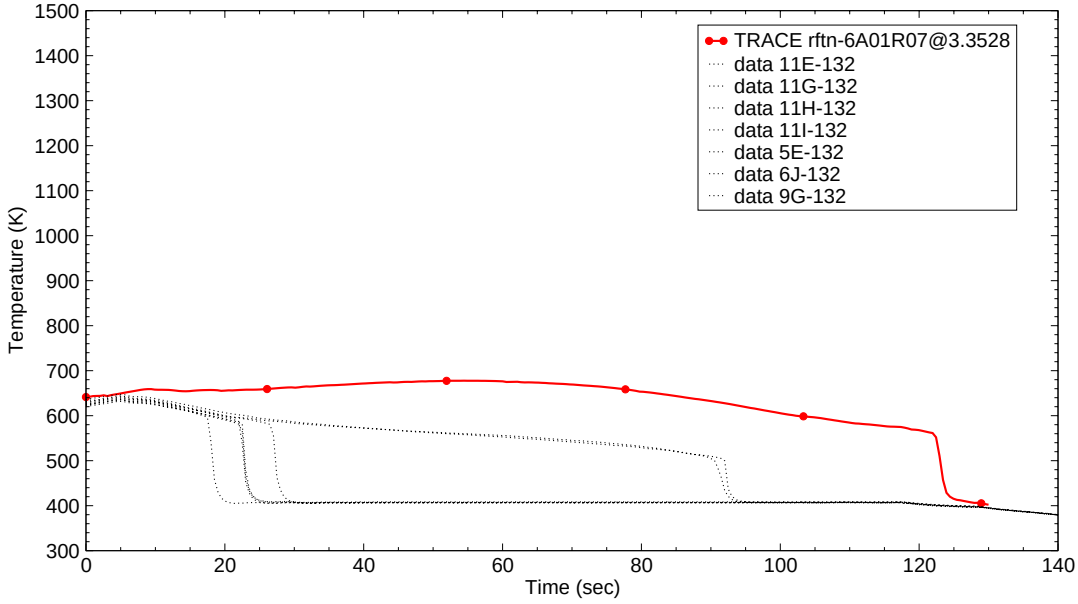

Figure B.7-125. Rod Clad Temperatures at 11 ft from Heated Bottom for Test 31701

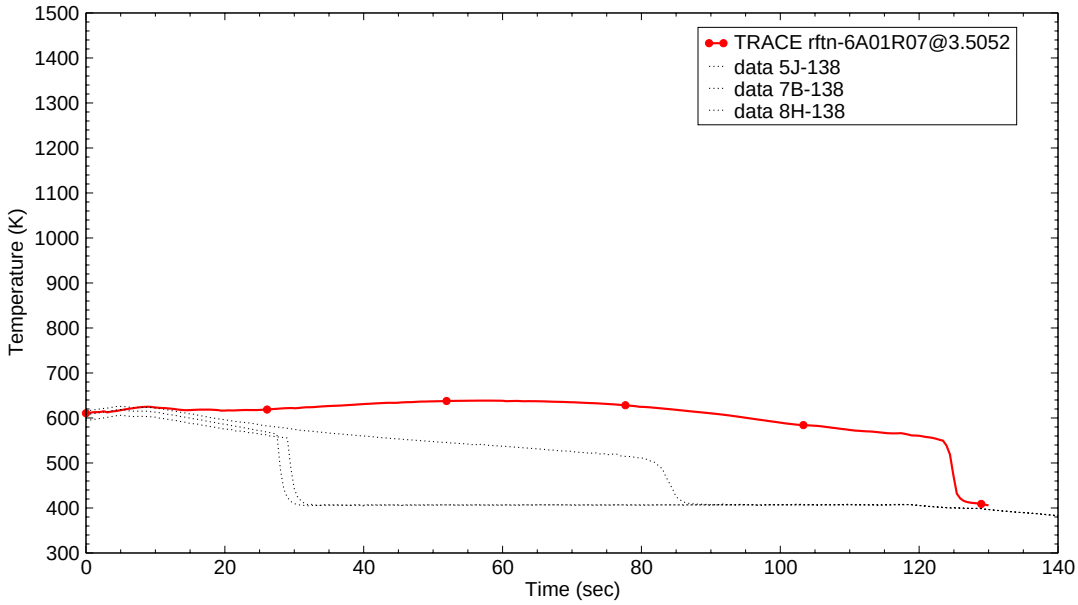

Figure B.7-126. Rod Clad Temperatures at 11.5 ft from Heated Bottom for Test 31701

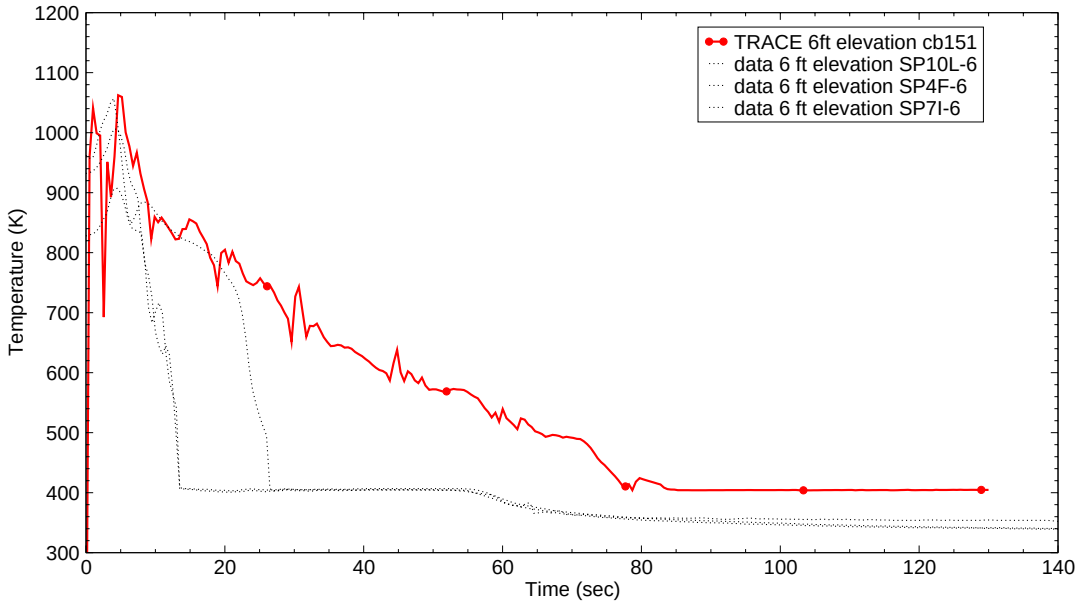

Figure B.7-127. Vapor Temperatures at 6 ft from Heated Bottom for Test 31701

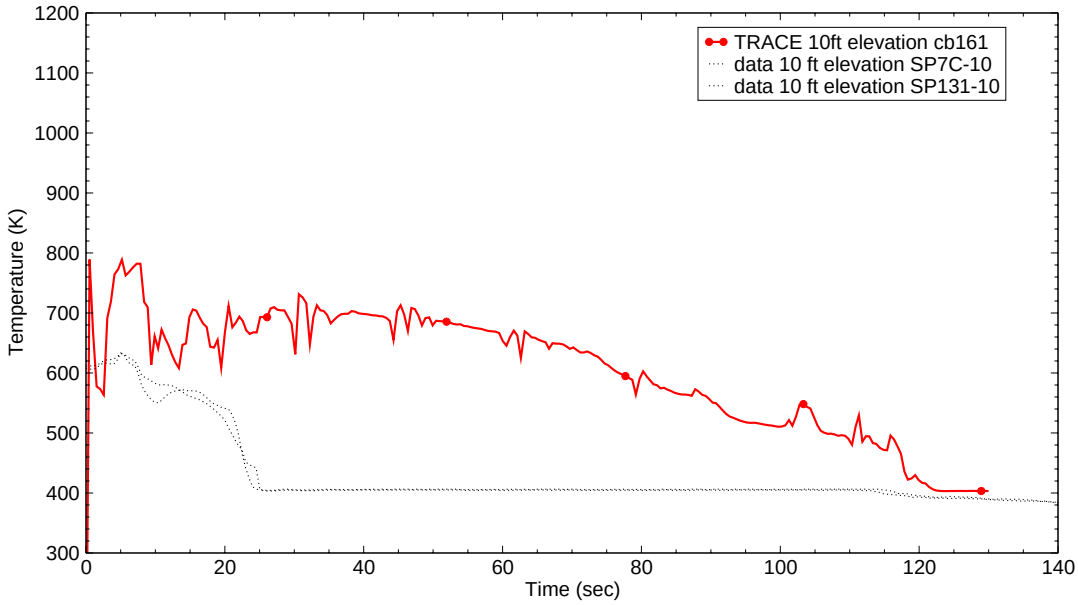

Figure B.7-128. Vapor Temperatures at 10 ft from Heated Bottom for Test 31701

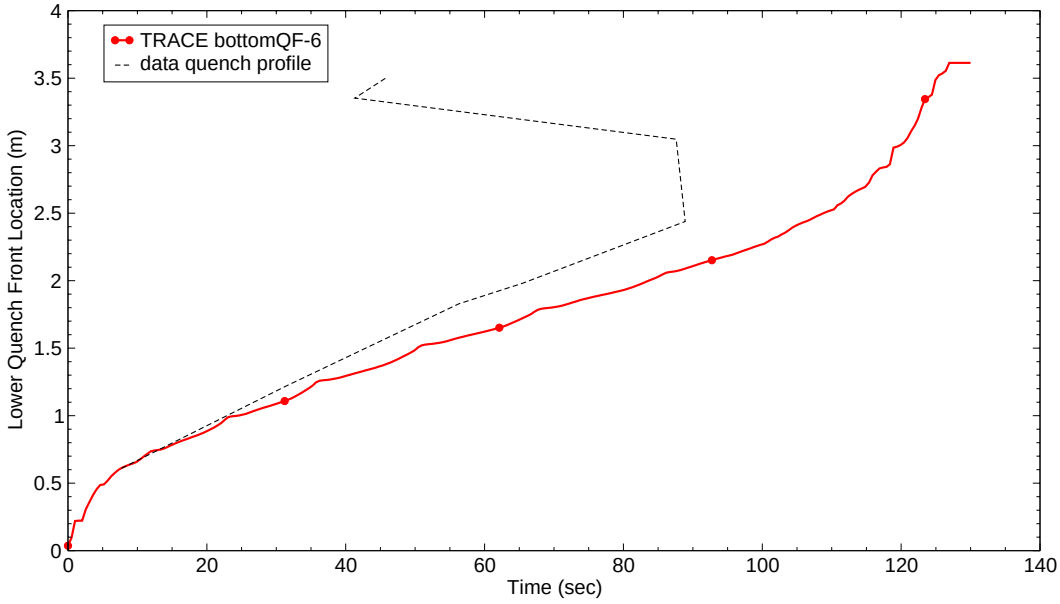

Figure B.7-129. Quench Profile as a Function of Time for Test 31701

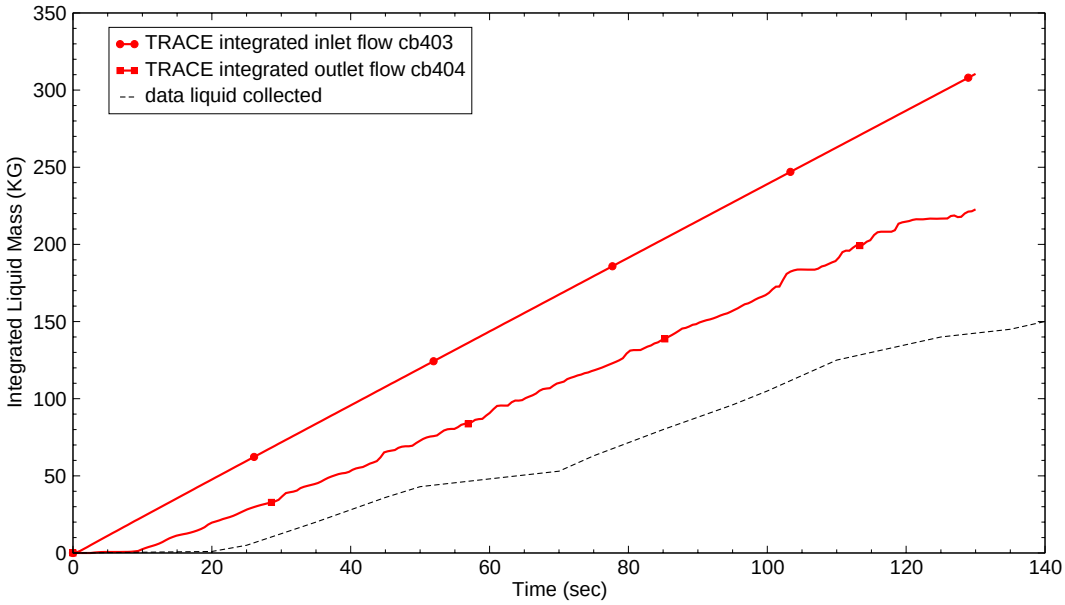

Figure B.7-130. Integrated Liquid Mass Flow into and out of Bundle for Test 31701

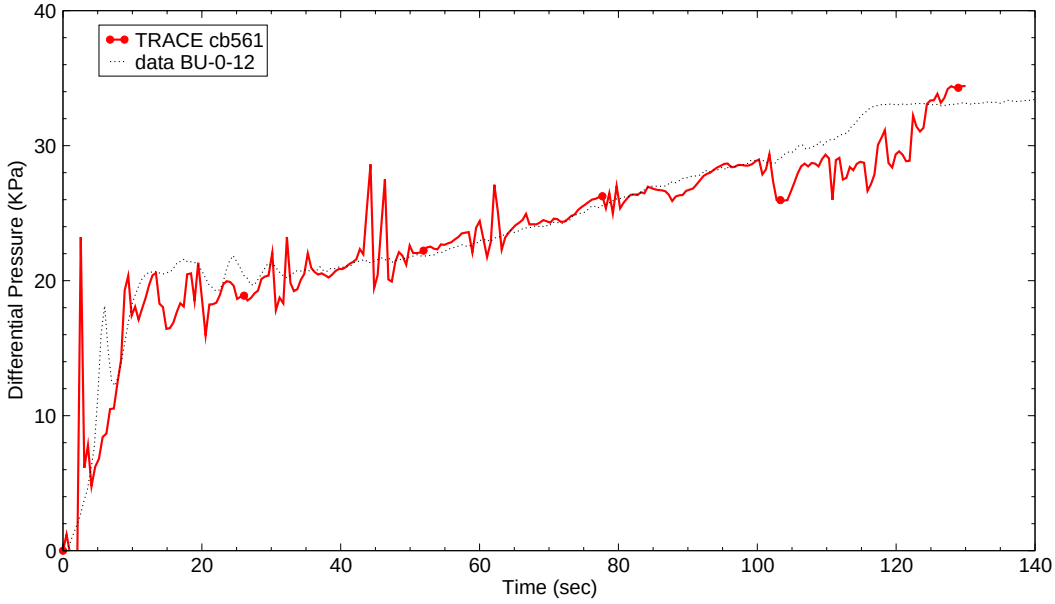

Figure B.7-131. Differential Pressure for the Entire 12 ft Core for Test 31701

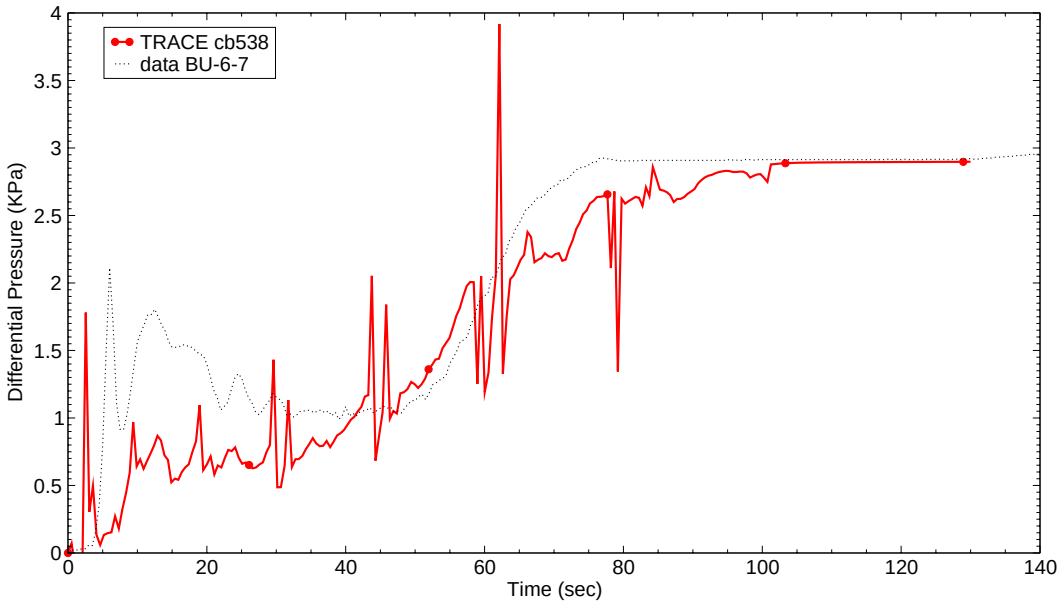

Figure B.7-132. Differential Pressure at 6-7 ft Elevation for Test 31701

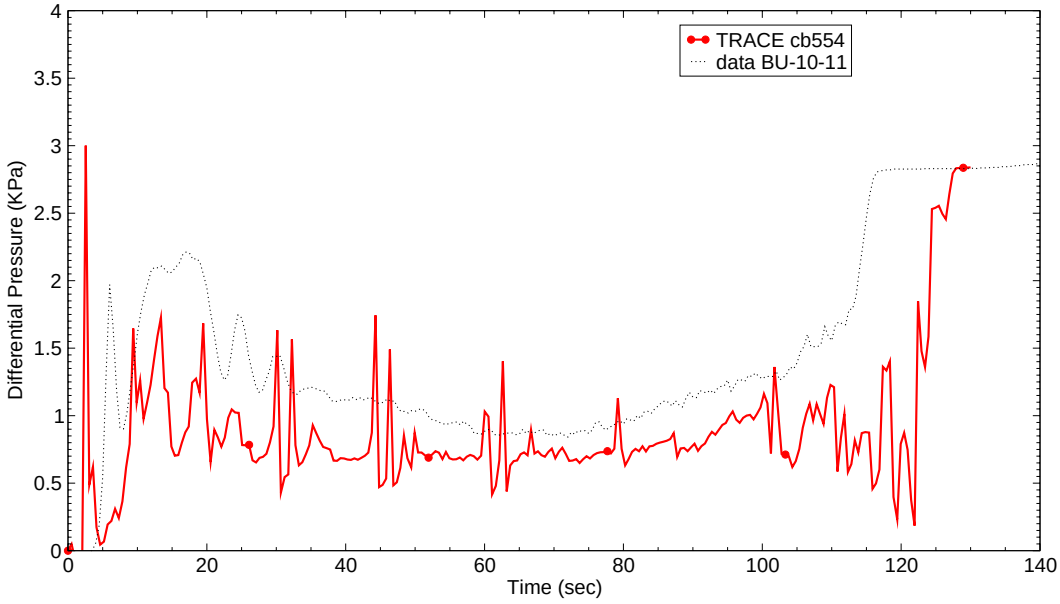

Figure B.7-133. Differential Pressure at 10-11 ft Elevation for Test 31701

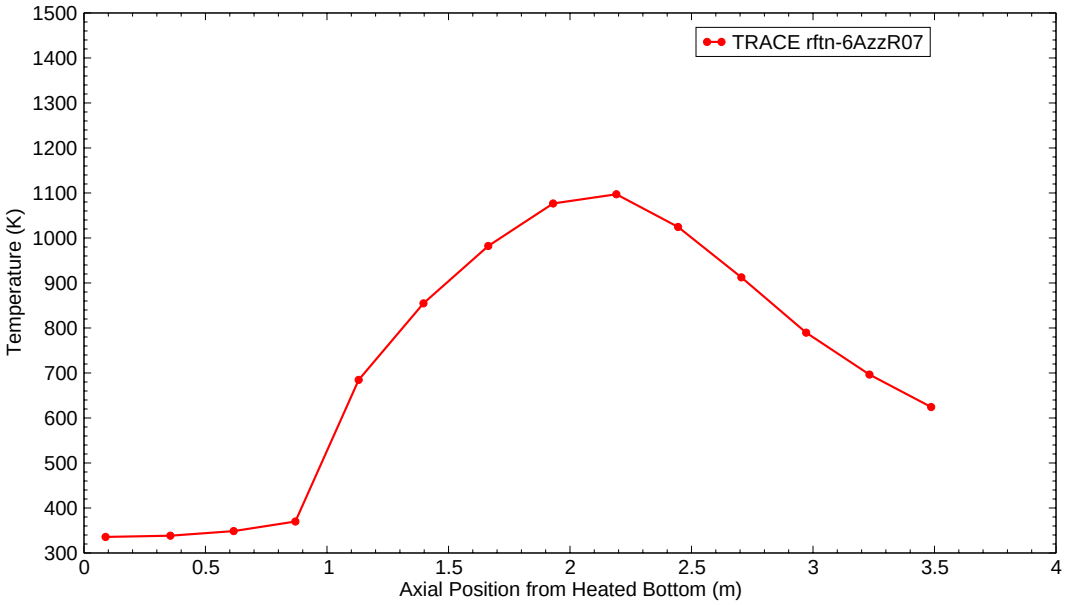

Figure B.7-134. Clad Temperature Profile at 30 sec after Reflood Start for Test 31701

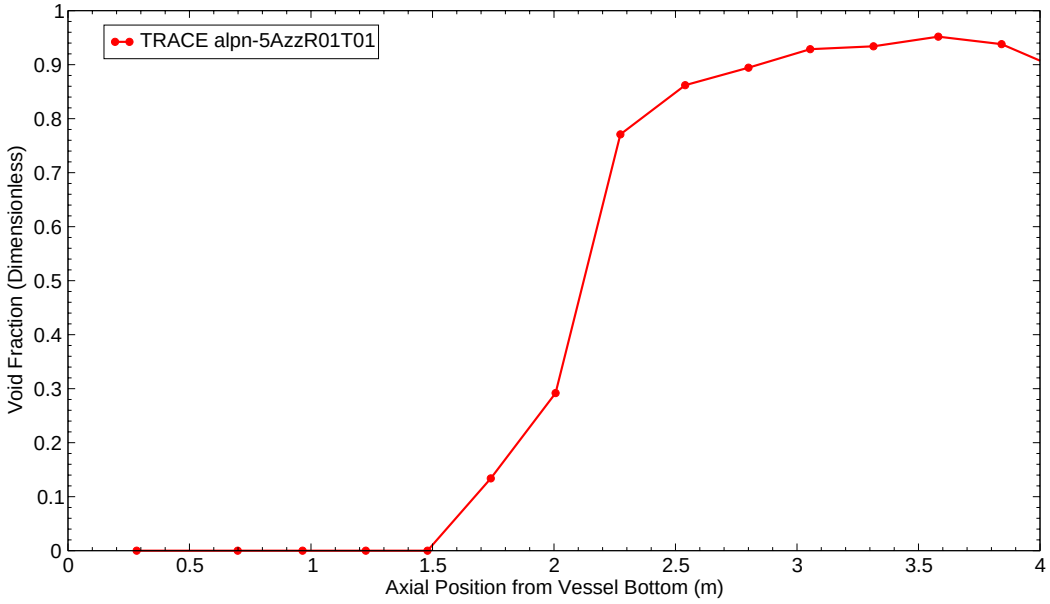

Figure B.7-135. Void Fraction Profile at 30 sec after Reflood Start for Test 31701

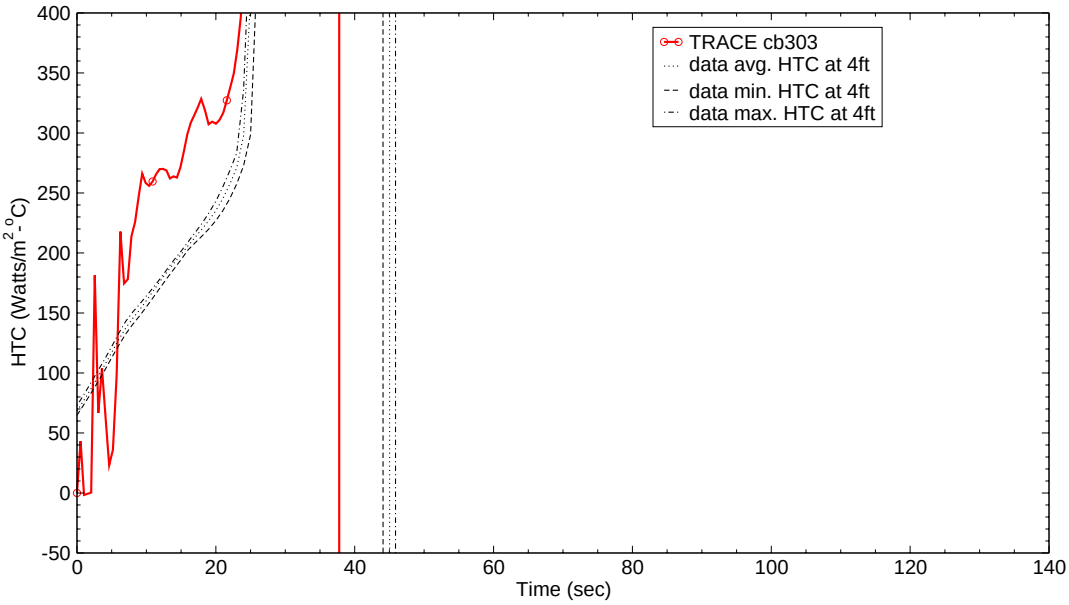

Figure B.7-136. Heat Transfer Coefficient at 4 ft from Heated Bottom for Test 31701

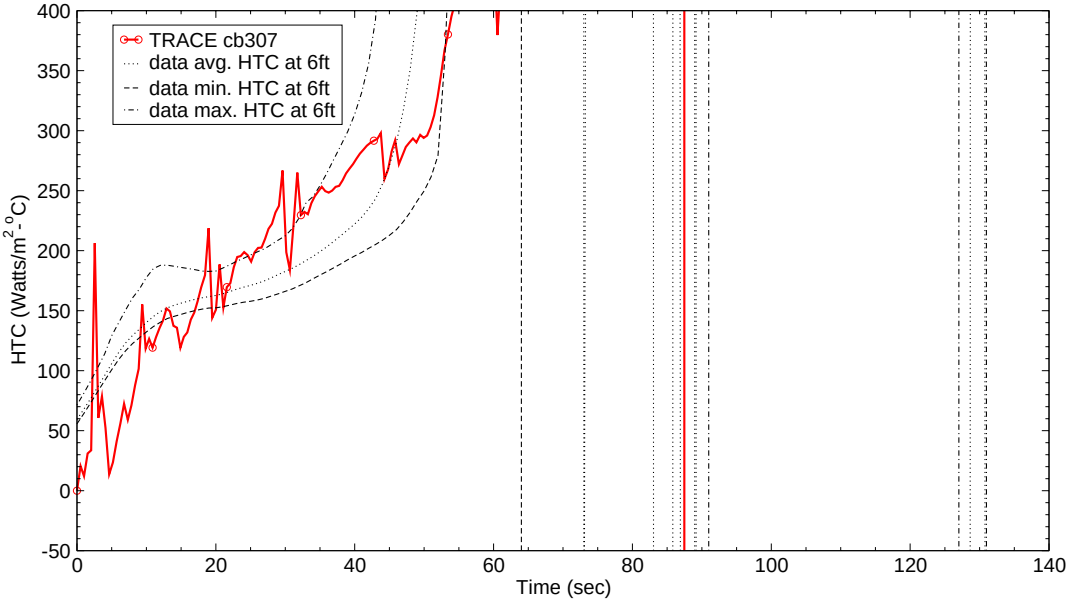

Figure B.7-137. Heat Transfer Coefficient at 6 ft from Heated Bottom for Test 31701

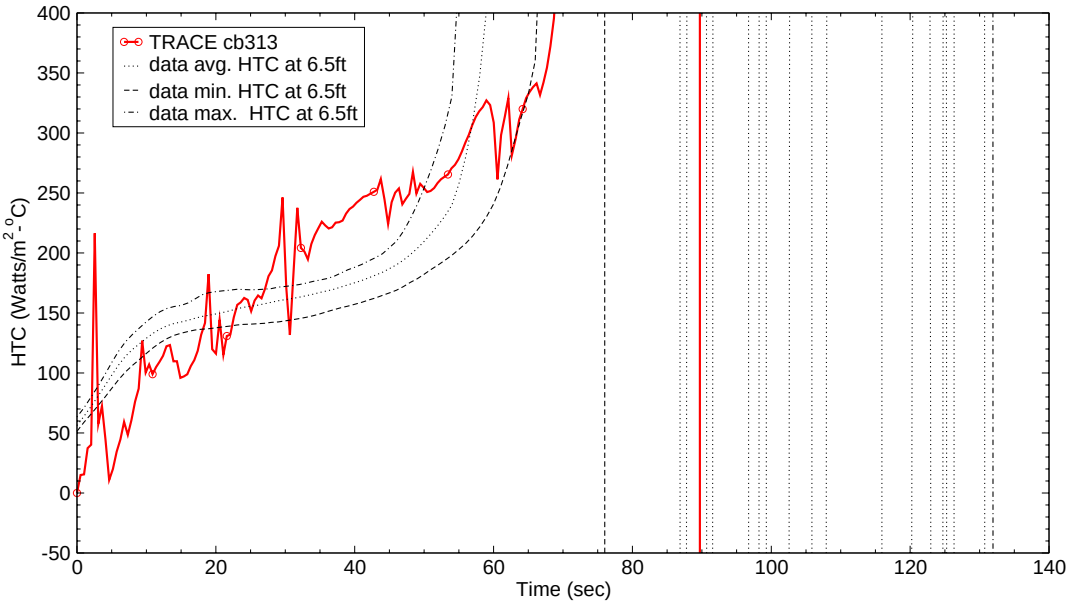

Figure B.7-138. Heat Transfer Coefficient at 6.5 ft from Heated Bottom for Test 31701

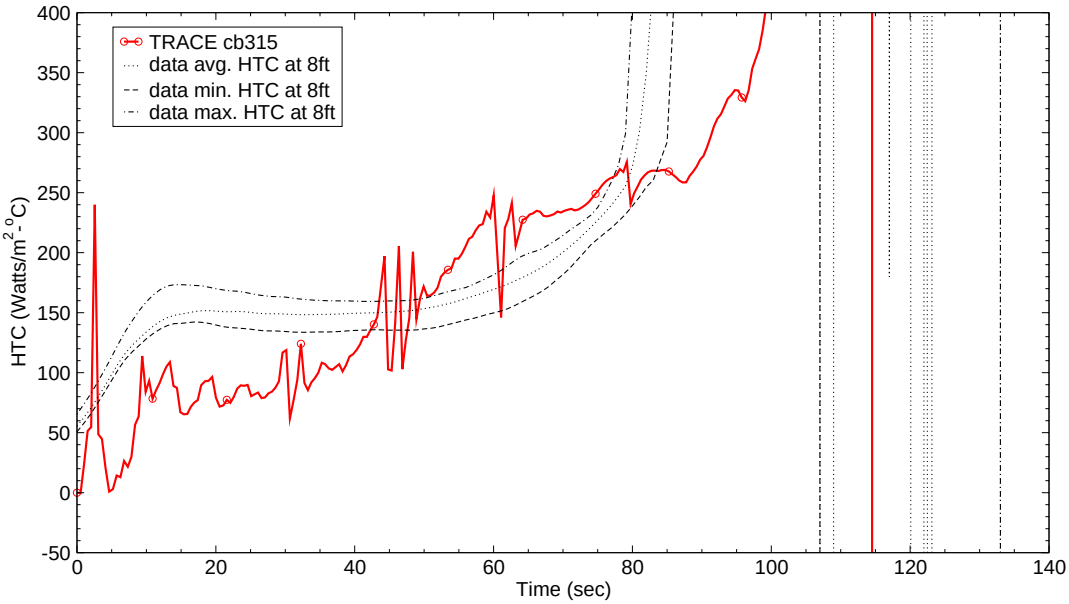

Figure B.7-139. Heat Transfer Coefficient at 8 ft from Heated Bottom for Test 31701

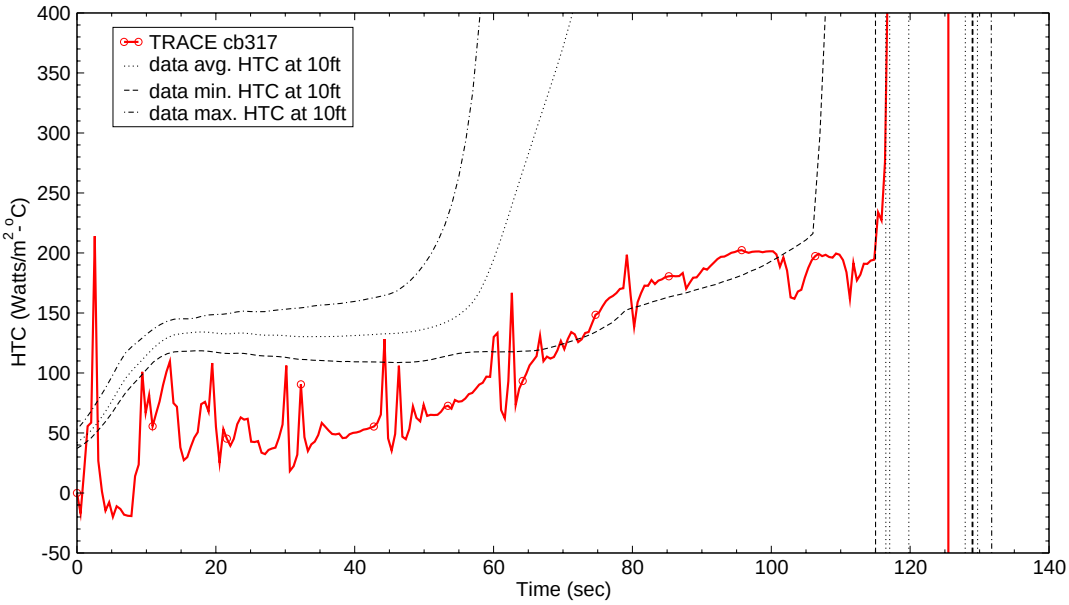

Figure B.7-140. Heat Transfer Coefficient at 10 ft from Heated Bottom for Test 31701

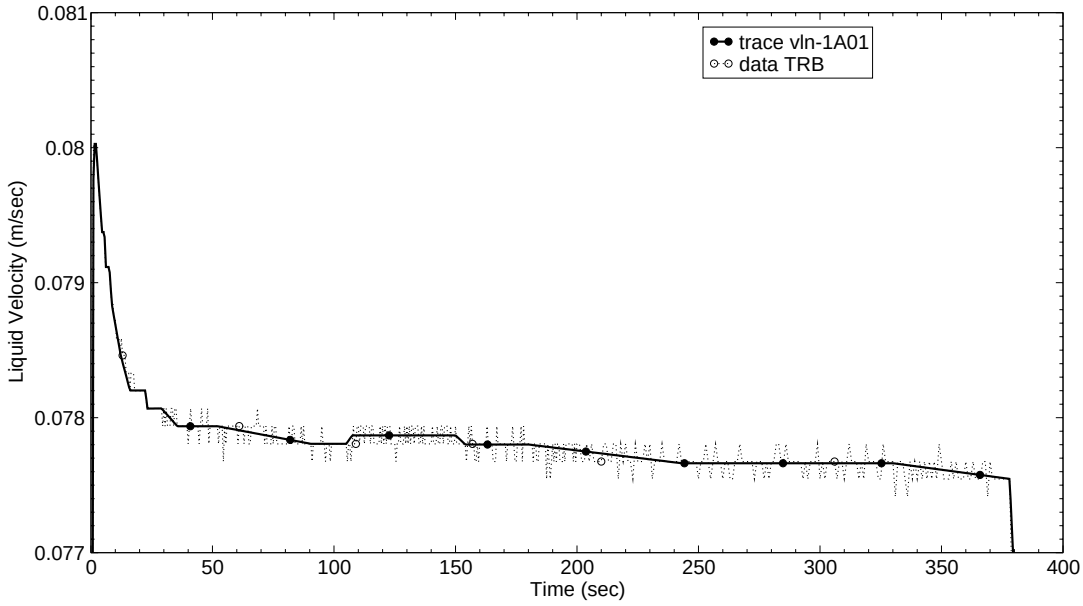

Figure B.7-141. Liquid Inlet Flow Rate for Test 31108

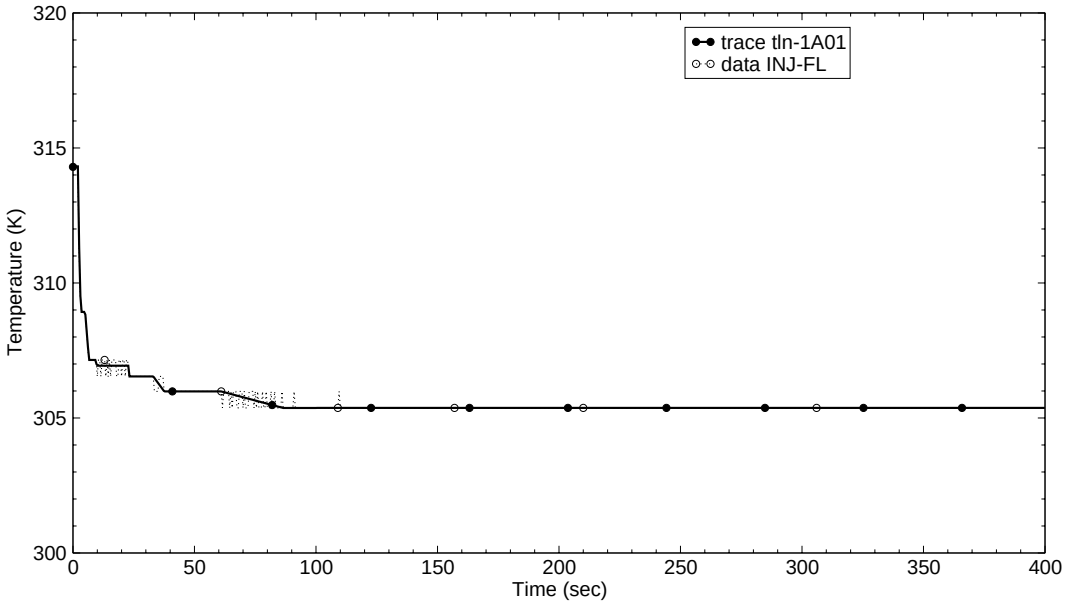

Figure B.7-142. Liquid Inlet Temperature for Test 31108

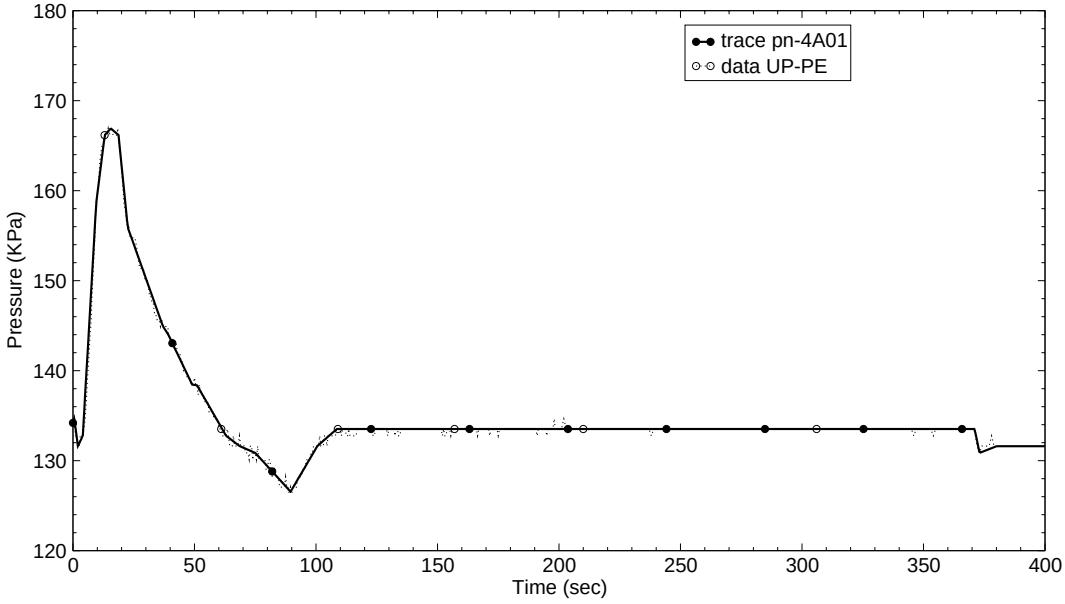

Figure B.7-143. Upper Plenum Exit Pressure for Test 31108

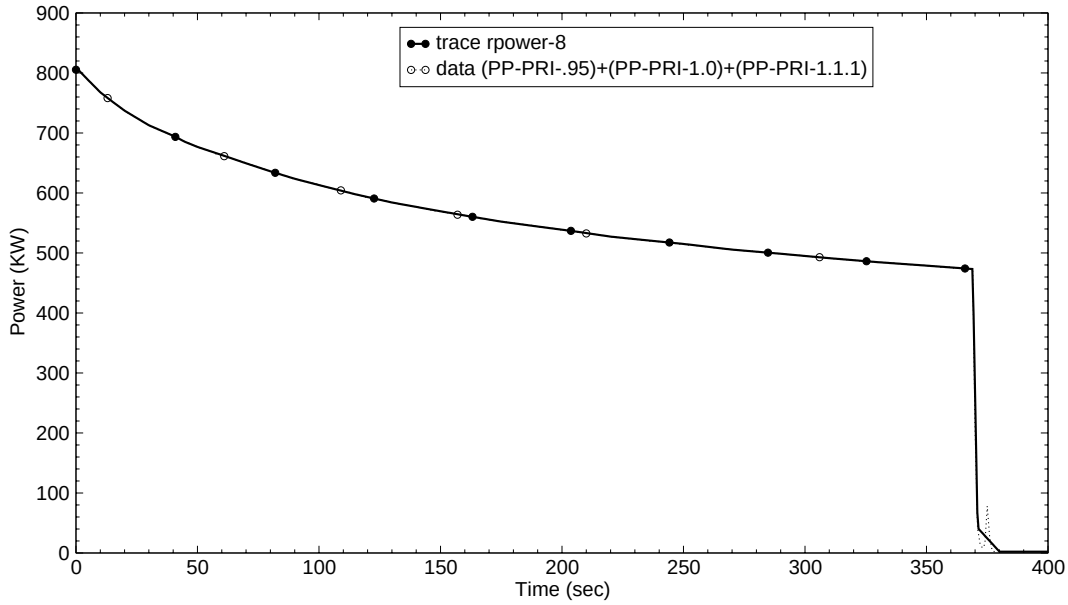

Figure B.7-144. Total Power to the Bundle for Test 31108

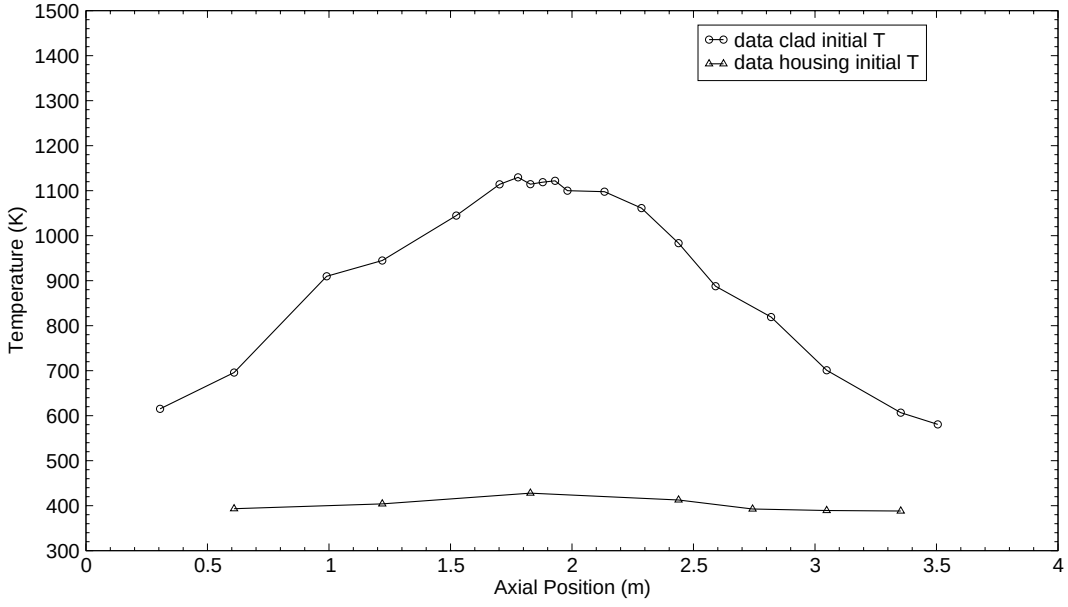

Figure B.7-145. Heater Rod Clad and Housing Initial Temperatures for Test 31108

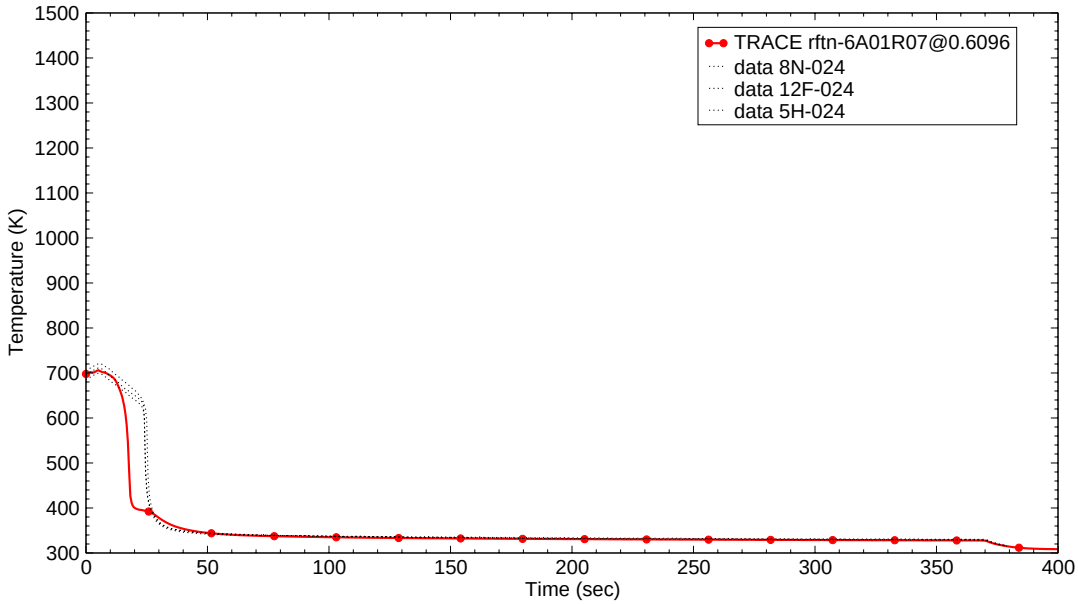

Figure B.7-146. Rod Clad Temperatures at 2 ft from Heated Bottom for Test 31108

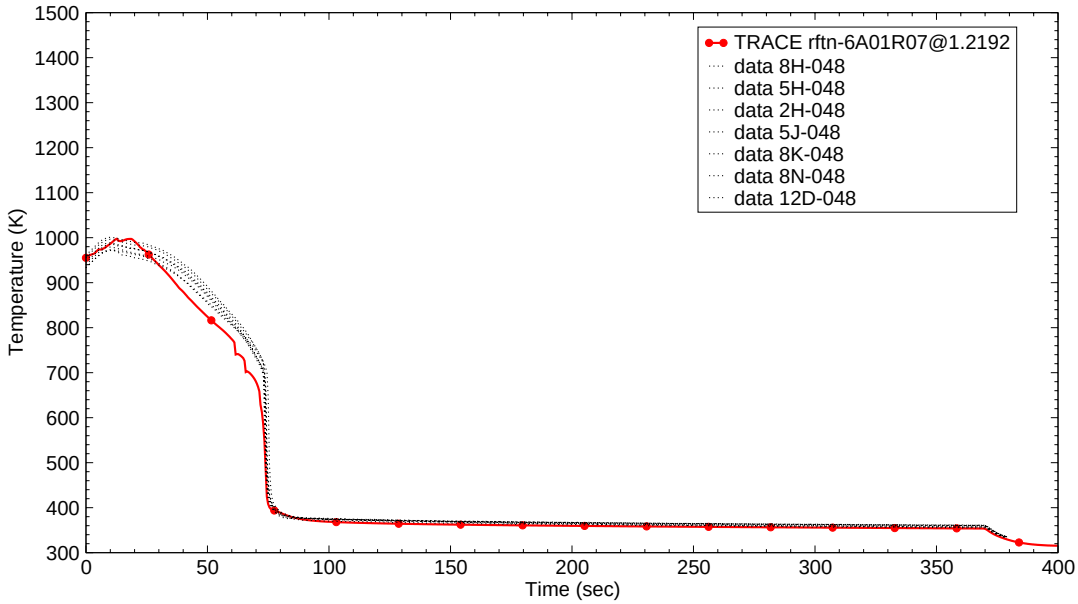

Figure B.7-147. Rod Clad Temperatures at 4 ft from Heated Bottom for Test 31108

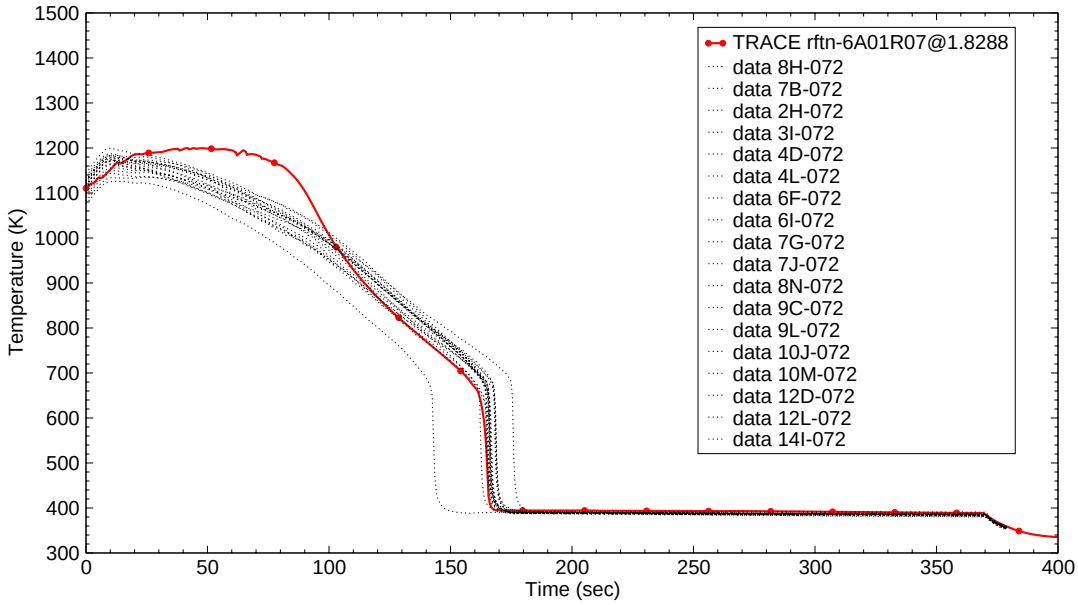

Figure B.7-148. Rod Clad Temperatures at 6 ft from Heated Bottom for Test 31108

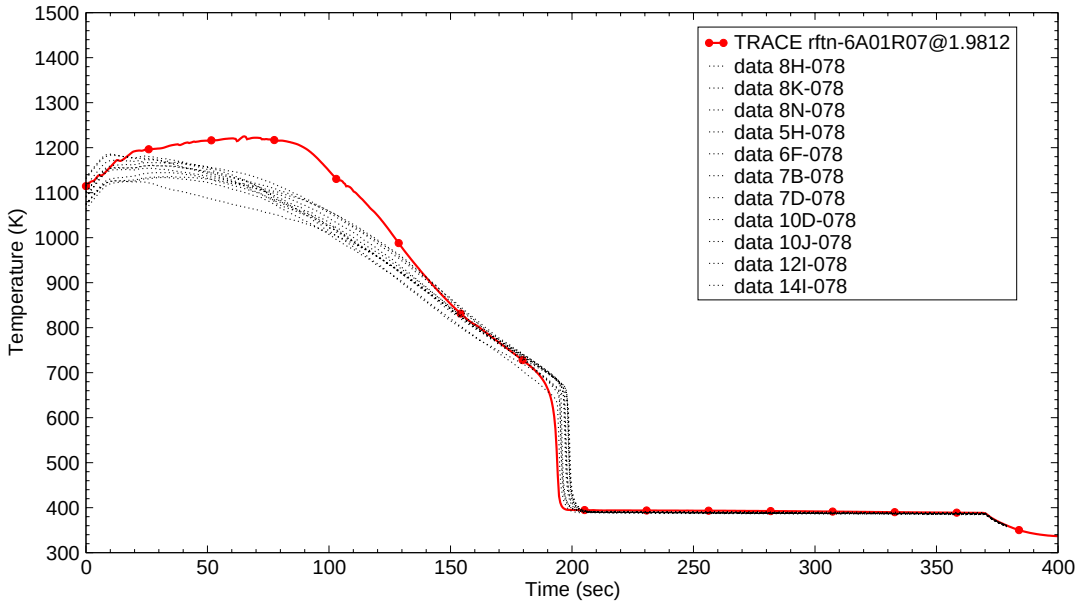

Figure B.7-149. Rod Clad Temperatures at 6.5 ft from Heated Bottom for Test 31108

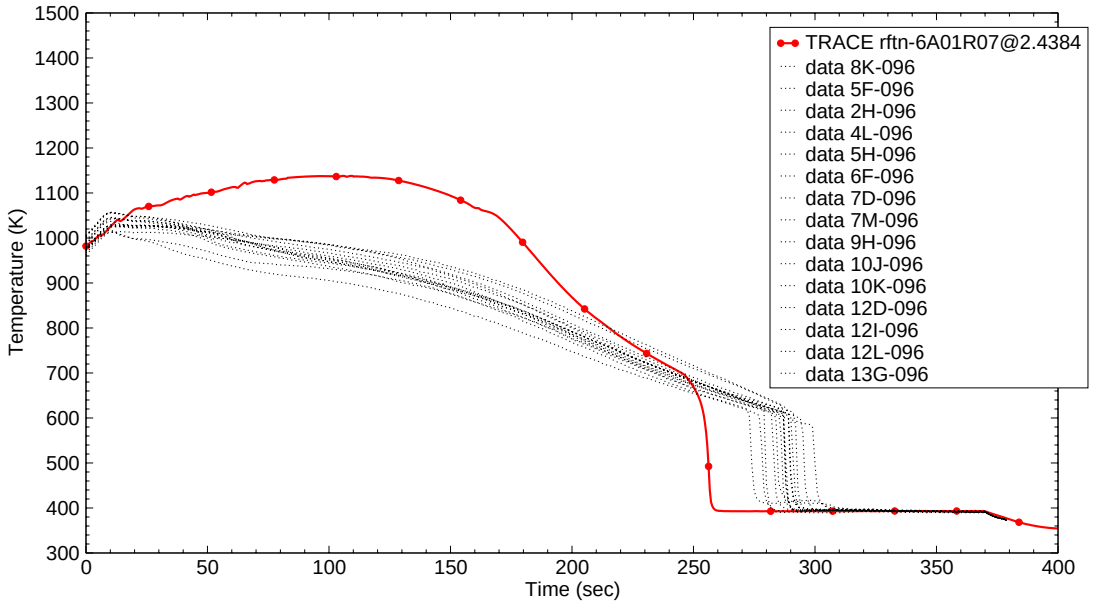

Figure B.7-150. Rod Clad Temperatures at 8 ft from Heated Bottom for Test 31108

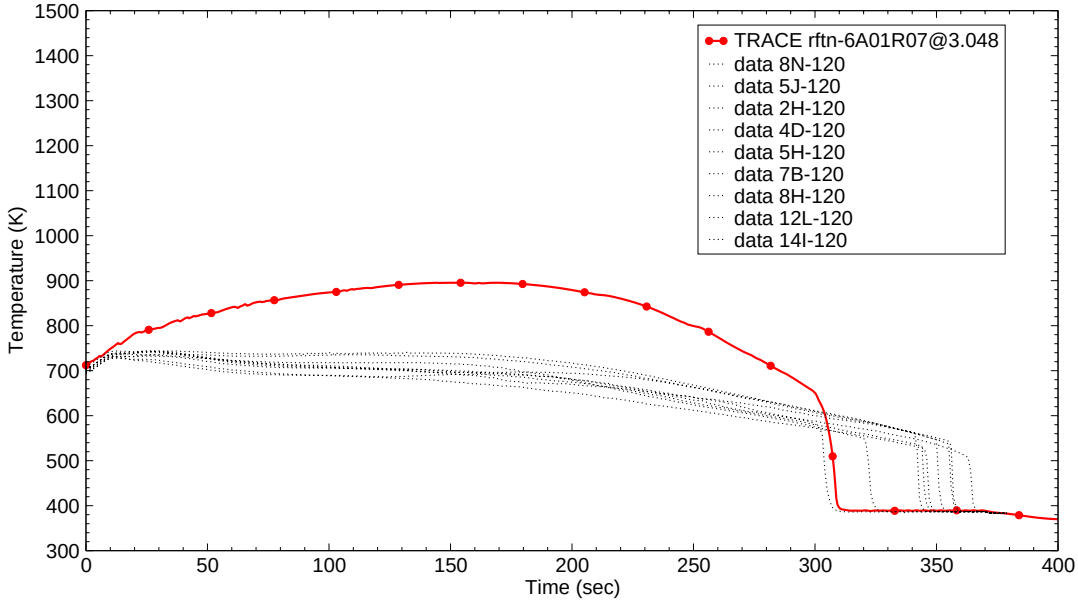

Figure B.7-151. Rod Clad Temperatures at 10 ft from Heated Bottom for Test 31108

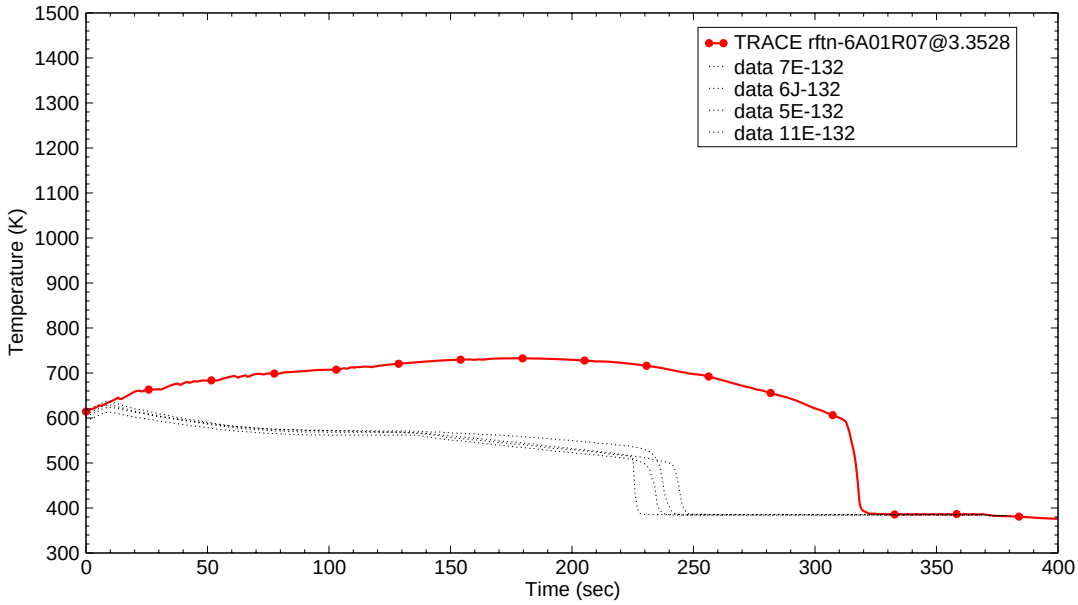

Figure B.7-152. Rod Clad Temperatures at 11 ft from Heated Bottom for Test 31108

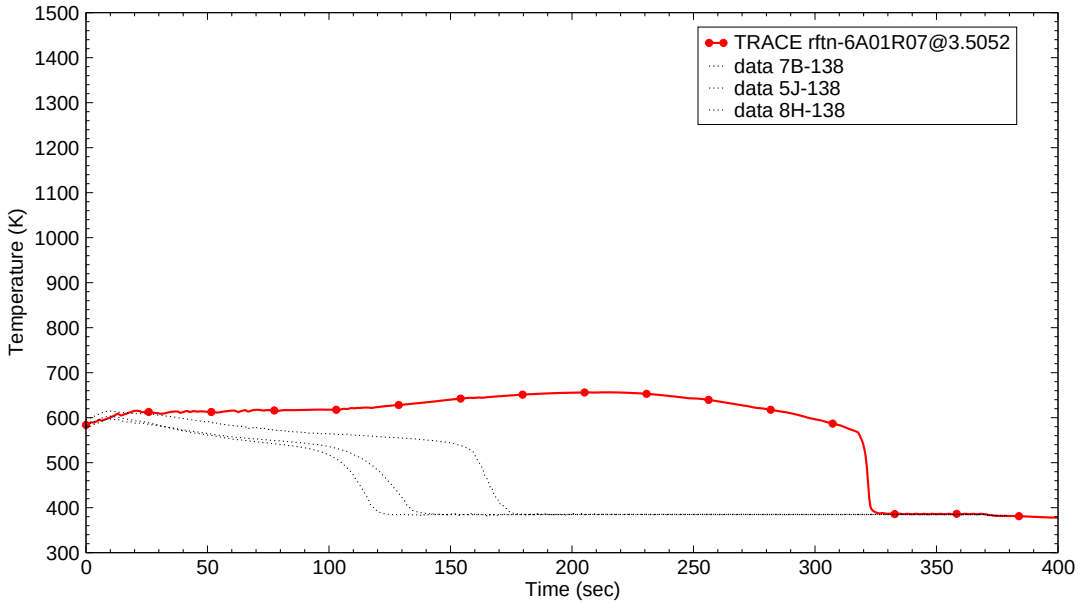

Figure B.7-153. Rod Clad Temperatures at 11.5 ft from Heated Bottom for Test 31108

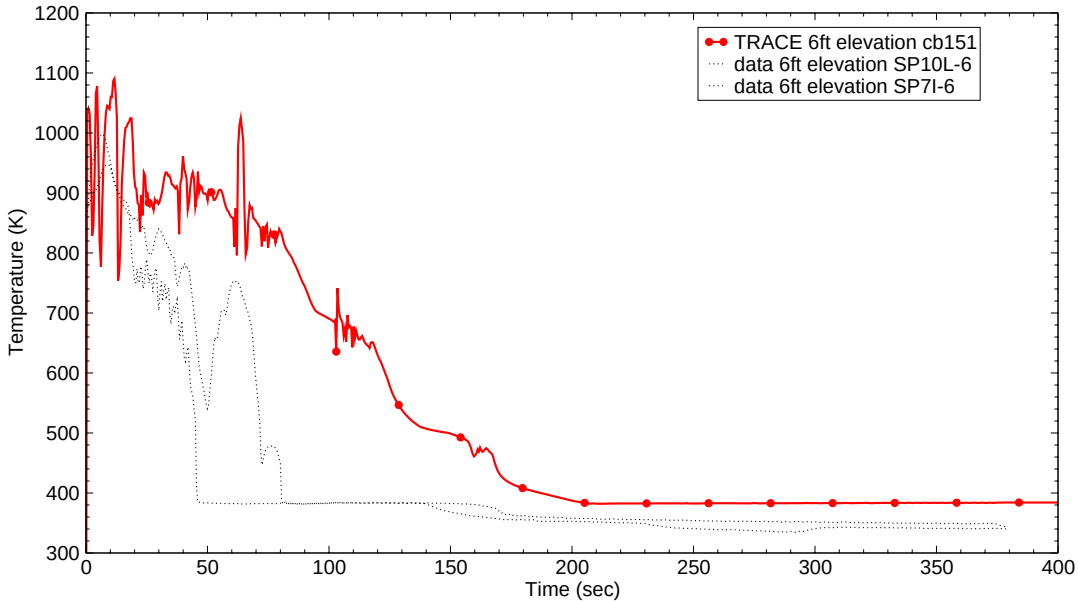

Figure B.7-154. Vapor Temperatures at 6 ft from Heated Bottom for Test 31108

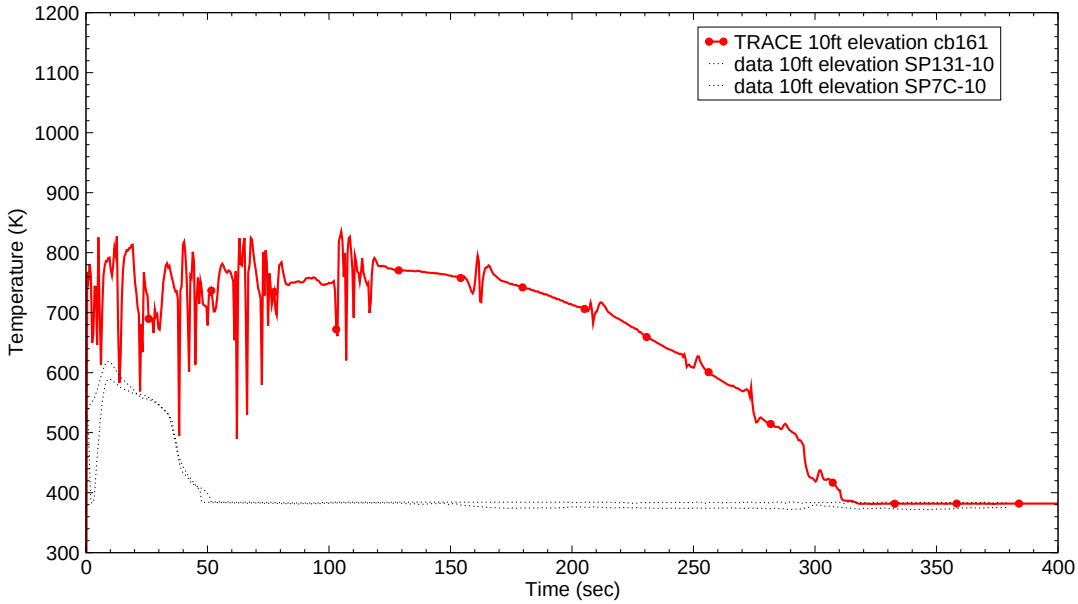

Figure B.7-155. Vapor Temperatures at 10 ft from Heated Bottom for Test 31108

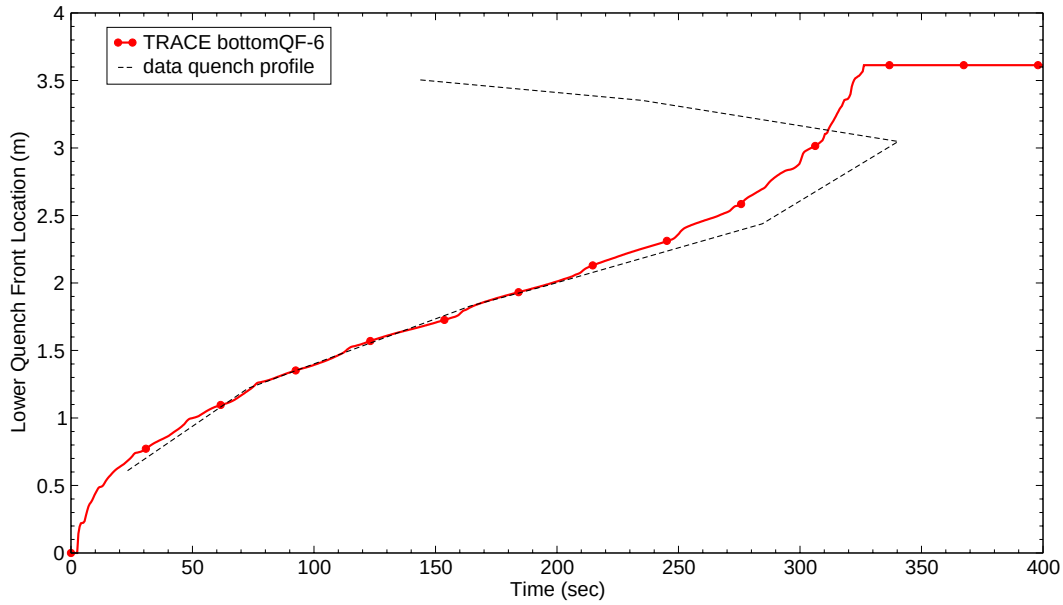

Figure B.7-156. Quench Profile as a Function of Time for Test 31108

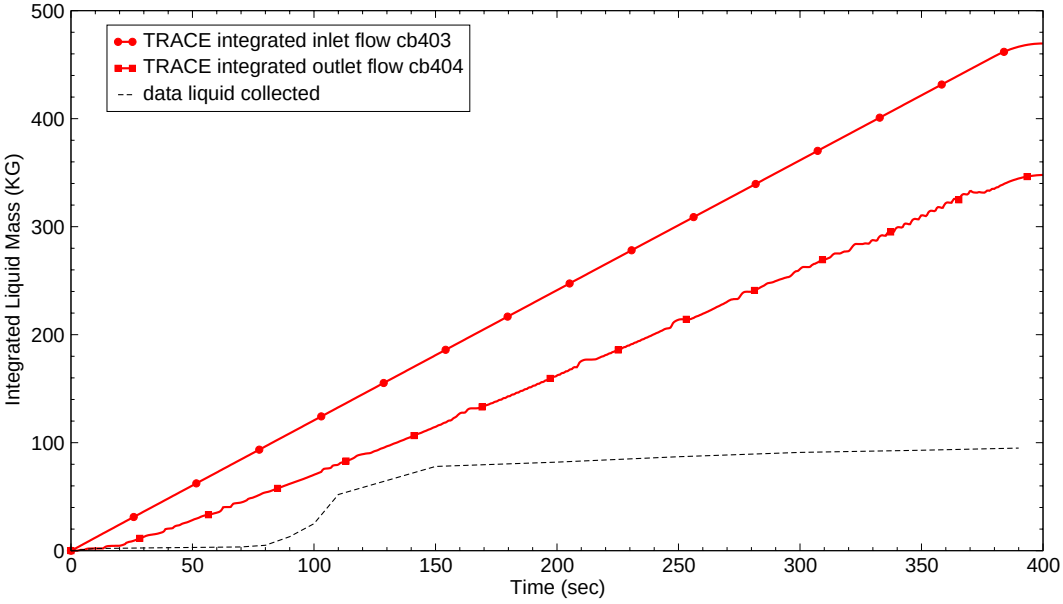

Figure B.7-157. Integrated Liquid Mass Flow into and out of Bundle for Test 31108

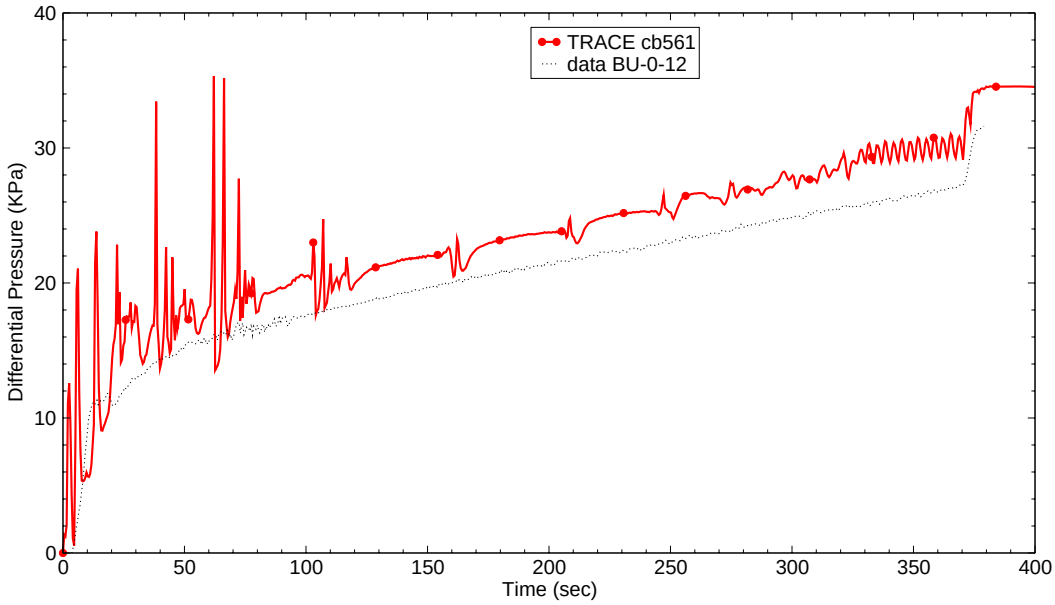

Figure B.7-158. Differential Pressure for the Entire 12 ft Core for Test 31108

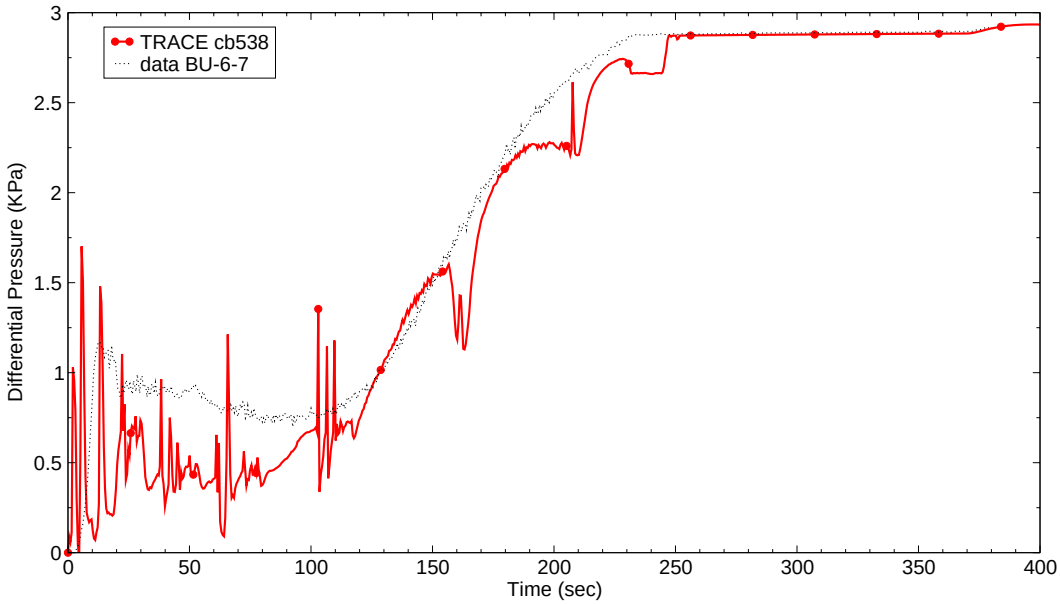

Figure B.7-159. Differential Pressure at 6-7 ft Elevation for Test 31108

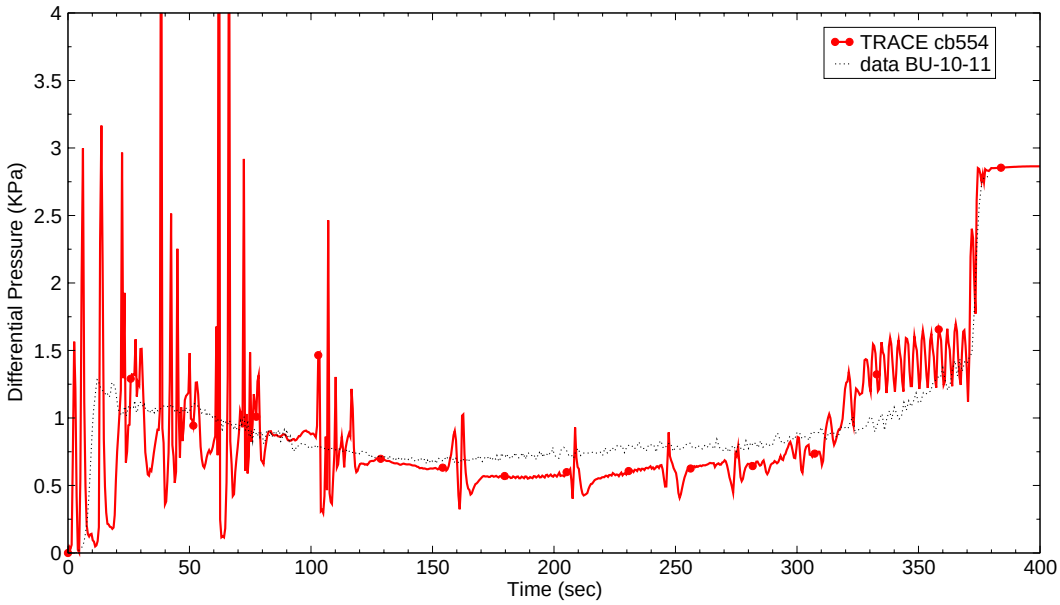

Figure B.7-160. Differential Pressure at 10-11 ft Elevation for Test 31108

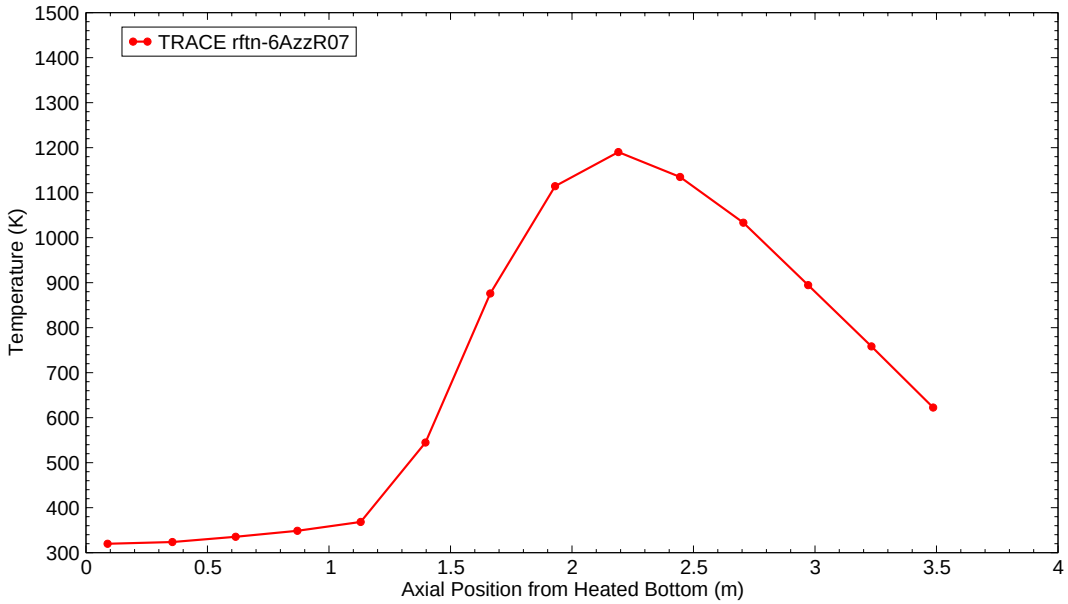

Figure B.7-161. Clad Temperature Profile at 100 sec after Reflood Start for Test 31108

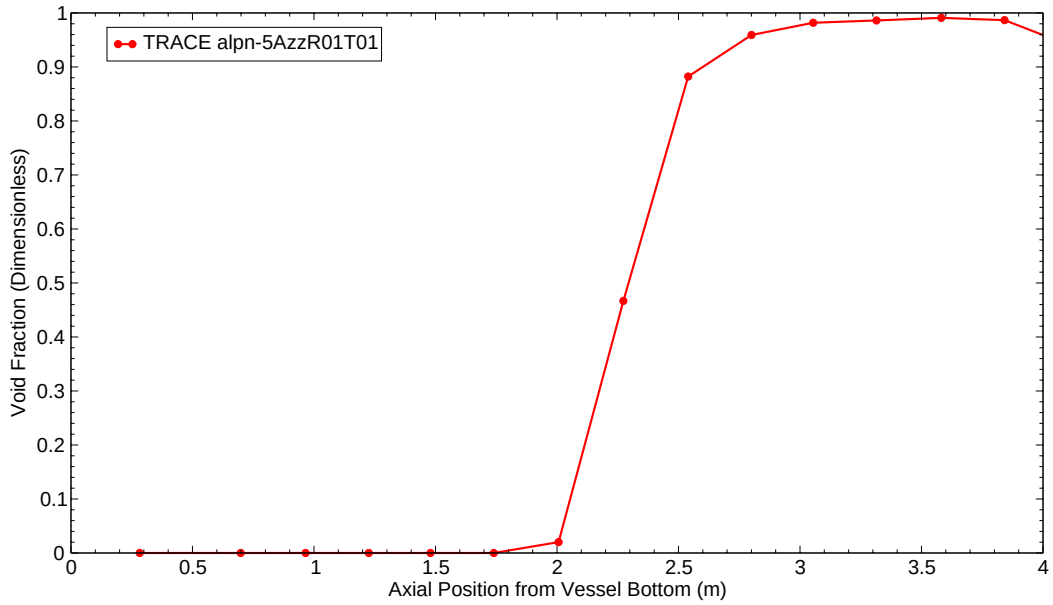

Figure B.7-162. Void Fraction Profile at 100 sec after Reflood Start for Test 31108

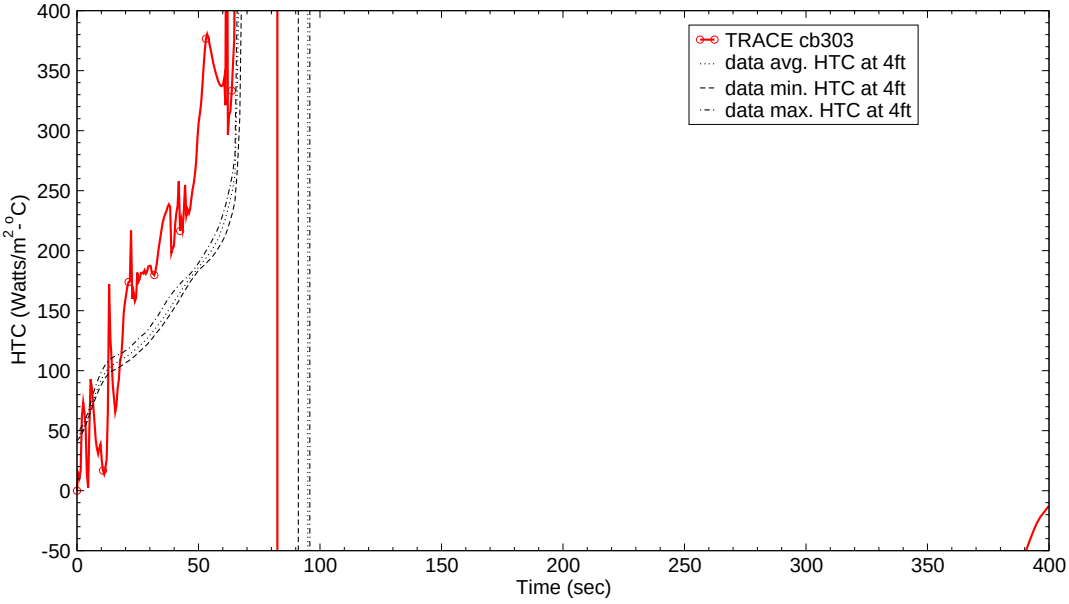

Figure B.7-163. Heat Transfer Coefficient at 4 ft from Heated Bottom for Test 31108

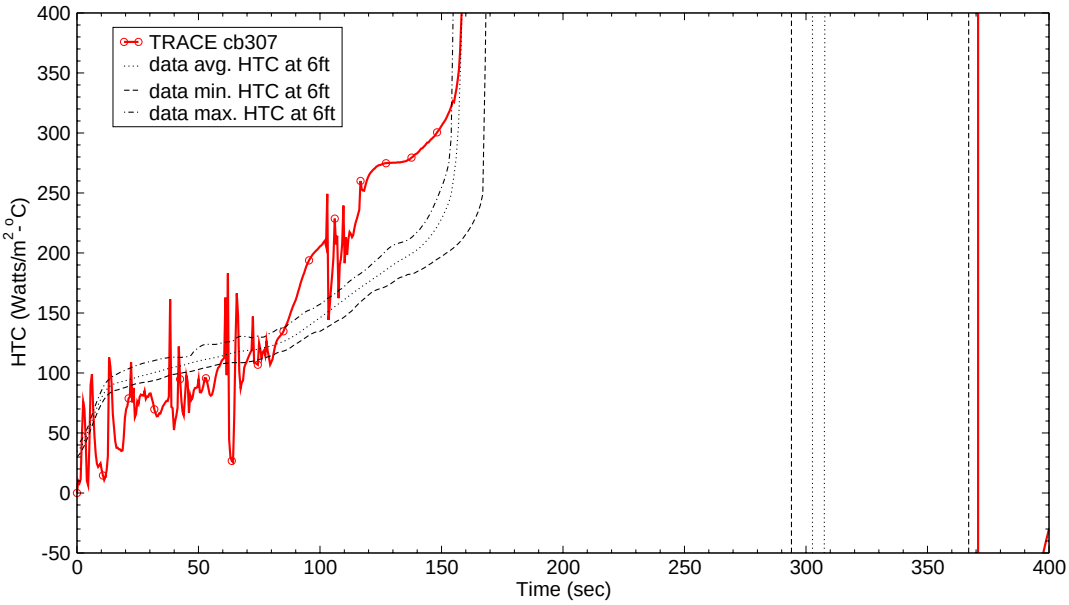

Figure B.7-164. Heat Transfer Coefficient at 6 ft from Heated Bottom for Test 31108

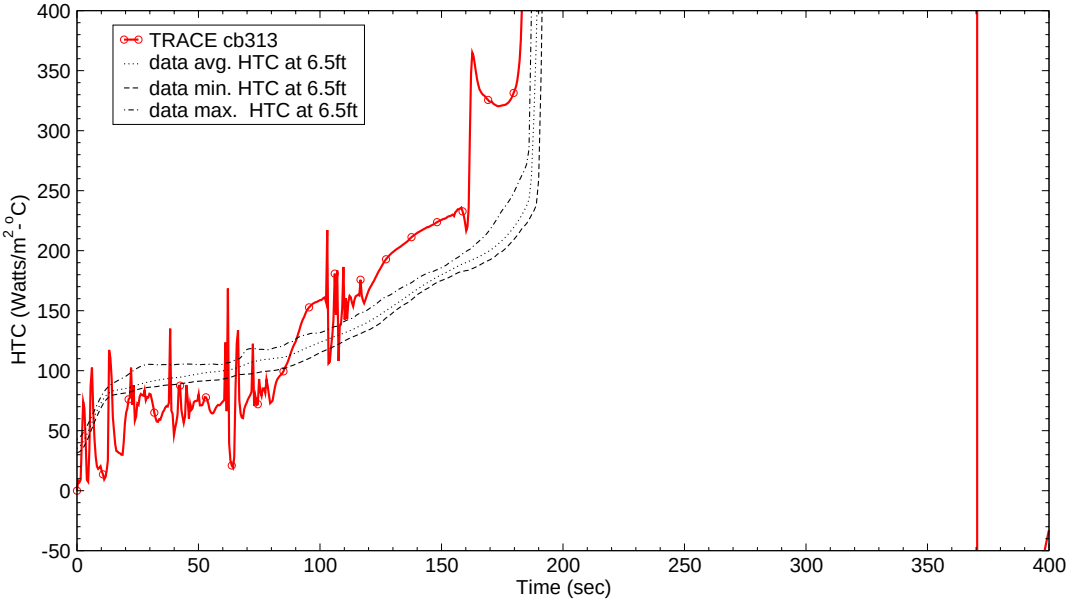

Figure B.7-165. Heat Transfer Coefficient at 6.5 ft from Heated Bottom for Test 31108

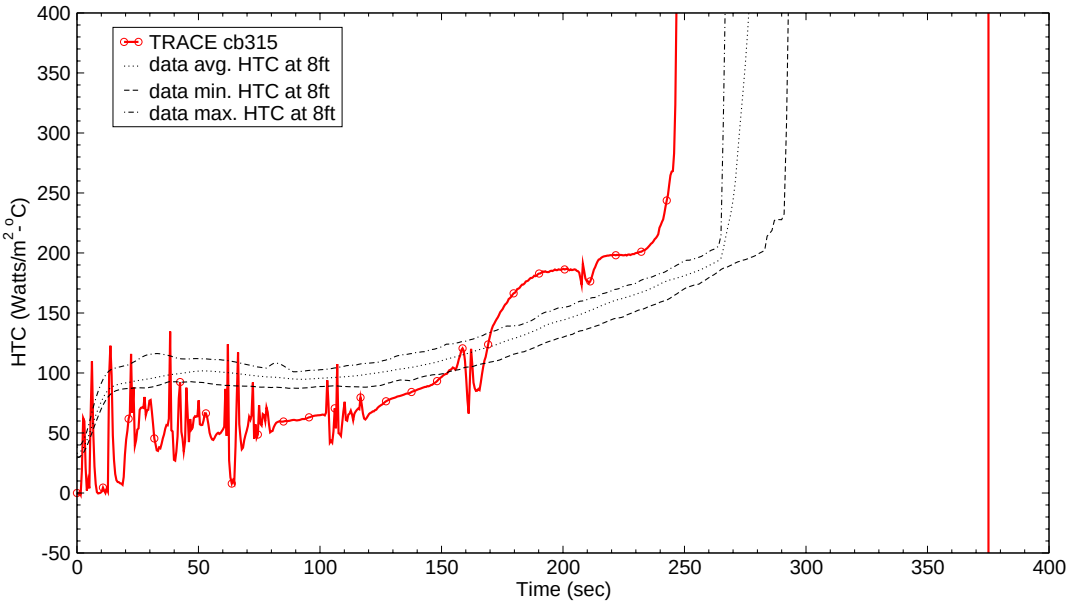

Figure B.7-166. Heat Transfer Coefficient at 8 ft from Heated Bottom for Test 31108

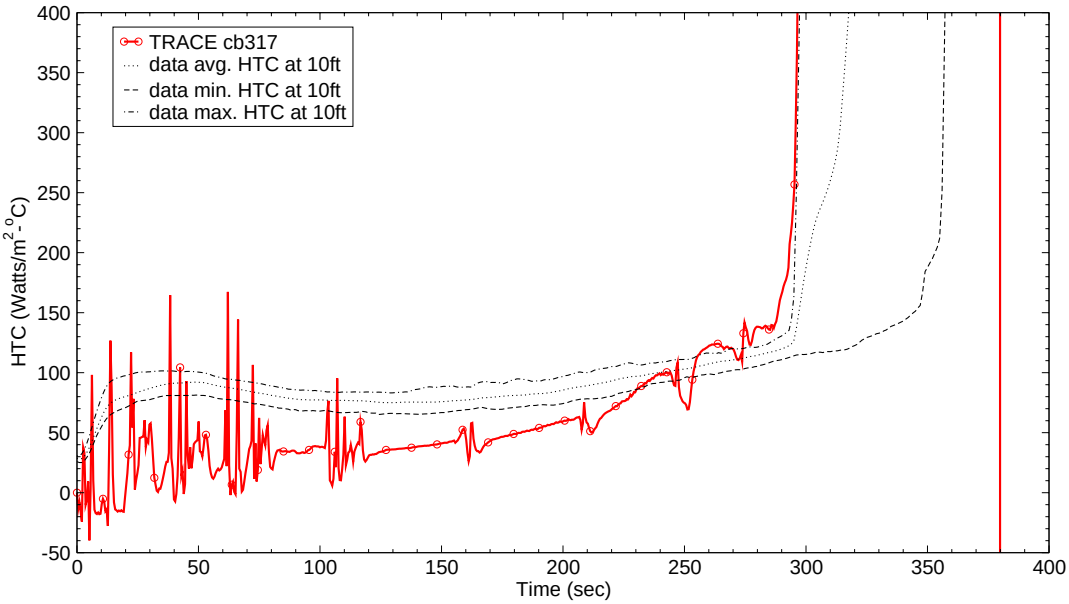

Figure B.7-167. Heat Transfer Coefficient at 10 ft from Heated Bottom for Test 31108

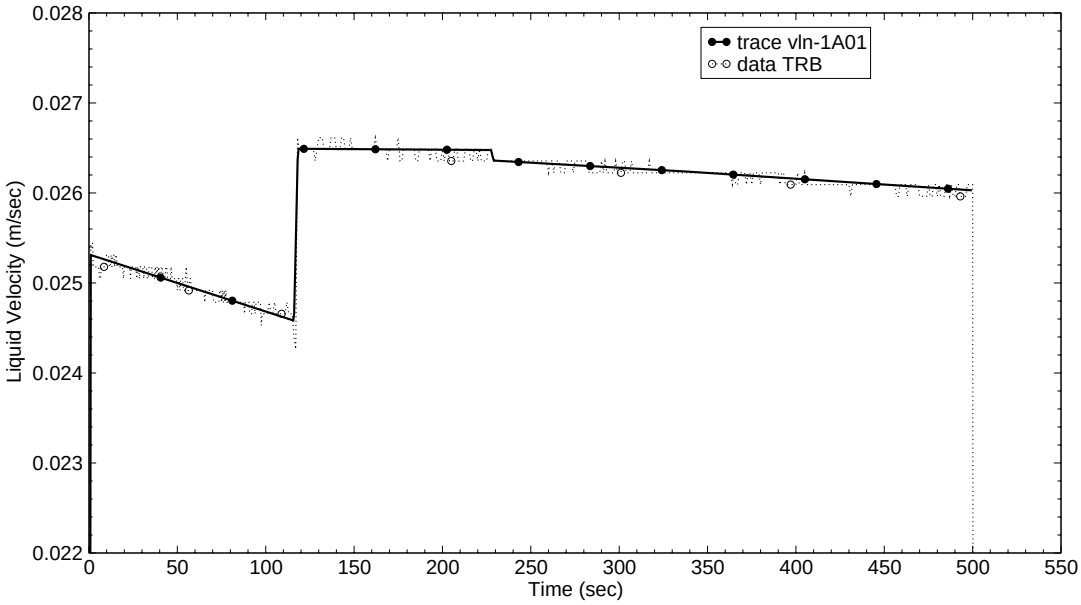

Figure B.7-168. Liquid Inlet Flow Rate for Test 32013

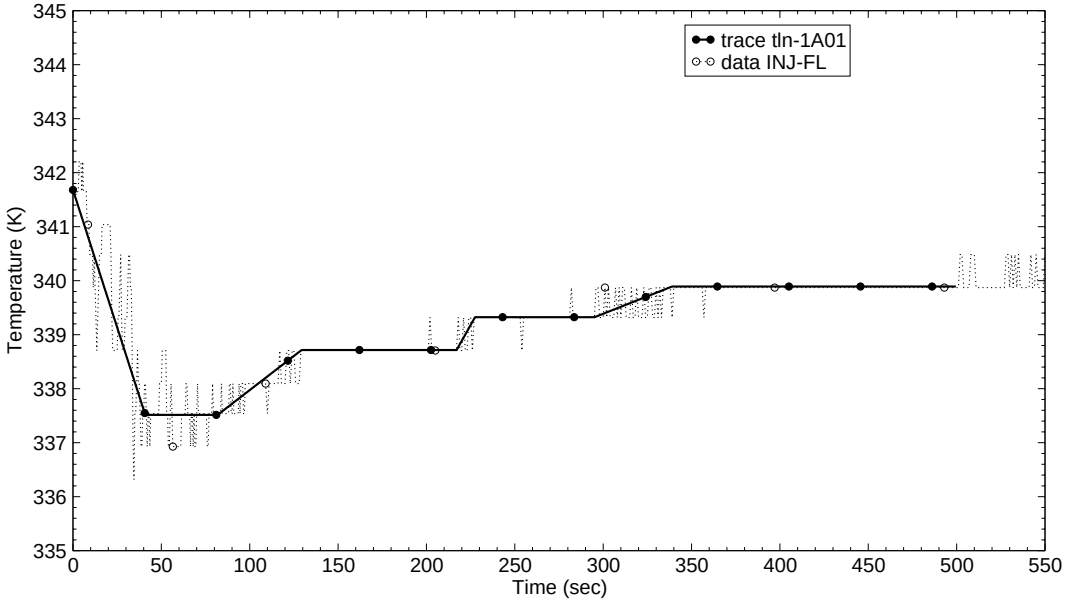

Figure B.7-169. Liquid Inlet Temperature for Test 32013

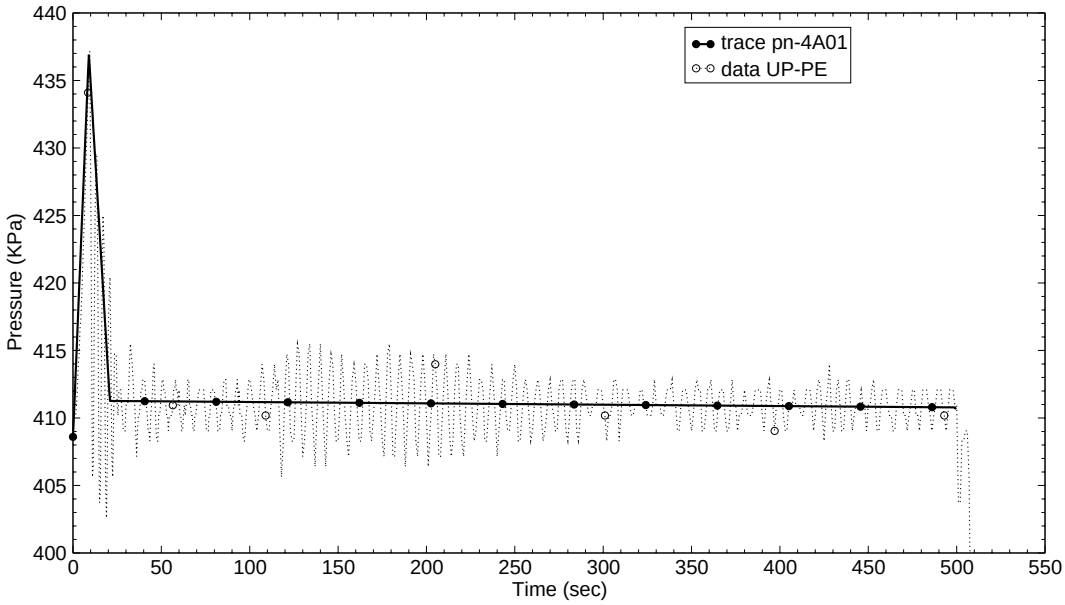

Figure B.7-170. Upper Plenum Exit Pressure for Test 32013

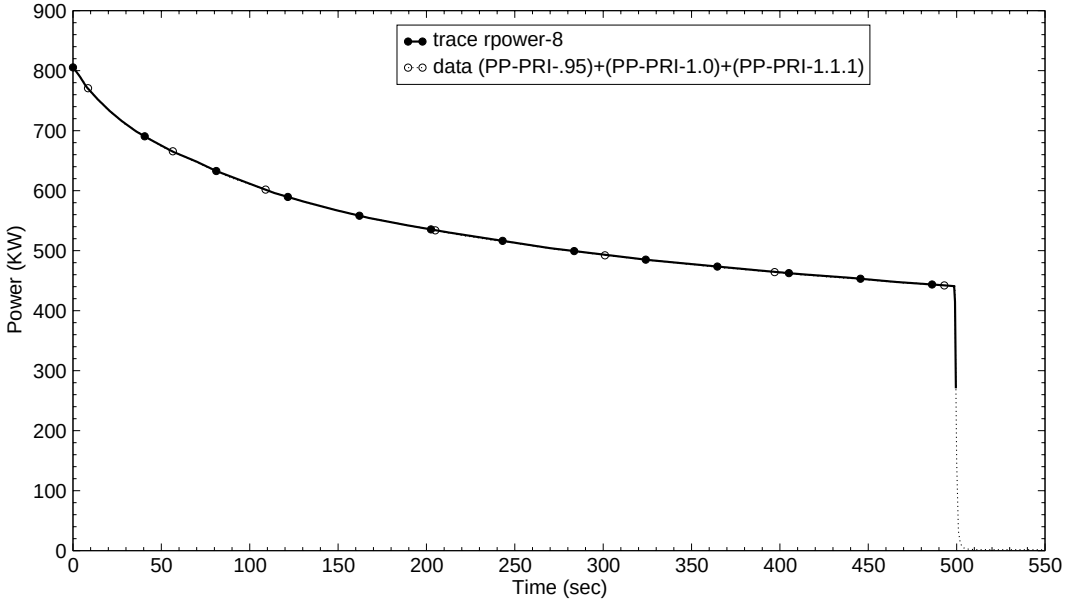

Figure B.7-171. Total Power to the Bundle for Test 32013

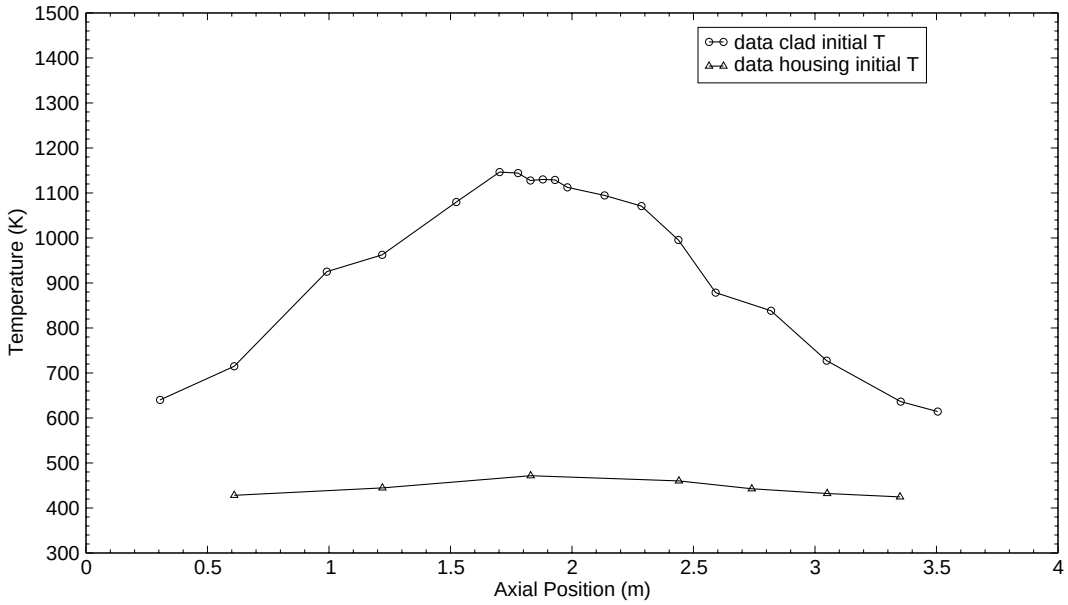

Figure B.7-172. Heater Rod Clad and Housing Initial Temperatures for Test 32013

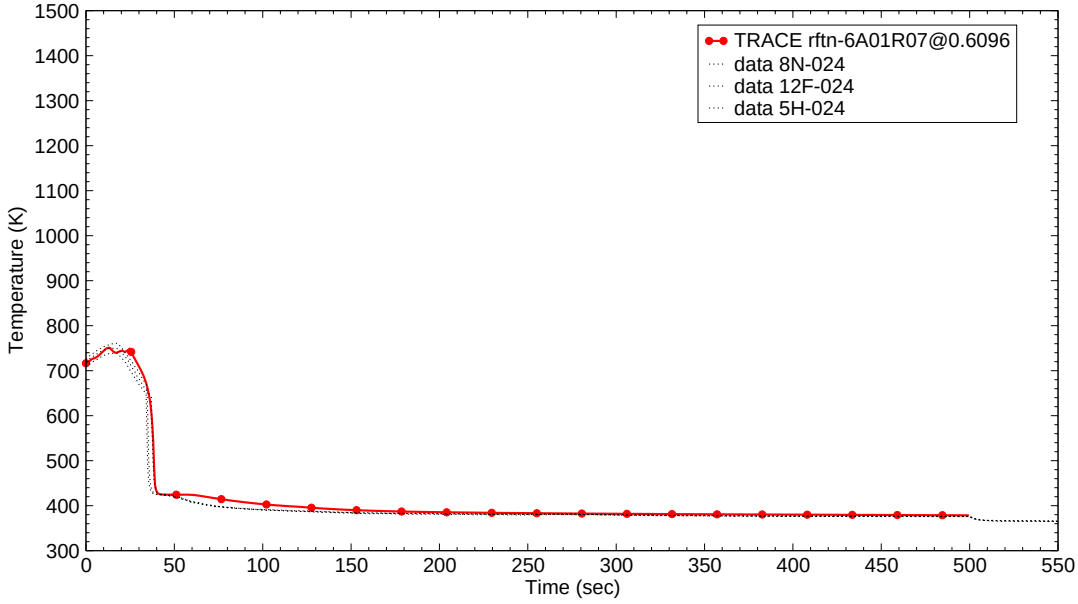

Figure B.7-173. Rod Clad Temperatures at 2 ft from Heated Bottom for Test 32013

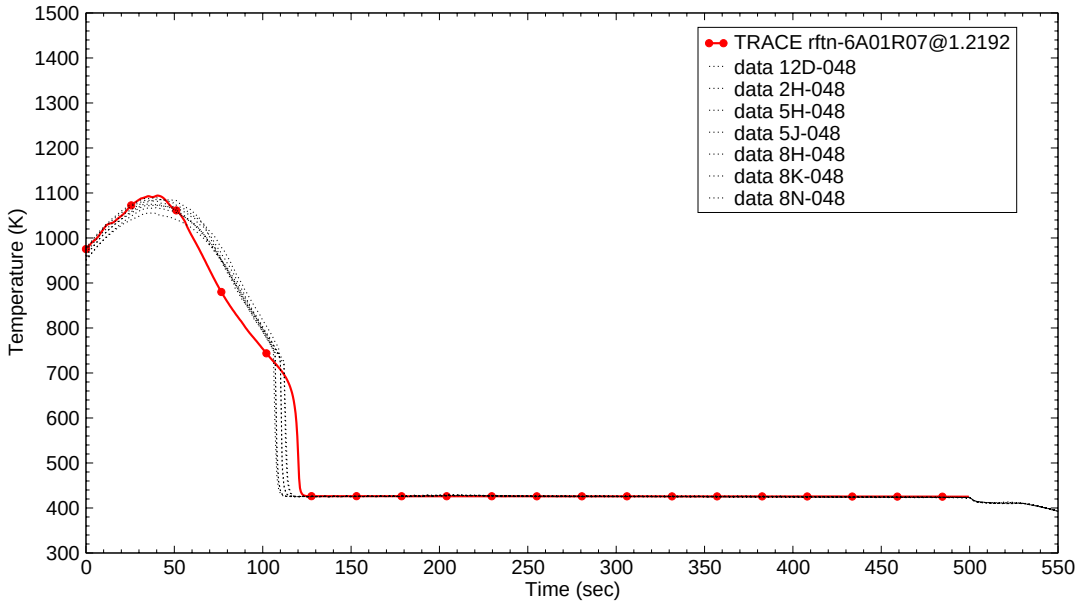

Figure B.7-174. Rod Clad Temperatures at 4 ft from Heated Bottom for Test 32013

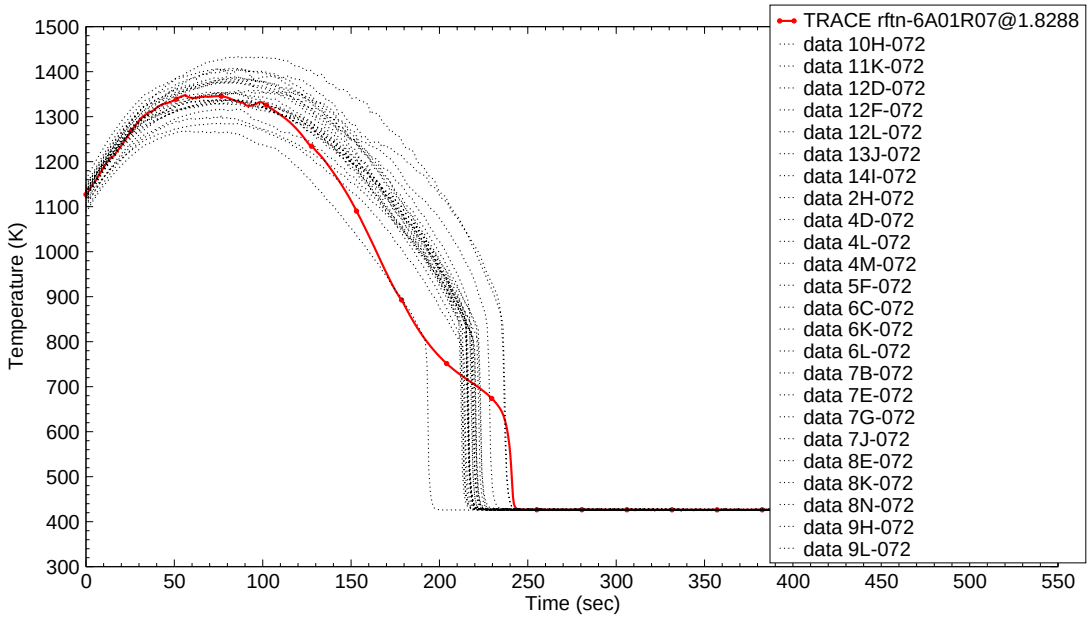

Figure B.7-175. Rod Clad Temperatures at 6 ft from Heated Bottom for Test 32013

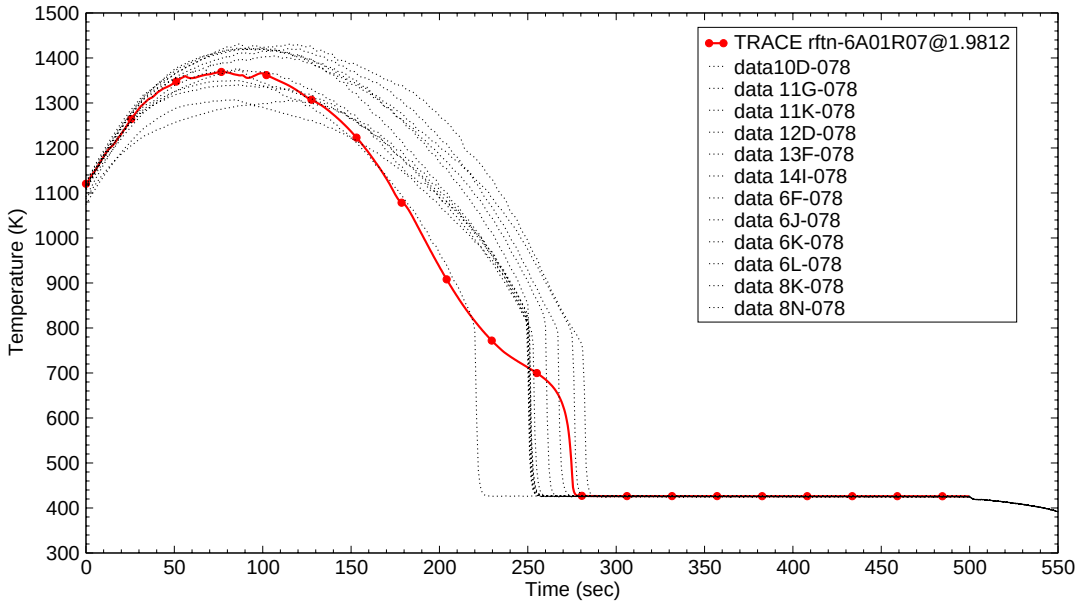

Figure B.7-176. Rod Clad Temperatures at 6.5 ft from Heated Bottom for Test 32013

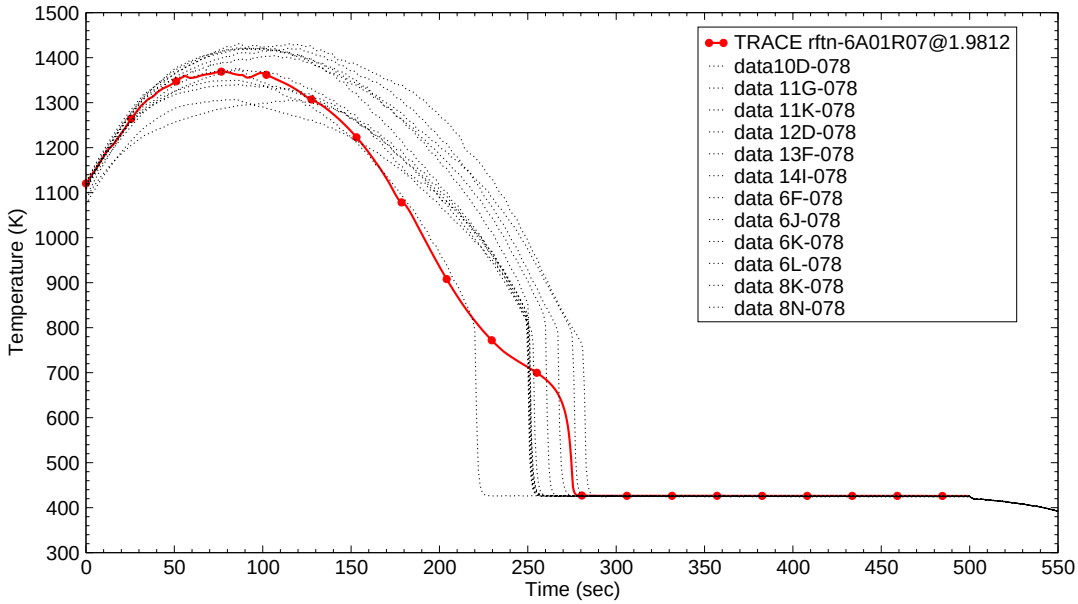

Figure B.7-177. Rod Clad Temperatures at 8 ft from Heated Bottom for Test 32013

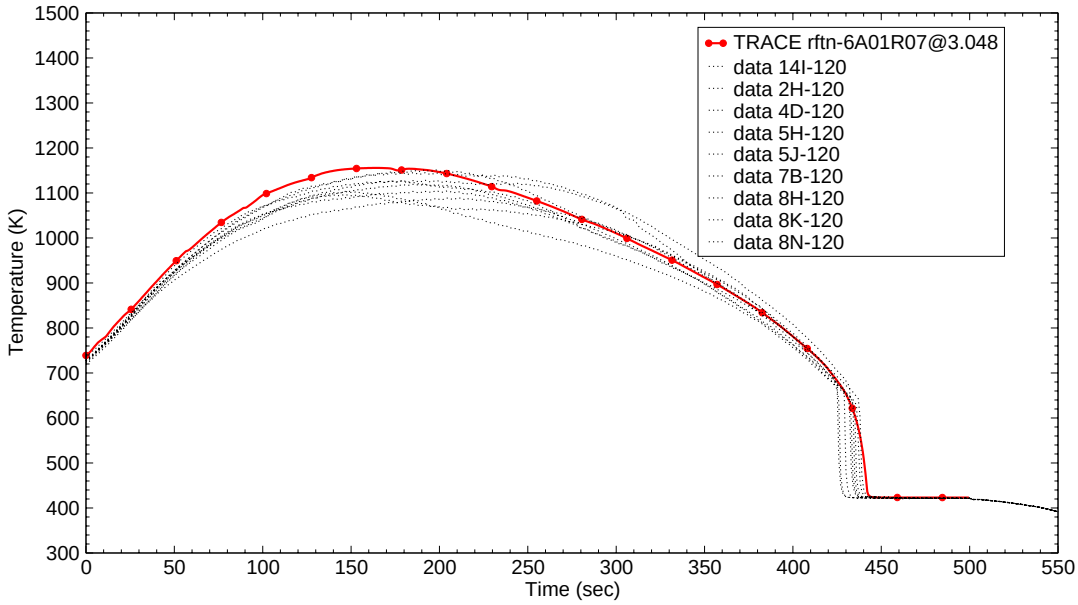

Figure B.7-178. Rod Clad Temperatures at 10 ft from Heated Bottom for Test 32013

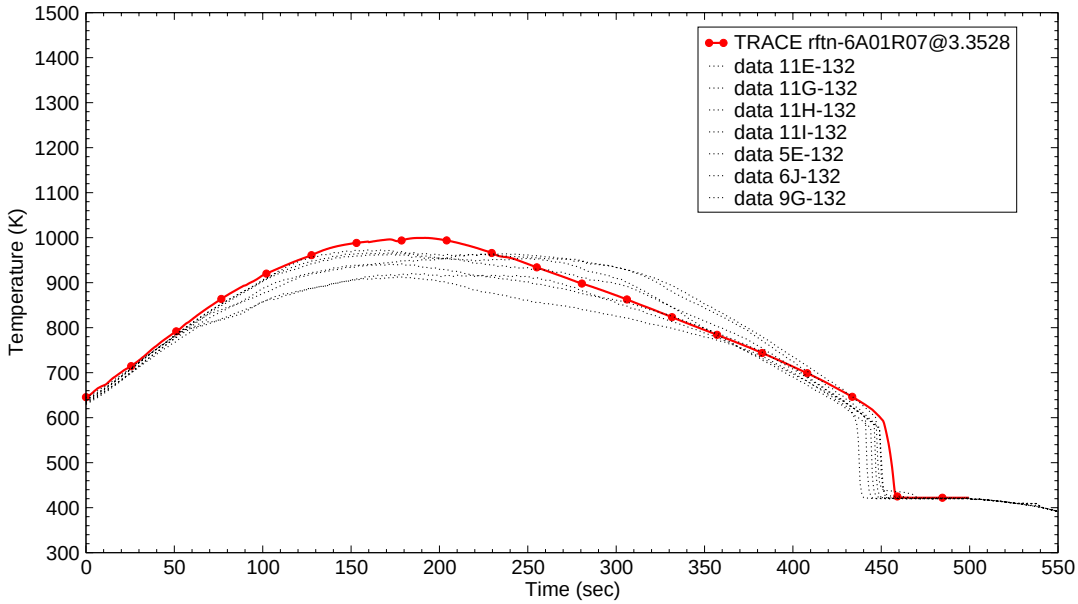

Figure B.7-179. Rod Clad Temperatures at 11 ft from Heated Bottom for Test 32013

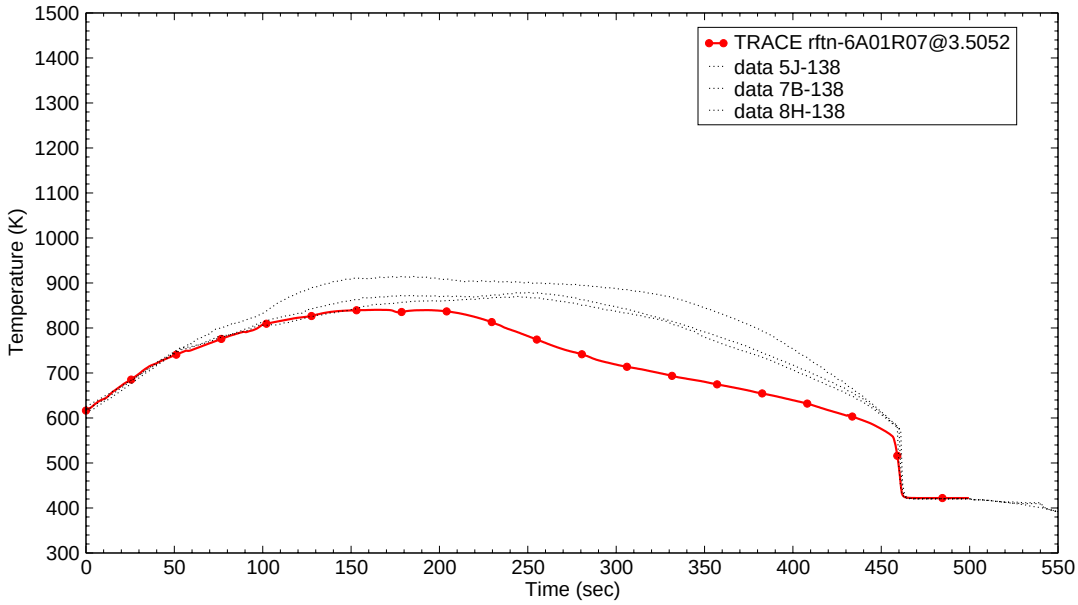

Figure B.7-180. Rod Clad Temperatures at 11.5 ft from Heated Bottom for Test 32013

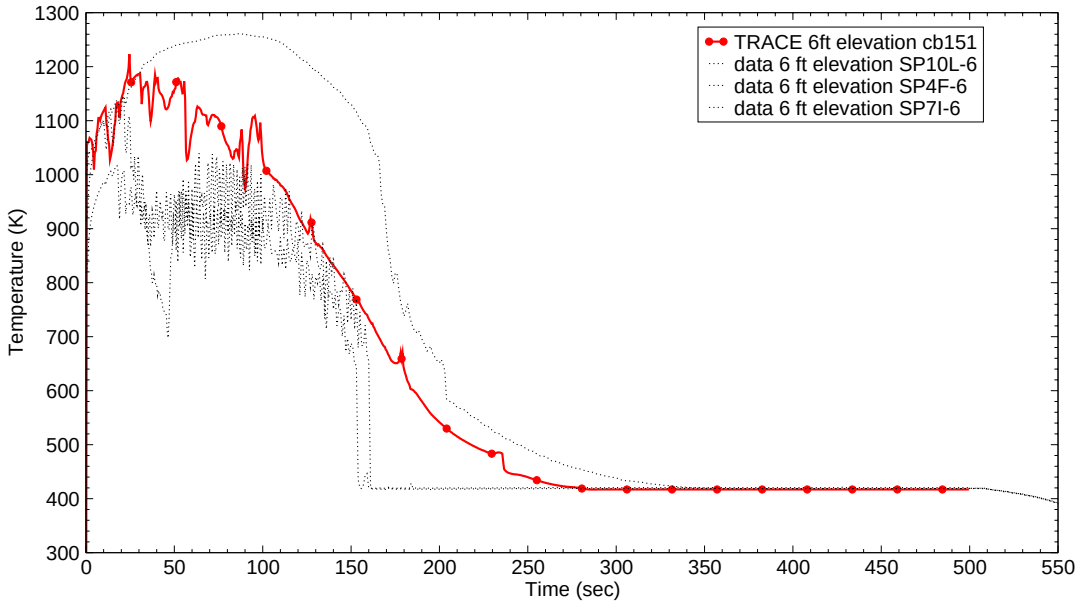

Figure B.7-181. Vapor Temperatures at 6 ft from Heated Bottom for Test 32013

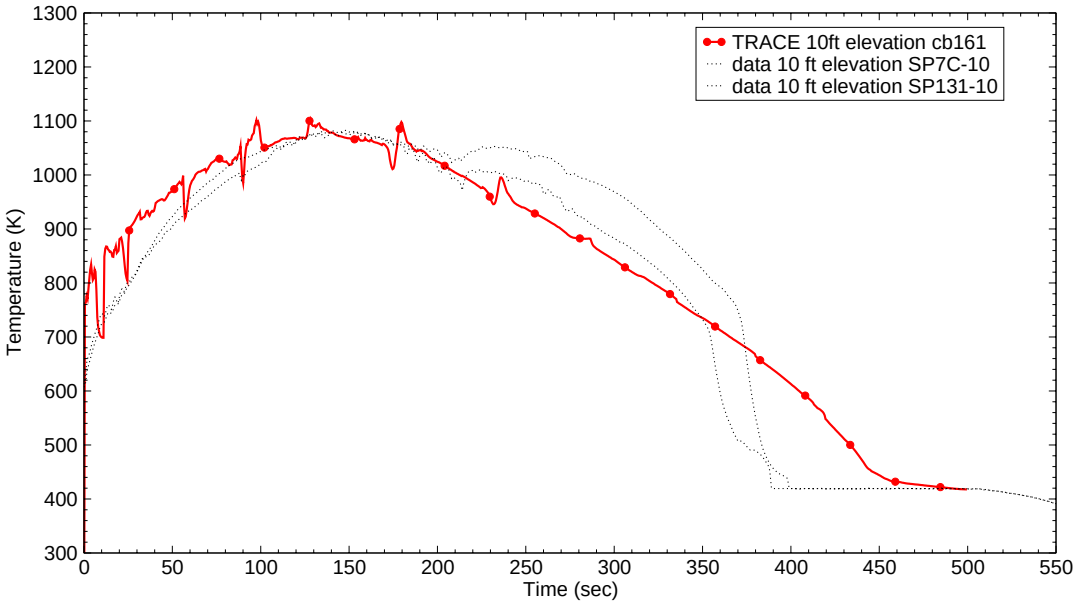

Figure B.7-182. Vapor Temperatures at 2 ft from Heated Bottom for Test 32013

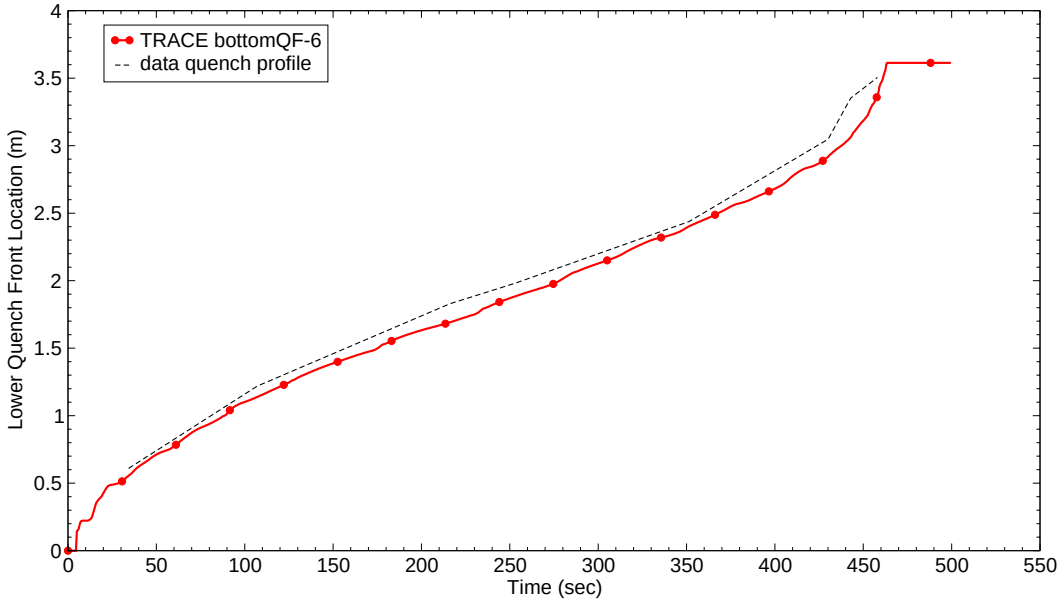

Figure B.7-183. Quench Profile as a Function of Time for Test 32013

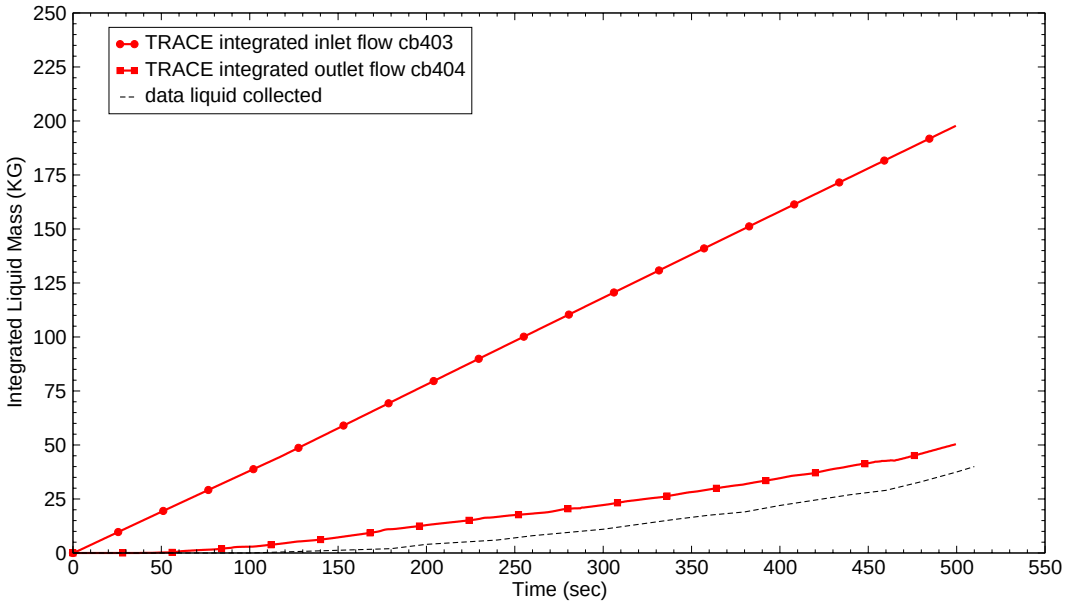

Figure B.7-184. Integrated Liquid Mass Flow into and out of Bundle for Test 32013

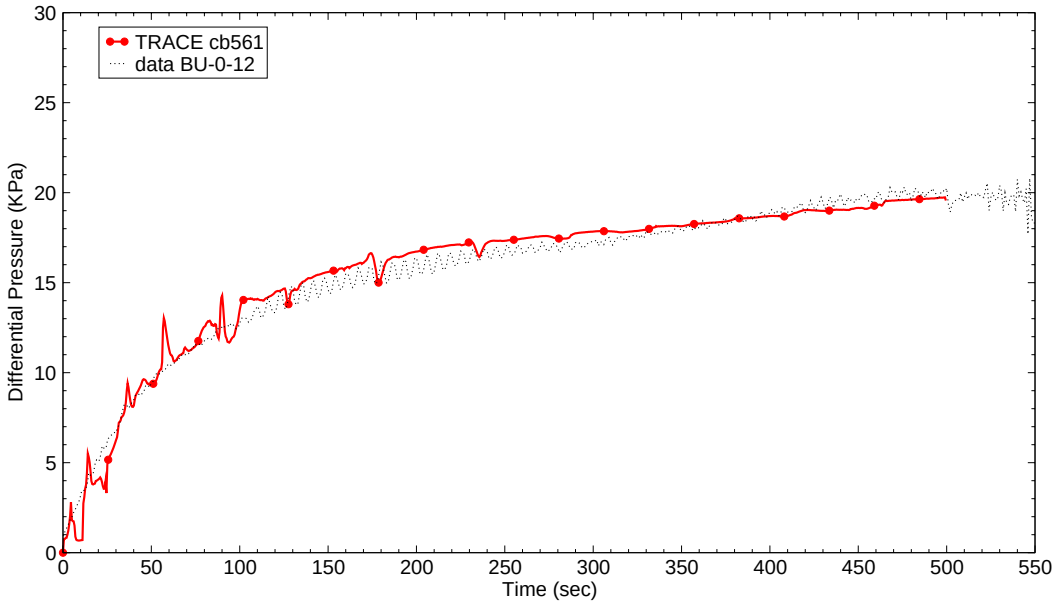

Figure B.7-185. Differential Pressure for the Entire 12 ft Core for Test 32013

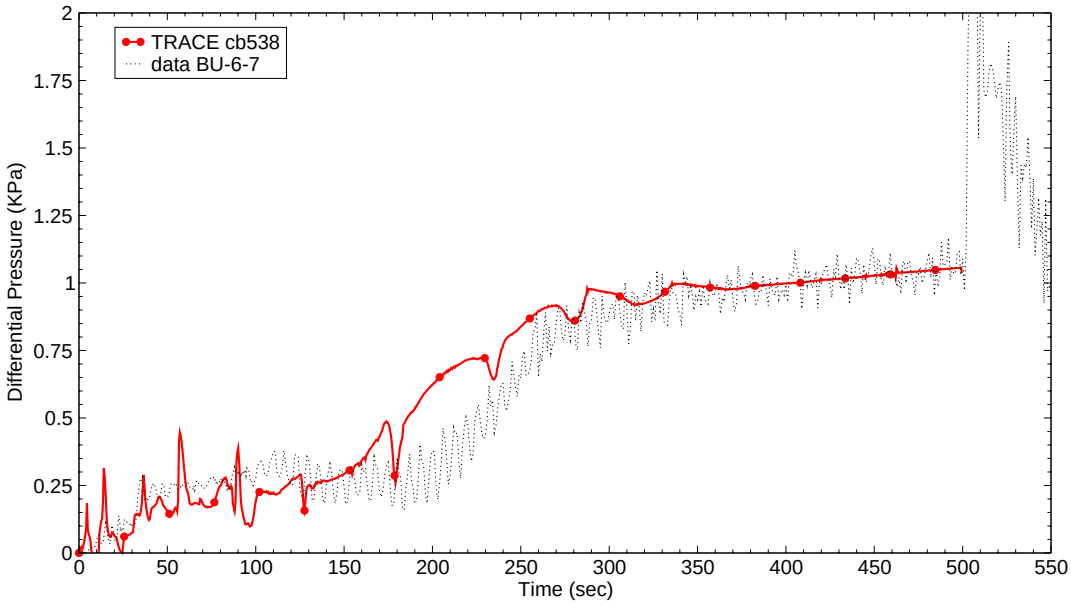

Figure B.7-186. Differential Pressure at 6-7 ft Elevation for Test 32013

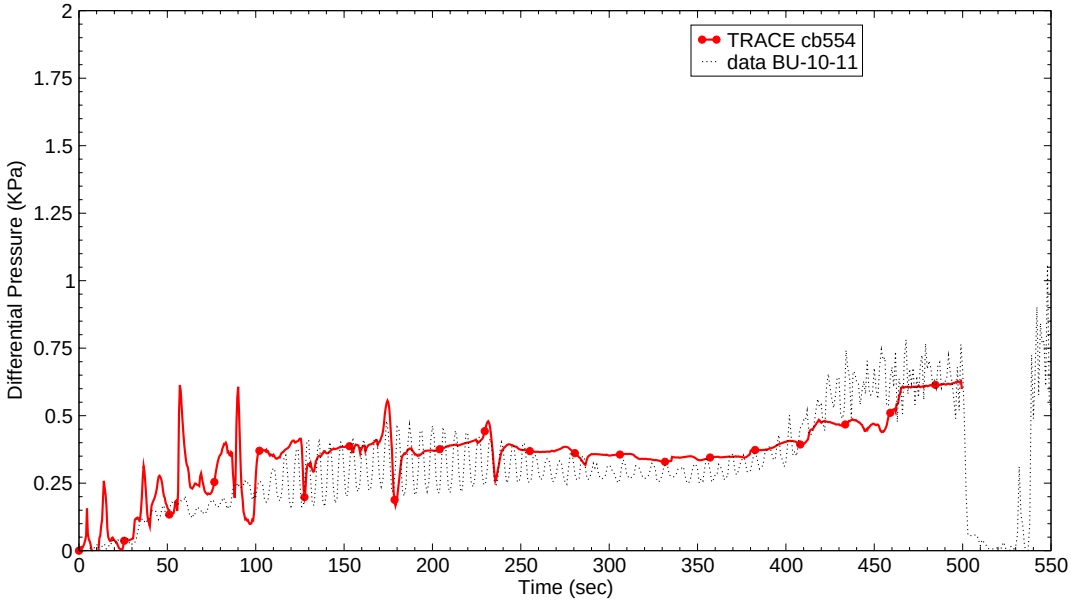

Figure B.7-187. Differential Pressure at 10-11 ft Elevation for Test 32013

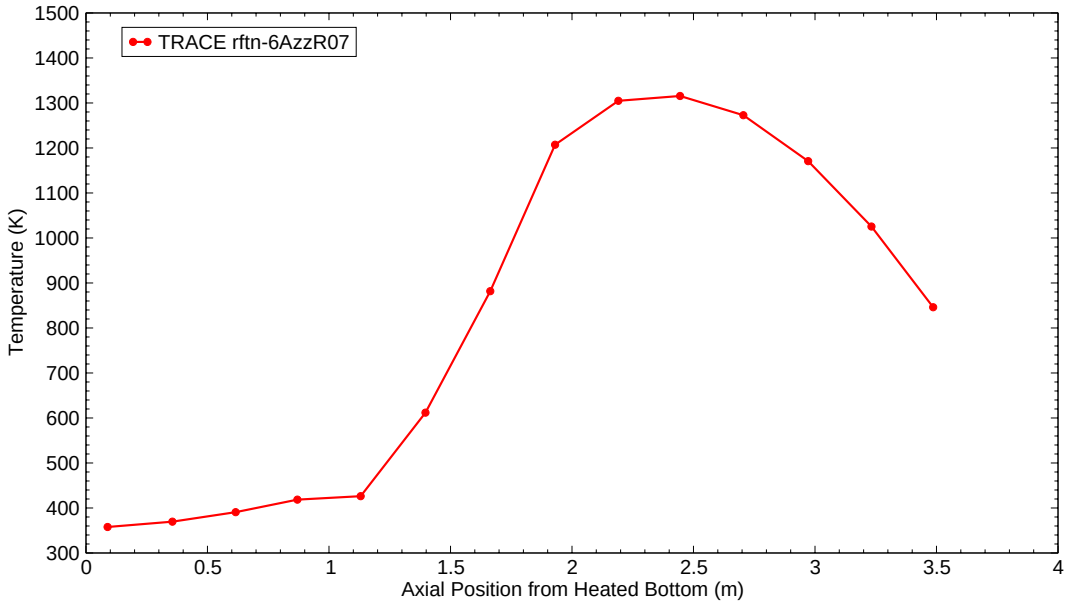

Figure B.7-188. Clad Temperature Profile at 150 sec after Reflood Start for Test 32013

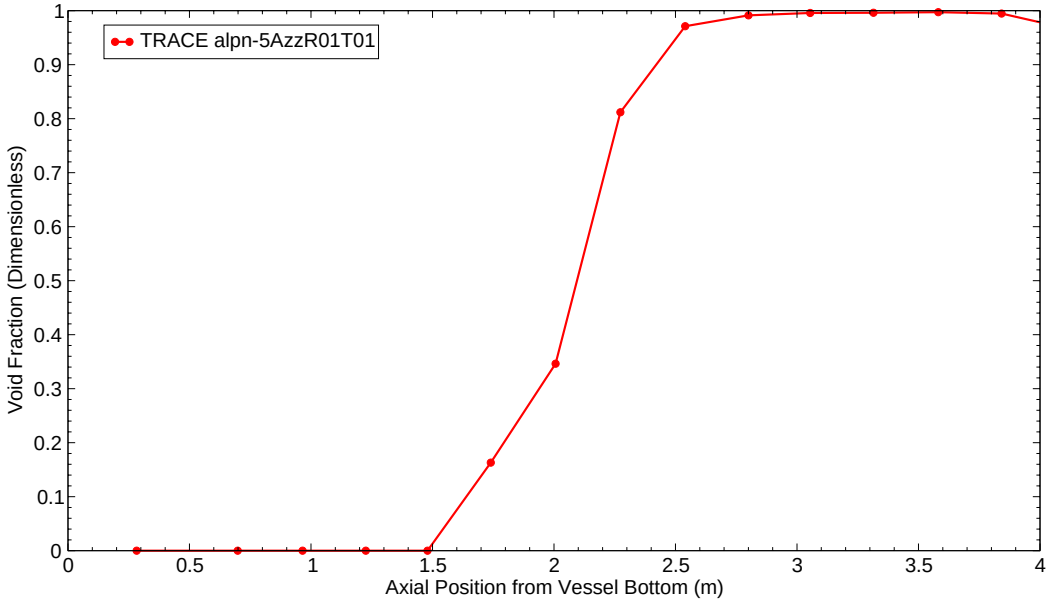

Figure B.7-189. Void Fraction Profile at 150 sec after Reflood Start for Test 32013

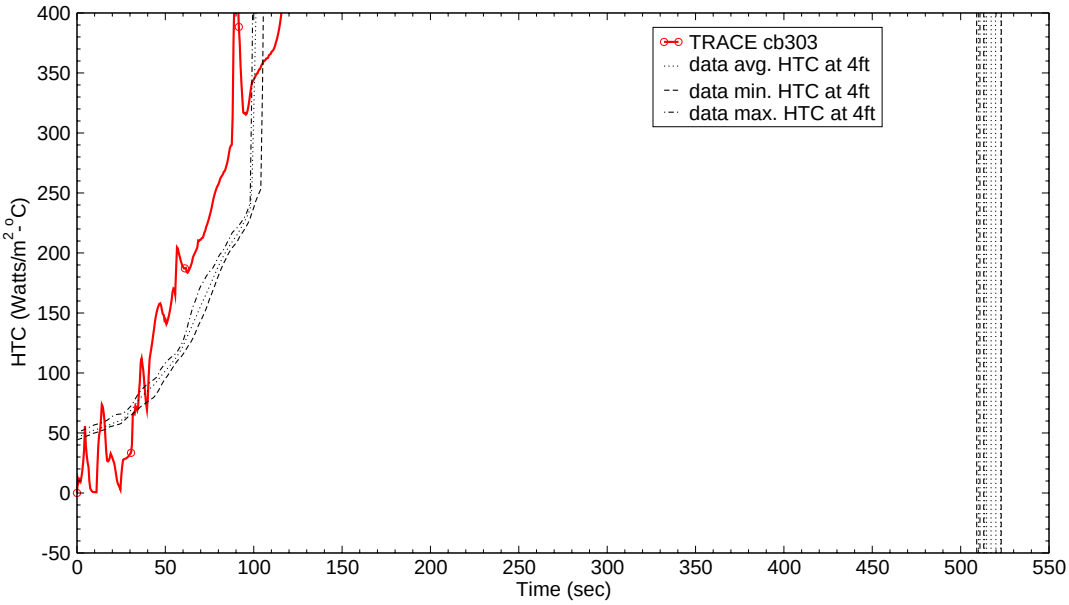

Figure B.7-190. Heat Transfer Coefficient at 4 ft from Heated Bottom for Test 32013

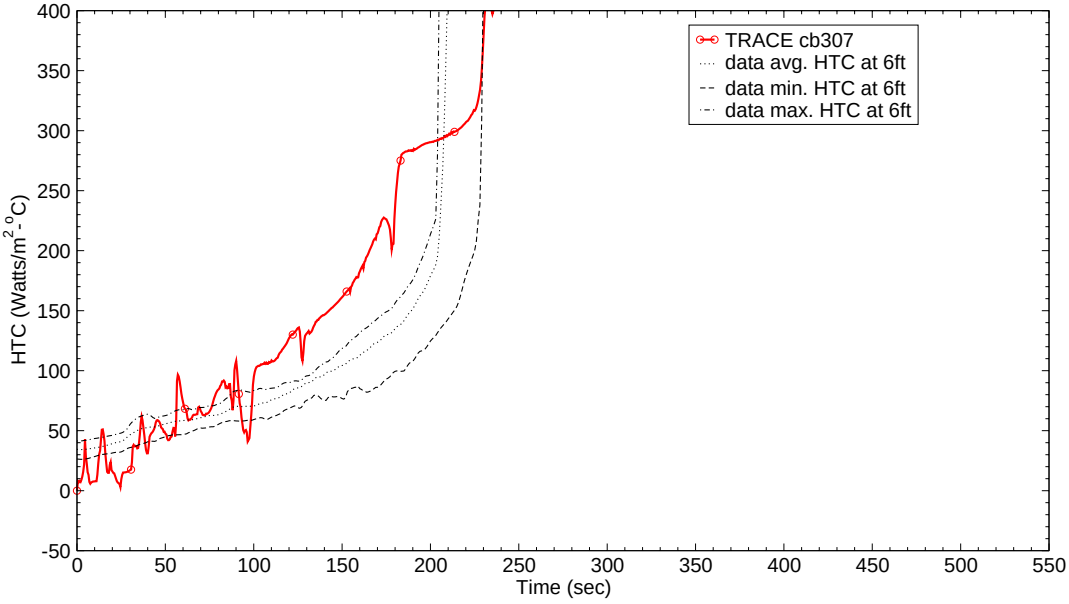

Figure B.7-191. Heat Transfer Coefficient at 6 ft from Heated Bottom for Test 32013

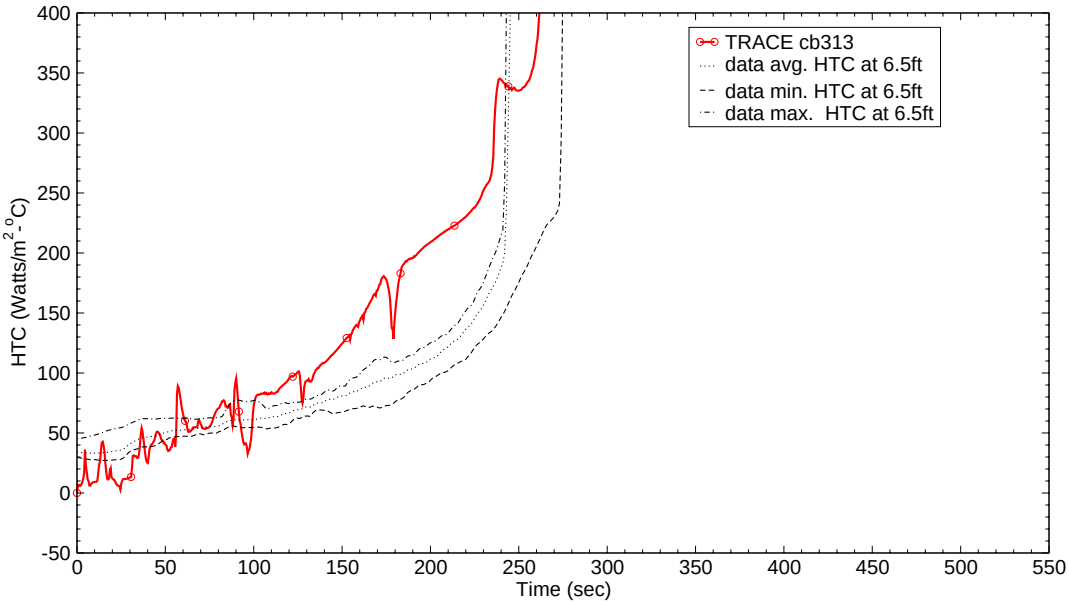

Figure B.7-192. Heat Transfer Coefficient at 6.5 ft from Heated Bottom for Test 32013

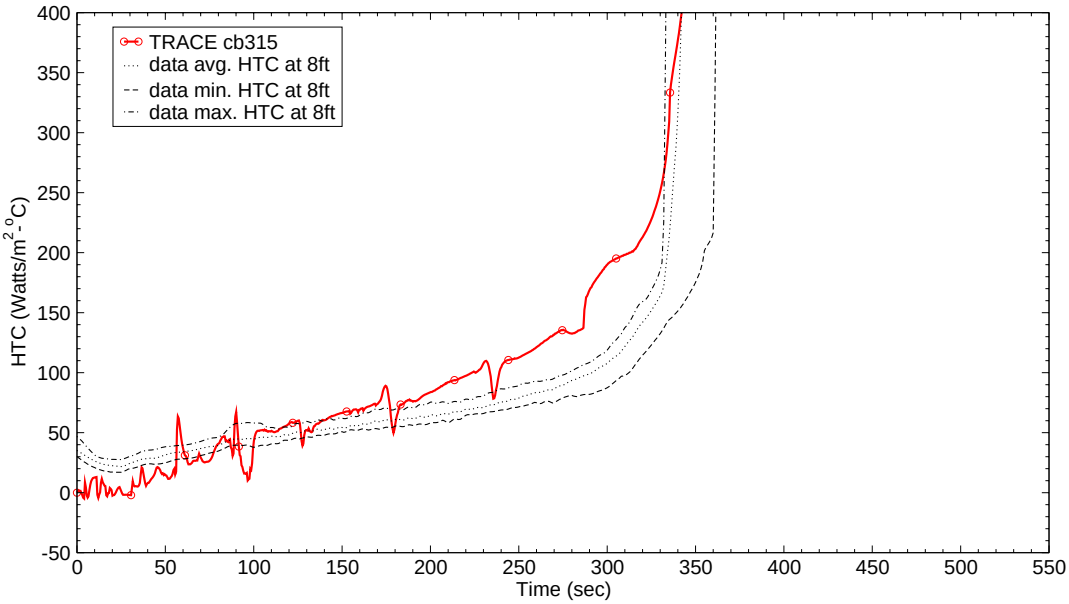

Figure B.7-193. Heat Transfer Coefficient at 8 ft from Heated Bottom for Test 32013

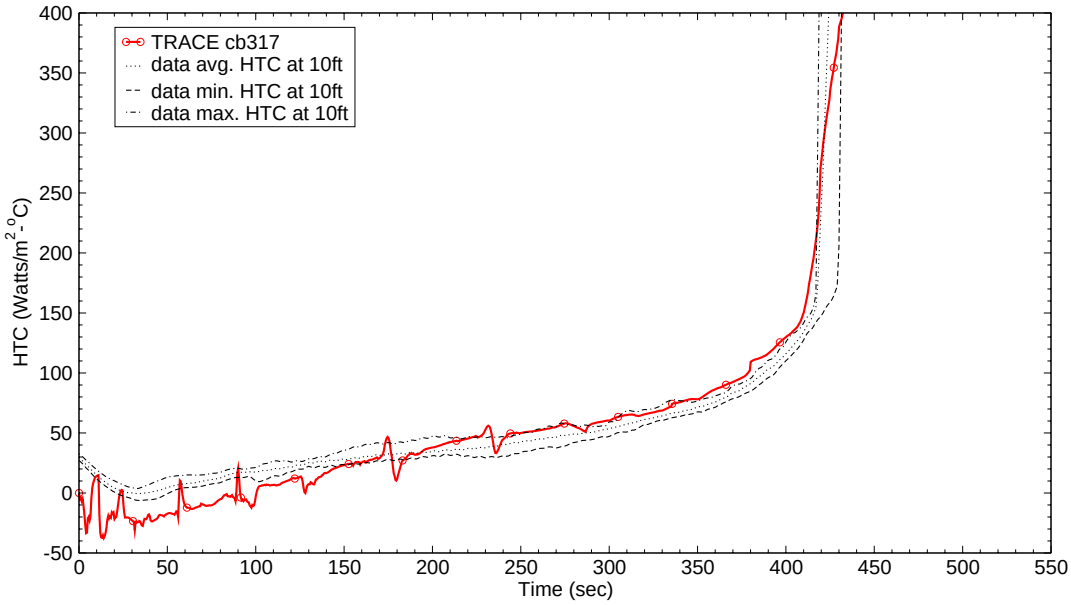

Figure B.7-194. Heat Transfer Coefficient at 10 ft from Heated Bottom for Test 32013

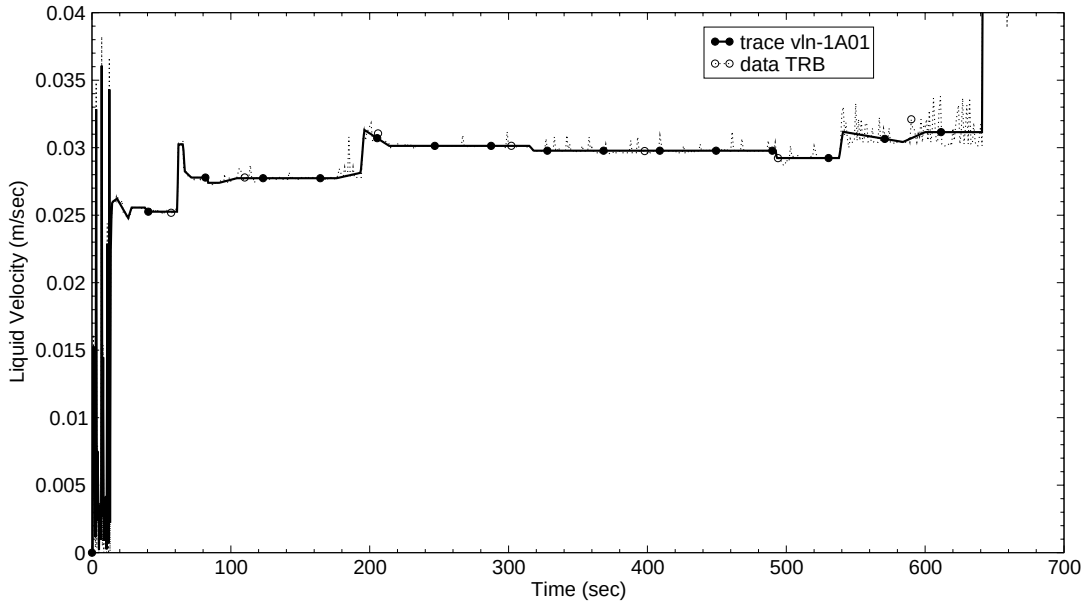

Figure B.7-195. Liquid Inlet Flow Rate for Test 32114

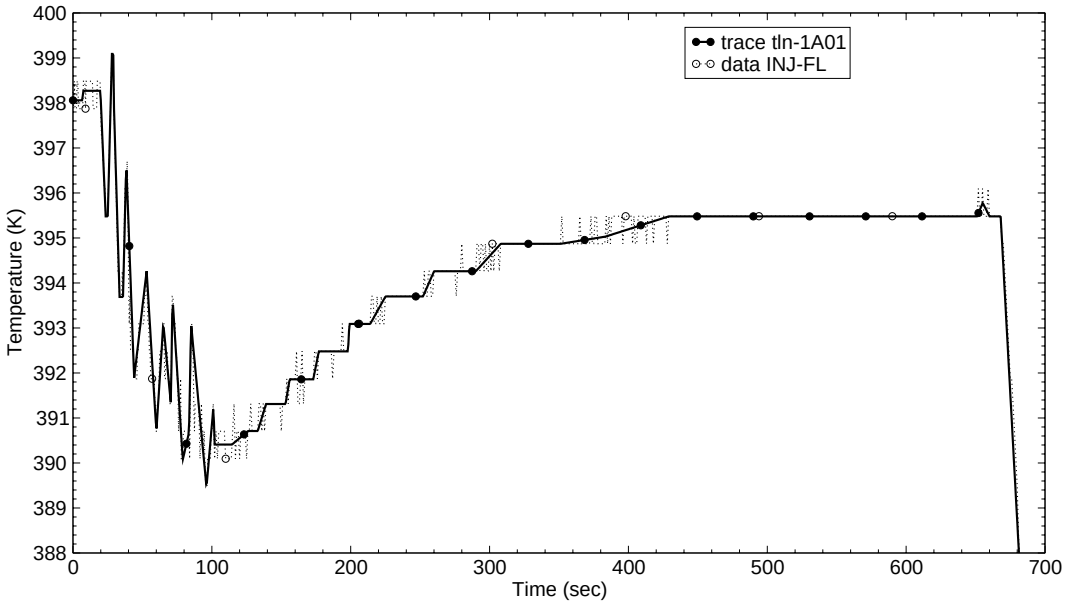

Figure B.7-196. Liquid Inlet Temperature for Test 32114

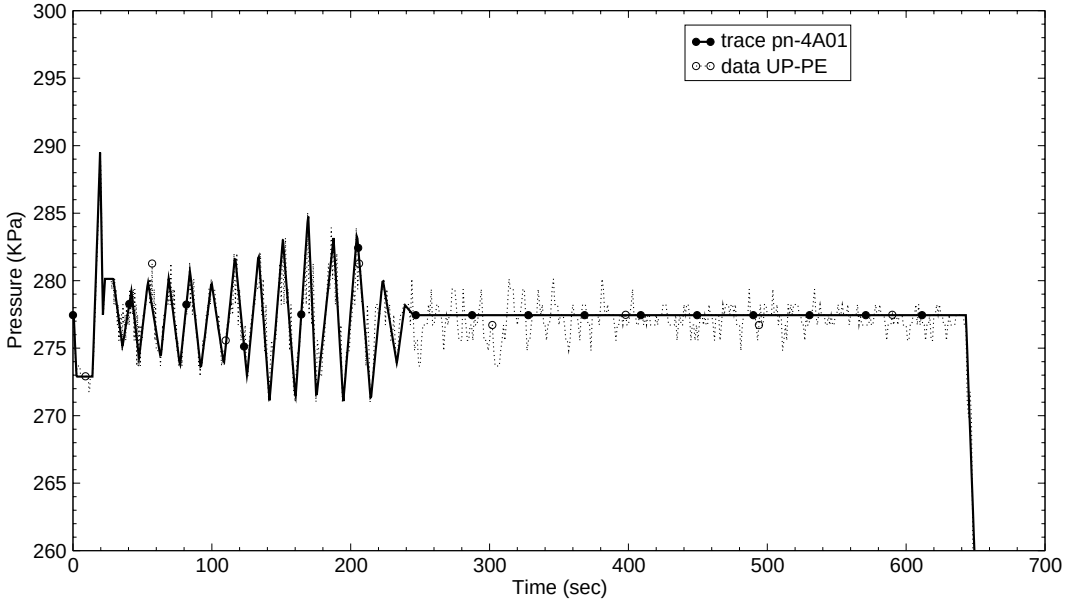

Figure B.7-197. Upper Plenum Exit Pressure for Test 32114

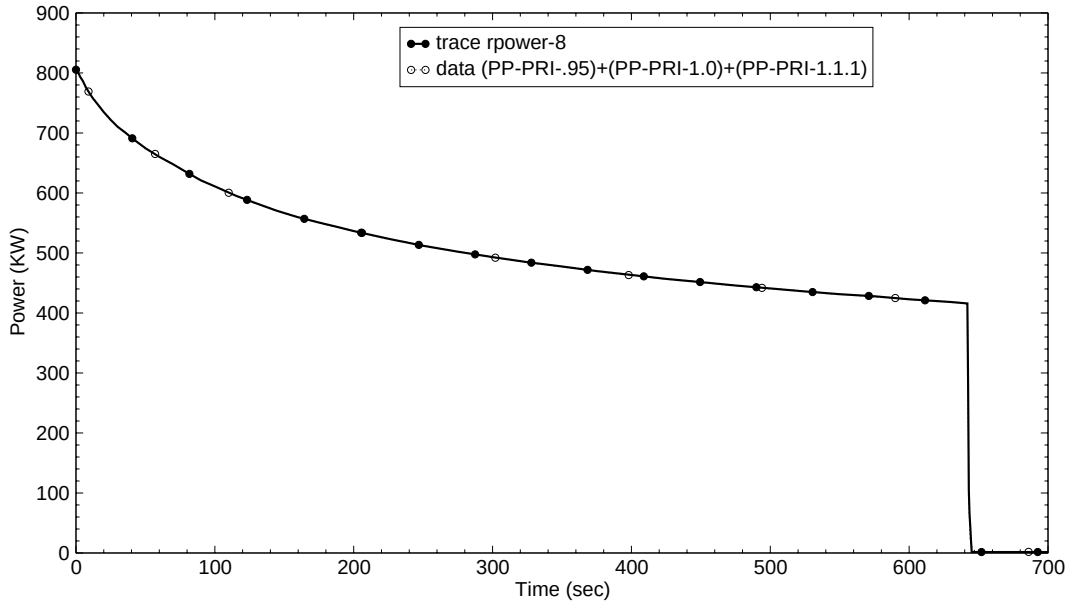

Figure B.7-198. Total Power to the Bundle for Test 32114

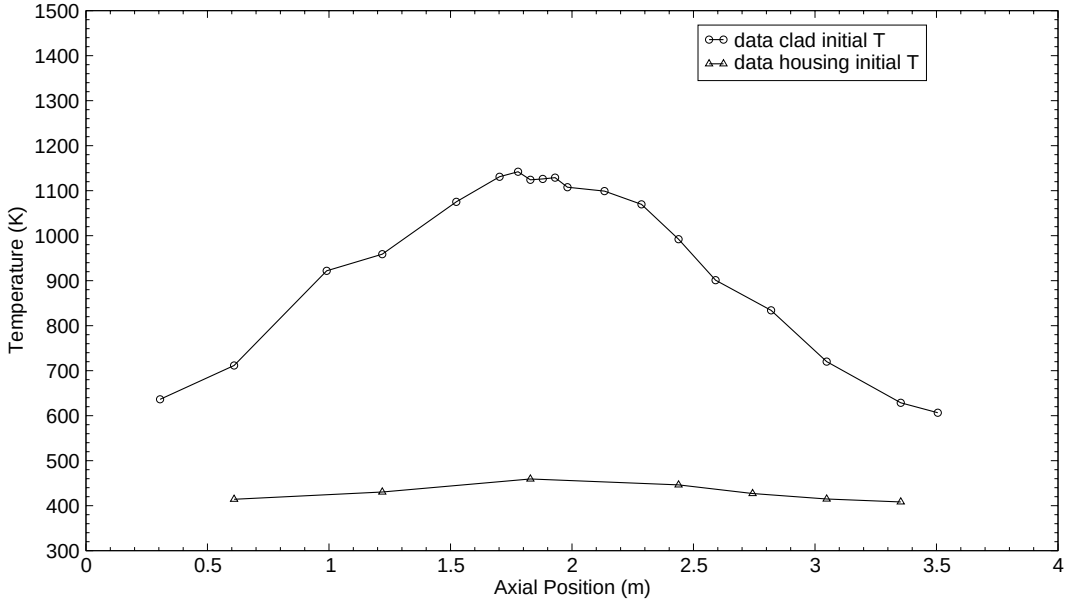

Figure B.7-199. Heater Rod Clad and Housing Initial Temperatures for Test 32114

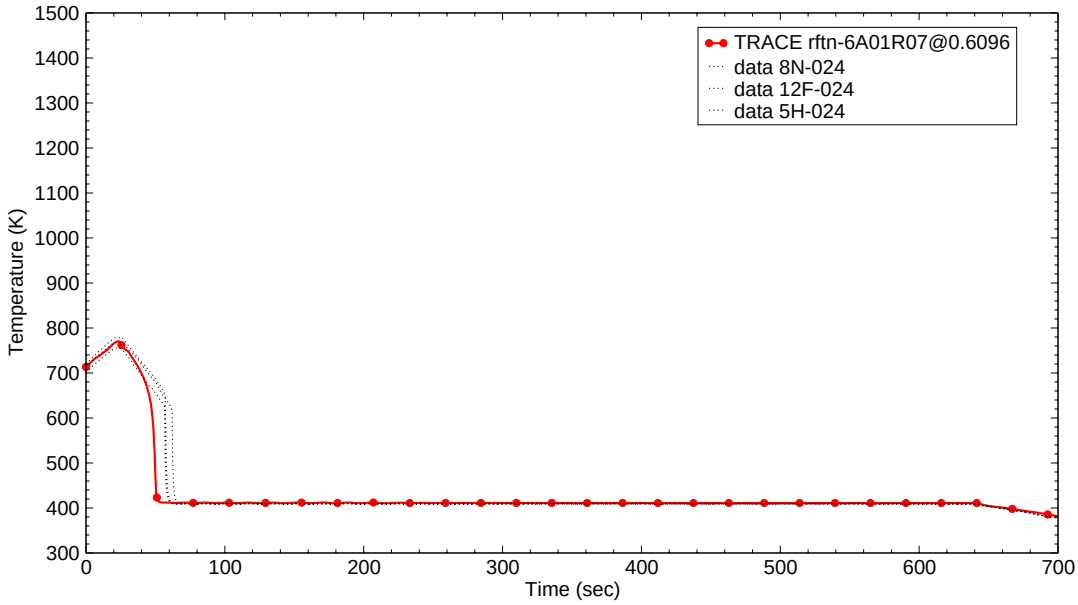

Figure B.7-200. Rod Clad Temperatures at 2 ft from Heated Bottom for Test 32114

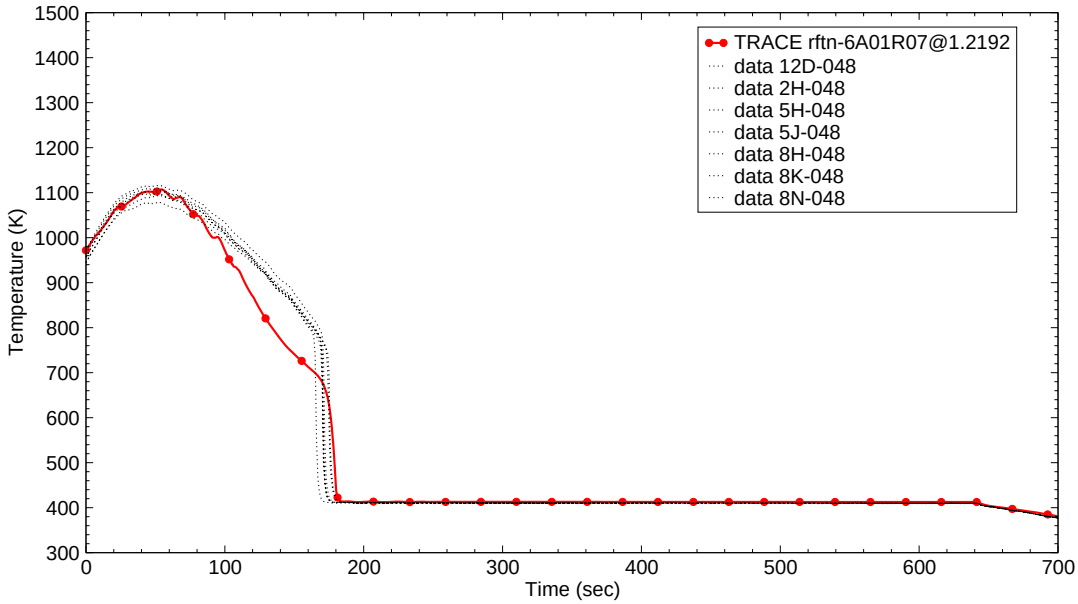

Figure B.7-201. Rod Clad Temperatures at 4 ft from Heated Bottom for Test 32114

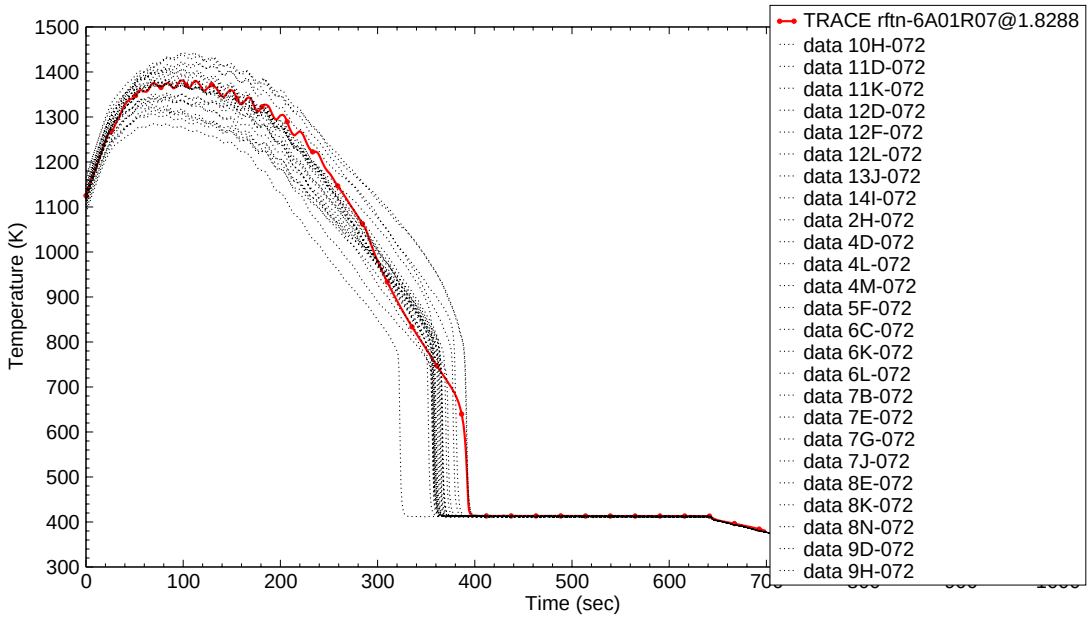

Figure B.7-202. Rod Clad Temperatures at 6 ft from Heated Bottom for Test 32114

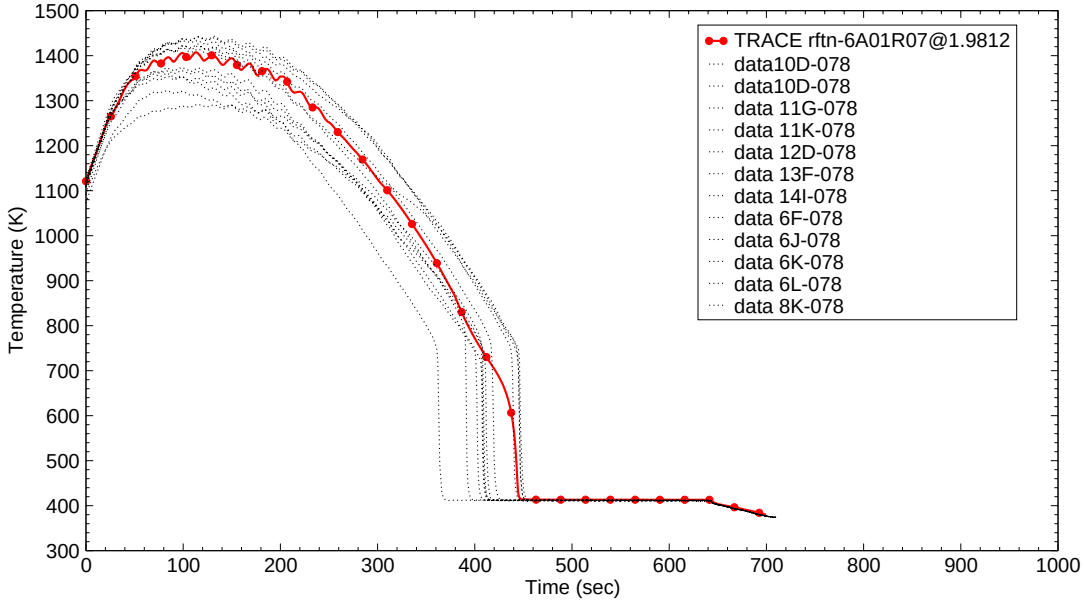

Figure B.7-203. Rod Clad Temperatures at 6.5 ft from Heated Bottom for Test 32114

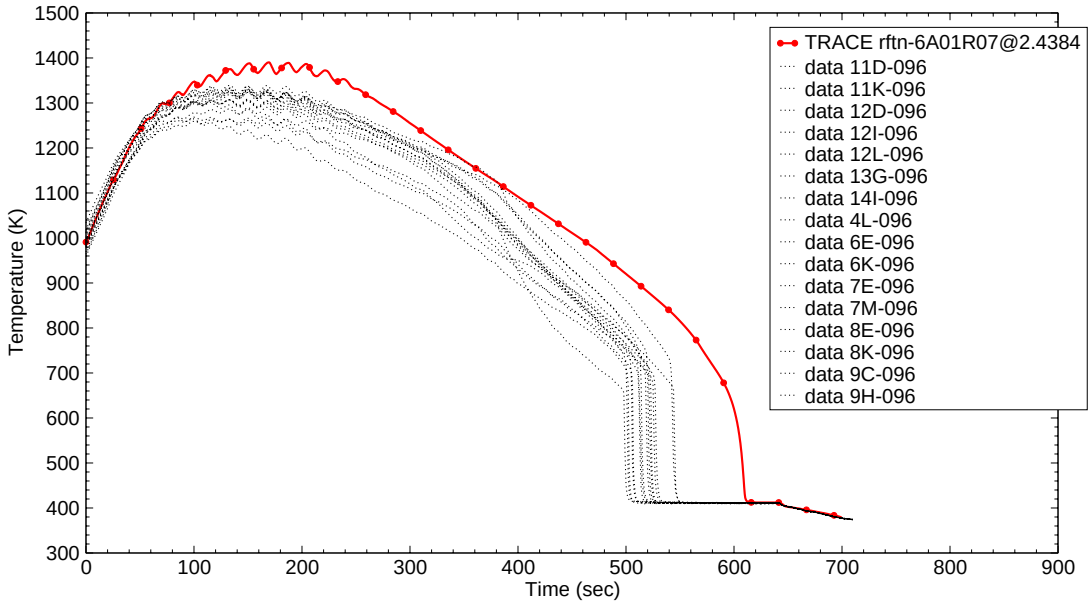

Figure B.7-204. Rod Clad Temperatures at 8 ft from Heated Bottom for Test 32114

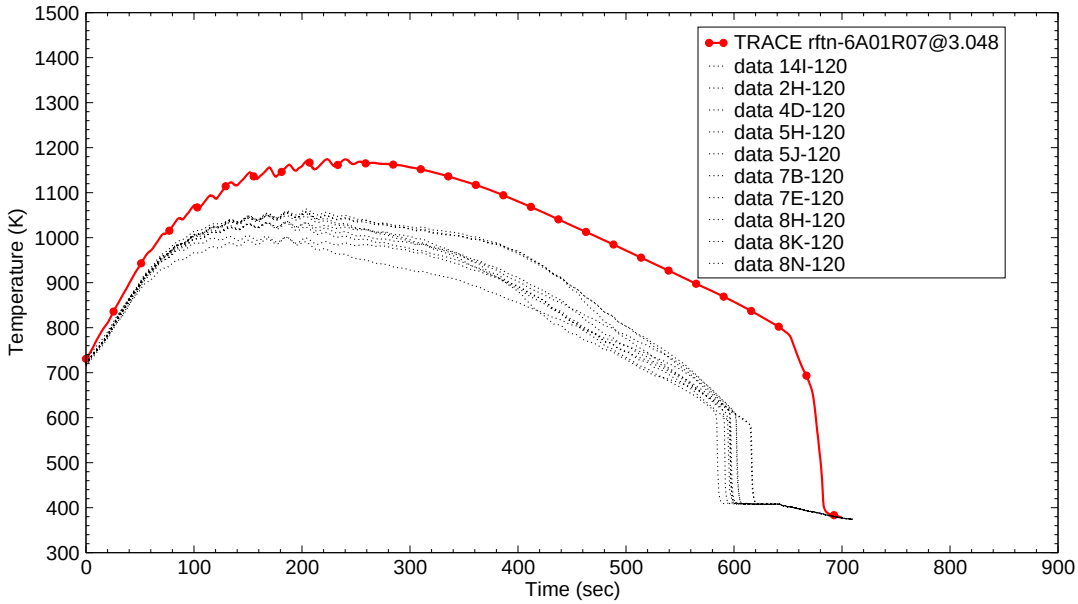

Figure B.7-205. Rod Clad Temperatures at 10 ft from Heated Bottom for Test 32114

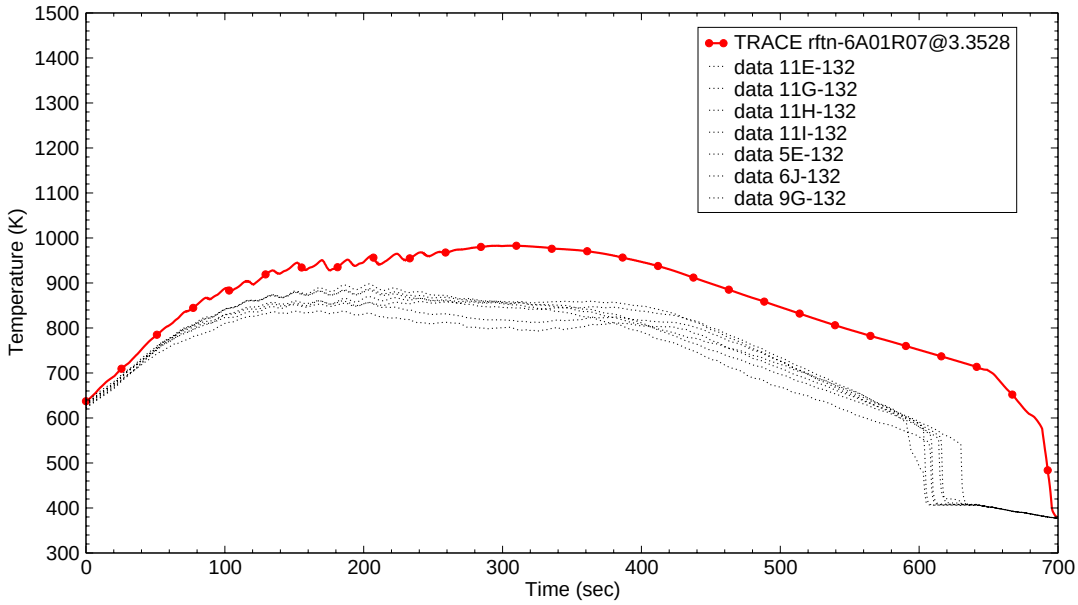

Figure B.7-206. Rod Clad Temperatures at 11 ft from Heated Bottom for Test 32114

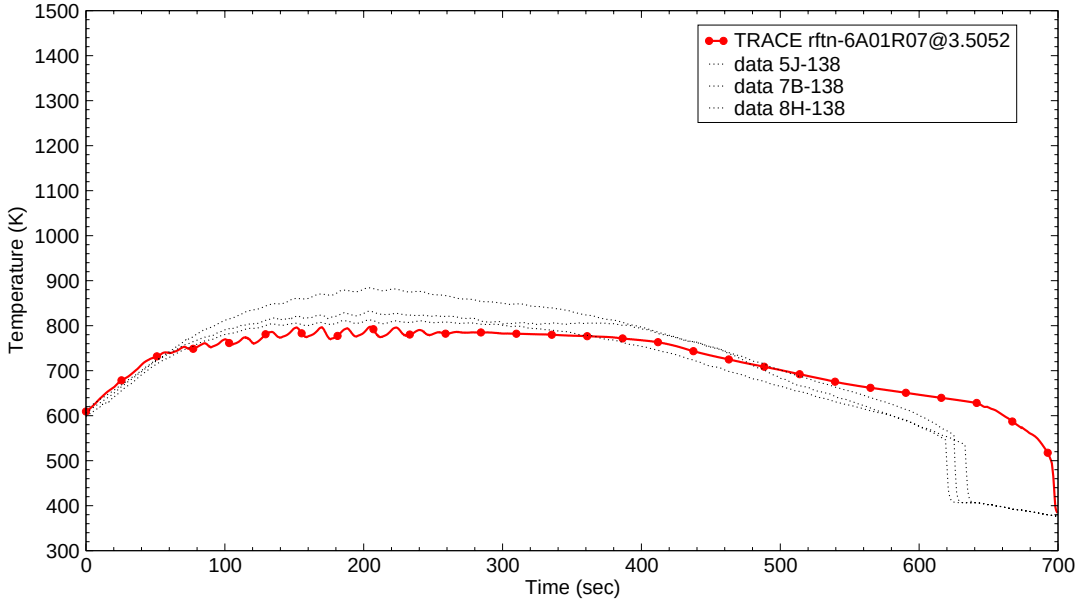

Figure B.7-207. Rod Clad Temperatures at 11.5 ft from Heated Bottom for Test 32114

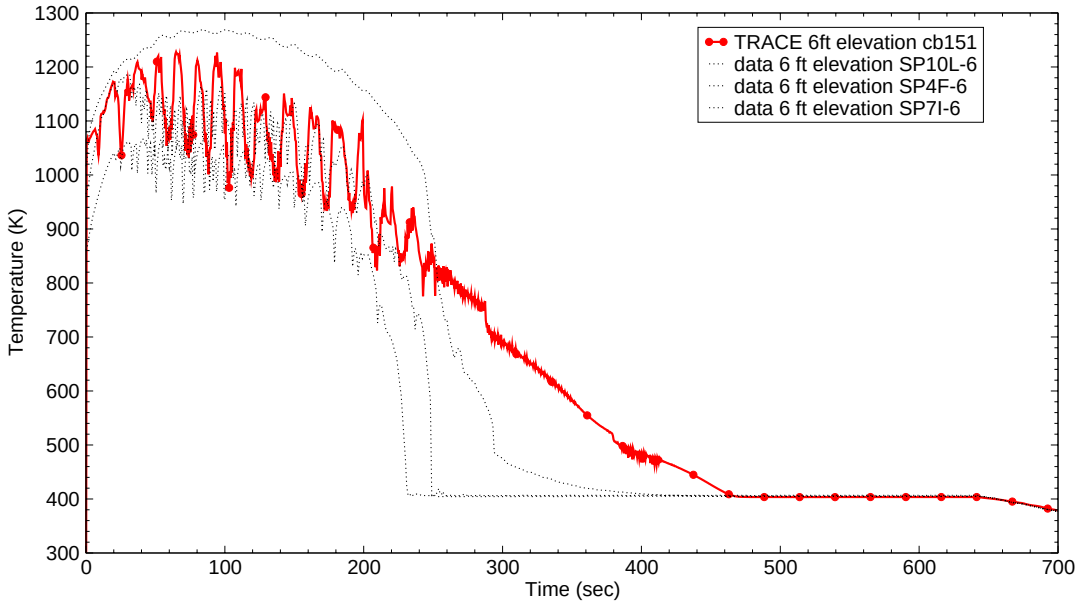

Figure B.7-208. Vapor Temperatures at 6 ft from Heated Bottom for Test 32114

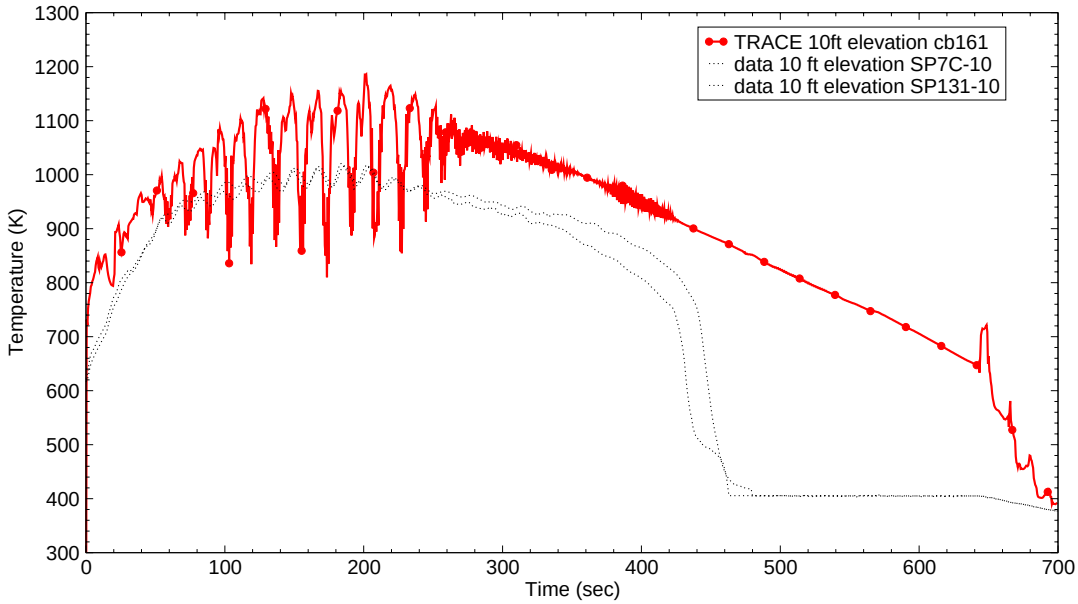

Figure B.7-209. Vapor Temperatures at 10 ft from Heated Bottom for Test 32114

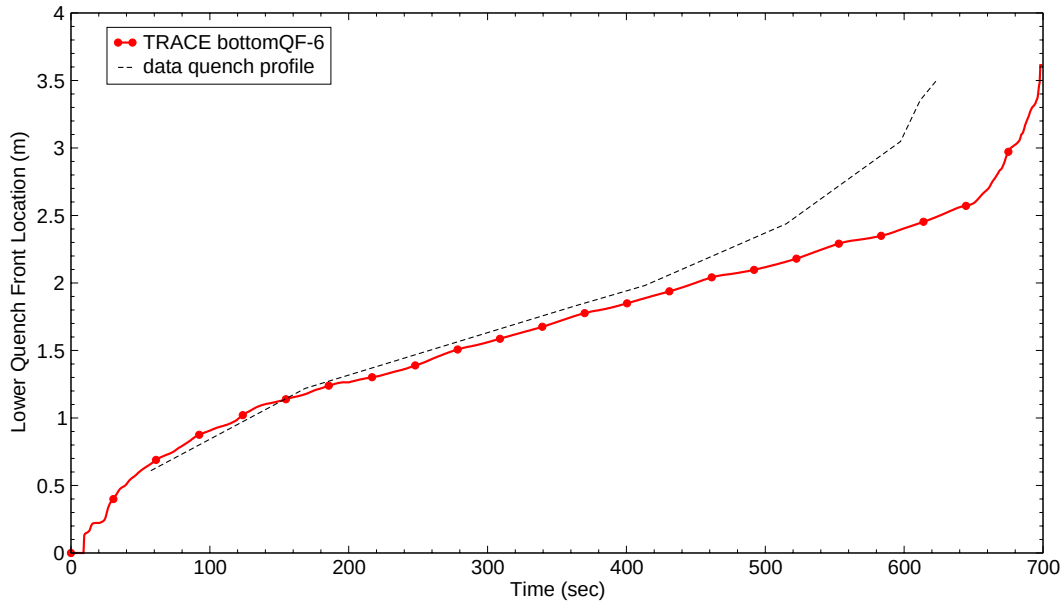

Figure B.7-210. Quench Profile as a Function of Time for Test 32114

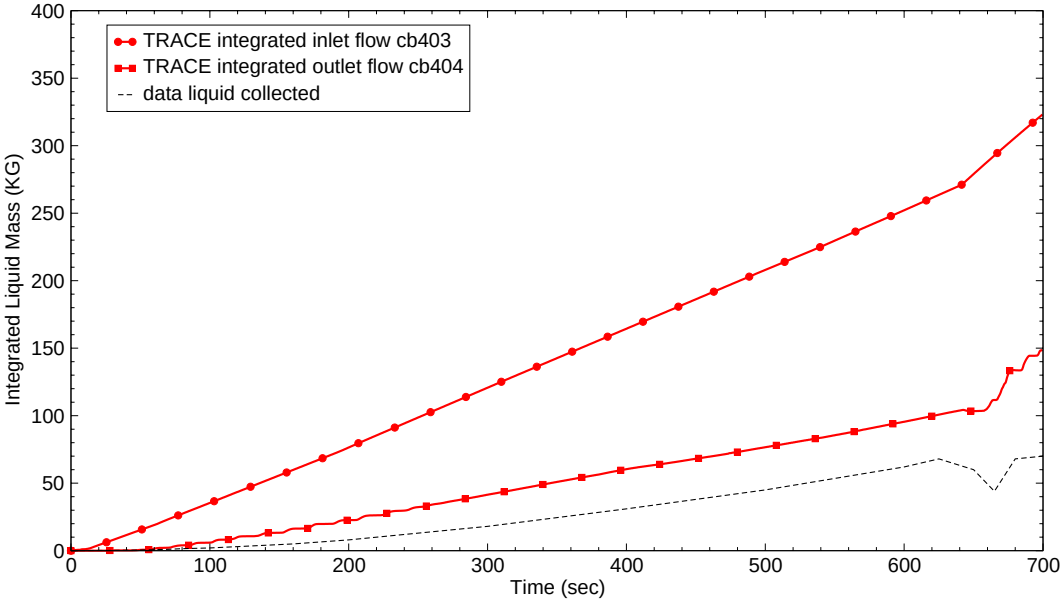

Figure B.7-211. Integrated Liquid Mass Flow into and out of Bundle for Test 32114

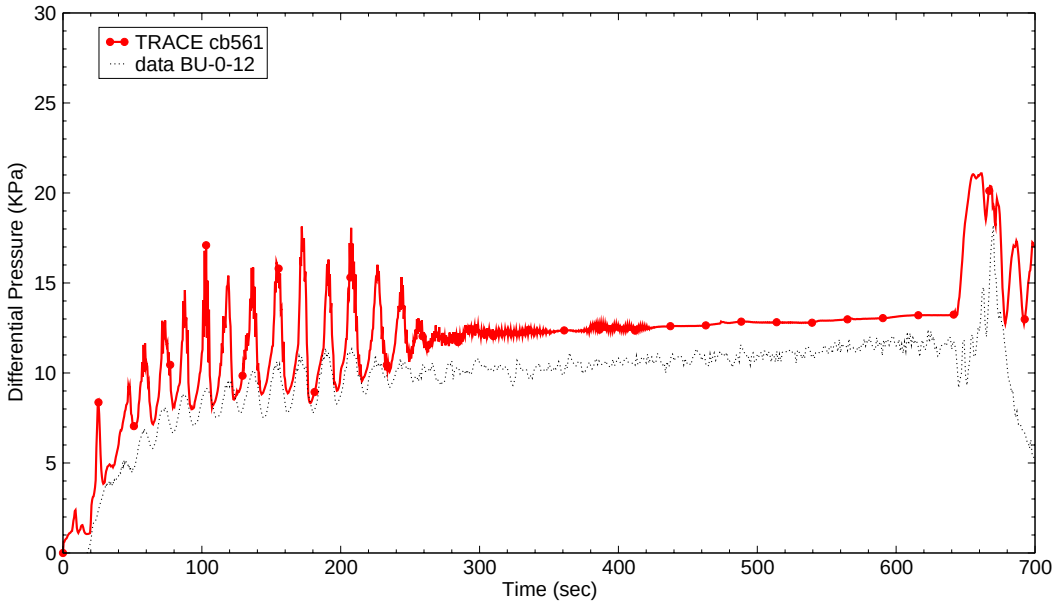

Figure B.7-212. Differential Pressure for the Entire 12 ft Core for Test 32114

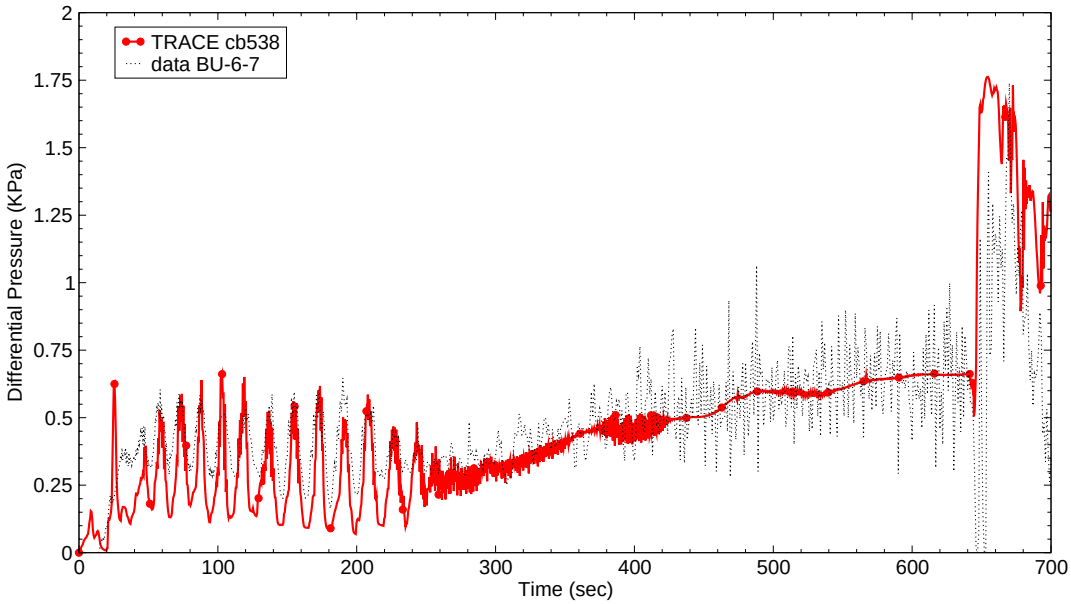

Figure B.7-213. Differential Pressure at 6-7 ft Elevation for Test 32114

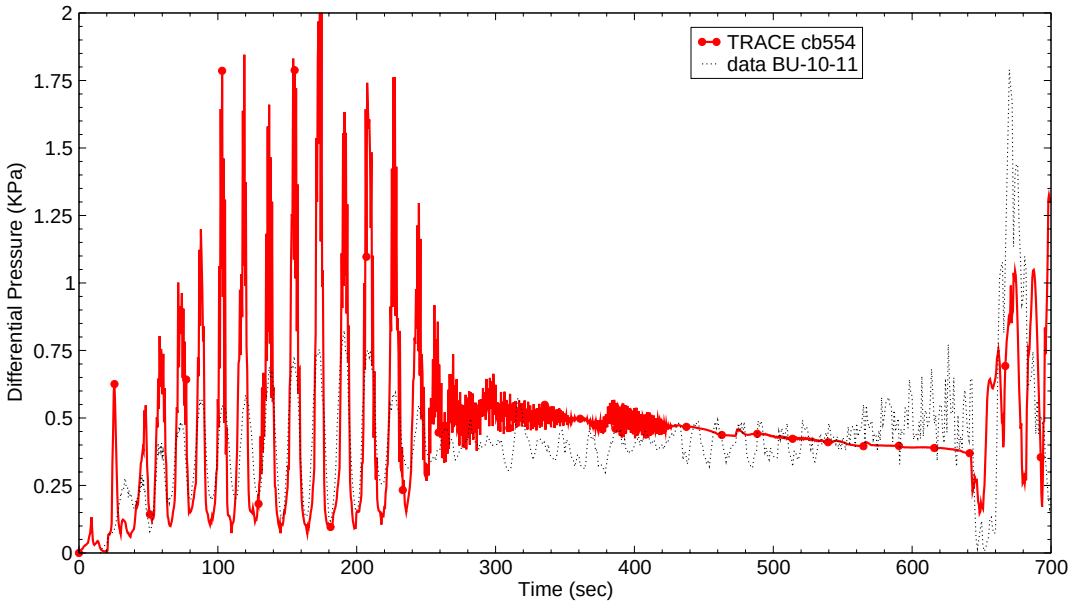

Figure B.7-214. Differential Pressure at 10-11 ft Elevation for Test 32114

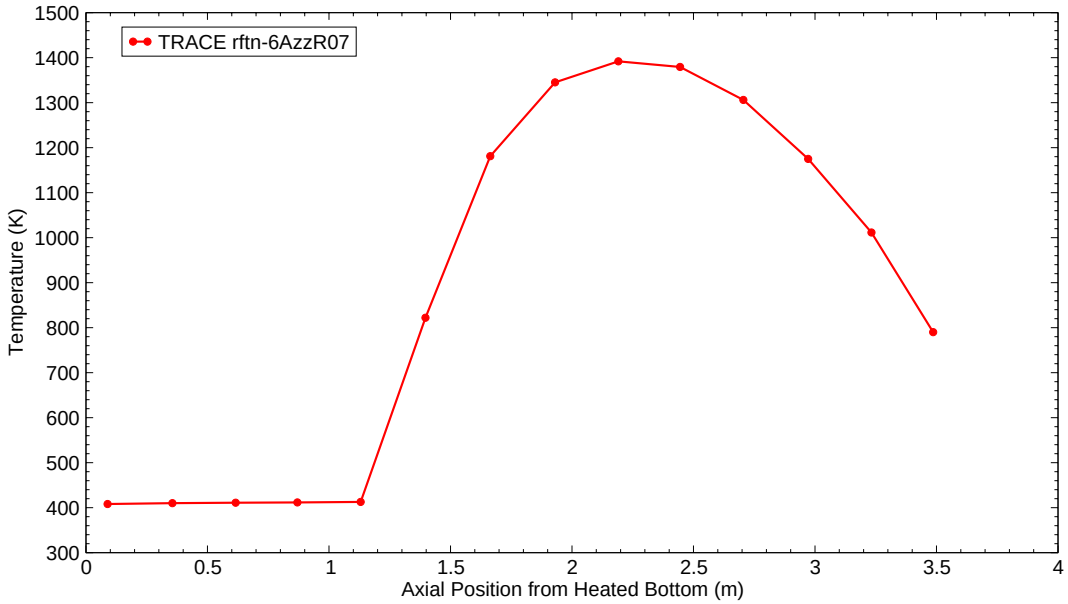

Figure B.7-215. Clad Temperature Profile at 200 sec after Reflood Start for Test 32114

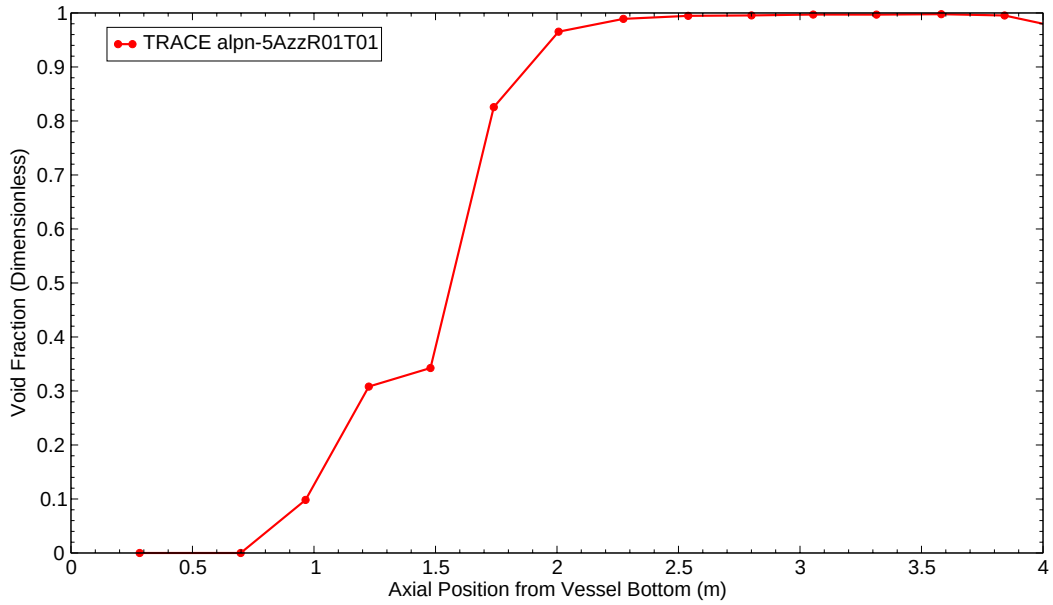

Figure B.7-216. Void Fraction Profile at 200 sec after Reflood Start for Test 32114

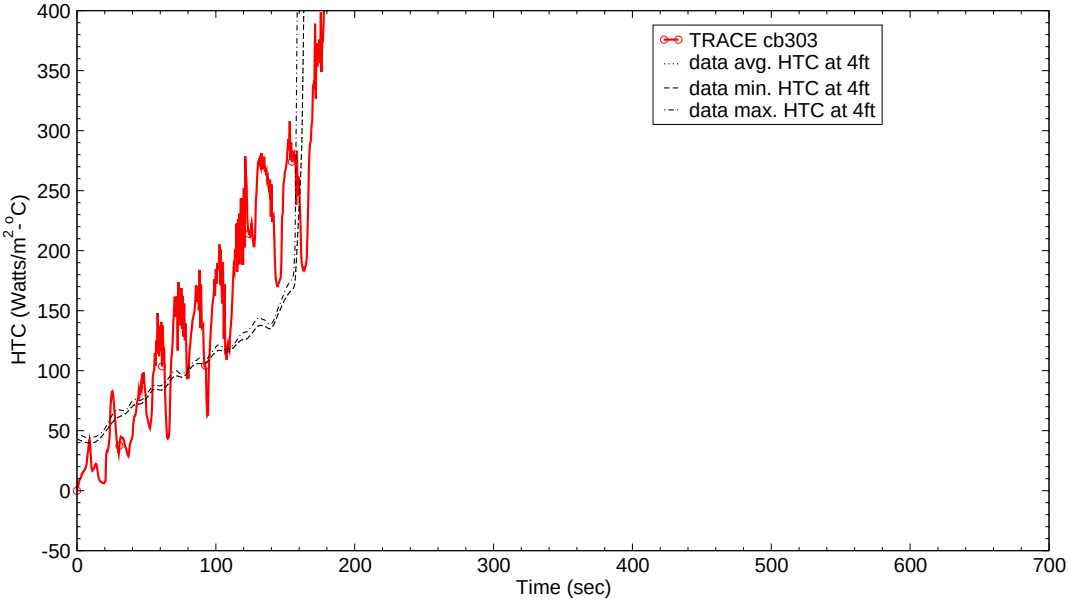

Figure B.7-217. Heat Transfer Coefficient at 4 ft from Heated Bottom for Test 32114

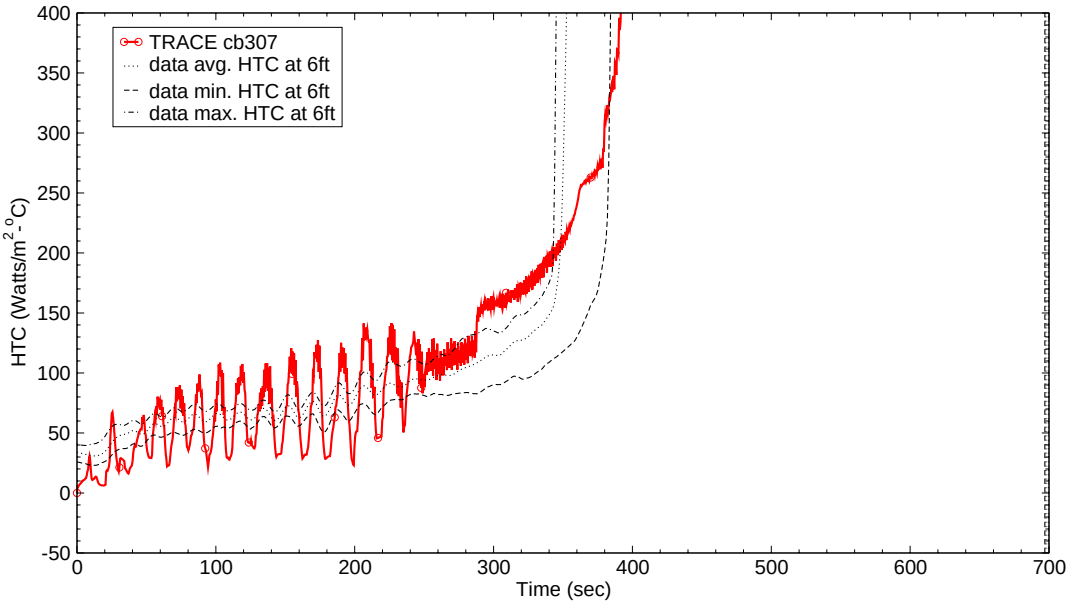

Figure B.7-218. Heat Transfer Coefficient at 6 ft from Heated Bottom for Test 32114

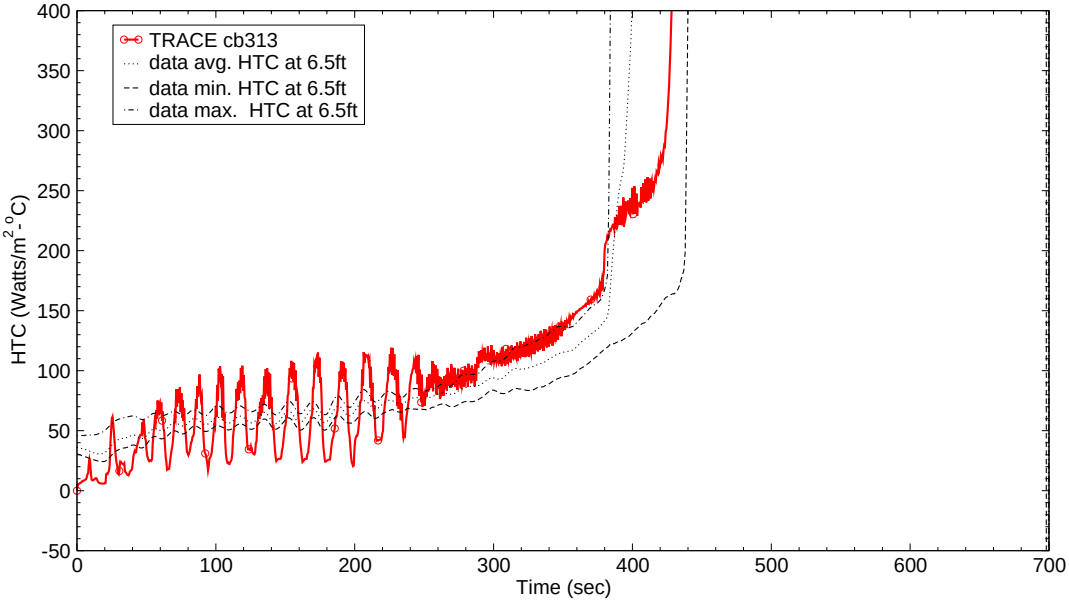

Figure B.7-219. Heat Transfer Coefficient at 6.5 ft from Heated Bottom for Test 32114

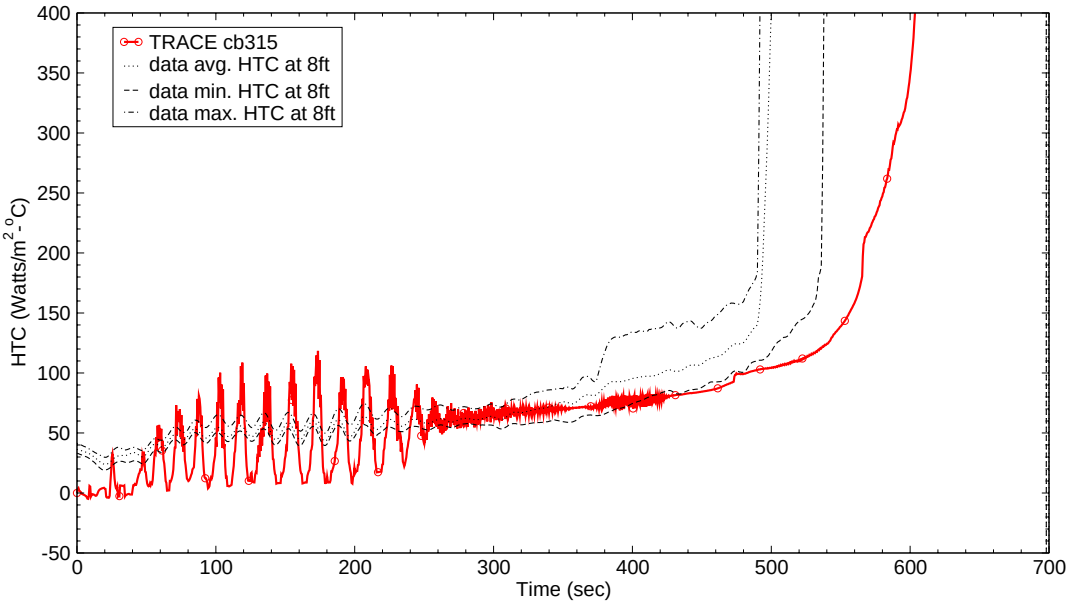

Figure B.7-220. Heat Transfer Coefficient at 8 ft from Heated Bottom for Test 32114

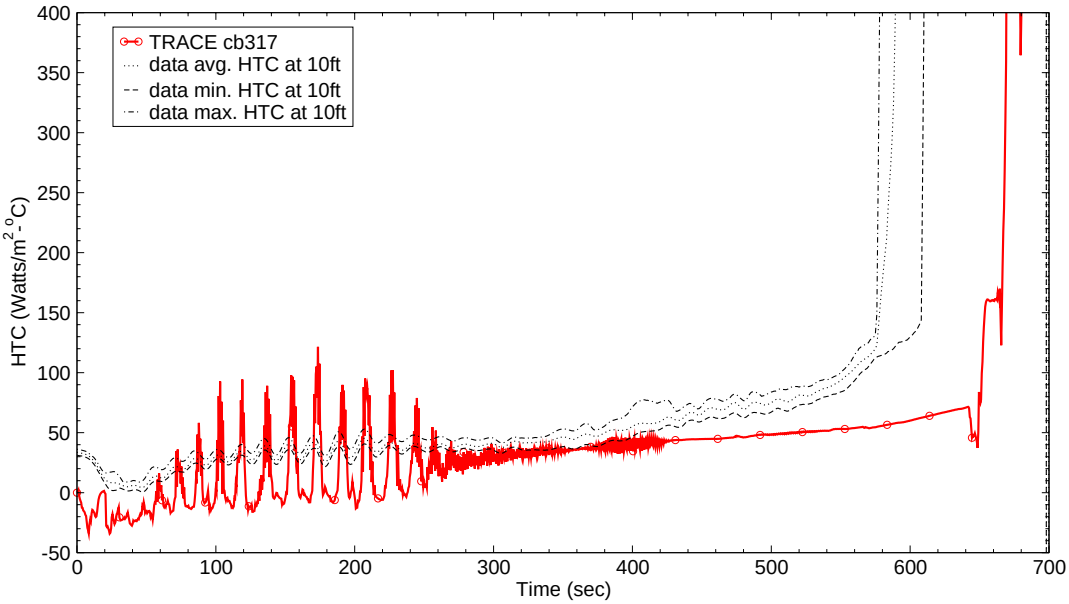

Figure B.7-221. Heat Transfer Coefficient at 10 ft from Heated Bottom for Test 32114

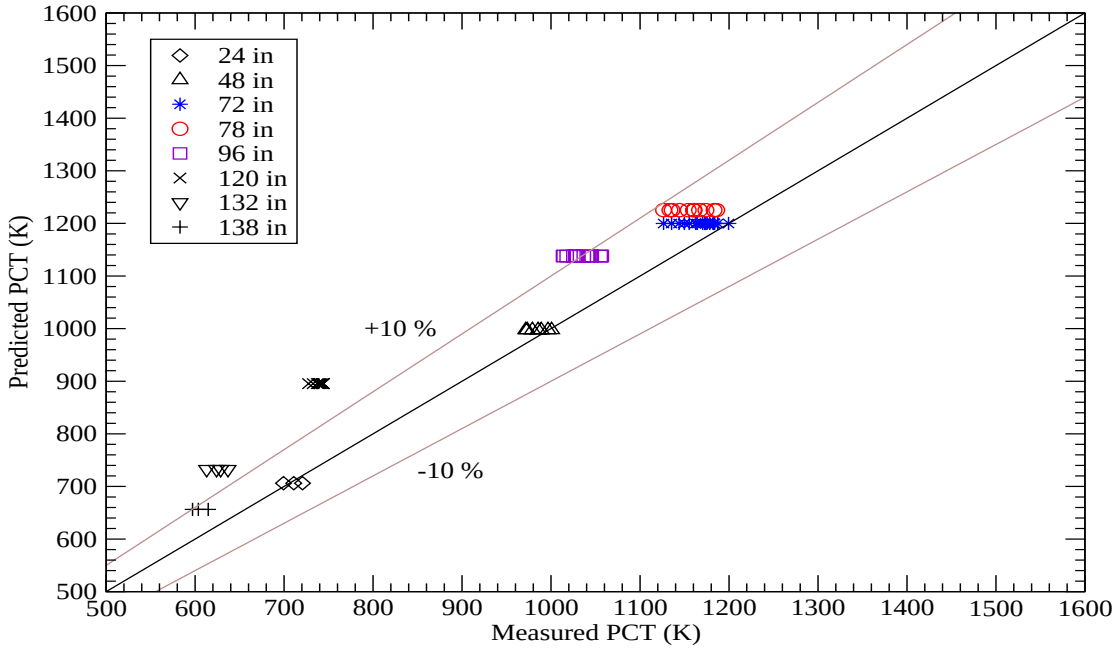

Figure B.7-222. Comparison of Calculated and Measured PCTs for Test 31108

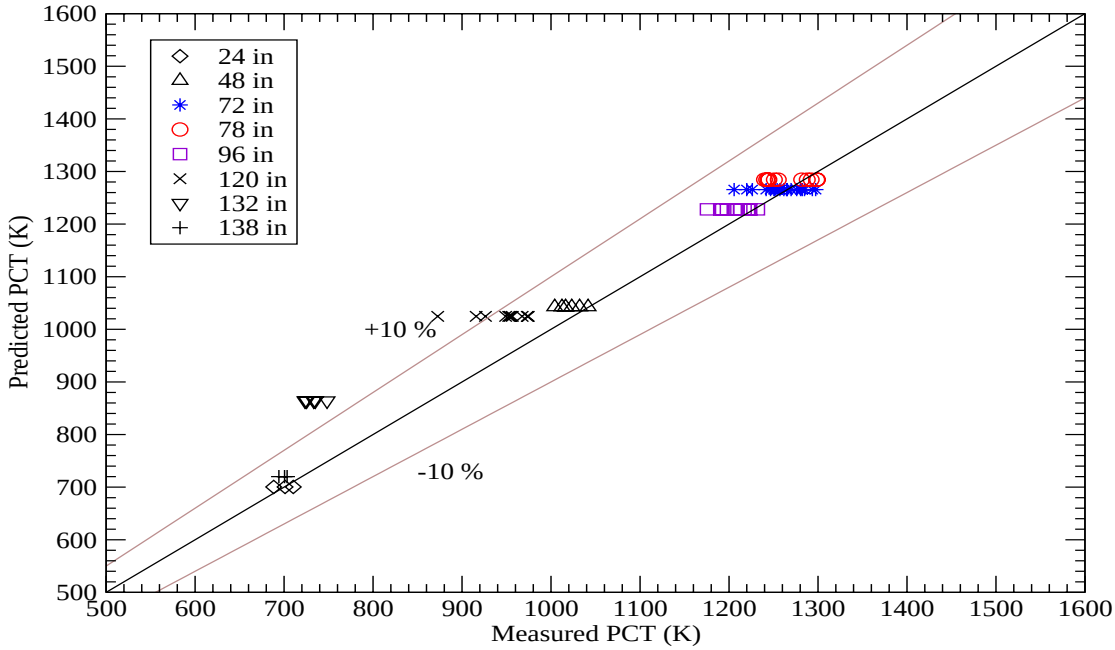

Figure B.7-223. Comparison of Calculated and Measured PCTs for Test 31203

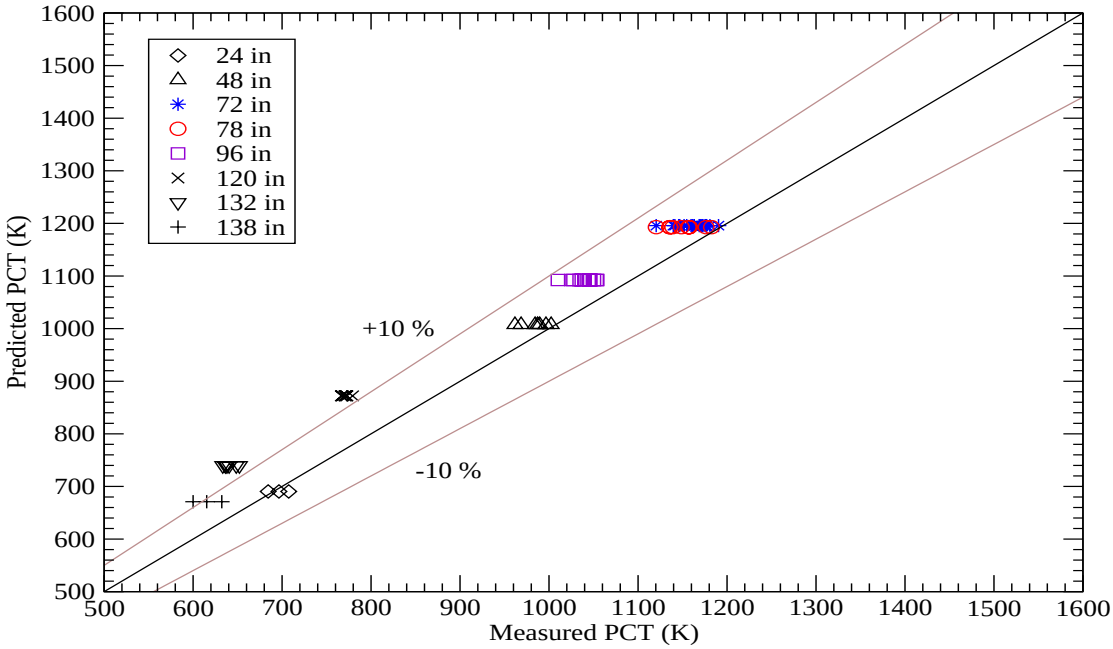

Figure B.7-224. Comparison of Calculated and Measured PCTs for Test 31302

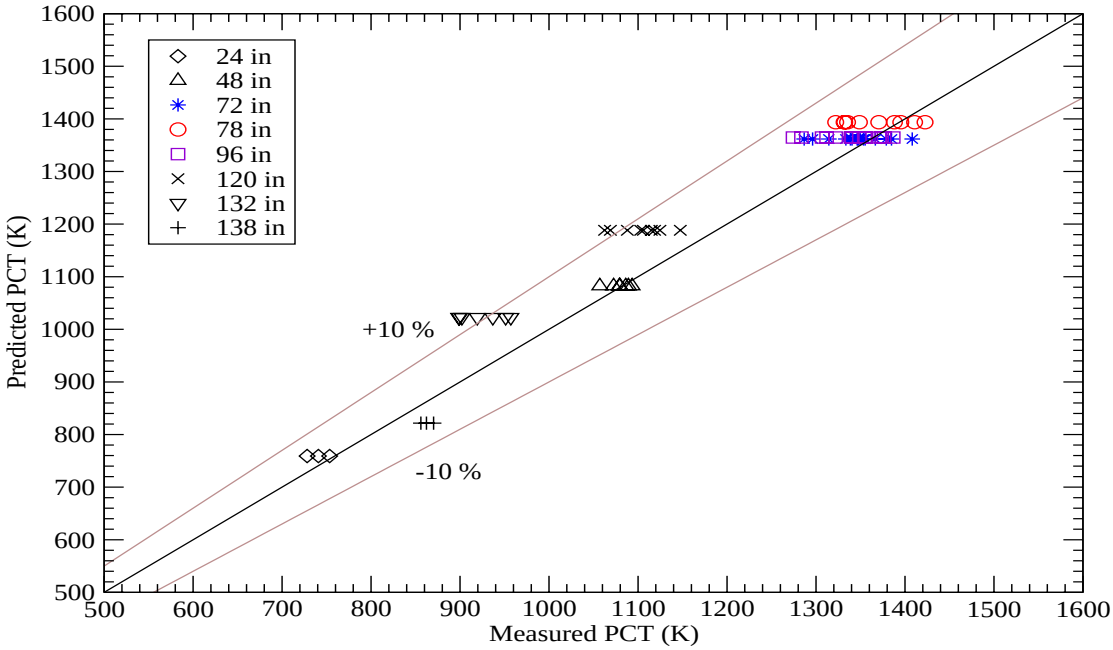

Figure B.7-225. Comparison of Calculated and Measured PCTs for Test 31504

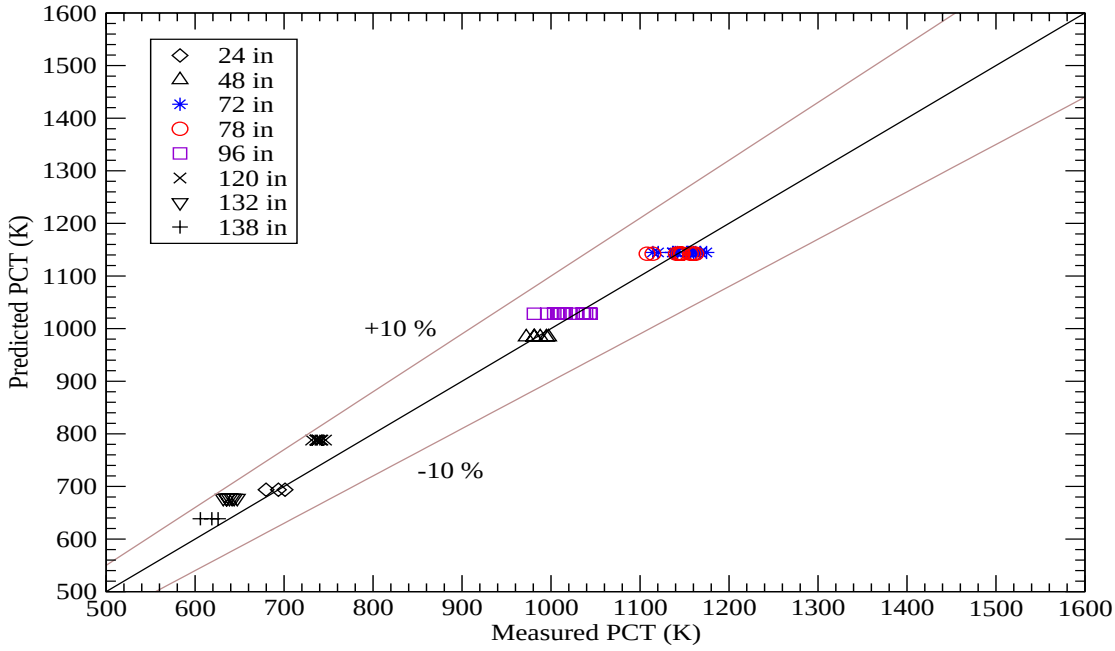

Figure B.7-226. Comparison of Calculated and Measured PCTs for Test 31701

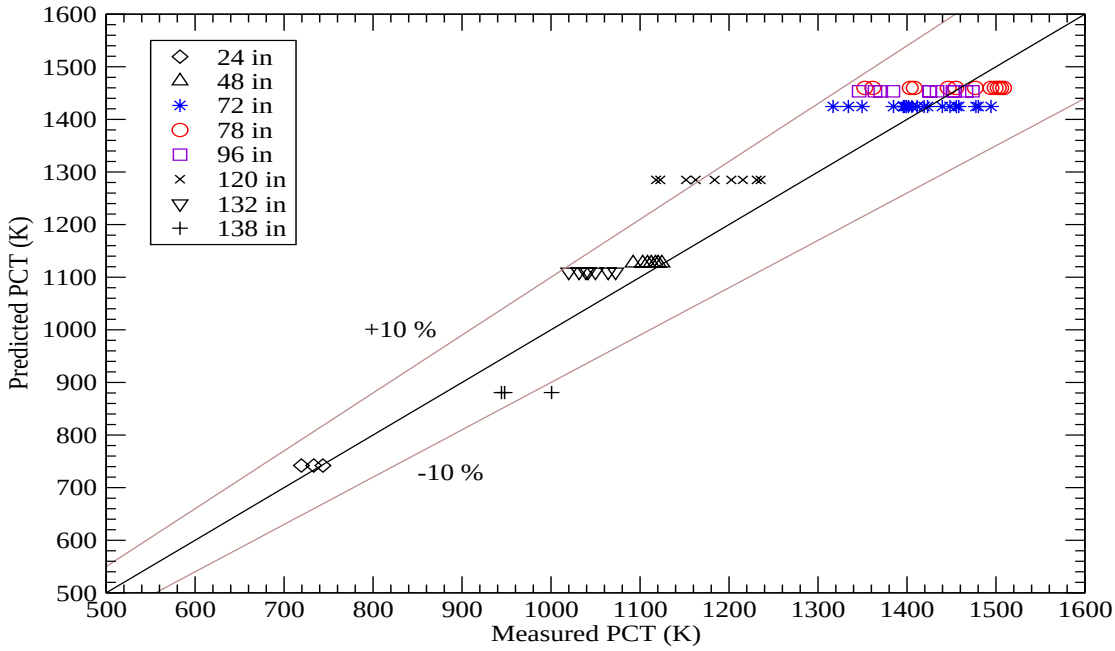

Figure B.7-227. Comparison of Calculated and Measured PCTs for Test 31805

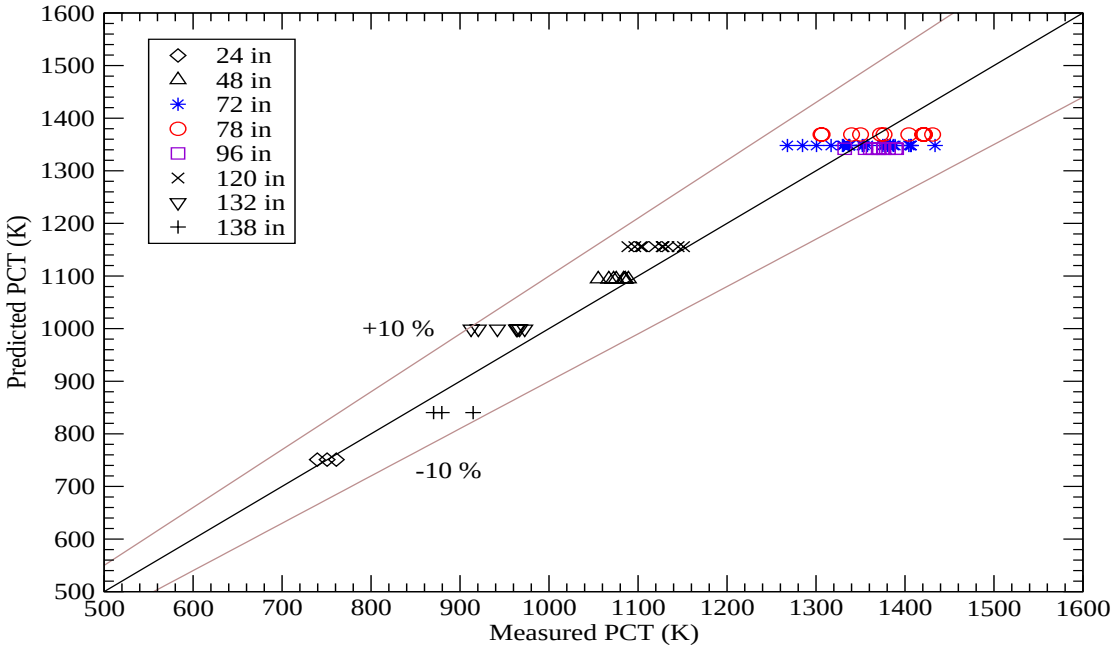

Figure B.7-228. Comparison of Calculated and Measured PCTs for Test 32013

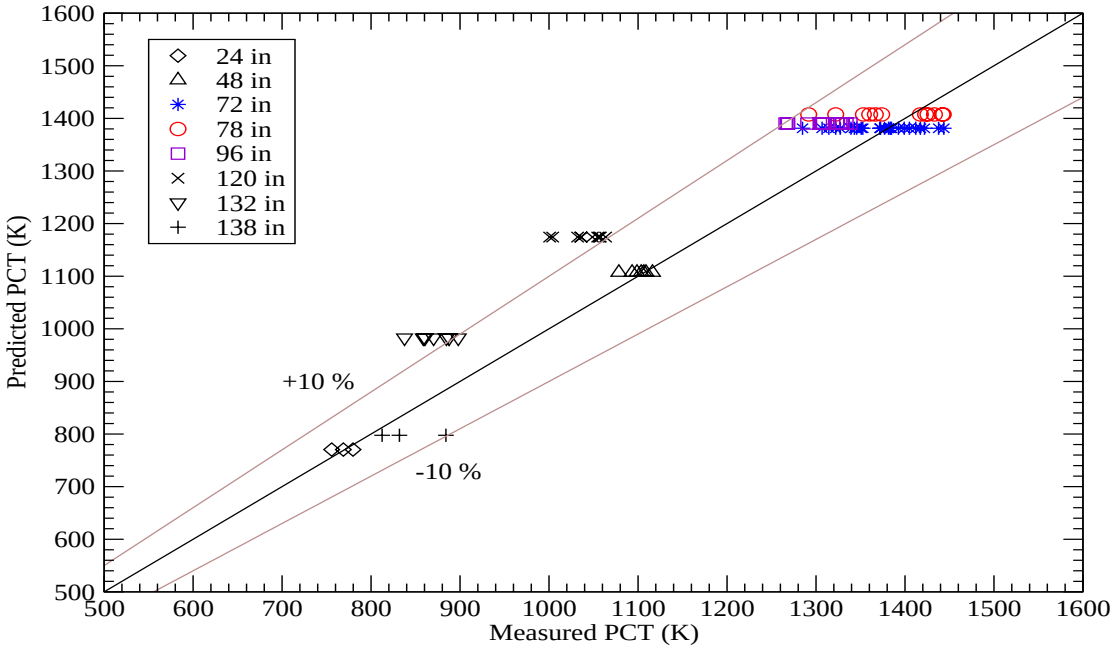

Figure B.7-229. Comparison of Calculated and Measured PCTs for Test 32114

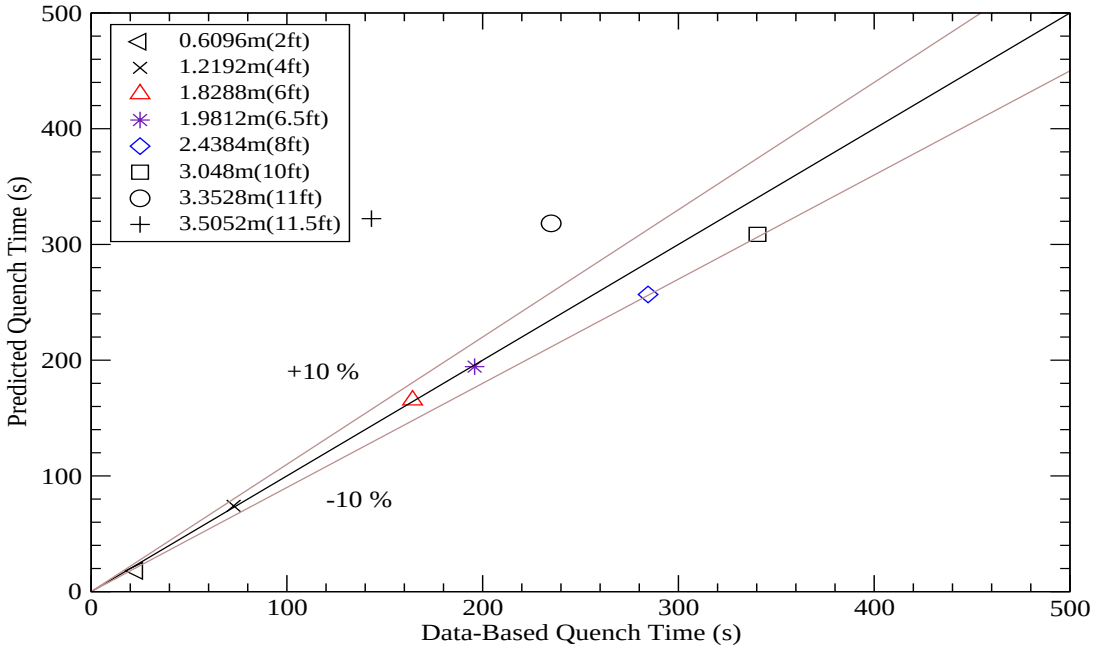

Figure B.7-230. Comparison of Calculated and Experimental Quench Times for Test 31108

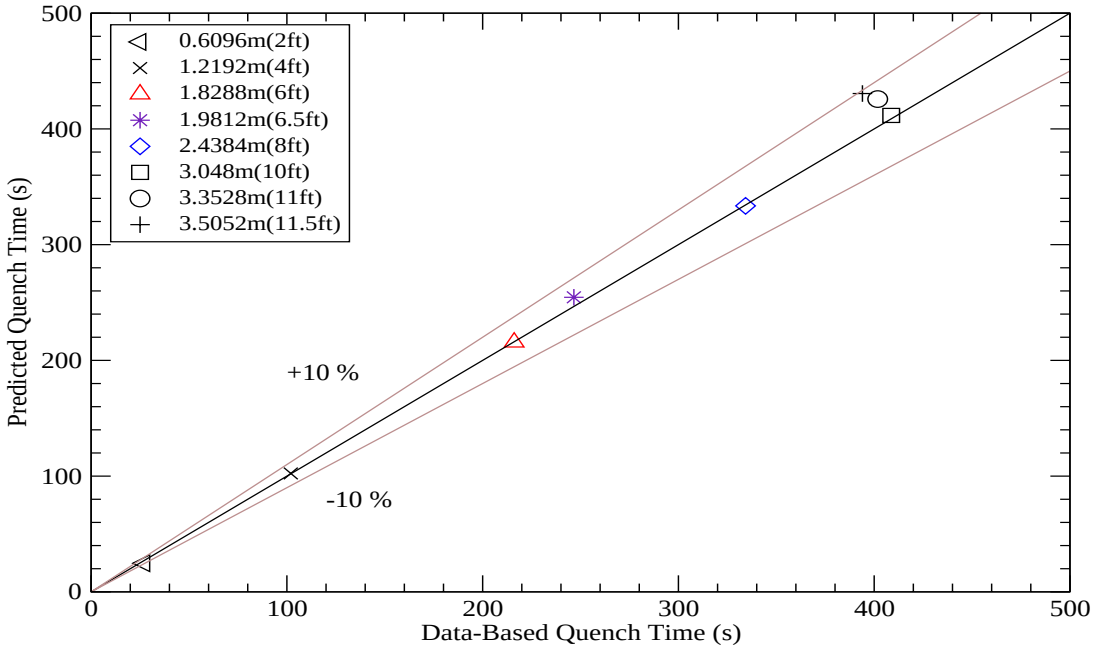

Figure B.7-231. Comparison of Calculated and Experimental Quench Times for Test 31203

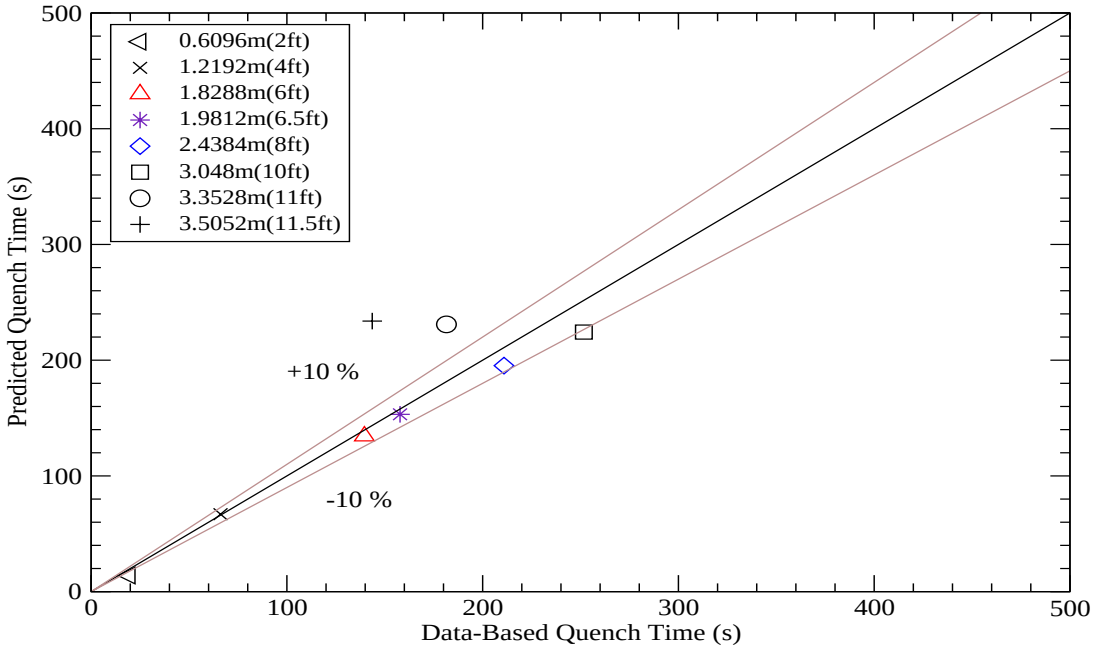

Figure B.7-232. Comparison of Calculated and Experimental Quench Times for Test 31302

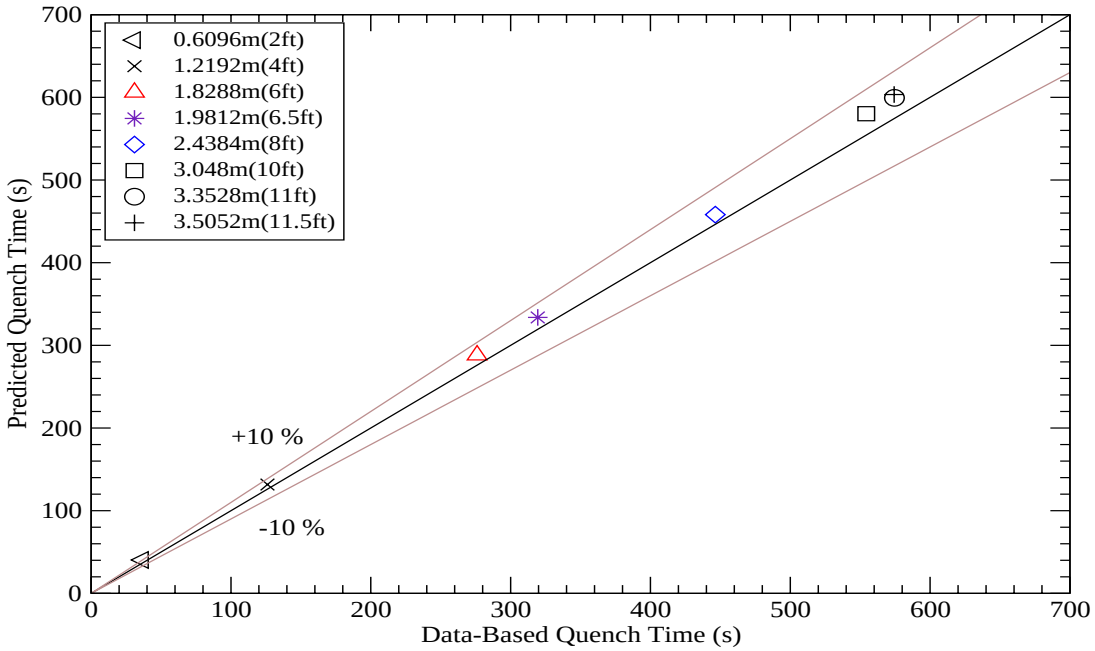

Figure B.7-233. Comparison of Calculated and Experimental Quench Times for Test 31504

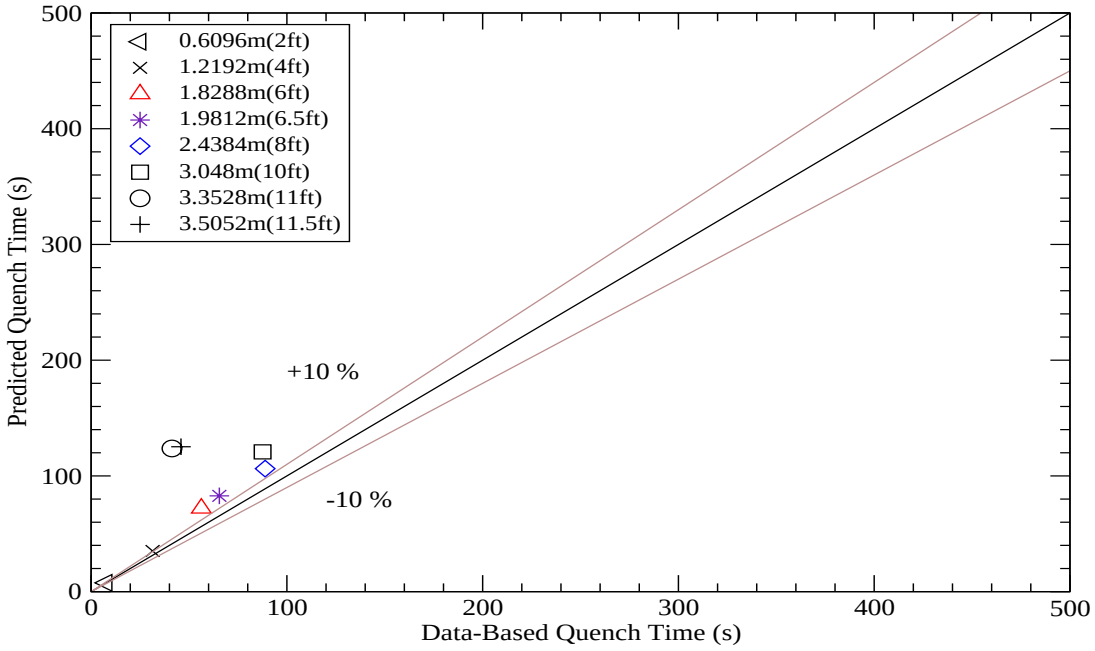

Figure B.7-234. Comparison of Calculated and Experimental Quench Times for Test 31701

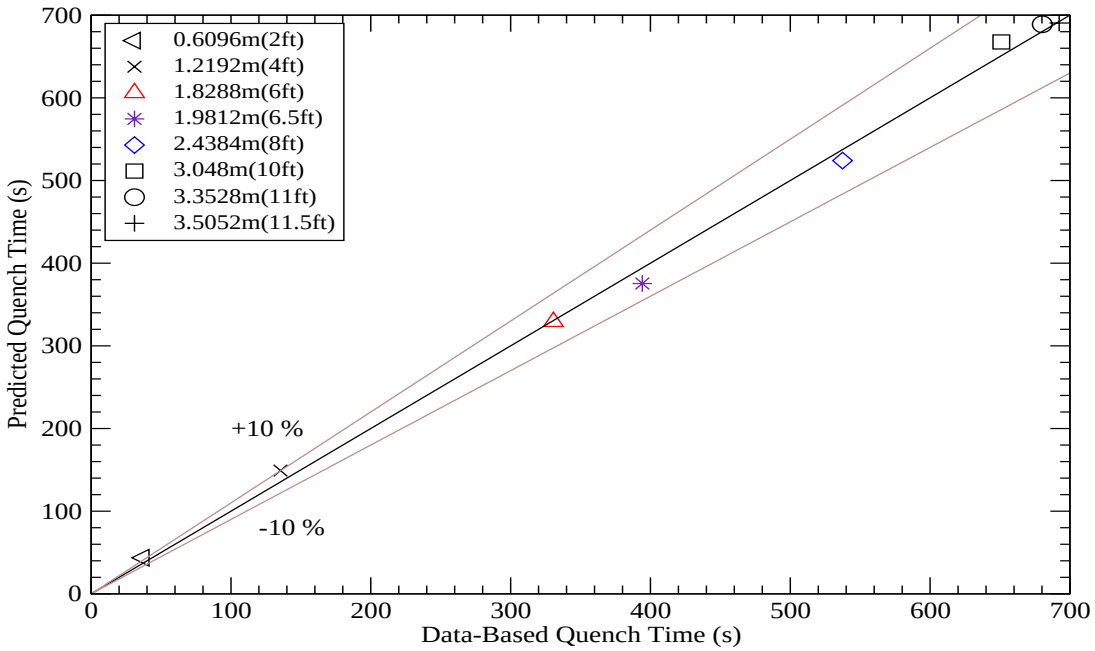

Figure B.7-235. Comparison of Calculated and Experimental Quench Times for Test 31805

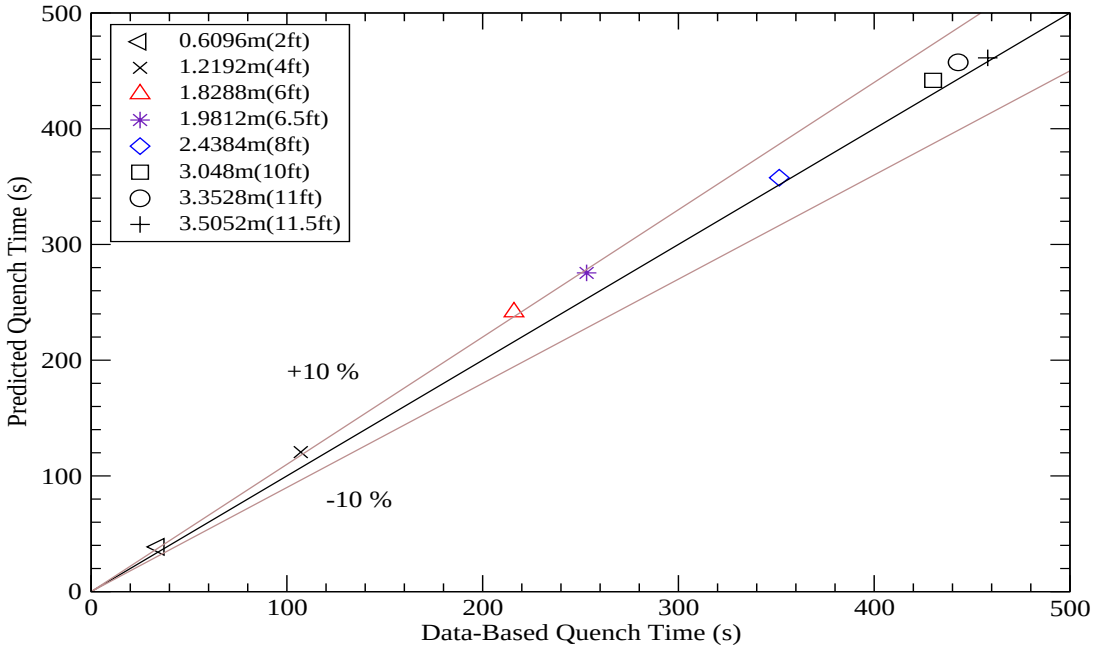

Figure B.7-236. Comparison of Calculated and Experimental Quench Times for Test 32013

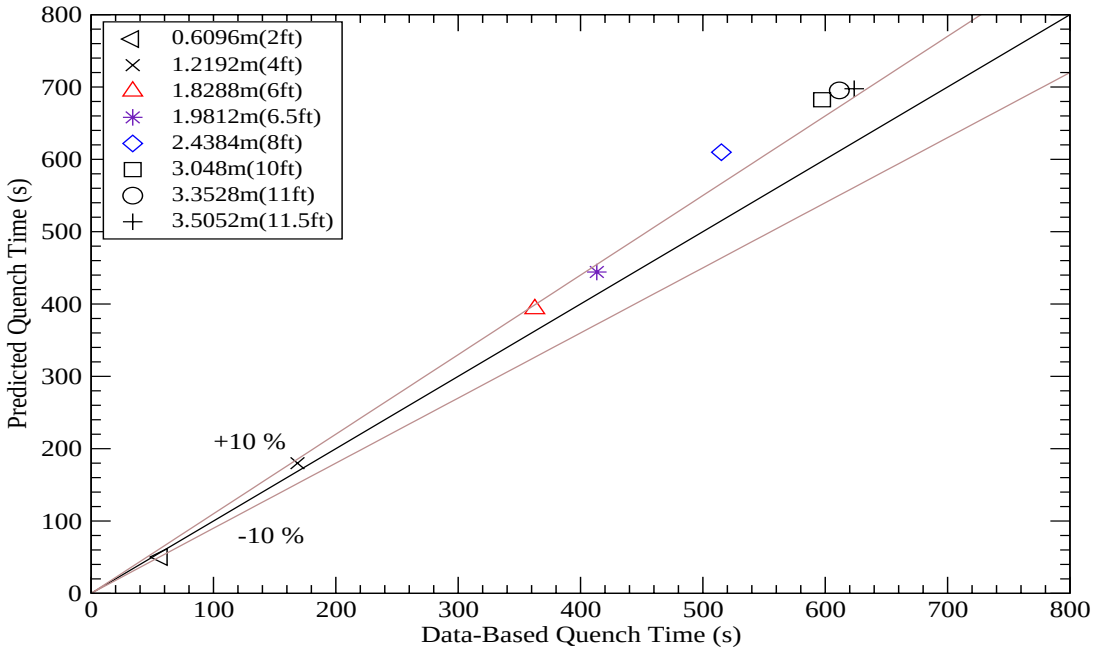

Figure B.7-237. Comparison of Calculated and Experimental Quench Times for Test 32114

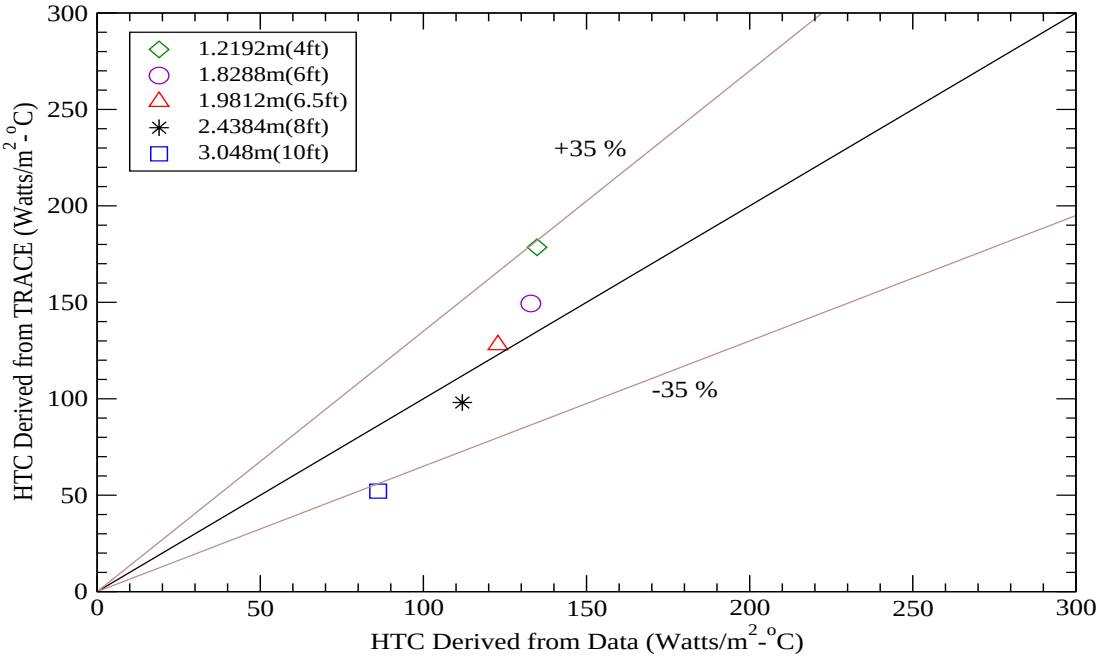

Figure B.7-238. Comparison of Calculated and Experimental HTCs for Test 31108

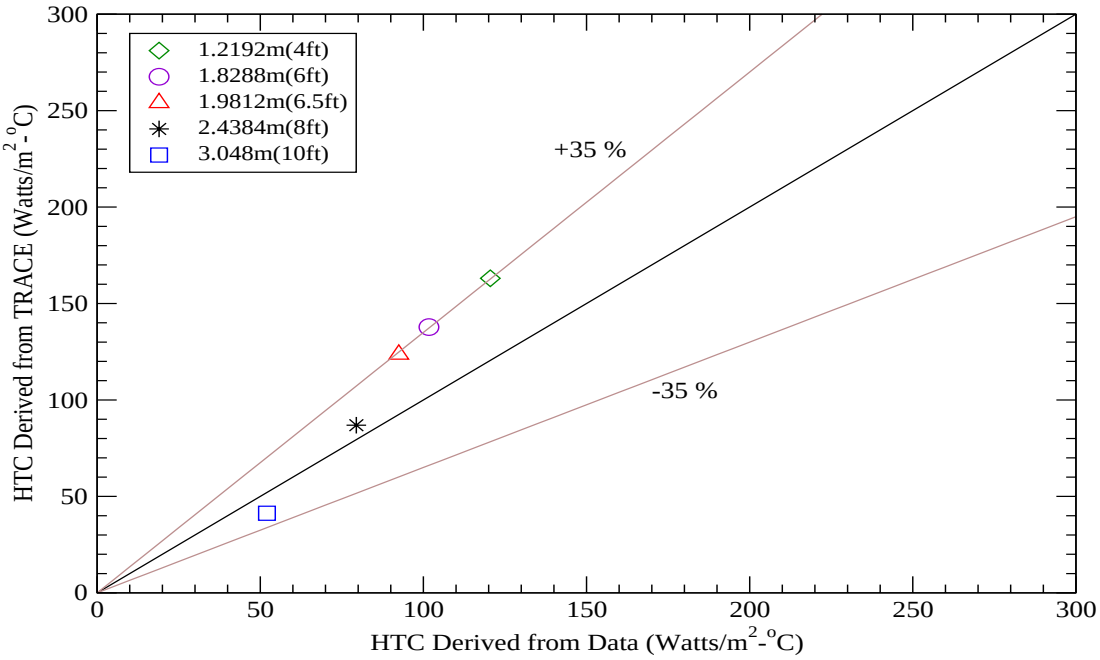

Figure B.7-239. Comparison of Calculated and Experimental HTCs for Test 31203

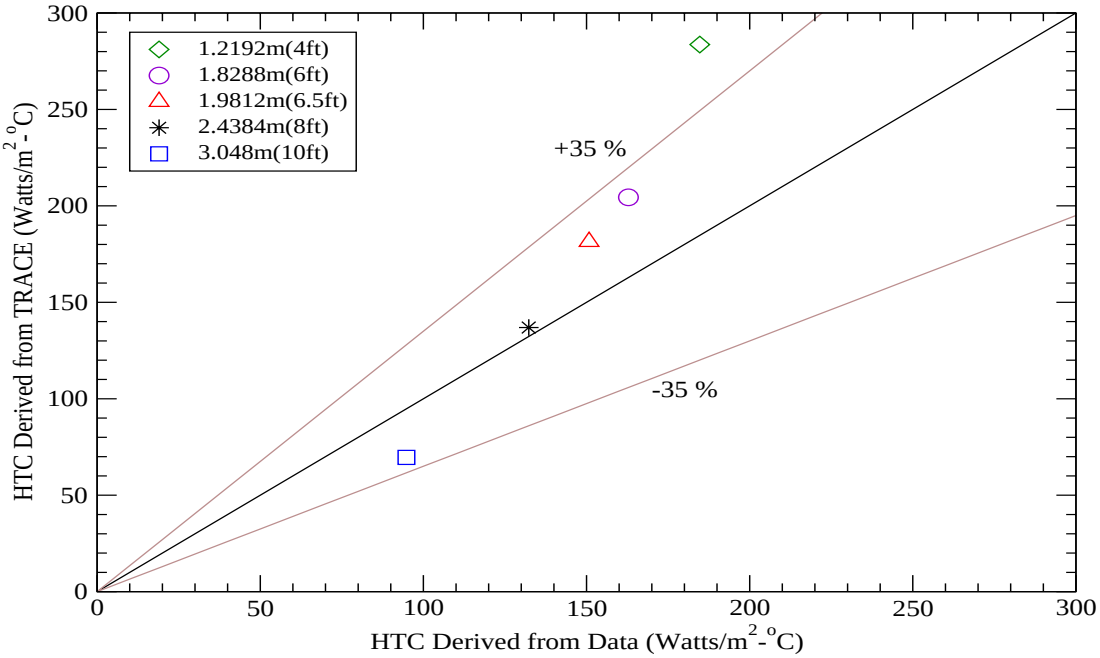

Figure B.7-240. Comparison of Calculated and Experimental HTCs for Test 31302

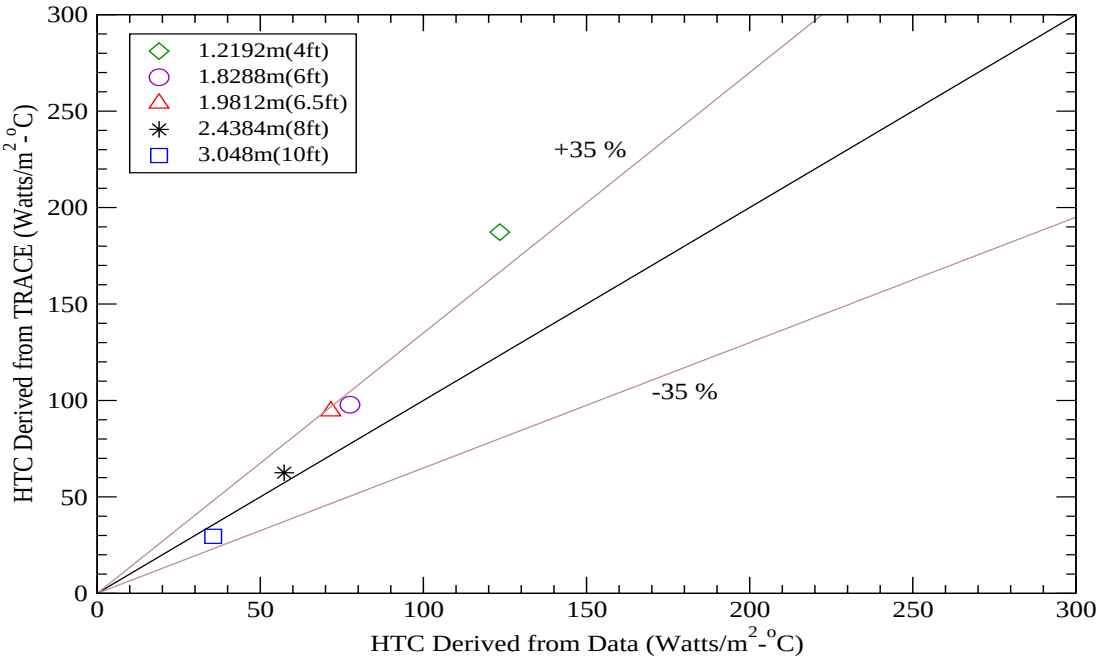

Figure B.7-241. Comparison of Calculated and Experimental HTCs for Test 31504

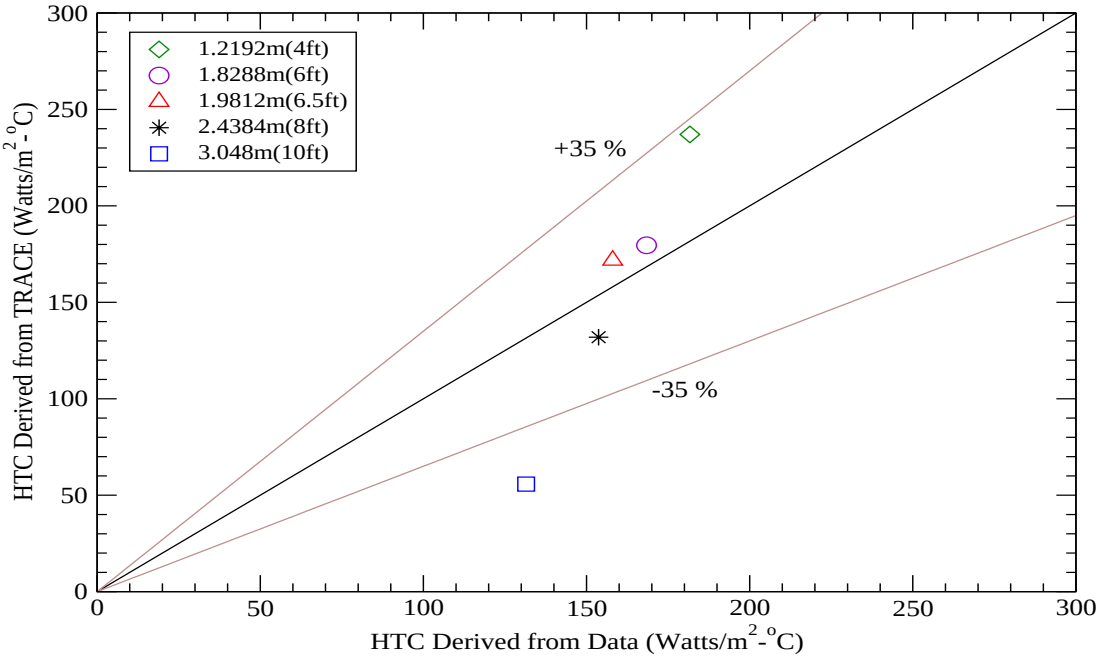

Figure B.7-242. Comparison of Calculated and Experimental HTCs for Test 31701

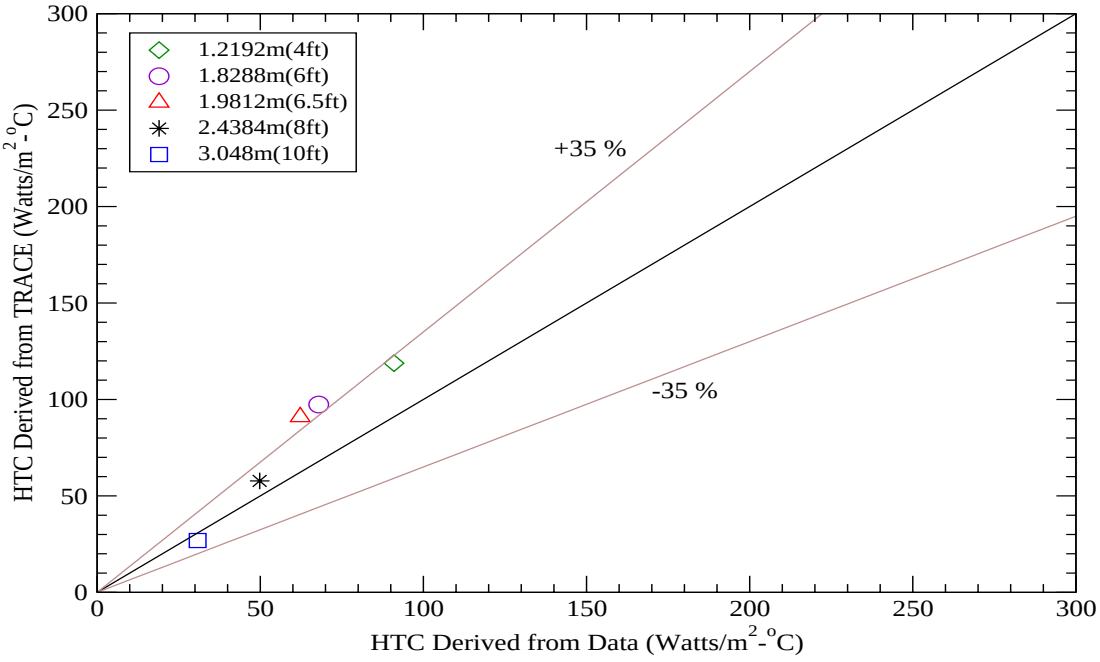

Figure B.7-243. Comparison of Calculated and Experimental HTCs for Test 31805

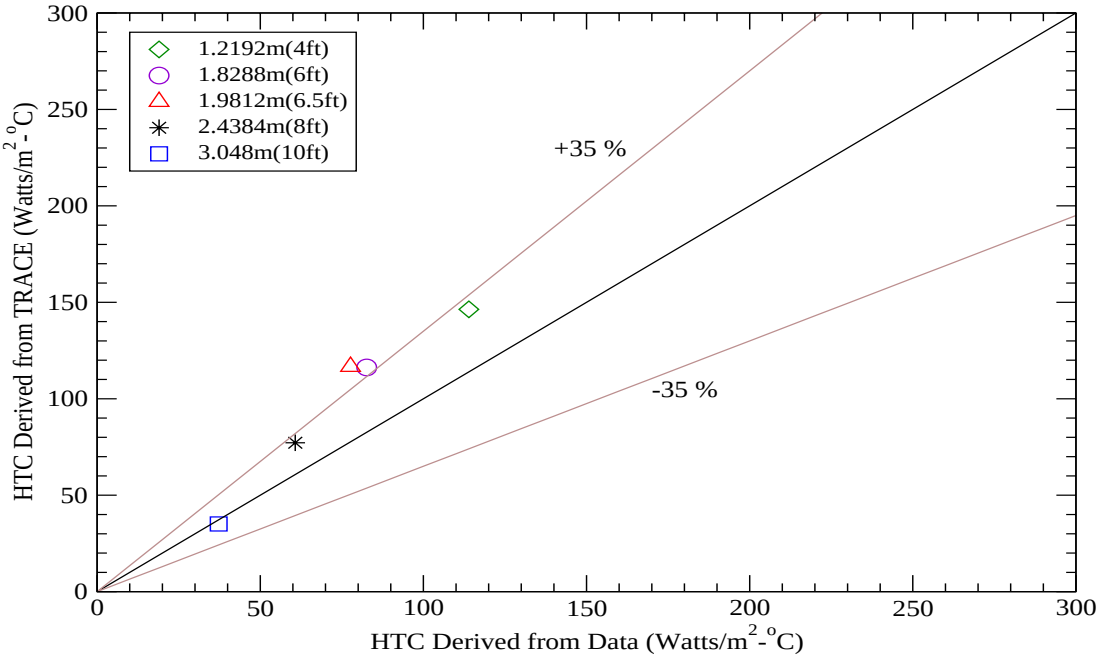

Figure B.7-244. Comparison of Calculated and Experimental HTCs for Test 32013

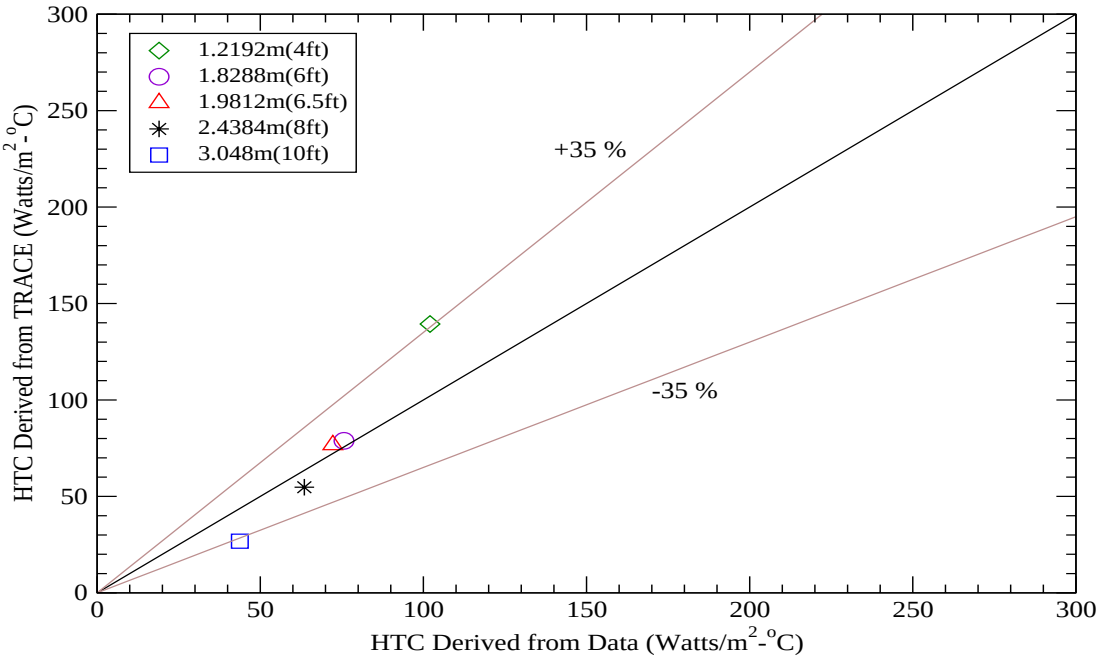

Figure B.7-245. Comparison of Calculated and Experimental HTCs for Test 32114

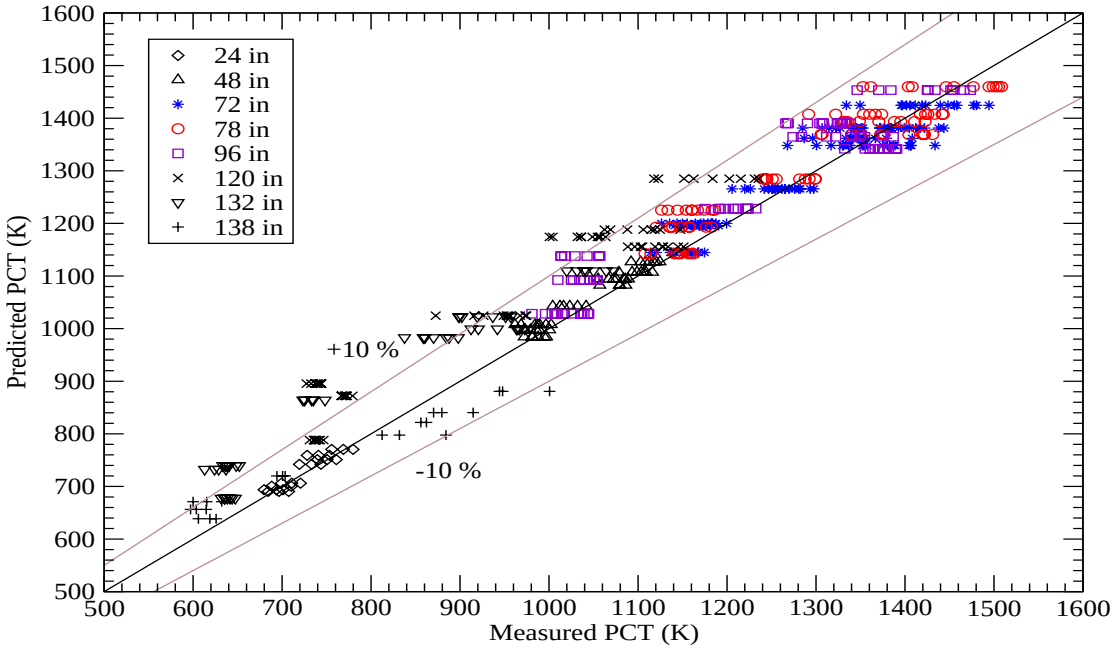

Figure B.7-246. Comparison of Calculated and Measured PCTs for All Tests

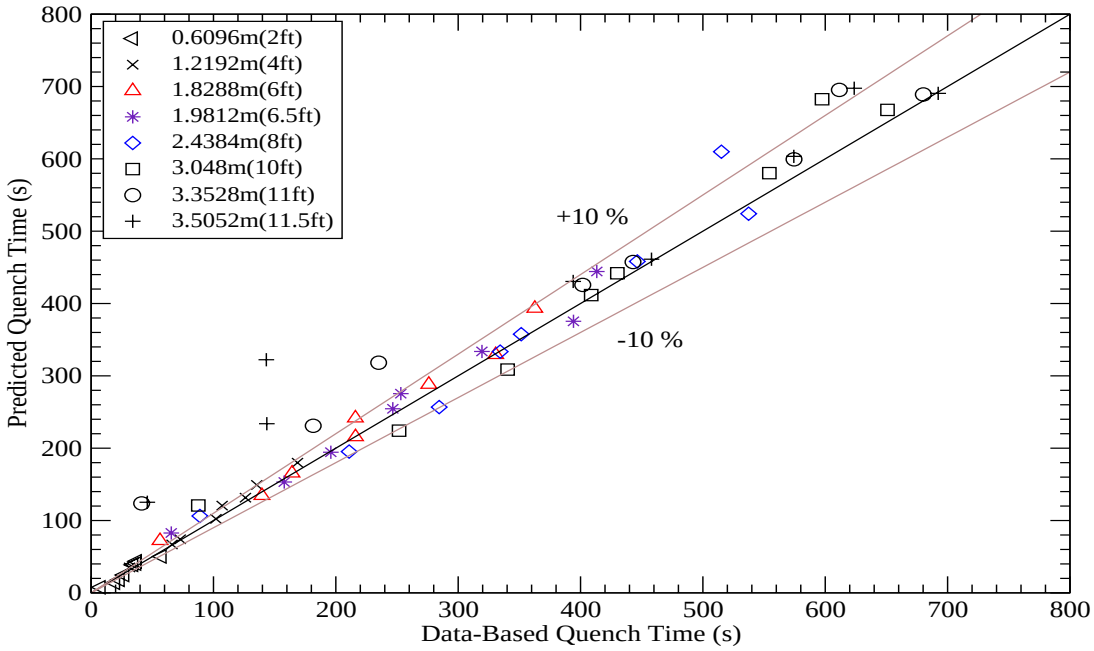

Figure B.7-247. Comparison of Calculated and Experimental Quench Times for All Tests

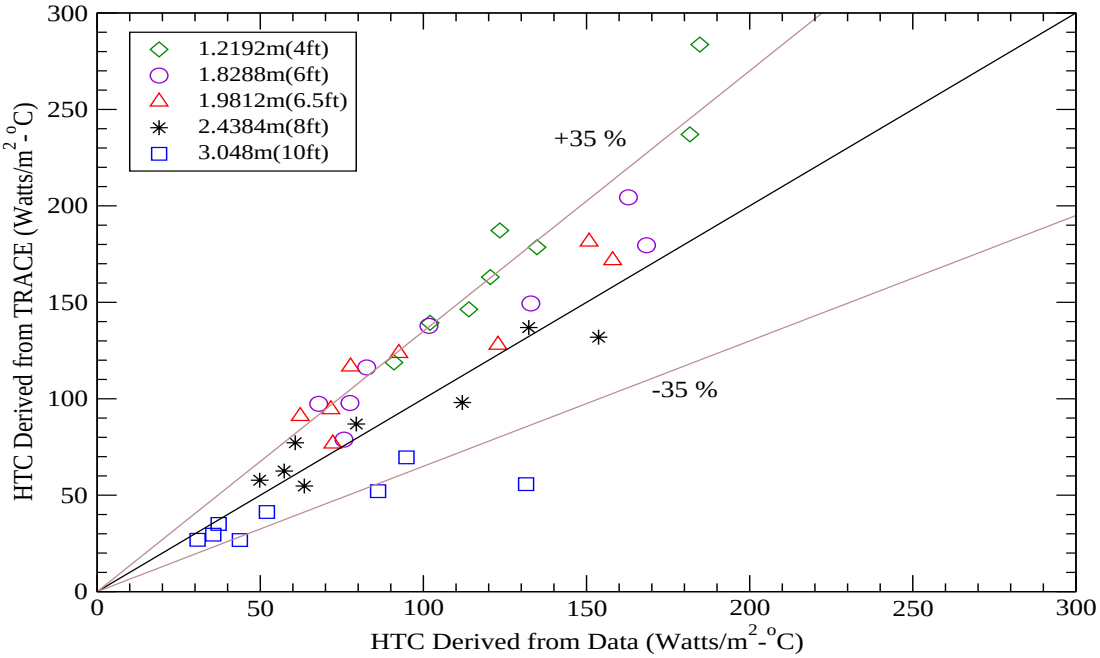

Figure B.7-248. Comparison of Calculated and Experimental HTCs for All Tests

B.8. GOTA Reflood (Run 42) Simulation

Author(s): Millan Straka, David Ebert

Affiliation: Advanced Systems Technology and Management, Inc. (AdSTM)

Code Version: TRACE V5.0

Platform and Operating System: Intel x86, Windows XP

B.8.1. Introduction

A series of experiments were performed on the GOTA separate effects test facility to investigate the effectiveness of the Emergency Core Cooling System (ECCS) used in Swedish BWRs (Ref. 1). From this series, two experiments were selected for simulation with the TRACE thermal-hydraulic code to assess its performance - Run 27 (to investigate radiation heat transfer in channeled rod bundles) and Run 42 (to investigate bottom-up and top-down reflood including rod quenching in channeled rod bundles). The purpose of this chapter is to present the results for Run 42. The results for Run 27 will be presented in a follow-on chapter.

B.8.2. Test Facility Description

The GOTA test facility was scaled to a ratio of 1/676. It had a pressure vessel with one channel, downcomer, bypass, and spray equipment simulating the BWR ECCS. Some ancillary components were: separator, pressurizer, circulation and drain pumps, and other necessary piping and equipment to perform reflood experiments. The full length (12 ft) heated bundle consisted of 63 electrically heated rods plus one water rod. A channel cross-section is shown in Figure B.8-1.

The rod axial power was cosine-shaped with 1.5 peaking in the middle of the heated section. The maximum radial peaking was 1.2 on the highest powered rods.

The facility description, data, and model description were obtained from Reference 1 and the previous assessment report (Ref. 3), respectively. The ECCS delivery by means of sprayed water could be activated in downcomer, bypass, and channel. Figure B.8-2 shows a schematic of the GOTA facility.

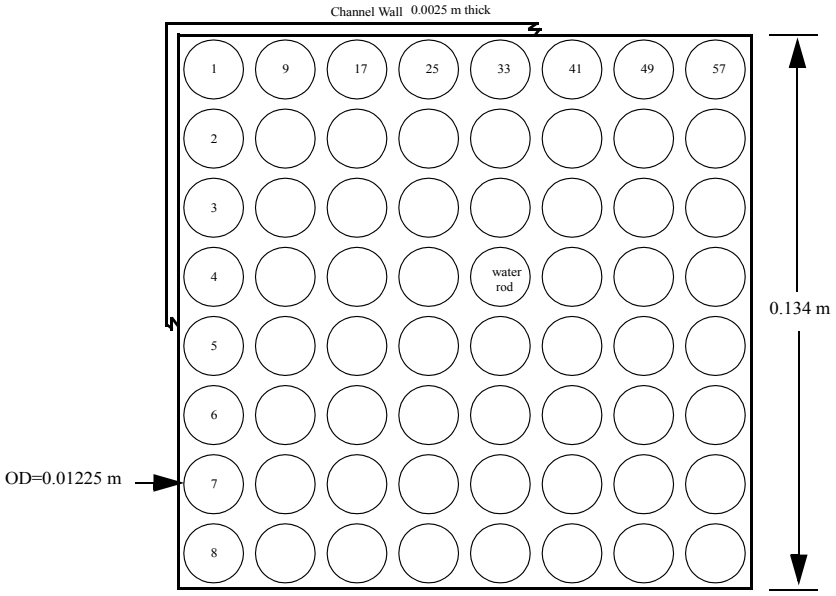

Figure B.8-1. GOTA Channe

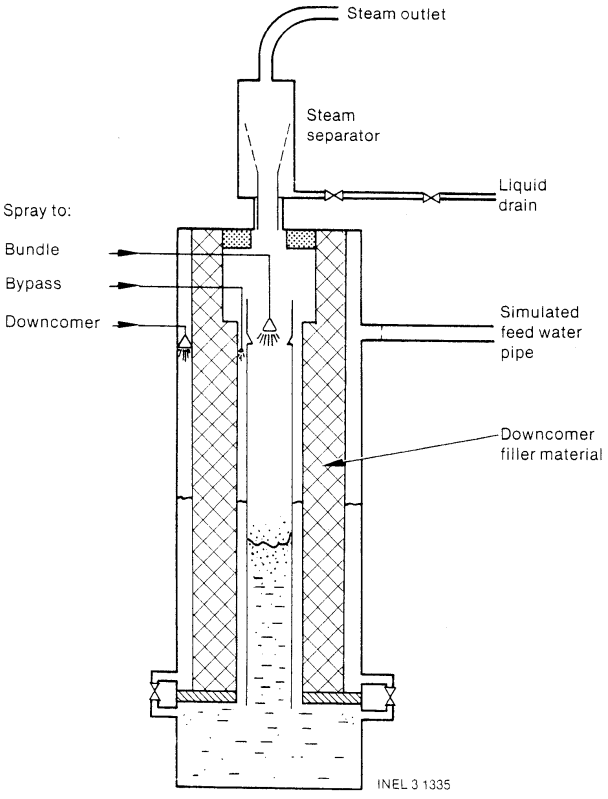

Figure B.8-2. GOTA Test Section

B.8.3. TRACE Model Description

B.8.3.1. Description of the GOTA Reflood Model

Referring to Figure B.8-1, the GOTA 64 rod bundle is symmetrical about the diagonal between Rods 8 and 57. Because of the symmetry, 36 rod groups would suffice in the TRACE CHAN input to model separately the 8 diagonal rods and 28 pairs of symmetric rods. However, experience has shown that a lesser number of rod groups provide satisfactory results, which will be shown in the first simulated case below.

A model of the bundle, which uses 5 rod groups is shown in Figure B.8-3. (The water rod has been lumped with two other low powered rods in rod group 5.)

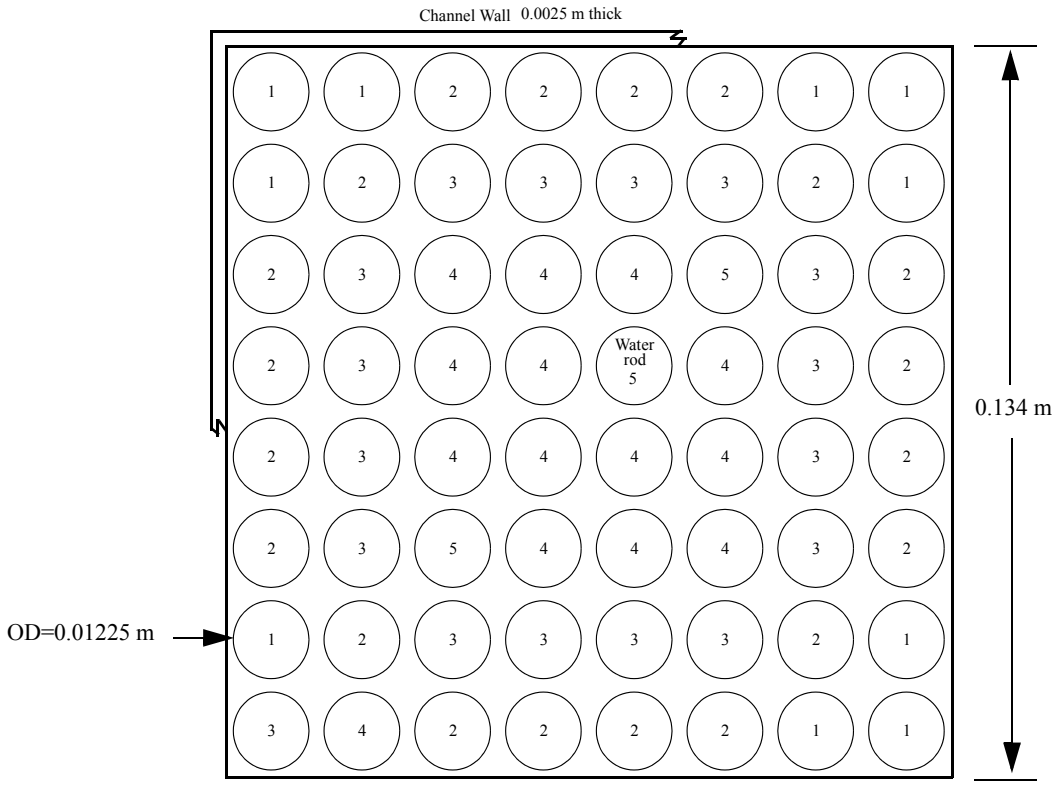

Figure B.8-3. TRACE Model for GOTA Radiation Test

An axial view of the CHAN nodalization is shown in Figure B.8-4. The CHAN component has 10 axial cells (9 heated cells 2 - 10 and one unheated cell 1). There were 7 spacer grids and lower and upper tie plate built into the GOTA bundle. Reference 1 does not provide, however, any other information except other than to state that this hardware was typical of ASEA BWR (Forsmark-1) type channels. There was in GOTA no leak path between the channel and bypass.

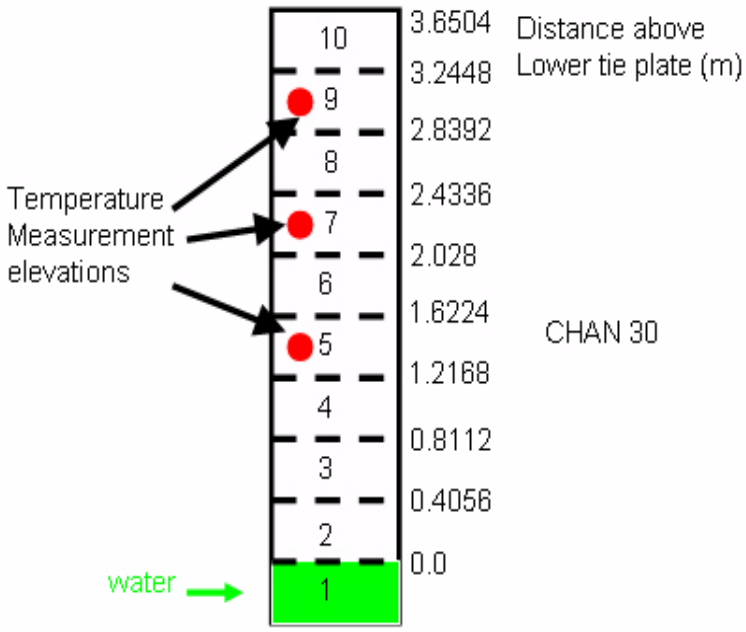

Figure B.8-4. Axial view of CHAN and Measurement Elevations

The pressure VESSEL, shown in Figure B.8-5, uses 13 axial levels and 2 radial rings. It includes the downcomer region, bypass, and components to model ECCS spray. The downcomer and bypass regions communicate via the lower vessel plenum with the channel. Some volume between the bypass and downcomer was occupied by a filler material, as depicted in Figure B.8-2, to reduce the downcomer volume to that scaled for the prototype plant.

The channel extension, added in the facility to the top of the channel box to facilitate distribution of spray to the bundle, is modeled with a TEE component with water injected into the center cell of the three cell primary side (see Figure B.8-5).

Coolant injection to the bundle, bypass, and downcomer regions was fed by fills (FILL components 52-channel spray, 54-bypass spray, and 56-downcomer spray, respectively). Steam from the test section was received by BREAK component 60. PIPE components 55, 57, and 61 connected FILL 54, 56 and BREAK 60 to VESSEL, respectively. FILL component 52 was connected to the VESSEL by a TEE component.

In the simulated test, the initial water level was at the top of the VESSEL level 2 (top of Cell 1 in the CHAN).

On the rods, the reflood model is initiated with 3 fine mesh rows in each heated channel cell. An option is provided for insertion of supplemental rows if the axial temperature difference is >2 K in any heat transfer mode. The minimum axial spacing of supplemental rows is 0.01 m. Fine mesh nodalization is used on the channel wall as well with 3 fixed fine mesh rows, and up to 54 moving mesh rows.

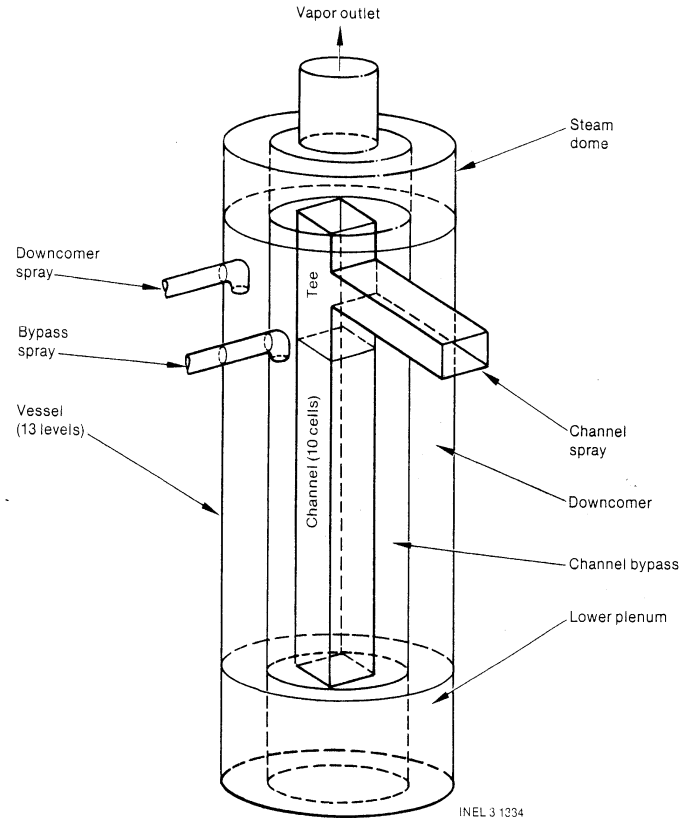

Figure B.8-5. TRACE Model for GOTA Reflood Test

B.8.4. Tests Simulated with TRACE

One experiment was simulated with TRACE V. 5.0: Run 42[1].

B.8.4.1. Simulation of GOTA Test 42

In the reflood test, Run 42, all three sprays (bundle, downcomer, and bypass) were activated. Except for ECCS, there was no other flow into the vessel and channel during the transient portion of this experiment.

Prior to initiation of the transient, the loop was filled with deionized water, air was purged, and instrumentation was zeroed. The system was then heated to the desired initial conditions using an electric pre-heater and applying power to the bundle rods. Once the desired initial conditions were achieved, the system was drained to the level of the bottom of the heated length. The bundle power was then adjusted to the initial test value and, when the selected heater rod temperatures

reached the test target values, the transient began with the initiation of ECCS spray and power decrease to simulate the reactor power decay. The vessel was vented to a pressurizer, where pressure was maintained by the pressurizer control system. The experiment continued until rod surface quenching was observed at all heater rod elevations, at which time bundle power and ECCS spray were terminated.

The initial conditions for Run 42 are summarized in Table B.8.1. Total power to the bundle was 338.8 kW, i.e. ~0.448 kW/ft (1.470 kW/m).

Table B.8.1. Initial and Boundary Conditions for GOTA Run 42

Parameter	Value
Initial system pressure	0.7-1.0 MPa
Initial core power	338.8 kW
Initial water level	Bottom of heated length (Top of Cell 1)
Spray temperature	363 K (~90 K subcooled)
Total spray flow	0.44 kg/s
Spray distribution: Downcomer Bypass Bundle	 35% (0.154 kg/s) 15% (0.066 kg/s) 50% (0.220 kg/s)

Measurements included various differential pressures such as across the heated channel part, bypass, and downcomer, and temperatures on the canister wall and rod cladding.

Time histories of the measured rod temperatures are provided at three bundle elevations 1.425, 2.225, and 3.025 m (see the CHAN schematic in Figure B.8-4) and one time history of the bundle water level with 0 m being the beginning of the heated bundle portion. For each elevation, three temperatures are provided which were measured at "cold", "average", and "hot" location, respectively. Figure B.8-6 depicts the temperature comparison at the lowest elevation. After an initially good agreement (up to about 60 sec) with the "average" measured temperature and the characteristic heat-up increase, the simulation result begins to diverge but the calculated peak clad temperature (PCT) is still higher than what was measured at the "cold" location. At the next higher elevation (2.225 m), as shown in Figure B.8-7, the simulated rod temperature follows very closely the "average" temperature all the time - up to the time of total quench (~235 sec). The calculated rod temperature at the highest elevation available for comparison (3.025 m) is in the range between the "average" and "hot" temperatures, as shown in Figure B.8-8. The calculated and observed quench times agree well.

Figure B.8-9 shows a comparison of collapsed water levels in the bundle. While the slope of calculated and measured water level time histories, and hence the reflood velocities, agree quite well, there appears to be a larger delay (~40 sec) in the GOTA reflood not observed in the simulation. It is noted, however, that in this time period the experimentally measured dP signal

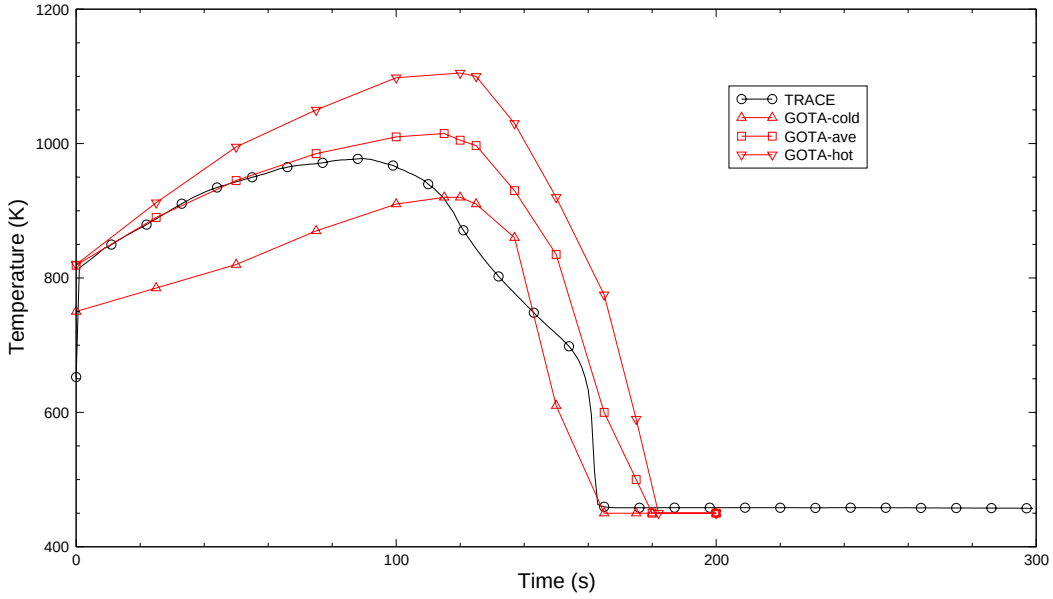

Figure B.8-6. Rod Temperatures at 1.425 m

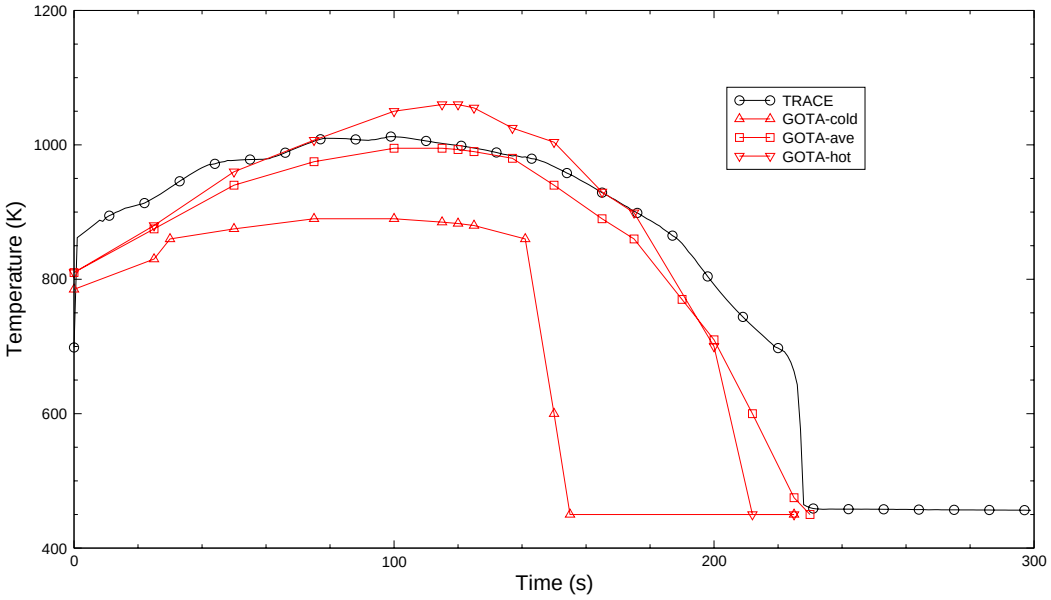

Figure B.8-7. Rod Temperatures at 2.225 m

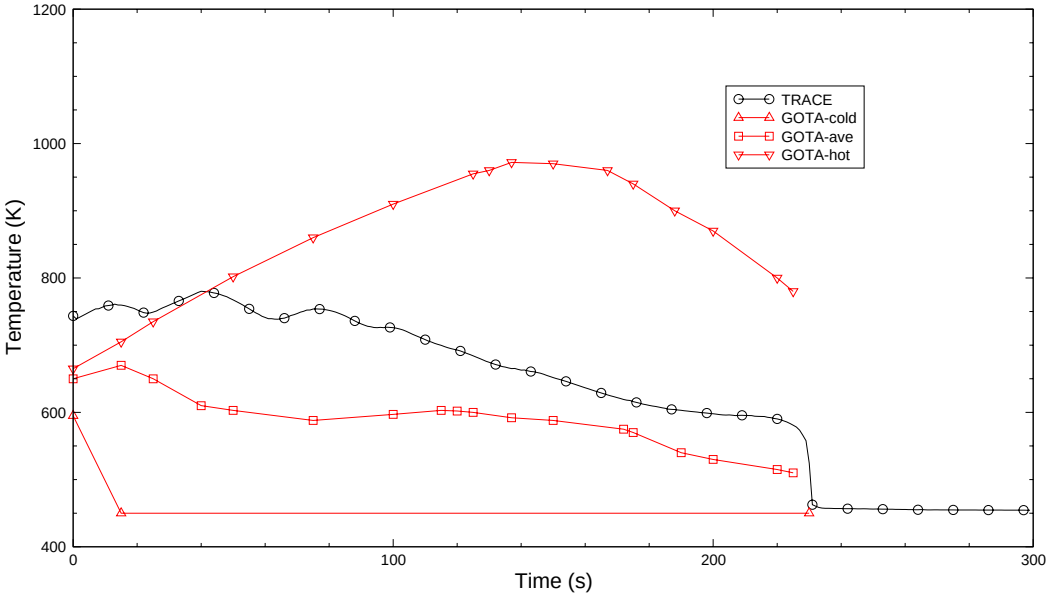

Figure B.8-8. Rod Temperatures at 3.025 m

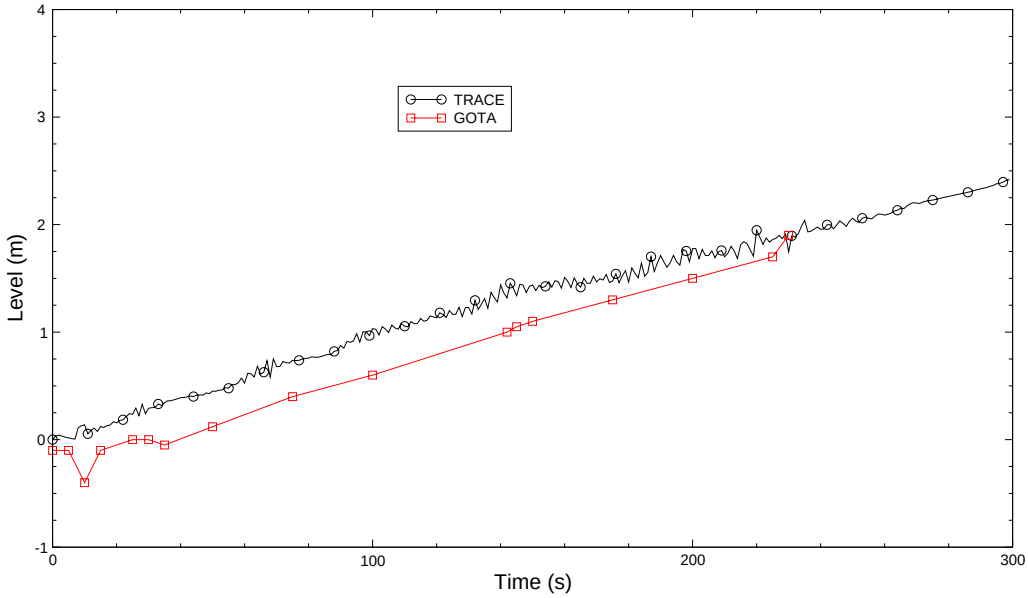

Figure B.8-9. Water Level in Bundle

exhibits somewhat suspicious behaviour going from zero to negative in the time period between 5 and 15 sec.

B.8.5. Assessment Results Summary

In the simulation of the reflood experiment, GOTA Run 42, the calculated rod temperatures typically follow the "average" measured temperature up to the point of quenching. The time of quenching for the two lower elevations is very close to the time observed in Run 42. The data for the "average" temperature at the highest elevation indicate that quenching is imminent but the data stop before that.

Slopes of the calculated and measured collapsed water levels in the bundle agree quite well after 40 sec. In the time period between 0 and 40 sec, the measurement is difficult to interpret but it appears that not much (if any) water entered the bundle, while the TRACE simulation indicates water presence within about 10 sec.

B.8.6. References

1 L. Nilsson, L, Gustafson and R. Harju, “Experimental Investigation of Cooling by Top Spray and Bottom Flooding of a Simulated 64 Rod Bundle for a BWR” STUDSVIK/RL-78/59, Norhav S-046, June 30, 1978.

2 U.S. Nuclear Regulatory Commission (NRC), TRACE V5.0 User's Manual, Volume 1, not yet published.

3 Rex W. Shumway, "GOTA Radiation Test 27 and Reflood Test 42" Report Task Order No.6 Task 4, ISL-NSAD-TR-02-20, Contract # NRC-04-02-054, Dec. 2002.

B.9. GOTA Radiation Test 27 Simulation

Author(s): Mark Bolander

Affiliation: Information Systems Laboratories, Inc.

Code Version: TRACE V5.0

Platform and Operating System: Intel x86, Windows XP

B.9.1. Introduction

The GOTA test facility in Sweden was used to conduct several reflooding experiments to provide data for evaluation of the effectiveness of the emergency core cooling systems (ECCS) in Swedish Boiling Water Reactors (BWRs) when reflooding of the core is expected (Ref. 1). These experiments examined thermal-hydraulic behavior for a combination of top spray and bottom flooding in a simulated 8 x 8 rod bundle. Four radiation only tests were performed during the test series to determine the emissivities of rod and inner canister surfaces and to record any changes in these values.

Data taken from these radiation tests is very useful for validating TRACE because they have the characteristics of steady-state, high temperature, high temperature gradient, stagnant steam near atmospheric pressure, and 64 simulated fuel bundle rods (over half instrumented). The bundle canister wall temperature was maintained at 373 K (212^{o}F) by cooling water on the outside.

Test 27, the third radiation only test, was simulated with TRACE. The purpose of the assessment was to verify the code's ability to predict rod cladding temperature under radiation heat transfer conditions.

B.9.2. GOTA Facility Description

The GOTA facility consists of a full length [3.66 m (12 ft.)] 63 rod electrically heated bundle, plus one water rod, that was placed in a vessel with a steam separator, upper plenum, lower plenum, core bypass, and downcomer. Spray water could be activated in the downcomer, bypass and upper plenum. A schematic of the test bundle is shown in Figure B.9-1 Components peripheral to the test bundle include a circulation pump for injecting coolant into the test vessel (lower plenum, downcomer, bypass, and upper plenum), pressurizer for collecting steam generated in the test

vessel, coolers, and various control valves. A detailed description of the test facility is given in Reference 1.

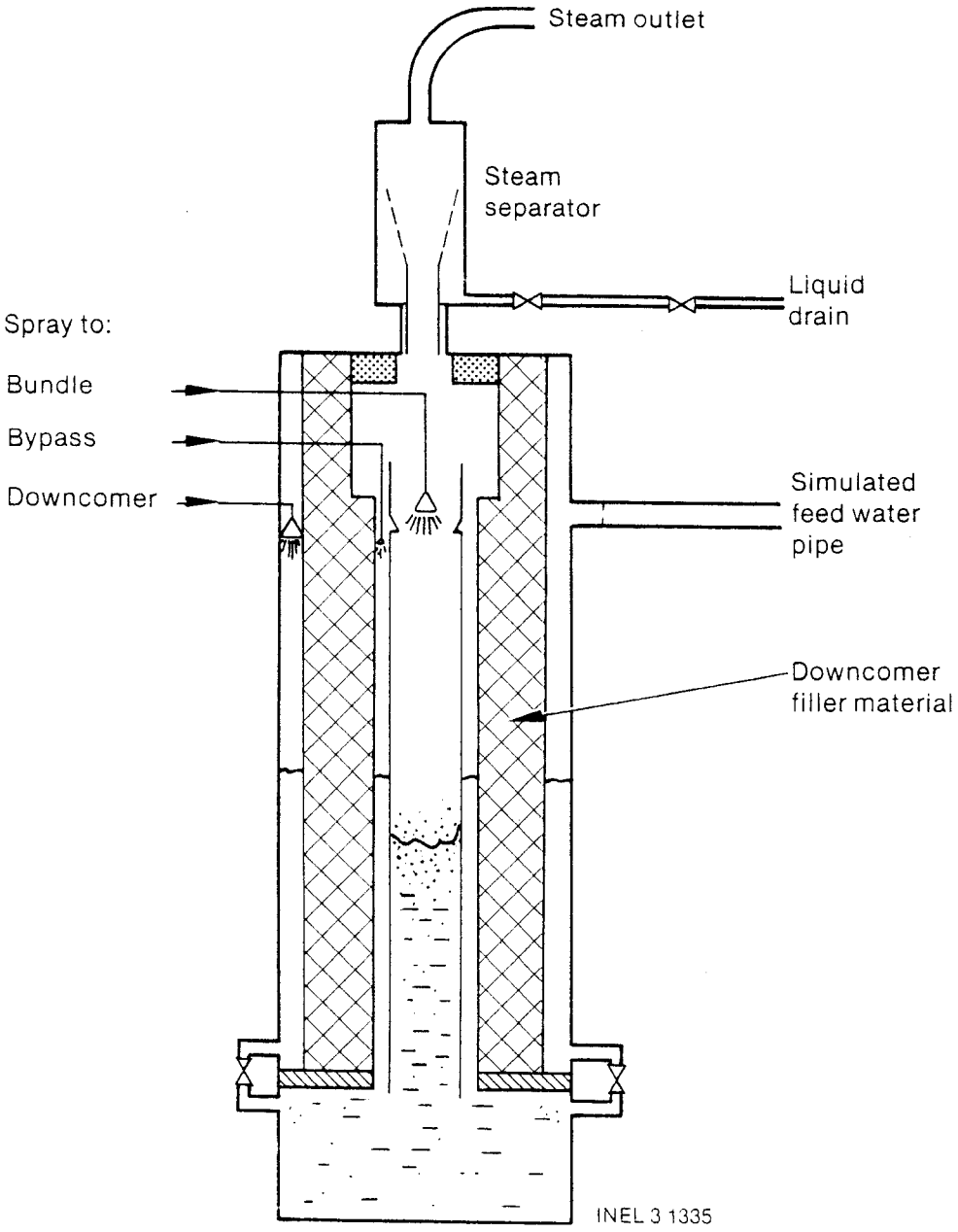

Figure B.9-1. GOTA Test Facility

The rod bundle axial power was cosine shaped with a 1.5 peaking factor. Radial peaking was 1.1 on the highest powered rods. Bundle symmetry existed along the diagonal.

Rod cladding temperatures were recorded at the mid-plane for the radiation only tests. Figure B.9-2 shows the rod positions in the bundle and the number of thermocouples associated with each rod.

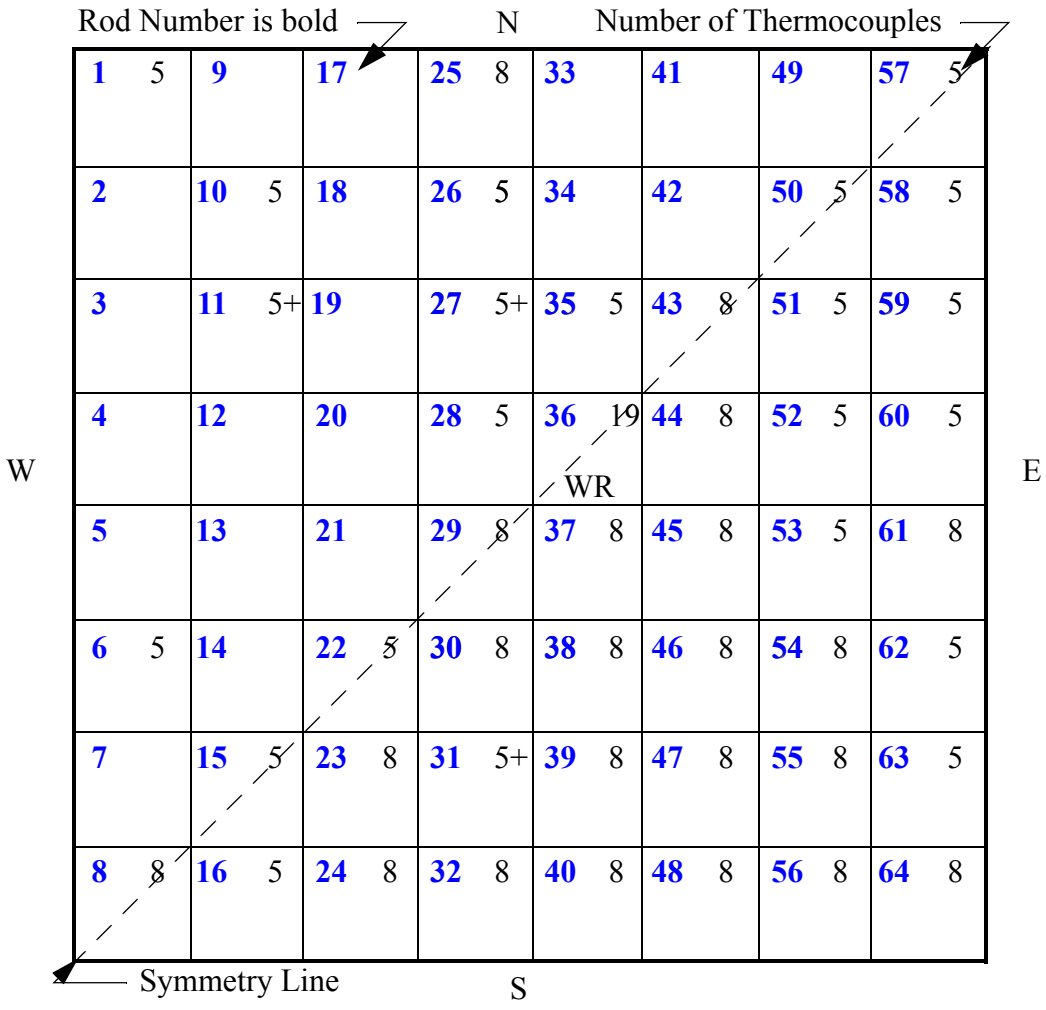

1 5	**9**	**17**	**25** 8	**33**	**41**	**49**	**57** 5
2	**10** 5	**18**	**26** 5	**34**	**42**	**50** 5	**58** 5
3	**11** 5+	**19**	**27** 5+	**35** 5	**43** 8	**51** 5	**59** 5
4	**12**	**20**	**28** 5	**36** 19	**44** 8	**52** 5	**60** 5
5	**13**	**21**	**29** 8	**37** 8	**45** 8	**53** 5	**61** 8
6 5	**14**	**22** 5	**30** 8	**38** 8	**46** 8	**54** 8	**62** 5
7	**15** 5	**23** 8	**31** 5+	**39** 8	**47** 8	**55** 8	**63** 5
8 8	**16** 5	**24** 8	**32** 8	**40** 8	**48** 8	**56** 8	**64** 8

Figure B.9-2. Rod Number and Location of Instrumented Rods

B.9.3. TRACE Model Description

The TRACE nodalization representing the GOTA bundle consisted of four components; a zero velocity FILL, a one celled CHAN, a BREAK, and a POWER component. The input model was based on a TRAC-B input file that was used to assess TRAC-B against GOTA test 27 data (Ref. 2). The input file was also used in assessing the implementation of the CHAN component into TRACE (Ref. 3). The input deck used in this assessment is documented in Reference 4.

The CHAN component represented the 0.4 m length of the mid-section of the GOTA rod bundle. Five rod groups were used to represent the 64 rods in the test bundle. The water rod was lumped

with two other low powered rods as rod group 5. The zero velocity FILL is attached to the bottom of the CHAN. The BREAK component sets the pressure at the top [0.101 MPa (14.7 psia)]. The value of 0.67 for the emissivity, used by the experimenters to make convective heat transfer coefficient calculations for test 27, was also used for the emissivity input for the CHAN component.

The total power to the bundle was 49 kW. Since only 0.4 meters of mid-section length was modeled, only 8.05 kW was used in the POWER component.

A TRACE nodalization diagram of the GOTA radiation test is shown in Figure B.9-3 Figure B.9-4 shows the rod grouping scheme.

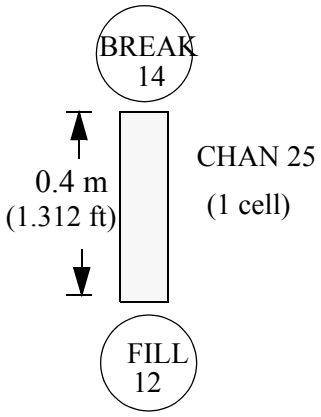

Figure B.9-3. TRACE Nodalization for the GOTA Radiation Simulation

B.9.4. Test Simulated with TRACE

Test 27 was conducted at a constant power of 49 kW to the bundle, atmospheric pressure and without any coolant being introduced to the bundle from the top spray nozzle. The lower plenum was drained to prevent water from accumulating there and evaporating. The inner canister was cooled to about 373 K (212^{o}F) on its outside surface by the bypass injection spray. The rod cladding temperatures were allowed to increase till steady-state conditions were reached. At steady conditions the cladding temperatures were recorded.

B.9.4.1. Simulation of GOTA Test 27

Predicted rod cladding temperatures along the diagonal at the mid-plane level are compared to data in Figure B.9-5 Predicted temperatures for some modeled rod groups are repeated in Figure B.9-5 since there are only 5 rod groups and 8 actual rods on the diagonal. Table B.9.1 shows the

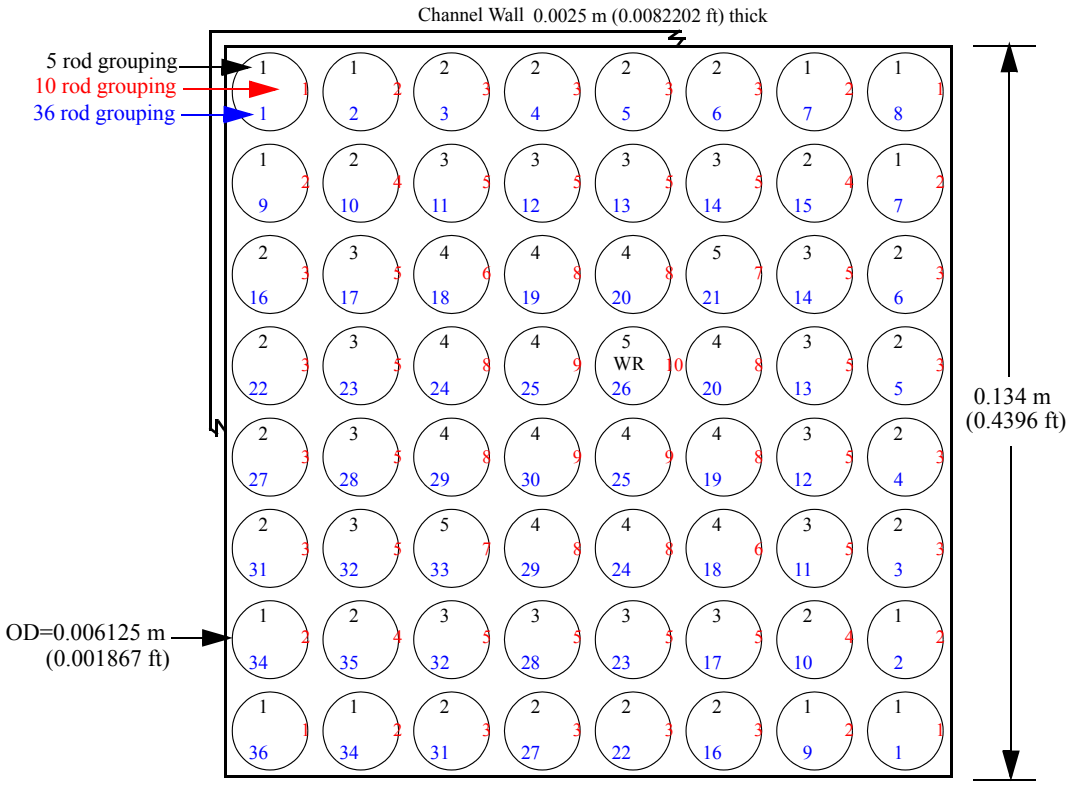

Figure B.9-4. GOTA Test 27 Bundle Cross Section Rod Grouping Scheme

relationship of the diagonal rod position number with the actual rod number along the diagonal and the modeled rod group number.

Table B.9.1. Diagonal Rod Number to Rod Group Number Mapping

Diagonal Rod Position Number	1	2	3	4	5	6	7	8
Actual Diagonal Rod Number	8	15	22	29	36	43	50	57
Diagonal Rod Group Number - 5 Rod Groups	1	2	5	4	5	5	2	1
Diagonal Rod Group Number - 10 Rod Groups	1	4	7	9	10	7	4	1
Diagonal Rod Group Number - 36 Rod Groups	36	35	33	30	26	21	15	8

The predicted rod clad temperatures using five rod groups compare well with the data. Data had a ± 5 K uncertainty. TRACE over-predicts the clad temperature in the edge rods and under-predicts the temperature in the central rods along the diagonal.

The calculated heat transfer coefficients for the rods range between 2.52 and 5.31 W/m^2-K (0.44 and 0.94 Btu/hr/ft^2-^{o}F). The heat transfer regime is convection to single phase vapor and uses the correlation:

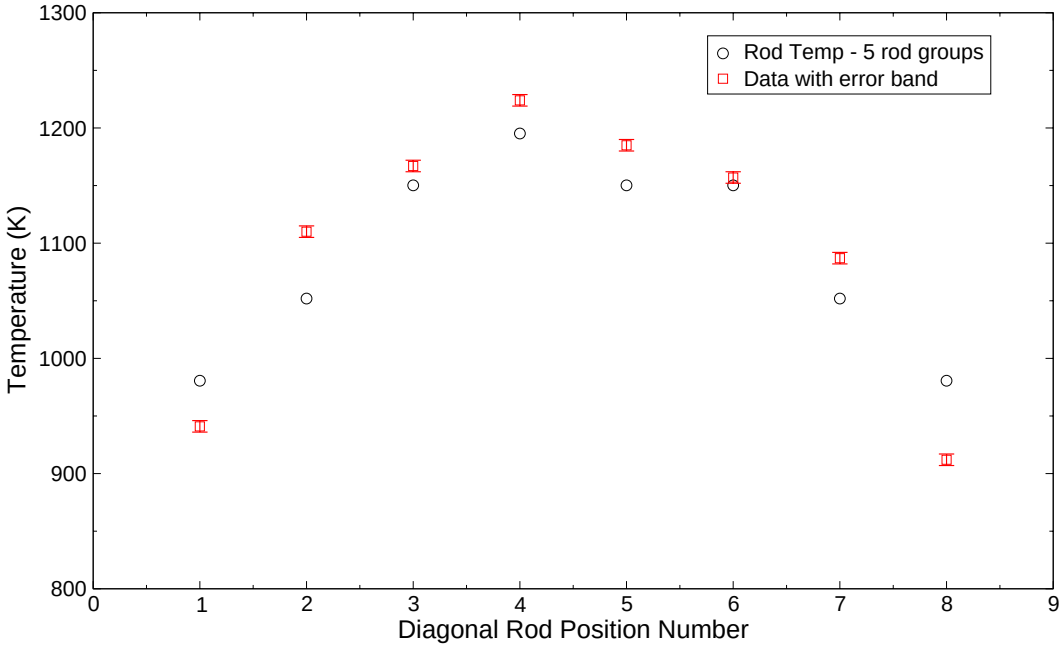

Figure B.9-5. Rod Clad Temperature Comparison with 5 Rod Groups

$$Nu = 0.13(GrPr)^{\frac{1}{3}} \tag{9-1}$$

The heat transfer coefficients estimated from the experiment however were not available.

The calculation was repeated with 10 and 36 rod groups to determine how much the added details improved the accuracy of the rod-to-rod and rod-to-canister radiation heat transfer (see Figure B.9-4). Thirty-six rod groups model all the rods along the diagonal and the rods above the diagonal individually. Table B.9.1 shows the relationship of the diagonal rod position number with the actual rod number along the diagonal and the modeled rod group number for the 10 and 36 rod group input. Improvements in the predictions are shown in Figure B.9-6 The central rod temperatures increased and the edge temperatures decreased. The predicted rod cladding temperatures along the diagonal improved significantly using more rod groups. There is not a significant difference in the results between 10 rod groups and 36 rod groups. Although the results using 5 rod groups are reasonable, 10 rod groups result in excellent agreement with the data. Using 10 rod groups for modeling fuel bundles captures the radiation heat transfer phenomena.

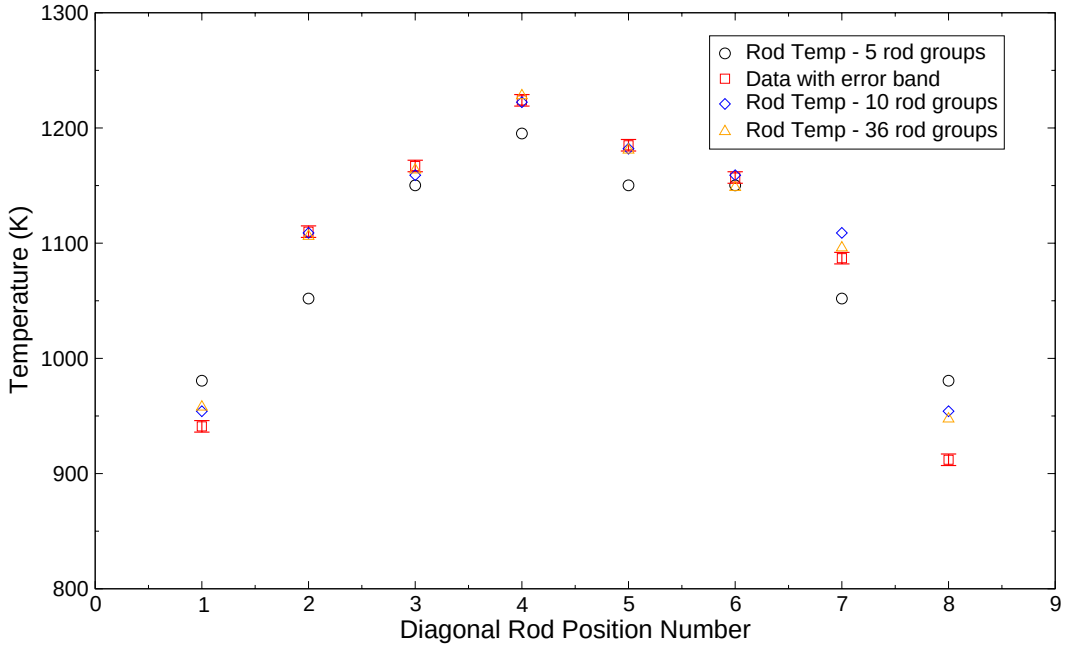

Figure B.9-6. Rod Clad Temperature Comparison with 10 and 36 Rod Group

B.9.4.2. Figure of Merit

Rod cladding temperature along the bundle diagonal was chosen as a figure of merit to illustrate how well the code predicts the measured data. Measured versus predicted rod cladding temperature along the bundle diagonal for each of the three different modeled rod groupings is shown in Figure B.9-7. In general, the measured versus predicted rod cladding temperature lies along the 45^{o} line. The outliers are those rods on the ends of the diagonal that are mostly exposed to the canister wall. It is clearly shown that 10-rod groups result in a much better prediction of the data than the 5-rod groups. There is only small improvement in the predicted rod temperature with the 36-rod groups.

B.9.5. Assessment Results Summary

TRACE predicts GOTA Test 27 mid-plane rod cladding temperatures very well. The prediction using 5 rod groups over-predicts the rod cladding temperature in the edge rods and under-predicts the clad temperature of the central rods on the bundle diagonal. Excellent agreement was shown with 10 and 36 rod groups, although 36 rod groups did not show any improvement over the 10 rod grouping. Ten rod groups were sufficient to capture the radiation heat transfer phenomena.

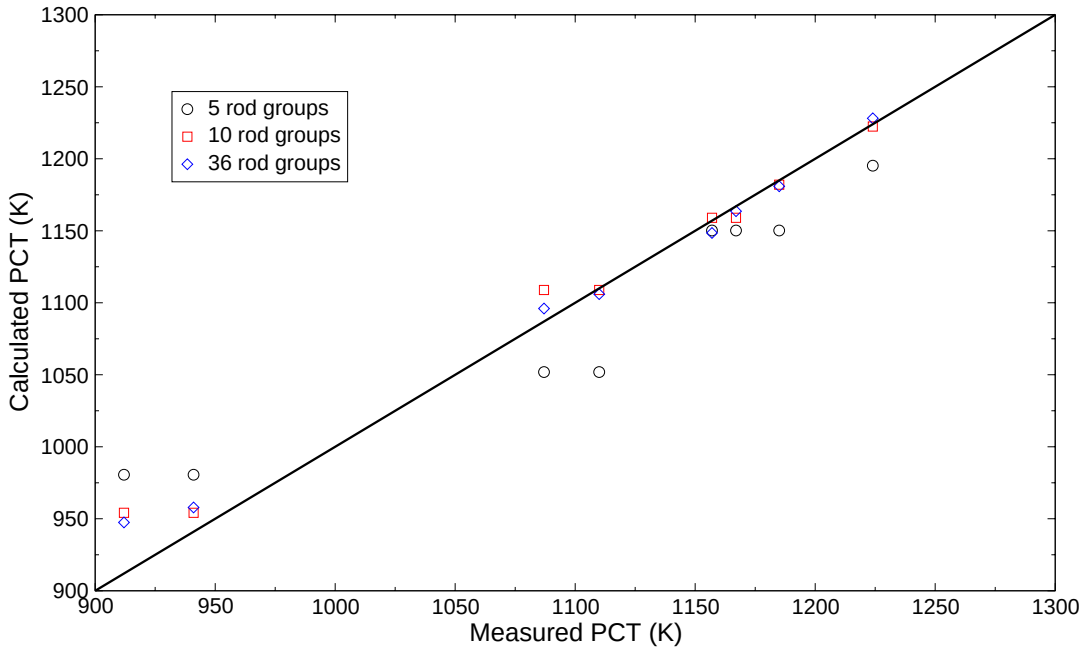

Figure B.9-7. Measured Versus Predicted Rod Cladding Temperature.

B.9.6. References

1 Nilsson, L., L. Gustafson and R. Harju, “Experimental Investigation of Cooling by Top Spray and Bottom Flooding of a Simulated 64 Rod Bundle for a BWR,” STUDSVIC/RL-78/59, Norhav S-046, June 30, 1978.

2 Shumway, R.W., et al., "TRAC-BD1/MOD1, Volume 4: Developmental Assessment," NUREG/CR-3633, EGG-2294, Volume 4, August 1985.

3 Shumway, R.W., "Consolidation of TRAC Codes: Task CHAN," SCIE-NRC-375-99, Scientech, Inc., January 12, 1999.

4 Bolander, M. and R.W. Shumway, "TRACE Calculation Notebook - GOTA Radiation Test 27," ADAMS ML061710616, January 2006.

B.10. RBHT Reflood Tests

Author(s): Kent B. Welter

Affiliation: USNRC RES:DRASP:NRCA

Code Version: TRACE V5.0

Platform and Operating System: Intel x86, Windows XP

B.10.1. Introduction

The simulations presented in this section examine the ability of TRACE to calculate peak cladding temperature (PCT), heat transfer coefficients, quench times, liquid carry-over, steam temp, and two-phase level swell at low pressure during a reflood test. The simulations were compared to Tests 1096, 1108, 1170, 1196, 1285, and 1383 performed at the Penn State/NRC Rod Bundle Heat Transfer (RBHT) facility. The RBHT facility is designed to simulate a full-length portion of a Pressurized Water Reactor (PWR) fuel assembly. The facility consists of a 7x7-rod bundle with 45 electrically heated rods, mixing vane grids, and over 500 instrument channels for measuring temperature, differential and absolute pressure, steam and liquid flow rates, power, etc. The axial differential pressure measurements can be used, along with appropriate temperature and flow corrections, to calculate the bundle void fraction.

The six RBHT reflood tests used in this assessment covered a range of injection flow rates from 0.12 to 0.75 kg/s, pressure from 0.13 to 0.28 MPa, and subcooling from 16 to 86 K. The maximum rod linear heat rate was 1.53 kW/m. The quench time, PCT, liquid carry-over rate, and steam temperature were used as figures of merit to quantify the code's accuracy.

B.10.2. Test Facility Description

The RBHT Facility is designed to conduct systematic separate-effects tests under well-controlled conditions in order to generate fundamental rod bundle transfer data from single phase steam cooling tests, low flow boiling tests, and dispersed flow film boiling heat transfer tests (Ref. 2). The facility is capable of operating in both forced and variable reflood modes covering a wide range of flow and heat transfer conditions at pressures from 0.13 to 0.42 MPa. The test facility consists of the following major components (shown schematically in Figure B.10-1):

- Test section consisting of a lower plenum, test section with heater rods, and an upper plenum.

- Cooling injection and steam injection systems.
- Closely coupled phase separation and liquid collection systems.
- Pressure fluctuation damping tank and steam exhaust piping.

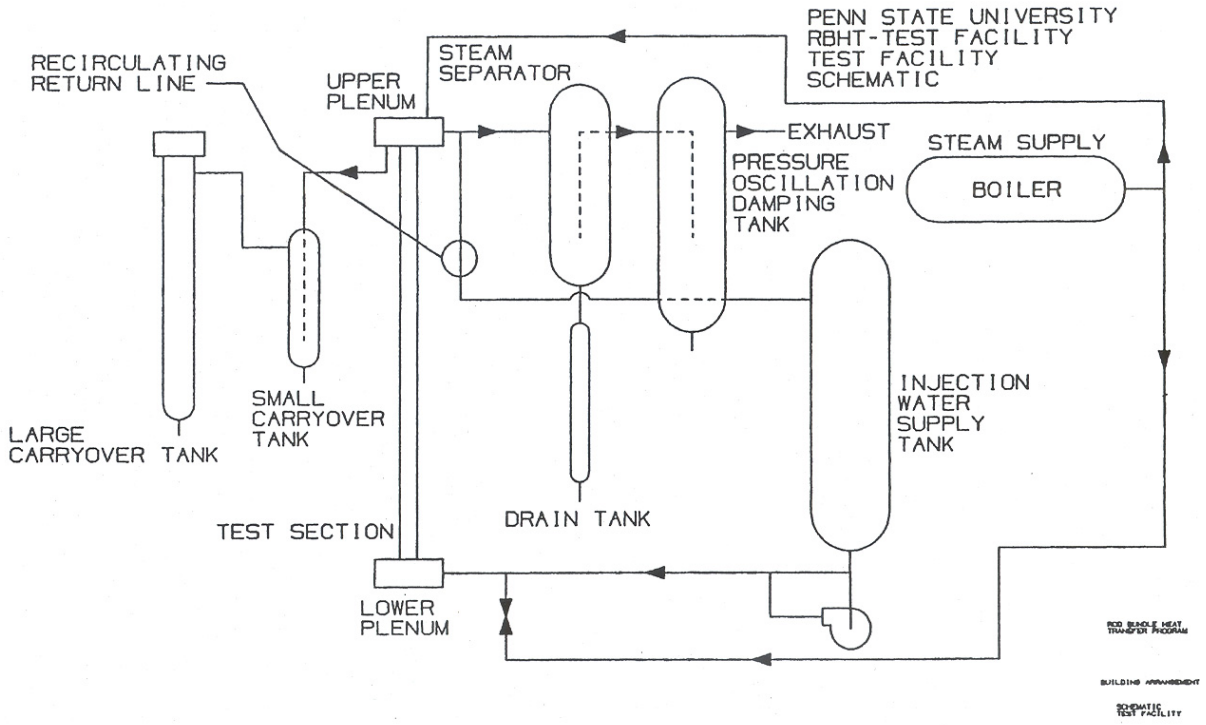

Figure B.10-1. RBHT Test Facility Schematic

The test section shown in Figure B.10-1 consists of the heater rod bundle, the flow housing, and the lower and upper plenums. The heater rod bundle simulates a small portion of a 17x17 reactor fuel assembly. The electrically heated rods have a diameter of 9.5 mm and are arranged in a 7x7 array with a 12.6 mm pitch with 45 heater rods and four unheated rods (at each corner). The facility has over 500 instrument channels to measure temperature, differential and absolute pressure, flow rates, power, etc. For this study, of particular interest are the bundle differential pressure cells (used to calculate void fraction), inlet injection flow rate (chan-412), liquid injection temperature (chan-407), heater rod voltage (chan-395) and current (chan-396), and upper and lower plenum pressures (chan-411 and chan-393, respectively). Table B.10.1 contains a list of the 22 axial bundle differential pressure cells used in this assessment, along with the axial locations of the 7 mixing vane grids. The grids are 5.72 cm high.

Radiation only experiments were conducted to characterize the test section heat loss and were conducted under a vacuum. Based on a total power of 114 kW, the heat loss for a typical reflood

Table B.10.1. Differential Pressure Cell and Grid Locations

Instrument ID	Lower Tap, Axial Location (m)	Upper Tap, Axial Location (m)	Grid Bottom, Axial Location (m)
chan-363	0.0	0.330	0.330
chan-364	0.330	0.640	-
chan-365	0.640	0.940	0.690
chan-366	0.940	1.092	-
chan-367	1.092	1.168	-
chan-368	1.168	1.346	1.212
chan-369	1.346	1.448	-
chan-370	1.448	1.524	-
chan-371	1.524	1.600	-
chan-372	1.600	1.702	-
chan-373	1.702	1.823	1.734
chan-374	1.823	1.905	-
chan-375	1.905	1.981	-
chan-376	1.981	2.057	-
chan-377	2.057	2.159	-
chan-378	2.159	2.362	2.256
chan-379	2.362	2.465	-
chan-380	2.465	2.540	-
chan-381	2.540	2.743	-
chan-382	2.743	3.048	2.778
chan-383	3.048	3.378	3.301
chan-384	3.378	3.657	-

test was calculated to be approximately 2.5 kW, which is a small fraction (~2%) of the total power supplied to the heater rods.

B.10.3. TRACE Model Description

The RBHT main test section was modeled in TRACE using VESSEL and HTSTR components as shown in Figure B.10-2. The VESSEL component was divided into 17 axial levels with a nodalization chosen such that there are two cells between each grid and that the bottom of every other cell corresponds to the bottom of a grid. The mixing vane grids were modeled by specifying a loss coefficient of 2.0 (Ref. 1). Forty-five heated rods were modeled in a 7x7 array, with four non-heated rods in the corners. Two PIPE components (shown in Figure B.10-2), one at the bottom and one at the top, were used to connect the FILL and BREAK to the VESSEL. Liquid

injection flow was provided by the FILL component at the bottom of the lower plenum, while a BREAK, at a specified initial pressure, was used at the top. The VESSEL component spans the entire heated length, but an additional cell at the top and bottom of the VESSEL were added to model the upper and lower plenums, respectively. The shape of the power curve applied to the HTSTR peaks at 2.7781 m as shown in Figure 2. The heater rods were modeled using 8 radial nodes, which is also shown in Figure B.10-2, and included the Constantan heater wire insulated with Boron-Nitride insulation, clad with Inconel, Type 600. A flow housing HTSTR was added to the model to account for heat loss to the environment and was based on user specified ambient conditions.

The heater rod was modeled with 8 radial HTSTR cells (shown in Figure B.10-2) using TRACE predefined materials for the insulation (Boron-Nitride) and for the outer cladding and heater wire (both Inconel Type 600). However, a check of material properties of Boron-Nitride (BN) insulation showed several inconsistencies. For example, BN material property data was collected from different sources to compare to the material property tests conducted on the RBHT heater rods by TPRL (Ref. 1). There is a slight variation in the density of the sample tested TPRL as a function of temperature, but in most cases, can be considered to be constant at 1,918 kg/m3. The variation in specific heat between the TPRL tests and the TRACE manual is noticeable (Ref. 4).

Accurate simulation of rod bundle reflood experiments require detailed data on the initial temperature of the test apparatus. For the tests simulated in this assessment, a detailed initial temperature map was calculated (based on the thermocouple readings from the central rods in the bundle) for the heater rods and support rods on thermocouple measurements. A fourth-order polynomial curve fit was then applied to the axial temperature profile (examples shown in Figure B.10-3 and Figure B.10-4) for each test in the reflood assessment matrix to allow for translation of the temperature measurements to the axial VESSEL and HTSTR noding. The axial temperatures were translation from the fourth-order polynomial to the TRACE nodes by simple linear interpolation and are listed in Table B.10.2. Table B.10.3 is a list of injection flow rates (based on RBHT chan-412) and power (based on RBHT chan-397 and chan-398) for each test.

The simulations were started right at the time of reflood, which corresponds to the initial injection of cold water into the RBHT test section from chan-412.

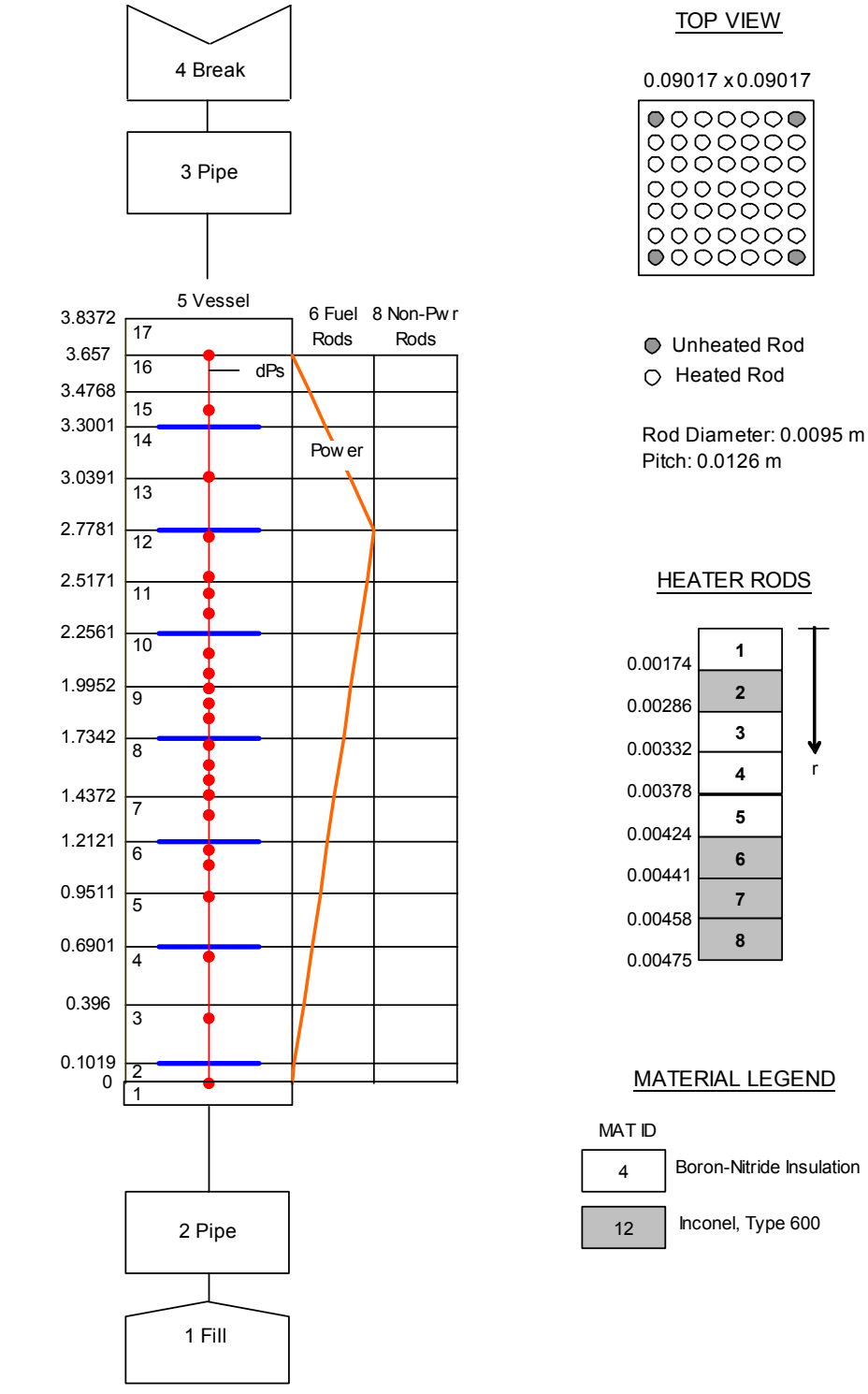

*Note: all dimensions in meters (m)

Figure B.10-2. TRACE Nodalization for the RBHT Facility

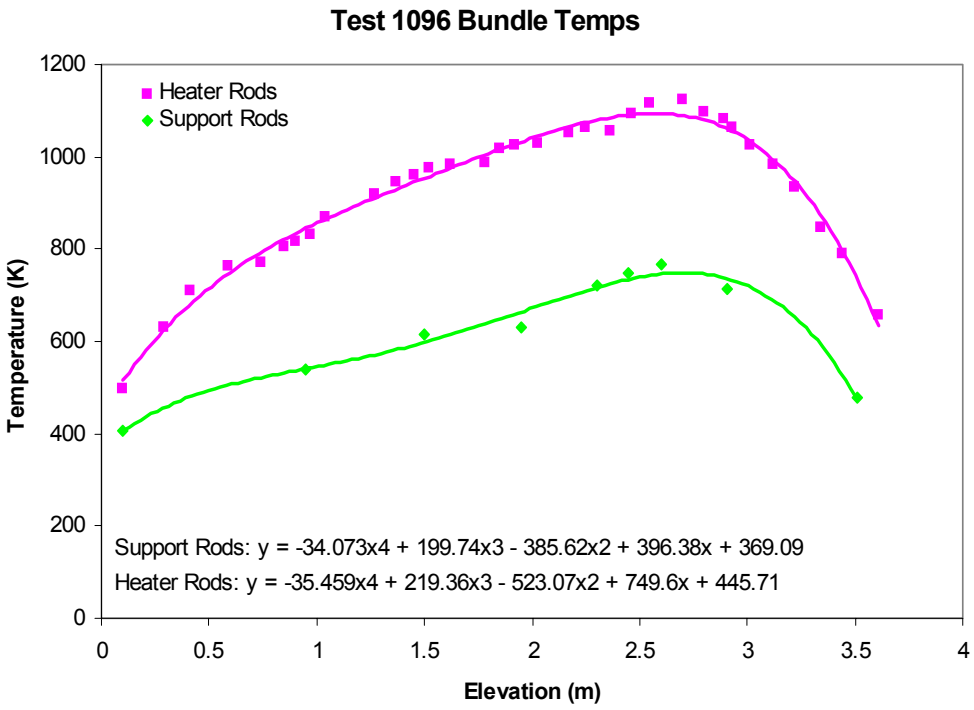

Figure B.10-3. Test 1096 Initial Bundle Temperatures

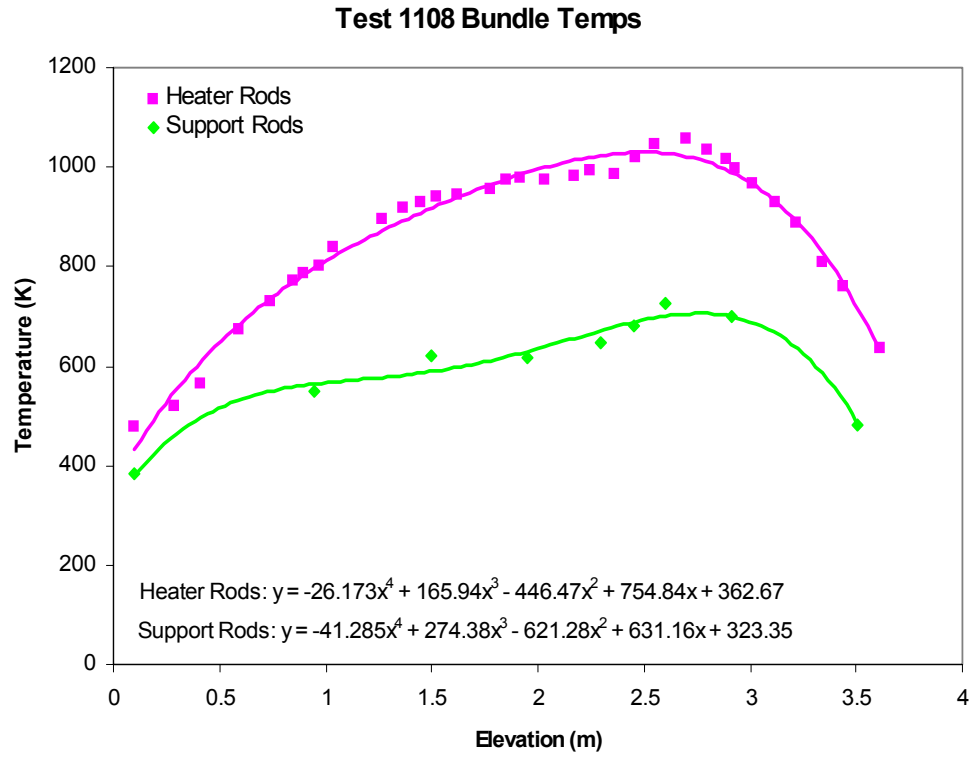

Figure B.10-4. Test 1108 Initial Bundle Temperatures

Table B.10.2. Initial Bundle Temperatures for Reflood Assessment

Elevation (m)	Test 1096 (P=0.13 MPa)		Test 1108 (0.13 MPa)		Test 1170 (0.27 MPa)	
	Heater Rod Temp (K)	Sup. Rod Temp (K)	Heater Rod Temp (K)	Sup. Rod Temp (K)	Heater Rod Temp (K)	Sup. Rod Temp (K)
0.05095	482.57	388.31	399.99	353.93	411.29	376.62
0.24895	603.15	446.82	525.38	446.05	599.09	466.05
0.54305	730.57	499.65	665.22	523.23	787.57	543.12
0.8206	813.74	529.61	761.27	555.82	897.32	578.01
1.0816	873.59	552.80	830.95	569.88	964.19	594.99
1.34265	924.92	578.85	887.89	580.73	1012.45	608.49
1.6037	972.79	611.46	936.25	596.30	1052.95	625.77
1.8647	1018.29	650.49	977.27	619.88	1091.16	649.80
2.1257	1058.59	692.06	1009.31	650.22	1127.27	679.24
2.3867	1086.91	728.45	1027.76	681.41	1156.06	708.47
2.6477	1092.51	748.18	1025.15	703.00	1167.01	727.57
2.9087	1060.71	735.95	991.06	699.90	1144.23	722.33
3.1697	972.86	672.68	912.16	652.44	1066.51	674.24
3.38945	838.96	563.14	799.15	560.39	939.09	583.90
3.5679	678.54	424.88	667.83	438.25	780.30	465.41
	Test 1196 (0.27 MPa)		Test 1285 (0.27 MPa)		Test 1383 (0.27 MPa)	
0.05095	534.18	381.35	494.43	387.13	476.70	438.32
0.24895	655.38	458.34	623.02	448.76	582.40	509.69
0.54305	782.97	530.93	759.38	511.34	700.54	565.15
0.8206	865.15	570.59	847.63	551.40	781.94	584.93
1.0816	922.85	595.03	909.33	581.47	841.15	591.84
1.34265	970.81	615.33	959.91	609.79	889.53	598.71
1.6037	1014.18	636.32	1004.78	639.07	930.42	612.11
1.8647	1054.28	659.55	1045.59	669.25	964.63	634.23
2.1257	1088.61	683.32	1080.22	697.52	990.49	662.90
2.3867	1110.85	702.63	1102.74	718.31	1003.85	691.51
2.6477	1110.87	709.23	1103.42	723.27	998.04	709.09
2.9087	1074.68	691.61	1068.77	701.31	963.90	700.30
3.1697	984.50	634.96	981.48	638.57	889.76	645.37
3.38945	850.94	543.83	851.81	541.99	786.01	545.75
3.5679	692.81	431.47	698.05	425.81	666.81	416.73

Table B.10.3. Reflood Test Injection Flow Rates and Power

Test 1096 (P=0.13 MPa)				Test 1108 (0.13 MPa)			
Time (s)	Inj. Flow (kg/s)	Time (s)	Power (W)	Time (s)	Inj. Flow (kg/s)	Time (s)	Power (W)
0.00	0.00	0.00	0.00	0.00	0.0000	0.00	0.00
0.50	0.04	0.50	72021.00	0.50	0.0626	0.50	71764.00
1.00	0.1232	1.00	143603.00	1.00	0.1251	1.00	143528.00
2.00	0.1245	1684.00	143603.00	2.00	0.1251	1610.00	143528.00
73.00	0.1245	1685.00	72021.00	1610.00	0.1251	1611.00	71764.00
197.00	0.1241	1686.00	0.00	1611.00	0.0626	1612.00	0.00
1702.00	0.1241			1612.00	0.0000		
1703.00	0.0618						
1704.00	0.0000						
Test 1170 (0.27 MPa)				Test 1196 (0.27 MPa)			
Time (s)	Inj. Flow (kg/s)	Time (s)	Power (W)	Time (s)	Inj. Flow (kg/s)	Time (s)	Power (W)
0.00	0.0000	0.00	0.00	0.00	0.0000	0.00	0.00
15.00	0.3768	0.50	125645.00	15.00	0.3700	0.50	125595.00
30.00	0.7536	1.00	251289.00	30.00	0.7400	1.00	251190.00
100.00	0.7536	774.00	251289.00	100.00	0.7400	723.00	251190.00
774.00	0.7536	775.00	125645.00	723.00	0.7400	724.00	125595.00
775.00	0.3768	776.00	0.00	724.00	0.3700	725.00	0.00
776.00	0.0000			725.00	0.0000		
Test 1285 (0.27 MPa)				Test 1383 (0.27 MPa)			
Time (s)	Inj. Flow (kg/s)	Time (s)	Power (W)	Time (s)	Inj. Flow (kg/s)	Time (s)	Power (W)
0.00	0.0000	0.50	0.00	0.00	0.00	0.50	0.00
15.00	0.4136	1.00	125944.00	0.50	0.05	1.00	71801.00
22.00	0.7334	308.00	251887.00	1.00	0.1000	891.00	143603.00
308.00	0.7415	309.00	251887.00	2.00	0.1300	892.00	143603.00
309.00	0.0000	310.00	125944.00	33.00	0.1220	893.00	71807.00
		311.00	0.00	43.00	0.1290	894.00	0.00
				70.00	0.1290		
				108.00	0.1380		
				893.00	0.1340		
				894.00	0.1340		
				895.00	0.00		

B.10.4. Simulations with TRACE

Six RBHT reflood tests were chosen for this assessment covering a range of power from 144 (0.88 kW/m) to 251 kW (1.53 kW/m), subcooling from 16 to 86 K, liquid injection flow rate from 0.12 to 0.75 kg/s, and upper plenum or system pressure from 0.13 to 0.28 MPa. A summary of the assessment matrix is provided in Table B.10.4, while a more detailed discussion of heat transfer characteristics is presented in the next section.

Table B.10.4. RBHT Reflood Test Assessment Matrix

Test ID	Reflood Rate (kg/s)	Pressure (MPa)	Linear Power/ Rod (kW/m)	Subcooling (K)	Reflood Time (s)
1383	0.73	0.28	0.88	17	310
1108	0.13	0.13	0.88	82	110
1096	0.12	0.13	0.88	16	225
1170	0.75	0.28	1.53	16	300
1196	0.74	0.28	1.53	59	227
1285	0.74	0.28	1.53	86	115

B.10.4.1. Heat Transfer Characteristics

Before looking at comparisons between RBHT data and TRACE for each specific test, it is useful to examine in detail the underlying heat transfer characteristics of the RBHT reflood tests. To better explain the underlying heat transfer phenomena, a detailed analysis of RBHT Test 1383 will be used as an example.

Figure B.10-5 is a plot of heater rod temperature and heat transfer coefficients (as calculated by the Penn State program DATARH) at the 1.40 and 1.88 m elevations for Test 1383. This figure clearly illustrates the initial rod heatup, cooling during reflood, and eventual quench. It also shows the large increase in heat transfer coefficient as the rod is quenched. The time at quench has been indicated on Figure B.10-5 as a vertical line.

Figure B.10-6 is basically the same as Figure B.10-5, however, in this figure, the HTC y-axis scale has been reduced to show the HTC before rod quench. In this figure, the HTC during the initial rod heatup is linear in nature, yet decreasing, and transitions to a mixed convective HTC during reflood. The cooling of the rod during reflood at these relatively high elevations is dominated by steam cooling and water droplets impacting the rod locally.

Figure B.10-7 contains several graphs. The top one is of the inlet and outlet liquid mass flow in the bundle. The middle plot is of the integrated liquid mass flow out of the bundle, while the bottom plot is of the bundle collapsed liquid level and quench front. As shown in Figure B.10-7, the liquid carryover rate slowly increases as the bundle is refilled, and reaches a steady carryover

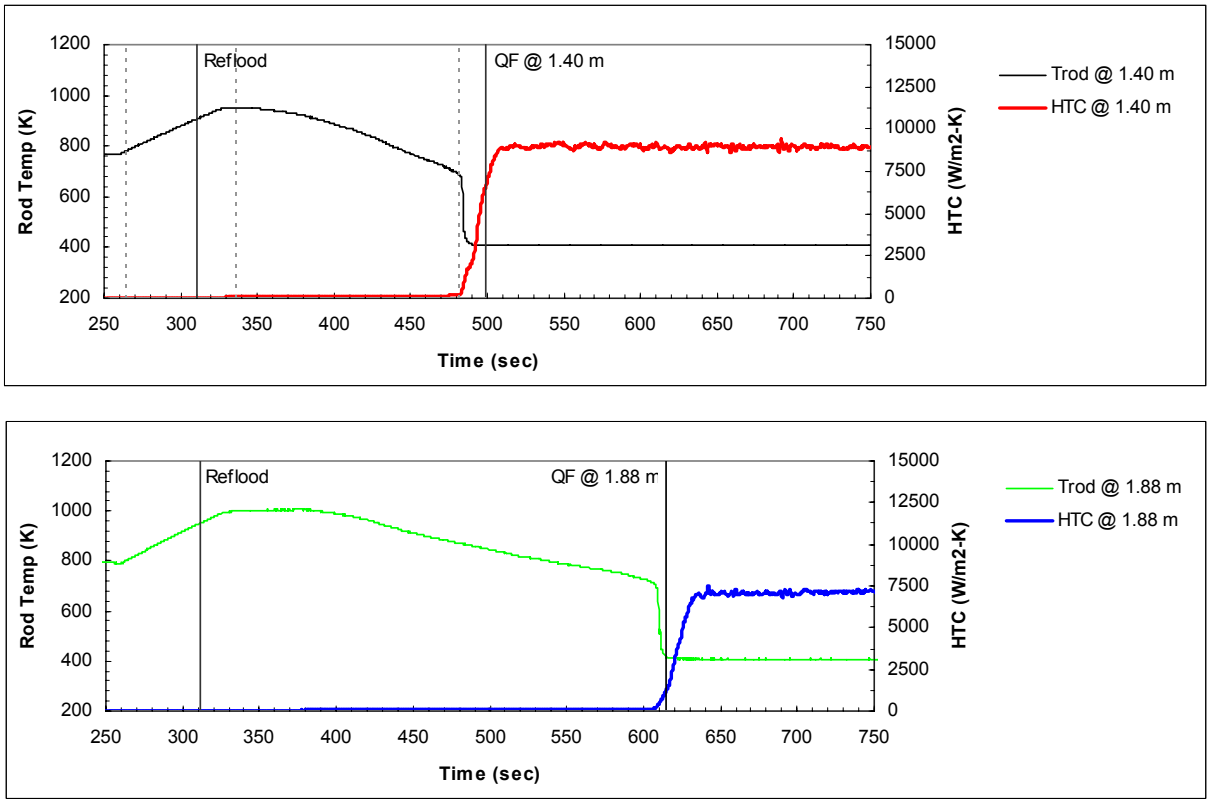

Figure B.10-5. Test 1383 Rod Temperature and HTC at 1.40 and 1.88 m elevations

rate of ~0.05 kg/s. A total of about 15 kg of liquid was carried out. The quench time was plotted along with the collapsed liquid level and illustrates several things. First, when the collapsed liquid level is above the quench location (t < 400 sec), it is likely that the two-phase flow in the bottom part of the bundle is inverted annular. As the bundle is filled the internal water core in the inverted annular structure is warmed up to saturated conditions. It is at this time that the collapsed liquid level and quench front are almost at the same elevation (t ~ 450 sec). After this time (t > 450 sec), the quench front leads the collapsed liquid level, as would be expected as the rods experience a pronounced two-phase mixture level swell as nucleate boiling continues. Figure B.10-7 also shows the time at which rods at 1.40 and 1.88 m are quenched.

Figure B.10-8 is a plot of the rod temperature, fluid temperature, saturation temperature, and HTC at the 1.40 m elevation for Test 1383. As would be expected, during the reflood cooling period before quench (340 - 480 sec), the HTC increases as the fluid and rod temperature decrease. Of special note is the fluid temperature measured by exposed thermocouples. It is proposed that the sudden reductions in fluid temperature are caused by droplets impacting the exposed fluid thermocouples. Therefore, the steam temperature would be some smooth curve fit joining the top peaks of the fluid temperature measurement. For Test 1383, a sigmodial curve fit was selected as shown in Figure B.10-8.

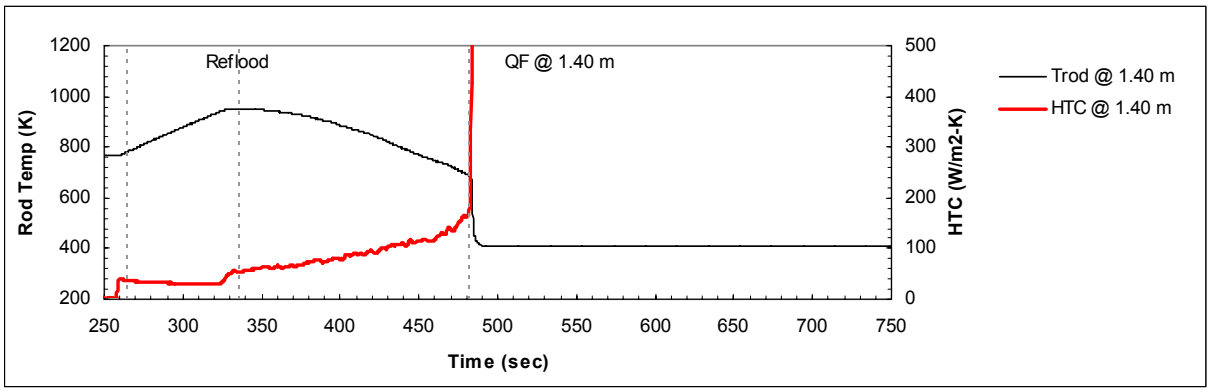

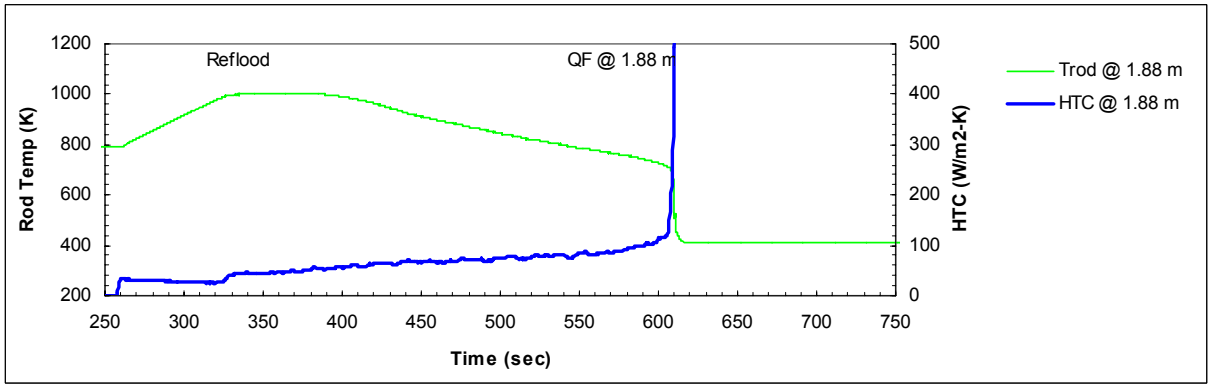

Figure B.10-6. Test 1383 Rod Temperature and HTC at 1.40 and 1.88 m elevations (zoom)

B.10.4.2. Test 1383 Comparisons

RBHT Test 1383 was a 0.73 kg/s (6 in/sec) reflood test at 0.28 MPa, 17 K subcooling, and 0.88 kW/m linear power. This test is the same as 1096, except for an increase in pressure and injection flow rate. The test began by preheating the bundle with steam from the small steam boiler. The power was turned on and when the bundle reached a predetermined maximum temperature, liquid was injected to begin the reflood portion of the test. The collapsed liquid level in the bundle rose steadily as cold water was injected and was sightly over predicted by TRACE as shown in Figure B.10-9. Figure B.10-10 is a plot of upper plenum pressure, which was fairly stable during the test. However, there was a slight increase in pressure at ~275 sec when the initial slug of cold water into the bottom of the bundle was rapidly vaporized.

The heater rod temperatures at various elevations are plotted in Figure B.10-11 through Figure B.10-17. TRACE predictions match the RBHT reflood data well at low bundle elevations ($z < 0.85$ m), but consistently over predicts the peak temperature and under predicts the quench time at high elevations.

The bundle exit gas and liquid mass flow rates are shown in Figure B.10-18 and Figure B.10-19. TRACE slightly under predicts the gas mass flow rate and noticeably over predicts the liquid

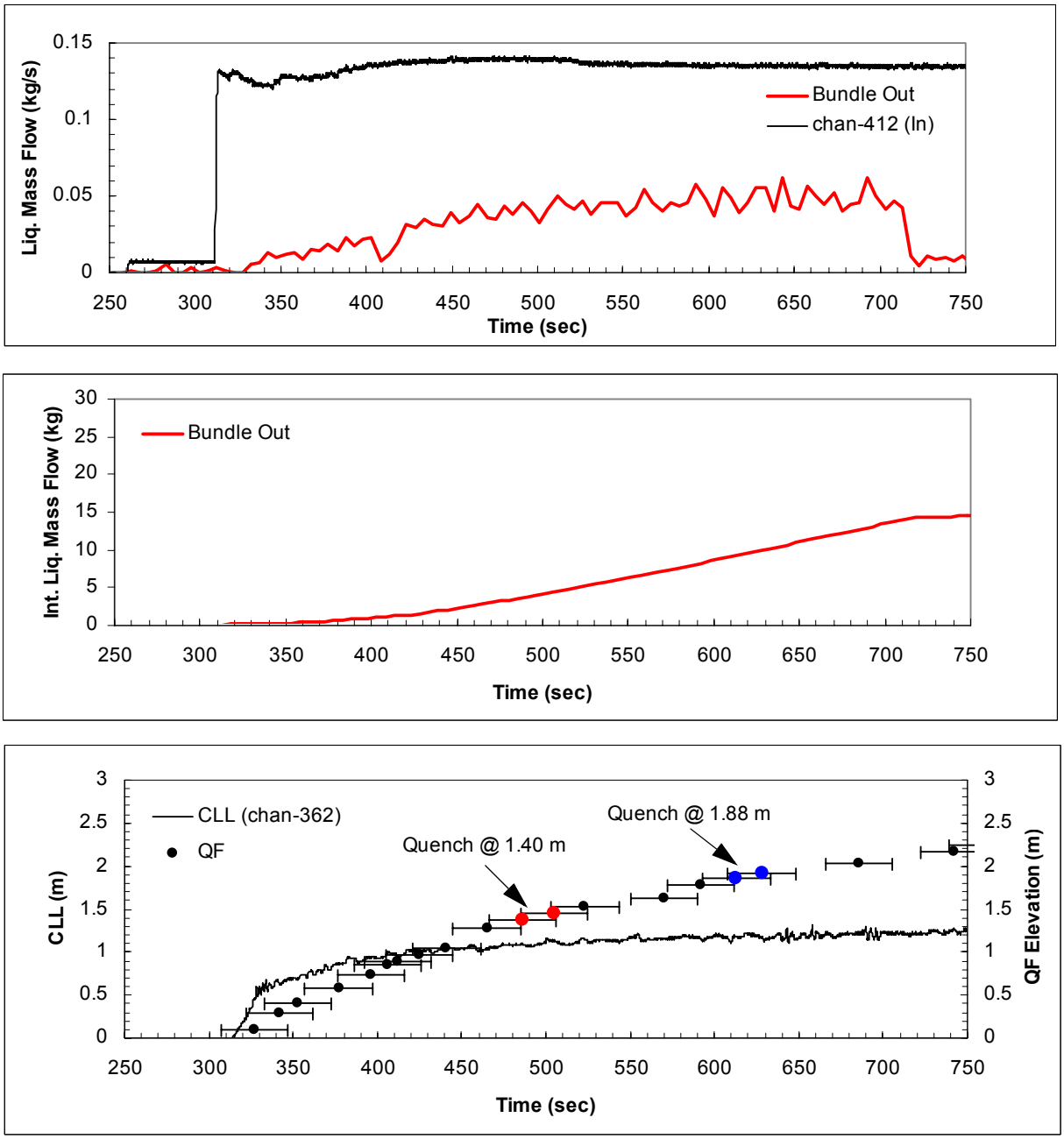

Figure B.10-7. Test 1383 Liquid Injection and Carryover, Collapsed Liquid Level, and Quench Front

carryover. In Figure B.10-19, the liquid carryover rate decreases suddenly at ~ 720 sec. This is due to the fact that the small and large catch tanks have filled with water and it takes approximately 90 seconds for the carryover liquid to stop flowing to the catch tanks and start flowing through the separator. During this time, water is held up in the upper plenum. During the very beginning of the reflood, a large increase in exist steam flow rate is shown in Figure B.10-18. This is indicative of a rapid quenching in the bottom portion of the bundle in the RBHT

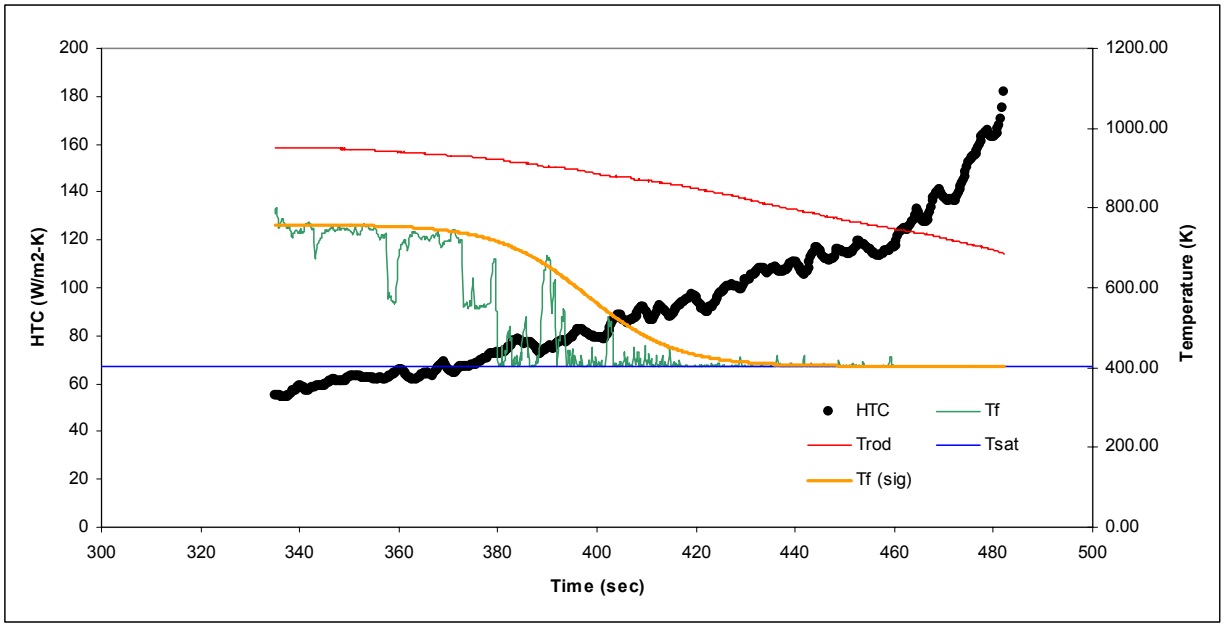

Figure B.10-8. Test 1383 Bundle Temperatures and HTC at z = 1.40 m

experiment. This sudden increase in steam flow rate entrains a small amount of droplets (as shown in Figure B.10-19) and cools the entire bundle as the exit the test section; some of the droplets evaporate on the way up the bundle.

This cooling in the RBHT experiment can also be seen in Figure B.10-24 and Figure B.10-25, which are graphs of the steam temperatures at the middle elevation in the bundle. This initial cooling of the bundle is not enough to completely quench the rods, but is one reason why TRACE significantly over predicts the initial rod heatup immediately after reflood. This phenomena is observed in all of the reflood tests covered in this assessment. The under prediction of quench times observed in the rod temperature figures may be due to the way in which TRACE maps void fractions to fine mesh heat structure cells. The small quench front (~1 cm in height) can be difficult for TRACE to predict using 0.2 m high fluid nodes.

The HTCs in Figure B.10-20 through Figure B.10-23. In some cases, the time scales on these figures have been changed to zoom in on the HTCs during the heatup and cooldown period at each specific axial location. TRACE seems to do a better job predicting HTCs at higher elevations for higher injection flow rate cases during the reflood portion of the test, but this is somewhat subjective, since although the average HTC predicted by TRACE during reflood is close to that of the data (Figure B.10-22 and Figure B.10-23), the trend is not.

B.10.4.3. Test 1108 Comparisons

RBHT Test 1108 was a 0.12 kg/s (1.0 in/sec) reflood test at 0.13 MPa, 82 K subcooling, and 0.88 kW/m linear power. The test began by preheating the bundle with steam from the small steam

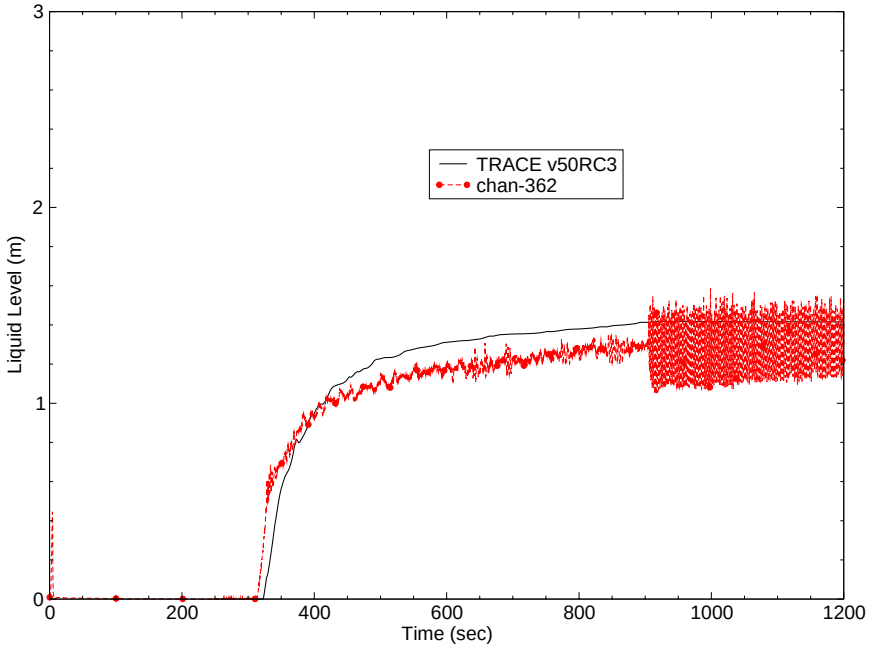

Figure B.10-9. Test 1383 Bundle Collapsed Liquid Level

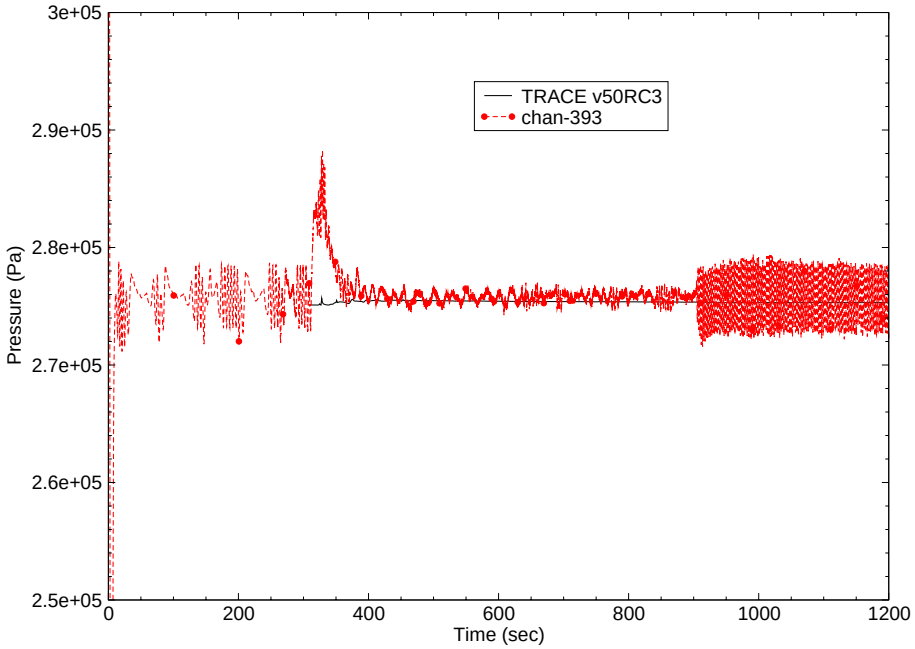

Figure B.10-10. Test 1383 Upper Plenum Pressure

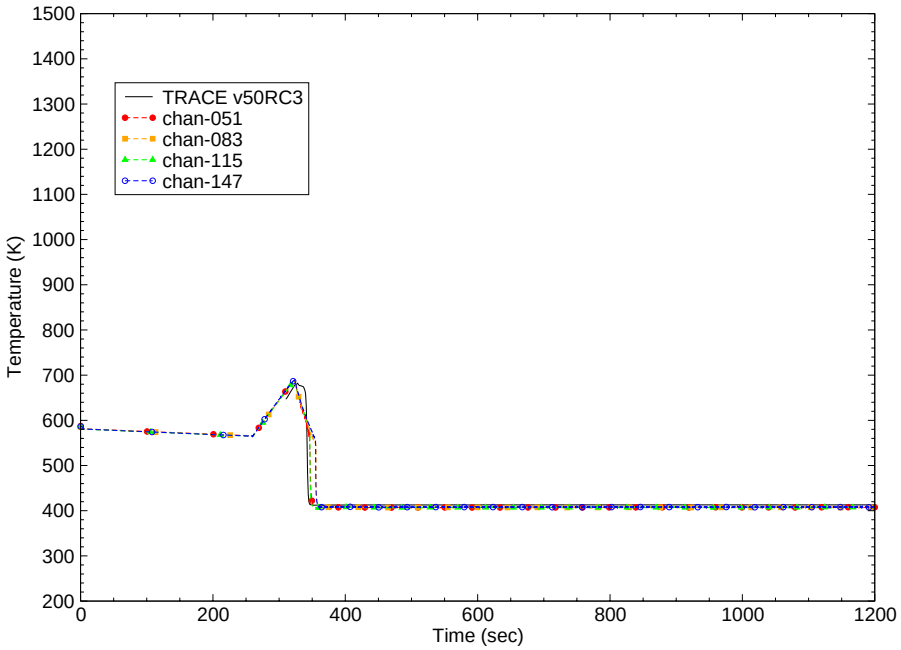

Figure B.10-11. Test 1383 Heater Rod Temperature at z = 0.41 m

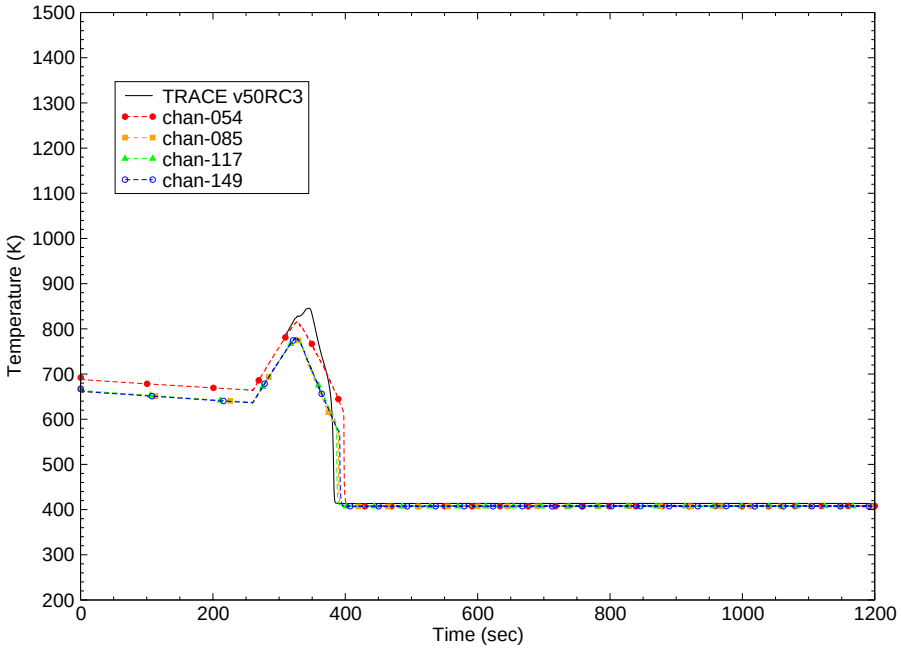

Figure B.10-12. Test 1383 Heater Rod Temperature at z = 0.85 m

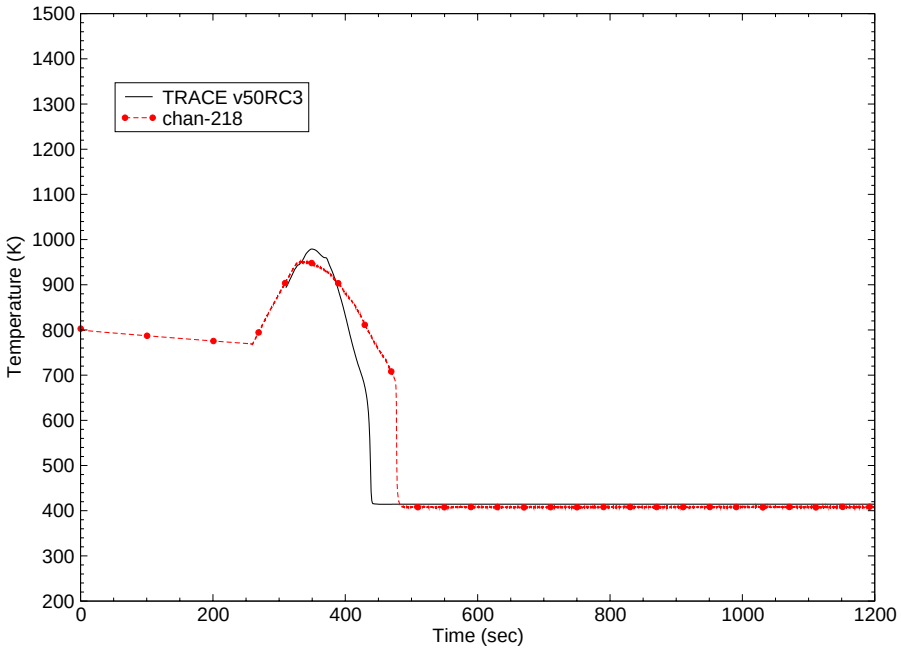

Figure B.10-13. Test 1383 Heater Rod Temperature at z = 1.37 m

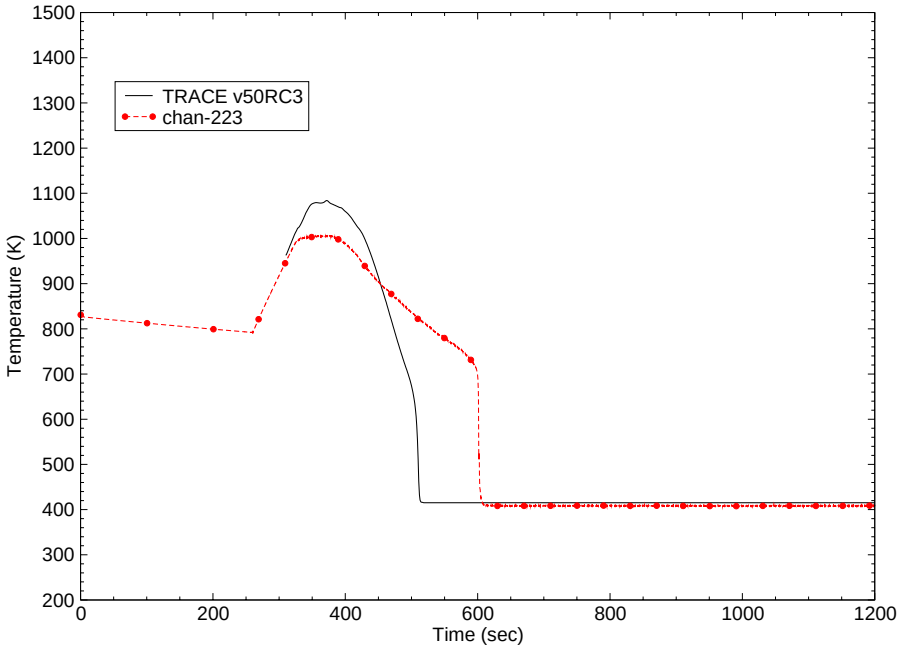

Figure B.10-14. Test 1383 Heater Rod Temperature at z = 1.85 m

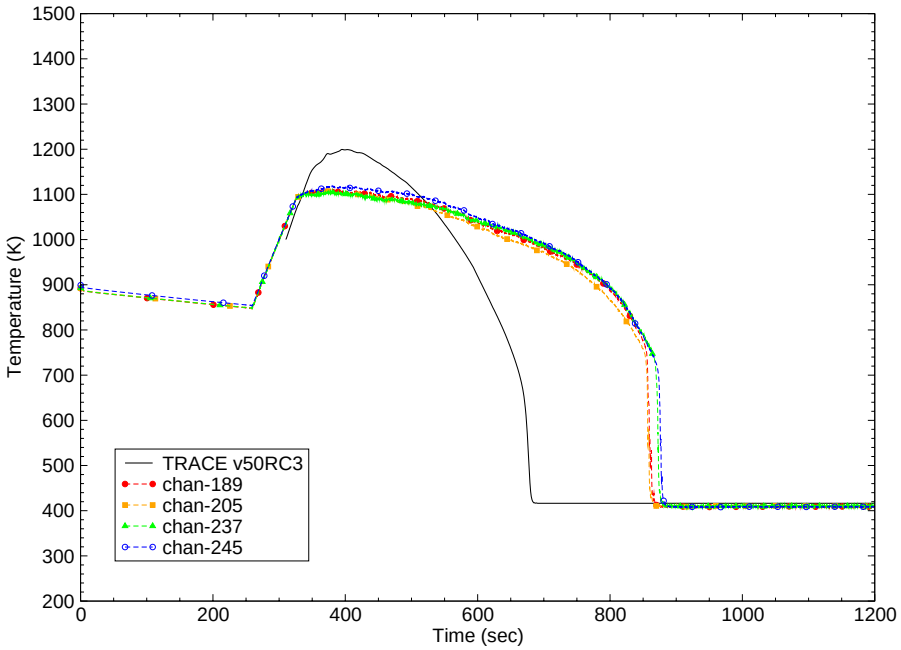

Figure B.10-15. Test 1383 Heater Rod Temperature at z = 2.55 m

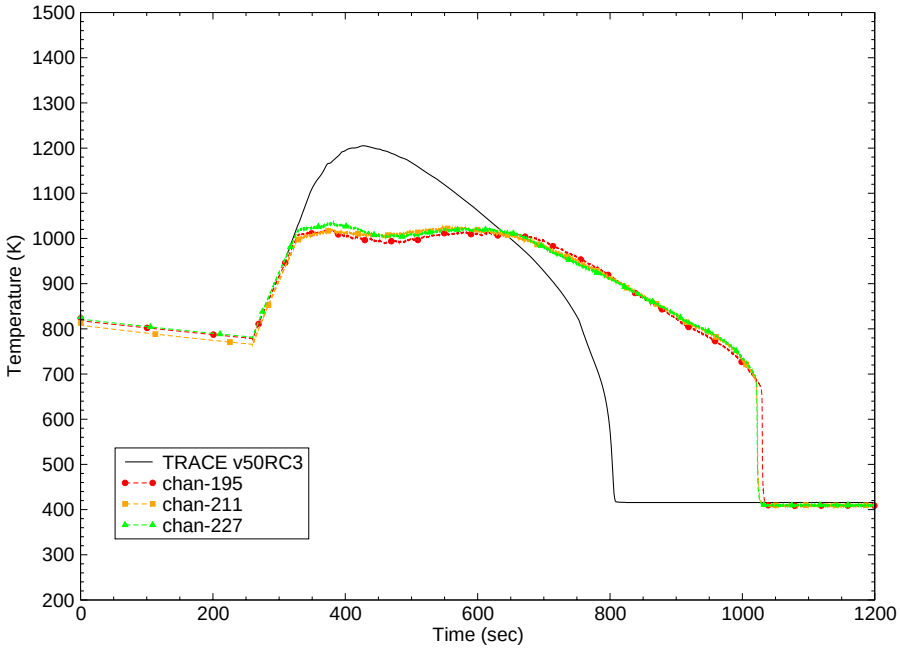

Figure B.10-16. Test 1383 Heater Rod Temperature at z = 2.93 m

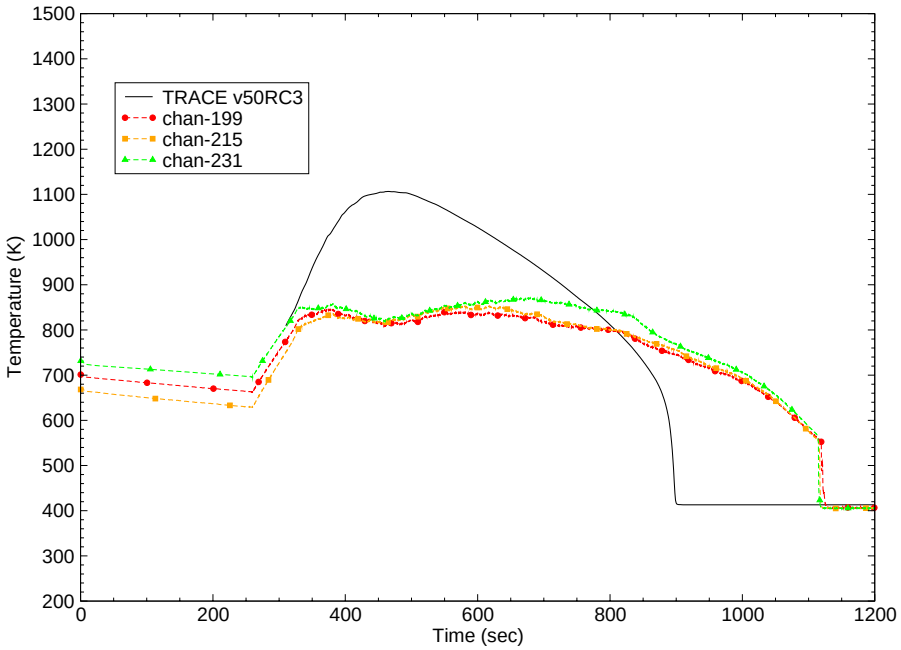

Figure B.10-17. Test 1383 Heater Rod Temperature at z = 3.34 m

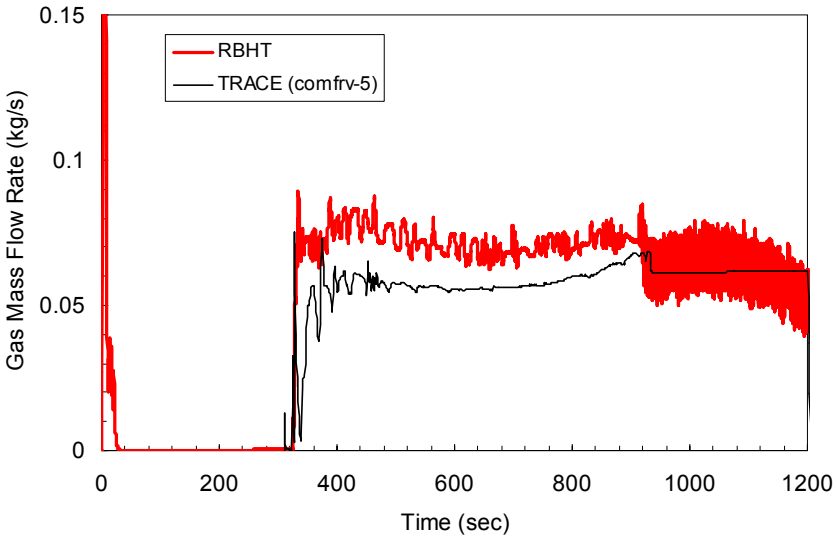

Figure B.10-18. Test 1383 Bundle Exit Gas Mass Flow Rate

boiler. The power was turned on and when the bundle reached a predetermined maximum temperature, liquid was injected to begin the reflood portion of the test. The collapsed liquid level in the bundle rose steadily as cold water was injected and boiled off as shown in Figure

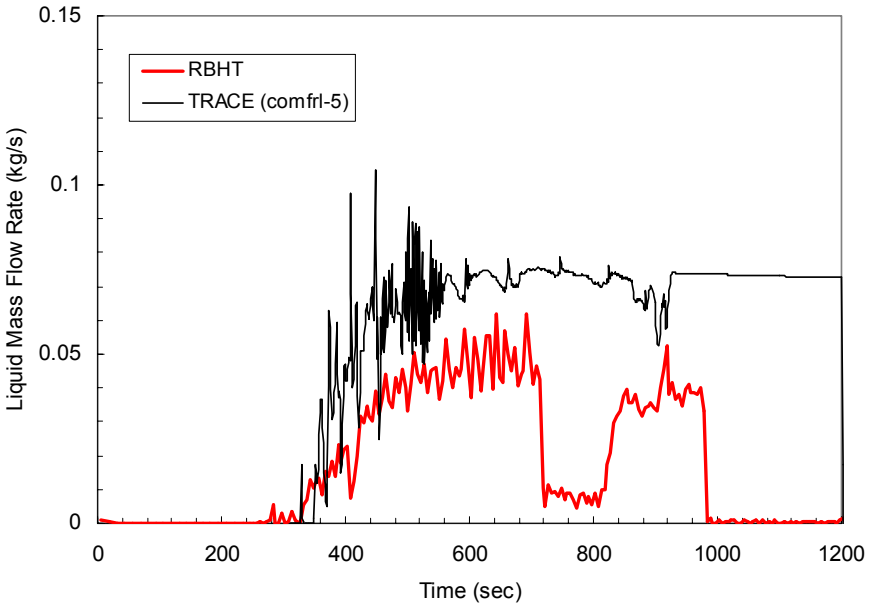

Figure B.10-19. Test 1383 Bundle Exit Liquid Mass Flow Rate

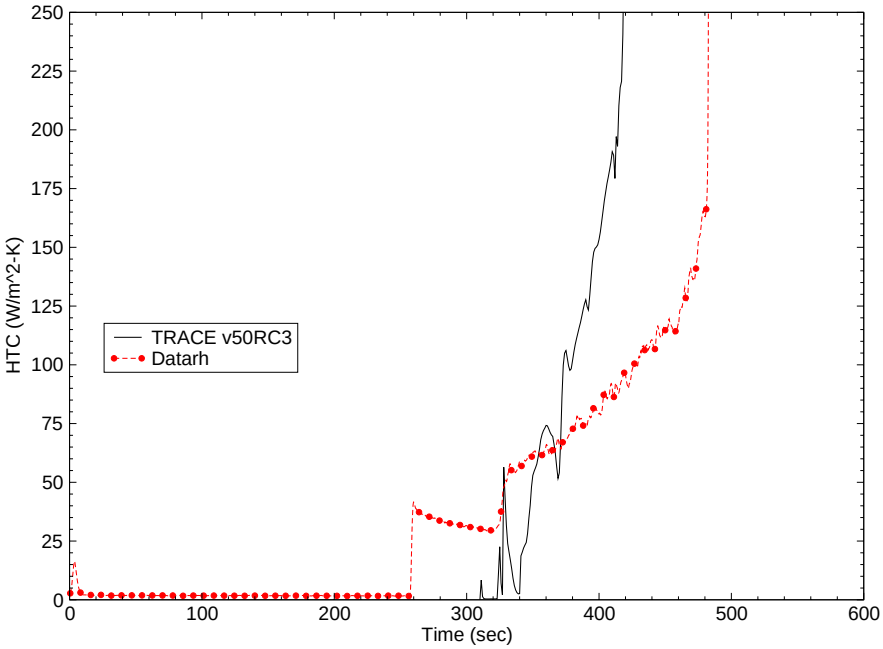

Figure B.10-20. Test 1383 HTC at z = 1.40 m

B.10-26. Figure B.10-27 is a plot of upper plenum pressure, which was fairly stable during the test. The heater rod temperatures at various elevations are plotted in Figure B.10-28 through

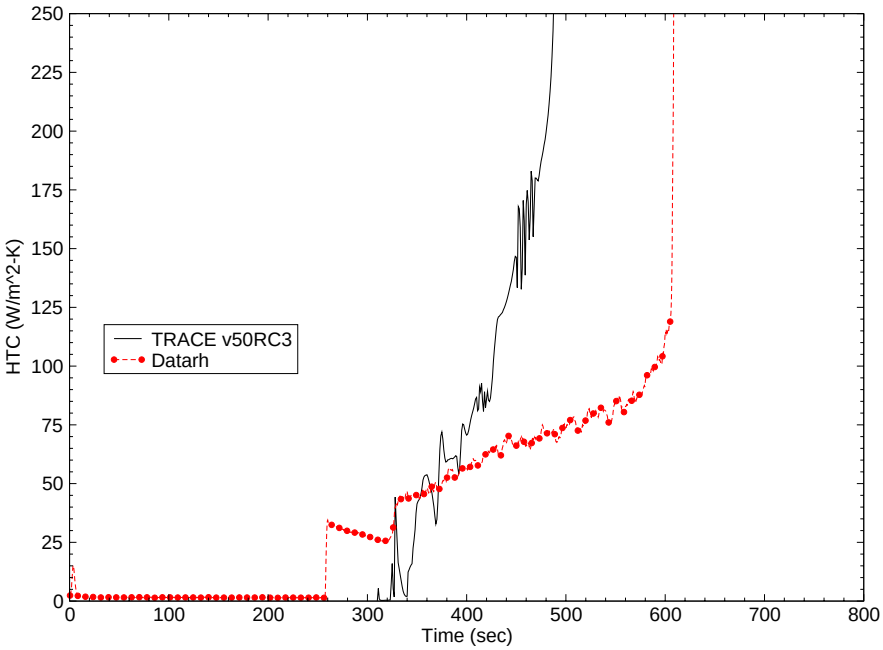

Figure B.10-21. Test 1383 HTC at z = 1.88 m

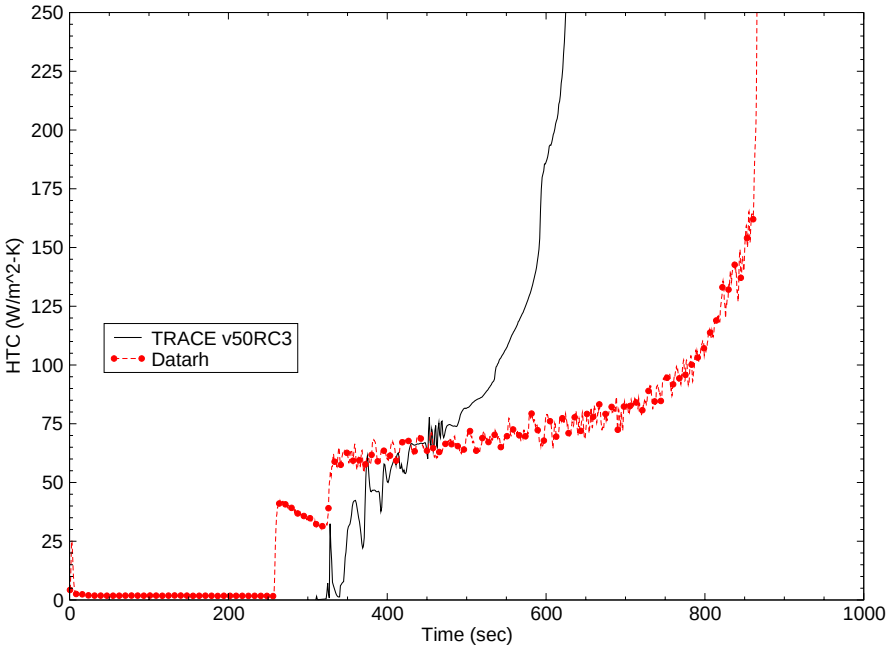

Figure B.10-22. Test 1383 HTC at z = 2.54 m

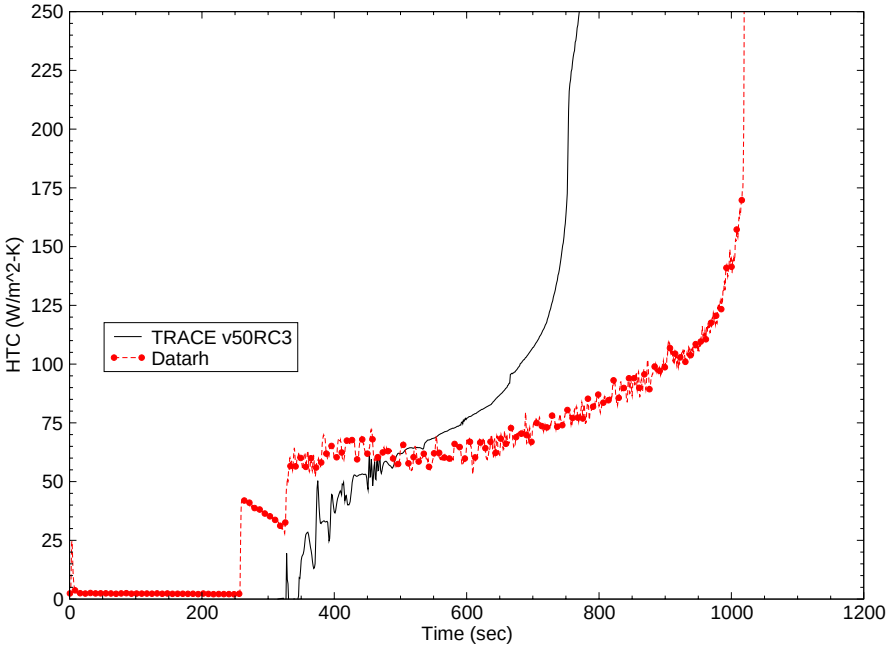

Figure B.10-23. Test 1383 HTC at z = 2.93 m

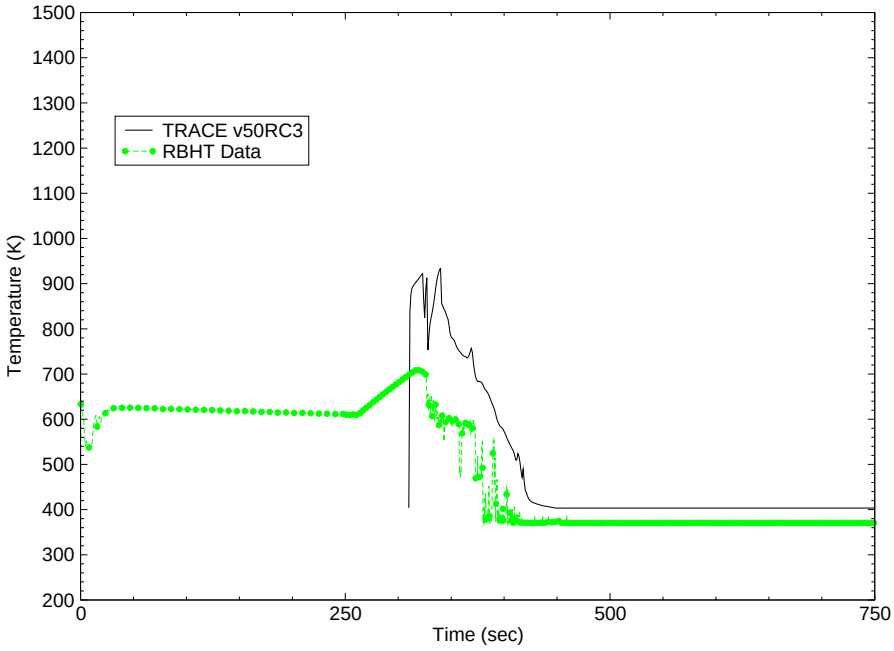

Figure B.10-24. Test 1383 Steam Temperatures at z = 1.40 m

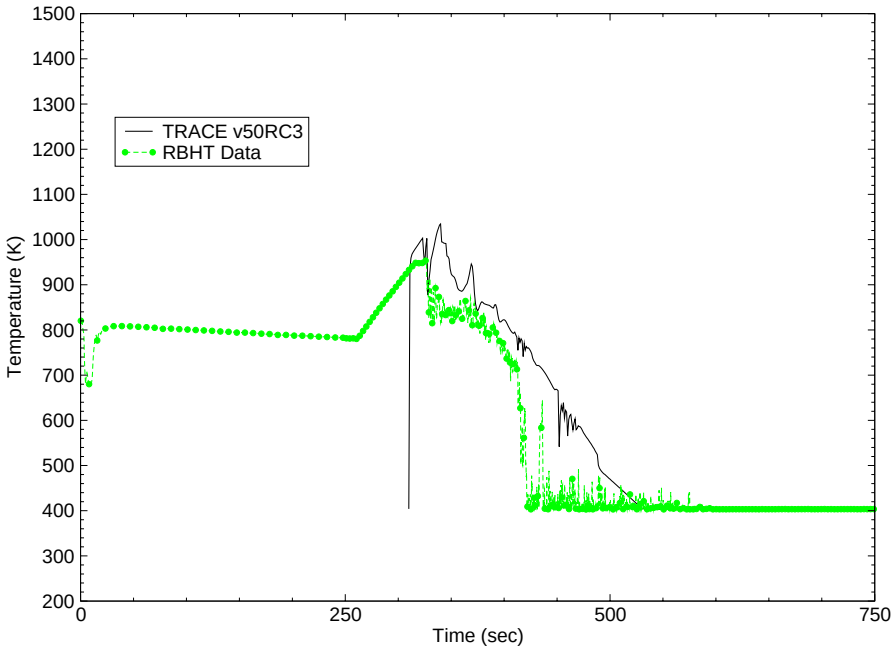

Figure B.10-25. Test 1383 Steam Temperatures at z = 1.88 m

Figure B.10-34. As in Test 1383, TRACE consistently over predicts the peak rod temperature and under predicts quench times at higher elevations. However, in this case, TRACE does a little better at z = 1.37 m. It would seem that the high subcooling cases are predicted slightly better than the low subcooling cases for the same conditions. This assertion is consistent with the HTCs plotted in Figure B.10-35 through Figure B.10-38. The steam temperature at two elevations are plotted in Figure B.10-39 and Figure B.10-40. TRACE does a pretty good job predicting the steam temperature at both elevations. It should be noted that the RBHT steam temperature data is based on an exposed fluid thermocouple. Thus, as previously mentioned, the RBHT steam temperature is the maximum reading and the drops in temperature are due to water droplets hitting the exposed thermocouple.

B.10.4.4. Test 1096 Comparisons

RBHT Test 1096 was a 0.12 kg/s (1 in/sec) reflood test at 0.13 MPa, 16 K subcooling, and 0.88 kW/m linear power. The test began by preheating the bundle with steam from the small steam boiler. The power was turned on and when the bundle reached a predetermined maximum temperature, liquid was injected to begin the reflood portion of the test (Figure B.10-41). Figure B.10-43 is a plot of upper plenum pressure, which varies significantly as the test progresses. It is not clear why there is such a large variation in pressure (chan-393), however, it was deemed that this test was still useful for analysis, because the oscillation does not appear to impact rod temperatures. The bundle collapsed liquid level is plotted in Figure B.10-44. From this figure, the data (chan-362) shows a sharp increase in the initial liquid level at ~ 250 sec, that TRACE

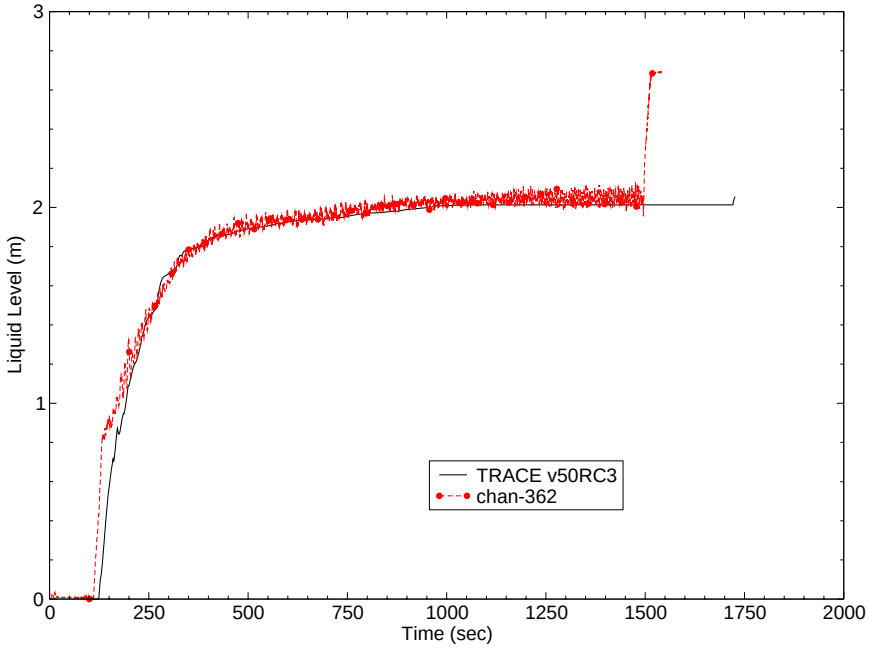

Figure B.10-26. Test 1108 Bundle Collapsed Liquid Level

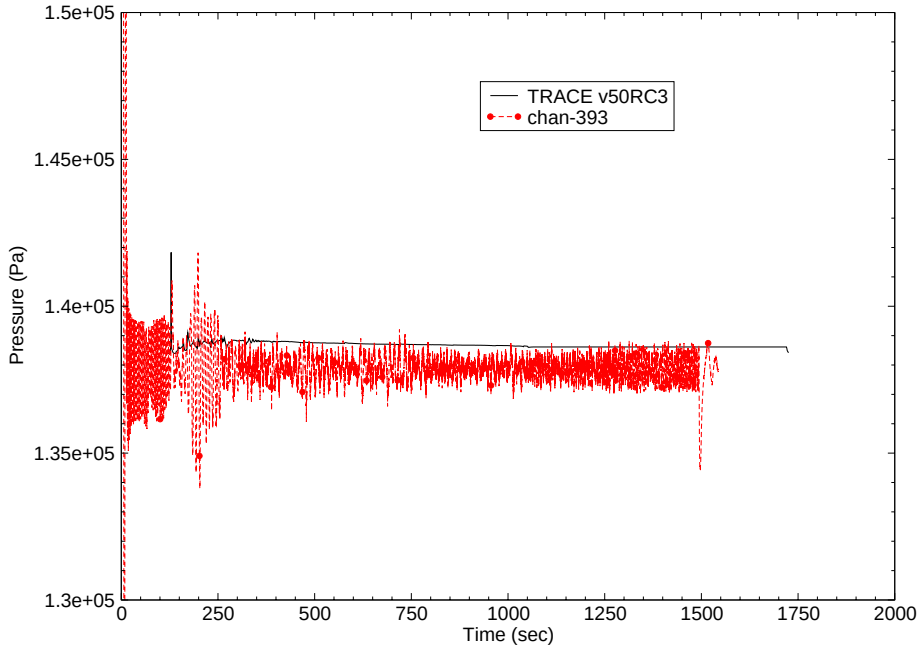

Figure B.10-27. Test 1108 Upper Plenum Pressure

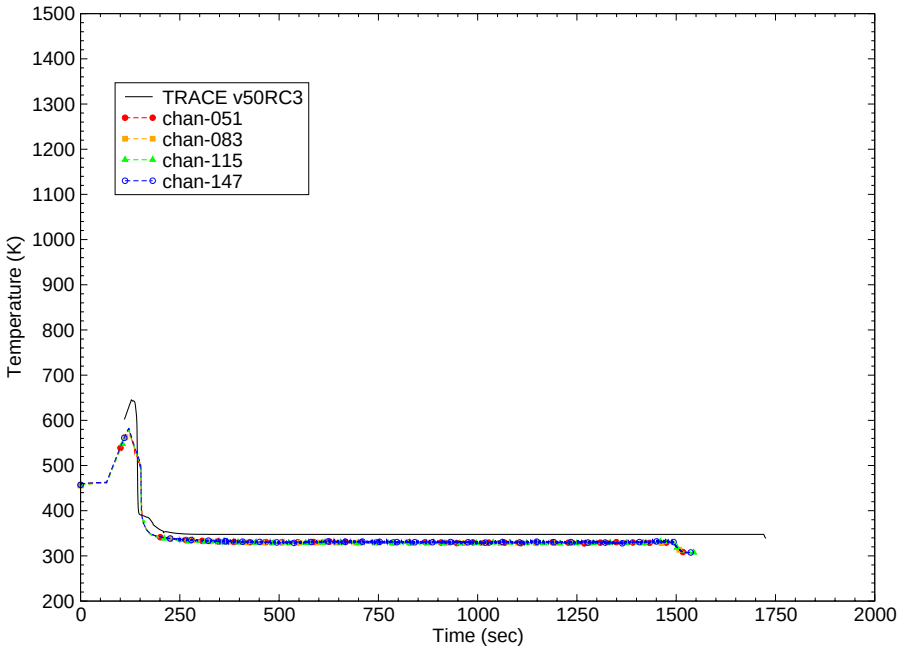

Figure B.10-28. Test 1108 Heater Rod Temperate at z = 0.41 m

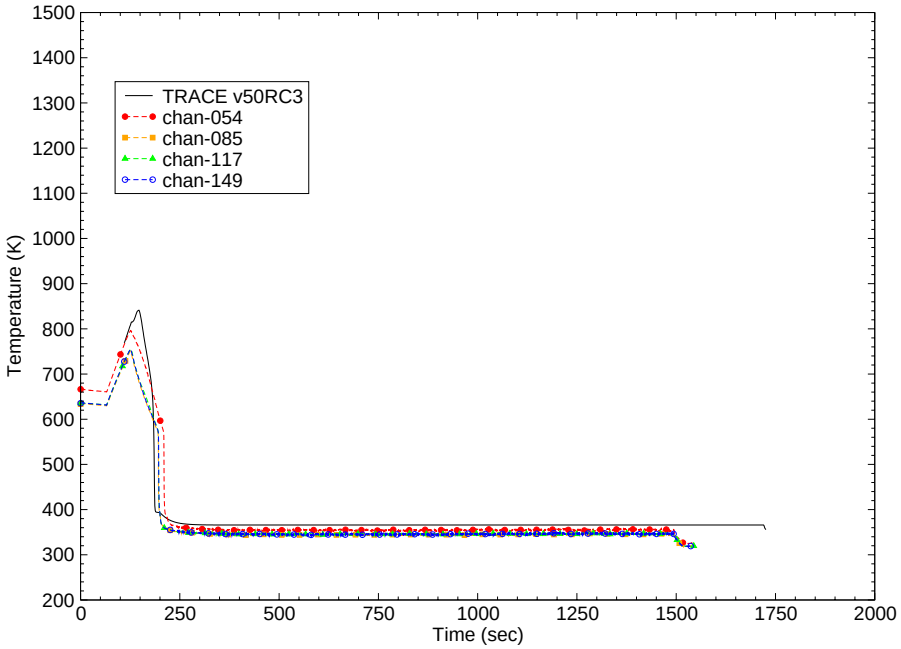

Figure B.10-29. Test 1108 Heater Rod Temperature at z = 0.85 m

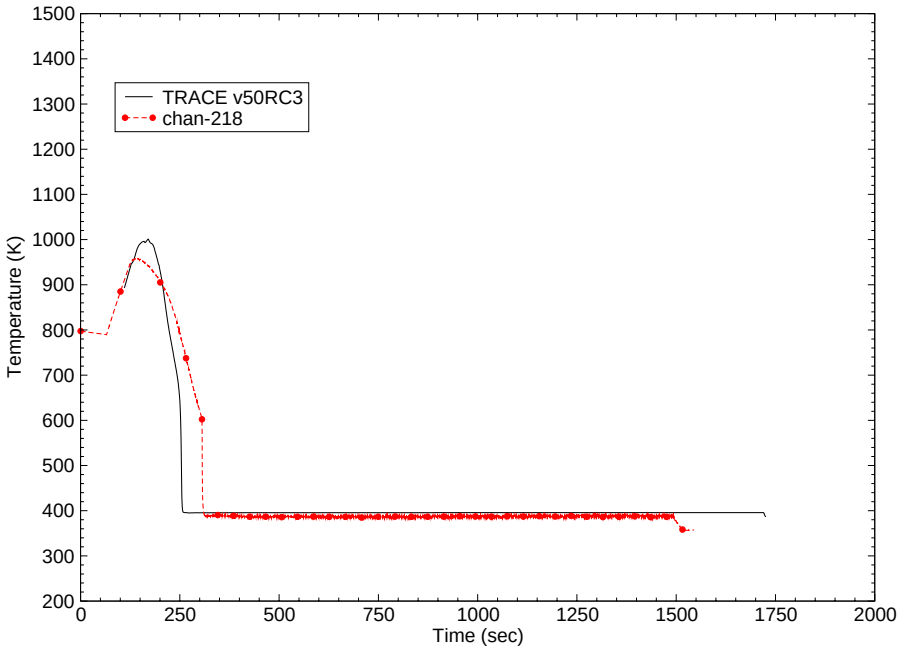

Figure B.10-30. Test 1108 Heater Rod Temperature at z = 1.37 m

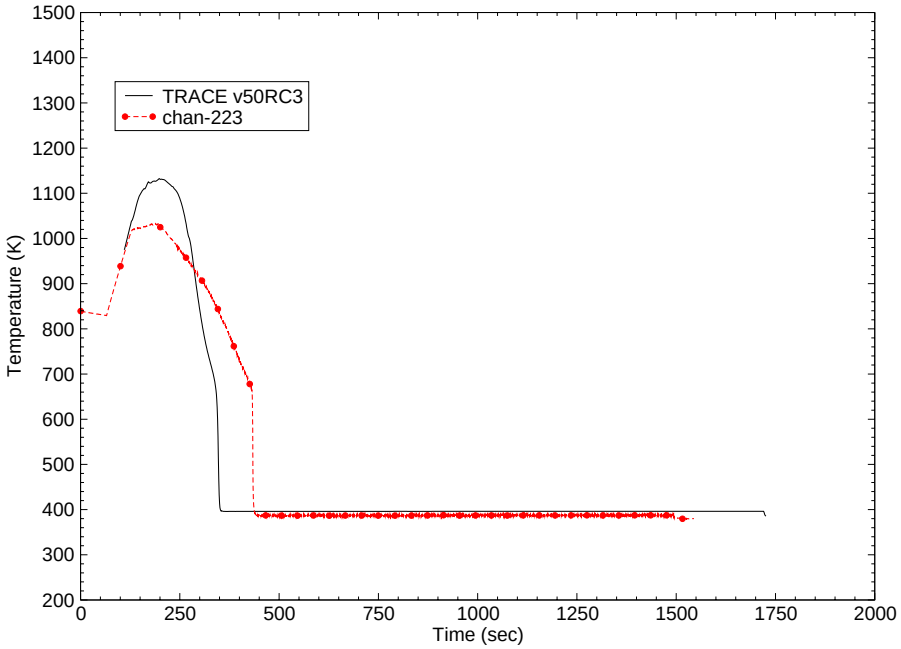

Figure B.10-31. Test 1108 Heater Rod Temperature at z = 1.85 m

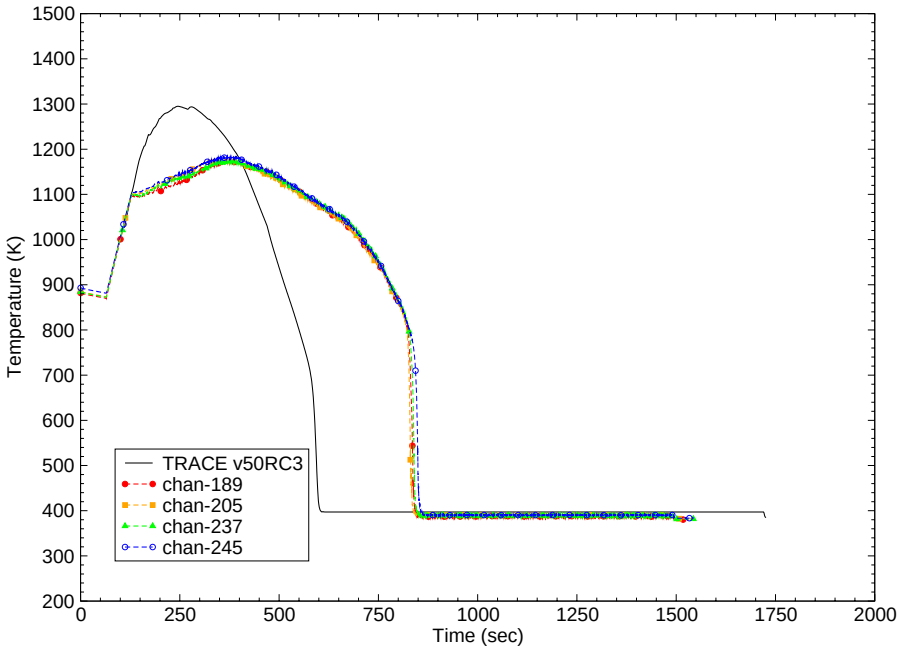

Figure B.10-32. Test 1108 Heater Rod Temperature at z = 2.55 m

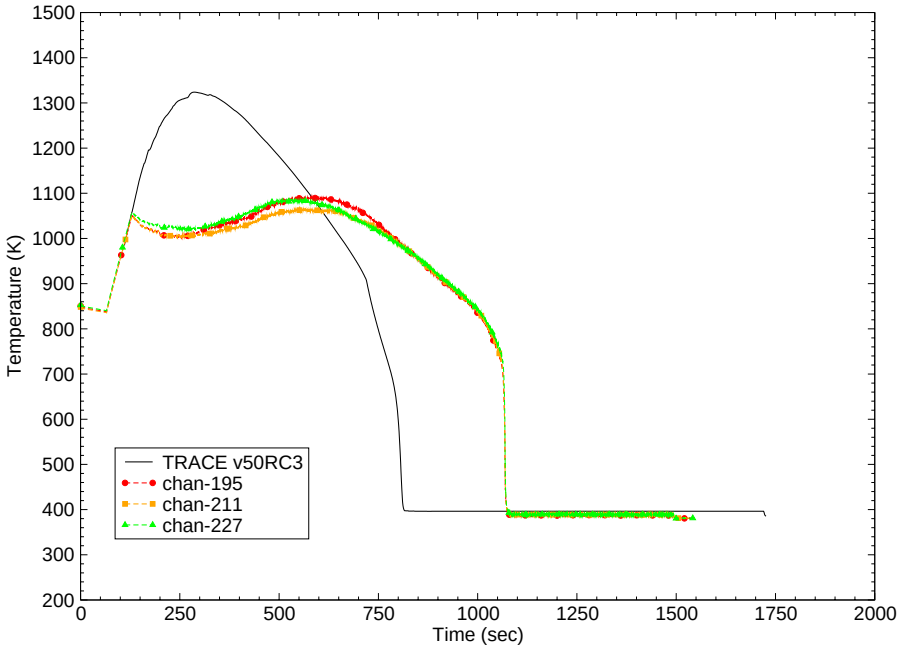

Figure B.10-33. Test 1108 Heater Rod Temperature at z = 2.93 m

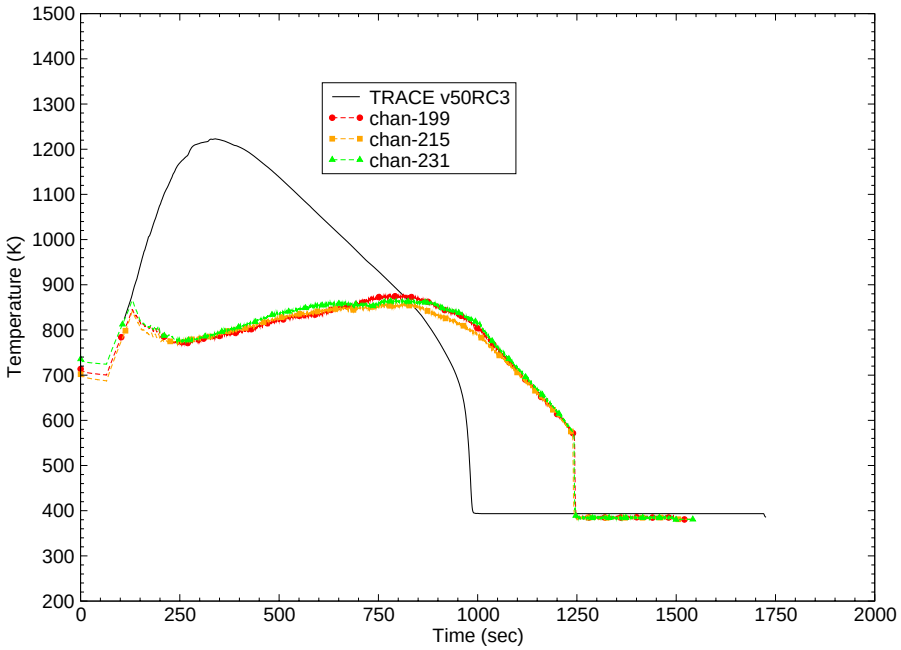

Figure B.10-34. Test 1108 Heater Rod Temperature at z = 3.34 m

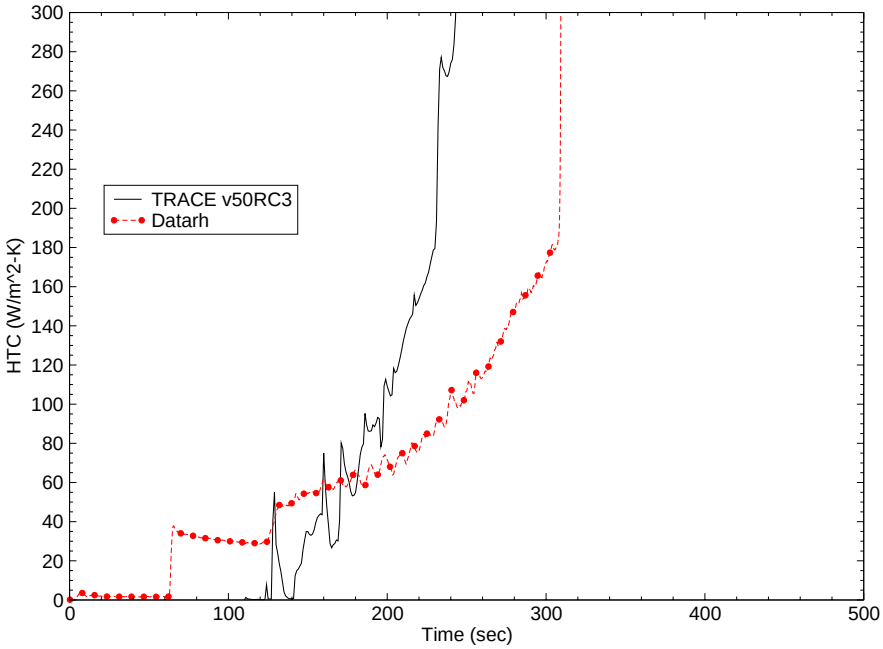

Figure B.10-35. Test 1108 HTC at z = 1.40 m

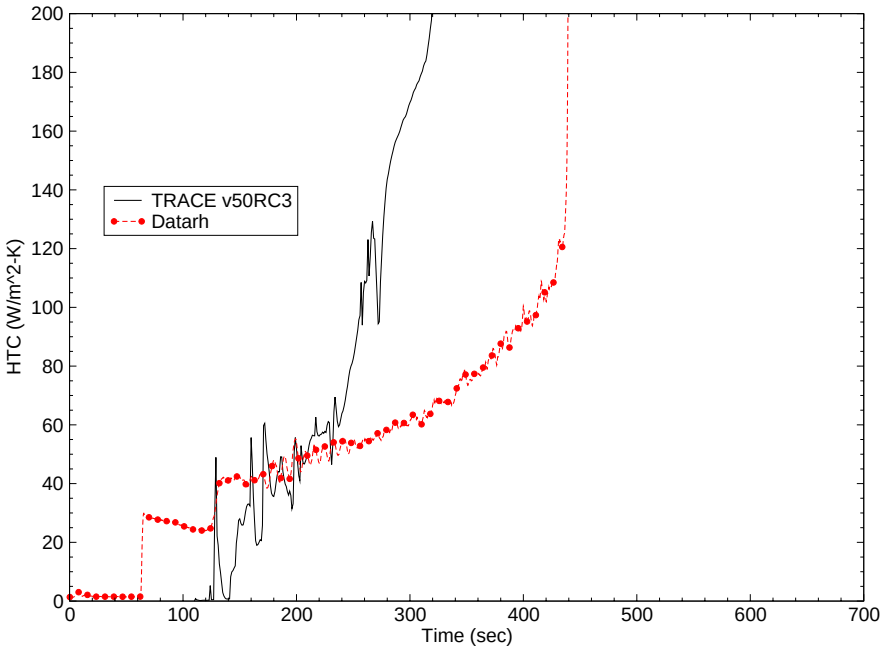

Figure B.10-36. Test 1108 HTC at z = 1.88 m

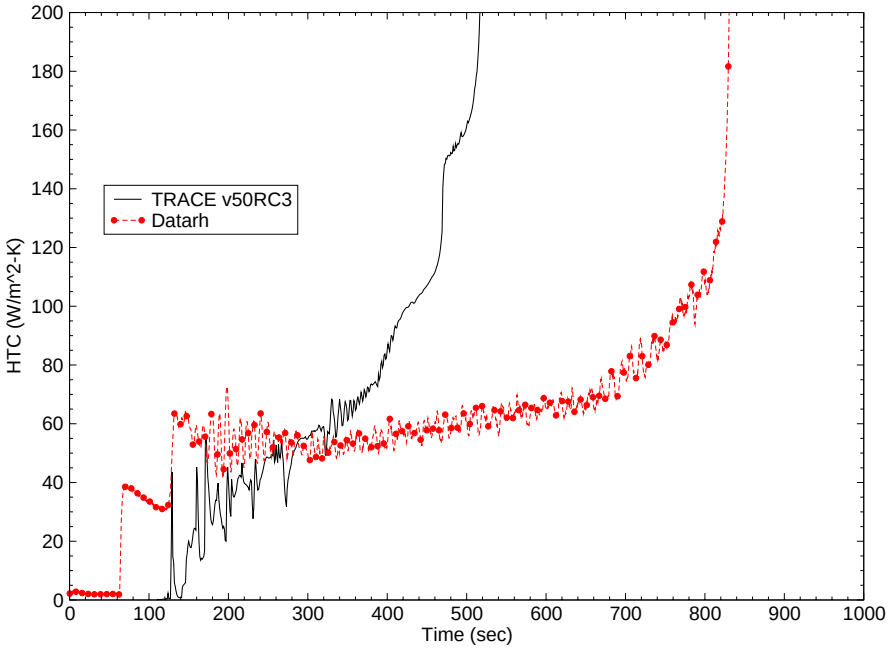

Figure B.10-37. Test 1108 HTC at z = 2.54 m

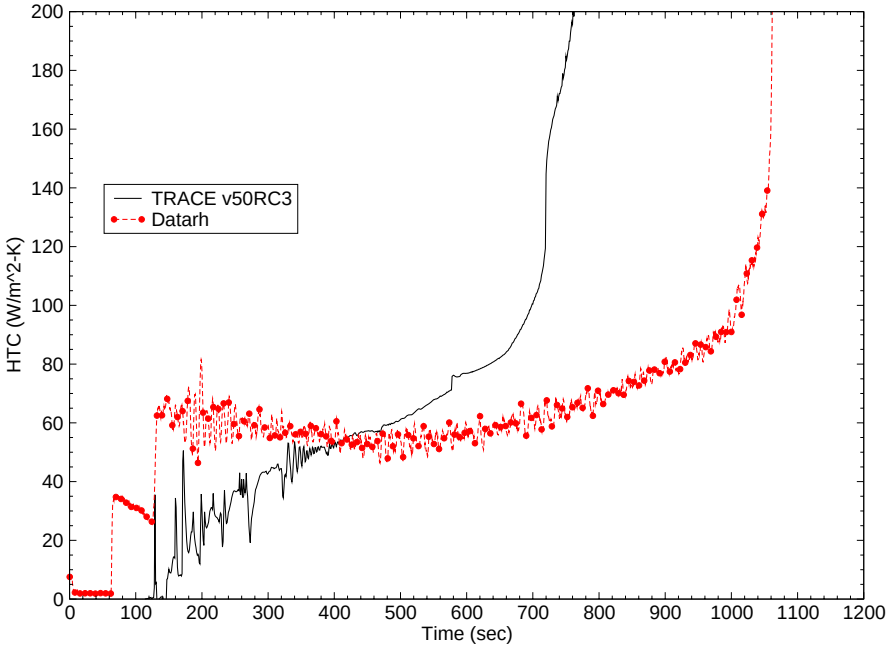

Figure B.10-38. Test 1108 HTC at z = 2.93 m

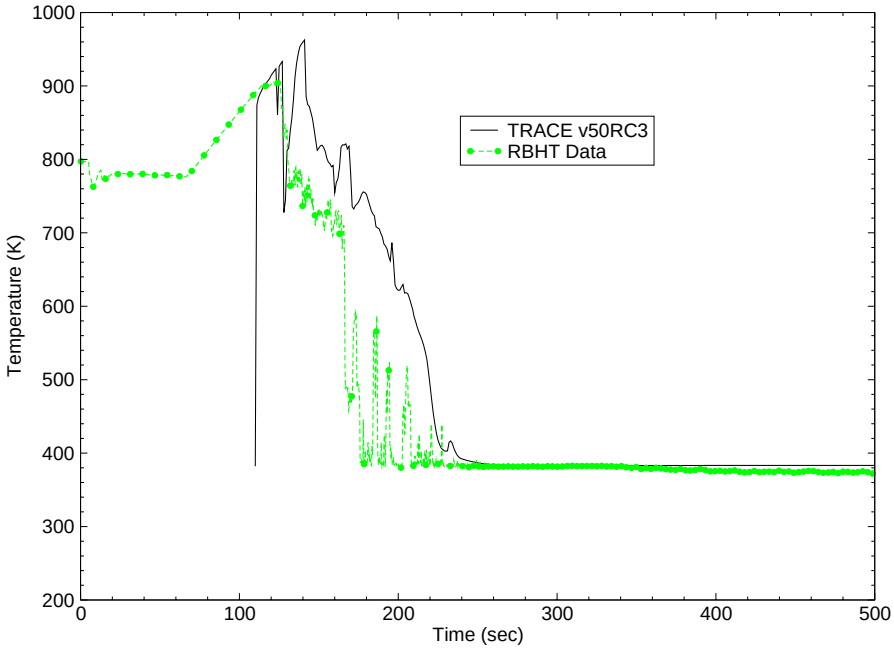

Figure B.10-39. Test 1108 Steam Temperature at z = 1.40 m

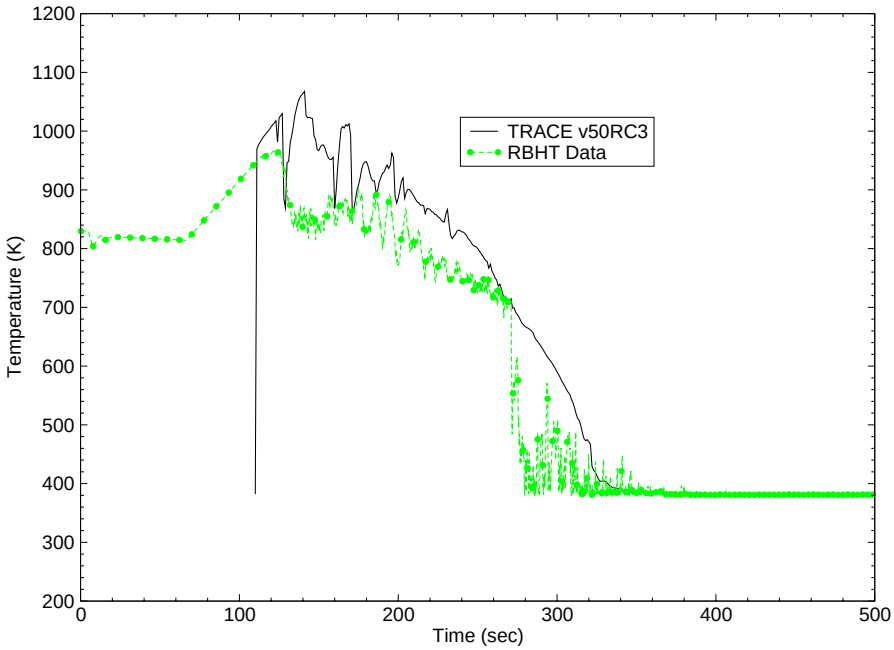

Figure B.10-40. Test 1108 Steam Temperatures at z = 1.88 m

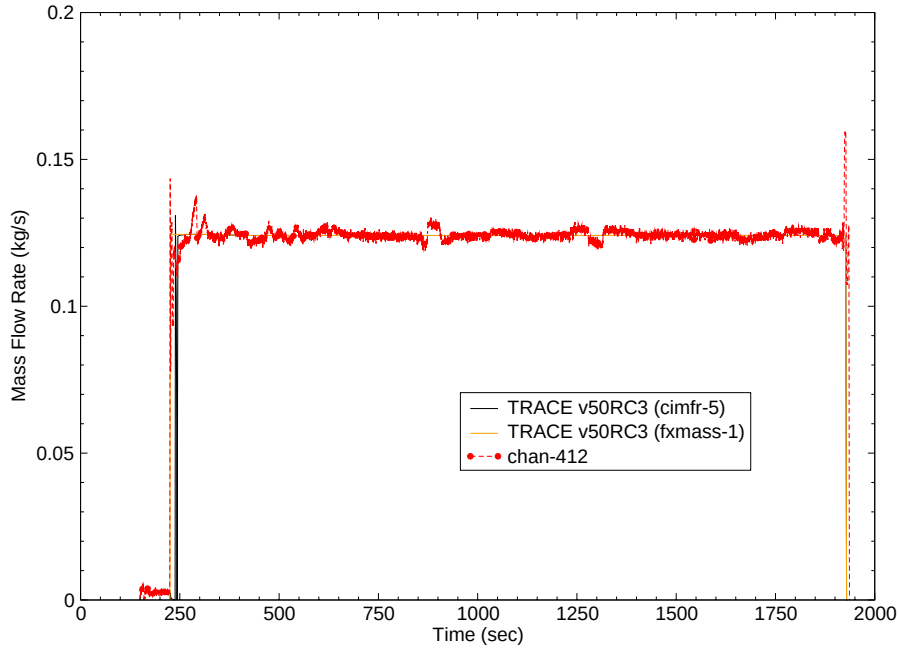

Figure B.10-41. Test 1096 Liquid Injection Flow Rate

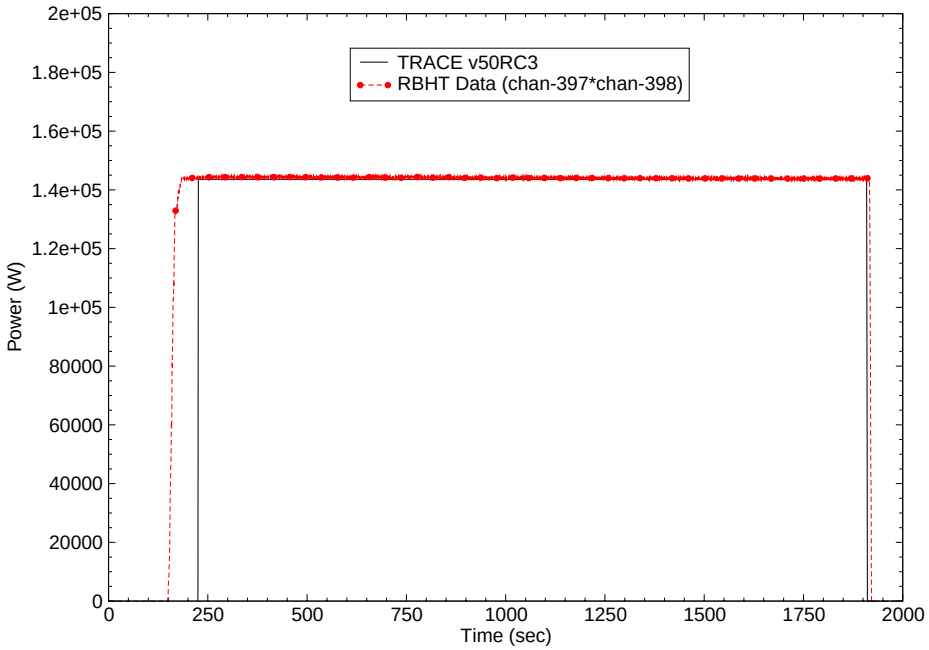

Figure B.10-42. Test 1096 Total Bundle Power

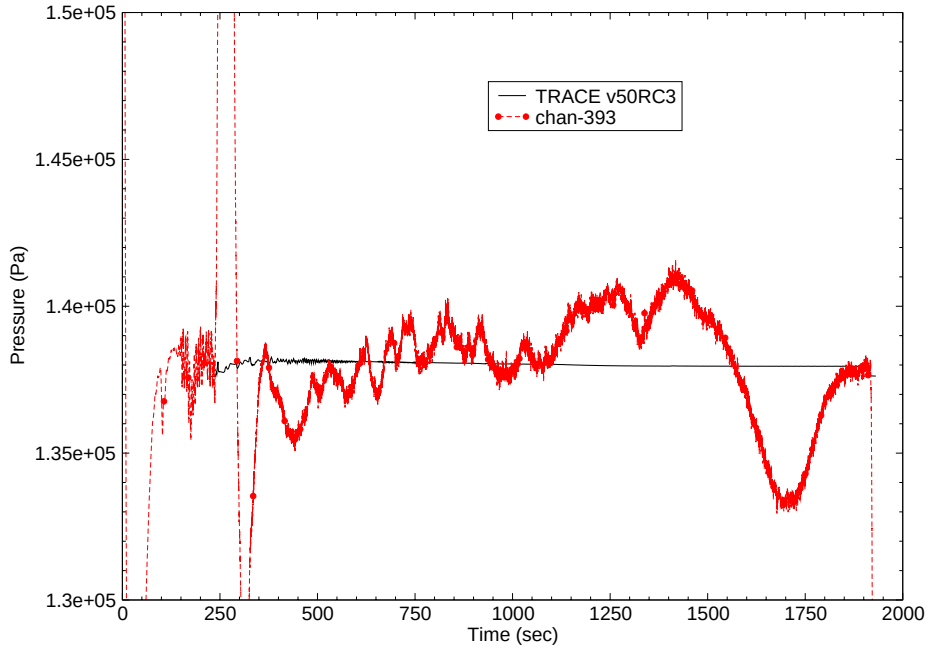

Figure B.10-43. Test 1096 Upper Plenum Pressure

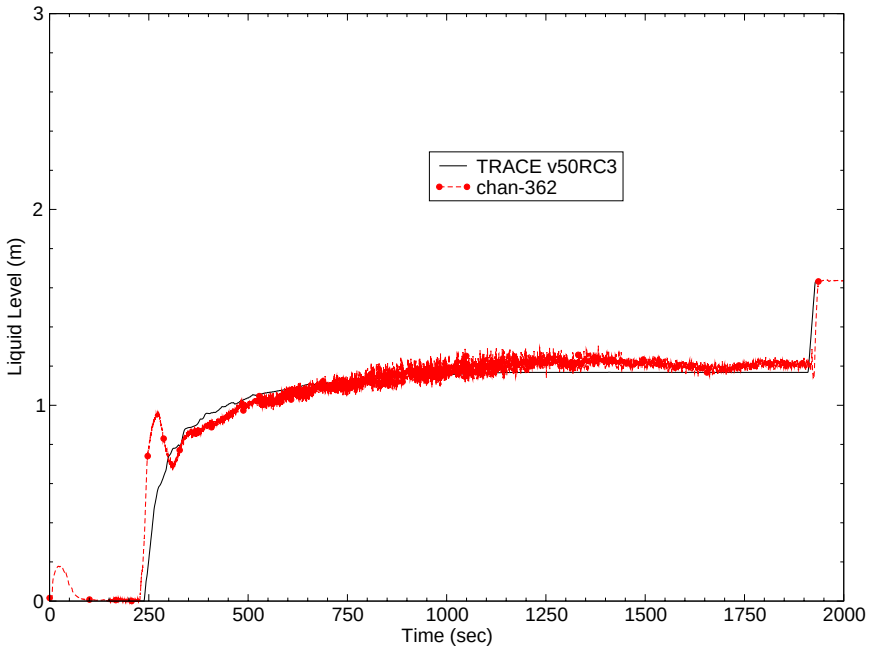

Figure B.10-44. Test 1096 Bundle Collapsed Liquid Level

does not predict. This sharp increase in level corresponds to an increase in exit steam mass flow. This would suggest that the first slug of cold liquid that enters the rod bundle was vaporized quite rapidly, while subsequent water was boiled off in a more controlled manner. This phenomena is more common in the higher power reflood tests, but since this test has a small amount of subcooling (~16 K), it was not unexpected.

Figure B.10-45 through Figure B.10-51 are plots of the heater rod temperature at various elevations along the bundle (starting with the lowest elevation and ending with the highest). TRACE predictions match the RBHT reflood data well at low bundle elevations ($z < 0.85$ m), but consistently over predicts the peak temperature and under predicts the quench time at high elevations. This characteristic is also illustrated in Figure B.10-52 through Figure B.10-55, which are plots of the HTC at various elevations. As shown in Figure B.10-52, the HTC is under predicted by TRACE at the beginning of reflood, and is over predicted as the rods are cooled. Higher in the bundle (Figure B.10-53 through Figure B.10-55), this tendency for TRACE to under predict the HTC is more pronounced, as rods at these higher elevations take longer to quench. Thus rod temperatures at higher elevations are significantly over predicted by TRACE (Figure B.10-50 and Figure B.10-51). The steam temperature at two elevations are plotted in Figure B.10-56 and Figure B.10-57. TRACE does a pretty good job predicting the steam temperature at $z = 1.40$, but seems to predict a faster cooling of the steam at $z = 1.88$ m. It should be noted that the RBHT steam temperature data is based on an exposed fluid thermocouple. Thus, as previously mentioned, the RBHT steam temperature is the maximum reading and the drops in temperature are due to water droplets hitting the exposed thermocouple.

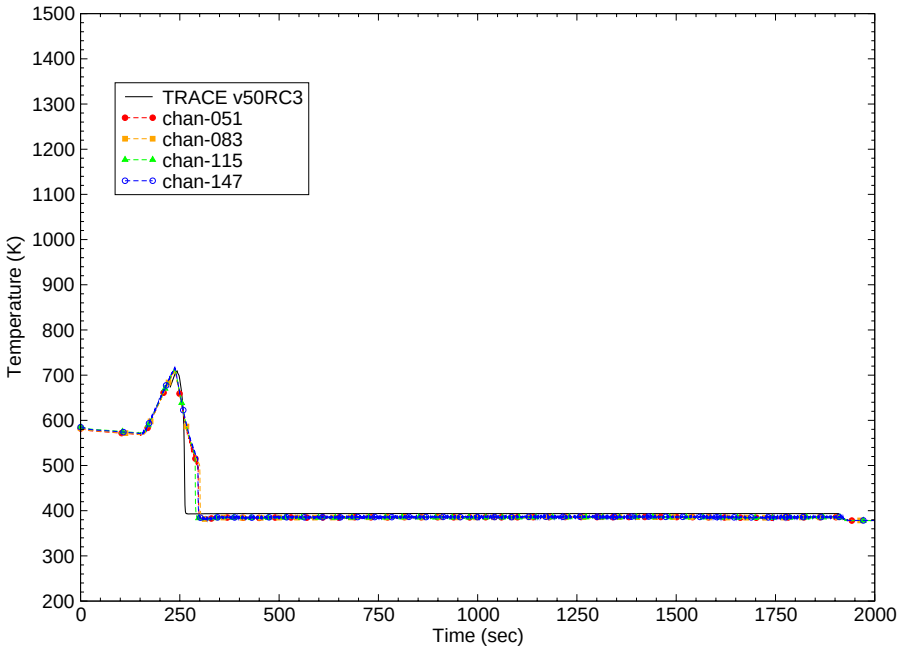

Figure B.10-45. Test 1096 Rod Temperature at z = 0.41 m

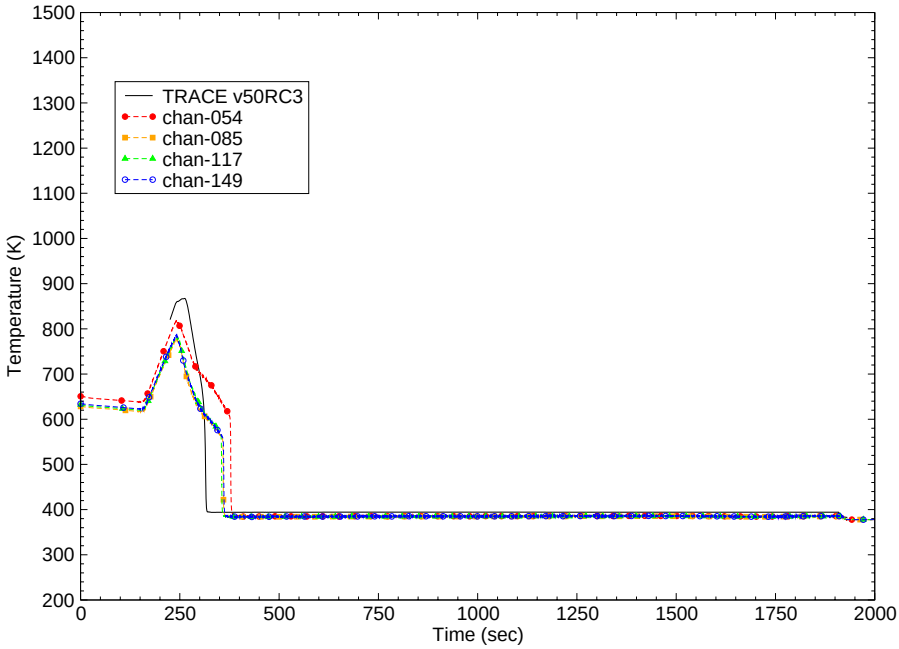

Figure B.10-46. Test 1096 Rod Temperature at z = 0.85 m

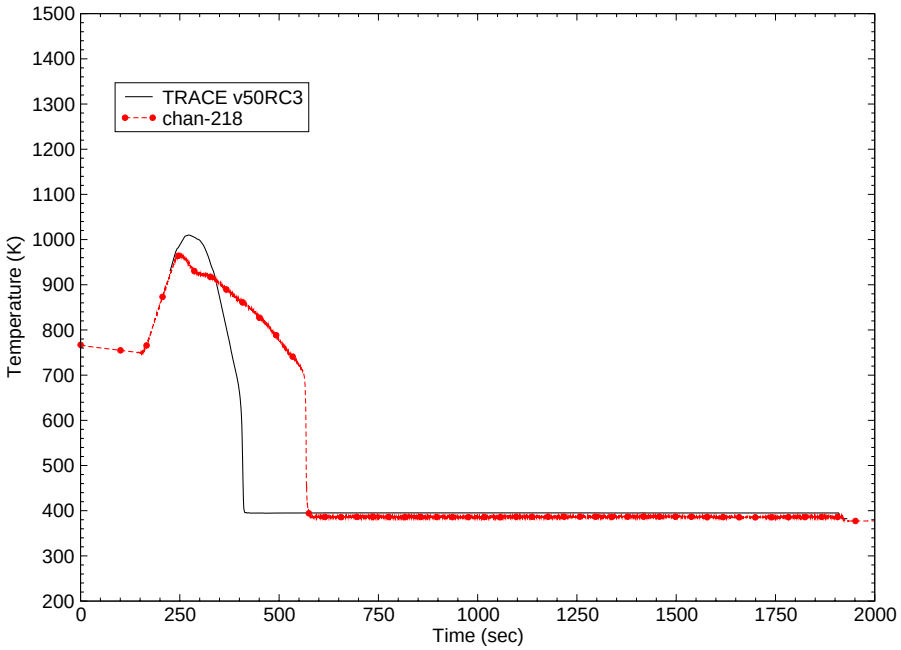

Figure B.10-47. Test 1096 Rod Temperature at z = 1.37 m

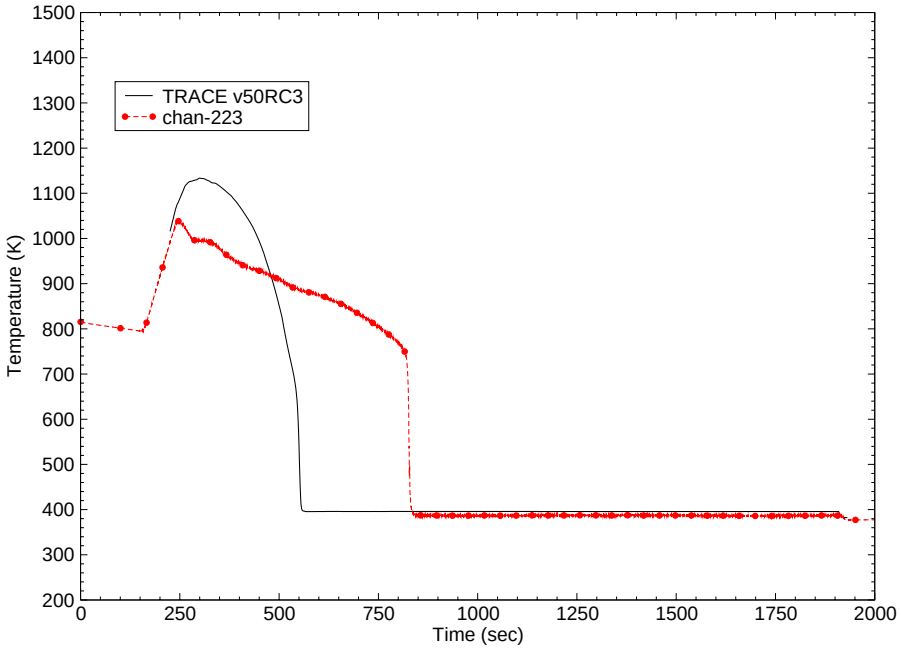

Figure B.10-48. Test 1096 Rod Temperature at z = 1.85 m

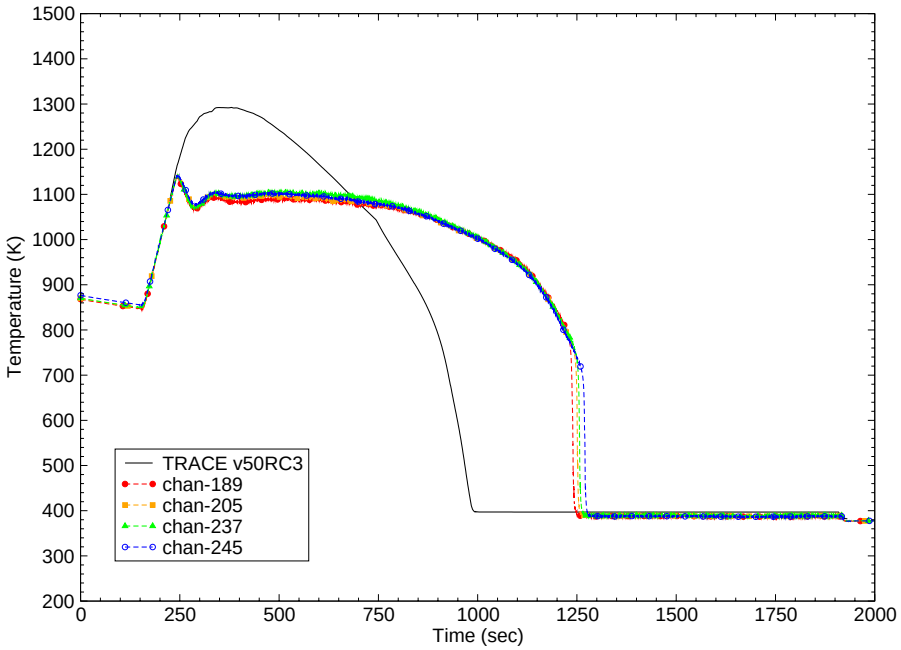

Figure B.10-49. Test 1096 Rod Temperature at z = 2.55 m

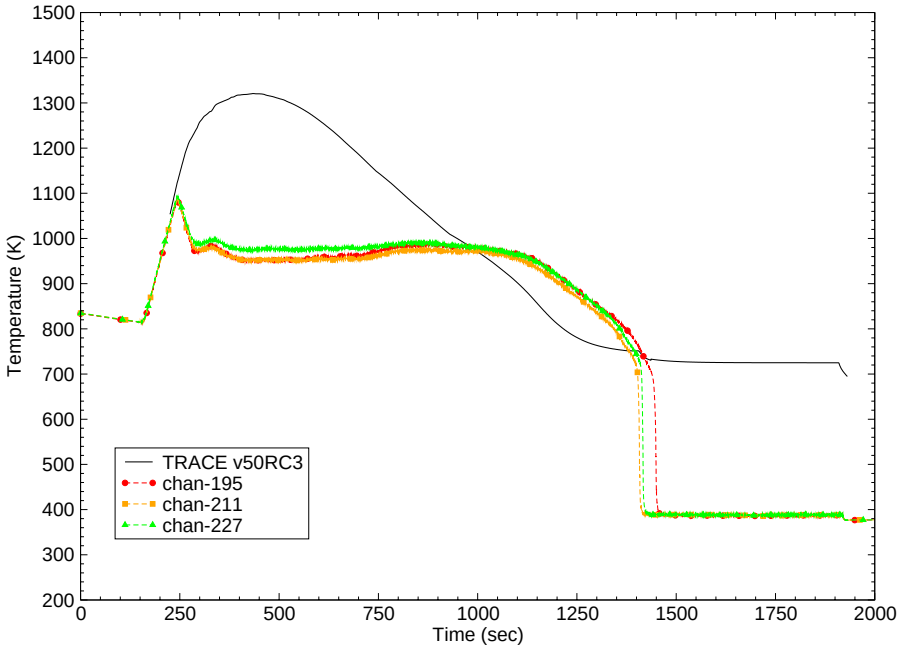

Figure B.10-50. Test 1096 Rod Temperature at z = 2.93 m

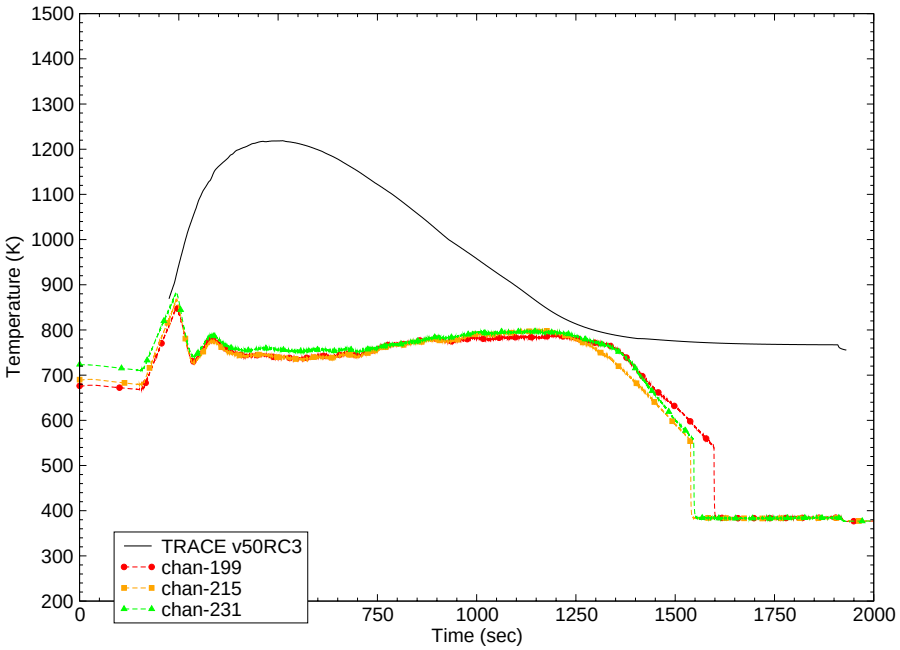

Figure B.10-51. Test 1096 Rod Temperature at z = 3.34 m

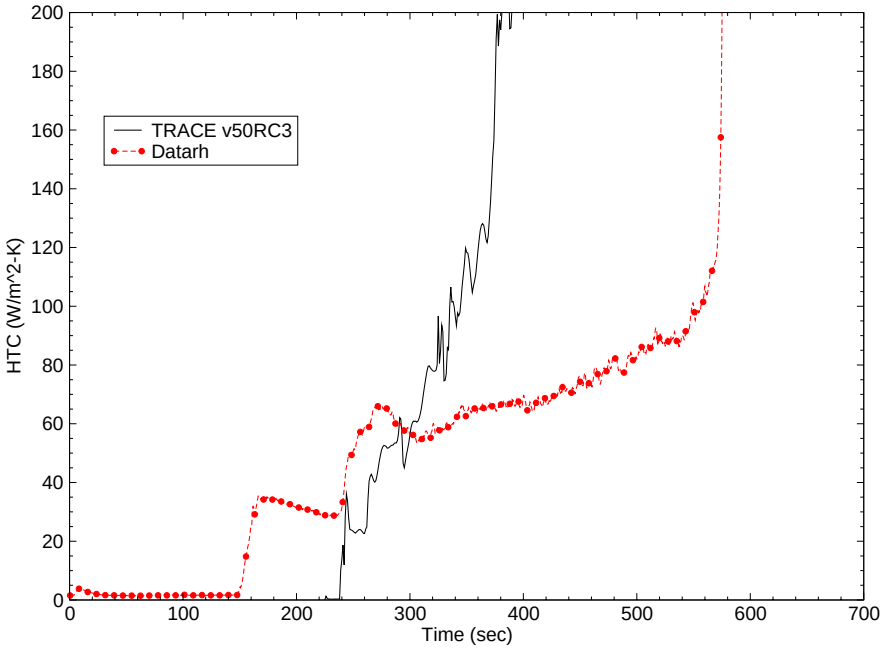

Figure B.10-52. Test 1096 HTC at z = 1.40 m

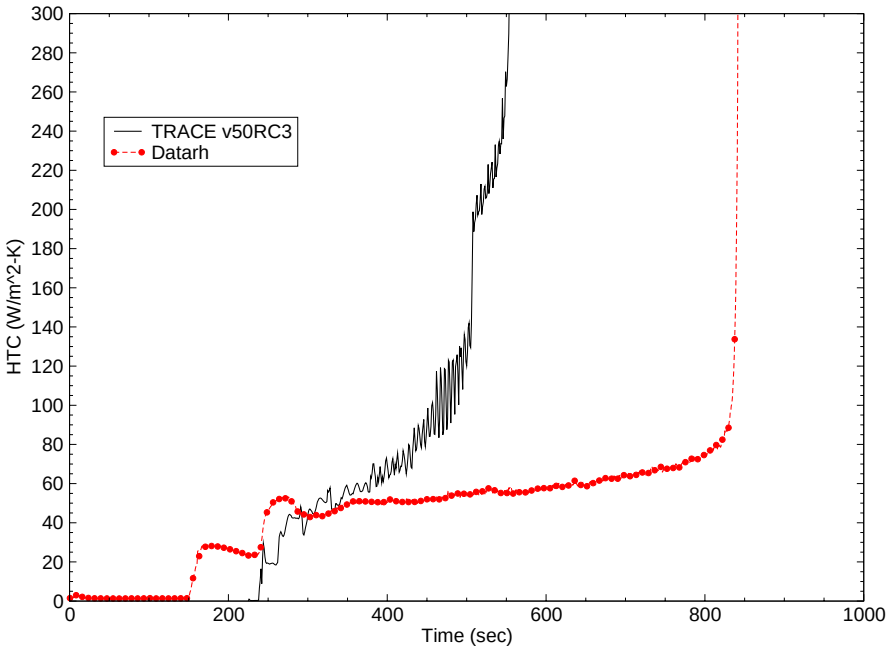

Figure B.10-53. Test 1096 HTC at z = 1.88 m

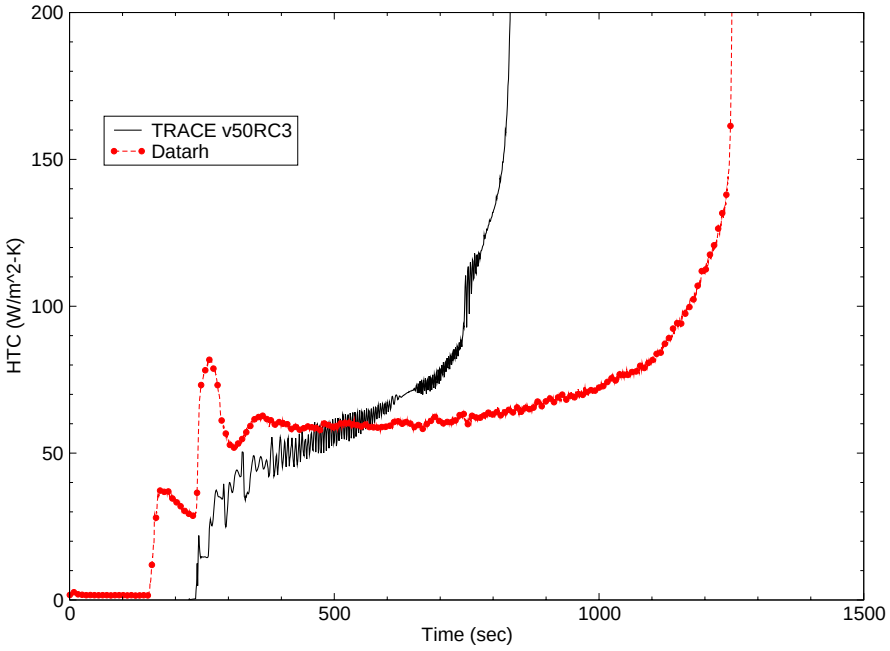

Figure B.10-54. Test 1096 HTC at z = 2.54 m

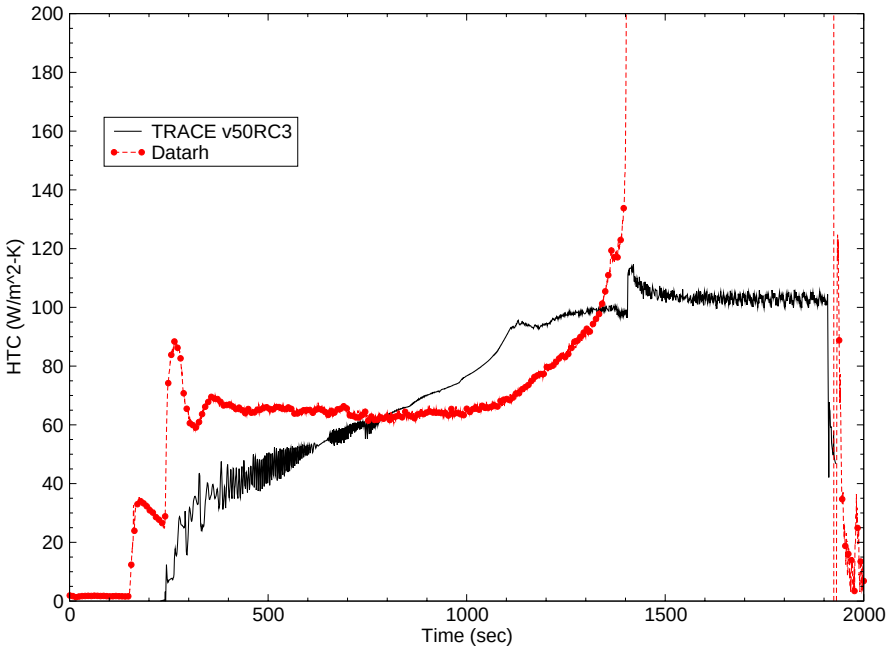

Figure B.10-55. Test 1096 HTC at z = 2.93 m

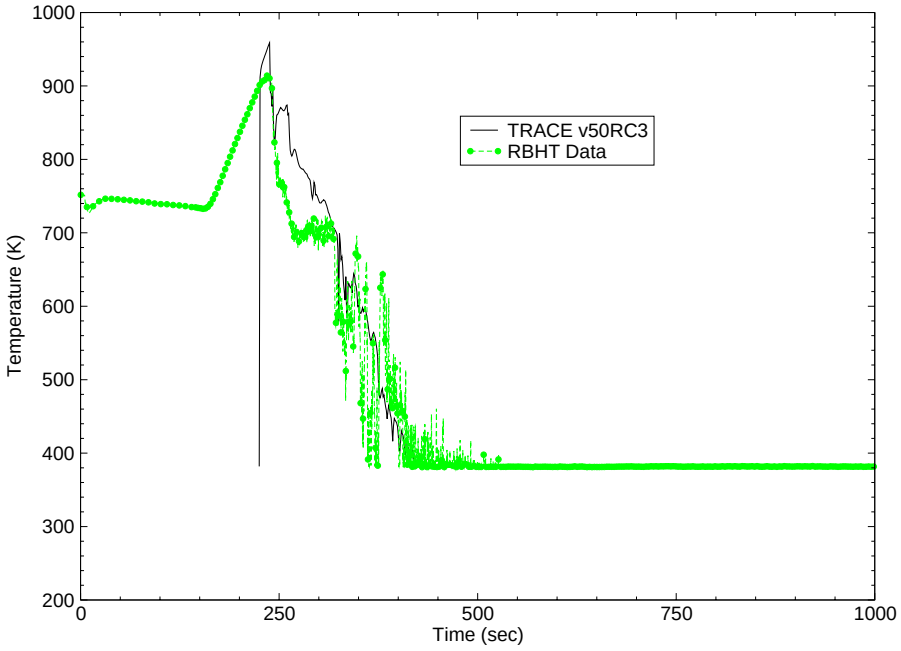

Figure B.10-56. Test 1096 Steam Temperature at z = 1.40 m

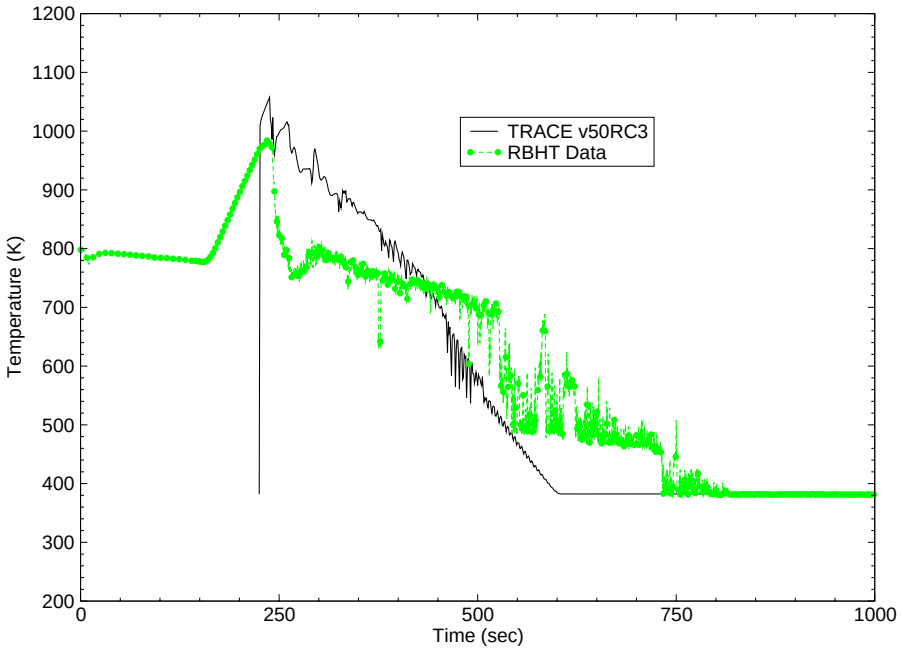

Figure B.10-57. Test 1096 Steam Temperature at z = 1.88 m

B.10.4.5. Test 1170 Comparisons

RBHT Test 1170 is the first of three high power (P = 251 kW), high liquid injection rate reflood cases that will be presented in this report. The previous three assessments discussed in this report (Tests 1096, 1108, and 1383) can be considered the low power (P = 143 kW) cases. RBHT Test 1170 was conducted at 0.23 MPa, an injection flow rate of 0.74 kg/s (6 in/sec), which is a relatively high pressure and high injection flow rate, and a subcooling of 16 K. Figure B.10-58 is a plot of the collapsed liquid level for this test and shows that TRACE significantly under predicted the liquid level at all times. This is due in part because of a rapid quenching of the RBHT rods in the lower portion of the bundle, which caused a sudden increase in pressure and large steam flow rate. Figure B.10-59 is a plot of the upper plenum pressure and was fairly stable throughout the test, with exception to the initial vaporization just mentioned. Although the bundle inventory was significantly under predicted by TRACE, the heater rod temperature were fairly well predicted up to z = 1.85 m as shown in Figure B.10-60 through Figure B.10-63. TRACE did a good job predicting peak rod temperature at all elevations, but significantly over predicted quench times at higher elevations (z > 2.55 m). The HTCs for this test are shown in Figure B.10-67 through Figure B.10-70 and illustrate that TRACE does a better job predicting heat transfer at lower elevations for high power, high injection flow rate cases. Some HTC trends are predicted well in the beginning of the reflood transient, but there is a large variation in TRACE's ability to predict HTCs at all elevations.

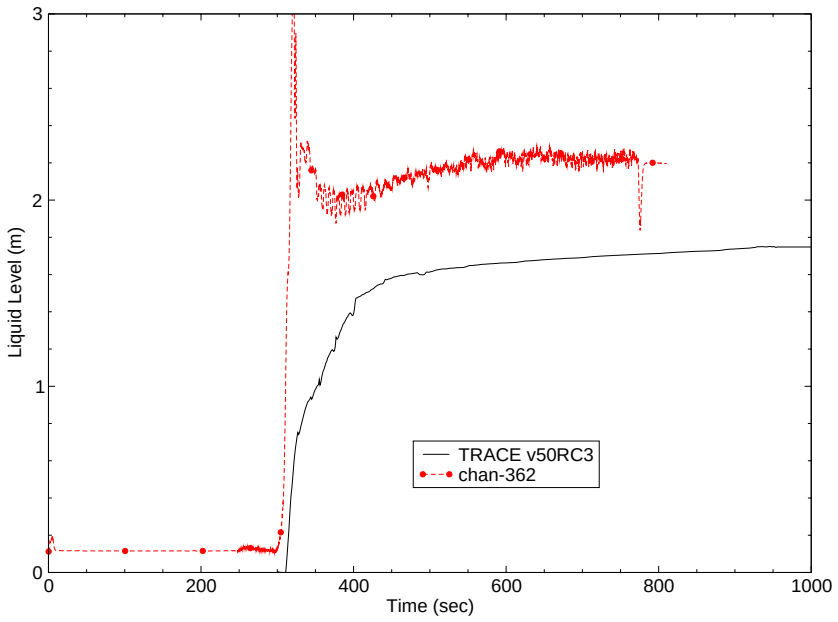

Figure B.10-58. Test 1170 Bundle Collapsed Liquid Level

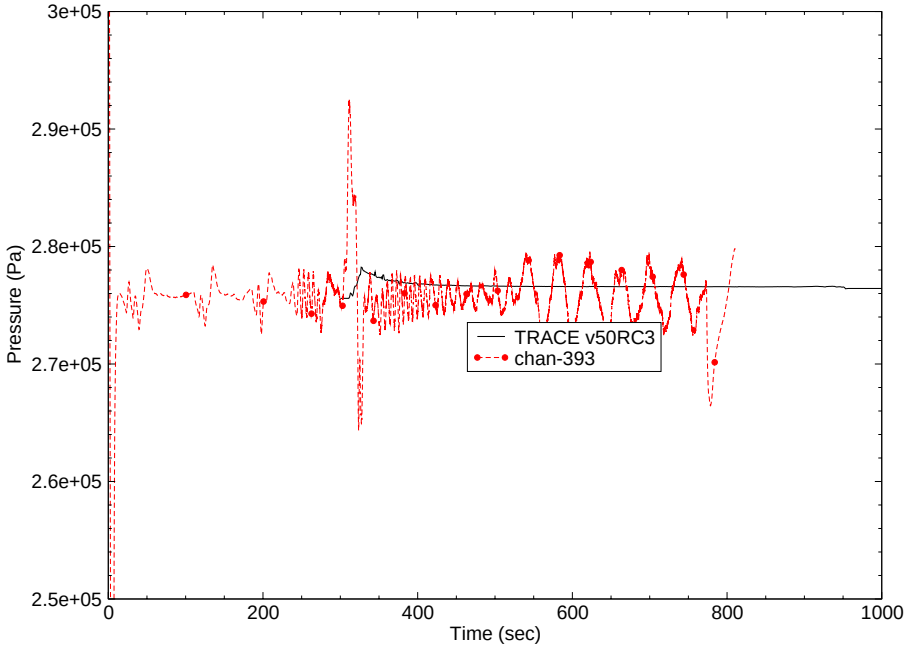

Figure B.10-59. Test 1170 Upper Plenum Pressure

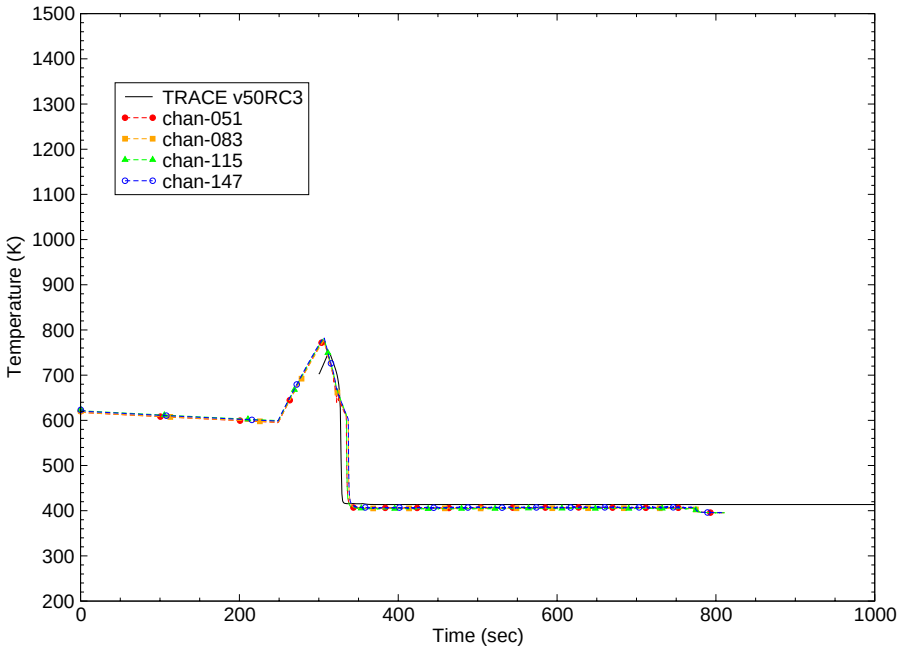

Figure B.10-60. Test 1170 Heater Rod Temperature at z = 0.41 m

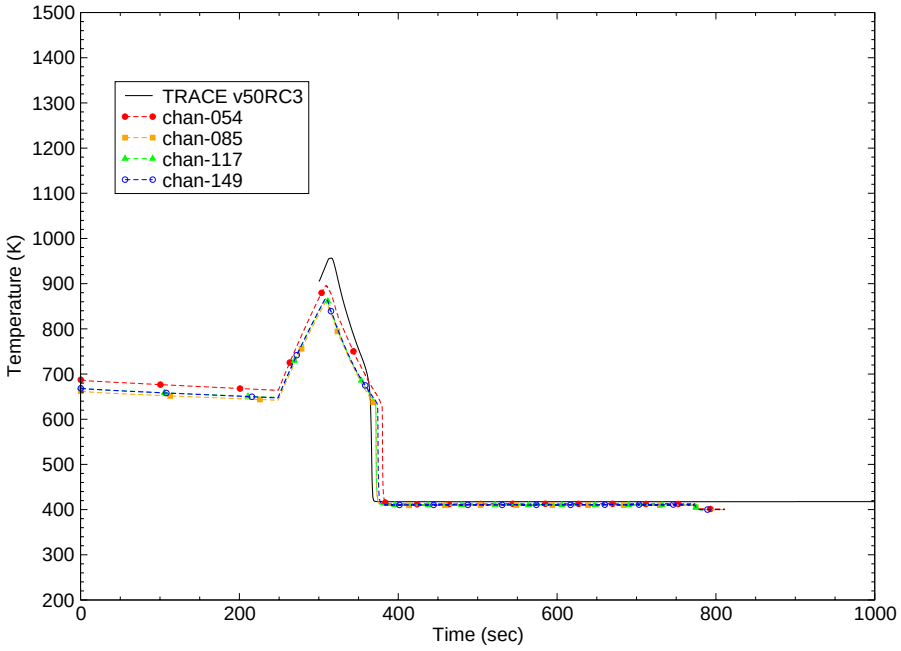

Figure B.10-61. Test 1170 Heater Rod Temperature at z = 0.85 m

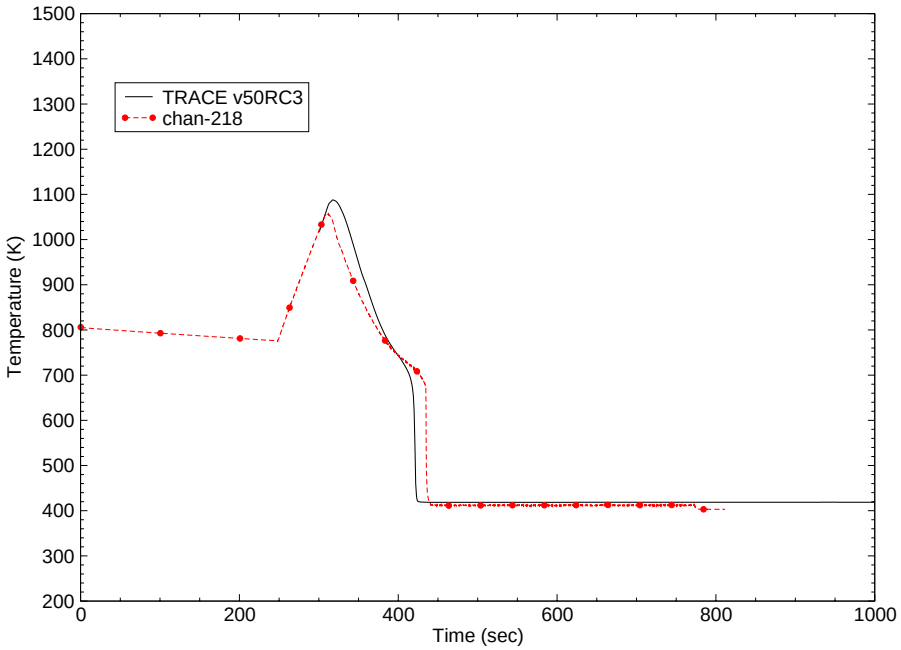

Figure B.10-62. Test 1170 Heater Rod Temperature at z = 1.37 m

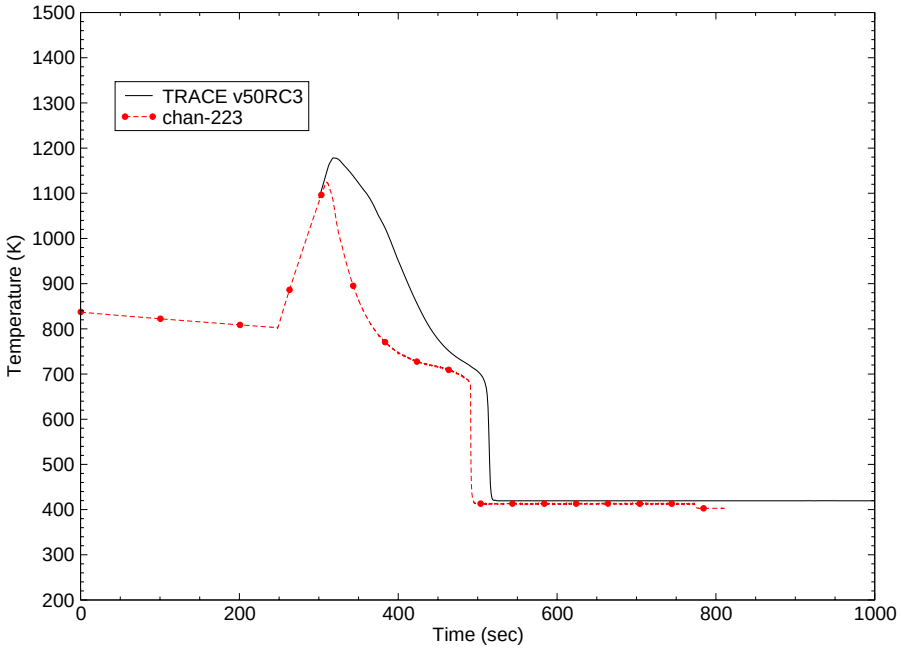

Figure B.10-63. Test 1170 Heater Rod Temperature at z = 1.85 m

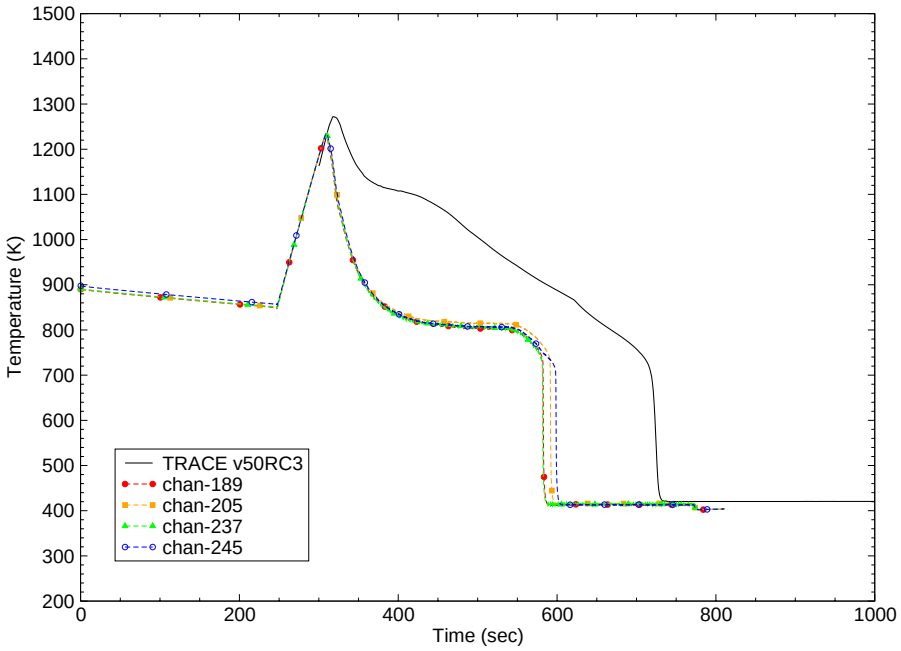

Figure B.10-64. Test 1170 Heater Rod Temperature at z = 2.55 m

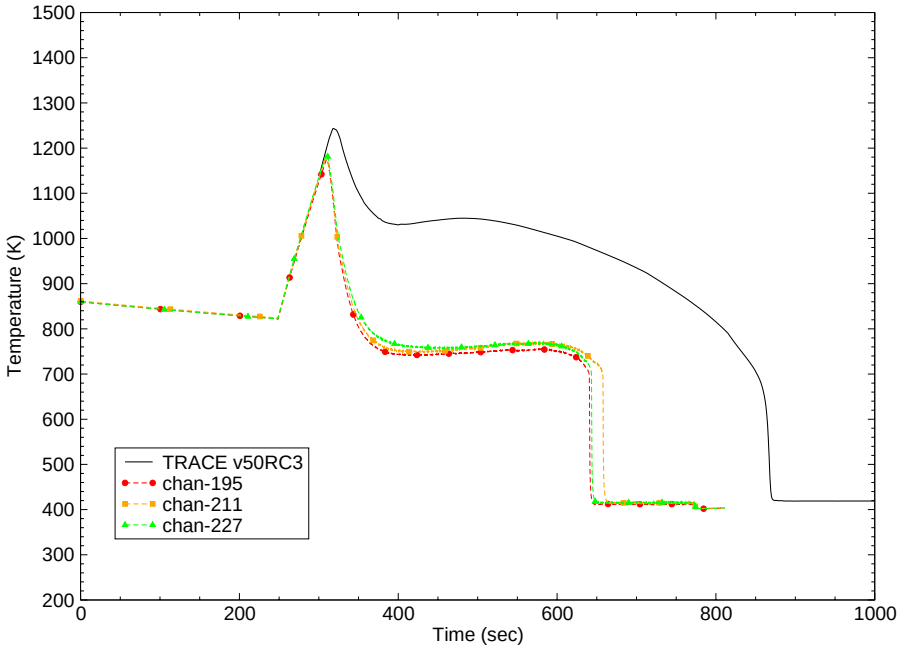

Figure B.10-65. Test 1170 Heater Rod Temperature at z = 2.93 m

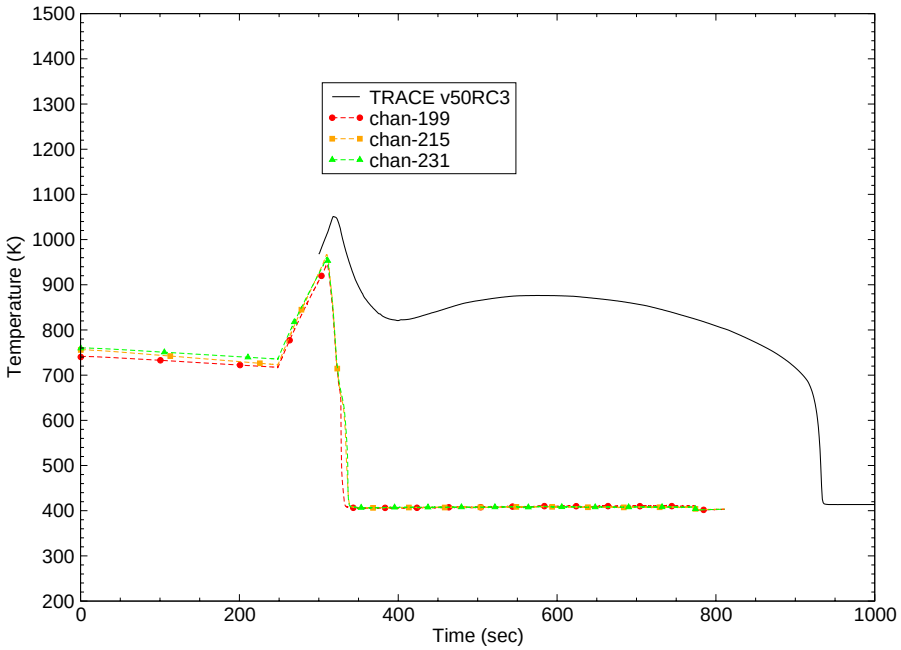

Figure B.10-66. Test 1170 Heater Rod Temperature at z = 3.34 m

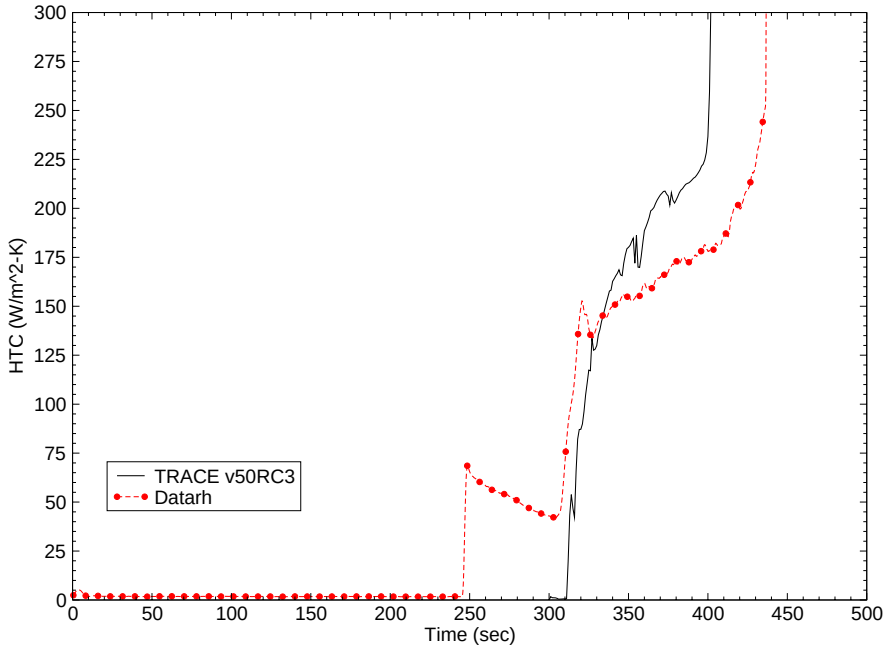

Figure B.10-67. Test 1170 HTC at z = 1.40 m

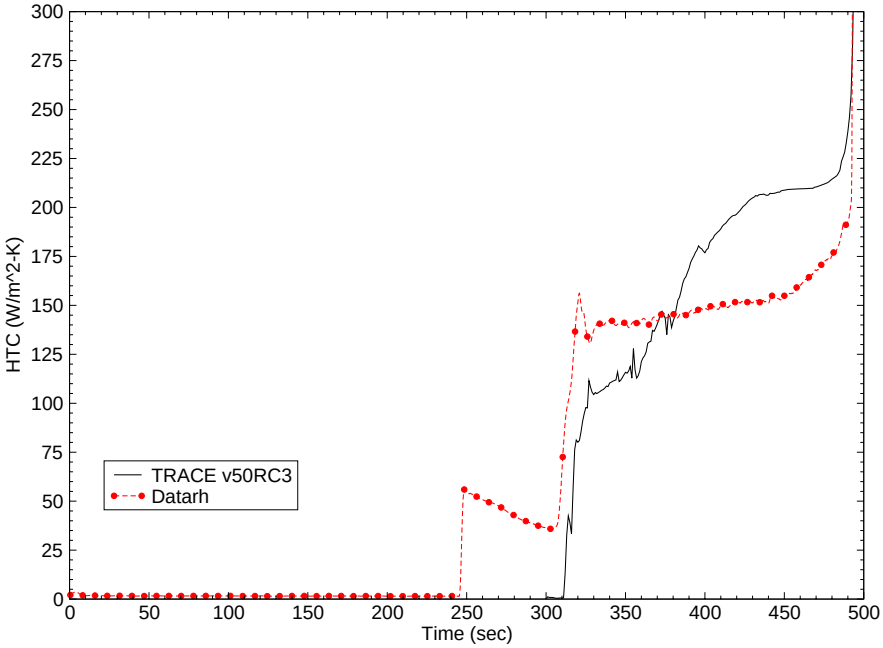

Figure B.10-68. Test 1170 HTC at z = 1.88 m

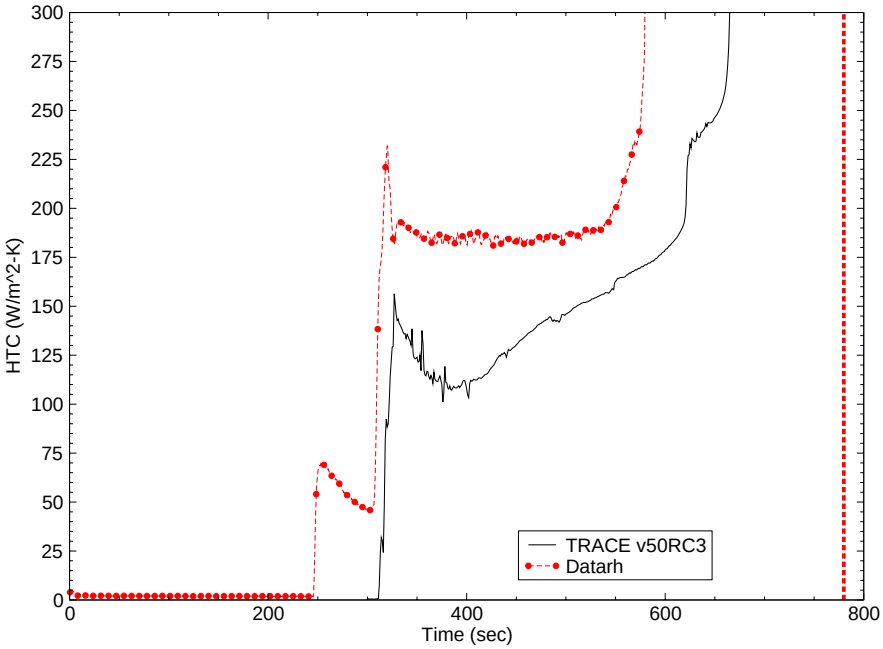

Figure B.10-69. Test 1170 HTC at z = 2.54 m

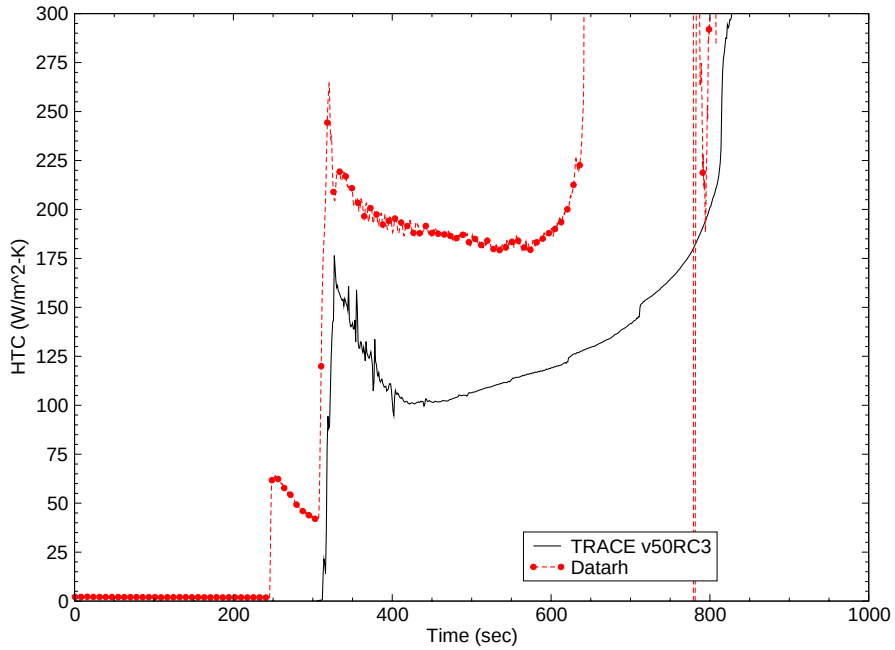

Figure B.10-70. Test 1170 HTC at z = 2.93 m

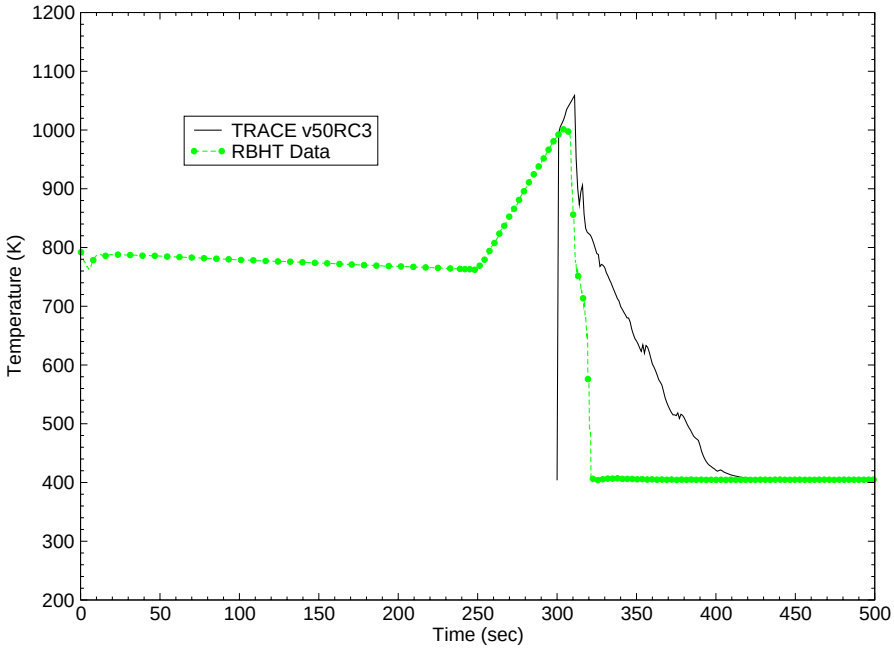

Figure B.10-71. Test 1170 Steam Temperatures at z = 1.40 m

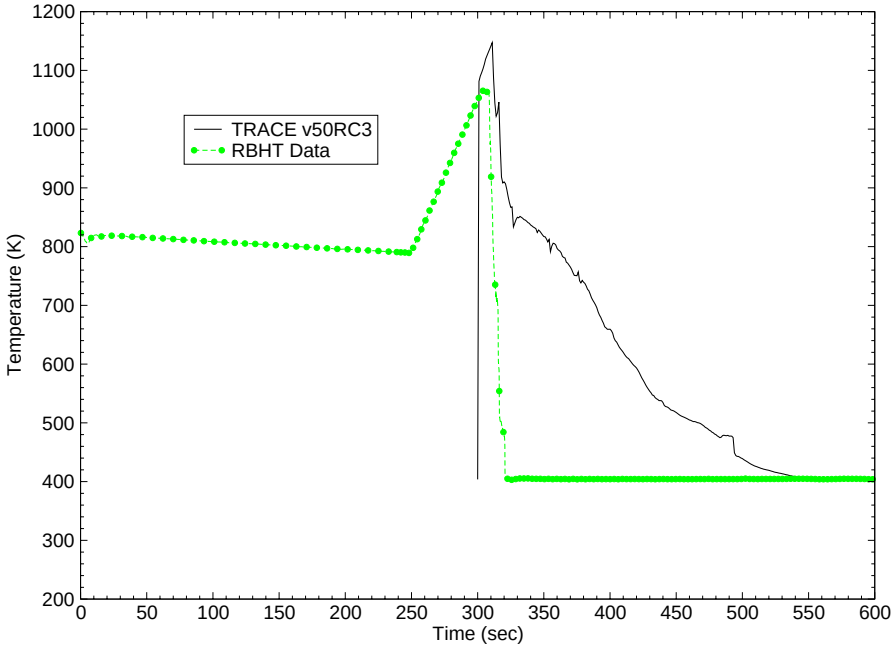

Figure B.10-72. Test 1170 Steam Temperatures at z = 1.88 m

The steam temperature at two elevations are plotted in Figure B.10-71 and Figure B.10-72. TRACE over predicts the steam temp at both elevations for all times, which is consistent with previous plots of rod temperature and HTCs.

B.10.4.6. Test 1196 Comparisons

RBHT Test 1196 was conducted at 0.23 MPa, an injection flow rate of 0.74 kg/s (6 in/sec), which is a relatively high pressure and high injection flow rate, and a subcooling of 59 K. Basically, the same conditions as Test 1170, except for 43 K increased in subcooling. Figure B.10-73 is a plot of bundle collapsed liquid level and Figure B.10-74 is a plot of upper plenum pressure. In this test, TRACE did a good job predicting bundle inventory and the upper plenum pressure was relatively stable during the entire test. Figure B.10-75 through Figure B.10-81 are plots of heater rod temperature for Test 1196. Similar to Test 1170, TRACE only slightly over predicts peak rod temperature, but for Test 1196, TRACE also does a reasonable job predicting quench times at all elevations. However, the rod heater temperature trend during reflood (300 sec < t < 400 sec) at higher elevations (z > 2.55 m) is not predicted well by TRACE. Figure B.10-82 through Figure B.10-85 show large oscillations in the HTC at all elevations during the initial rod heatup. These oscillations are consistent with the oscillations seen in the collapsed liquid level (Figure B.10-73) and are most likely due to the intermittent way TRACE handles boiling in a vertical rod bundle.

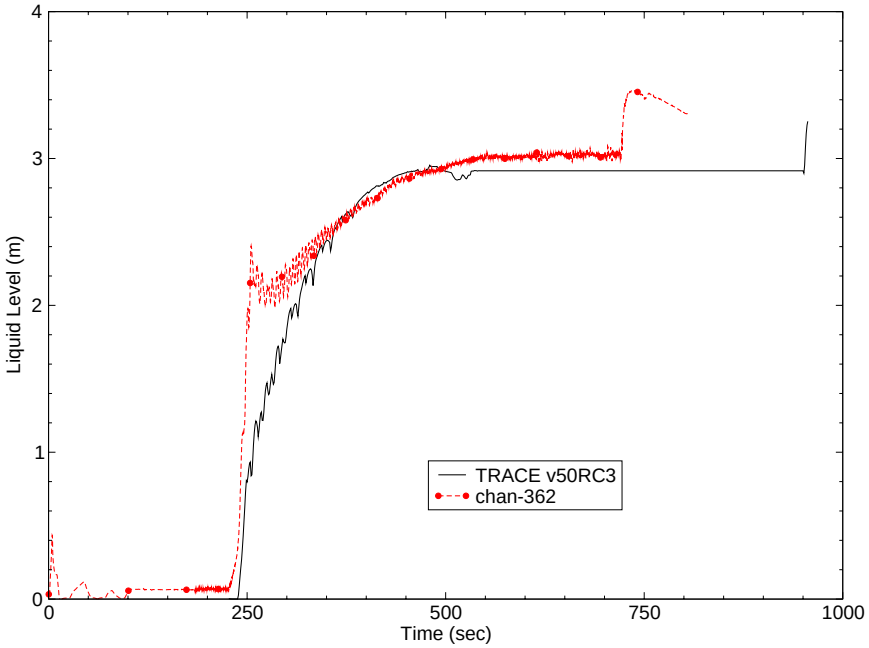

Figure B.10-73. Test 1196 Bundle Collapsed Liquid Level

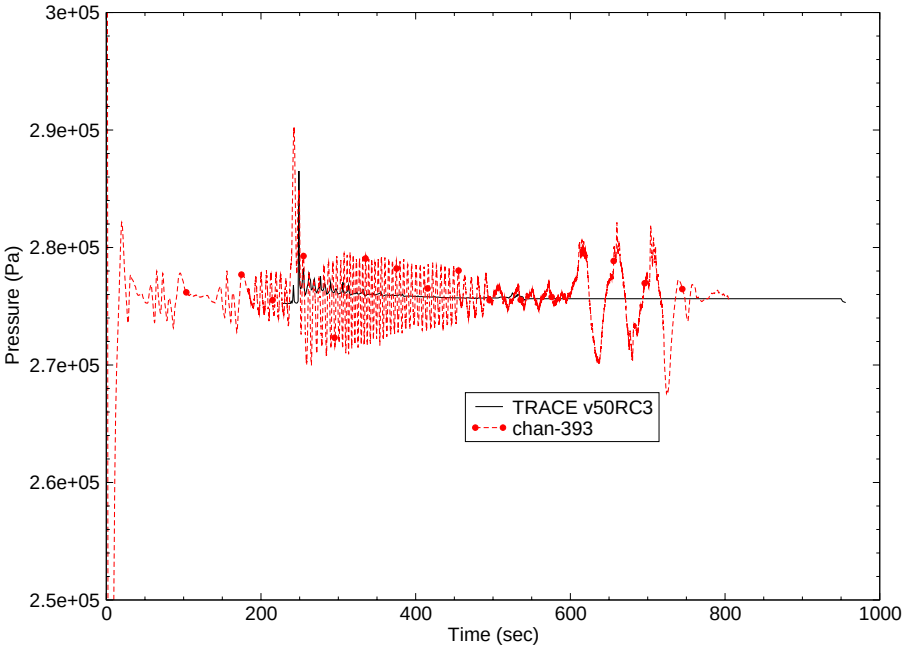

Figure B.10-74. Test 1196 Upper Plenum Pressure

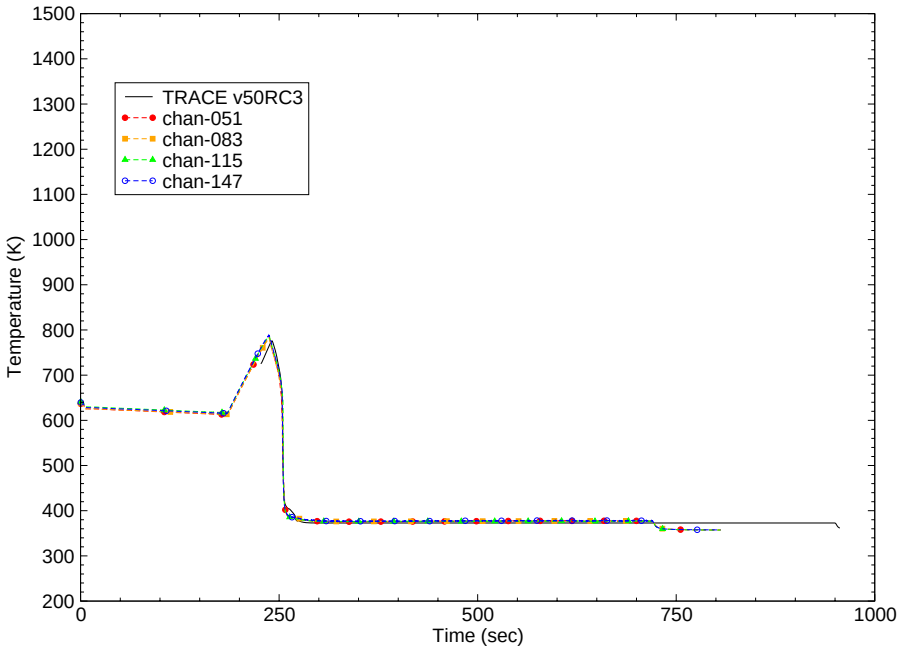

Figure B.10-75. Test 1196 Heater Rod Temperature at z = 0.41 m

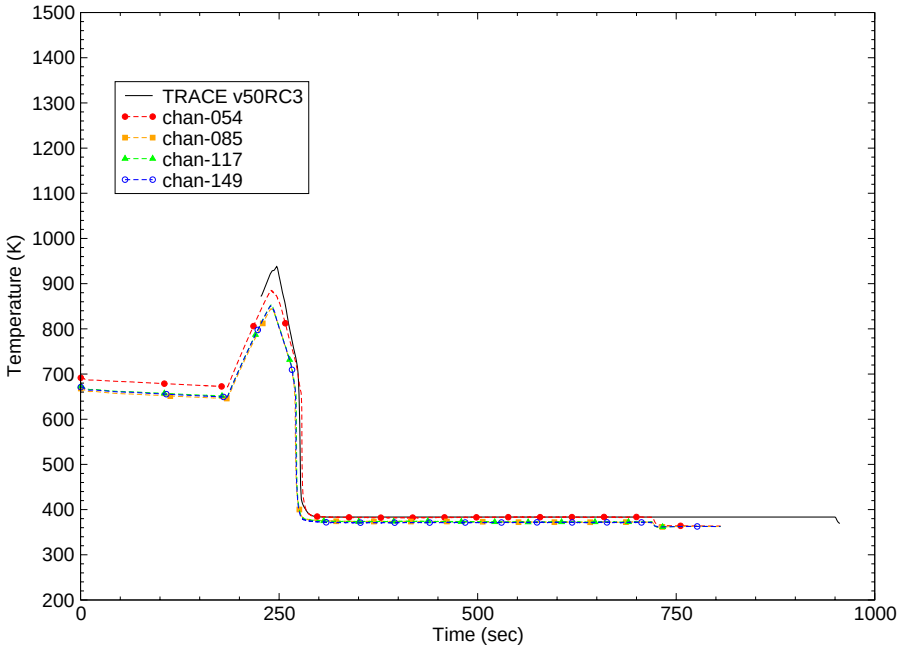

Figure B.10-76. Test 1196 Heater Rod Temperature at z = 0.85 m

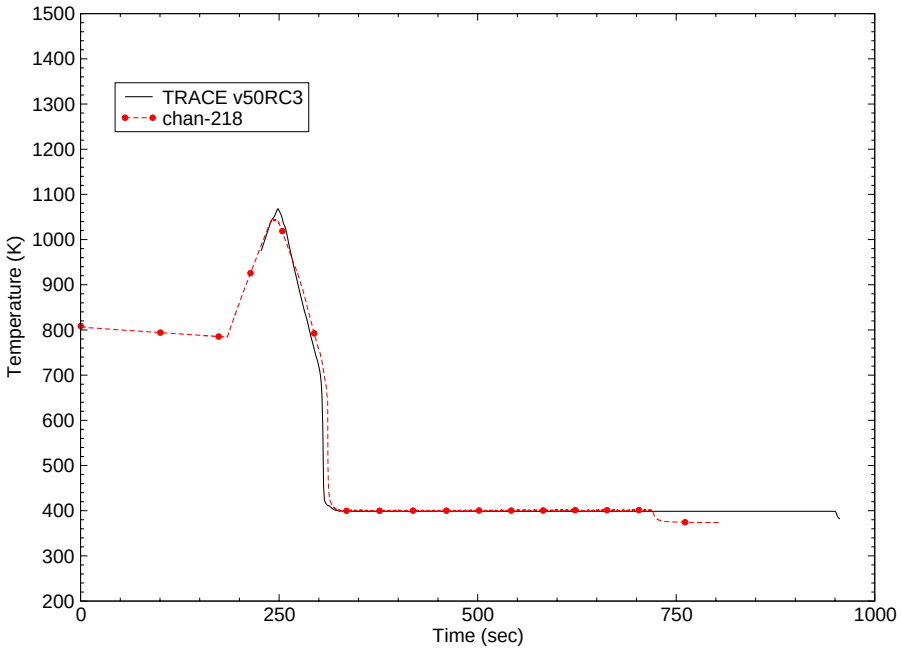

Figure B.10-77. Test 1196 Heater Rod Temperature at z = 1.37 m

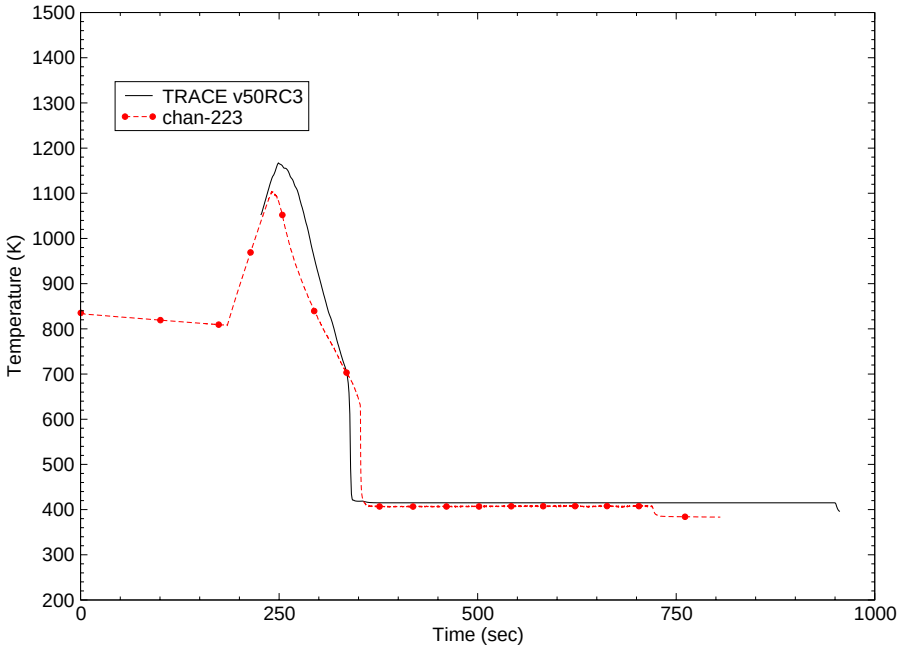

Figure B.10-78. Test 1196 Heater Rod Temperature at z = 1.85 m

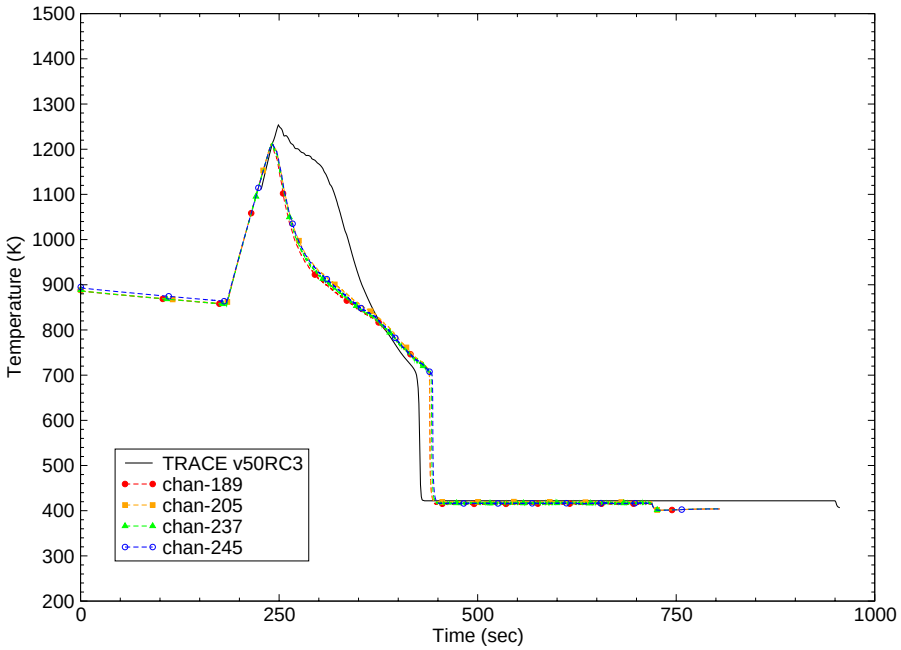

Figure B.10-79. Test 1196 Heater Rod Temperature at z = 2.55 m

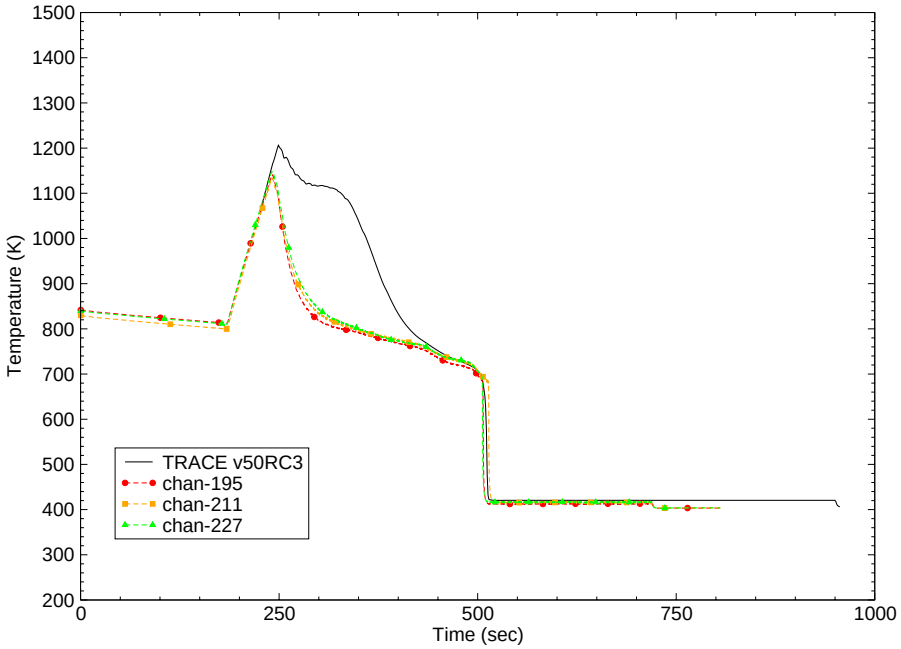

Figure B.10-80. Test 1196 Heater Rod Temperature at z = 2.93 m

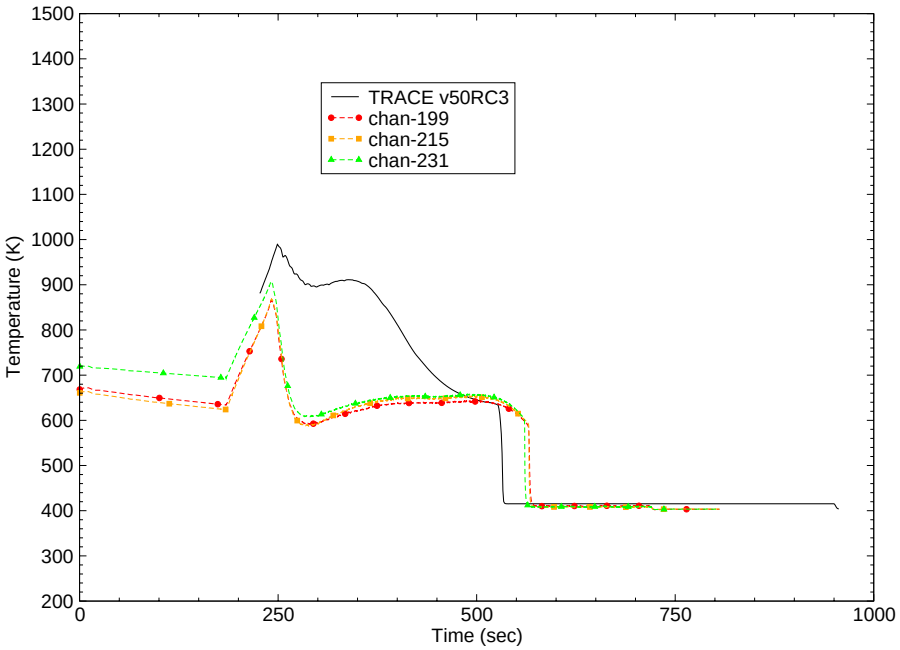

Figure B.10-81. Test 1196 Heater Rod Temperature at z = 3.34 m

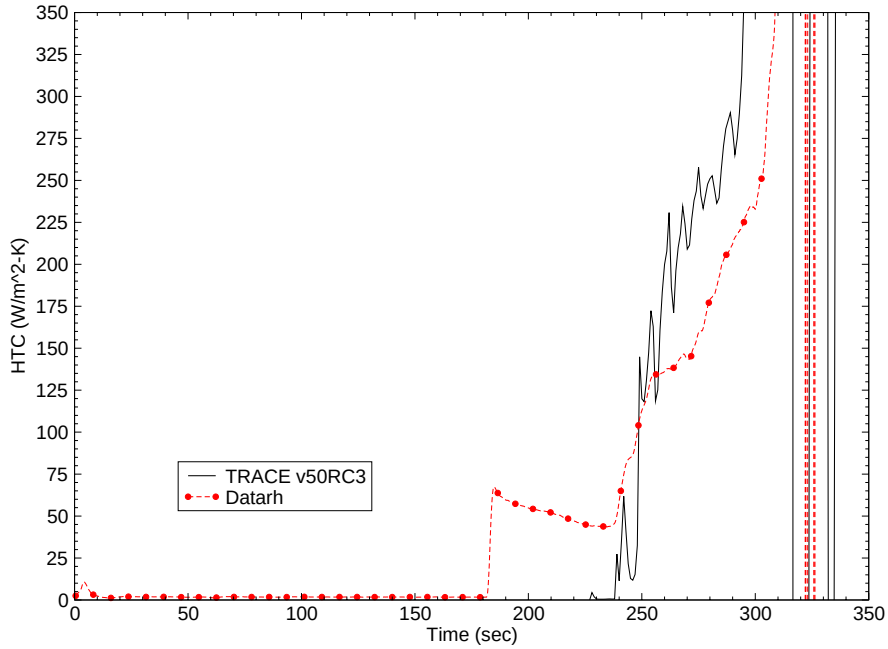

Figure B.10-82. Test 1196 HTC at z = 1.40 m

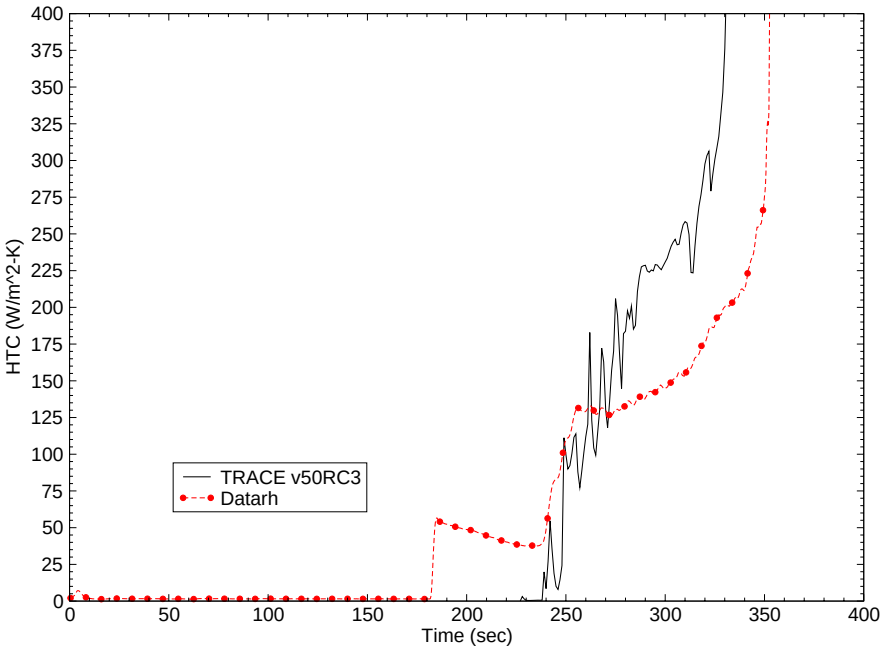

Figure B.10-83. Test 1196 HTC at z = 1.88 m

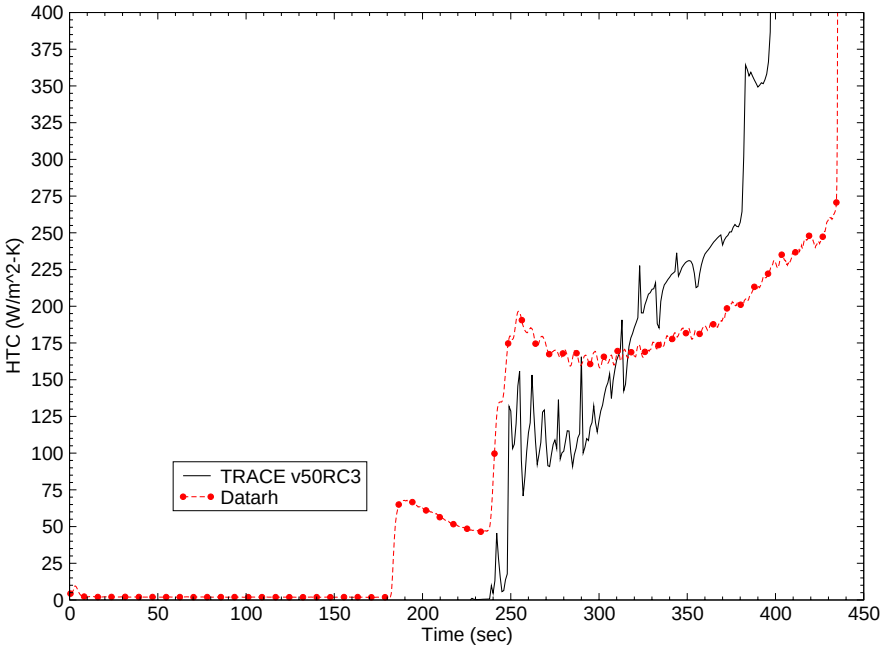

Figure B.10-84. Test 1196 HTC at z = 2.54 m

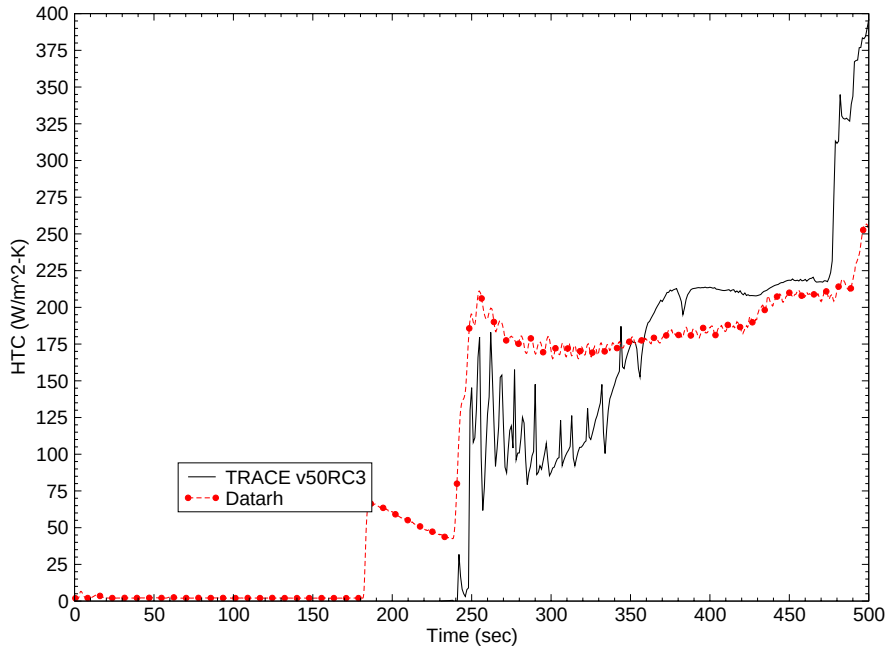

Figure B.10-85. Test 1196 HTC at z = 2.93 m

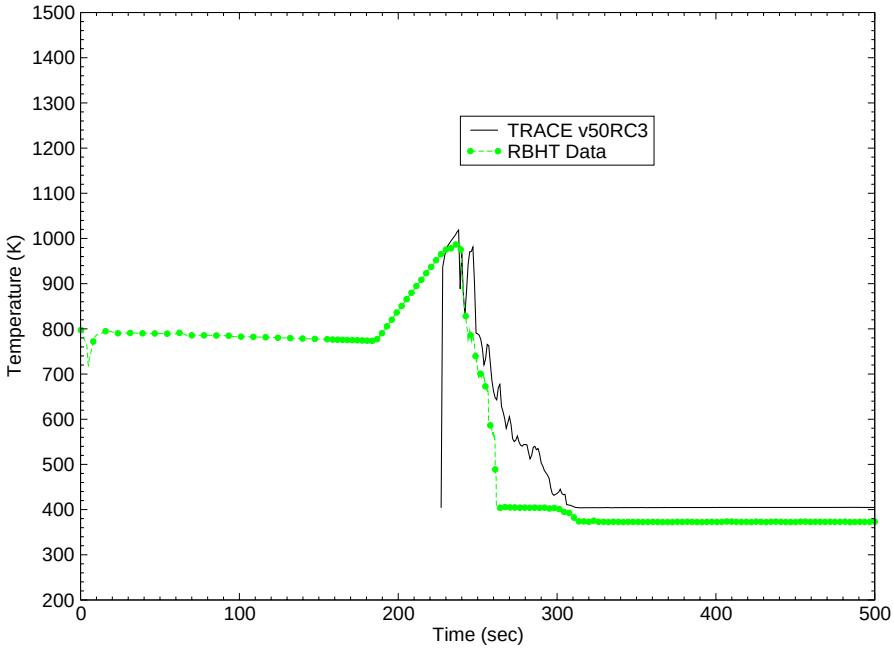

Figure B.10-86. Test 1196 Steam Temperatures at z = 1.40 m

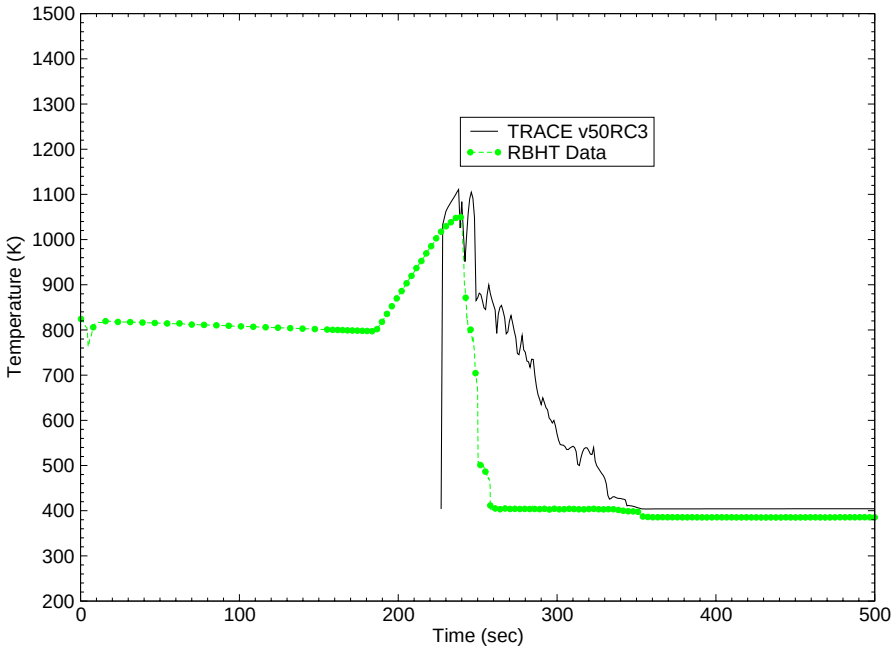

Figure B.10-87. Test 1196 Steam Temperatures at z = 1.88 m

The steam temperature at two elevations are plotted in Figure B.10-86 and Figure B.10-87. TRACE over predicts the steam temp at both elevations for all times, which is consistent with previous plots of rod temperature and HTCs.

B.10.4.7. Test 1285 Comparisons

RBHT Test 1285 was conducted at 0.23 MPa, an injection flow rate of 0.74 kg/s, which is a relatively high pressure and high injection flow rate, and a subcooling of 86 K. Basically, the same conditions as Test 1170, except for 70 K increased in subcooling. Figure B.10-73 is a plot of bundle collapsed liquid level and Figure B.10-74 is a plot of upper plenum pressure. In this test, TRACE did a good job predicting bundle inventory, except during the initial rapid vaporization, and the upper plenum pressure was relatively stable during the entire test. Figure B.10-75 through Figure B.10-81 are plots of heater rod temperature for Test 1285. Similar to Test 1170, TRACE only slightly over predicts peak rod temperature, but for Test 12856, TRACE also does a reasonable job predicting quench times at all elevations. However, the rod heater temperature trend during reflood (300 sec < t < 400 sec) at higher elevations (z > 2.55 m) is not predicted well by TRACE. Figure B.10-82 through Figure B.10-85 show large oscillations in the HTC at all elevations during the initial rod heatup. These oscillations are consistent with the oscillations seen in the collapsed liquid level (Figure B.10-73) and are most likely due to the intermittent way TRACE handles boiling in a vertical rod bundle. Test 1285 assessment results are essentially the same as for Test 1196, except that TRACE does a slightly better job predicting peak rod temperatures and quench times as compared to Tests 1170 and 1196.

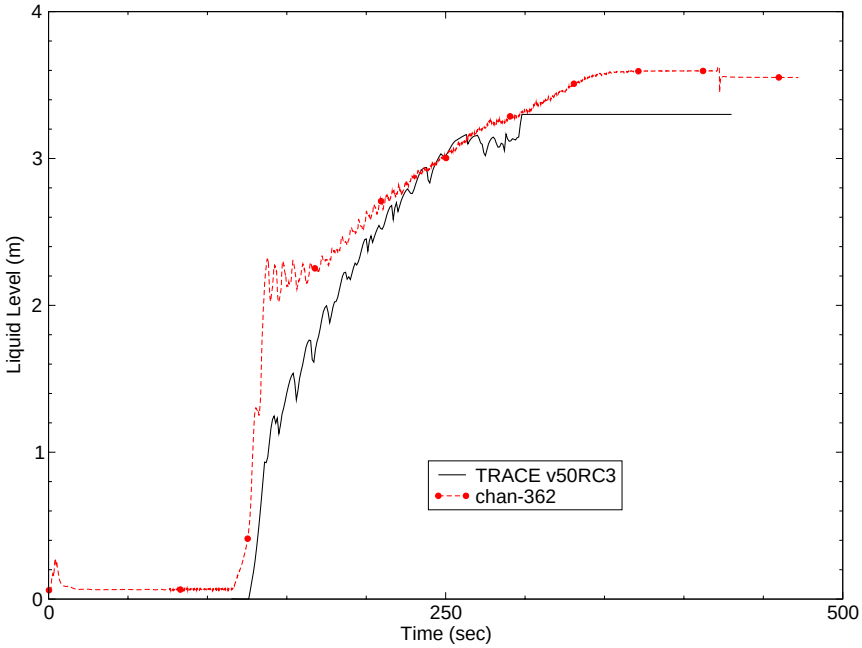

Figure B.10-88. Test 1285 Bundle Collapsed Liquid Level

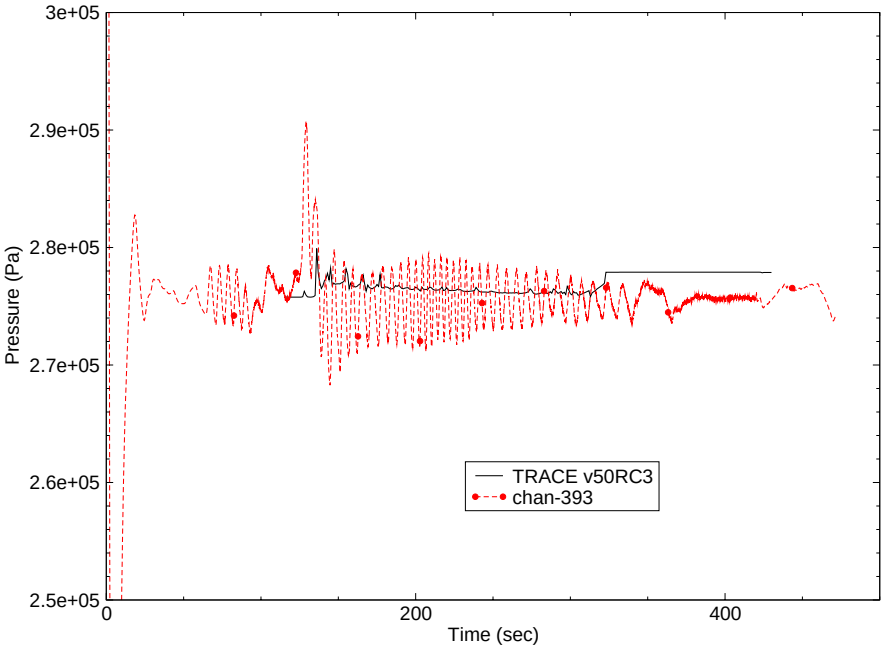

Figure B.10-89. Test 1285 Upper Plenum Pressure

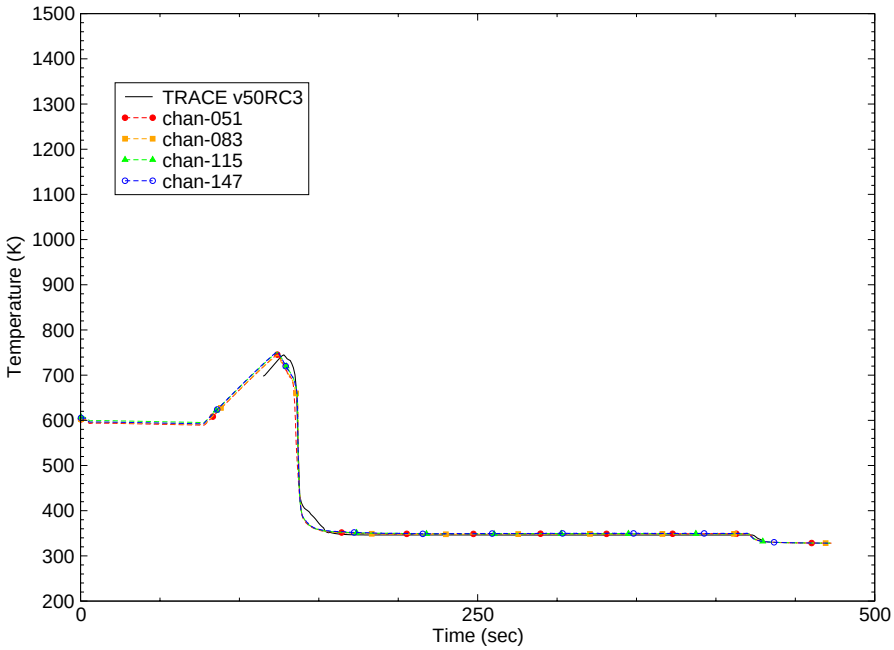

Figure B.10-90. Test 1285 Heater Rod Temperature at z = 0.41 m

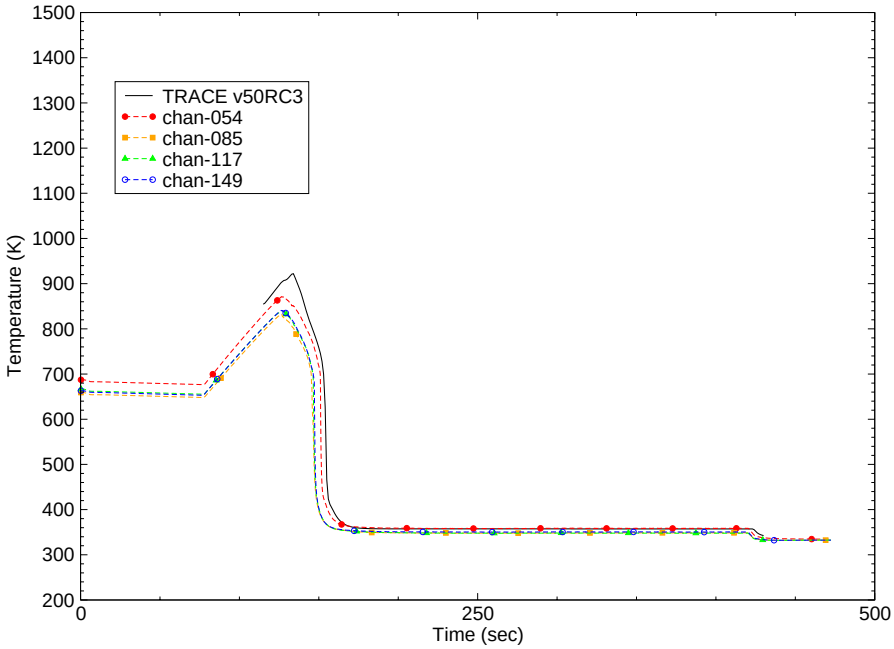

Figure B.10-91. Test 1285 Heater Rod Temperature at z = 0.85 m

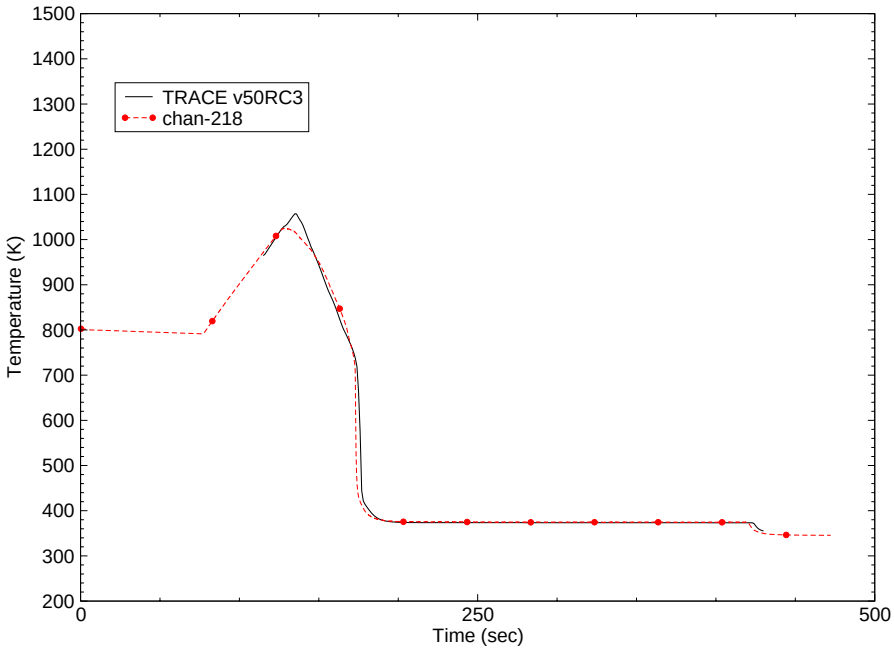

Figure B.10-92. Test 1285 Heater Rod Temperature at z = 1.37 m

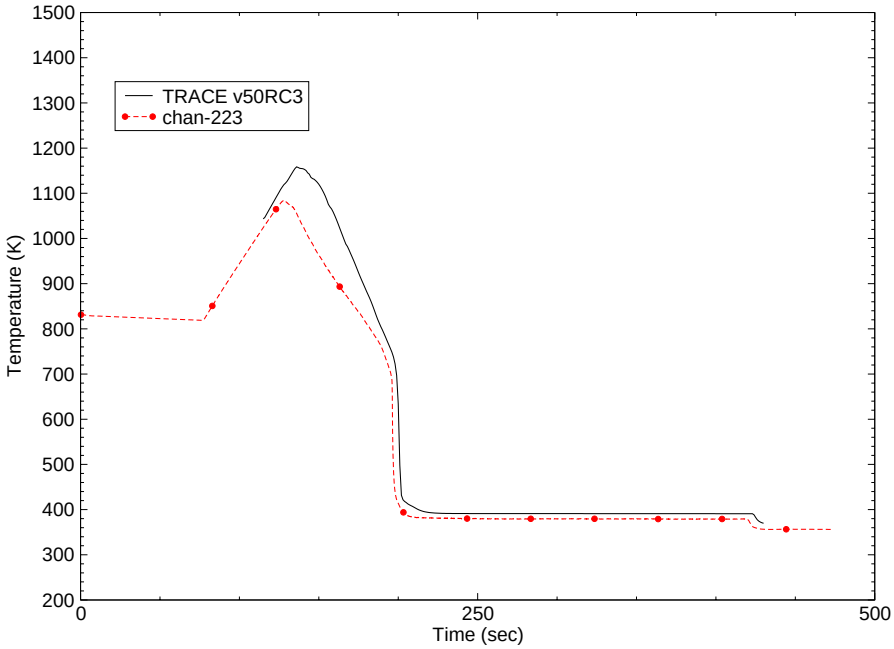

Figure B.10-93. Test 1285 Heater Rod Temperature at z = 1.85 m

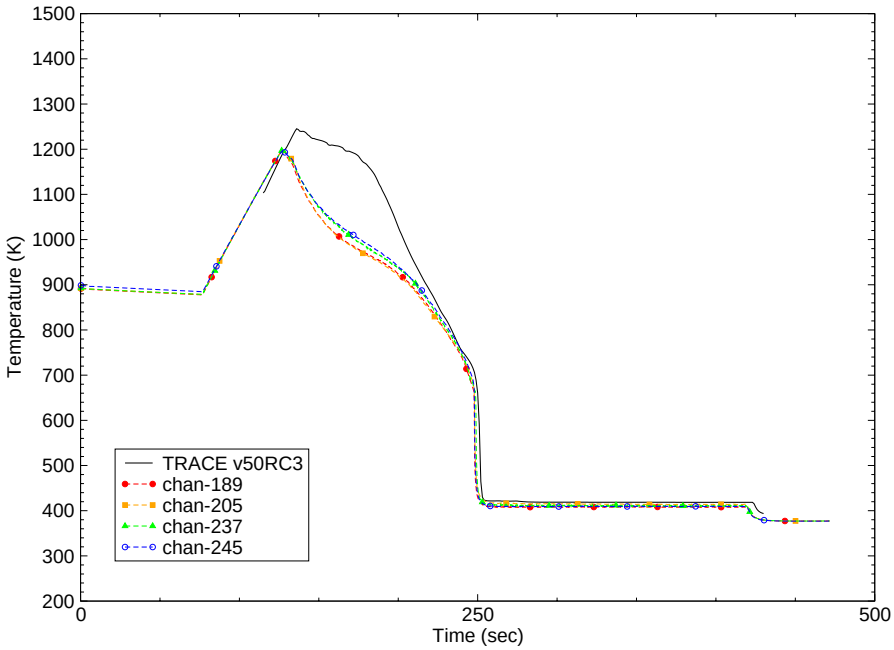

Figure B.10-94. Test 1285 Heater Rod Temperature at z = 2.55 m

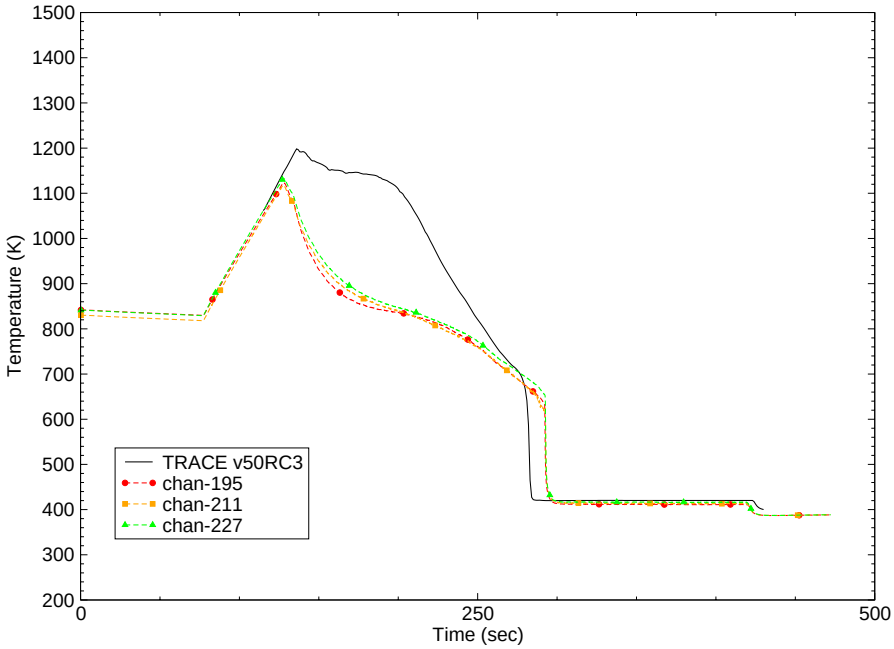

Figure B.10-95. Test 1285 Heater Rod Temperature at z = 2.93 m

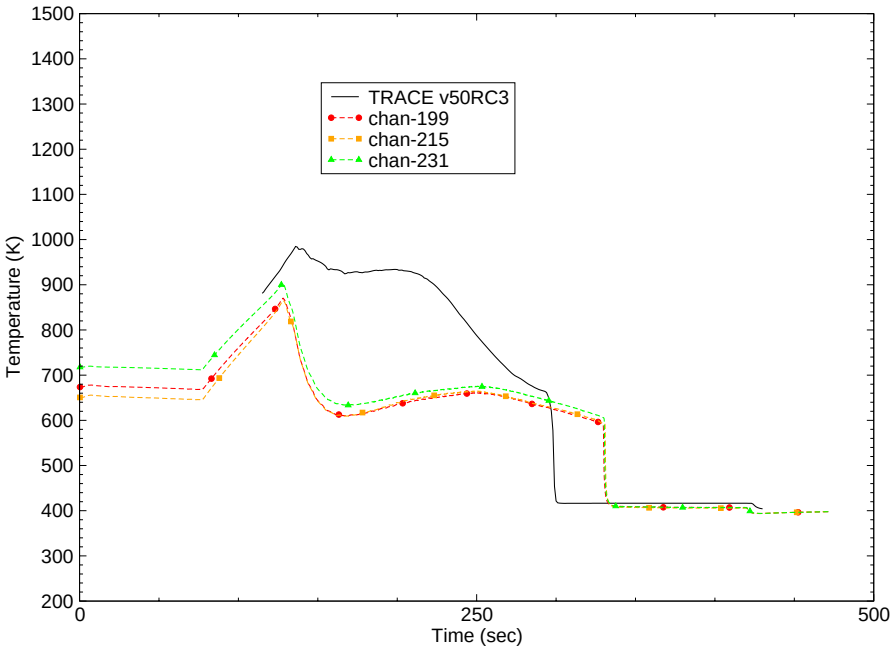

Figure B.10-96. Test 1285 Heater Rod Temperature at z = 3.34 m

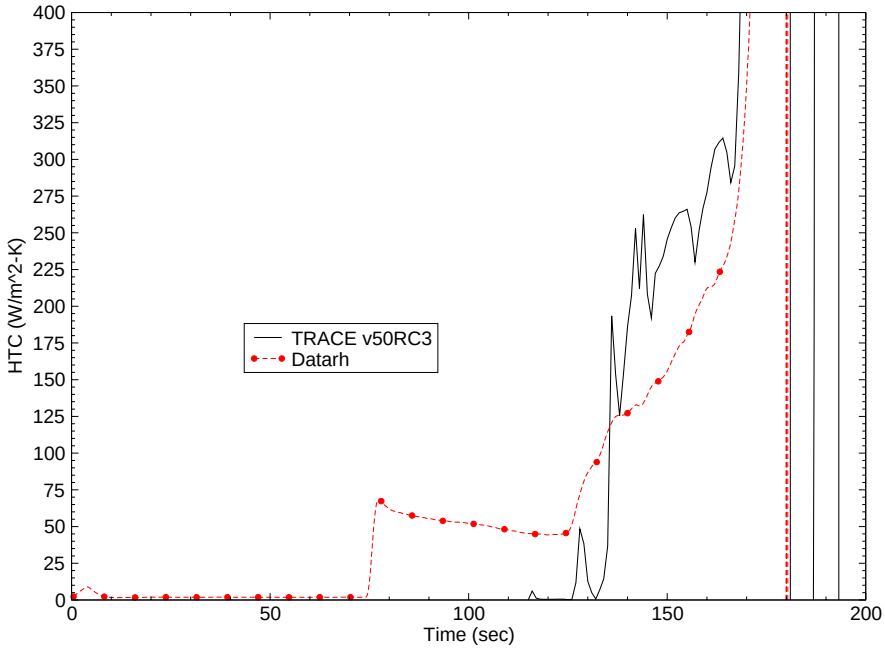

Figure B.10-97. Test 1285 HTC at z = 1.40 m

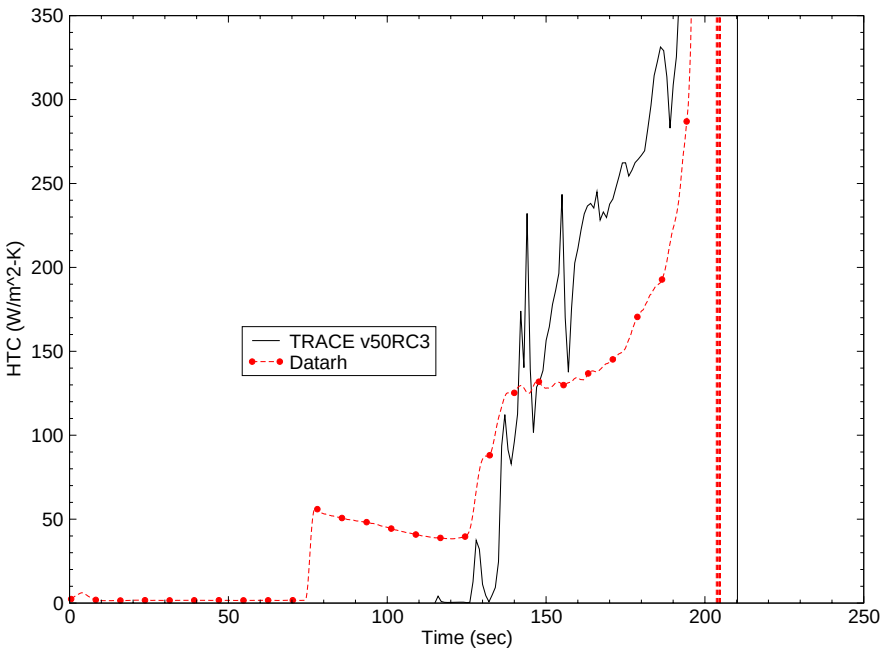

Figure B.10-98. Test 1285 HTC at z = 1.88 m

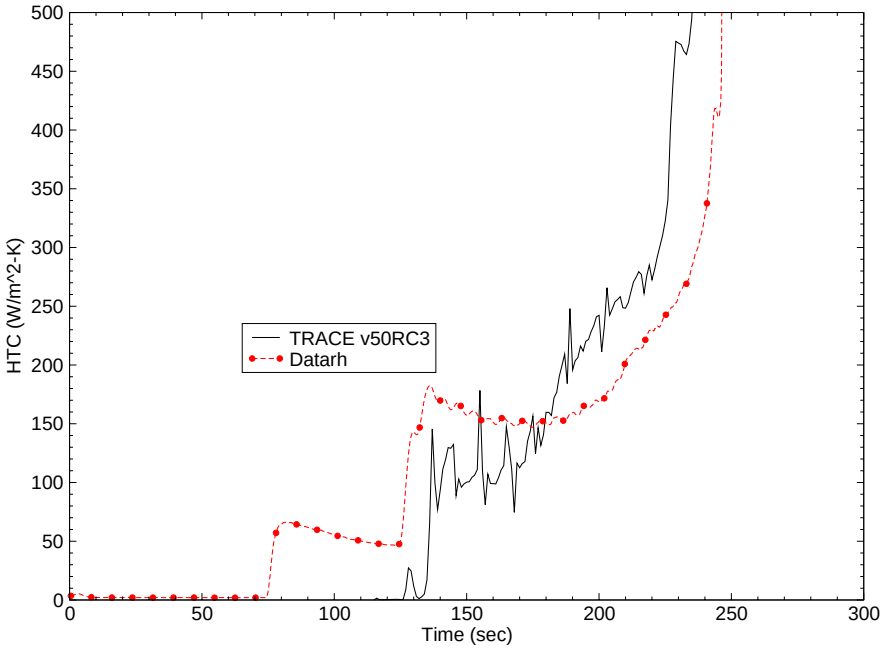

Figure B.10-99. Test 1285 HTC at z = 2.54 m

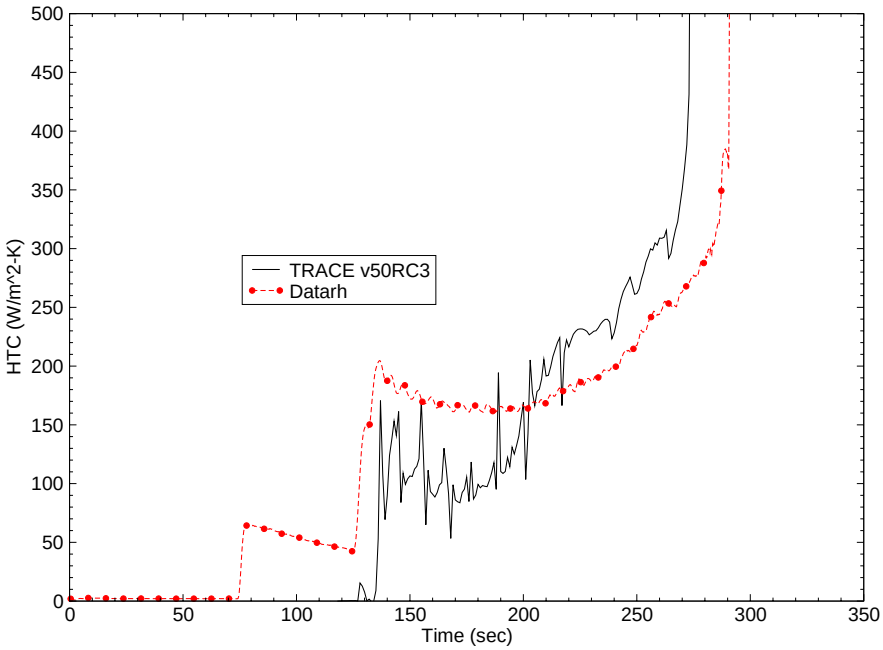

Figure B.10-100. Test 1285 HTC at 2.93 m

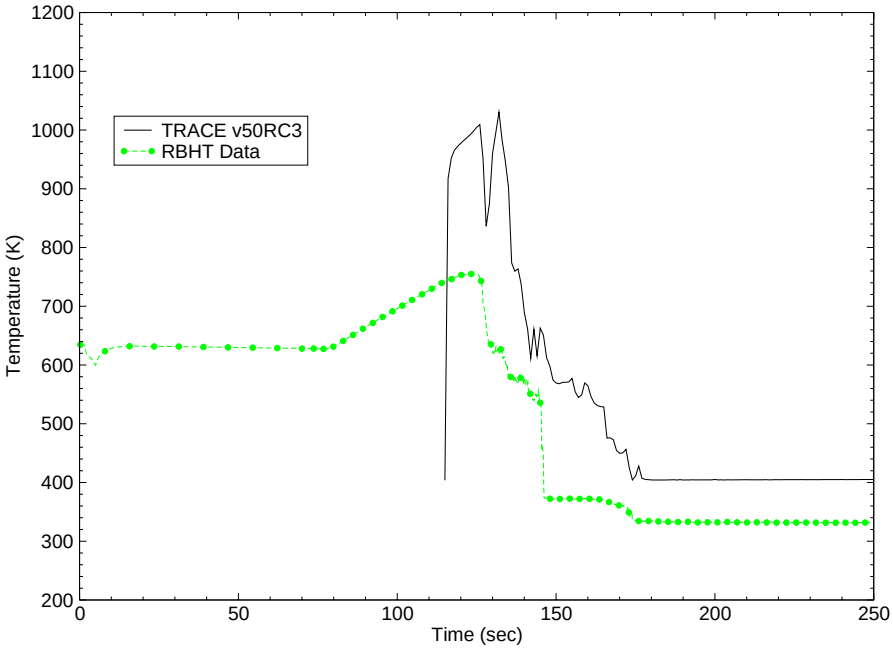

Figure B.10-101. Test 1285 Steam Temperatures at z = 1.40 m

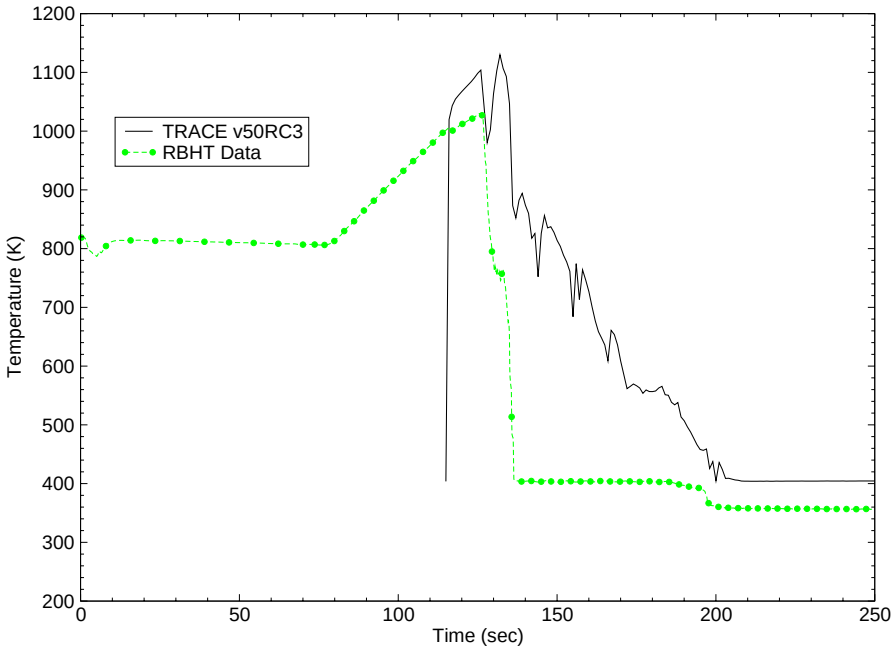

Figure B.10-102. Test 1285 Steam Temperatures at z = 1.88 m

The steam temperature at two elevations are plotted in Figure B.10-101 and Figure B.10-102. TRACE over predicts the steam temp at both elevations for all times, which is consistent with previous plots of rod temperature and HTCs.

B.10.5. Summary and Conclusions

In general, TRACE over predicts peak rod temperatures at higher bundle elevations. TRACE has a tendency to under predict quench times for low power and low flow cases and over predict quench times for high power and high flow cases. In addition, TRACE seems to have the most difficulty with low subcooling cases. The worst predictions were seen in low power, low flow, low subcooling cases, while the best predictions were seen with high power, high flow, high subcooling cases. Table B.10.5 is a comparison of actual and predicted values for important figures of merit for the RBHT reflood assessment. Figure B.10-103 through Figure B.10-105 are plots of the measure versus predicted values for these figures of merit.

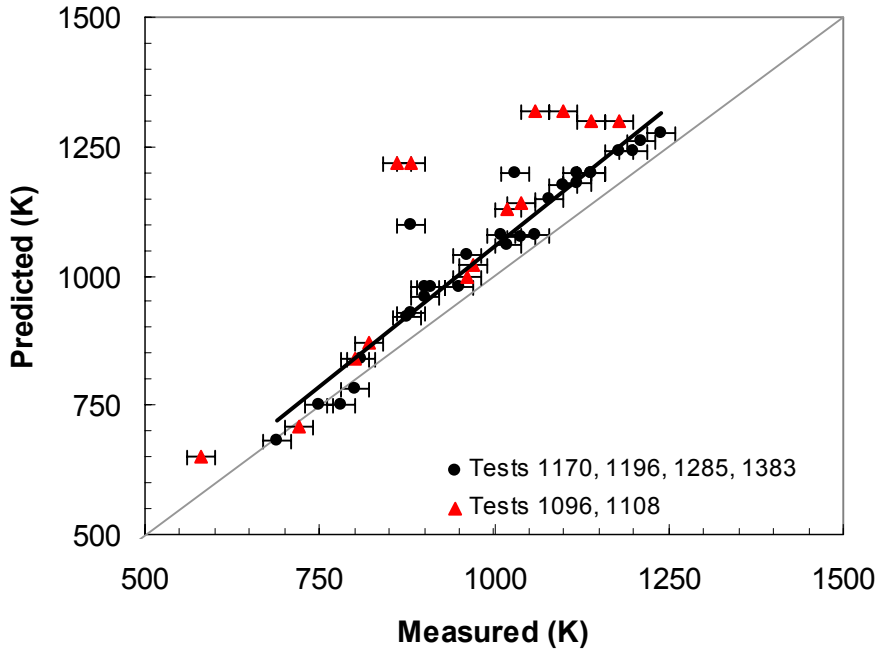

Figure B.10-103. Measured vs Predicted Peak Cladding Temperature

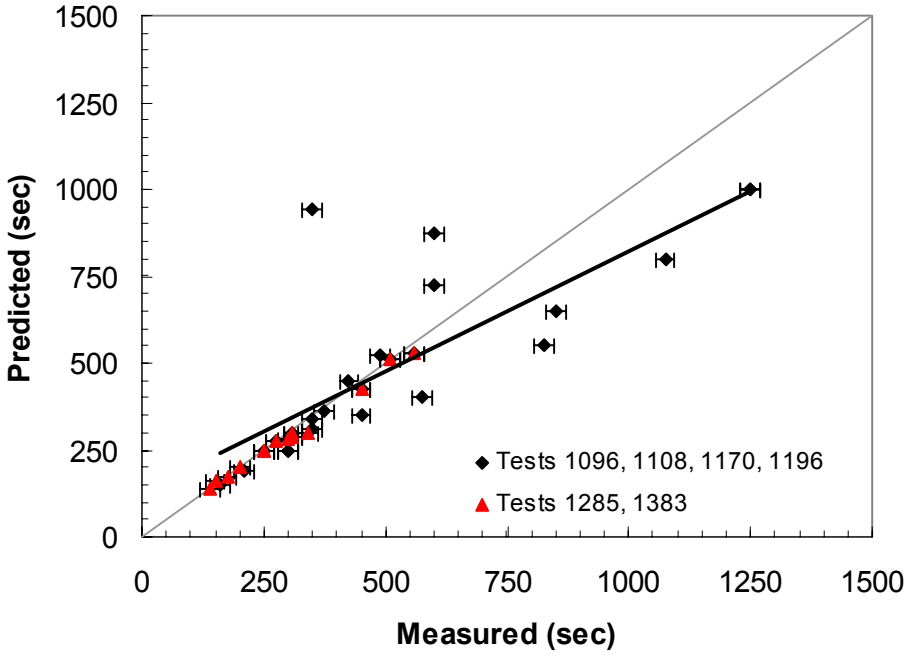

Figure B.10-104. Measured vs Predicted Quench Time

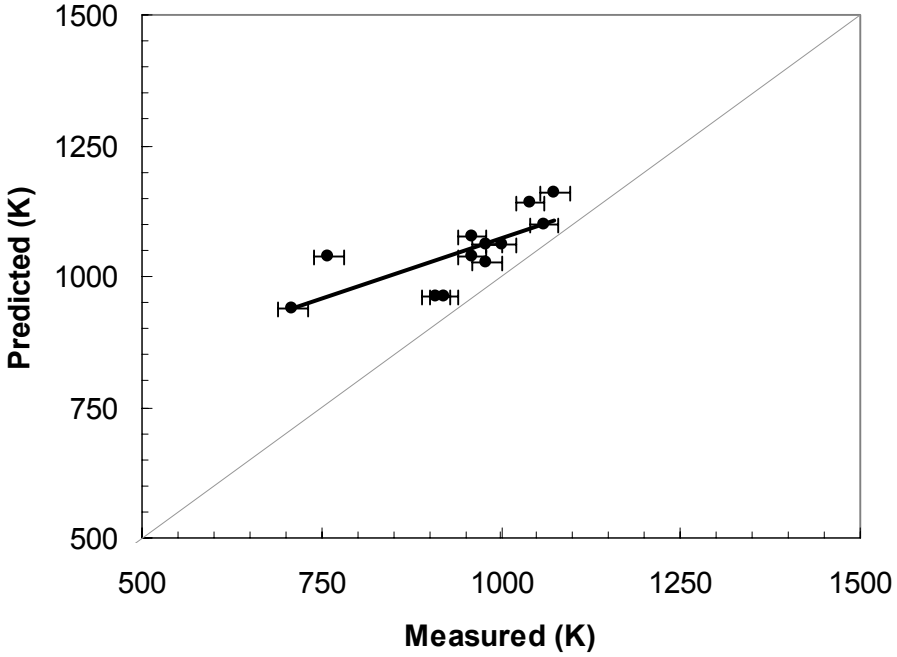

Figure B.10-105. Measured vs Predicted Maximum Steam Temperature

Table B.10.5. Figures of Merit Comparison

Parameter	RBHT Data	TRACE	% Difference
PCT	R^2 = 0.79 (linear regression)		- 8.37
Quench Time	R^2 = 0.75 (linear regression)		+ 2.92
Max Steam Temp (z ~ 1.6 m)	R^2 = 0.54 (linear regression)		- 11.62

B.10.6. References

1 Rosal, E.R., Lin, T.F., McClellan, I.S., Brewer, R.C., "Rod Bundle Heat Transfer (RBHT) Test Facility Description Report," Department of Mechanical Engineering, The Pennsylvania State University, 2005.

2 Hochreiter, L.E. et. al., "RBHT Facility - Reflood Heat Transfer Experiments," Department of Mechanical Engineering, The Pennsylvania State University, November 2005.

3 *Boron Nitride: Thermal Properties*, http://www.ioffe.ru/SVA/NSM//Semicond/BN/thermal.html.

4 Welter, K.B., Bajorek, S.M., "RBHT Reflood Calculation Notebook," Office of Nuclear Regulatory Research, U.S. Nuclear Regulatory Commission, March 2007.

B.11. RBHT Steam Cooling Tests

Author(s): S. M. Bajorek

Affiliation: RES/DRASP/NRCA

Code Version: TRACE V5.0

Platform and Operating System: Intel x86, Windows XP

B.11.1. Introduction

Single phase convection heat transfer in a rod bundle is one of the several fundamental processes that occurs during many hypothetical loss of coolant accidents. Steam cooling, as it is frequently referred to, is important during the uncovery period of a small break LOCA, and is the dominant heat transfer mechanism in the hot assembly during a large break LOCA near the time at which the peak cladding temperature is attained. To assess the ability of TRACE to calculate single phase convective heat transfer in a rod bundle, tests from the RBHT Steam Cooling Test Series were simulated. The simulations presented in this section examine the ability of TRACE to calculate single phase convective heat transfer for a wide range of Reynold's numbers. The Steam Cooling tests were performed at the Penn State/NRC Rod Bundle Heat Transfer (RBHT) facility. The RBHT facility is designed to simulate a full-length portion of a Pressurized Water Reactor (PWR) fuel assembly. The facility consists of a 7x7-rod bundle with 45 electrically heated rods, mixing vane grids, and over 500 instrument channels for measuring temperature, differential and absolute pressure, steam and liquid flow rates, power, etc. The detailed axial distribution of rod thermocouples and steam probes were used in these simulations to compare predicted and measured axial temperature profiles. In addition, heat transfer coefficients obtained from the experiments were compared to the those predicted by the TRACE code.

For this study, 7 steady-state RBHT steam cooling tests were assessed against TRACE: Tests 3173A, 3216D, 3205A, 3216A, 3216G, 3205G, and 3214A. Results of these experiments are described in References 1 and 2. These tests constitute an assessment base that covers Reynolds numbers from 2000 to 20000, which is approximately the range expected during hypothetical small break accidents and during the reflood period of a large break LOCA. In these tests the pressure ranged from 0.138 to 0.414 MPa (20 to 60 psia), and total bundle power ranged from 10 to 95 kW. The results of these tests were compared to steady-state TRACE calculations using the rod cladding temperature, steam temperature, heat transfer coefficient and wall to fluid temperature difference.

B.11.2. Test Facility Description

The Rod Bundle Heat Transfer (RBHT) Facility is designed to conduct systematic separate-effects tests under well-controlled conditions in order to generate fundamental rod bundle transfer data from single phase steam cooling tests, low flow boiling tests, and dispersed flow film boiling heat transfer tests (Ref. 3). The facility is capable of operating in both forced and variable reflood modes covering a wide range of flow and heat transfer conditions at pressure from 0.13 to 0.42 MPa. The test facility consists of the following major components, shown schematically in Figure B.11-1

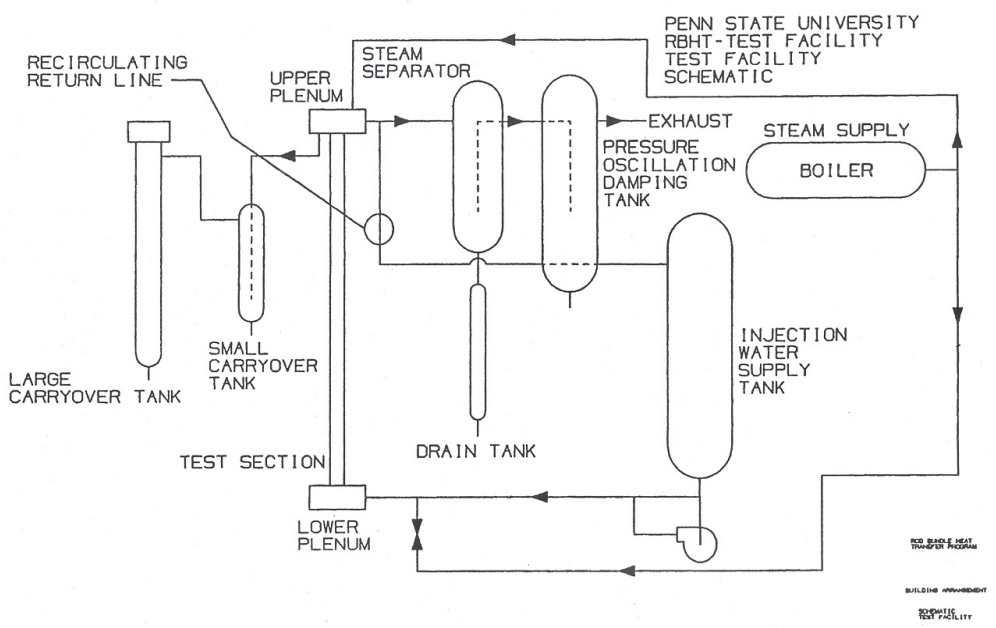

Figure B.11-1. RBHT Schematic

The test section consists of the heater rod bundle, the flow housing, and the lower and upper plenums. The heater rod bundle simulates a small portion of a 17x17 reactor fuel assembly. The electrically heated rods have a diameter of 9.5 mm and are arranged in a 7x7 array with a 12.6 mm pitch with 45 heater rods and four unheated rods (at each corner). The facility has over 500 instrument channels to measure temperature, differential and absolute pressure, flow rates and power. Reference 3 provides a complete description of the RBHT facility and instrumentation.

B.11.3. TRACE Model Description

The RBHT main test section was modeled with TRACE as shown in Figure B.11-2. The VESSEL component was divided into 16 axial levels with a nodalization selected such that there are two cells between each spacer grid except at the very bottom of the model. The VESSEL component spans the entire heated length, with an additional cell at the top of the VESSEL in order to help reduce void fraction oscillations at the top of the rod bundle, which is a standard TRACE

modeling practice. With this axial nodalization, the bottom of every other cell corresponds to the bottom of a grid. The mixing vane grids were modeled as a hydraulic form loss, assuming a loss coefficient of K = 2.0 constant with Reynolds number.

A constant inlet injection flow was provided by the FILL component at the bottom of the lower plenum, while a BREAK, at a specified initial pressure, was used as the exit boundary condition. Two PIPE components are required to connect the FILL to the lower plenum and the upper plenum to the BREAK component.

There are forty-five heated rods in RBHT, arranged in a 7x7 array, with four non-heated rods providing support for the bundle in the corners. There are no thimble tubes. The heater rods, unheated corner rods and housing were modeled using three HSTRC components. The 45 heater rods were represented using Component 6, with the radial nodalization shown in Figure B.11-2. The heater rods have 8 material regions (nine nodes), with three outermost representing the Inconel Type 600 cladding. The heater wire represents the power generating region and was assumed to have the properties of nichrome. The insulator was boron nitride.

Component 7 is a POWER Component, which provides information on axial power shape and power history for the heater rods. The axial shape of the power curve applied to the HSTRC Component 6 with a peak at 2.7432 m (9.0 ft) as shown in Figure B.11-2

.

Table B.11.1. Steady-State Initial and Boundary Conditions

Parameter	Instrument ID	Units
Steam Injection Flow Rate	chan-417	m3/min
Steam Pressure at Flow Meter	chan-416	psig
Steam Temperature at Flow Meter	chan-414	K
Steam Temperature at Bundle Inlet	chan-360, chan-361	K
Lower Plenum Pressure	chan-411	Pa
Upper Plenum Pressure	chan-393	Pa
Voltage	chan-397	volts
Current	chan-398	amps

Each TRACE simulation assumes a constant steam injection flow at a constant heater rod power. At the start of each simulation, the test section was initialized full of steam with an approximate axial temperature that was allowed to reach a new steady state profile following application of the rod power. The case was run as a transient for approximately 2500 seconds. Table B.11.1 is a list of parameters and corresponding facility channels that were used to determine the boundary conditions for each subcase.

Additional details on the TRACE input model for RBHT are documented in References 4 and 5.

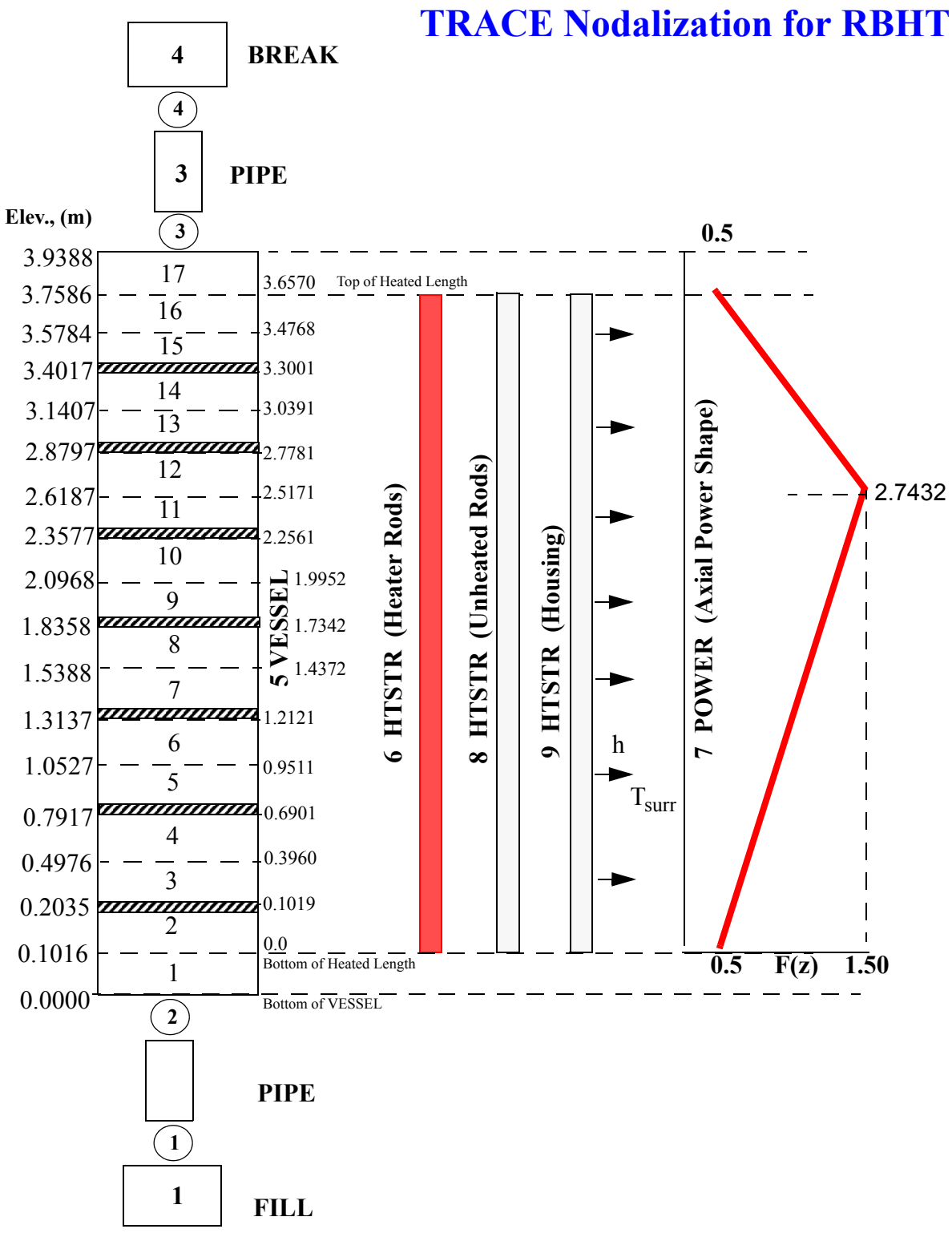

Figure B.11-2. TRACE Nodalization for the RBHT Facility

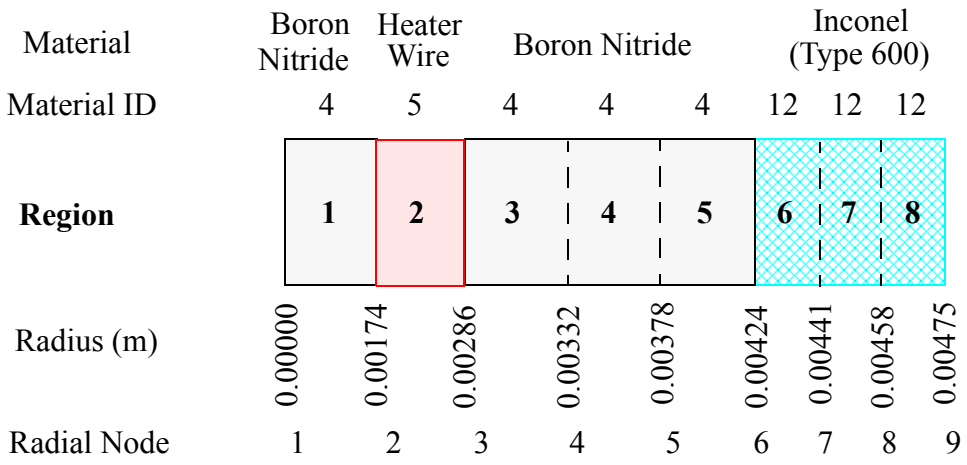

Figure B.11-3. Heater Rod Radial Nodalization

B.11.4. Tests Simulated with TRACE

A total of 7 steady-state cases were assessed using TRACE. In the experiments themselves, each RBHT steam cooling test was actually composed of several steady-state subcases. Each subcase was given a test number designation, and defined for a specific time period. A summary of the subcases simulated in this section are listed in Table B.11.2 Figure B.11-4 is a graphical representation of the assessment matrix and shows which specific tests were simulated with TRACE. The tests cover a range of pressure from 0.138 to 0.414 MPa (20 to 60 psia) and inlet Reynolds numbers up to 20000. These conditions are typical of those in a hot assembly during the reflood period of a LOCA.

Table B.11.2. RBHT Steam Cooling Tests Simulated

Test Number	Tstart (sec)	Tend (sec)	Re	P (MPa)	Q (kW)
3173A	11340	12240	4000	0.276	10
3216D	21300	21800	20000	0.276	95
3205A	10800	12000	10000	0.276	50
3216A	14000	14600	20000	0.138	95
3216G	25200	25600	20000	0.414	93.6
3205G	16100	17500	2000	0.276	14
3214A	11000	11500	15000	0.276	70

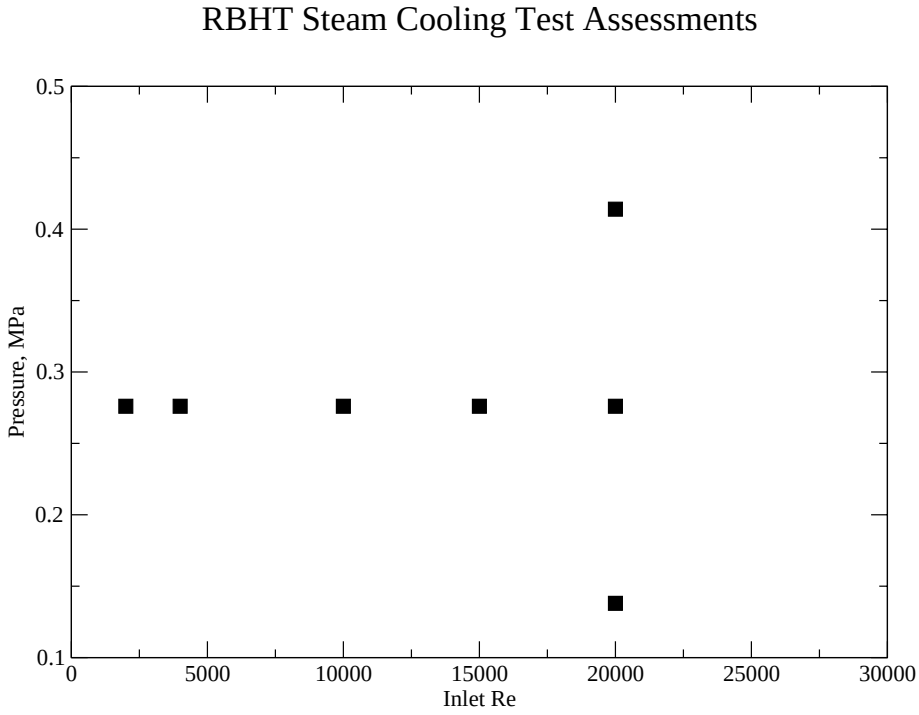

Figure B.11-4. Matrix of RBHT Steam Cooling Tests Simulated with TRACE.

The TRACE simulation assumed a constant steam injection flow at a constant heater rod power. For each case simulated, the test section was initially steam-filled at a representative initial temperature profile. Each case was simulated for 2500 seconds in order to insure that steady state conditions were achieved in the simulation.

B.11.4.1. Simulation of Turbulent Flow Tests.

Four tests were simulated in which conditions at the inlet could be characterized as turbulent. Tests 3216D, 3216A, and 3216G were each conducted such that the Reynolds number of the steam at the inlet was Re=20000. The primary difference between these three tests was the bundle pressure, which ranged from 0.138 MPa (20 psia) in Test 3216A to 0.414 MPa (60 psia) in Test 3216G. The bundle power of approximately 95 kW produced steam at the bundle exit at nominally 800 K (980 deg F).

The fourth test of this set was Test 3214A. The inlet Reynolds number for this test was Re=15000. The bundle power for this test, 70 kW, was also sufficient to produce steam temperatures at the exit of approximately 800 K (980 deg F).

Results for these tests are shown from Figure B.11-5 to Figure B.11-20 The results of each simulation are presented in a set of four figures comparing the axial distribution of cladding temperature, steam temperature, wall to fluid ΔT, and heat transfer coefficient. In general, there is good agreement between TRACE and data for the cladding and steam temperatures. There is considerable scatter however in the comparisons for wall to fluid ΔT and heat transfer coefficient however. The cause of this in the experimental data is due to the grid spacers. Downstream of the grids there is a large increase in the heat transfer coefficient. This increase decays rapidly with distance downstream of the spacer grid.

TRACE, because it lacks models to account for the spacer grid effect, tends to underpredict most of the data. TRACE is closer to the fully developed flow points that lower bound the data at each elevation.

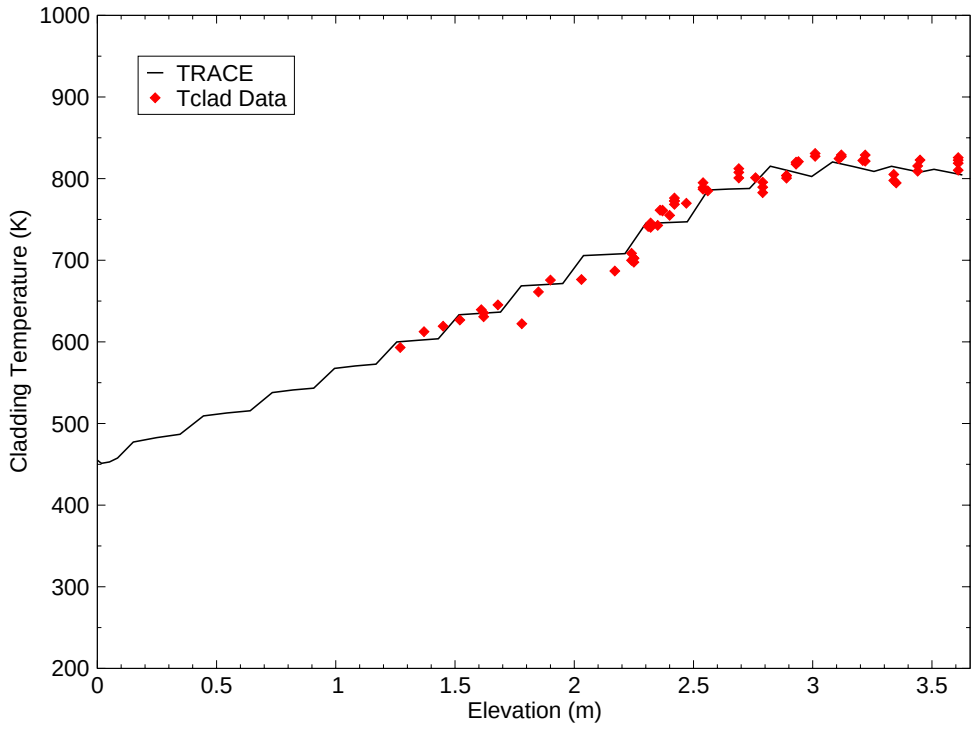

Figure B.11-5. RBHT Test 3216D Cladding Temperature Comparison.

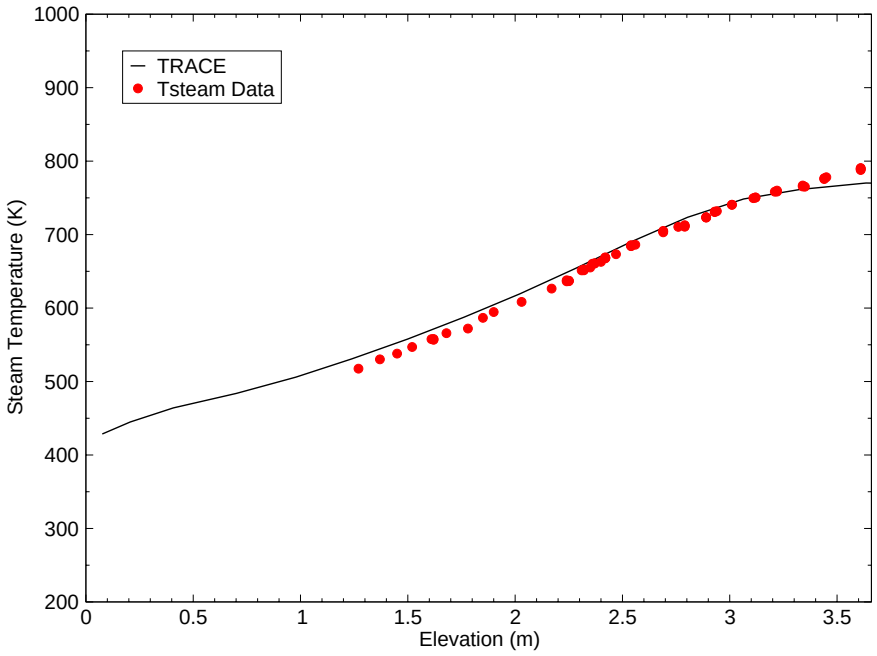

Figure B.11-6. RBHT Test 3216D Steam Temperature Comparison.

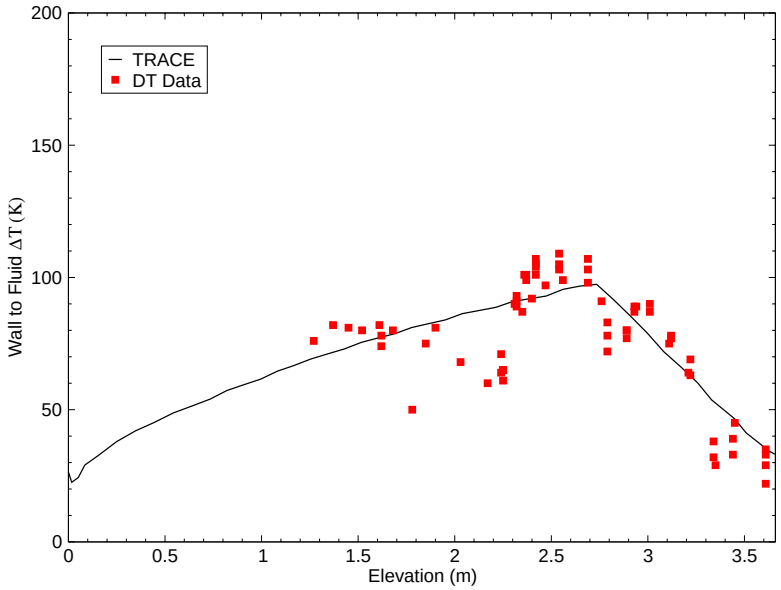

Figure B.11-7. RBHT Test 3216D Wall to Fluid DT Comparison.

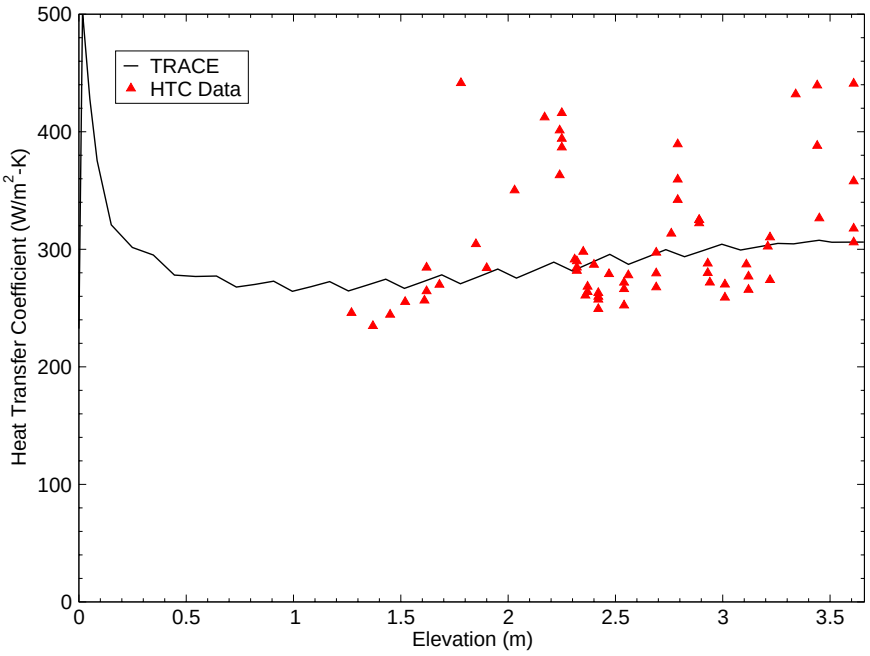

Figure B.11-8. RBHT Test 3216D Heat Transfer Coefficient Comparison.

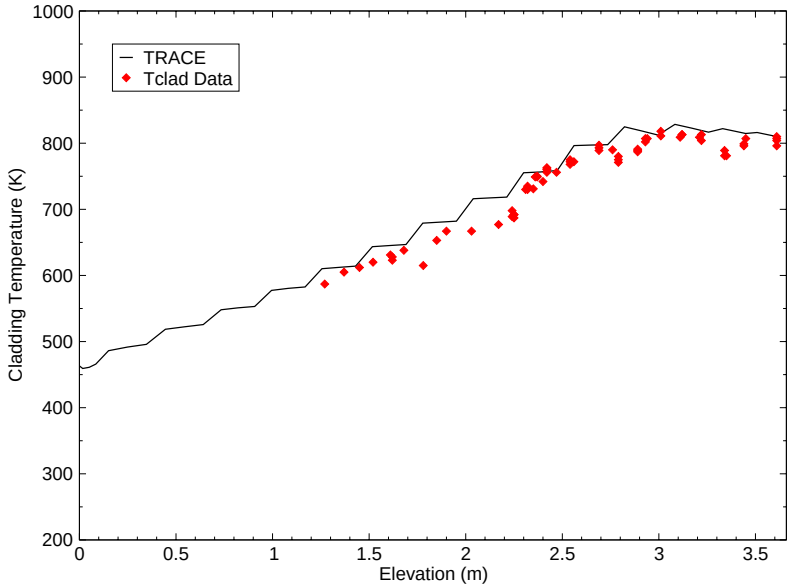

Figure B.11-9. RBHT Test 3216A Cladding Temperature Comparison.

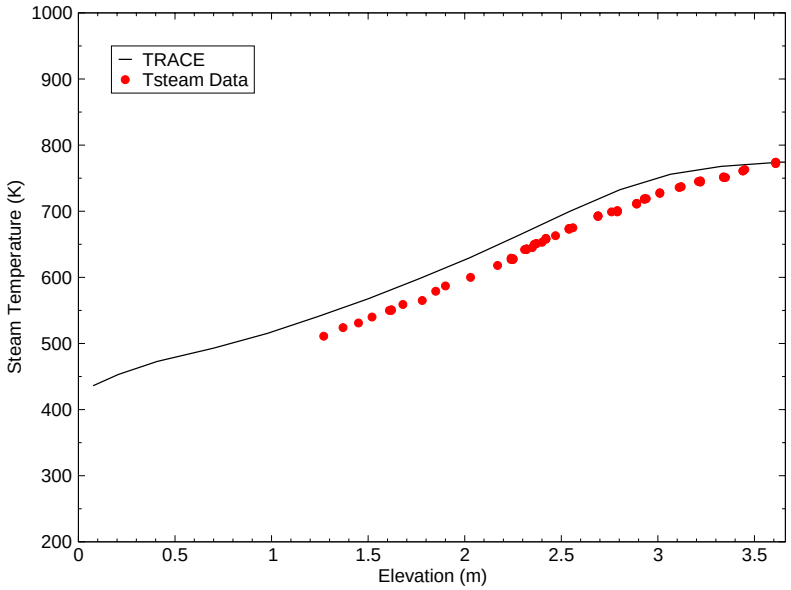

Figure B.11-10. RBHT Test 3216A Steam Temperature Comparison.

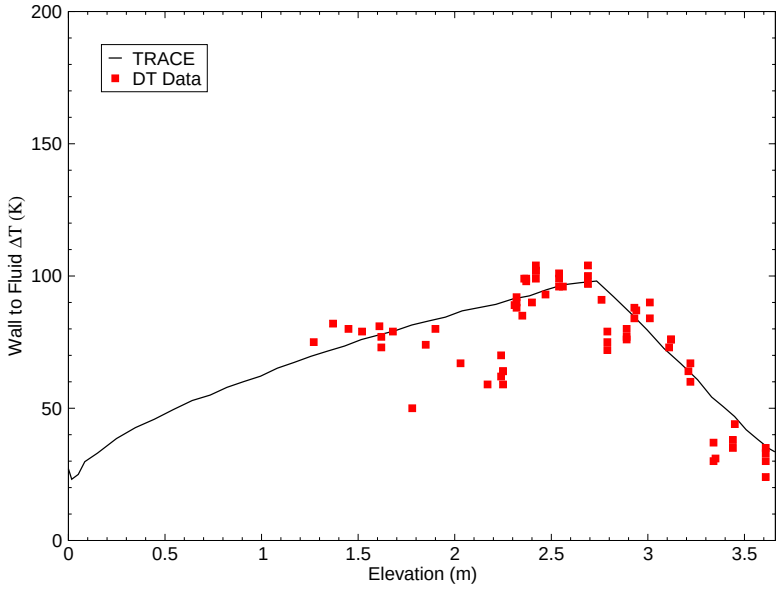

Figure B.11-11. RBHT Test 3216A Wall to Fluid DT Comparison.

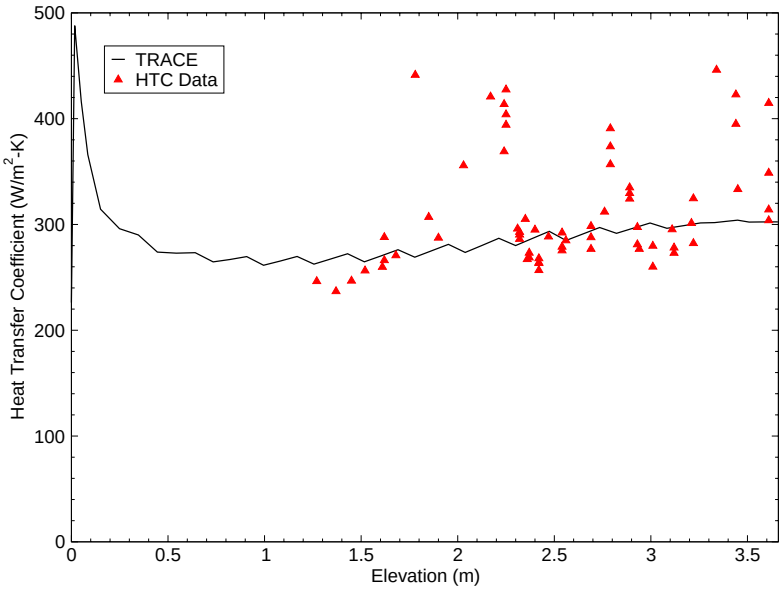

Figure B.11-12. RBHT Test 3216A Heat Transfer Coefficient Comparison.

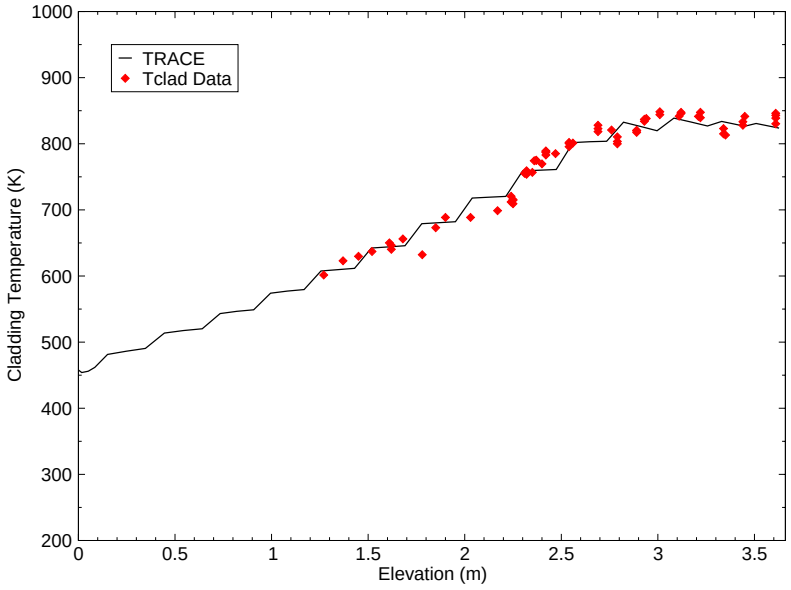

Figure B.11-13. RBHT Test 3216G Cladding Temperature Comparison.

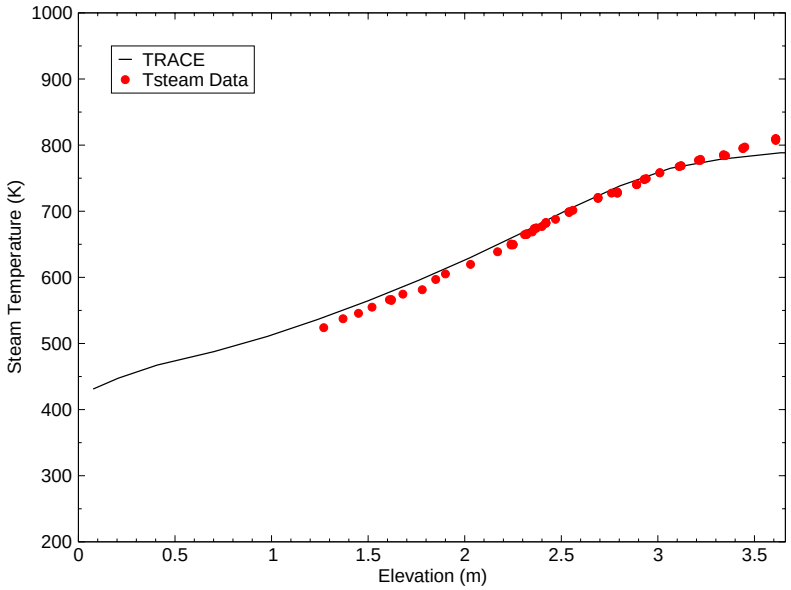

Figure B.11-14. RBHT Test 3216G Steam Temperature Comparison.

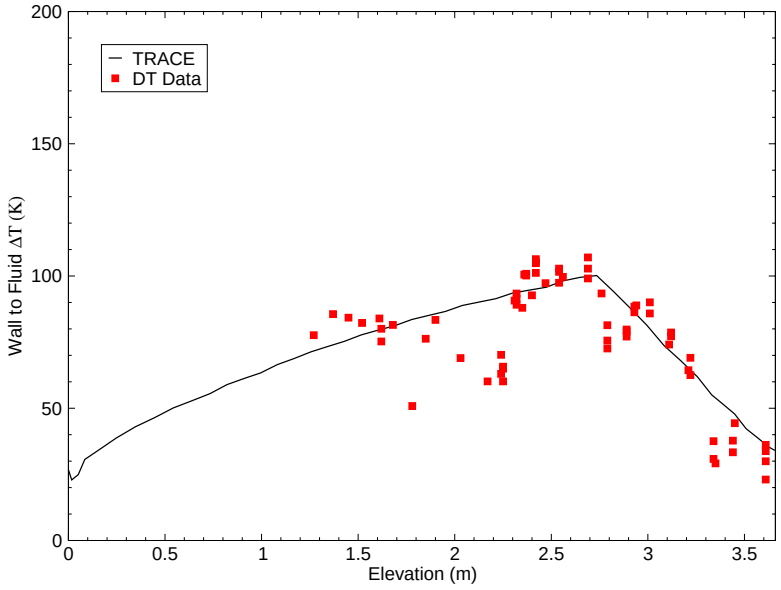

Figure B.11-15. RBHT Test 3216G Wall to Fluid DT Comparison.

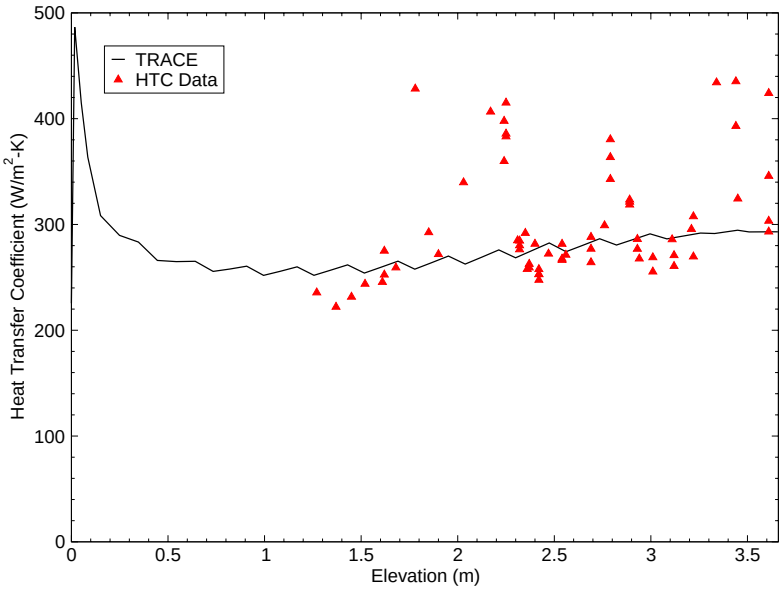

Figure B.11-16. RBHT Test 3216G Heat Transfer Coefficient Comparison.

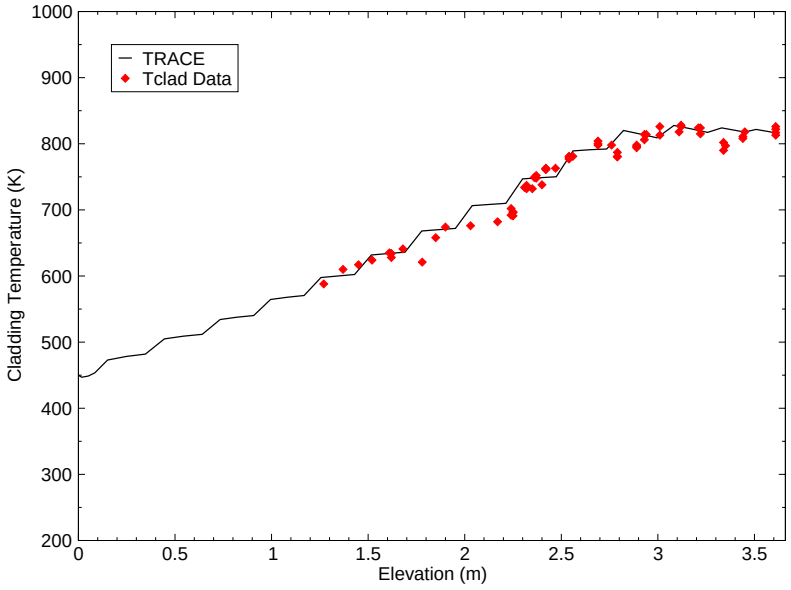

Figure B.11-17. RBHT Test 3214A Cladding Temperature Comparison.

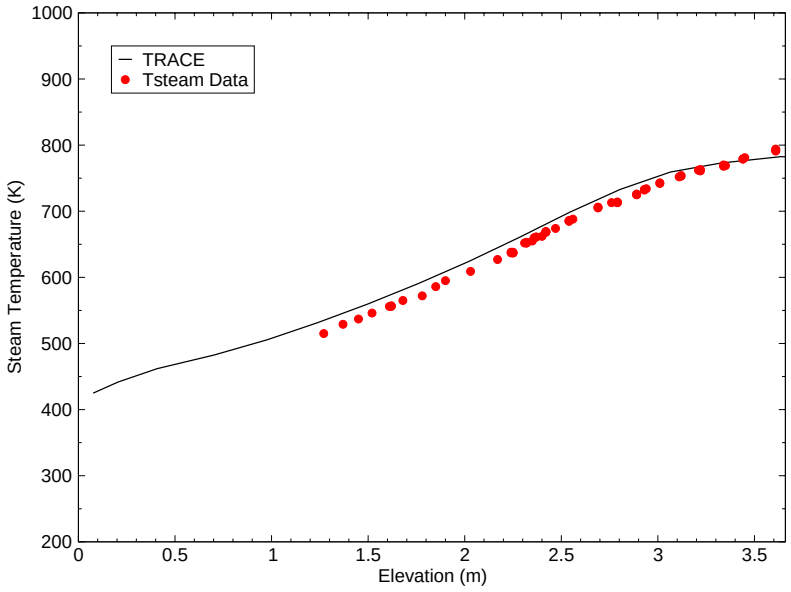

Figure B.11-18. RBHT Test 3214A Steam Temperature Comparison.

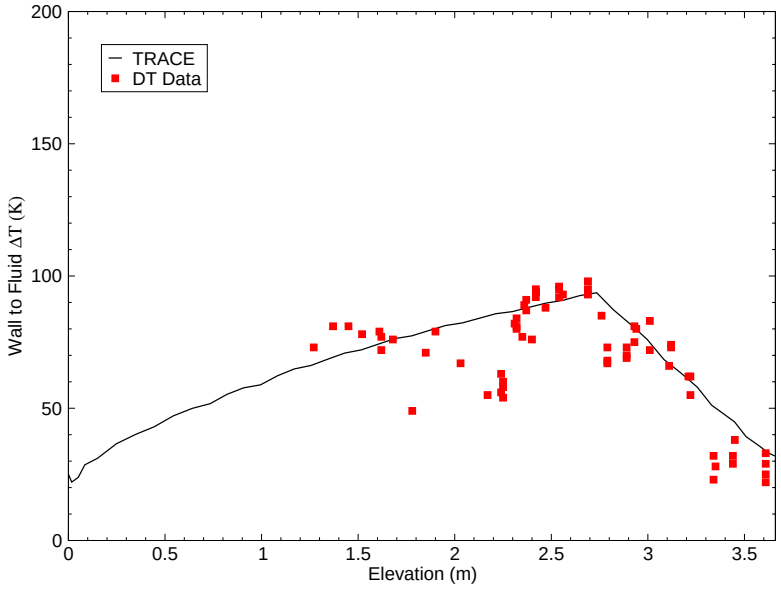

Figure B.11-19. RBHT Test 3214A Wall to Fluid DT Comparison.

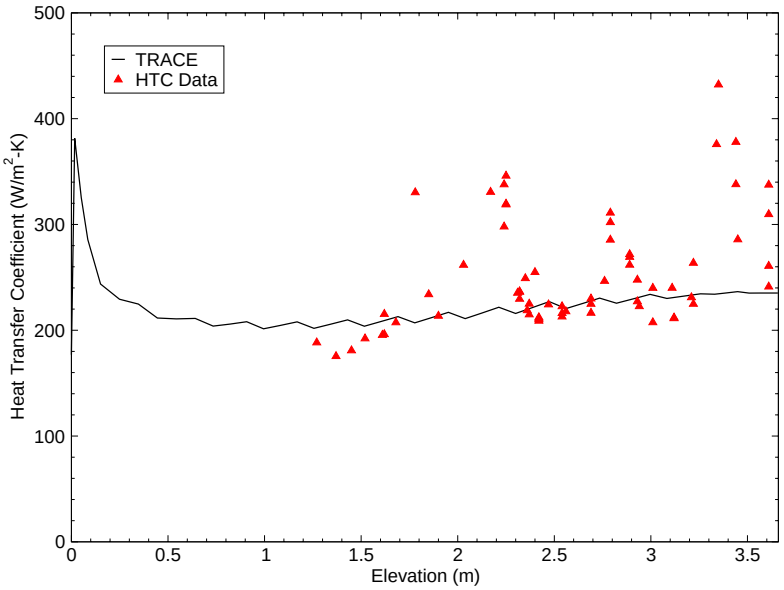

Figure B.11-20. RBHT Test 3214A Heat Transfer Coefficient Comparison.

B.11.4.2. Simulation of Laminar and Transition Flow Tests.

Three tests were simulated in which conditions at the inlet could be characterized as laminar or within the laminar-turbulent transition range of Re. Tests 3205G, 3173A, and 3205A were each conducted such that the Reynolds number of the steam at the inlet was Re=10000 or less. The bundle pressure was 0.276 MPa (40 psia) for each of these tests.

Results for these tests are shown from Figure B.11-21 to Figure B.11-32 The results of each simulation are again presented in a set of four figures comparing the axial distribution of cladding temperature, steam temperature, wall to fluid ΔT, and heat transfer coefficient. The agreement for these test is not as good as it was for the higher Re cases. In general, there is reasonable agreement between TRACE and data for the cladding and steam temperatures. There is considerable scatter in the comparisons for wall to fluid ΔT and heat transfer coefficient and for the low Re cases the underprediction of the heat transfer coefficient is more apparent. This is again due to the lack spacer grid models to enhance the local heat transfer coefficients. Agreement is poor for RBHT Test 3205G, which had an inlet Re of 2000. This test is in the mixed convection regime, in which both natural convection and forced convection are expected to a role. TRACE does not have a specific model for this heat transfer regime, but assumes laminar forced convection.

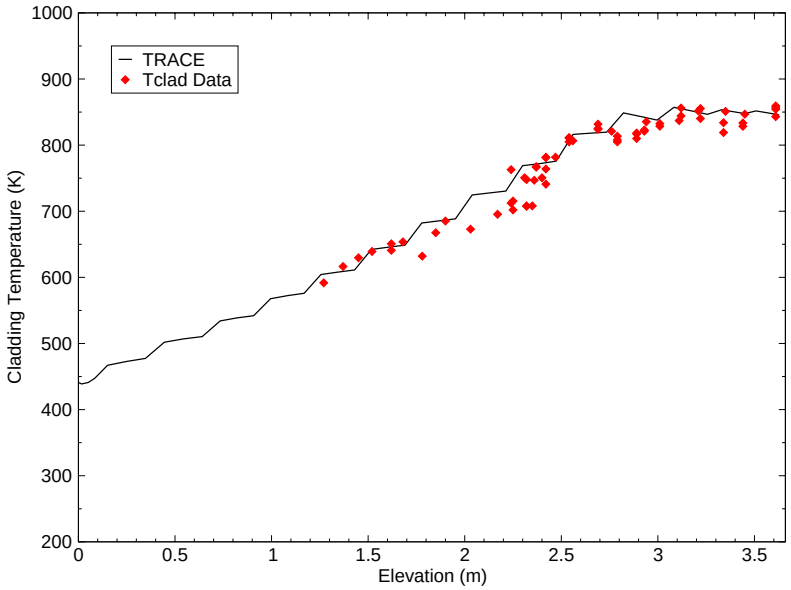

Figure B.11-21. RBHT Test 3205A Cladding Temperature Comparison.

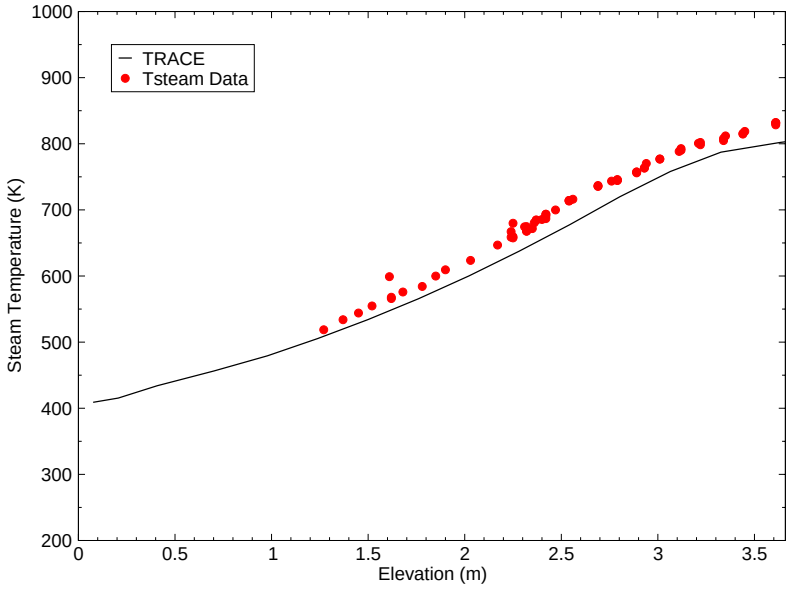

Figure B.11-22. RBHT Test 3205A Steam Temperature Comparison.

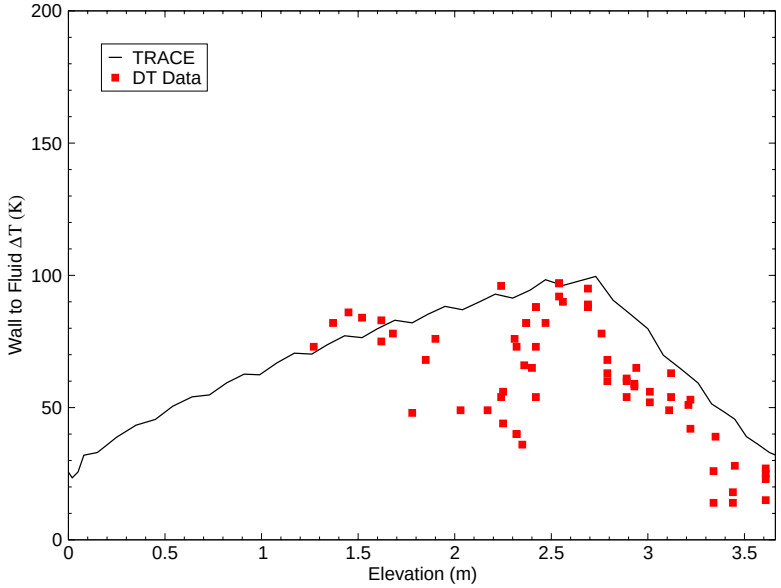

Figure B.11-23. RBHT Test 3205A Wall to Fluid ΔT Comparison.

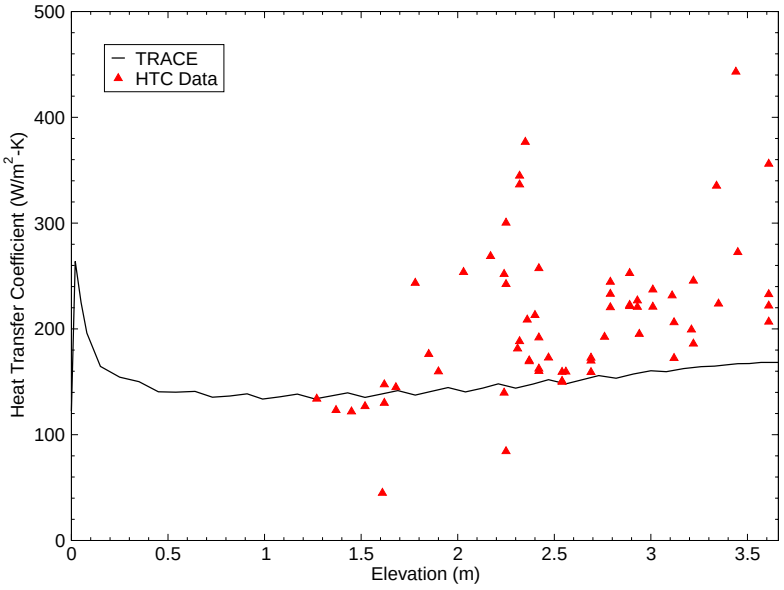

Figure B.11-24. RBHT Test 3205A Heat Transfer Coefficient Comparison.

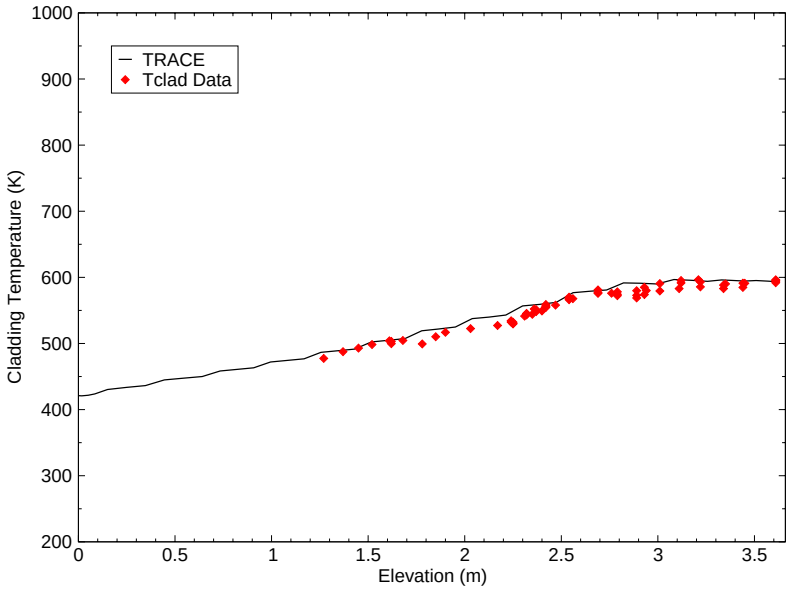

Figure B.11-25. RBHT Test 3173A Cladding Temperature Comparison.

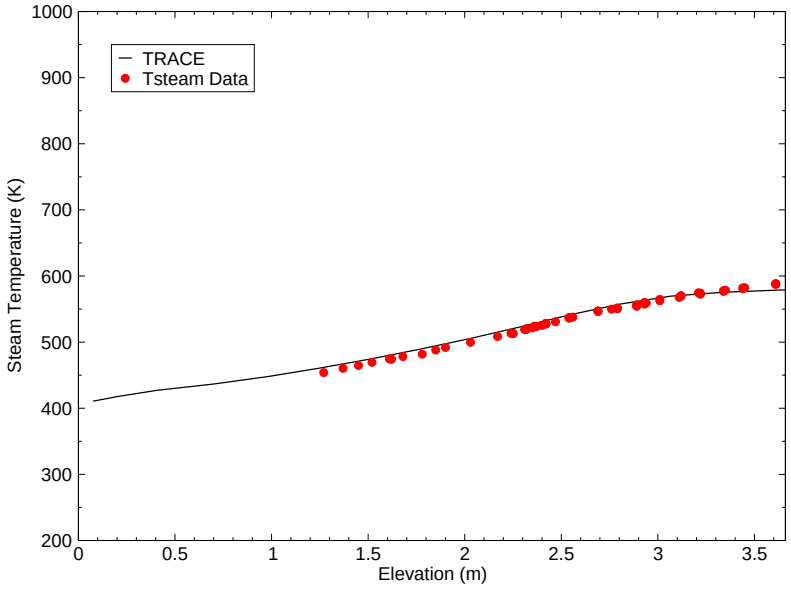

Figure B.11-26. RBHT Test 3173A Steam Temperature Comparison.

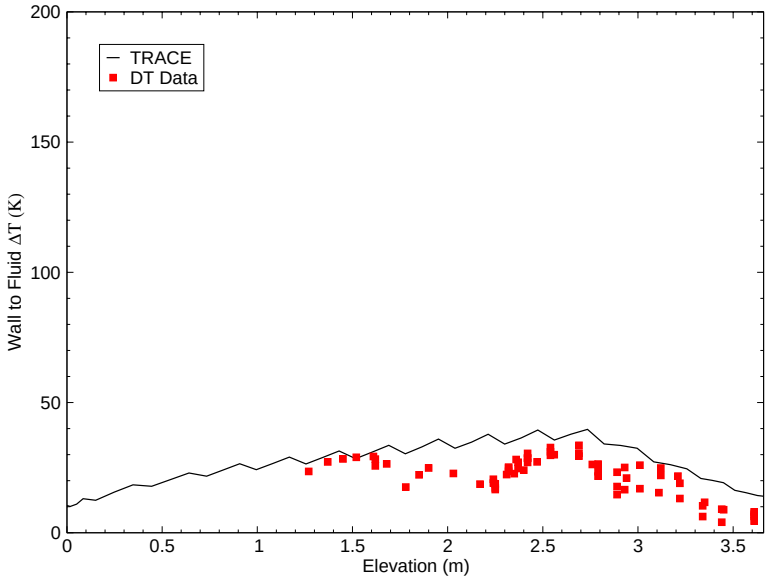

Figure B.11-27. RBHT Test 3173A Wall to Fluid ΔT Comparison.

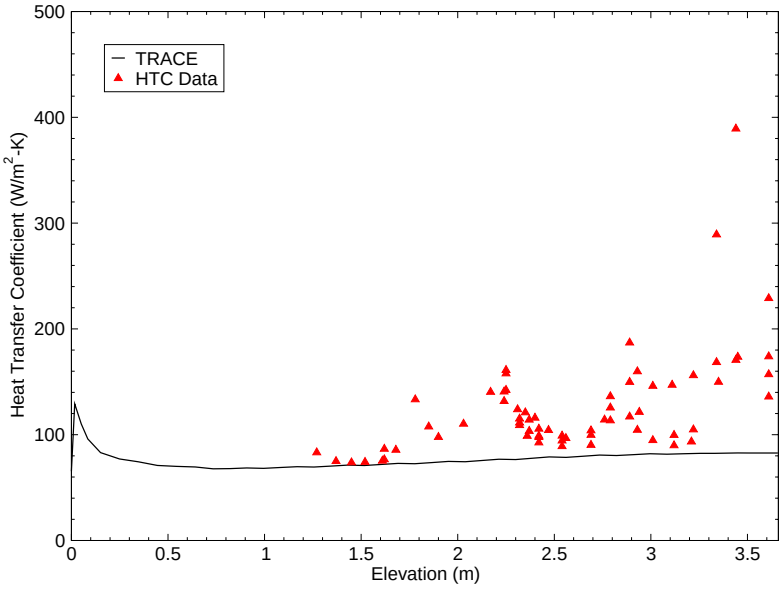

Figure B.11-28. RBHT Test 3173A Heat Transfer Coefficient Comparison.

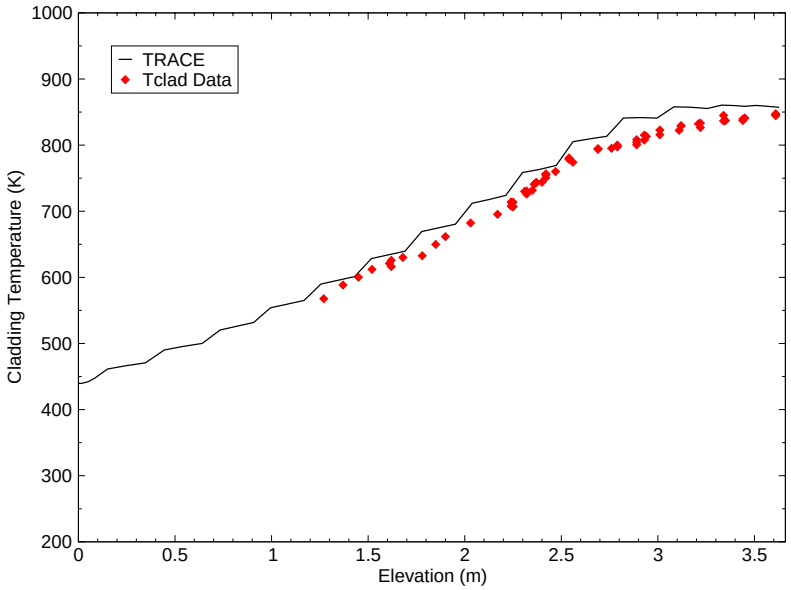

Figure B.11-29. RBHT Test 3205G Cladding Temperature Comparison.

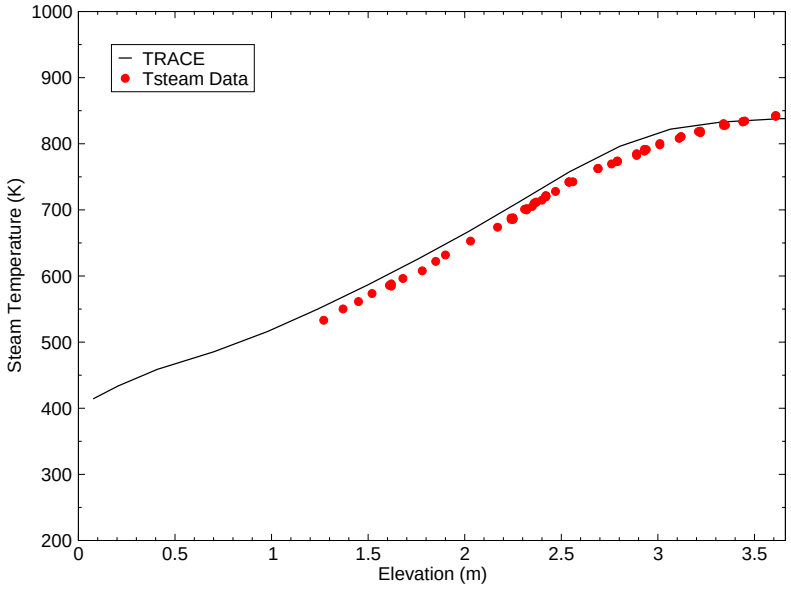

Figure B.11-30. RBHT Test 3205G Steam Temperature Comparison.

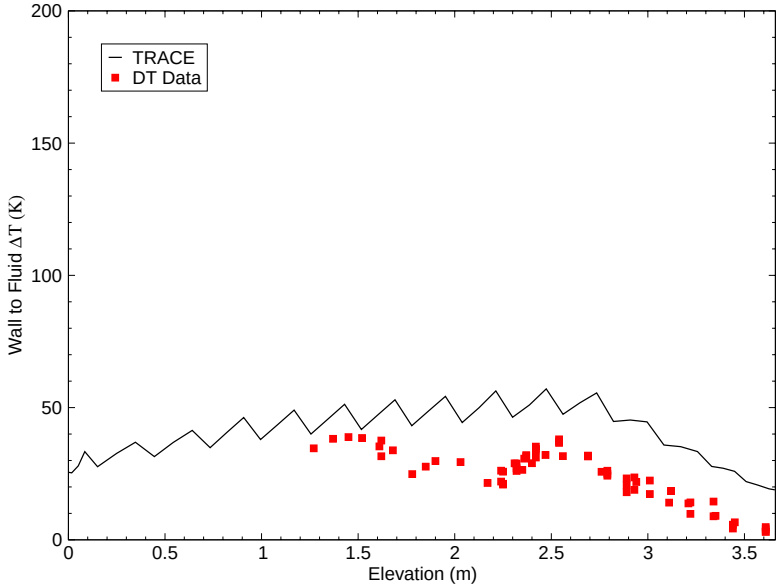

Figure B.11-31. RBHT Test 3205G Wall to Fluid ΔT Comparison.

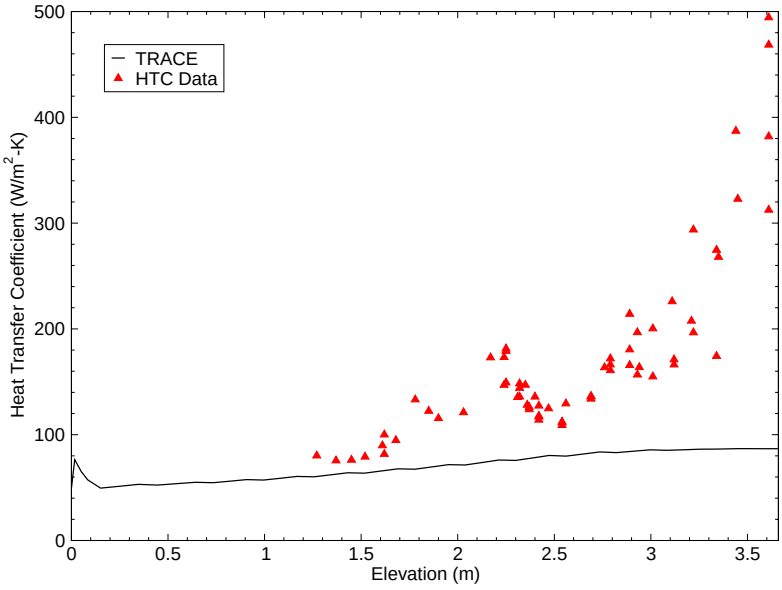

Figure B.11-32. RBHT Test 3205G Heat Transfer Coefficient Comparison.

B.11.5. RBHT Steam Cooling Test Assessment Summary

A total of seven RBHT Steam Cooling Tests were simulated using TRACE Version 5.0RC3. In general, there was good agreement between the predicted and measured results for cladding and steam temperatures. A comparison of wall-to-fluid temperature difference and heat transfer coefficients however showed some deficiencies in the TRACE calculation of rod bundle thermal-hydraulics. Table B.11.3 shows a comparison of the seven simulations with each other. For all cases, the wall to fluid ΔT is overpredicted, while the heat transfer coefficients are underpredicted. (The mean error was calculated as data minus code.) The cause of this underprediction is the lack of spacer grid models to enhance the local heat transfer coefficient immediately downstream of the grid. The largest deviation occurs at low Re. This is seen more clearly by comparison with the normalized mean error (or other Figures of Merit from ACAP). In Table B.11.4, the Raw Error in heat transfer coefficient, and a Normalized Mean Error are shown for each test. The Normalized Mean Error increases with Re, indicating better agreement with data at higher Reynolds number, as shown in Figure B.11-33. At low Re, TRACE can expected to underpredict the heat transfer coefficient by a significant margin.

Table B.11.3. Summary of Steam Cooling Test Assessment Results

Test	Re	P (MPa)	Tclad Mean Error (K)	Tsteam Mean Error (K)	ΔT Mean Error (K)	HTC Mean Error (W/m2-K)
3205g	2000	0.276	-22.0288	-2.80092	-19.2276	96.4666
3173a	4000	0.276	-7.66014	1.43249	-9.09188	41.0837
3205a	10000	0.276	-8.57278	5.25872	-13.8032	59.2462
3214a	15000	0.276	-7.74876	-1.58307	-6.06217	32.5356
3216a	20000	0.138	-20.9745	-15.2452	-5.80771	36.5156
3216d	20000	0.276	0.092913	4.04015	-3.95007	30.4847
3216g	20000	0.414	0.390282	6.01709	-5.62729	36.6822
Ave			-9.500	-0.411	-9.081	47.574

Table B.11.4. Summary of RBHT Assessment Heat Transfer Coefficient Results

Test	Re	P (MPa)	Mean Error (Raw) (W/m2-K)	Mean Error (Normalized)
3205g	2000	0.276	98.5572	0.637629
3173a	4000	0.276	42.5587	0.735837
3205a	10000	0.276	59.9484	0.777594
3214a	15000	0.276	41.9636	0.858200
3216a	20000	0.138	47.5747	0.871555
3216d	20000	0.276	42.2389	0.883142
3216g	20000	0.414	46.8681	0.869546
Ave			54.244	0.805

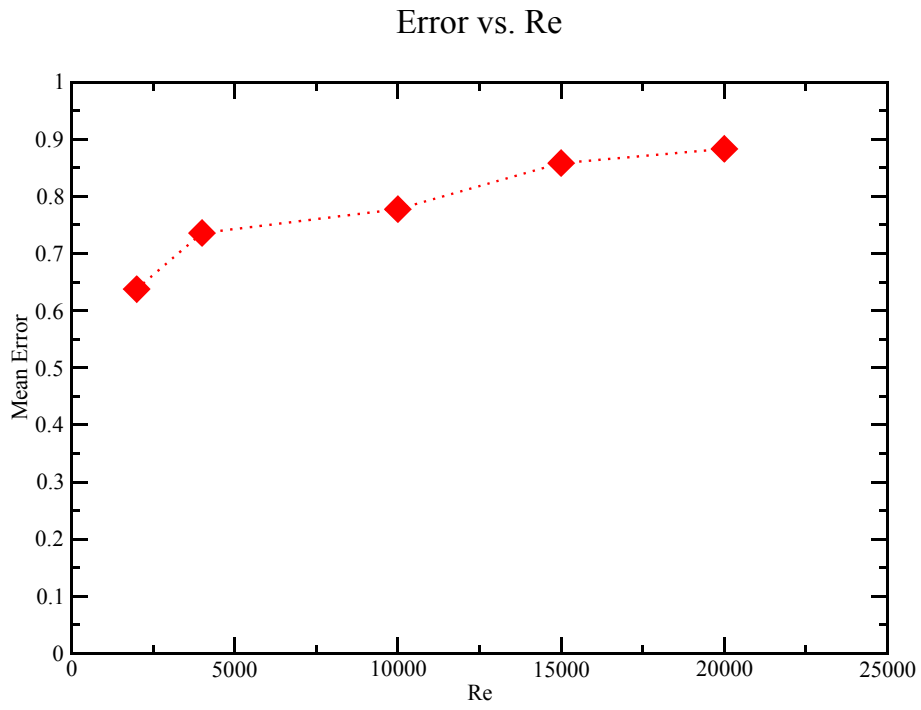

Figure B.11-33. Mean (Normalized) Error in HTC as a Function of Re.

B.11.6. References

1 McLaughlin, D. M., Jr., "Rod Bundle Heat Transfer Facility Steam Cooling Experiments, M.S. Thesis, The Pennsylvania State University, December 2005.

2 Hochreiter, L. E., et al.,"RBHT Steam Cooling Test Data Report," (in preparation).

3 Rosal, E.R., Lin, T.F., McClellan, I.S., Brewer, R.C., "Rod Bundle Heat Transfer (RBHT) Test Facility Description Report," Department of Mechanical Engineering, The Pennsylvania State University, 2005.

4 Bajorek, S. M., "RBHT Steam Cooling Tests, ADAMS No. ML062640589/ML062640275, September, 2006.

5 Bajorek, S. M., "Simulation of RBHT Steam Cooling Heat Transfer Tests Using TRACE Version 5.0RC3, ADAMS No. ML070890386, March, 2007.

Interfacial Drag and Mixture Level Swell Tests

B.12. FRIGG Tests

Author(s): Chester Gingrich

Affiliation: USNRC

Code Version: TRACE V5.0

Platform and Operating System: Intel x86, Windows XP

B.12.1. Introduction

FRIGG is a Swedish test loop facility that was used to study the thermal-hydraulic performance of a simulated fuel bundle for the then-proposed Marviken boiling-water reactor (BWR). The power supply for the FRIGG loop was capable of providing a maximum of 8 MW of direct current to the test section. This current was sufficient to power an electrically heated rod bundle at near prototypical plant conditions. The FRIGG loop was used to investigate single- and two-phase pressure drops, axial and radial void distributions, burnout in natural and forced circulation, and natural-circulation mass velocity, as well as the stability limit and some limited transient conditions. The facility was well instrumented with many thermocouples, pressure transducers, flow meters, and a gamma densitometer that could be moved up and down to obtain void measurements at predetermined axial locations. The gamma densitometer was designed to measure radial void fractions, as well as axial void fractions.

The purpose of this assessment is to document the performance of the TRACE code with respect to predicting the void fraction along the axial length of the channel. The quality of this prediction is heavily dependent on the interfacial drag model and the heat transfer model implemented in TRACE. Note that while the purpose of the FRIGG loop tests indicate that natural and forced circulation data was obtained, the only data report for the FRIGG tests currently available (Ref. 2) does not contain sufficient information to model the natural circulation loop effects in any meaningful way.

B.12.2. Test Facility Description

A simplified flow diagram of the FRIGG test facility is shown in Figure B.12-1. A more detailed view of the test section only is shown in Figure B.12-2. A detailed view of the test section inlet is pictured in Figure B.12-4. The FRIGG facility provided the capability for testing the full height Marviken fuel bundle under both forced and natural circulation conditions. A cross-section view showing the fuel bundle geometry is shown in Figure B.12-3. The tests examined featured 36

identical rods arranged in concentric rings of 6, 12, and 18 rods each. The facility was designed to measure other quantities besides the void profile. However, the documentation does not contain adequate detail on the balance of plant or the test section inlet to allow for the preparation of meaningful TRACE models.

The FRIGG tests were used to investigate typical BWR phenomena. Inlet conditions involved subcooled flows that, upon being heated in the test section, achieved saturation by top of the bundle. Subcooling of the inlet flow ranged from 22.6K to 2.4K. All of the tests were performed at approximately 50 bars. For the tests used in this assessment, the rod power ranged from 1470 kW to 4560 kW and the mass flow rate through the channel ranged from 9.8 kg/s to 21.3 kg/s. Along most of the bundle, subcooled nucleate boiling occurred, giving rise to an increasing void fraction with height. Above the heated section was an unheated section that ends just before a perforated tube that acts as a steam separator.

B.12.3. TRACE Model Description

Two different basic TRACE models were developed to model this facility. One model uses the CHAN component to model the test section, and the other uses the VESSEL component to model the test section. The purpose of using both the CHAN and the VESSEL components to model the test section was to assess the performance of the 1D interfacial drag model and the 3D interfacial drag model. A calculation notebook indicating how parameter and modeling choices were made in each of these models is provided in <reference calc-notebook>. Brief descriptions of each of these models is described in the following sections.

B.12.3.1. Channel Based Model

The nodalization for the CHAN (channel component) based model is presented in Figure B.12-5. In the CHAN-based model a CHAN component with 16 axial nodes is used to model the heated length of the fuel rods. A 5 cell pipe is used for the upper plenum to reach the elevation of the pressure transducer just below the steam separators. The TRACE model represents a single pass of coolant starting from the recirculation loop just after leaving the steam separator through the downcomer, the test section and the upper plenum to the pressure transducer (see the pressure transducer location labeled P28 in Figure B.12-1) before entering the steam separators. For simplicity, all recirculation flow (feedwater, condensate, and thermally controlled steam separator effluent) is provided at the FILL just after the steam separator, rather than at their true varied locations along the top section of the loop.

The TRACE model does not model any of the steam separators, condensers, loop heat exchangers, control valves, the forced circulation pump or heaters outside of the simulated fuel elements. The test section is modeled completely with the exception of pipe wall heat loss. Adiabatic conditions are assumed throughout due to a lack of information as to how much, if any, insulation was provided. Experimentally determined values for flow losses at the spacer locations were included in the model. No effort was made to align the cell centers with the experimental locations for void measurement. The model of the recirculation loop does account for the pipe

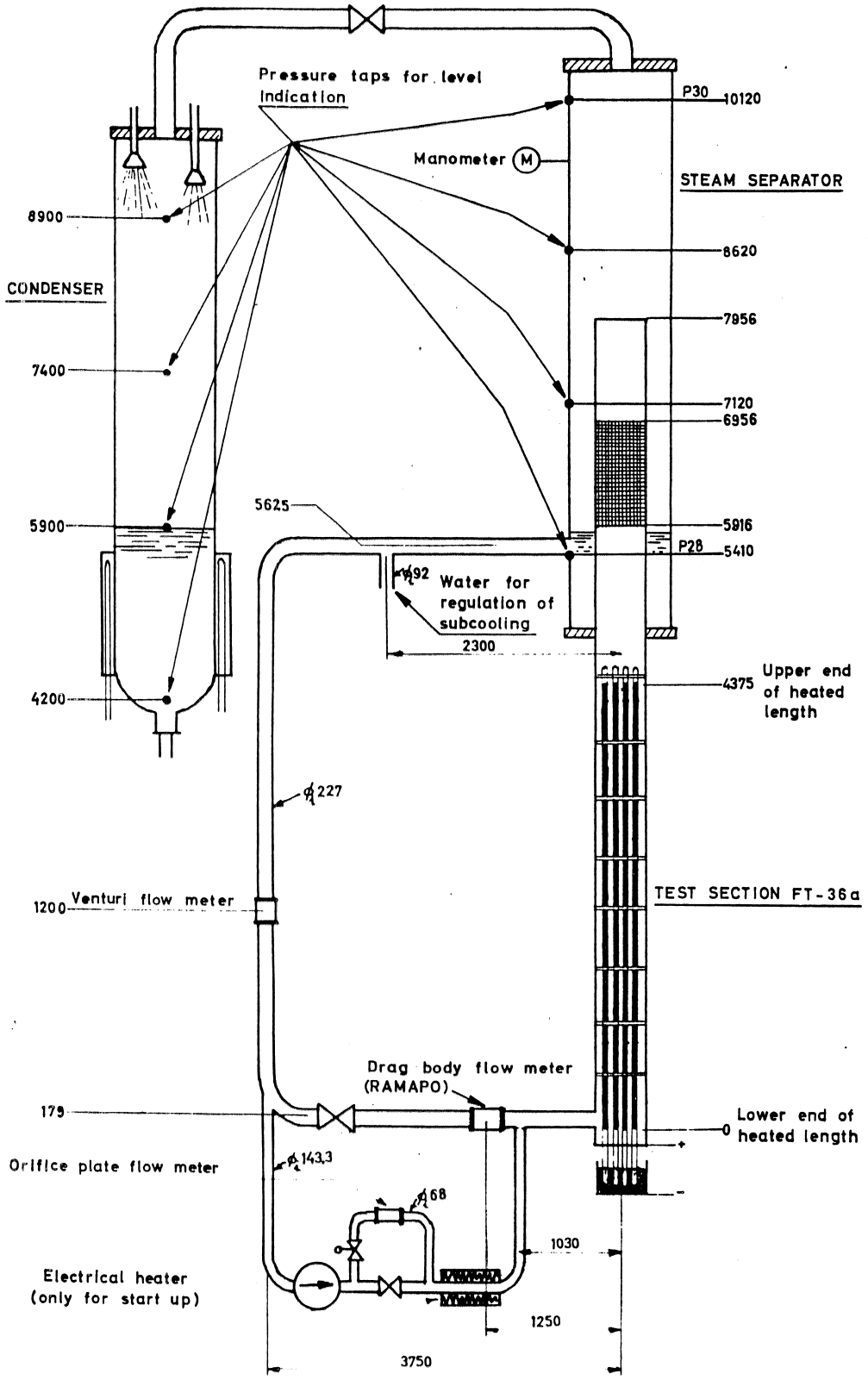

Figure B.12-1. FRIGG Loop geometry

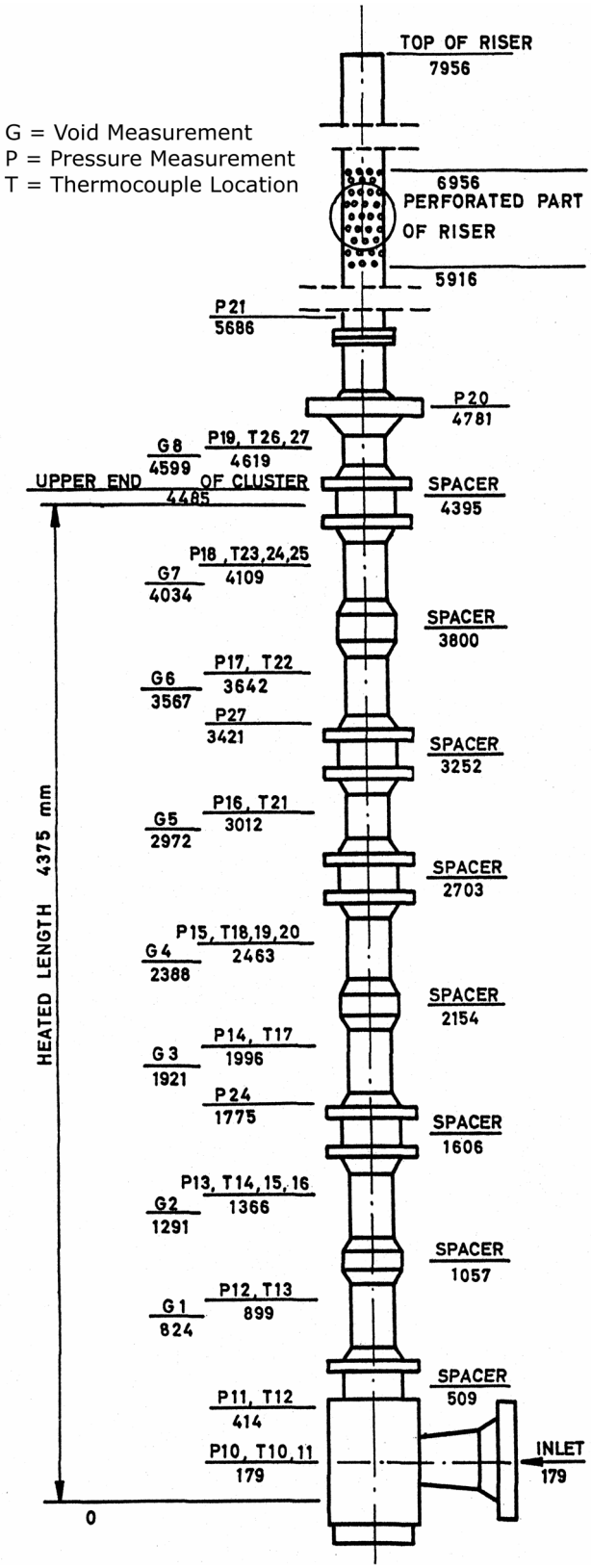

Figure B.12-2. FRIGG Test Section

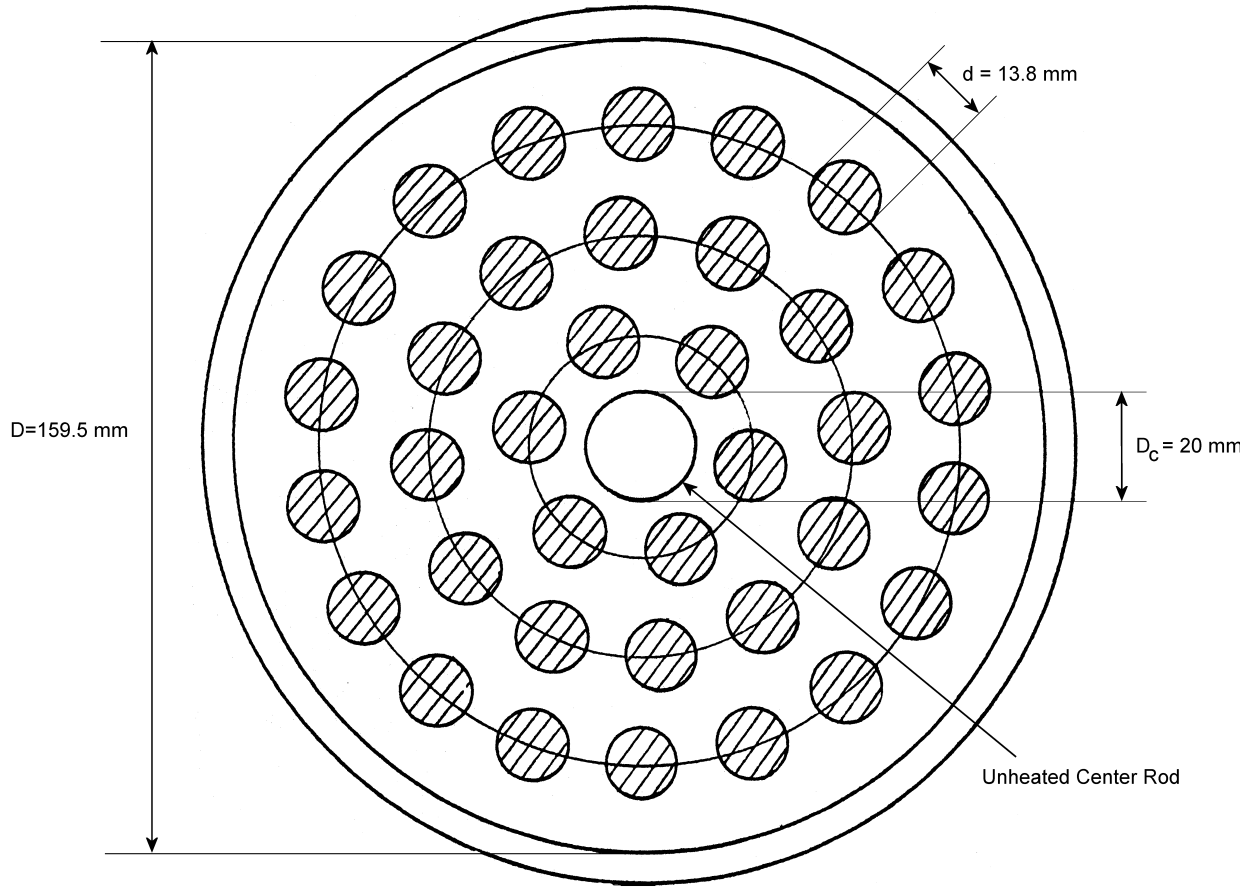

Figure B.12-3. Cross Section View of Test Section

length, diameter, and various flow losses located throughout the loop. No attempt to model the different paths for forced or natural circulation was made; the model contains the piping for natural circulation, less the forced circulation valves, piping, pump, and heater.

The decision to model the test facility in a once through design rather than its true loop basis was made due to the lack sufficient data on the losses associated with the supporting equipment and instrumentation. This includes the lower plenum geometry, the venturi flow meter at elevation 1200mm on the downcomer, as well as much of the steam separator and condenser details. Without these details it was judged impossible to model natural circulation properly, hence the fluid flow was controlled by way of a FILL component set at the specified experimental flow rate.

As there is insufficient detail in the documentation to properly model the test section inlet, the lower plenum geometry shown in Figure B.12-4 is not modeled at all; instead the downcomer is extended to come in from the bottom with a smooth taper to the actual test section geometry. With the exception of the first run, which is used to demonstrate how quickly the model approaches steady state, a total of 6 input parameters are varied between runs. These parameters are located in

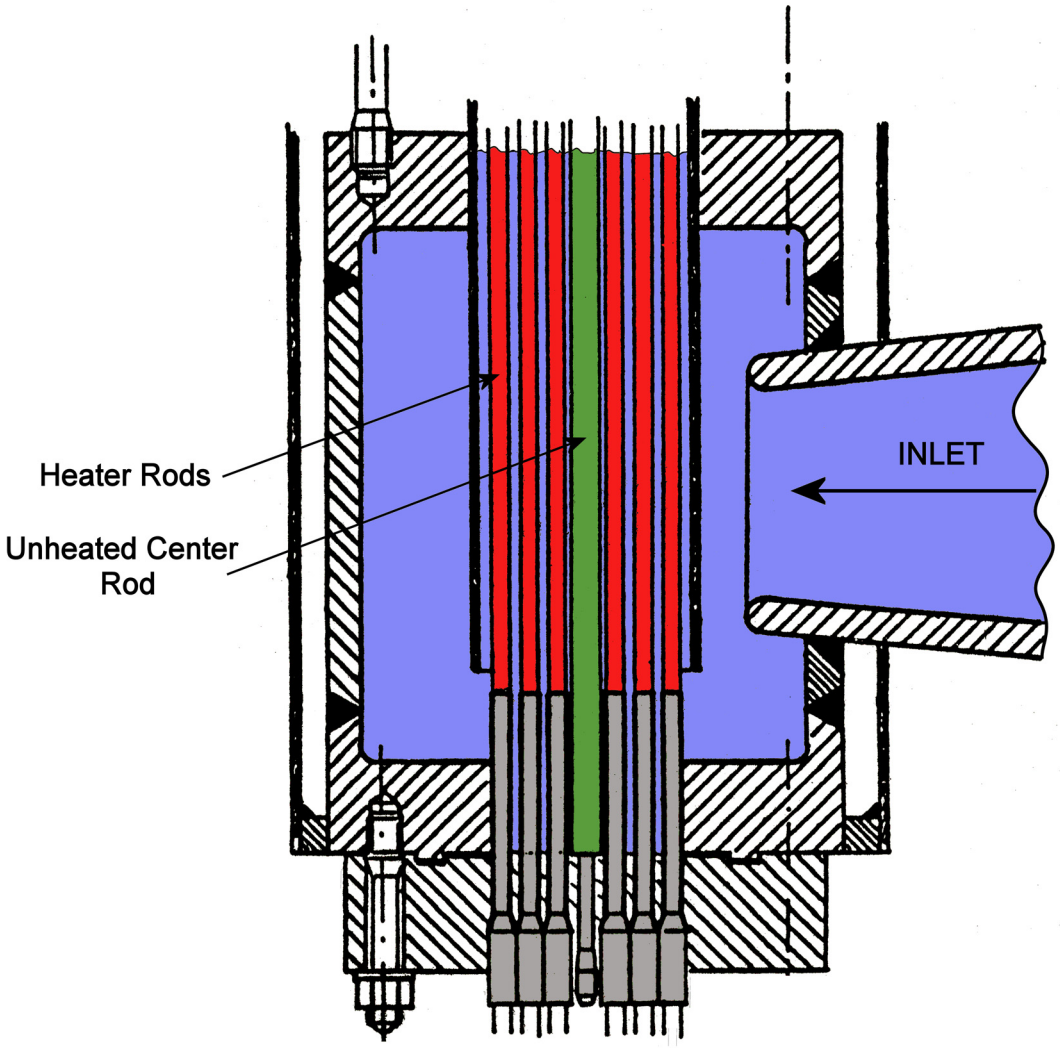

Figure B.12-4. Close-up Diagram Showing Coolant In-let to Test Section

the BREAK, FILL and POWER components, and as such, are common to both models. These parameters are provided in Table B.12.1 below.

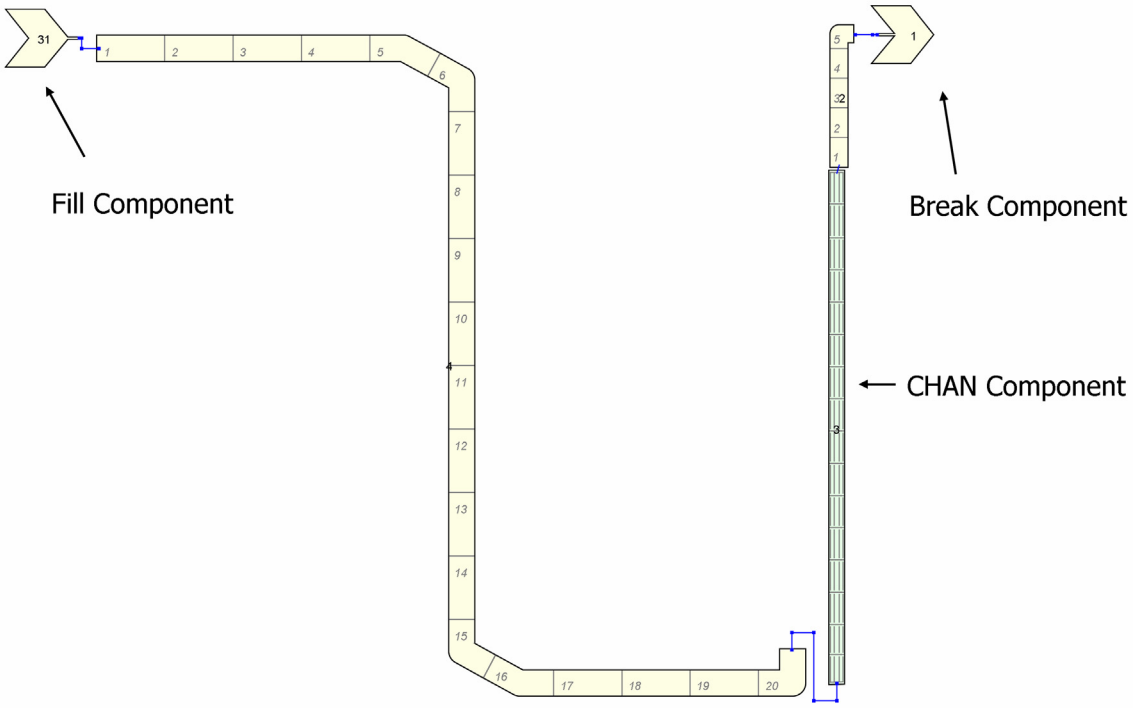

Figure B.12-5. Nodalization Diagram for CHAN Based TRACE Model

Table B.12.1. Significant FRIGG Test Parameters

Test Number	Pressure (bars)	Inlet Coolant subcooling (degrees K)	Total Power to Rods (kW)	Coolant Flow Rate Through Test Section (kg/s)
313001	49.6	5.0	1500	21.31
313002	49.6	2.6	1500	15.65
313003	49.6	2.6	1500	15.65
313004	49.8	3.7	1500	15.75
313005	49.8	3.7	1500	15.85
313006	50	3.7	1500	10.41
313007	50	11.7	1500	15.85
313008	50	4.3	3000	21.01
313009	50	4.4	2980	15.81
313010	50	4.6	2980	9.81
313011	50	4.5	4440	20.61
313012	49.7	4.2	1430	20.81

Table B.12.1. Significant FRIGG Test Parameters

Test Number	Pressure (bars)	Inlet Coolant subcooling (degrees K)	Total Power to Rods (kW)	Coolant Flow Rate Through Test Section (kg/s)
313013	49.7	4.6	2930	16.00
313014	49.7	11.0	2930	16.61
313015	49.7	11.0	2920	16.61
313016	49.6	19.3	2910	17.25
313017	49.6	2.4	4400	20.91
313018	49.7	3.7	4390	16.05
313019	49.5	8.6	4390	16.81
313020	49.7	22.4	4415	16.55
313024	49.7	4.2	1475	12.25
313027	50	4.9	2820	12.65
313030	50	5.1	4560	11.75
313034	50	4.6	1500	14.45
313037	50	4.4	3000	14.65
313040	50	4.4	1500	11.31
313043	50	3.5	3000	11.75
313056	49.9	9.5	3000	13.11
313060	49.4	10.5	1470	11.31

B.12.3.2. Vessel Based Model

The second basic model type utilizes a VESSEL component for the primary test section and a heat structure for thermal transfer. The VESSEL based model nodalization is presented in Figure B.12-6. The only other significant differences between the CHAN and the VESSEL based models are in the length of the CHAN as compared to the VESSEL. In both the CHAN-based and VESSEL based models a 5 cell pipe is used for the upper plenum to reach the elevation of the pressure transducer just below the steam separators. In the VESSEL-based model, however, the length of the pipe cells are lessened. The corresponding length is incorporated into the top vessel cell (which is unheated), so that the transition from bundle to upper plenum occurs inside the vessel.

B.12.4. Tests Simulated with TRACE

In order to simulate the tests described in the following sections TRACE model parameters were adjusted for the FILL, BREAK and POWER components. The FRIGG tests modeled in this assessment used a near constant pressure (50 bars) and had saturated conditions at the bottom of

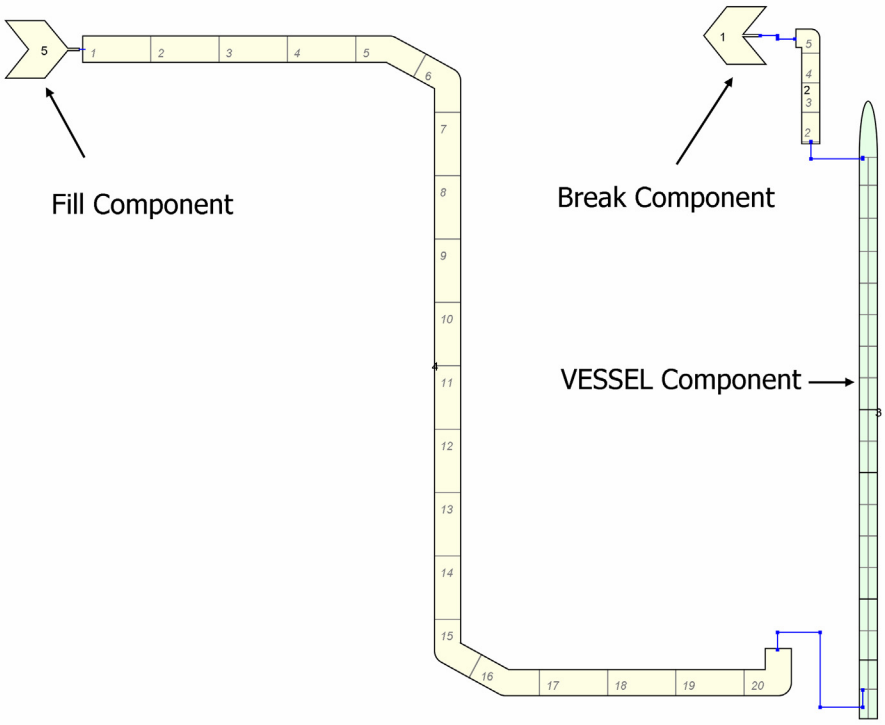

Figure B.12-6. Nodalization Diagram for VESSEL Based TRACE Model

the steam separator/perforated pipe. Therefore, the parameters for the BREAK component where varied only slightly from the tests target of 50 bars and 537.2 K and where based on the actual measured values for the pressure and temperature at that location. The primary parameters varied in the tests were the inlet coolant subcooling, coolant flowrate, and total power to the rods. The inlet subcooling and flowrate parameters are set in the FILL component and the power to the heater rods is set in the POWER component.

The total-power-to-rod parameter was varied between 1430 kW and 4560 kw. However, this parameter was not varied uniformly, but rather there are three distinct groupings of values. The highest powered group ranges from 4390 to 4560 kW power. The next highest group ranges from 2820 to 3000 kW. The lowest powered group ranges from 1430 to 1500 kW. The uncertainty in the power parameter is estimated as +/- 50 kW (Ref. 2)

The mass-flux through the test section parameter was varied from 687 to 1492 kg/m^{2}s. The actual values in this range are fairly uniform, however, a group ranging from 1443 to 1492 kg/m^{2}s is slightly offset on the high end of this parameter's range.

The degree of subcooling in the inlet liquid to the test section was varied from 2.4 to 22.4 degrees K. However, two of the tests that had the most subcooling were considerably far away from the next nearest group of tests. Test 313016 (19.3 degree K subcooling) and test 313020 (22.4 degree K subcooling) were over 7 degrees of subcooling away from the next closest group of tests. The

next closest range had subcooling ranging between 8.6 and 11.7 degree K of subcooling; this range will be referred to as the "high subcooled" range in this report. There was also a group of tests where the range of subcooling was lower and varied between from 2.4 to 5.1 degree K; this range will be referred to as the "low subcooled" range in this report.

B.12.4.1. Simulation of FRIGG Test 313001

Run 313001 is a low power (1500 kW), high flow, (1492 kg/m^{2}s) forced convection run with little subcooling (5 K). The void fraction profile at the end of 95 seconds is presented in Figure B.12-10 In nearly all of the runs, TRACE over-predicts the void at the bottom of the bundle and under-predicts the void at the top. Also shown at the top is a sudden decrease in void fraction on exiting the core.

B.12.4.2. Simulation of FRIGG Tests 313002 and 313003

Runs 313002 and 313003 differ from Run 313001 in that they exhibit very little subcooling (2.6K) and about two-thirds the flow, leading to almost double the exit quality. The void fraction profile at the end of 95 seconds for run 313002 is presented in Figure B.12-11, though approximately half of the experimental measurement positions are unreported. The void fraction profile at the end of 95 seconds for run 313003 is presented in Figure B.12-12. There is better agreement between the CHAN and the VESSEL components for these runs than run 313001, though somewhat at the expense of the more accurate CHAN values. The errors are similar to those of the VESSEL component for run 313001 falling in the range of 20-30% over the active length until the last cell.

B.12.4.3. Simulation of FRIGG Tests 313004 and 313005

Runs 313004 and 313005 are positioned as midpoint run in between the conditions of 313001 and 313002 and 313003 they have 3.7 degrees of sub cooling, right in the middle of the former runs, with approximately the same flow as Run 313002 so it will exhibit slightly less void generation. The void fraction profile at the end of 95 seconds for run 313004 is presented in Figure B.12-13. The void fraction profile at the end of 95 seconds for run 313005 is presented in Figure B.12-14. We continue to see good agreement between the CHAN and the VESSEL components as in Runs 313002 and 312003, but with significant over-prediction of the void fraction along all but the upper end of the test section particularly in run 313004. Most values for run 313004 and nearly all values for run 313005 are within a factor of 2 with predictive quality improving significantly with elevation.

B.12.4.4. Simulation of FRIGG Test 313006

Run 313006 is a small adjustment from run 313005 and run 313004. All of the parameters are kept approximately the same except for the flow rate which is reduced to approximately half of

the initial run 313001. This generates the greatest exit quality seen thus far in the test series. The void fraction profile at the end of 95 seconds is presented in Figure B.12-15. As we have seen in most runs, we continue to see good agreement between the, CHAN and the VESSEL components, with over-prediction of the void fraction along the lower end of the test section, improving with elevation and void. All values are well within a factor of 2 with predictive quality improving significantly as a whole with elevation.

B.12.4.5. Simulation of FRIGG Test 313007

Run 313007 is an adjustment from run 313002 and run 313003. All of the parameters are kept approximately the same except for the subcooling which is more quadrupled to 11.7 degrees. This generates the lowest exit quality of the entire test series. The void fraction profile at the end of 95 seconds is presented in Figure B.12-16. As was seen in most runs, good agreement exists between the CHAN and the VESSEL components, with over-prediction of the void fraction along the lower end of the test section, improving with elevation. All values are well within a factor of 2 with predictive quality improving significantly as a whole with elevation.

B.12.4.6. Simulation of FRIGG Test 313008

Run 313008 is generally speaking the same as run 313001 but with double the power, and slightly less (4.3 instead of 5K) subcooling. This generates an exit quality similar to run 313006. The void fraction profile at the end of 95 seconds is presented in Figure B.12-17. As we have seen in most runs, we continue to see good agreement between the CHAN and the VESSEL components, with over-prediction of the void fraction along the low to middle region of the test section, with a typical dip to under-prediction at the top of the test section. All values agree within 50%.

B.12.4.7. Simulation of FRIGG Test 313009

Run 313009 parallels run 313002, by reducing the flow to similar values (1107 kg/m^{2}s). All other values are nominally the same as run 313008. With the increased power and decreased flow, this generates an exit quality that is the highest of the runs so far. The void fraction profile at the end of 95 seconds is presented in Figure B.12-18. As was seen in most of the runs, good agreement exists between the CHAN and the VESSEL components, with significant over-prediction of the void fraction along the lower region of the test section, with a typical dip to mild under-prediction at the top of the test section. All values agree within 50%.

B.12.4.8. Simulation of FRIGG Test 313010

Run 313010 is a third flow rate (687 kg/m^{2}s) at the increased power conditions, giving even higher exit qualities; all other values are nominally the same as run 313008 and 313009. The void fraction profile at the end of 95 seconds is presented in Figure B.12-19 As was seen in most of the runs, good agreement exists between the CHAN and the VESSEL components, with very mild

over-prediction of the void at the along the lowest region of the test section, with a typical dip to mild under-prediction at the top of the test section. All values agree within 30%.

B.12.4.9. Simulation of FRIGG Test 313011

Run 313011 is a third nominal power (4440 kW) at the other nominal conditions of run 313001. Because this run contains approximately as high a power as ever achieved under forced convection in the FRIGG test series, the exit quality is substantial. The void fraction profile at the end of 95 seconds is presented in Figure B.12-20 This particular run has little experimental data with only 2 locations reporting measured values. As was seen in most of the runs, good agreement exists between the CHAN and the VESSEL components, but the agreement with experiment appears to be quite poor, though the only experimental values are those that have been in the region with the least predictive capability.

B.12.4.10. Simulation of FRIGG Test 313012

Run 313012 is a run much like run 313001. It has slightly less subcooling (4.2 vs. 5 K) and slightly less power (1413 vs. 1500 kW), with all other parameters nominally the same as run 313001. The void fraction profile at the end of 95 seconds is presented in Figure B.12-21 The results from this run mirror those of Run 313001, the agreement between the CHAN and the VESSEL is poorer at the lower end of the test section and better at the higher end.

B.12.4.11. Simulation of FRIGG Test 313013

Run 313013 is a run that appears to be a duplicate of run 313009. It has mid level power (2930 kW) nominally typical subcooling (4.6 K) and mid- level flow (1120 kg/m^2s). The void fraction profile at the end of 95 seconds is presented in Figure B.12-22. The results from this run are nearly indistinguishable from Run 313009.

B.12.4.12. Simulation of FRIGG Tests 313014 and 313015

Run 313014 and 313015 are runs with high subcooling (11.0 K), mid-range power levels (2930 and 2920 kW respectively) and a mid-range flow rate (1163 kg/m^2s). As these runs are essentially higher subcooled versions on runs 313009 and 313013, the anticipated exit qualities are somewhat lower. The void fraction profile at the end of 95 seconds for run 313014 is presented in Figure B.12-23 and the profile for run 313015 is presented in Figure B.12-24 The results from these runs are nearly indistinguishable but differ markedly from the previous high subcooling run 313007, both in the level of agreement between the CHAN and the vessel at low elevations as well as the overall quality of prediction.

B.12.4.13. Simulation of FRIGG Test 313016

Run 313016 is one of two ultra-high subcooling experiments performed (19.3 K). The other conditions were kept nominally similar to runs 313013-313015 with mid-range power levels and flow rates. As this run is a much higher subcooled version of runs 313009 and 313013, the anticipated exit qualities are much lower. The void fraction profile at the end of 95 seconds for run 313016 is presented in Figure B.12-25. The results from this run bear a strong resemblance to 313007, though there is an anomalous value at the lowest end of the vessel.

B.12.4.14. Simulation of FRIGG Test 313017

Run 313017 is the first of three low to midrange subcooling, high power runs. Run 313017 has the smallest subcooling (2.4K) of any of the runs, with nearly the highest power (4400 kW). To compensate for that, the flow rate has been set at the high range (1464 kg/m^{2}s), which results in a middle of the road exit quality. The void fraction profile at the end of 95 seconds for run 313017 is presented in Figure B.12-26 The results from this run bears more resemblance to run 313011, a high power run than to run 313002 or 313003, both very small subcooling runs. This would seem to indicate that the TRACE prediction is more sensitive to power than subcooling.

B.12.4.15. Simulation of FRIGG Test 313018

Run 313018 is the middle run of three with smaller than typical subcooling, at high power. Run 313018 is a parallel run to runs 313004 and 313005 with parameters nominally the same for subcooling, (3.7K), and flow (1124 kg/m^{2}s). With high power levels, a mid-range flow rate and less than typical subcooling, run 313018 sports the second highest exit quality for any of the forced circulation runs. The void fraction profile at the end of 95 seconds for run 313018 is presented in Figure B.12-27 The results from this run show some of the best agreement with experiment of all of the forced circulation runs.

B.12.4.16. Simulation of FRIGG Test 313019

Run 313019 is the last run of three with smaller than typical subcooling at high power. Run 313019 is the only run to feature a subcooling between the nominal low range of 5 and the midrange of approximately 11 K. The other parameters are nominally the same as run 313018. As the subcooling was increased from run 313018, run 313019 should exhibit flow qualities slightly above the middle range. The void fraction profile at the end of 95 seconds for run 313019 is presented in Figure B.12-28. The results from this run again show some of the best agreement with experiment of all of the forced circulation runs.

B.12.4.17. Simulation of FRIGG Test 313020

Run 313020 is the last run of in the forced circulation series that we have analyzed. It sports the largest degree of subcooling (22.4 K) of any run. This is matched with a high power level and mid-range flow rate yielding a mid-range exit quality. The void fraction profile at the end of 95 seconds for run 313019 is presented in Figure B.12-29 The results show the most pronounced discrepancy between the CHAN and VESSEL components. Other than at the very low end of the test section agreement with experiment appears to be on par with the other test runs.

B.12.4.18. Simulation of FRIGG Test 313024, 313034, and 313040

Runs 313024, 313034, and 313040 are a natural circulation runs approximating run 313002 or 313003. There appears to be some level of control over the flow rate as power, subcooling and condenser level are nominally the same for the three runs, but the flow rates differ by up to a fifth. The void fraction profile at the end of 95 seconds for run 313024 is presented in Figure B.12-30. The void fraction profile at the end of 95 seconds for run 313034 is presented in Figure B.12-33 The void fraction profile at the end of 95 seconds for run 313040 is presented in Figure B.12-35. The results for run 313024 are nominally of the same predictive quality as runs 313002 and 313003, however the results for run 313034 show considerably less agreement, particularly at the lower end of the test section. Run 313040 has better agreement than run 313034 but worse than 313024.

B.12.4.19. Simulation of FRIGG Tests 313027 and 31037

Runs 313027 and 313037 are natural circulation runs that differ from runs 313024 and 313034 primarily in the power level of the electric heaters (2820 kW and 3000kW respectively), approximately double the power of the former runs. While the power has nominally doubled, the natural circulation flow rates only increased slightly, 3.3% for run 313027 and 1.0% for 313037, resulting in a near doubling in exit quality from the test section. The void fraction profile at the end of 95 seconds for run 313027 is presented in Figure B.12-31. The void fraction profile at the end of 95 seconds for run 313037 is presented in Figure B.12-34. The results for run 313027 show very good agreement with experiment, while the results for run 313037 are some what degraded by comparison.

B.12.4.20. Simulation of FRIGG Test 313030

Run 313030 has the single highest power level (4560 kW) of all the runs evaluated. It is somewhat anomalous that the steady state natural circulation flow is less for high power than for either of the previous lower powers but run 3130034 (nominally similar to run 313024 but with a differing flow rate) suggests that the steady state flow velocity is a somewhat independent parameter. The combination of low flow, high power results in this run exhibiting the highest exit quality from the test section of any of the runs evaluated. The void fraction profile at the end of 95

seconds for run 313030 is presented in Figure B.12-32 The results show excellent agreement with experiment.

B.12.4.21. Simulation of FRIGG Test 313043

Run 313043 is nominally similar to runs 313027 and 313037 other than in the degree of subcooling (3.5 vs. 4.4 or 4.9 K), and the flow rate is smaller than either of the previous runs. The combination of low subcooling, low flow rate and moderate power results in this run exhibiting a high exit quality from the test section. The void fraction profile at the end of 95 seconds for run 313043 is presented in Figure B.12-36 Similar to run 313027, the results show excellent agreement with experiment.

B.12.4.22. Simulation of FRIGG Test 313056

Run 313056 is one of two moderately subcooled (9.5 K) test runs. With moderate power (3000 kW) and average flow rates, this run generates one of the higher exit qualities of the natural circulation runs. The void fraction profile at the end of 95 seconds for run 313056 is presented in Figure B.12-37 Similar to run 313027, the results show very good agreement with experiment.

B.12.4.23. Simulation of FRIGG Test 313060

Run 313060 is the second of two moderately subcooled (10.5 K) test runs. With low power (1470 kW) and slightly below average flow rates, this run generates the lowest natural circulation exit quality of any natural circulation runs. The void fraction profile at the end of 95 seconds for run 313060 is presented in Figure B.12-38. The results strongly resemble run 313020 with the divergent results for the CHAN and VESSEL at the lowest end of the test section improving to values that agree well with experiment at the top.

B.12.5. Assessment Results Summary

There is generally reasonable agreement between experimental void fractions in the FRIGG tests and those predicted by TRACE. A comparison of predicted void fraction versus experimental values for the CHAN model is shown in Figure B.12-39 and for the VESSEL model in Figure B.12-40. On average, both the CHAN and VESSEL Components overpredict the void fraction by less than 1% and all points within 7%. For both the CHAN and VESSEL Components, the prediction of the void fraction deviates from the experimental values as the void fractions become large. For both the CHAN and VESSEL Component models, TRACE underpredicts the void fractions at high void fractions. Figure B.12-47 shows a series of plots of predicted versus data values for the void fraction at the various levels measured in the experiment. It is seen that the predicted values of void fraction deviate from experimental values in a more pronounced degree at the higher values of void fraction, irrespective of the level in the channel. However, it is also noticed that there is a greater measurement error at level 3.56m than for the other levels.

B.12.6. References

1 O. Nylund et al., "Measurements of Hydrodynamic Characteristics, Instability Thresholds, and Burnout Limits for 6-Rod Clusters in Natural and Forced Circulation," ASEA and AB Atomenergi report FRIGG-1, Sweden (1967)

2 O. Nylund et al., "FRIGG Loop Project: Hydrodynamic and Heat Transfer Measurements on a Full Scale Simulated 36-Rod Marviken Fuel Element with Uniform Heat Flux Distribution," ASEA and AB Atomenergi report FRIGG-2, Sweden (1968).

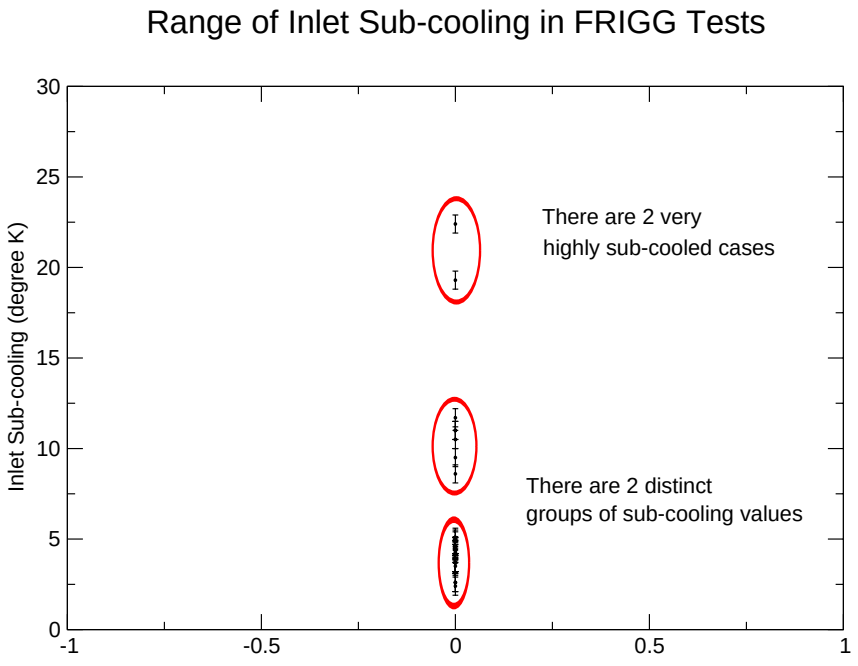

Figure B.12-7. Range of subcooling in FRIGG Tests.

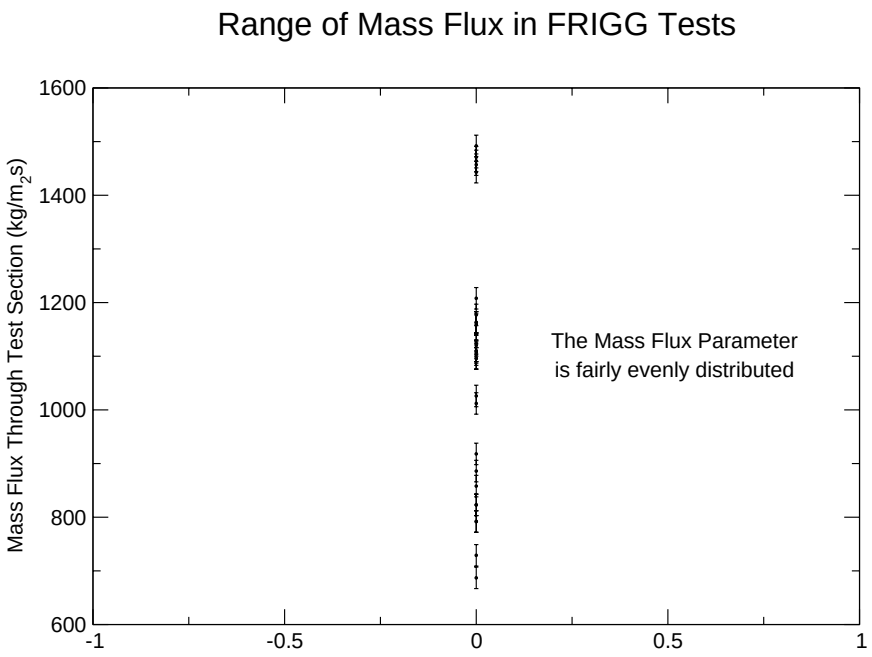

Figure B.12-8. Range of Mass Flux in FRIGG Tests

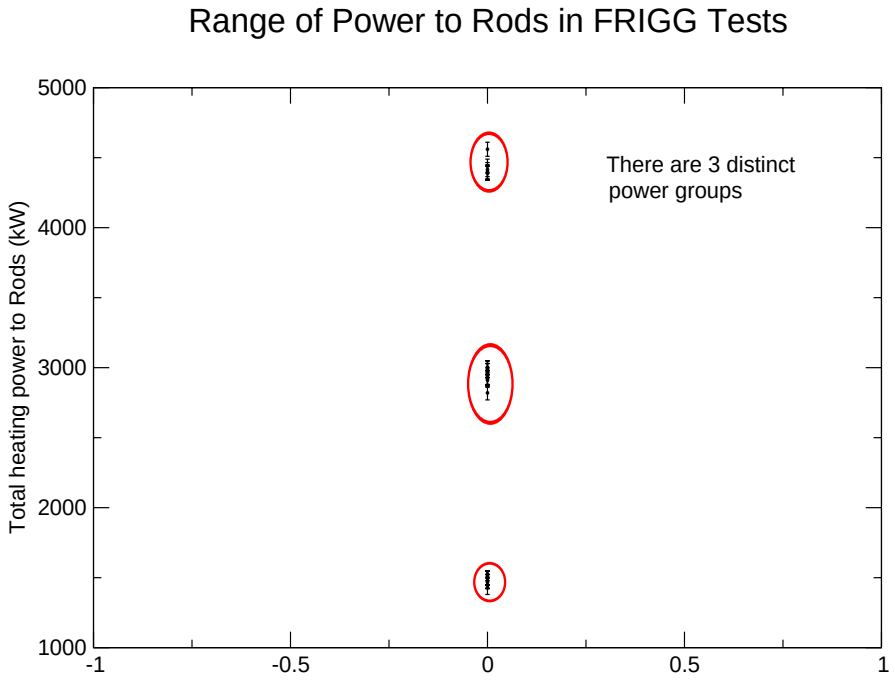

Figure B.12-9. Range of the Power Parameter in the FRIGG Tests

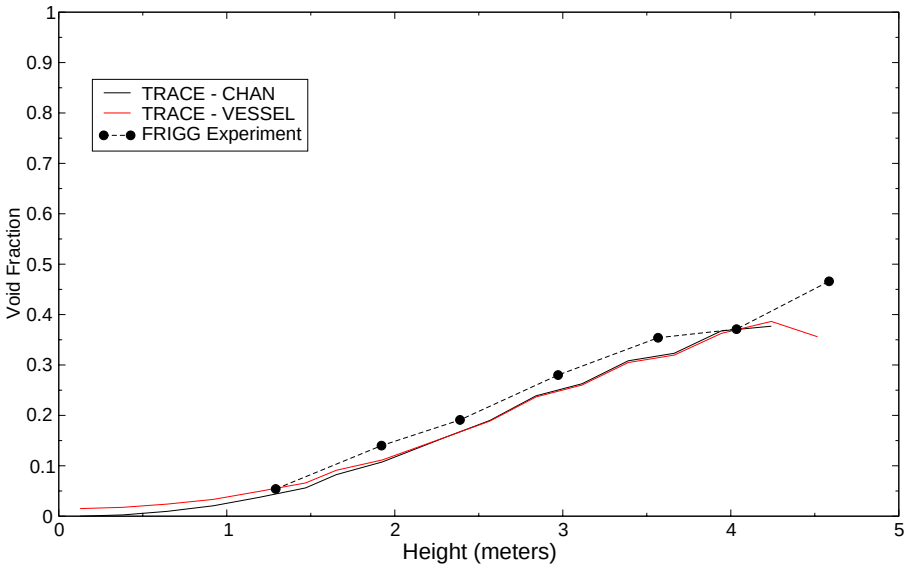

Figure B.12-10. Plot of void fraction vs. height for FRIGG Run 313001

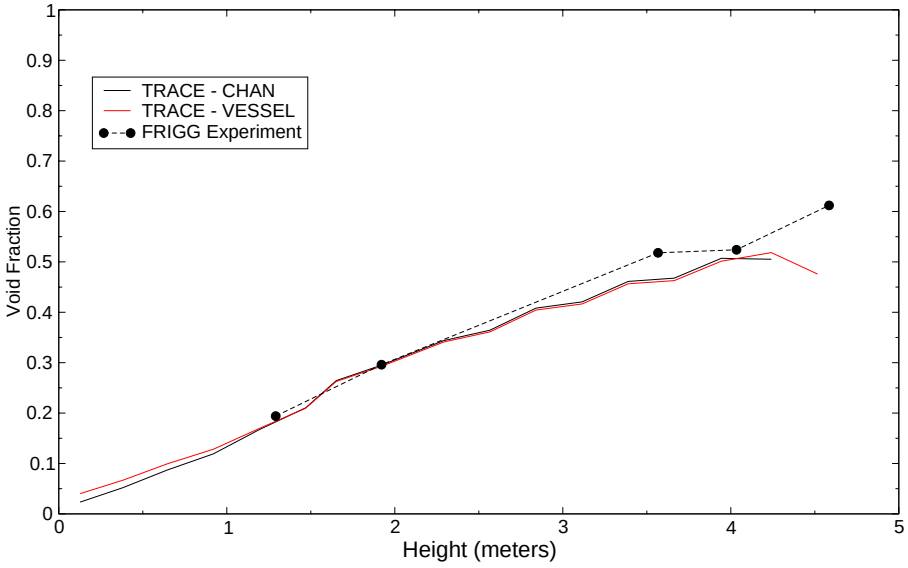

Figure B.12-11. Plot of void fraction vs. height for FRIGG Run 313002

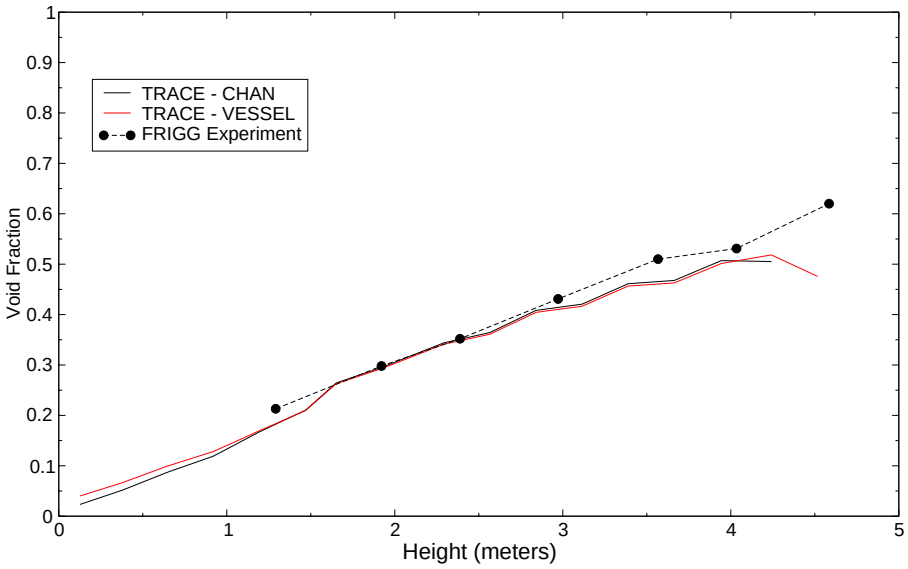

Figure B.12-12. Plot of void fraction vs. height for FRIGG Run 313003

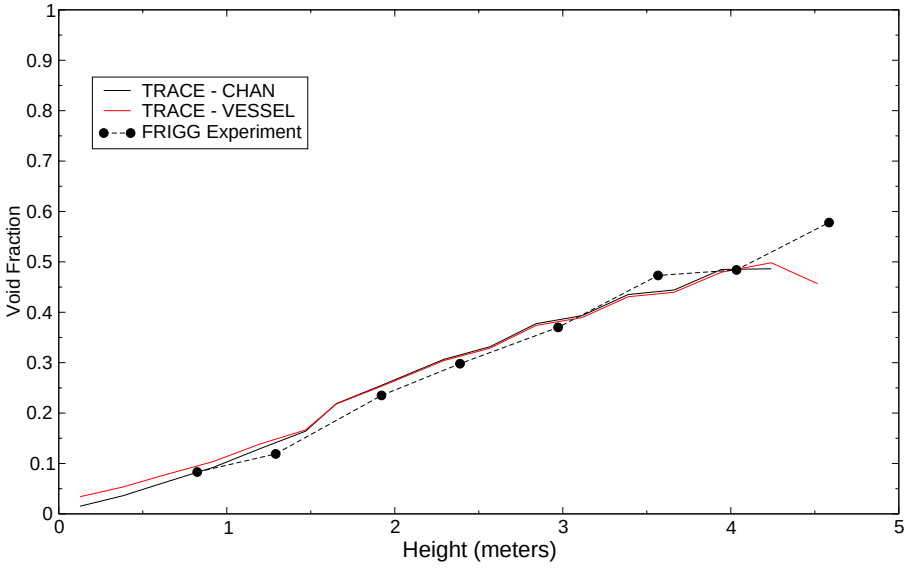

Figure B.12-13. Plot of void fraction vs. height for FRIGG Run 313004

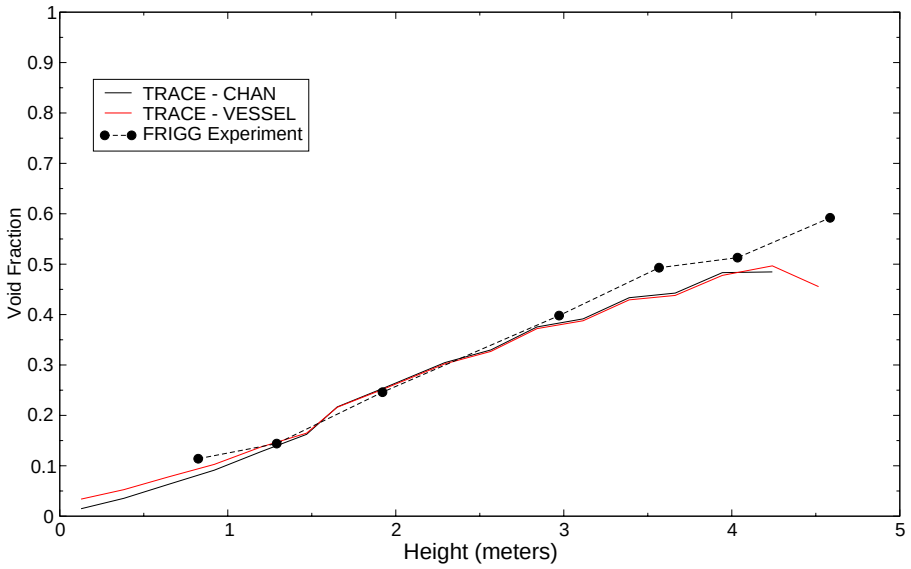

Figure B.12-14. Plot of void fraction vs. height for FRIGG Run 313005

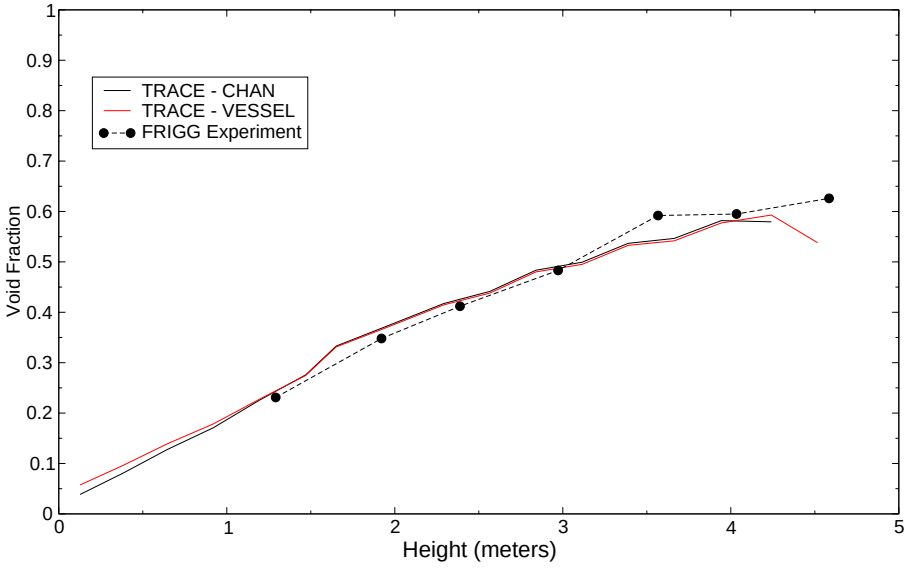

Figure B.12-15. Plot of void fraction vs. height for FRIGG Run 313006

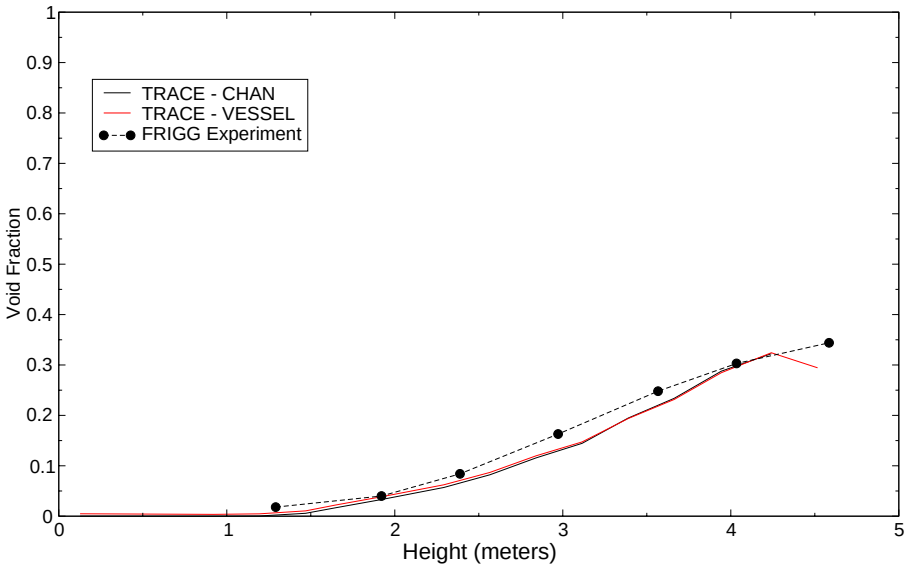

Figure B.12-16. Plot of void fraction vs. height for FRIGG Run 313007

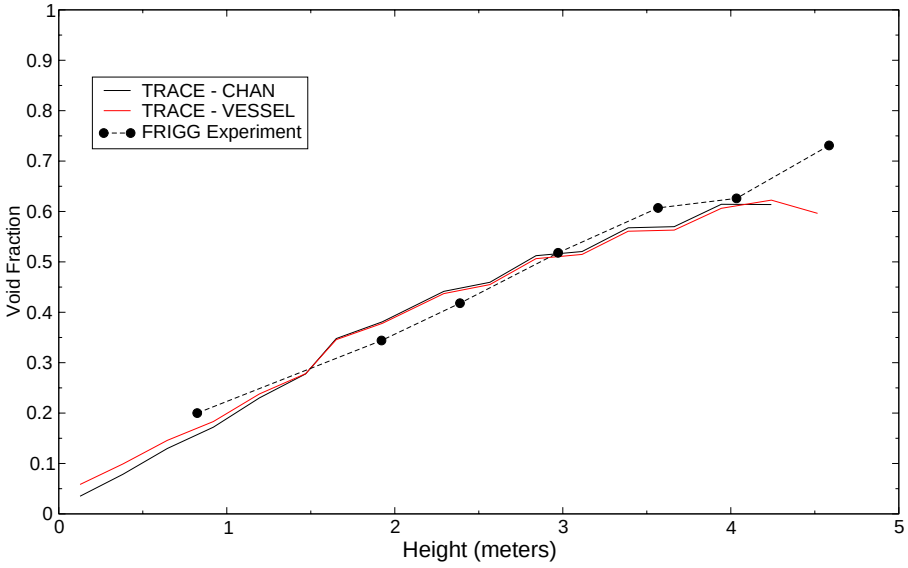

Figure B.12-17. Plot of void fraction vs. height for FRIGG Run 313008

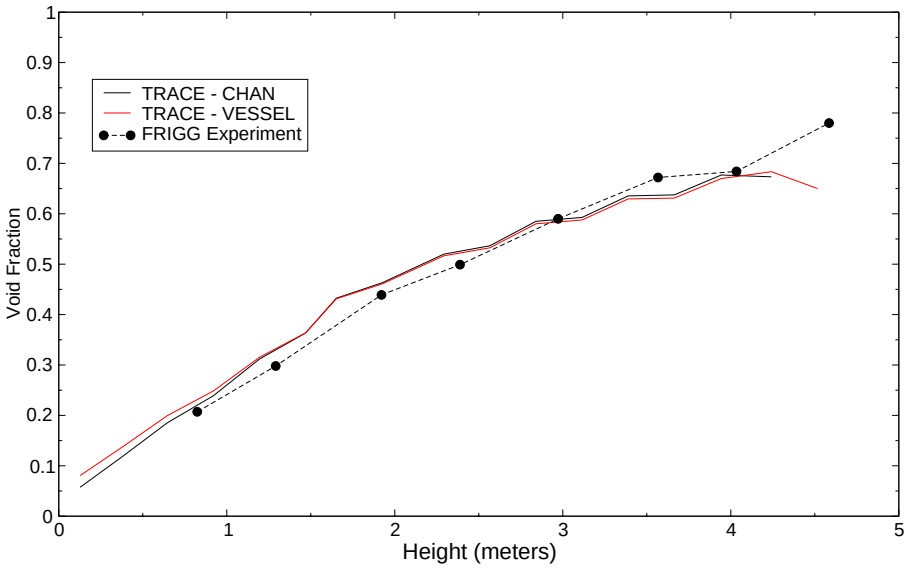

Figure B.12-18. Plot of void fraction vs. height for FRIGG Run 313009

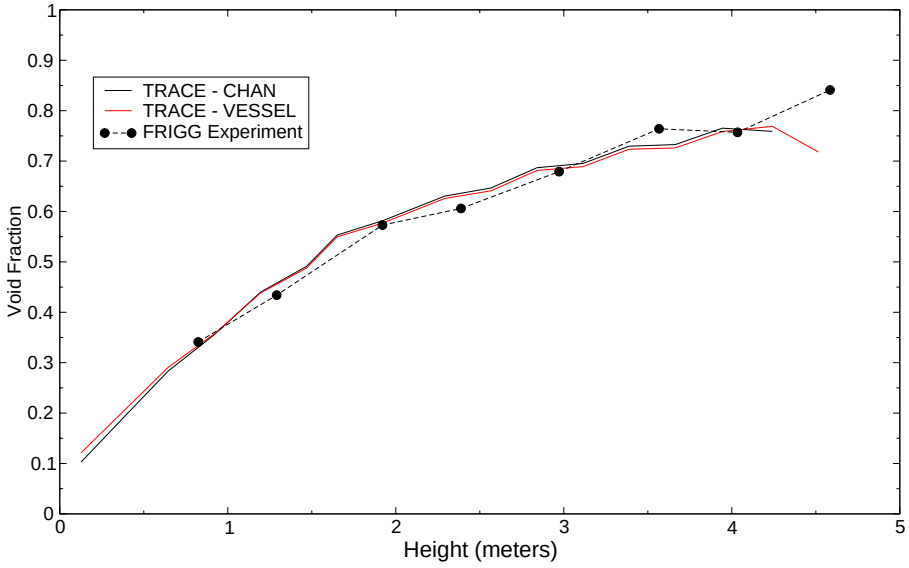

Figure B.12-19. Plot of void fraction vs. height for FRIGG Run 313010

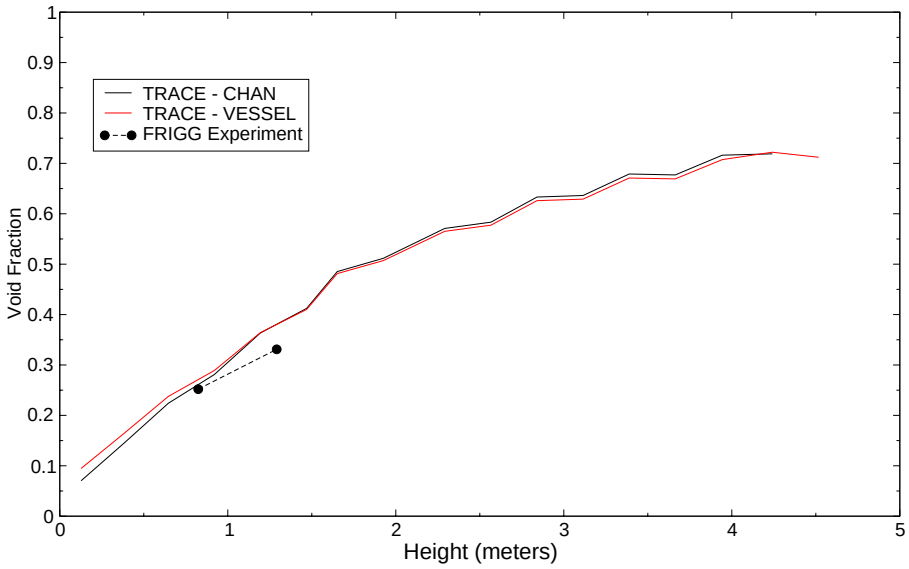

Figure B.12-20. Plot of void fraction vs. height for FRIGG Run 313011

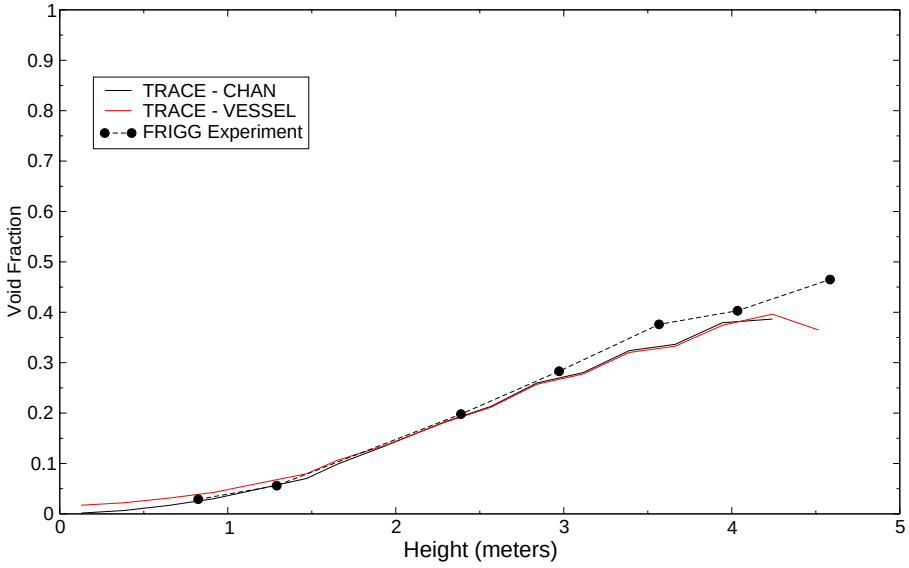

Figure B.12-21. Plot of void fraction vs. height for FRIGG Run 313012

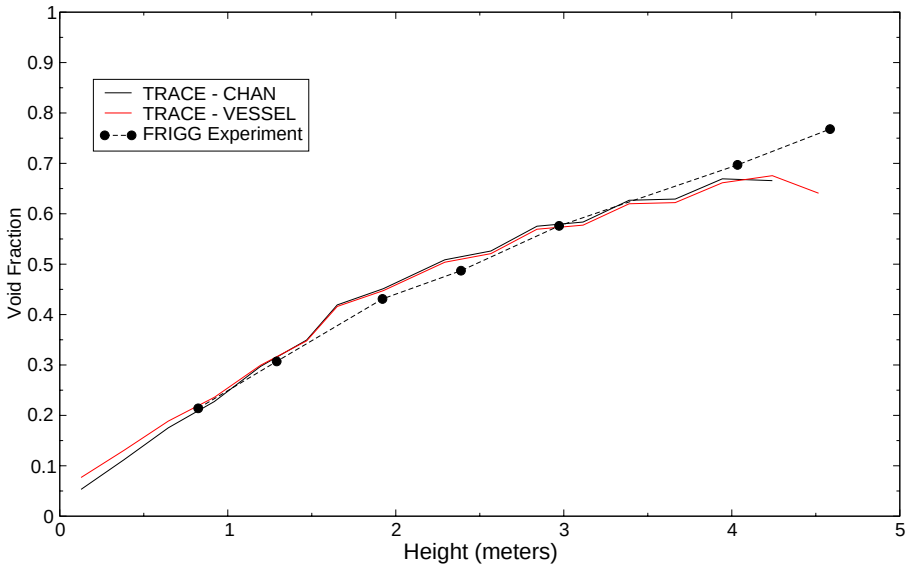

Figure B.12-22. Plot of void fraction vs. height for FRIGG Run 313013

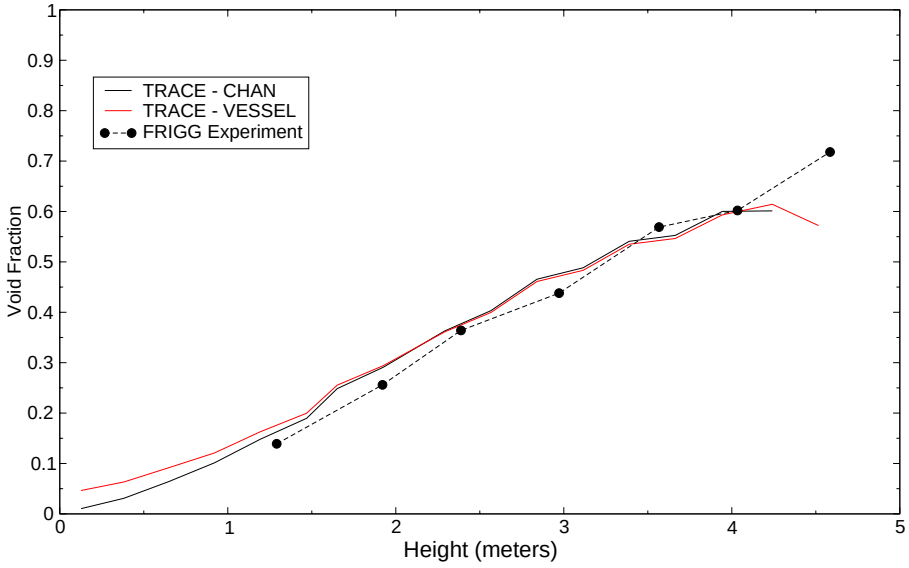

Figure B.12-23. Plot of void fraction vs. height for FRIGG Run 313014

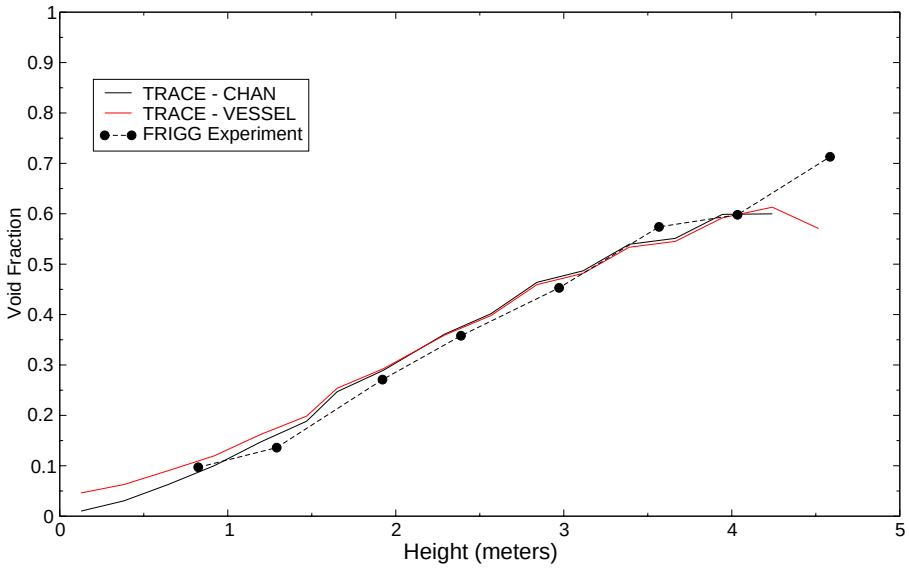

Figure B.12-24. Plot of void fraction vs. height for FRIGG Run 313015

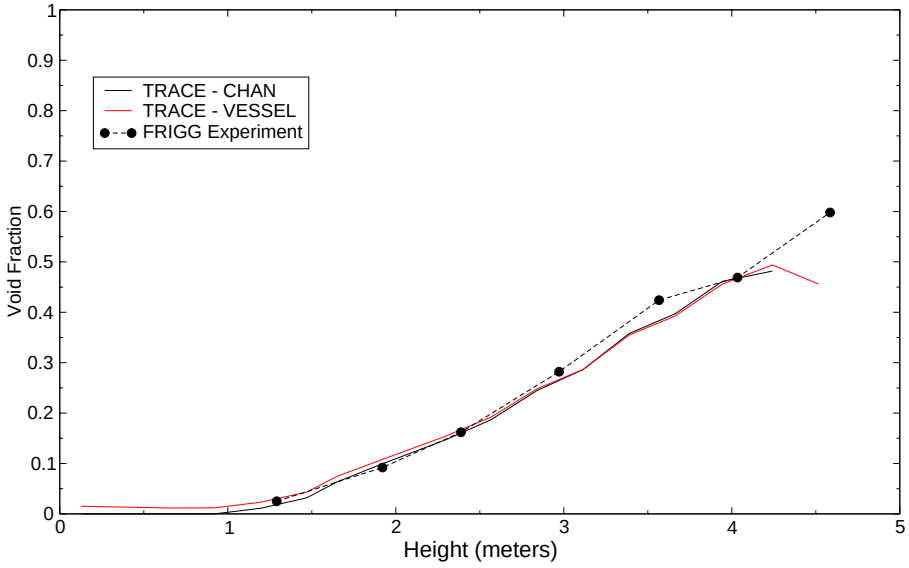

Figure B.12-25. Plot of void fraction vs. height for FRIGG Run 313016

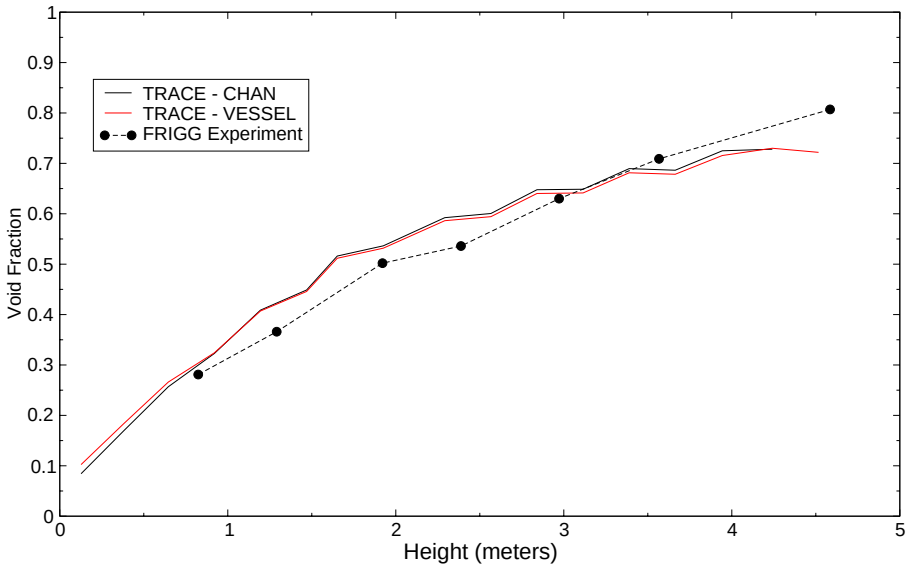

Figure B.12-26. Plot of void fraction vs. height for FRIGG Run 313017

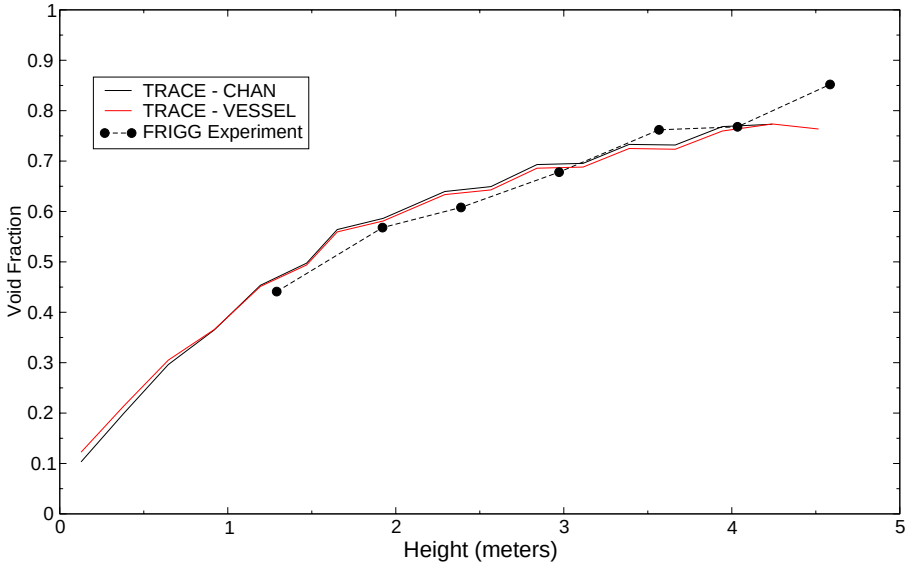

Figure B.12-27. Plot of void fraction vs. height for FRIGG Run 313018

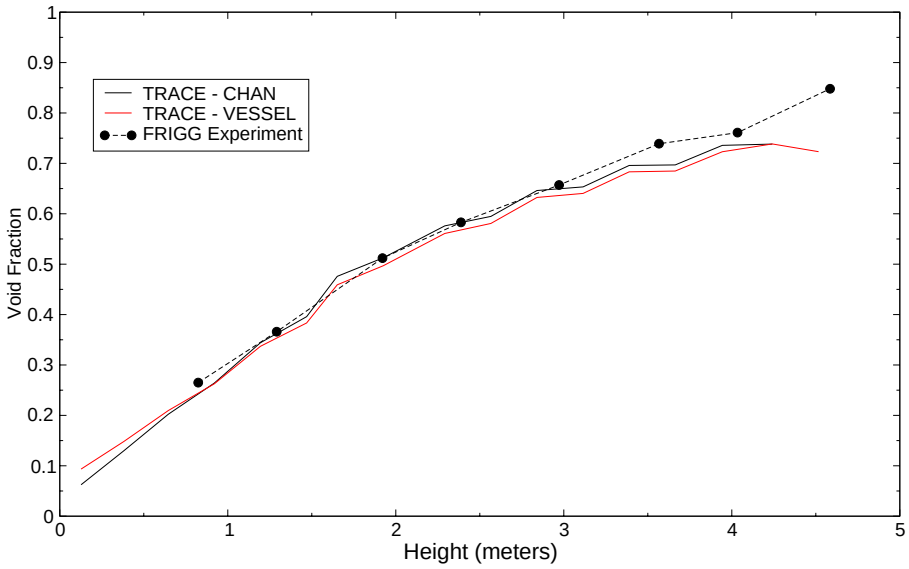

Figure B.12-28. Plot of void fraction vs. height for FRIGG Run 313019

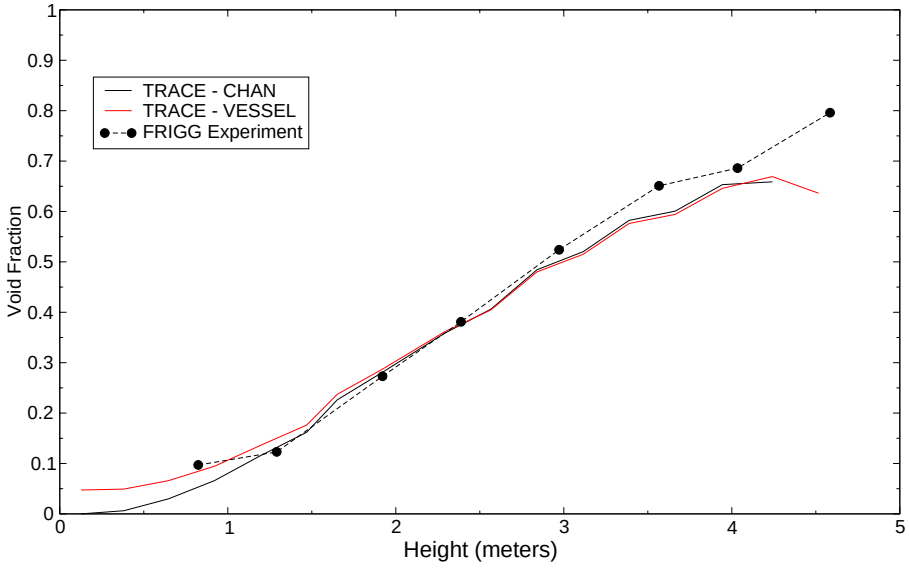

Figure B.12-29. Plot of void fraction vs. height for FRIGG Run 313020

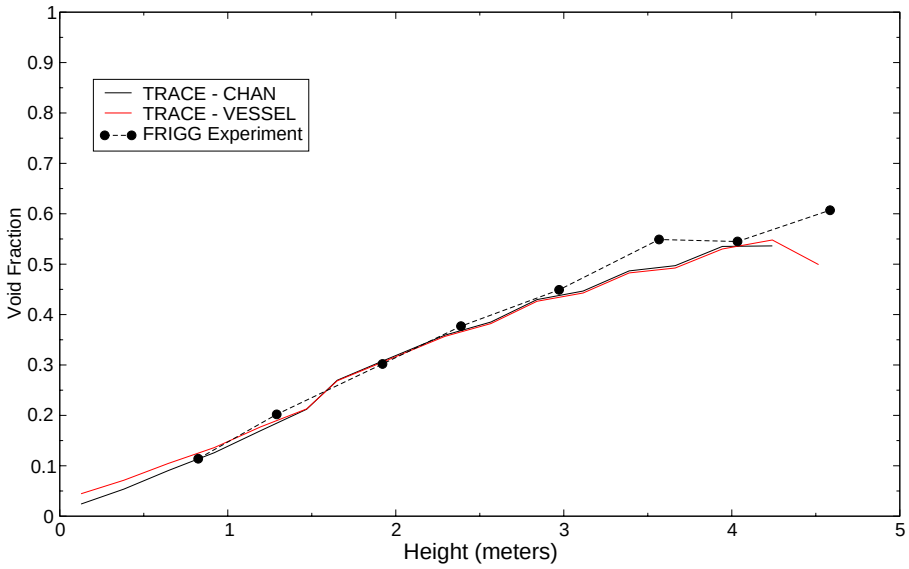

Figure B.12-30. Plot of void fraction vs. height for FRIGG Run 313024

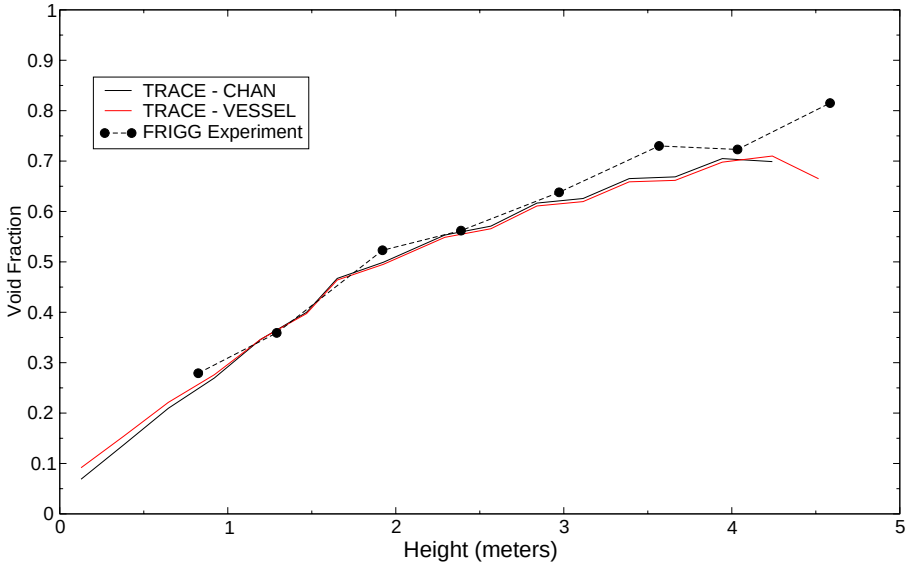

Figure B.12-31. Plot of void fraction vs. height for FRIGG Run 313027

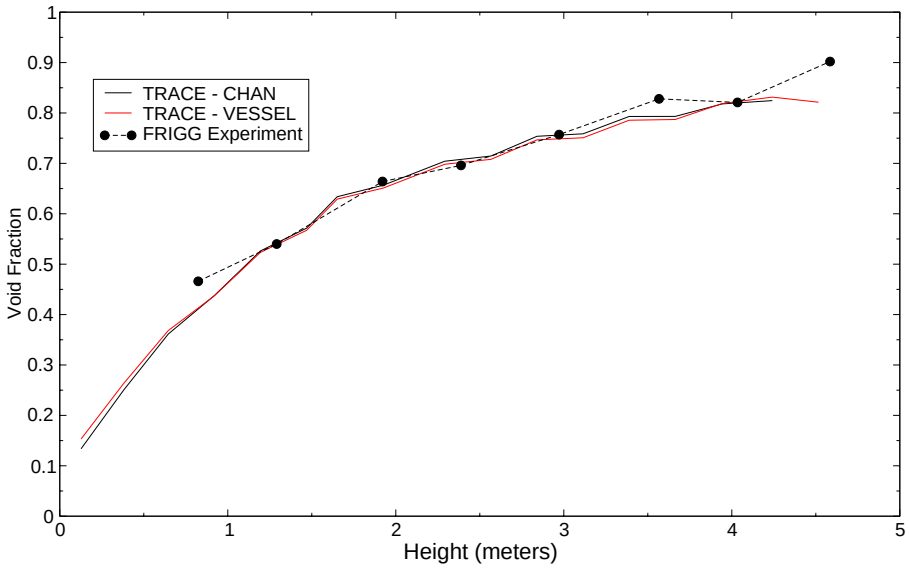

Figure B.12-32. Plot of void fraction vs. height for FRIGG Run 313030

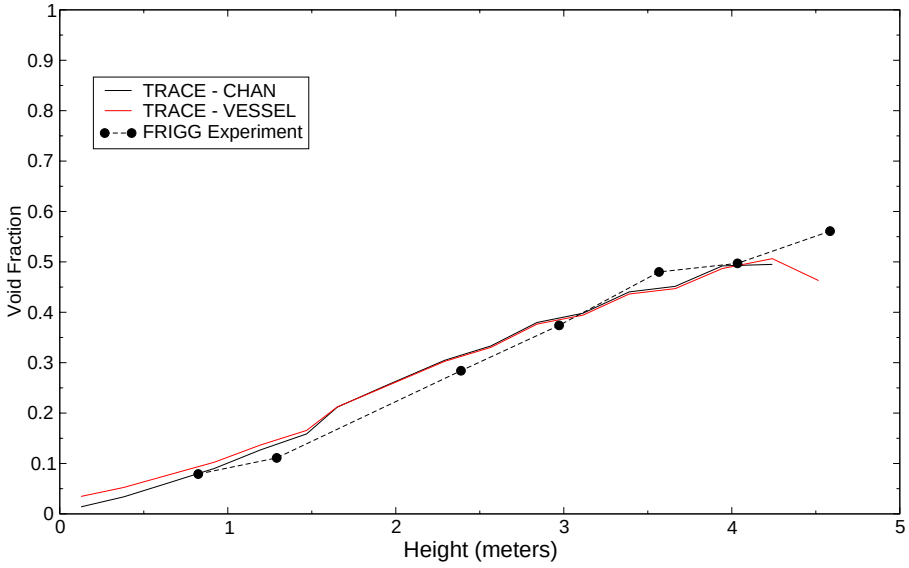

Figure B.12-33. Plot of void fraction vs. height for FRIGG Run 313034

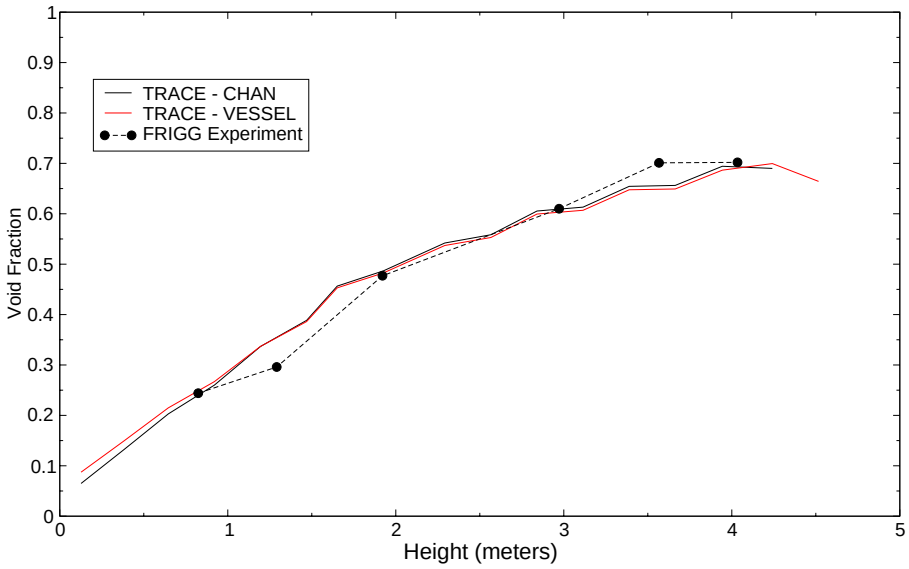

Figure B.12-34. Plot of void fraction vs. height for FRIGG Run 313037

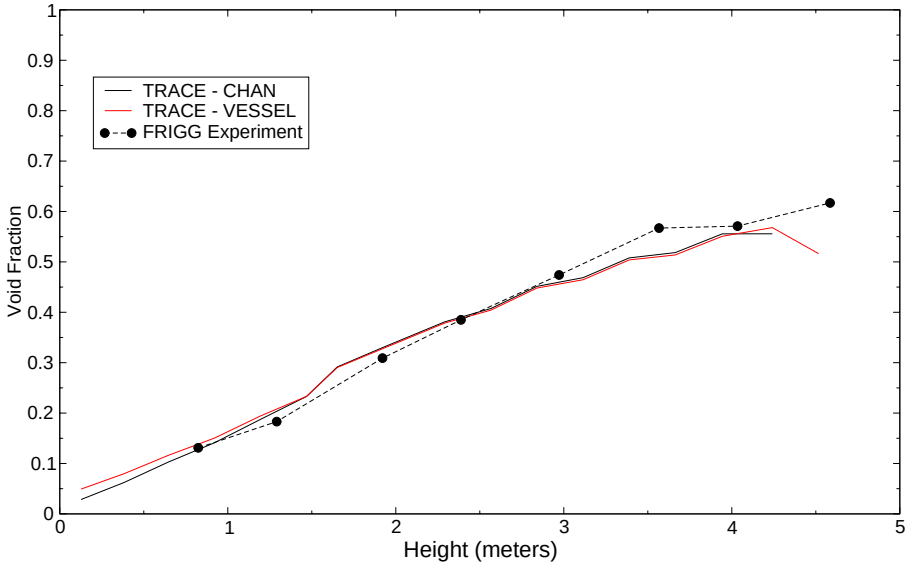

Figure B.12-35. Plot of void fraction vs. height for FRIGG Run 313040

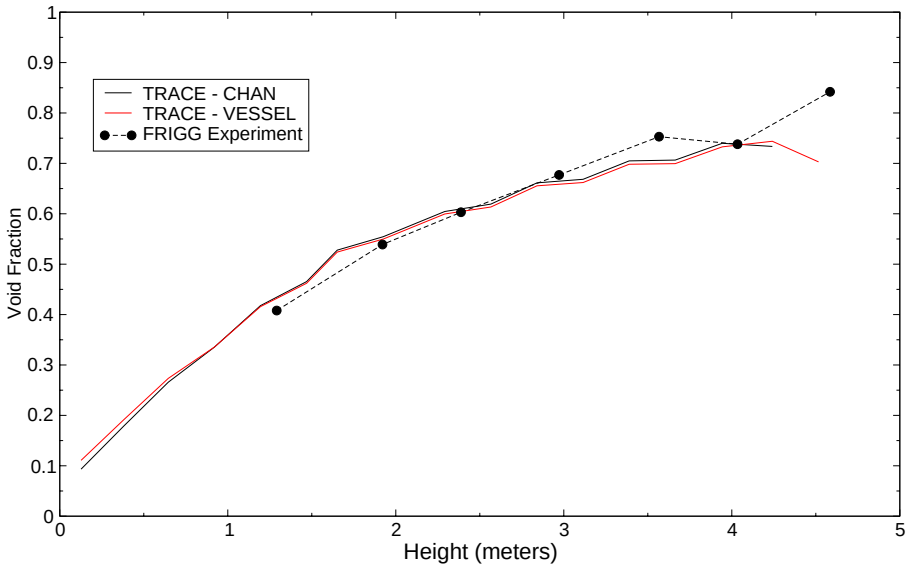

Figure B.12-36. Plot of void fraction vs. height for FRIGG Run 313043

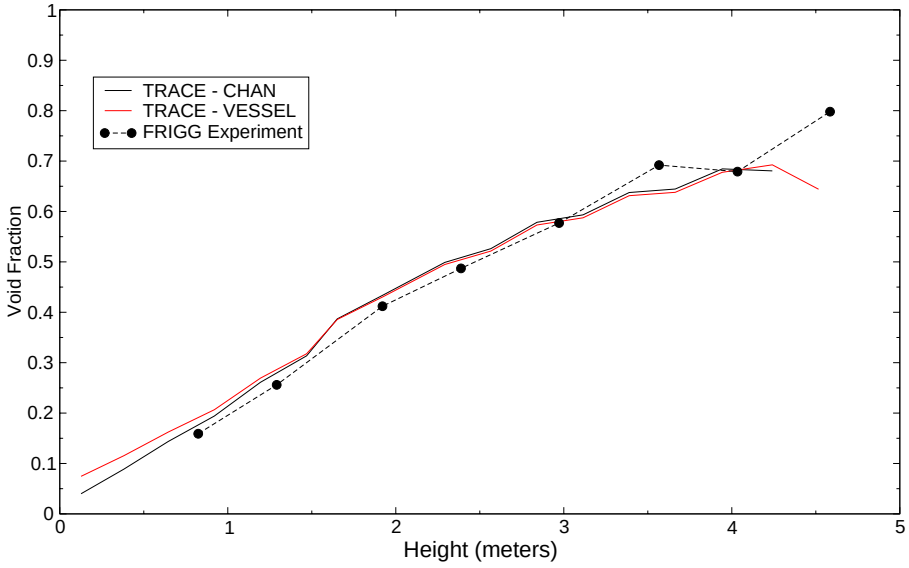

Figure B.12-37. Plot of void fraction vs. height for FRIGG Run 313056

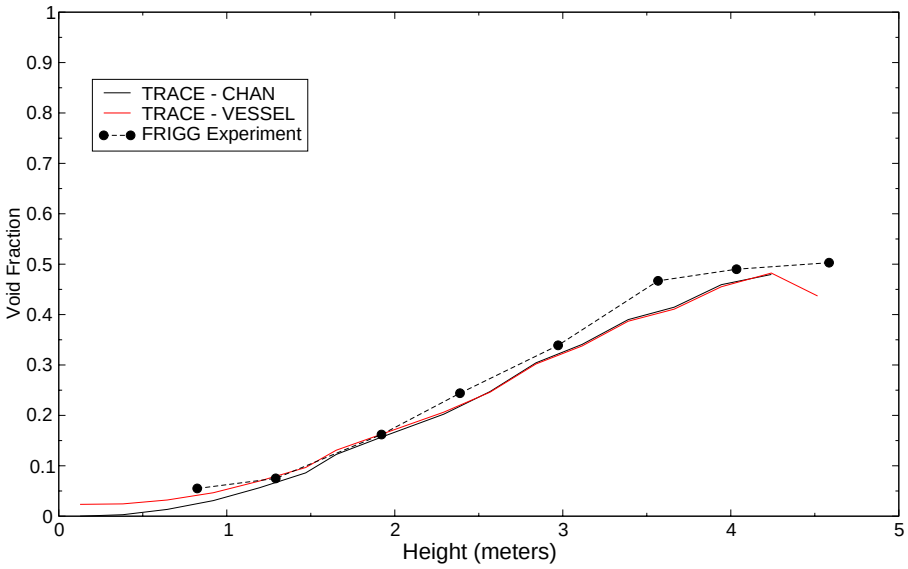

Figure B.12-38. Plot of void fraction vs. height for FRIGG Run 313060

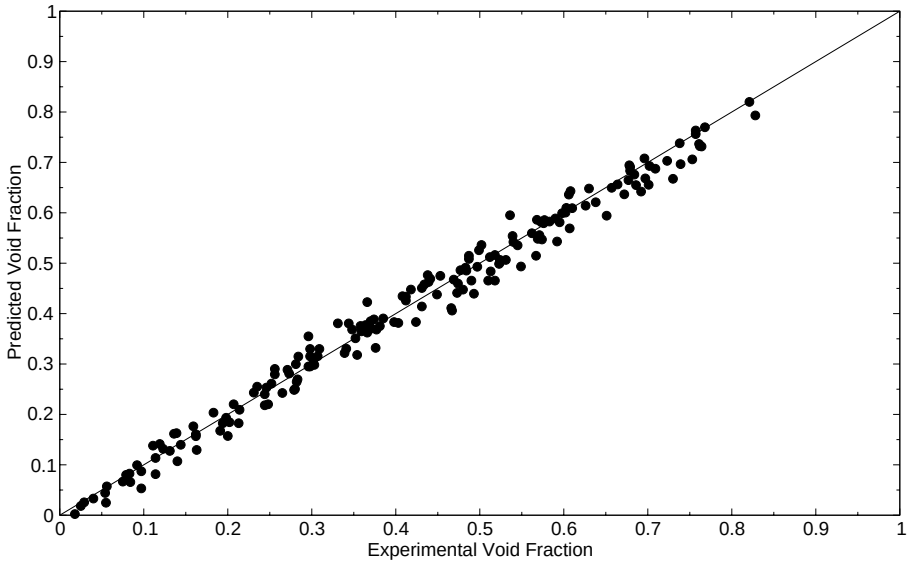

Figure B.12-39. Plot of predicted vs. measured void fractions for the CHAN-based TRACE

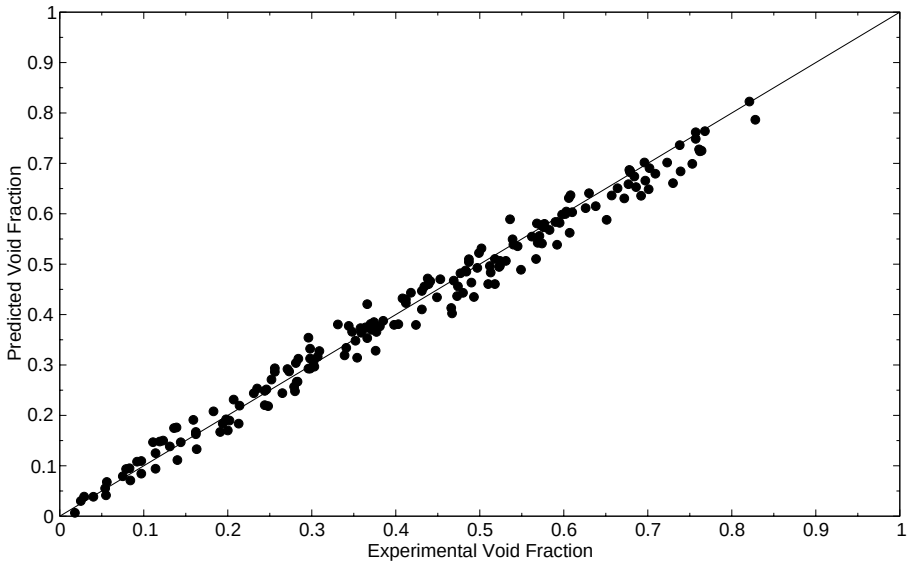

Figure B.12-40. Plot of predicted vs. measured void fractions for the VESSEL-based TRACE

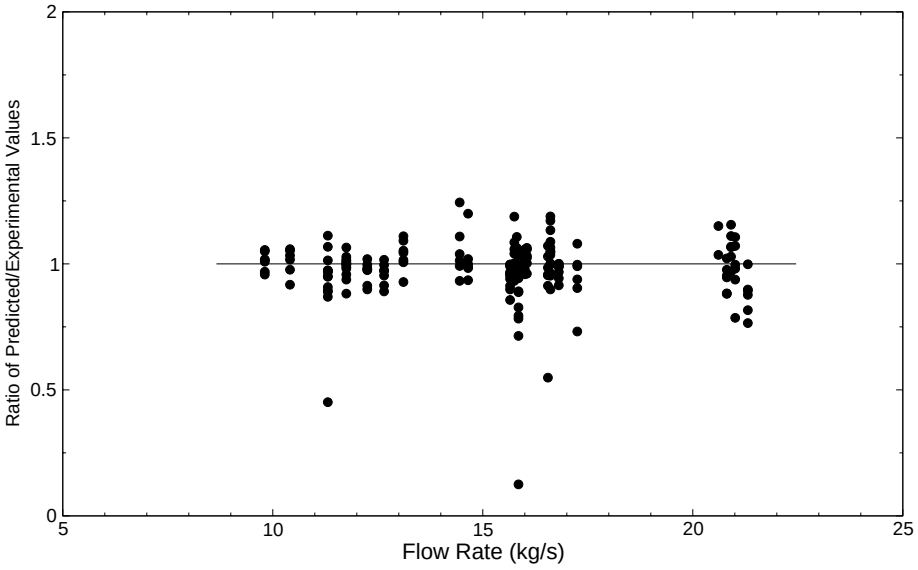

Figure B.12-41. Predicted to Experimental Value Ratio Versus Flow Rate for CHAN Model

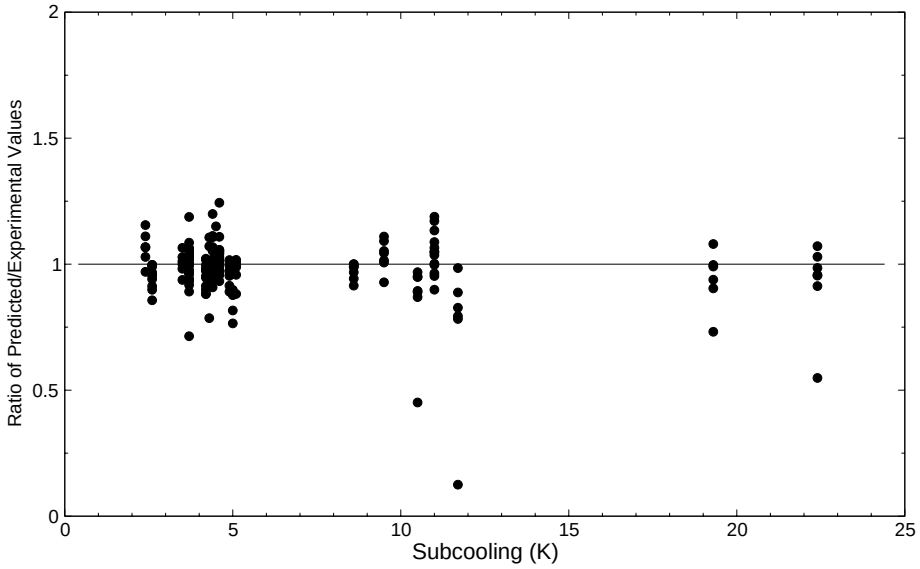

Figure B.12-42. Predicted to Experimental Value Ratio Versus Subcooling for CHAN Model

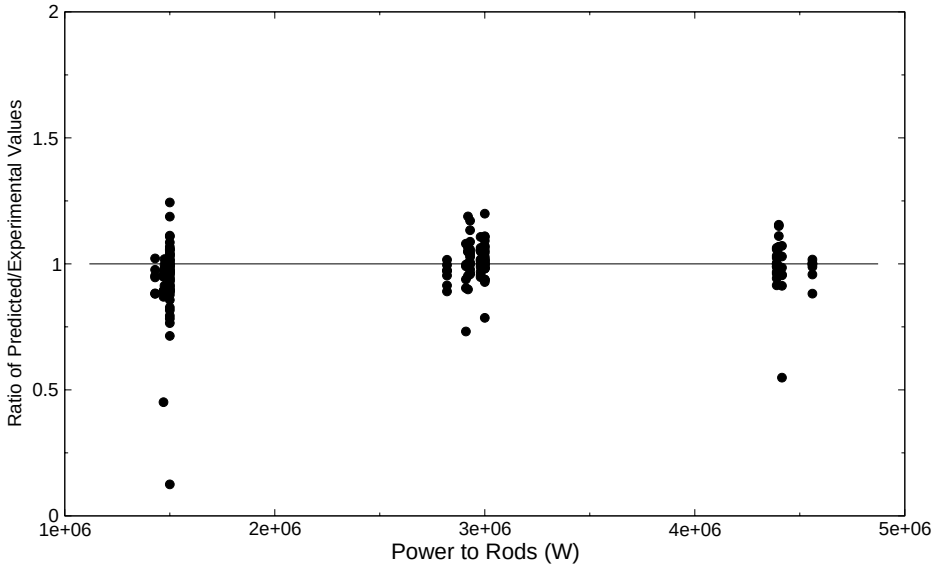

Figure B.12-43. Predicted to Experimental Value Ratio Versus Power for CHAN Model

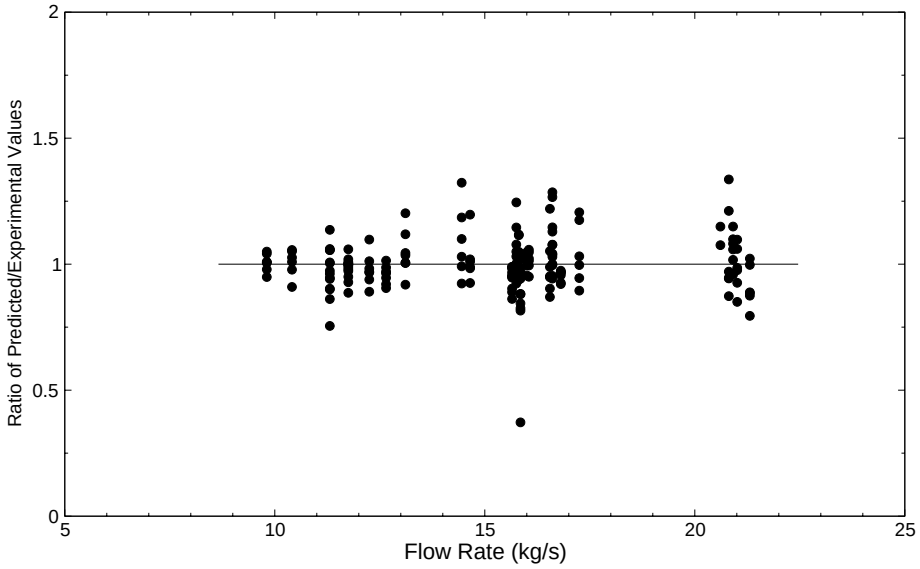

Figure B.12-44. Predicted to Experimental Value Ratio Versus Flow Rate for VESSEL Model

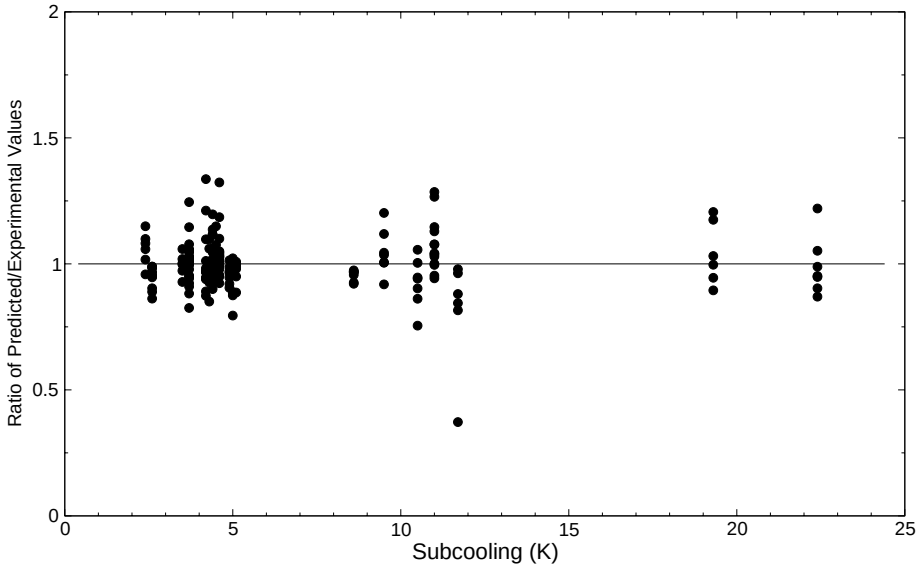

Figure B.12-45. Predicted to Experimental Value Ratio Versus Subcooling for VESSEL Model

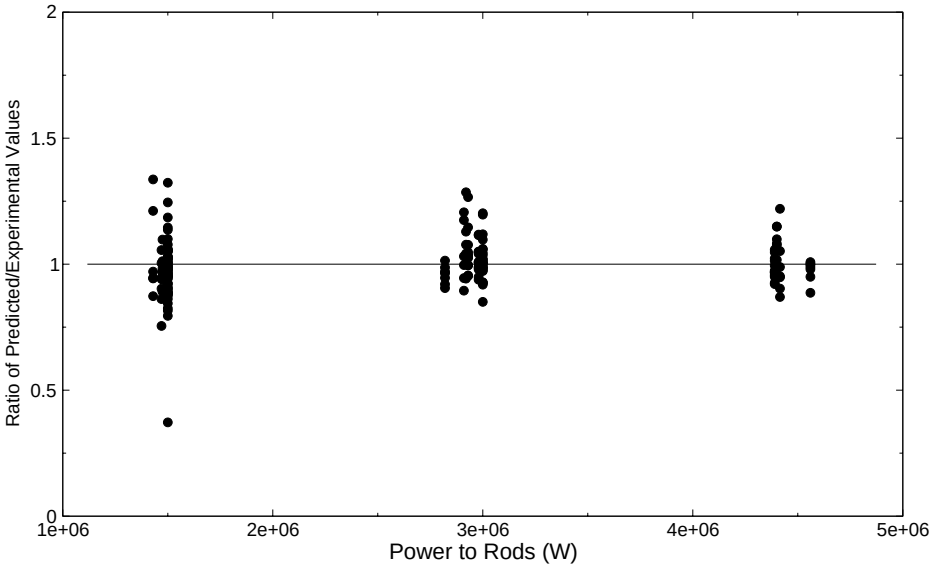

Figure B.12-46. Predicted to Experimental Value Ratio Versus Power for all VESSEL runs

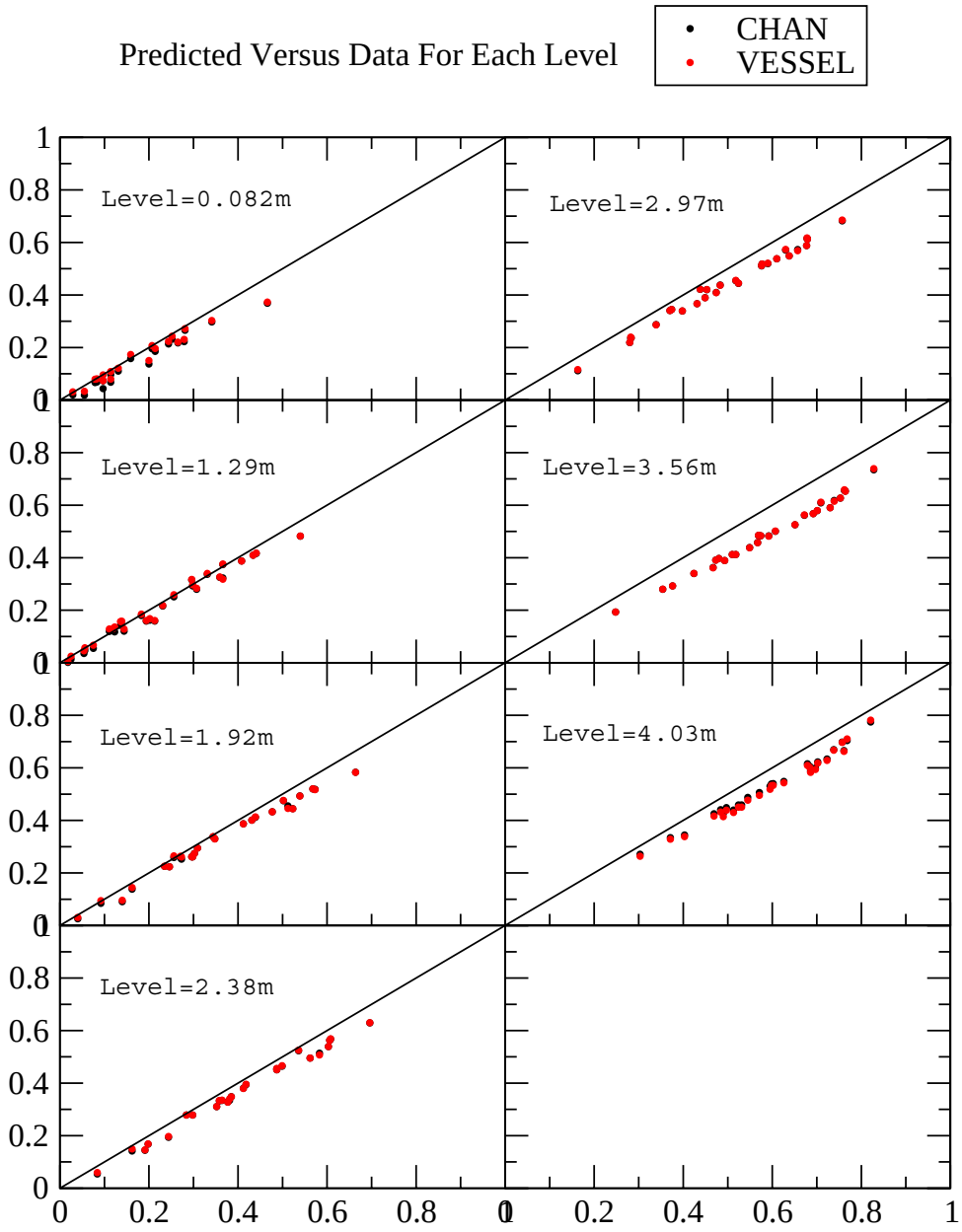

Figure B.12-47. Predicted Values Versus Data Values at Indicated Channel Level (CHAN and VESSEL Models shown)

B.13. THTF - ORNL Mixture Level and Core Uncovery Tests

Author(s): Millan Straka, Andrew Ireland

Affiliation: AdSTM, Inc. (M. Straka), NRC (A. Ireland)

Code Version: TRACE V5.0

Platform and Operating System: Intel x86, Windows XP

B.13.1. Introduction

This section describes the assessment of TRACE using the THTF mixture level swell and core uncovery tests. In particular, this assessment assesses the TRACE capability to predict the axial steam void distribution in general, and the degree of swell in boiling two-phase mixtures in particular. To this end, twelve THTF boiling experiments at low constant velocity and nuclear reactor decay heat level were selected for the assessment (Ref. 1).

The latest TRACE version available at the time of the analysis was applied; namely version 5.0. This assessment applies two TRACE components: VESSEL and CHAN. Based on the current TRACE user guidelines, a VESSEL component is applied to a PWR design and a CHAN (channel) component is used for BWR applications (i.e., modeling a BWR fuel bundle or collection of fuel bundles) (Ref. 2). Therefore, two sets of TRACE input decks were utilized. The first set models the THTF test section with a VESSEL component and the second set applies a CHAN component for the test section.

Topics in this report include presentation of computationally determined axial void-fraction profiles and two-phase mixture swell parameters for each of the selected THTF experiments. Comparison to the THTF experimental data and an assessment of the TRACE code and its ability to predict the two-phase mixture level in boiling bundles are provided.

This assessment report is based largely on the assessment report of Millan Straka for the same mixture level swell tests simulated with TRACE version 4.190 (Ref. 3).

B.13.2. Test Facility Description

Under the sponsorship of the U.S. Nuclear Regulatory Commission, Oak Ridge National Laboratory (ORNL) experimentally and analytically investigated rod bundle heat transfer under high- and medium-pressure and low heat-flux conditions in the Thermal-Hydraulic Test Facility (THTF) (Ref. 3). The THTF was an electrically heated bundle test loop configured to produce conditions similar to those in a small-break loss-of-coolant accident. A schematics of the THTF test section is shown in Figure B.13-1.

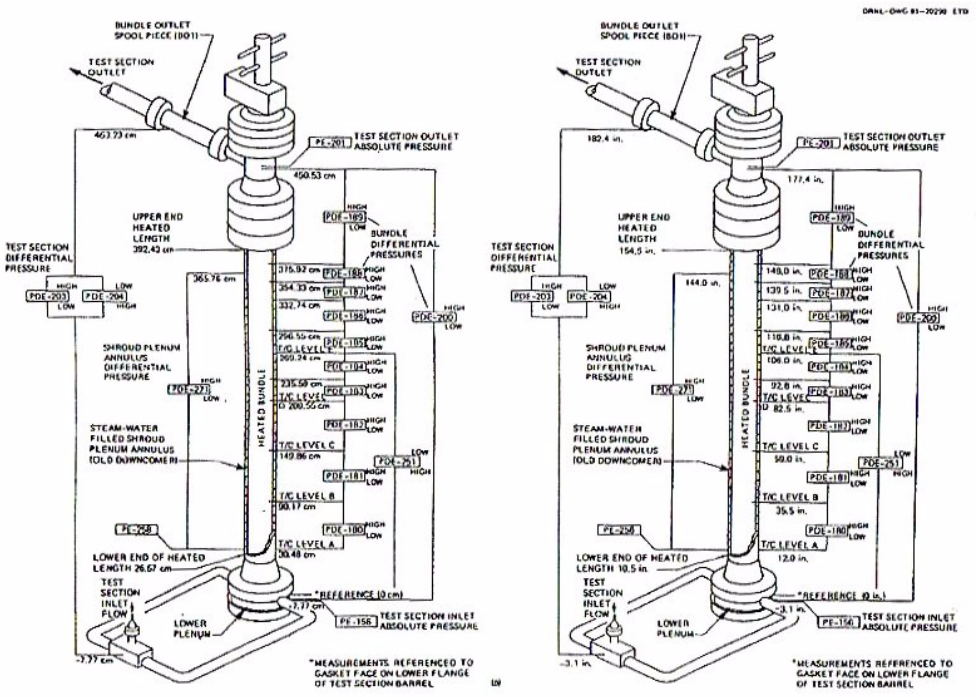

THTF in-bundle pressure instrumentation. (a) Metric units; (b) English units.

Figure B.13-1. THTF Test Section Schematics

The bundle test section consisted of 64 full reactor length fuel rod simulators, 60 of them heated electrically. Figure B.13-2 shows a cross section of the bundle. The four unheated rods were designed to represent control-rod guide tubes in a nuclear fuel assembly. Rod diameter and pitch are typical of a 17 x 17 PWR fuel assembly.

The key THTF design parameters and important bundle geometry data are given in Table B.13.1 below.

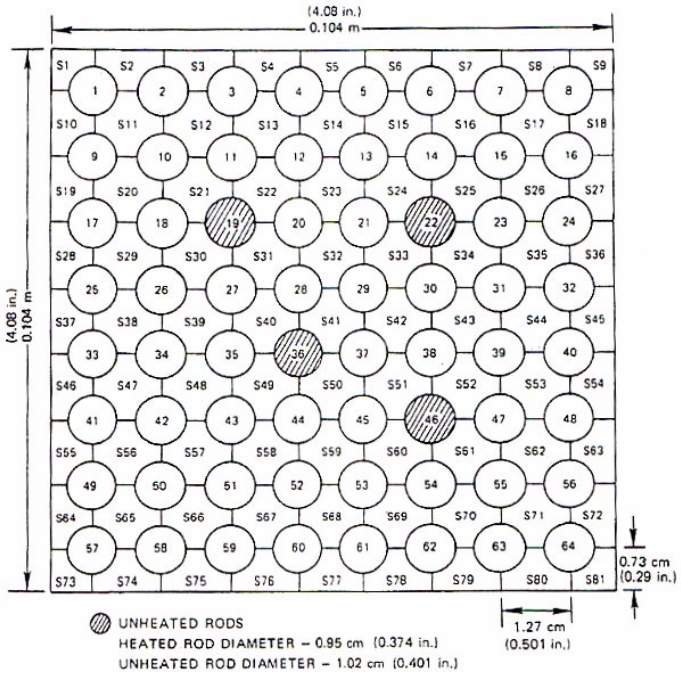

Figure B.13-2. THTF Bundle Cross Section

.

Table B.13.1. THTF Design Summary

Parameter	**Quantity**
Design pressure, MPa (psia)	17.2 (2500)
Pump capacity, m^3/s (gpm)	0.044 (700)
Heated length, m (ft)	3.66 (12.0)
Power profile	Flat
FRS diameter, cm (in.)	0.95 (0.374)
Pitch, cm (in.)	1.27 (0.501)
Subchannel hydraulic diameter, cm (in.)	1.23 (0.48)
Number of heated rods	60
Number of unheated rods	4
Unheated rod diameter, cm (in.)	1.02 (0.40)
Bundle shroud configuration	Square
Bundle shroud thickness, 2 sides, cm (in.) 2 sides, cm (in.)	2.54 (1.0) 1.91 (0.75)
Number of grid spacers	7

Details about the axial location of spacer grids and thermocouple instrumentation are provided in Reference 3.

Two sets of six THTF experiments each have been selected for this assessment. They are 3.09.10I through 3.09.10N, which were experiments intended to investigate heat transfer in an uncovered bundle, and 3.09.10AA through 3.09.10FF, which were designed to measure the axial void distribution in a boiling bundle.

All experiments were performed in a quasi-steady-state manner. The initial and boundary conditions for each respective experiment are shown in Table B.13.2 below.

Table B.13.2. THTF Test Conditions

3.09.10 Test	Pressure (MPa)	Inlet Temperature (K)	Mass Flow (kg/s)	Power (kW/m)
I	4.50	473.0	1.840E-01[a]	2.22
J	4.20	480.3	7.991E-02	1.07
K	4.01	466.5	1.375E-02	0.32
L	7.52	461.3	1.799E-01[a]	2.17
M	6.96	474.4	8.269E-02	1.02
N	7.08	473.1	2.679E-02	0.47
AA	4.04	450.9	1.307E-01	1.27
BB	3.86	458.2	5.836E-02	0.64
CC	3.59	467.6	4.463E-02	0.33
DD	8.09	453.4	1.225E-01	1.29
EE	7.71	455.9	6.800E-02	0.64
FF	7.53	451.4	2.985E-02	0.32

a. Bundle outlet

B.13.3. TRACE Model Description

To model the THTF bundle test section two TRACE models have been designed. The first one made use of the CHAN component and the second make use of the VESSEL component (Ref. 2). Both input files were created to have very similar geometry and each model incorporates uniform axial nodes of height 0.1525 m. The VESSEL model, however, includes an additional axial level below the heated length. The nodalization diagram for the CHAN component is shown in Figure B.13-3 and the nodalization diagram for the VESSEL component is shown in Figure B.13-4. Each test was executed until steady-state conditions were achieved in each simulation run.

Both models consider (and include input for) rod spacer grids at the cell boundaries corresponding to THTF bundle grid elevations.

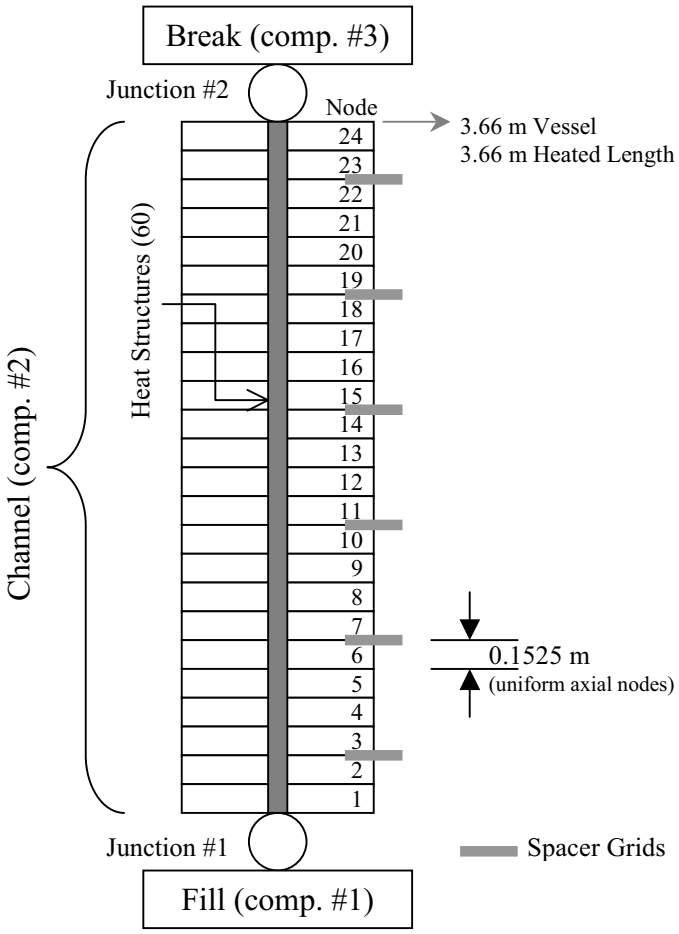

Figure B.13-3. THTF Nodalization with CHAN Component

B.13.4. Tests Simulated with TRACE

All TRACE calculations were performed using code version 5.0 compiled for a Windows operating system.

It is important to note that in the analysis of the TRACE results the same procedure steps have been followed as used for analysis of the THTF experiments (Ref. 3). To determine the calculated two-phase mixture level, the location of interface between the region of nucleate boiling and dry-out has been determined using the calculated rod temperatures. This step is shown in Figure B.13-5 that depicts the rod outer temperatures at the bundle elevations 16, 17, 18, and 19 in the simulation of the experiment 3.09.10I with the TRACE VESSEL component at steady-state conditions. It also shows the corresponding saturation temperature and the temperature of steam. It is noted that dry-out is indicated to occur between the nodal elevations 17 and 18. The mid-point between these elevations corresponds to the axial elevation of 2.5925 m. Therefore, for this case, the calculated two-phase mixture level Z2PH is assumed to be located at 2.59 m (2.62 m

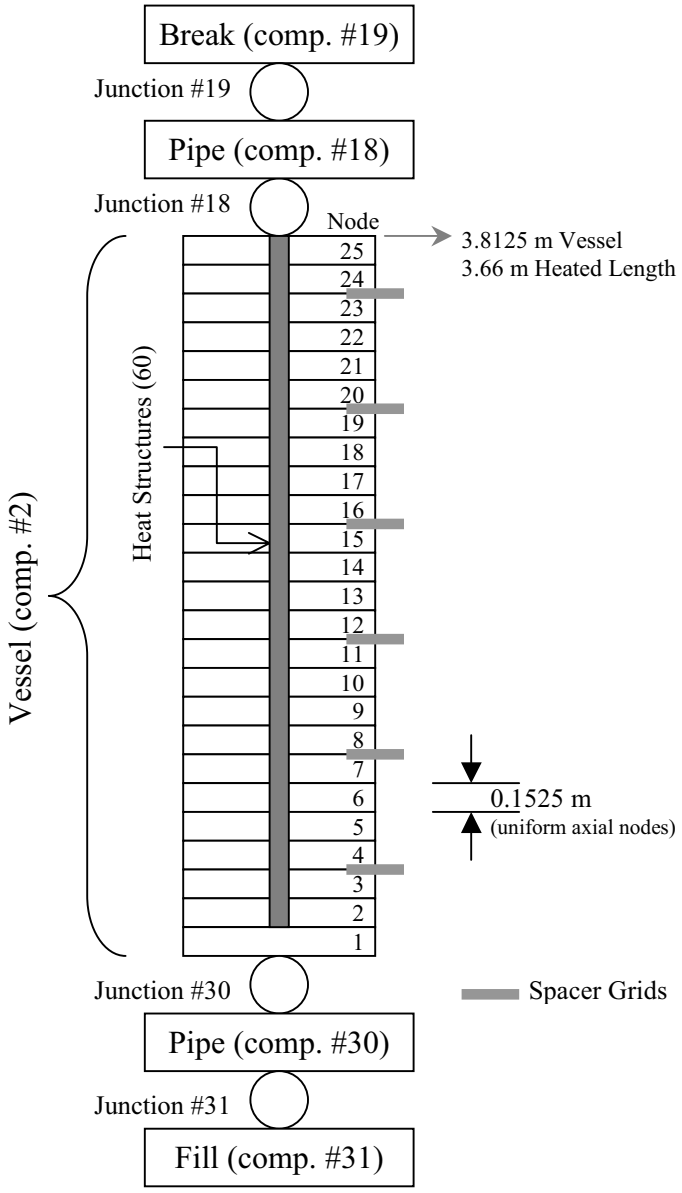

Figure B.13-4. THTF Nodalization with VESSEL Component

measured in the experiment). The two-phase mixture level in each of the remaining simulated experiments (J - N and AA - FF) has been determined in the same fashion. The corresponding temperature plots, for both the VESSEL and CHAN analysis, are shown in Figures B.13-10 through B.13-33.

The axial distribution of steam void for the experiment 3.09.10I is shown in Figure B.13-6. It compares experimental data with the results obtained by the TRACE components CHAN and VESSEL. Except for over-prediction in the lower part of the bundle (discussed above), the trend

is acceptable - especially in the upper part of the bundle and in the transition region from boiling to steam cooling.

The liquid collapsed level Z_{CL} has been determined (as in Reference 3) by summing all liquid fractions along the bundle and multiplying each by the corresponding spatial increment dz. It is shown for all subject tests and calculations in Figure B.13-7. It is underpredicted, as would be expected based on the review of the calculated void fraction distribution.

The results of the void distribution calculated for the remaining simulated experiments are shown in Figures B.13-34 through B.13-45.

The principal figure of merit (FOM) chosen for the present analysis is the so-called mixture level swell parameter, *S*, defined in Reference 3, as:

$$S = \frac{Z_{2PH} - Z_{CL}}{Z_{CL}^*} \tag{13-1}$$

Where Z_{CL}* is the collapsed liquid level over the bundle boiling region, which is equal to the collapsed liquid level over the entire length minus the level of the onset of nucleate boiling (Figure B.13-5). The calculated mixture swell parameter, S is depicted in Figure B.13-8. This figure shows *S* resulting from the analysis of the calculations using the VESSEL and CHAN model component. The calculated parameter *S* has been plotted against its measured value published in Reference 3 (Table 6). It is noted that, in general, *S* has been overpredicted. The suspected reason for this behavior is the performance of the interfacial drag model in TRACE. This appears to be substantiated, e.g. in Figure B.13-6, which shows the axial void profile for the experiment 3.09.10I. As stated above, an overprediction of the void fraction is clearly seen in the lower half of the test bundle. (This fact has also been noted while calculating the collapsed liquid level, Z_{CL}.) It indicates that too much liquid is carried out from each nodalization cell within the lower portion of the boiling region.

A brief survey of pertinent literature shows that this problem has been observed in other works as well. For example, Reference 5 shows that a reduction of the interfacial drag coefficient for calculations with TRACE 4.05 facilitates better agreement with measurements. In Reference 6, the interfacial drag model of the WCOBRA/TRAC computer code was assessed against G1 and G2 test series. The calculation results indicated the tendency of the nominal interfacial drag model to overpredict the mixture level swell. It was reported that when “a multiplier” of 0.8 was applied to the interfacial drag coefficient, the calculation results improved with the test data having been captured within 20%.

As shown above, the calculated level swell, *S* is overpredicted while the collapsed level, Z_{CL} is underpredicted. Because of their multiplicative relationship, these two errors tend to compensate each other and as a result the calculated mixture level agrees relatively well with the measured one (generally within 10% or better) as shown in Figure B.13-9.

During the run execution it was noted that all runs with the exception of 3.09.10K executed in a smooth manner with no error/warning messages. Run 3.09.10K did not reach a reasonable steady-state condition before the rod temperature exceeded the bounds of the material property tables. This is due to the very high power to flow ratio. For this case, results were obtained at 1500 seconds, rather than at a fully steady-state condition. Also, it should be noted that case 3.09.10CC did not experience DNB for the TRACE calculation.

B.13.4.1. Simulation of Important Parameters.

Table B.13.3 through Table B.13.5 lists the THTF experiment measurements and TRACE simulation results. The data in each table are provided for each of the twelve experiments and for each TRACE model (i.e., CHAN and VESSEL) and plotted in Figure B.13-7, Figure B.13-8, and Figure B.13-9, respectively. For the VESSEL model, the results are presented for the heated length only, so that the elevations are consistent with the CHAN model.

B.13.5. Assessment Results Summary

With a few exceptions, the results calculated for the principal figure of merit, mixture swell, are overpredicted. The majority of the results is concentrated within the error line +50%. (Experimental error is on the average 3%.) The reason for this seems to be the overprediction of interfacial drag by the interfacial drag model. It is noted that in similar investigations - with other codes - the same problem has been reported.

Finally, it is noted that one case (3.09.10K, Vessel model) did not reach steady-state before the rod temperatures exceeded the maximum values in the material property tables and one case did not experience DNB in the TRACE calculations (3.09.10CC).

B.13.6. References

1 Ireland, A., “THTF - ORNL Calculation Notebook,” U.S. Nuclear Regulatory Commission, November 2006.

2 U. S. Nuclear Regulatory Commission, TRACE V4.160 User's Manual, Vol. 1-3, July 2005.

3 Straka, M., "THTF - ORNL Mixture Level and Core Uncovery Tests," for the U.S. Nuclear Regulatory Commission, by Advanced Systems Technology and Management, Inc., March 2006, ML061560248.

4 Anklam, T.M.; R.J. Miller; and M.D. White, "Experimental Investigations of Uncovered-Bundle Heat Transfer and Two-Phase Mixture-Level Swell Under High-Pressure Low Heat-Flux Conditions," NUREG/CR-2456, ORNL-5848, March 1982.

5 Viani, P.; R. Macian; and P. Coddington, "The Influence of the Interfacial Drag Models in the TRACE v. 4.05 Predictions for a Large Rod Bundle Void Fraction Data Base," NURETH-11, Avignon, France, October 2005.

6 Frepoli, C.; K. Ohkawa, and R.M. Kemper, "Simulation of Westinghouse G1 and G2 Low Pressure Boil-Off Experiments Using WCOBRA/TRAC," 2004 International Congress on Advances in Nuclear Power Plants (ICAPP '04), Pittsburgh, PA, USA, June 13-17, 2004.

Table B.13.3. Collapsed Levels

THTF Experiment	Pressure & Power Conditions	Measured (m)	TRACE using CHAN Component (m)	TRACE using VESSEL Component (m)
3.09.10I	MPr-HPwr	1.34	1.28	1.31
3.09.10J	MPr-HPwr	1.62	1.45	1.48
3.09.10K	MPr-LPwr	1.62	1.12	1.22[a]
3.09.10L	HPr-HPwr	1.76	1.63	1.61
3.09.10M	HPr-HPwr	1.89	1.81	1.77
3.09.10N	HPr-LPwr	1.86	1.47	1.48
3.09.10AA	MPr-HPwr	2.0	1.95	1.99
3.09.10BB	MPr-LPwr	2.32	2.10	2.09
3.09.10CC	MPr-LPwr	2.88	2.80	2.81
3.09.10DD	HPr-HPwr	2.39	2.10	2.13
3.09.10EE	HPr-LPwr	2.85	2.67	2.70
3.09.10FF	HPr-LPwr	2.9	2.65	2.67

MPr-LPwr: Medium Pressure - Low Power; MPr-HPwr: Medium Pressure - High Power; HPr-LPwr: High Pressure - Low Power; HPr-HPwr: High Pressure - High Power.

a. The TRACE vessel model simulation for experiment 3.09.10K does not reach steady-state. The rod temperatures increase beyond the limits of the material property tables. The results shown for the vessel model are for a simulation time of 1500 seconds.

Table B.13.4. Level Swell Figure of Merit Values

THTF Experiment	Pressure & Power Conditions	Measured	TRACE using CHAN Component	TRACE using VESSEL Component
3.09.10I	MPr-HPwr	1.3	1.35	1.27
3.09.10J	MPr-HPwr	0.63	0.65	0.69
3.09.10K	MPr-LPwr	0.38	0.26	0.15
3.09.10L	HPr-HPwr	0.93	1.29	1.15
3.09.10M	HPr-HPwr	0.54	0.59	0.51
3.09.10N	HPr-LPwr	0.20	0.31	0.17
3.09.10AA	MPr-HPwr	0.98	1.17	1.10
3.09.10BB	MPr-LPwr	0.53	0.53	0.54
3.09.10CC	MPr-LPwr	0.29	0.36	0.36
3.09.10DD	HPr-HPwr	0.57	0.80	0.76
3.09.10EE	HPr-LPwr	0.32	0.48	0.45
3.09.10FF	HPr-LPwr	0.16	0.21	0.20

MPr-LPwr: Medium Pressure - Low Power; MPr-HPwr: Medium Pressure - High Power; HPr-LPwr: High Pressure - Low Power; HPr-HPwr: High Pressure - High Power.

Table B.13.5. Mixture Level

THTF Experiment	Pressure & Power Conditions	Measured (m)	TRACE using CHAN Component (m)	TRACE using VESSEL Component (m)
3.09.10I	MPr-HPwr	2.62	2.59	2.59
3.09.10J	MPr-HPwr	2.47	2.29	2.29
3.09.10K	MPr-LPwr	2.13	1.37	1.37
3.09.10L	HPr-HPwr	2.75	2.75	2.59
3.09.10M	HPr-HPwr	2.62	2.59	2.44
3.09.10N	HPr-LPwr	2.13	1.83	1.68
3.09.10AA	MPr-HPwr	3.42	3.51	3.51
3.09.10BB	MPr-LPwr	3.31	3.05	3.05
3.09.10CC	MPr-LPwr	3.60	3.66[a]	3.66[a]
3.09.10DD	HPr-HPwr	3.23	3.05	3.05
3.09.10EE	HPr-LPwr	3.47	3.51	3.51
3.09.10FF	HPr-LPwr	3.23	3.05	3.05

MPr-LPwr: Medium Pressure - Low Power; MPr-HPwr: Medium Pressure - High Power; HPr-LPwr: High Pressure - Low Power; HPr-HPwr: High Pressure - High Power.

a. The TRACE models for experiment 3.09.10CC do not predict dryout. The two-phase level for this test is assumed to occur at the end of the heated length.

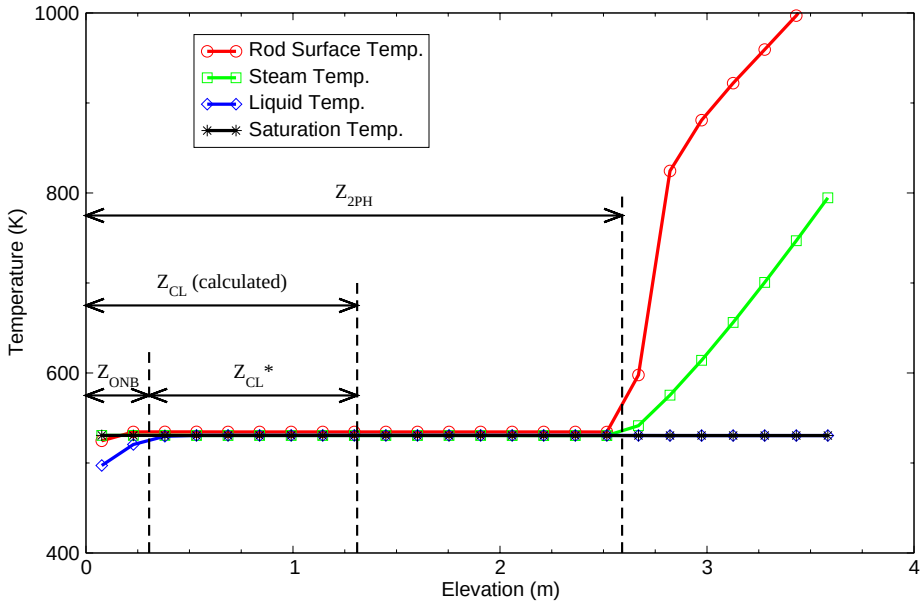

Figure B.13-5. Rod Outer Temperatures in TRACE VESSEL Calculation, THTF 3.09.10I

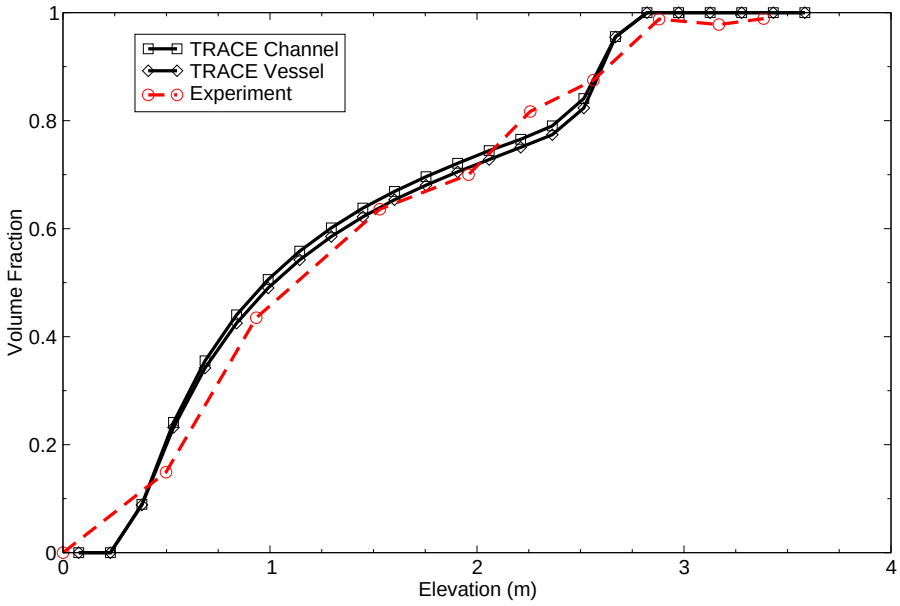

Figure B.13-6. Axial Void Profile Comparison for THTF 3.09.10I

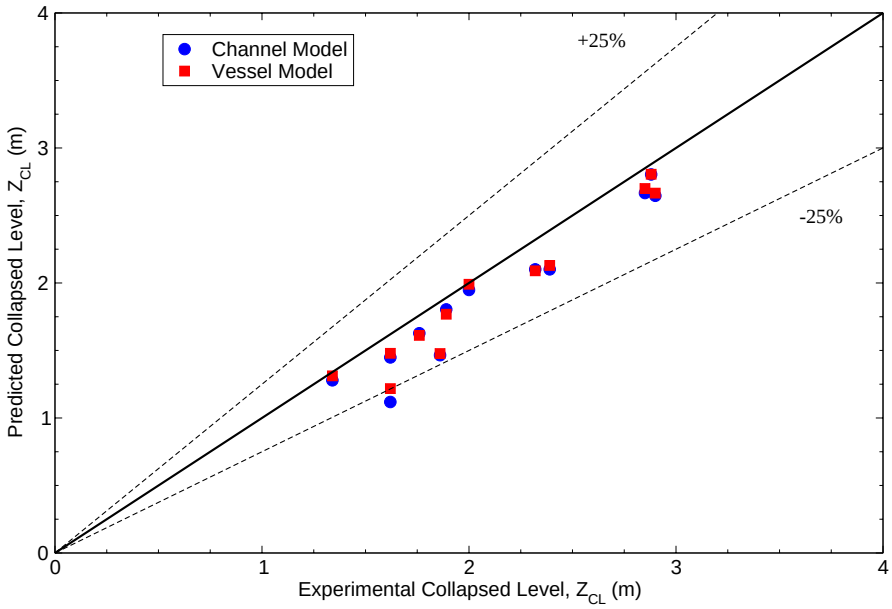

Figure B.13-7. Collapsed Level, Z_{CL}

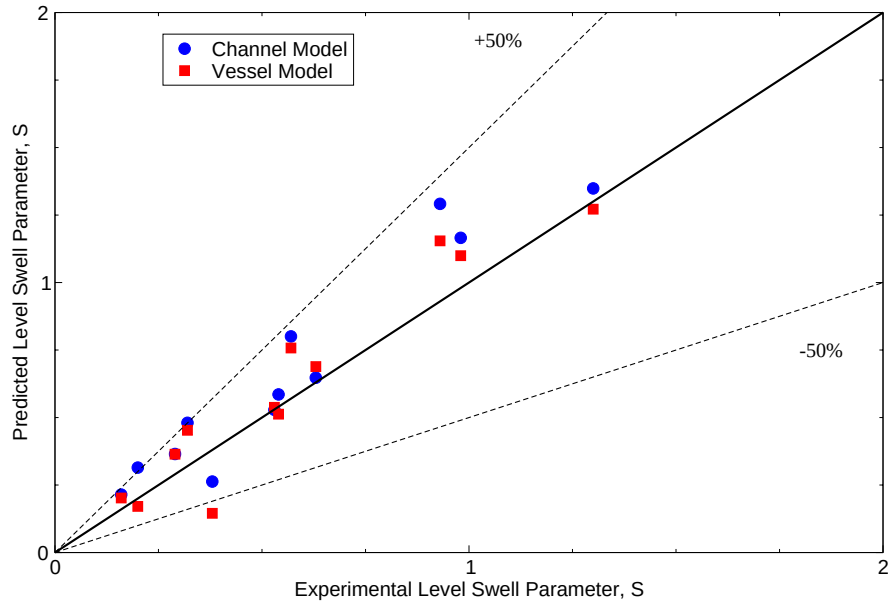

Figure B.13-8. Level Swell, S

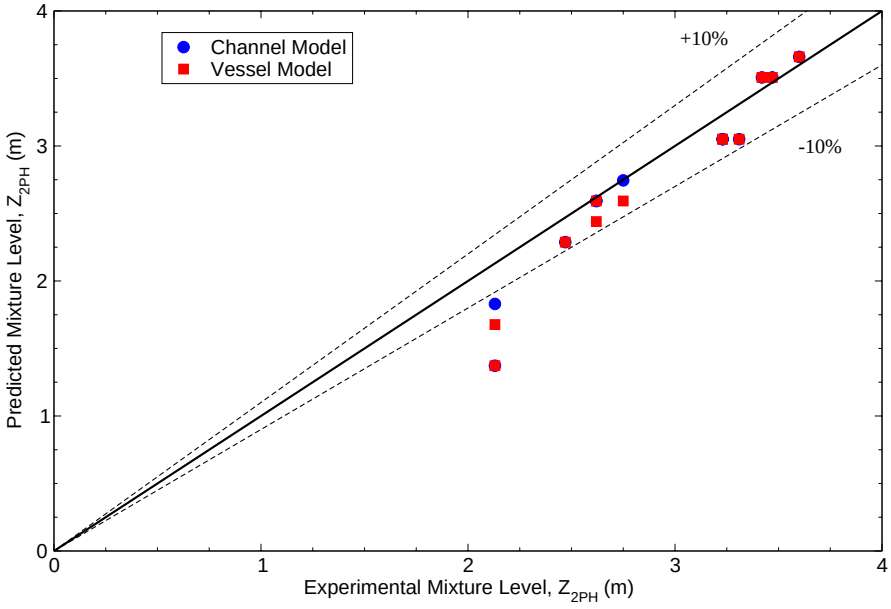

Figure B.13-9. Mixture Level, Z_{2PH}

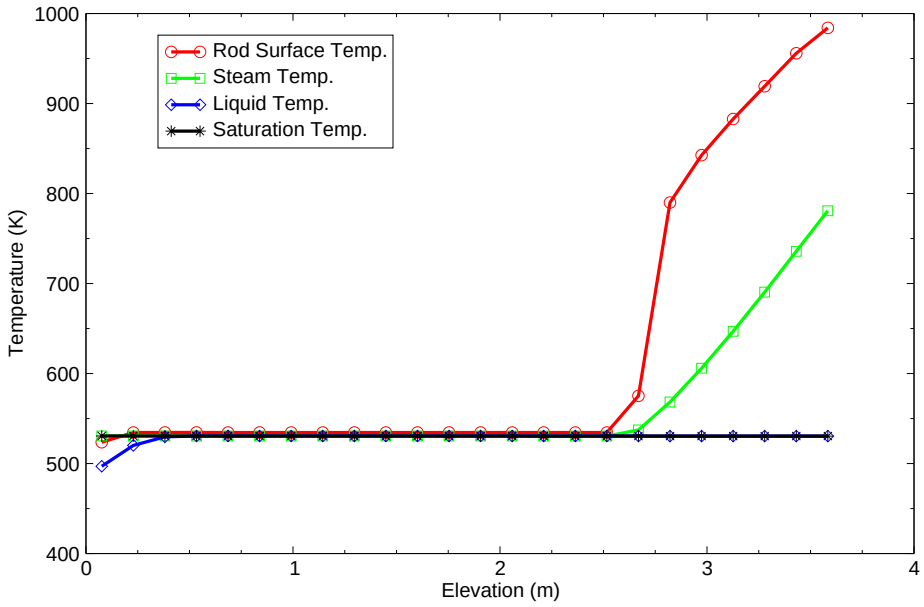

Figure B.13-10. TRACE-calculated axial temperatures for THTF 3.09.10I, CHAN model

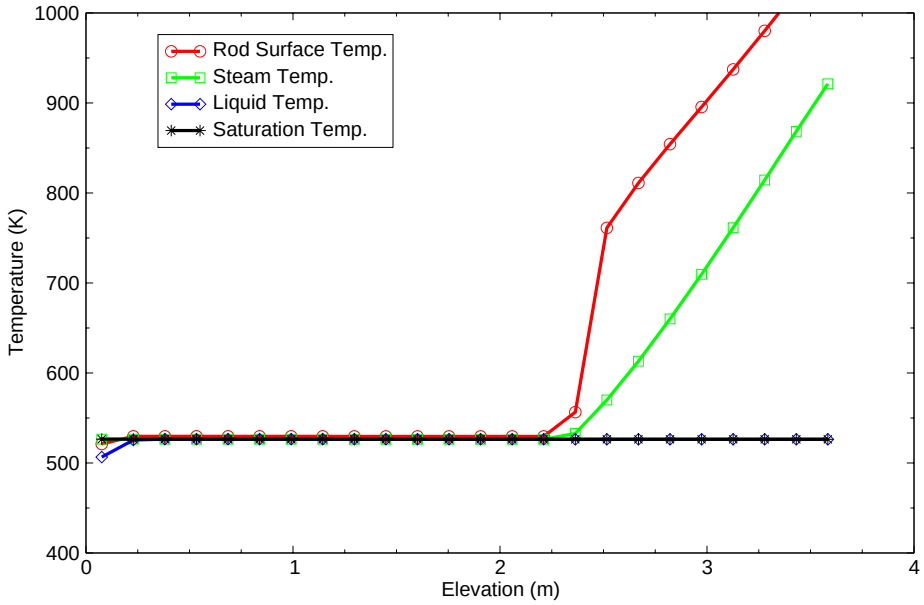

Figure B.13-11. TRACE-calculated axial temperatures for THTF 3.09.10J, CHAN model

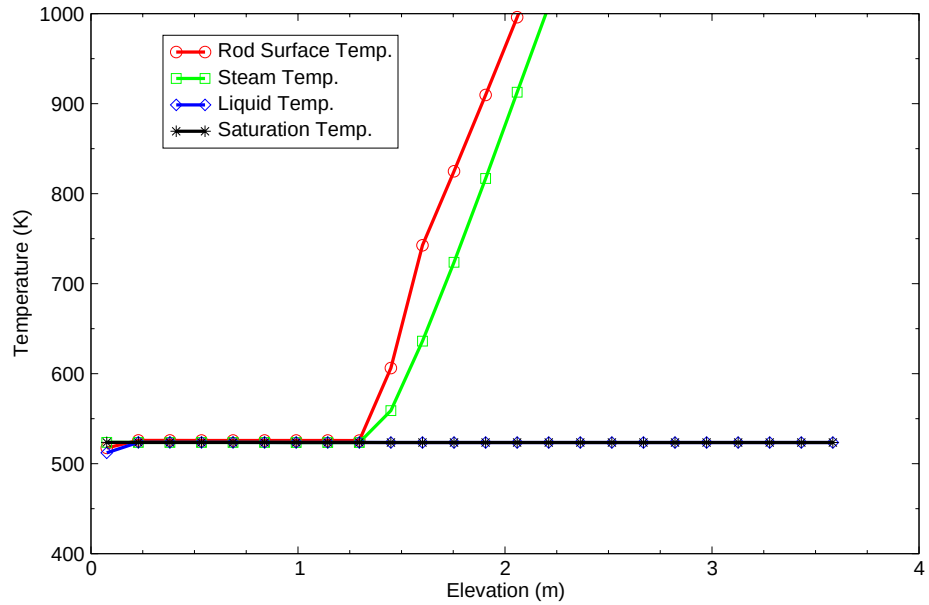

Figure B.13-12. TRACE-calculated axial temperatures for THTF 3.09.10K, CHAN model

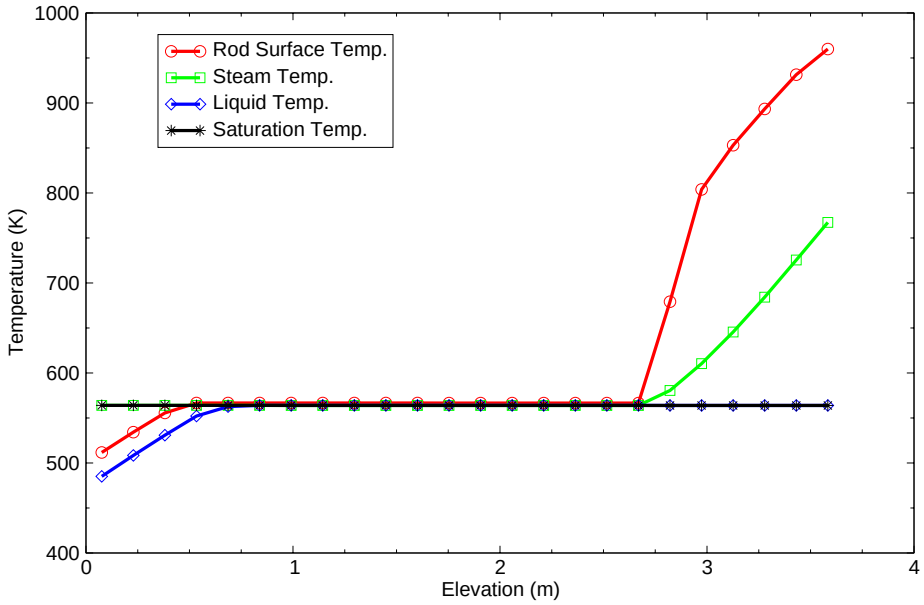

Figure B.13-13. TRACE-calculated axial temperatures for THTF 3.09.10L, CHAN model

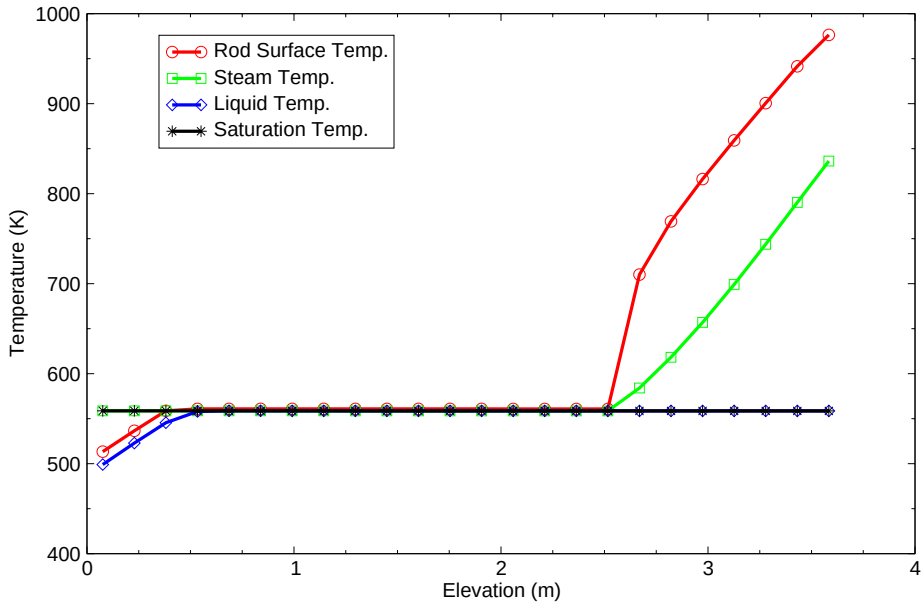

Figure B.13-14. TRACE-calculated axial temperatures for THTF 3.09.10M, CHAN model

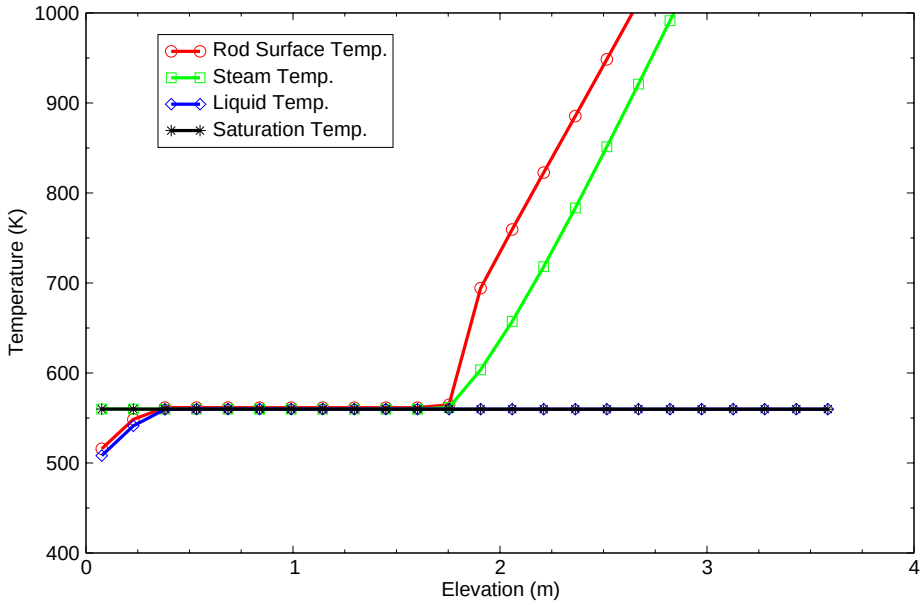

Figure B.13-15. TRACE-calculated axial temperatures for THTF 3.09.10N, CHAN model

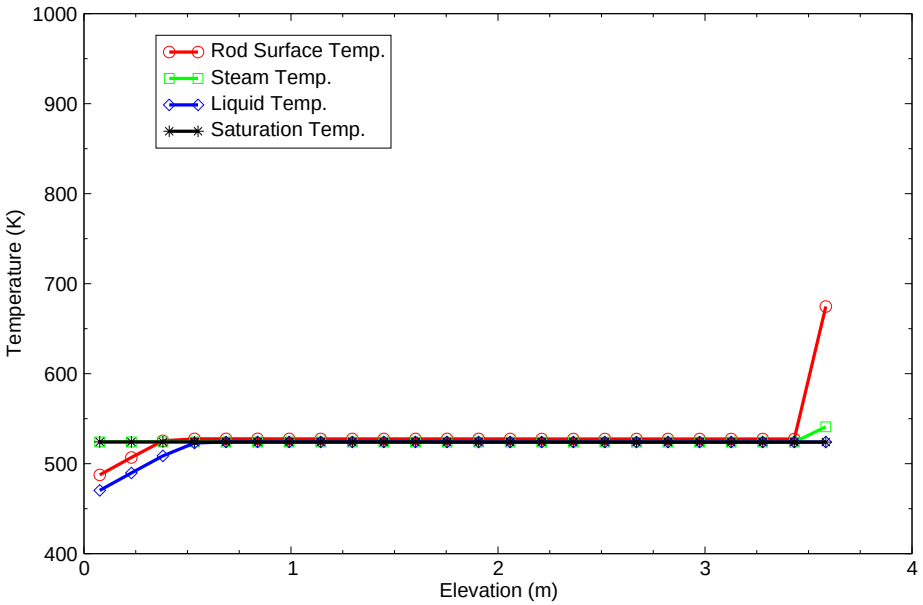

Figure B.13-16. TRACE-calculated axial temperatures for THTF 3.09.10AA, CHAN model

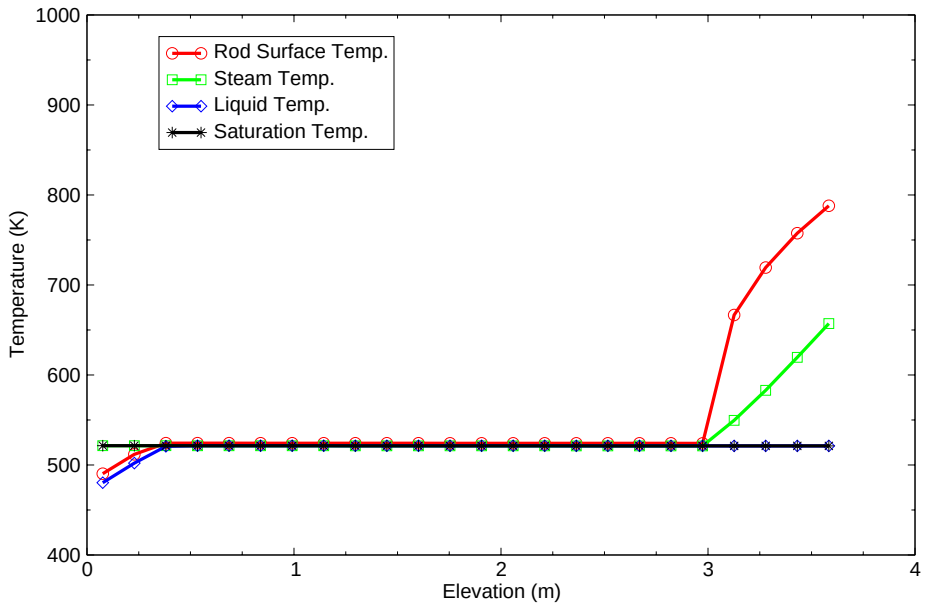

Figure B.13-17. TRACE-calculated axial temperatures for THTF 3.09.10BB, CHAN model

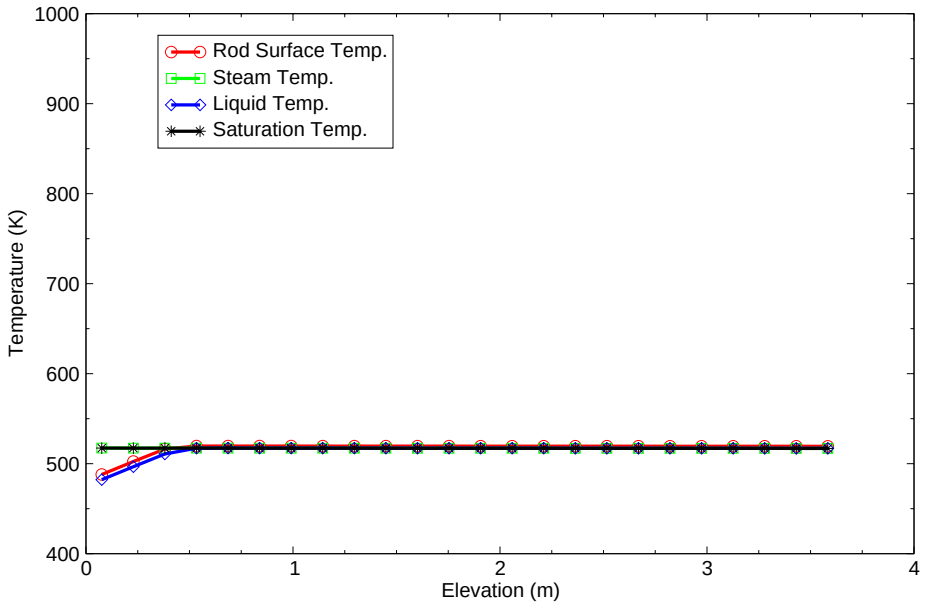

Figure B.13-18. TRACE-calculated axial temperatures for THTF 3.09.10CC, CHAN model

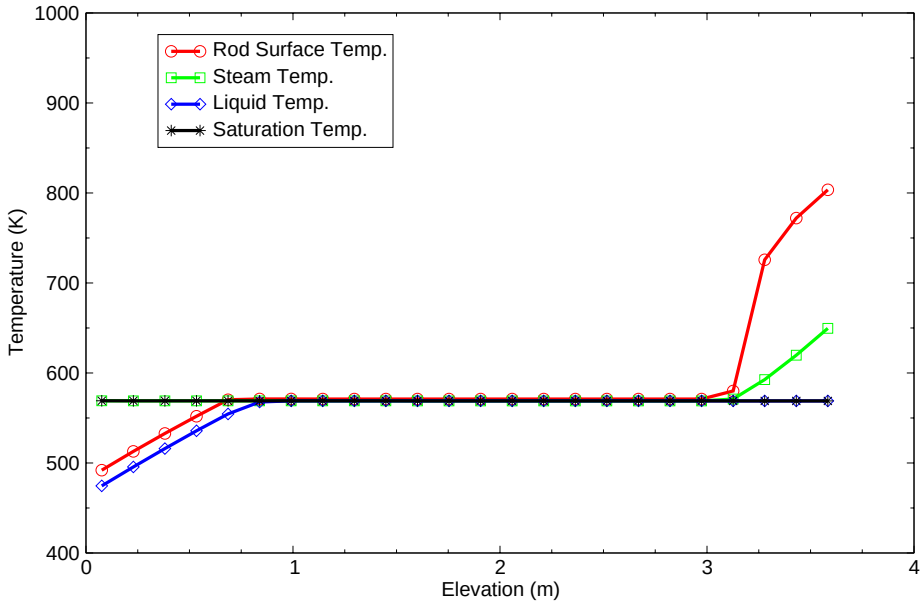

Figure B.13-19. TRACE-calculated axial temperatures for THTF 3.09.10DD, CHAN model

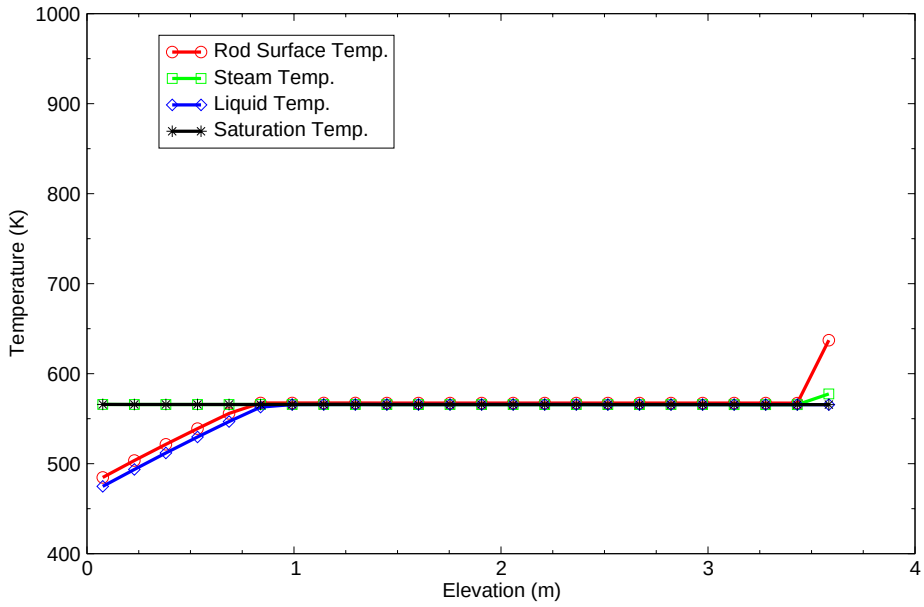

Figure B.13-20. TRACE-calculated axial temperatures for THTF 3.09.10EE, CHAN model

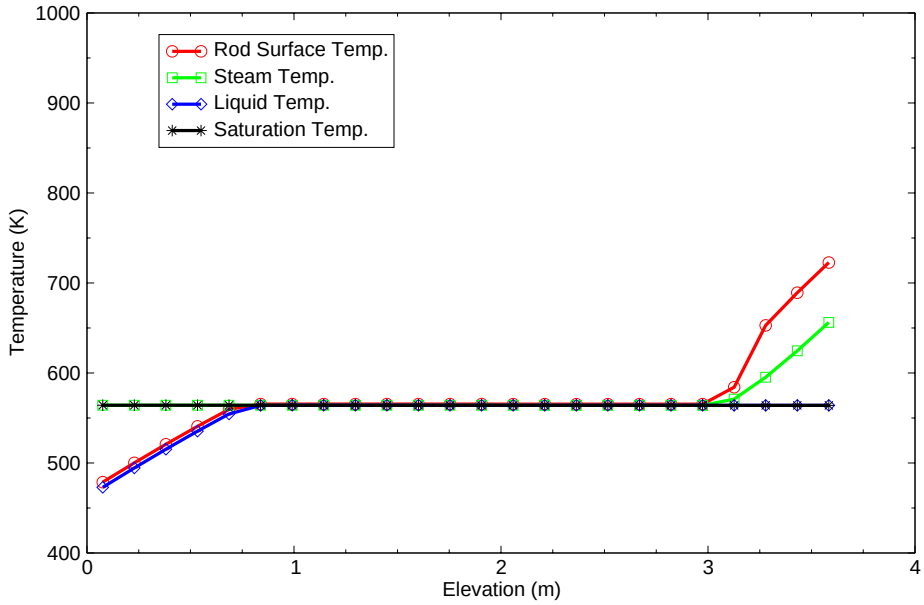

Figure B.13-21. TRACE-calculated axial temperatures for THTF 3.09.10FF, CHAN model

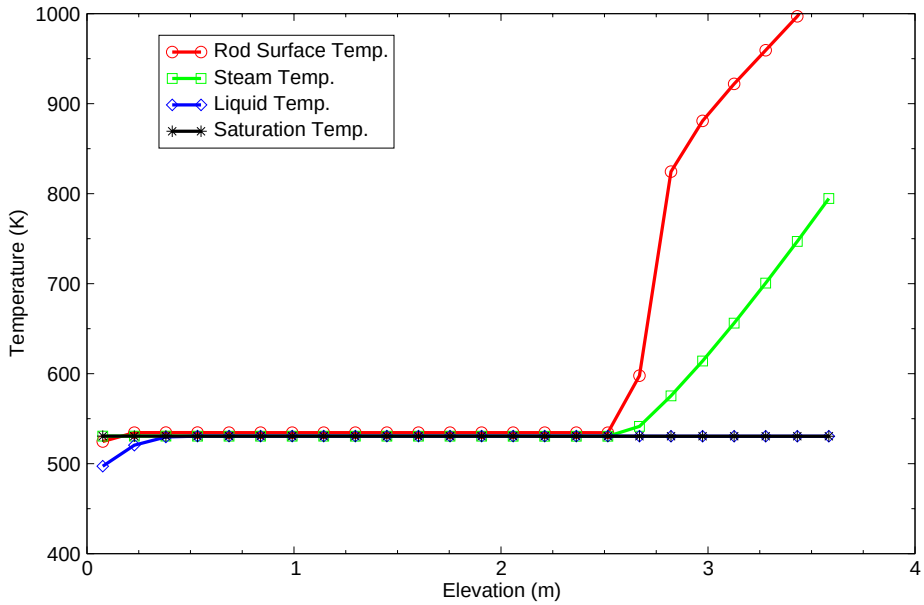

Figure B.13-22. TRACE-calculated axial temperatures for THTF 3.09.10I, VESSEL model

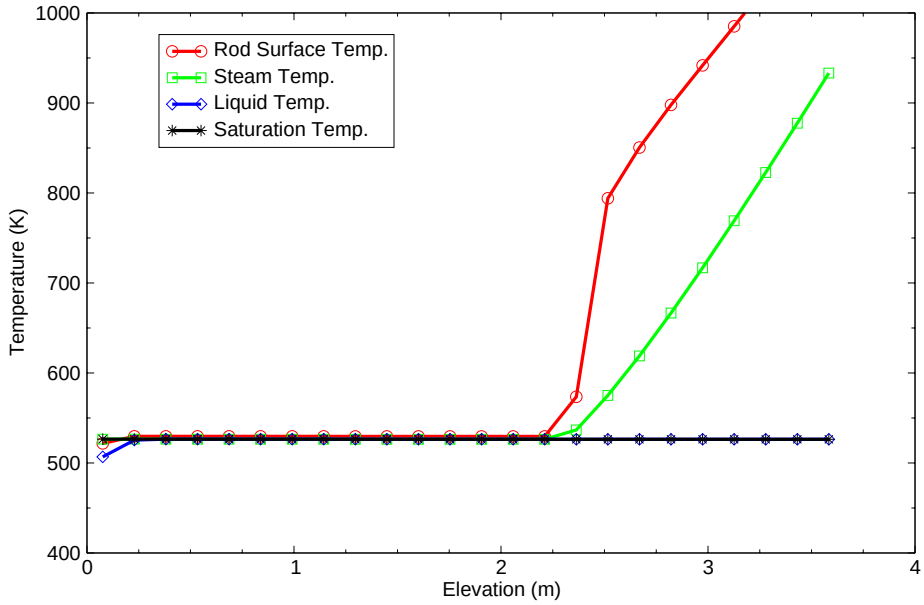

Figure B.13-23. TRACE-calculated axial temperatures for THTF 3.09.10J, VESSEL model

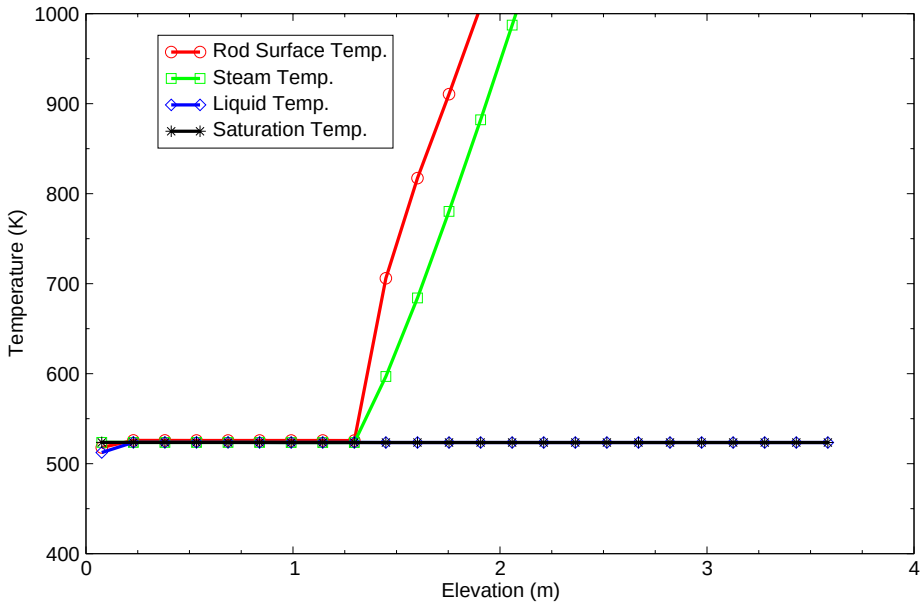

Figure B.13-24. TRACE-calculated axial temperatures for THTF 3.09.10K, VESSEL model

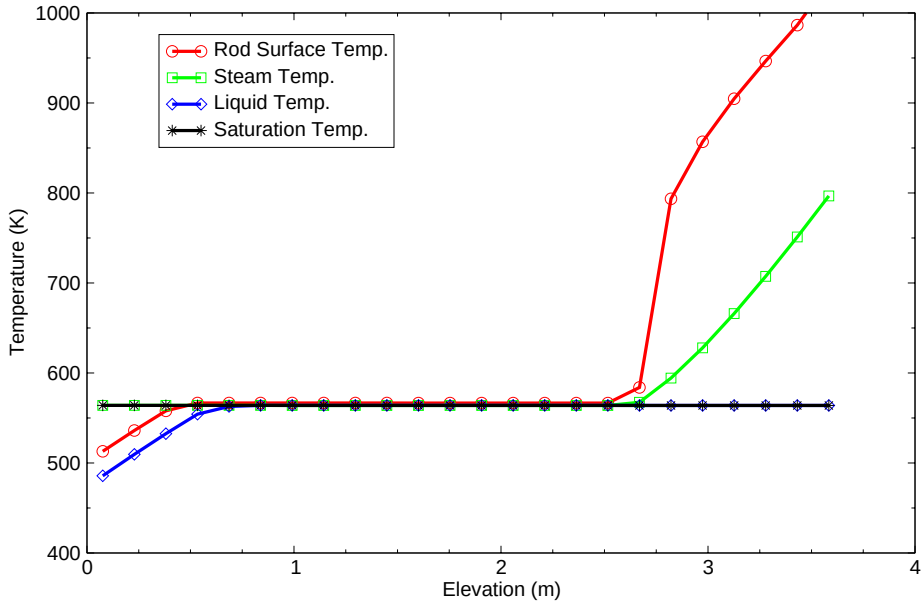

Figure B.13-25. TRACE-calculated axial temperatures for THTF 3.09.10L, VESSEL model

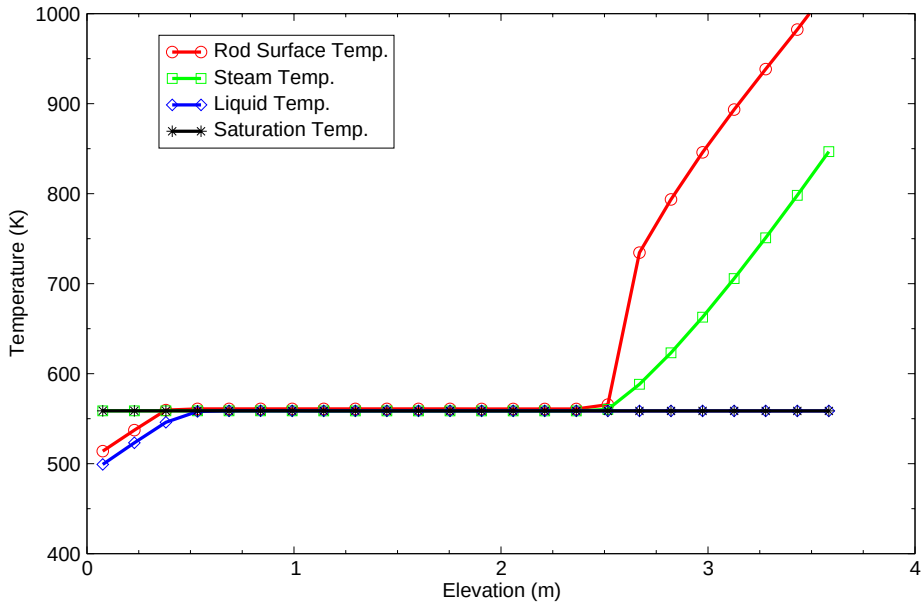

Figure B.13-26. TRACE-calculated axial temperatures for THTF 3.09.10M, VESSEL model

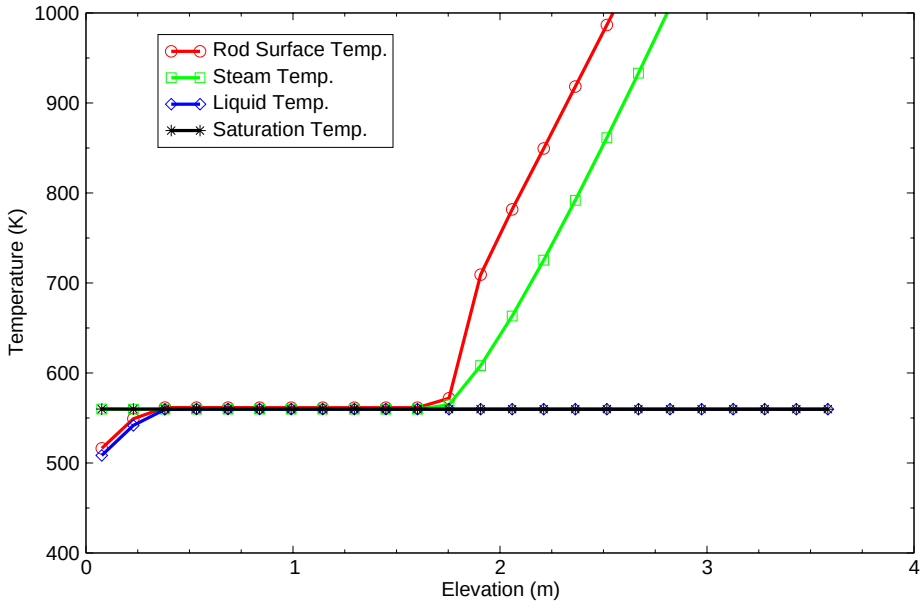

Figure B.13-27. TRACE-calculated axial temperatures for THTF 3.09.10N, VESSEL model

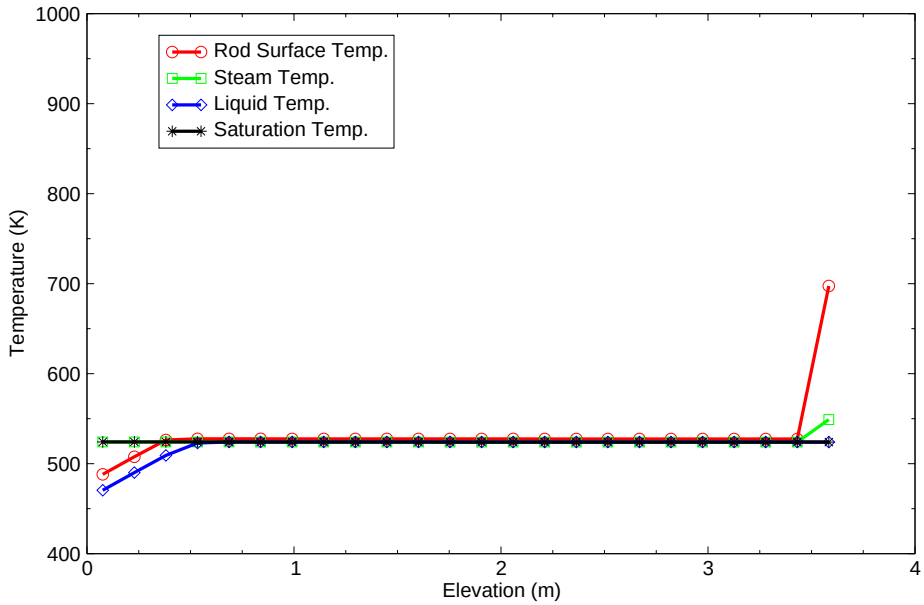

Figure B.13-28. TRACE-calculated axial temperatures for THTF 3.09.10AA, VESSEL model

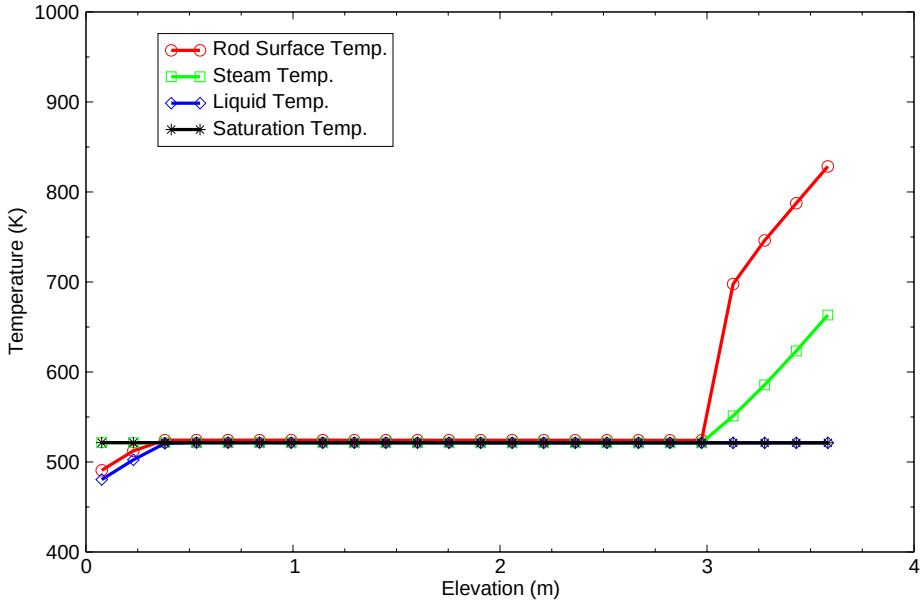

Figure B.13-29. TRACE-calculated axial temperatures for THTF 3.09.10BB, VESSEL model

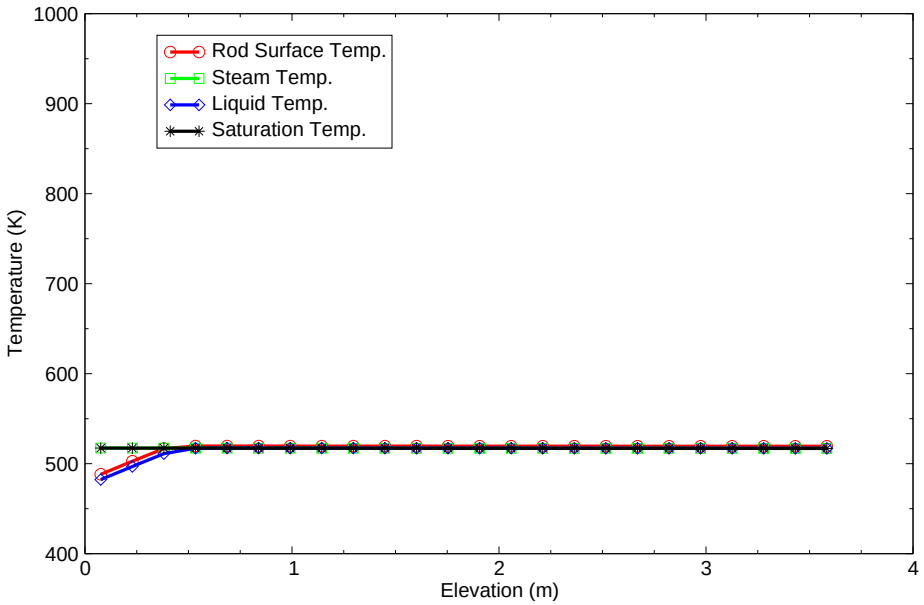

Figure B.13-30. TRACE-calculated axial temperatures for THTF 3.09.10CC, VESSEL model

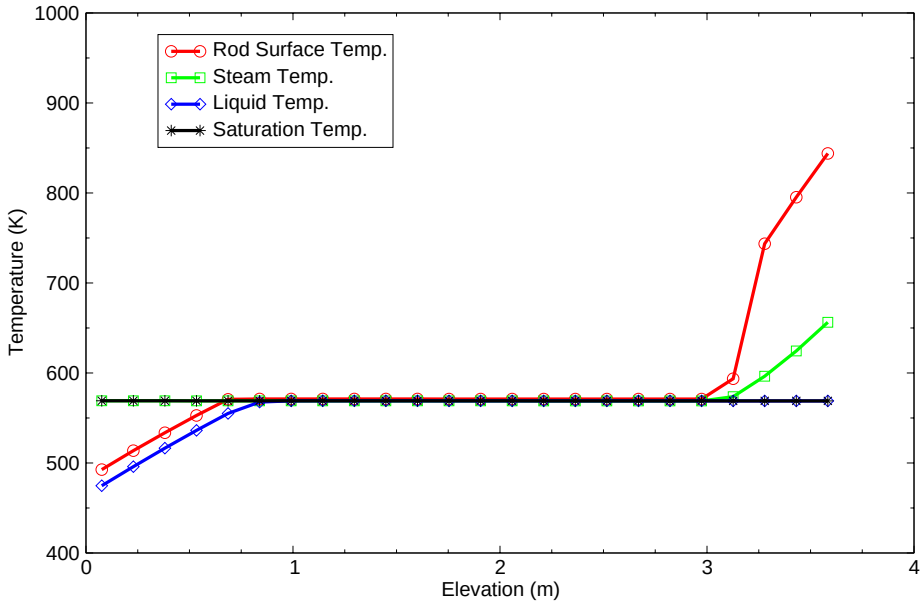

Figure B.13-31. TRACE-calculated axial temperatures for THTF 3.09.10DD, VESSEL model

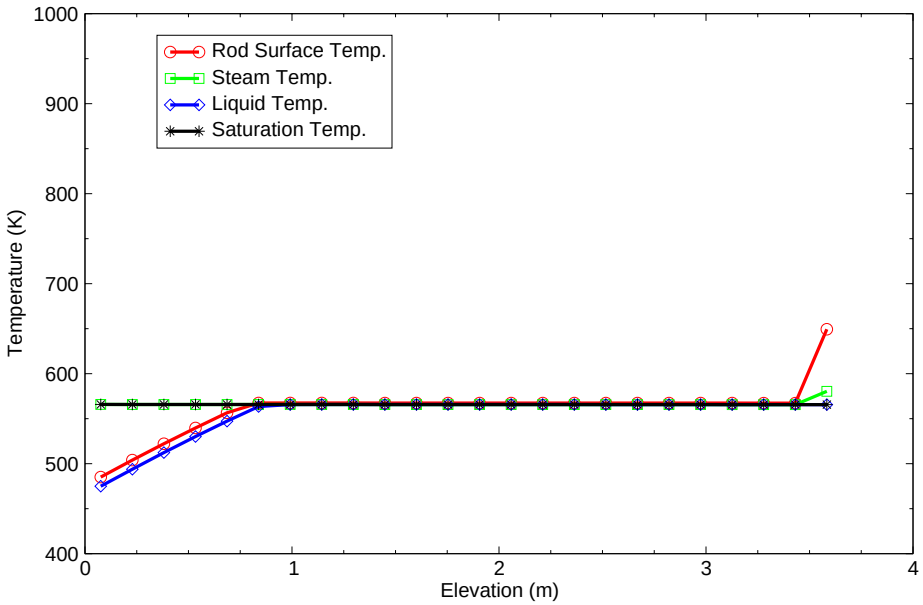

Figure B.13-32. TRACE-calculated axial temperatures for THTF 3.09.10EE, VESSEL model

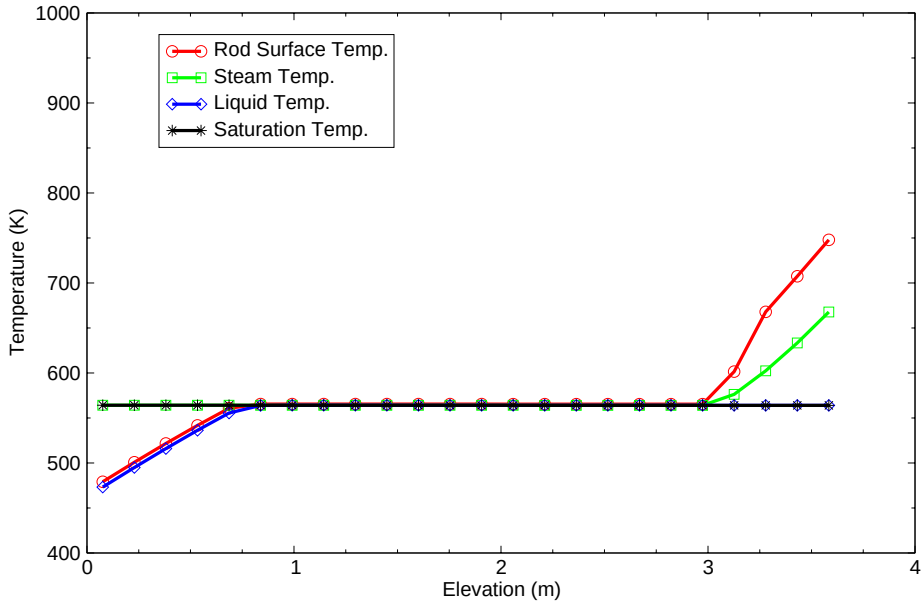

Figure B.13-33. TRACE-calculated axial temperatures for THTF 3.09.10FF, VESSEL model

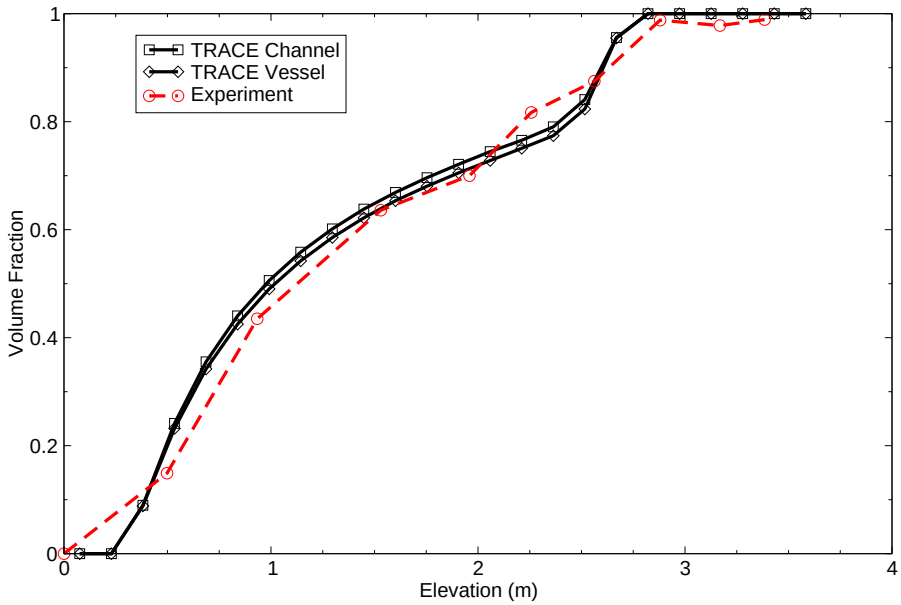

Figure B.13-34. Axial void profile comparison for THTF 3.09.10I

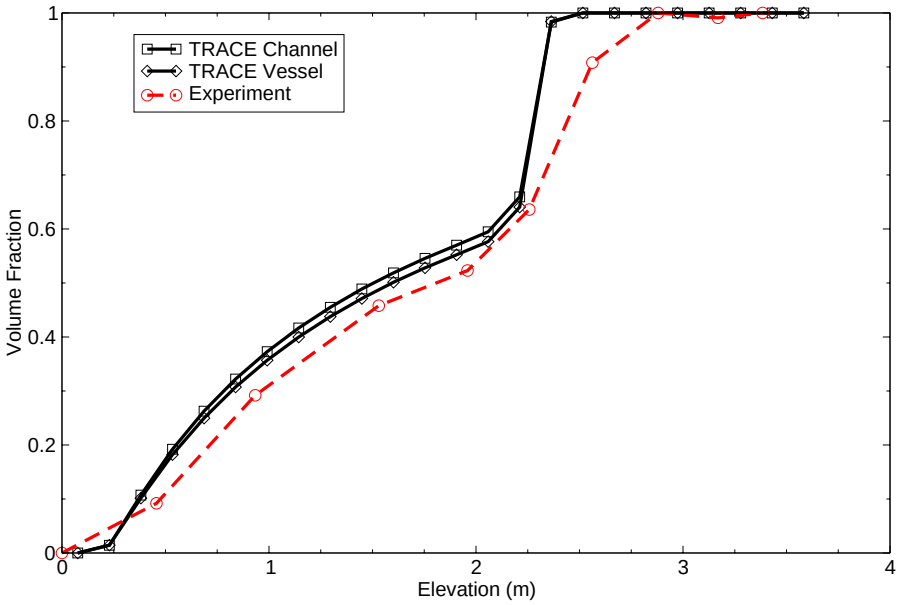

Figure B.13-35. Axial void profile comparison for THTF 3.09.10J

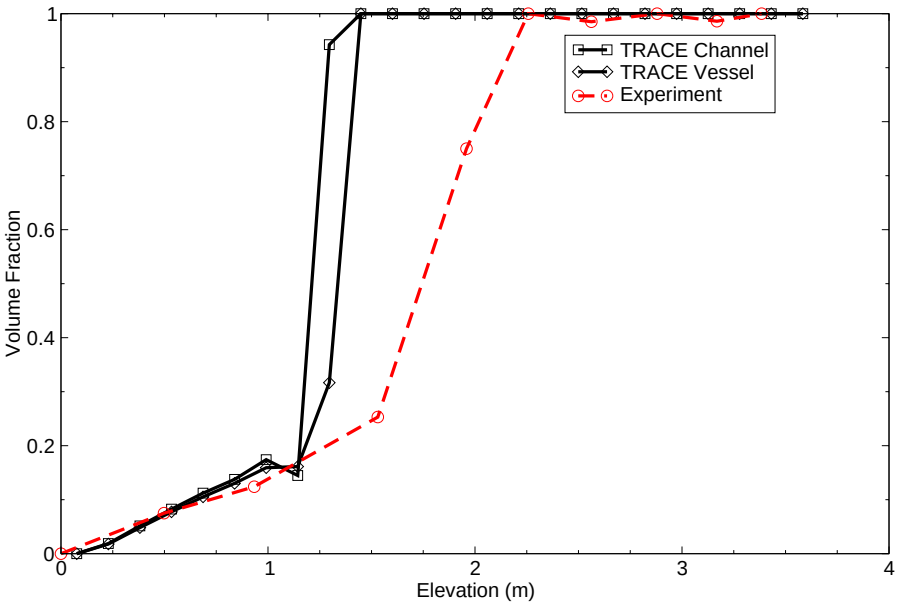

Figure B.13-36. Axial void profile comparison for THTF 3.09.10K

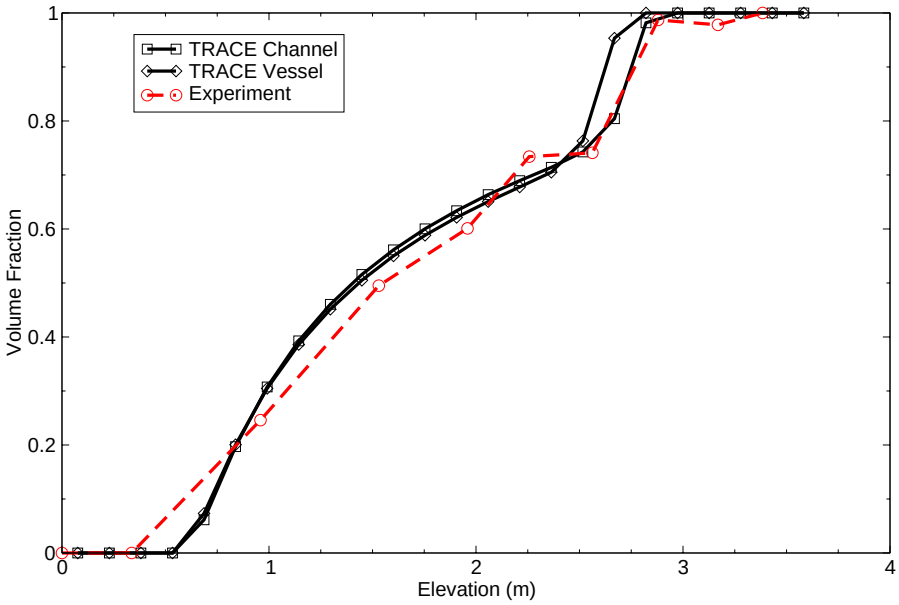

Figure B.13-37. Axial void profile comparison for THTF 3.09.10L

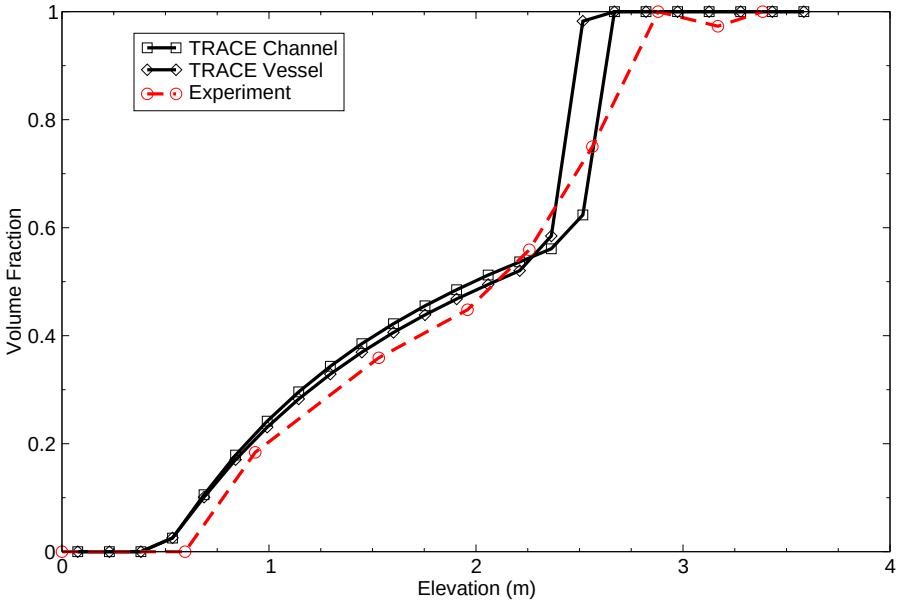

Figure B.13-38. Axial void profile comparison for THTF 3.09.10M

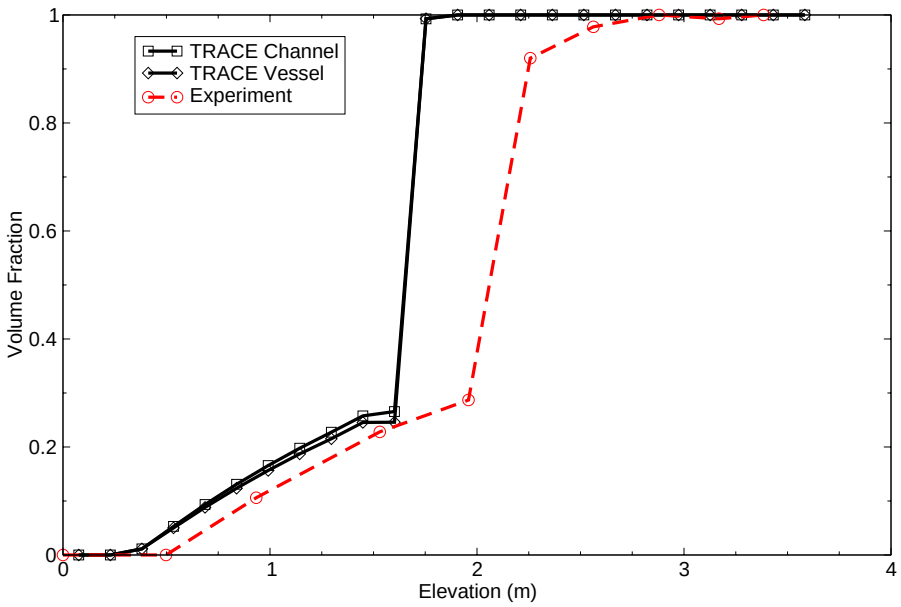

Figure B.13-39. Axial void profile comparison for THTF 3.09.10N

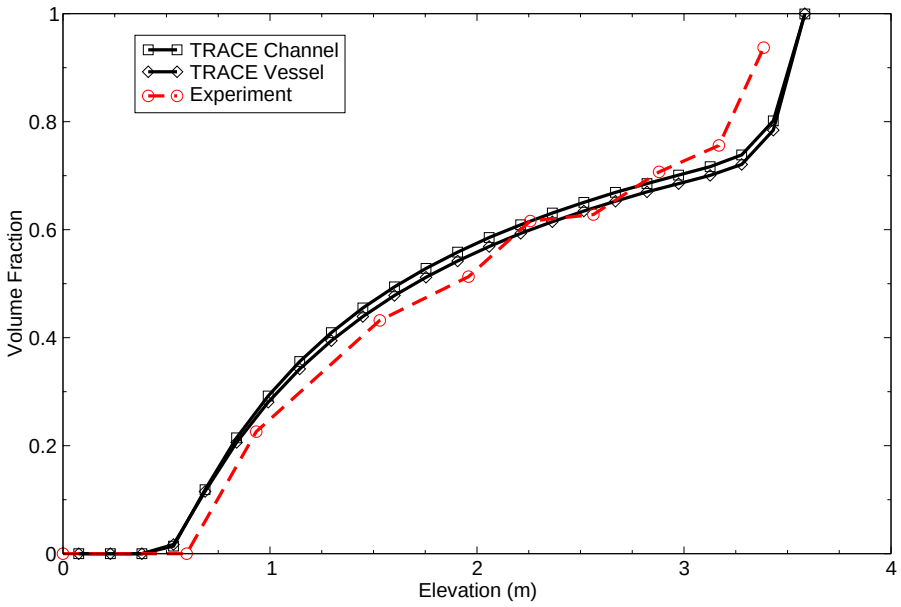

Figure B.13-40. Axial void profile comparison for THTF 3.09.10AA

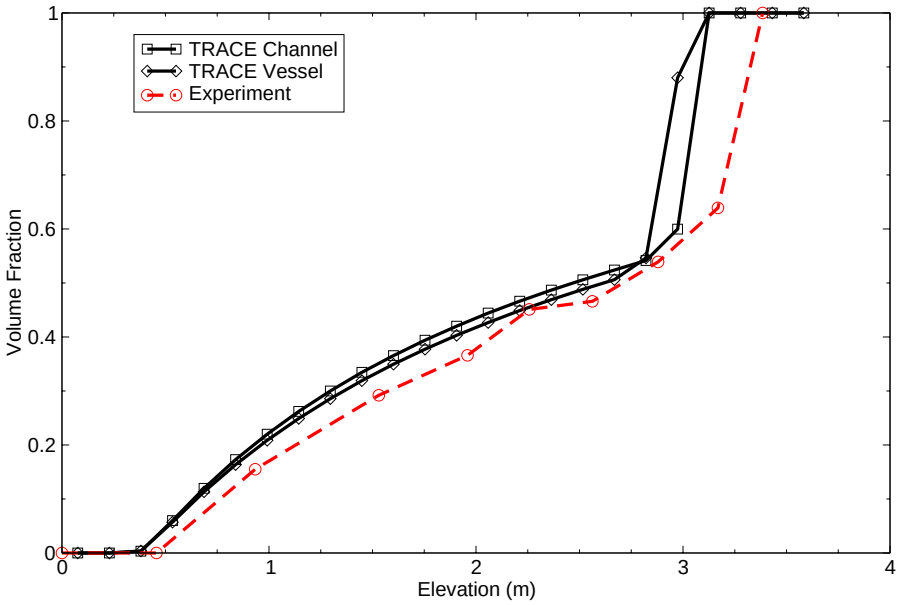

Figure B.13-41. Axial void profile comparison for THTF 3.09.10BB

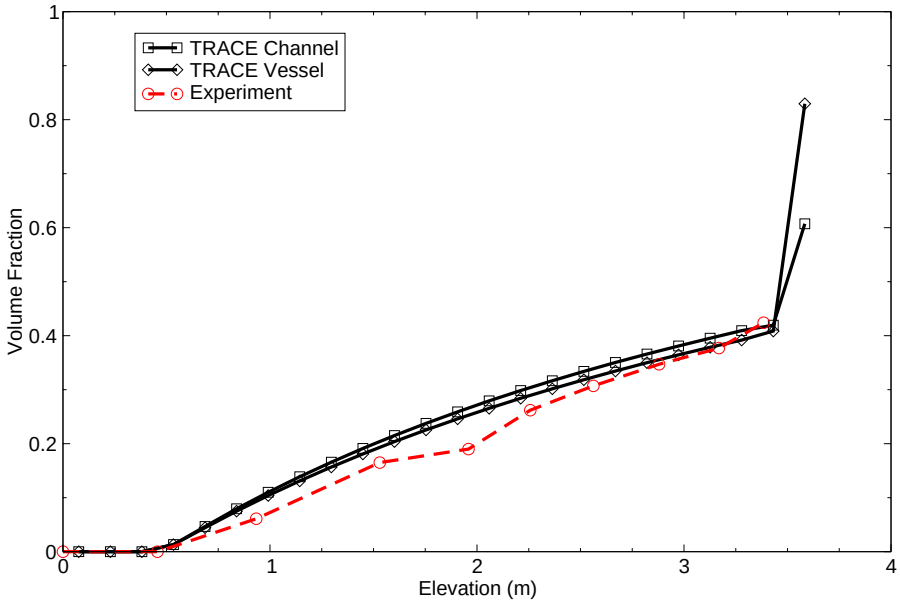

Figure B.13-42. Axial void profile comparison for THTF 3.09.10CC

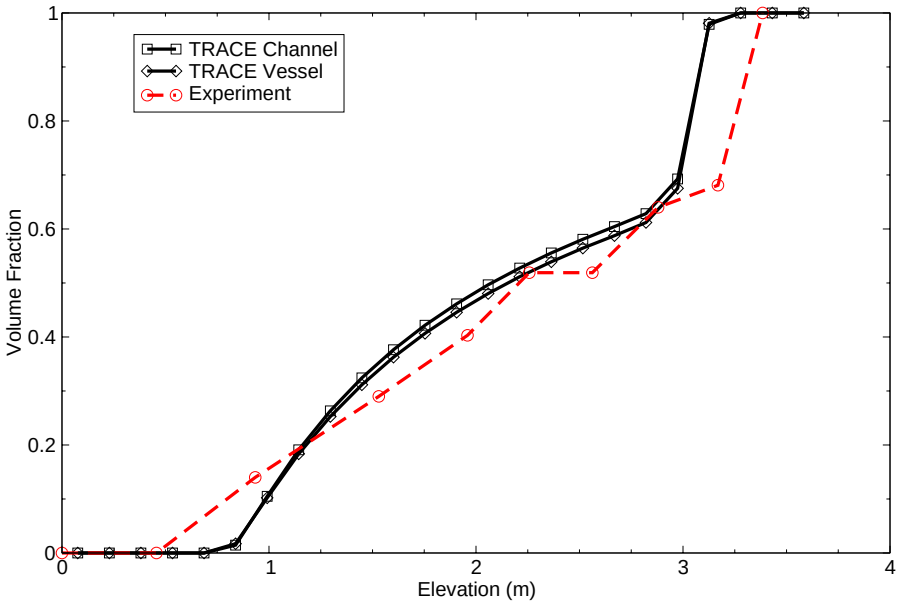

Figure B.13-43. Axial void profile comparison for THTF 3.09.10DD

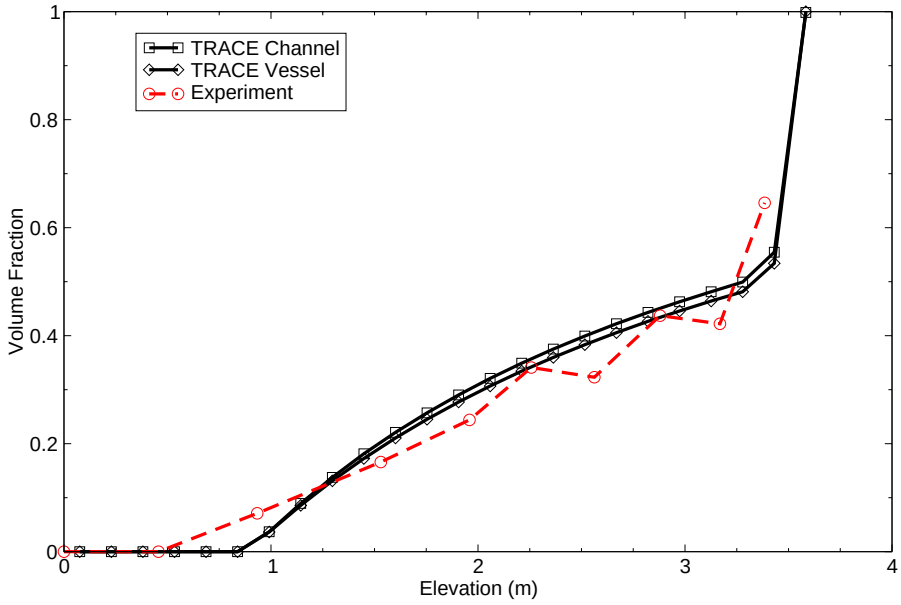

Figure B.13-44. Axial void profile comparison for THTF 3.09.10EE

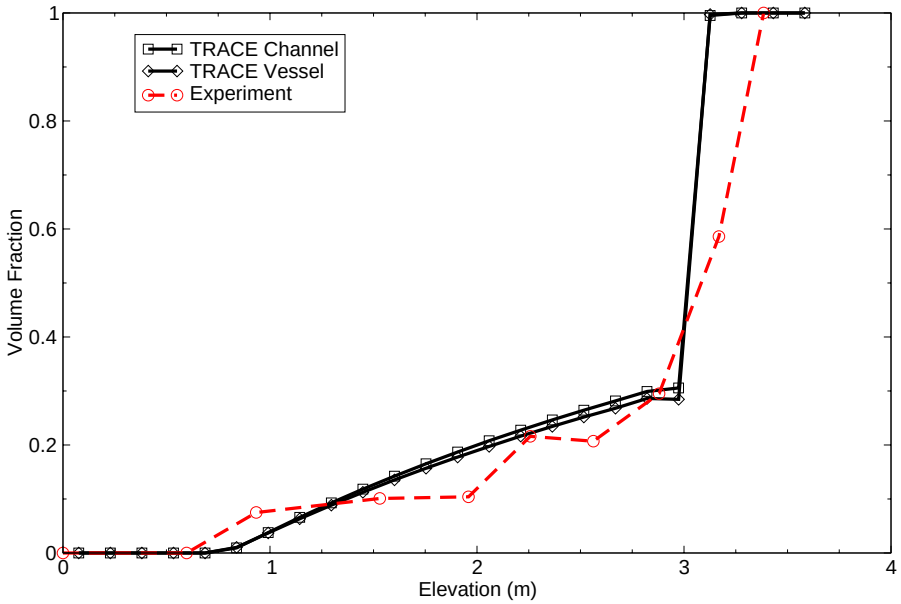

Figure B.13-45. Axial void profile comparison for THTF 3.09.10FF

B.14. RBHT Steady-State Uncovery Tests

Author(s): Kent B. Welter

Affiliation: USNRC RES:DRASP:NRCA

Code Version: TRACE V5.0

Platform and Operating System: Intel x86, Windows XP

B.14.1. Introduction

The two-phase level swell and void distributions at low pressure conditions in the reactor core are important parameters that must be calculated during a safety review to determine the safety margins for core heatup and/or uncovery. The simulations presented in this section examine the ability of TRACE to calculate interfacial drag and mixture swell at low pressure. The simulations were compared to a series of interfacial drag experiments performed at the Penn State/NRC Rod Bundle Heat Transfer (RBHT) facility. The RBHT facility is designed to simulate a full-length portion of a Pressurized Water Reactor (PWR) fuel assembly. The facility consists of a 7x7-rod bundle with 45 electrically heated rods, mixing vane grids, and over 500 instrument channels for measuring temperature, differential and absolute pressure, steam and liquid flow rates, power, etc. The axial differential pressure measurements can be used, along with appropriate temperature and flow corrections, to calculate the bundle void fraction.

For this study, 9 steady-state RBHT interfacial drag tests were assessed against TRACE: Tests 1560, 1566, 1570, 1572, 1582, 1637, 1648, 1651, and 1659. Each of these tests included several subperiods with differring thermal-hydraulic conditions. These tests constitute an assessment base that covers the typical range of parameters during passive plant post-accident conditions. The power was varied from 14.2 to 39.1 kW/m, the pressure from 0.16 to 0.42 MPa, the amount of subcooling from 15 to 60 K, and the liquid injection flow rate from 0.017 to 0.200 kg/s. The results of these tests were compared to steady-state TRACE calculations using the onset of significant voiding, bundle exit void fraction, and collapsed liquid level.

B.14.2. Test Facility Description

The Rod Bundle Heat Transfer (RBHT) Facility is designed to conduct systematic separate-effects tests under well-controlled conditions in order to generate fundamental rod bundle transfer data from single phase steam cooling tests, low flow boiling tests, and dispersed flow film boiling heat transfer tests (Ref. 1). The facility is capable of operating in both forced and variable reflood

modes covering a wide range of flow and heat transfer conditions at pressure from 0.13 to 0.42 MPa. The test facility consists of the following major components (shown schematically in Figure B.14-1):

- Test section consisting of a lower plenum, low-mass housing containing the heater rod bundle, and an upper plenum.
- Cooling injection and steam injection systems.
- Closely coupled phase separation and liquid collection systems.
- Pressure fluctuation damping tank and steam exhaust piping.

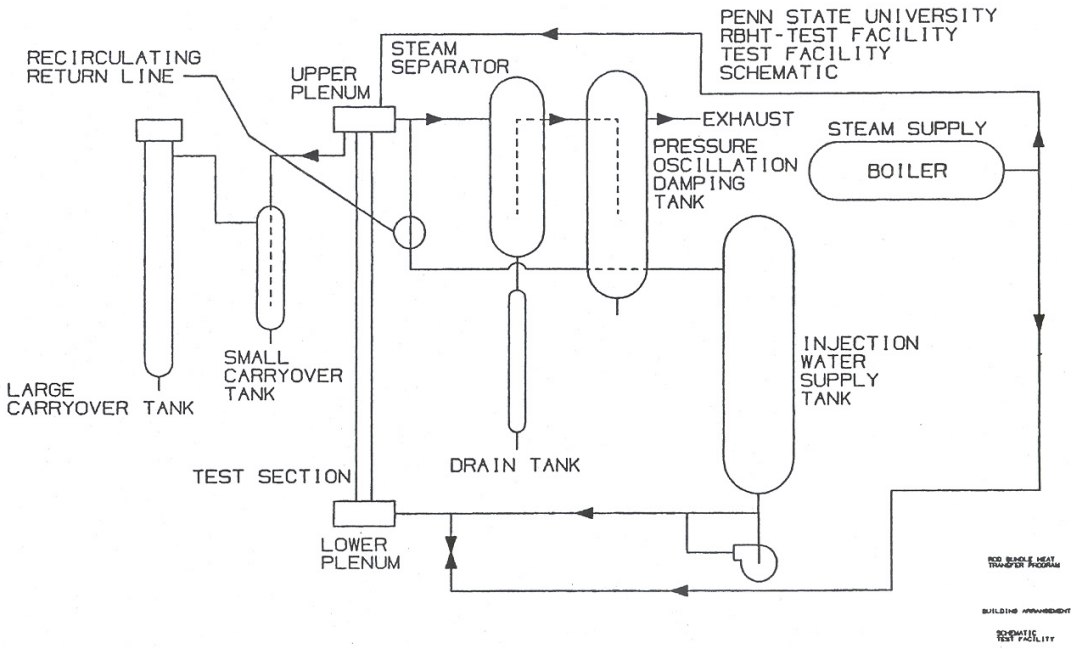

Figure B.14-1 RBHT Test Facility Schematic

The test section shown in Figure B.14-1 consists of the heater rod bundle, the flow housing, and the lower and upper plenums. The heater rod bundle simulates a small portion of a 17x17 reactor fuel assembly. The electrically heated rods have a diameter of 9.5 mm and are arranged in a 7x7 array with a 12.6 mm pitch with 45 heater rods and four unheated rods (at each corner). The facility has over 500 instrument channels to measure temperature, differential and absolute pressure, flow rates, power, etc. For this study, of particular interest are the bundle differential pressure cells, wich are used to calculate void fraction, inlet injection flow rate (chan-412), liquid injection temperature (chan-407), heater rod voltage (chan-395) and current (chan-396), and upper and lower plenum pressures (chan-411 and chan-393, respectively). Table B.14.1 contains a list of the 22 axial bundle differential pressure cells used in this assessment, along with the axial locations of the 7 mixing vane grids. The grids are 5.72 cm high.

Table B.14.1. Differential Pressure Cell and Grid Locations

Instrument ID	Lower Tap, Axial Location (m)	Upper Tap, Axial Location (m)	Grid Bottom, Axial Location (m)
chan-363	0.0	0.330	0.330
chan-364	0.330	0.640	
chan-365	0.640	0.940	0.690
chan-366	0.940	1.092	
chan-367	1.092	1.168	
chan-368	1.168	1.346	1.212
chan-369	1.346	1.448	
chan-370	1.448	1.524	
chan-371	1.524	1.600	
chan-372	1.600	1.702	
chan-373	1.702	1.823	1.734
chan-374	1.823	1.905	
chan-375	1.905	1.981	
chan-376	1.981	2.057	
chan-377	2.057	2.159	
chan-378	2.159	2.362	2.256
chan-379	2.362	2.465	
chan-380	2.465	2.540	
chan-381	2.540	2.743	
chan-382	2.743	3.048	2.778
chan-383	3.048	3.378	3.301
chan-384	3.378	3.657	

Radiation only experiments were conducted to characterize the test section heat loss and were conducted under a vacuum. Based on a total power of 114 kW, the heat loss for a typical reflood test was calculated to be approximately 2.5 kW, which is a small fraction (~2%) of the total power supplied to the heater rods.

B.14.3. TRACE Model Description

The RBHT main test section was modeled in TRACE using VESSEL and HSTRC components as shown in Figure B.14-2. The VESSEL component was nodalized with 14 axial levels over the heated region. There are two cells between each mixing vane grid and that the bottom of every

other cell corresponds to the bottom of a grid. The mixing vane grids were modeled by specifying a loss coefficient of 2.0 (Ref. 2). Forty-five heated rods were modeled in a 7x7 array, with four non-heated rods in the corners. Two PIPE components (shown in Figure B.14-2), one at the bottom and one at the top, were used to model the upper and lower plenums, respectively. A constant inlet injection flow was provided by the FILL component at the bottom of the lower plenum, while a BREAK, at a specified initial pressure, was used at the top. The VESSEL component spans the entire heated length, but an additional cell at the top of the VESSEL was added to help reduce void fraction oscillations at the top of a rod bundle, which is a standard TRACE modeling practice. The shape of the power curve applied to the HSTRC peaks at 2.7781 m as shown in Figure B.14-2. The heater rods were broken into 8 radial nodes, also shown in Figure B.14-2, which modeled the Constantan heater wire insulated with Boron-Nitride insulation, clad with Inconel, Type 600.

The TRACE model assumes a constant liquid injection flow at a constant heater rod power. For each case simulated, the test section was initially full of cold water at a specified temperature to investigate the effects of subcooling on interfacial drag. The model was then run as a transient, and when the bundle void fraction and collapsed liquid level reach a constant value (usually after ~500 seconds), the simulation was assumed to be steady-state. Most of the simulations were run to 500 seconds, but in some instances, when the TRACE calculation showed uncontrolled heatup of the bundle, the simulation was run out to around 2000 seconds to capture the heatup. In these heatup cases, a steady-state point was chosen around 1800 seconds after the bundle achieved a steady-state temperature.

For each RBHT test there was a series of steady-state subcases of ~2 minutes in duration. An input deck was created for each subcase using time averaged RBHT data for the initial and boundary conditions. Table B.14.2 is a list of parameters and corresponding facility channels that were used for each subcase.

Table B.14.2. Steady-State Initial and Boundary Conditions

Parameter	**Instrument ID**	**Units**
Liquid Injection Flow Rate	chan-412	kg/s
Supply Line Pressure/Lower Plenum Pressure	chan-411	Pa
Upper Plenum Pressure	chan-393	Pa
Liquid Injection Temperature	chan-407	K
Power = Voltage x Current	chan-395 x chan-396	V x Amp = W

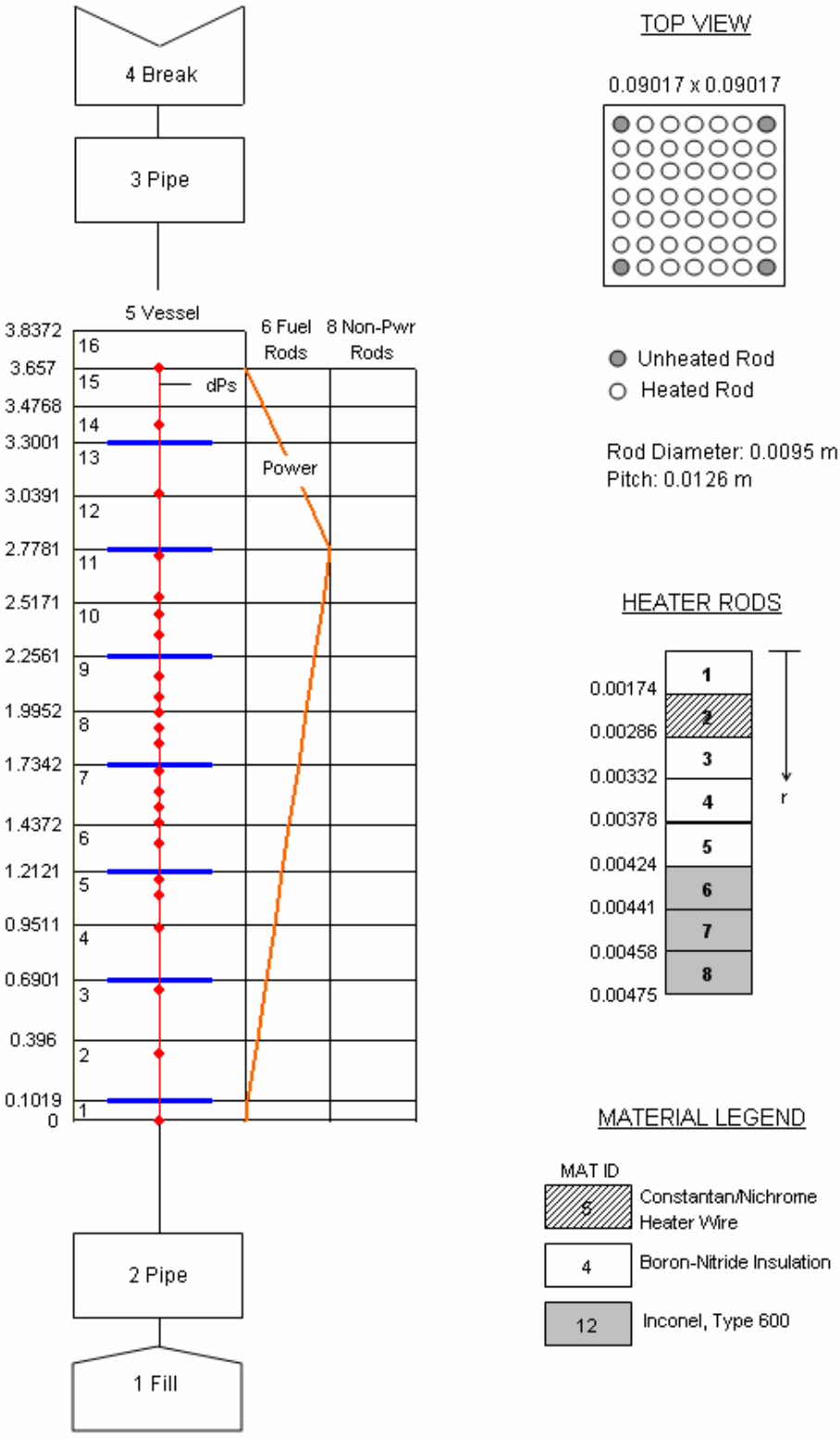

Figure B.14-2. TRACE Nodalization for the RBHT Facility

B.14.4. Tests Simulated with TRACE

A total of 73 steady-state cases were assessed using TRACE. Each RBHT interfacial drag test was composed of several steady-state subcases which are listed in Table B.14.3 Figure B.14-3 is a graphical representation of the assessment matrix and shows how specific tests were to be compared to each other. Figure B.14-4 is an example of a typical transient of the liquid injection flow rate for an RBHT test. The subcases or cases can be identified as periods of time (~2 minutes) of constant injection flow rate. During this time period, important parameters such as pressure and power are also held constant, allowing allowing the test section to reach a steady-state condition. It is important to note that error bars are not included in the figures of RBHT data, since at the time of this report, experimental error has not been quantified. In addition, all figures of bundle void fraction are uncorrected for two-phase conditions. In general, not employing a two-phase correction factor when calculating the bundle void fraction, will tend to result in lower void fractions at the top of the bundle than can be expected. In other words, when a two-phase flow correction factor is used the void fractions at the top part of the bundle will tend to increase (maybe by as much as 15%).

The next few sections of this report examine the ability of TRACE to predict RBHT data over a range of power, subcooling, pressure, and injection flow rate. Changes in pressure do not have a noticable effect on TRACE's ability to predict the bundle void fraction. In some instances, not all available cases are graphed, since plotting two or three cases of a particular class should provide sufficient information for the reader to draw inferences as to the general ability of TRACE to predict RBHT interfacial drag data.

Table B.14.3. RBHT Interfacial Drag Assessment Matrix

Case ID	Test ID	Beg Time	End Time	Inj Flow	Mass Flx	Inj Temp	Subcool	Inj Press	UP* Press	Lin Heat	Power
(-)	(-)	(sec)	(sec)	(kg/s)	(kg/m^2-s)	(K)	(K)	(MPa)	(MPa)	(kW/m)	(kW)
Case 1	Test 1560	1600	1800	0.1247	25.8	370.4	15	0.158	0.138	20.5	75.0
Case 2	Test 1560	1900	2020	0.0873	18.0	370.6	15	0.155	0.138	20.5	75.0
Case 3	Test 1560	2090	2180	0.0593	12.3	370.7	15	0.154	0.138	20.5	75.0
Case 4	Test 1560	2220	2310	0.0378	7.82	370.7	15	0.153	0.138	20.5	75.0
Case 5	Test 1566	500	700	0.0999	20.7	370.6	15	0.159	0.138	20.5	75.0
Case 6	Test 1566	3300	3400	0.0742	15.3	371.1	15	0.155	0.138	20.5	75.0
Case 7	Test 1566	4100	4220	0.0495	10.3	371.1	15	0.154	0.138	20.5	75.0
Case 8	Test 1566	4380	4460	0.0364	7.53	371.2	15	0.153	0.138	20.5	75.0
Case 9	Test 1566	4600	4650	0.0249	5.14	371.3	15	0.151	0.138	20.5	75.0
Case 10	Test 1570	12208	12300	0.1998	41.3	371.0	15	0.155	0.138	39.1	143.0
Case 11	Test 1570	12495	12530	0.1727	35.7	371.0	15	0.155	0.138	39.1	143.0
Case 12	Test 1570	12990	13060	0.1239	25.6	371.1	15	0.152	0.138	39.1	143.0
Case 13	Test 1570	13300	13380	0.1497	30.9	371.0	15	0.153	0.138	39.1	143.0
Case 14	Test 1570	13537	13620	0.0999	20.7	371.0	15	0.151	0.138	39.1	143.0
Case 15	Test 1570	13770	13800	0.0750	15.5	371.0	15	0.150	0.138	39.1	143.0
Case 16	Test 1572a	11384	11526	0.1244	25.7	383.8	15	0.228	0.207	21.7	80.0
Case 17	Test 1572a	11672	11750	0.1253	25.9	383.7	15	0.227	0.207	21.7	80.0
Case 18	Test 1572a	12089	12210	0.1242	25.7	383.7	15	0.227	0.207	21.7	80.0
Case 19	Test 1572b	12482	12575	0.1235	25.5	383.6	15	0.231	0.207	14.2	52.0
Case 20	Test 1572b	13079	13148	0.1244	25.7	383.4	15	0.232	0.207	14.2	52.0
Case 21	Test 1572b	13358	13478	0.0871	18.0	383.1	15	0.231	0.207	14.2	52.0
Case 22	Test 1572b	13845	14001	0.0624	12.9	382.8	15	0.231	0.207	14.2	52.0
Case 23	Test 1572b	14172	14259	0.0377	7.80	382.3	15	0.230	0.207	14.2	52.0

Table B.14.3. RBHT Interfacial Drag Assessment Matrix

Case ID	Test ID	Beg Time	End Time	Inj Flow	Mass Flx	Inj Temp	Subcool	Inj Press	UP* Press	Lin Heat	Power
(-)	(-)	(sec)	(sec)	(kg/s)	(kg/m^2-s)	(K)	(K)	(MPa)	(MPa)	(kW/m)	(kW)
Case 24	Test 1572b	14376	14469	0.0248	5.13	381.8	15	0.228	0.207	14.2	52.0
Case 38	Test 1582	1010	1080	0.1920	39.7	327.7	60	0.161	0.138	39.1	143.0
Case 39	Test 1582	1694	1748	0.1933	39.9	327.7	60	0.161	0.138	39.1	143.0
Case 40	Test 1582	2039	2100	0.1693	35.0	327.7	60	0.160	0.138	39.1	143.0
Case 41	Test 1582	2231	2291	0.1446	29.9	327.7	60	0.158	0.138	39.1	143.0
Case 42	Test 1582	2430	2490	0.1210	25.0	327.7	60	0.157	0.138	39.1	143.0
Case 43	Test 1582	2630	2690	0.0970	20.1	327.7	60	0.155	0.138	39.1	143.0
Case 44	Test 1582	2822	2894	0.0733	15.1	327.8	60	0.153	0.138	39.1	143.0
Case 45	Test 1582	3600	3668	0.0607	12.6	327.8	60	0.152	0.138	39.1	143.0
Case 46	Test 1582	4103	4200	0.0486	10.1	327.8	60	0.151	0.138	39.1	143.0
Case 66	Test 1637	3722	3805	0.1168	24.1	384.0	15	0.231	0.207	14.2	52.0
Case 67	Test 1637	4090	4172	0.1169	24.2	384.1	15	0.230	0.207	14.2	52.0
Case 68	Test 1637	4667	4838	0.0818	16.9	384.1	15	0.230	0.207	14.2	52.0
Case 69	Test 1637	5096	5300	0.0582	12.0	384.0	15	0.228	0.207	14.2	52.0
Case 70	Test 1637	5576	5705	0.0578	12.0	384.0	15	0.229	0.207	14.2	52.0
Case 71	Test 1637	5905	6100	0.0349	7.20	384.0	15	0.227	0.207	14.2	52.0
Case 72	Test 1637	6307	6467	0.0352	7.27	384.0	15	0.227	0.207	14.2	52.0
Case 73	Test 1637	6805	6960	0.0234	4.83	383.8	15	0.226	0.207	14.2	52.0
Case 74	Test 1637	6990	7110	0.0234	4.84	383.7	15	0.227	0.207	14.2	52.0
Case 75	Test 1637	7170	7270	0.0234	4.83	383.7	15	0.227	0.207	14.2	52.0
Case 76	Test 1637	7378	7589	0.0173	3.57	383.5	15	0.225	0.207	14.2	52.0
Case 77	Test 1637	7790	7937	0.0175	3.61	383.1	15	0.223	0.207	14.2	52.0
Case 81	Test 1648	909	987	0.1175	24.3	372.4	26	0.233	0.207	14.2	52.0

Table B.14.3. RBHT Interfacial Drag Assessment Matrix

Case ID	Test ID	Beg Time	End Time	Inj Flow	Mass Flx	Inj Temp	Subcool	Inj Press	UP* Press	Lin Heat	Power
(-)	(-)	(sec)	(sec)	(kg/s)	(kg/m^2-s)	(K)	(K)	(MPa)	(MPa)	(kW/m)	(kW)
Case 82	Test 1648	1220	1287	0.0948	19.6	372.5	26	0.232	0.207	14.2	52.0
Case 83	Test 1648	1458	1545	0.0935	19.3	372.4	26	0.232	0.207	14.2	52.0
Case 84	Test 1648	1734	1800	0.0941	19.4	372.5	26	0.232	0.207	14.2	52.0
Case 85	Test 1648	2040	2133	0.0710	14.7	372.6	26	0.231	0.207	14.2	52.0
Case 86	Test 1648	2313	2470	0.0706	14.6	372.63	26	0.231	0.207	14.2	52.0
Case 87	Test 1648	2709	2862	0.0468	9.66	372.7	26	0.230	0.207	14.2	52.0
Case 88	Test 1648	3285	3465	0.0235	4.85	372.5	26	0.227	0.207	14.2	52.0
Case 89	Test 1648	4005	4080	0.0178	3.67	371.9	26	0.224	0.207	14.2	52.0
Case 90	Test 1648	4380	4440	0.0175	3.61	371.8	26	0.224	0.207	14.2	52.0
Case 91	Test 1648	5510	5640	0.0177	3.65	371.7	26	0.224	0.207	14.2	52.0
Case 94	Test 1651	2985	3060	0.1449	30.0	348.6	60	0.306	0.276	19.1	70.0
Case 95	Test 1651	3270	3322	0.1439	29.7	348.6	60	0.306	0.276	19.1	70.0
Case 96	Test 1651	3520	3610	0.1428	29.5	348.6	60	0.305	0.276	19.1	70.0
Case 97	Test 1651	4050	4125	0.1194	24.7	348.7	60	0.304	0.276	19.1	70.0
Case 98	Test 1651	4770	4845	0.1187	24.5	348.8	60	0.304	0.276	19.1	70.0
Case 99	Test 1651	5030	5100	0.0965	19.9	348.8	60	0.302	0.276	19.1	70.0
Case 100	Test 1651	5280	5379	0.0955	19.7	348.8	60	0.302	0.276	19.1	70.0
Case 101	Test 1651	5960	6257	0.0480	9.93	349.0	60	0.298	0.276	19.1	70.0
Case 116	Test 1659	1950	2040	0.1424	29.4	363.2	60	0.443	0.414	19.1	70.0
Case 117	Test 1659	2210	2300	0.1431	29.6	363.3	60	0.443	0.414	19.1	70.0
Case 118	Test 1659	2490	2557	0.1416	29.3	363.3	60	0.443	0.414	19.1	70.0
Case 119	Test 1659	2730	2820	0.1191	24.6	363.3	60	0.442	0.414	19.1	70.0
Case 120	Test 1659	3680	3730	0.1180	24.4	363.3	60	0.442	0.414	19.1	70.0

Table B.14.3. RBHT Interfacial Drag Assessment Matrix

Case ID	Test ID	Beg Time	End Time	Inj Flow	Mass Flx	Inj Temp	Subcool	Inj Press	UP* Press	Lin Heat	Power
(-)	(-)	(sec)	(sec)	(kg/s)	(kg/m^2-s)	(K)	(K)	(MPa)	(MPa)	(kW/m)	(kW)
Case 121	Test 1659	4127	4270	0.0949	19.6	363.4	60	0.441	0.414	19.1	70.0
Case 122	Test 1659	4550	4660	0.0713	14.7	363.4	60	0.439	0.414	19.1	70.0
Case 123	Test 1659	4980	5100	0.0475	9.82	363.4	60	0.437	0.414	19.1	70.0
Case 124	Test 1659	5310	6120	0.0237	4.90	363.1	60	0.432	0.414	19.1	70.0

*UP = Upper Plenum

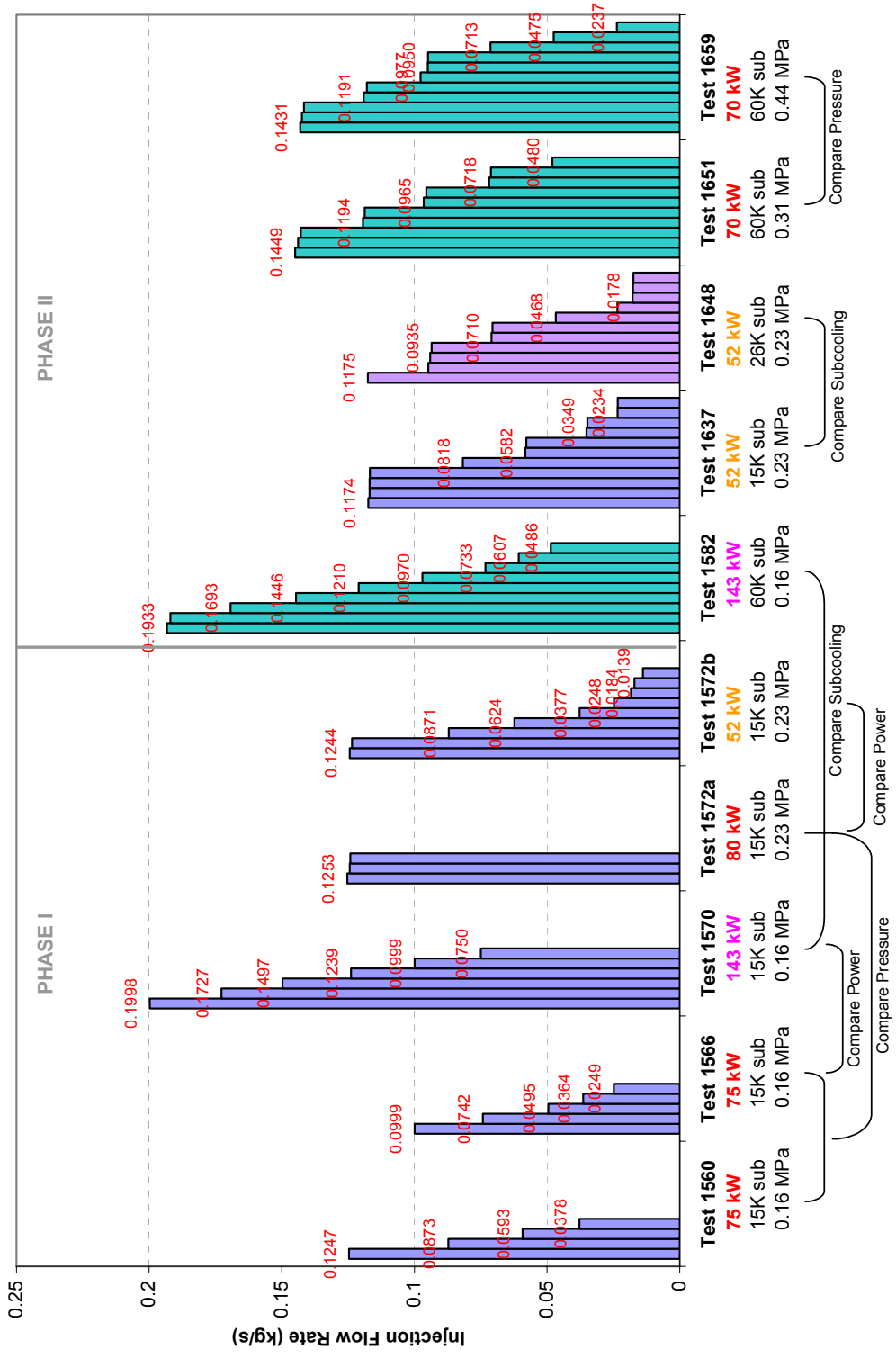

Figure B.14-3. Graphical Representation of RBHT Interfacial Drag Assessment Matrix

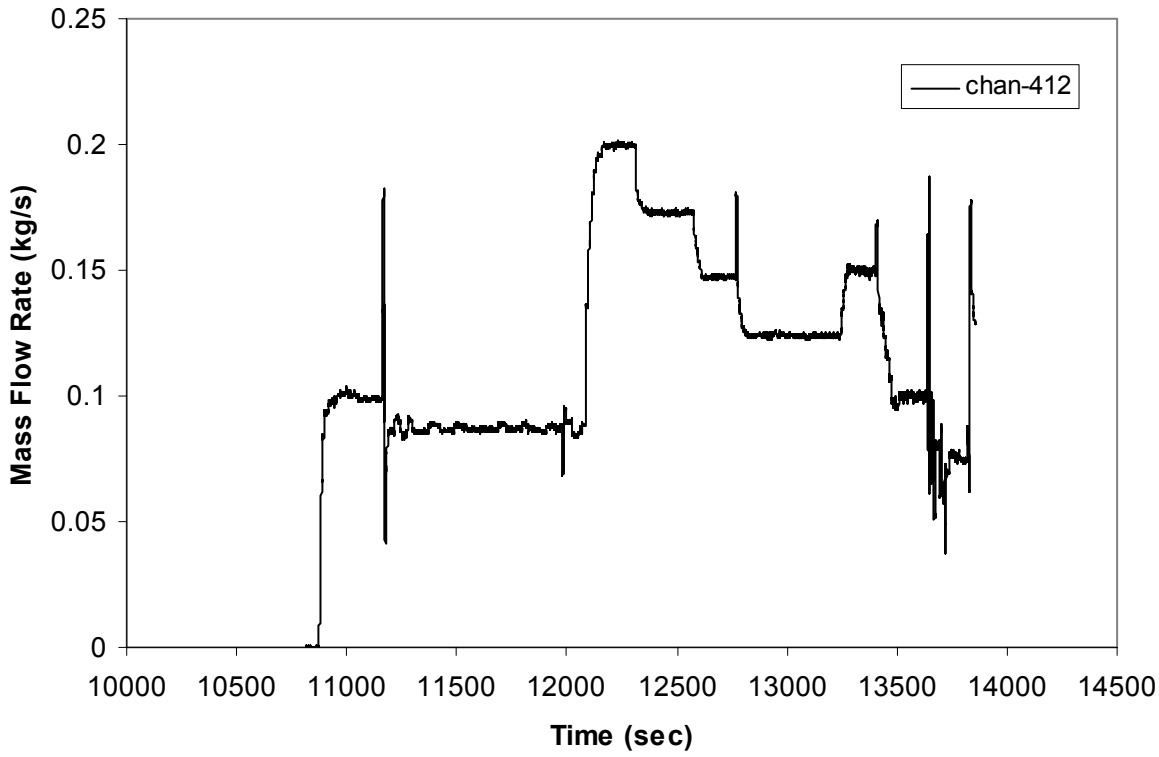

Figure B.14-4. Test 1570 Injection Mass Flow Rate

B.14.4.1. Low Power Cases

The low power cases have a power of 52.0 kW or 14.2 kW/m (4.3 kW/ft) and include Cases 19-24 and 67-91 from Table B.14.3. Figure B.14-5 through Figure B.14-8 are comparisons of TRACE simulations against RBHT data, with respect to axial bundle void fraction, for four representative Cases 19, 20, 67, and 68. The comparisons to data show that TRACE slightly over predicts the axial bundle void fraction. This over prediction is most noticable at the middle and top of the bundle. However, it should be repeated that the RBHT void fraction data has not been corrected for two-phase flow conditions; such corrections could cause the RBHT void fraction data at higher elevations to increase, thus potentially matching the TRACE simulations more closely. In addition, there exists a significant amount of scattering of the axial bundle void fraction data due to a combination of the effects of mixing vane grids and the difficulty in using static dP cells to calculate void fractions near the grids. Figure B.14-9 shows the measured versus predicted void fraction for all low power cases. All of the cases shown in Figure B.14-9 have slight varations in injection flow rate, subcooling, and pressure, and in general, are predicted reasonably well by TRACE.

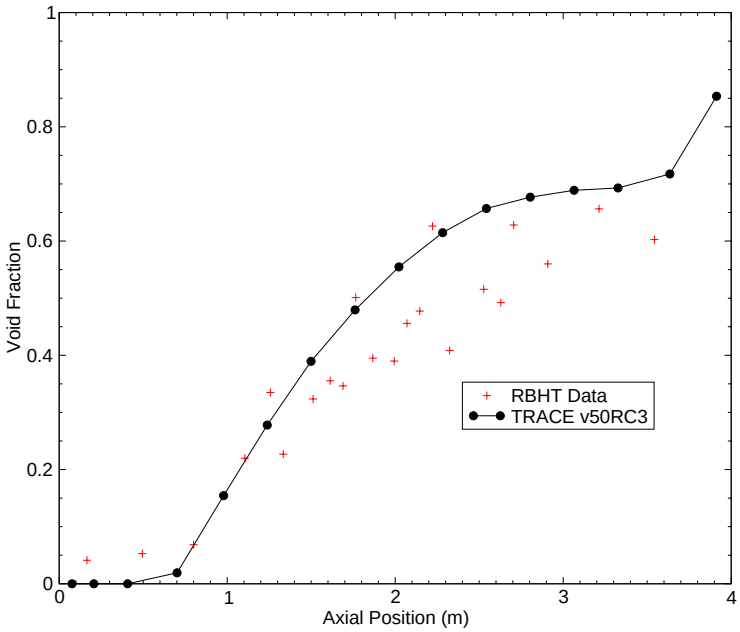

Figure B.14-5. Case 19 (0.1235 kg/s, 0.231 MPa, 52.1 kW) Axial Void Fraction

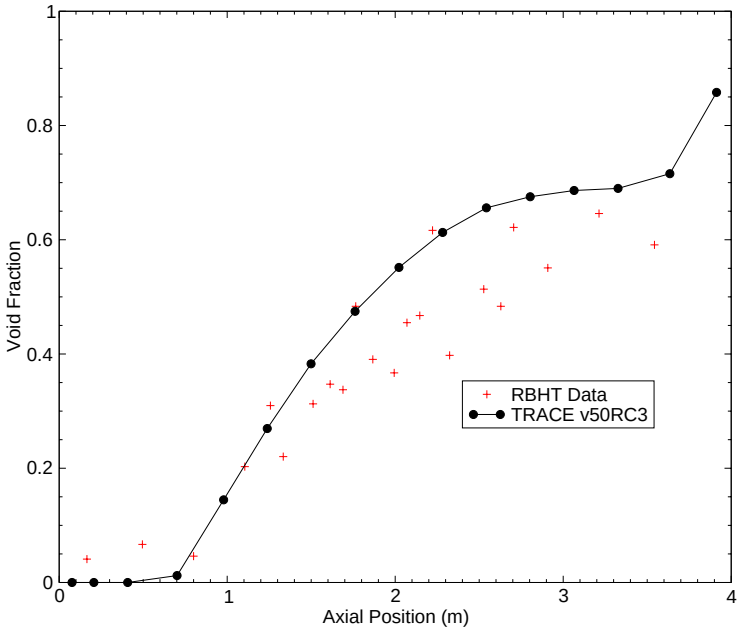

Figure B.14-6. Case 20 (0.1244 kg/s, 0.232 MPa, 52.1 kW) Axial Void Fraction

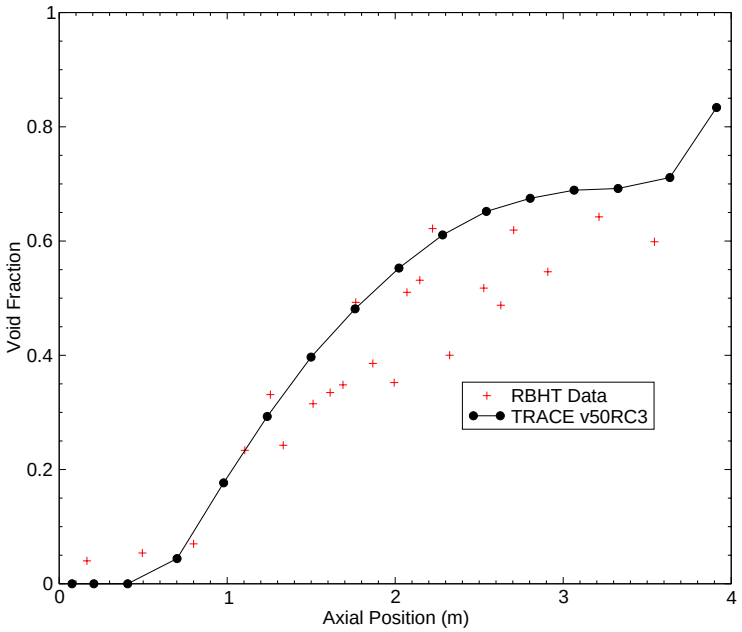

Figure B.14-7. Case 67 (0.1169 kg/s, 0.230 MPa, 52.0 kW) Axial Void Fraction

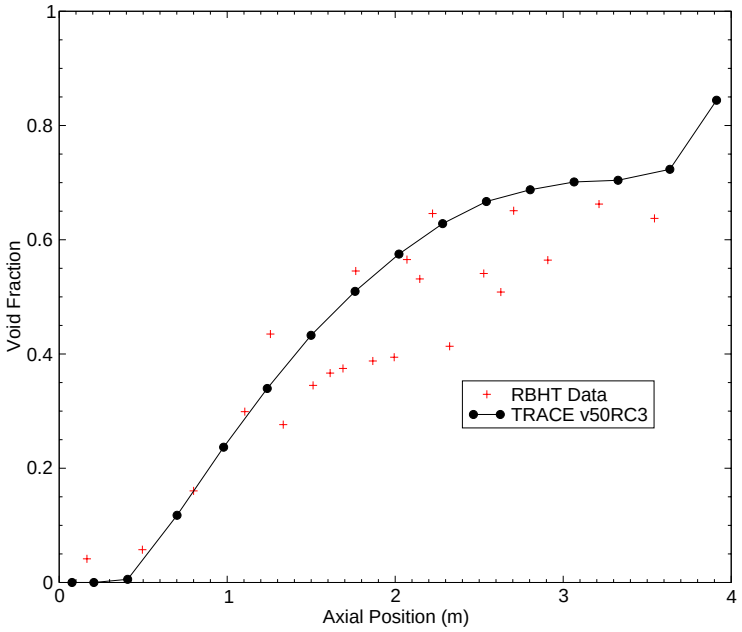

Figure B.14-8. Case 68 (0.0818 kg/s, 0.230 MPa, 52.0 kW) Axial Void Fraction

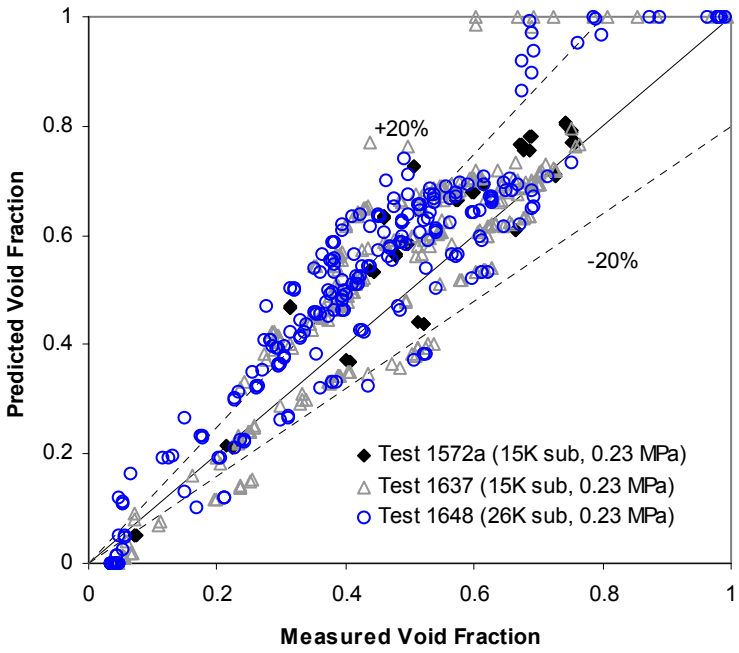

Figure B.14-9. Low Power (52 kW) Cases (Tests 1572a, 1637, and 1648)

B.14.4.2. High Power Cases

The high power cases have a power of 143.0 kW or 39.1 kW/m (11.9 kW/ft), but vary slightly in injection flow rate and degree of subcooling, and include Cases 10-15 and 38-46 from Table B.14.3 Figure B.14-10 through Figure B.14-13 are comparisons of TRACE simulations against RBHT data, with respect to axial bundle void fraction, for four representative Cases 10-13. Due to the high degree of subcooling in Test 1582, 60 K, it has been excluded from this comparison. These comparisons to data show that TRACE significantly over predicts the axial bundle void fraction at higher bundle elevations. However, it should be repeated that the RBHT void fraction data has not been corrected for two-phase flow conditions. TRACE shows slightly more heatup in some cases (Figure B.14-14), while the data does not, which may be partially due to an over prediction of the axial void fraction at higher elevations. Figure B.14-15 shows the measured versus predicted void fraction for all high power cases. All of the cases shown in Figure B.14-15 have slight varations in injection flow rate. In general, TRACE was found to have difficulty predicting axial bundle void fractions at the top of the bundle for high power cases.

B.14.4.3. Low Subcooling Cases (High Power Cases Excluded)

The low subcooling cases have a subcooling of 15 K, but vary slightly in injection flow rate, and include Cases 1-24 and 66-77 from Table B.14.3 Figure B.14-16 through Figure B.14-19 are comparisons of TRACE simulations against RBHT data, with respect to axial bundle void

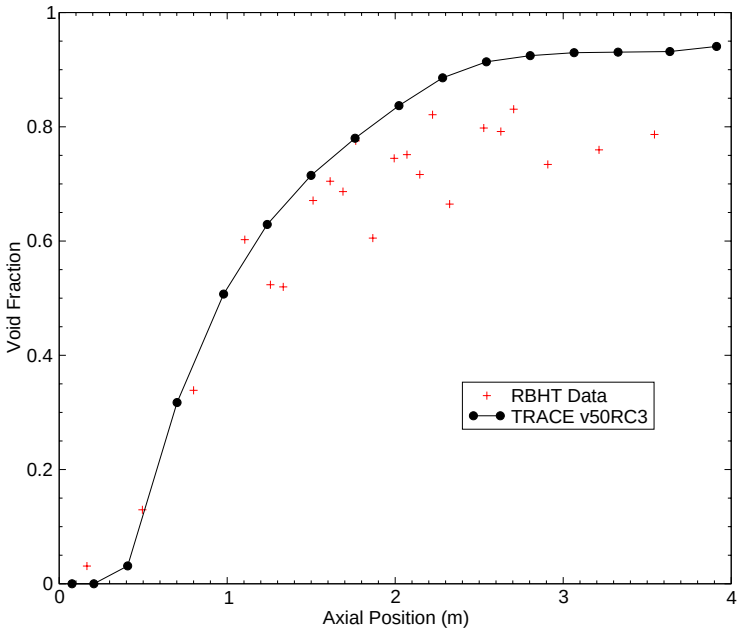

Figure B.14-10. Case 10 (0.1998 kg/s, 0.156 MPa, 143 kW) Axial Void Fraction

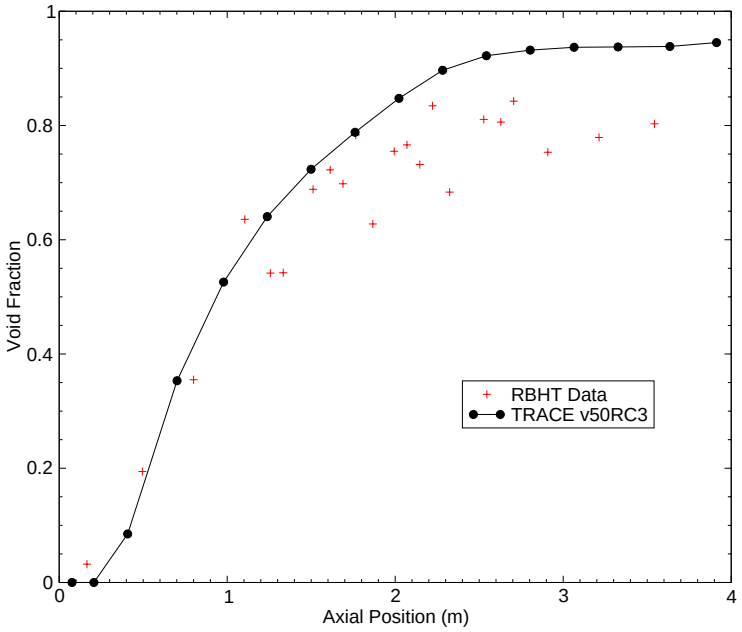

Figure B.14-11. Case 11 (0.1727 kg/s, 0.155 MPa, 142 kW) Axial Void Fraction

fraction, for four representative Cases 1, 7, 21, and 65. The higher power cases were excluded in this comparison. The comparisons to data show that TRACE does a good job predicting the axial

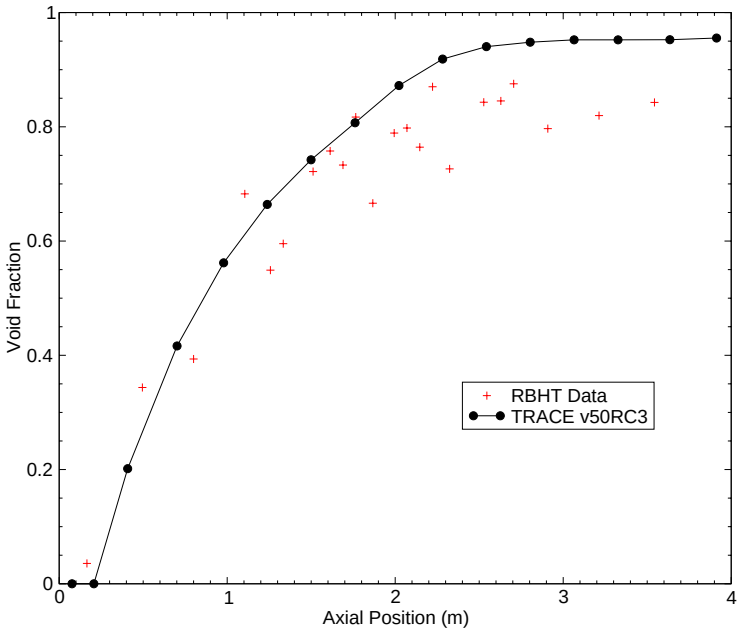

Figure B.14-12. Case 12 (0.1239 kg/s, 0.152 MPa, 142 kW) Axial Void Fraction

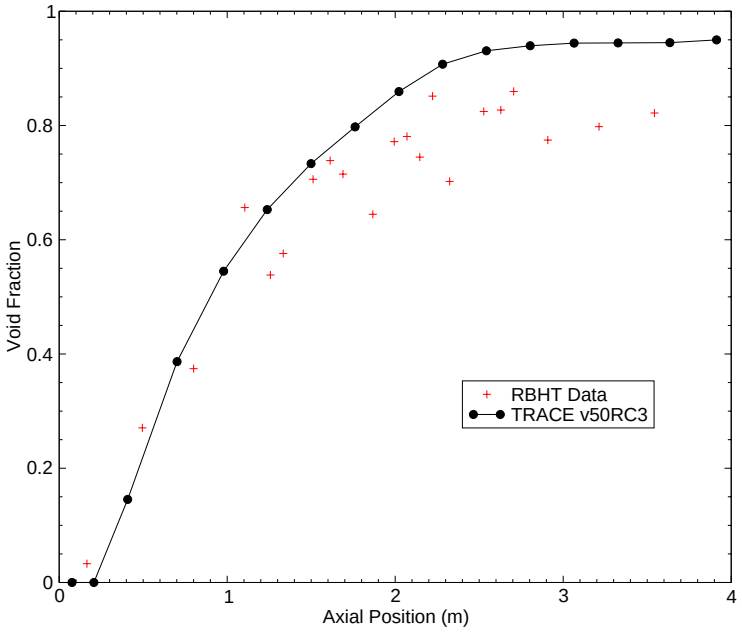

Figure B.14-13. Case 13 (0.1497 kg/s, 0.152 MPa, 143 kW) Axial Void Fraction

bundle void fraction for all bundle elevations. For all of these cases (except for the extremely low flow cases as shown in Figure B.14-21 for Case 26) no heatup was predicted in the TRACE

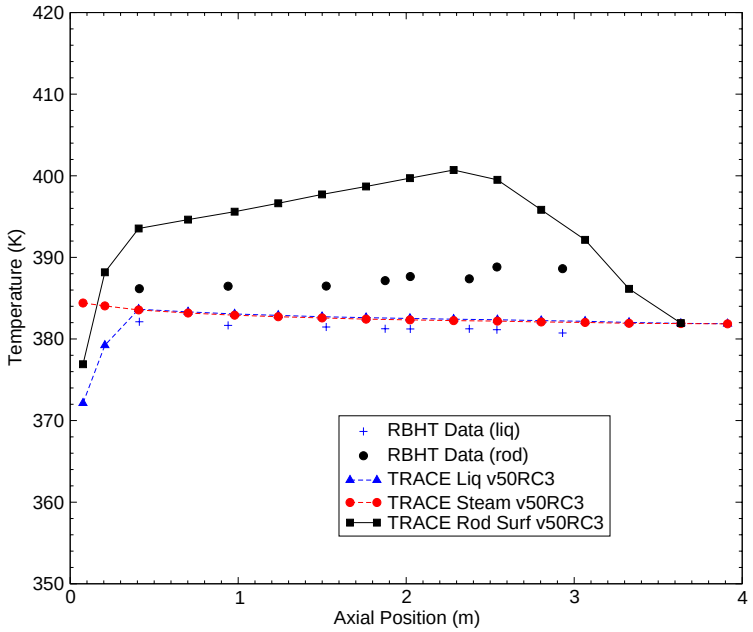

Figure B.14-14. Case 13 (0.1497 kg/s, 0.152 MPa, 143 kW) Axial Bundle Temperature

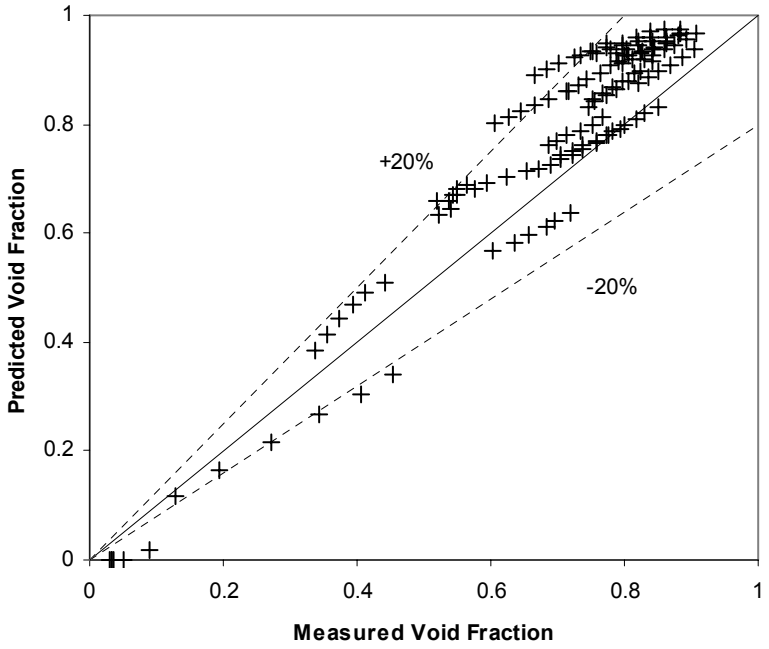

Figure B.14-15. High Power (143 kW) Cases (Test 1570)

simulations or observed in the data. Figure B.14-22 shows the outer surface area heat flux calculated by TRACE for Case 26 at several axial locations in the top portion of the bundle. In this case, TRACE under predicted the rod-to-liquid heat transfer coefficient, which is consistent with the RBHT transient uncovery and reflood assessments. Because Case 26 had a very low injection flow rate, this under prediction had a larger impact on the convective heat transfer and uncovery of the bundle was simulated. Figure B.14-22 shows the measured versus predicted void fraction for all cases that had a small degree of subcooling. In general, TRACE does a reasonably good job predicting most of the low subcooling cases.

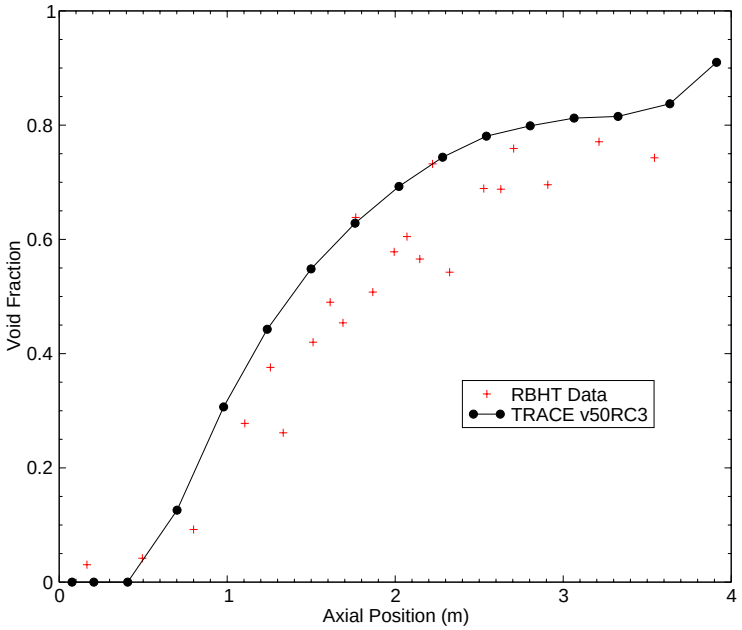

Figure B.14-16. Case 1 (0.1247 kg/s, 0.158 MPa, 75.2 kW) Axial Void Fraction

B.14.4.4. High Subcooling Cases (High Power Cases Excluded)

The high subcooling cases have a subcooling of 60 K, but vary slightly in injection flow rate and pressure, and include Cases 38-46, 94-101, and 116-124 from Table B.14.3 Figure B.14-23 through Figure B.14-26 are comparisons of TRACE simulations against RBHT data, with respect to axial bundle void fraction, for four representative Cases 95, 96, 117, and 118. The higher power cases were excluded in this comparison. The comparisons to data show that TRACE significantly over predicts the void fraction at all bundle elevations. For almost all of these cases no heatup was experienced in the TRACE simulations or data due to the large amount of subcooling present. Figure B.14-27 shows the measured versus predicted void fraction for all cases that had a large degree of subcooling. In general, TRACE has difficulty predicting the axial bundle void fraction at lower void fractions for cases with high subcooling.

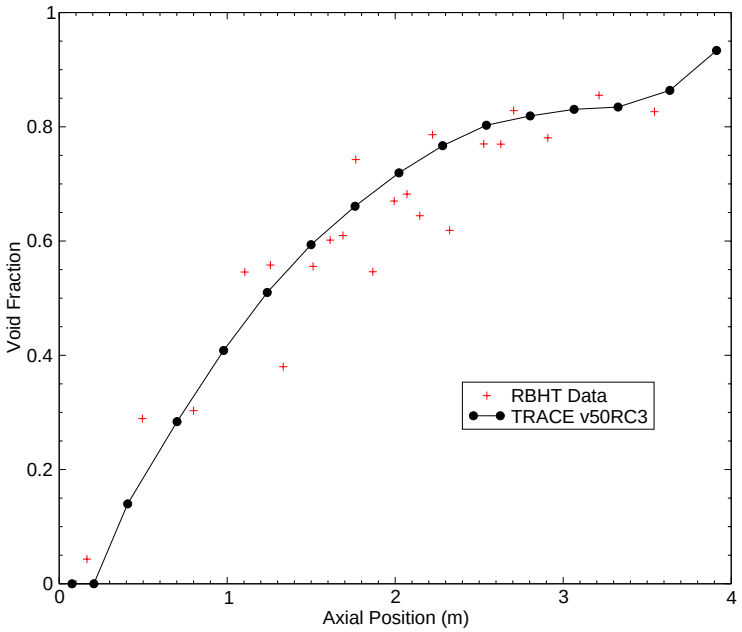

Figure B.14-17. Case 7 (0.0496 kg/s, 0.154 MPa, 74.8 kW) Axial Void Fraction

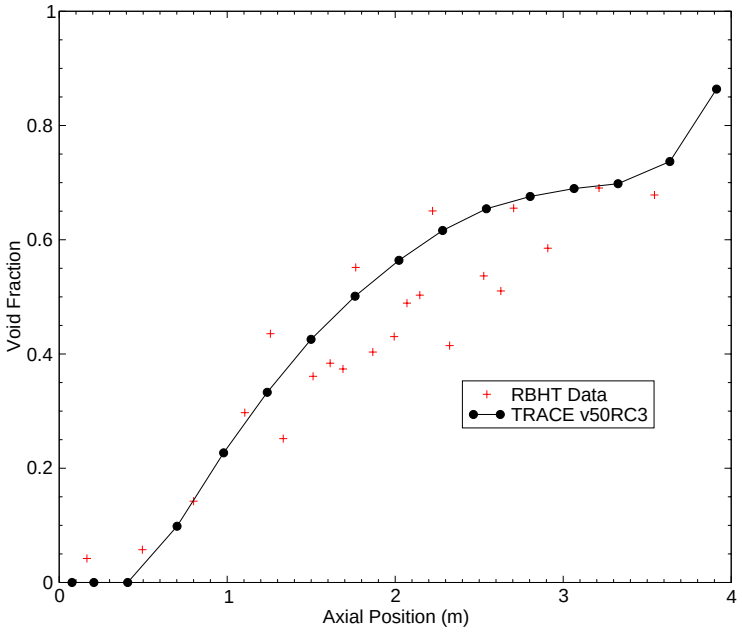

Figure B.14-18. Case 21 (0.0871 kg/s, 0.231 MPa, 52.1 kW) Axial Void Fraction

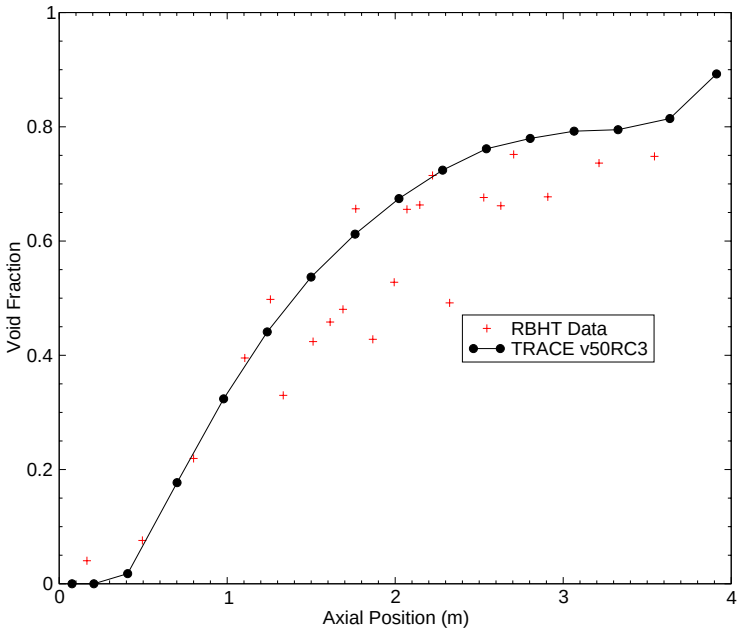

Figure B.14-19. Case 65 (0.1174 kg/s, 0.230 MPa, 52 kW) Axial Void Fraction

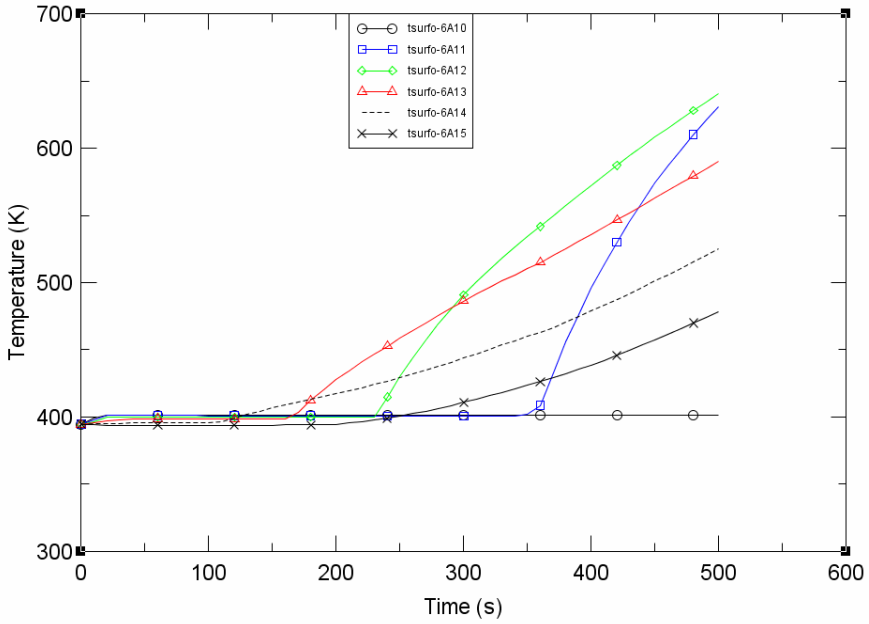

Figure B.14-20. Case 26 TRACE Outer Rod Surface Temperature

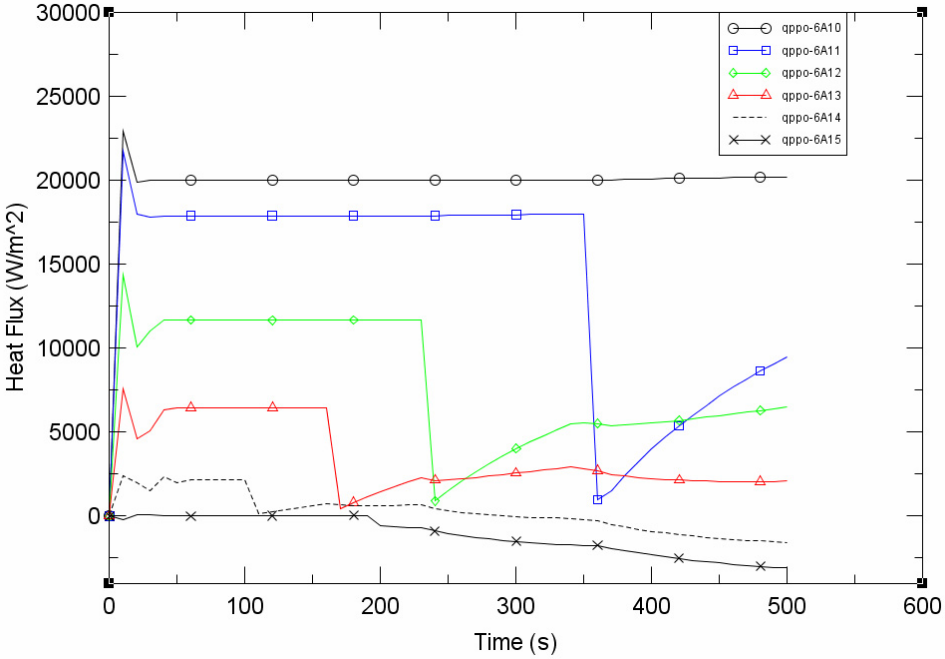

Figure B.14-21. Case 26 TRACE Outer Rod Surface Heat Flux

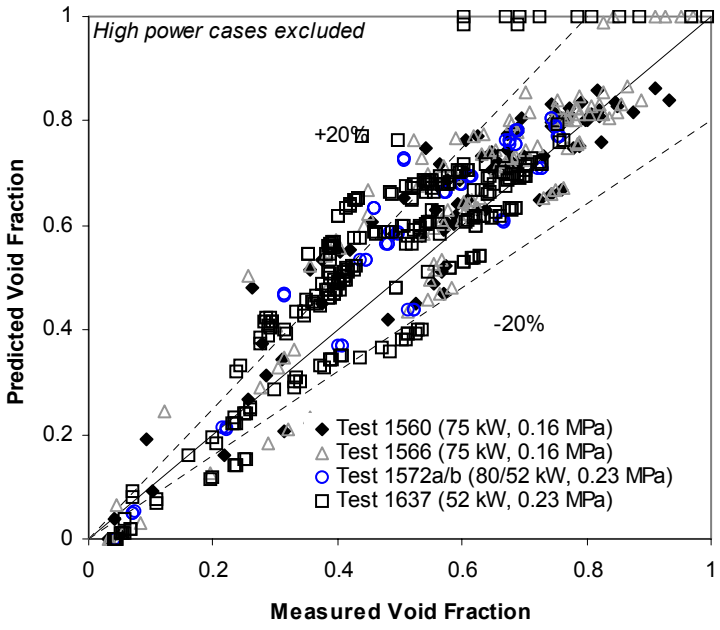

Figure B.14-22. Low Subcooling (15 K) Cases (Tests 1560, 1566, 1572a/b, and 1637)

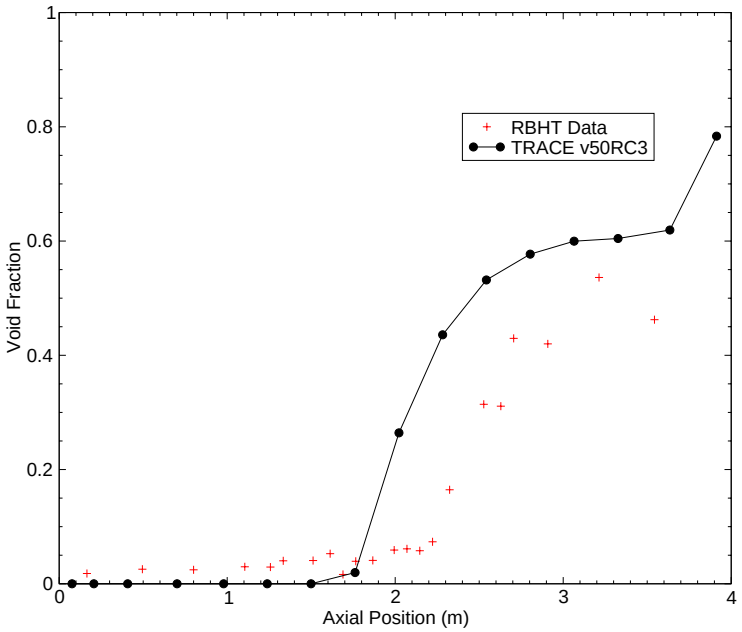

Figure B.14-23. Case 95 (0.1439 kg/s, 0.30 MPa, 70 kW) Axial Void Fraction

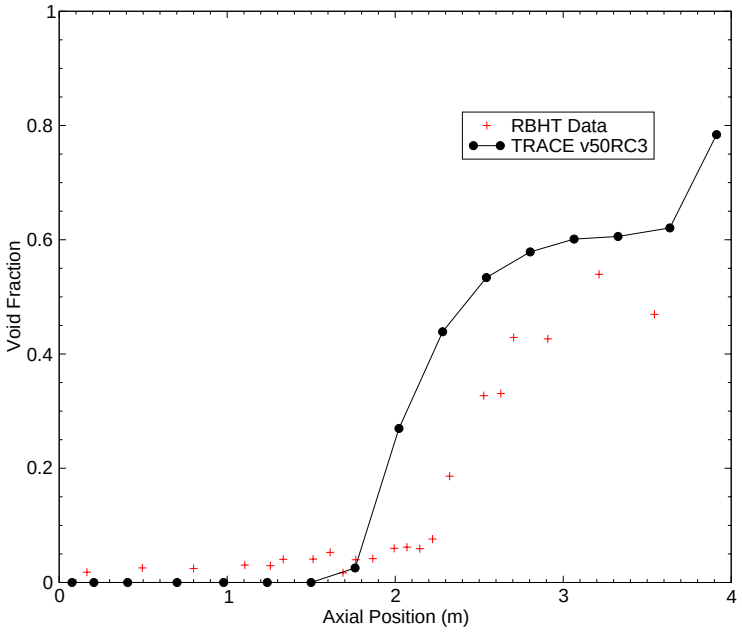

Figure B.14-24. Case 96 (0.1428 kg/s, 0.30 MPa, 70 kW) Axial Void Fraction

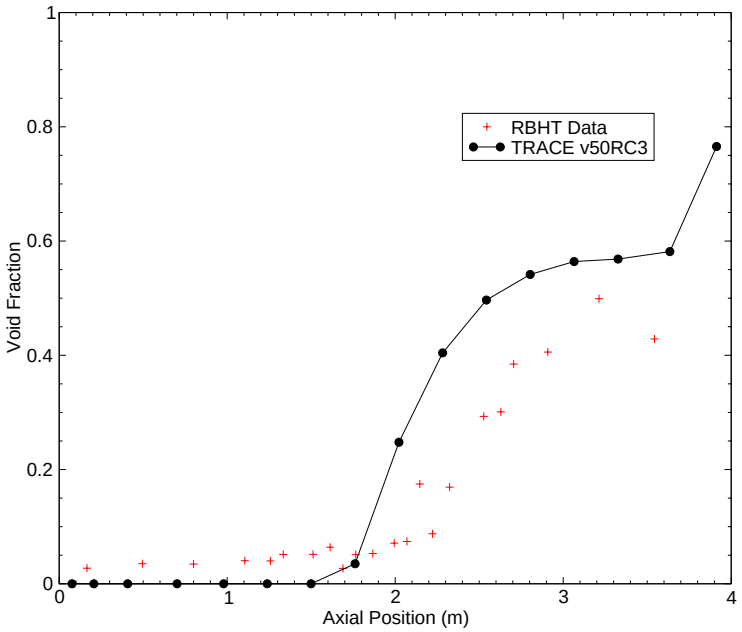

Figure B.14-25. Case 117 (0.1431 kg/s, 0.44 MPa, 70 kW) Axial Void Fraction

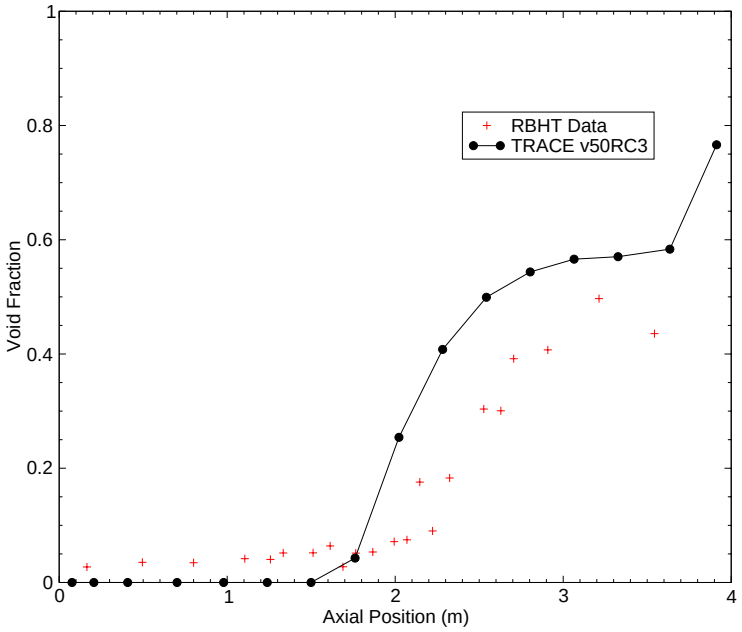

Figure B.14-26. Case 118 (0.1416 kg/s, 0.44 MPa, 70 kW) Axial Void Fraction

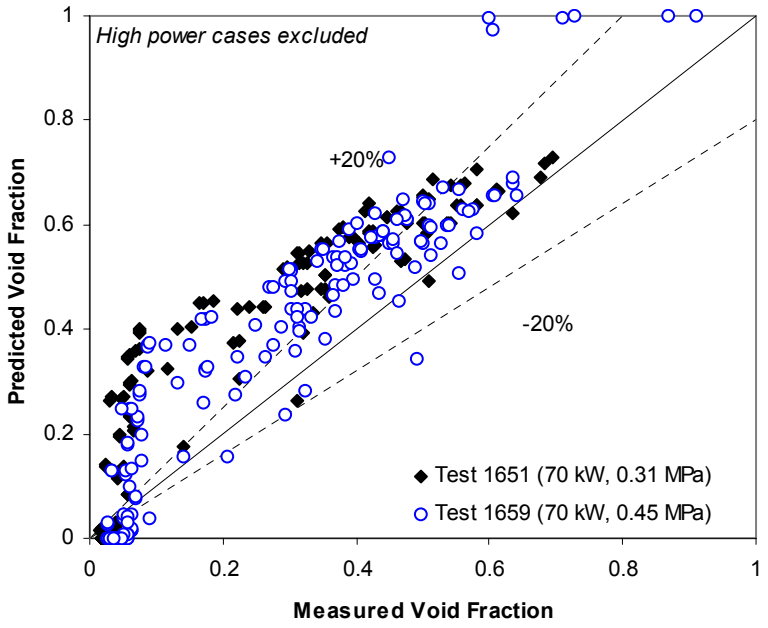

Figure B.14-27. High Subcooling (60 K) Cases (Tests 1651 and 1659)

B.14.4.5. Low Flow Cases (High Power Cases Excluded)

The low flow cases have a liquid injection flow rate less than 0.04 kg/s, but vary slightly in pressure and subcooling, and include Cases 4, 8, 9, 23, 24, 71-77, and 88-91 from Table B.14.3 Figure B.14-28 through Figure B.14-31 are comparisons of TRACE simulations against RBHT data, with respect to axial bundle void fraction, for four representative Cases 4, 9, 77, 91. The higher power large subcooling cases were excluded in this comparison. The comparisons to data show that TRACE slightly over predicts the void fraction at the highest bundle elevations, but does a good job at all other axial locations. Figure B.14-32 shows the measured versus predicted void fraction for all low flow cases. All of the cases shown in Figure B.14-32 have slight varations in pressure, power, and subcooling and, in general, TRACE does a good job predicting the axial bundle void fraction for low flow cases.

B.14.4.6. High Flow Cases (High Power Cases Excluded)

The high flow cases have an injection flow rate greater than 0.10 kg/s, but vary slightly in pressure and subcooling, and include Cases 1, 10-13, 16-20, 38-42, 66, 67, 81, 94-98, and 116-120 from Table B.14.3 Figure B.14-33 through Figure B.14-36 are comparisons of TRACE simulations against RBHT data, with respect to axial bundle void fraction, for four representative Cases 16, 17, 18, and 64. The higher power and large subcooling cases were excluded in this comparison. The comparisons to data show that TRACE does a good job predicting axial bundle void fraction at all elevations. Figure B.14-37 shows the measured versus predicted void fraction

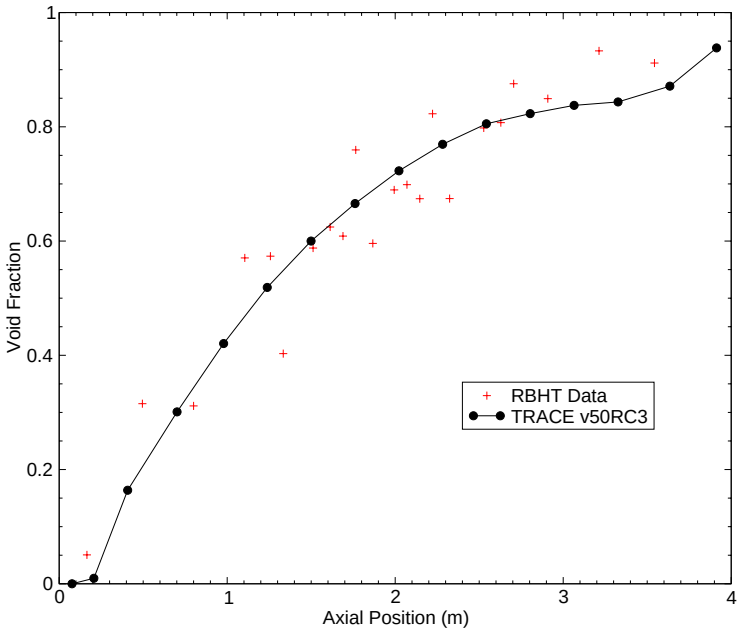

Figure B.14-28. Case 4 (0.0378 kg/s, 0.153 MPa, 75.1 kW) Axial Void Fraction

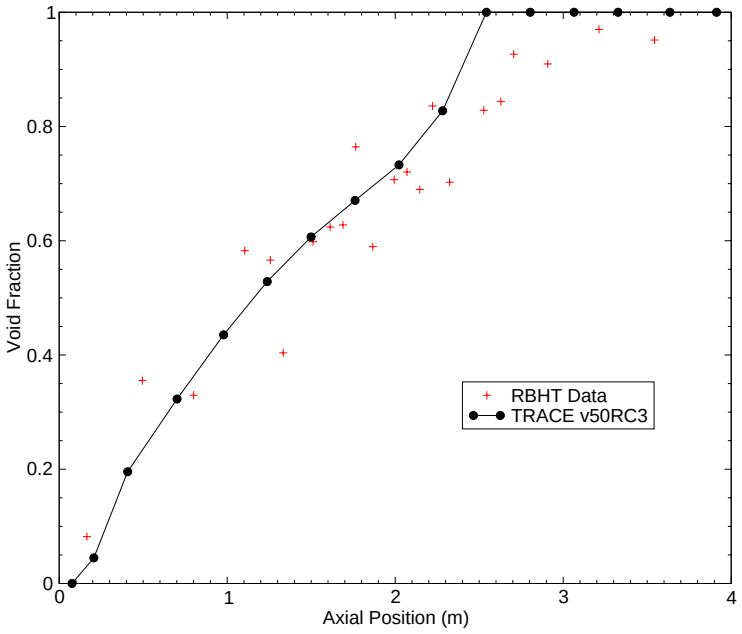

Figure B.14-29. Case 9 (0.0249 kg/s, 0.151 MPa, 74.6 kW) Axial Void Fraction

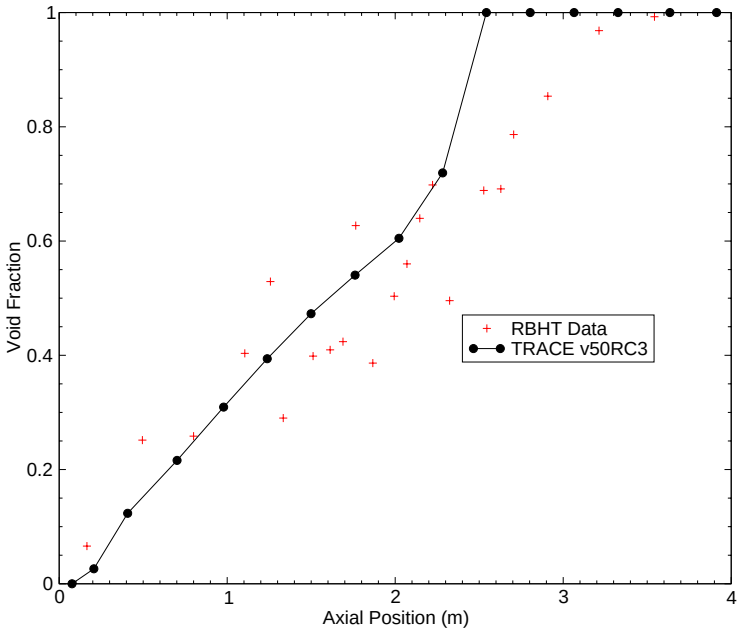

Figure B.14-30. Case 77 (0.0175 kg/s, 0.23 MPa, 52 kW) Axial Void Fraction

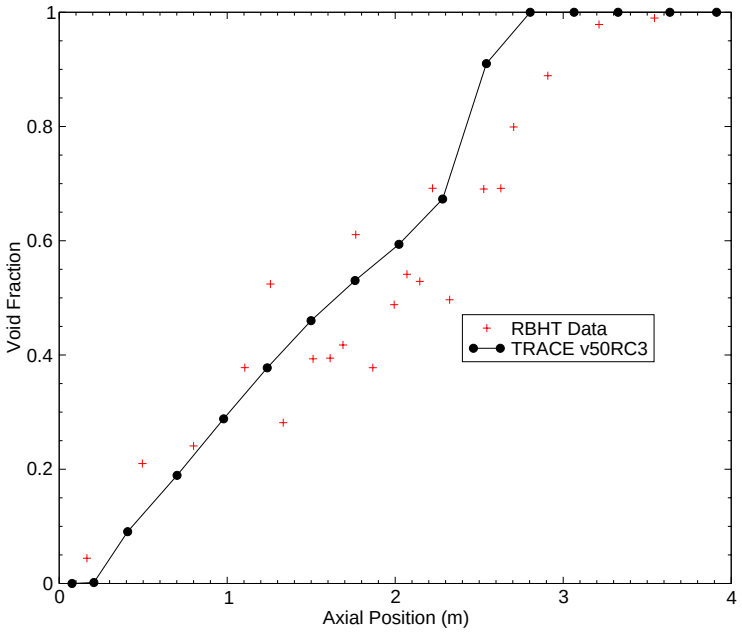

Figure B.14-31. Case 91 (0.0177 kg/s, 0.230 MPa, 52 kW) Axial Void Fraction

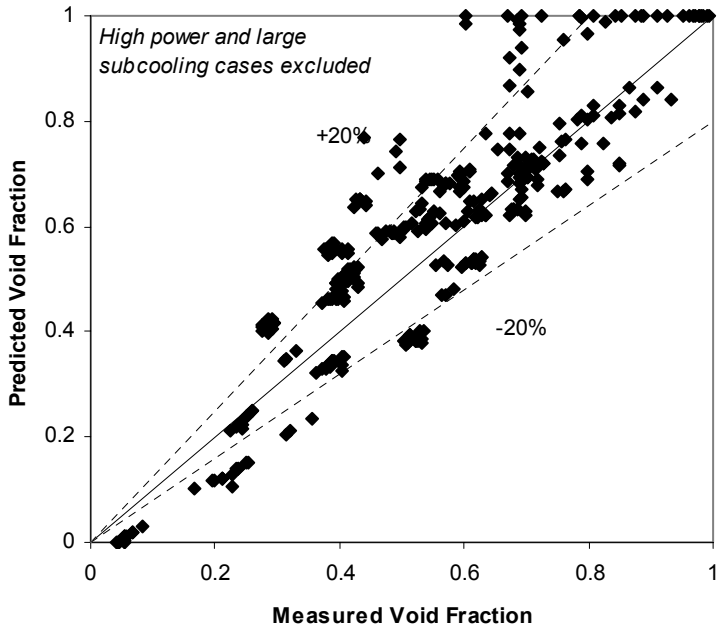

Figure B.14-32. Low Flow (Injection Flow Rate < 0.04 kg/s) Cases 4, 8, 9, 23, 24, 71-77, and 88-91

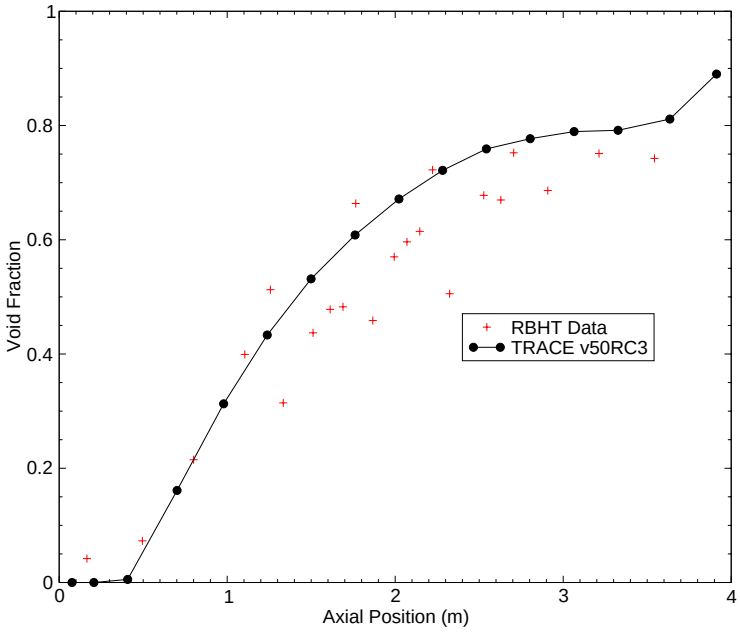

Figure B.14-33. Case 16 (0.1244 kg/s, 0.228 MPa, 80 kW) Axial Void Fraction

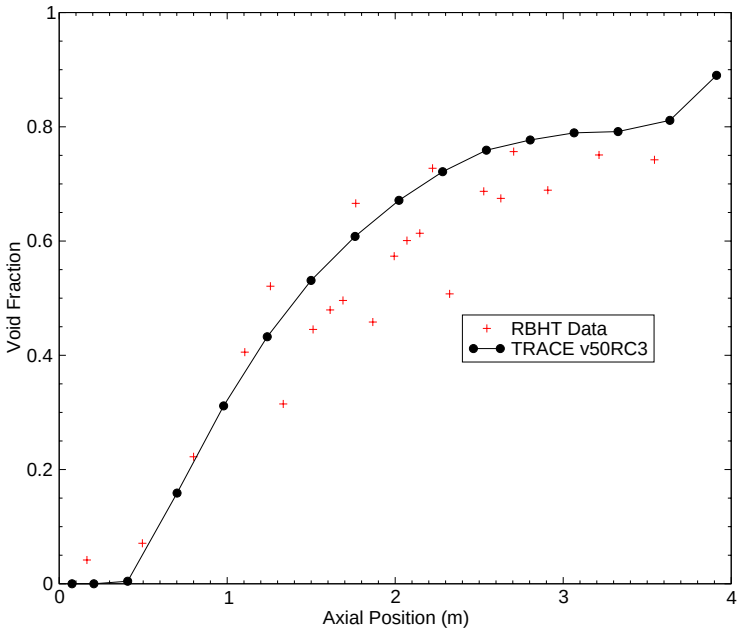

Figure B.14-34. Case 17 (0.1253 kg/s, 0.227 MPa, 79.1 kW) Axial Void Fraction

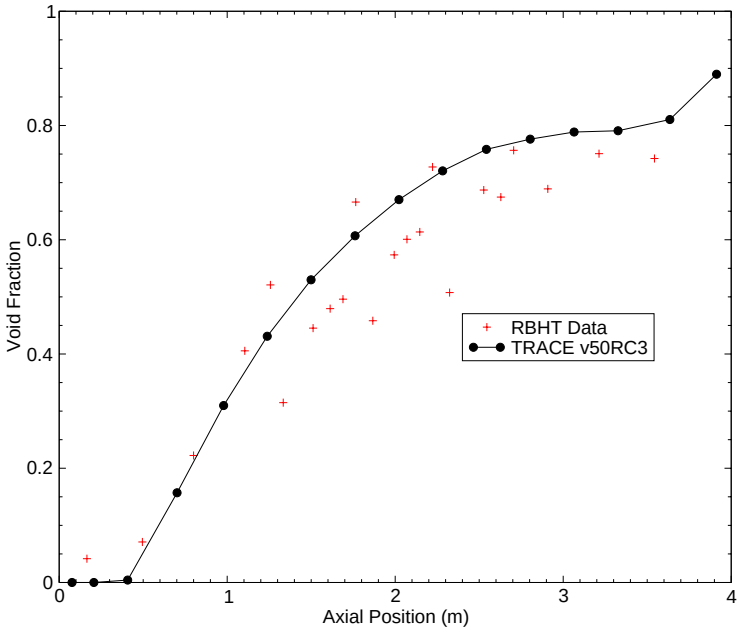

Figure B.14-35. Case 18 (0.1242 kg/s, 0.227 MPa, 78.8 kW) Axial Void Fraction

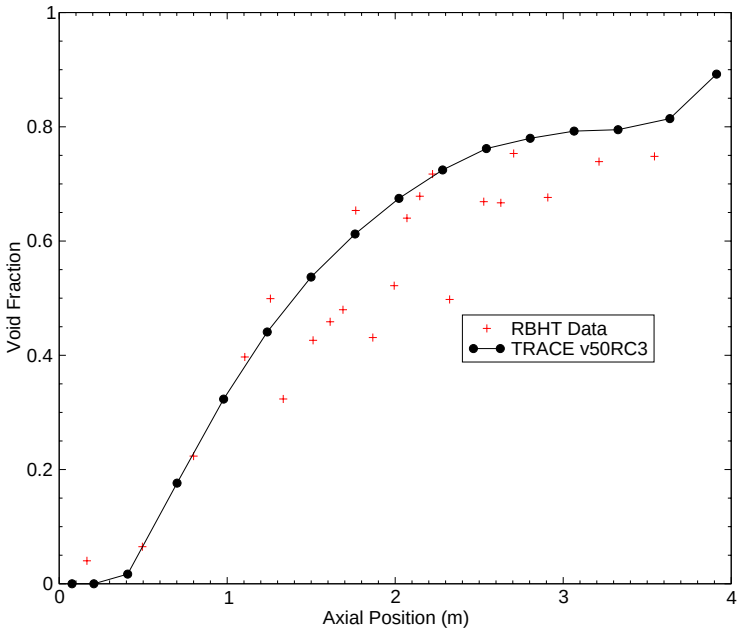

Figure B.14-36. Case 64 (0.1169 kg/s, 0.230 MPa, 52 kW) Axial Void Fraction

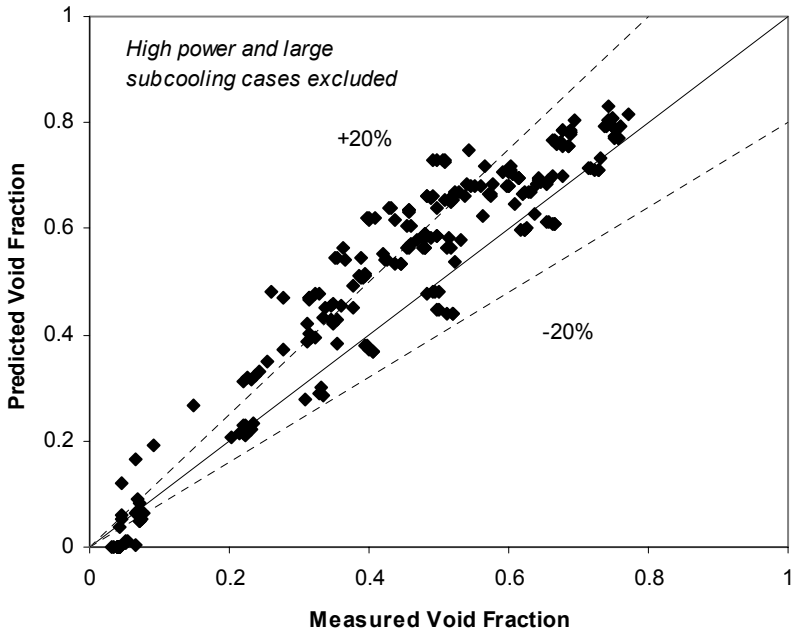

Figure B.14-37. High Flow (Injection Flow Rate > 0.10 kg/s) Cases 1, 16-20, 64-67, and 81

for all high flow cases. In general, TRACE does a good job predicting axial bundle void fractions for high flow cases.

B.14.5. Assessment Results Summary

Parameters were selected to quantify the code's ability to predict RBHT interfacial drag data: the onset of significant voiding, bundle exit void fraction, local void fraction, and collapsed liquid level. Table B.14.4 provides a measure of the total bias (or accuracy) and uncertainty (or precision) in the code's predictive capabilities for all cases with respect to each parameter. For this assessment the bias was defined as the average percentage difference between the calculated and measured quanitities, while the uncertainty was defined as the measure of goodness-to-fit (R^2) value found by conducting a linear interpolation between the measured and predicted values.

Table B.14.4. RBHT Interfacial Drag Assessment Parameters

Parameter	Bias (%)	R^2	Comments
Exit Void Fraction	-12.5	0.88	slightly over predicts, excellent precision
Local Void Fraction	-19.6	0.89	slightly over predicts, excellent precision
Onset of Significant Void	-32.3	0.01	significantly over predicts, poor precision
Collapsed Liquid Level	+11.5	0.96	slightly under predicts, excellent precision

Figure B.14-38 through Figure B.14-41 are comparisons of measured to calculated onset of significant voiding, bundle exit void fraction, collapsed liquid level, and local void fraction for all 73 assessment cases listed in Table B.14.4. For this assessment, the onset of significant voiding is defined as the first measured void fraction (determined axially starting from the bottom of the bundle) greater than 0.10 in the bundle. In general, TRACE has difficulty predicting the onset of significant voiding, with the high power and large degree of subcooling cases being the most difficult to predict. Figure B.14-39 shows the bundle exist void fraction for all assessment cases and shows that TRACE does a good job predicting this FOM with good precision. TRACE does a good job predicting the bundle collapsed liquid level with excellent precision as shown in Figure B.14-40.

In general, TRACE has the most difficulty predicting the high power, subcooling, and flow cases, but does a good job predicting the rest of the RBHT interfacial drag data over the full range of injection flow rates and pressures tested. In addition, TRACE has the most difficulty predicting low (< 0.3) and high (> 0.6) bundle void fractions as shown in Figure B.14-41. In general the low void fraction cases correspond to the cases with a high degree of subcooling, while the high void fraction cases usually correspond to the high power cases. Figure B.14-42 shows the same data in Figure B.14-41, but in this figure, the vertical axis is the measured minus predicted void fraction, which illustrates TRACE's tendency to over predict the bundle void fraction (majority of the data below the horizontal axis). It is useful to note that TRACE consistently under predicts the collapsed liquid level, while significantly over predicts the onset of significant void for the high power, low subcooling, and flow cases, but then under predicts the onset of significant void for

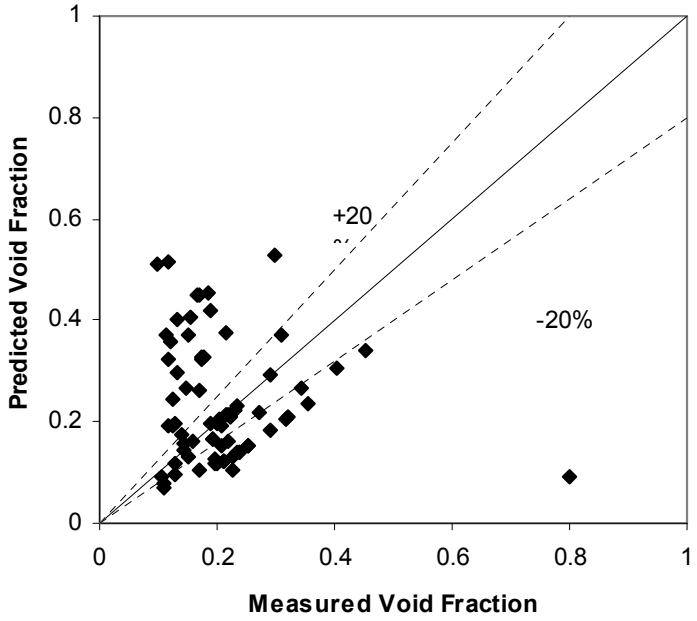

Figure B.14-38. Onset of Significant Voiding (First $\alpha_{meas} > 0.10$) Comparison

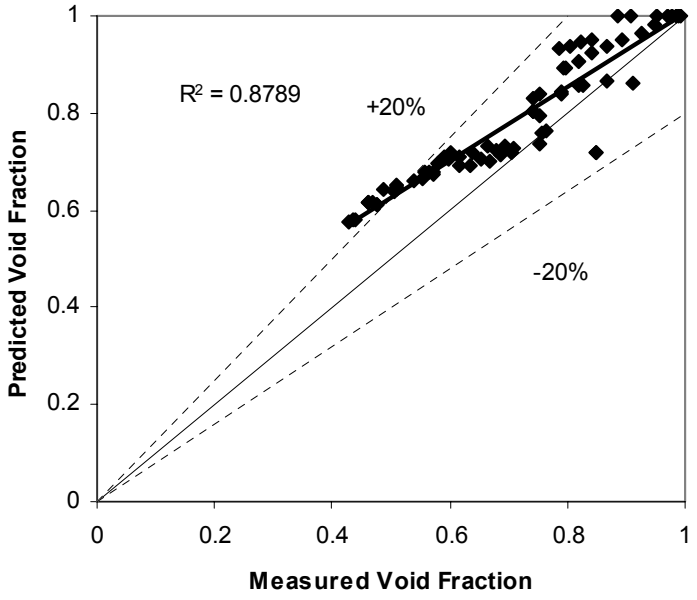

Figure B.14-39. Bundle Exit Void Fraction Comparison

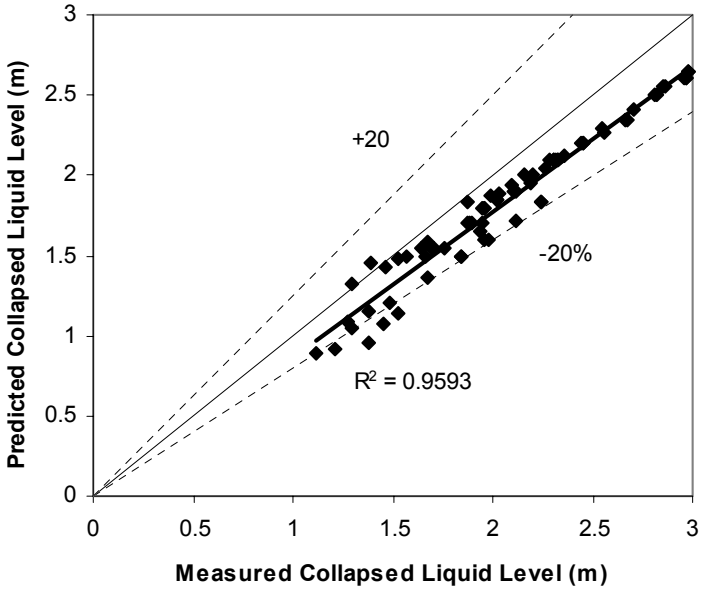

Figure B.14-40. Collapsed Liquid Level Comparison

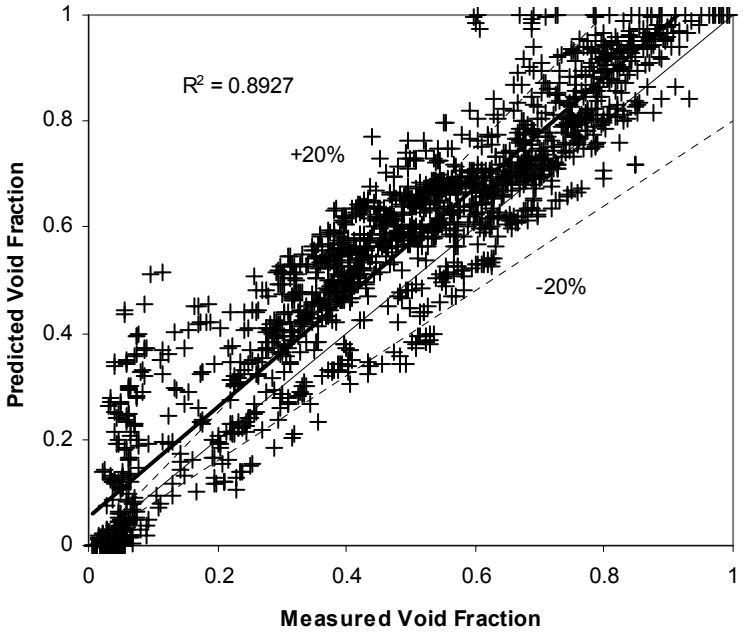

Figure B.14-41. Measured versus Predict Void Fraction for All Cases

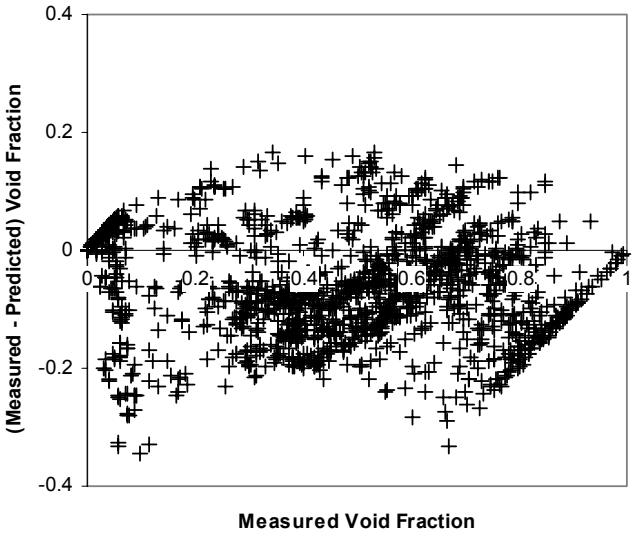

Figure B.14-42. Measured Minus Predicted Void Fraction for All Cases

the low power, subcooling, and flow cases. This "flip-flop" prediction of the onset of significant void suggests issues with the calculation of the interfacial drag in subcooled region of the simulated bundle.

It is important to note that this assessment is based on RBHT data that has not been corrected for two-phase flow conditions and that when such a correction is implimented, it will most likely result in the higher void fraction data (i.e. void fractions at higher elevations) to increase. This would then cause the TRACE predictions at higher void fractions to better match the data. In addition, the mixing vane grids caused large variations in measured local void fractions. This could be due to a combination of a real effect of the mixing vanes and/or due to difficulty in calculating the axial void fraction based on static dPs near the grids.

B.14.6. References

1 Rosal, E.R., Lin, T.F., McClellan, I.S., Brewer, R.C., "Rod Bundle Heat Transfer (RBHT) Test Faciltity Description Report," Department of Mechanical Engineering, The Pennsylvania State University, 2005.

2 Hochreiter, L.E. et. al., "Analysis of the Rod Bundle Heat Transfer Facility Two-Phase Interfacial Drag Experiments," Department of Mechanical Engineering, The Pennsylvania State University, June 2005.

3 Welter, K.B., Bajorek, S.M., "RBHT Steady-State Uncovery Calculational Notebook," Office of Nuclear Regulatory Research, U.S. Nuclear Regulatory Commission, January 17, 2005.

B.15. RBHT Transient Uncovery Test

Author(s): Kent B. Welter

Affiliation: USNRC RES:DRASP:NRCA

Code Version: TRACE V5.0

Platform and Operating System: Intel x86, Windows XP

B.15.1. Introduction

The simulations presented in this section examine the ability of TRACE to calculate peak cladding temperatures, heat transfer coefficients, void distributions, and two-phase level swell at low pressure during a transient boil-off or uncovery test. The simulations were compared to Test 1690 performed at the Penn State/NRC Rod Bundle Heat Transfer (RBHT) facility. The RBHT facility is designed to simulate a full-length portion of a Pressurized Water Reactor (PWR) fuel assembly. The facility consists of a 7x7-rod bundle with 45 electricity heated rods, mixing vane grids, and over 500 instrument channels for measuring temperature, differential and absolute pressure, steam and liquid flow rates, power, etc. The axial differential pressure measurements can be used, along with appropriate temperature and flow corrections, to calculate the bundle void fraction.

RBHT Test 1690 was run at 0.207 MPa (30 psia) with a variable liquid injection flow rate that ranges from 0.014 to 0.071 kg/s. The maximum rod linear heat rate was 0.49 kW/m (0.15 kW/ft). The axial void fraction, peak cladding temperature (PCT), and bundle heat transfer coefficient at PCT were used as figures of merit to quantify the code's accuracy.

B.15.2. Test Facility Description

The RBHT Facility is designed to conduct systematic separate-effects tests under well-controlled conditions in order to generate fundamental rod bundle transfer data from single phase steam cooling tests, low flow boiling tests, and dispersed flow film boiling heat transfer tests (Ref. 2). The facility is capable of operating in both forced and variable reflood modes covering a wide range of flow and heat transfer conditions at pressures from 0.13 to 0.42 MPa. The test facility consists of the following major components (shown schematically in Figure B.15-1):

- Test section consisting of a lower plenum, low-mass housing containing the heater rod bundle, and an upper plenum.

- Cooling injection and steam injection systems.
- Closely coupled phase separation and liquid collection systems.
- Pressure fluctuation damping tank and steam exhaust piping.

The test section shown in Figure B.15-1 consists of the heater rod bundle, the flow housing, and the lower and upper plenums. The heater rod bundle simulates a small portion of a 17x17 reactor fuel assembly. The electrically heated rods have a diameter of 9.5 mm and are arranged in a 7x7 array with a 12.6 mm pitch with 45 heater rods and four unheated rods (at each corner). The facility has over 500 instrument channels to measure temperature, differential and absolute pressure, flow rates, power, etc. For this study, of particular interest are the bundle differential pressure cells (used to calculate void fraction), inlet injection flow rate (chan-412), liquid injection temperature (chan-407), heater rod voltage (chan-395) and current (chan-396), and upper and lower plenum pressures (chan-411 and chan-393, respectively). Table B.15.1 contains a list of the 22 axial bundle differential pressure cells used in this assessment, along with the axial locations of the 7 mixing vane grids. The grids are 5.72 cm high.

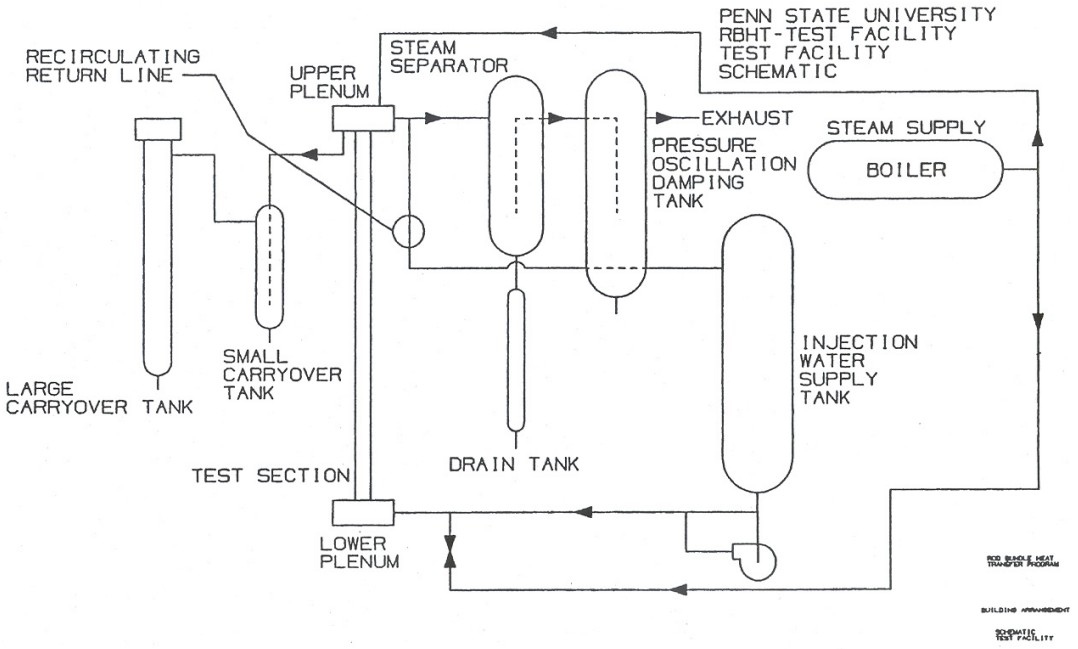

Figure B.15-1. RBHT Test Facility Schematic

Table B.15.1. Differential Pressure Cell and Grid Locations

Instrument ID	Lower Tap, Axial Location (m)	Upper Tap, Axial Location (m)	Grid Bottom, Axial Location (m)
chan-363	0.0	0.330	0.330
chan-364	0.330	0.640	
chan-365	0.640	0.940	0.690
chan-366	0.940	1.092	
chan-367	1.092	1.168	
chan-368	1.168	1.346	1.212
chan-369	1.346	1.448	
chan-370	1.448	1.524	
chan-371	1.524	1.600	
chan-372	1.600	1.702	
chan-373	1.702	1.823	1.734
chan-374	1.823	1.905	
chan-375	1.905	1.981	
chan-376	1.981	2.057	
chan-377	2.057	2.159	
chan-378	2.159	2.362	2.256
chan-379	2.362	2.465	
chan-380	2.465	2.540	
chan-381	2.540	2.743	
chan-382	2.743	3.048	2.778
chan-383	3.048	3.378	3.301
chan-384	3.378	3.657	

Radiation only experiments were conducted to characterize the test section heat loss and were conducted under a vacuum. Based on a total power of 114 kW, the heat loss for a typical reflood test was calculated to be approximately 2.5 kW, which is a small fraction (~2%) of the total power supplied to the heater rods.

B.15.3. TRACE Model Description

The RBHT main test section was modeled in TRACE using VESSEL and HSTRC components as shown in Figure B.15-2. The VESSEL component was divided into 16 axial levels with a nodalization chosen such that there are two cells between each mixing vane grid and that the

bottom of every other cell corresponds to the bottom of a grid. The mixing vane grids were modeled by specifying a loss coefficient of 2.0 (Ref. 2). Forty-five heated rods were modeled in a 7x7 array, with four non-heated rods in the corners. Two PIPE components (shown in Figure B.15-2), one at the bottom and one at the top, were used to model the upper and lower plenums, respectively. Liquid injection flow was provided by the FILL component at the bottom of the lower plenum, while a BREAK, at a specified initial pressure, was used at the top. Table B.15.15.2. provides a list of the initial and boundary conditions simulated in TRACE for Test 1690. The VESSEL component spans the entire heated length, but an additional cell at the top of the VESSEL was added to help reduce void fraction oscillations at the top of a rod bundle, which is a standard TRACE modeling practice. The shape of the power curve applied to the HSTRC peaks at 2.7781 m as shown in Figure B.15-2. The heater rods were modeled using 8 radial nodes, which is also shown in Figure B.15-2, and included the Constantan heater wire insulated with Boron-Nitride insulation, clad with Inconel, Type 600. A flow housing HSTRC was added to the model to account for heat loss to the environment and was based on user specified ambient conditions.

Table B.15.15.2. is a list of the initial and boundary conditions used in the TRACE model to simulate RBHT Test 1690. In general, the liquid injection flow rate and power were specified explicitly during the entire transient, along with initial values for component temperature, pressure, and void fraction.

B.15.16. Simulations with TRACE

RBHT Test 1690 was a boil-off and recovery test. This test was run at 0.207 MPa (30 psia) with a liquid injection flow rate from 0.014 to 0.071 kg/s. The maximum rod linear heat rate was 0.49 kW/m (0.15 kW/ft). The sequence of events for Test 1690 is listed in Table B.15.3. Figure B.15-3 is a comparison between the specified TRACE liquid injection flow rate and that of the experiment, while Figure B.15-4 is a comparison of the total rod bundle power.

A comparison of the collapsed liquid level is shown in Figure B.15-5, where TRACE underpredicts the RBHT data. Figure B.15-6 through Figure B.15-9 compare the rod surface temperatures predicted by TRACE with experimental data at four bundle elevations: 2.029, 2.471, 2.921, and 3.215 m. Figure B.15-6 shows that the rod temperature calculated by TRACE at 2.029 m is very close to the data, but is consistently higher. In Figure B.15-7, TRACE is showing a slight heatup at ~2600 sec, while the data does not. Higher in the bundle, Figure B.15-8 shows that TRACE is overpredicting the rod surface temperature for all times at the 2.921 m elevation. In addition, TRACE is calculating a lower mixture level compared to the data, as shown by the earlier heatup in the TRACE calculations. Figure B.15-9 is a comparison of rod surface temperatures at 3.215 m in the bundle. At this elevation, TRACE does a better job predicting the RBHT data compared to the 2.921 elevation. It is not clear why this is the case, however, the 2.921 m location is closer to the peak power, which is at 2.771 m. The time of initial heatup (~1850 sec) for the 2.921 m location shown in Figure B.15-9 is well predicted by TRACE.

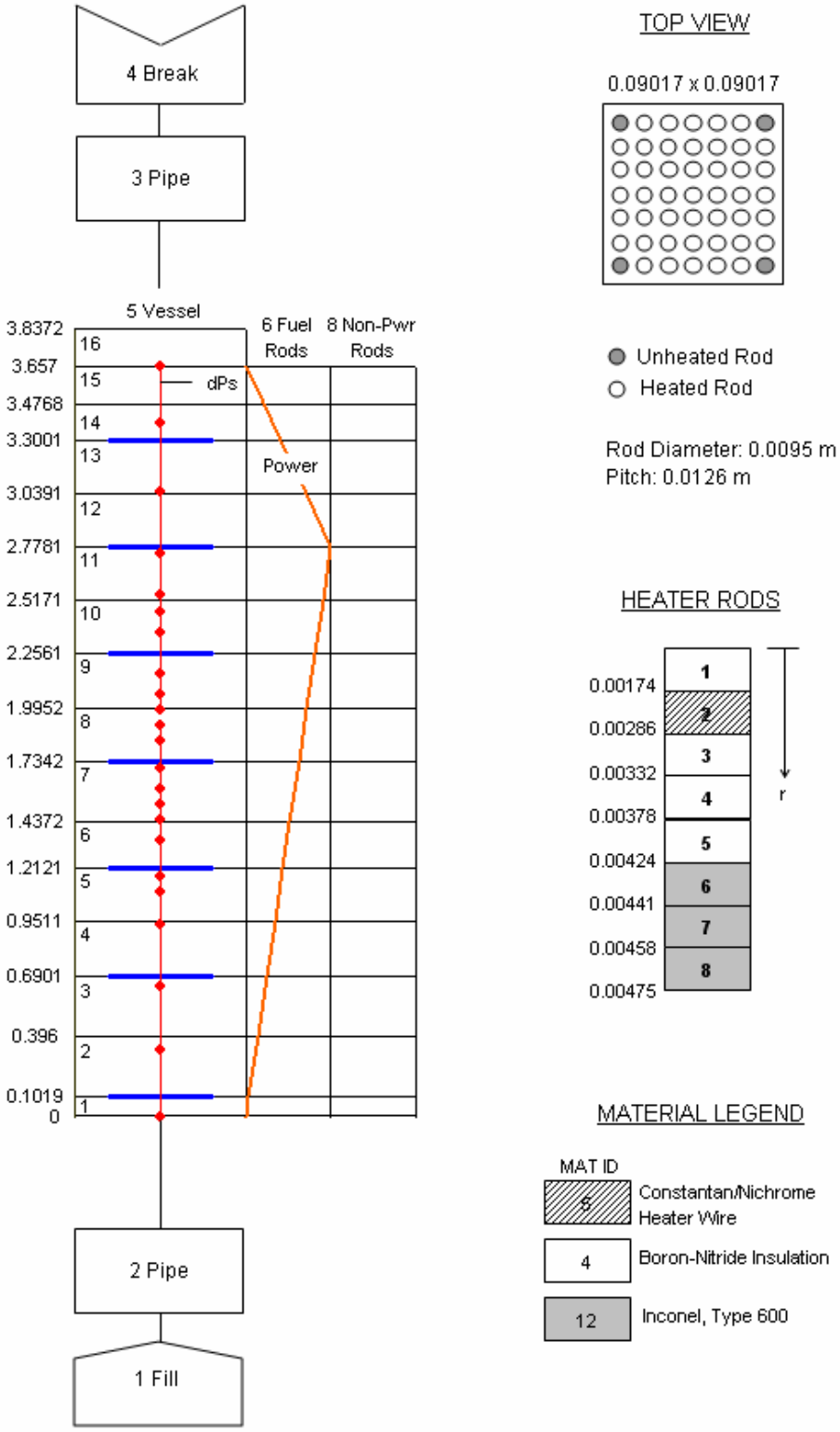

Figure B.15-2. TRACE Nodalization for the RBHT Facility

Table B.15.15.2. Test 1690 Initial and Boundary Conditions

Component	Parameter	Instrument ID	Time (sec)	Value	Units
1 FILL (Inlet) Vol=1.65214E-3 m^3	Liquid Injection Velocity	chan-412	0.0 610 614 1400 1410 1510 1530 2582 2737 3500	0.0 0.0 0.00908 0.00908 0.00454 0.00394 0.00182 0.00182 0.00908 0.00908	m/s
	Liquid Injection Temperature	chan-407	0.0 612 624 645 675 733 817 909 1072 3500	326 326 326 326 330 346 358 363 366 367	K
	Supply Line Pressure/Lower Plenum Pressure	chan-411	0-3500	206842.8	Pa
	Void Fraction	-	0-3500	0.0	-
2 PIPE (Lower Plenum) Vol=1.65214E-3 m^3	Initial Liquid Temperature	chan-407	0.0	334	K
	Initial Vapor Temperature	-	0.0	372	K
	Initial Pressure	chan-411	0.0	206843	Pa
	Initial Void Fraction	-	0.0	0.0	-
3 PIPE (Upper Plenum) Vol=9.82700E-3 m^3	Initial Liquid Temperature	-	0.0	334	K
	Initial Vapor Temperature	-	0.0	372	K
	Initial Pressure	-	0.0	206843	Pa
	Initial Void Fraction	-	0.0	1.0	-
4 BREAK Vol=1.0160E-3 m^3	Initial Temperature	-	0.0	334	K
	Initial Pressure	-	0.0	206643	Pa
	Initial Void Fraction	-	0.0	1.0	-
5 VESSEL (Rod Bundle)	Initial Liquid Temperature	-	0.0	334	K
	Initial Vapor Temperature	-	0.0	372	K
	Initial Pressure	-	0.0	206842	Pa
	Initial Void Fraction	-	0.0	0.0	-

Table B.15.15.2. Test 1690 Initial and Boundary Conditions

Component	Parameter	Instrument ID	Time (sec)	Value	Units
6 HTSTR (Fuel Rods)	Initial Temperature	-	0.0	334	K
7 POWER	Power = Voltage x Current	chan-395 x chan-396	0.0 620 669 1021 1058 2014 3263 3282 3500	0.0 0.0 8.10924E4 8.09056E4 5.38281E4 5.38281E4 5.38281E4 0.0 0.0	V x Amp = W
	Axial Power Profile	-	0-3500	0.5000 0.5371 0.6443 0.7516 0.8467 0.9419 1.0370 1.1322 1.2273 1.3224 1.4176 1.4619 1.1764 0.8910 0.6959 0.5007	
8 HTSTR (Non-conducting Rods)	Initial Temperature	-	0.0	334	K
9 HTSTR (Rod Bundle Outer Housing)	Initial Temperature	chan-033	0.0	409	K
	Liquid Heat Transfer Coefficient	-	0-3500	15	W/m-K
	Reference Liquid Temperature	-	0-3500	300	K

Table B.15.3. RBHT Test 1690 Sequence of Events

Time (sec)	Event
0.0	Begin test
600	Start liquid injection to bundle
620	Increase rod bundle power to ~80 kW
620-1390	Steady-state nucleate boiling
1020	Reduce bundle power to ~53 kW
1400	Decrease liquid injection flow rate ~75%
1500-2680	Rod bundle heatup
2590	Increase liquid injection flow rate
~2680	PCT
2680-2805	Rod bundle quench
3394	End of test

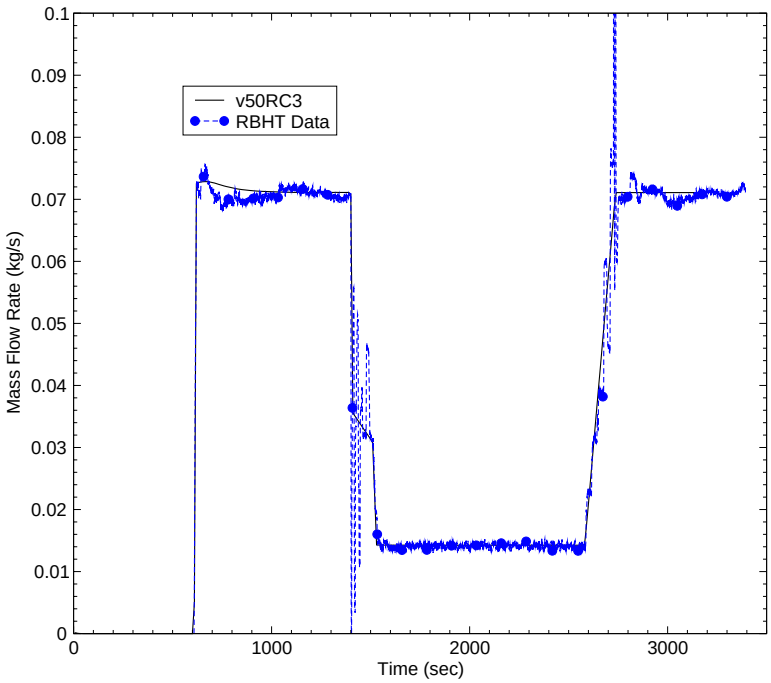

Figure B.15-3 Liquid Injection Flow Rate

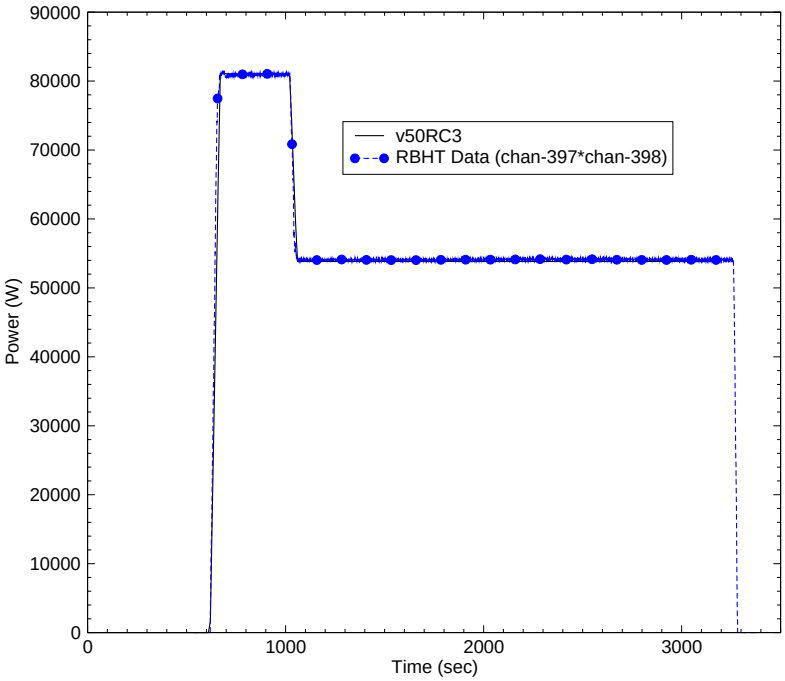

Figure B.15-4 Total Rod Bundle Power

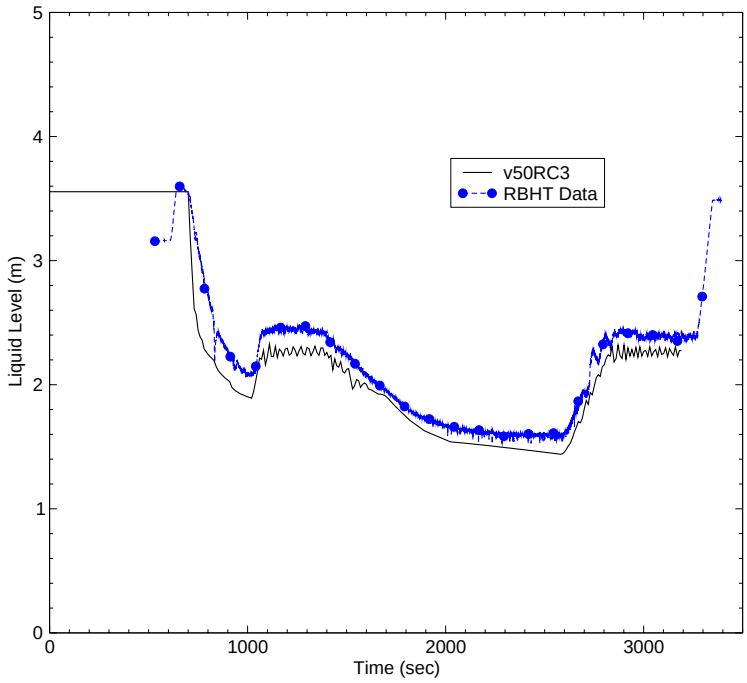

Figure B.15-5 Collapsed Liquid Level

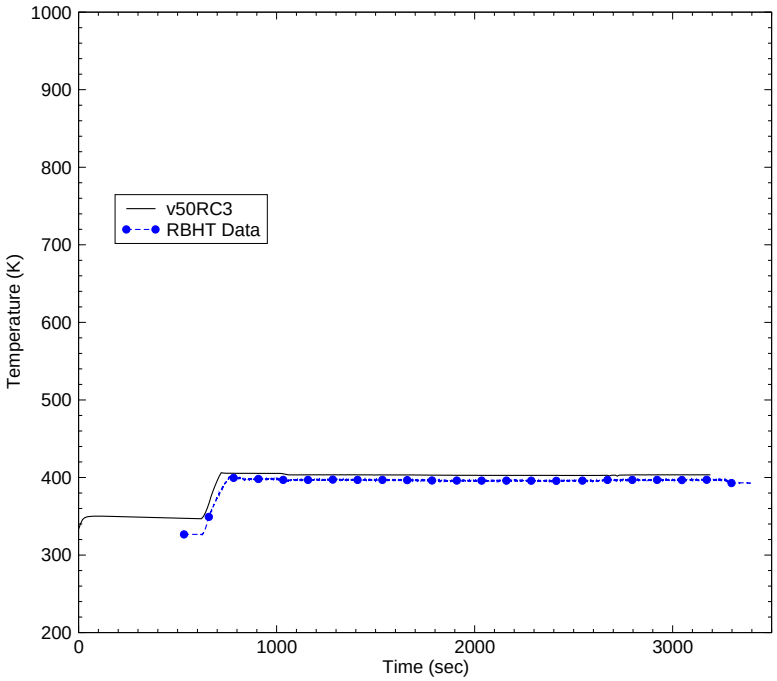

Figure B.15-6 Rod Surface Temperature at 2.029 m.

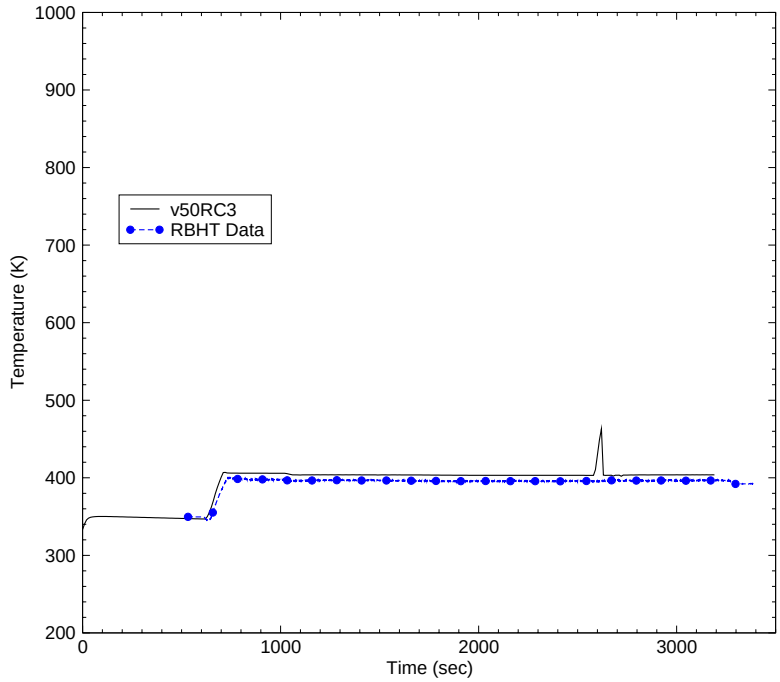

Figure B.15-7 Rod Surface Temperature at 2.471 m.

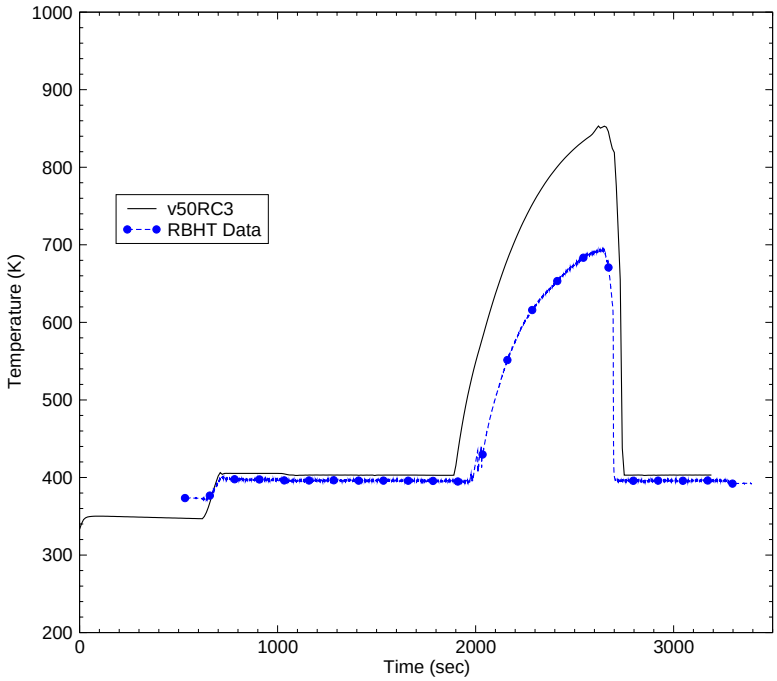

Figure B.15-8 Rod Surface Temperature at 2.921 m.

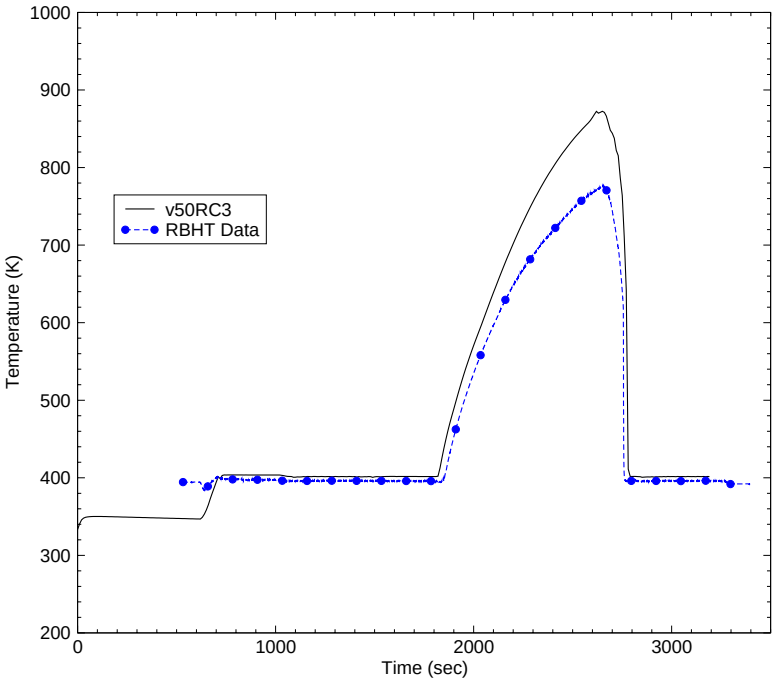

Figure B.15-9 Rod Surface Temperature at 3.215 m.

Figure B.15-10 and Figure B.15-11 show the axial rod surface temperatures at 1020 and 2620 sec. Comparison to data shows that TRACE consistently overpredicts the rod temperature at all elevations. However, TRACE does seem to predict the two-phase mixture level accurately, as shown in Figure B.15-12 by a significant increase in temperatures at ~2.5 m. Figure B.15-12 is a comparison of the two-phase mixture level during the heatup period of the test, where TRACE underpredicts the two-phase level swell as expected by examination of previous rod temperature plots. Only the uncovery portion of this test was plotted in Figure B.15-12, since bundle recovery and quench is addressed in the RBHT reflood assessments. Also apparent is that TRACE seems to stair-step the calculation of two-phase level. This same behavior was seens in similar rod bundle assessments such as THTF and has to due with the way in which TRACE calculates CHF during boil-off. However, this stair-stepping in two-phase liquid level was not seen in other assessments during reflood (i.e., during bundle fill).

Comparisons to data show that TRACE slightly overpredicts the void fraction at all elevations during the steady-state nucleate boiling period of the test as shown in Figure B.15-13. During the time of peak cladding temperature, TRACE has more difficulty predicting the axial void fraction at the higher elevations as shown in Figure B.15-14.

An important figure of merit for predicting rod bundle heatup is the heat transfer coefficient (HTC) at PCT. Figure B.15-15 is a plot of the rod surface to liquid HTC from 1500 to 3000 sec. at 2.921 m and shows that TRACE underpredicts the HTC at PCT (~2680 sec) by ~15 W/m^2-K.

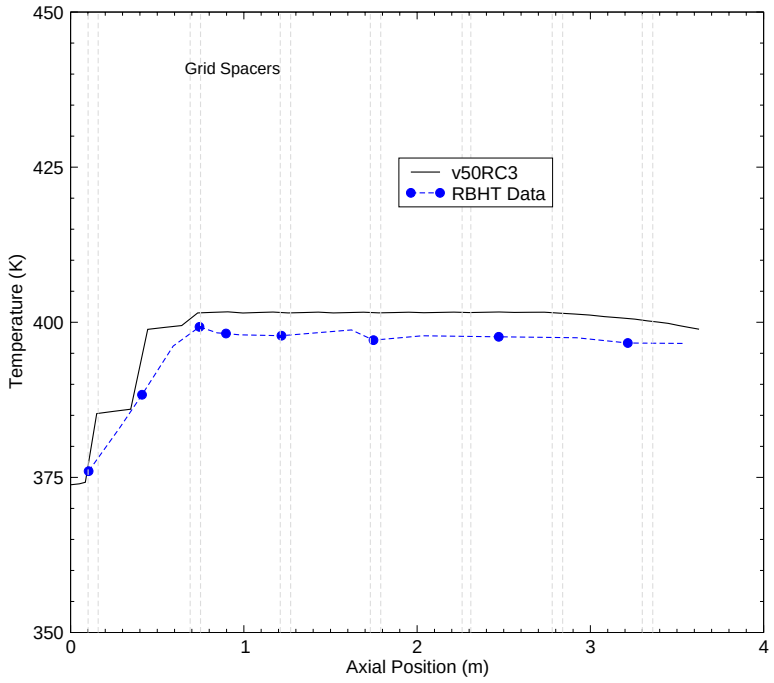

Figure B.15-10 Axial Rod Temperatures at 1020 seconds.

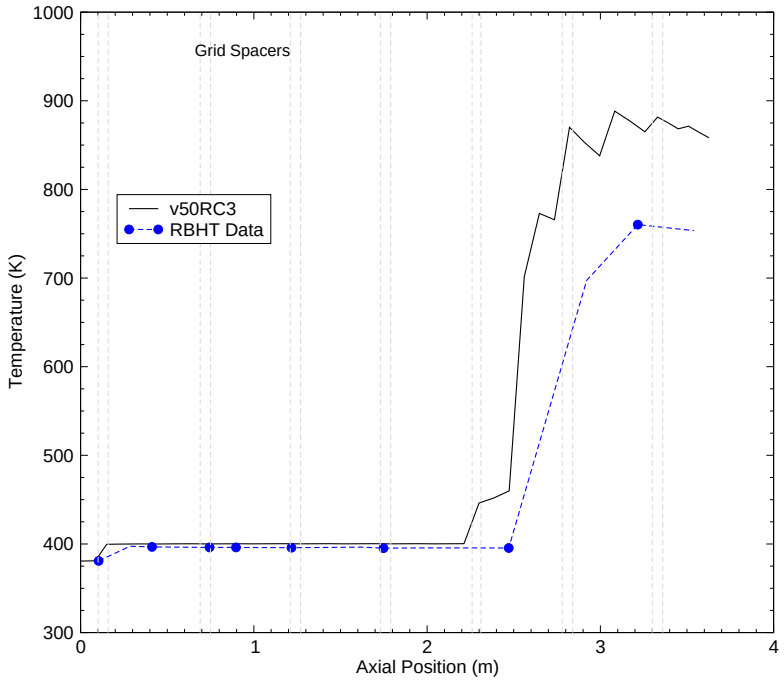

Figure B.15-11 Axial Rod Temperatures at 2620 seconds.

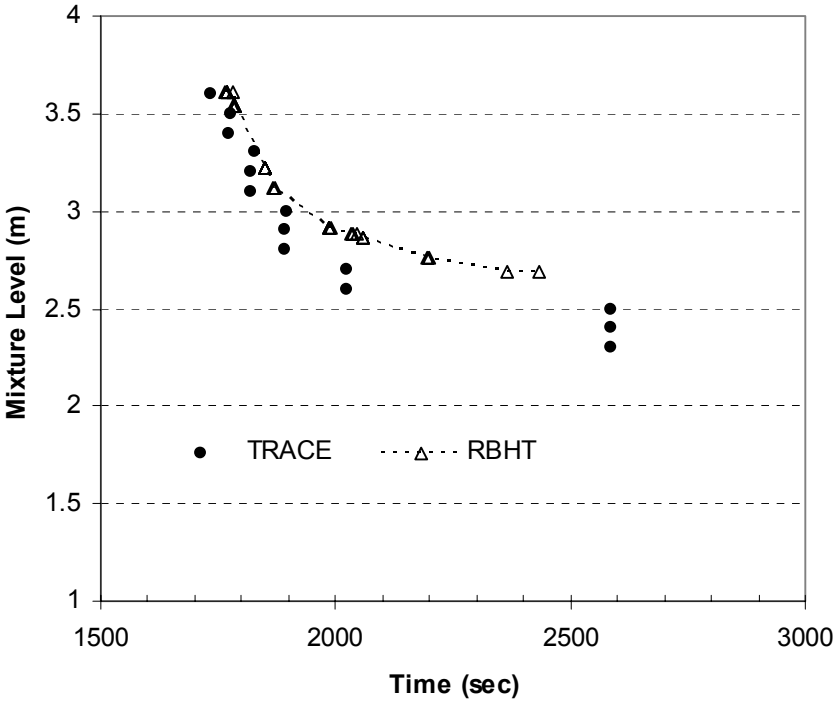

Figure B.15-12 Two-Phase Bundle Mixture Level

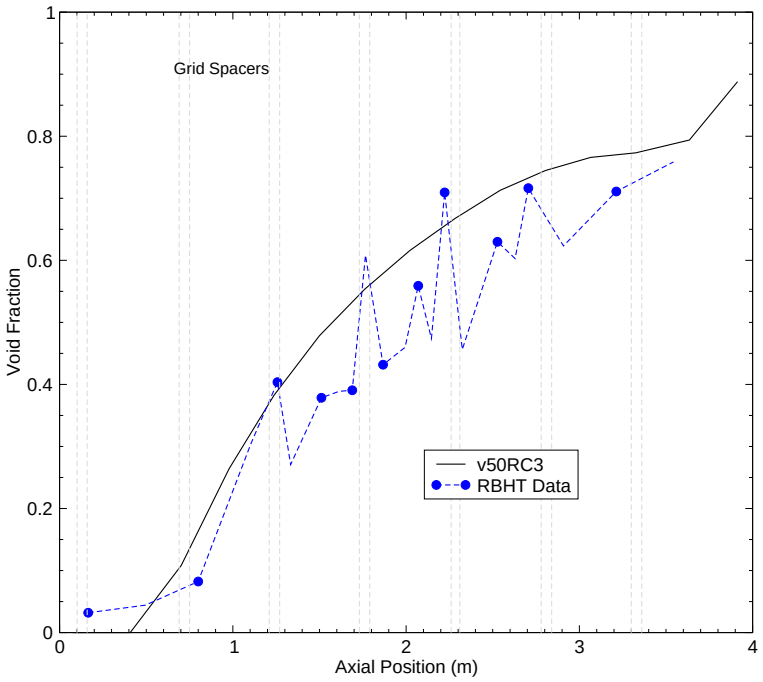

Figure B.15-13 Axial Bundle Void Fraction at 1020 seconds.

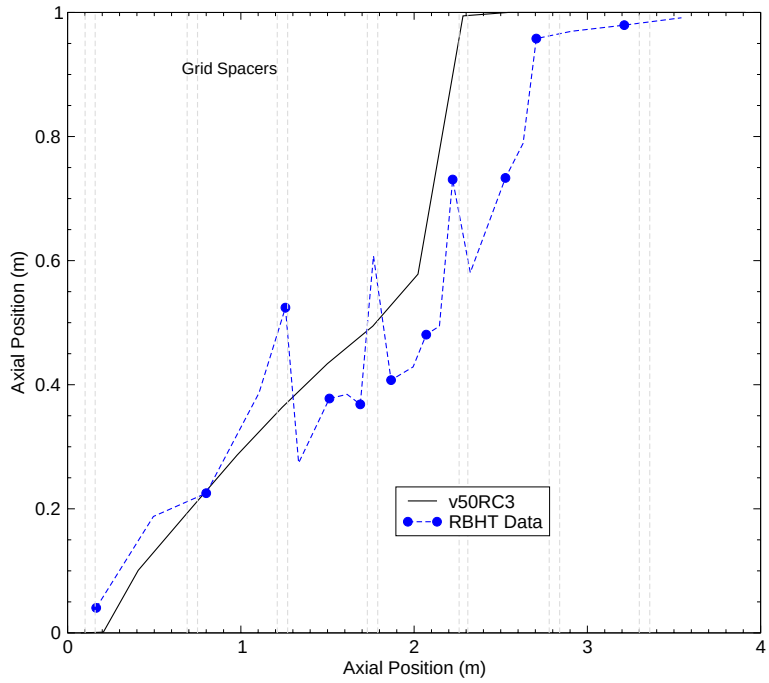

Figure B.15-14 Axial Bundle Void Fraction at 2620 seconds.

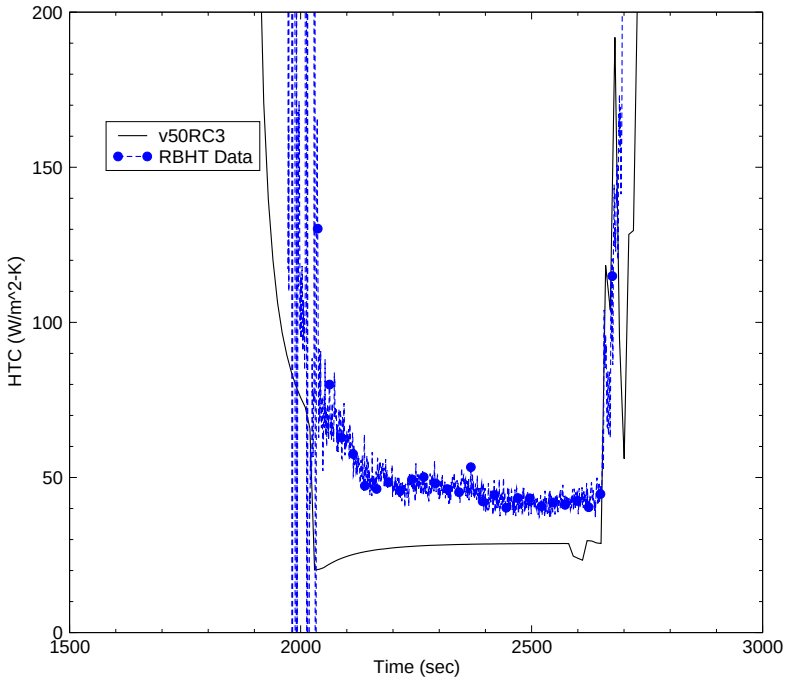

Figure B.15-15 HTC at 3.215 m Elevation.

B.15.17. Summary and Conclusions

In general, TRACE overpredicts cladding temperatures at all elevations during the test, suggesting an overprediction in the interfacial drag. The void fraction comparisons show good agreement with the code, except at higher elevations (z > 2.2 m), while the HTC was underpredicted. Table B.15.4 is a quantitative comparison of TRACE against RBHT Test 1690 for several parameters. Figure B.15-16 is a plot of the measured versus predicted axial bundle void fractions.

Table B.15.4. Figures of Merit Comparison

Parameter	**RBHT Test 1690**	**TRACE**	**% Difference**
Axial Bundle Void Fraction at 1020, 2420, and 2620 seconds	-13.1 %, R^2 = 0.87 (linear regression)		
Rod Temp at PCT @ 2.921 m	700 K	860 K	-22.9
HTC at PCT @ 2.921 m	43 W/m^2-K	29 W/m^2-K	+32.6
Collapsed Liquid Level @ PCT	1.63 m	1.45 m	+11.0

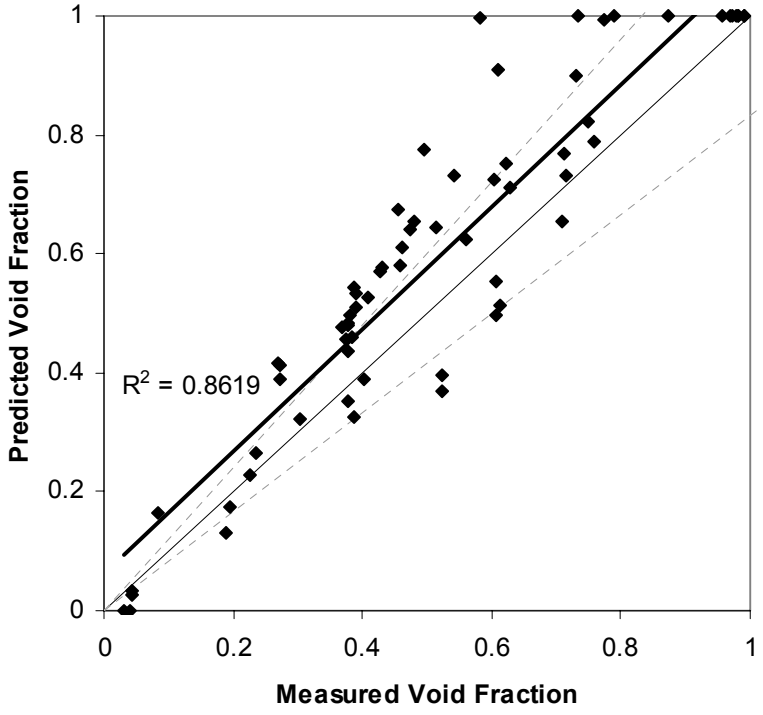

Figure B.15-16 Measured Versus Predicted Bundle Void Fraction

B.15.18. References

1 Rosal, E.R., Lin, T.F., McClellan, I.S., Brewer, R.C., "Rod Bundle Heat Transfer (RBHT) Test Facility Description Report," Department of Mechanical Engineering, The Pennsylvania State University, 2005.

2 Hochreiter, L.E. et. al., "RBHT Test 1690 Quick Look Report," Department of Mechanical Engineering, The Pennsylvania State University.

3 Welter, K.B., Bajorek, S.M., "RBHT Test 1690 Calculational Notebook," Office of Regulatory Research, U.S. Nuclear Regulatory Commission, June 2, 2006.

B.16. GE Level Swell Experiments

Author(s): Millan Straka, Andrew Ireland

Affiliation: AdSTM, Inc. (M. Straka), NRC (A. Ireland)

Code Version: TRACE V5.0

Platform and Operating System: Intel x86, Windows XP

B.16.1. Introduction

General Electric (GE) performed a series of experiments to investigate thermal-hydraulic phenomena such as critical flow, void distribution, and liquid-vapor mixture swell during blowdown conditions. Two experiments of the GE level swell test series were to be simulated with the TRACE thermal-hydraulics code package. For this purpose two vessels were used: one with a nominal diameter of 1 ft (0.3048 m), called "small" vessel, and other one - called appropriately "large" vessel - with a 4 ft (1.219 m) diameter.

This report is based in large part on the GE Level Swell Assessment Report of Millan Straka (AdSTM), for the same level swell experiments simulated with TRACE version 4.190 (Ref. 1).

B.16.2. Test Facility Description

The description of the test facilities is provided in References 3, 4, 5, and 7. The small vessel was made of 1 ft (0.3048 m) diameter, Schedule 80, carbon steel pipe. Its height was 14 ft (4.267 m). It was instrumented with differential pressure (DP) and pressure (P) gauges and thermocouples (TC) located along the vessel. The vessel discharge was guided to a suppression tank via a blowdown pipe, which included an orifice mounted near the vessel. The vessel was designed to accommodate a perforated plate at about the mid-point of its height. (No plate was used in Experiment 1004-3.) Figure B.99.6-1 shows schematically the experiment arrangement and elevations of the DP gauges.

The large vessel was 4 ft (1.219 m) in diameter (47 in., 1.194 m ID), 14 ft (4.267 m) high, made out of carbon steel. For top blowdown experiments, the vessel was equipped with an inverted dip tube, which accommodated a venturi tube located near the vessel wall and exited to an atmospheric tank. The large vessel was equipped with the same kind of instrumentation as the small vessel. Figure B.99.6-2 shows schematically the experiment arrangement and elevations of the DP gauges.

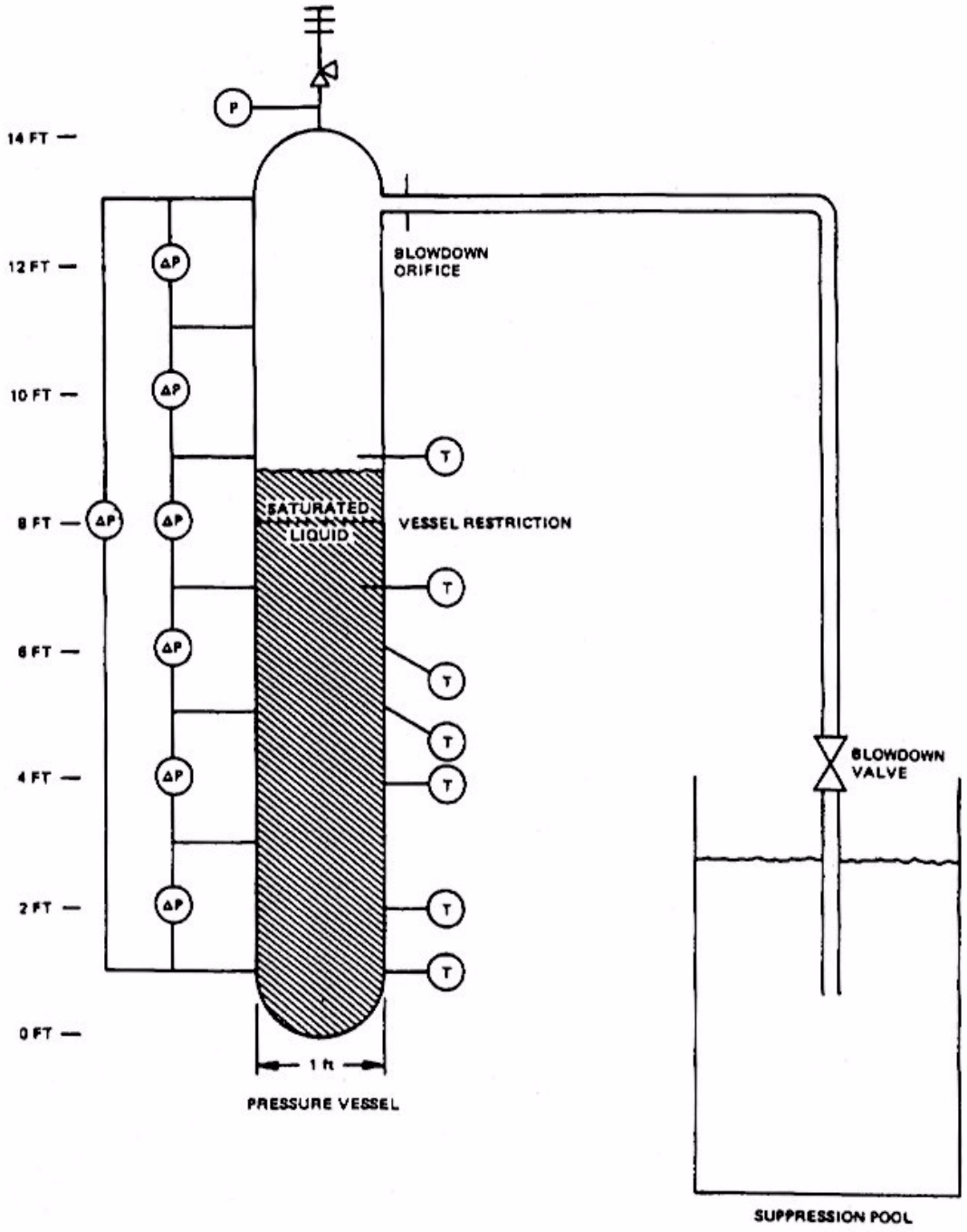

Applied Instrumentation in Small GE Blowdown and Level Swell Test Facility
(Temperatures Not Published by GE)

Figure B.16-1. Small vessel test facility

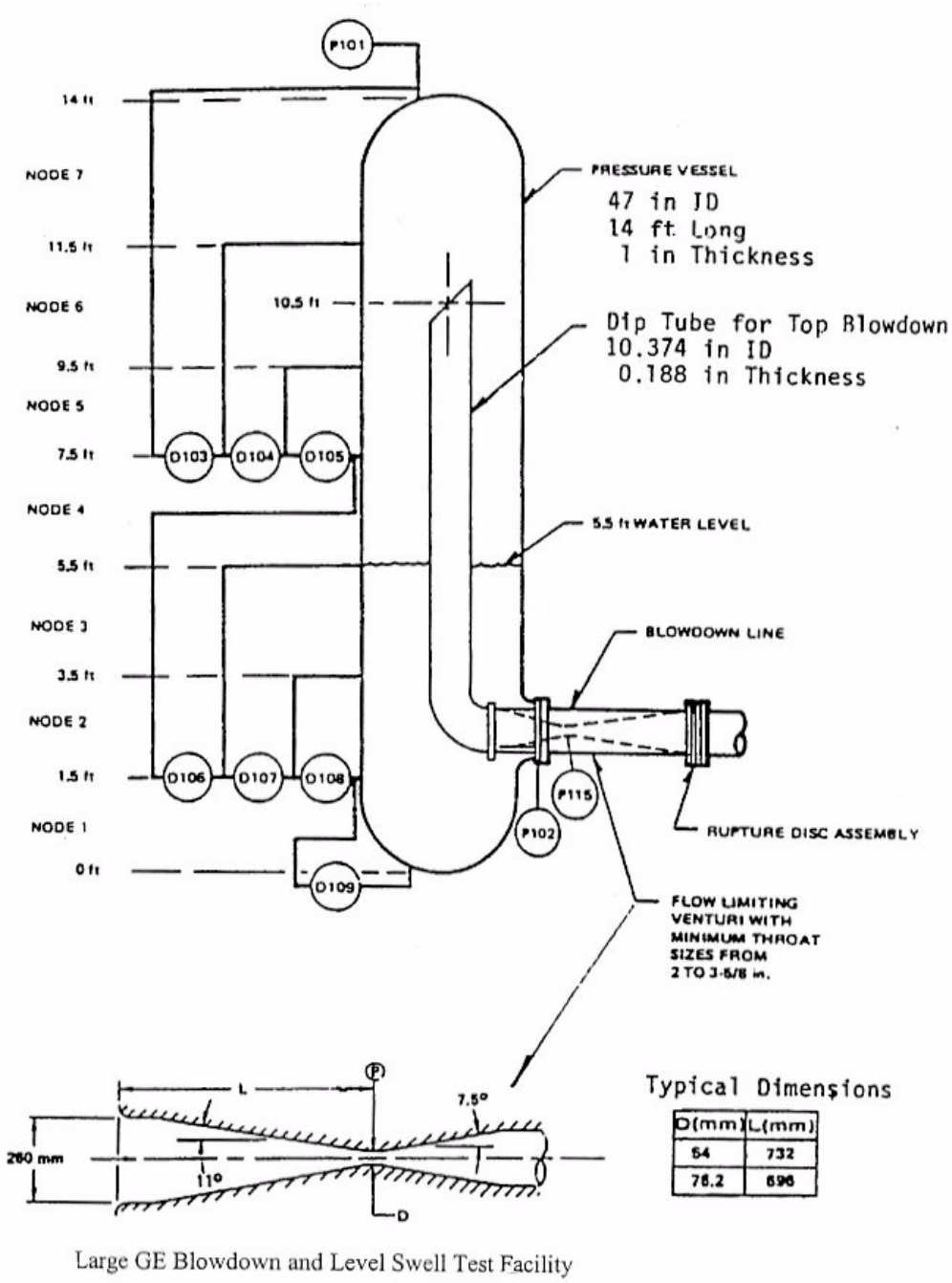

Figure B.16-2. Large vessel test facility

B.16.3. TRACE Model Description

The TRACE model used for the small vessel simulation is shown in Figure B.99.6-3. It consists of 8 nodes whose elevation correspond to the elevations of the DP gauges of the vessel

instrumentation. Thus, a quantity calculated at the mid-points of a node can be compared to the quantity, such as void fraction, measured in the experiment. The design of the present TRACE model was a conversion of the available TRAC-BD1 model (Ref. 3), but otherwise the present model includes the true geometry (as far as could be verified from the available documents) - in particularly, the geometry of the blowdown pipe and orifice (Ref. 4).

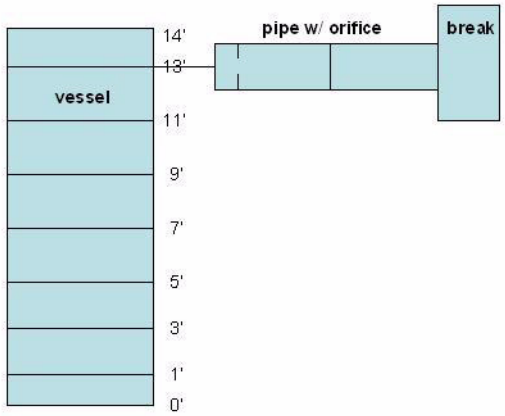

Figure B.16-3. Small vessel TRACE model.

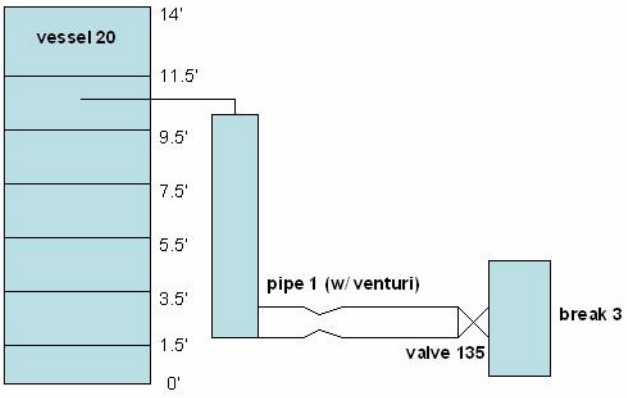

Figure B.16-4. Large vessel TRACE model

The TRACE model of the large vessel is depicted in Figure B.99.6-4. It consists of 7 nodes whose elevations correspond to the elevations of the DP gauges of the vessel instrumentation. Thus, a quantity calculated at the mid-points of a node can be compared to the quantity measured in the experiment, such as void fractions.

B.16.4. Tests Simulated with TRACE

Two experiments were simulated with TRACE (V. 4.190): Test 1004-3 and Test 5702-16. Test 1004-3 was performed in the small vessel with a 3/8 in (0.00952 m) orifice located near the vessel outlet. The vessel was filled with saturated water and steam with water reaching up to the axial level of 10.5 ft (3.20 m). It was pressurized to 1011 psia (6.971 MPa). Subsequently, a blowdown was initiated. The time window of the data acquisition extended up to 180 seconds.

Test 5702-16 was performed in the large vessel with a dip tube installed in the inverted fashion (Figure B.99.6-2). The size of the venturi tube located in the dip pipe near the vessel was 3.625 in (0.0921 m). The vessel was filled with saturated water and steam with water reaching up to the axial level of 5.5 ft (1.676 m). It was pressurized to 1060 psia (7.308 MPa). Subsequently, a blowdown was initiated. The time window of the data acquisition extended from 20 to 30 seconds.

B.16.4.1. Simulation of Test 1004-3

The data measured in this experiment consist essentially of the system pressure and void fractions (determined at six - equally distributed - axial levels). The test was first simulated with a TRACE input file, which was assembled using the code "default" values for the parameter and options to be selected by user (Ref. 2). It was noted that after an initial agreement between the calculation and experiment (up to about 10 seconds) the system pressure began to be considerably underestimated (Figure B.99.6-5). Ideally, a measure of the break flow would be used to modify the two-phase multiplier (TPM) at the location of the choked flow. However, break flow was either not measured or not reported for this experiment, so a match to the experimental pressure response was used instead. The two-phase pressure multiplier (TPM) should be reduced to a value of 0.7 (reducing the TPM is consistent with experience in similar blowdown calculations) in order to obtain the "best" agreement with the experimental pressure data. This value was then retained for all subsequent analysis runs.

Figures B.99.6-6 through B.99.6-11 show a comparison between the calculated and measured void fractions at each respective axial level. The void measurement error for all of the GE level swell experiments was approximately +/–0.1. Figure B.99.6-6 depicts temporary presence of water in the upper vessel part (such as Node 7 at the elevation of 12 ft [3.658 m]) - filled previously with steam - with a considerable amount of water being present in both the experiment and calculation. Also during this time period, the TRACE calculation indicates that the mixture level rapidly moved from Node 6 (its initial location) to Node 7 in approximately 1.25 seconds and returned to Node 6 after approximately 35 seconds. (See discussion below.)

Figure B.99.6-7 shows the process of voiding at the 10 ft (3.048 m) elevation (Node 6). Initially, the node was filled with water and steam (initial void fraction was 0.3). This node began to empty at about 35 seconds in the test and 38 seconds in the TRACE calculation. Figure B.99.6-8 depicts the same process for the node below: Node 5. It is noted that the mixture level receded to this node at about 95 seconds (see Figure B.99.6-16) and remained there for much of the remainder of the simulation.

Figures B.99.6-9 through B.99.6-11 show the process of voiding in Nodes 4, 3, and 2, at elevations 6, 4, and 2 ft (1.829, 1.219, and 0.6096 m), respectively. A quasi steady-state was eventually reached at each of these elevations. The calculated values are within the approximate error band (Ref. 7). Notwithstanding this fact, it is noted, however, that TRACE consistently underpredicts the amount of voiding at the lower elevations.

The axial void distribution between the elevations 2 (0.6096 m) and 12 ft (3.658 m) for four different time snapshots is shown in Figures B.99.6-12 through B.99.6-15. As already stated above, TRACE tends to slightly underpredict voiding at lower elevations. As a consequence, a void fraction that is slightly higher than the experimental value is predicted at higher elevations, as depicted in Figure B.99.6-13 by elevation 12 ft (3.658 m).

The mixture level location on a nodal basis has been determined using the TRACE calculation. The mixture level is considered to enter a particular level when the void fraction drops below 95%. The calculation indicates that the mixture level rapidly moved from Node 6 (its initial location) to Node 7 (elevation 12 ft [3.658 m]) and then at about 35 seconds receded back to Node 6 (elevation 10 ft [3.658 m]) as shown in Figure B.99.6-16. Gradually, the mixture level dropped to lower nodes with the ever increasing time.

The simulation of this experiment was continued up to 1000 seconds (Figure B.99.6-17). Between the times 600 and 700 seconds, minor oscillations occurred in the four lowest level void fractions. It is noted that these oscillations coincide with (and are believed to be the consequence of) oscillations observed in the interfacial drag coefficients (not shown here) at the corresponding vessel levels.

B.16.4.2. Simulation of Test 5702-16

The data measured in this experiment consist essentially of the system pressure and temporal void fractions (determined at six axial levels). The test was first simulated using a TRACE input file assembled using the code "default" values for the parameters and options selected by user (Ref. 2). (An exception was the TPM, which was set to 0.9 - based on the present experience with the small vessel calculations and personal experience with the RELAP5 critical flow model.) It was noted that after an initial agreement between the calculation and experiment (for about 0.25 seconds) the system pressure began to be overestimated (Figure B.99.6-18). This is caused by water entrainment into the blowdown pipe (up to 15% volumetrically) which appears to occur in the calculation earlier than in the experiment. This situation persists until about 9 seconds at which time the agreement between the calculated and measured pressure is very good and continues to remain so. (It is noted that the 9 seconds mark is the time at which the experimental

mixture level recedes below the inlet of the blowdown pipe, as depicted in Figure B.99.6-23 and discussed below.)

A time step sensitivity run was performed in an attempt to capture the short spike in the measured pressure around 0.9 second. Its duration is about 0.5 second. It is noted that this spike is typical of large-break loss-of-coolant-accidents in light-water reactors and is due to a temporary imbalance between the steam production (flashing) and steam removal through the break opening. However, the sensitivity run (with dt=0.001 sec) has not been able to reproduce the phenomenon. It is believed that early flashing and entrainment of water into the pipe entrance observed in the calculation prevent its simulation by TRACE. Another sensitivity calculation was performed to investigate the effect of keeping the TPM at 1.0. Void fractions remained nearly the same.

The axial void distribution between the elevations 0.75 and 12.75 ft (0.229 and 3.886 m) is shown in Figures B.99.6-19 through B.99.6-22 for four different time snapshots: 2, 5, 10, and 14 seconds, respectively. It is noted that TRACE tends to show a much greater difference in void fraction between the lower and upper elevations than does the experiment. The experimental void fraction tends to show a more uniform increase with elevation. Later in time, the predicted and experimental void fractions tend to be in better agreement.

The mixture level location on a nodal basis has been determined using the TRACE calculation. The mixture level is considered to enter a particular level when the void fraction drops below 95%. The calculation indicates that the mixture level rapidly moved from 4.5 ft (1.372 m) (the cell center of the node that has its top at 5.5 ft (1.676 m)) through Node 4 to Node 5 (elevation 8.5 ft [2.59 m]) where it remains up to about 27.5 seconds (Figure B.99.6-23). After that, the level remained at Node 4 until gradually receding back to Node 3 (elevation 4.5 ft [1.372 m]). The blowdown is over in less than 20 seconds.

B.16.5. Assessment Results Summary

An assessment analysis of the TRACE code (V. 4.190) was carried out simulating two GE level swell experiments performed in small (1 ft [0.3048 m]) and large (4 ft [1.219 m]) vessels. The results obtained in the simulations were compared against the experimental data. The input files for TRACE were prepared using the experiment and facility descriptions and recommended approaches for modeling and selection of the TRACE input values. Besides these so-called "base" input files, a second TRACE file - called "best" - was prepared for simulation of each experiment. The goal was to perform TRACE input sensitivity analyses aimed at improving the comparison with experimental data and identifying the parameters which decisively control the simulation outcome. The best input was "frozen" when best match with the measured vessel pressure has been obtained during the entire blowdown process.

Overall, TRACE predicted axial transient voiding at different times reasonably well for the small vessel and somewhat worse for the large vessel. Using the base input file, TRACE calculated too much liquid carried toward the blowdown pipe entrance during the first 8 seconds of the large vessel blowdown test. Even with the best input (and very small time steps), TRACE did not

capture the brief pressure spike at the beginning of blowdown nor did TRACE capture the brief delay in onset of flashing at the beginning of the large vessel blowdown as observed in the experiment.

Adjusting the TPM in the TRACE simulation, a reasonably good agreement was obtained between the calculated and measured vessel pressure. Most of the simulation time, the calculated temporal void fractions are slightly lower for the small vessel albeit they are still within the error bars of the measured values. The axial void distributions measured and calculated agree quite well for the small vessel. For the large vessel, the TRACE simulation shows a much higher difference in void fraction between the lower and upper portions of the vessel, compared to the experiment. For one run, the simulation time was extended up to 1000 seconds. Intermittent oscillations (of not too big amplitude) in the calculated void fractions were identified. It is noted that in this calculation similar oscillations were also identified in the interfacial drag variable.

B.16.6. References

1 Straka, M., "GE Level Swell Experiments," for the U.S. Nuclear Regulatory Commission, by Advanced Systems Technology and Management, Inc., January 2006, ML061570481.

2 U.S. Nuclear Regulatory Commission (NRC), TRACE V4.160 User's Manual, Volume 1, July 2005.

3 Tyler, T., L. Wolf (PI), G. Woods, and C. Greenwell, “TASK 4: TRAC-M Calculations for the GE Level Swell Tests,” Task Order 9: BWR Model Development and Assessment, University of Maryland Report to the U.S. Nuclear Regulatory Commission, October 2000.

4 Aumiller, D.L., E.T. Tomlinson, and W.G. Clarke, “A new assessment of RELAP5-3D using a GE level swell problem,” 2000 RELAP5 Users Seminar, September 2000.

5 Bandini, B.R., D.L. Aumiller, and E.T. Tomlinson, “A new assessment of the large-tank GE swell problem using RELAP5-3D,” 2002 RELAP5 Users Seminar, September 2002.

6 Idelchik, I.E., *Handbook of Hydraulic Resistance*, 3rd Ed., Begell House, New York, 1996.

7 Findlay, J.A., BWR Refill-Reflood Program Task 4.8 - Model Qualification Task Plan, NUREG/CR-1899, EPRI NP-1527, GEAP-24898, General Electric Company, August 1981.

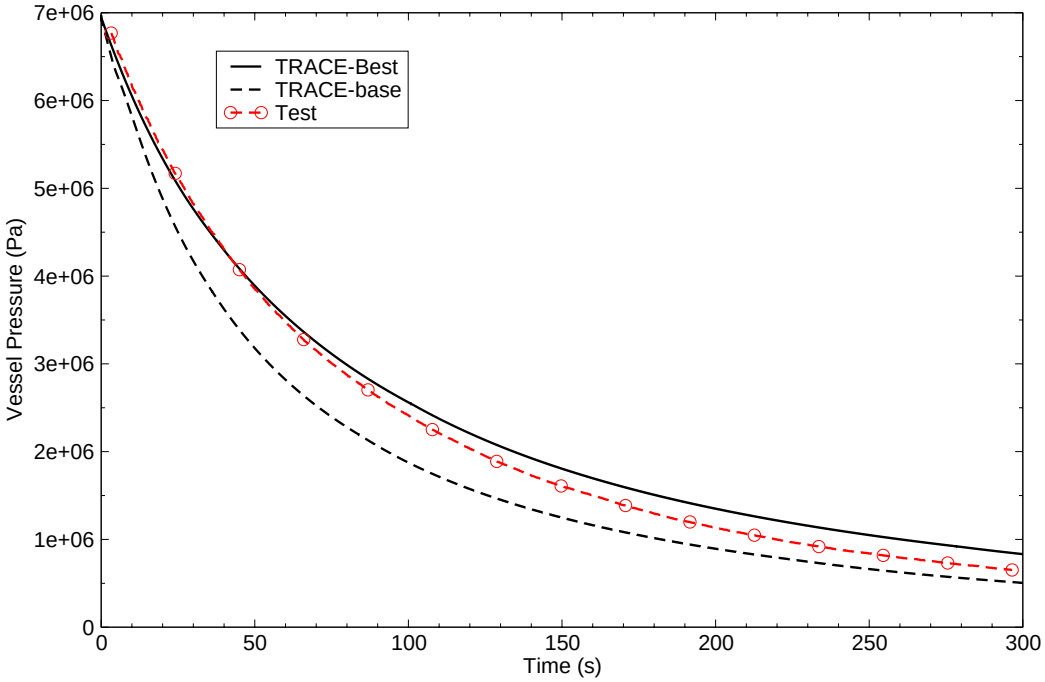

Figure B.16-5. Test 1004-3 pressure response.

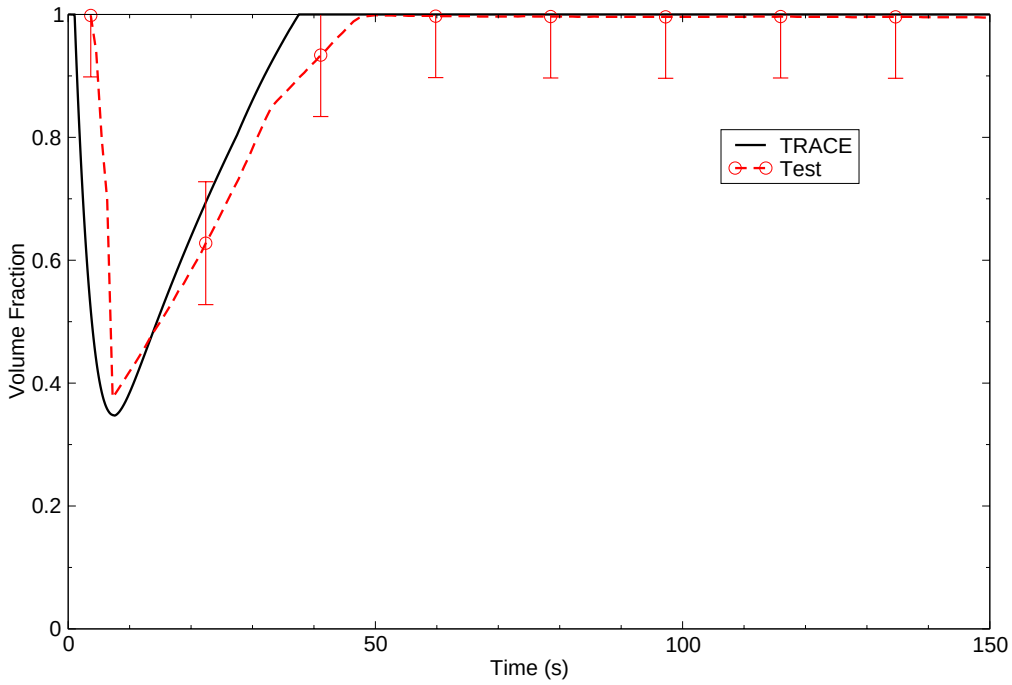

Figure B.16-6. Test 1004-3 void fraction response at 12 ft.

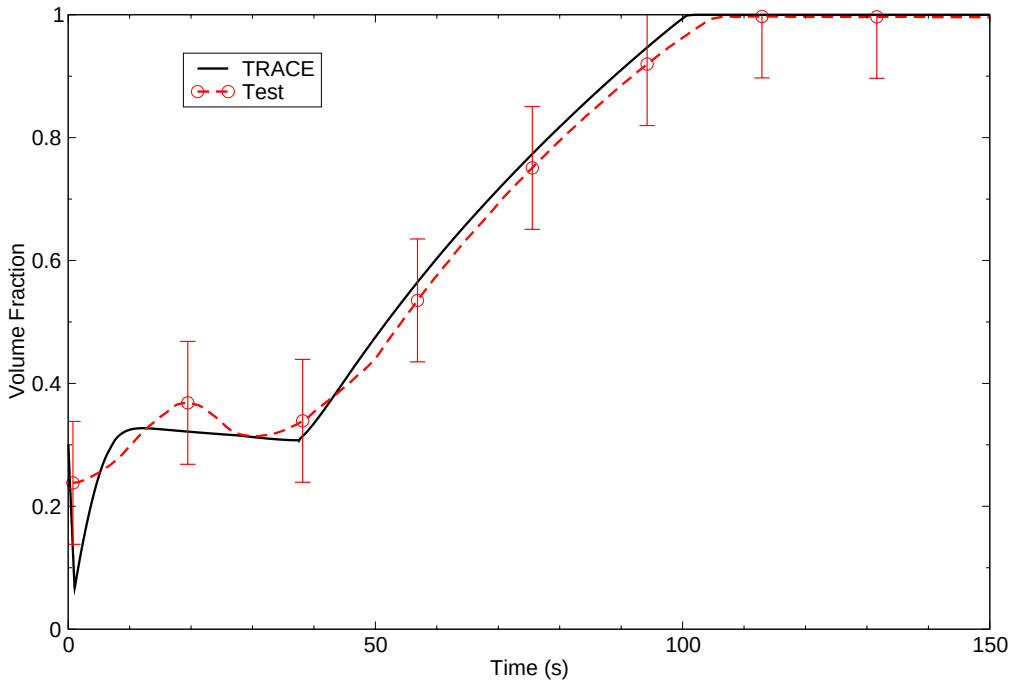

Figure B.16-7. Test 1004-3 void fraction response at 10 ft.

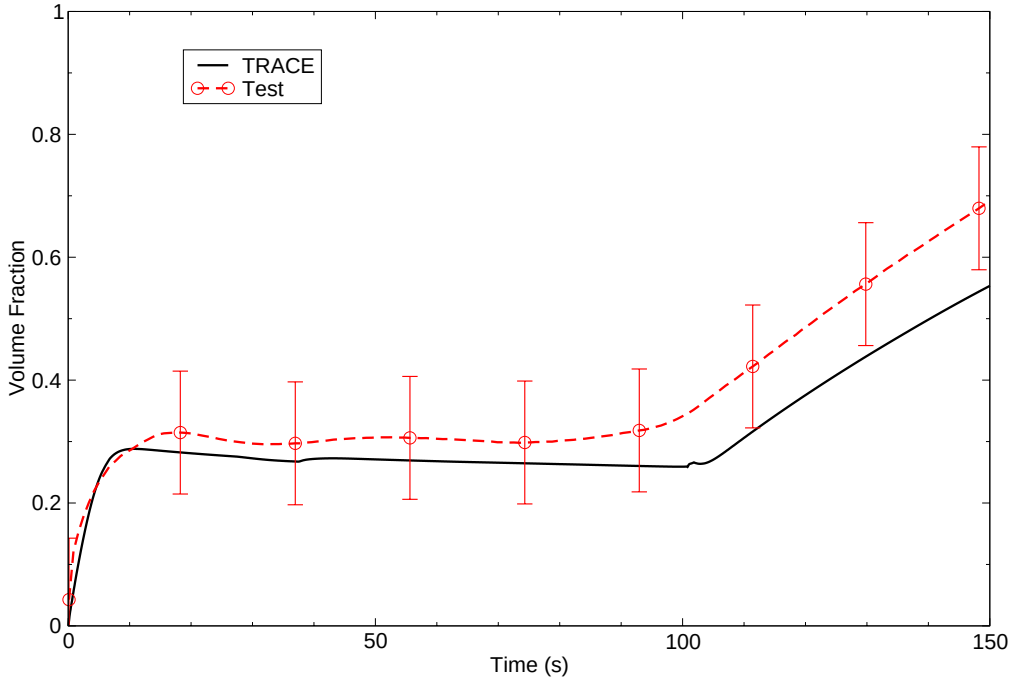

Figure B.16-8. Test 1004-3 void fraction response at 8 ft.

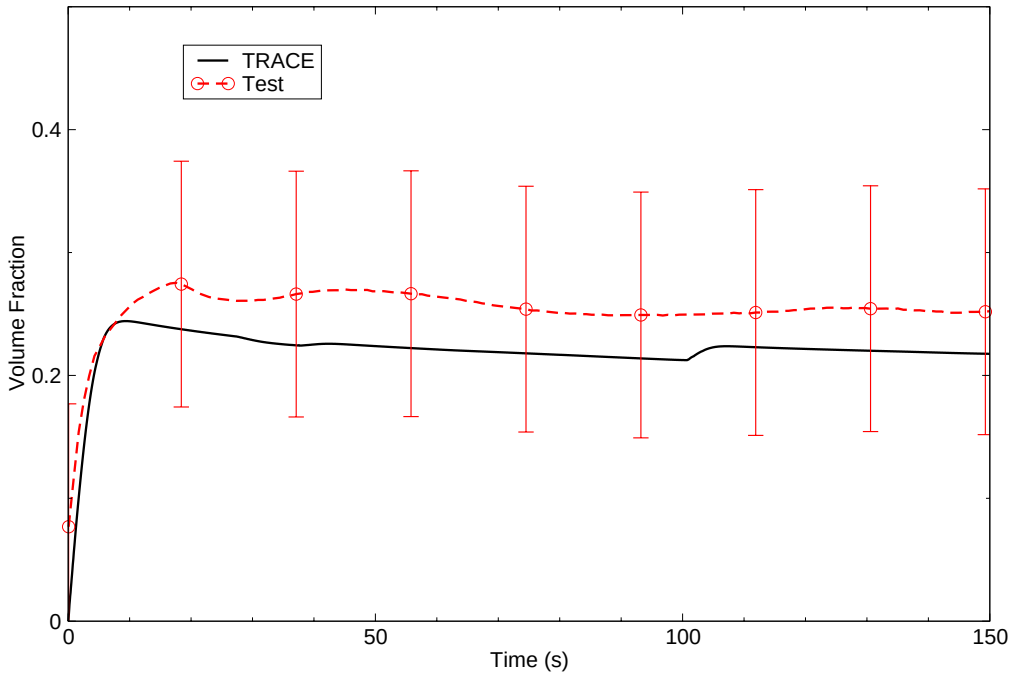

Figure B.16-9. Test 1004-3 void fraction response at 6 ft.

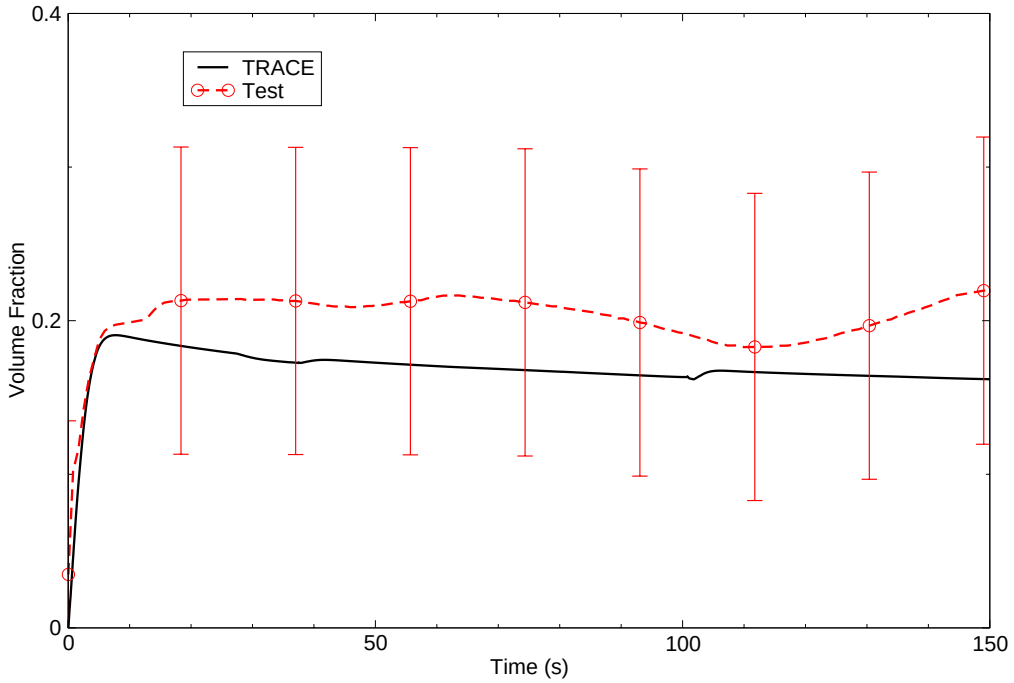

Figure B.16-10. Test 1004-3 void fraction response at 4 ft.

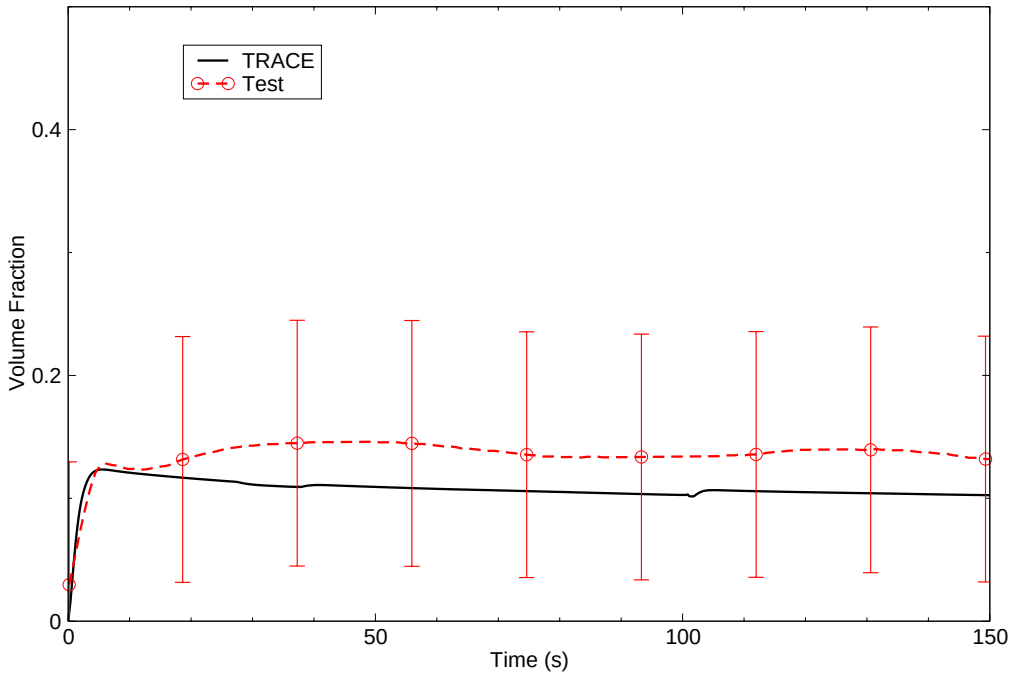

Figure B.16-11. Test 1004-3 void fraction response at 2 ft.

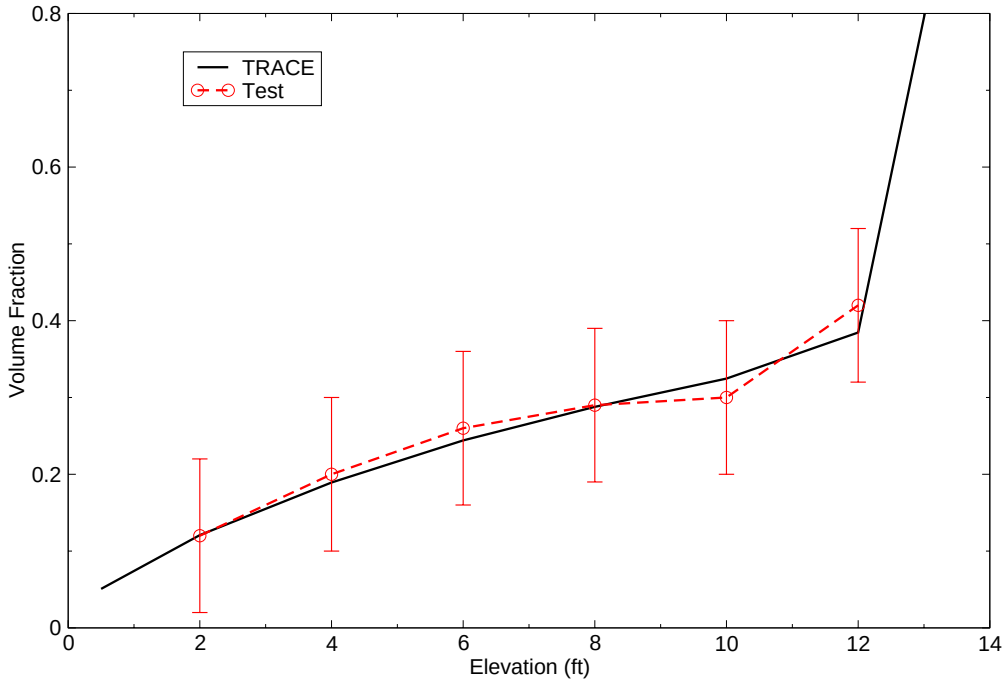

Figure B.16-12. Test 1004-3 axial void distribution at 10 seconds.

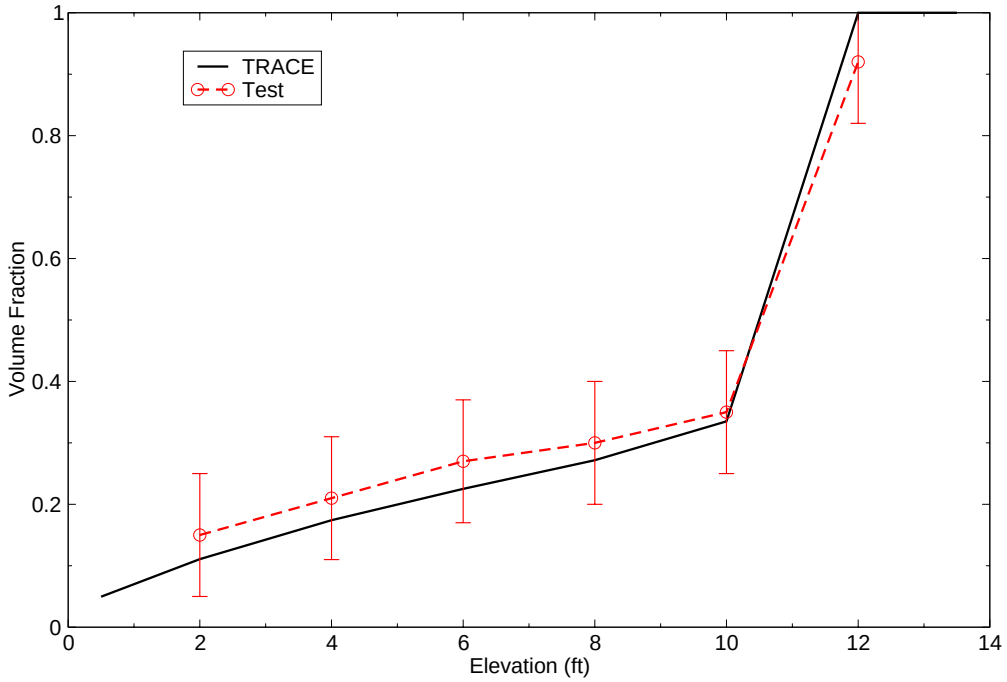

Figure B.16-13. Test 1004-3 axial void distribution at 40 seconds.

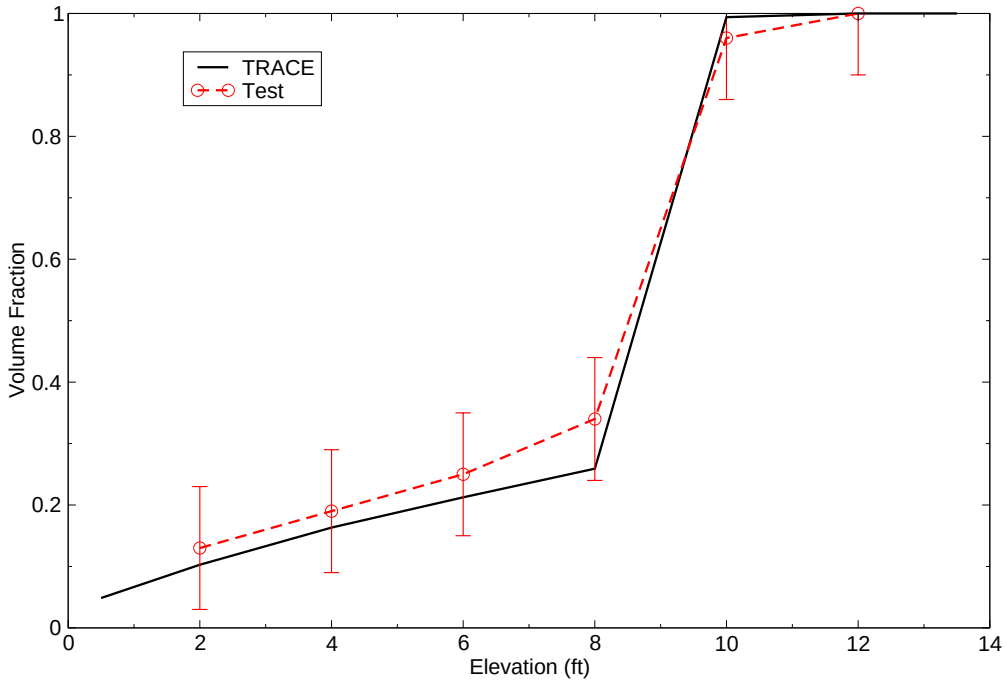

Figure B.16-14. Test 1004-3 axial void distribution at 100 seconds.

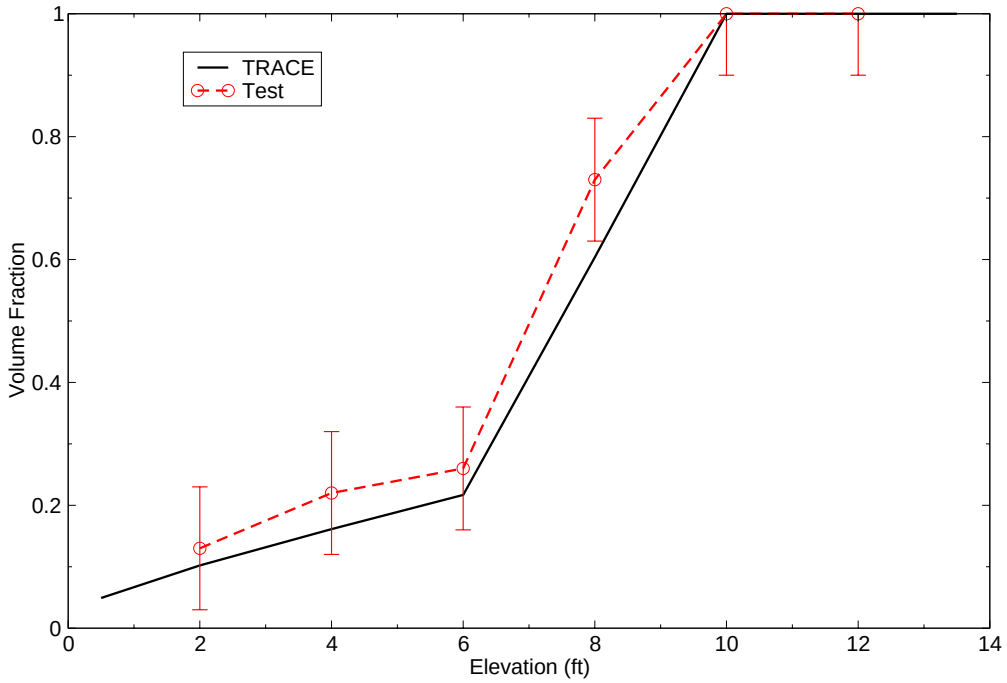

Figure B.16-15. Test 1004-3 axial void distribution at 160 seconds.

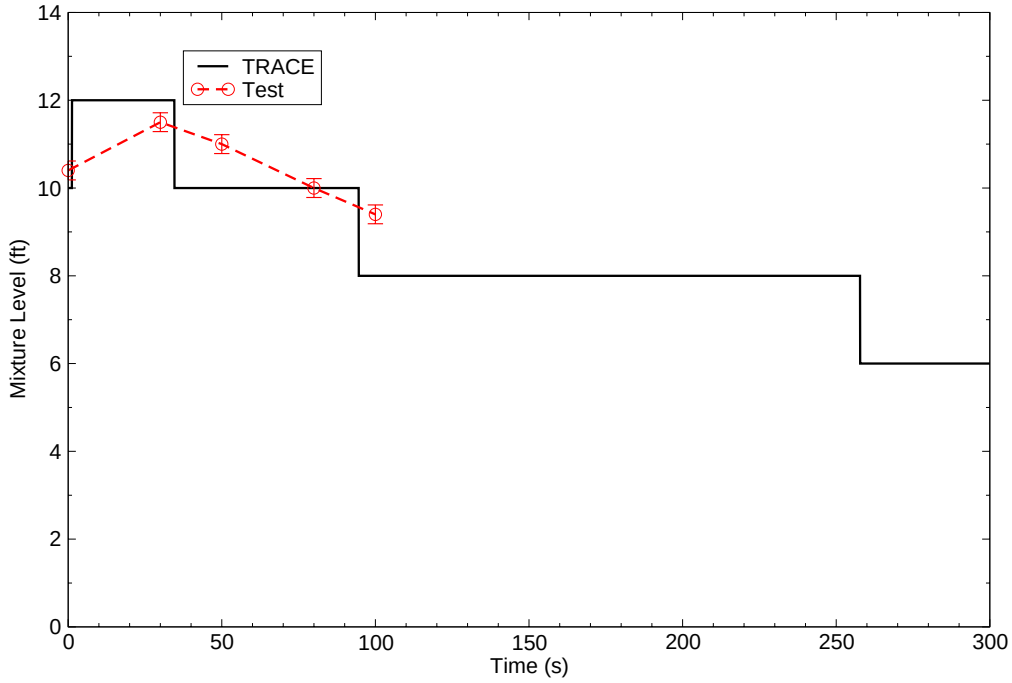

Figure B.16-16. Test 1004-3 approximate mixture level response.

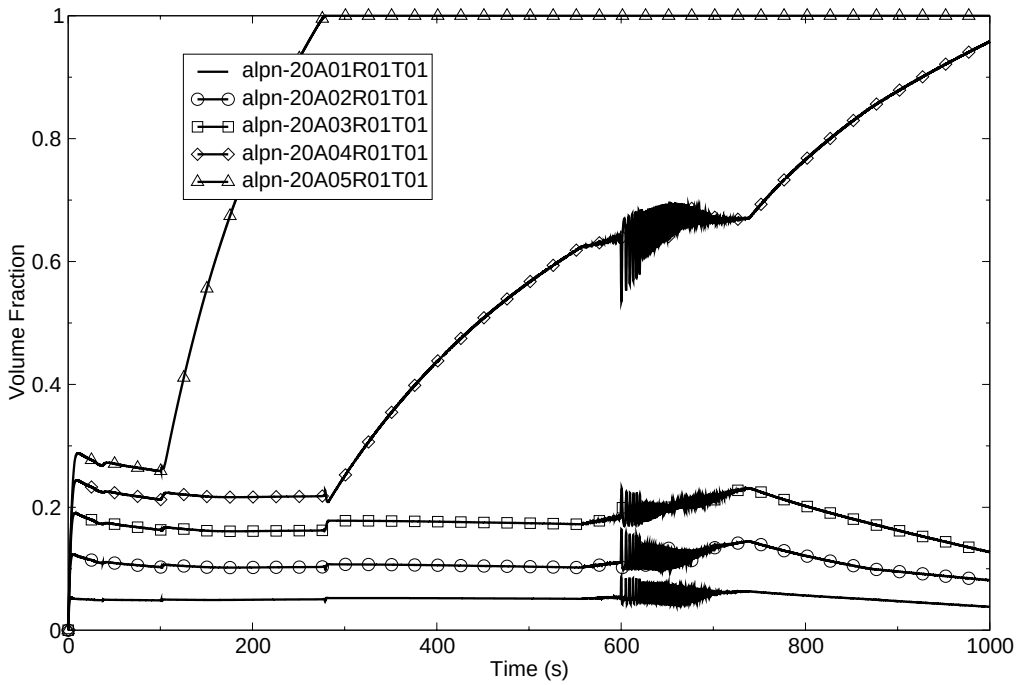

Figure B.16-17. Test 1004-3 TRACE axial void fractions out to 1000 seconds.

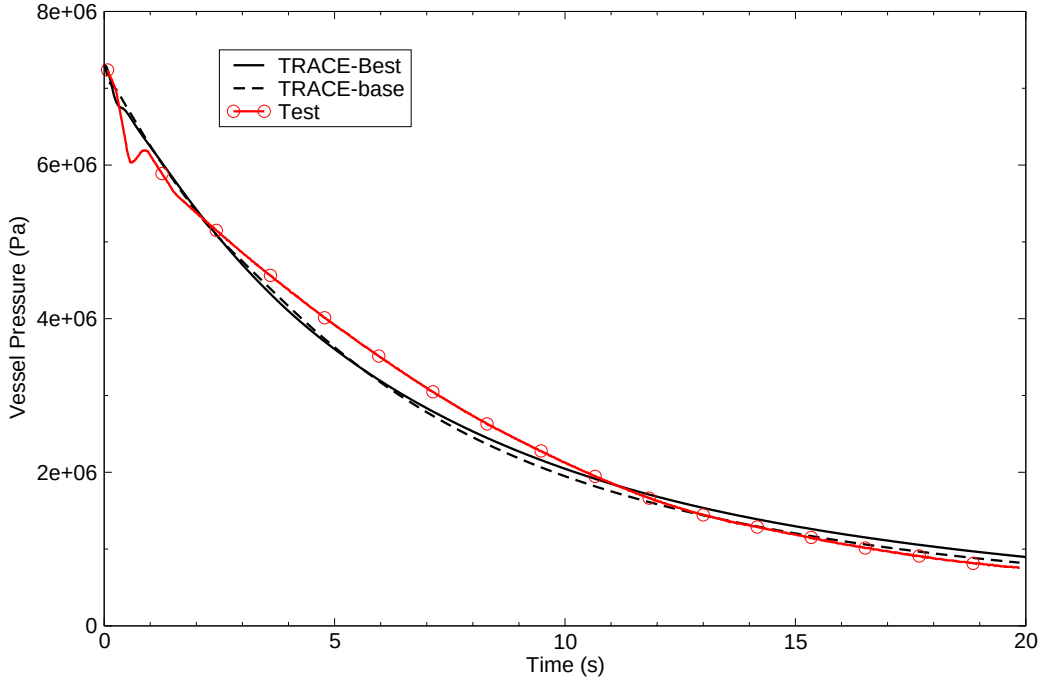

Figure B.16-18. Test 5702-16 pressure response.

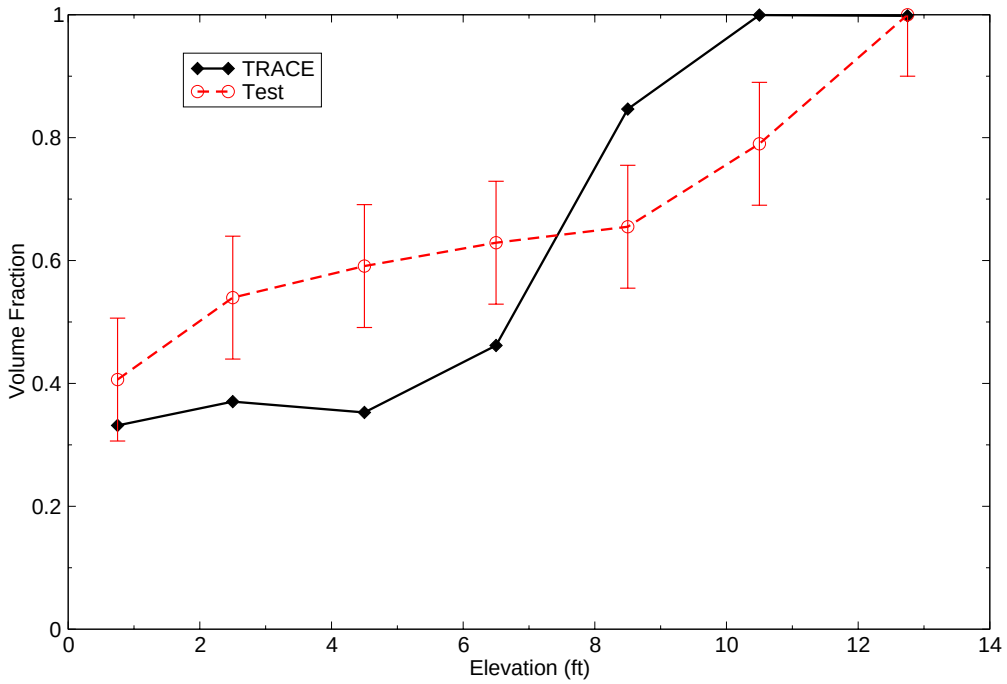

Figure B.16-19. Test 5702-16 axial void distribution at 2 seconds.

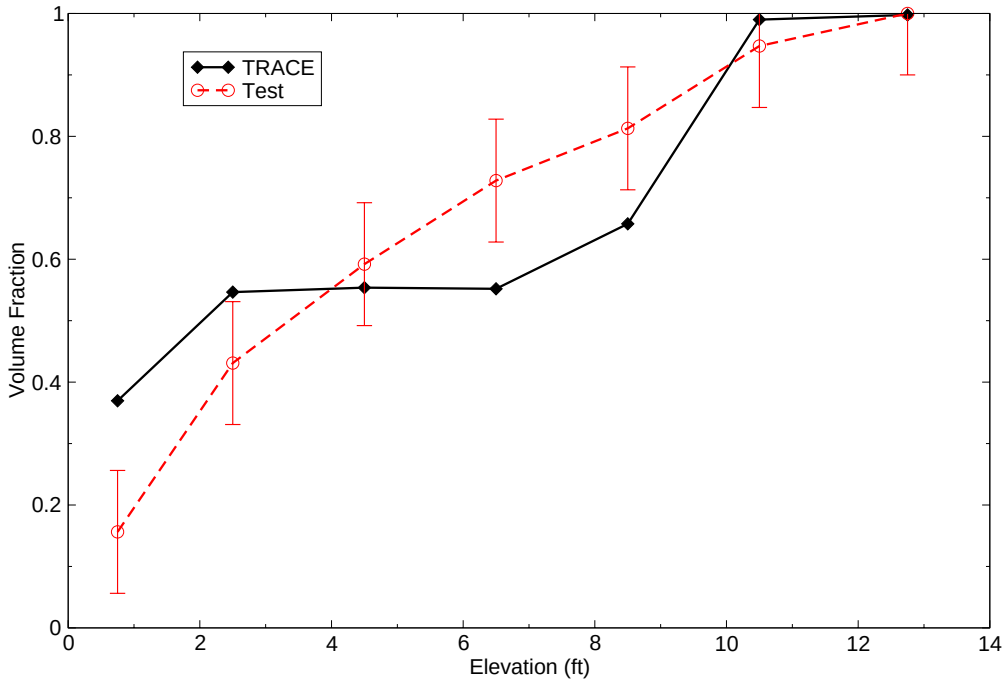

Figure B.16-20. Test 5702-16 axial void distribution at 5 seconds

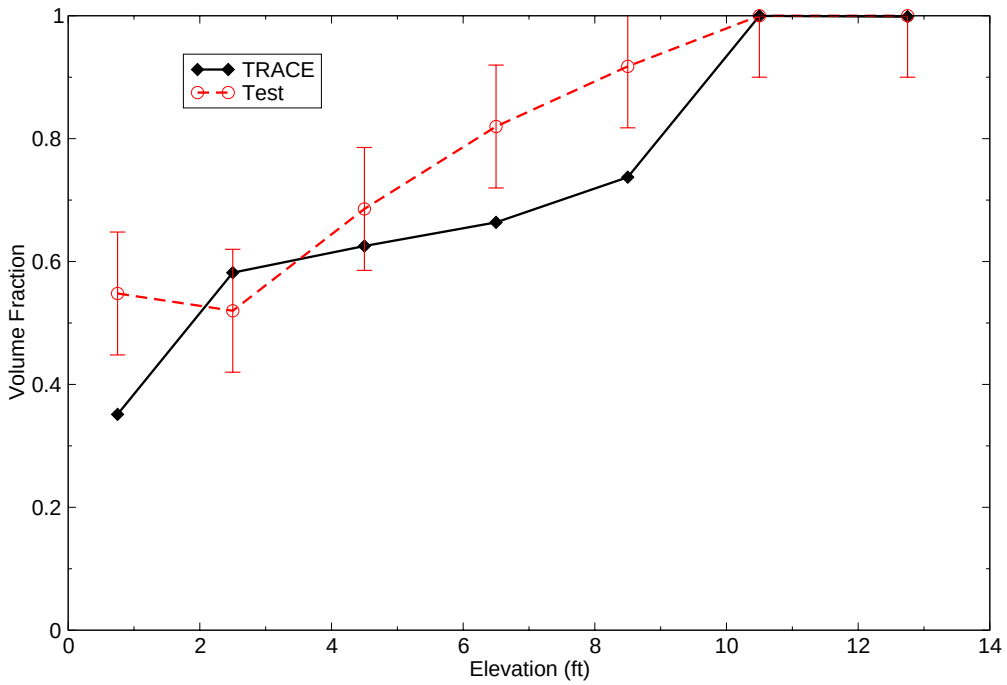

Figure B.16-21. Test 5702-16 axial void distribution at 10 seconds.

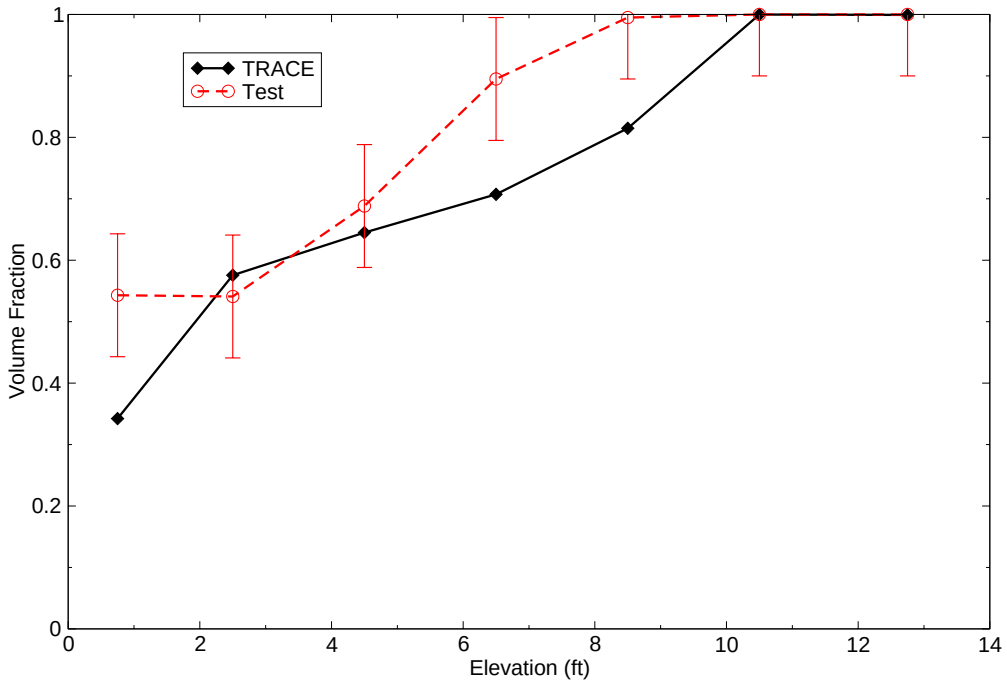

Figure B.16-22. Test 5702-16 axial void distribution at 14 seconds.

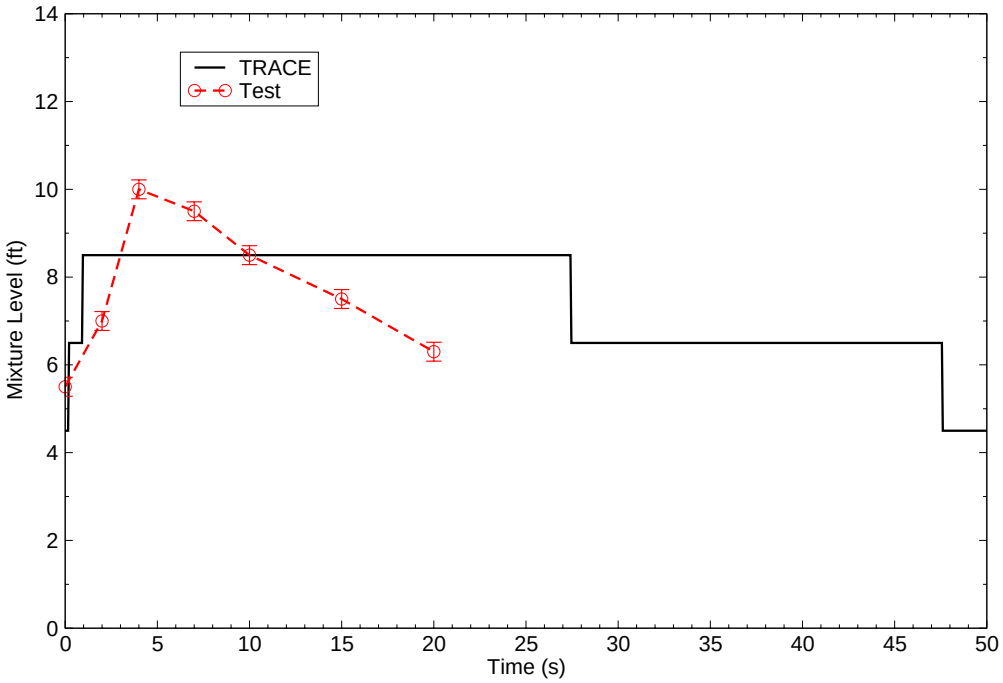

Figure B.16-23. Test 5702-16 approximate mixture level response.

B.17. Wilson Bubble Rise Tests

Author: Donald Palmrose*, Dan Prelewicz#

Affiliation: *AdSTM, Inc., # ISL, Inc.

Code Version: TRACE V5.0

Platform and Operating System: Intel x86, Windows XP

B.17.1. Introduction

In the 1960's, the United States and the European Atomic Energy Community (Euroatom) cooperated in conducting research and development programs for the advancement of the peaceful applications of atomic energy. One program was to carry out a series of steam-water and air-water tests under various thermodynamic conditions (Refs. 1, 2). In particular, one test was to perform a series of high pressure steam-water tests to determine the void fractions in a bubbling two-phase mixture. As a conclusion to this test, an equation was developed to predict the void fractions in both flowing and non-flowing two-phase mixtures.

The purpose of this assessment is to compare TRACE calculation results with the test data for the prediction of void fractions in non-flowing two-phase mixtures. The initial assessment was performed by Palmrose (Refs. 3, 4). These non-flowing tests will be denoted in this report as the "Wilson Bubble Rise" tests. This work includes the development of a TRACE model for the Wilson Bubble Rise tests, performance of a series of calculations at the appropriate test conditions (saturated pressure & temperature conditions, mass flow rates, and associated superficial steam velocities), and assessment of how well TRACE predicts the measured void fraction under the saturated two-phase mixture conditions.

B.17.2. Test Facility Description

The test facility description is provided in two documents, namely a conference paper presented at the 1964 Winter Meeting of the American Nuclear Society (Ref. 2) and the Joint US/Euroatom R&D program report published by Allis-Chalmers, herein denoted as ACNP-65002, published in 1965 (Ref. 1). The specific Wilson bubble rise test applied in this assessment is for the non-flowing conditions as presented in Section 4.3 of Reference 1. The test facility and test program descriptions are quoted from these two documents.

The tests were conducted in a 36-inch (0.91 m) diameter by 25-ft (7.62 m) tall pressure vessel, as shown in Figure B.17-1, located at an electrical power generating station of the then Wisconsin Electric Power Company. This test facility had a steam flow capacity of 60,000 pounds per hour (lb/hr) [7.576 kilograms/second, kg/s] and a pressure rating of 2150 psig (14.82 MPa). For the non-flowing tests, the internal baffling consisted of an 18-inch (0.46 m) diameter duct which ran the entire height of the vessel. Steam was injected through a flange attachment into the side of the vessel into a plenum volume which then bubbled through a perforated plate into non-flowing water at saturated conditions. The channel caused the void fractions to reach appreciable values for the steam flow rates available. Void fraction measurements were made with manometer probes connected to differential pressure cells, which extended into the 18-inch channel. The manometer probes were located well below the two-phase interface to ensure that the readings were not affected by the axial void fraction gradient near the interface (flange elevations of 18 feet, 3 1/4 inches [5.57 m] and 21 feet, 8 1/4 inches [6.61 m]). Three series of probes were used. These probes measured the voids at the channel wall, the quarter-diameter (or half-radius), and at the centerline of the channel.

A test was performed by first slowly heating the vessel and bringing the conditions to equilibrium at the desired test pressure. The water level was adjusted to the desired height and the steam flow was set at 5,000 lb/hr (0.631 kg/s). After the system reached equilibrium, the necessary instrument readings were taken. These readings were the vessel pressure, steam flow, and the three void fraction readings. After the readings were taken, the next steam flow was set and the process repeated. The steam flow was varied from 5,000 to 60,000 lb/hr (0.63 to 7.56 kg/s) and the pressures adjusted from 600 to 2000 psig (4.24 to 13.89 MPa). A total of 60 test cases were performed in the test facility. These test cases were broken into six pressure settings with anywhere from seven to eleven separate steam flows for each pressure setting.

Data from the series of tests were reduced using a FORTRAN program which then produced a set steam flows, superficial steam velocities, and the three void fraction measurements. Table B.17.1 provides the results of the Wilson bubble rise tests as published in Reference 1. The analysis of the experimental data showed that for a given superficial steam velocity, the void fraction increases with increasing pressure. A radial gradient in the void fraction was also observed. Wilson, et al., provided an explanation for the larger gradient at higher superficial steam velocities: "At low steam flows, a homogenous mixture exists, hence the radial gradient is very small and may not be noticeable. As the steam flow through the test section increases, the void fraction increases and the radial gradient becomes noticeable. This was attributed to the migration of bubbles toward the center of the column, caused by a lateral lift force on the bubble due to unequal flow around it."

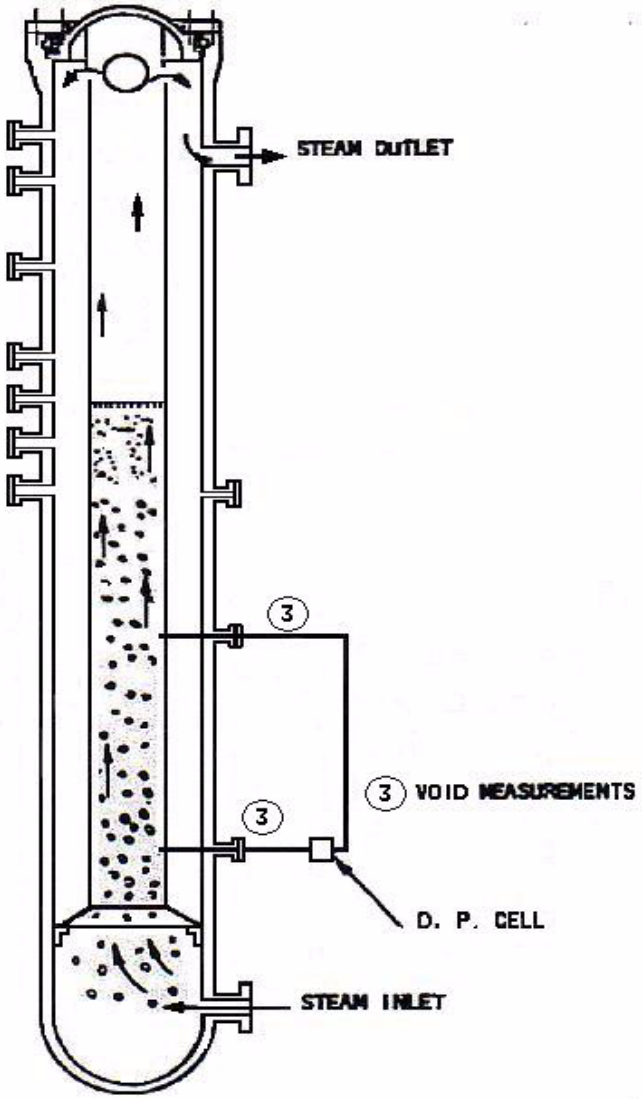

Figure B.17-1. Steam-Water Apparatus (Reference 1)

Wilson, et al., also correlated the data by the use of dimensional analysis and derived a correlation (i.e., Equation 6 of Reference 1) using the data from this program and previous low pressure data as follows:

$$\alpha = \kappa\left(\frac{\rho_g}{\rho_f - \rho_g}\right)^a \left(\frac{d}{\sqrt{\frac{\sigma}{g(\rho_f - \rho_g)}}}\right)^{-0.11033} \left(\frac{V_g}{\left(g\sqrt{\frac{\sigma}{g(\rho_f - \rho_g)}}\right)^{0.5}}\right)^b \tag{17-1}$$

Where $\kappa = 0.56157$, $a = 0.0917$, $b = 0.62086$ when

$$\frac{V_g}{\left(g\sqrt{\frac{\sigma}{g(\rho_f - \rho_g)}}\right)^{0.5}} < 2 \tag{17-2}$$

and $\kappa = 0.68728$, $a = 0.10736$, $b = 0.41541$ when

$$\frac{V_g}{\left(g\sqrt{\frac{\sigma}{g(\rho_f - \rho_g)}}\right)^{0.5}} > 2 \tag{17-3}$$

Data points from this correlation will also be applied in the comparison of the TRACE calculations to the experimental data. Void fraction values calculated using this correlation are also shown in Table B.17.1

Table B.17.1. Experimental Data and Wilson Correlation Void Fractions

Test No.	Steam Flow (kg/s)	Steam Velocity (m/s)	Wall Void Fraction	1/2 Radius Void Fraction	Mid-Duct (mid) Void Fraction	Average Void Fraction	ACNP-65002 Eq. 6
600 psig (4.24 MPa)							
1	0.630	0.183	0.2560	0.2560	0.2670	0.260	0.266
2	1.260	0.367	0.3460	0.3460	0.3690	0.354	0.386
3	1.890	0.550	0.4260	0.4370	0.4480	0.437	0.456
4	2.520	0.733	0.4930	0.4930	0.5160	0.501	0.514
5	3.150	0.917	0.5270	0.5720	0.5390	0.531	0.564
6	3.780	1.100	0.5610	0.5610	0.6060	0.576	0.609
7	4.410	1.284	0.5730	0.5840	0.6180	0.592	0.649
800 psi (5.62 MPa)							
1	0.630	0.135	0.2520	0.25200	0.2750	0.260	0.231
2	1.260	0.271	0.3350	0.3350	0.3820	0.351	0.355
3	1.890	0.406	0.4060	0.4060	0.4420	0.418	0.421
4	2.520	0.542	0.4650	0.4650	0.4890	0.473	0.474
5	3.150	0.677	0.5370	0.5370	0.5610	0.545	0.520
6	3.780	0.813	0.5370	0.5490	0.5490	0.545	0.561
7	4.410	0.948	0.5490	0.5610	0.5690	0.569	0.598
8	5.040	1.084	0.5250	0.5960	0.6680	0.596	0.632
9	5.544	1.192	0.4770	0.6080	0.7150	0.600	0.658
1000 psia (6.70 MPa)							
1	1.260	0.212	0.3030	0.3030	0.3400	0.315	0.317
2	1.890	0.318	0.3650	0.3770	0.4140	0.385	0.394
3	2.520	0.425	0.4270	0.4390	0.4640	0.443	0.444
4	3.150	0.531	0.4770	0.5260	0.5020	0.490	0.488
5	3.780	0.637	0.5140		0.5390	0.526	0.526
6	4.410	0.743	0.5640	0.5640	0.6010	0.576	0.561
7	5.040	0.849	0.5890	0.6010	0.6260	0.605	0.593
8	5.680	0.955	0.6010	0.6260	0.6510	0.626	0.622
9	6.300	1.062	0.6510	0.6630	0.7130	0.676	0.650
10	6.930	1.168	0.6880	0.7250	0.7880	0.734	0.677
11	7.560	1.274	0.7630	0.8000	0.8750	0.813	0.702
1200 psia (8.38 MPa)							
1	1.260	0.172	0.3080	0.3080	0.3340	0.317	0.353
2	1.890	0.258	0.3730	0.3860	0.4260	0.395	0.445
3	2.520	0.345	0.4250	0.4250	0.4510	0.434	0.503
4	3.150	0.431	0.4640	0.4770	0.5040	0.482	0.552
5	3.780	0.517	0.5300	0.5040	0.5430	0.526	0.589
6	4.410	0.603	0.5430	0.5430	0.5620	0.549	0.615
7	5.040	0.690	0.5820	0.5950	0.6210	0.599	0.640
8	5.670	0.776	0.5820	0.6080	0.6600	0.617	0.660
9	6.300	0.862	0.6340	0.6470	0.6990	0.660	0.675
10	6.930	0.948	0.6210	0.6340	0.6730	0.643	0.690
11	7.560	1.035	0.6470	0.6860	0.7250	0.686	0.701
1400 psi (9.75 MPa)							
1	1.260	0.143	0.2990	0.2720	0.2990	0.290	0.354

Test No.	Steam Flow (kg/s)	Steam Velocity (m/s)	Wall Void Fraction	1/2 Radius Void Fraction	Mid-Duct (mid) Void Fraction	Average Void Fraction	ACNP-65002 Eq. 6
2	1.890	0.215	0.3680	0.3400	0.3820	0.363	0.445
3	2.520	0.287	0.3820	0.3950	0.4230	0.400	0.503
4	3.150	0.358	0.4230	0.4500	0.4780	0.450	0.551
5	3.780	0.430	0.4910	0.4780	0.5190	0.496	0.589
6	4.410	0.502	0.5320	0.5320	0.5730	0.546	0.615
7	5.040	0.574	0.5870	0.6010	0.6280	0.605	0.640
8	5.670	0.646	0.6010	0.6150	0.6560	0.624	0.660
9	6.300	0.717	0.6280	0.6420	0.7110	0.660	0.675
10	6.930	0.789	0.6560	0.6690	0.7240	0.683	0.690
11	7.560	0.861	0.6690	0.6830	0.7520	0.701	0.701
2000 psi (13.89 MPa)							
1	1.260	0.089	0.1770	0.1770	0.2420	0.199	0.275
2	1.890	0.134	0.2910	0.3070	0.3890	0.329	0.349
3	2.520	0.179	0.3240	0.3400	0.4220	0.362	0.420
4	3.150	0.224	0.3400	0.3890	0.4710	0.400	0.464
5	3.780	0.268	0.3890	0.4540	0.5190	0.454	0.509
6	4.410	0.313	0.4380	0.5030	0.5850	0.509	0.539
7	5.040	0.358	0.4710	0.4430	0.6170	0.510	0.570
8	5.670	0.402	0.4870	0.5520	0.6340	0.558	0.592
9	6.300	0.447	0.5360	0.5850	0.6500	0.590	0.614
10	6.930	0.492	0.5680	0.6170	0.6660	0.617	0.630
11	7.560	0.537	0.6170	0.6340	0.6830	0.645	0.648

B.17.3. TRACE Model Description

The TRACE model applied the given information from ACNP-65002 for geometric data and test conditions. The geometric data was obtain either directly from the text (diameters and overall height), Figure 1 (i.e., internal arrangements), or from Figure 14 (i.e., flange elevations) of Reference 1. Figure B.17-2 shows the nodalization scheme applied to the Wilson Bubble Rise tests. To model the main test apparatus, a VESSEL component (VESSEL 2) was used with two rings, 9 levels, and one azimuthal zone. No radial flow is allowed between Ring 1 and Ring 2 except at Level 1 and Level 9 along with no axial flow between Ring 2 of Level 1 and Level 2. Steam flows are produced by a FILL component (FILL 1). Vapor flows are removed from the outer ring, as in the test apparatus, via a connection on Ring 2 of Level 7 to a PIPE component (PIPE 3), and then to a BREAK component (BREAK 4) set to the saturated VESSEL conditions.

None of the references provide information on the water level applied for each test or for the dimensions of the flow area at the top of the duct where the steam flows from the inner region to the outer ring and then to the outlet flange. For the purposes of this assessment, the water level was set to the top of Level 6 to ensure that there would be enough fluid height so as not to influence the void fraction at Level 3. The flow area from the inner ring to the outer ring on Level 9 was assumed to be half of the full boundary area between the two rings at this level and is intended to be large enough as to not affect the flow out of the test apparatus.

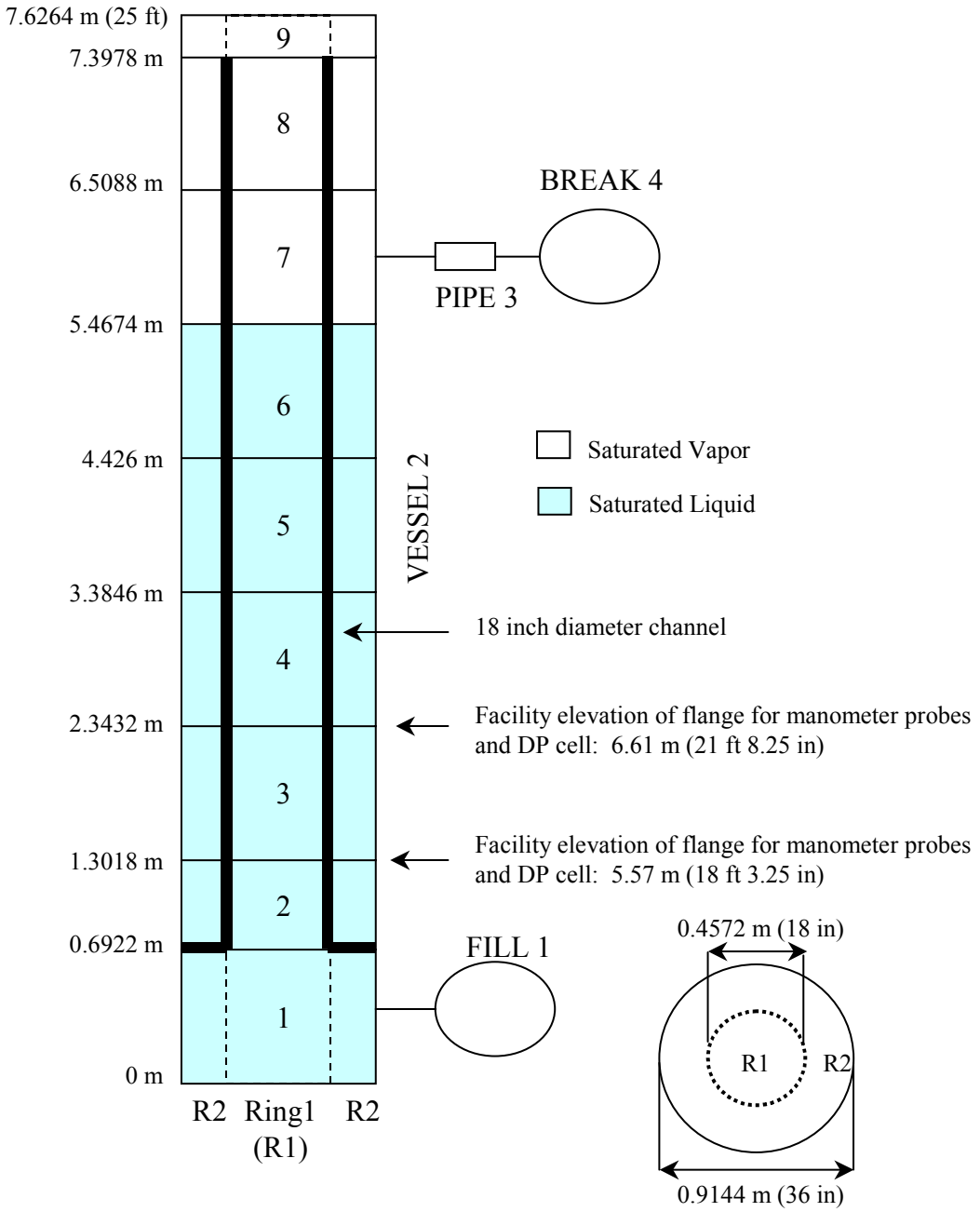

Figure B.17-2. TRACE Nodalization Scheme.

B.17.4. Test Simulated with TRACE

For each of the six pressure groups shown in Table B.17.1, the TRACE volumes' fluid conditions were set to the saturated properties for that pressure and an initial void fraction of 0.0 for liquid volumes and 1.0 for vapor volumes as shown in Figure B.17-2. The inlet conditions for the steam flow from the FILL component (FILL 1) were set to the specific mass flows and superficial steam

velocities given in Table B.17.1 for each individual run. All other initial velocities were set to zero.

B.17.4.1. Simulation of Wilson Tests.

A total of six calculation runs were performed using TRACE code version 5.0 for each test condition with a total transient time of 300 seconds for each steam flow rate. This was found to provide enough time for the calculation to obtain steady-state conditions across the Wilson apparatus. The time dependent void fraction response for the 300 second steady-state run for each of the six pressure cases is shown in Figure B.17-3. The transient cases were initiated from the conditions at the end of these runs. Because the VESSEL volume boundaries for Level 3, Ring 1 match the facility elevations for the flanges used by the manometers (see Figure B.17-2), the calculated void fraction for this VESSEL cell should directly correspond to the experimental measurements. The void fractions calculated using the Wilson correlation (Equation 6 of Reference 1) for each case are provided in Table B.17.1 along with the experimental measurements.

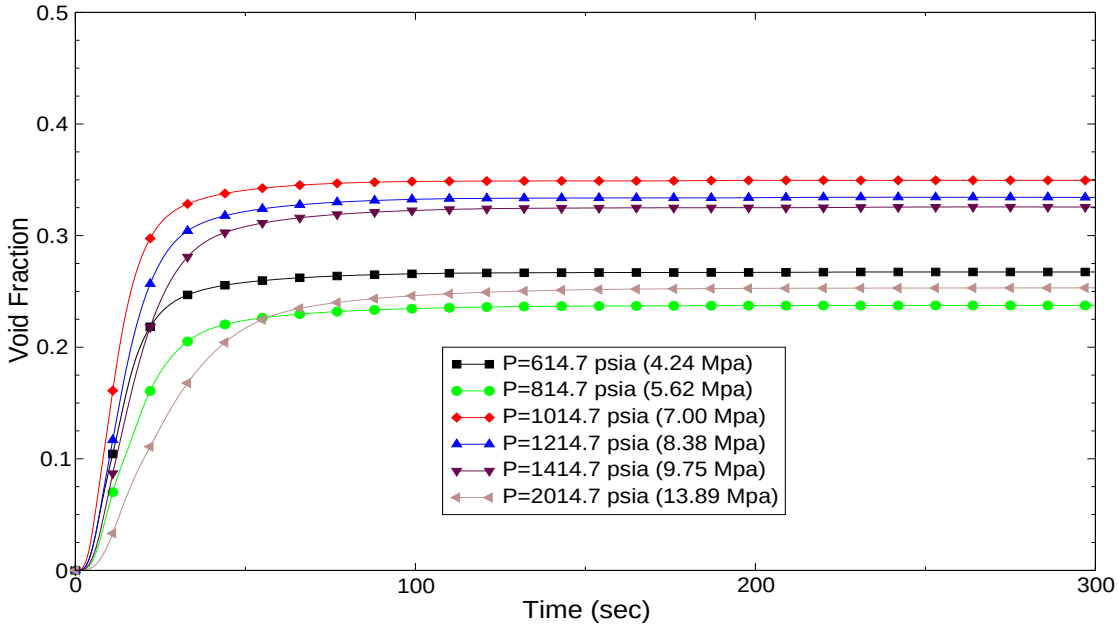

Figure B.17-3. VESSEL Void Fractions for Steady-State Runs.

The calculated void fractions, over the same volume as the data measurements (Level 3, Ring 1), have "Excellent Agreement" using the acceptance criteria of NUREG-1737 (i.e., the calculated results are judged to agree closely with the data). This is demonstrated in Figure B.17-4 through Figure B.17-15. All but one of the runs are within the expected measurement error of ±0.1 (shown as error bars for the measurements in the Figures) with most runs within 0.05 of the measured

mid-channel void fraction. For each pressure group, two figures are shown. The first figure compares TRACE calculated void fractions to the average void fraction of all three measurements across the duct (i.e., at the wall, 1/2 radius, and middle of the duct). The second figure plots the TRACE predicted void fraction against the average measured values providing a Figure of Merit for each specific pressure.

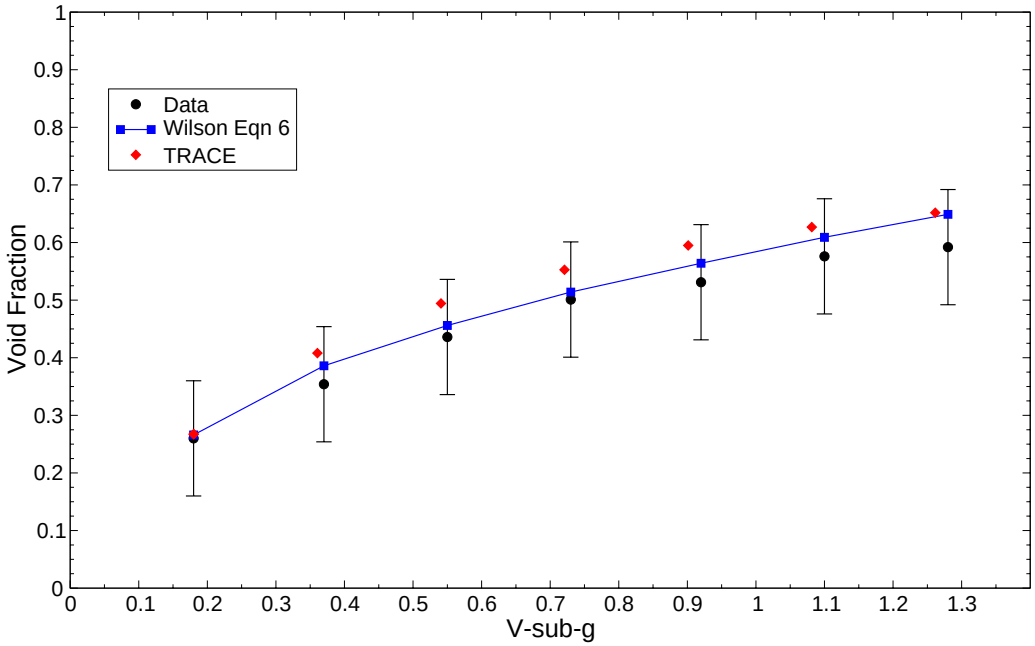

Figure B.17-4. Average Measured, TRACE, and Equation 6 Void Fractions at 600 psig.

B.17.5. Assessment Results Summary

TRACE Version 5.0 can predict the void fraction in a vertical duct under saturated and non-flowing conditions. A measure of how well TRACE does in predicting the void fraction under these conditions can be seen from the Figure of Merit for all of the cases shown in Figure B.17-16. Fifty-nine out of 60 cases have the TRACE values within 0.1 of the experimental measurements' average void fraction and of these 59 cases, the majority are within 0.05. However, the majority of cases have TRACE slightly over-predicting the void fraction.

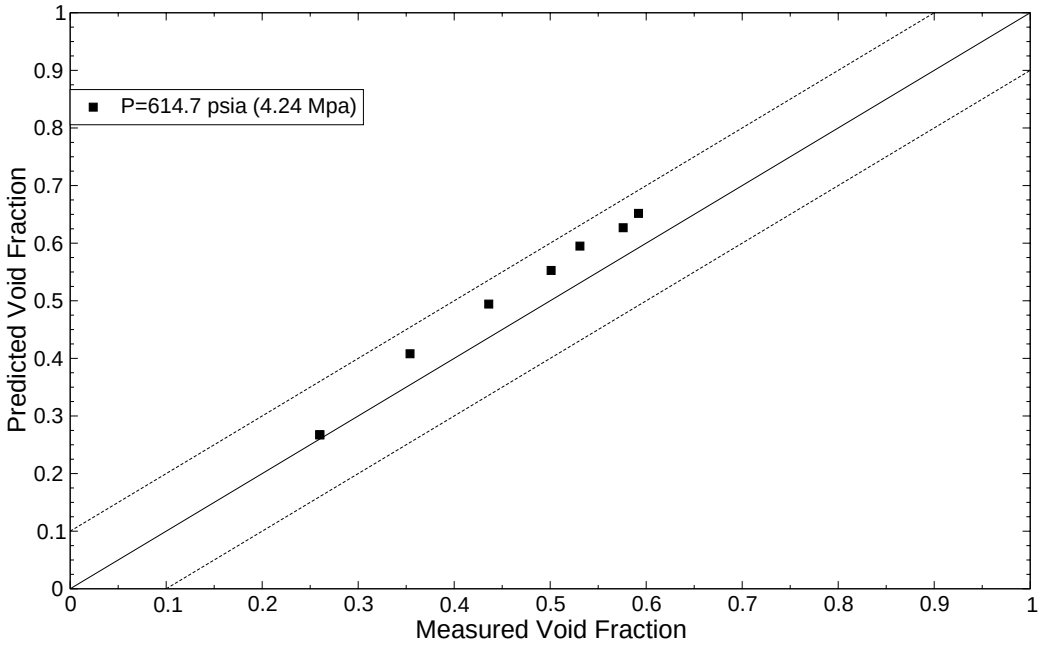

Figure B.17-5. Predicted Versus Measured Void Fractions at 600 psig.

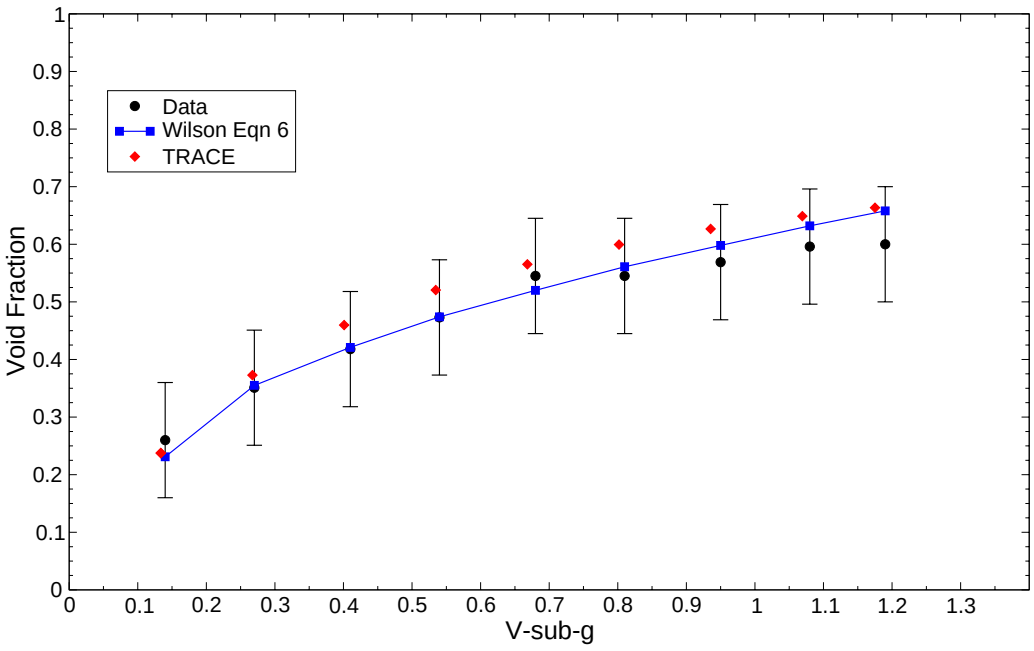

Figure B.17-6. Average Measured, TRACE, and Equation 6 Void Fractions at 800 psig.

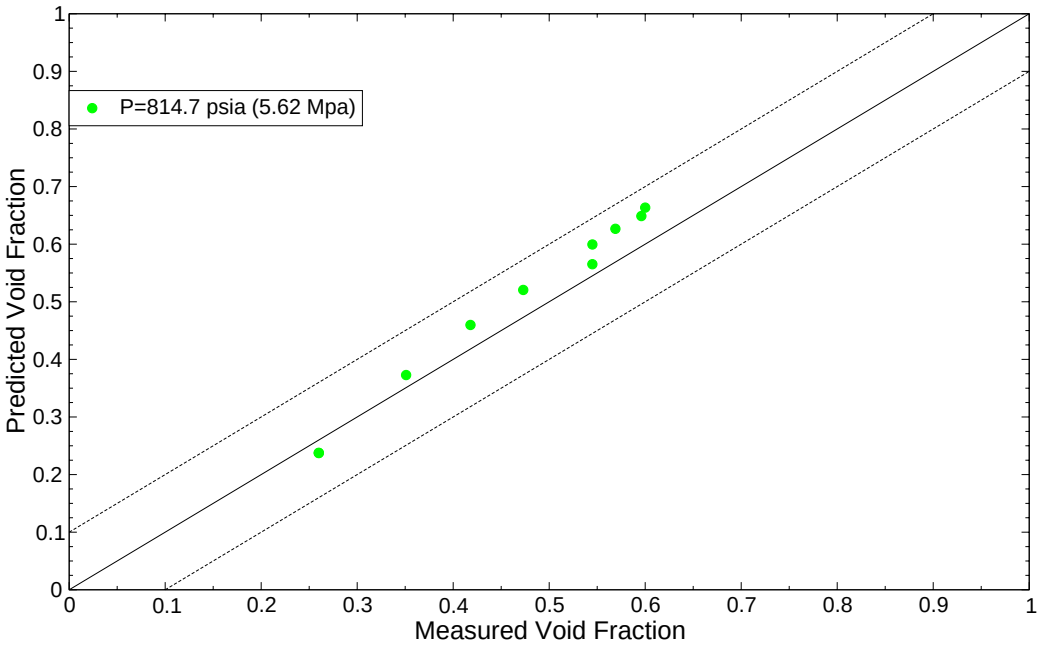

Figure B.17-7. Predicted Versus Measured Void Fractions at 800 psig.

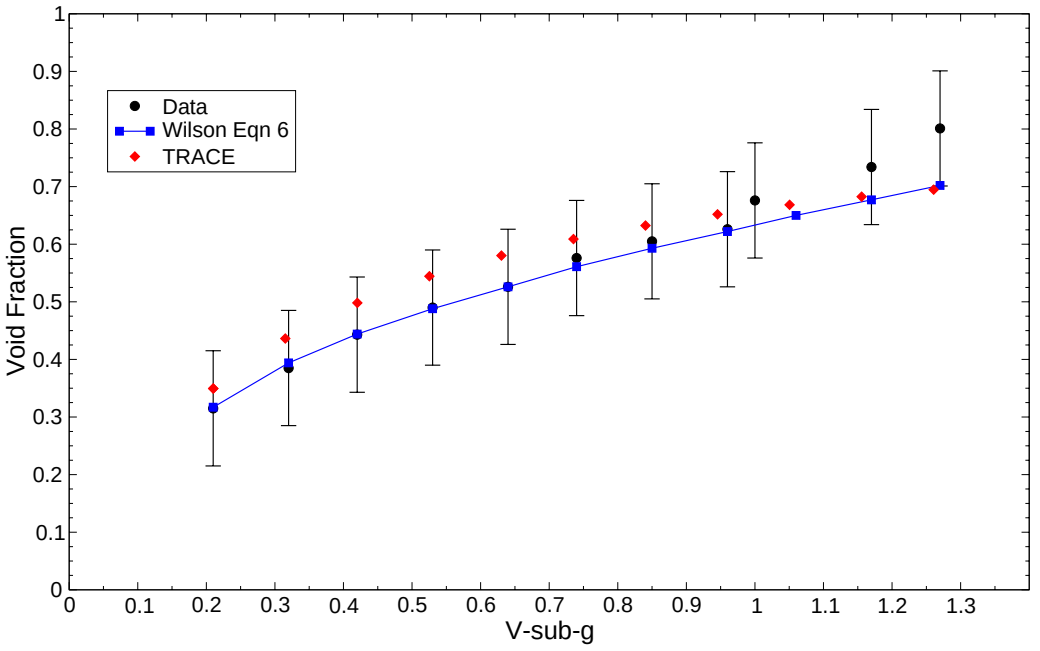

Figure B.17-8. Average Measured, TRACE, and Equation 6 Void Fractions at 1000 psig.

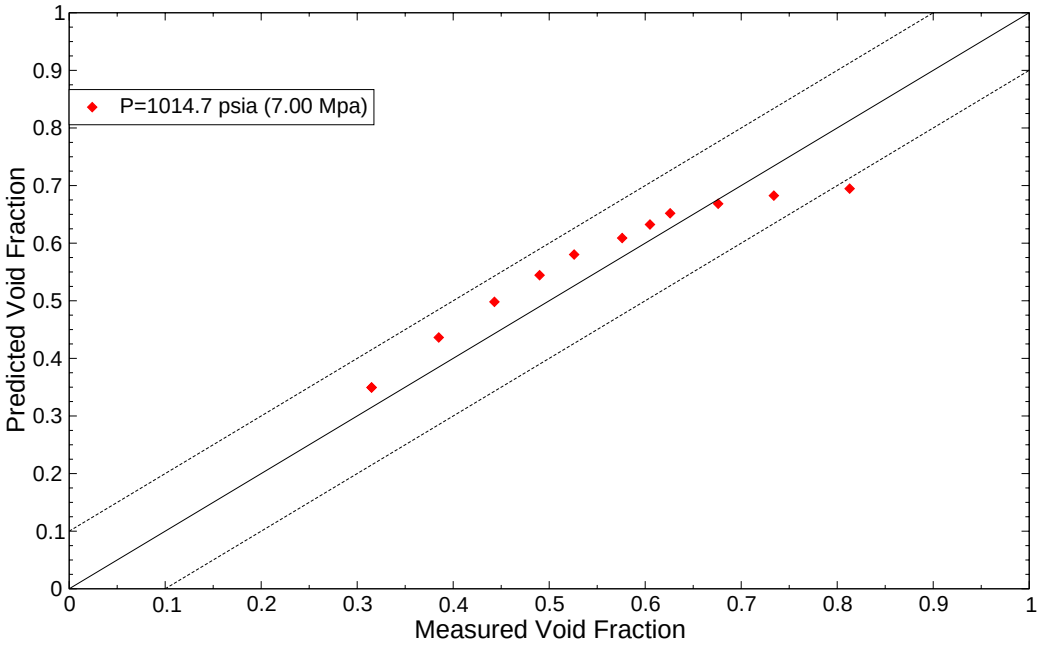

Figure B.17-9. Predicted Versus Measured Void Fractions at 1000 psig.

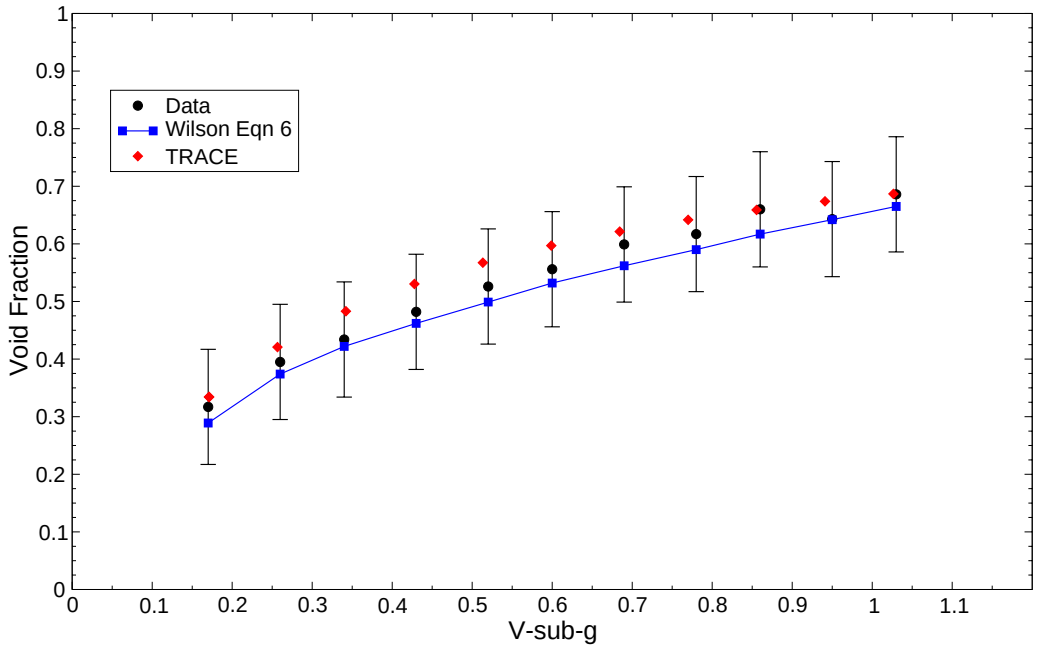

Figure B.17-10. Average Measured, TRACE, and Equation 6 Void Fractions at 1200 psig.

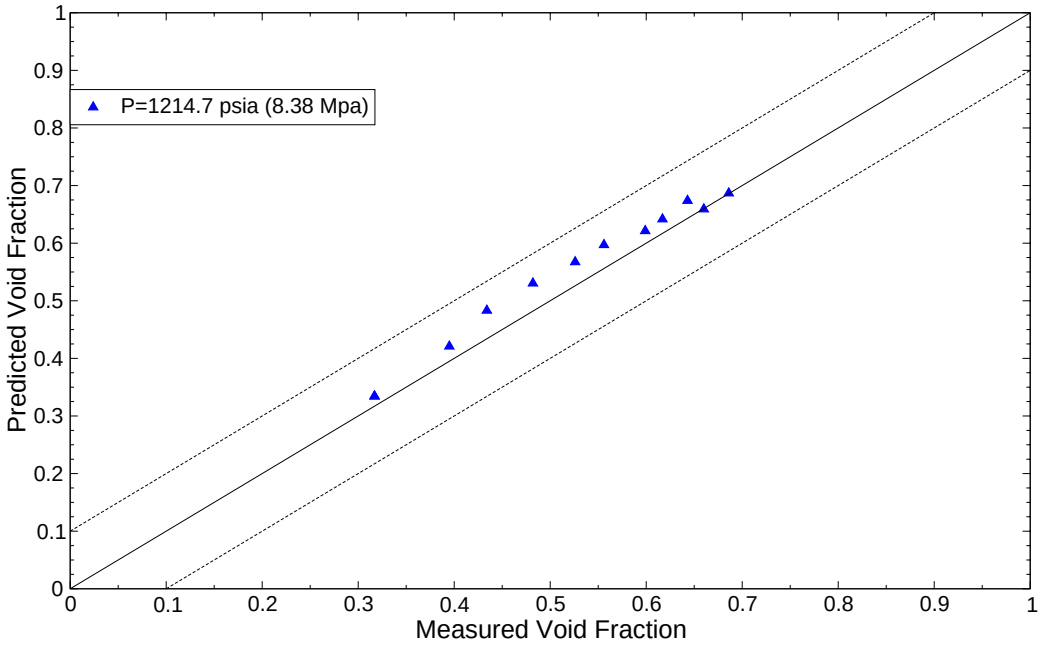

Figure B.17-11. Predicted Versus Measured Void Fractions at 1200 psig.

B.17.6. References

1 Wilson, J.F., W.E. Littleton, H.W. Yant, and W.C. Meyer, "TOPICAL REPORT - Part I: Primary Separation of Steam from Water by Natural Separation," Joint US/Euroatom R&D Program at (11-1)-1186, Allis-Chalmers, Atomic Energy Division, Milwaukee, Wisconsin, April 15, 1965.

2 Meyer, W.C., J.F. Wilson, "Steam Volume Fractions in Flowing and Non-Flowing Two-Phase Mixtures," CONF-654-71, 1964 Winter Meeting, American Nuclear Society, San Francisco, California, November 30 - December 3, 1964.

3 D. Palmrose, "TRACE Calculation Notebook - Wilson Bubble Rise", January 19, 2006, ADAMS Accession Number ML062010392.

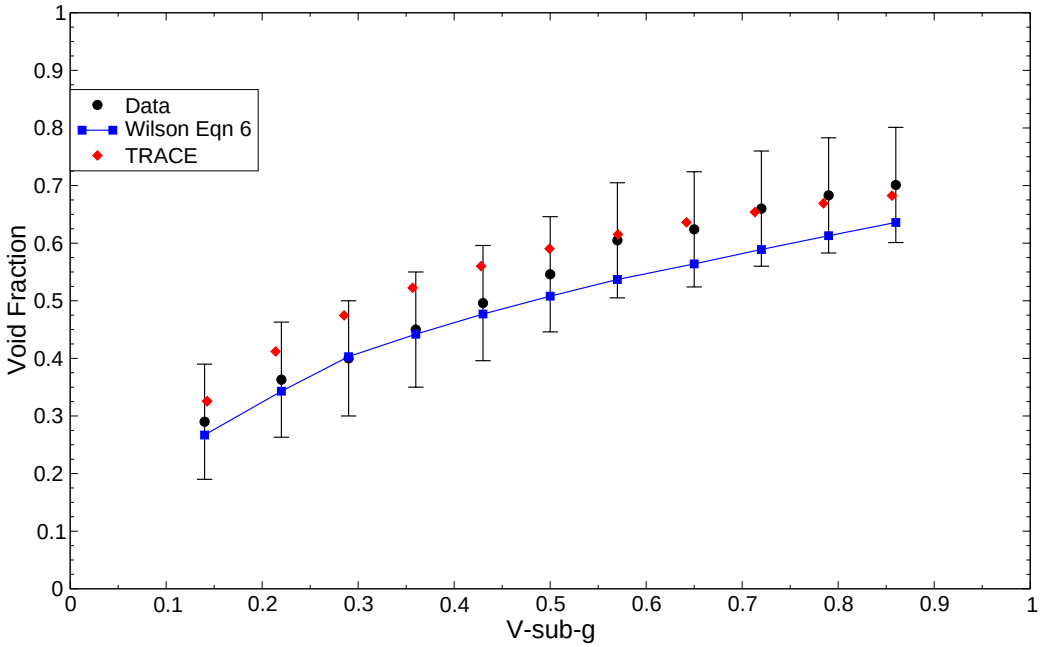

Figure B.17-12. Average Measured, TRACE, and Equation 6 Void Fractions at 1400 psig.

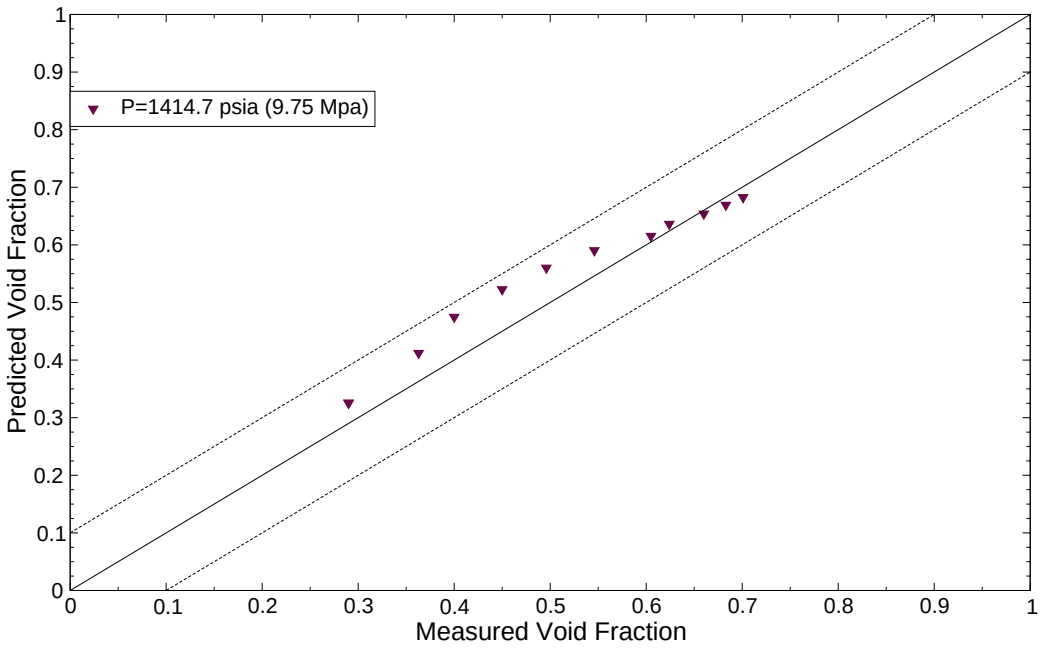

Figure B.17-13. Predicted Versus Measured Void Fractions at 1400 psig.

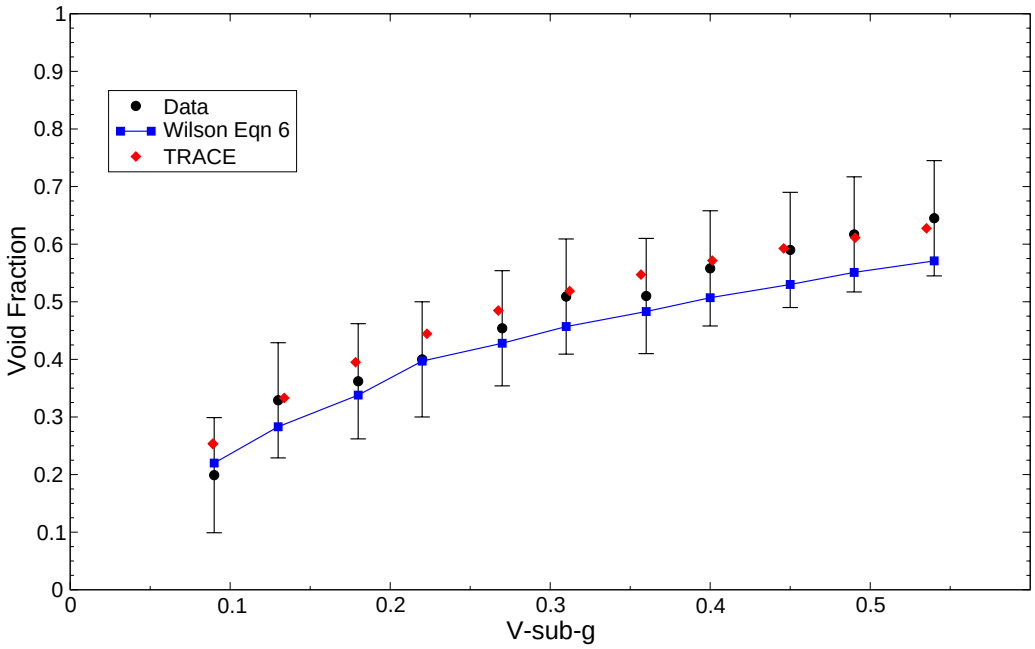

Figure B.17-14. Average Measured, TRACE, and Equation 6 Void Fractions at 2000 psig.

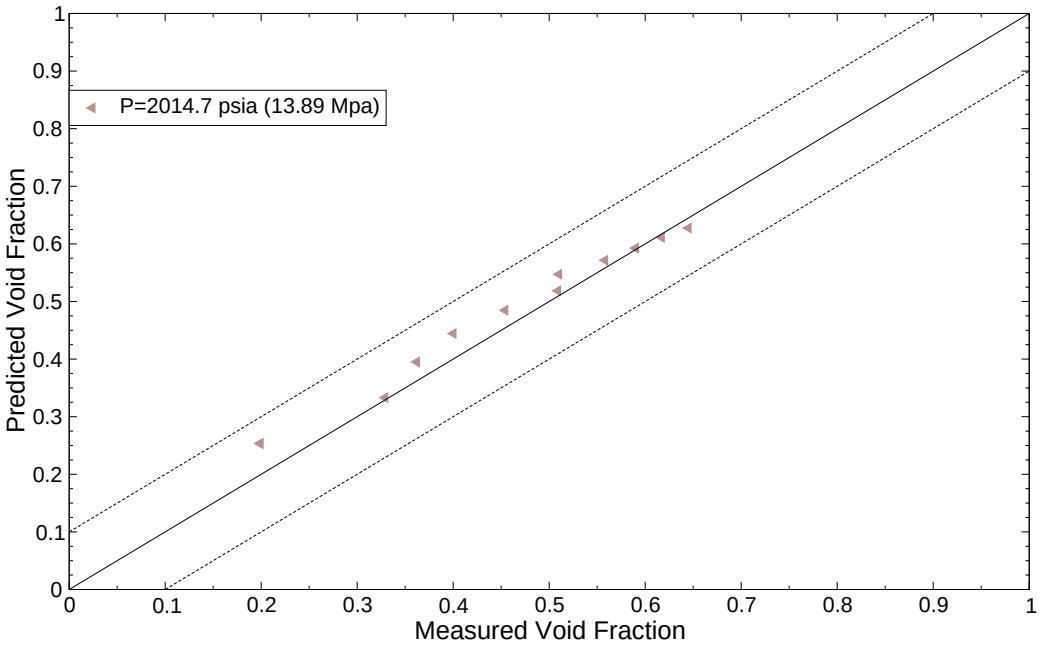

Figure B.17-15. Predicted Versus Measured Void Fractions at 2000 psig.

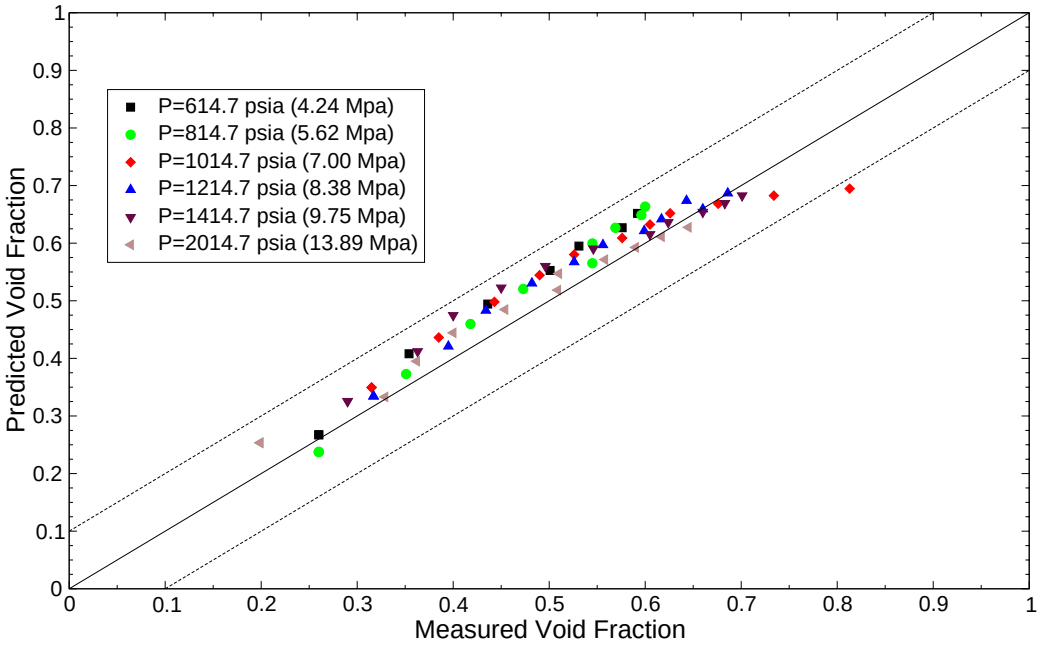

Figure B.17-16. Figure of Merit for Complete Data Set.

4 D. Palmrose, TRACE Assessment Manual Section B.99.33, "TRACE Assessment of Wilson Bubble Rise Tests (DRAFT)", December 23, 2005, ADAMS Accession Number ML061720346.

Flooding and CCFL Tests

B.18. Bankoff Perforated Plate CCFL

Author(s): Dan Prelewicz

Affiliation: Information Systems Laboratories, Inc.

Code Version: TRACE V5.0

Platform and Operating System: Intel x86, Windows XP

B.18.1. Introduction

Counter-current flow limiting (CCFL) is a phenomenon important in several hypothetical accident scenarios. Of particular interest during the reflood period of a large break LOCA, is CCFL and pool formation above the upper core plate. Water that de-entrains in the upper plenum and that is held there by CCFL cannot drain back into the core and contribute to core cooling.

This section examines the ability of the TRACE code to predict CCFL. The tests conducted by Bankoff, et. al. (Refs 1-3) are used in this assessment. Bankoff, et. al. conducted air/water and steam/water countercurrent flow tests in a small scale test apparatus where the countercurrent flow occurred through perforated plates of various geometries. Additional testing of steam/water countercurrent flow testing with a 15-hole plate is reported in Reference 3. The TRAC-P code was assessed (Ref. 4) against air/water data for countercurrent flow through a 15-hole plate 20 mm thick with a geometry that corresponds to a small segment of a PWR upper tie plate. Experimental data for this same case from Reference 1 was used here to assess the ability of TRACE to model countercurrent flow in the absence of condensation effects.

The Bankoff CCFL correlation can be invoked by the TRACE code user at specific locations as a user option. The Bankoff correlation combines Wallis scaling and Kutateladze scaling, either of which can be invoked as special cases of the Bankoff corrlation. Bankoff's form of the CCFL correlation was developed using data from eight different plate geometries, including the 15-hole plate used for this assessment. The 15-hole plate geometry was used as a basis in this assessment because it was considered by Bankoff, et.al. to be most representative of a PWR upper tie plate. The assessment shows that the correlation is correctly implemented in TRACE, includes comparison to the complete data set for the 15-hole plate and indicates limitations of the model for low values of the air flow. The model was also run with saturated steam instead of with air as the gas phase. Results for the saturated steam case followed the correlation for all values of the gas flow. The assessment documented in Reference 4 used saturated steam as the gas phase.

B.18.2. Test Facility Description

The Bankoff perforated plate countercurrent flow apparatus is shown schematically in Figure B.18-1. Air is introduced below the perforated plate while water is introduced through a vertical tube above the plate. The water forms a bubbly pool above the perforated plate and overflows to a drain. The height of the pool above the plate could be adjusted by moving the plate. All of the tests considered here were conducted with a 267 mm height pool. Water was drained from the lower plenum through a drain tube, preventing water from accumulating in the "soft volume" below the plate. Air exited the top of the test section. All of the tests were run at atmospheric pressure, taken to be 1.0E+5 Pa. Water temperature was reported to have varied between 276 and 288 K.

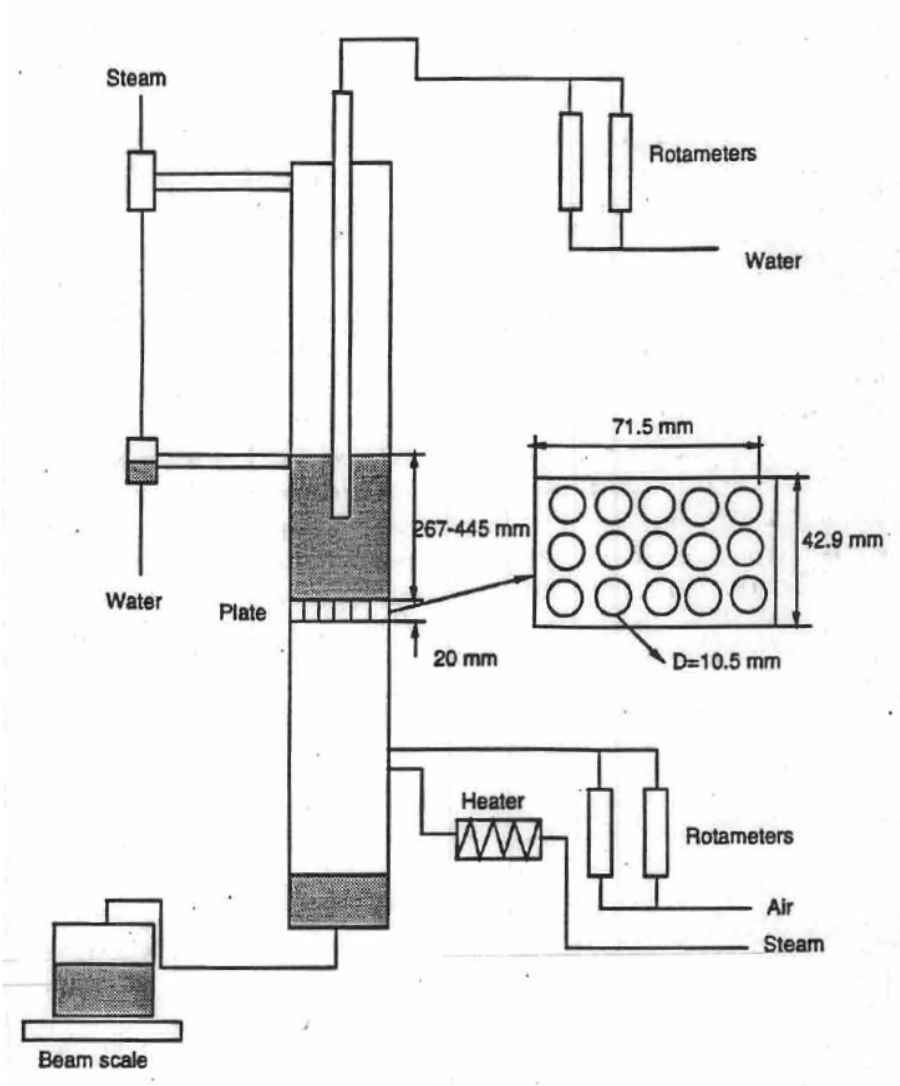

Figure B.18-1. Schematic of Bankoff Countercurrent Flow Test Apparatus

The test procedure consisted of establishing the water inlet flow rate and then increasing the air flow rate in steps. At each step, the water delivery rate to the lower plenum was determined,

ending with the point of essentially zero downward flow, the countercurrent flow limit, or weep point. Measurements made by Bankoff include the air delivery rate and the delivery rate of water to the plenum below the perforated plate.

For a range of plate geometries Bankoff, et. al. were able to correlate their data using H^* scaling as:

$$(Hg^*)^{\frac{1}{2}} + (Hf^*)^{\frac{1}{2}} = C \tag{18-1}$$

where

$$H^*_k = j_k \left(\frac{\rho_k}{gw(\rho_f - \rho_g)} \right)^{\frac{1}{2}}, \qquad (k = f, g) \tag{18-2}$$

H_g^* and H_f^* are dimensionless superficial gas and liquid velocities. In Equation 1-1, the coefficient C is given by:

$$C = (1.07 + 0.00433 \times L^*)\,, L^* \leq 200.$$
$$C = 2\,, L^* > 200. \tag{18-3}$$

$$L^* = n\pi D \sqrt{g \times (\rho_f - \rho_g)/\sigma} \tag{18-4}$$

where L^* is the Bond Number defined as:

In the above equations, D is the hole diameter, g is the gravitational constant, j_k is the superficial velocity, n is the number of holes in the plate, ρ_k is density, σ is surface tension and w is an interpolative reference length between Wallis and Kutateladze scaling defined as.

$$w = D^{(1-\beta)} L^{\beta} \tag{18-5}$$

where L is the Laplace capillary constant used by Kutateladze

$$L = \sqrt{\sigma/(g(\rho_f - \rho_g))} \tag{18-6}$$

and β is an empitical parameter defined as

$$\beta = \tanh(\gamma k_c D) \tag{18-7}$$

In equation (18-7), γ is the perforation ratio, i.e. the fraction of the plate area occupied by holes, and $k_c = 2\pi/t_p$, where t_p is the plate thickness. The results of correlating the experimental data in this manner are shown in Figure B.18-2. Only the data for the 15-hole plate were used. The experimental data was obtained by digitizing the 15 hole points from this figure.

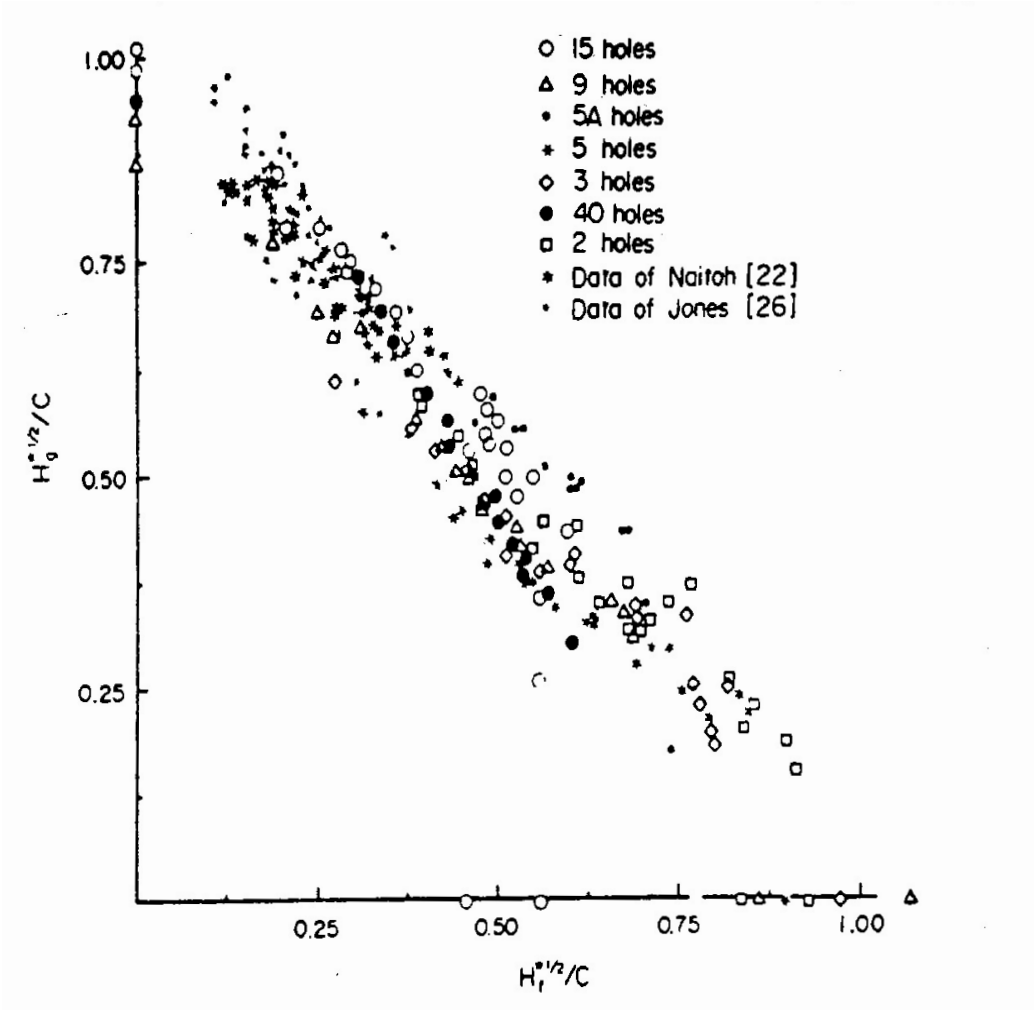

Figure B.18-2. Bankoff Experimental Data

B.18.3. TRACE Model Description

The TRACE input model of the Bankoff apparatus consists of 11 components as shown in Figure B.18-3. A one-dimensional VESSEL with eleven axial nodes represents the test section, while five single node pipes are used to connect the VESSEL to FILLS or BREAKS. BREAKS are

used for the water overflow and the air/steam outlet. FILLS are used to model the water and air injection. The water drain from the lower plenum is modeled using a FILL with the flow set by a control system to match the delivery to the lower plenum, so as to prevent buildup of liquid and maintain the level essentially constant.

The perforated plate was modeled as a restriction in the flow area between the fifth and sixth VESSEL cells. Each of the 15 holes in the plate is 0.0105 m in diameter and the rectangular cross section of the VESSEL is 0.0715 m by 0.0429 m, giving a perforation ratio of 0.4235. Additive liquid and gas loss coefficients of 1.0 were used to model the area change losses.

The gas was treated as steam and a noncondensable gas (air) mixture. A second case was run with the gas treated as saturated steam at the total test section pressure. The complete Bankoff correlation was used with the same parameters as Reference 1.

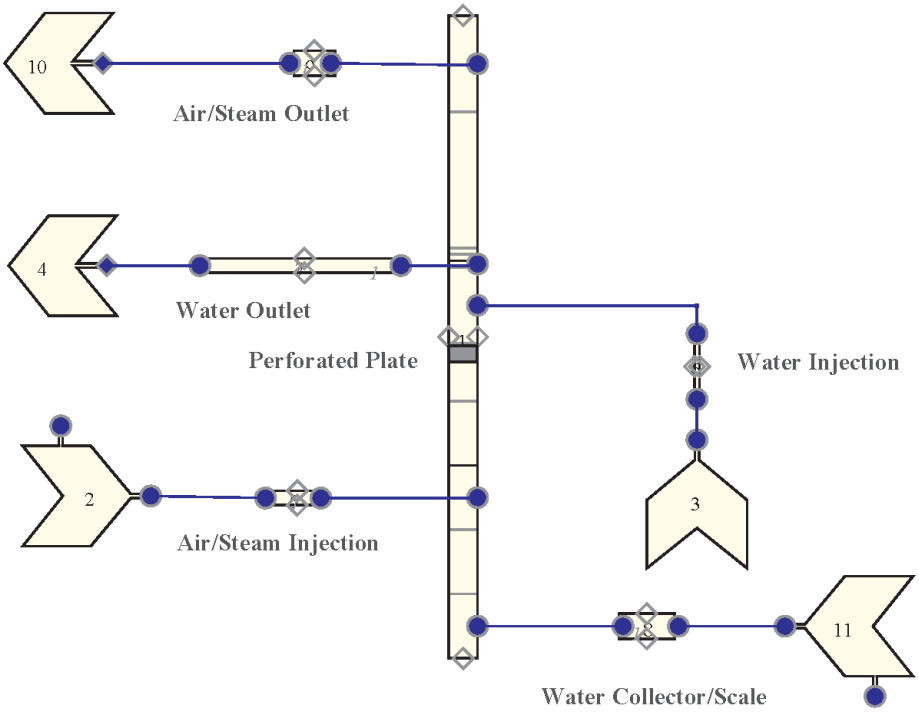

Figure B.18-3. TRACE Noding Diagram for Bankoff Test Apparatus

Experimental air/water data for the 15-hole plate tests was digitized from plotted results in Reference 1, shown here in Figure B.18-2. The input air flow rate was calculated from the gas superficial velocity data using control variables, and input to the TRACE model using FILL component 2. Predicted dimensionless superficial liquid velocity for comparison to data was calculated from the mass flow rate of liquid through the plate using control variables.

B.18.4. Tests Simulated with TRACE

The air/water test with the 15-hole plate was simulated as a single TRACE run by starting with the air flow rate at zero and stepping the air flow from zero to the low value in the tests and then increasing the air flow in steps up to the high value. The air flow was ramped over a five second period and then held at each air flow step for 25 seconds before ramping to the next air flow rate.

Figure B.18-4 shows a plot of TRACE calculated dimensionless square root of superficial gas and liquid velocities. The calculated liquid velocity has reached a steady-state at the end of each step, except for oscillations over part of the range, showing that the 25 second hold period is sufficient. A comparison to the Bankoff data is shown in Figure B.18-5. All points lie on the correlation curve for $H^*_g{}^{1/2}/C$ values above 0.6. For values less than this the response lies below the correlation curve.

Figure B.18-6 shows a comparison of predicted versus measured values of $H^*_f{}^{1/2}/C$. This Figure of Merit shows that values are generally within a 7% band, except for the cluster of points that do not line up with the correlation in Figure B.18-5, i.e. those points below with $H^*_g{}^{1/2}/C$ below 0.6.

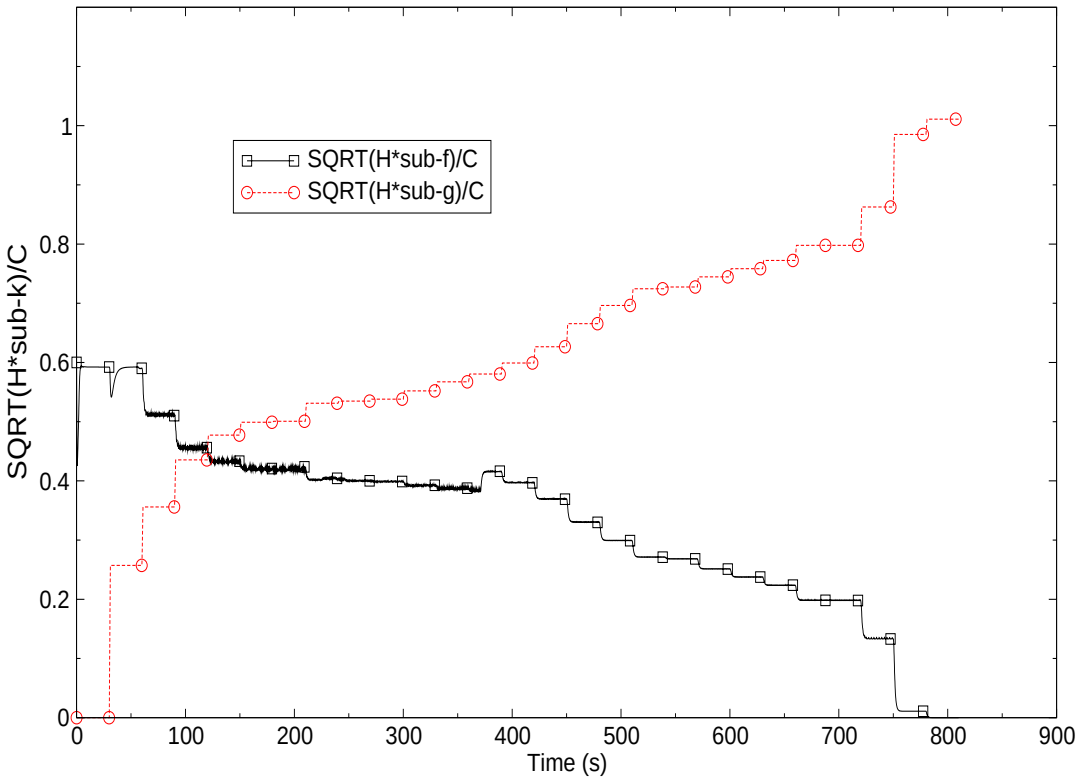

Figure B.18-4. Liquid and Gas Dimensionless Superficial Velocities

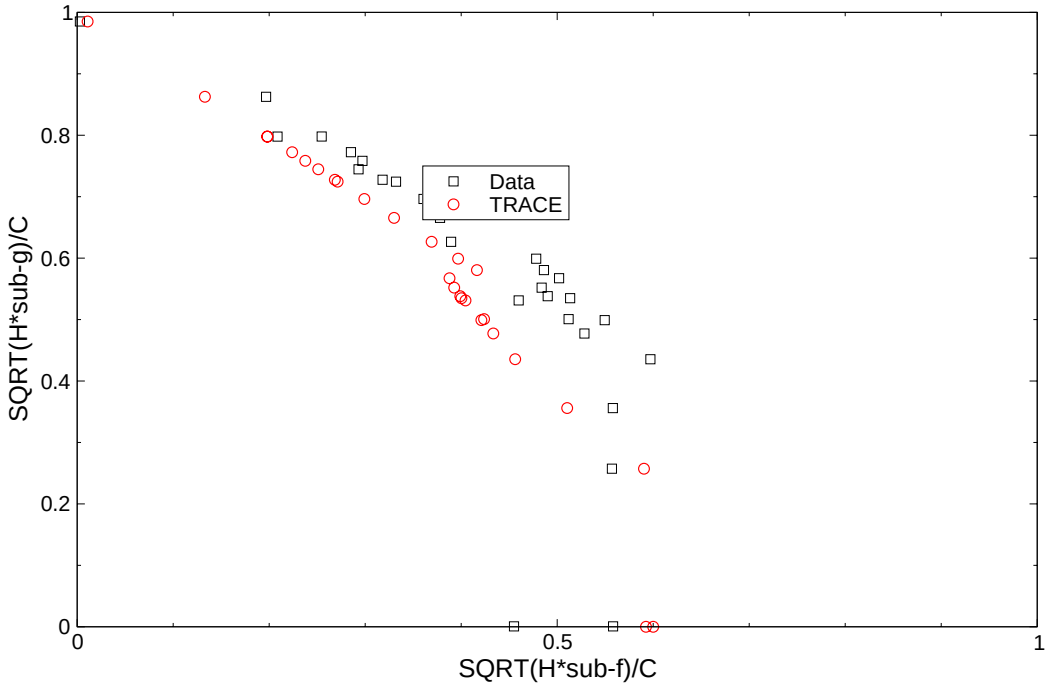

Figure B.18-5. Comparison of TRACE Calculated Velocities to Bankoff Data

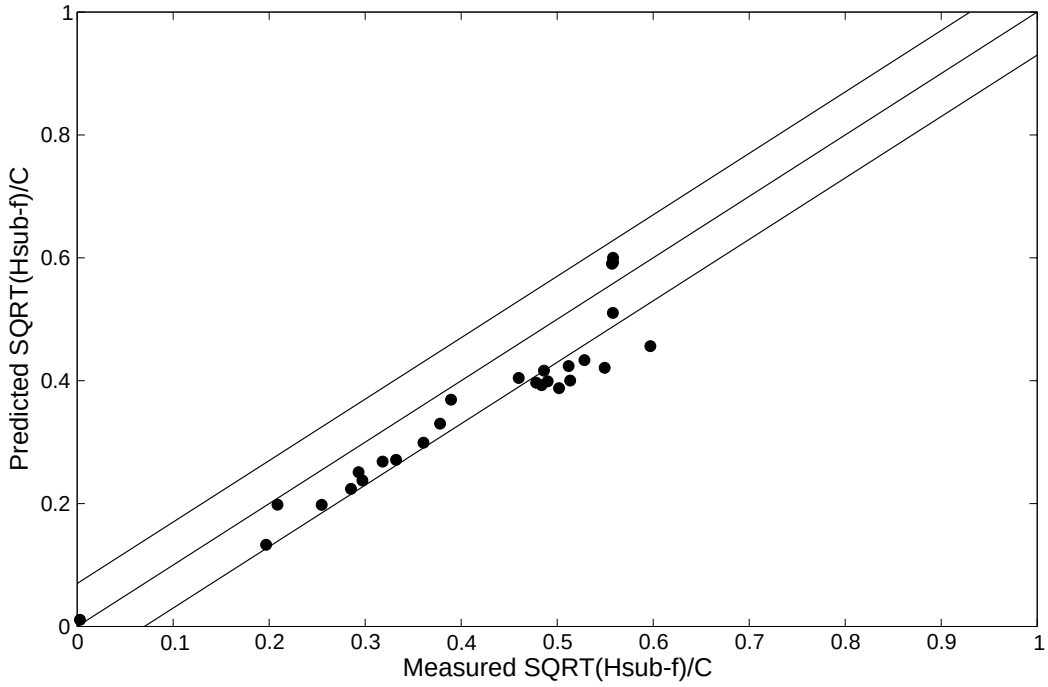

Figure B.18-6. Figure of Merit for Air/Steam CCFL Simulation

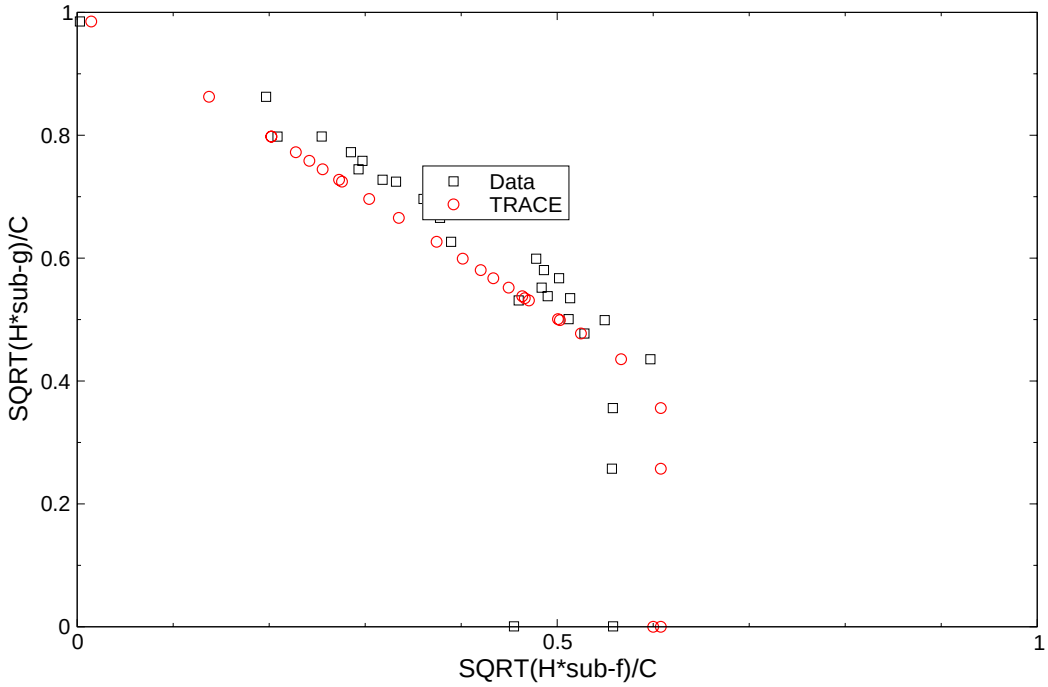

Figure B.18-7. Comparison of TRACE Calculated Velocities to Bankoff Data for Saturated Steam Case

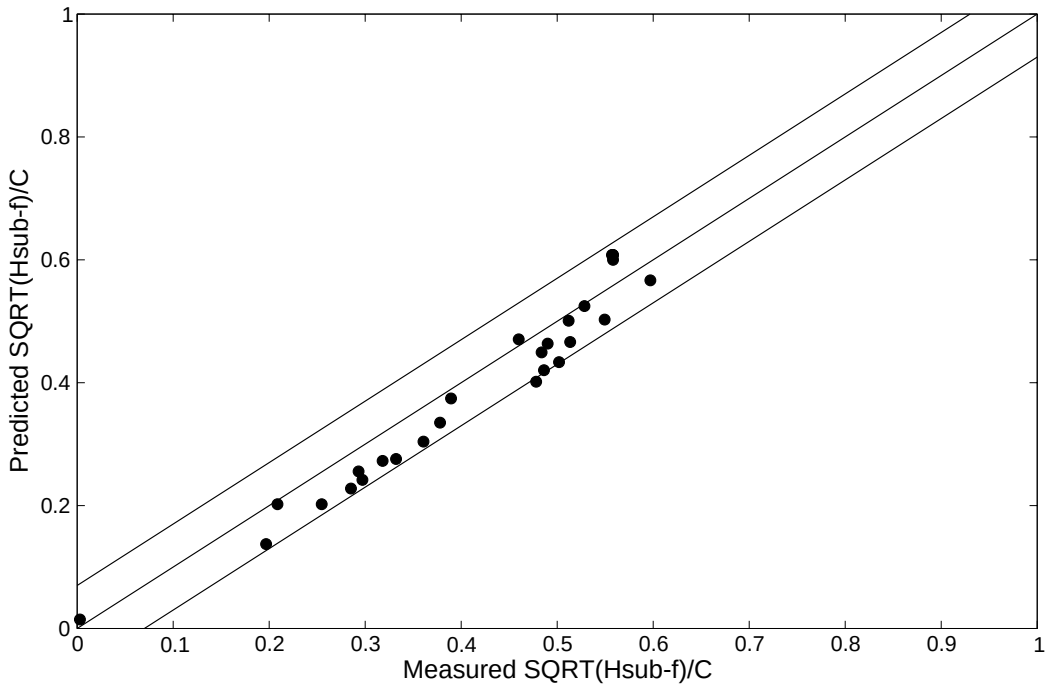

Figure B.18-8. Figure of Merit for Saturated Steam CCFL Simulation

The simulation was run again with saturated steam as the injected gas in place of air. Figure B.18-7 shows a comparison to the Bankoff data. In this case, where there is sufficient liquid flow, all points lie on the correlation line. Figure B.18-8 shows the Figure of Merit for the saturated steam case. In this case all points are very close to being within the 7% error band.

B.18.5. Assessment Results Summary

The assessment shows that TRACE can predict the air/water countercurrent flow data for the 15-hole plate over a significant range of air flows. The predictions are better when saturated steam is used as the gas instead of air. There were more oscillations in the response when air was used and this may contribute to the degradation of the comparison.

Applications involving reflood, where CCFL can be an important phenomenon, will not involve significant amounts of non condensable gases. When steam is used as the gas, the comparisons to data are very good and within the correlation error band.

B.18.6. References

1 S. G. Bankoff, R. S. Tankin, M. C. Yuen and C. L. Hsieh, "Countercurrent Flow of Air/Water and Steam/Water Through a Horizontal Perforated Plate", Int. J. Heat Mass Transfer, Vol. 24, No. 8 pp 1381-1395, 1981.

2 C. L. Hsieh, S. G. Bankoff, R. S. Tankin, and M. C. Yuen, "Countercurrent Air/Water and Steam/Water Flow above a Perforated Plate", NUREG/CR-1808, November 1980.

3 3I. Dilber, S. G. Bankoff, R. S. Tankin, M. C. Yuen, "Countercurrent Steam/Water Flow Above a Perforated Plate-Vertical Injection of Water", NUREG/CR-2323, September 1981.I. Dilber, S. G. Bankoff, R. S. Tankin, M. C. Yuen, "Countercurrent Steam/Water Flow Above a Perforated Plate-Vertical Injection of Water", NUREG/CR-2323, September 1981.

4 J. C. Lin, V. Martinez and J. W. Spore, "TRAC-PF1/MOD2 Developmental Assessment Manual", Los Alamos National Laboratory, TRAC DAM-Ver. 5.4, August 20, 1993.

Condensation Tests

B.19. UCB-Kuhn Condensation Tests

Authors: Claudio Delfino and Dean Wang

Affiliation: Information Systems Laboratories, Inc.

Code Version: TRACE V5.0

Platform and Operating System: Intel x86, Windows XP

B.19.1. Introduction

Condensation in the presence of non-condensable gases inside vertical tubes is an important process in several reactor system components during LOCA transients. Condensation within the tubes of passive containment cooling condensers (PCCCs) such as those in the ESBWR design are driven by natural circulation and remove heat from the primary system. In order to assess the ability of TRACE to predict in-tube condensation heat transfer in the presence of non-condensable gases, experiments reported by Kuhn et al. (References 1 and 2) were modeled and simulated. This section describes the tests, referred to as the UCB-Kuhn tests, the TRACE models and comparison of predicted and measured condensation heat transfer coefficients.

Initial assessment against the UCB-Kuhn data was performed using earlier versions of TRACE and reported by Delfino for Test Series 1 and 2 (Reference 3), and by Wang for Test Series 3 and 4 (Reference 4). The assessment described here used TRACE Version 5.0 and covers all four Test Series. The following subsections describe the UCB-Kuhn tests and the TRACE input model. Simulations of the tests and comparison to applicable data follow.

B.19.2. UCB Test Facility Description

The UCB condensation experimental apparatus consists of six different systems, namely the steam and gas supply, condenser test section, condenser end section, cooling systems, instrumentation, and data acquisition system. The purpose of the test was to provide data for film condensation of downward flowing mixtures of steam and non-condensable gases inside vertical tubes to support design of the PCCS for the Simplified Boiling Water Reactor (SBWR). The condenser section is shown in Figure B.19-1. The mixture of steam and non-condensable gases was directed downward through the condenser section. Condensation occurred as heat was removed from the gaseous mixture through the condenser tube wall (O.D. = 50.8 mm, I.D. = 47.5 mm) by an upward flow of cooling water in the outer annulus. The test section was cooled over a length of 2.418 m.

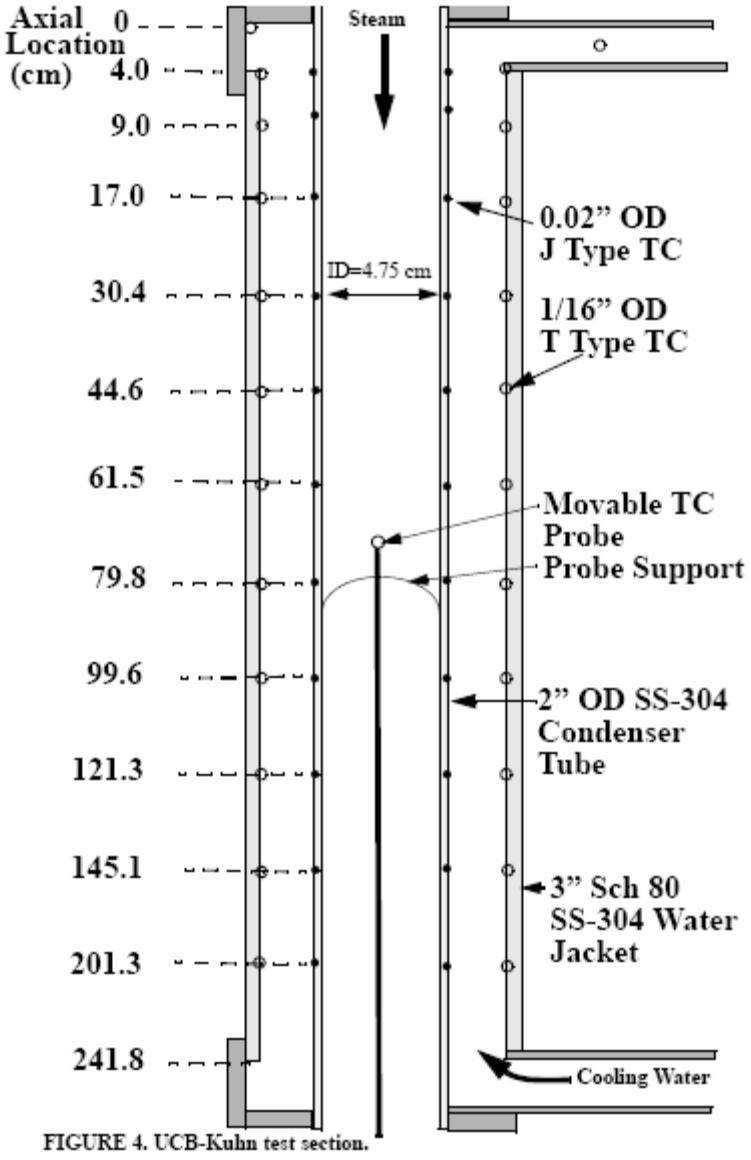

Figure B.19-1. Test Section (not to scale)

B.19.3. TRACE Model Description

A schematic of the TRACE model for the UCB test section is shown in Figure B.19-2 It consists of four components, a "FILL", a "PIPE", a "BREAK" and a "HTSTR", in a vertical configuration.

The flow is directed downward from the inlet "FILL 1" to the outlet "BREAK 3". For each run, the "FILL 1" component specifies the flow rate and the non-condensable gas partial pressure at the inlet. The non-condensable gas partial pressure is calculated based on the steam and gas mass flow rates as shown below.

From Dalton's law of partial pressures, and by the perfect gas law, we have

$$P = P_s + P_g = \frac{m_s R_s T}{V} + \frac{m_g R_g T}{V} \tag{19-1}$$

and

$$P_g = \frac{P}{1 + \frac{P_s}{P_g}} = \frac{P}{1 + \frac{m_s R_s}{m_g R_g}} \tag{19-2}$$

where,

P: total pressure
T: temperature
P_g: gas partial pressure
P_s: steam pressure
M_s: steam mass (mass flow rate used)
M_g: gas mass (mass flow rate used)
R_s = 462 J/kg
R_g = 286 J/kg (air)

"PIPE 2" is divided into fifteen computational cells. Twelve cells model the UCB test section. Three additional cells at the outlet avoid perturbations in the test section due to the "BREAK 3" exit conditions.

A "HTSTR" is connected to "PIPE 2" in order to model the condenser wall. "HTSTR 4" component is divided in twelve cells coupled with the twelve hydraulic cells of "PIPE 2", along the test section length. The nodalization was specified so that the cell centers are aligned with the thermocouple elevations. The axial temperature profiles from the experiments are enforced as boundary conditions on the outer surface of the "HTSTR 4" component. It should be noted that the outer surfaces at 5.15 cm of "HTSTR 4" used the same temperatures as those at 17 cm in the TRACE inputs because there are no experimental temperature data available at 5.15 cm. A sensitivity analysis for Run 4.3-3 indicated that this treatment had no significant effect on results except for the first cell of the pipe as shown in Figure B.19-3 This also applies to the other test cases. An additional noding sensitivity analysis also showed that a 12-cell model for the test section is adequate, as shown in Figure B.19-4.

In order to provide for a consistent comparison between experimental and code-calculated quantities, a set of TRACE "signal variables" and "control blocks" was developed in the TRACE input files. The experimental heat transfer coefficient (HTC) was calculated as the ratio of the heat flux over the difference between the saturation temperature (at the local vapor partial pressure) and the wall temperature. Hence, a series of "post-processing" calculations is performed in TRACE, by user-specified control blocks, in order to output a HTC that would be obtained as the ratio between heat flux and temperature difference consistent with the test data reduction procedure.

Additional information on the TRACE input model is documented in Reference 5.

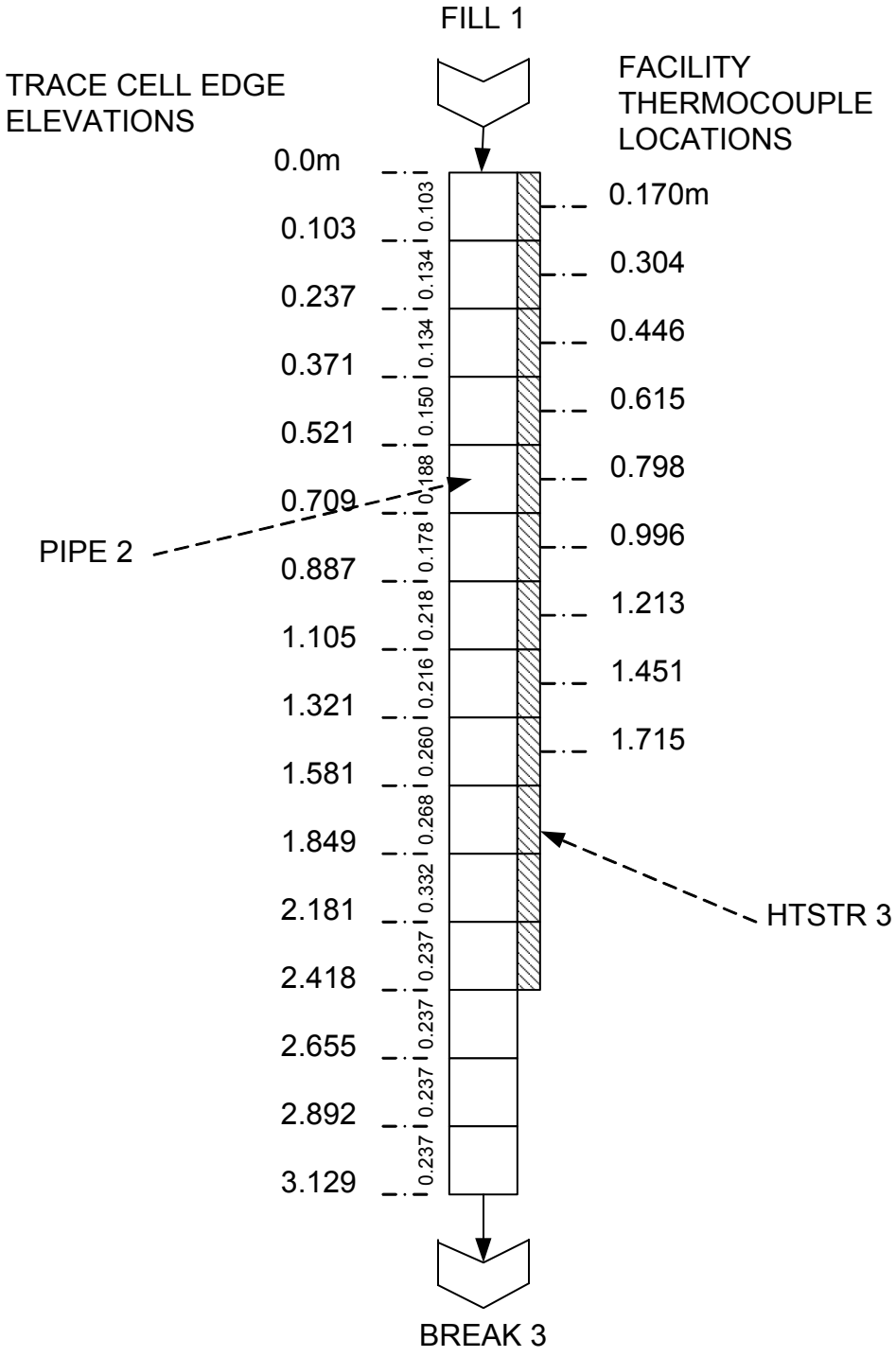

Figure B.19-2. TRACE Model of the UCB Condensation Test Section

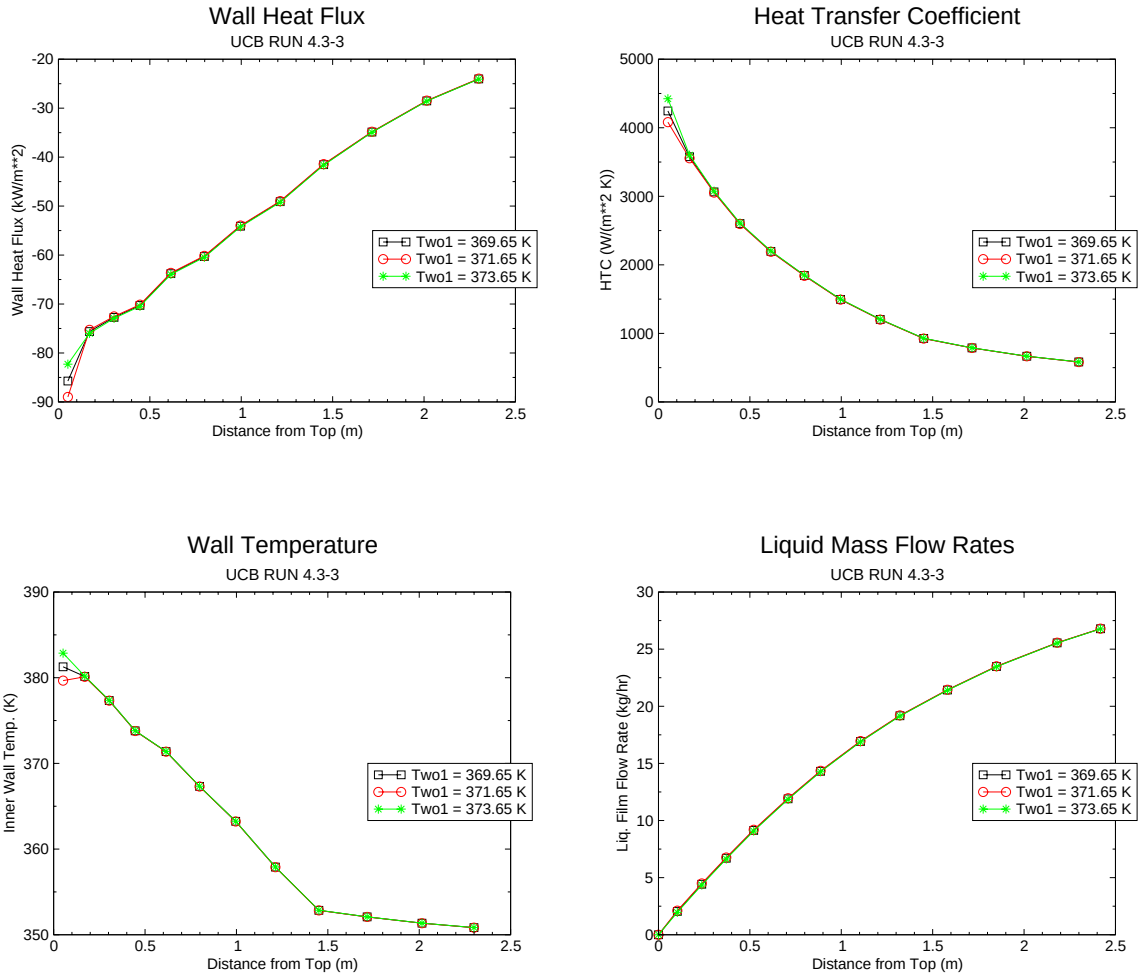

Figure B.19-3. Sensitivity Analysis of the Outer Surface Temperature of the First Cell of the Heat Structure for Run 4.3-3

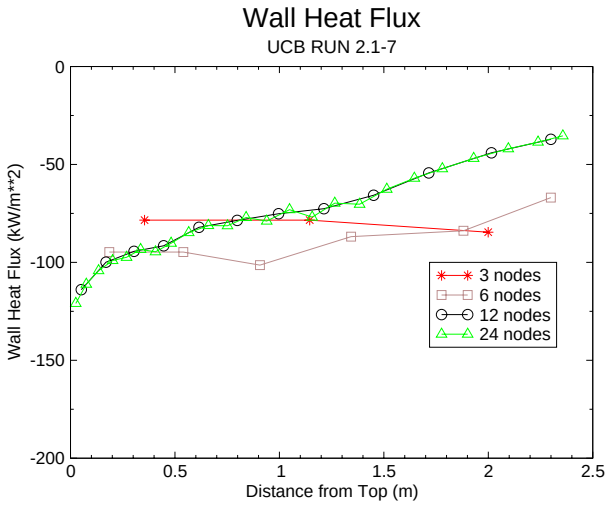

Figure B.19-4. Sensitivity Analysis of the axial profile of the wall heat flux upon the number of computational cells

B.19.4. Tests Simulated with TRACE

A total of 30 tests were selected for TRACE verification and assessment, as given in Table B.19.1 The assessment matrix includes condensation tests in laminar film mode at different pressures and for varying non-condensable (air) qualities, including cases involving pure steam. For all tests, the inlet mixture was in saturation conditions.

TRACE version 5.0 was employed to perform all the simulations for this task. The calculations were run in transient mode for a 50 second simulation time with maximum time step size of 0.1 s. The "null" transient plots were checked to make sure that the calculated variables were stabilized during the simulation. Figure B.19-5 reports the null transient plots of four key variables for Run 3.1-4. The null transient plots for the other tests are qualitatively similar and therefore not reported.

In the following pages, figures B.19-6 through B.19-35 illustrate the results of the assessment for all test cases. For each case, comparisons are made between predicted and measured axial profiles for heat flux, heat transfer coefficient, inner surface temperature, and liquid film flow rate. The values of parameters of interest in the figures for TRACE were taken at the end of the calculation.

Table B.19.1. Test Matrix for TRACE Verification and Assessment[a]

Run No.	Pressure (bar)	Inlet Steam Flow (kg/hr)	NC Gas Mass Fraction (%)
1.1-1	1	60	(pure steam)
1.1-2	2	60	(pure steam)
1.1-3R	3	60	(pure steam)
1.1-4R1	4	60	(pure steam)
1.1-5R1	5	60	(pure steam)
2.1-1	4	50	1
2.1-4	4	50	4
2.1-7	4	50	10
2.1-9	4	60	20
2.1-13	4	50	40
3.1-4	4	60	1
3.2-4	4	60	5
3.3-4	4	60	10
3.5-4	4	60	35
3.1-3	3	60	1
3.2-3	3	60	5
3.3-3	3	60	10
3.4-3	3	60	20
3.5-3	3	60	40
4.1-3	3	30	1
4.2-3	3	30	5
4.3-3	3	30	10
4.4-3	3	30	20
4.5-3	3	30	40
4.1-2	2	30	1
4.2-2	2	30	5
4.3-2	2	30	10
4.4-2	2	36	17
4.5-2	2	30	40
3.4-2	2	60	20

a. All values in the table are rounded. See Reference 1 for the actual figures.

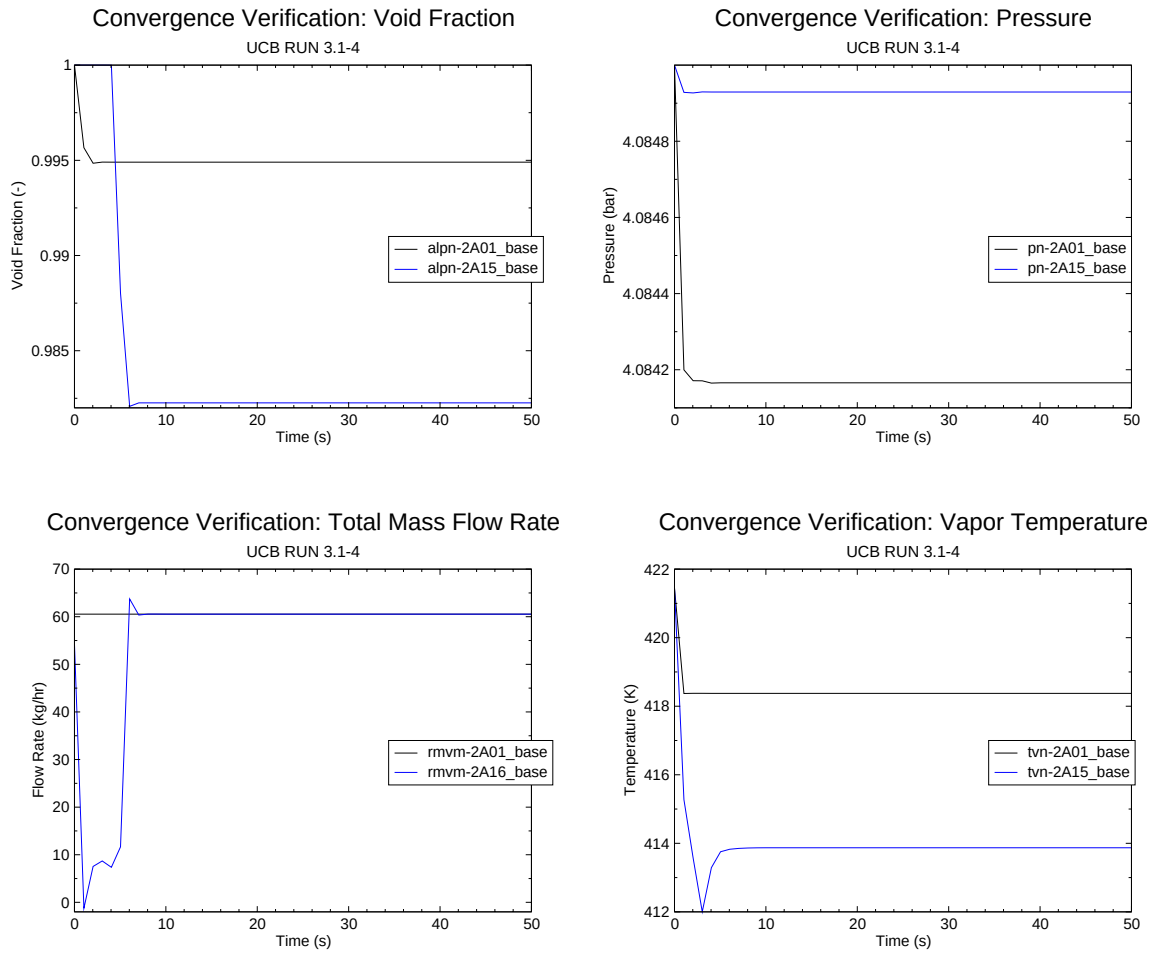

Figure B.19-5. Null Transient Plots for Run 3.1-4

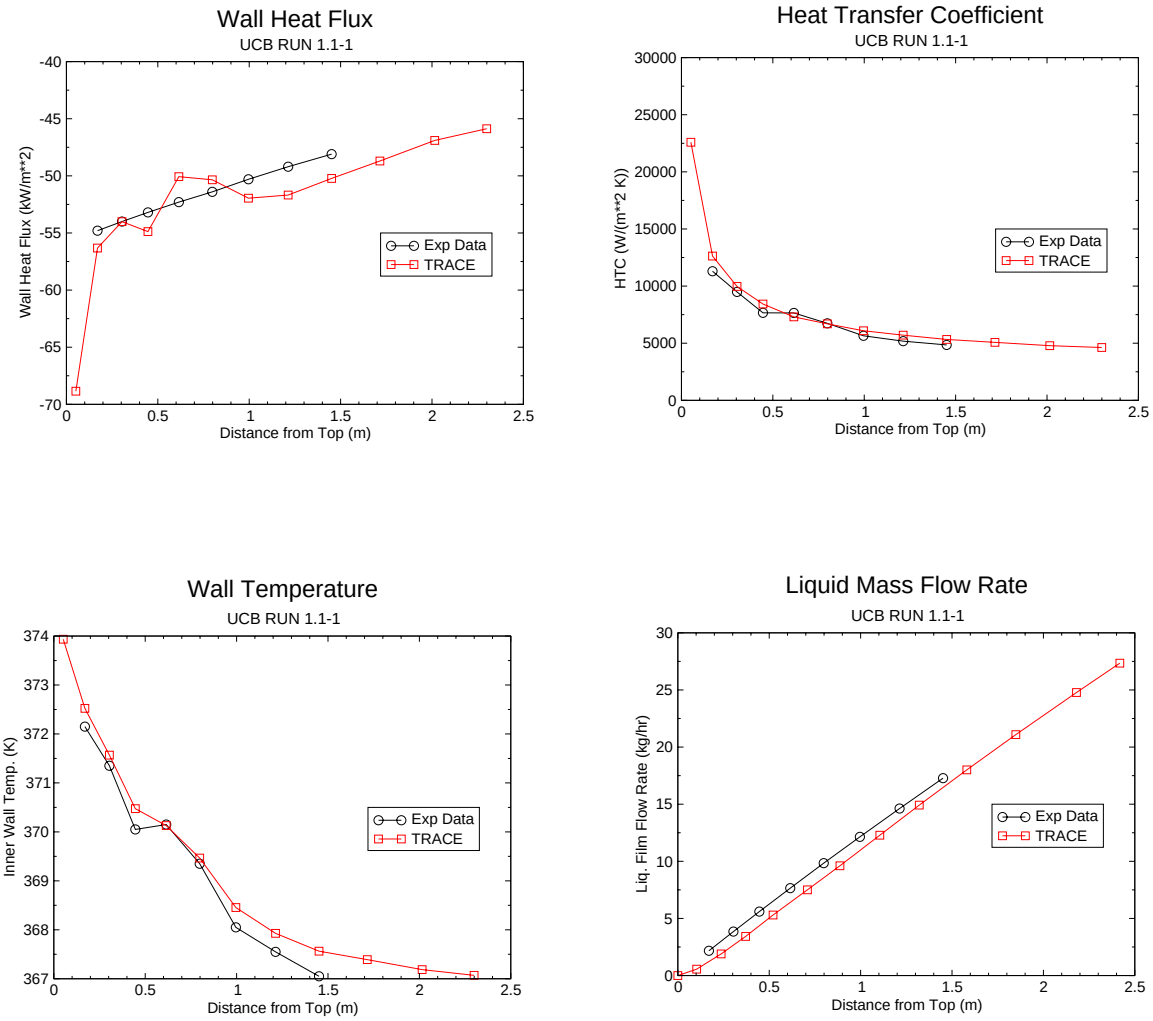

Figure B.19-6. TRACE Results for Run 1.1-1

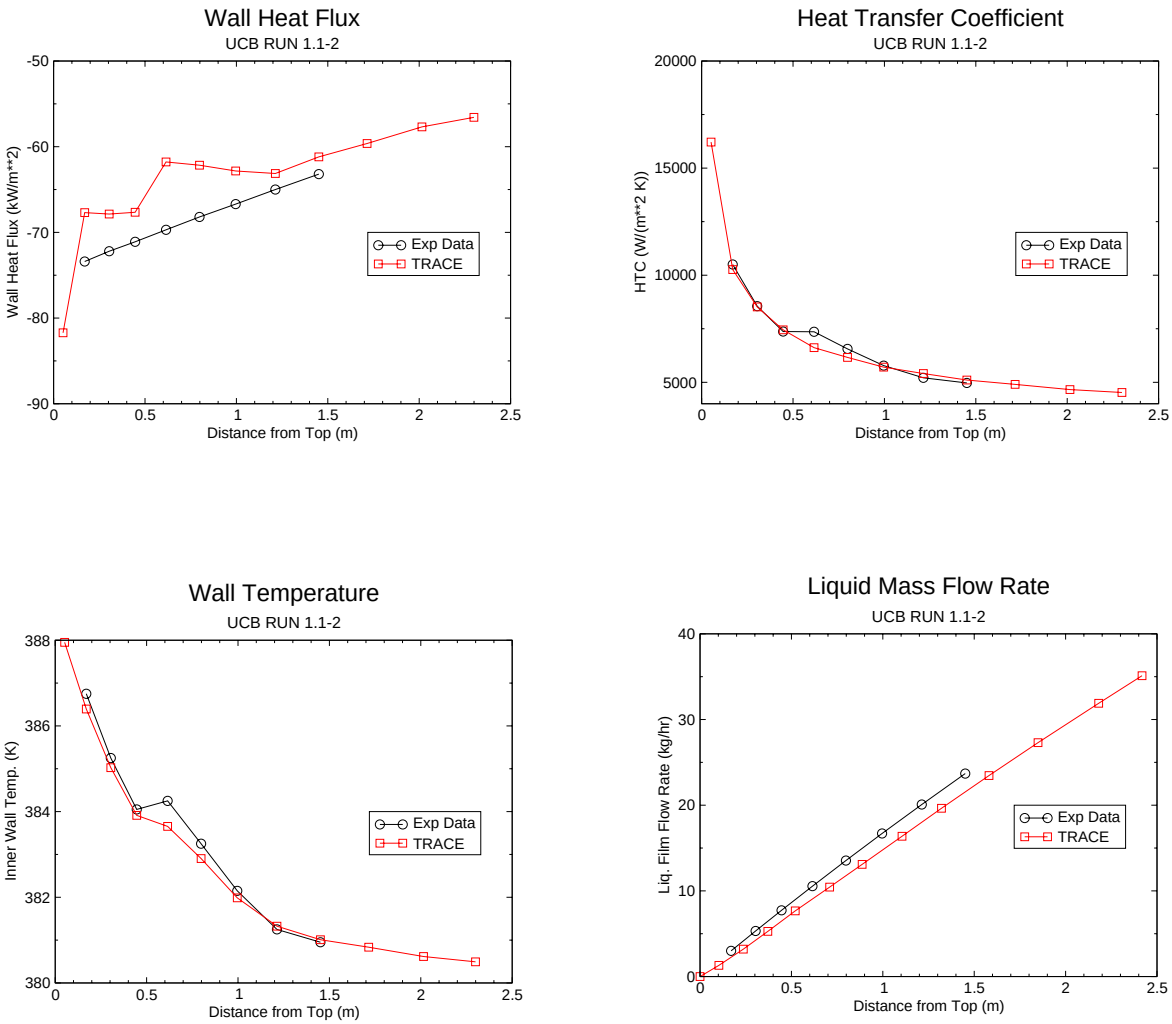

Figure B.19-7. TRACE Results for Run 1.1-2

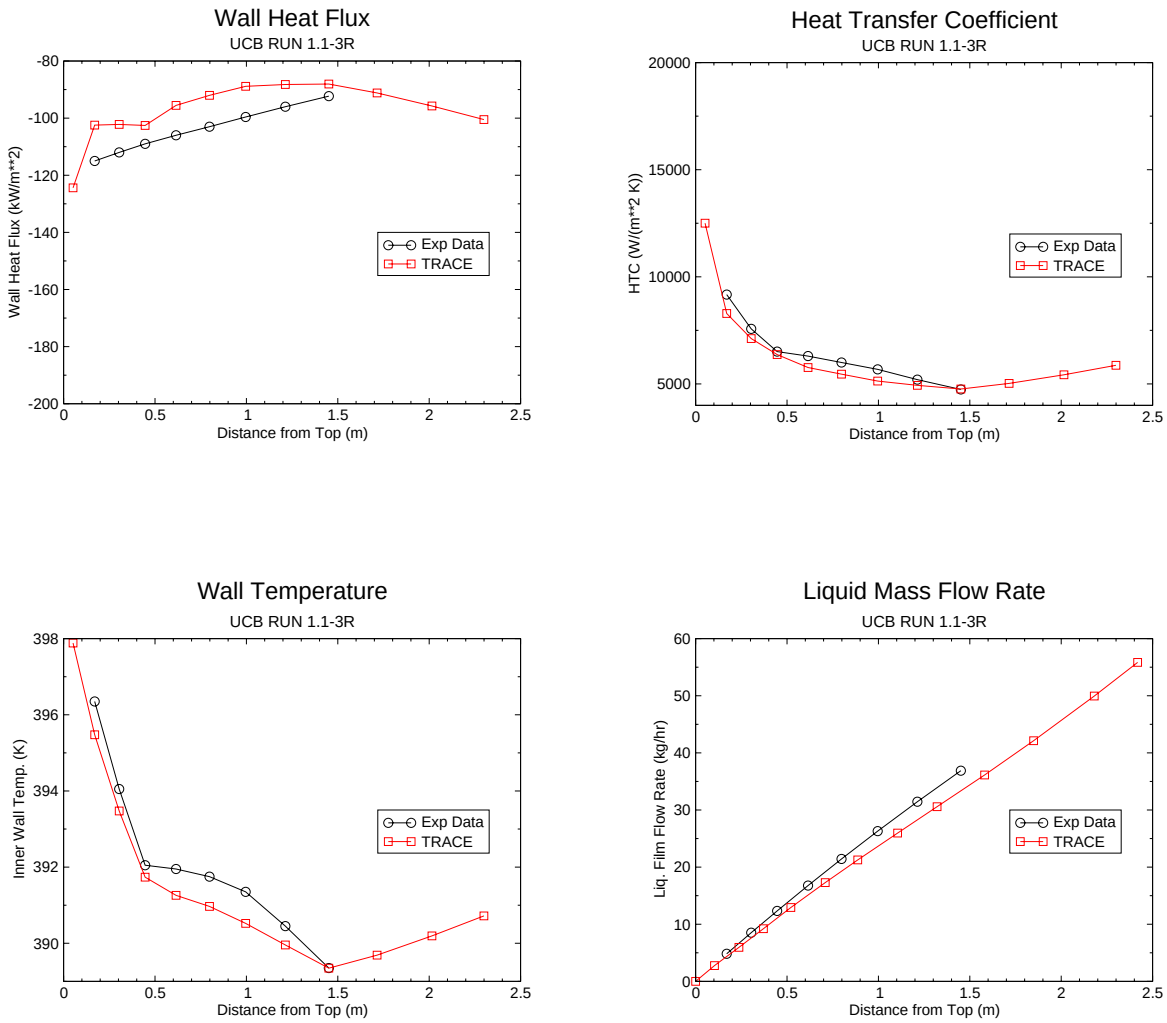

Figure B.19-8. TRACE Results for Run 1.1-3R

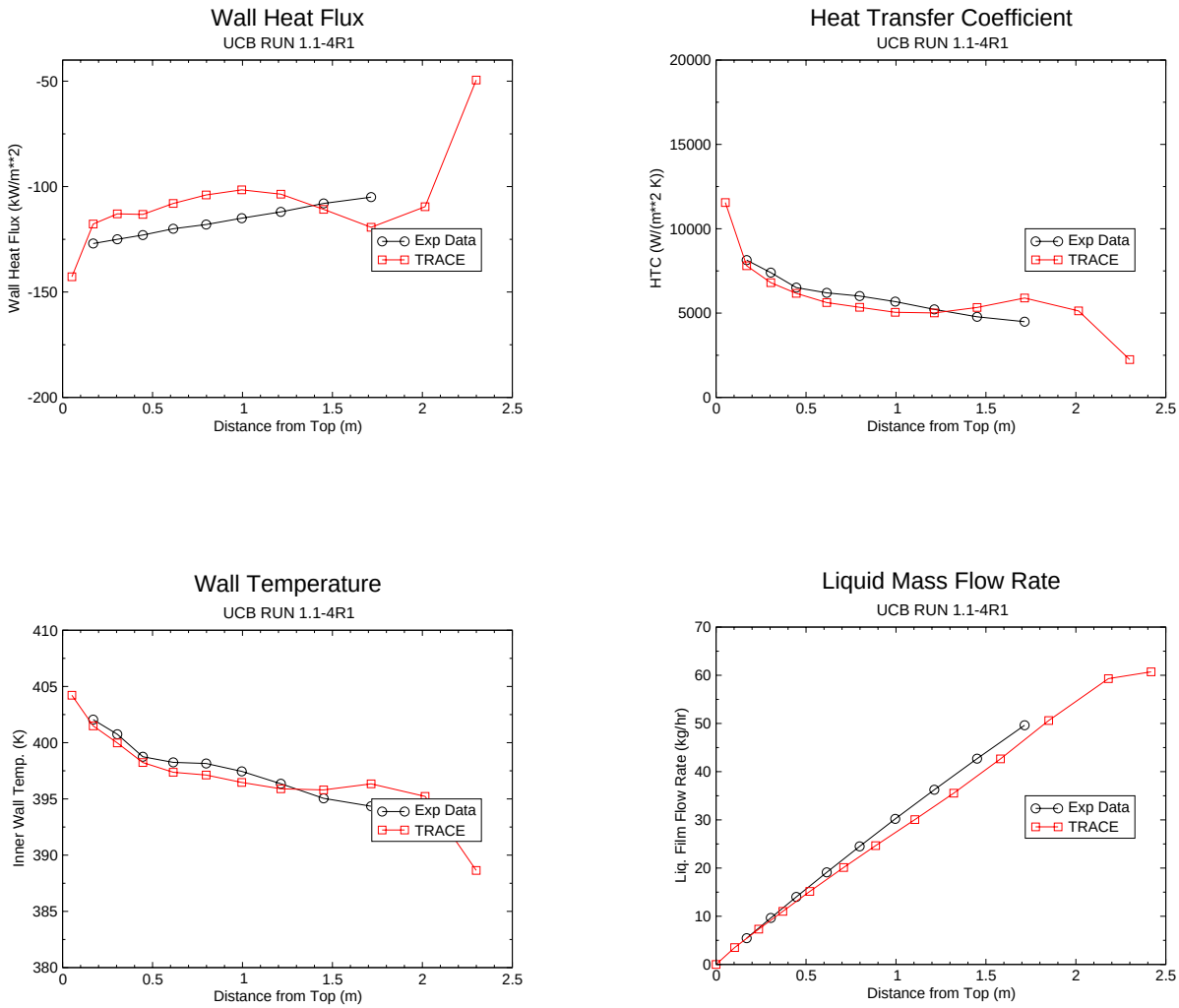

Figure B.19-9. TRACE Results for Run 1.1-4R1

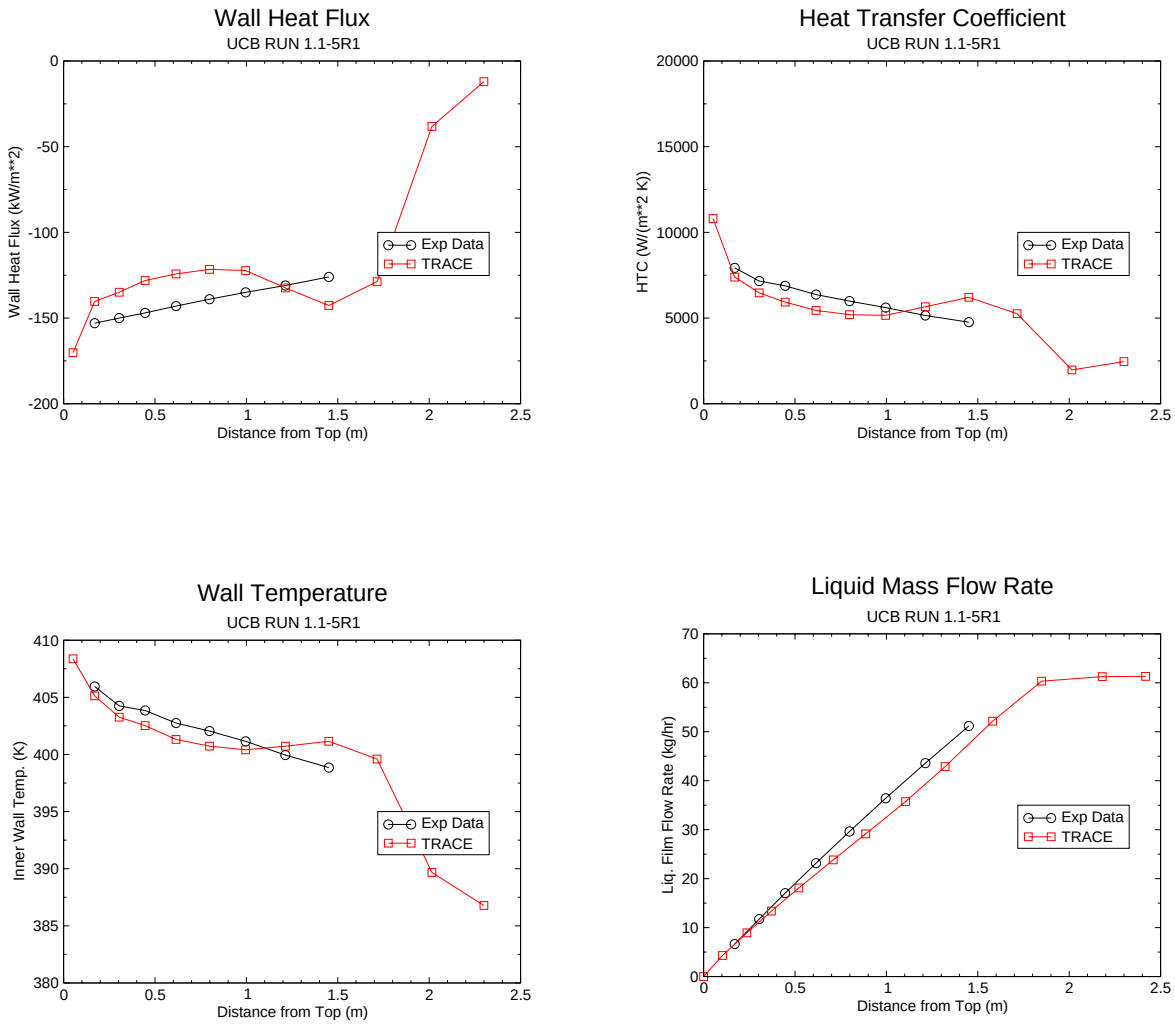

Figure B.19-10. TRACE Results for Run 1.1-5R1

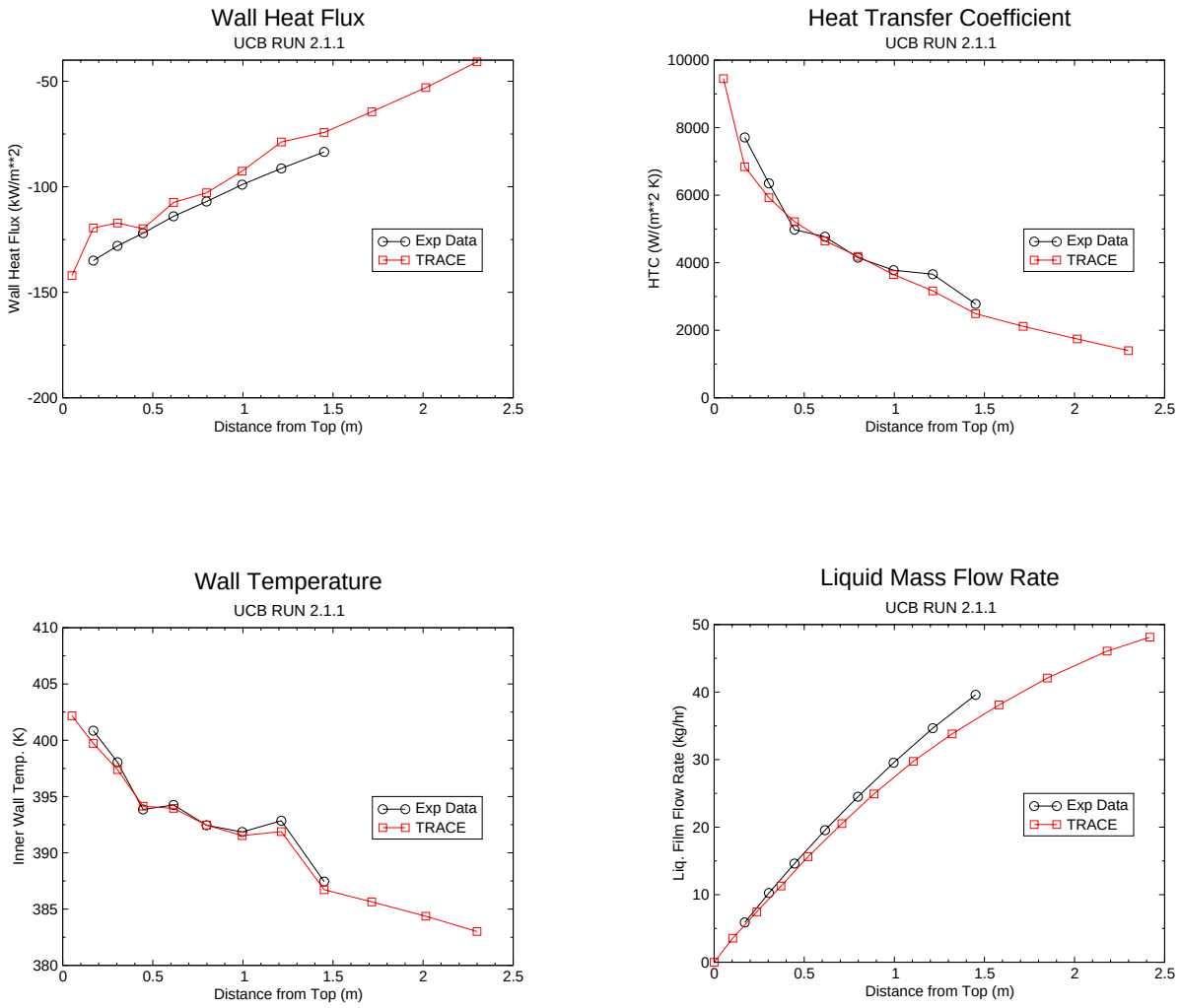

Figure B.19-11. TRACE Results for Run 2.1-1

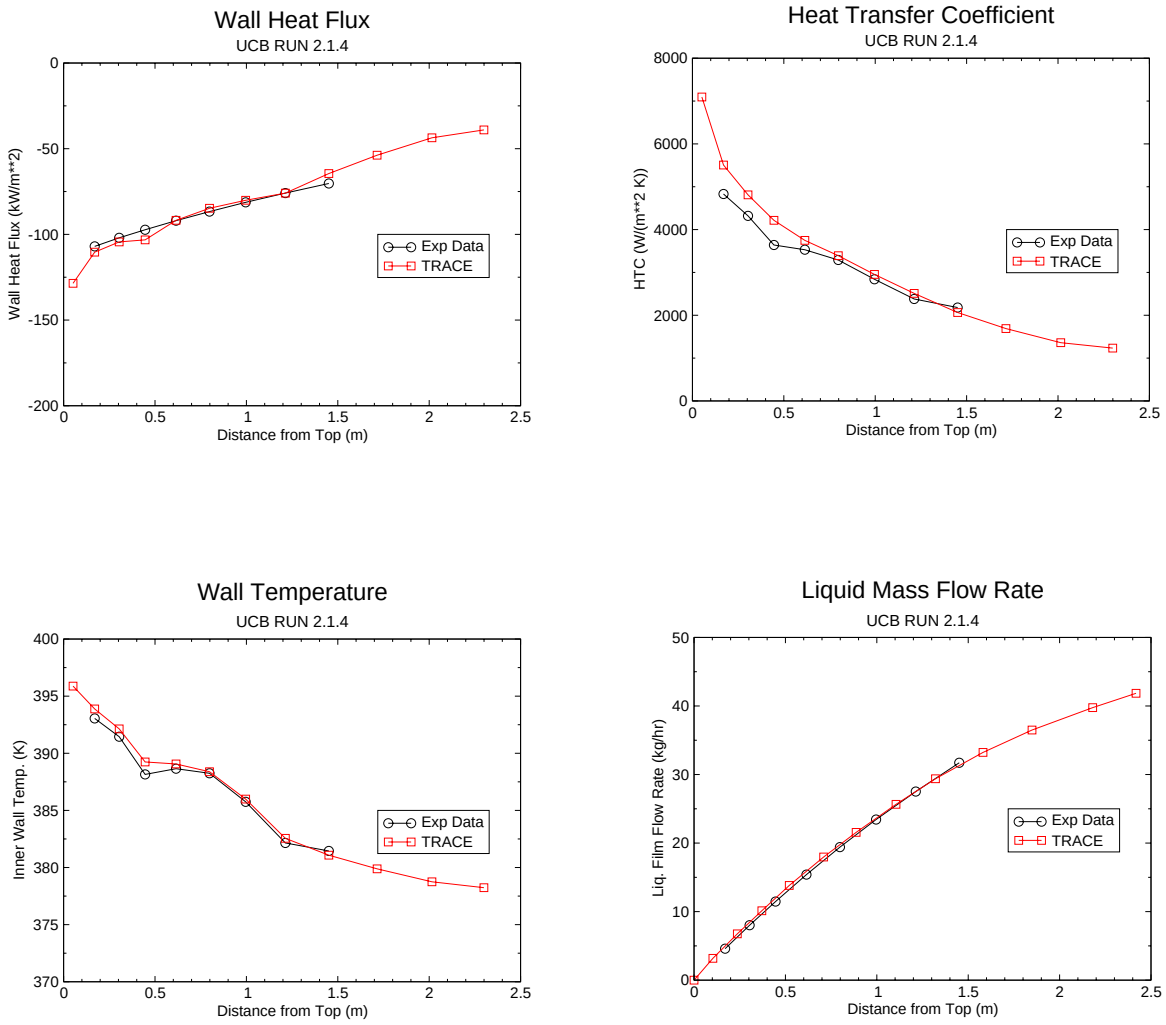

Figure B.19-12. TRACE Results for Run 2.1-4

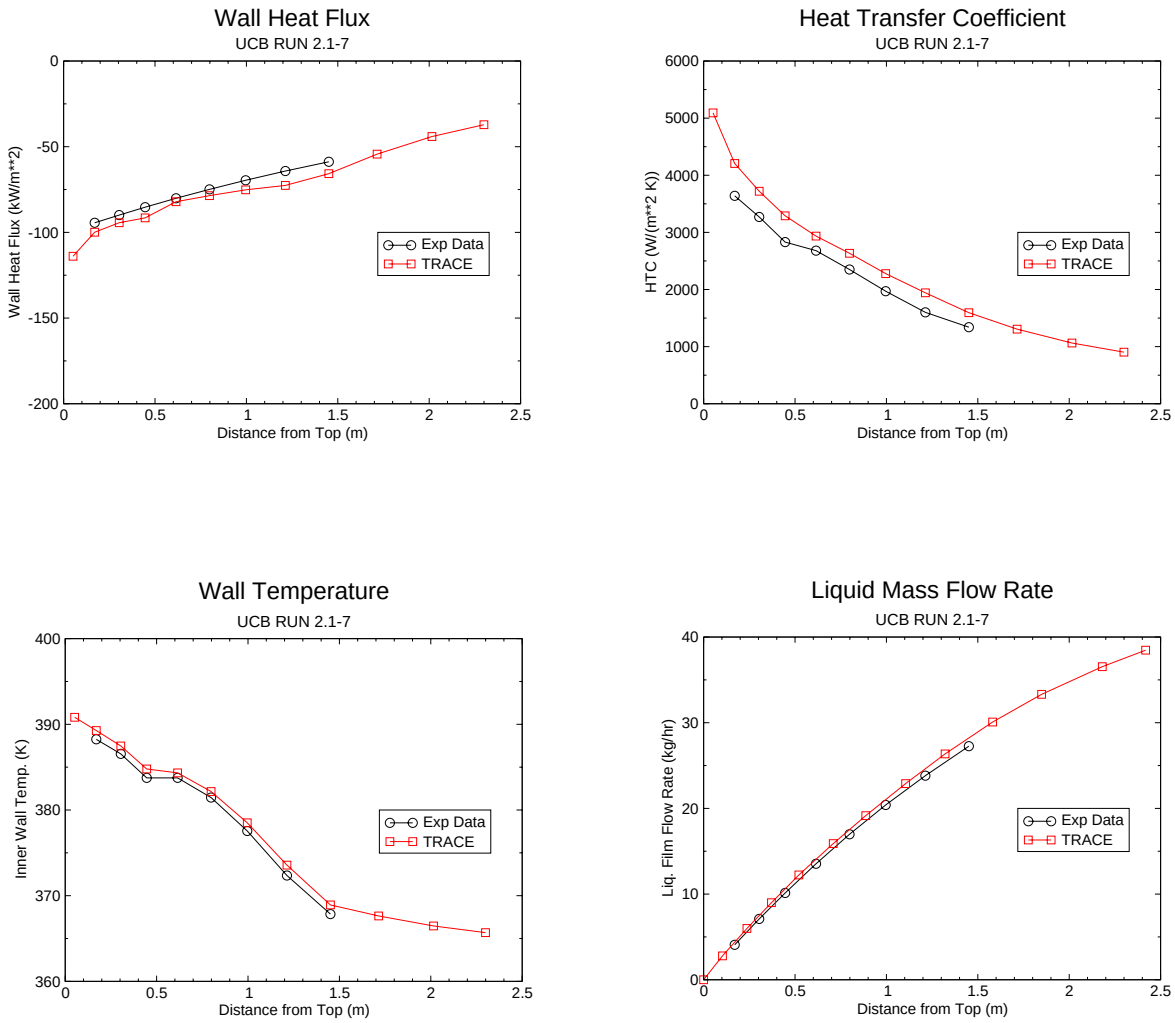

Figure B.19-13. TRACE Results for Run 2.1-7

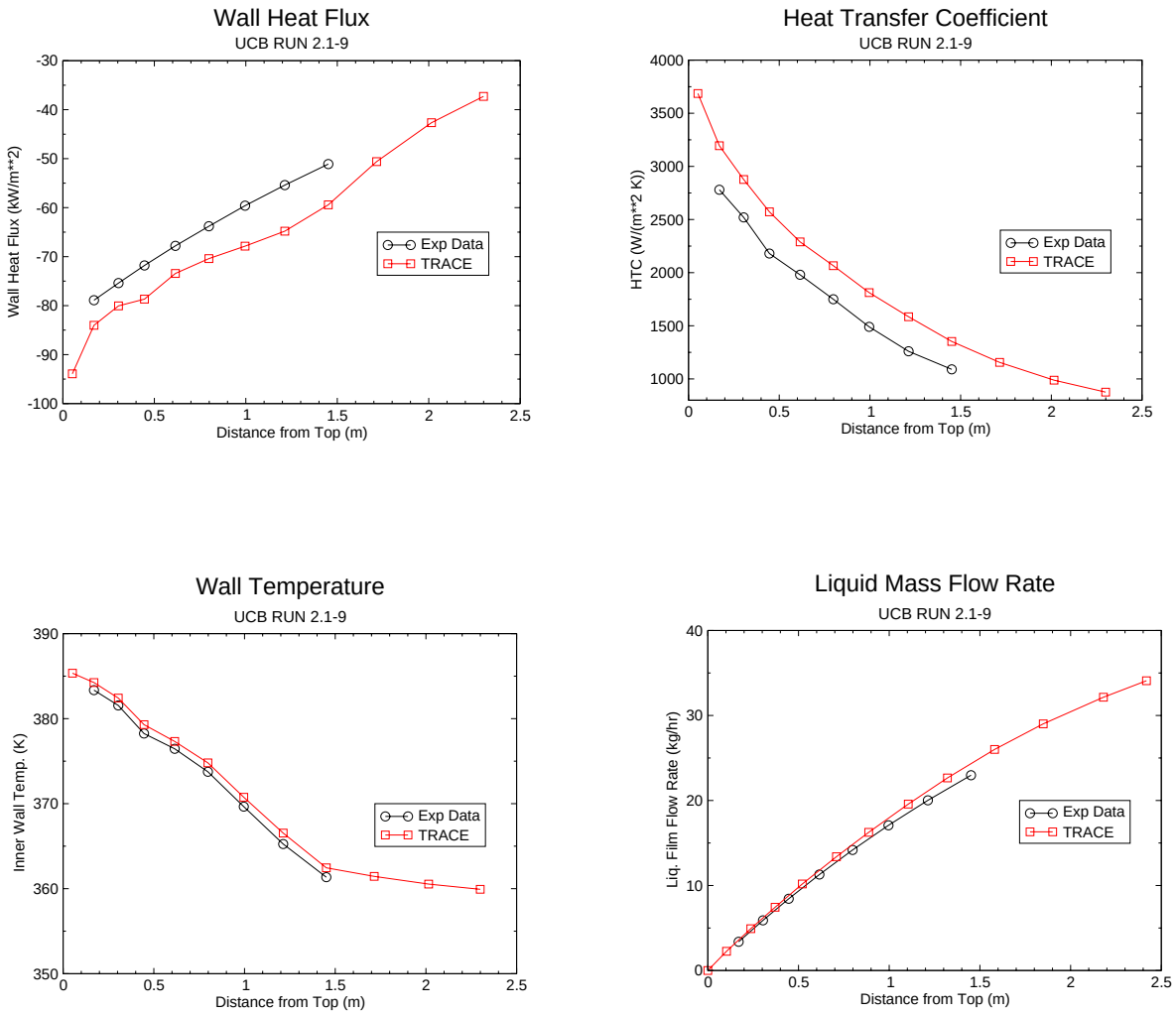

Figure B.19-14. TRACE Results for Run 2.1-9

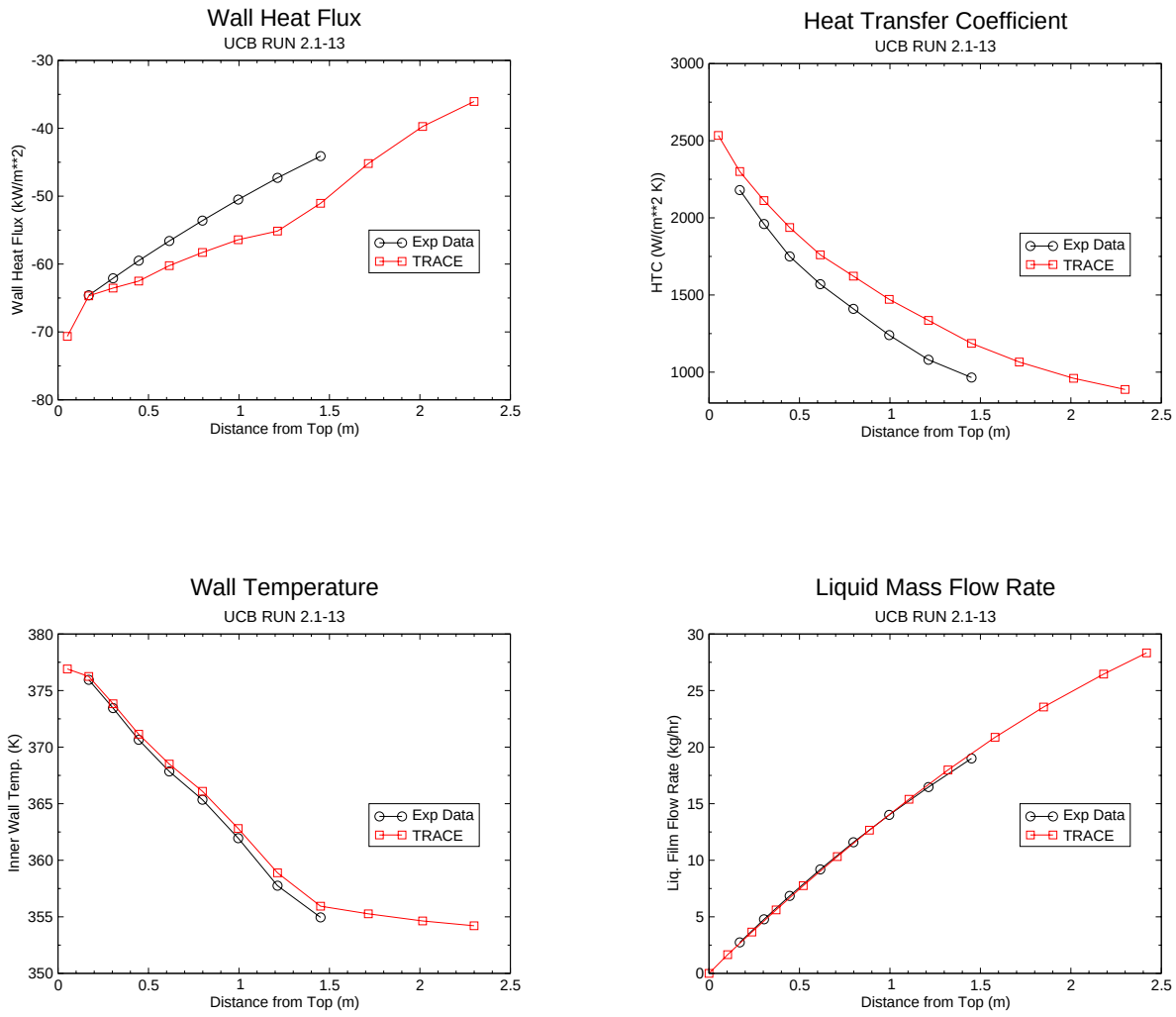

Figure B.19-15. TRACE Results for Run 2.1-13

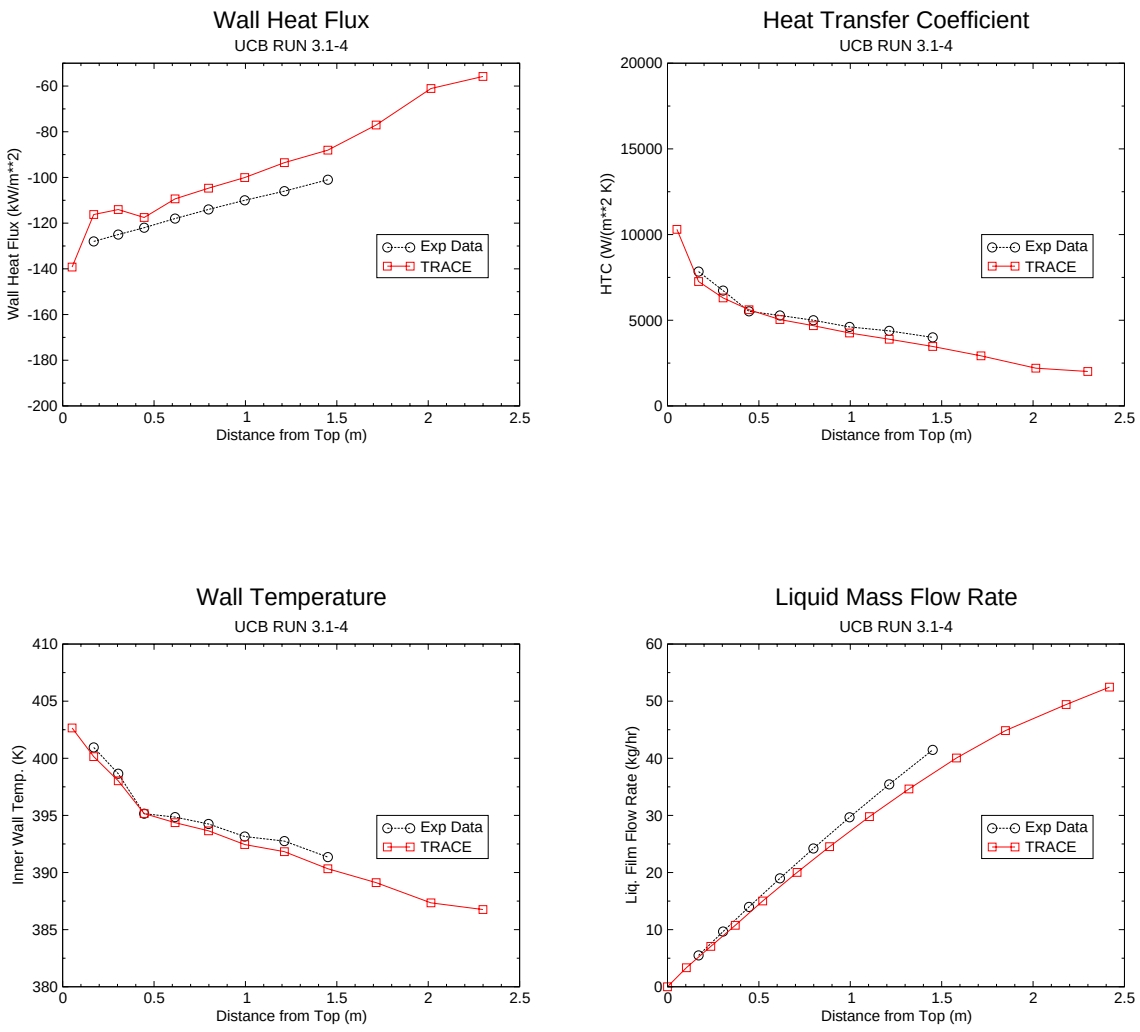

Figure B.19-16. TRACE Results for Run 3.1-4

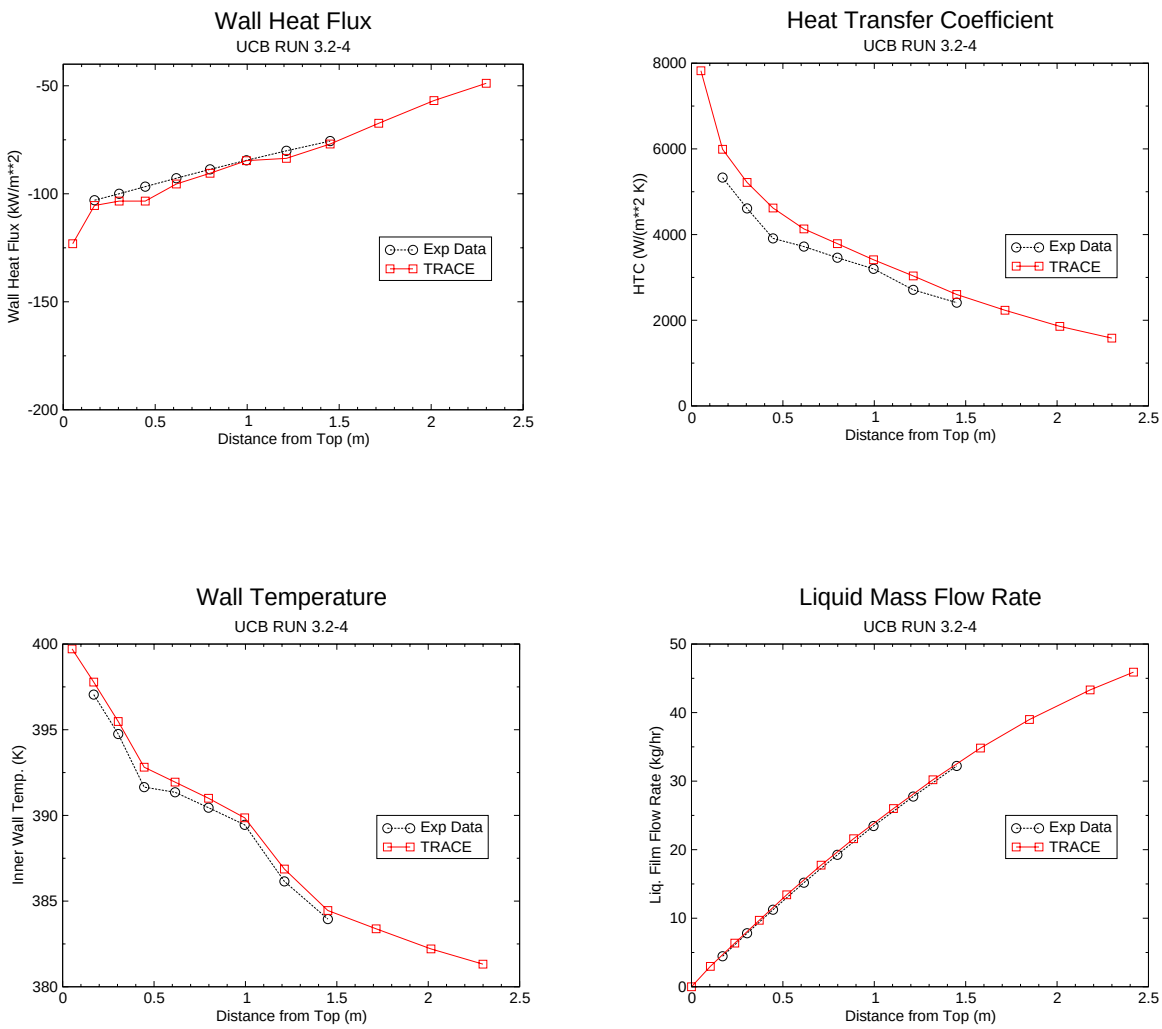

Figure B.19-17. TRACE Results for Run 3.2-4

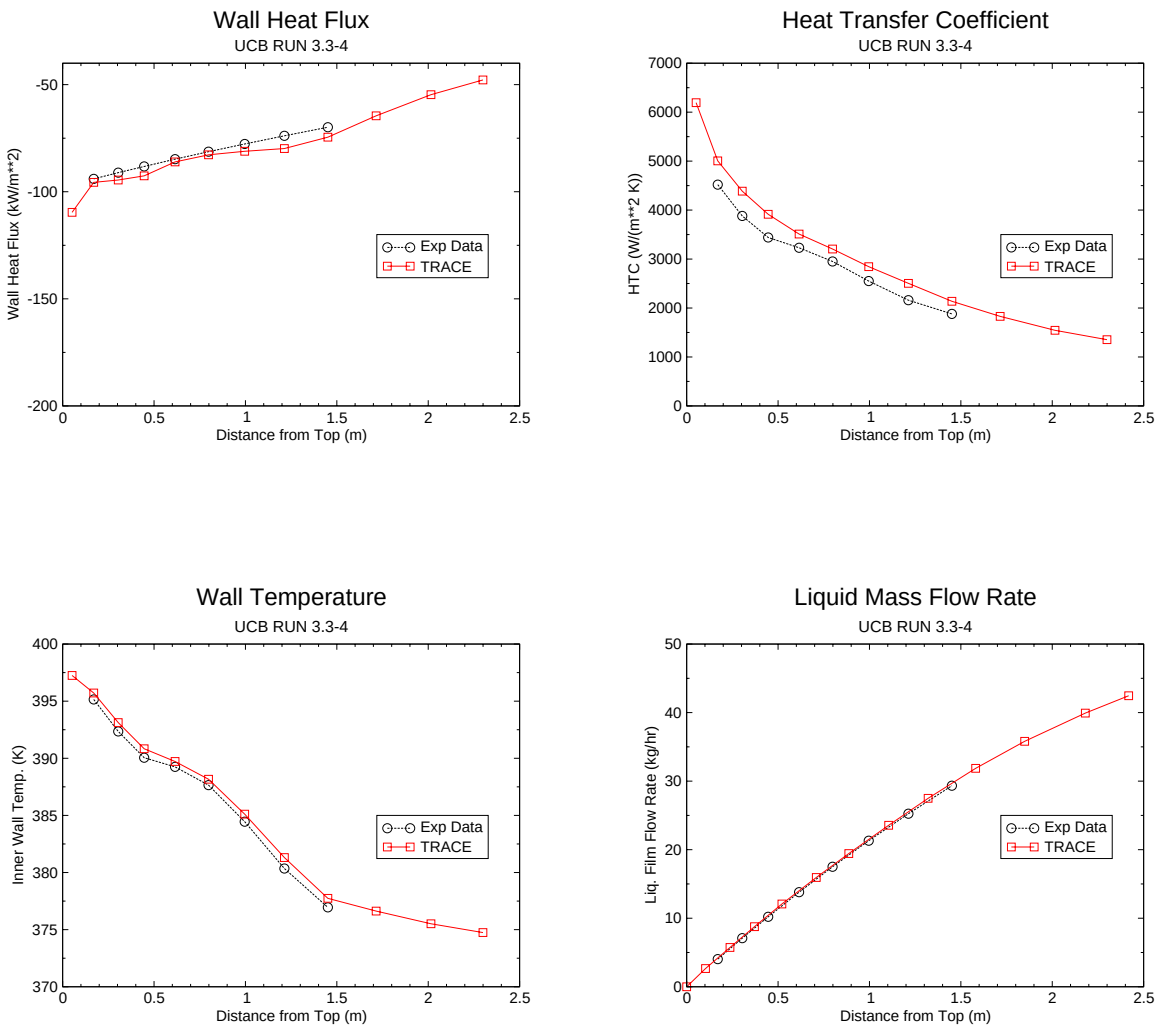

Figure B.19-18. TRACE Results for Run 3.3-4

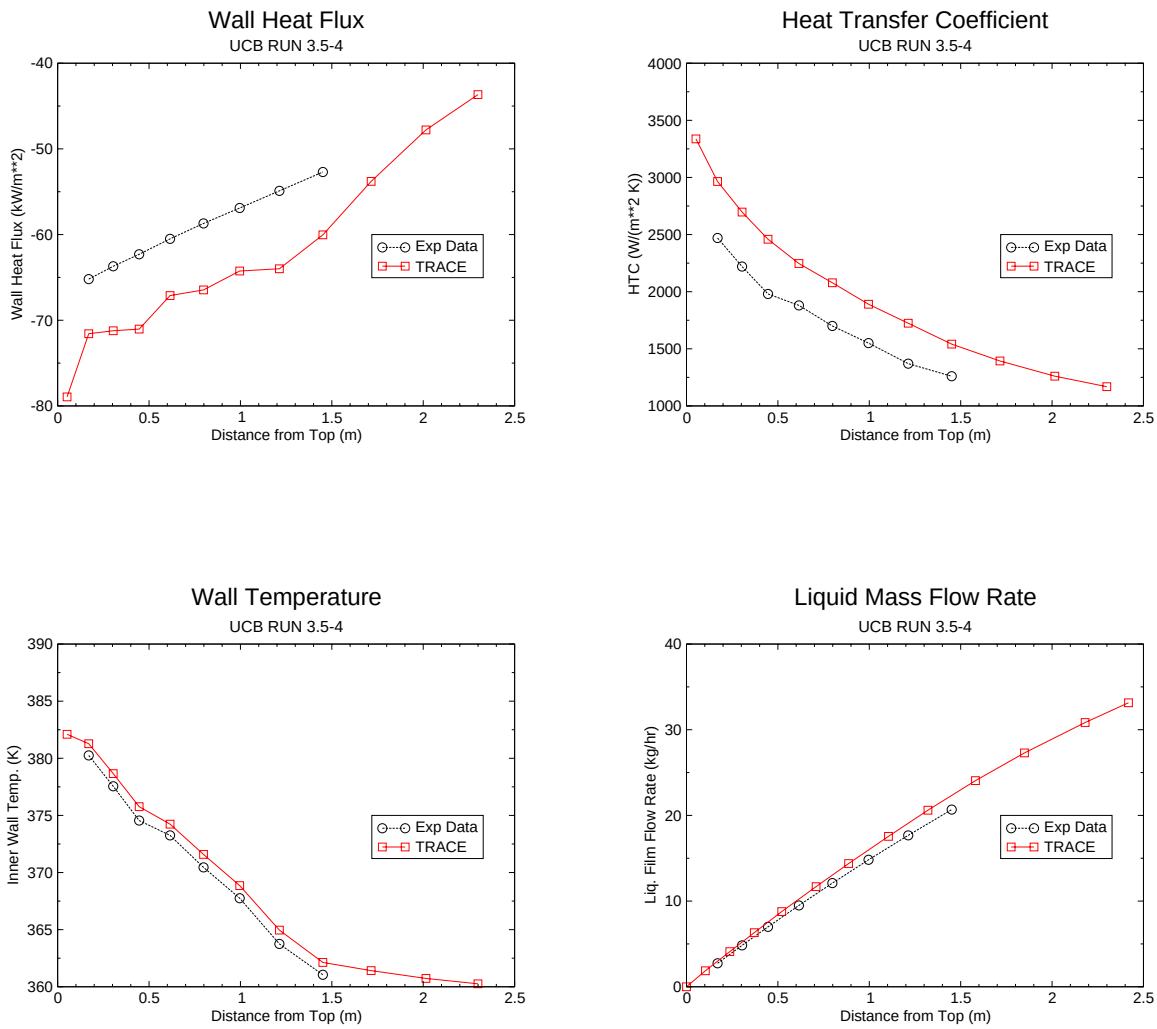

Figure B.19-19. TRACE Results for Run 3.5-4

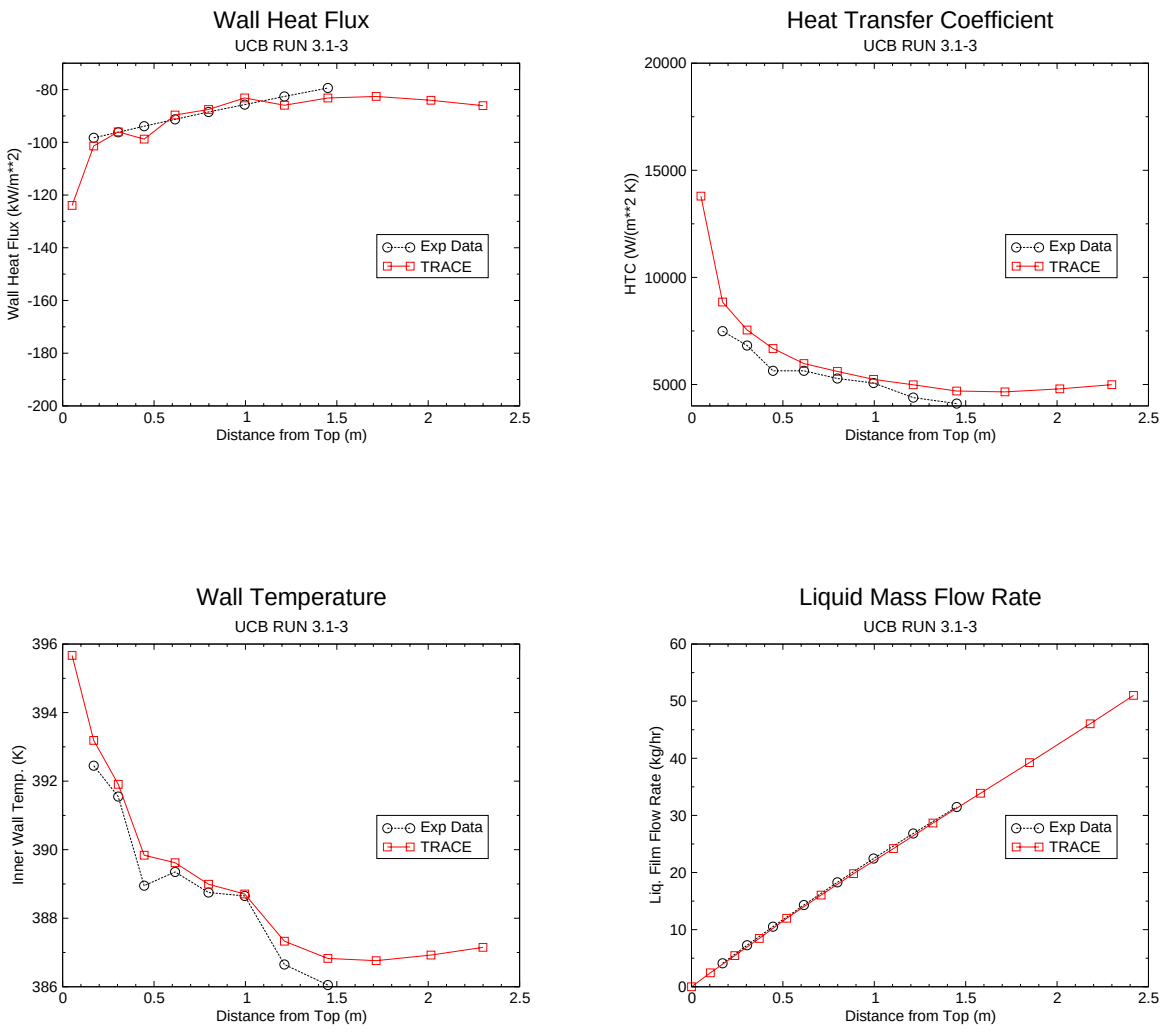

Figure B.19-20. TRACE Results for Run 3.1-3

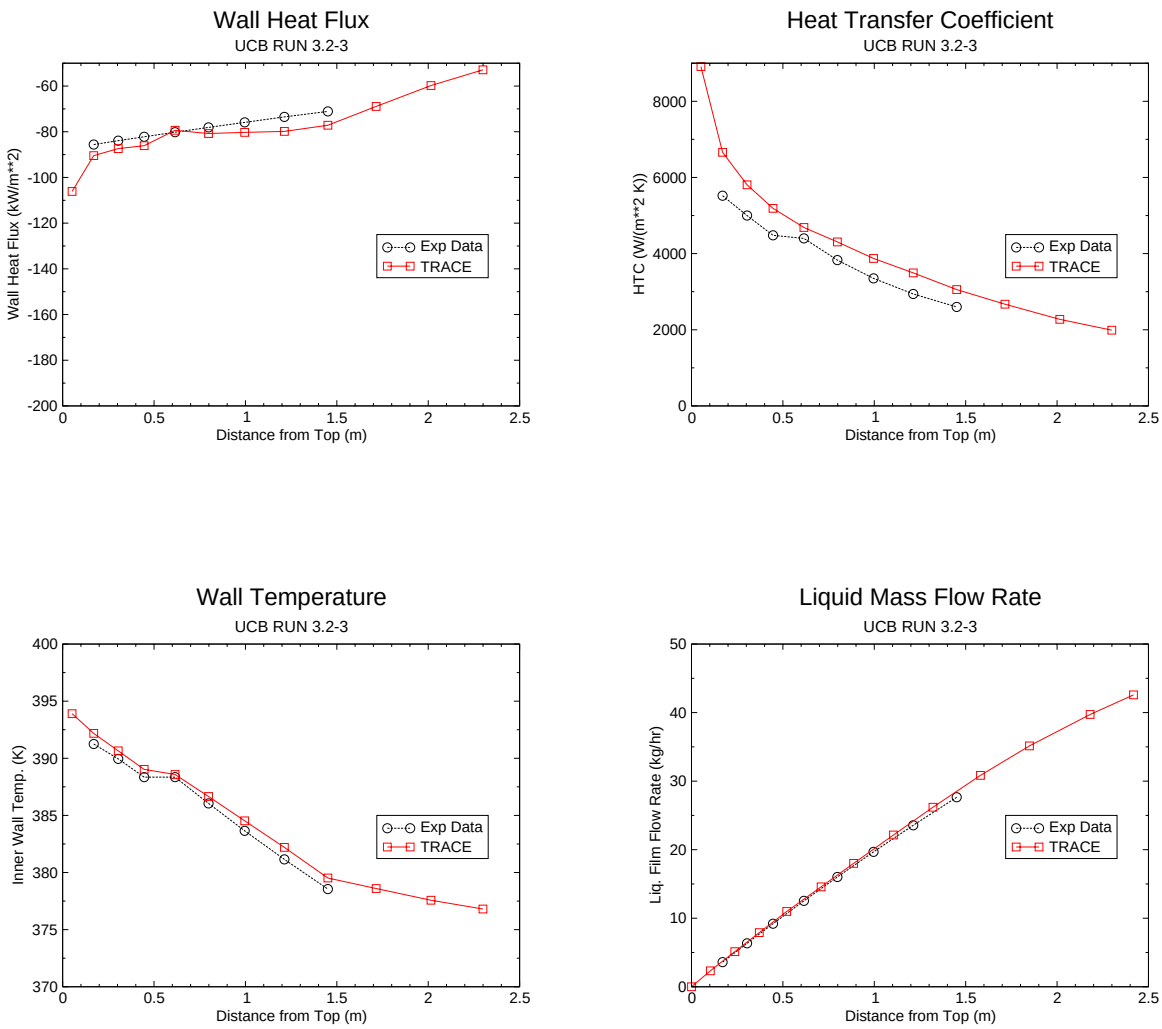

Figure B.19-21. TRACE Results for Run 3.2-3

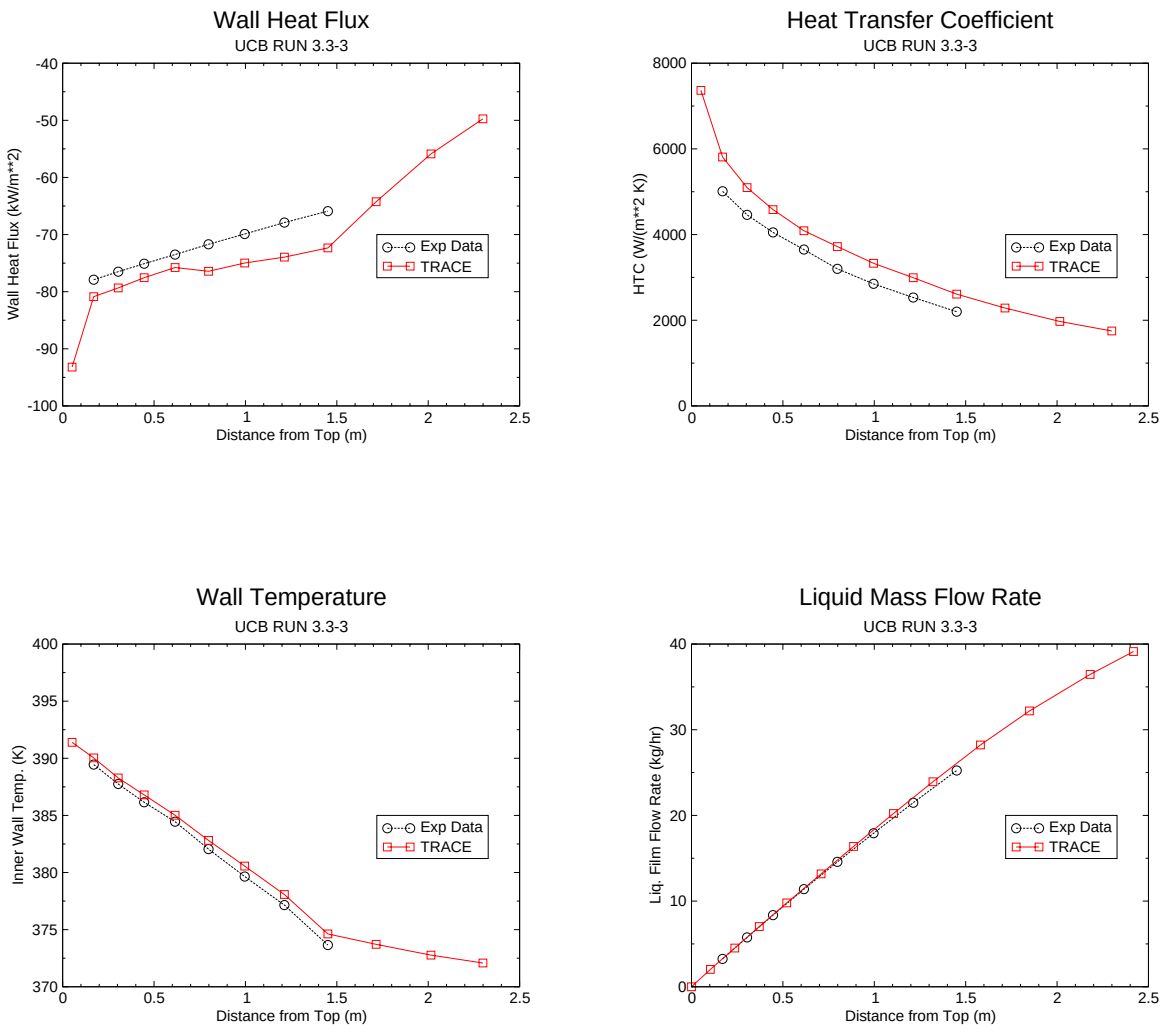

Figure B.19-22. TRACE Results for Run 3.3-3

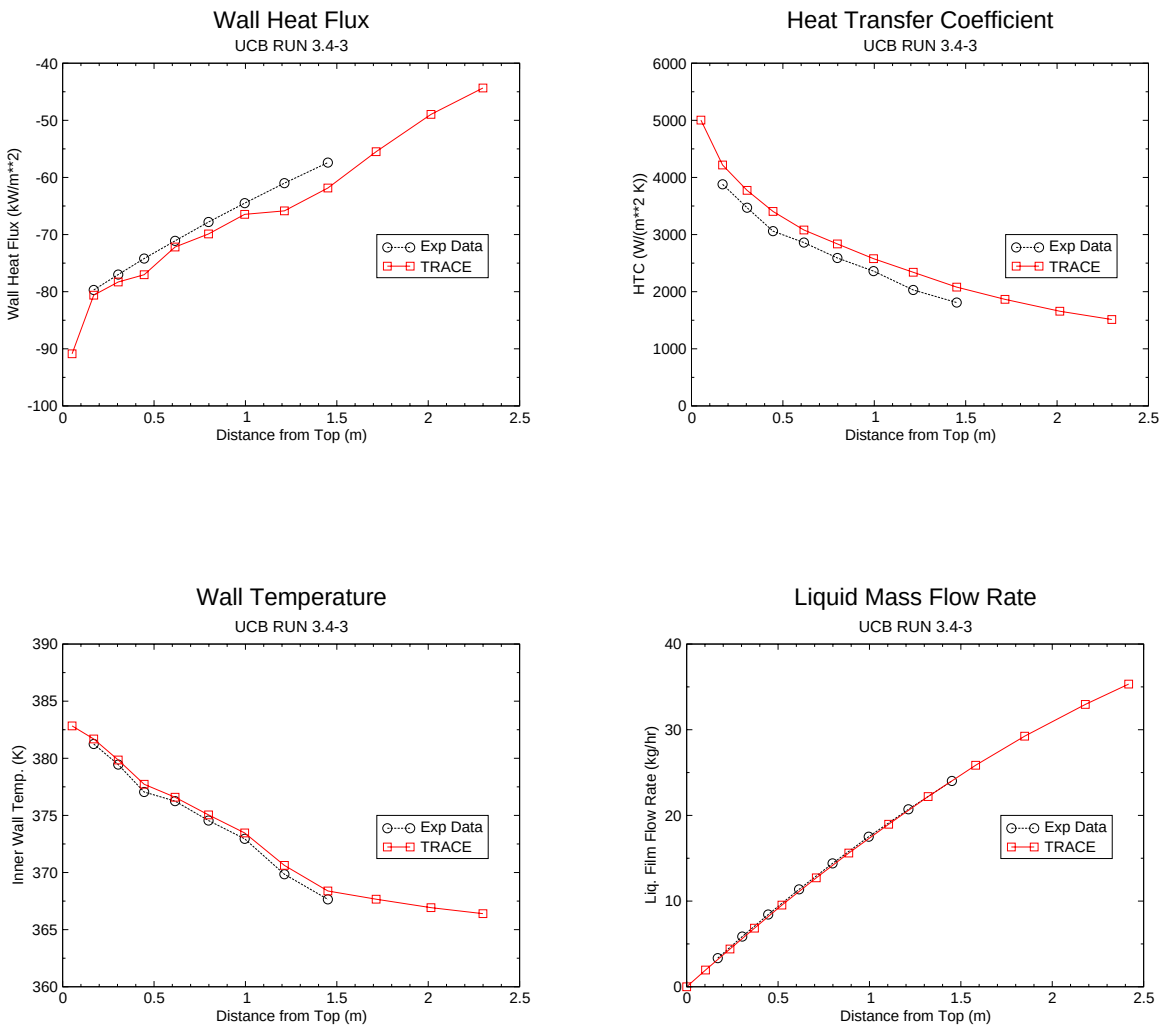

Figure B.19-23. TRACE Results for Run 3.4-3

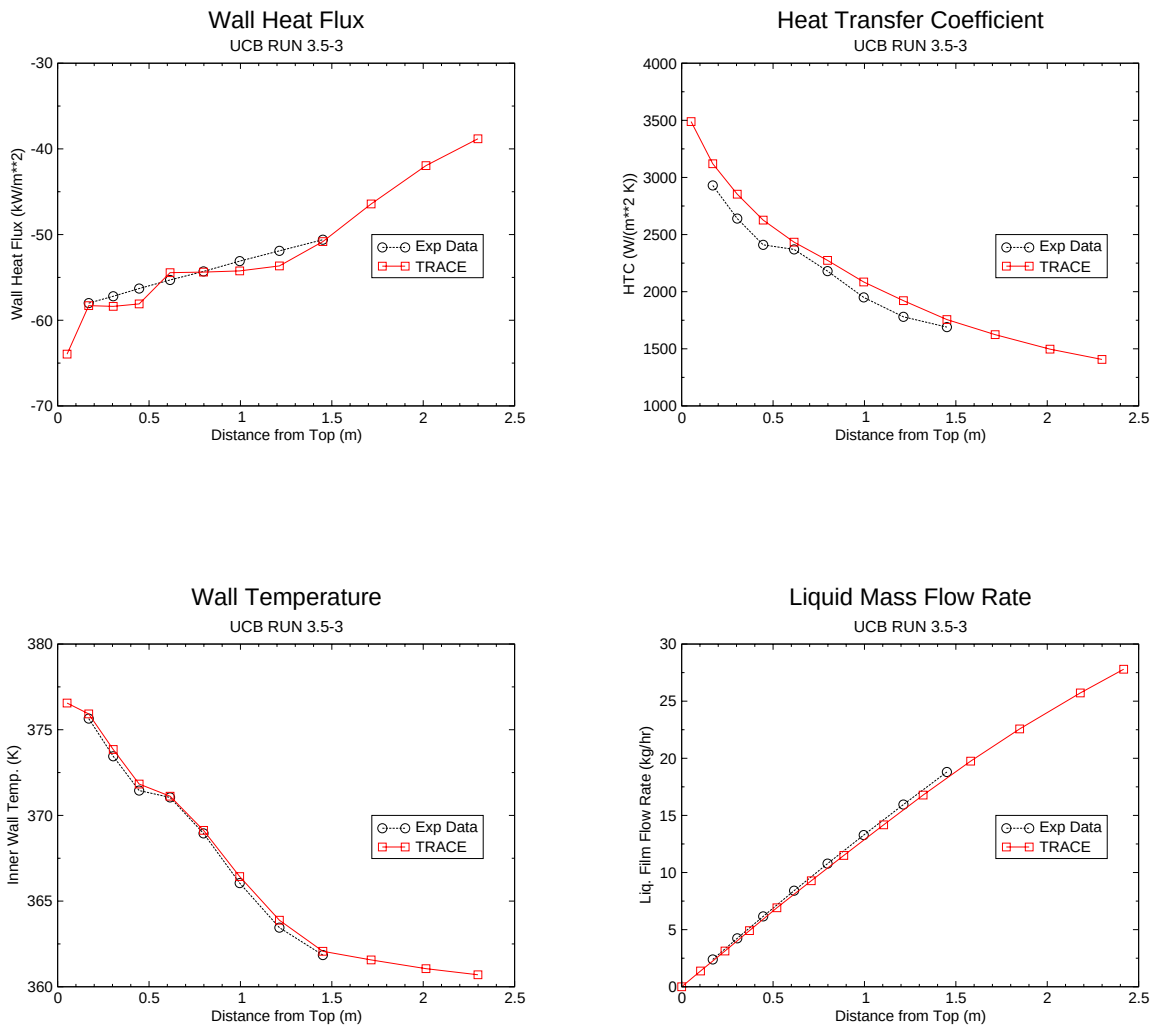

Figure B.19-24. TRACE Results for Run 3.5-3

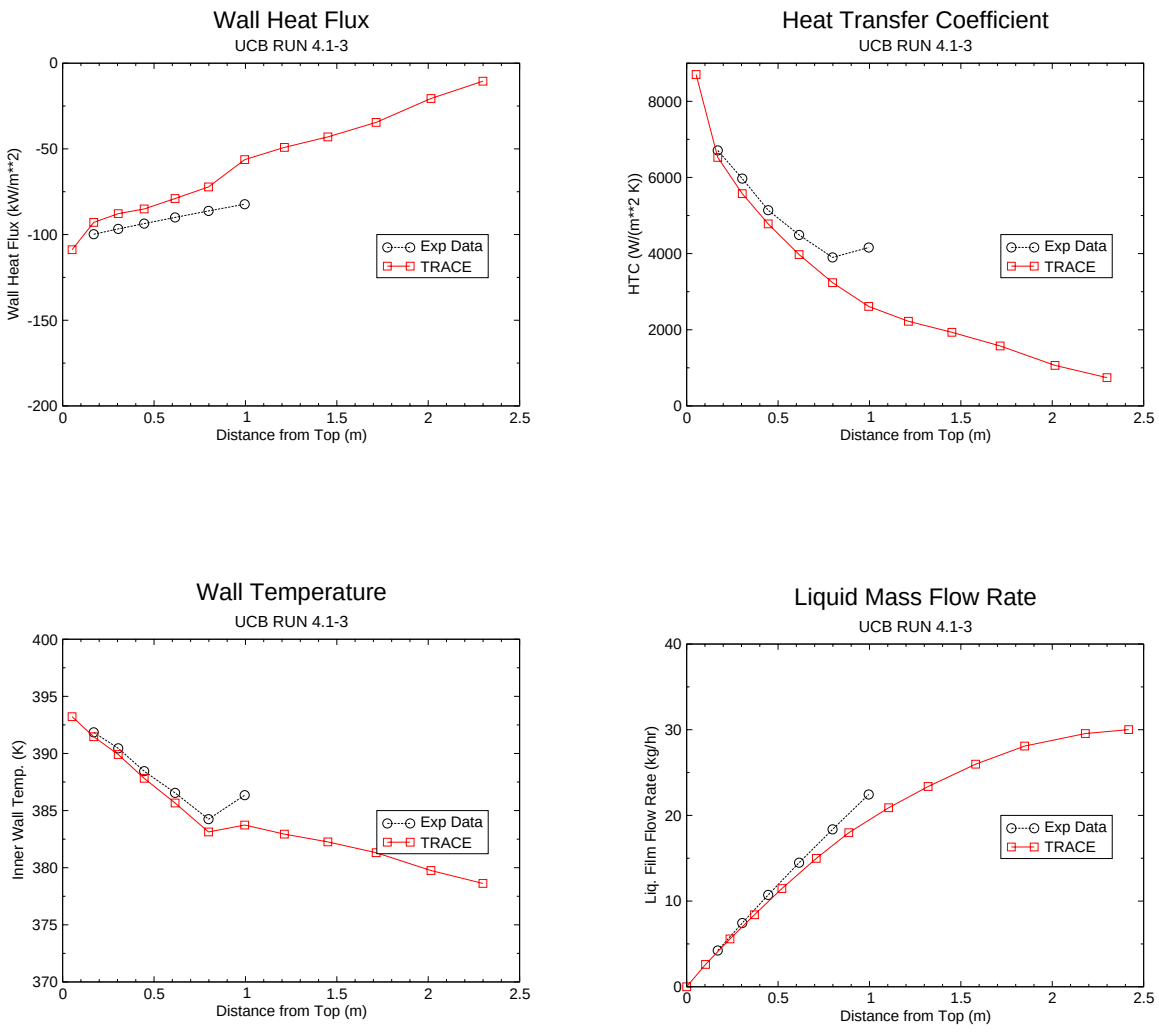

Figure B.19-25. TRACE Results for Run 4.1-3

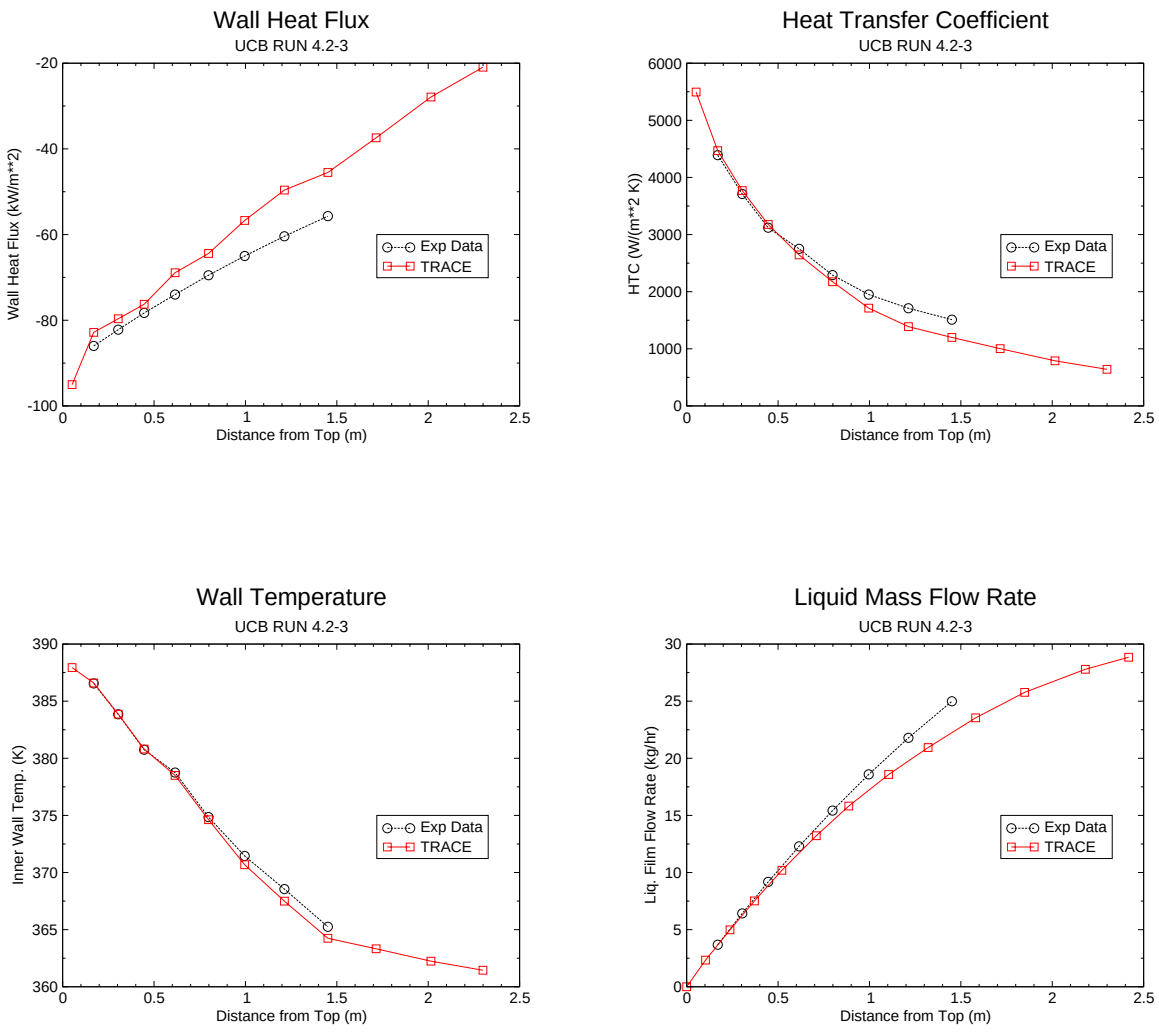

Figure B.19-26. TRACE Results for Run 4.2-3

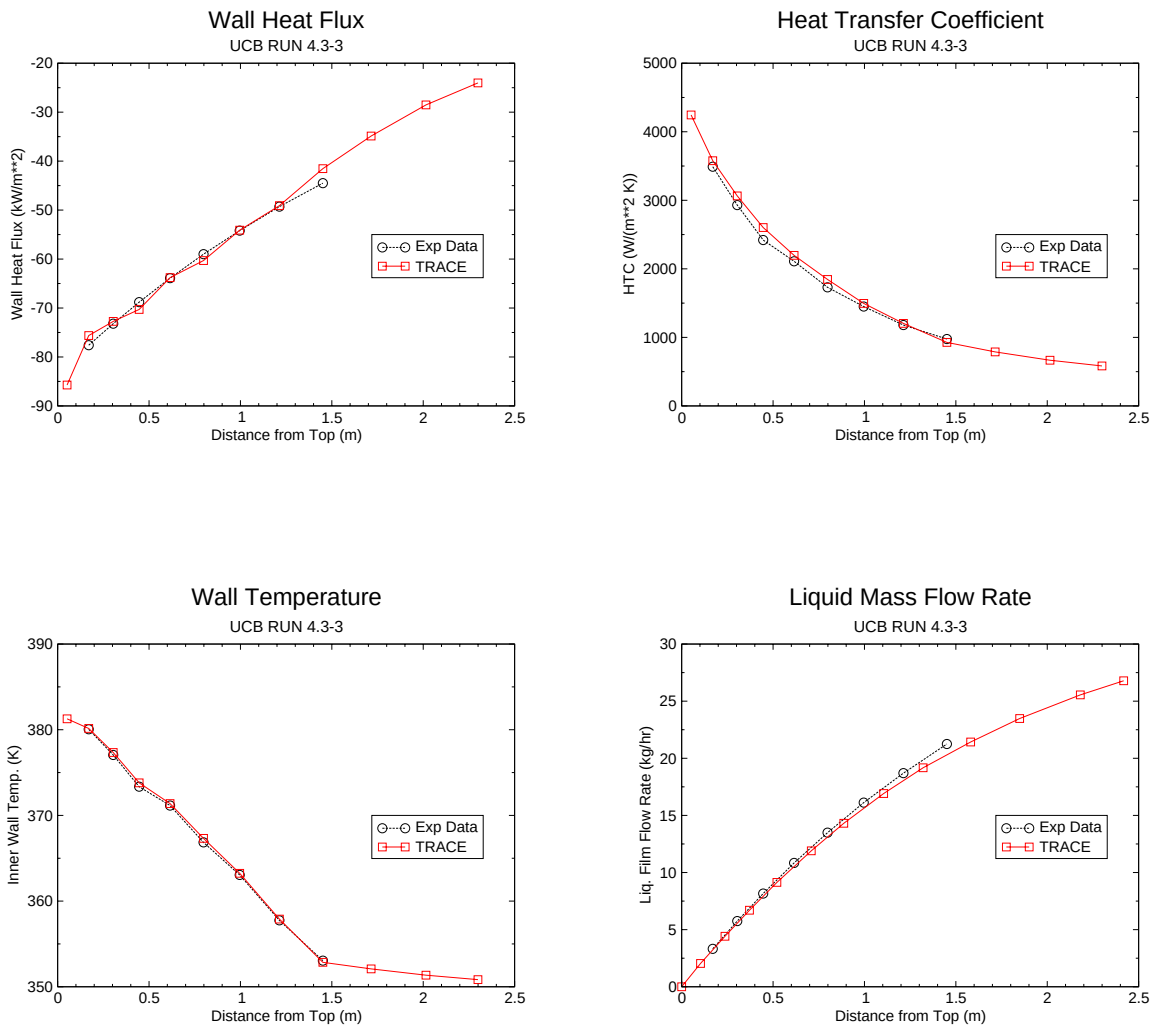

Figure B.19-27. TRACE Results for Run 4.3-3

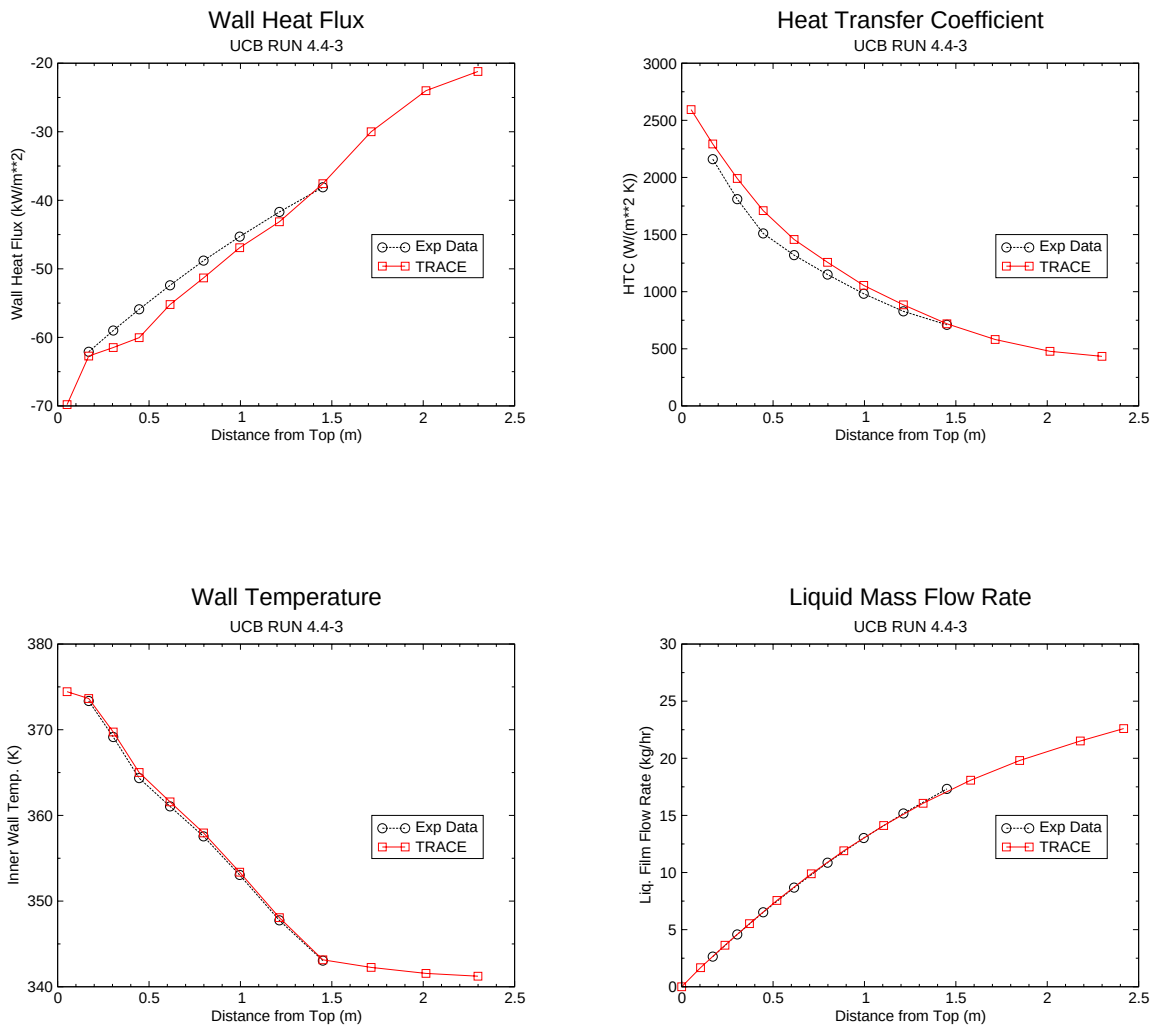

Figure B.19-28. TRACE Results for Run 4.4-3

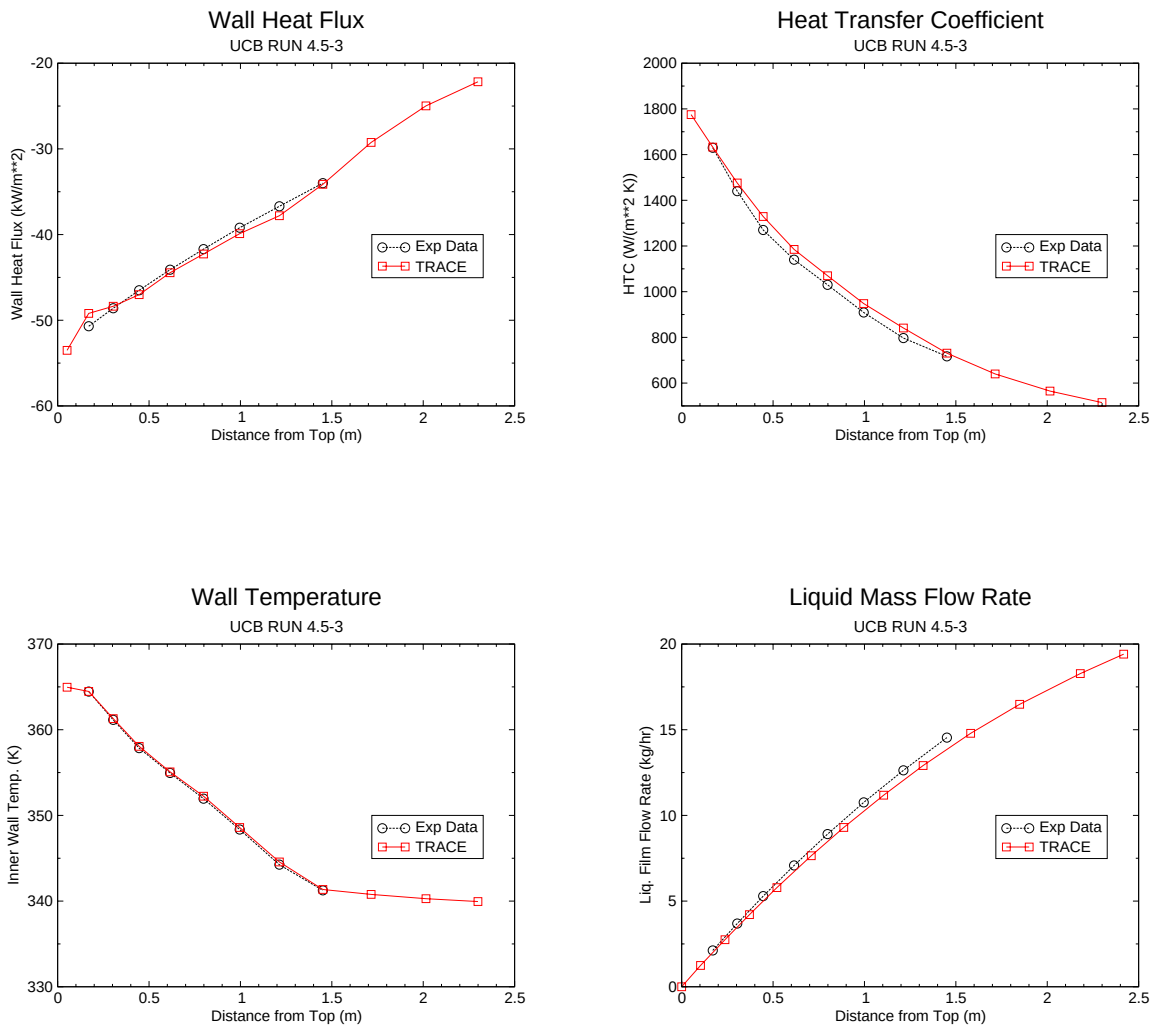

Figure B.19-29. TRACE Results for Run 4.5-3

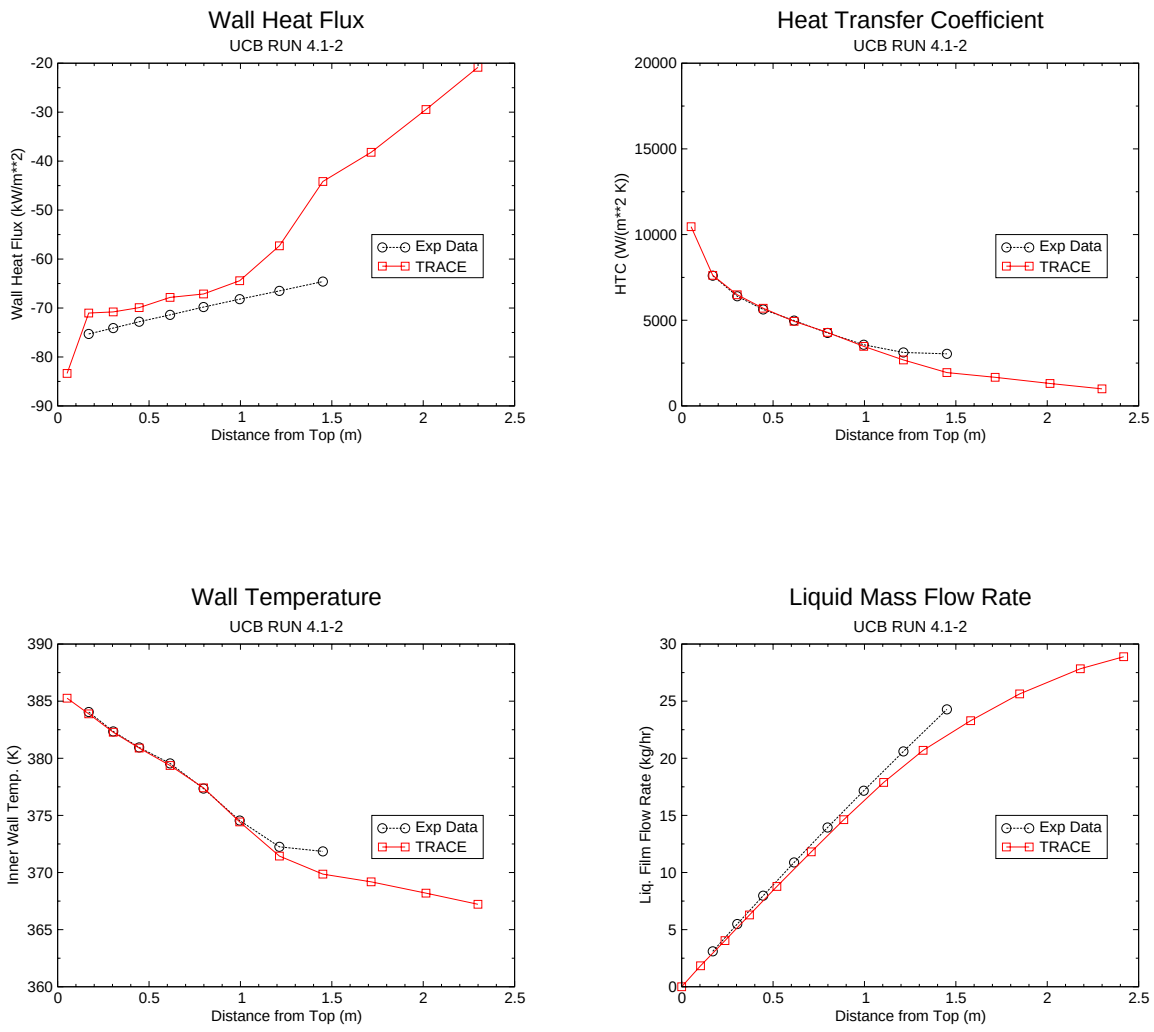

Figure B.19-30. TRACE Results for Run 4.1-2

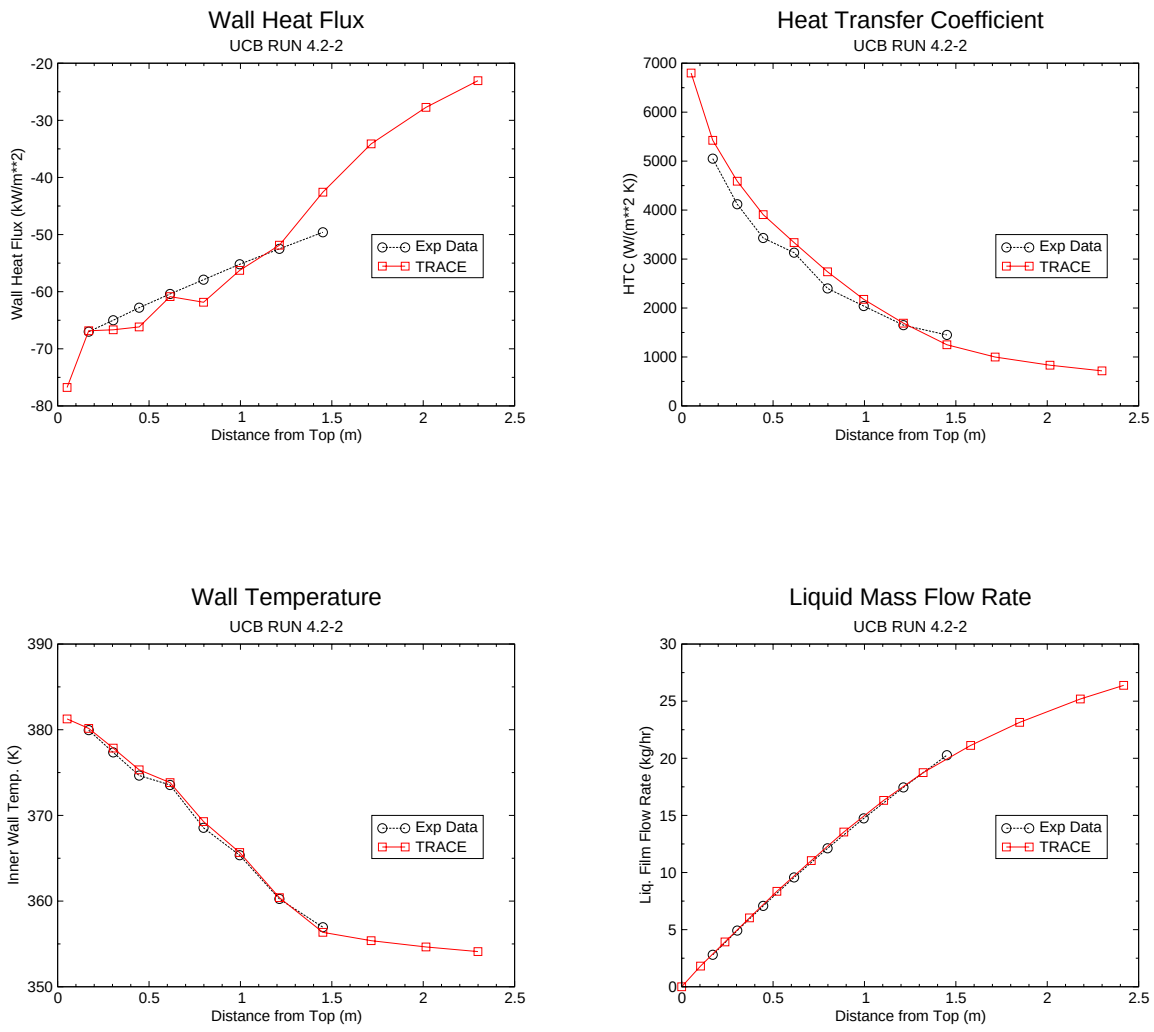

Figure B.19-31. TRACE Results for Run 4.2-2

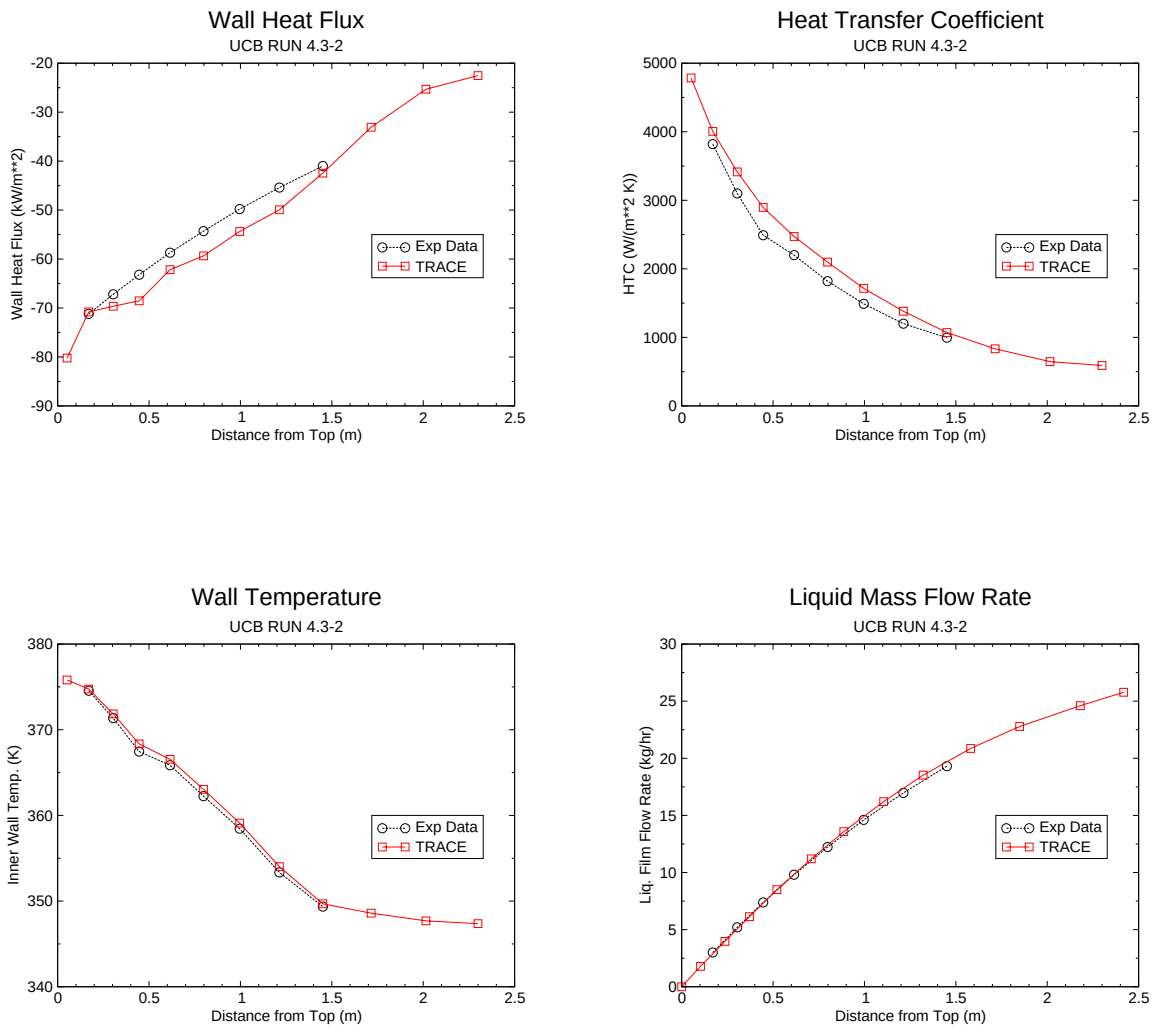

Figure B.19-32. TRACE Results for Run 4.3-2

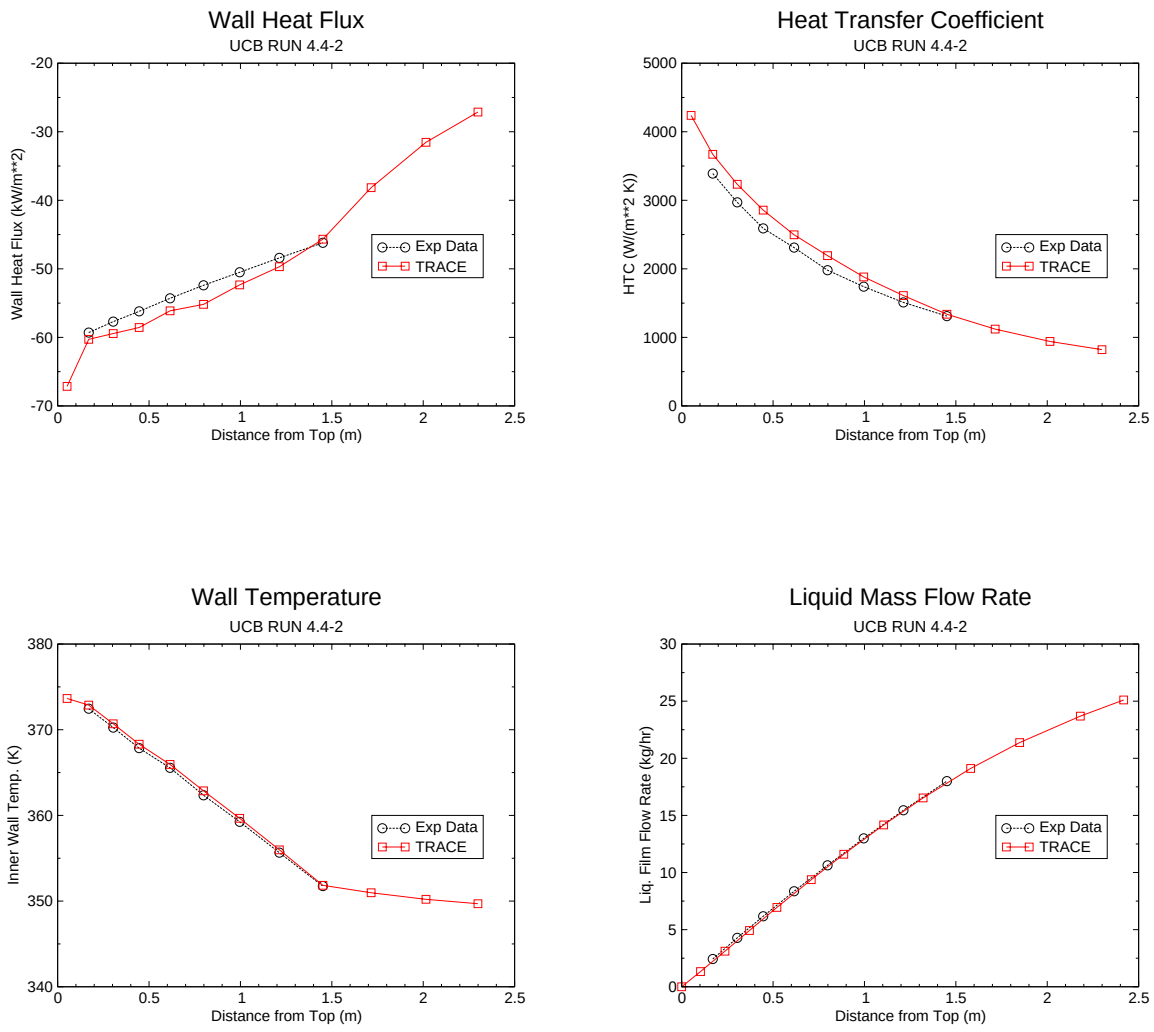

Figure B.19-33. TRACE Results for Run 4.4-2

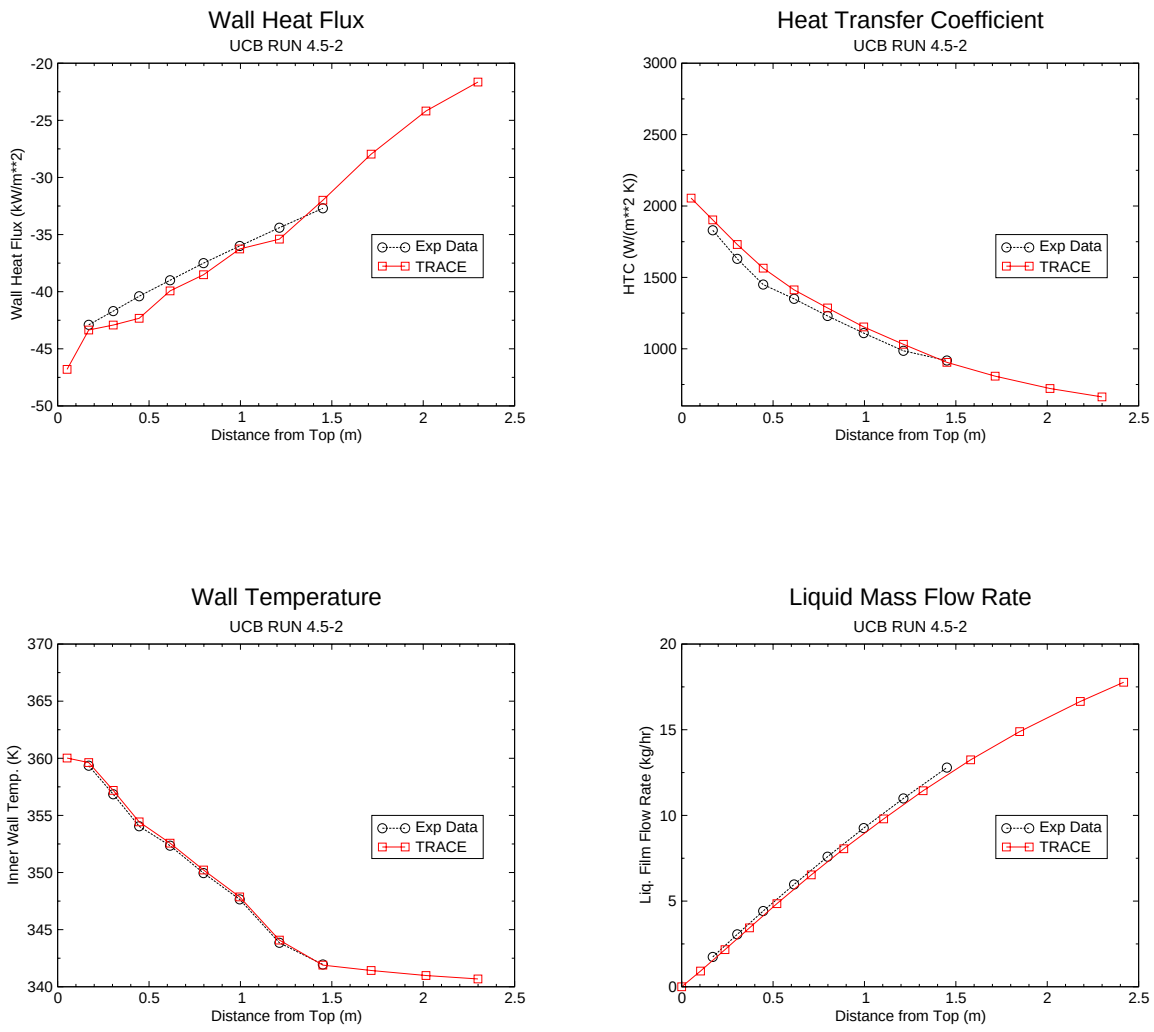

Figure B.19-34. TRACE Results for Run 4.5-2

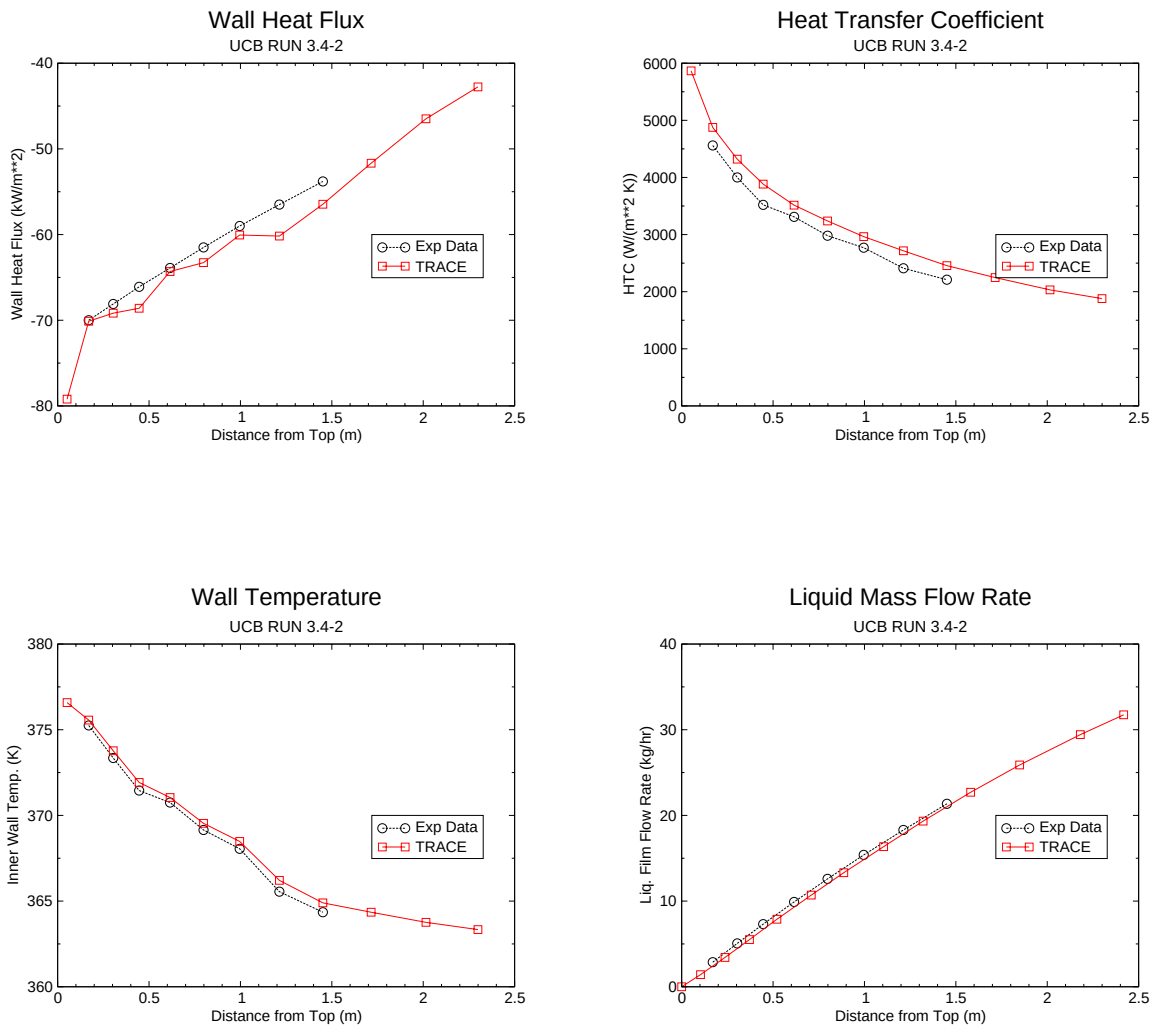

Figure B.19-35. TRACE Results for Run 3.4-2

B.19.5. Summary of the Assessment Results

Comparisons of the predicted and measured heat transfer coefficients, and for the wall heat flux are shown in Figure B.19-36 and Figure B.19-37. From these comparisons, a relative error can be defined as:

Relative Error (%) = (Calculated Value - Measured Value)/(Measured Value) *100.

Figure B.19-38 and Figure B.19-39 show the root mean square (RMS) of the error for all test cases as a function of the test pressure and the concentration of non-condensable gas, respectively.

From figures B.19-36 and B.19-37, it can be seen that with the exception of very few data points, the predictions agree with the measurements to within 20%, which is comparable to the experimental uncertainty of 18.7% indicated by Kuhn et al. for the heat transfer coefficient (Reference 1). Since the TRACE condensation model (which is based on the same UCB-Kuhn correlation) is valid for condensation with laminar film flow, it can be expected that the model predictions would deviate the most from the experimental data for higher film Re numbers, which correspond to the higher condensation rates.

In figures B.19-38 and B.19-39 it can be seen that the RMS of the error increases with increasing test pressures, while there may be a weak tendency for errors to decrease with increasing non-condensable gas fractions can be recognized if we exclude as outliers the three data points from Figure B.19-39 with large error. For the same inlet mixture flow rate, the condensation rates are higher for higher pressures and lower concentration of non-condensable gases, thus from figures B.19-38 and B.19-39, it can be affirmed that the code has slightly better performance (i.e., smaller RMS error) at low condensation rates.

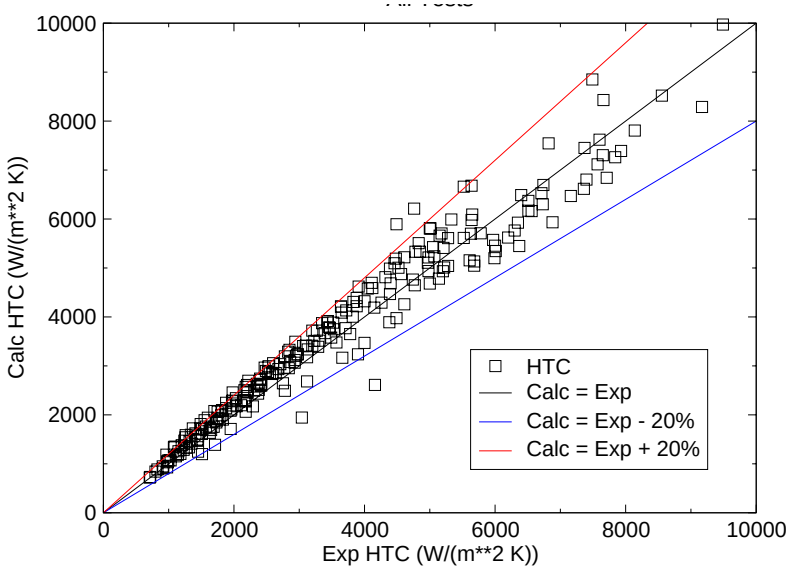

Figure B.19-36. Comparison of Predicted and Measured Heat Transfer Coefficients for UCB-Kuhn Tests.

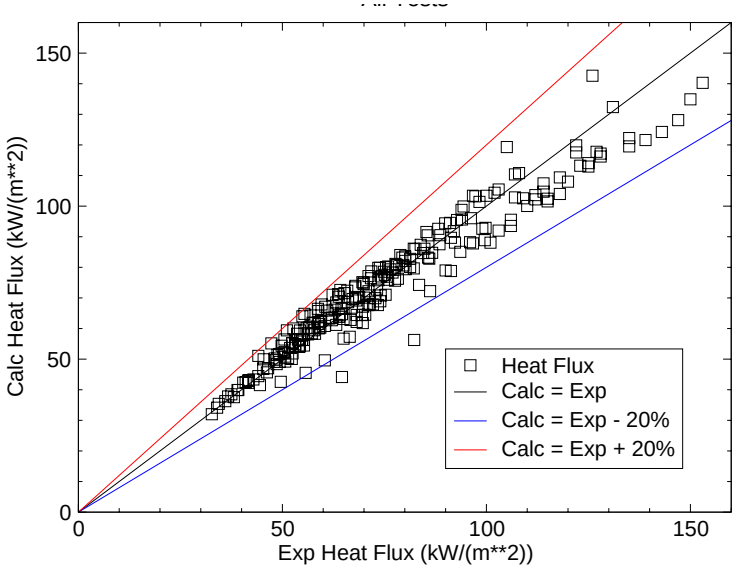

Figure B.19-37. Comparison of Predicted and Measured Heat Flux for UCB-Kuhn Tests

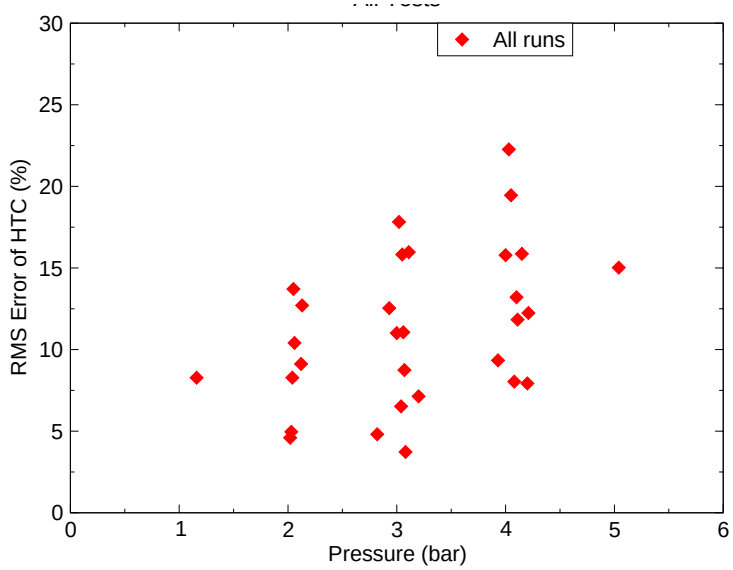

Figure B.19-38. Relative RMS Error of the HTC as a Function of the Pressure

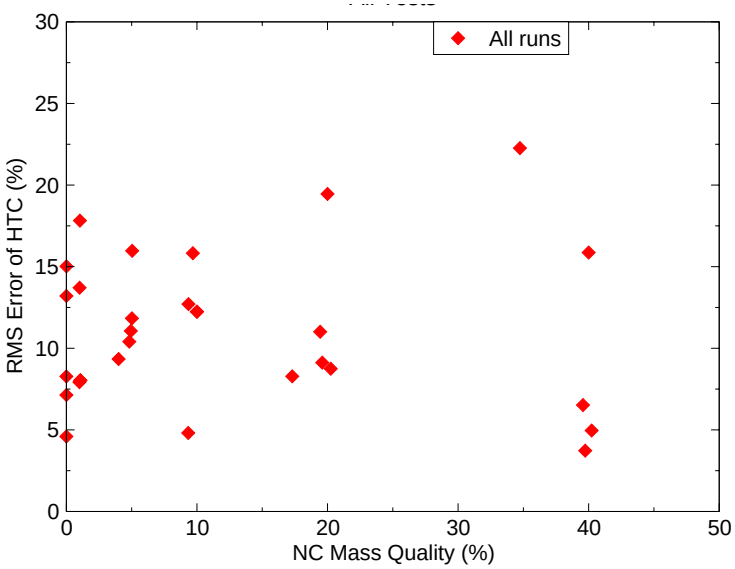

Figure B.19-39. Relative RMS Error of the HTC as a Function of the Non-condensable Gas Quality

B.19.6. Conclusions

The assessment of TRACE Version 5.0 with the UCB-Kuhn condensation tests shows that the TRACE predictions have reasonable to excellent agreement with the test data. Predicted and measure results agree to within 20%, which is roughly the measurement accuracy. Trends with pressure and non-condensable gas fraction were reasonably well predicted. Results appear to be slightly better at low condensation rate when the condensate film is laminar.

B.19.7. References

1. Kuhn, S. Z., Schrock, V. E., and Peterson, P. F., "Final Report of the U.C. Berkeley Single Tube Condensation Studies", Dept. of Nuclear Engineering, UCB-NE-4201, 1994

2. Kuhn, S. Z., Schrock, V. E., and Peterson, P. F., "An investigation of condensation from steam-gas mixtures flowing downward inside a vertical tube," Proc. of NURETH-7, pp. 312-331, 1995.

3. Claudio Delfino, "Assessment of TRACE V.4.190 on the UCB Single Tube Condensation Tests," Information Systems Laboratories, Inc., ISL-NSAD-TR-05-04, July 2005.

4. Dean Wang, "UCB Kuhn Test Series 3 and 4", ADAMS Accession Number ML06171780160.

5. Dean Wang, TRACE Calculation Notebook, "UCB Kuhn Test Series 3 and 4", January 25, 2006, ADAMS Accession Number ML0616500418.

B.20. Dehbi-MIT Condensation Tests

Author(s): C. Delfino, Dean Wang

Affiliation: ISL/NSAD

Code Version: TRACE V5.0

Platform and Operating System: Intel x86, Windows XP

B.20.1. Introduction

In the event of a reactor accident involving a pipe break, a large amount of steam may be released. Condensation of steam on cold containment surfaces will act as a passive heat sink and mitigate the containment pressurization. In order for an analyst to estimate the condensation heat transfer rates in such a scenario, the presence of a large amount of non-condensable gas and its suppression effect on heat transfer rates must be taken into account. The inhibitive effect of non-condensable gases on steam condensation is a well known phenomenon that is due to the formation of a layer of noncondensable gas adjacent to the liquid film through which the steam must diffuse to condense. Therefore, the heat transfer rates are controlled by a mass diffusion process as well as heat conduction into the wall.

TRACE will be employed in the safety analysis of nuclear plant systems including containment analysis. Therefore analytical models for condensation of steam on cool walls in the presence of noncondensable gases were identified and implemented in a developmental version of the code. The implementation in TRACE of these models, which are suitable for modeling of condensation processes occurring on walls such as those inside a containment building, extends the pre-existing TRACE logic suitable for modeling of condensation in a pipe geometry.

The purpose of this section is to report on the assessment of the implemented condensation models against an experimental correlation and data on steam condensation on external walls, in the presence of a noncondensable gas. The experimental investigation performed by A.A. Dehbi at MIT (Ref. 1) is used to assess the capabilities of this TRACE developmental version.

B.20.2. Test Facility Description

An experimental and theoretical investigation was conducted at MIT to determine the effects of noncondensable gases on steam condensation under free convection conditions, as documented in A.A. Dehbi's doctoral dissertation (Ref. 1).

The test section used in the Dehbi-MIT condensation experiments consisted of a 3.5 m long, 3.8 cm diameter, copper cylinder located centrally inside a 4.5 m long, 0.45 m diameter stainless steel vessel (see Figure B.20-1). Steam was generated at the bottom of the vessel by a set of immersion heaters. Air was injected in the vessel from an air supply source. Cooling water was forced to flow inside the copper tube (bottom-up) to refrigerate the wall where condensation occurred. The vessel was fully insulated so that condensation took place only on the cold copper wall. Wall, coolant and steam thermocouples were installed to measure the temperatures and thus obtain the heat transfer rates when a given coolant flow rate was imposed.

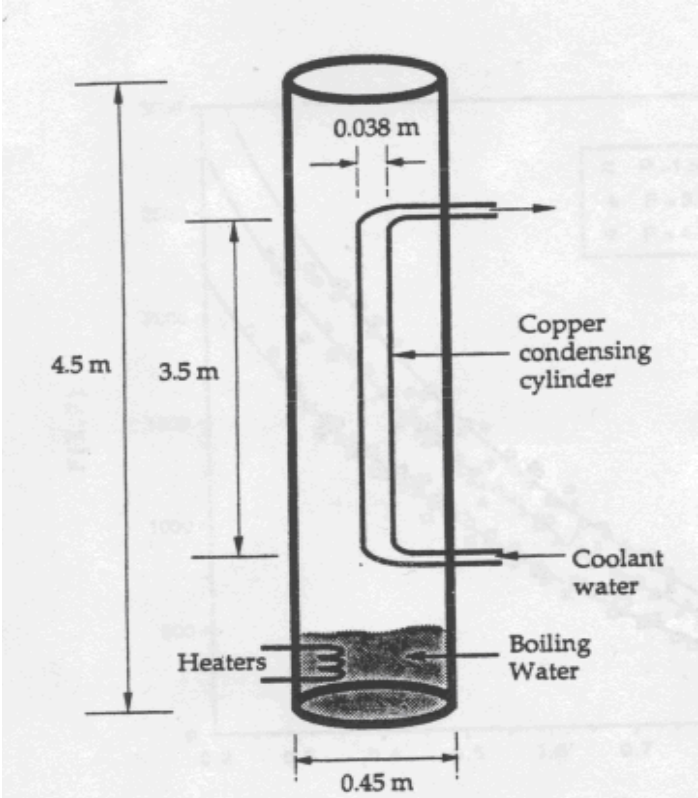

Figure B.20-1. Schematic of the Dehbi-MIT Facility

Known amounts of air or an air-helium mixture were admitted inside the vessel while steam was produced at the bottom of the vessel in the pool of boiling water. The steam-gas mixture was allowed to reach a steady-state in which natural circulation currents were the only driving mechanism. In the steam-air investigation, which is the only case considered for the TRACE assessment, three sets of experiments were performed. In each set, the system pressure was held constant while the air content and the wall temperature subcooling were varied. The three sets of runs had pressures of 1.5, 3.0 and 4.5 atmospheres. The cylinder wall subcooling ranged from 15 to 50 K. The air mass fraction varied from 25% to 90%.

Dehbi found that the heat transfer coefficient decreased slowly with subcooling, increased mildly with height, and significantly with pressure. Based on the collected experimental database, Dehbi

then built a theoretical model and developed a correlation for predicting the heat and mass transfer which accompanies steam condensation in the presence of a noncondensable gas.

The experimental heat transfer coefficients were fit by Dehbi with the formula (Ref. 1):

$$h_L = \frac{L^{0.05}[(3.7 + 28.7p) - (2438 + 458.3p)\log(W)]}{(T_b - T_W)^{0.25}} \quad (20\text{-}1)$$

(L is the condensing length in meters, p is the pressure in atmospheres, W is the mass fraction of air, T_b (bulk) and T_w (wall) are temperatures expressed in degrees K; the heat transfer coefficient is obtained in $W/m^2/K$).

The correlation was obtained for the following range:

Length: 0.3 m < L < 3.5 m

Pressure: 1.5 atm < p < 4.5 atm

Subcooling: 10 K < (T_b - T_w) < 50 K.

B.20.3. TRACE Model Description

The numerical simulations were executed with TRACE Version 5.0CR3. In this version, the new wall condensation model is optionally available to the user as an alternative to the pre-existing TRACE logic.

B.20.3.1. Wall Condensation Model Activation Flags

To model wall condensation processes, such as those occurring in the event of a reactor accident involving release of steam into the containment building, a few specialized models have been installed in TRACE. So that these models are called only for the intended purpose and do not interfere with the correct operation of other models, an option flag for vessel and pipe components has been added. The wall condensation model can be activated in a vessel component by setting (in the input file) the "VessType" flag equal to 1 (0 is the default value used for a regular vessel component). "VessType" has been added to the input requirements as word 5 of Card 6 for a vessel component. The wall condensation model is available also for pipe components. In this case, the model is activated by setting PipeType=8 in the input file. The wall condensation model applies to both the hydraulic components and the heat structures connected to the hydraulic components that have the wall condensation flag activated. Such heat structures are automatically flagged as "wall condensation heat structures" without requiring additional user input. This approach is the same as that used in the development of the tube condensation models.

B.20.3.2. TRACE Modeling of the Dehbi-MIT Tests

These tests focus on the impact of noncondensable gases upon wall condensation in a stagnant environment. The geometry of this facility poses a challenge to modeling with TRACE. The heat transfer surface is a small diameter copper tube (0.038 m OD) enclosed in a larger vessel (0.45 m ID) and in an almost stagnant atmosphere. The condensate from the copper tube drips into a reservoir at the bottom of the vessel where a heater evaporates enough liquid to maintain a steady state for the specific pressure.

The first difficulty in using TRACE to model these experiments concerns the experimenter's assumption that natural convection currents will essentially uniformly mix the evaporated steam with the resident noncondensable gas. In TRACE, if a 1-D vessel is used, then only limited mixing would occur, as both the steam and the noncondensable gas share the same velocity field. A multi-dimensional model could be used where the air-steam density difference would drive macroscopic convection currents to promote mixing but, while an improvement, this too does not guarantee complete mixing.

The simplest configuration was adopted and the system was modeled as an open loop as shown in Figure B.20-2.The VESSEL component has 14 levels and 2 rings, but the inner ring, with radius equal to the copper tube, is input with null volumes and flow area. Therefore, the VESSEL is essentially a 1-D component. The HTSTR modeling the copper tube wall is connected to the inner face of the outer VESSEL ring (at the central 10 VESSEL levels), where the gas mixture resides. The constant wall temperature from the experiments is imposed as a boundary condition in the HTSTR. The FILL component at the top of the configuration assures that the steam flow rate is larger than the condensation rate, so that steam depletion does not hinder the condensation. However, in order to model a natural circulation environment, the inlet velocities are kept to low values. The BREAK at the outlet prescribes the test pressure. The two PIPE components are merely connection elements between the VESSEL and the inlet and outlet boundaries. Reference 2 documents the TRACE input deck. .

Another issue in modeling these experiments is related to the specification of the hydraulic diameter for the VESSEL component. In addition to the air-steam mass ratio, the condensation rate will be affected by the thickness and Reynolds number of the liquid film. In turn, these quantities are dependent on the wall drag models and the input hydraulic diameter. Since the wall drag for the annular flow regime and film condensation is applied to the liquid film only, the input hydraulic diameter should be calculated based on the perimeter wetted by the liquid film only. Therefore, the wetted perimeter used for calculating the hydraulic diameter is the perimeter of the small copper tube where the liquid film flows ("cooled" perimeter). The perimeter of the VESSEL is not included because there is no liquid film on it.

B.20.4. Tests Simulated with TRACE

The results of the Dehbi tests simulations are shown in Figure B.20-3 through Figure B.20-5 for the three pressure levels of 1.5 atm, 3.0 atm and 4.5 atm. The plots in the figures show the average

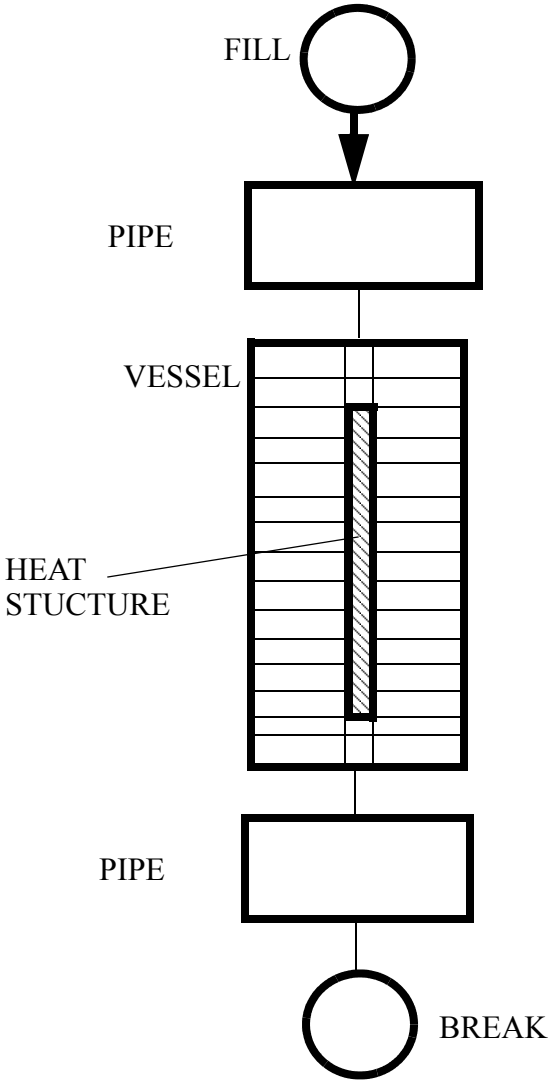

Figure B.20-2. TRACE Model Schematic for the Dehbi-MIT Condenastion Tests

condensation heat transfer coefficient over the entire condensing surface, as a function of the air mass fraction. TRACE results, the Dehbi correlation and the experimental data are reported.

The correlation data was obtained for a constant subcooling of 30 K, and for seven increasing values of air mass fraction from 0.3 to 0.9, whereas the experimental data refers to a range of different subcooling and air mass fractions, depending on the particular data point. The TRACE heat transfer coefficients are computed as the average of the heat transfer coefficients over the axial meshes of the heat structure modeling the condensing surface. This was achieved with a Perl script that makes use of the TRACE axial profile plot data created with AVScript.

Seven TRACE calculations were executed for each pressure level, with the same constant subcooling of 30 K and the same range of air mass fraction as that input to the correlation. Since the wall temperature is imposed as a boundary condition and the gas/mixture is in saturation

conditions at the given pressure, the comparison of TRACE-calculated heat transfer coefficients against the Dehbi correlation is representative of a comparison between the heat fluxes (the imposed thermal-hydraulic conditions are exactly the same). Because the experimental data points were obtained in a scattered range of subcooling values (with average subcooling about 30 K), the comparison of TRACE results against the experimental data is somewhat less consistent. In all cases, the TRACE results follow the trend of data and correlation, with maximum error about 18%, and decreasing errors for increasing noncondensable gas quality. The experimental uncertainty for these test cases was reported at about 15%. Thus, the overall performance of the new model can be defined as satisfactory. This is especially true if we consider the results of the old model, which overestimated the heat transfer coefficients by more than an order of magnitude (as will be shown in the next section).

A sensitivity study was performed on the number of vessel levels (and therefore, on the node size). It was found that the average heat transfer coefficient (over the entire wall) did not vary significantly with varying node sizes from 0.35 m to 3.5 m.

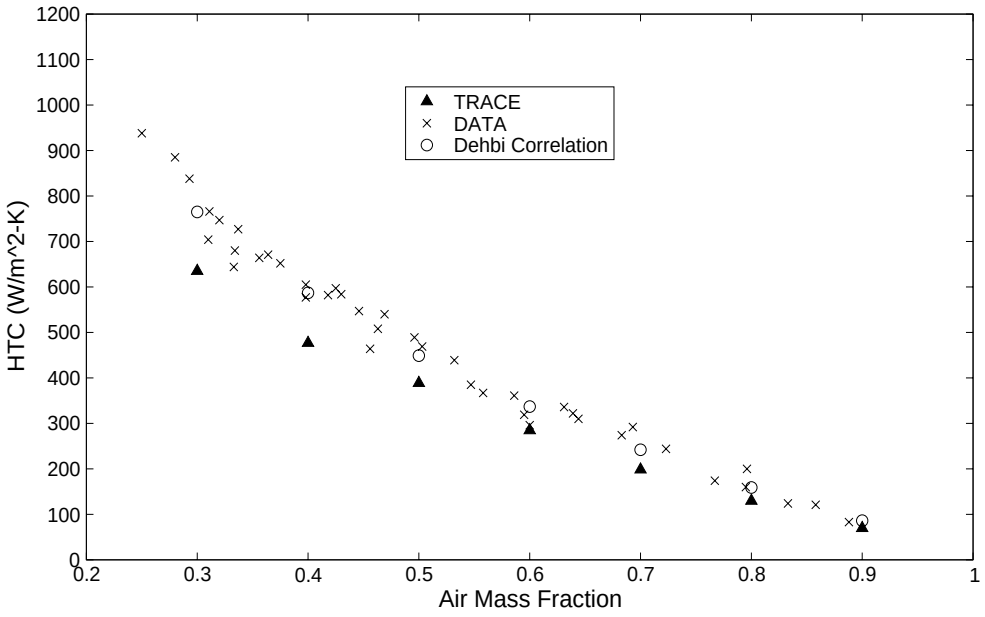

Figure B.20-3. Heat Transfer Coefficient as a function of air mass fraction, Pressure = 1.5 atm, $\Delta T = 30K$

B.20.5. Assessment Results Summary

The assessment of the new wall condensation model implemented in TRACE shows that the code can predict accurately the heat transfer coefficients for steam condensation in film mode along

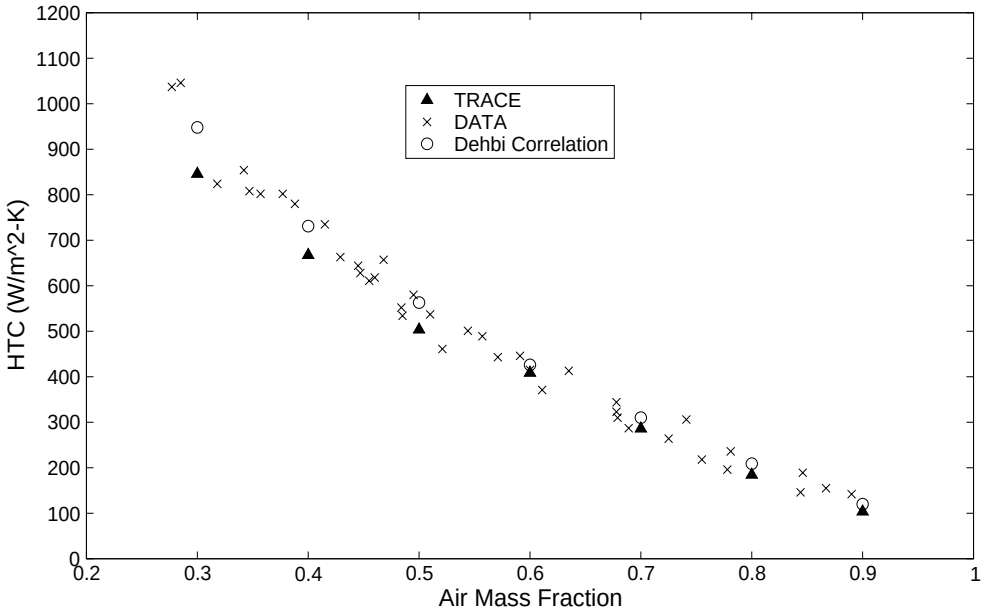

Figure B.20-4. Heat Transfer Coefficient as a function of air mass fraction, Pressure = 3.0 atm, $\Delta T = 30K$

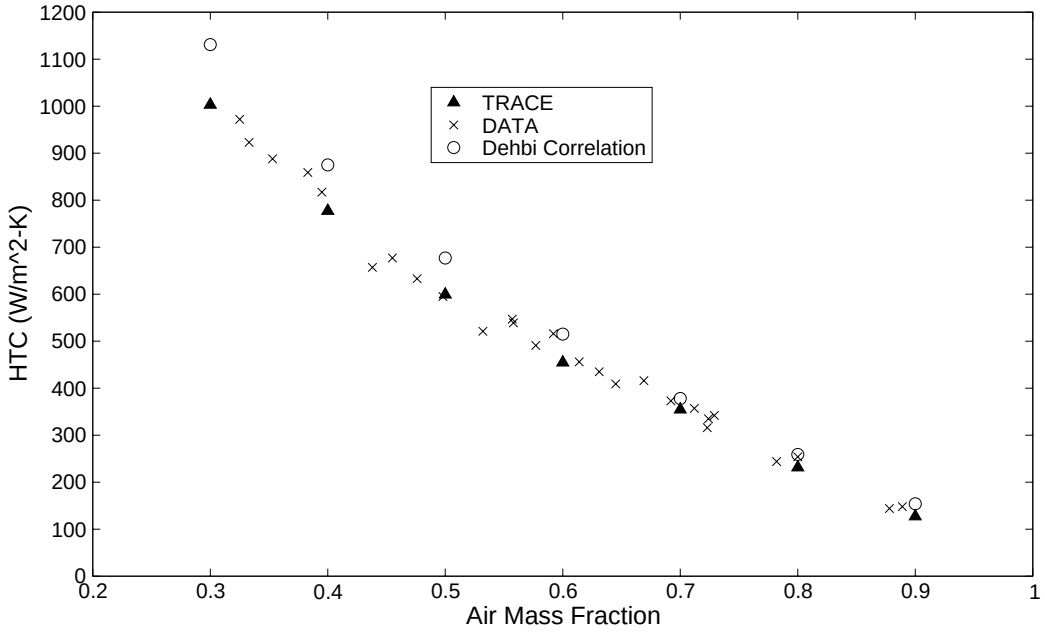

Figure B.20-5. Heat Transfer Coefficient as a function of air mass fraction, Pressure = 4.5 atm, $\Delta T = 30K$

cooled walls, in the presence of noncondensable gases. This assessment against an empirical correlation and experimental data for the condensation heat transfer coefficient shows that the code results are generally within a 20% accuracy range. The new model improves the results obtained with the default condensation model, which largely overestimated the condensation heat transfer rates.

B.20.5.1. Comparison to the Default TRACE Logic

The default condensation logic implemented in TRACE (derived from TRAC-P and hereby called the TRAC model) was found to have many deficiencies. The inadequacy of the TRAC condensation model can be itemized as follows:

- The TRAC model was overly complicated; it superposed wall/liquid and wall/vapor heat fluxes over a wide range of conditions, so that it was difficult to identify which specific correlation was actually being used.

- The wall drag was partitioned between liquid and gas, leading to calculation of unphysical velocities in the case of liquid film condensation.

- The TRAC model inappropriately used the physical correlations; the correlations integrated the condensate rate over the entire heat transfer surface to obtain an average film thickness, but TRAC applied the correlations to each individual node as the condensation surface, thus introducing errors and an explicit node-size effect.

- The effect of the interfacial shear on the heat transfer was not accounted for, except through the flow factor of Chen for wall/liquid heat transfer only.

- The treatment of condensation with non-condensable gases was especially defective. TRAC used an experimental correlation for the wall/liquid heat transfer of questionable applicability to conditions other than cross flow of gas-vapor mixtures on liquid jets.

The TRAC model over-predicted the heat transfer coefficient by an order of magnitude and fails to predict the decreasing heat transfer coefficients for increasing air mass fractions.

B.20.5.2. Recommendations for Input Modeling

During the implementation of the new wall condensation models and the preparation of the input files for the assessment study, a few issues were identified as potential recommendations for the code user when modeling wall condensation. The following is a list of such recommendations:

- The hydraulic diameter of those volumes where film condensation is expected to occur should be based on the perimeter wetted by the liquid film only (“cooled” perimeter).

- When the film thickness is the largest heat transfer resistance, that is for pure steam condensation, then the radial dimension of the vessel nodes attached to the heat structures where condensation occurs should be limited to about a hundred times the expected film thickness (a value of 0.1 m for the radial dimension was verified to work properly in this assessment).

- On the other hand, when the mass transfer is the limiting heat transfer resistance, that is in the presence of non-condensable gases, then the new condensation model seems to be rather insensitive on the axial node length, which suggests the possibility of using large axial node sizes (a maximum axial node size of 3.5 m was verified to work properly in this study). However, at the uppermost elevations where the liquid film has minimum thickness, it is suggested to use smaller axial node sizes in order to capture the initial growth of the liquid film.

B.20.6. References

1 A. A. Dehbi, “The Effects of Noncondensable Gases on Steam Condensation Under Turbulent Natural Convection Conditions,” Ph.D. Thesis, Massachusetts Institute of Technology, February 1991.

2 Delfino, C., "TRACE Calculational Notebook for Dehbi-MIT Natural Convection Condensation Test ," ADAMS ML071760489, July 2006.

B.21. University of Wisconsin Condensation Tests

Author(s): C. Delfino and Dean Wang

Affiliation: ISL/NSAD

Code Version: TRACE V5.0

Platform and Operating System: Intel x86, Windows XP

B.21.1. Introduction

During a LOCA, a large amount of steam may be released to containment where it can condense on cold surfaces. Condensation of steam on these containment surfaces represents an important heat removal mechanism and helps to reduce containment pressurization during the event. In a passively cooled containment, condensation processes play an even more important role. However, the presence of non-condensable gasses can suppress condensation rates. The inhibitive effect of non-condensable gases on steam condensation is a well known phenomenon that is due to the collection of the non-condensable components adjacent to the liquid film. Steam must diffuse through this layer of non-condensables in order to reach the condensing surface. Thus, condensation rates can be controlled by the relatively slow mass diffusion process rather than by conduction through the liquid film.

It is expected that TRACE may be used in the analysis of either conventional or advanced plants where it may be necessary to include a model for the containment. During a LOCA containment pressure is an important boundary condition on the primary system. Therefore analytical models for condensation of steam on walls in the presence of non-condensable gases have been included in TRACE Version 5.0. The implementation of these models in TRACE extends the pre-existing logic which has previously been restricted to condensation within pipes.

The purpose of this section is to report on the assessment of the TRACE condensation models against experimental data on steam condensation in the presence of non-condensable gases and wall geometry. The experimental investigation at the University of Wisconsin (Ref. 1) is used in this section to assess the capabilities of this TRACE model.

B.21.2. Test Facility Description

An experimental investigation to examine the effect of surface orientation and forced convection on the condensation of steam in the presence of a non-condensable gas was performed by researchers at the University of Wisconsin under Westinghouse sponsorship (Ref. 1).

The test section consisted of 1.095 m long polycarbonate plates that formed a square duct of 15.24x15.24 cm. Figure B.21-1 shows the test section geometry. The test section was designed to withstand temperatures of 140 C and pressures up to 2 bars. The first 84 cm of the test section served as the entrance length. The condensation took place in the section following the entrance length. The condensing section consisted of a cooled aluminum plate mounted as the ceiling of the duct. The cooling of the test wall was provided by independent coolant plates mounted on the backside of the aluminum plates and arranged on top of heat flux meter stations. The arrangement of the coolant system ensured an even heat flux profile along the test plate.

The facility included a variety of instruments to acquire the necessary data. The overall goal in performing the measurements was that the measurement accuracy of the heat transfer coefficient would be within 10%. The overall heat transfer coefficients were calculated from the heat flux measurements using two different methods: with heat flux meters; and from a calculated coolant energy balance.

An air-steam mixture was directed into a rectangular flow channel over a condensing aluminum surface which had a wetting surface finish. In the Univ. of Wisconsin tests the orientation of the condensing surface was varied from 0 to 90 degrees (plate surface facing downwards at 0 degree), with variable air/steam mass ratios ranging from 0.24 to 0.80, and an inlet mixture velocity of 1-3 m/s. Film-wise condensation prevailed throughout all tests. The heat transfer coefficient was measured and found to vary from 100 to 600 W/(m^2-K). For the present TRACE assessment, only data from vertical orientation (downward flow) have been used.

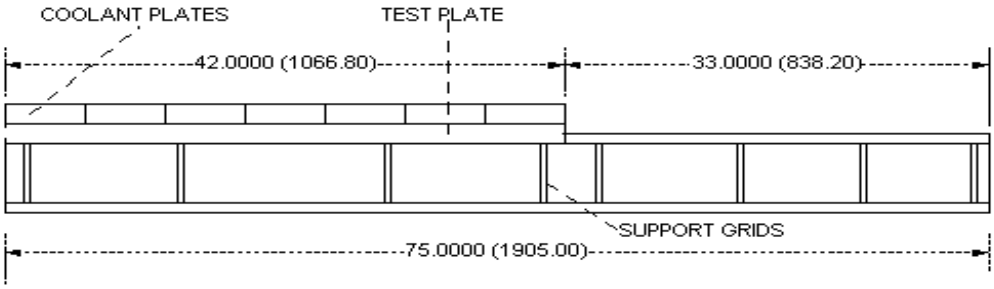

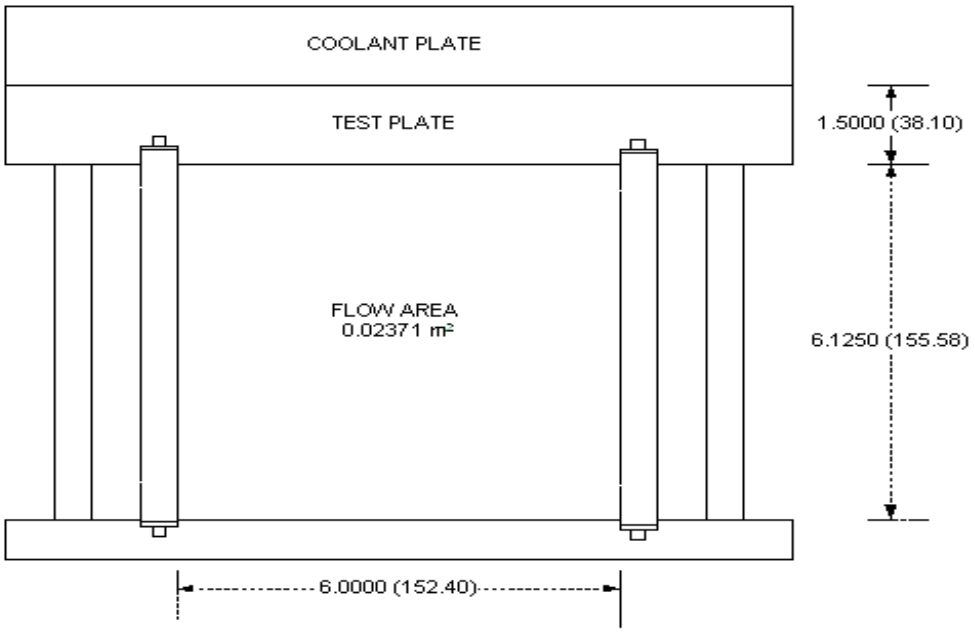

Figure B.21-1. Schematic of the University of Wisconsin Flat Plate Condensation Facility

B.21.3. TRACE Model Description

All simulations were performed with TRACE Version 5.0RC3. In this version, the specialized wall condensation model is available to the user as an option to the normal TRACE logic. So that the models are called only for the intended regions and so that they do not interfere with the operation of other models, an option flag for VESSEL and PIPE Components was added. The wall condensation model is activated in a VESSEL Component by setting the "VessType" flag equal to 1 (0 is the default value for the VESSEL Component). The same wall condensation model is available also for PIPE Components. In this case, the model is activated by setting PipeType=8 for that particular PIPE in its input. The wall condensation model applies to both the hydraulic components and the heat structures connected to the hydraulic components that have the wall condensation flag activated. Such heat structures are automatically flagged as "wall condensation heat structures" without requiring additional user input. This approach is the same as that used in the development of the tube condensation models.

The TRACE nodalization of this facility is shown in Figure B.21-2 The scheme (FILL-PIPE-VESSEL/HTSTR-PIPE-BREAK) is very similar to the nodalization of the Dehbi-MIT tests. The FILL component imposes the inlet mixture velocity, temperature and air mass fraction; the VESSEL component makes use of cartesian coordinates and models the test section together with the HTSTR component. Five VESSEL levels were specified to model the test section, in addition to an entry and an exit cells. Therefore, the VESSEL component is essentially a 1-D component with seven axial levels. The hydraulic diameter of the VESSEL is based on the perimeter wetted by the liquid film. The constant wall temperature from the experiments is imposed as a boundary condition in the HTSTR. The BREAK at the outlet prescribes the test pressure. The two PIPE components are merely connection elements between the VESSEL and the inlet and outlet boundaries.

The TRACE input deck is documented in Reference 2.

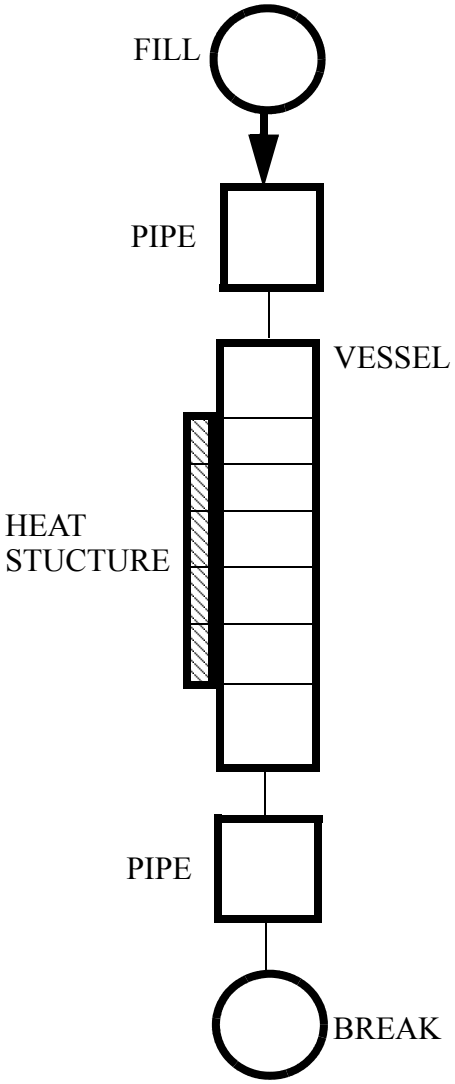

Figure B.21-2. TRACE Model Schematic of the University of Wisconsin Flat Plate Condensation Tests.

B.21.4. Tests Simulated with TRACE

The results of the simulations of the University of Wisconsin tests are summarized in Table B.21.1. Following the same procedure adopted in the experiments, the average TRACE heat transfer coefficient over the condensing surface was determined and compared to the experimental value. It was observed in the TRACE simulations, that the TRACE local condensation heat transfer coefficient at the first mesh of the HTSTR representing the wall was generally exceeded the experimental value and was often oscillatory in the simulation. Those points were not included in the calculation of the average condensation heat transfer coefficient, as the condensation model was not being used at those elevations. This effect can be corrected by adopting a finer nodalization at the boundary of the heat structure.

For inlet velocity of 1 m/s, the calculated results show a maximum deviation from the experimental value of 14.29% (test #5). The experimental uncertainty for these tests is 6%. At the higher inlet velocity of 3 m/s, the TRACE predictions underestimate the measured value with an error in the order of 60%. This fact is not surprising, as the wall condensation models implemented in the code are not suitable for prediction of the increased Sherwood number above its natural convection value due to the increased Reynolds number. It is therefore suggested that a multiplier of the Nu/Sh numbers be implemented in TRACE (in form of an additional NAMELIST variable) as on option for the user to model forced convection condensation.

Table B.21.1. Results of the Simulations of the University of Wisconsin Tests

Test #	**delta T [K]**	**Air Quality [%]**	**Velocity [m/s]**	**HTC [W/(m^2 K)]**		**Error [%]**	**Exp. Unc. [%]**
				TRACE	**EXP**		
1	40	77.8	1	104.16	111.1	-6.66	10
2	40	77.8	3	134.32	213.9	-59.25	10
3	50	64.0	1	163.74	163.9	0.10	10
4	50	64.0	3	182.90	305.6	-67.09	10
5	60	40.5	1	298.09	255.5	14.29	10
6	50	22.5	1	537.18	546.0	-1.75	10

B.21.5. Assessment Results Summary

The assessment of the new wall condensation model implemented in TRACE shows that the code can accurately predict the heat transfer coefficients for steam condensation in film mode along cooled walls in the presence of non-condensable gases for gas velocities up to 1 m/s. In this velocity range, this assessment against the University of Wisconsin experiments confirms the results obtained for the Dehbi tests, i.e., the code predictions of the condensation heat transfer coefficient are within a 20% accuracy range. For higher velocities, TRACE underestimates the condensation heat transfer coefficient.

B.21.6. References

1 Huhtiniemi, I. K., and Corradini, M. L., “Condensation in the Presence of Noncondensable Gases,” Nucl. Eng. Des., 141, pp. 429-446, 1993.

2 Delfino, C., "TRACE Calculational Notebook for University of Wisconsin Flate Plate Condensation Tests," ADAMS ML071770144, July 2006.

Steam Binding and Steam Generator Thermal-Hydraulics Tests

B.22. FLECHT-SEASET Steam Generator Tests

Author(s): Shawn O. Marshall, Michael Salay

Affiliation: USNRC-RES/DRASP/NRCA/CDB

Code Version: TRACE V5.0

Platform and Operating System: Intel x86, Windows XP

B.22.1. Introduction

The ability of the TRACE code to accurately predict the detailed thermal-hydraulic response of LWRs during accident conditions is being assessed as part of the comprehensive, generic assessment of TRACE that is currently being conducted by the USNRC's Office of Research. One of the important separate effects to be considered in this assessment is the steam binding effect that occurs during the reflood stage of the PWR LOCA. This phenomenon is characterized by a pressure increase in the upper plenum of the reactor, which is caused by the boiling of entrained liquid that has been carried over into the steam generator.

In this section, the ability of the TRACE code to predict steam binding is assessed against data collected from tests conducted on the Full-Length Emergency Cooling Heat Transfer Systems Effects Test (FLECHT SET) Phase B steam generator, as part of the Westinghouse/NRC/EPRI Full-Length Emergency Cooling Heat Transfer for the Separate Effects and Systems Effects Test (FLECHT SEASET) reflood program. In this program, a series of heat transfer tests were run in a model steam generator operating under simulated LOCA conditions. The model steam generator contained 32 full-length U-tubes instrumented with thermocouples to measure secondary fluid, tube wall, and primary steam temperatures. The purpose of these tests was to measure and characterize the steam generator secondary side to primary side heat release under fluid conditions for a hypothetical PWR LOCA.

B.22.2. Test Facility Description

Figure B.22-1 provides a detailed schematic diagram of the FLECHT SET Phase B steam generator test loop used in conducting the separate effects tests (Ref. 1). The major components in the loop are the boiler, accumulator, steam/water mixer, steam generator, and containment tank. The boiler and accumulator supply steam and water to a mixing chamber which generates a two-phase flow to the steam generator. Steam separators in the steam generator discharge flow path

separate the two-phase effluent from the steam generator tube bundle to allow each component of the two-phase flow to be measured.

The facility steam supply is a 1.23 MW steam boiler, with a thermal output rating of 1.2255 MW and equivalent steam rating of 1956 kg/hr at 373 K. The unit operated at 0.69 MPa for all tests. The water supply tank, which provides the water for the mixer section, has a capacity of approximately 0.946 m^3 (250 gallons) and is designed for 2.06 MPa at 616 K. Strip heaters on the tank wall along with a mixing pump are used to bring the water to the saturation temperature corresponding to the specified test pressure. A constant nitrogen gas overpressure supplies the driving head for injecting water into the mixer section. The steam-water mixer is shown in Figure B.22-2 and consists of a liquid spray nozzle located inside the steam flow line in the horizontal run of hot leg pipe upstream of the steam generator.

The steam generator used for the separate effects task is the large steam generator simulator used in the FLECHT SET Phase B test program. Of the 33 tubes available in the facility, no less than 32 must be used to preserve the desired flow area scaling relationship.

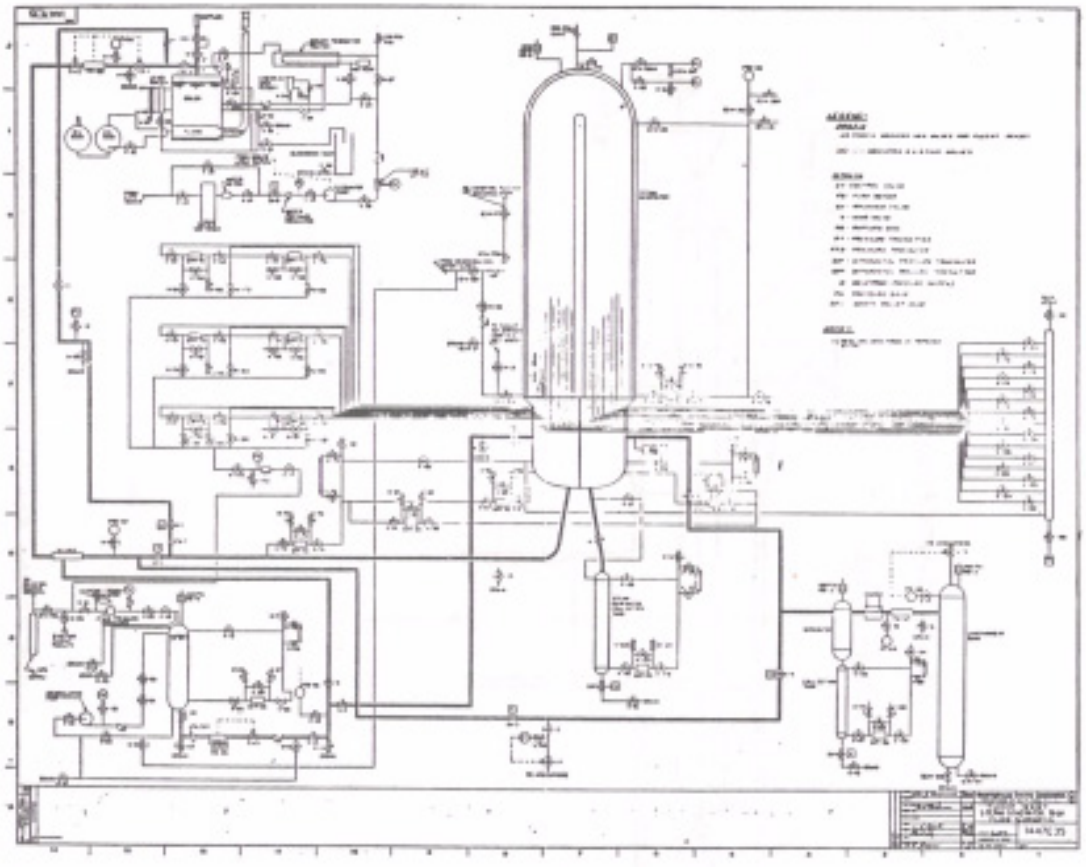

Figure B.22-1. Schematic of FLECHT SET Phase B steam generator test loop

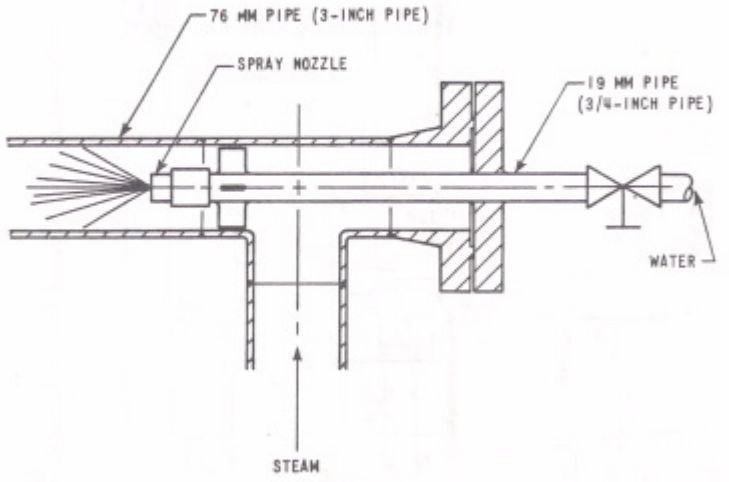

Figure B.22-2. Mixer configuration

A steam separator located downstream of the steam generator is used to separate any remaining entrained liquid so that a accurate single-phase steam flow measurement can be made by the vortex meter located downstream of the separator. The separator uses centrifugal force to drive the heavier moisture against the walls of the vessel, where it drains to a 3-inch diameter, 7-ft. long collection tank.

The containment tank is the same vessel used in the FLECHT SET test program to provide the containment back pressure simulation. It is made from 24-inch diameter pipe, and has a volume of approximately 450 gallons. The containment tank serves as a convenient point from which to control system pressure, since its large volume helps to dampen any system pressure fluctuations in the test loop.

The loop instrumentation is designed to measure mass and energy transport across the primary side inlet and outlet boundaries of the steam generator. Flow meters in the boiler steam line, liquid supply tank feed line, and steam separator exhaust feed line establish the steam and liquid mass flow rates. Within the tube bundle, the heat transfer process is monitored by thermocouples in the secondary fluid and on the tube wall, and by steam probes inside the tubes. The tube bundle instrumentation is specifically designed to measure a radial variation in heat transfer rate due to expected nonuniform two-phase flow in the inlet plenum. The distribution of secondary fluid and tube wall thermocouples is skewed toward the bottom of the bundle, because prior FLECHT SET Phase B data showed that most secondary temperature variation occurred below the 2-ft. elevation. The steam probe axial spacing is based on calculations of vapor temperature versus tube length from a model of the two-phase heat transfer process in the tubes. Photographic techniques were used to identify the tow-phase flow regime in the steam generator inlet and outlet plena. Droplet size and velocity information were obtained from high-speed movies and still photographs.

B.22.3. Model Description

The nodalization of the TRACE model of the FLECHT SET Phase B steam generator is shown in Figure B.22-3. The system is modeled as follows: Water is injected into the mixer (TEE 2) by FILL 11 via PIPE 1. Steam is injected into the mixer by FILL 12. The mixture then flows from the mixer, through the inlet plenum (represented by PIPE 3), to the steam generator tubes, all of which are modeled by PIPE 4. The downhill side of the steam generator tubes is connected to BREAK 13 where primary flow leaves the system. A total of 24 heat structures were used to model heat transfer between the primary and secondary side (PIPE 5) of the steam generator, one for each of PIPE 4 cells 2 through 25, each of which is connected to the cell in PIPE 5 at the same elevation (cells 1 through 12). Further modeling details are provided in the calculation notebook (Ref. 4).

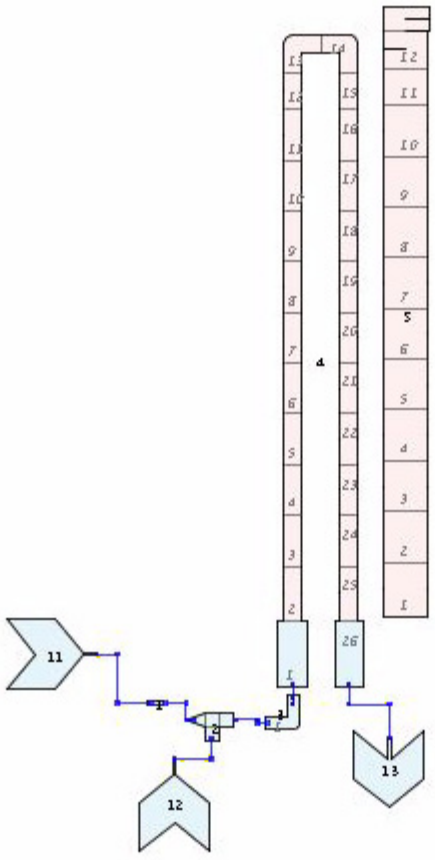

Figure B.22-3. TRACE nodalization

B.22.4. Test Description

Before performing the experiments, the facility and the steam generator were brought to the desired initial conditions. Electrical strip heaters and a low-pressure recirculation pump were

used to produce a uniform temperature distribution on the secondary side. The primary side piping was heated to the primary side saturation temperature using bleed steam from the boiler. Once the system had been heated, the steam and liquid flows were adjusted to their desired values at the mixer, with the resulting two-phase flow being bypassed to the drain while these conditions were being established. When the desired inlet flow conditions had been established, the inlet two-phase flow was directed into the steam generator by proper alignment of the loop valves, to start the transient. Loop pressure and inlet flow were thereafter maintained constant by control valves.

B.22.5. Code Boundary Conditions and Steady State Predictions

Four test runs with different boundary and initial conditions were simulated using TRACE. Test 22701 served as the reference case, tests 21806 and 23605 were used tot test quality sensitivity, and test 23402 was used to test flow sensitivity. The initial conditions and boundary conditions for these tests are shown in Table B.22.1.

Table B.22.1. Run Conditions

	Time-Averaged Boundary Conditions			SG Secondary Initial Conditions	
Plant Parameters	Total Flow (kg/s)	Quality	Pressure (MPa)	Temperature (K)	Level (m)
21806	0.227	0.2	0.174	544	10.7
22701	0.225	0.798	0.174	546	10.8
23402	0.449	0.799	0.174	546	10.5
23605	0.224	0.496	0.173	546	11.0

B.22.6. Principal Figure(s) of Merit

The performance of TRACE in simulating the characteristics of the steam binding effect in the FLECHT SET Phase B steam generator is based on how closely its predictions compare with the experimental measurements taken during each of the four chosen tests. Of primary interest are the total energy transported from the secondary to the primary side and the amount of liquid that remains in the two-phase flow after traveling the superheated circuit of the steam generator tubes. The steam superheat an another indicator of liquid carryover in that energy transferred to the fluid that does not contribute to steam superheating results in liquid vaporization.

Figures B.22-4 through B.22-9 compare measured and predicted results for test 22701. Figures B.22-10 through B.22-15 compare measured and predicted results for test 21806. Figures B.22-16 through B.22-21 compare measured and predicted results for test 23402. Figures B.22-22 through B.22-27 compare measured and predicted results for test 23605.

B.22.6.1. Simulation of test 22701

Test 22701 served as the reference run for the series with a quality of 0.8 and a total flow of 0.225 kg/s.

The steam generator tube predicted primary volume fractions at selected locations on the uphill side are shown for test 22701 in Figure B.22-4. For the first 300 s, no liquid water is predicted to enter into the steam generator tubes. During this period the inlet plenum is predicted to accumulate liquid water. This continues until the void fraction in the inlet plenum reaches approximately 0.33 at which point water abruptly begins to be carried up through the steam generator tubes. When the void fraction in the steam generator tubes drops below 1.0, the predicted heat transfer regime in the lower 3 steam generator cells changes from single phase vapor heat transfer to transition boiling. Other uphill side cells are predicted to change to transition boiling throughout the test. The predicted cell heat transfer regimes later transition to nucleate boiling. This transition occurs sequentially and at regular intervals, starting at the lowest steam generator cell and moving upwards, indicating the prediction of a liquid film advancing at a near constant rate, as was observed in the experiment.

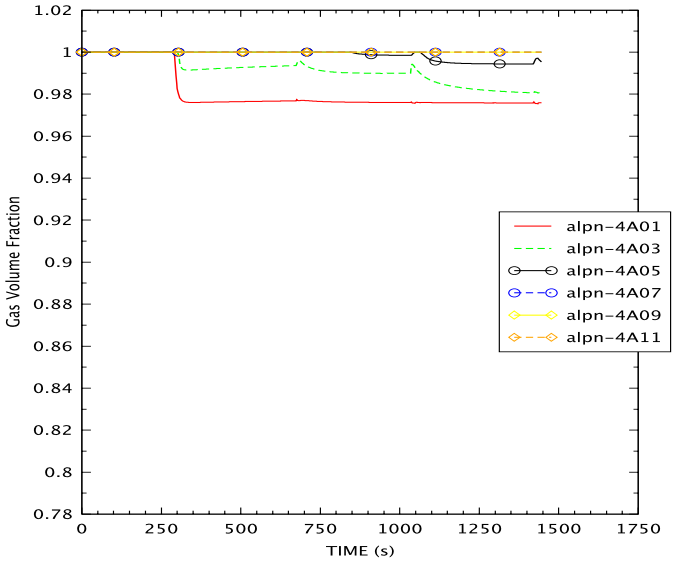

Figure B.22-4. Test 22701 steam volume fraction in SG tube cells

Predicted and experimental primary steam temperature distributions in the steam generator tubes at the end of test 22701 are compared in Figure B.22-5. Both the vapor and liquid temperatures are shown for TRACE. The steam temperature is well predicted both in the distance within the steam generator tubes that the vapor is in equilibrium and also the peak superheat. The entire predicted curve, including the saturation temperature, falls approximately 10 K below the data, indicating that the predicted system pressure is lower than that of the experiment.

The bundle exit liquid flow for test 22701 is shown in Figure B.22-6. In the experiment, a constant amount of liquid carryover was observed throughout the test with 4.5 kg of liquid

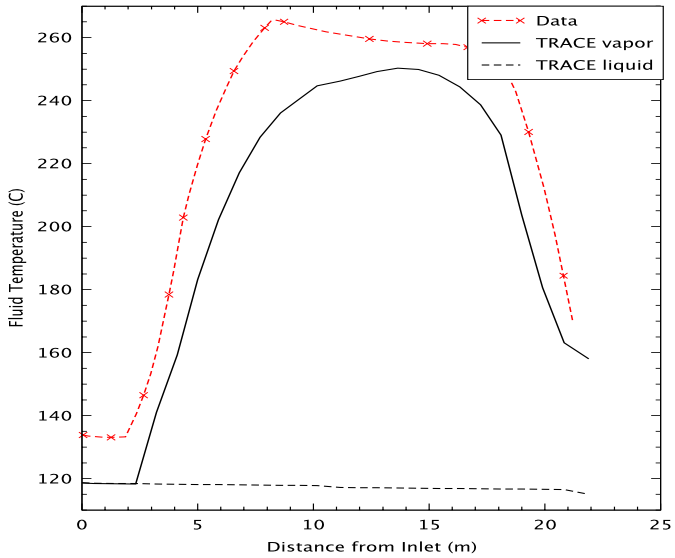

Figure B.22-5. Test 22701 SG tube fluid temperature at 1450 s

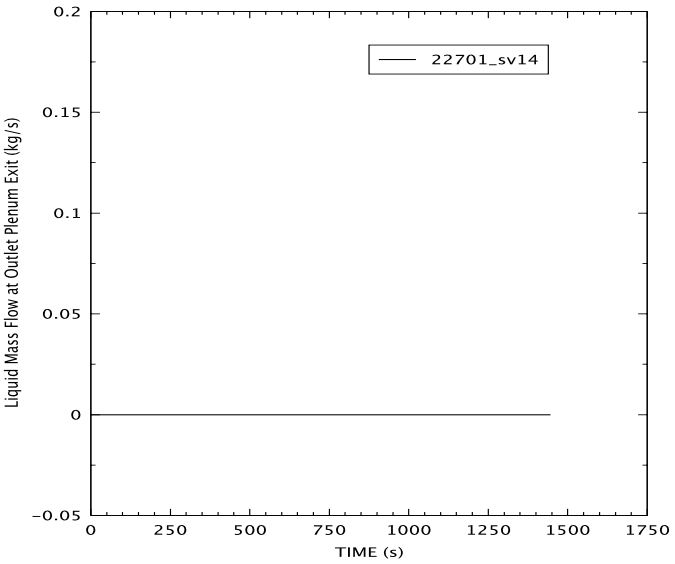

Figure B.22-6. Test 22701 SG tube exit liquid flow

collected in the outlet plenum by the termination of the test. TRACE predicted no liquid leaving the steam generator tubes with all entering liquid being evaporated on the uphill side.

The comparison of pressure drop across the bundle for test 22701 is shown in Figure B.22-7. The pressure drop is overpredicted by approximately 30% before 300 s. When the liquid is predicted to enter the steam generator primary side, the predicted pressure drop jumps, resulting in a prediction double the experimental pressure drop. This overprediction continues until the end of the test. The 3 periodic jumps in the predicted pressure drop occur when heat structures 1, 2, and 3 at elevations of 0.49 m, 1.43 m, and 2.32 m, respectively, are predicted to switch to nucleate boiling heat transfer.

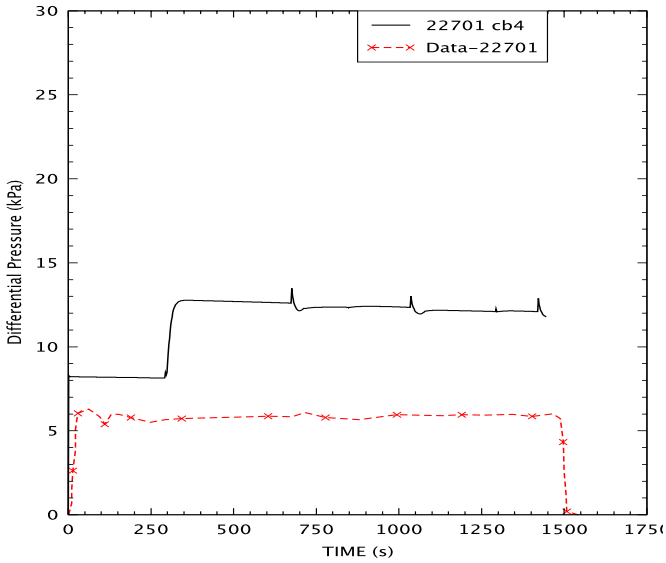

Figure B.22-7. Test 22701 bundle differential pressure

A comparison of the predicted and experimental total heat transfer rate for test 22701 is shown in Figure B.22-8. Before the liquid water is predicted to enter the steam generator tubes at approximately 300 s, the heat transfer rate is under predicted by 2/3. After the liquid is predicted to enter the steam generator tubes, the heat transfer, like the pressure drop, jumps due to the additional heat transfer from the wall to the liquid, and exceeds the experimental heat transfer by nearly 30%. The overprediction decreases to less than 10% by the end of the test. The periodic jumps in the predicted heat transfer rate, occurring during a switch in the predicted heat transfer regime, coincide with the jumps seen in the bundle differential pressure. Additional heat transfer can result in either more primary evaporation, greater superheat, or a combination of the two, either of which increase the steam velocity and thus the pressure drop.

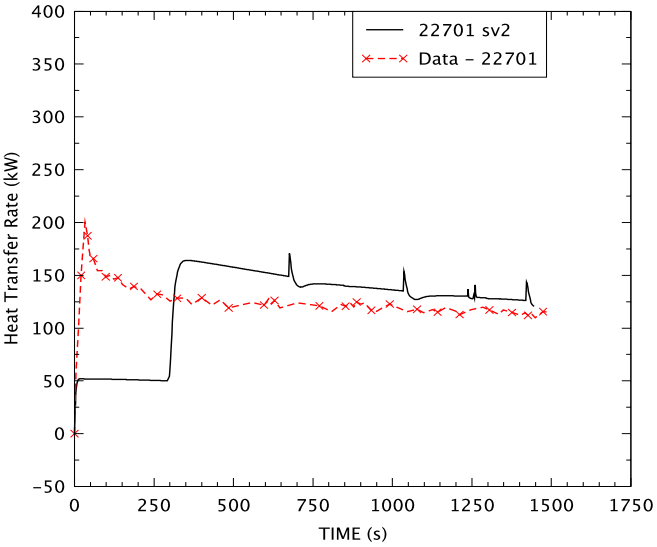

Figure B.22-8. Test 22701 total heat transfer rate

A comparison steam generator tube wall temperature at an elevation of 1.22 for test 22701 is shown in Figure B.22-9. Temperatures at the two nearest bounding elevations (0.49 m and 1.43 m) are provided for TRACE. The predicted quench front is significantly broader than that of the experiment as the predicted wall temperature cools gradually and does not exhibit the experimentally observed sudden drop in temperature with the arrival of the quench front. The predicted drop at 300 s occurs when liquid is predicted to enter the steam generator tubes. This drop coincides with the changes in void fraction, differential pressure, and heat transfer rate which were predicted at this time.

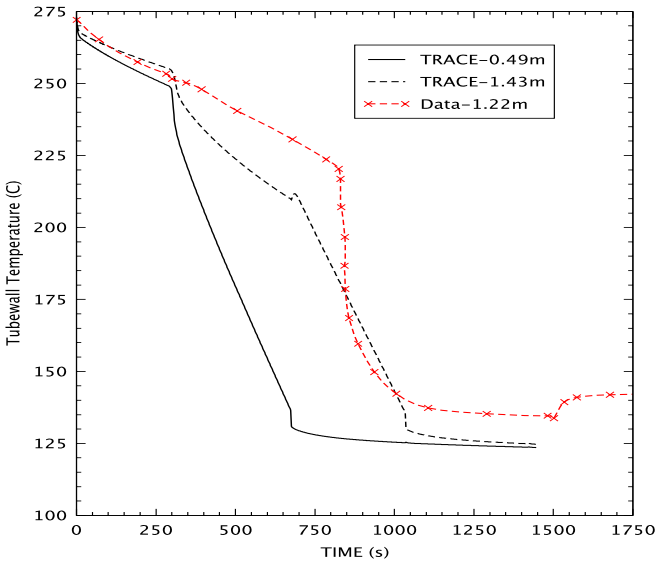

Figure B.22-9. Test 22701 SG tube wall temperature at 1.22 m (4 ft)

B.22.6.2. Simulation of test 21806

Test 21806 served as part of the quality sensitivity study. This test used the lowest inlet quality, 0.2, while maintaining the same mass flow rate as the reference case. The additional cooling capacity greatly affected the system response compared to the reference case. Other conditions were similar to the reference case.

The steam generator tube predicted primary volume fractions at selected locations on the uphill side are shown for test 21806 is shown in Figure B.22-10. As in the reference case, liquid water was not predicted to immediately enter the steam generator tubes but instead collected in the inlet plenum. Liquid collection in the inlet plenum for this test was considered to be the cause for similar quench times observed at 1.22 m for this test and the 50% quality sensitivity run (23605). The predicted void fraction in the steam generator tubes stabilizes at a much lower value than in the reference case, approximately 0.8 instead of 0.98. The predicted void fraction drop, along with transition of heat transfer regime from single phase vapor to transition boiling and then to nucleate boiling, which is indicative of the advancing quench front, progresses much more rapidly than in the reference case.

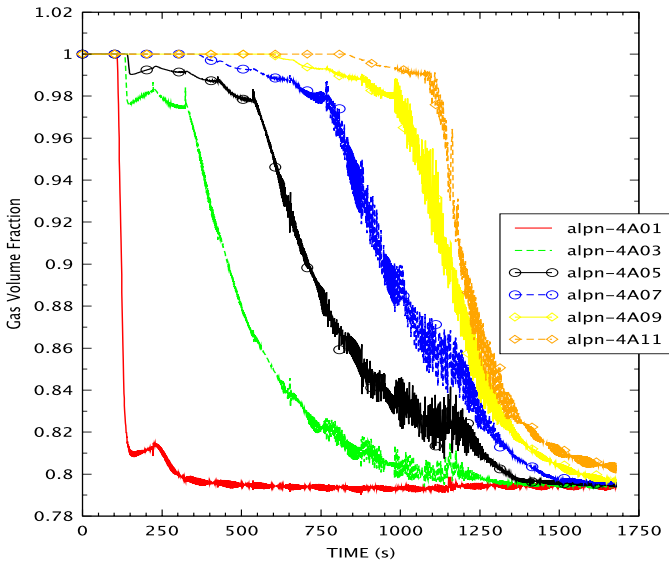

Figure B.22-10. Test 21806 steam volume fraction in SG tube cells

Predicted and experimental primary steam temperature distributions in the steam generator tubes at the end of test 21806 are compared in Figure B.22-11. As in the reference case, both the vapor and liquid temperatures are shown for TRACE. All steam is predicted to be saturated by approximately 1250 s whereas, although decreasing, some superheated steam was observed in the experiment until the end of the test near 1750 s. The predicted cooling was more rapid than in the experiment, enough that the temperature of the entire secondary side was predicted to have decreased to near that of the primary saturation temperature by 1250 s. This was not the case in the experiment in which the upper regions of the secondary side remained warm throughout, although cooler at 20% of the original temperature difference between the secondary side and the primary side saturation temperature by the end of the test.

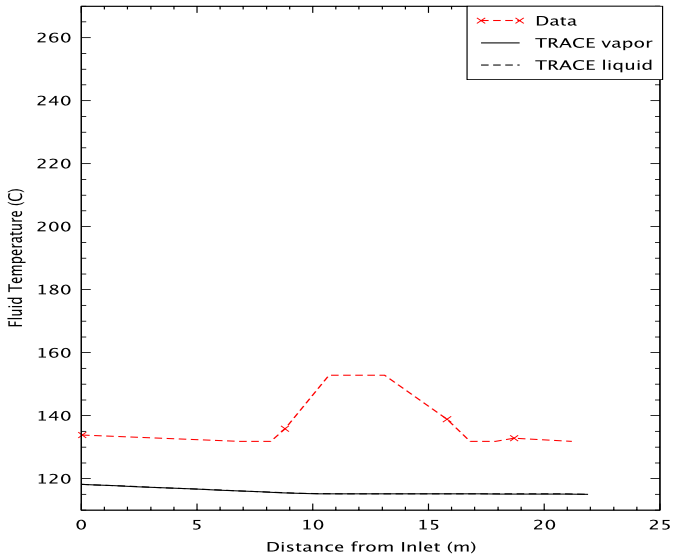

Figure B.22-11. Test 21806 SG tube fluid temperature at end of test

The bundle exit liquid flow for test 21806 is shown in Figure B.22-12. No liquid was predicted leaving the steam generator tubes until the primary side became saturated. Before this, all liquid was predicted to have been evaporated on the uphill side. After all the steam became saturated, liquid was predicted to exit the steam generator tubes. This behavior is not consistent with the experimental report which lists an average liquid collection rate of 0.0059 kg/s until the entire bundle quenched at 1250 s, with a increase in the liquid collection rate after quenching.

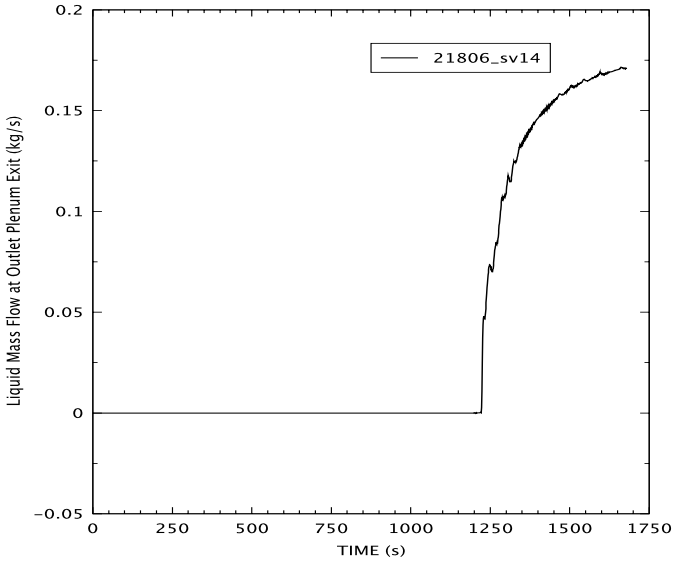

Figure B.22-12. Test 21806 SG tube exit liquid flow

The comparison of pressure drop across the bundle for test 21806 is shown in Figure B.22-13. The pressure drop was significantly underpredicted before liquid was predicted to enter the steam generator tubes and was overpredicted after the liquid was predicted to enter the tubes. The predicted differential pressure dropped from about 1100 s to 1250 s as uphill side tube wall became completely cooled, reducing the vapor generation rate. Although complete quenching occurred somewhat later in the experiment, a similar pressure drop was not observed in the experiment. Unlike the reference case, the bundle pressure drop increased throughout the test. After the predicted heat transfer regime on the last uphill side cell switched to nucleate boiling, the heat transfer regimes on the downhill side rapidly followed. As in the reference case, periodic differential pressure spikes were predicted when heat structures connecting the primary side to the secondary side are predicted to switch to nucleate boiling heat transfer.

A comparison of the predicted and experimental total heat transfer rate for test 21806 shown in Figure B.22-14. In this test both the experiment and prediction have a period during which the inner plenum fills before liquid water begins to enter the steam generator tubes. Some liquid does appear to have entered the tubes at the beginning of the test in the experiment as indicated by the elevated heat transfer at the beginning of the test, which dips back down as the inlet plenum fills. The predicted duration of inlet plenum filling of about 150 s is twice as long as that of the experiment. As in the reference case, once liquid is predicted to enter the steam generator tubes, the heat transfer rate is overpredicted, by 20% at first which decreases gradually. The predicted heat transfer rate begins to drop about 150 s before the experiment due to earlier quenching of the

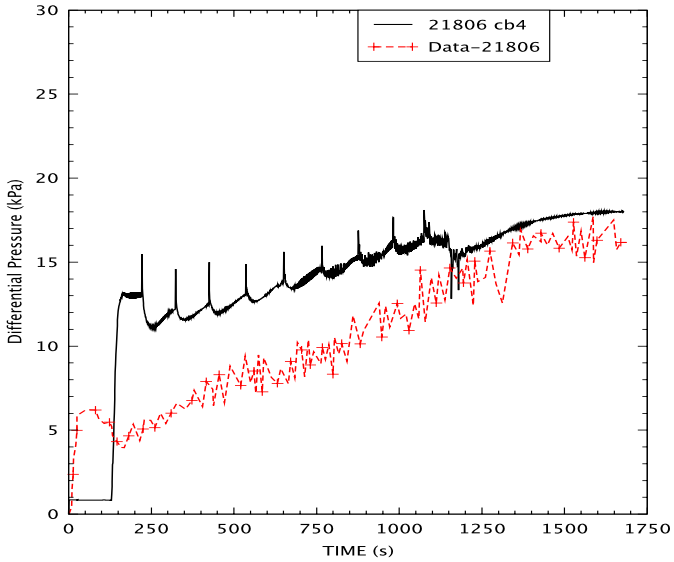

Figure B.22-13. Test 21806 bundle differential pressure

entire rods, associated loss of superheating, and nearly complete cooling of the secondary side. As in the prediction of the reference case, the periodic jumps in heat transfer, caused by the change of heat transfer regimes, coincide with the periodic jumps in pressure drop.

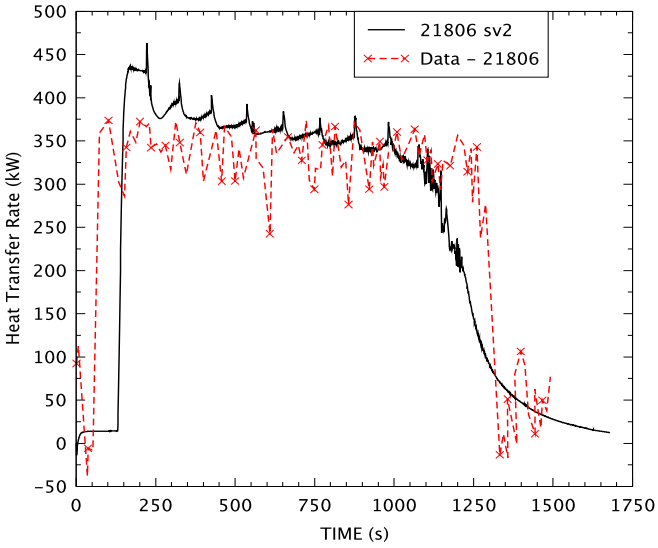

Figure B.22-14. Test 21806 total heat transfer rate

A comparison steam generator tube wall temperature at an elevation of 1.22 for test 21806 is shown in Figure B.22-15. Temperatures at the two nearest bounding elevations (0.49 m and 1.43 m) are provided for TRACE. As in the reference case, the predicted quench front is significantly broader than that of the experiment as the predicted wall temperature cools gradually and does not exhibit the experimentally observed sudden drop in temperature with the arrival of the quench front. The predicted sharp drop at 150 s occurs when liquid is predicted to enter the steam

generator tubes. This drop coincides with the changes in void fraction, differential pressure, and heat transfer rate which were predicted at this time. The predicted wall cooling rate is greatly overpredicted once the liquid is predicted to enter the steam generator tubes.

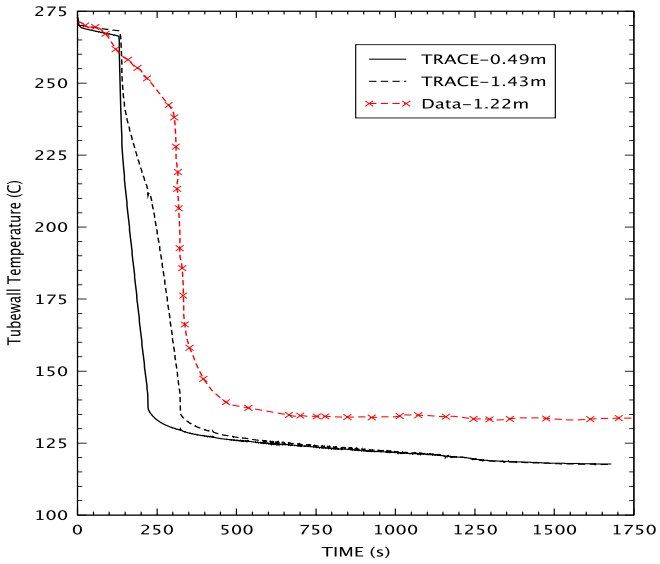

Figure B.22-15. Test 21806 SG tube wall temperature at 1.22 m (4 ft)

B.22.6.3. Simulation of test 23402

Test 23402 was used to investigate the effect of mass flow rate. This test had the same inlet quality as the reference case with double the flow rate of the other tests. Other conditions were similar to the reference case.

The steam generator tube predicted primary volume fractions at selected locations on the uphill side are shown for test 23402 is shown in Figure B.22-16. Behavior is similar to that of the reference case with the lowest volume fraction achieved being 0.98. The time before liquid starts entering the steam generator tube is less than halved, and the rate of decrease in the void fraction occurs more rapidly.

Predicted and experimental primary steam temperature distributions in the steam generator tubes at the end of test 23402 are compared in Figure B.22-17. Although the distance until superheating begins, indicative of the quench location, is well predicted, the peak superheat at this time is underpredicted by about 60%. Either wall cooling by droplets is being overpredicted resulting in less wall temperature available to superheat the vapor, wall heat transfer to the vapor is being underpredicted, or vapor heat transfer to the liquid is being overpredicted.

The steam generator tube exit liquid flow for test 23402 is shown in Figure B.22-18. A constant amount of liquid carryover was observed throughout the test in the experiment with nearly 5 kg of liquid collected in the outlet plenum by the end of the test. TRACE predicted no liquid leaving the steam generator tubes with all entering liquid being evaporated on the uphill side.

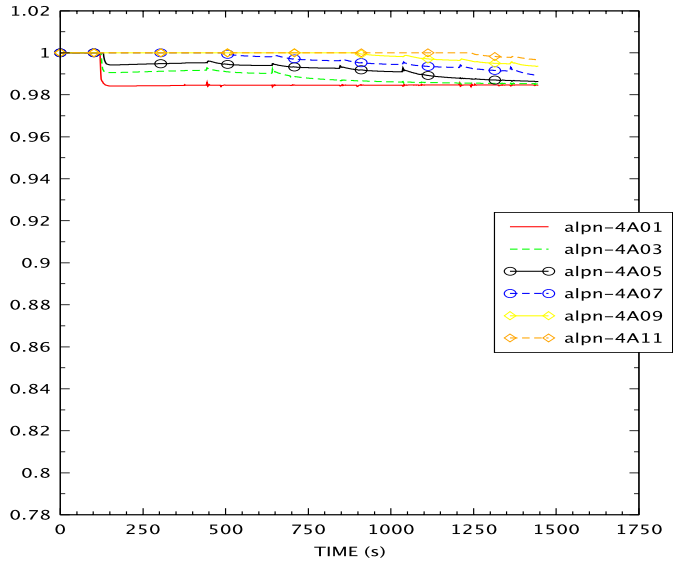

Figure B.22-16. Test 23402 steam volume fraction in SG tube cells

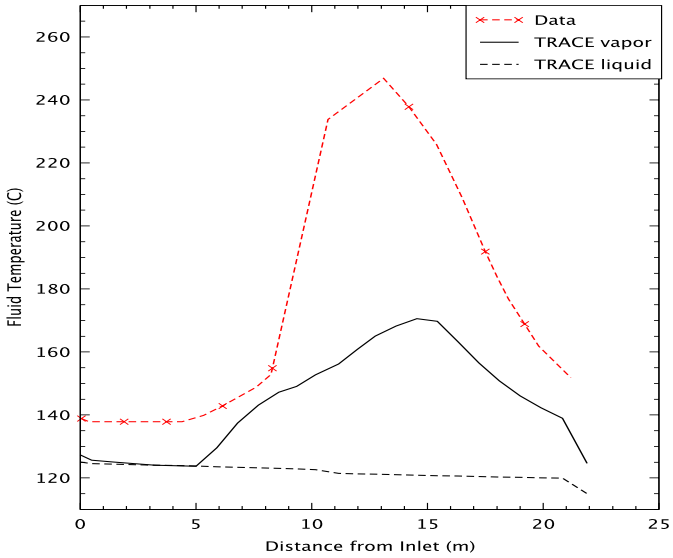

Figure B.22-17. Test 23402 SG tube fluid temperature at 1450 s

The comparison of pressure drop across the bundle for test 23402 is shown in Figure B.22-19. As in the reference case, the pressure drop is over predicted throughout, even before liquid is predicted to enter the steam generator tubes. The initial over prediction by about 40% jumps to approximately double the experimental value when liquid is predicted to enter the steam generator tubes. As in the other tests, periodic spikes in the predicted differential pressure can be seen when the heat transfer regimes in different heat structures transition to nucleate boiling.

A comparison of the predicted and experimental total heat transfer rate for test 23402 is shown in Figure B.22-20. As in the other tests, due to predicted accumulation of liquid in the beginning of the test, the heat transfer is significantly underpredicted for the first 150 seconds, before liquid is

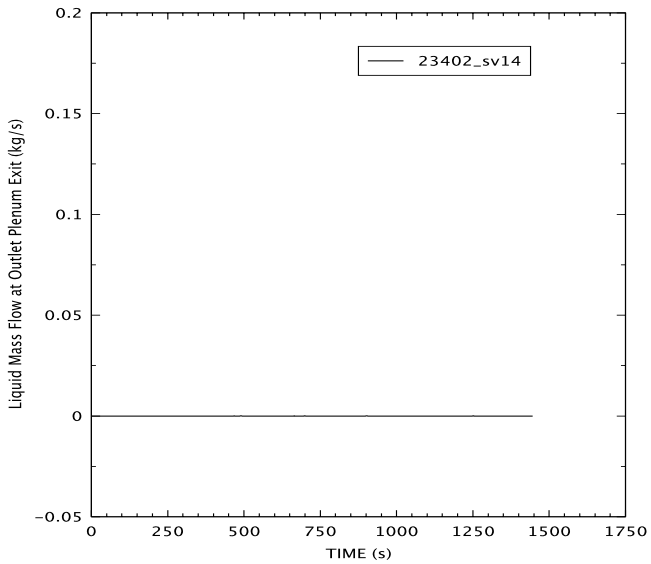

Figure B.22-18. Test 23402 SG tube exit liquid flow

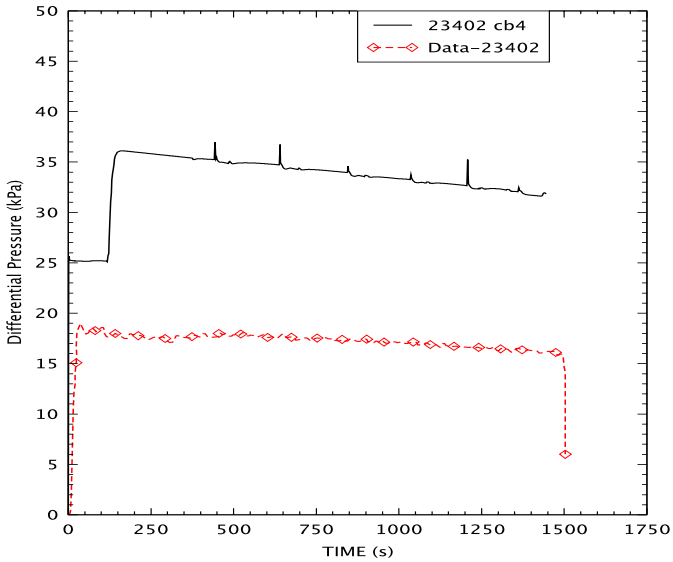

Figure B.22-19. Test 23402 bundle differential pressure

predicted to enter the SG tubes, and overpredicted by about 20% immediately after. The subsequent decrease in heat transfer rate is predicted to be greater than observed in the experiment leading to a reasonable match in the heat transfer rate for the last 500 s of the test. The periodic jumps in the predicted total heat transfer coincide with those of the predicted pressure drop.

A comparison steam generator tube wall temperature at an elevation of 1.22 for test 23402 is shown in Figure B.22-21. Again, bounding curves are provided for the simulation. As in the other tests, the predicted quench front is significantly broader than that of the experiment as the predicted wall temperature cools gradually and does not exhibit the experimentally observed sudden drop in temperature with the arrival of the quench front. The predicted drop at 150 s

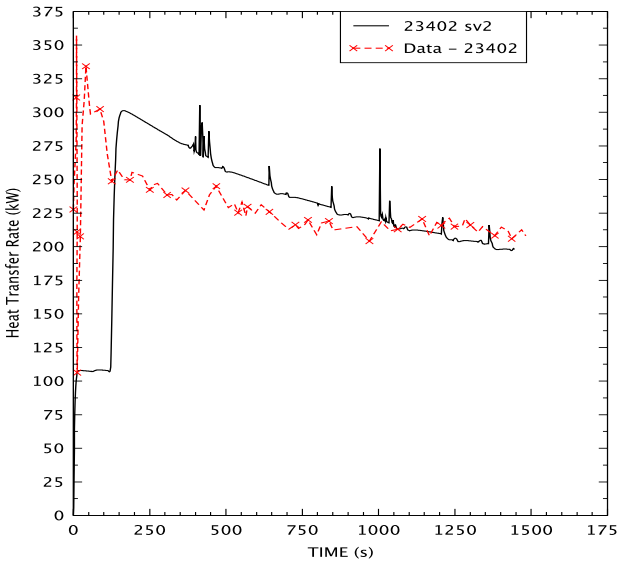

Figure B.22-20. Test 23402 total heat transfer rate

occurs when liquid is predicted to enter the steam generator tubes. This drop coincides with corresponding changes in void fraction, differential pressure, and heat transfer rate.

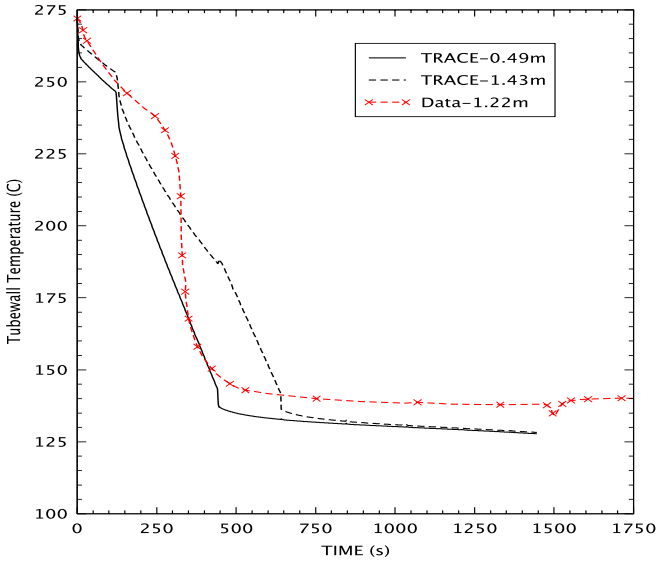

Figure B.22-21. Test 23402 SG tube wall temperature at 1.22 m (4 ft)

B.22.6.4. Simulation of test 23605

Test 23605 served as part of the quality sensitivity study along with the previously discussed test 21806. This test had an inlet quality of 0.5, in between that of the reference case and test 21806. Other conditions were similar to the reference case.

The steam generator tube predicted primary volume fractions at selected locations on the uphill side are shown for test 23605 is shown in Figure B.22-22. As in the other cases, liquid water was not predicted to immediately enter the steam generator tubes but instead collected in the inlet plenum. The void fractions stabilize at approximately 0.9, less than the 0.98 reached by the reference run (22701) and the flow sensitivity run (23402), but greater than 0.8 reached by the run with a quality of 0.2 (21806).

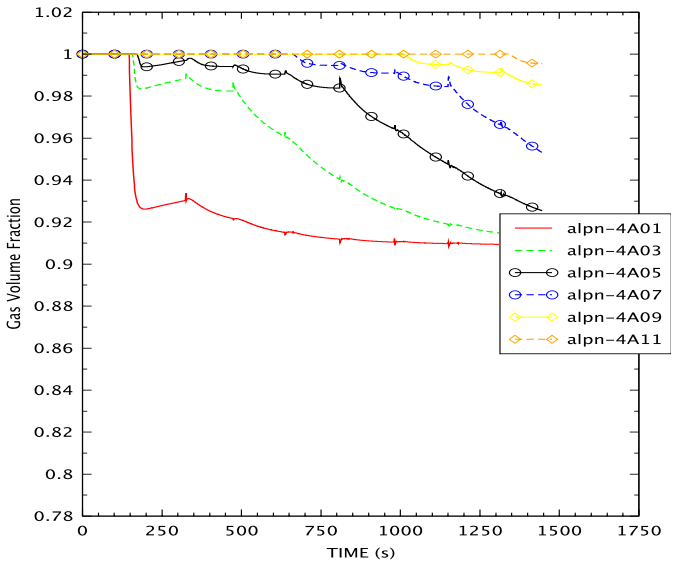

Figure B.22-22. Test 23605 steam volume fraction in SG tube cells

Predicted and experimental primary steam temperature distributions in the steam generator tubes at the end of test 23605 are compared in Figure B.22-23. As in the other tests, saturation temperature is predicted low, predicted distance along the steam generator tubes in which fluid is in thermal equilibrium is well predicted (except for test 21806 in which the entire steam generator length was predicted to be saturated at the end of the test), and the amount of superheating is underpredicted although the predicted superheat profile is similar to that observed in the experiment.

The exit liquid flow for test 23605 is shown in Figure B.22-24. As in all tests but 21806, no liquid is predicted to exit the steam generator tubes, all liquid is evaporated on the uphill side of the steam generator tubes and thus no liquid is carried over.

The comparison of pressure drop across the bundle for test 23605 is shown in Figure B.22-25. The bundle pressure drop is underpredicted until liquid is predicted to enter the steam generator primary side, at which time the predicted pressure drop jumps to approximately double the experimental pressure drop. This overprediction continues until the end of the test but the difference shrinks as the experimental pressure drop increases while the predicted pressure drop remains constant. As in the other tests, the periodic jumps in the predicted pressure drop occur when heat structures are predicted to switch to nucleate boiling heat transfer.

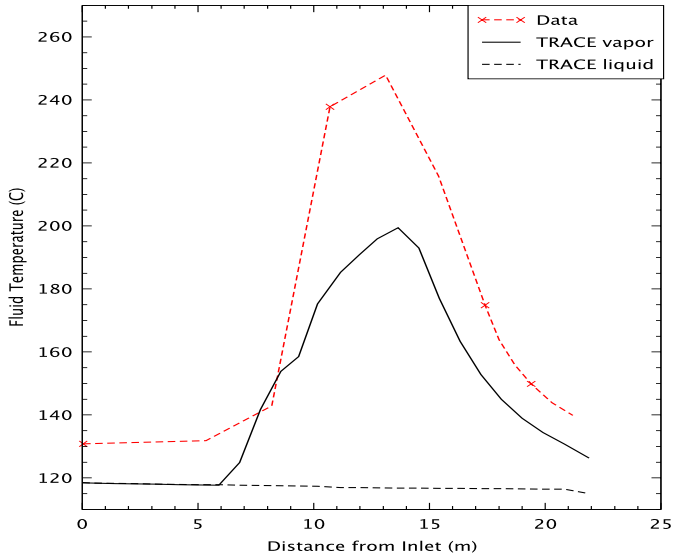

Figure B.22-23. Test 23605 SG tube fluid temperature at 1450 s

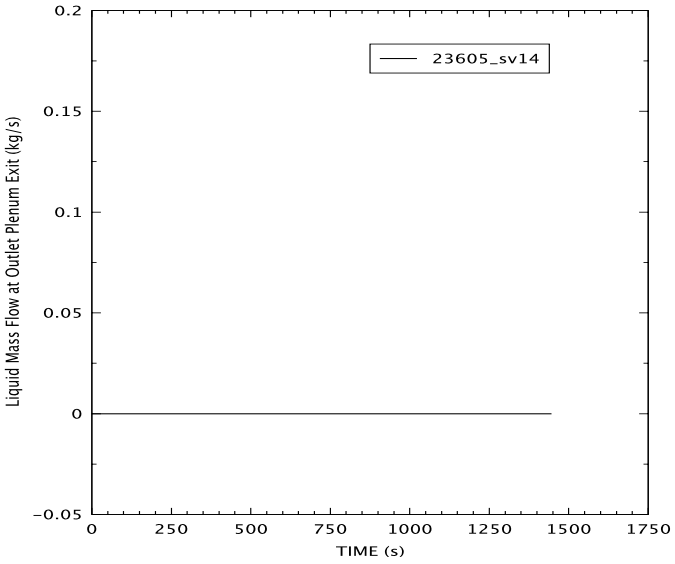

Figure B.22-24. Test 23605 SG tube exit liquid flow

A comparison of the predicted and experimental total heat transfer rate for test 23605 is shown in Figure B.22-26. As in the other tests, the heat transfer is underpredicted until liquid is predicted to enter the steam generator tubes. After liquid is predicted to enter the steam generator tubes, the heat transfer is over predicted by about 20%. The over prediction diminishes, however, resulting in a good prediction of the heat transfer rate for during the second half of the test. The periodic jumps in the predicted total heat transfer rates occur at the same time as those in the predicted differential pressure.

The SG tube wall temperature at 1.22 for test 23605 is shown in Figure B.22-27. Wall temperatures at the two available bounding levels are plotted for TRACE. As in the other tests,

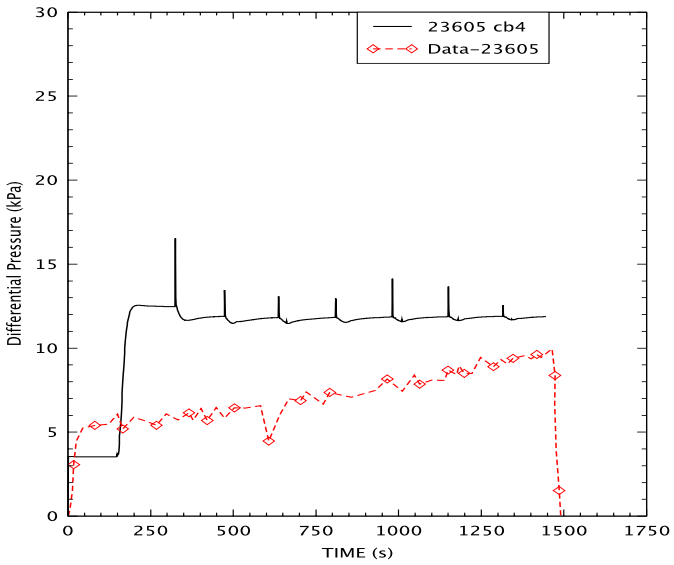

Figure B.22-25. Test 23605 bundle differential pressure

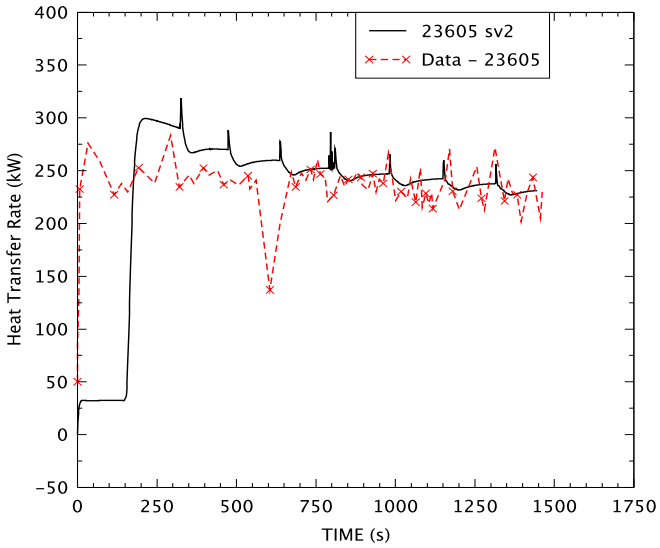

Figure B.22-26. Test 23605 total heat transfer rate

the predicted wall temperature drops sharply when liquid is predicted to enter the steam generator but the cooling rate decreases such that, when the quench front reaches 1.22 m in the experiment, the experimental wall temperature at 1.22 m drops below the predicted wall temperature at 1.43 m.

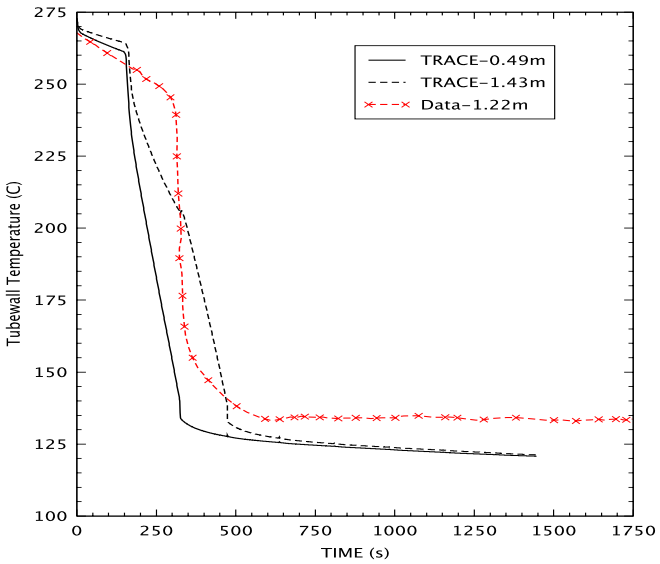

Figure B.22-27. Test 23605 tube wall temperature at 1.22 m (4 ft)

B.22.7. Assessment Results Summary

The performance of TRACE in predicting the primary figures of merit, along with primary-side inlet flow quality, is shown in Table B.22.2. The average ratio of the vapor to flow-mixture mass flow rates, evaluated over the code execution time, is used to calculate primary flow quality at the entrance of the SG tubes. The experimental quality values shown in the table are simply the ratio of the injected vapor and liquid mass flows, whereas the predicted values were taken at the entrance to the SG tubes. In the simulation of test 21806 the flow velocities and qualities at the entrance to the bundle continuously fluctuated over the course of the transient.

Table B.22.2. Run Conditions and Test Results

Run No.	Total Flow (kg/s)	Inlet Plenum Quality			Mass of Liquid Exiting Outlet Plenum (kg)			Total Energy Transport (MW-s)		
		Data	TRACE	%Error	Data	TRACE	%Error	Data	TRACE	%Error
21806	0.227	0.200	0.209	4.42	65.2	64.4	1.23	429	445	3.73
22701	0.225	0.798	0.871	9.15	4.48	1.68e-4	>>50	177	191	7.91
23402	0.449	0.799	0.819	5.12	4.94	3.16e-4	>>50	330	357	8.18
23605	0.224	0.496	0.512	3.16	10.1	1.67e-4	>>50	338	358	5.92

In the experiment, the uphill side tube wall temperature cooled at a constant rate until the quench front arrived. As the quench front arrives the tube wall cooling rate increased significantly until the temperature became close to the primary side saturation temperature. The transition from the initial cooling rate to the quench rate occurs later with increasing tube elevation. In the

predictions, however, a few hundred seconds passed before the void fraction began to drop in the primary side of steam generator tubes, indicating liquid entry into the tubes. During this time, liquid water was predicted to accumulate in the inlet plenum until the inlet plenum void fraction reached a value at which liquid water was predicted to cross through to the steam generator tubes. The predicted inlet plenum void fraction stabilized at a different value for all tests before liquid was predicted to enter into the steam generator tubes. The predicted stable void fraction ranged from 0.1 to 0.5. When liquid was predicted to enter the tubes, transition boiling began to be predicted in the lowest 3 to 5 uphill side cells, and the tube wall cooling rate along the entire uphill side was predicted to increase at this time. Heat transfer and pressure spikes were predicted when heat structures later switched to nucleate boiling on the primary side. The liquid accumulation in the inlet plenum, although also occurring in the experiment to some extent, was significantly overpredicted leading to behavior different than the experiment in the first few hundred seconds of the tests.

After liquid was predicted to enter the steam generator tubes, the predicted heat transfer rate and wall cooling rate become significantly greater than that observed in the data. Despite this, the steam superheat is generally underpredicted. The predicted excess energy transferred to the primary fluid serves to completely vaporize all liquid water on the up hill side of the steam generator tubes resulting in no predicted liquid carryover of entrained liquid drops within the superheated vapor. The liquid drops are predicted to evaporate, either through overpredicted wall to liquid heat transfer or overpredicted interfacial heat transfer. The one exception is the lowest quality run (21806) in which liquid carryover is predicted only after the up hill side tube wall is quenched, thus greatly reducing heat transfer to the primary fluid. The steam is already predicted to be saturated by this time. Although the amount of liquid that was predicted to reach the outer plenum was within 1.5% of that of the experiment, liquid is predicted to reach the outlet plenum after tube wall quenching whereas, in the experiment, although most of the liquid was also transferred after quenching, significant amounts of liquid carryover were observed throughout.

TRACE predicts an advancing liquid film as indicated by an advancing predicted nucleate boiling regime. However the predicted quench front is generally less defined than in the experiment, as indicated by the primary liquid and steam generator tube wall temperature profiles. Given that both the heat transfer and primary side liquid vaporization were both overpredicted, one would expect steam binding during a reactor reflood would also be somewhat overpredicted.

The predicted system pressure was low for all tests, with saturation temperature indicating a pressure offset of approximately 1 atmosphere below experiment.

B.22.8. References

1 R. C. Howard and L. E. Hochreiter, "PWR FLECHT SEASET Steam Generator Separate Effects Task data Analysis and Evaluation Report, NRC/EPRI/Westinghouse Report No. 9," NUREG/CR-1534, Westinghouse Electric Corporation, February 1982

2 L. N. Kmetyk, "RELAP5 Assessment: FLECHT SEASET Steam Generator Test 23402," NUREG/CR- 2887, Sandia National Laboritory, 1982.

3 J. J. Ginoux, Two-Phase Flow and Heat Transfer with Application to Nuclear Reactor Design Problems, Hemisphere Publishing, Washington, 1978.

4 Shawn Marshall, "TRACE Calculation Notebook: FLECHT SEASET STEAM GENERATOR," RES/DRASP/NRCA/CDB, June 2006

B.23. Westinghouse Model Boiler No. 2 (MB2)

Author(s): Shawn O. Marshall, Michael Salay

Affiliation: USNRC-RES/DRASP/NRCA/CDB

Code Version: TRACE V5.0

Platform and Operating System: Intel x86, Windows XP

B.23.1. Introduction

The ability of the TRACE code to simulate the operation of the Westinghouse Model Boiler No. 2 (MB2) is being assessed as part of the comprehensive, generic assessment of TRACE that is currently being conducted by the USNRC's Office of Research. The objective of the MB2 assessment is to evaluate how well the code predicts the response of the MB2 to certain accident transients.

To determine code accuracy, test data from the MB2 test program conducted in 1986 will be used for comparisons. The MB2 is a 0.8% power-scaled model that was designed to be geometrically and thermal-hydraulically similar to the Model F steam generator. In 1986, an MB2 test program was devised to provide test data to improve the analytical methods and promote physical understanding of the PWR steam generator response to certain accident transients.

B.23.2. Test Facility Description

The MB2 test facility is a pressurized water heat supply loop and steam cycle complex that consists of three main systems: primary, secondary, and tertiary, with the attendant process instrumentation and control systems (Ref. 1). Dry saturated steam is generated by the transfer of heat from high-pressure water at 15.51E6 Pa (2250 psia) on the primary side to a steam and water mixture on the secondary side. The primary water enters the inlet side of the channel head, flows through a bundle of U-tubes, and leaves through the exit side of the channel head. Steam formed in the secondary side flows up into a primary separator that removes the water by centrifugal action and returns it to the tube bundle region via a downcomer circuit. The steam, with entrained moisture, then enters the secondary separator where the moisture is removed by a single-tier vane-type separator. The moisture is again returned to the downcomer while dry steam exits the vessel through the outlet nozzle. For steady, constant pressure conditions, the steam is vented from the annular space (dead space) between the wrapper box encasing the tube bundle and the steam generator outer shell. Figure B.23-1 is a schematic of the MB2 that shows the tube bundle

region, wrapper box, key elevations, and secondary side internals. The cross section in the lower right corner of the figure shows the dead space in relation to the rectangular array of tubes.

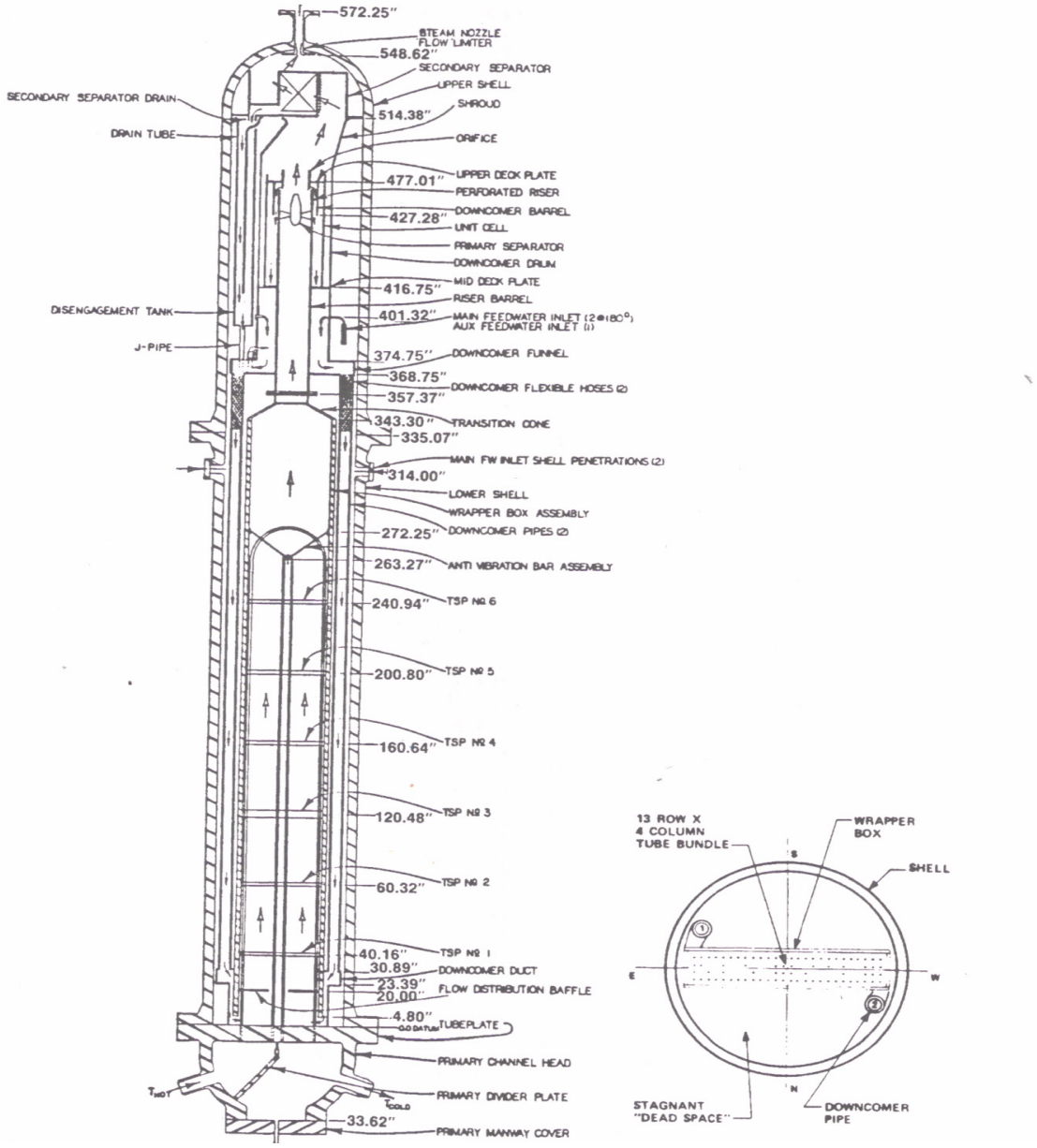

Figure B.23-1. Model Boiler Elevation and Cross Section Through Tube Bundle

The primary or heat supply system is a closed loop pressurized water loop, consisting of a pump, a flow control valve, a 10 MWt natural-gas-fired- heater as the primary heat source, two 3.5 MWt gas-fired heaters used for isothermal or low-power operation, a pressurizer, and a model steam generator as a heat sink. The test loop has a design pressure of 17.2 MPa (2500 psia) and a design temperature of 616.5 K (650 °F).

The tube bundle is composed of 52 tubes arranged in a rectangular array, having 13 tube rows and 4 tube columns. All tubes are fabricated from Inconel 600. They have the same outside diameter of .01746 m (11/16 in) and wall thickness of 1.016E-3 m (.040 in) as the tubes in the Model F and are configured in the same square-pitch array. As a result, the primary and secondary unit cell flow areas for the model and the full-size steam generator are identical.

The secondary system of the facility consists of a model steam generator as the steam supply source, a steam flow system, a condensate system, and a feedwater supply system. The steam leaving the model generator passes through an orifice flow meter, through the shell side of the feedwater heater, and into the condenser, which it leaves as saturated or slightly subcooled water. The temperature of the condensed water is further lowered in the subcooler before the water enters a surge tank. Then the liquid continues to the feedwater pump, which circulates the water through the single-stage feedwater heater and back into the downcomer of the model. Instrumentation was provided to monitor temperature, pressure, and flow rates.

The tertiary loop is the facility's cooling water system. It serves a number of components, to include the condenser, the subcooler, the primary pump, and feedwater pump bearings.

B.23.3. Model Description

The TRACE model of the MB-2 facility consisted of an array of PIPEs, TEEs, VALVEs, BREAKs, and HTSTRs arranged and connected in a manner suitable for replicating the facility's form and function. The components and processes vital to achieving the assessment objective were modeled using the thermal and hydraulic components available in TRACE. Components and processes deemed unessential were either not modeled or were modeled with little detail. Figure B.23-2 shows the MB2 nodalization. All of the nodalized components geometries correspond to the test report specifications. (Ref. 1)

The primary side is modeled with a FILL, three PIPEs and a BREAK. The fill supplies the hot leg injection flow; the three pipes represent the inlet plenum, steam generator tubes, and outlet plenum; and the break maintains the cold leg pressure. The steam generator tube PIPE is a single pipe with the cumulative flow area of 52 pipes but with the hydraulic diameter of a single pipe. On the secondary side, a series of pipes represent the wrapper box, upper and lower downcomers, drains, and the steam dome. TEEs are used to represent the primary and secondary separators, and a check valve is used to regulate the pressure in the steam dome. A FILL connected to the upper downcomer supplies the feedwater flow. In the wrapper box, the tube support plates (TSPs) that stabilize the tube bundle are modeled using K-factors at the cell edges. The wrapper box nodalization was constructed so that the cell edges coincided with the TSP locations.

To account for the heat transfer, heat structures were applied to all of the pipe and tee components. For more detailed modeling, the heat transfer diameters of these structures were also specified.

The final aspect of the modeling was the development of the control system to generate the collapsed water level in the bundle region and to achieve an accurate pressure differential prediction across the TSPs. The differential pressure control systems were needed because of the

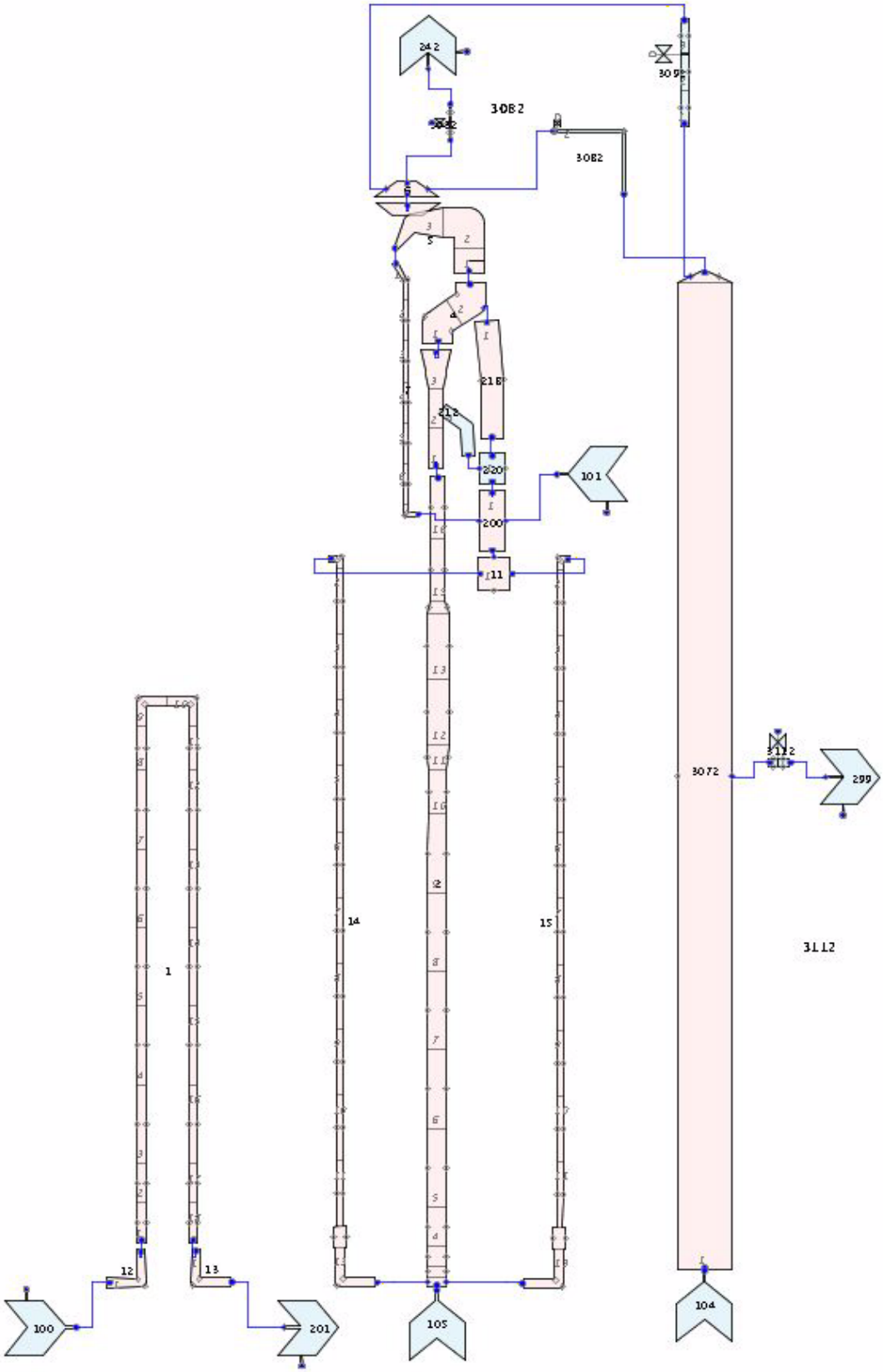

Figure B.23-2. MB2 Nodalization

difference in elevation between the experimental pressure taps and the corresponding cell centers of the TRACE model.

B.23.4. Test 2013 Description

Test 2013 simulated the behavior of the MB2 in response to a 100% steam line break (SLB) under hot standby conditions. In this transient, the MB2 experiences a steam line break and subsequent loss of feedwater flow which causes a complete loss of secondary side liquid inventory. Described below are the steps taken to simulate this transient in the MB2 facility.

To initiate test 2013, steady conditions were maintained in the model boiler while a small amount of steam from the steam dome was allowed to vent through the external moisture separators and piping, heating them up to approximately 372 K (210 °F) to minimize condensation during the transient. Prior to the test, the condensate was drained from the dead space, allowing steam to flow to the void space through the steam dome check valves.

With the boiler operating at steady-state conditions, testing was initiated by commencing data acquisition at t = 0 seconds. At t = 50 seconds, the moisture separator warm-up steam flow was terminated. At t = 60, seconds the transient was initiated by opening a valve located at the top of the MB2 shell. At t = 70 seconds, the auxiliary feed flow was terminated and the model boiler was allowed to boil dry and depressurize to approximately 791 kPa (100 psig). During the blowdown phase, the MB2 dead space was allowed to depressurize in parallel with the MB2 test section to prevent a rupture or collapse of the test section.

B.23.4.1. Code Boundary Conditions and Steady State Predictions

To simulate test 2013 with TRACE, the initial conditions for the primary and secondary components were set at the values of Table B.23.1. The data channels listed provide this information. During the first 60s of the test, these values were monitored to ensure that the initial conditions were being maintained as they should.

Table B.23.1. Test 2013 Steady-State Conditions

	Steady-State Values	
Plant Parameters	**Data Channel**	**TRACE Value**
Hot leg temperature, K (°F)	T-1150	567 (560)
Cold leg pressure, MPa (psia)	P-13	14.143 (2051.3)
Primary mass flow, kg/s (lbm/s)	WF109	41.5 (91.5)
Feedwater flow, kg/s (lbm/s)	WF299	0.115 (0.254)
Feedwater pressure, MPa (psia)	P-299	11.000 (1595.4)

Table B.23.1. Test 2013 Steady-State Conditions

Plant Parameters	Steady-State Values	
	Data Channel	TRACE Value
Feedwater temperature, K (°F)	T-299	309 (96.5)
Secondary pressure, MPa (psia)	P-91	7.591 (1101)

B.23.4.2. Transient Test Initialization

Once steady-state operation had been established, the code was restarted and appropriate boundary conditions were set at the specified times. At t = 60s, the cold leg pressure was set using a break which followed table values that matched those observed in the experiment. This was done because, during the experiment, a reduction in primary pressure was observed that was caused by the rapid cooling of the primary coolant which was brought on by the rapid depressurization of the secondary side. As a result, the gas-fired primary heaters, though ramped up to full power, were unable to provide the required heat to the system to maintain the primary pressure. At t = 60 seconds, the transient was initiated by opening value 3032 in the steam dome pipe component and valve 299 connected to the dead space. Valve 299 was opened to allow the dead space to depressurize along with the internal system. The flow area of valve 3032 was set at 1.35 in, which is the same throat diameter of the flow limiter located at the top of the MB2 steam dome. The break attached to this valve used a table of values that followed experimental pressure readings. At t = 70 seconds, the auxiliary flow rate was reduced as in the experiment by using a table of values in fill component 260.

B.23.4.3. Principal Figure(s) of Merit

The performance of TRACE in simulating the MB2 steam line break is based on how closely its predictions compare with the measurements taken during test 2013. The key parameters of interest were cold leg temperature, primary fluid temperature distribution, break flow, water level, and secondary side differential pressures.

The cold leg predictions demonstrate how well the code calculates the heat transfer from the primary to the secondary side of the MB2. Figure B.23-3 shows the primary side temperature histories during the transient. At the initiation of the transient, the cold leg temperature drops until all of the water in the bundle region boils away. This is shown in Figure B.23-3 with the first temperature decrease in the experimental data, which occurs around 80s into the transient. At approximately 90s, water from the downcomers enter the bundle region and the temperature begins another rapid decrease until a second and final dryout period is reached. At this point, the cold leg temperature begins to rise rapidly. TRACE does not capture the first dryout period, predicts the second dryout period late with substantial water remaining in the bundle region well after 110s. Further evidence of this is shown in Figure B.23-4, which is a figure of the collapsed water level inside the bundle over time. TRACE predicts a significant amount of water flowing from the downcomers and remaining in the bundle region after the data shows complete dryout.

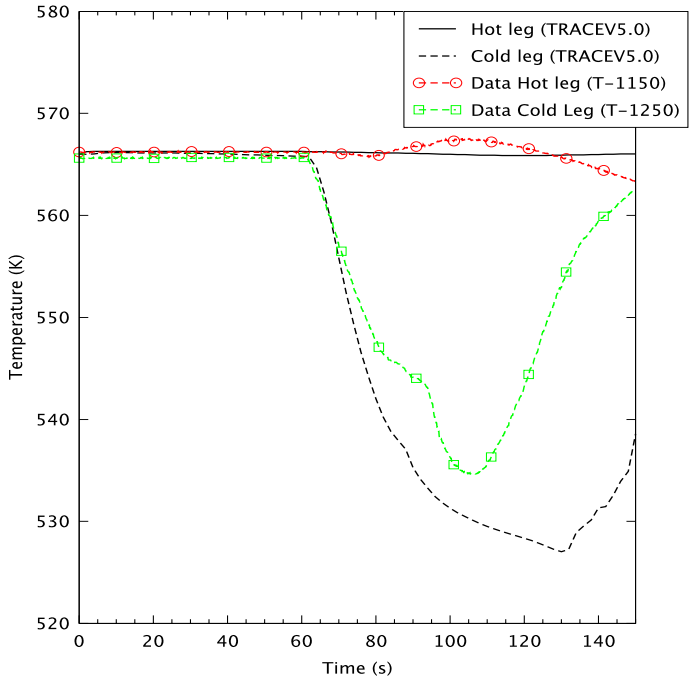

Figure B.23-3. Test 2013 Primary Side Temperatures

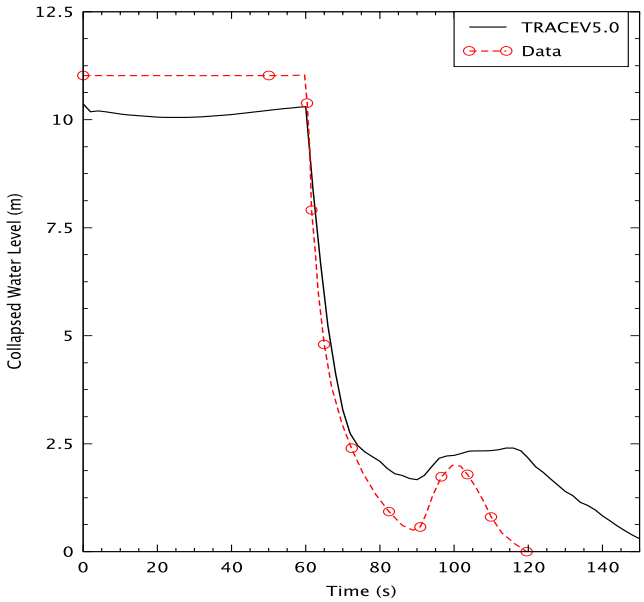

Figure B.23-4. Test 2013 Collapsed Water Level in Bundle Region

Another indication of code heat transfer prediction performance is the primary fluid temperature distribution. Figure B.23-5 shows the temperature distribution in the primary fluid at 100s into the transient. The temperatures along both the hot and cold legs are under-predicted throughout

by as much as 5.5 K (10 °F) with a slight over-prediction of the total temperature difference between the inlet and outlet to the tube bundle. The elevation differences between the measurements and the predictions are due to the differences in the locations of the thermocouples and the cell centers.

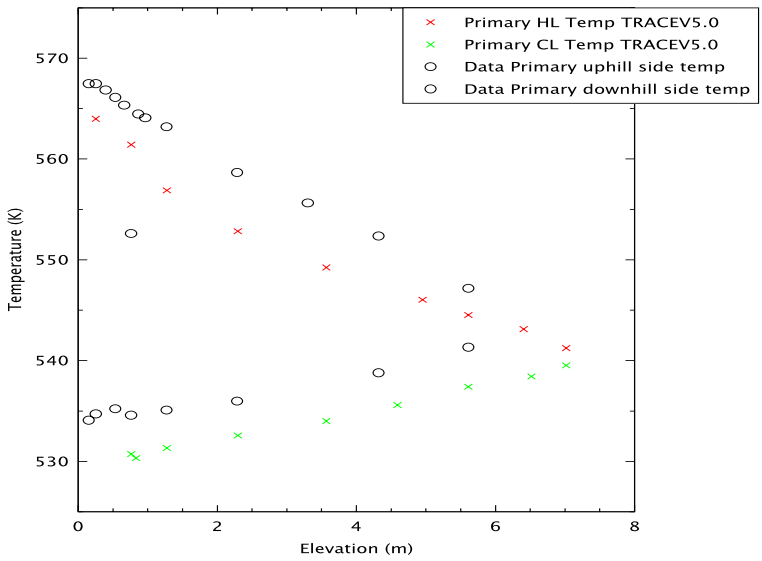

Figure B.23-5. Test 2013 Primary Temperature in U-tubes at 100s

The amount of steam flow exiting the break is shown in Figure B.23-6 This gives an indication of how well the steam-water separation process is being simulated by the code. TRACE over-predicts the steam flow exiting the break throughout the test, peaking significantly higher than the data for the first 20 s following the break, remaining reasonable but high until experimental steam flow begins to decrease with bundle dryout. The peak coincides with an under-prediction of liquid ejected from the break. Therefore more liquid inventory is predicted in the bundle region that in the experiment after the initial peak. Because of this, more liquid water is predicted to be in contact with the bundle than observed in the experiment resulting in more vapor generation and higher steam flow than observed the experiment for the remainder of the test.

Figure B.23-7 shows comparisons in the secondary side collapsed water level in the upper downcomer region, which is an indication of how well the code is predicting mass distribution. TRACE maintains a steady water level during the steady-state portion of the test and predicts the sudden rise in level at the initiation of the transient. Although the TRACE predicted rise is less than that of the spike seen in the experimental curve, the experimental collapsed level exceeds the elevation of the upper pressure tap used to calculate the level, which located at an elevation of 12.243 m (482.0"), and therefore can not be representative of the actual collapsed level during this initial rise. TRACE also predicts a second level rise that does not occur in the experiment.

Figures B.23-8 - B.23-13 show differential pressure comparisons, which are also an indication of how well the code distributes mass. These measurements were taken between pressure taps that were separated by a single tube support plate (TSP). In each figure, the predictions show

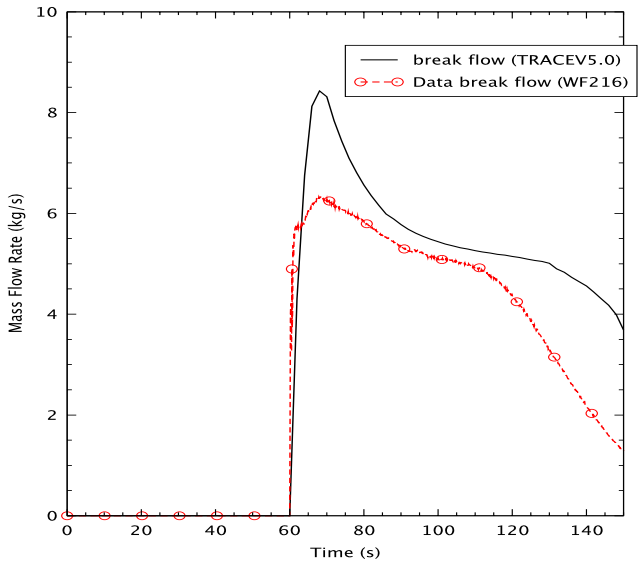

Figure B.23-6. Test 2013 Break Steam Flow

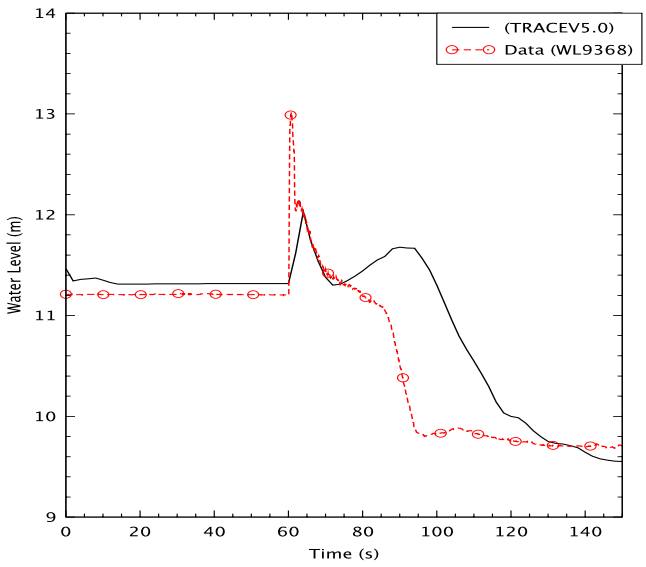

Figure B.23-7. Test 2013 Upper Downcomer Water Level

reasonable agreement with data until the second dryout. After the dryout the predictions overestimate the differential pressure.

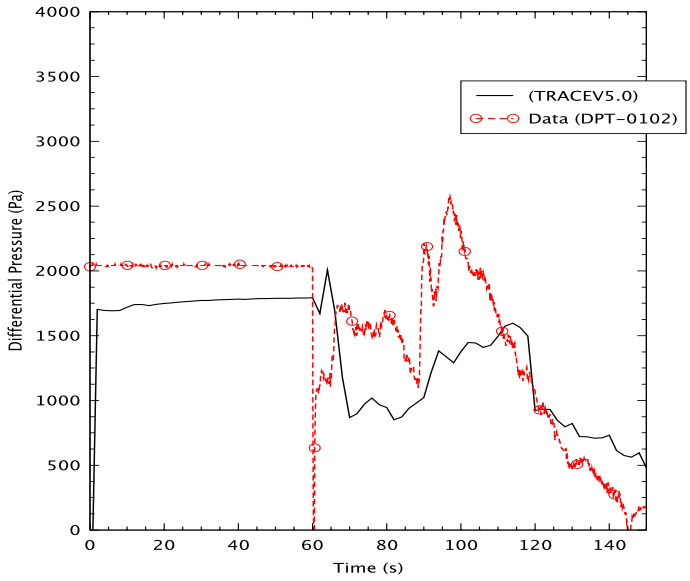

Figure B.23-8. Test 2013 Pressure differential across TSP 1 measured between pressure taps P01 at 43.18 cm (17.00") and P02 at 66.95 cm (26.36")

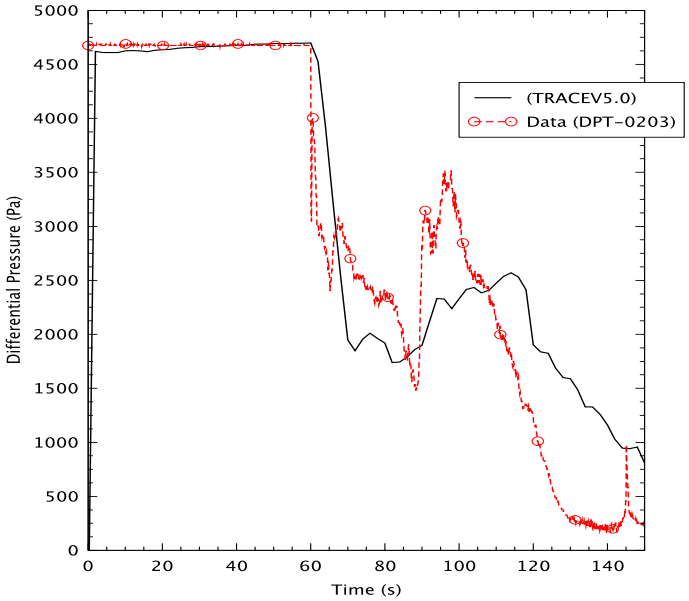

Figure B.23-9. Test 2013 Pressure differential across TSP 2 measured between pressure taps P02 at 66.95 cm (26.36") and P03 at 131.62 cm (51.82")

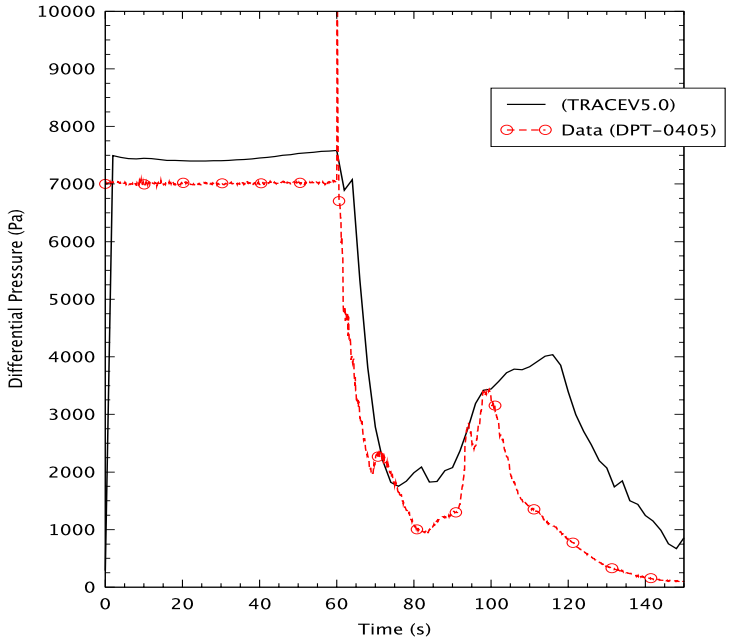

Figure B.23-10. Test 2013 Pressure differential across TSP 5 measured between pressure taps P04 at 493.24 cm (194.19") and P05 at 599.33 cm (235.96")

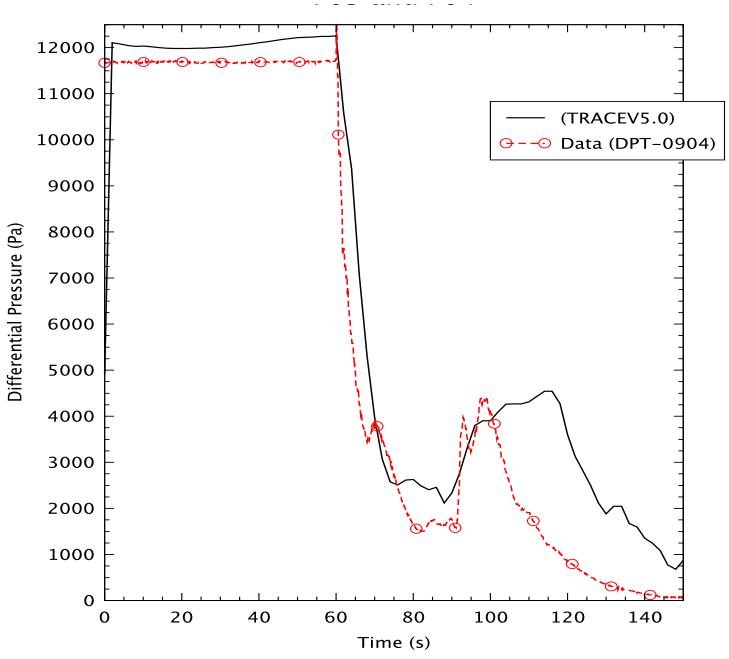

Figure B.23-11. Test 2013 Pressure differential across TSP 4 measured between pressure taps P09 at 322.12 cm (126.82") and P04 at 493.24 cm (194.19")

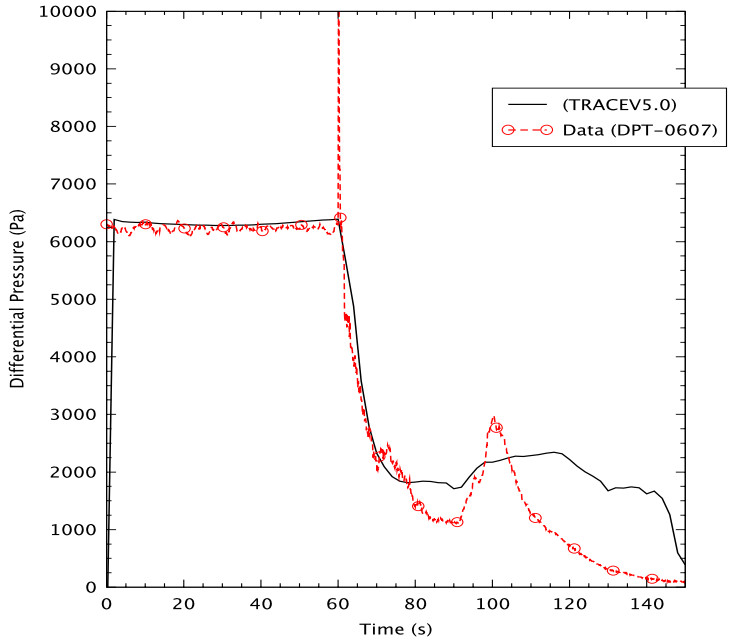

Figure B.23-12. Test 2013 Pressure differential between pressure taps P06 at 637.44 cm (250.96") and P07 at 727.94 cm (286.59")

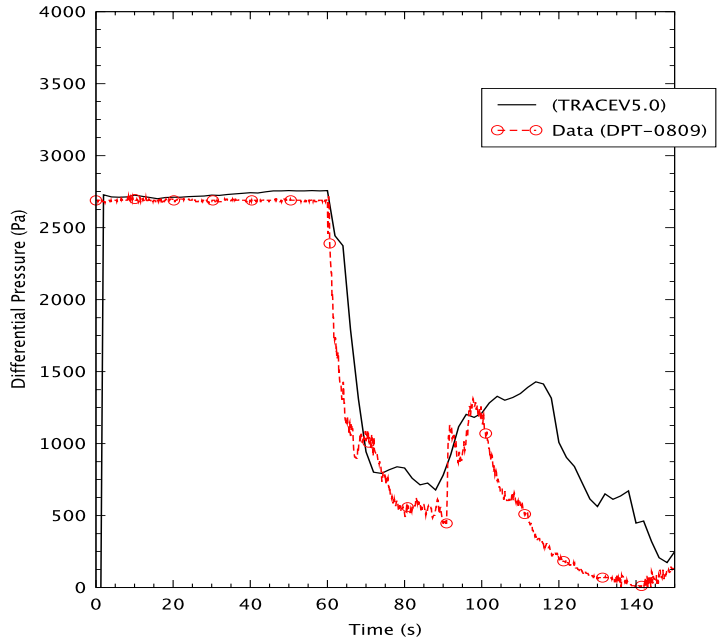

Figure B.23-13. Test 2013 Pressure differential across TSP 3 measured between pressure taps P08 at 284.02 cm (111.82") and P09 at 322.12 cm (126.82")

B.23.4.4. Subsidiary Figures of Merit

In addition to the figures of merit that have been discussed, other areas of the code calculation were evaluated to ensure the reliability of the predictions. These areas include the total heat transfer from the primary side, secondary side pressure, and lower downcomer temperature.

Comparisons of the total bundle heat transfer are shown in Figure B.23-14. After initiation of the transient, the heat transfer from the primary side is rapid and reaches approximately 7.4 MW (7000 Btu/s) before descending in like fashion. The TRACE predictions show continued heat transfer from the primary side to liquid, resulting in an overprediction of void fraction.

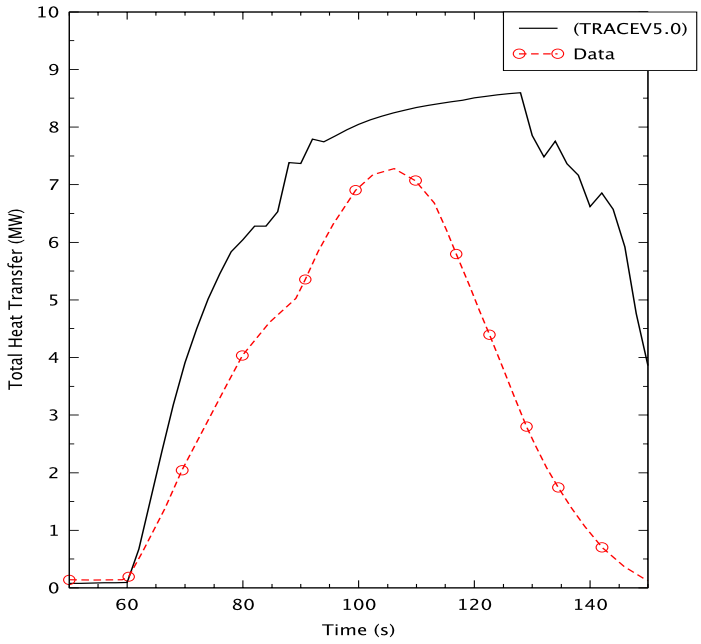

Figure B.23-14. Test 2013 Total Heat Transfer Rate from the Tube Bundle

Figures B.23-15 and B.23-16 show the secondary side pressure and lower downcomer temperature, respectively. These figures reinforce the previous discussions.

B.23.4.5. Sources of Discrepancy

The largest discrepancy between the code predictions and the data is the prediction of excess water in the bundle region by TRACE primarily caused by the underprediction of liquid mass lost through the break. The data shows a very fast two-phase level swell occuring during the first 5 seconds into the transient which results in an almost immediate discharge of predominantly liquid wheras TRACE predicts a break discharge consisting almost exclusively of vapor throughout the test. The liquid fraction in the experimental discharge continuously decreased until a single phase vapor discharge was observed at 93 s, at which time liquid held up in the downcomer flowed into

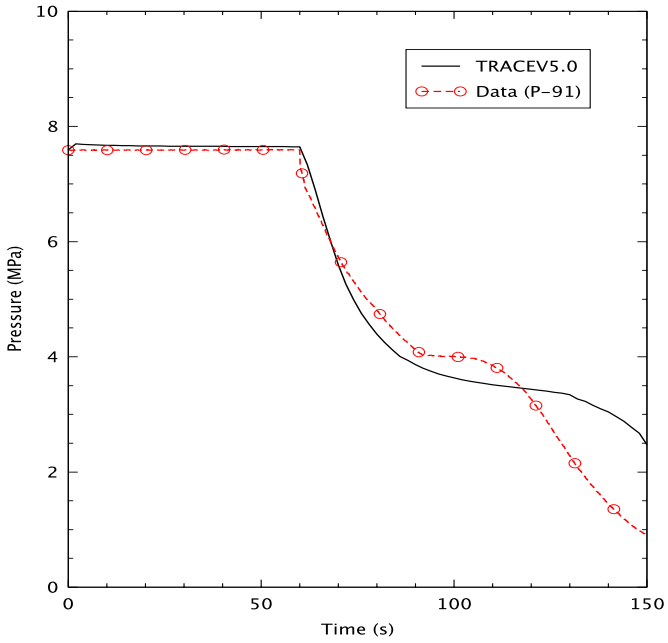

Figure B.23-15. Test 2013 Secondary side Pressure

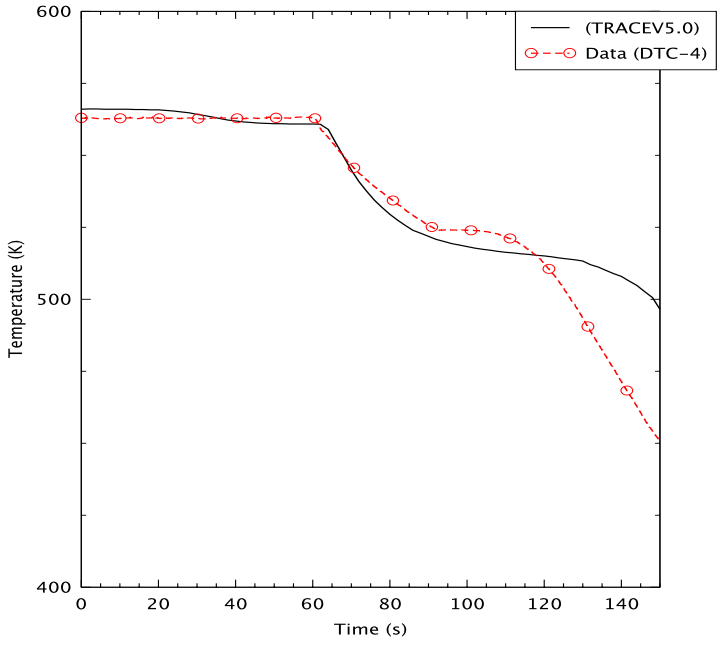

Figure B.23-16. Test 2013 Upper Downcomer Temperature

the bundle region. TRACE significantly underpredicts the liquid lost from the break, predicts less level swell, and the decrease in its prediction of post-surge level is more gradual than the data.

B.23.5. Assessment Results Summary

TRACE V5.0 was used to simulate the response of the MB2 to a SLB from a no-load hot standby state. TRACE underpredicted the liquid mass lost immediately following the break and consequently overpredicted the liquid inventory in the boiler, which leads to some discrepancies in the data comparisons.

B.23.6. References

1 O. J. Mendler, K. K. Takeguchi, M. Y. Young, Loss-of-Feedwater, Steam Generator Tube Rupture, and Steam Line Break Experiments: Steam Generator Transient Response Test Program, NUREG/CR-4751, Westinghouse Electric Corporation, Pittsburgh, PA (1987).

2 F. M. White, *Fluid Mechanics*, 2nd Ed, McGraw-Hill, New York (1986).

3 S. Marshall, TRACE Calculation Notebook, Model Boiler No. 2, (2006).

PWR & BWR Component Tests

B.24. MIT Pressurizer

Author(s): Mark Bolander and Dean Wang

Affiliation: Information Systems Laboratories, Inc.

Code Version: TRACE V5.0

Platform and Operating System: Intel x86, Windows XP

B.24.1. Introduction

A research program involving both experimental and analytical work on pressurized water reactor pressurizers was performed at MIT by Saedi and Griffith (Ref. 1) and Kim and Griffith (Ref. 2).

Several types of tests were performed: insurge of subcooled water into a pressurizer partially full of saturated water, insurge of subcooled water into a hot empty pressurizer, insurge of subcooled water into a partially full pressurizer followed by outsurge, and outsurge when the pressurizer is partially full. Phenomena occurring are: compression or expansion of steam, condensation of steam on the water (free surface) and walls, heating of steam by the walls (during expansion), water flashing and mixing, and thermal stratification in the water.

Two of these tests, ST4 and Insurge-Outsurge, are simulated with TRACE. Test ST4 was an insurge only test and Insurge-Outsurge forced water into the bottom of the pressurizer and then sucked it back out. The purpose of the assessment was to verify the code's ability to predict pressure response where the wall and interfacial condensation and flashing effects and thermal stratification in the water are important.

B.24.2. Test Facility Description

The MIT pressurizer experimental apparatus is shown schematically in Figure B.24-1. It consisted of two cylindrical steel tanks: the primary tank (pressurizer) and the storage tank. The pressurizer was a stainless steel tank 1.143 m (3.75 ft.) tall with an ID of 0.203 m (8 in) and a wall thickness of 0.0095 m (0.374 in). The pressurizer had six windows and was equipped with six immersion heaters with a power of 9kW. The storage tank was pressurized with nitrogen to force the liquid into the pressurizer. The pressurizer was insulated to diminish energy losses. Calibration tests were used to estimate the losses at 1.1kW. A more detailed description of the test facility is given in Reference 3.

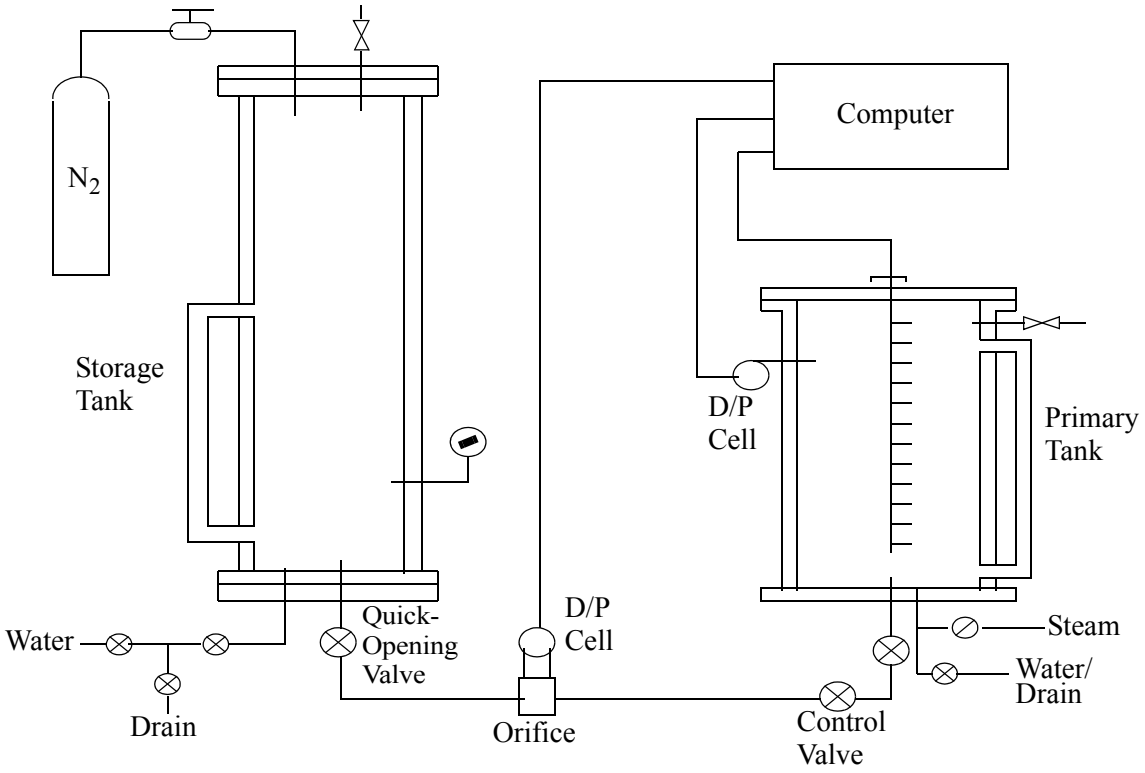

Figure B.24-1. Schematic of the Experimental Apparatus for the MIT Pressurizer Test.

The tests were initiated by opening two quick-opening valves which resulted in the insurge of subcooled water into the bottom of the pressurizer. During the tests the insurge of subcooled water was terminated and the pressurizer allowed to come to equilibrium or the water was drained out of the pressurizer through the bottom water/drain connection (see Figure B.24-1).

Pressure measurements were taken at the top of the pressurizer. Thermocouples were placed along the pressurizer centerline to measure fluid temperatures and along the outside wall to measure steel temperatures.

Phenomena occurring during the tests are: compression or expansion of steam, condensation of steam on the water (free surface) and walls, heating of steam by the walls (during expansion), water flashing and mixing, and thermal stratification in the water.

B.24.3. TRACE Model Description

The TRACE input model of the MIT pressurizer apparatus included five components. A vertically oriented PIPE component with ten nodes represented the pressurizer. A FILL component was attached to the bottom of the PIPE to set the flow and fluid temperature conditions during the simulations. A HTSTR component was used to simulate the pressurizer wall and insulation surrounding the pressurizer. A PIPE component was used to represent the surrounding

environment. Finally, a FILL component was attached to the environment PIPE to set the conditions outside of the pressurizer. A nodalization diagram of the TRACE model is shown in Figure B.24-2.

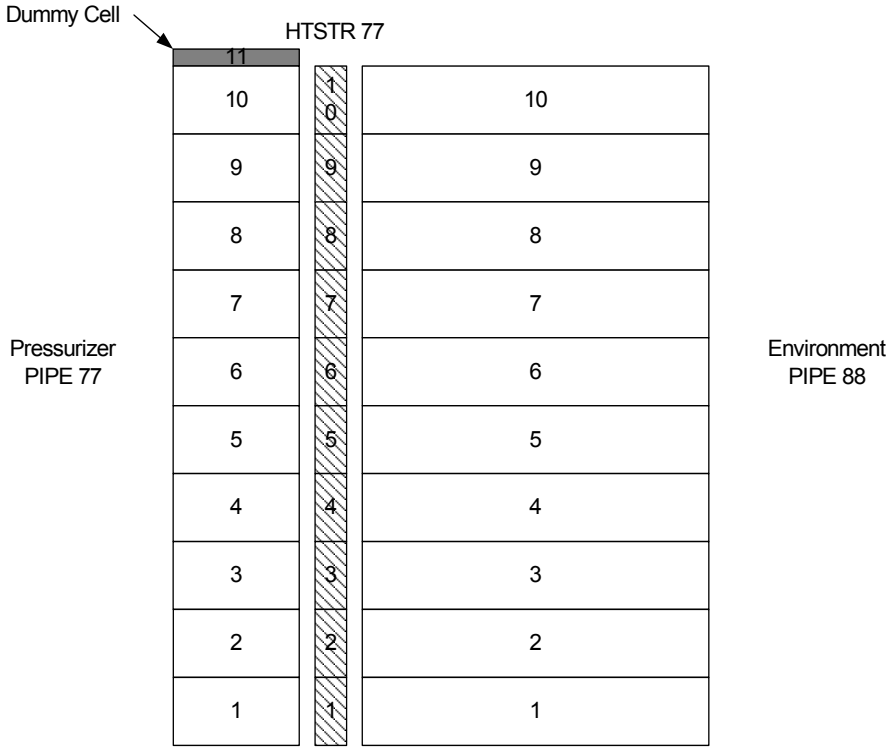

Figure B.24-2. TRACE Nodalization of the MIT Pressurizer.

It is found that the previous 10-cell model has a poor prediction of the pressure with TRACE. So the pressurizer is remodeled using 11 fluid cells in PIPE 77 in which the top cell (Cell 11) is an additional dummy cell with very small cell length and volume. It is expected a more accurate prediction could be obtained with more cells, however, models of reactor pressurizers usually have less than 10 cells.

The level tracking option was turned on for the simulation of Test ST4 (insurge). The level tracking option was also turned on for the Insurge-Outsurge test simulation. However, preliminary results showed un-physical behavior relating to the flashing interfacial heat transfer as the liquid level crossed into Cell 9 during the insurge portion of the transient. Thus the level tracking option for the Insurge-Outsurge test was turned off.

The vessel was insulated to diminish energy losses. Calibration tests were used to estimate the losses at 1.1 kW (Ref. 2). The experimenters did not report on the type and thickness of the insulation covering the vessel. The code model used 8.9 cm (3.5 in) of fiber glass insulation. Ten nodes were used in the steel and five in the insulation. Steady state calculations were performed to adjust the insulation conductivity so the steady state heat loss agreed with the reported value of 1.1 kW.

A detailed description of the input model is given in Reference 5.

B.24.4. Tests Simulated with TRACE

Flow insurge Test ST4 (Ref. 3) was an insurge only experiment while Insurge-Outsurge (Ref. 4) forced water into the bottom of the pressurizer and then allowed it to flow back out. Water was subcooled by 130 K (234 ^{o}F) in ST4 and 140 K (252 ^{o}F) in the Insurge-Outsurge test. The stainless steel vessel was initially partially filled with saturated water at a pressure of 0.49 MPa (71.1 psia) in Test ST4 and 0.7 MPa (101.5 psia) in the Insurge-Outsurge test.

The initial water levels in the pressurizer were 0.4318 m (1.42 ft.) for Test ST4 and 0.5207 m (1.72 ft.) for Test Insurge-Outsurge.

Water injection into the bottom of the vessel varied over the first 40.6 seconds during Test ST4 at which time it was stopped. The injection rate translated into a vessel water level rise rate of about 1 cm/s (0.3937 in/s). Water injection into the bottom of the pressurizer began at about 14 seconds for Test Insurge-Outsurge. At about 64.5 seconds the injection into the pressurizer was terminated and fluid was sucked out of the pressurizer over the next seconds. The injection rate for Test Insurge-Outsurge translated into an average pressurizer water level rise and fall rate of about 0.9 cm/s (0.3543 in/s). Injected flow rates for both tests are shown in Figure B.24-3.

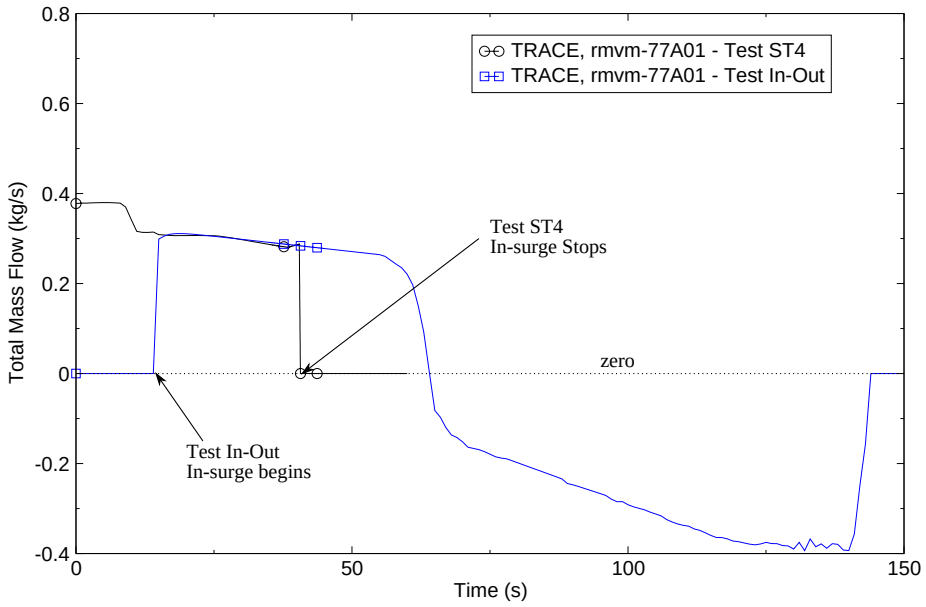

Figure B.24-3. Liquid Injection Rates.

The vessel was insulated to diminish energy losses. Calibration tests were used to estimate the losses at 1.1 kW (Ref. 2).

There is no electronic data file for these experiments. Data reported here comes from digitizing figures in the referenced reports.

B.24.4.1. Simulation of Test ST4.

The water level in the pressurizer was initially in cell 4 (the void fraction was 0.22) and reached its maximum value in cell 8 (the void fraction was 0.69).

Steam in the upper part of the vessel was compressed as the water level rose. As the saturation temperature rose, the vessel walls became subcooled and film condensation occurred. The condensate ran down the walls to meet a rising water level. A balance between interfacial and wall steam condensation and steam compression determined the pressure response.

The measured pressure in the top of the vessel peaked at about 0.59 MPa (85.57 psia) as shown in Figure B.24-4. After the subcooled water insurge stopped, the pressure fell due to further steam condensation. The complex physical processes occurring are: wall heat transfer, steam-water interfacial heat transfer, and thermal mixing between the cold and hot water.

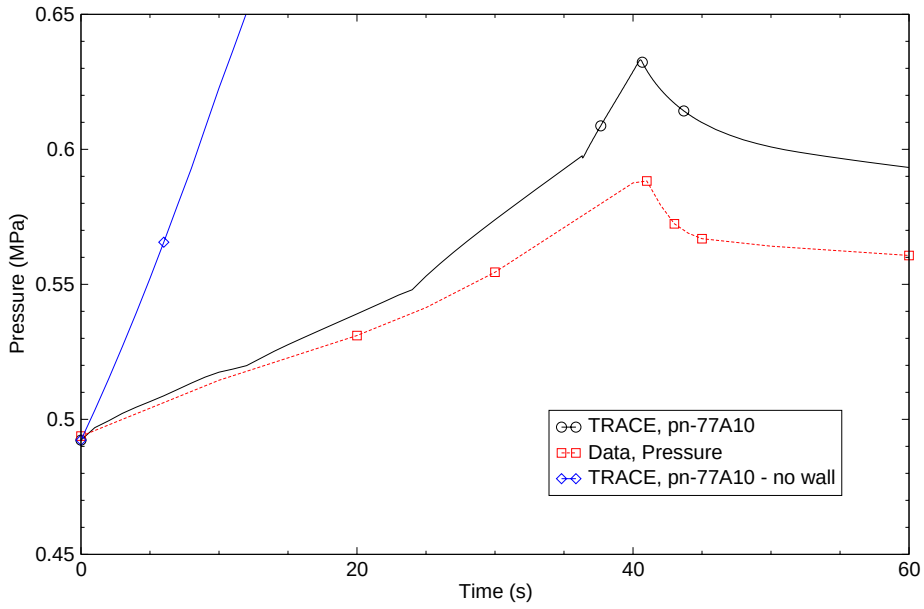

Figure B.24-4. Test ST4 Pressure Prediction.

TRACE shows excellent agreement with the measured data during the steam compression period. However, after the insurge stopped, TRACE predicted less condensation and the pressure was over-predicted.

The dominant factor in controlling the pressure is the wall heat transfer rather than the interfacial heat transfer. A sensitivity calculation was made with no wall heat transfer. The predicted pressure response is shown in Figure B.24-4. Without wall heat transfer the predicted pressure increased more rapidly and peaked at about 1.4 MPa (203.1 psia).

The change in the slope of the predicted pressure response (see Figure B.24-4 at approximately 12, 24, and 36 seconds) was caused when the liquid level crossed a cell boundary. It is shown in Figure B.24-5 and Figure B.24-6 that when the liquid level crosses over the cell boundary, the HTC regime predicted by TRACE changes from 7 (convection to two-phase mixture) to 8 (reference is not available), and stays there for a very short time. Then it comes down to 1 (forced convention to single-phase liquid). However, after the water level enters a cell the heat transfer coefficient should be between wall condensation and liquid convection since both mechanisms influence the heat transfer rate. Shutting off wall condensation when the water level reached cell 8 caused the noticeable pressure increase change at 36 seconds in Figure B.24-4

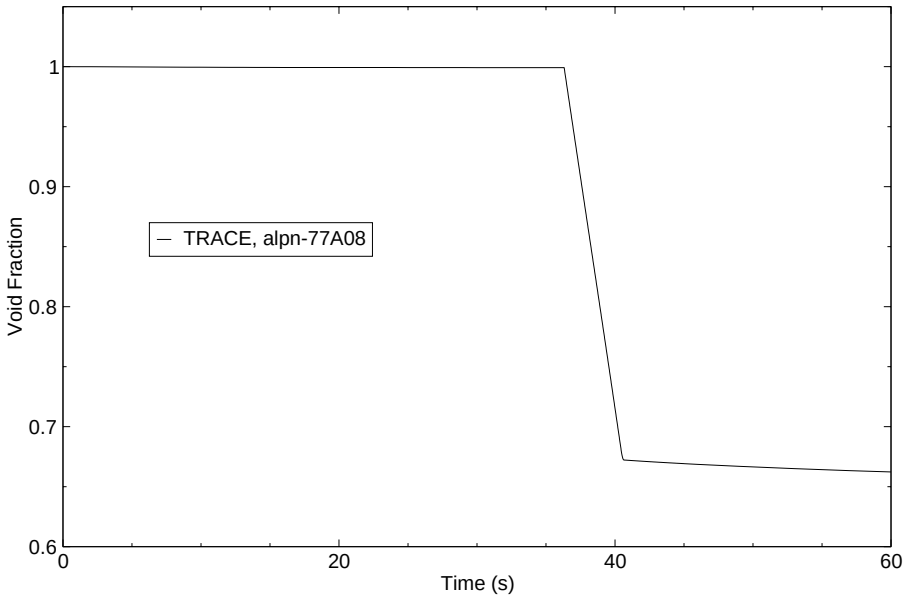

Figure B.24-5. Void Fraction in Cell 8 - Test ST4.

Figure B.24-7 shows the predicted inside wall vapor heat transfer coefficient in the top cell (cell 10). After 5 seconds, TRACE predictions show no heat is transferred directly through vapor.

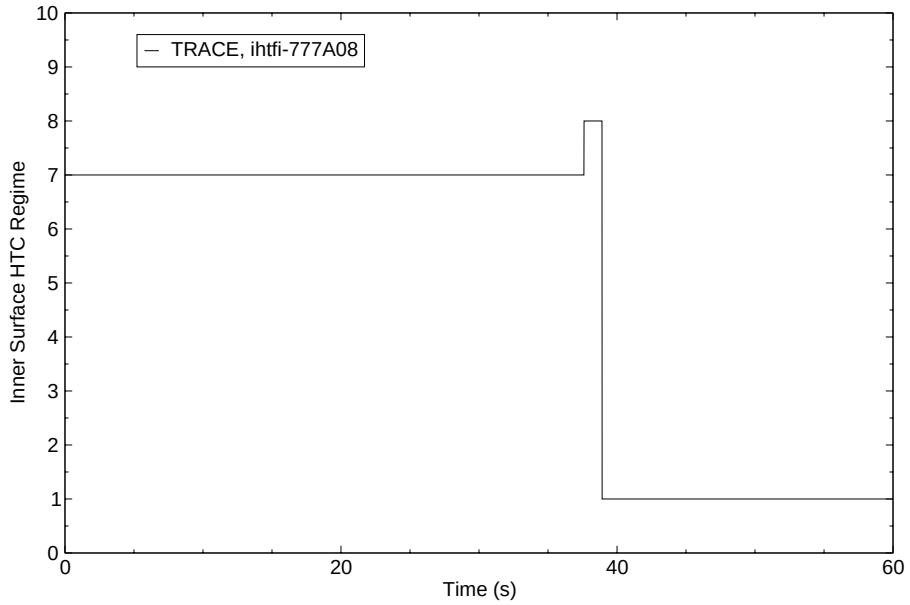

Figure B.24-6. Inner Surface Heat Transfer Coefficient Regime for Cell 8 - Test ST4

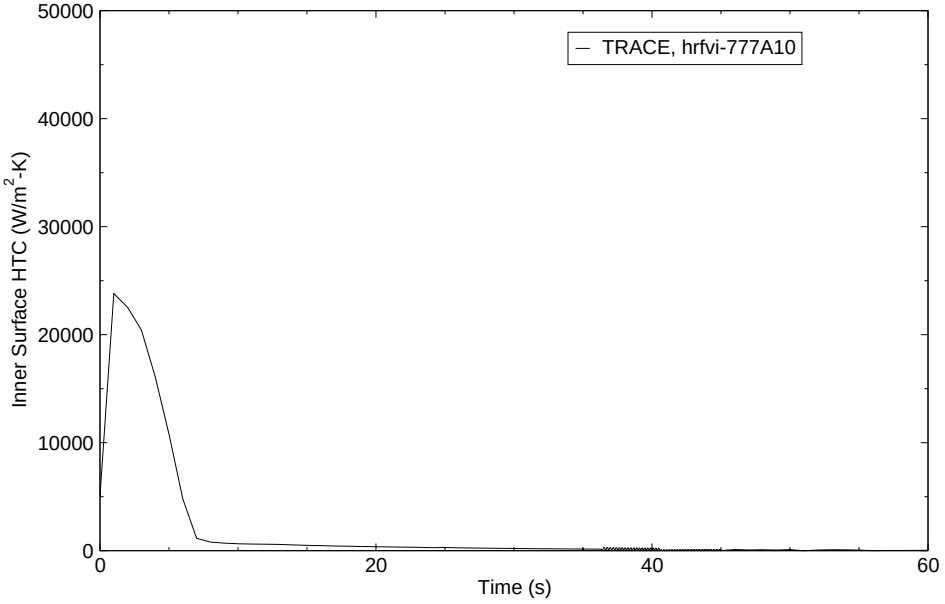

Figure B.24-7. Inner Surface Vapor Heat Transfer Coefficient in Cell 10 - Test ST4.

The axial fluid temperature profiles are compared in Figure B.24-8. Numerical diffusion caused the thermal gradient to be more smeared than shown by the data.

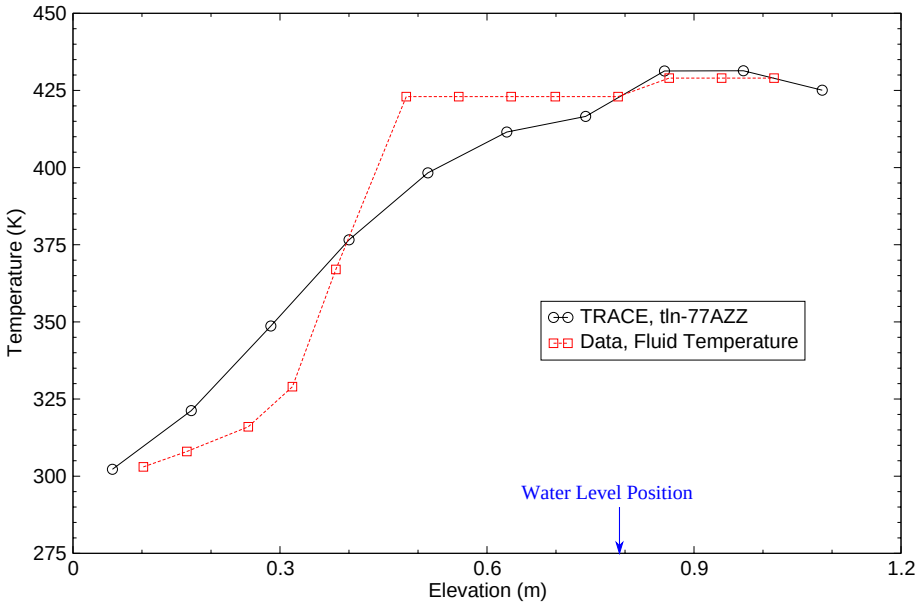

Figure B.24-8. Axial Fluid Temperature Profile at 35 s - Test ST4.

Sensitivity calculations were performed to study the effect of cell nodalization on the predicted results. The number of axial cells used in PIPE components 77 and 88 and HTSTR 777 were increased from 10 to 20 and from 20 to 40, and both with an additional dummy cell on the top. Figure B.24-9 shows the predicted pressure in the top of the pressurizer for the 10, 20, and 40 cell nodalization compared to data. Generally, the finer the nodalization resulted in better pressure predictions. Figure B.24-10 and Figure B.24-11 show the predicted axial inside wall temperature and fluid temperature compared to data at 35 seconds respectively. The finer nodalization did a better job in predicting the wall temperature and the fluid temperature.

In the past users have modeled pressurizer with ten cells or less. Based on the prediction of Test ST4 ten cells appears to be a reasonable number to capture pressurizer insurge behavior with an additional dummy cell on the top.

B.24.4.2. Simulation of Test Insurge-Outsurge.

The water level in the pressurizer was initially in cell 5 (the void fraction was 0.445) and reached its maximum value in cell 9 (the void fraction was 0.79).

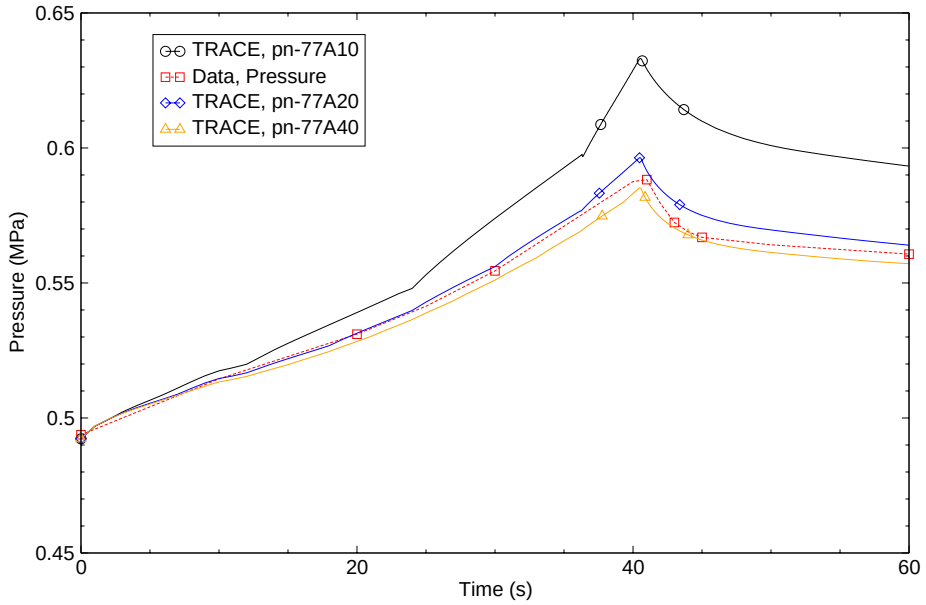

Figure B.24-9. Test ST4 Pressure Prediction for Cell Nodalization Sensitivity Study.

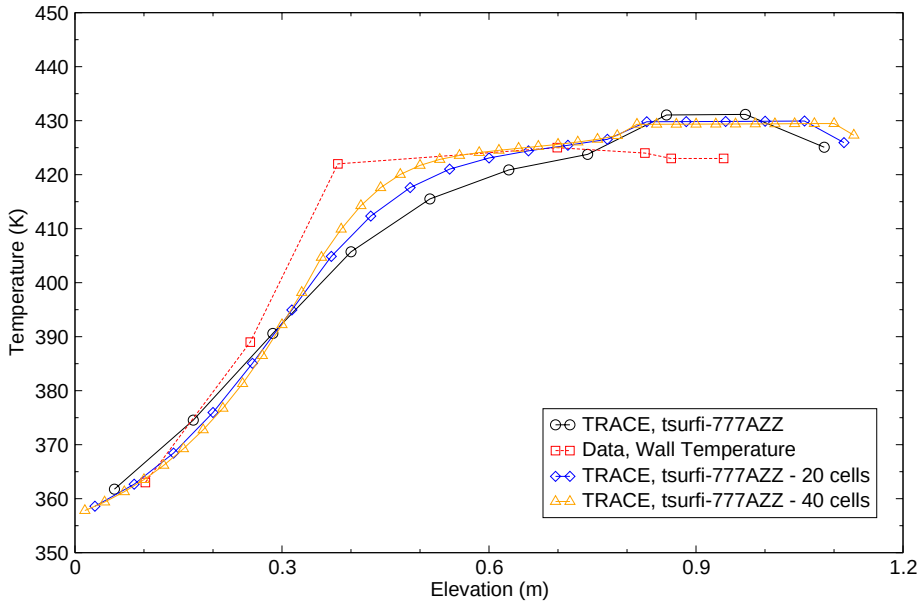

Figure B.24-10. Axial Wall Temperature Profile at 35 s for Cell Nodalization Sensitivity Study

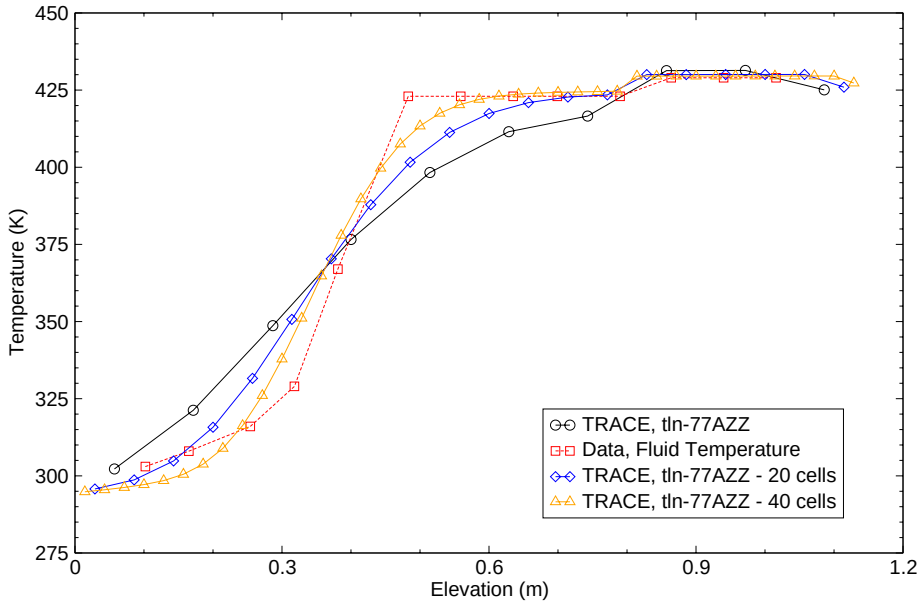

Figure B.24-11. Axial Fluid Temperature Profile at 35 s for the Cell Nodalization Sensitivity Study.

Inlet flow was zero for about 14.5 seconds, positive until 64.5 seconds, negative until 143.8 seconds and then zero as shown in Figure B.24-3.

The pressure change in the top cell is compared to data in Figure B.24-12. Unlike Test ST4, there was not quite enough condensation predicted during the insurge period and the peak pressure was over predicted. The predicted depressurization rate was larger than the experimental rate during the first part of the outsurge. By about 80 seconds, TRACE was transferring wall energy back to the steam and the rate of depressurization slowed down just as occurred in the experiment. However, the transfer of energy from the wall back into the fluid was not as large as indicated by the data and the pressure declined at a faster rate. When the outsurge stopped at 143.8 seconds, the prediction showed a reduction in the depressurization rate similar to the data. The noticeable change in pressure response during the insurge and outsurge periods are caused by the liquid level crossing a cell boundary similar to the prediction for Test ST4.

A noding sensitivity study was done to see if the outsurge part of the transient could be more accurately predicted. Fifty cells were used in the study. The level tracking option was activated, but resulted in a code failure due to water property errors during the outsurge portion of the transient. Therefore level tracking was turned off.

Figure B.24-13 compares the pressurizer pressure response using a fifty celled model with the ten celled model and data. The pressure response, during the insurge portion, using the fifty cell model showed similar behavior observed in the noding sensitivity done for the ST4 simulation,

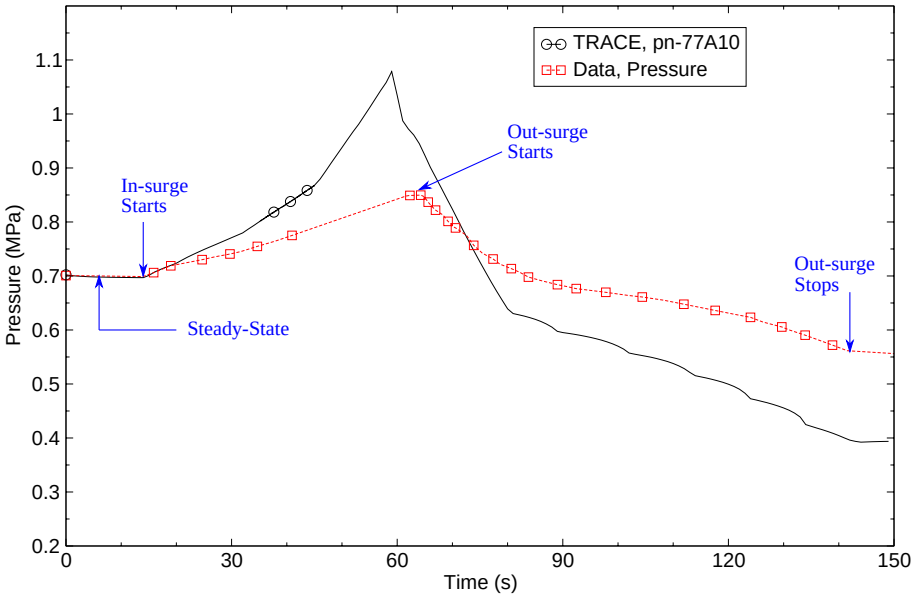

Figure B.24-12. Insurge-Outsurge Pressure Comparison.

i.e. the finer mesh cells allowed condensation to occur over a longer period of time for a given distance (one coarse cell versus five fine mesh cells).

The pressure response during the outsurge portion of the transient using the fifty celled model is more reasonable compared to data than the pressure response using the ten celled model. Numerical diffusion during the insurge portion of the transient resulted in a higher fluid temperature in the fifty celled case for a given coarse mesh cell as shown in Figure B.24-14 (The bottom cell edge of cell 36 of the fifty celled model is the same elevation as the bottom cell edge of cell 8 in the ten celled model. The combination of cells 36, 37, 38, 39, and 40 of the fifty celled model is equivalent to cell 8 of the ten celled model). As a result, during the outsurge portion, when the system was depressurizing a combination of wall energy transfer back to the fluid and fluid flashing resulted in keeping the pressure up higher in the fifty celled model.

B.24.4.3. Figure of Merit

Peak pressure and the pressure at the end of the transient were chosen to illustrate how well the code predicts the measured data. Peak pressure occurred at the time the liquid insurge flow ended. A comparison of the peak pressure tell how good the code performs in calculating the compression of the steam during insurge and the condensation of steam on the rising water surface and vessel walls. A comparison of the end time pressure indicates how well the code performs in calculating the cooling of the steam after the insurge (Test ST-4) or steam expansion and heating of the steam from the hot walls during the outsurge period (Test In-Out). Figure B.24-

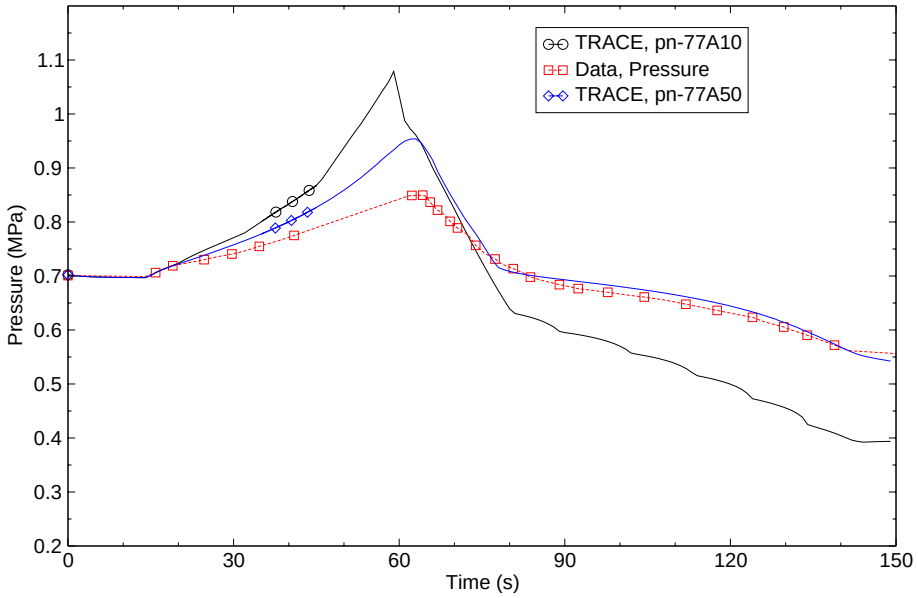

Figure B.24-13. Insurge-Outsurge Pressure Comparison using 50-celled model.

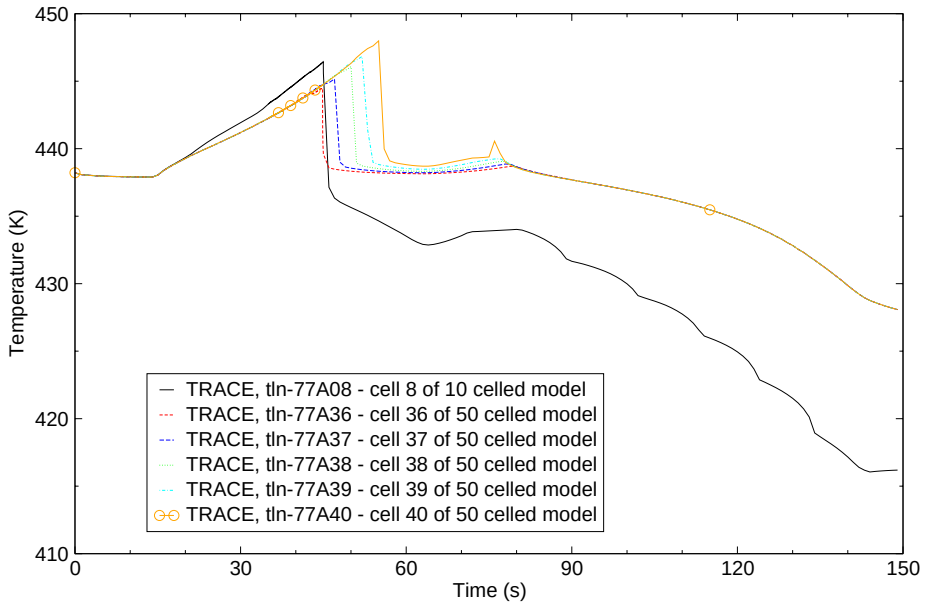

Figure B.24-14. Comparison of Fluid Temperature in Cell 8 of the Coarse Node Model and Cells 36, 37, 38, 39, and 40 of the Fine Node Model.

15 shows the measured versus calculated peak pressure as well as the measured versus calculated end time pressure for Tests ST-4 and In-Out. The code simulation of Test ST-4 did reasonably well calculating the peak and end time pressures. The code prediction of Test In-Out did not perform as well. Improvements are noted when the input model was expanded from 10 cells to 50 cells, especially calculating the pressure during the outsurge portion of the transient.

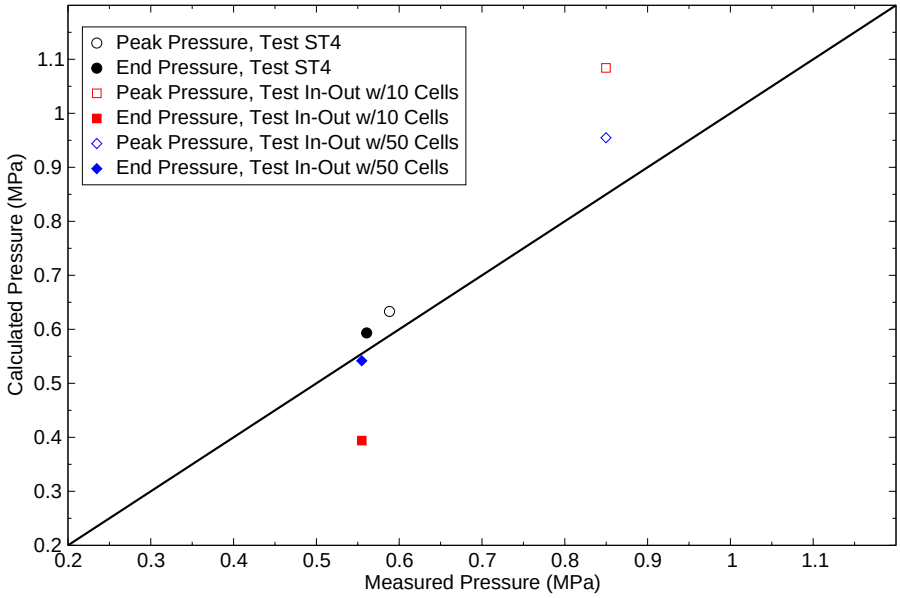

Figure B.24-15. Measured Versus Calculated Peak and End Time Pressures for the Simulation of Tests ST-4 and In-Out.

B.24.5. Assessment Results Summary

TRACE predicted the MIT pressurizer pressure response reasonably well for Test ST4 with an additional dummy added on the top.

Noding sensitivity studies showed that changing the number of cells from 10 to 20 and 40 improved the pressure response. The predicted axial wall and fluid temperature response was improved with the finer noded models. Based on the prediction of Test ST4 at least twenty cells are needed to capture pressurizer insurge behavior.

The base TRACE prediction of the Insurge-Outsurge test was not as good as the prediction of Test ST4. The prediction was improved when fifty cells were used. When the level tracking problems that cause code failure are corrected, this assessment will be rerun to determine whether pressure predictions are improved during the outsurge.

B.24.6. References

1 H. R. Saedi, and P. Griffith, “The Pressure Response of a PWR Pressurizer During an Insurge Transient,” Transactions of ANS, 1983 Annual Meeting, Detroit, Michigan, June 12-16, pp. 606-607.

2 S. N. Kim, and P. Griffith, “PWR Pressurizer Modeling”, *Nuclear Engineering and Design 102*, 1987, pp. 199-209.

3 H. R. Saedi, "Insurge Pressure Response and Heat Transfer for PWR Pressurizer", Partial Fulfillment of the Requirements for the Degree of Master of Science in Mechanical Engineering at the Massachusetts Institute of Technology, November 1982.

4 S. Kim, "Experimental and Analytical Model of a PWR Pressurizer During Transients", Submitted to the Department of Nuclear Engineering in Partial Fulfillment of the Requirements for the Degree of Doctor of Philosophy at the Massachusetts Institute of Technology, February 1984.

5 M. Bolander, "TRACE Calculation Notebook - MIT Pressurizer", February 2006.